

12th Carolus Magnus Summer School on Plasma and Fusion Energy Physics

Leuven (Belgium), August 24 – September 4 2015

Editor: Kristel Crombé (Scientific Secretary CMSS 2015)



Energie & Umwelt /
Energy & Environment
Band / Volume 298
ISBN 978-3-95806-107-1

 **JÜLICH**
FORSCHUNGSZENTRUM

Forschungszentrum Jülich GmbH
Institute of Energy and Climate Research
Plasma Physics IEK-4

12th Carolus Magnus Summer School on Plasma and Fusion Energy Physics

Leuven (Belgium), August 24 – September 4 2015

Editor: Kristel Crombé (Scientific Secretary CMSS 2015)

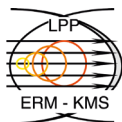
Schriften des Forschungszentrums Jülich
Reihe Energie & Umwelt / Energy & Environment

Band / Volume 298

ISSN 1866-1793

ISBN 978-3-95806-107-1

Bibliographic information published by the Deutsche Nationalbibliothek. The Deutsche Nationalbibliothek lists this publication in the Deutsche Nationalbibliografie; detailed bibliographic data are available in the Internet at <http://dnb.d-nb.de>.



Publisher and
Distributor: Forschungszentrum Jülich GmbH
Zentralbibliothek
52425 Jülich
Tel: +49 2461 61-5368
Fax: +49 2461 61-6103
Email: zb-publikation@fz-juelich.de
www.fz-juelich.de/zb

Cover Design: Grafische Medien, Forschungszentrum Jülich GmbH

Printer: Grafische Medien, Forschungszentrum Jülich GmbH

Copyright: Forschungszentrum Jülich 2015

Schriften des Forschungszentrums Jülich
Reihe Energie & Umwelt / Energy & Environment, Band / Volume 298

ISSN 1866-1793
ISBN 978-3-95806-107-1

The complete volume is freely available on the Internet on the Jülicher Open Access Server (JuSER) at www.fz-juelich.de/zb/openaccess.

Neither this book nor any part of it may be reproduced or transmitted in any form or by any means, electronic or mechanical, including photocopying, microfilming, and recording, or by any information storage and retrieval system, without permission in writing from the publisher.

**Proceedings of the
12th Carolus Magnus Summer School
on Plasma and Fusion Energy Physics**

Preface

The 12th edition of the Carolus Magnus Summer School on Plasma and Fusion Energy Physics is hosted by the Katholieke Universiteit Leuven. The Carolus Magnus Summer School has been organised once every 2 years since 1993. It is a joint initiative of the Laboratory for Plasma Physics of the Royal Military Academy in Brussels (Belgium), the Belgian Nuclear Research Centre (SCK/CEN) in Mol (Belgium), the Dutch Institute for Fundamental Energy Research (DIFFER) in Eindhoven (The Netherlands) and the Institute of Energy and Climate Research (IEK-4) of the Forschungszentrum Jülich (Germany). All institutes are members of the EUROfusion Consortium. For the 12th CMSS edition, the Centre for mathematical Plasma-Astrophysics (CmPA) of the KU Leuven joined the team. KU Leuven is the oldest university in the Low Countries. It is internationally renowned for the high quality of its alumni, and ranks among the top 10 European universities in terms of its scholarly output.

The summer school aims at graduate and postgraduate students active in or becoming active in controlled thermonuclear fusion, a field of research striving to offer an alternative base load energy “production” method that can - if political will and scientific endeavor are side by side - become available when both fossil and nuclear fission fuels will either be depleted or their consumption drastically reduced on ecological grounds. Whereas peaceful use of fission was demonstrated more than half a century ago, controlled fusion has proven to be a much more demanding challenge on the experimental, engineering as well as theoretical fronts. Many insights have matured over the last decades but there are still various open questions. Whereas the present generation of researchers paves the path towards fusion by building ITER in Cadarache (France) - “iter” is the latin word for “the way” - and making sure the underlying physics is sufficiently well understood to take this next step, it is the young generation of researchers that is presently trained that will ultimately prove or disprove to the world that fusion exploitation claims made decades ago were indeed justified or merely were overly optimistic predictions based on too shallow insight of a demanding research field, requiring simultaneous knowledge of a wide variety of topics such as magneto-hydrodynamics, plasma physics, quantum physics, relativity, solid state physics, cryogenics and chemistry.

Well over 70 CMSS12 participants attend courses on the physics governing the behavior of plasmas in experimental thermonuclear fusion devices. As in the previous summer schools of this type, the accent is on machines relying on magnetic confinement of the highly energetic particles that spontaneous fusion requires. The scope of the Carolus Magnus schools is purposely rather wide: The treated subjects range from basic principles of magnetic confinement, heating, equilibrium and instabilities, classical and neoclassical transport as well as fundamental kinetic theory to leading-edge and occasionally far from fully understood fusion physics topics such as anomalous transport and transport barriers. Aside from describing the actual processes in the plasma, various speakers also explain how the dynamics of the hot plasma medium can be diagnosed. And the closer we get to a burning plasma, the more aspects such as neutron protection, neutron diagnostics and the development of proper materials allowing to contain the fusion furnace need to come to the foreground. Since 2011, the Joint European Torus (JET) - a machine of the tokamak type and the flagship of the European fusion efforts - has metallic rather than carbon walls. Lacking the proper tools a few decades ago, allowing to reach fusion relevant temperatures temporarily required giving up high Z wall materials and gave rise to a generation of experimental devices with low Z and quickly eroding plasma facing materials. But unless fundamentally new insights are gained in the coming years, fusion machines necessarily need to have metallic walls. The solution that was chosen for ITER (Beryllium vessel walls and a Tungsten divertor) is presently being tested in JET and so far no major obstacles have been encountered.

JET may be the biggest and the only machine to be fully capable to handle tritium by having sophisticated remote handling robotics that allow manipulating components of an activated machine, it is not the only European experimental device, nor is the tokamak necessarily the machine that has the highest probability to become a fusion reactor. The EUROfusion Consortium supports various other machines. Wendelstein 7-X, for example, explores the potential of stellarators as fusion machines. CMSS12 aims at discussing the broad scope of theoretical as well as experimental tools presently thought to have the potential of helping making fusion a reality.

To optimally transfer knowledge to the new generation, the school has always had a large number of lecturers, each of whom speaking about their own field of interest and specialization. Most of the speakers are from one of the organizing institutes, but subjects falling outside the main focus of the organizing institutes are taught by specialists from other European laboratories. With pleasure, the efforts of internal as well as external lecturers are gratefully acknowledged.

Many of the papers appearing in this volume are reprinted, with minor revisions in some cases, by permission of the American Nuclear Society, Transactions of Fusion Science and Technology, Tenth Carolus Magnus Summer School on Plasma and Fusion Energy Physics, Copyright February 2012.

Some CMSS texts are directly taken from scientific magazines. The paper of S. Brezinsek has a 'golden' copyright status and is gratefully reprinted from *Journal of Nuclear Materials* [S. Brezinsek et al., *JNM* **463** (2015) 1121]. Thanks to the courtesy of IAEA, the paper of A. Murari could be reproduced from *Nuclear Fusion* [A. Murari et al., *NF* **55** (2015) 073009].

To make room for other, more recent topics some talks were merged while the available texts still date from an earlier summer school and/or author. Whenever this is the case, it is duly flagged in the table of contents. The relevant reading material for the evening lecture by EUROfusion Programme Manager Tony Donn e is the booklet on the Fusion Road Map. It is available on the www site but can also be downloaded from <https://www.eurofusion.org/wpcms/wp-content/uploads/2013/02/JG12.356-web.pdf>. For a very limited number of papers no text is available at all.

The vast majority of the slides of the summer school is available at the password protected summer school web site.

Dirk Van Eester (chairman)
Laboratory for Plasma Physics
Trilateral Euregio Cluster
EUROfusion Consortium member
Royal Military Academy
Renaissancelaan 30 Avenue de la Renaissance
B-1000 Brussels
Belgium

Stefaan Poedts (local chairman)
Centre for mathematical Plasma-Astrophysics (CmPA)
KU Leuven
Celestijnenlaan 200-B
B-3001 Leuven
Belgium

List of summer school lectures

AT-1	D. Hogeweij	Degraded confinement and turbulence in tokamak experiments (1)
AT-2	D. Hogeweij	Degraded confinement and turbulence in tokamak experiments (2)
AT-3	D. Reiser	Introduction to drift wave turbulence (1)
AT-4	D. Reiser	Introduction to drift wave turbulence (2)
AT-5	M. Vergote	Radial electric fields
BT-1	H. de Blank	Guiding centre motion (1)
BT-2	H. de Blank	Guiding centre motion (2)
CO-1	M. de Baar	How to fly a tokamak? (no text available)
DI-1	T. Donné	Plasma diagnostics in view of ITER
DI-2	A. Murari	Bridging the gap between theory and experiment: advanced data analysis for the extraction of mathematical models directly from the data (reprinted from <i>Nuclear Fusion</i>)
DI-3	A. Krämer-Flecken	Microwave diagnostics
DI-4	R. Jaspers	Active and passive plasma spectroscopy
DI-5	A. Kreter	Diagnostics for plasma-material interaction studies
DI-6	V. Kiptily	Fusion product diagnostics
DI-7	S. Brezinsek	In-situ plasma-wall interaction diagnostics (no text available)
EI-1	H. de Blank	Plasma equilibrium in tokamaks
EI-2	H. de Blank	MHD instabilities in tokamaks
EI-3	R. Koslowski	Operational limits and limiting instabilities in tokamak machines
EI-4	S. Sharapov	Energetic particle-driven instabilities: theory and experiment
EI-5	H. Wilson	Neoclassical tearing modes
EI-6	H. Wilson	Edge localized modes in tokamaks
EP-1	U. Samm	Plasma-wall interaction of magnetically confined fusion plasmas (1)
EP-1	U. Samm	Plasma-wall interaction of magnetically confined fusion plasmas (2)
EP-3	B. Unterberg	Transport processes in the plasma edge (1)
EP-4	B. Unterberg	Transport processes in the plasma edge (2)
EP-5	M. Tokar	Impurity transport and radiation
EP-6	Y. Liang	Plasma with stochastic boundaries
EP-7	I. Uytendhouwen	Erosion and deposition mechanisms in fusion plasmas (1; no text available)
EP-8	I. Uytendhouwen	Erosion and deposition mechanisms in fusion plasmas (2; no text available)
EP-9	D. Reiter	Recycling and transport of neutrals (1)
EP-10	D. Reiter	Recycling and transport of neutrals (2)
EP-11	G. van Rooij	Laboratory experiments to study plasma surface interaction
EV-1	T. Donné	Evening lecture: The EUROfusion Consortium (no text available)
EV-2	J. Beckers et al.	Evening lecture: Exotic Plasma Show
FM-1	M. Van Schoor	Fusion machines (1)
FM-2	M. Van Schoor	Fusion machines (2)
FM-3	D. Hartmann	Stellarators (1)
FM-4	D. Hartmann	Stellarators (2)
FM-5	J. Ongena	Confinement in tokamaks
HC-1	Y. Kazakov	Heating the plasma
HC-2	F. Louche	Coupling EM waves to the plasma
HC-3	E. Lerche	Ion cyclotron, lower hybrid and Alfvén heating (text by R. Koch)
HC-4	E. Westerhof	Electron cyclotron waves
HC-5	E. Westerhof	Current drive
HC-6	P. Dumortier	Antenna design and matching issues
IN-1	J. Ongena	Energy for future centuries: prospects for fusion
IN-2	R. Jaspers	Thermonuclear burn criteria
KT-1	S. Poedts	Kinetic theory (1)
KT-2	G. Lapenta	Kinetic theory (2)
KW-1	E. Lerche	Kinetic theory of plasma waves (1; texts KW-1 & 2 merged)
KW-2	D. Van Eester	Kinetic theory of plasma waves (2; texts KW-1 & 2 merged)
KW-3	D. Van Eester	Fast particle heating (NBI) and Modelling particle heating and current drive in tokamaks (merged talk with 2 separate texts, one on fast particles and one on numerics)
MA-1	J. Coenen	Tungsten as a plasma facing component; advanced fusion materials
MA-2	C. Linsmeier	Beryllium and mixed materials: surface compounds and hydrogen retention (no text available)
MA-3	J. Linke	High heat flux performance of plasma facing components
MA-4	S. Brezinsek	Plasma-surface interaction in all-metal tokamaks (reprinted from <i>Journal of Nuclear Materials</i>)
MA-5	M. Rubel	Structure materials in fusion reactors
P-1		Poster session I
P-2		Poster session II
SF-1	W. Biel	Status and outlook of fusion research
SF-2	J. Ongena	The big step from ITER to DEMO
SF-3	V. Massaut	The nuclear aspects of a fusion power plant: new constraints and challenges
SF-4	G. De Temmerman	ITER status and challenges (no text available)
TT-1	P. Helander	Classical transport in plasmas
TT-2	P. Helander	Neoclassical transport in plasmas

TIME	MON 24/8/2015	TUE 25/8/2015	WED 26/8/2015	THU 27/8/2015	FRI 28/8/2015
08:45 - 09:35	Welcome	BT-1	EI-1	-	AT-3
09:40 - 10:30	IN-1	BT-2	EI-2	KT-1	AT-4
Coffee					
10:45 - 11:35	IN-2	TT-1	EI-3	AT-1	EP-3
11:40 - 12:30	FM-1	TT-2	EI-4	AT-2	EP-4
Lunch					
14:00 - 14:50	FM-2	EI-5	HC-1	EP-1	MA-1
14:55 - 15:45	FM-5	DI-1	-	EP-2	KT-2
Coffee					
16:00 - 16:50	FM-3	MA-2	P-1	AT-5	CO-1
16:55 - 17:45	FM-4	EI-6	P-1	-	-
Dinner					
	Evening walk through Leuven (20h)	EV-1 (19:30-21:30)	-	Visit InBev brewery (19:30-??)	-

TIME	MON 31/8/2015	TUE 1/9/2015	WED 2/9/2015	THU 3/9/2015	FRI 4/9/2015
08:45 - 09:35	HC-2	Excursion to FZ Juelich	EP-7	DI-7	SF-1
09:40 - 10:30	HC-3	Bus leaves Leuven at 8h30	EP-8	DI-6	SF-2
Coffee					
10:45 - 11:35	HC-4	EP-5	EP-11	MA-3	SF-4
11:40 - 12:30	HC-5	EP-6	DI-2	MA-4	Closing
Lunch					
14:00 - 14:50	HC-6	EP-9	DI-5	DI-3	
14:55 - 15:45	KW-1	EP-10	DI-4	MA-5	
Coffee					
16:00 - 16:50	KW-2	-	P-2	SF-3	
16:55 - 17:45	KW-3	-	P-2	-	
Dinner		BBQ in Juelich Bus leaves Juelich at 20h30		summer school diner (18:30-??)	
	EV-2 (19:30-21:30)		-		

**Participants
of the
12th Carolus Magnus Summer School
on
Plasma and Fusion Energy Physics
at the
Katholieke Universiteit Leuven
2015**



Manuscripts of Lectures - Table of Contents

Introduction

IN-1

J. Ongena and G. Van Oost

ENERGY FOR FUTURE CENTURIES,

PROSPECTS FOR FUSION POWER AS A FUTURE ENERGY SOURCE

1-14

IN-2

G. Van Oost and R. Jaspers

THERMONUCLEAR BURN CRITERIA

15-24

Fusion Machines

FM-1-2

M. Van Schoor and R. R. Weynants

FUSION MACHINES

25-31

FM-3-4

D. Hartmann

STELLARATORS

32-45

FM-5

J. Ongena

CONFINEMENT IN TOKAMAKS

46-59

Basic Theory

BT-1-2

H. J. de Blank

GUIDING CENTER MOTION

60-65

Kinetic Theory

KT-1

S. Poedts

KINETIC PLASMA THEORY

66-75

KT-2

G. Lapenta

KINETIC PLASMA SIMULATION: PARTICLE IN CELL METHOD

76-85

Equilibrium and Instabilities

EI-1

H. J. de Blank

PLASMA EQUILIBRIUM IN TOKAMAKS

86-92

EI-2

H. J. de Blank

MHD INSTABILITIES IN TOKAMAKS

93-105

EI-3

H. R. Koslowski

*OPERATIONAL LIMITS AND LIMITING INSTABILITIES
IN TOKAMAK MACHINES*

106-113

EI-4

S. E. Sharapov

MHD AND FAST PARTICLES IN TOKAMAKS

114-121

EI-5

H. R. Wilson

NEOCLASSICAL TEARING MODES

122-130

EI-6

H. R. Wilson

EDGE LOCALIZED MODES IN TOKAMAKS

131-139

Transport Theory**TT-1-2**

P. Helander

CLASSICAL AND NEOCLASSICAL TRANSPORT IN TOKAMAKS

140-148

Anomalous Transport**AT-1-2**

G. M. D. Hogeweij

*DEGRADED CONFINEMENT AND TURBULENCE
IN TOKAMAK EXPERIMENTS*

149-156

AT-3-4

D. Reiser

INTRODUCTION TO DRIFT WAVE TURBULENCE MODELS

157-166

AT-5

M. Vergote and K. Cromb 

RADIAL ELECTRIC FIELDS AND TRANSPORT BARRIERS

167-177

Edge Physics and Exhaust**EP-1-2**

U. Samm

*PLASMA-WALL INTERACTIONS IN MAGNETICALLY
CONFINED FUSION PLASMAS*

178-184

EP-3-4

B. Unterberg

TRANSPORT PROCESSES IN THE PLASMA EDGE

185-198

EP-5	M. Z. Tokar and M. Koltunov <i>IMPURITY TRANSPORT AND RADIATION</i>	199-207
EP-6	Y. Liang <i>STOCHASTIC BOUNDARY PLASMA IN TOKAMAKS WITH RESONANT MAGNETIC PERTURBATIONS</i>	208-217
EP-7-8	A. Kirschner <i>EROSION AND DEPOSITION MECHANISMS IN FUSION PLASMAS</i>	218-232
EP-9-10	D. Reiter <i>RECYCLING AND TRANSPORT OF NEUTRALS</i>	233-242
EP-11	G. J. van Rooij <i>LABORATORY EXPERIMENTS AND DEVICES TO STUDY PLASMA SURFACE INTERACTION</i>	243-249

Materials and Plasma Surface Interaction

MA-1	J. W. Coenen <i>TUNGSTEN AS A PLASMA FACING COMPONENT AND DEVELOPMENT OF ADVANCED MATERIALS FOR FUSION INTERACTION</i>	250-259
MA-3	J. Linke <i>HIGH HEAT FLUX PERFORMANCE OF PLASMA FACING MATERIALS AND COMPONENTS UNDER SERVICE CONDITIONS IN FUTURE FUSION REACTORS</i>	260-269
MA-4	S. Brezinsek and JET-EFDA contributors (reprint of Journal of Nuclear Materials 463 (2015) 1121, doi:10.1088/0029-5515/55/7/073009) <i>PLASMA-SURFACE INTERACTION IN THE BE/W ENVIRONMENT: CONCLUSIONS DRAWN FROM THE JET-ILW FOR ITER</i>	270-280
MA-5	M. Rubel <i>STRUCTURE MATERIALS IN FUSION REACTORS: ISSUES RELATED TO TRITIUM, RADIOACTIVITY AND RADIATION-INDUCED EFFECTS</i>	281-289

Heating and Current Drive

HC-1	Y. Kazakov, D. Van Eester and J. Ongena <i>PLASMA HEATING IN PRESENT-DAY AND FUTURE FUSION MACHINES</i>	290-297
-------------	--	---------

HC-2

F. Louche and R. Koch

THE COUPLING OF ELECTROMAGNETIC POWER TO PLASMAS

298-306

HC-3

R. Koch

THE ION CYCLOTRON, LOWER HYBRID AND ALFVEN WAVE HEATING METHODS

307-314

HC-4

E. Westerhof

ELECTRON CYCLOTRON WAVES

315-322

HC-5

E. Westerhof

NON-INDUCTIVE CURRENT DRIVE

323-330

HC-6

P. Dumortier and A. M. Messiaen

ICRH ANTENNA DESIGN AND MATCHING

331-338

Kinetic Wave Theory**KW-1-2**

D. Van Eester and E. Lerche

KINETIC THEORY OF PLASMA WAVES

339-354

KW-3a

R. Koch and D. Van Eester

FAST PARTICLE HEATING

355-365

KW-3b

D. Van Eester

MODELING PARTICLE HEATING AND CURRENT DRIVE IN FUSION MACHINES: BRIEF OVERVIEW OF ADOPTED TECHNIQUES

366-373

Diagnostics**DI-1**

A. J. H. Donné

PLASMA DIAGNOSTICS IN VIEW OF ITER

374-381

DI-2

A. Murari , E. Peluso, M. Gelfusa , I. Lupelli and P. Gaudio

(reprint of Nucl. Fusion 55 (2015) 073009, doi:10.1088/0029-5515/55/7/073009)

A NEW APPROACH TO THE FORMULATION AND VALIDATION OF SCALING EXPRESSIONS FOR PLASMA CONFINEMENT IN TOKAMAKS

382-395

DI-3

A. Krämer-Flecken

MICROWAVE AND FAR INFRARED DIAGNOSTICS

396-403

DI-4
R. J. E. Jaspers
PLASMA SPECTROSCOPY 404-413

DI-5
A. Kreter
DIAGNOSTICS FOR PLASMA-MATERIAL INTERACTION STUDIES 414-423

DI-6
V. Kiptily
FUSION PRODUCT DIAGNOSTICS OF TOKAMAK PLASMAS 424-431

Status of Fusion

SF-1
W. Biel
STATUS AND OUTLOOK OF FUSION RESEARCH 432-441

SF-2
J. Ongena, R. Koch and Y .O. Kazakov
THE BIG STEP FROM ITER TO DEMO 442-456

SF-3
V. Massaut
*THE NUCLEAR ASPECTS OF A FUSION POWER PLANT:
NEW CONSTRAINTS AND CHALLENGES* 457-468

ENERGY FOR FUTURE CENTURIES

Prospects for fusion power as a future energy source

J. Ongena¹ and G. Van Oost²

¹Laboratorium voor Plasmafysica - Laboratoire de Physique des Plasmas
Koninklijke Militaire School - Ecole Royale Militaire
Association "EURATOM - Belgian State", B-1000 BRUSSELS (Belgium)
Partner in the Trilateral Euregio Cluster (TEC)

² Department of Applied Physics, Ghent University,
Rozier 44, B-9000 Gent.

ABSTRACT

The current power consumption and an estimate of the future energy needs of the world are discussed. The present energy supplies and prospects, the possible consequences of a continued massive fossil fuel consumption, and the potential of non-fossil candidates for long-term energy production are outlined. An introduction to the potential contribution of future fusion reactors is given. The resources, safety, environmental and economic aspects of magnetic fusion energy are discussed.

I. INTRODUCTION

Mankind currently has an addiction to fossil fuels which is non sustainable and dangerous for several reasons: (i) burning of fossil fuels is having a measurable impact on our atmosphere and could trigger serious changes in climate (ii) much more interesting use could be made from this resource (iii) they will run out at some point.

The number of conceivable non-fossil candidates which in the long-term could substantially contribute to energy production is very limited: renewables, nuclear fission and fusion. Fusion is the least developed of the three, but has particularly valuable environmental and safety advantages and has virtually inexhaustible resources.

Before starting the discussion let us briefly discuss some of the basic physical quantities used in this paper. Energy is the capacity for doing work by any system and its SI unit is Joule. Power is the amount of energy produced, transferred, or used per unit of time and its SI unit is Joule per second or Watt. Other units often used to express an energy quantity are e.g. kWh, MWd, TWyr etc. Energy (or power) in the form that it is first accounted for i.e. before any conversion to secondary or tertiary forms of energy (or power) is called primary energy (or power). Energy has several forms, some of which can be changed to another form useful for work. According to the second law of thermodynamics, each thermal conversion process is associated with losses. This is especially true when using a heat flow from a hot source to a cold sink in the conversion process: only a fraction of the heat can be converted in that way into work, the amount depending on the difference in temperature

between the hot source and cold sink (Carnot cycle). This difference becomes very clear in discussions on electricity production, where the efficiency is often as low as 30%, and thus a distinction has to be made between thermal power and electrical power (indicated in this paper by the suffix "el").

II. THE WORLD ENERGY PROBLEM

II.A. CURRENT AND FUTURE ENERGY NEEDS.

COUNTRY	PER CAPITA POWER CONSUMPTION IN 2010 (kW)
United Arab Emirates	21.35
Iceland	20.00
Qatar	19.30
Kuwait	15.20
Bahrain	14.20
Norway	12.00
Canada	11.50
USA	9.50
Australia	8.10
Belgium	7.90
The Netherlands	7.70
Russia	6.20
South Korea	6.60
Japan	5.10
Germany	5.10
Europe of 27	4.10
South Africa	3.40
China	2.30
Brazil	1.75
Vietnam	0.62
India	0.56
Zimbabwe	0.42
Mozambique	0.24
Congo (Kinshasa)	0.05
Chad	0.01
World	2.23

Table 1 Per capita total primary power consumption for selected countries (total annual primary power consumption per country divided by the number of its inhabitants [1,2])

Table I gives an overview of the total primary power consumption per capita for different regions in

the world. This is the equivalent amount of power consumed per person 24 hours a day, 365 days per year. It is interesting to note that the largest consumers are often to be found among those countries which are also large energy producers and exporters (Qatar, Bahrain, Kuwait, etc) or dispose of cheap and abundant energy (Iceland, Canada, etc...). Lowest consumption is found in developing countries. Outstanding is also the difference between the USA and the Japanese or European average power consumption: about twice as much power is used for essentially a comparable standard of living.

With over 7 billion people in 2011 and a primary power consumption per capita (world average) of about 2.2kW, the total amount of energy currently consumed in the world is about $2.2 \text{ kW} \times 7 \text{ billion people} \times 1 \text{ year} \approx 15.4 \text{ TWyr}$. An estimate of what might be needed in the future can be found with the following two assumptions:

- (i) primary power consumption per capita (world average) will increase by 800W from 2.2kW to about 3kW (i.e. about half of what is already used in Europe and one fourth of what is currently used in the USA), and
- (ii) world population will rise to about 10 billion in the next 50 years, (medium variant prediction) by the UN [3] (see also Fig. 1)

Thus, in 50 years we expect the world to consume yearly an amount of primary energy equal to $3 \text{ kW} \times 10 \text{ billion people} \times 1 \text{ year} = 30 \text{ TWyr}$ or about two times more than what is consumed now!

The first assumption fits with energy data from the past decades: in the last ~25 years (1980-2006), the primary power consumption per capita (world average) has increased by about 300W (associated with an increase in total primary energy consumption in the world by about 66%). Extrapolating linearly (if justified) would amount to 600W in 50 years.

Another confirmation comes from the study of the World Energy Council and the International Institute for Applied System Analysis [4], which considers three different scenarios for the future development of the world energy consumption: (i) a high growth scenario with impressive technological developments and high economic growth [Case A], (ii) a “middle course” scenario with less ambitious and perhaps more realistic technological improvements and a more intermediate economic growth [Case B] and (iii) an ecologically driven scenario which represents a “rich and green” future, both with substantial technological improvements, strict environmental control mechanisms and an unprecedented international collaboration for environmental protection [Case C]. The predicted energy future for the three scenarios described above is shown in Fig. 1. The middle course scenario, Case B, considered as the most realistic scenario, predicts about 25TWyr for 2050, close to the estimate above.

Note that the numbers above would imply that we need an additional power production capacity (for electricity, direct heating, transportation, etc) of about 15TW in the next 50 years. If true, this means 300GW/year, or equivalently a capacity of 1GW nearly every day for the next 50 years. Taking into account that on top of this, old power or heat generation systems will have to be replaced (also amounting to about 15TW), a total of 30GW greener power systems has to be constructed in the next 50 years. This clearly shows the staggering task that lies in front of us. We can only hope that this will indeed be greener systems, but unfortunately and as will be shown in what follows, there are currently not sufficient clean alternatives ready to replace fossil fuels on such a large scale.

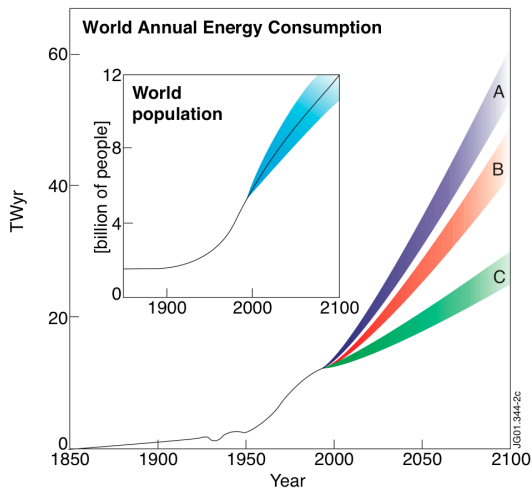


Fig. 1 Past and projected evolution of the annual world primary energy consumption according to three different scenarios, as documented in [4]. The inset shows the projected evolution of the world population [3]. The bands reflect the uncertainties in the predictions.

What is then the best way forward? As we will see below, there is no simple answer to this question.

II.B. CURRENT ENERGY SUPPLY AND FUTURE PROSPECTS

An overview of the present proved recoverable reserves for various energy options is given in Table II, together with an estimate of the period still available for use at the current rate of consumption.

In addition, one has to be careful with these numbers, as huge political and economic interests (for a frightening example, see [5]) might lead to under- or overestimates depending on who is providing the data. In addition, future prospection could result in updates of these numbers. It is clear from Table II that we can indeed go on for at least a few decades.

But is this really desirable?

As can be seen in Table III, about 90% of our energy is currently produced by burning fossil fuels. This could pose serious problems in the future.

FUEL	PROVED RECOVERABLE RESERVES (2009)	YEARS OF USE AT THE CURRENT RATE OF CONSUMPTION
Coal	0.9 10^{12} tons	210
Crude oil	1.3 10^{12} barrels	30-40
Natural gas	190 10^{12} m ³	60-70
Uranium (ore)	4.7 10^6 tons	85-270* (2600-8000)**
Uranium (sea water)	4.5 10^9 tons	81000-260000

* assuming Light Water Reactor, once through

** if breeder technology is employed.

Table II Years of use of different fuels at the current rate of consumption [1,2,6-9]

First, depletion of the world energy resources will inevitably lead to political instabilities (and has already caused tensions) in the world. The energy crisis of the 1970's, the Iraq war in the 1990s, etc. are small reminders of what we could face. Note that more and more institutions are warning about peaking of conventional oil reserves [10, 11] with possible shortages and/or price increases in the near future. The oil peak discussion is complex: different concepts of "reserves" are often used, changes in price could have big influences on the economical recoverability of a source, financial speculation can interfere etc. Moreover, there are very large in-place resources of both conventional and various non-conventional oils (primarily tar sands and shale oil). But many analysts calculate that once conventional oil peaks, it will be difficult to bring these other resources on-line fast enough to offset the decline in the production of conventional oil. These and various other facets of this discussion are documented in ref [12]. However, it should be clear that much better use could be made of these finite resources. They are invaluable for our chemical and pharmaceutical industry. From this point of view, our present energy production scheme causes irreplaceable basic chemicals to be literally 'going up in smoke' and thus lost forever on a gigantic scale.

The second, and most worrisome problem is the possible influence to our environment of the massive use of fossil fuels due to the inevitable release of gigantic quantities of CO₂. In 2012 alone, about 32 billion tons of CO₂ were released in the atmosphere [1]. This could still seem to be negligible, as it represents only a minor fraction of the total amount of CO₂ released (and subsequently recycled) by nature. But precisely because these natural flows balance out, any additional source of CO₂ will lead to

an increase. This is exactly what is observed: a steep increase of the CO₂ content in the atmosphere during the last few decades, as illustrated in Fig. II. This graph - compiled from analysis of air bubbles in the ice of the Antarctic and air samples at the top of the Mauna Loa mountain on Big Island (Hawaii) - compiled data up to 1996. It shows clearly the ever faster increase in CO₂ since the beginning of industrialisation around 1800. The out of graph star in Fig II indicates the current level (2013) of ~400ppm [13] and illustrates the increase of 40ppm that took place over the last ~17 years. Comparing this with the previous period it took for a similar increase in CO₂, about 70 years - from 1930 to 1996 - it shows that we are far from curbing CO₂ emissions. ★

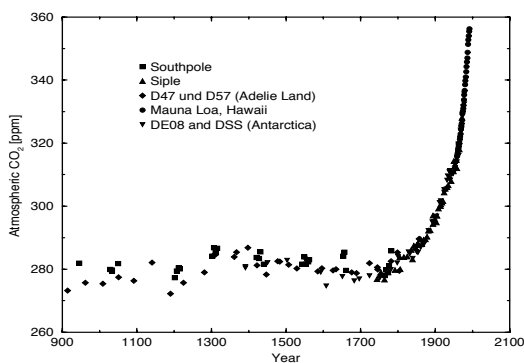


Fig. II Evolution of the CO₂ concentration in the atmosphere (in ppm) during the last 1000 years up to 1996 [14]. The out of graph black star added at the top right of the figure indicates current CO₂ levels (2008, ~ 385ppm [13]).

Note also that all this CO₂ has accumulated in about 200 years. This is very short on a geological time scale and rather frightening in view of additional evidence that the CO₂ concentration has remained at about 280 ppm for the last 160000 years [15]. Carbon sequestration or carbon capture and storage (CCS) could perhaps help to reduce future CO₂ increases [16], but is of no use to decrease present atmospheric levels.

What are the possible consequences of such a sudden change in the composition of the atmosphere?

CO₂ is a greenhouse gas, and a higher concentration of this gas will lead to an increased absorption in the atmosphere of the infrared radiation re-emitted by the earth. This has led to a continuous increase in the mean global temperature in past years. The consequences are becoming visible, e.g. the last decade being the warmest since early 1800 [15, 17] and effects in Greenland, on glaciers worldwide and

polar ice are very impressive (see e.g. ref. [18] for truly frightening examples) and do raise serious concern. To what will all this lead on the long-term? The answer to this question is not evident, because our ecosystem is very complex, with many feedback channels, some of them still partly or fully unknown and thus impossible to take correctly into account in modelling. Some buffering against changes probably exists, but there are surely limits to the adaptability of our ecosystem and two main questions are: what are these limits, and in which direction will the ecosystem evolve as soon as the stability thresholds are crossed? We should also not forget that the climate system is inherently unstable: climate records from the past have indicated that variations of more than 7 °C have taken place in the average sea water temperature in the course of a few tens of years [19].

PRIMARY ENERGY SOURCE	CONTRIBUTION TO PRIMARY ENERGY PRODUCTION (2008)
Oil	33.7 %
Coal	23.8 %
Gas	29.6 %
Fission	5.2 %
Hydro-electricity	6.4 %
Solar, wind, wood, waste,..	1.3 %

Table III Contribution of different primary energy sources to the primary energy production in the world [8].

What makes things even more frightening is that the excess CO₂ decays exponentially with a very long time constant (100-200 years), mainly determined by the slow exchange of carbon between surface waters and the deep ocean [15]. This means also that as soon as changes are visible in our climate, we will have to deal with these effects for very long times, even if we could shut down all sources of CO₂ immediately. Even worse, returning to previous levels is no guarantee neither as it cannot be ascertained that the whole ecosystem will return in a reversible way to the previous situation once critical (unknown!) thresholds have been crossed.

This is the most threatening consequence of our energy production scheme nowadays. We are conducting a possibly irreversible large-scale geophysics experiment. We have to remember that we have only one atmosphere and that it is irreplaceable, in other words, we are all "sitting in the test tube". It cannot be excluded that certain parts of the world could become no longer inhabitable due to rising sea levels or desert formation; in addition, food-producing areas could shift, with hunger, poverty, migration of people, etc. as possible consequences. This would constitute a serious threat to peace and international security.

Is this the prospect we would like to offer our children and grand children?

In this context, it seems nearly unavoidable to reduce or stop burning fossil fuels and try to use other energy sources as soon as possible. It seems also unwise to use uncertainties in the predictions for future climate change as an excuse for delaying necessary actions. The only thing we are left with currently is to try to limit the impact (see [15]) and thus one of the consequences could be environmentally imposed reductions on the use of fossil fuels, well before the effects of resource limitations are felt. But this can only be realistically imposed if there are sufficient non-fossil alternatives. To make things worse, efforts to reduce emissions of greenhouse gases may be alone insufficient to avert unacceptable levels of climate change. Therefore geo-engineering methods (e.g. increasing the albedo of the earth by injecting aerosols in the stratosphere) are beginning to be considered as a possible option to "keep the earth cool" (see e.g. [20, 21]). It underlines very clearly that there is 'no easy fix' to the problems we are facing.

There are only two classes of long-term alternatives to burning fossil fuels: renewables and nuclear energy (fission and fusion).

However, there should be no illusions that bringing on-line massive quantities of non-fossil solutions will take time. It should be done wisely and with vision, and with respect for scientific and economic realities. Unfortunately, except for fission, none of the possible alternatives at present is sufficiently mature (see Sect. II.C); but even fission is (i) only short term with the current type of reactors (implying the need for breeder technology, unless one could use seawater extraction [6], see below) and (ii) has a low level of acceptance by the general public. A revival of nuclear energy seems a necessity, but it will still take a while before a large-scale increase can be realised. Fear of nuclear energy is often misused as a 'source of votes' from a general public that is in many cases very badly informed. Political decisions also often backfire (and the public is left uninformed): in the case of Germany, closing down 7 nuclear plants in the aftermath of Fukushima has led to a 7% increase in CO₂ production, despite really enormous investments (~ 10-12 billion Euro/year for the last 10 years) in green energy systems. The low quality of the public discussion, frequently lacking reference to realistic numbers or using the numbers very selectively, is a matter of serious concern and correct and neutral education of the general public is an absolute necessity. To make things worse, there are strong economic and political powers trying to maintain the current situation by all possible means, see e.g. the frightening report in Ref. [5].

II.C. LONG-TERM NON-FOSSIL ENERGY SOURCES

Although renewable energy resources in the world are large and inexhaustible, they have, unfortunately, only a limited potential [22]. Natural obstacles met by renewables are low energy density

and/or fluctuations in time, implying the need for storage, which reduces again the efficiency and leads to extra costs.

A useful insight in this respect can be gained from a very simple example on hydropower, at this moment the most important renewable energy source. The energy needed to boil 1 liter of water (from 0 to 100C) is equivalent to the energy gained from 100 liters of water falling over 426m (nearly half a km) assuming complete conversion of gravitational potential energy into heat. Two important conclusions follow immediately: (i) we consume a lot of energy without realizing, (ii) it requires a large effort to extract these amounts from sustainable sources.

RENEWABLE CATEGORY	RENEWABLE SOURCE	POWER OUTPUT (W/m ²)
Sun based	Solar heating	53
	Concentrating solar power (deserts)	15
	Solar photovoltaics	5-20
	Solar chimney	0.1
	Ocean thermal	5
	Wind	2-3
	Waves (Pelamis farm)	30
Gravitation based	Tidal power	6
	Tide pool	3
	Hydro-electricity	11
Agriculture based	Biogas	0.02
	Rape seed oil	0.13
	Bio-ethanol (sugar cane)	1.2
	Energy crops	0.5
	Wood	0.1-0.2
Earth based	Geothermal Heat	0.017

Table IV Power production per m² of land or sea surface occupied. Renewable energy is rather diffuse, leading to large, country-sized facilities in order to contribute substantially (from [22]).

The potential of renewables is further illustrated in Table IV compiling values for the power output per

unit land or sea area occupied for a number of possible options. Best solutions seem solar heating, wave power, concentrated solar power and hydro electricity. These numbers can be put into context by comparing with the power output per m² of a large (1000MW_{el}) coal or nuclear power plant (~150kW/m²) or the surface of the lake behind a dam (>100km²) to provide 1000MW_{el}.

Renewable and nuclear energy systems have the common feature that emissions of greenhouse gases and other atmospheric pollutants are 'indirect', that is, they arise from stages of the life-cycle other than power generation. In the case of nuclear energy, this arises mainly from mining and processing ore, and is only a minor effect. In the case of renewables, the low power density, illustrated in Table IV, unavoidably implies important land use and/or investment in materials. E.g. in the case of biomass this implies areas of several 1000 km² even for a relatively low power production of 100MW and CO₂ emissions from fertilizer/pesticide production, harvesting, drying and transportation have to be taken into account. It could lead for some 'low carbon' technologies to an outperformance of their potential to contribute effectively to CO₂ reductions. For interesting analysis see [23,24]. The production of e.g. solar cells causes quite some pollution if one is not careful, and have already led to protests e.g. in China [22a]. Some of the estimates of the world wide potential also seem not to take into account fundamental restrictions. E.g. in the case of wind energy, a bottom-up estimation seems to easily lead to overestimations [22b]. For a very interesting discussion on sustainability, energy efficiency and subsidies see [22c]; a critical assessment of the consequences of the recent German energy policy is given in [22d]. These and other arguments should be carefully taken into account in discussing energy options.

We would like to stress that we do not mean to imply that renewables are useless. The purpose is to point out important aspects of renewables that should not be forgotten in discussions on our energy future. Land use and indirect emissions are two of them. It certainly makes sense to try to exploit these as much as is realistically possible, as every non-fossil energy source will be needed in the future. But one should be realistic in assessing their potential [22, 25] to produce energy and effectively reduce CO₂ emissions.

The other main non-fossil option is nuclear power generation by fission and for the future, by fusion.

In the case of fission, issues raising concern are waste, safety and proliferation. Concerning waste, indeed highly radioactive waste is produced, but the volume is rather low: only about 28 tons of fuel is needed per GW_{yr,el}, resulting in the same amount of irradiated material. (Note that this is less fuel than expected on the basis of 3-4% ²³⁵U enrichment alone, the reason being that about 40% of the heat is generated from fission of ²³⁹Pu and ²⁴¹Pu formed from ²³⁸U by neutron capture). But about 27 tons of the

irradiated fuel can in principle be reprocessed and reused in other reactors [26] as it consists of a mixture of about 224 kg ²³⁵U, 26400 kg ²³⁸U and 170 kg of fissile Pu isotopes, the rest - fission products and non-fissile elements - must be disposed of. In essence, only 1 ton or about 50 dm³ of highly active waste is produced per GWyr,el. Moreover, with the right techniques this can be handled safely and new methods are being developed to store [27], or even eliminate it by transmutation thereby producing energy [28]. Reprocessing is unfortunately no longer an option for many countries, so the irradiated rods are stored after cooling in special containers. For the Belgian reactors Doel 1 and 2 (~ 830MW,el total) this results in one container per year, still a small volume for the amount of power produced, certainly if compared with greenhouse gases and other pollutants generated by burning fossil fuels. The radiological danger of nuclear power generation should also be put in perspective comparing with coal power plants. Trace elements in coal like thorium and uranium accumulate in the ash and add to the natural background radiation. Comparing radiation doses from airborne effluents of 1000MW,el coal-fired and nuclear power plants and assuming a 1 percent ash release to the atmosphere (Environmental Protection Agency regulation) and 1 part per million of uranium and 2 parts per million of thorium in the coal (approximately the U.S. average), population doses from the coal plant are typically higher than those from pressurized-water or boiling-water reactors that meet government regulations. [28a, 28b].

With the present reactor types the lifetime of our uranium resources from ore is comparable to that of oil or gas - about 80 years. Using breeder technology to transform non-fissile fuel into fissile elements, we could stretch our resources by a large factor (30 or more [9, 29, 30]) although the safety and environmental problems are potentially more difficult to cope with. Perhaps the need for breeders could be avoided altogether, if uranium extraction from seawater would become an economical option [6].

METHOD	ANNUAL FUEL CONSUMPTION FOR 1000MW,el. (typical size of a single large electric power plant)
Coal	2 700 000 tonnes
Oil	1 900 000 tonnes
Fission	28 tonnes of U
Fusion	100 kg D and 150 kg T

Table V Fuel consumption for different energy production methods

Concerning safety, new reactor concepts, which rely on passive safety systems, will surely contribute to increase public acceptance [31]. In this context, the Tchernobyl incident should be mentioned, as it was not the result of a malfunction under normal working circumstances, but rather due to negligence and total disregard of safety rules. As such it is close to an unbelievable criminal act, a fact hardly ever mentioned by the mass media. The Tchernobyl reactor (RBMK-1000) was of a dangerous design (among others, it has a positive temperature coefficient). All reactors of this type are closed worldwide. The reactor was not protected from the environment (as in the West) by a concrete and steel dome. Worst of all, the accident was triggered by trying out a dangerous and badly prepared experiment. Operators were put under severe pressure from local officials. In the panic of the last minutes, the control system was disabled and all control rods were fully extracted, leaving no room for a fast intervention in case of a runaway reaction. No wonder that under such conditions the worst possible happened. A hair raising and detailed account of the events on 26 April 1986 can be found in e.g. refs. [32, 33].

The recent events in Fukushima, Japan, although very serious, should not be over dramatised, or lead to panic reactions. It should be underlined that the earthquake itself, although of an extremely large magnitude, did lead to a correct and timely shutdown of all nuclear plants in Japan. It was the arrival of a tsunami of enormous proportions that was the major problem and killed an estimated 20000 people. Nobody died so far from the nuclear incident itself. Conclusions should be (and are) drawn on justified critiques of certain aspects of the construction and localization of those damaged Japanese plants. But it seems unwise to plan a complete nuclear shutdown if no good alternative is immediately ready to take over the nuclear share, or if as a result one has to import power from other nuclear nations or end up with an increased dependency on fossil fuels. The danger is also real that due to inappropriate decisions very valuable know-how could get lost for a technology that could serve good purposes in the coming decennia

The other nuclear option is fusion. It is the least developed of the three but it holds the promise of being a safe, inexhaustible and rather clean energy production method. As such it could become the best compromise between nature and the energy needs of mankind. Recent studies carried out for the European Commission [34] confirm this point of view. Energy quality criteria will become most important in the future: energy production must be not only economically, but also environmentally and societally acceptable.

The huge contrast in fuel consumption between fossil and nuclear methods to generate energy becomes clear from a look at Table V. This results of course from the large difference in energy gained from a nuclear reaction compared to a chemical one - per

reaction a factor of around 10^6 for fission and 10^7 for fusion. The numbers mentioned reflect what is needed for just one electric power plant. A good idea of the gigantic quantities of CO_2 released in the atmosphere yearly is found by calculating the equivalent length of a train carrying 2 700 000 tonnes of coal: it has a length of 540 km, i.e. the distance between Paris and Amsterdam. Per power plant of 1000MW_{el} and per year, this quantity of coal gets (nearly totally) converted into 10 000 000 tonnes of CO_2 . The equivalent of many hundreds of such plants are in operation at present...

There is every reason to be worried for the future, as reflected by the projected numbers of electric power capacity to be installed in the next ~50 years, estimated by the Indian and Chinese governments [35, 36]. These numbers are respectively equal to 480 GW_{el} and 1500 GW_{el}. In the case of China alone, it is estimated that burning coal will generate half of this number in 50 years. However, to reach this level, China will have to build and put into operation each month at least one new electric power plant with a capacity of 1 GW_{el} - fired by coal - and this for the next 50 years... Note that the reality surpasses by far projections: an average capacity of 5GW_{el}/month (coal, gas) has been installed in China over the period 2003-2007 (see Ref. [1]). Consequences of this massive development are becoming visible: data analysis of water samples indicate that mercury levels in the North Pacific Ocean have risen about 30 percent over the last 20 years, attributed to increases in global mercury atmospheric emission rates from coal burning [37] in Asia. This mercury is now accumulating via fish in the food chain.

III. NUCLEAR FUSION AS AN ENERGY SOURCE FOR THE FUTURE.

The development of nuclear fusion as an energy source is one of the most complex scientific and technical tasks ever undertaken for non-military purposes and will still span several human generations. There exist presently two approaches to realise nuclear fusion on earth: inertial and magnetic fusion. Inertial fusion consists of micro-explosions of small

fuel pellets by means of powerful lasers or particle beams. Confinement of the fuel is based on the inertia of the pellet fuel mass, which resists the natural expansion when it is heated to thermonuclear fusion temperatures. Magnetic fusion uses magnetic fields to confine the fuel. The European fusion effort is concentrated on the latter (with tokamaks, stellarators and reversed field pinches) and hence we will briefly review only this method here. The interested reader can find a wealth of additional information in the references [34, 38, 39, 40].

Fantastic progress has been made in magnetic fusion in the last decades. Three generations of tokamaks with doubling of characteristic dimensions at each step led to a 10000 times higher value of the fusion triple product (density times temperature times confinement time) in the last 30 years. Since the start of controlled fusion research, a 10 million-fold improvement in the fusion triple product has been obtained verging to reactor conditions, as illustrated in Fig. III.

Since 1991 several megawatts of fusion power have been released in a controlled way in deuterium-tritium experiments in JET (Joint European Torus, Culham, UK) and TFTR (Tokamak Fusion Test Reactor, Princeton, USA). Peak values of about 16 MW have been obtained on JET in 1997 corresponding to Q_{DT} values (i.e. the ratio of the power released from deuterium-tritium fusion reactions to the power applied to heat the fuel) of more than 0.6; in a stationary way fusion powers of more than 4 MW have been obtained for more than 5 seconds on JET. A comparison of high performance D-T pulses is given in Fig. IV. Break-even in deuterium-tritium experiments, i.e. $Q_{DT} = 1$, is expected at JET in the coming years.

Fusion research entered a new era in 2005 with the international agreement (28 June 2005) on the construction site of ITER at Cadarache (close to Aix-en-Provence in France). Construction has started this year (2009), first (H or ^4He) plasmas are projected for 2018 and first D-T plasmas in 2028 [42]. We all look forward to a swift realization of these plans, and hope that they could be realized earlier than planned now - the world urgently needs clean energy solutions for the long term!

III.A. NUCLEAR FUSION PROCESSES AND FUTURE FUSION REACTORS

The least difficult fusion reaction to initiate on earth is that between the hydrogen isotopes D and T:

$\text{D} + \text{T} \rightarrow ^4\text{He} (3.5\text{MeV}) + \text{n} (14.1\text{MeV})$
 in which D stands for deuterium (the stable isotope of hydrogen with a nucleus consisting of one proton and one neutron) and T for tritium (the radioactive hydrogen isotope with a nucleus of 2 neutrons and 1 proton, see Section III.B). To produce sufficient fusion reactions, the temperature of the plasma has to be on the order of 100 to 200 million C for this reaction.

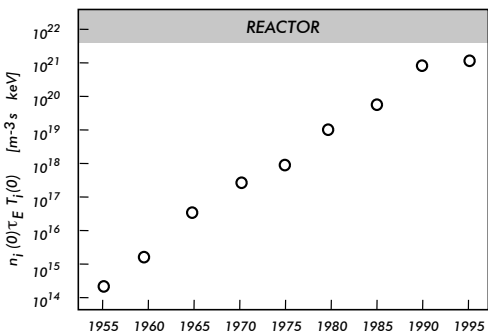


Fig. III Evolution of the value for the fusion triple product since the beginning of fusion research [41]

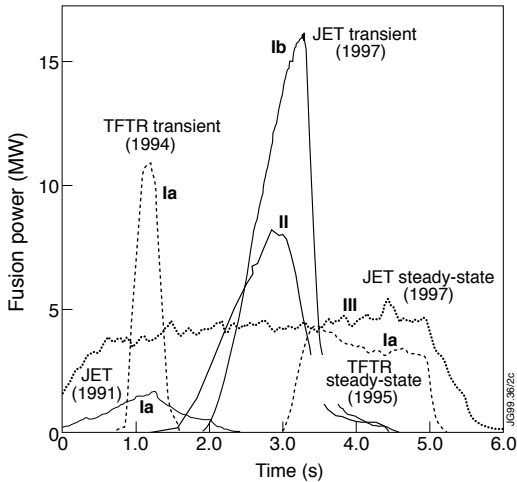


Fig. IV Fusion power development in the D-T campaigns of JET (full and dotted lines) and TFTR (dashed lines), in different regimes: (Ia) Hot-Ion Mode in limiter plasma (Ib) Hot-Ion H-Mode, (II) Optimized shear and (III) Steady-state ELMY-H Modes [43].

A first generation of future fusion reactors would be based on this reaction. The reaction products are thus an α -particle (helium nucleus) and a very energetic neutron. Twenty percent of the energy is taken by the α -particles that are confined, owing to their charge, and deliver their energy to the background plasma. In this way they compensate for losses and might make the reaction self-sustaining. The kinetic energy of the fast neutrons will be converted into heat in a blanket and then into electricity using conventional technology (steam). About one million times more energy is released from a fusion reaction in comparison with a chemical one (MeV's instead of eV's for the latter). This is the reason why so little fuel can produce so much energy: when burnt in a fusion reactor, the deuterium contained in 1 l of water (about 33 mg) will produce as much energy as burning 260 l of gasoline.

The D-T reaction is not the only possibility for controlled fusion. Other conceivable reactions are:



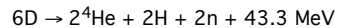
These are more difficult to achieve and have a much lower power density than the D-T reaction [40, 44] but show even more benign environmental features. The D-D reaction would eliminate the need for tritium and produce neutrons with lower energies and are therefore easier to absorb and shield. A

reactor based on the D- ${}^3\text{He}$ reaction would proceed with very low neutron production (some neutrons would be produced in competing but much less occurring D-D reactions) with minor radioactivity produced in the reactor structures. This reaction also releases its total energy in the form of charged particles, enabling in principle the possibility of direct energy conversion to electrical energy. However, the prospects for these 'advanced' fuels are still too speculative and only the D-T reaction has immediate future prospects.

III.B. INEXHAUSTIBLE ENERGY SOURCE?

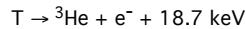
The most obvious advantage of fusion is the virtual inexhaustibility of the fuels that are cheap and widely accessible. Table VI summarises the presently estimated reserves.

Deuterium, a non-radioactive isotope of hydrogen is extremely plentiful as it can be obtained from ordinary water (about 33 g from 1 ton) with cheap extraction techniques using conventional technology. Complete burning of deuterons and the first generation fusion products (T and ${}^3\text{He}$) results in the overall equation:



providing $350 \cdot 10^{15}$ J/ton D. The deuterium content of the oceans is estimated at $4.6 \cdot 10^{13}$ tons [26], thus equivalent to about $5 \cdot 10^{11}$ TWh.

Tritium is the radioactive isotope of hydrogen. It decays to ${}^3\text{He}$ by emission of an electron:



with the rather short half-life of 12.3 years. The quantities available in nature are not sufficient for technical applications. The neutrons produced in the fusion reactions will be used to breed it by bombarding a blanket around the burn chamber containing a lithium compound, according to:



Thus the real consumables in the D-T fusion process are D and Li, while T is an intermediate product burned in the fusion reaction.

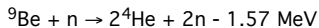
Lithium, like deuterium, is a widely available element. There are two isotopes ${}^6\text{Li}$ and ${}^7\text{Li}$, which occur naturally (7.5% and 92.5% respectively). ${}^6\text{Li}$ is the most useful isotope as it reacts with neutrons in the lower energy range ($E < 1\text{MeV}$). Model calculations [34] show that the burn up of ${}^7\text{Li}$ in a future fusion reactor would be negligible and thus only ${}^6\text{Li}$ is relevant to resource considerations. Per ${}^6\text{Li}$ atom, one T atom is formed, with an extra energy of 4.78 MeV. Including the energy released in D-T fusion reactions, 22.38 MeV is released per ${}^6\text{Li}$ atom. The energy content of natural Li is therefore about $27 \cdot 10^{15}$ J/ton. Estimated reserves of natural Li are somewhat less than 29 million tons in known ore deposits and

brines [45] and about 200 billion tons dissolved in sea water (0.1-0.2ppm) [46], equivalent to about $2.4 \cdot 10^4$ and $1.7 \cdot 10^8$ TWyr. The amount of energy needed to extract Li is negligible compared to the energy released in thermonuclear reactions.

FUSION FUEL	ENERGY CONTENT (TWyr)	YEARS OF USE TO SUPPLY WORLD ELECTRICITY NEEDS (AT 2006 LEVELS)
D	5×10^{11}	100 billion yr
Li (known reserves)	2.4×10^4	5000 year
Li (in sea water)	1.7×10^8	35 million yr

Table VI Estimated reserves of fusion fuels [45,46].

Since only one neutron is produced in each fusion reaction and since each new tritium nucleus to be bred from Li requires one neutron, it is necessary to provide a small additional neutron source, to balance losses in the breeding blanket. A possible suitable neutron multiplier is beryllium, using the (n,2n) reaction:



Another question related to inexhaustibility is if we dispose of enough suitable materials (e.g. structural and superconducting materials for the magnets) for a large-scale use of fusion energy over many centuries. Also here there seem to be no significant constraints [34]

III.C. SAFETY ASPECTS

- Inherent and passive safety

- Can Chernobyl-type accidents occur?

First, the amount of fuel available at each instant is sufficient for only a few tens of seconds, in sharp contrast with a fission reactor where fuel for several years of operation is stored in the reactor core. Second, fusion reactions take place at extremely high temperatures and the fusion process is not based on a neutron multiplication reaction. With any malfunction or incorrect handling the reactions will stop. An uncontrolled burn (nuclear runaway) of the fusion fuel is therefore excluded on physical grounds. Even in case of a total loss of active cooling, the low residual heating excludes melting of the reactor structure [34].

- Radioactivity

The basic fuels (D and Li) as well as the direct end product (He) of the fusion reaction are not

radioactive. However, a fusion reactor will require radiation shielding since it has a radioactive inventory consisting of (i) tritium and waste contaminated by tritium and (ii) reactor materials activated by the neutrons of the fusion reaction. Studies [34, 38, 39] indicate, however, that an adequate choice of the latter can minimise the induced radioactivity such that recycling should become possible after some decades to a century. Thus, radioactivity does not have to be inherent to nuclear fusion, in contrast to nuclear fission where the fission reaction itself leads to dangerous long-lived radioactive products.

The tritium cycle is internally closed, and the total tritium inventory in the fusion power plant will be on the order of a few kg, of which only about 200 grams could be released in an accident. Special permeation barriers will have to be used to inhibit discharge into the environment of tritium diffusing through materials at high temperature [34]. As tritium is chemically equivalent to hydrogen, it can replace normal hydrogen in water and all kinds of hydrocarbons. It could thus contaminate the food chain when released in the atmosphere. The absorption of tritium contaminated food and water by living organisms is a potential hazard. However, possible damage is reduced owing to the short biological half-life of tritium in the body of about 10 days.

- Links to nuclear weaponry?

The operation of pure (i.e. non-hybrid) fusion reactors (see Section III.E) is not accompanied by the production of fissile materials required for nuclear weapons. Only a significant modification of the fusion reactor - the introduction of a special breeding section containing fertile material - would make the production of weapons grade fissile materials possible. However, according to the conclusion of experts (see e.g. [47]), the presence of such a section (in an environment where none at all should be present) could be easily discovered by qualified inspectors. This is in sharp contrast to a fission reactor where production of these materials occurs in the reactor core itself and where in addition a delicate balance has to be made of large inventories of ingoing and out coming nuclear material to discover any possible diversion of fissile material.

- Other non-nuclear risks

Reactor designers will have to minimise non-nuclear risks such as Li-fires, release of chemical toxins like Be, sudden loss of vacuum or cooling liquids, etc... But none of the possible issues currently appear to be sufficiently serious to weigh importantly in societal discussions about the attractiveness of fusion compared to other energy systems.

III.D. ENVIRONMENTAL ASPECTS

- Environmental pollution?

The primary fuels (D and Li) and the direct end product (He) are not radioactive, do not pollute the atmosphere, and do not contribute to the greenhouse effect or the destruction of the ozone layer. Helium is in addition chemically inert and very useful in industry. There are no problems with mining (Li) and fuel transportation. No ecological, geophysical and land-use problems exist such as those associated with biomass energy, hydropower and solar energy.

Measures for tritium containment and detritiation of substances contaminated with tritium will have to be taken. During normal operation the dose for the public in the neighbourhood of the plant will only be a fraction of the dose due to natural radioactivity.

- Dangerous waste?

An important advantage of fusion is the absence of direct radioactive reaction products, in contrast to fission, where radioactive waste is unavoidable since the products of the energy releasing nuclear reaction are radioactive.

Adequate disposal of radioactive waste is especially difficult if the products are volatile, corrosive or long-lived. The neutron-activated structural materials of a fusion reactor would not pose such problems and because of their high melting point and their low decay heat, will not necessitate active cooling during decommissioning, transport or disposal. Recent studies [34] show that over their life time, fusion reactors would generate, by component replacement and decommissioning, activated material similar in volume to that of fission reactors but qualitatively different in that the long-term radio toxicity is considerably lower (no radioactive spent fuel).

Fusion could be made even more attractive by the use of advanced structural materials with low activation as e.g. vanadium alloys or silicon carbides. These materials offer in principle the prospect of recycling after about 100 years after shutdown of the reactor as the radioactivity would fall to levels comparable to those of the ashes from coal-fired plants [34] (which contain always small amounts of thorium and other actinides). It is not yet clear if they will meet a number of technical specifications with regard to thermo-mechanical properties and the ability to withstand a high neutron flux and further research is necessary to clarify these points [48]. But even if existing structural materials like stainless steel are used, the induced radioactivity in a fusion reactor is still about 10 times less than in a fission reactor of comparable power [29, 39].

III.E. ECONOMIC ASPECTS

- Economic viability of future fusion plants?

It is obviously difficult to estimate with any useful precision the cost of a system that will only be put into service several decades from now. In comparison with other energy sources, environmental and safety-related advantages and the virtual inexhaustibility of the fuel sources should be taken into account, as well as the evolution of the cost of electricity based on (exhaustible) resources. Present studies, embodying many uncertainties, produce cost estimates, which are close to those of present power plants. Investment costs (reactor chamber, blanket, magnets, percentage of recirculating power...) will probably be higher, but the fuel is cheap and abundant. Fusion is likely to be a centralised energy source. On the basis of present knowledge, technologically sophisticated power plants will probably have an electrical output larger than 1GW to be economic. The fast neutrons produced in the D-T reaction could be used to produce fissile material in fusion-hybrid breeder reactors [40]. This complementary role for fusion might improve system economics compared with pure fusion systems; however, it would increase societal concerns related to safety, environment and weaponry.

- Cost of fusion research?

Public expenditure on fusion research in the European Community is presently about 500 million Euro per year. Every comparison unavoidably has its disadvantages, but in the case of fusion – being an important possible option for our energy future, generating electricity – it seems fair to compare this number to (i) the present cost of electricity in Europe and (ii) to the investments in other energy systems under development.

Concerning (i): The total electricity bill spent in 2006 in the European Community by end users can be estimated as the product of the net consumption times an average electricity price or roughly $3.3 \cdot 10^9 \text{ kWh} \times 0.1 \text{ Euro/kWh} = 330 \text{ billion Euro}$ [1]. The fusion effort in Europe is thus equivalent to about 0.3% of the yearly European electricity bill. Alternatively one can calculate the cost of fusion research per European citizen: with over 400 million Europeans, the fusion effort comes down to about 1 Euro for every European per year.

Concerning (ii): All funds for fusion research are and have to be public, due to the long period still needed before a fusion reactor can become a commercially available system. These public funds are very well known. For the other energy sources (especially wind and solar), it is not so easy to get a complete picture of the money spent on research as several private companies are contributing with own research investments. In addition, subsidies or tax reductions may be applied to promote these systems, which should be included in the public expenditure on

the system. To illustrate these points and to show that the public expenditure on energy research for the other sources is certainly not less than for fusion, we take the case of Germany. Total investments in fusion research currently are about 150 millions Euro / yr. This number should be compared to the cost alone of subsidising/investing in renewables in Germany in the last 10 years, which is estimated at about 120 billion Euro... [49].

IV. CONCLUSIONS

In a most profound sense, mankind's quality of life depends on an acceptable response to the continually rising demand for energy. To be able to satisfy our future energy needs, we therefore have to invest in all viable energy options, compatible with our environment.

Fusion is one of these options and is characterised by exclusive properties, some of which represent distinct advantages over the other major energy sources. They can be grouped around three aspects:

- **Fuel:** abundant supply of cheap fuels (D and Li); they are non-radioactive, and their extraction does not cause any significant ecological problem.
- **Safety:** fusion reactors offer inherent, passive safety. They are not based on a neutron multiplication reaction and do not contain a large supply of fuel in their core. An uncontrolled burn of the Chernobyl type is excluded.
- **Environment:** Fusion reactions produce energy and no direct radioactive waste. However, in current fusion reactor concepts there is radioactivity from two sources. First, from tritium, which is bred locally from lithium, but consumed directly. Second, by activation of reactor structures by neutrons. Future reactor concepts might strongly limit this radioactivity. Anyhow, by carefully choosing structural materials, the radioactive waste will not constitute a burden for many generations. In addition there is no production of combustion gases. Hence, there is no contribution to the greenhouse effect, to acid rain and to the destruction of the ozone layer.

There should be no illusions about the technical difficulty or the time required bringing even the D-T reaction to a commercially viable system. However, there is no indication up to now to doubt that fusion could be made practical and successful. History has repeatedly proven that major technological projects (not hampered by scientific limits) have finally reached a breakthrough. Who would have believed 80 years ago that highly sophisticated planes would provide transport of passengers across the Atlantic on a large scale and at prices far below those by ship?

Given the potential advantages of nuclear fusion compared to the risks and dangers of all other alternatives for base load electricity generation and given its potential contribution to long-term

sustainable world development, is it not our duty towards future generations to continue the fusion effort without delay and with full commitment?

ACKNOWLEDGEMENTS

Many thanks to Dr.D.Bartlett, Prof.R.Bentley, Dr.A.Pritchard and Ir.K.Mertens for interesting discussions and feedback to this paper. Ms. P.Hickmott is thanked for the careful perusal of the manuscript.

FURTHER READING

1. David JC MacKay, "Sustainable Energy - without the hot air", UIT Cambridge UK (2009), ISBN 978-0-9544529-3-3. Also freely downloadable from www.withouthotair.com. This book provides clear physical arguments on the potential of main renewable alternatives. It is a unique book, with a lucid and didactic style, ideal to prepare (e.g.) an energy discussion with the general public, politicians, policy makers and pressure groups. Very strongly recommended.
2. Bernard L.Cohen, "The nuclear energy option", Plenum Press, New York and London (1990). ISBN-13: 978030643567. A superb and still very actual reference containing a clear and very well documented scientific discussion on all aspects of energy production by nuclear fission. Online at: www.phyast.pitt.edu/~blc/book/BOOK.html
3. John H.Fremlin, "Power Production: What are the risks" Adam Hilger, Bristol and New York (1989), ISBN 0-85274-133-2. A very interesting reference on the risks involved in energy production by renewables, nuclear and fossil burning.
4. Douglas R.O.Morrison, "World Energy and Climate in the Next Century", in Proc. of the 24th Session of the International Seminar on Nuclear War and Planetary Emergencies, Erice (Italy) - August 19-24, 1999, pp.347-387. World Scientific Publishing Co, Singapore (2000), ISBN 981-02-4362-6. A very detailed reference dealing with many issues on energy production, now and in the future.
5. Thomas E.Graedel, Paul J.Crutzen "Atmosphere, Climate, and Change", Scientific American Library, W.H.Freeman and Co, New York and Basingstoke 1997, ISBN-13: 9780716750499. An excellent reference dealing with many aspects of world climate in the past and the difficulties to predict future climate.
6. Kenneth.S.Deffeyes, "Hubbert's peak: The impending World Oil Shortage (New Edition)", Princeton University Press (2009), ISBN13: 978-0-691-14119-0. A clearly written overview of the current status and future evolution of world oil production, for the general public. This important book with its shocking predictions by a geologist and Princeton University professor specialized in petroleum prospecting is not easy to dismiss. Highly

recommended. The 2001 Edition got the Honorable Mention of the Association of American Publishers for Best Professional/Scholarly Book in Geography and Earth Science

7. Vaclav Smil, "Energy at the crossroads", The MIT Press, Cambridge, Massachusetts (2005), ISBN-13: 9780262194921. Overview of various energy options for the future, with interesting (and sometimes particular) views on the applicability of various energy systems in the future.

REFERENCES

[1] "International Energy Annual 2010", US Department of Energy, Energy International Annual (DOE-EIA); see <http://www.eia.gov>

[2] Statistical Tables from the International Energy Agency, available on <http://data.iaea.org>

[3] "World Population Prospects: the 2008 Revision", United Nations Population Division, data up to 2050 available on <http://esa.un.org/unpp/>. For estimates beyond 2050 see the long range report on www.un.org/esa/population/publications/longrange2/Long_range_report.pdf

For an interesting discussion on this subject see the controversial article by M.Singer and the accompanying notes by Jean-Marie Robine, "Vers un monde moins peuplé que les États-Unis", *La Recherche*, **327**, 84-86 (January 2000).

[4] N.Nakicenovic (Editor), Arnulf Grubler (Editor), Alan McDonald (Editor), A. Grubler, A. McDonald "Global Energy Perspectives", IASA and World Energy Council, Cambridge University Press 1998, ISBN 0-521-64569-7

[5] R.Gelbspan, "The Heat is On: The Climate Crisis, The Cover-up, The prescription", updated edition, Perseus Books, Reading Massachusetts (1998) ISBN-13: 9780738200255; original edition reviewed by T. O'Riordan, "Betrayers of a global truth", *Nature*, **389**, 685 (1997).

[6] Masao Tamada, JAEA, in Proc. of the 42th Session of the International Seminar on Nuclear War and Planetary Emergencies, Erice (Italy) – August 19-24, 2009.

[7] "Energy Statistics Yearbook 2006", United Nations, Department of Economic and Social Affairs, New York 2009.

[8] "Statistical Review of World Energy 2009"; see www.bp.com

[9] "Uranium 2005: Resources, Production and Demand", OECD Publishing (2006), ISBN 9789264024250. Read-only available from www.oecdbookshop.org/oecd/display.asp?K=5L9TOF75B3KC&DS=Uranium-2005

[10] K.S.Deffeyes, "Hubbert's peak: The impending World Oil Shortage (New Edition)", ISBN-13: 978-0-691-14119-0, Princeton University Press (2009)

[11] Richard A.Kerr, "The next oil crisis looms large – and perhaps close", *Science*, **281**, 1128-1131 (21 Aug 1998); see also: C.Bond Hatfield "Oil back on the global agenda", *Nature*, **387**, 121 (8 May 1997).

[12] UK Energy Research Centre Study: "Global Oil Depletion" October 2009. See <http://www.ukerc.ac.uk/support/tiki-index.php?page=GlobalOilDepletion>

[13] Dr. Pieter Tans, NOAA/ESRL (www.esrl.noaa.gov/gmd/ccgg/trends/)

[14] F.Joos, "The Atmospheric Carbon Dioxide Perturbation", *Europhysics News*, **27**, 6, 213-218 (1996).

[15] "Climate Change 2007: Synthesis Report" and related reports. (IPCC Fourth Assessment Report) Core editors R.K.Pachauri and A.Reisinger, Cambridge IPCC, Geneva, Switzerland (2007). Available from: www.ipcc.ch/publications_and_data/publications_ipcc_fourth_assessment_report_synthesis_report.htm

[16] D.Reichle, J.Houghton et al., "Carbon Sequestration, State of the Science", US Department of Energy, Office of Science, Office of Fossil Energy, Washington 1999.

[17] M.Verrall, "Climate group rejects criticism of warnings", *Nature*, **371**, 274 (1994); E.Masood, "New IPCC report set to confirm earlier warming conclusions", *Nature*, **377**, 189 (1995)

[18] Several impressive photo compilations became available recently: (i) "Fragile Earth: Views of a Changing Earth", ISBN-13: 9780061137310, HarperCollins Publishers (2006); a summary is available on the web: www.bartholomewmaps.com/fragile_earth_movie/index.html. (ii) "Extreme Ice Survey" by James Balog, www.extremeicesurvey.org; (iii) "Home" by Yann Arthus-Bertrand, www.home-2009.com/us/index.html

[19] J.F.McManus, G.C.Bond, W.S.Broecker, S.Johnsen, L.Labeyrie and S.Higgins; "High-resolution climate records from the North Atlantic during the last interglacial." *Nature*, **317**, 326-329 (1994).

[20] Website of the Royal Society (UK): <http://royalsociety.org/document.asp?tip=0&id=8729>

[21] UK Parliamentary Office of Science and Technology, Postnote 327 (June 2009), www.parliament.uk/parliamentary_offices/post/environment.cfm

[22] David JC MacKay, "Sustainable Energy – without the hot air", UIT Cambridge UK (2009), ISBN 978-0-

9544529-3-3. Also freely downloadable from www.withouthotair.com

[22a] "China: Villagers protest at Zhejiang solar panel plant" BBC News 16 sept 2011, <http://www.bbc.co.uk/news/world-asia-pacific-14963354>

[22b] L. M. Miller, F. Gans, and A. Kleidon, "Estimating maximum global land surface wind power extractability and associated climatic consequences", *Earth Syst. Dynam.*, **2**, 1-12, (2011)

[22c] M. Jefferson, "Energy efficiency and sustainability", Proc. of the 44th Session of the International Seminar on Nuclear War and Planetary Emergencies, Erice (Italy) – August 19-24, 2011.

[22d] Frondel, M., Ritter, N., Schmidt, C.M., Vance, C.: "Economic Impacts from the Promotion of Renewable Energies: The German Experience", 'Energy Policy', **38** 4048 – 4056 (2010)

[23] M. Kleemann, "Aktuelle wirtschaftliche und ökologische Probleme bei der Nutzung regenerativer Energiequellen", *Elektrowärme International*, **49**, Issue A2, A62-70 (Juni 1991) Vulkan Verlag, Essen 1991.

[24] UK Parliamentary Office of Science and Technology, Postnote 268 (October 2006), www.parliament.uk/parliamentary_offices/post/environment.cfm

[25] M. Fuchs, M. Eingartner, "Grenzen der Nutzung regenerativer Energien", in "Kernenergie und andere Energieoptionen: Nutzen, Risiken, Wirtschaftlichkeit", *VDI Berichte*, **984**, 147-168 (1992); H. Schaefer, "Möglichkeiten und Grenzen der Nutzung regenerativer Energien", in "Zukunft der Energieversorgung - Energie der Zukunft", Ruhrgas AG, Essen (1994).

[26] B.L. Cohen, "High level radioactive waste from light-water reactors", *Rev. Mod. Phys.*, **49**, 1-20, (1977); "The Disposal of Radioactive Wastes from Fission Reactors", *Sci. Am* **236**, (6), 21-31 (1977).

[27] G. Collard, R. Andre-Jehan, A. Bonne et al., "The HADES project: an underground demonstration facility for the disposal of high-level waste in plastic clay" in Proceedings of the 3rd European Community Conference on Radioactive Waste Management and Disposal (Luxemburg, 17-21 Sept. 1990), Elsevier Science Publishers, London 1991, 418-436.

[28] C. Rubbia, J.A. Rubio, S. Buono, et al. "Conceptual Design of a fast neutron operated High Power Energy Amplifier", *Report CERN-AT-95-44 (ET)*, Geneva 1995.

[28a] J.P. McBride et al., "Radiological Impact of Airborne Effluents of Coal and Nuclear Plants", *Science*, **202**, no. 4372, 1045 – 1050 (1978).

[28b] Scientific America online, see <http://www.scientificamerican.com/article.cfm?id=coal-is-more-radioactive-than-nuclear-waste&page=2>

[29] W. Haefele et al., "Fusion and Fast Breeder Reactors", Report RR-77-8, International Institute for Applied Systems Analysis, Laxenburg, Austria (1977).

[30] S. Krawczynski and W. Krug, "Schnelle Brüter - ihre Technik und ihre Rolle zur langfristigen Energiebedarfsdeckung", *Chemie-Technik* **8**, (4), 135-142 (1979); A. Camplani and A. Zambelli, "Advanced nuclear power stations: Superphénix and fast-breeder reactors", *Endeavour, New Series*, **10**, (3), 132-138 (1986).

[31] M.W. Golay and N. Todreas, "Advanced Light-Water Reactors", *Sci. Am.*, **262**, (4), 58-65 (1990); J. Taylor, "Improved and Safer Nuclear Power", *Science*, **244**, 318-325 (1989).

[32] Richard F. Mould, "Chernobyl Record: The Definitive History of the Chernobyl Catastrophe", IOP, Philadelphia (2000), ISBN 0-7503-0670-X

[33] Grigori Medvedev, "The Truth about Chernobyl", Basic Books, New York (1992), ISBN 0-465-08776-0

[34] I. Cook et al., "Safety and Environmental Impact of Fusion" Report EFDA-S-RE-1, EUR(01) CCE-FU/FTC 8/5 (April 2001);

[35] P.K. Iyengar, Proc. of the 24th Session of the International Seminar on Nuclear War and Planetary Emergencies, Erice (Italy) – August 19-24, 1999, pp.156-163. World Scientific Publishing Co, Singapore (2000), ISBN 981-02-4362-6

[36] H. Yu Ping, Proc. of the 25th Session of the International Seminar on Nuclear War and Planetary Emergencies, Erice (Italy) – August 19-24, 2000, pp.331-344. World Scientific Publishing Co, Singapore (2001), ISBN 981-02-4669-2

[37] Elsie M. Sunderland et al., "Mercury sources, distribution, and bioavailability in the North Pacific Ocean: Insights from data and models", *Global Biogeochem. Cycles*, **23**, GB2010, doi:10.1029/2008GB003425 (1 May 2009).

[38] J.P. Holdren et al., "Summary of the report of the senior committee on environmental, safety and economic aspects of magnetic fusion energy", *Lawrence Livermore National Laboratory, Report UCRL-53766 (1987)*

[39] R.W. Conn et al. "Economic, safety and environmental prospects of fusion reactors", *Nucl. Fusion*, **30** (1990) 1919.

[40] J. Raeder et al., "Controlled Nuclear Fusion: Fundamentals of its Utilization for Energy Supply", John Wiley & Sons, New York (1986), ISBN-13: 978047110312

[41] J.Wesson, "Tokamaks", Third Edition, Oxford Science Series nr. 118, Clarendon Press, Oxford (2004), ISBN-0-19-850922-7.

[42] A.Loarte, Invited Talk at the ITER Session of the EPS Fusion Conference in Sofia (2009)

[43] J.Jacquinot and the JET Team, "Deuterium-tritium operation in magnetic confinement experiments: results and underlying physics", *Plasma Phys. Control. Fusion*, **41** (1999) A13-A46.

[44] E.Rebhan, "Heisser als das Sonnenfeuer", Piper Verlag, München und Zürich, 1992.

[45] R.Keith Evans, "An abundance of lithium" (July 2008), www.worldlithium.com

[46] R.Keith Evans, "Lithium Reserves and Resources", *Energy*, **3**, 379-385 (1978).

[47] "Status Report on Controlled Thermonuclear Fusion, Executive Summary and General Overview", prepared by the International Fusion Research Council (IFRC), International Atomic Energy Agency, Vienna (1990)

[48] E.E.Bloom, "Structural materials for fusion reactors", *Nucl. Fusion*, **33**, 1879-1896 (1990)

[49] Frankfurter Allgemeine Zeitung, 16 Dec. 1999.

THERMONUCLEAR BURN CRITERIA

Guido Van Oost¹ and Roger Jaspers²

1. *Department Applied Physics*
Ghent University
St. Pietersnieuwstraat 41, B-9000 Gent, Belgium
Guido.Vanoost@ugent.be

2. *Science and Technology of Nuclear Fusion,*
Faculty of Applied Physics,
Eindhoven University of Technology,
P.O. Box 513, 5600 MB Eindhoven, The Netherlands

I. INTRODUCTION

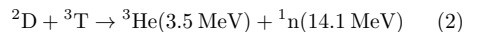
After more than 50 years of fusion research the time has arrived when fusion processes in experimental plasmas are increasingly getting important. In JET the genuine fuel (deuterium-tritium) of a fusion reactor was used for the first time in late 1991, in TFTR the same happened in 1993, and in JET an extended period of experiments of this kind was performed in 1997. Therefore, it is getting more and more rewarding to deal with the problems related to the ignition and burning of plasmas.

Nuclear fusion played and still plays an important role in the Universe. About 1 million years after the big-bang large amounts of ${}^4\text{He}$ were created by the fusion of protons on a global scale, and later on heavier elements were and are created in the huge fusion reactors provided by the interior of the stars. On earth, the concepts envisaged for a fusion reactor are *thermonuclear fusion* by magnetic plasma confinement in tokamaks or stellarators, laser- or beam-induced *inertial fusion*, and muon catalyzed *cold fusion*. In this lecture we shall concentrate on magnetic confinement, in particular on the D-T fusion reaction ${}^2\text{D} + {}^3\text{T} \rightarrow {}^4\text{He} + \text{n}$, which has a mass defect $\Delta m = m_{\text{D}}^+ + m_{\text{T}}^+ - (m_{\text{He}}^+ + m_{\text{n}}) = 3.1 \cdot 10^{-29}$ kg, i.e. about 4 per thousand of the reactant's mass, that according to Einstein's equation $E = mc^2$ corresponds to an energy $E = 17.6$ MeV released as kinetic energy in the reaction products. Starting from the 5 nucleons in the D&T nuclei, this means 3.5 MeV per nucleon or about 4 times the 0.85 MeV which is released per nucleon during the fission of U235. The distribution of fusion energy among the reaction products is determined by the momentum conservation law. Since the momentum of the reaction products is much larger than that of the reaction partners before the reaction, in a D-T reaction we essentially have $m_{\text{n}}v_{\text{n}} = -m_{\text{He}}v_{\text{He}}$.

From this, with $E = mv^2/2$ we immediately obtain

$$E_{\text{n}}/E_{\text{He}} = m_{\text{He}}/m_{\text{n}} = 4 \quad (1)$$

Usually this process is described by the chemical notation



Since the binding energy B of the nucleons (neutrons and protons) must be expended for their separation from the nucleus, it is released in the reverse process, fusion. And since each nucleus possesses *negative* binding energy, its mass is always smaller than the sum of the masses of all neutrons and protons (total number A) of which it consists. In Fig. 1 we see how B/A depends on A . In the range $A \leq 60$ the average binding energy per nucleon can be increased (brought to larger negative values) by the *fusion* of smaller nuclei into larger ones; in the range $A \geq 60$ the same effect is achieved by the fission of larger nuclei into smaller fragments.

While the first fusion reactions had already been observed in 1919 by the physicist Ernest Rutherford, nuclear fission was only discovered in 1938 by the two chemists Otto Hahn and Fritz Strassmann. Nevertheless it was only four years until the physicist Enrico Fermi obtained the first controlled chain reactions in an experimental fission reactor. On the other hand we shall have to wait far into this century until the first fusion reactor will hopefully go into operation. This is an indication of how much more difficult it is to obtain controlled fusion reactions with an net energy gain. The obstacles in nuclear fusion are well illustrated by the following estimate: The energy needed to overcome the Coulomb-wall of mutual repulsion for two hydrogen nuclei is about 0.4 MeV, and the temperature of a plasma needed

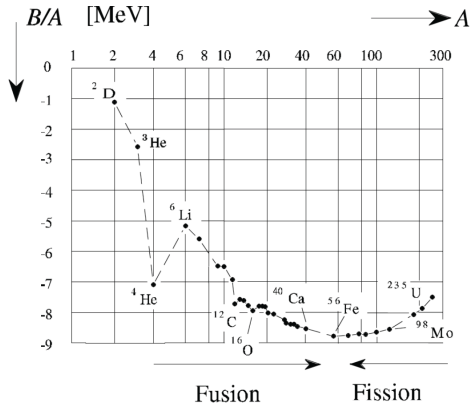


Figure 1: Binding energy per nucleon, B/A , as a function of A

for the particles to achieve this in a classical process with the help of their thermal energies is $T \approx 3 \cdot 10^9$ K. Fortunately the tunnelling effect makes considerably lower temperatures possible. In a D-T reaction the quantum probability for penetrating the Coulomb wall is given by the *Gamow factor*

$$w \approx \exp\left(-34.4\sqrt{\text{keV}/E_{\text{kin}}}\right) \quad (3)$$

For $E_{\text{kin}} = 10$ keV we obtain a tunnelling probability of $w \approx 1.9 \cdot 10^{-5}$, indicating that markedly lower temperatures than the classically required 3 billion Kelvin can lead to fusion. All this is included in the fusion reaction cross-section below (Section II).

According to the curve of binding energies the direct fusion of the ${}^4\text{He}$ -nucleus out of its four nucleons would be even more energetic than the D-T reaction because a total binding energy of 28 MeV would be released in this process, i.e. 7 MeV per nucleon. However, a reaction of this kind would require the simultaneous collision of four nuclei, a process that is so highly improbable at normal densities in magnetic fusion that it practically does not occur. Indeed, as we have seen before, the fusion of two reaction partners is already a rather improbable process, so only two-particle collisions can be envisaged for fusion reactions in a reactor.

Altogether more than 80 different fusion reactions are currently known. Since singly charged nuclei have the lowest Coulomb repulsion, fusion reactions between hydrogen isotopes require the lowest plasma temperatures. The D-T reaction (2) is accompanied by a number of side-reactions, the most important of which are D-D and T-T reactions. However, we will neglect these side reactions because of their small fusion cross-sections.

In the D-T reaction the main portion of the energy is released to the neutron. Although the fast fusion neutrons created this way lead to secondary radioactivity in some materials surrounding the plasma (first wall, supports, etc.), in magnetic confinement schemes this must, at least at present, be considered an advantage. Since they don't carry electric charge the neutrons are not held back by the confining magnetic field, and they can also easily penetrate the confinement vessel. Outside of this their energy can be extracted by a moderator.

II. CROSS-SECTIONS, REACTION RATES AND POWER DENSITY OF FUSION REACTIONS

A fusion reaction which releases a lot of energy but occurs very rarely is of little use. Thus the reaction frequency is a crucial issue. Let us consider a beam of D-nuclei with density n_D , moving at constant relative velocity v through T-nuclei. The number dn_D of beam particles that is lost due to interaction processes such as scattering collisions or fusion reactions when the beam advances by a distance ds is proportional to ds , to the density n_T of target particles and to that of the beam particles, n_D :

$$dn_D = \sigma n_D n_T ds \implies R := \dot{n}_D = \dot{n}_T = n_D n_T \langle \sigma(v) v \rangle, \quad (4)$$

where $\langle \rangle$ denotes the averaging over particles of all possible velocities. R is the *reaction rate* (or the collision frequency in the case of scattering collisions; for both processes independently a corresponding equation applies). σ is the D-T *fusion cross-section*, v the relative velocity between the reacting particles. The evaluation of the average rate coefficient $\langle \sigma(v) v \rangle$ requires some thermodynamics, involves the Gamow factor, and yields the results shown in Fig. 2 for some typical fusion reactions. It is seen that it assumes by far the largest values in the D-T reaction, and this even at much lower temperatures than in the other fusion reactions.

It is only a small fraction of highly energetic particles that are reacting and being lost through fusion (see eq. 3). This tail is repopulated by scattering collisions that cause the plasma to approach a Maxwellian distribution closely. This collisional process for the replacement of highly energetic particles lost by fusion is an essential characteristic of thermonuclear fusion. Thus while scattering collisions have the unpleasant side effect of causing diffusion and particle losses from the reaction vessel on the one hand, on the other hand they have the important task of replenishing highly energetic particles lost by fusion. In a fusion reactor each fusion collision will be accompanied by a sufficiently high number of scattering collisions. Closer investigation shows that at the temperature of a fusion reactor (≈ 10 keV)

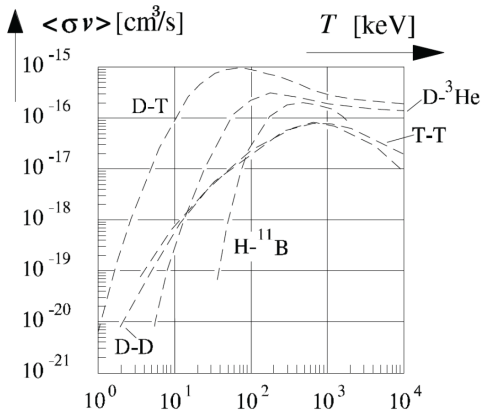


Figure 2: Temperature dependence of the rate coefficient for some typical fusion reactions

on average for each fusion collision there are about 8000 scattering collisions (Note: this is the reason that beam-target fusion concepts will not produce net energy, and a thermonuclear approach is needed).

The quantity which characterizes the efficiency of a fusion reaction is the *power density* P_{fus} , the energy released per second in a unit volume:

$$P_{\text{fus}} = RE_{\text{fus}} = n_{\text{D}}n_{\text{T}}\langle\sigma v\rangle E_{\text{fus}}, \quad E_{\text{fus}} = 17.6\text{MeV} \quad (5)$$

Both ions and electrons exert a pressure p_{i} and p_{e} , respectively, adding to a total pressure p ,

$$p_{\text{i}} = n_{\text{i}}kT_{\text{i}} = (n_{\text{D}} + n_{\text{T}})kT_{\text{i}}, \quad (6)$$

$$p_{\text{e}} = n_{\text{e}}kT_{\text{e}}, \quad p = p_{\text{i}} + p_{\text{e}} \quad (7)$$

Due to stability reasons, there is an upper limit β_{max} to the ratio between average plasma pressure and magnetic pressure

$$\beta = \langle p \rangle / \langle B^2 / 2\mu_0 \rangle \quad (8)$$

From this and (6)-(7) it follows that there is an upper limit to the fusion particle density that for $n_{\text{D}} = n_{\text{T}}n_{\text{i}}/2$ and $n_{\text{e}} = n_{\text{D}} + n_{\text{T}}$ (quasi-neutrality) is given by $\langle \hat{n}_{\text{i}} \rangle \approx \langle B^2 \beta_{\text{max}} / (8\mu_0 kT) \rangle$. The maximum fusion power density associated with this is

$$\hat{P}_{\text{fus}} = \left\langle \frac{B^4 \beta^2}{64\mu_0^2 k^2} \frac{\langle\sigma v\rangle}{T^2} E_{\text{fus}} \right\rangle \quad (9)$$

Figure 3 shows \hat{P}_{fus} for a given β_{max} as a function of the temperature for several fusion reactions. Comparison with Fig. 2 reveals that the highest power output is

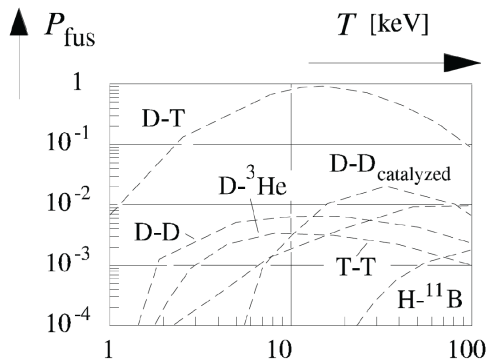


Figure 3: Maximum fusion power density P_{fus} [W/cm³] vs. T .

obtained at a much lower temperature than the maximum value of $\langle\sigma v\rangle$. This is due to the factor $1/T^2$ in \hat{P}_{fus} that, with increasing temperature, causes \hat{P}_{fus} to decrease before $\langle\sigma v\rangle$ has reached its maximum value. Equation (9) also demonstrates the importance of high magnetic fields.

III. BALANCE EQUATIONS

A. Particle balance

A general particle balance equation has the form

$$\partial n_k / \partial t + \text{div}(n_k v_k) = Q_k \quad (10)$$

$n_k v_k$ is the current of particles consisting of a diffusive and a convective part, and Q_k is a local source term. The equation accounts for (a) particle supply, (b) particle gains and losses through the burning of the fuel, and (c) for losses by diffusion and convection. Averaging eq. (10) over the whole plasma volume V (with surface S_V) yields

$$d\bar{n}_k/dt + \int_{S_V} n_k v_k \cdot dS/V = \bar{Q}_k \quad (11)$$

where $\bar{n}_k = \int n_k dV/V$ is the average particle density and $\bar{Q}_k = \int Q_k dV/V$ the average source term. $\int n_K \cdot dV/V = \bar{n}_K \cdot V$ is the total number of particles N_K (i.e. the particle content).

The source term is composed of the fuel losses described by (4) and a term \bar{s}_k accounting for the fuel supply: $\bar{Q}_i = -n_i n_j \langle\sigma v\rangle + \bar{s}_i$. After multiplication with V the total loss of particles per second from the plasma, $dN_k^{\text{loss}}/dt = \int n_k v_k \cdot dS$, yields an average particle loss

rate per volume. This leads to the definition of a particle loss time τ_k through

$$\tau_k = \frac{\bar{n}_k V}{\int n_k v_k \cdot dS} \quad (12)$$

Its precise meaning can be seen from the reformulation

$$\tau_k \int_V n_k v_k \cdot dS = \tau_k dN_k^{\text{loss}}/dt = \bar{n}_k V = N_k$$

Under stationary conditions obtained when all particle losses are compensated for by supply, τ_k is the time elapsed until just as many particles are lost from the plasma through diffusion and convection as it momentarily contains. (We assume that effects of particle recycling[12] are included in τ_k). Assuming approximately equal diffusion loss times, $\tau_i = \tau_j = \tau_p$, and using the approximations

$$\overline{n_i n_j \langle \sigma v \rangle} \approx \bar{n}_i \bar{n}_j \overline{\langle \sigma v \rangle}, \quad \overline{\langle \sigma v \rangle (T)} \approx \langle \sigma v \rangle (\bar{T}) \quad (13)$$

from (11) and (12) we obtain the *burn equations*

$$dn_i/dt = -n_i/\tau_p - n_i n_j \langle \sigma v \rangle + s_i \quad (14)$$

where the volume-averaging bars have been omitted for further convenience. These “zero-dimensional” equations can be improved by taking into account profile effects: For profiles of a given (not self-consistently determined) shape each term is modified by a shape factor (see e.g. Ref. 2).

Equations (14) must be supplemented by the *quasi-neutrality condition*

$$\sum n_k Z_k = n_e \quad (15)$$

in which Z_k is the charge number of ion species k .

B. Energy balance

With the simplifying assumption $T_e = T_D = T_T = T$ (this implies that all ions created by fusion are thermalized) the general energy balance equation has the form

$$\frac{\partial}{\partial t} \frac{3}{2} \left(n_e + \sum_{\lambda} n_{\lambda} \right) kT + \text{div} J = p_{\text{OH}} + p_{\text{ext}} + p_{\alpha} + p_{\text{rad}} \quad (16)$$

where J is the total heat flow current due to heat convection and heat conduction, is the ohmic heating power, p_{OH} the additional external heating power, p_{α} the alpha particle heating power; the work $v_e \cdot \nabla p_e + \sum_{\lambda} v_{\lambda} \nabla p_{\lambda}$ performed by the pressures has been neglected in comparison with the much larger heat source terms.

- Ohmic heating:** At fusion temperatures $P_{\text{OH}} = \eta j^2$ can usually be neglected in comparison with

p_{α} since $\eta \propto 1/T^{3/2}$ (this would not be possible in tokamaks with extremely strong magnetic fields because in these much stronger currents would be allowed).

- External heating:** It is useful to express the external heating power as a fraction of the fusion power through

$$p_{\text{ext}} = p_{\text{fus}}/Q = 5p_{\alpha}/Q \quad (17)$$

Q is called the *power enhancement factor* (see also IV). It is the ratio of the thermonuclear power produced to the heating power supplied and is a measure of the success in approaching reactor condition.

- Alpha particle heating:** In our calculations we shall assume that the energy released to the alpha particles through fusion processes is fully delivered to the plasma through collisions. The heating power thus obtained is approximately given by (5) with E_{fus} replaced by E_{α} , i.e.

$$P_{\alpha} = n_D n_T \langle \sigma v \rangle E_{\alpha} = n_D n_T \langle \sigma v \rangle E_{\text{fus}}/5 \quad (18)$$

This is only an approximation for the following reasons:

- Some alpha particles may already diffuse out, before they have delivered their surplus energy to the plasma.
- The expression for P_{α} is a function of the position and time of alpha particle creation; however, the real position and time of energy deposition are somewhat apart or later respectively. Due to $P_{\alpha} = E_{\text{fus}}/5$ the temperature dependence of P_{α} is the same as that of P_{fus} shown in Fig. 3.

- Radiation losses:** There are radiation losses through *bremstrahlung*, synchrotron radiation, and through line and recombination radiation. At the temperatures of a D-T reactor, 10 – 20 keV, synchrotron radiation can be neglected in comparison with *bremstrahlung*. For *bremstrahlung*, which originates mainly from the acceleration of electrons in the field of ions, we employ the formula

$$P_B = \frac{e^6}{24\pi e_0^3 c^3 m_e h} n_e^2 Z^2 \sqrt{\frac{8kT_e}{\pi m_e}} g_{\text{ff}} \left(\frac{Z^2}{T_e} \right) \quad (19)$$

in which g_{ff} is a slowly varying function of its argument called *Gaunt-factor* (accounting for quantum effects). In the D-T reaction there are separate contributions of this kind from D and T with charge number $Z = 1$ and from ${}^4\text{He}$ with $Z = 2$ (helium

is fully ionised under reactor conditions).

In a pure D-T plasma line and recombination radiation do not play an essential role except for the much cooler plasma boundary region, because all ions are fully ionized and the central plasma is too hot for recombinations. The situation is different if the plasma is polluted by nuclei of higher charge number. We shall only rather crudely take into account such radiation, employing for it again eq. (19) with some effective charge number for the impurities.

5. **Transport losses:** Integrating the heat flow J through diffusion and convection of energy over the plasma boundary yields the total energy losses by transport.

By analogy with (12) we introduce an *energy confinement time* τ_E through

$$\tau_E = \frac{\int_V \frac{3}{2} (n_e + \sum_\lambda n_\lambda) kT \cdot dV}{\int_{S_V} J \cdot dS} \quad (20)$$

Frequently, especially by experimentalists, a different energy confinement time τ_E^* (called global confinement time) is used that is defined through

$$\tau_E^* = \frac{\int_V \frac{3}{2} (n_e + \sum_\lambda n_\lambda) kT \cdot dV}{P_{\text{rad}} + \int_{S_V} J \cdot dS} \quad (21)$$

It is the time in which the plasma, due to all losses including radiation, loses the same amount of energy as it presently contains and is easier to measure than τ_E .

6. **Averaged energy balance equation:** Integrating eq.(16) over the whole plasma volume, dividing by V and using (17), (20) plus the same approximations as in (13), with omission of the bar for averages we obtain

$$\begin{aligned} \frac{d}{dt} e_{\text{tot}} = P_\alpha \left(1 + \frac{5}{Q} \right) - \frac{e_{\text{tot}}}{\tau_E} - P_{\text{rad}} = \\ P_\alpha \left(1 + \frac{5}{Q} \right) - \frac{e_{\text{tot}}}{\tau_E^*} \end{aligned} \quad (22)$$

Where $e_{\text{tot}} = (n_e + \sum_\lambda n_\lambda) kT$ is the total energy density and the expressions for P_α and P_{rad} must be evaluated at the average temperature and density.

C. Basic equations for the D-T reaction

We now make a further approximation in neglecting all side reactions (D-D, T-T etc.) due to their small fusion cross-sections. With this we obtain from (14) the *particle balance equations*

$$\frac{dn_D}{dt} = -\frac{n_D}{\tau_p} - n_D n_T \langle \sigma v \rangle_{DT} + s_D \quad (23)$$

$$\frac{dn_T}{dt} = -\frac{n_T}{\tau_p} - n_D n_T \langle \sigma v \rangle_{DT} + s_T \quad (24)$$

$$\frac{dn_\alpha}{dt} = -\frac{n_\alpha}{\tau_\alpha} - n_D n_T \langle \sigma v \rangle_{DT} \quad (25)$$

and from (22) and (18) the energy balance equation

$$\begin{aligned} \frac{d}{dt} \left[\frac{3}{2} (n_e + n_I + n_\alpha + n_Z) kT \right] = \\ -\frac{3}{2} (n_e + n_I + n_\alpha + n_Z) kT / \tau_E \\ + n_D n_T \langle \sigma v \rangle_{DT} E_\alpha (1 + 5/Q) - P_B \end{aligned} \quad (26)$$

where n_I is the total number of ions and n_Z is the density of impurity ions considered as a single species with effective charge number Z . We shall consider n_Z as a given parameter. In contrast to our previous intentions, we have introduced a separate particle confinement time $\tau_\alpha \neq \tau_p$ for the alpha particles, the purpose being that this will facilitate the transition to a limiting case to be considered (see IV.A). In addition, we have the quasi-neutrality condition

$$n_I + 2n_\alpha + Zn_Z = n_e = n_{\text{tot}}/2 \quad (27)$$

For P we have to take into account the radiation caused by hydrogen isotopes ($Z = 1$), alpha particles ($Z = 2$) and impurities (charge number Z), from (19) obtaining the formula

$$P_B = n_e^2 [c_I R_I(T) + c_\alpha R_\alpha(T) + c_Z R_Z(T)] \quad (28)$$

in which we employed the concentrations

$$c_I = \frac{n_I}{n_e}, \quad c_\alpha = \frac{n_\alpha}{n_e}, \quad c_Z = \frac{n_Z}{n_e} \quad (29)$$

and where

$$\begin{aligned} R_I = C_B \sqrt{T} g_{ff}(1/T), \quad R_\alpha = 4C_B \sqrt{T} g_{ff}(4/T), \\ R_Z = Z^2 C_B \sqrt{T} g_{ff}(Z^2/T) \end{aligned} \quad (30)$$

with

$$C_B = \frac{e^6 \sqrt{8k}}{24\pi \epsilon_0^3 c^3 m_e h \sqrt{\pi m_e}} \quad (31)$$

IV. EQUILIBRIA: BREAK-EVEN AND IGNITION

We now want to determine equilibria, i.e. we are looking for stationary solutions $d/dt = 0$. When an equilibrium is achieved with $P_{\text{ext}} = P_{\text{fus}}$ or $Q = 1$ resp. this is called *break-even*. *Ignition* (notice the analogy with the burning of fossil fuels) is achieved when all external heat sources can be turned off, $P_{\text{ext}} = 0$ or $Q = \infty$. The confinement conditions are then such that the plasma temperature can be maintained against the

energy losses solely by α -particle heating. From (23)-(24) for stationary conditions we get

$$\begin{aligned} s_D &= \frac{n_D}{\tau_p} + n_D n_T \langle \sigma v \rangle_{DT} + s_D, \\ s_T &= \frac{n_T}{\tau_p} + n_D n_T \langle \sigma v \rangle_{DT} + s_D \end{aligned} \quad (32)$$

the magnitude of the particle sources is fixed by the requirement of stationarity. The maximum fusion power is obtained for $n_D = n_T = n_I/2$ (see II), i.e. the particle sources must satisfy

$$s_D = s_T = \frac{n_I}{2\tau_p} + \frac{n_I^2}{4} \langle \sigma v \rangle \quad (33)$$

With this equations (23) and (24) are satisfied and must no longer be considered concerning equilibrium.

The remaining equations to be solved are (25), (26) and (15) viz

$$c_I + 2c_\alpha + Zc_Z = 1 \quad (34)$$

The latter one is satisfied when we eliminate c_I by using $c_I = 1 - 2c_\alpha - Zc_Z$. Inserting this we are left with only two equations (for particles and energy respectively),

$$\frac{c_\alpha n_e}{\tau_\alpha} = \frac{1}{4} (1 - 2c_\alpha - Zc_Z)^2 n_e^2 \langle \sigma v \rangle, \quad (35)$$

$$\begin{aligned} \frac{3}{2} [2 - c_\alpha - (Z - 1)c_Z] n_e kT / \tau_E &= \\ \frac{1}{4} (1 - 2c_\alpha - Zc_Z)^2 n_e^2 \langle \sigma v \rangle E_\alpha (1 + 5/Q) - P_B \end{aligned} \quad (36)$$

A. Ideal ignition condition, minimum burn temperature, and ideal break-even

In a first quantitative approach we shall neglect the presence of impurities as well as that of the helium ash, i.e. we set $c_\alpha = 0$, $c_Z = 0$. This way we not only get a widely used result for the ignition condition but also one which is very easily comprehensible. Of course this can only be a rough approximation because the accumulation of helium ash can, in principle, not be avoided. $c_\alpha = 0$ is compatible with the equilibrium equations if in (35) we set τ_α and don't consider this equation any longer. (This is the reason why we introduced a separate confinement time τ_α .) For the bremsstrahlung we have $P_B = n_e^2 R_I(T)$ and the only equation left is the energy equation (36) which becomes

$$3n_e kT / \tau_E = \frac{1}{4} n_e^2 \langle \sigma v \rangle E_\alpha (1 + 5/Q) - n_e^2 R_I(T) \quad (37)$$

Dividing it by n_e^2 and then solving it with respect to $n_e \tau_E$ we finally obtain the ideal ignition criterion

$$n_e \tau_E = \frac{3kT}{\frac{1}{4} \langle \sigma v \rangle E_\alpha (1 + 5/Q) - R_I(T)} \quad (38)$$

The product $n_e \tau_E$ is a measure of the quality of the plasma confinement, and the value required according to this formula in order to get an ignited equilibrium or break-even depends only on the temperature. This temperature dependence is shown in Fig. 4. The minimum temperature required for ignition ($Q = \infty$) is obtained by equating the denominator of our result for $n_e \tau_E$ to zero (becoming infinite). It is given by the smaller temperature obtained as a solution from

$$R_I(T) = \frac{1}{4} \langle \sigma v \rangle E_\alpha \quad (39)$$

and is typically about 6 keV.

We shall now transform the ideal ignition curve into a diagram employing our second energy confinement time τ_E^* defined in (21). Applying this definition,

$$P_{\text{rad}} + e_{\text{tot}} / \tau_E = e_{\text{tot}} / \tau_E^* \quad (40)$$

to the present situation yields

$$n_e^2 R_I + 3n_e kT / \tau_E = 3n_e kT / \tau_E^* \quad (41)$$

$$\tau_E = \frac{3kT \tau_E^*}{3kT - n_e \tau_E^* R_I} \quad (42)$$

Since τ_E must be nonnegative, from this we get the condition

$$n_e \tau_E^* \leq 3kT / R_I \quad (43)$$

The limit $n_e \tau_E^* \leq 3kT / R_I$ is called *radiation limit* because $\tau_E = \infty$ for it, and all losses are due to radiation. With (42) and multiplication by T the condition (38) transforms into

$$n_e \tau_E^* T = \frac{12kT^2}{\langle \sigma v \rangle E_\alpha (1 + 5/Q)} \quad (44)$$

The so-called *fusion product* $n_e \tau_E^* T$ employed in this formula is widely used for characterizing the performance of a fusion device because it combines the two quantities $n_e \tau_E^*$ (also a measure for the quality of confinement) and T , which both have to be large for ignition, into a single quantity. Its temperature dependence is shown in Fig. 4 together with the radiation limit. According to (43) only states below the radiation limit are physically meaningful. The two intersection points between the radiation limit and the ignition curve describe *radiative equilibria*. The temperature at the left point is the minimum temperature for which ignition is possible (about 4.4 keV). Please note that this is only true for plasmas which are transparent for the radiation losses considered; the *sun* burns at lower temperatures. In the temperature range of a fusion reactor a good approximation for $\langle \sigma v \rangle$ is provided by [13]

$$\langle \sigma v \rangle = 1.1 \times 10^{-24} T^2 \text{ ms}^{-1}, \quad T \text{ in eV} \quad (45)$$

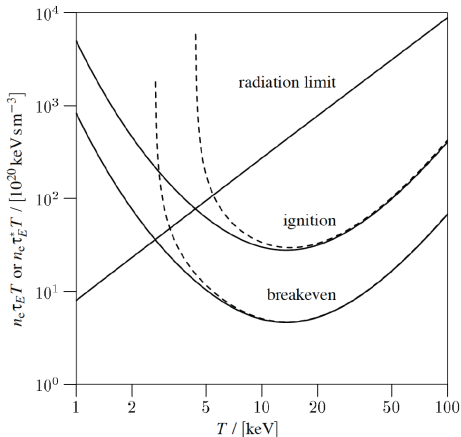


Figure 4: Curves $n_e \tau_E T = f_1(Q; T)$ (dashed lines) and $n_e \tau_E^* T = f_2(Q; T)$ (solid lines) for ideal ignition and ideal break-even. Also shown is the radiation limit (only relevant for the description by τ_E^*). (Figure adapted from Ref. [2].)

Inserting this in (44) yields the ideal conditions $n_e \tau_E^* T = 3 \cdot 10^{21} \text{ m}^{-3} \text{ keV s}$ for ignition, e.g. reached with $n = 10^{20} \text{ m}^{-3}$, $T = 10 \text{ keV}$ and $\tau_E^* = 3 \text{ s}$, and $n_e \tau_E^* T = 0.5 \cdot 10^{21} \text{ m}^{-3} \text{ keV s}$ for break-even.

B. Non-ideal ignition and break-even

We shall now discuss the influence of the helium ash and impurities on the conditions for ignition and break-even.

For $\tau_\alpha \neq 0$ from (35) we also get $c_\alpha \neq 0$, and since according to (15) each α -particle displaces two fuel particles and according to (19) radiates twice as much as the two together, too high alpha particle concentrations will inevitably cause the nuclear fire to suffocate. Thus, welcome as they are with respect to heating, the alpha particles may lead to a dangerous fuel dilution and provide a rather unpleasant pollution if they become too numerous. It is therefore important that they disappear due to diffusion and convection, thereby unfortunately being accompanied by fuel particles.

Diffusion and convection are the only loss mechanisms for particles, and there is no mechanism that could be compared with the loss of energy by radiation. Although the mechanisms of particle and of energy diffusion are quite different, there is a strong coupling between them. The scaling ansatz [1, 2]

$$\tau_p / \tau_E = \rho = \text{const.} \quad (46)$$

appears as a good approximation for the helium ash particles in the plasma core because in this particular

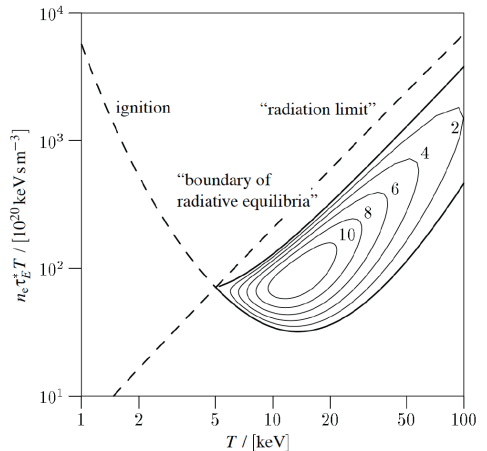


Figure 5: Curves $n_e \tau_E^* T = f(T)$ for non-ideal ignited equilibria, radiation limit, and boundary of radiative equilibria assuming an impurity concentration of $f_Z = 2\%$ beryllium ($Z = 4$). (Fig. adapted from Ref. [2].)

case (distinct from other species in the plasma) the particle and energy source profiles are identical. Since particles are somewhat better confined than energy, a value ≥ 5 is expected for the ratio.

The statements made above can now be quantified by solving equations (35)-(36) together with (28) and the scaling ansatz (46). After c_α is eliminated from the equations, one can again derive an equation for $n_e \tau_E T$ this time as a function of T and ρ , that can be put into the form [2]

$$\rho = \rho(n_e \tau_E T, T) \quad (47)$$

Figure 5 shows the ignition curves $\rho = \text{const}$ numerically obtained from this for $Q = \infty$. For $\rho = 0$ (corresponding to $\tau_\alpha = 0$) our previous ideal curves are recovered. For $\rho > 0$ one obtains closed ignition curves, and it was shown in Ref. [2] that one also obtains closed ignition curves for $n_e \tau_E^* T(T)$ if the scaling assumption (46) with τ_E is being kept. The most important outcome of these calculations is that ignited equilibria exist in a pure D-T plasma only for $\rho \leq 15$ (or $\rho \leq 10$ for an impurity concentration of 2% beryllium). If ρ becomes larger, the helium concentration becomes too large and ignition is impossible as predicted by our qualitative arguments. However, the helium concentration requirement is relaxed if elastic scattering by collisions between helium and D/T ions are taken into account [3]. The ignition curves shrink in size with ρ even faster with increasing Z and c_Z . Modelling of impurity seeded ITER discharges [7] has shown that the interplay be-

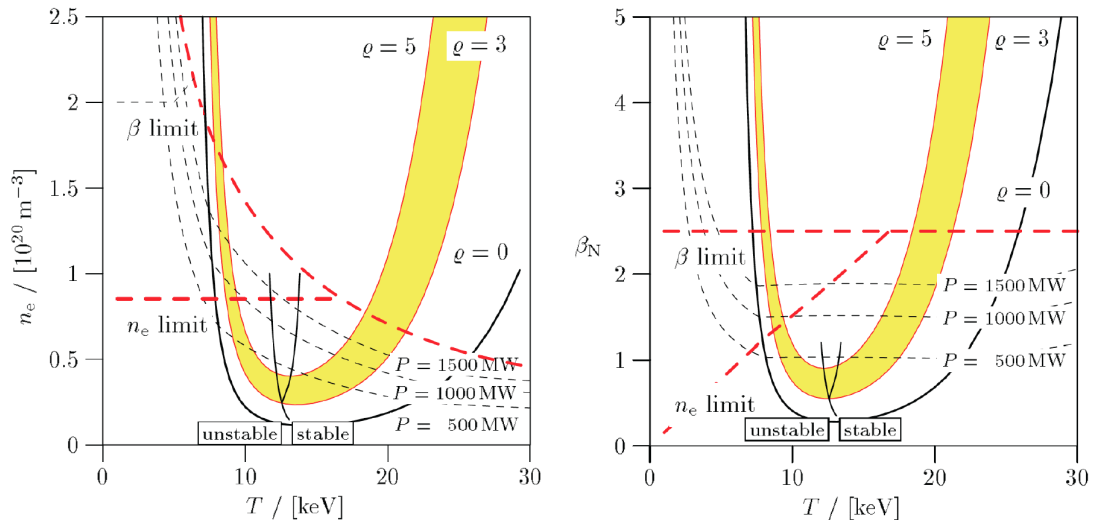


Figure 6: Ignition curve $\rho = 5$ (together with curves $\rho = 3$ and 0 for comparison) (a) in a n_e, T -plane and (b) in a β_N, T -plane. $\beta_N = \beta/(I/aB)$ is the so-called normalized beta). In both diagrams the boundary of stability with respect to thermal instabilities is also shown. The stable regime is to the right of all stability curves. (Figures taken from Ref. [11].).

tween He and sputtered impurities may under certain circumstances result in a rather weak dependence of Q on He confinement. This would relieve the concern about helium ash removal.

V. ITER CONFINEMENT SCALING LAWS AND TRANSFORMATION OF IGNITION CURVES TO THE N, T AND β, T PLANE

The initially designed Ignition ITER has been replaced by a High- Q ITER, the construction of which in Cadarache has been decided in June 2005. The design of the High- Q ITER does not preclude the possibility of ignition but the objective is extended burn with $Q \geq 10$ and with a duration sufficient to reach stationary conditions with respect to the characteristic time scales. Furthermore, the design also aims at demonstrating steady-state operation using non-inductive current drive with $Q > 5$.

For the planning of a burning plasma experiment like ITER it is important to have some idea about what confinement properties may be expected. Theoretically plasma transport is a very difficult and not yet satisfactorily solved problem, so the answers to this question must be essentially extrapolated from experimental data. In huge international databases the transport properties of many different tokamaks under many

different circumstances have been collected and evaluated, applying as constraints certain theoretical criteria [13, 4, 5]. One expects that the energy confinement time τ_E will depend on design parameters according to scaling laws such as ITER 89-P [6],

$$\tau_E = 0.048 f_H M^{0.5} I^{0.85} B^{0.2} R^{1.2} a^{0.3} \kappa^{0.5} P^{-0.5} n_e^{0.1} \quad (48)$$

where f_H is the H-mode enhancement factor ($f_H = 2.0$ in Fig. 6), M the isotopic mass (2.5 for a 50:50 D-T mixture), I the plasma current in MA, B the toroidal magnetic field in Teslas, R and a the major and minor tokamak radius in meters, κ the elongation of the plasma cross-section, n_e the electron density in 10^{20} m^{-3} , and $P = P_{QH} + P_{ext} + P_\alpha$ the net heating power in MW. Using the equilibrium equation (36), P can be replaced by $\frac{3}{2} n_{tot} T / \tau_E$ and (48) rewritten as:

$$\tau_E = (0.048 f_H M^{0.5} I^{0.85} B^{0.2} R^{1.2} a^{0.3} \kappa^{0.5})^2 n_e^{-0.8} T^{-1.0} \quad (49)$$

With this relation the ignition contours (47) can be translated from the $n_e \tau_E T, T$ -plane directly into the n_e, T -plane (for details see Ref. [10]; note, however, that there the ITER scaling laws were applied to the energy confinement time τ_E^* including radiation losses). Fig. 6(a) shows the ‘‘ignition curve’’ $\rho = 5$ (together with $\rho = 3$ and $\rho = 0$ for comparison) in a n_e, T -plane, and using $\beta = n_{tot} k T B^2 / 2 \mu_0$ a similar diagram can be

obtained in the β, T -plane (see Fig. 6(b)). The advantage of representing the ignition curve as $n_e = n_e(T)$ or $\beta = \beta(T)$ is that the impact of plasma stability limits like the β -limit or the Greenwald density limit can immediately be seen.[8]

VI. BURN STABILITY

In order to determine the stability of the burn equilibria with respect to thermal instabilities one has to solve the time dependent equations (23)-(27) for perturbations of the equilibrium states. This has extensively been done in Ref. [10], and here only the most important results are quoted. One problem arising in this context is, how to treat the confinement times during the evolution of instabilities. One possibility would be to keep them constant at their equilibrium values. Since the typical growth times of instabilities turn out to be several seconds under this assumption, it appears reasonable to assume the validity of the scaling law (49) also during this time dependent process because the plasma has time enough to adapt to these conditions which were originally derived for equilibrium states. Redoing the stability calculations with these adapted confinement times appreciably changes the stability behaviour, which for this case is shown in Figs. 6 (a) and (b). Stable behaviour is obtained to the right of the stability boundaries shown in the diagram. States to the left are unstable and undergo a transition to some state on the right branch of the corresponding ignition curve $\rho = \text{const.}$

VII. LAWSON CRITERION AND REACTOR EFFICIENCY CRITERION

If the plasma of a fusion reactor is ignited, this does not imply that there is also a net energy gain, because there are energy losses during the initial heating phase, and also energy is needed for feeding auxiliary devices to keep the reactor running. The first one to consider problems of this kind was Lawson who, in 1957, formulated the so-called *Lawson criterion*[9]. He asked the question: When does a fusion reactor deliver so much energy that it can run self-sustained, i.e. when does it neither need nor deliver energy? However, in this calculation Lawson neglected -particle heating, assumed that the plasma was heated from an external source, took for the discharge pulse length, and took only account of hydrogen bremsstrahlung radiation (which is small in a tokamak plasma).

In order to answer Lawsons question, we consider the sum of the internal plasma energy and the energy

released in the form of radiation and fusion energy during the burn time, all expressed as specific quantities per volume,

$$e_{\text{th}} + e_{\text{rad}} + e_{\text{fus}} \quad (50)$$

$$e_{\text{th}} = 3n_e kT, \quad e_{\text{rad}} = C_{B\text{gff}} n_e^2 \sqrt{T} \tau_b$$

$$e_{\text{fus}} = \frac{1}{4} n_e^2 \langle \sigma v \rangle E_{\text{fus}} \tau_b \quad (51)$$

This sum of energies is converted with efficiency η_{th} , and in a self-sustained power station it supplies the thermal energy of the plasma and the radiation losses:

$$(e_{\text{th}} + e_{\text{rad}} + e_{\text{fus}}) \eta_{\text{th}} = e_{\text{th}} + e_{\text{rad}} \quad (52)$$

After the explicit expressions for the different energy terms are inserted, one can solve with respect to $n_e \tau_b$ to obtain the *Lawson criterion*

$$n_e \tau_b \frac{12kT}{\langle \sigma v \rangle E_{\text{fus}} \eta_{\text{th}} / (1 - \eta_{\text{th}}) - 4C_{B\text{gff}} n_e^2 \sqrt{T}} \quad (53)$$

Similarly one can ask the question: When does a reactor yield the efficiency η ? In order to answer this question we assume a pulsed operation of the reactor with a start-up phase of duration τ_h for heating the plasma to ignition, and a burning time τ_b with stationary conditions at temperature T . In the start-up phase for each volume element a heating energy e_h must be supplied externally, from which a fraction

$$e_\alpha = \eta_\alpha e_h \quad (54)$$

is absorbed by the plasma for providing its internal energy and compensating all heat losses (transport and radiation). The net efficiency of the power station is defined through:

$$\eta = e_{\text{net}} / e_{\text{fus}} \quad (55)$$

where e_{fus} is the total fusion energy gain per volume (at present, probably not all fusion energy delivered to the alpha particles can be envisaged for conversion), and e_{net} is the energy per volume that can be supplied to the mains as electricity. Considering all important energy flows in the reactor station, the following *reactor efficiency criterion* can be derived:

$$n_e \tau_b = \frac{1}{\eta_\alpha (\eta_{\text{eff}} - \eta)} \frac{12kT(1 + \tau_h / \tau_{E,h}^*)}{\langle \sigma v \rangle E_{\text{fus}}} \quad (56)$$

where $\eta_{\text{eff}} \approx \eta_{\text{th}} \approx 1/3$. We can combine this efficiency criterion with the corresponding ideal ignition criterion (44). Dividing the first by the second yields (for $Q = \infty$)

$$\frac{\tau_b}{\tau_E^*} = \frac{(1 + \tau_h / \tau_{E,h}^*)}{5\eta_\alpha \eta_{\text{eff}} (1 - \eta / \eta_{\text{eff}})} \quad (57)$$

where $E_\alpha / E_{\text{fus}} = 1/5$ was used. This shows that the factor by which the burning time τ_b must exceed the

energy confinement time τ_E^* is independent of the temperature.

Assuming $\tau_h \approx \tau_{E,h}^*$ and $\eta_a/\eta_{\text{eff}} \approx 1/20$ we get $\tau_b \approx 8\tau_E^*/(1 - \eta/\eta_{\text{eff}})$. For $\eta = \eta_{\text{eff}} = 0.95$ this yields $\tau_b \approx 160\tau_E^*$ or $\tau_b \approx 560\text{s}$ for $\tau_E^* = 3.5\text{s}$ as expected in a fusion reactor.

In fact much longer burn times will be required for other reasons: A reactor must last for about 25 years at least in order to repay for the large expenses that are needed for its construction. A burn time of 200 s only would imply about 4×10^6 start-ups and thus changes between hot and cold during its lifetime. This is more than the reactor will stand according to all technical experience. A reasonable number of changes will be no more than about 100 000. In that case a burning cycle would have to last for about 2 h in order to sum up to a life time of 25 years.

REFERENCES

- [1] G. H. WOLF D. REITER and H. KEVER. Burn condition, helium particle confinement and exhaust efficiency. *Nucl. Fusion*, (30):2141–2155, 1990.
- [2] D. REITER E. REBHAN, U. VIETH and G. H. WOLF. Effect of helium concentration on ignition curves with energy confinement time including radiation losses. *Nucl. Fusion*, (36):264–269, 1996.
- [3] H.KUBO et al. The spectral profile of the he i single line (667.82 nm) emitted from the divertor region of jt-60u. *Plasma Phys. Control.Fusion*, 41: 747–757, 1999.
- [4] J. P. CHRISTIANSEN et al. Global energy confinement h-mode database for iter. *Nucl. Fusion*, (32):291–338, 1992.
- [5] K. THOMSEN et al. Iter h-mode confinement database update. *Nucl. Fusion*, (34):131–167, 1994.
- [6] P. N. YUSHMANOV et al. Scalings for tokamak energy confinement. *Nucl. Fusion*, (30):1999–2006, 1990.
- [7] R.ZAGORSKI et al G.TELESCA. Modelling of radiative power exhaust by sputtered and seeded impurities in fusion reactors with carbon and molybdenum target plates. *Nucl. Fusion*, (30):1625–1637, 2007.
- [8] H.R. KOSLOWSKI. Operational limits and limiting instabilities in tokamak machines. this volume.
- [9] J. D. LAWSON. Some criteria for a power producing thermonuclear reactor. *Proc. Phys. Soc.*, B 70: 6–10, 1957.
- [10] REBHAN and U. VIETH. Burn stability and safe operating regime of a tokamak reactor with iter scaling. *Nucl. Fusion*, 37:251–270, 1997.
- [11] E. REBHAN and U. VIETH. Parameter dependence of the operating regime and performance of d-t tokamak reactors in a current-versus-size diagram. In *Proc. 24th Eur. Conf. Berchtesgaden*, volume 21A, page 1029, 1997.
- [12] D. REITER. Recycling and transport of neutrals. this volume.
- [13] J. WESSON. *Tokamaks*. Oxford Engineering Science Series No. 48. Clarendon Press, third edition edition, 2004.

FUSION MACHINES

M. Van Schoor and R. R. Weynants
*Laboratory for Plasmaphysics,
Association 'Euratom-Belgian state',
Ecole Royale Militaire - Koninklijke Militaire School,
B-1000 Brussels, Belgium*

ABSTRACT

A concise overview is given of the principles of inertial and magnetic fusion, with an emphasis on the latter in view of the aim of this summer school. The basis of magnetic confinement in mirror and toroidal geometry is discussed and applied to the tokamak concept. A brief discussion of the reactor prospects of this configuration identifies which future developments are crucial and where alternative concepts might help in optimising the reactor design. The text also aims at introducing the main concepts encountered in tokamak research that will be studied and used in the subsequent lectures.

I. INTRODUCTION

Very soon after the discovery of nuclear fission in 1938, the possible peaceful application of this new source of energy was recognised and commercial power plants became available. Stimulated by this success, first concepts for the peaceful use of fusion energy emerged well over 50 years ago. In his opening speech to the first Conference on the Peaceful Uses of Atomic Energy held in Geneva in 1955, H.J. Bhabha ventured to predict that " *a method will be found for the liberating fusion energy in a controlled manner within the next two decades*". Nevertheless, some people at least were aware of the severe problems that would have to be solved. Indeed, in the first article on the fusion issue published in 1956, R.F. Post wrote; " *However, the technical problems to be solved seem great indeed. When made aware of these, some physicists would not hesitate to pronounce the problem impossible of solution*".

Despite the latter statement, but well aware of it, a world wide R & D campaign was launched to develop a nuclear fusion reactor. Surprisingly the basic concepts, which nowadays are considered to be the most successful and promising, had already been published at that time, albeit of course without all the plasma physics knowledge available today and without the techniques and insights needed for a proper scale demonstration[1].

Two main lines are pursued towards the realisation of thermonuclear fusion: inertial (ICF) and magnetic confinement (MCF). In both cases, a burn criterion must be satisfied which requires that a minimum quantity of fuel, represented by the fuel density n , be maintained together for a minimum time span τ_E (the energy confinement time) at a sufficiently high temperature T , brought

together in the fusion triple product $n\tau_E T$. Both of these lines have achieved considerable progress in recent years and in both instances the prospects for successful reactor application have been strengthened. In this lecture the basic principles of each of these lines are given, followed by a more in depth discussion of the configurations in which magnetic fusion research is pursued, with special emphasis on the tokamak

II. INERTIAL CONFINEMENT

Inertial confinement fusion[2] (ICF) uses laser or particle beams (called drivers) to heat frozen D-T pellets (radius R), either directly or indirectly via conversion into X-rays, to the necessary fusion temperatures[2]. The heating pulses are typically 1 to 10 ns long. A reactor based on this concept is inherently pulsed and, hence, the basic reactor requirement should be to produce a substantial target gain G , defined as the energy yield of the fusion reactions divided by the energy of the driver. High yield depends on the number of fusion reactions that can occur in the time before the fuel disassembles i.e. during the time the fuel is confined on account of its finite mass. A good approximation for the inertial confinement time τ_E is then the time it takes for an ion to move over the distance R , at its thermal speed V_{thi} , taken as the sound speed $\sqrt{kT/m}$. The ICF burn criterion is known as the ρR -criterion, also called the high-gain condition, and is essentially obtained by requiring that almost all the fuel contained in the pellet is indeed burned, i.e. that the number of reactions that take place during the time interval τ_E equals the number of fuel deuterons or tritons. The standard form reads[3]:

$$\rho R \geq 4\sqrt{mkT} < \sigma v >^{-1} \quad (1)$$

where m is the mean ionic mass, the mass density $\rho = nm$, and $< \sigma v >$ is the fusion reaction rate constant. For D-T $\rho R \geq 3g/cm^2$ at $T = 50keV$. The ρR -criterion can also be rewritten in terms of density and confinement time, as $n\tau_E = < \sigma v >^{-1}$. The triple product that results from this puts the reactor requirement typically 10 times higher than what is asked for MCF, a consequence of the inherent inefficiency in assembling the fuel. Please note also that in ICF the term ignition does not have the same meaning as in MCF, as it refers to the condition of efficient α -particle capture, a ρR value of at least $0.3g/cm^2$ being required to slow the α -particles down in the pellet[4].

Since DT-ice has a mass density $\rho = 0.2g/cm^3$, satisfying the ρR -criterion asks for massive targets, requiring for their heating unattainable amounts of driver energies. An escape from this apparent impasse is however possible. By compression of the pellet, ρ can be increased significantly. An increase by, for instance, a factor of 1000 would lower the energy demand by 10^6 , thus bringing it in the range of what is technically achievable. In addition, it is not obvious that the total amount of heat that is needed to bring the fuel to fusion temperatures must be provided by the lasers or beams. It might be enough to ignite a fraction of the pellet and let the fusion energy, thus liberated, heat the rest. The latter requirement is also dictated by considerations of the energy economy of the scheme. It is easy to show that the intrinsic gain G_i of a uniformly heated D-T pellet, defined as the ratio of the energy liberated by fusion to the energy needed to reach the fusion conditions, is at most about 200. The efficiencies in the external systems of the power plant and the low efficiencies of the driver generation, ask for reactor target gains of about 100. Noting that $G = \eta_T G_i$ requires in turn intrinsic gains of about 10^4 to account for a realistic coupling efficiency T of the driver. For inertial confinement to be attractive, it is therefore mandatory to demonstrate that it is possible to burn the whole pellet after bringing just a small fraction to ignition temperature at the densities imposed by the ρR -criterion. The reader is referred to Refs. [2]-[4] for more details on pellet compression and hot spot creation.

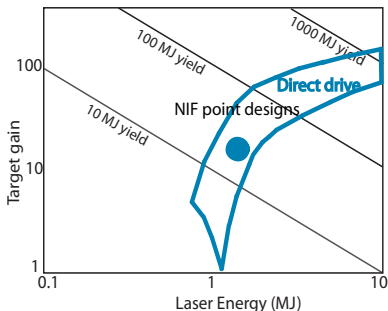


FIG. 1: Expected path of ICF towards achieving ignition and high gain.

Experiments show that satisfying Eq.(1) might be sufficient to achieve the high values of G needed. Figure 1 shows the calculated target gain as a function of direct drive energy [4, 5]. Based on the experimental progress and on the steady advances in system efficiency, it is predicted that ignition should be possible with a driver energy of $0.5 - 1 MJ$, whereas high gain reactor operation becomes feasible with a $5 - 10 MJ$ of driver energy. The projected operation point of the US National Ignition Facility (NIF), presently under construction[6] and in which ignition is predicted, is also shown.

III. ICF CONFIGURATIONS

At the heart of an inertial fusion explosion is a target that has to be compressed and heated to fusion conditions by the absorption of energy carried by a driver. For the so-called direct drive, the target consists of a spherical capsule that contains the DT fuel (Fig. 2b). For indirect drive, the capsule is contained within a cylindrical or spherical metal container or hohlraum which converts the incident driver energy into X-rays that then drive the capsule implosion (Fig. 2a). The drivers can be lasers, heavy ion beams or so-called Z-accelerators. The latter consists of a huge array of separate pulsed power devices timed to fire, all to within ten billionths of a second, a current of tens of millions of amperes into two spool-of-thread-sized arrays of 100 to 400 wires, symmetrically positioned with respect to the hohlraum (only one such array is shown in Fig. 2c). The currents vaporize the wires, thus creating a plasma, and produce powerful magnetic fields that pinches this plasma to densities and temperatures sufficient to generate an intense source of X-rays. The main challenge for ICF reactor implementa-

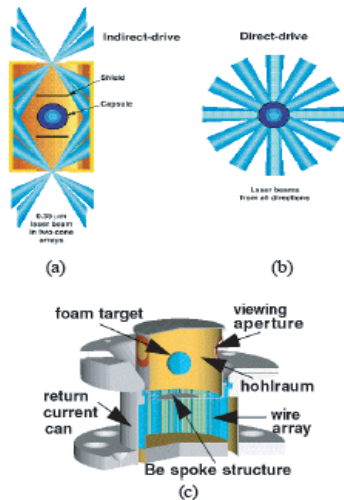


FIG. 2: Geometrical arrangements to implode ICF capsules.

tion will be the target manufacturing cost, the repetition rate and target standoff distance at which drivers and windows can be operated and the fusion target chamber construction.

IV. MAGNETIC CONFINEMENT [7, 9]

The Lorentz force makes charged particles move in helical orbits (Larmor orbits) about magnetic field lines. In a uniform magnetic field and in the absence of collisions

or turbulence, the particles (better: their guiding centers) remain tied to the field lines but are free to move along them. The distance between the actual particle orbit and the magnetic field line is the Larmor radius r_L . A magnetic field is thus capable of restricting the particle motion perpendicular to the magnetic field but does not prevent particles from moving along the magnetic field. This effect serves as the basis for all magnetic confinement schemes, while at the same time it points to the absolute necessity to cope with the particle losses along the magnetic field (end losses).

The perturbative effect of collisions and turbulence on the transport of particles and energy across the magnetic field can be understood in terms of a simple statistical diffusion process applied here to a cylindrical plasma. Let us first consider Coulomb collisions. The particles suffer collisions with a characteristic collision time τ_c . A collision allows the particle to step across B with a step length equal to r_L . This gives a diffusion coefficient $D \approx r_L^2/\tau_c$. The effect of (electrostatic) turbulence on the other hand can be estimated in a similar fashion. A simple model pictures the particles to be dragged along by the turbulent waves. The step length is now of the order of the wavelength perpendicular to the magnetic field k_\perp^{-1} and the effective collision time is that of the correlation time of the turbulence τ_{corr} , yielding[10] $D \approx 1/(k_\perp^2 \tau_{corr})$. In both cases however, the confinement time is linked to D by means of the simple diffusion relation

$$\tau \approx \frac{a^2}{D} \quad (2)$$

where a is the radius of the plasma, such that in any case high τ requires a large plasma cross-section.

In its motion around a magnetic field line, a gyrating particle constitutes a small current loop of magnetic moment μ that generates a magnetic field that opposes the imposed magnetic field by an amount that is proportional to the kinetic energy contained in the perpendicular particle motion: plasmas in magnetic fields are therefore naturally diamagnetic. The larger the sum of the kinetic energies of all the plasma particles, the lower will be the field. This obviously means that there is a limit to the total energy content ($3nkT$) that a given magnetic field can confine.

The same conclusion is reached by an alternative approach, in which the action of the magnetic field on the confined plasma can be viewed as a balance between the magnetic pressure $B^2/(2\mu_0)$ (μ_0 is the vacuum permeability) and the plasma pressure p according to the relation:

$$p + B^2/(2\mu_0) = \text{constant}. \quad (3)$$

The maximum pressure that possibly can be confined at a given B , is thus $B^2/(2\mu_0)$. Stability constraints prevent however the attainment of this maximum and the pressure thus reaches at most a fraction β (beta) of its theoretical limit[11, 12]. A large value of B is therefore the key to achieve large values of $p = nkT$.

From what we just have seen, it is to be expected that the fusion triple product in devices without end losses will increase with plasma cross section (Eq. 2) and magnetic field pressure (Eq. 3). Such a dependence is substan-

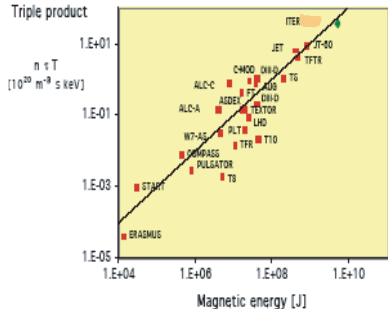


FIG. 3: $n\tau_E T$ values reached by MCF devices versus the magnetic energy stored in their plasma volume.

tiated in Fig. 3, showing the $n\tau_E T$ values experimentally achieved over 30 years of research in a large number of toroidal magnetic fusion devices as a function of $E_{mag} = B^2/\mu_0 V$, the total magnetic energy stored in the plasma. The scatter in the data is caused by differences in configuration as well as in secondary engineering parameters. This graph predicts that magnetic fusion will achieve reactor grade $n\tau_E T$ values in the projected ITER device (diamond).

V. MAGNETIC CONFIGURATIONS WITH END LOSSES

One could in principle conceive a magnetic confinement machine that consists of a long solenoid of length L in which particles are confined radially but flow out axially. By analogy with the ICF-case, one could define an effective energy confinement time:

$$\tau_E = \frac{L}{V_{thi}}. \quad (4)$$

For $L = 1 \text{ km}$, τ_E equals about 10^{-3} s at $T = 15 \text{ keV}$, meaning that burn is possible for $n > 2 \times 10^{23} \text{ m}^{-3}$. The pressure corresponding to these n and T values requires a confining field $B = 50 \text{ T}$. It is therefore clear that the end losses have to be curtailed in a fusion reactor. One way to achieve this is through an increase of the magnetic field strength at each end of the solenoid. The gyrating particles will then be repelled from these areas with higher field strength, which thus effectively act as "magnetic mirrors". The reflection is due to the so-called grad-B force:

$$F_z = -\mu \frac{\partial B_z}{\partial z}, \quad (5)$$

where $\mu = \frac{1}{2}mv_{\perp}^2/B$ is the magnetic moment of the particle. It can be shown that is an adiabatic invariant, meaning that its value does not change along the motion. The motion of a particle in such a mirror can then also be described by means of the two conservation relations

$$mv_{\perp}^2 + mv_z^2 = C^{st}, \quad (6)$$

and

$$\mu = \frac{\frac{1}{2}mv_{\perp}^2}{B} = C^{st}. \quad (7)$$

During the motion towards a higher field, v_{\perp} increases and v_z decreases. At sufficiently high values of B , v_z can even be reduced to zero, i.e. the particle reflects. Although the end losses can be significantly reduced in a mirror[13], the confinement of such a device proved to be too low and mirror machines have almost completely disappeared from the fusion scene.

VI. TOROIDAL PARTICLE CONFINEMENT.

An obvious recipe for the elimination of the end losses is to close the magnetic field lines on themselves. This

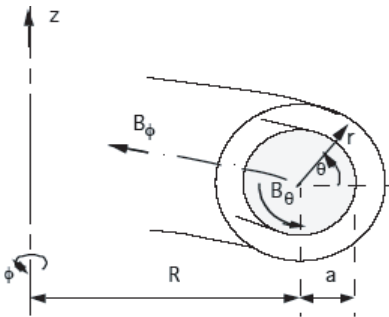


FIG. 4: Coordinates and fields in a toroidal system.

can for instance be done by aligning the field producing coils along a circumference of radius R , thus creating a toroidal magnetic field, B (see Fig. 4) having a gradient in the direction of R . During their motion along the toroidal field lines the plasma particles experience a radially outward directed force F_R which is the sum of a centrifugal force mv_{\parallel}^2/R and a grad-B force $\frac{1}{2}mv_{\perp}^2/Be\vec{r}$. As a result, a drift motion, the so-called toroidal drift v_D , occurs that is traverse to both the field and the field gradient and is given by:

$$\vec{v}_D = m \frac{v_{\parallel}^2 + \frac{1}{2}v_{\perp}^2}{q_c R B^2} e_{\vec{R}} \times \vec{B}. \quad (8)$$

Averaging over a Maxwellian, the value of the toroidal drift becomes

$$v_D = \frac{r_L}{R} V_{th}. \quad (9)$$

Because of the dependence on charge q_c , electrons and ions experience drifts in opposite directions, giving rise to the creation of an electric field. The latter than causes both electrons and ions to drift together radially outwards, thus shattering our hopes of creating the ideal confinement system.

The catastrophic effect of the toroidal drift can be avoided by twisting the magnetic field lines helicoidally[8, 14]. One uses the term rotational transform to characterise the twisting, which gives rise to a poloidal field component B_{θ} . The amount of rotational transform is measured by the ratio B_{θ}/B_{ϕ} , or by the rotational transform angle $\iota = 2\pi/q$ where q , the safety factor, is defined as:

$$q = \frac{rB_{\phi}}{RB_{\theta}}. \quad (10)$$

If one follows a given field line many times around the torus a closed flux tube is mapped, a so-called magnetic surface. Surfaces pertaining to different field lines form a set of nested surfaces around the torus axis. It should be noted that the rotational transform angle is in general different from surface to surface: the configuration therefore possesses magnetic shear, a property which is quite effective against large scale plasma instabilities.

By considering the trajectory of a single particle (with high enough velocity v_{\parallel} along the magnetic field), it is easy to show that the helical twist can compensate the toroidal drift. It suffices to show that, even in the presence of v_D , the trajectory of a charged particle is a closed orbit. Without the toroidal drift, the trajectory of the guiding centre of a particle coincides with a field line, such that its projection on a meridian plan (coordinates x and y) is a circle which the particle describes with an angular frequency $\omega = v_{\parallel}B_{\theta}/(aB_{\phi})$. Including the toroidal drift, the projected trajectory is found from:

$$\frac{dx}{dt} = \omega y + v_D \quad (11)$$

$$\frac{dy}{dt} = -\omega x.$$

the solution of which is a circle which is displaced with respect to the projection of the field line such that the maximum distance between the orbit and the magnetic surface equals:

$$d = 2 \frac{v_D}{\omega} \approx q r_L. \quad (12)$$

We therefore conclude that a toroidal system with rotational transform can indeed confine particles. The price to be paid to get rid of the end losses is an excursion of the particles away from a magnetic field line that is larger by the factor q than the Larmor radius. As this excursion turns out to be the step length for collisional transport, one sees that it is of great advantage to work with as low a q as possible, i.e. with the highest possible helical

twist. The maximally allowed amount of twist will result from stability considerations[11, 12]. Note also that the rotational transform provides a conductive path between the top and bottom zones of opposite charge polarity: the currents that thus flow are called the Pfirsch-Schlter currents. As these currents meet some resistance, the vertical electric field can not completely be short-circuited.

The dynamical behaviour of a plasma in a magnetic field is more intricate than just being the sum of the motions of the individual particles. One can show that a perfectly conducting plasma is capable of dragging the magnetic field lines along during its macroscopic motion. In this sense, we can conclude that the particle motion described earlier pertains to motion with respect to a fixed magnetic field, i.e. where any macroscopic motion of the field lines (and of plasma) is prevented. In a tokamak, we will see that the radial force F_R ($= 4\pi^2 a^2 p$ when summed over all Maxwellian plasma particles), has to be compensated by means of an additionally applied vertical magnetic field. This motion of plasma and field plays also an important role in the so-called pressure driven instabilities of the interchange and ballooning type.

VII. THE TOKAMAK[10, 16]

A tokamak is a toroidal device in which the poloidal magnetic field is created by a toroidal current I_p flowing through the plasma. Figure 5 gives a schematic diagram of a tokamak. A strong toroidal magnetic field is generated by a toroidal field coil system. The toroidal current is induced by means of a transformer. The plasma itself forms the secondary winding of the transformer, the primary being wound on an iron core.

The toroidal geometry of the plasma leads to two hoop forces which are both in the direction to expand the plasma ring. The first of these forces results from the natural tendency of a current loop to expand in an effort to lower its magnetic energy. The second force is the resultant F_R of the sum of centrifugal and grad-B forces experienced by the individual particles during their motion along the field lines.

Both these forces can be compensated by providing a vertical magnetic field B_v , that interacts with the toroidal current to give an inward force. The required magnitude of this field is:

$$B_v = \frac{\mu_0 I_p}{4\pi R_0} \left[\left(\ln \frac{8R_0}{a} + \frac{l_i}{2} - 1.5 \right) + \beta_p \right]. \quad (13)$$

In this expression, β_p is the ratio of the mean plasma pressure to the poloidal magnetic field pressure and describes that part of vertical field that is needed to compensate F_R . l_i is the internal inductance per unit length of the current loop and, together with the external inductance given by the other terms between the round brackets, sets the amount of field needed to balance the current force contribution.

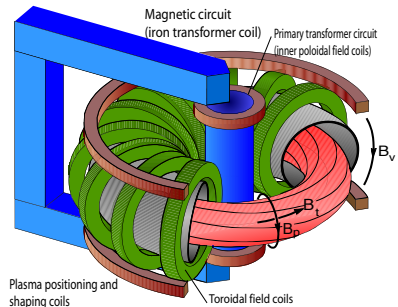


FIG. 5: Schematic diagram of a tokamak.

If the applied vertical field is spatial non-uniform and increases with major radius, the plasma is found to be vertically unstable. Such a vertical field shape is e.g. mandatory when, in an attempt to increase the plasma pressure, the plasma is pushed as much as possible to the high field side, thus creating a D-shaped plasma, i.e. having elongation and triangularity. An externally applied horizontal magnetic field B_h can then be used to maintain the plasma well centred. Both the horizontal and vertical position control is in all modern tokamaks achieved by means of feedback controlled vertical and horizontal magnetic field systems. The combination of the above fields can generate an equilibrium tokamak configuration. Whether this equilibrium will be stable or unstable can be found from a stability analysis. A tokamak plasma has essentially two origins of instability, i.e. two energy sources for the excitation of oscillations: the magnetic energy of the plasma current and the plasma thermal energy. At high pressures, these sources start to interact with each other, but at low pressure they can be studied separately. The poloidal field magnetic energy excites helical instabilities, named kink instability and tearing instability, while the thermal energy excites flute (or interchange) modes and ballooning modes.

VIII. THE MCF REACTOR

The tokamak is the most studied and most advanced fusion machine to date and is the most likely system to be converted into a reactor. Even when the confinement time of toroidal configurations still lacks a quantitative first-principle derivation on account of the intricate nature of plasma turbulence, important progress has been achieved through an empirical approach[17], akin to windtunneling, and has allowed to find the most important engineering parameters affecting confinement and has brought the attainment of the burn condition in a tokamak at hand.

It is however not clear today whether the tokamak is the optimal reactor concept. Some alternative approaches are therefore being pursued, in the first place

the Stellarator[18], and, on a more exploratory level, such devices like the Reversed Field Pinch[19], the Spheromak[20] and the Field Reversed Configuration[21]. It is however appropriate here to illustrate on the example of the tokamak which are the main developments required on the way to the reactor.

A first series of issues has to do with economical reactor operation and the likelihood to achieve unit sizes that are acceptable in power output, in physical volume or in cost of electricity. Mechanical endurance and duty cycle considerations require the burn to be sustainable for a long, in principle unlimited time. There are two problems here. Firstly, as long as its plasma current is generated by induction, the tokamak is a pulsed system. One might therefore have to develop alternative ways to generate I_p , known as current-drive methods, or possibly switch to an alternative confinement scheme like the stellarator.

Secondly, it is clear that sudden termination of the discharge, known as disruption, should be avoided (another plus for the stellarator) or by a burn quench due to ash or impurity accumulation.

This last problem falls under the heading heat and particle removal and is a prime object of present day's research. A reactor will have to exhaust power and particles associated with the thermalisation of the 3.5 MeV alpha particles. The power leaves the plasma in the form of radiation or of kinetic energy of the escaping particles. The problems and solutions will differ depending on how the plasma is limited. Direct contact of the plasma and the material wall is avoided because unavoidable imperfections in the magnetic configuration and motions of the plasma column might lead to concentrated heat deposition on areas that are difficult to control and cool.

To this end, a specially monitored, suitably clad and cooled piece of wall, somewhat protruding from the main wall, is often used to intercept the escaping particles. This element is called limiter. The limiter's exposed surface should be large enough to avoid too large power fluxes and it is therefore indicated to use a toroidal (or belt) limiter that runs around the circumference of the torus. The magnetic surface that touches the inner most part of the limiter is called the last closed flux surface (LCFS). It is also possible to exhaust the escaping particles into a separate chamber before they actually reach a material wall. By means of extra magnetic coils, the magnetic configuration inside the containing vessel can be divided in two zones, separated by a so-called sep-

aratrix (= LCFS). Inside the separatrix there exist the desired nested and closed magnetic surfaces. A particle escaping from this inner zone towards the outside (into the so-called scrapeoff layer) meets field lines that convey it to a target plate in the exhaust chamber, which can be situated quite far from the plasma boundary at the separatrix. When the extra field coils consist of conductors that are concentric with the plasma current, the configuration is called an axisymmetric or poloidal-field divertor. The point where the poloidal field is zero is called the X-point. The limiter or the divertor target plates are heated by the incoming exhausted power and bombarded by the escaping particles. As a result, material is released from their surfaces which can reach the plasma in the form of neutral particles, capable of deep penetration before being ionised. As such particles are impurities that can cause a lot of radiation loss from the plasma and in addition lead to fuel dilution, it is very important to (i) reduce the power density to the targets to levels that can be handled by state-of-the-art cooling techniques and (ii) decrease the kinetic energy of the incoming particles below the threshold energy at which target damage occurs. A special category of escaping particles are the helium atoms produced in the fusion reactions: care should be taken that these leave the plasma promptly and are not given the chance to reenter the discharge as impurities.

Providing the needed vacuum enclosure, the first wall is probably the most critical reactor component, as it is the target of very intense radiation from the plasma (14 MeV neutrons, energetic neutral particles produced by charge exchange, photons of various energies). Its mechanical strength will be weakened by lattice damage and swelling, by wall erosion through sputtering and by temperature excursions. In addition, neutron induced transmutation reactions can render the wall radioactive. Based on these extreme operational conditions, it is presently estimated that the time integrated neutron flux through the first wall will have to be lower than about 18 MW-y per m^2 . Upon reaching this limit, the first wall will have to be replaced[22]. Solving the heat and particle removal issue and finding adequate first wall materials are the prime tasks of present day's fusion research, presenting an equally large challenge to the tokamak and its possible alternatives. Many of these problems point to the urgent need for an irradiation facility for fusion materials, such as IFMIF[23].

[1] P. Vandenplas, G.H. Wolf, *Europhysics News*, 39 (2008) 21.
 [2] Hogan, W.J., *Editor: Energy from Inertial Fusion*, International Atomic Energy Agency, Vienna, Austria (1995).
 [3] M. Rosen, *Phys. Plasmas* 6 (1999) 1690.
 [4] J. Lindl, *Phys. Plasmas* 2 (1995) 3933.
 [5] J.D. Lindl, R.L. McCrory, E.M. Campbell *Physics Today* 45 (1992) 32.

[6] <http://www.llnl.gov/nif/nif.html>.
 [7] L. Spitzer *The Physics of fully Ionized Gases*, Interscience, New York (1956).
 [8] K. Miyamoto, *Plasma Physics for Nuclear Fusion* MIT Press, Cambridge, Mass., 1976.
 [9] F.F. Chen, *Introduction to Plasma Physics and Controlled Fusion*, Plenum Press, New York, 1984.
 [10] B.B. Kadomtsev, *Plasma turbulence*, Academic, New

- York (1965)., 1984.
- [11] V.D. Shafranov, *Reviews of Plasma Physics*, 2 (1963) 103.
 - [12] R.B. White *Theory of Tokamak Plasma* North Holland, Amsterdam (1989).
 - [13] R.F. Post *Nucl. Fusion* , 27 (1987) 1579.
 - [14] A.D. Sakharov *Plasma physics and problems of Controlled Fusion, Moscow, AN SSSR (in Russian)* , 1 (1958) 20.
 - [15] B.B. Kadomtsev *Tokamak Plasma: a Complex Physical System, Institute of Physics, Bristol* (1992).
 - [16] J. Wesson *Tokamaks, 2nd edition, Clarendon Press, Oxford* (1997).
 - [17] B.B. Kadomtsev, *Sov. Physics - Journal of Pl. Physics* , 1 (1975) 295.
 - [18] F. Wagner *Transact. of Fusion Technol.* , 33 (1998) 67.
 - [19] H.A.B. Bodin *Nucl. Fusion* , 30 (1990) 2033.
 - [20] T.R. Jarboe *Plasma Phys. Contr. Fusion* , 36 (1994) 36.
 - [21] M. Tuszewski *Nucl. Fusion* , 28 (1988) 1717.
 - [22] F. Najmabadi and the ARIES team: Fusion Engineering & Design *Nucl. Fusion* , 38 (1997) 33.
 - [23] A. Moslang et al., "Suitability and Feasibility of the International Fusion Materials Irradiation Facility (IFMIF) for Fusion Materials Studies" *Nucl. Fusion* , 40 (2000) 619.

STELLARATORS

D.A. Hartmann

Max-Planck Institut für Plasmaphysik, EURATOM Association
Wendelsteinstrasse 1
17491 Greifswald
Tel. (49) 3834882478, Fax (49) 3834882509

ABSTRACT

Stellarators are toroidal devices where the required rotational transform of the magnetic field lines is generated by external field coils and not via an induced net toroidal plasma current. This confinement scheme has the advantages that, in principle, steady-state plasma operation is possible and that it does not have to brace itself against disruptions of a toroidal plasma current. At the cost of having to give up toroidal symmetry the properties of the stellarator field can be tailored to suit reactor needs. Research focuses on the plasma confinement properties of different stellarator fields and investigates the problems arising when one extrapolates to reactor parameters

I. INTRODUCTION

In a toroidal device the magnetic field lines need to be helically twisted in order to prevent polarisation of the plasma by drifting particles and thus to provide plasma confinement [1]. In addition, during many toroidal revolutions the field lines need to trace out surfaces, the so called flux surfaces. Figure 1 shows a toroidal section of four nested flux surfaces with one magnetic field line highlighted. Such nested flux surfaces can be created (mainly) in two ways: In a tokamak a toroidal field is superposed with the poloidal field of a net toroidal current induced in the plasma. In a stellarator¹ the net toroidal current is zero and the confining magnetic field is generated solely by external field coils. This requires some of the coils to helically revolve around the plasma.

The goal of stellarator research - as well as tokamak research - is to prove that the concept is suitable for a fusion reactor. Thus it is necessary to determine the magnetic field structure that can confine a plasma at sufficiently high density, n , and temperature, T , with sufficiently long energy confinement time, τ_E , in order to meet the Lawson criterion [2].

¹ In this lecture the term "stellarator" is used in a generic sense for helical confinement systems encompassing traditional stellarators, helias stellarators, torsatrons, heliotrons, and heliacs. These terms will be explained further down.

Dirk Hartmann – Stellarator

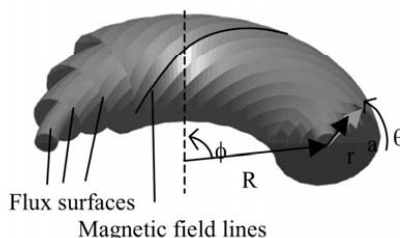


Figure 1 Nested flux surfaces ergodically covered by helical field lines.

In Table 1 the highest plasma parameters achieved in tokamaks and helical systems are summarised. Particularly the maximum central ion and electron temperatures of helical systems are lagging behind those of tokamaks and on first glance it is not obvious why this concept is still being pursued. According to present understanding, however, the differences are largely due to the different sizes of the present day experiments and not due to an inherent shortcoming of the stellarator concept.

	Tokamaks	Helical systems
$T_i(0)$ [keV]	44	4
$T_e(0)$ [keV]	15	7
$n_e(0)$ [10^{20}m^{-3}]	10	7
τ_E [s]	1	0.15
τ_{plasma} [s]	120	90
$\langle \beta \rangle$ [%]	12.3	2.9
P_{fusion} [MW]	17	-

Table 1 Maximal plasma parameters achieved in tokamaks and stellarators in different discharges.

Larger experiments are being developed because of the attractiveness of the concept: The stellarator field can be stationary thus steady-state operation with plasma is possible rather than a pulsed operation as may be necessary in tokamaks. This reduces material fatigue due to thermal cycles in a reactor and avoids the requirement to store thermal loads. Also (as will be seen in subsequent lectures) the net toroidal plasma current in a tokamak constitutes a large reservoir of free energy that can quickly be released

in sudden disruptions. This causes severe strain on the mechanical structure and since stellarators do not have a net toroidal current the engineering requirements can be relaxed. In addition, tokamak research of the last decade has shown that the energy confinement time, the maximum plasma pressure and the highest density all are proportional to the plasma current. Thus tokamaks are required to operate at higher plasma currents in order to obtain better plasma performance.

During the 1950s research on controlled thermonuclear fusion was classified until it became clear near the end of that decade that progress was arduous and required international collaboration rather than secrecy. Historically, one of the first toroidal magnetic confinement experiment was the model "C" stellarator built by the astrophysicist Lyman Spitzer [2] in the fifties. However, at the IAEA meeting in 1968 the Russian tokamak T-3 showed confinement times which were thirty-fold higher than the stellarator values. This led to a surge towards new tokamak experiments; for example, the C stellarator was converted into the ST tokamak. Stellarator research, on the other hand, was continued at four laboratories in Germany, United Kingdom, U.S.A. and Japan only. Since then the stellarator concept has undergone many changes and the original short-comings are understood. Whereas the size of the tokamaks steadily increased, stellarators did not keep up with them. Only the latest experiments: the Large Helical Device (LHD) in Japan ($R=3.9$ m, operational since 1998, [3]) and Wendelstein 7-X in Germany ($R=5.5$ m, operation planned for 2012, [5]) will have plasma volumes comparable with medium size tokamaks. Both have superconducting coils and will investigate near steady-state plasma discharges with a duration of 30 minutes. In addition, some smaller experiments, e.g. Quasi-helically Symmetric Experiment, HSX, ($R=1.2$ m, operation since 2000, [6]) and the National Compact Stellarator Experiment, NCSX, ($R=1.2$ m, operation planned for 2009) pursue the study of optimising the magnetic field with respect to different aspects of particle kinetics or the influence of the plasma on the confining magnetic field.

This paper gives a brief overview of some aspects of stellarator research. Section II classifies the multitude of possibilities of using external coils to generate a toroidal, helical field. Section III describes the properties of the vacuum magnetic field of helical devices. When a plasma is generated in a helical device, plasma currents flow that lead to a deviation of the magnetic field from the vacuum magnetic field. This is the subject of Section IV. Section V relates plasma confinement to the magnetic field properties. Section VI shows how neo-classical transport in a helical devices can be reduced by a radial electric field to such an extent that the stellarator concept becomes viable for a fusion reactor. Section VII summarizes stellarator research that is directly reactor relevant: high plasma β , long pulse operation, particle exhaust with helical and island divertors. Finally, Section XIII gives an overview of the problems that are the focus of current stellarator

research.

II. STELLARATOR GENEALOGY

The stellarator magnetic field is generated by a suitable assembly of external field coils only. Since there is no net toroidal current one obtains for the poloidal component of the magnetic field: $\int B_\theta(r) r d\theta = 0$. Besides having twisted magnetic field lines, it is also necessary for plasma confinement that the field lines trace out nested magnetic flux surfaces [1]. There is no general analytic proof that a stellarator field has nested flux surfaces. However, one can numerically trace the field lines and investigate whether such surfaces exist. If they do exist one can show that they cannot be toroidally symmetric. Thus whereas for an ideal tokamak field, $B = B(r, \theta)$, for the stellarator field $B = B(r, \theta, \varphi)$. At first glance this seems to be a disadvantage since this entails that the generalised momentum, p_φ , is not a separable quantity, i.e. is not conserved as it is in a tokamak. This has profound consequences on transport in a stellarator. However, this freedom can also be put to one's advantage and allows to tailor the magnetic field to the specific needs of a fusion reactor. This is done in most of the recent stellarator experiments.

There is a plethora of ways of how to externally produce a helical field [6]. They can be divided into two groups: In the first group the magnetic field is generated by an assembly of field coils of simple geometric forms, e.g. planar, helical. These devices require at least one coil to encircle the torus toroidally. The nomenclature of these helical devices is given by the number of helical coils and the direction of the current flowing in them. The second group are devices where the magnetic field is generated by modular field coils of complicated geometric shape that encircle the torus only poloidally. Optimising the properties of the magnetic field of helical devices became possible only after magnetic field coils were no longer required to be of simple geometric shape. These devices are labelled according to the principal optimisation criteria.

A classical stellarator consists of a set of planar field coils that generate a toroidal magnetic field and a set of l dipole coils that are wound around the torus circumference n times. Wendelstein 7-A (Germany) [8] was such a $l=2$, $n=5$ classical stellarator and is shown in Figure 2. The direction of the current in the helical coils is indicated. The currents in neighbouring coils flow in opposite directions. The last closed flux surface clearly shows the three-dimensional structure of the plasma. The plasma cross section is approximately elliptical and rotates with increasing toroidal angle.

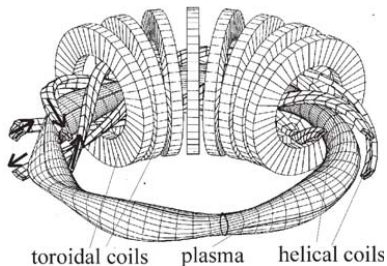


Figure 2. Cut open schematic of the $l=2, n=5$ -stellarator W7-A.

Helical magnetic field lines and nested flux surfaces can also be obtained if the currents in the helical coils all flow into the same direction; then the toroidal field component does not cancel and it is even possible to dispose of the toroidal field coils all together (lest one wants to retain them for some additional experimental freedom). Such a device is called a torsatron (heliotron in Japanese literature). In such a situation also the average vertical magnetic field does not vanish and it is necessary to add an additional vertical field (generated by horizontal coils) in order to form a magnetic axis. The advanced toroidal facility (ATF, U.S.A.) was a $l=2, n=6$ torsatron [9]. It is schematically shown in Figure 3.

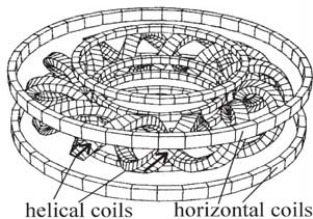


Figure 3 Coil system of the $l=2, n=6$ torsatron ATF.

In a heliac, finally, the centers of the toroidal field coils are no longer in one plane but follow a helical line. TJ-II [10] (Spain, operative since 1997) is an example and shown in Figure 4. There a horizontal coil for an additional vertical field has been added to increase the flexibility of the magnetic field configuration.

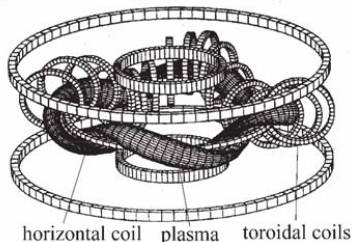


Figure 4 Schematic of the heliac TJ-II.

Dirk Hartmann – Stellarator

It is also possible to use non-planar coils altogether. Here one starts out with a magnetic field of desired properties and uses the fact that the magnetic field on an enclosing surface uniquely determines the magnetic field within. This magnetic field can be generated by a current distribution on another enclosing shell [11]. The current distribution might be continuous but one can approximate it with a set of discrete paths of constant current. These discrete paths define the coils. After calculating the magnetic field generated by the coils and comparing it with the desired field one can derive a set of coils in an iterative process.

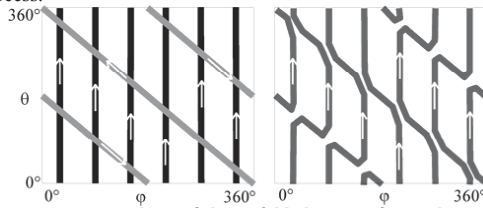


Figure 5 Current sheet of the unfolded torus of $n=1, l=1$ stellarator (left) and its equivalent set of modular coils. (right).

This procedure is illustrated in Figure 5 for the case of a standard $l=1, n=1$ -stellarator where the set of toroidal and helical coils is replaced by a set of modular coils that generate approximately the same magnetic field. Figure 5 left shows the currents in the toroidal and helical coils on the torus surface that has been projected into the ϕ, θ -plane. If the currents in the toroidal and helical coils are equal then rearranging the current paths is possible. In Figure 5 right the new set of current paths is shown. Note that all of them are linked only poloidally and the currents do not intersect with one another. Thus the magnetic field coils are modular.

Wendelstein 7-AS was the first stellarator that used such a modular coil system. The set of coils is shown in Figure 6. The additional toroidal coils are used to increase the experimental variability but are not essential. The magnetic field is based on the field of a $l=2, n=5$ -stellarator. The $n=5$ structure was retained such that the magnetic field has a five-fold symmetry, i.e. the magnetic field is invariant under rotation around the z -axis by $360^\circ/5=72^\circ$. The freedom gained by giving up the need to use coils of simple geometric shapes was used to optimize the magnetic field. Here, the magnetic field is similar to five magnetic mirrors that form the edges of a pentagon. Regions of high magnetic curvature, thus poor confinement, are located at the mirror ends with higher magnetic field, thus fewer particles. Other helical devices with modular coils are HSX with a magnetic field that is quasi-helical, W7-X optimized for reduced Shafranov shift and the formerly planned but since abandoned experiment QPS in the U.S.A. [12] with a quasi-poloidal field.

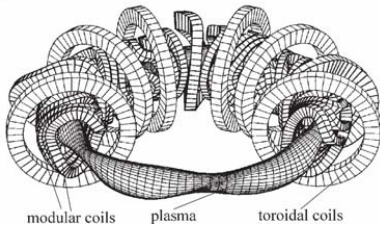


Figure 6 Schematic of the modular stellarator W7-AS.

III. VACUUM MAGNETIC FIELD

The vacuum magnetic is characterised by the poloidal cross-section of the flux surfaces, including magnetic islands, mod \underline{B} contours, profile of the rotational transform ι the magnetic well and particles orbits in the vacuum magnetic field.

The cross-section of the magnetic field in one poloidal plane can be obtained by tracing field lines and plotting their intersection with one poloidal plane, similar to Poincaré plots in real space. The surface of a magnetic flux tube is identified as the line that is traced out by the intersection points of one field line during many revolutions around the torus. Using different starting positions for the field line tracing yields different flux surfaces. These results can be compared with measurements done with an electron beam generated by an electron gun inside of the evacuated vacuum region. The beam electrons follow the magnetic field line at the location of the gun and circle around the torus several times until they are observed by an intersecting scintillating grid [13] or by a moving scintillating rod in one poloidal plane [13,15]. Moving the location of the beam gun to a different starting point in the poloidal plane one obtains the location of different flux surfaces. Figure 7 shows the measured and calculated flux surfaces on LHD.

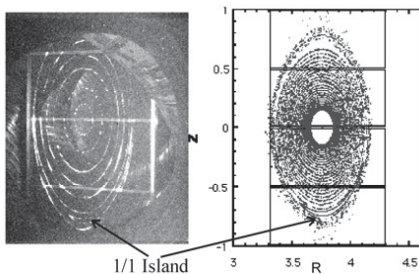


Figure 7 Measured (left) and calculated (right) flux surfaces of LHD.

One can identify three different regions: An inner region where the field lines form closed nested flux surfaces. This region can be perturbed by magnetic islands [16] that are caused by magnetic field errors. In Figure 7 an island is indicated that was caused by a field error that has a dominant $n=1, l=1$ component. This region can be

Dirk Hartmann – Stellarator

surrounded by an additional region of islands that are caused by the toroidicity of the field and are not necessarily due to field errors, i.e. they would not occur in a linear device. Therefore they are also referred to as "natural islands". Between the islands and the nested flux surfaces one can identify X- and O-points similar to the field of a divertor tokamak. Taking advantage of them one expects to be able to apply the successful concepts of a divertor in tokamaks also to stellarators [17]. Outside of the islands the field lines become stochastic with short connection lengths to the torus walls. Even though the flux surfaces have a complicated three-dimensional structure fast equilibrium processes along the field lines assure that they are also surfaces of constant plasma pressure. They can be ordered by assigning each surface the effective radius, r_{eff} , of a torus with cylindrical cross-section and the same major radius, R , that contains the same volume. The average twist of the magnetic field lines on a given flux surface is described by the rotational transform, ι , given by

$$\iota(r_{\text{eff}}) = \frac{R \cdot \langle B_{\theta} \rangle}{r_{\text{eff}} \cdot \langle B_{\phi} \rangle} \equiv \frac{2\pi}{q(r_{\text{eff}})}$$

which is proportional to the inverse of the safety factor, q . Geometrically, this is the number of toroidal rotations that are necessary for one poloidal rotation. Historically, tokamaks use the safety factor q and stellarators use the rotation ι . In Figure 8 the rotational transform profiles are shown for different stellarators and compared with a tokamak. In a tokamak the toroidal plasma current and therefore the contribution to the poloidal magnetic field decreases with distance from the center; thus the rotation decreases. In a stellarator field the poloidal field increases with distance from the center because the contribution of the (outside) helical coils increases.

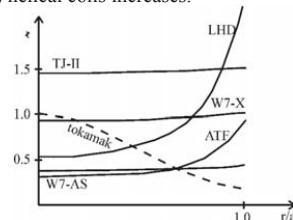


Figure 8 Radial profiles of the rotational transform of different helical devices and comparison with the tokamak profile.

Magnetic shear, $S = d\iota/dr$, describes the radial variation of the rotation. It is obvious from Figure 8 that stellarators and tokamaks have opposite sign of the shear and it is interesting to note that tokamak discharges with "reversed shear" that often have improved plasma confinement properties, locally have the same sign as a stellarator. If the ι profile is flat the pitch angle of the magnetic field on neighbouring flux surfaces changes. W7-AS and W7-X are examples for that. LHD (as all torsatrons) is an experiment with strong shear.

Devices with strong shear inevitably have flux surfaces with rotational transform $\iota = m/n$, with m and n

small natural numbers, so called “rational surfaces”. There local instabilities can develop that locally destroy these flux surfaces by island formation which themselves short-circuit the inner plasma core to the plasma boundary thus degrading the plasma confinement. As shown in Figure 7 field errors, b_{per} , of a particular toroidal and poloidal mode structure can also resonate with the corresponding rational flux surface and cause the formation of islands. The width of the islands W becomes smaller with increased shear, $W \approx \sqrt{b_{per}/S}$ [16]. Thus strong shear is favourable for plasma confinement. On the other hand in devices with nearly vanishing shear, it is possible to avoid low order rational surfaces all together by properly choosing the rotational transform at the edge. This also has beneficial effects on confinement (see Section IV).

It is instructive to unwrap a flux surface and plot the contours of the constant total magnetic field versus toroidal angle, ϕ , and poloidal angle, θ . $\theta=0$ denotes the outside horizontal midplane. Figure 9 shows mod B plots of an ideal tokamak and of the stellarator W7-AS. The solid line marks one representative field line as it wraps around the torus. An ideal tokamak (with infinitely many toroidal field coils, a finite number of coils causes an additional small ripple) is toroidally symmetric and the highest field is on the inboard side, $\theta = 180^\circ$, the lowest on the outboard side, $\theta = 0^\circ$. In a stellarator this toroidal symmetry is broken by the helical field coils leading to an additional fine structure of magnetic hills and valleys. The additional variation of the magnetic field along a field line is called magnetic ripple.

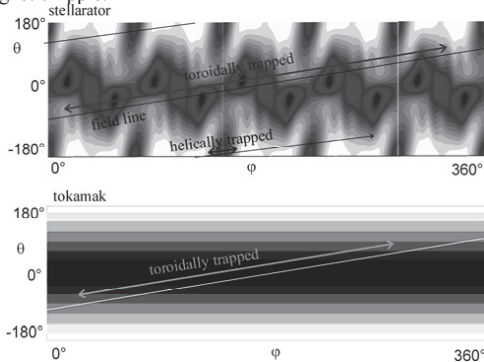


Figure 9 Mod B plots of W7-AS and an ideal tokamak.

As has been pointed out before [17] the undulating magnetic field leads to different classes of particle motion. In a tokamak there exist passing particles that approximately follow the magnetic field lines (and rotate toroidally) and toroidally trapped particles that are bouncing back and forth between the high magnetic field on the inside of the torus as indicated in Figure 9. In a stellarator there is an additional class of particles that are trapped in the local magnetic mirrors of the helical field. They are also shown in Figure 9.

The curvature and ∇B -drift [16] cause deviation of the particle orbits from the flux surface that is particularly pronounced for trapped particles. Figure 10 shows the traces of the three classes of particle motion projected into a poloidal plane of magnetic co-ordinates for W7-AS. The circles indicate magnetic flux surfaces. The high field side is on the left. Passing particles have orbits that stay close to the magnetic flux surface. Toroidally trapped particles have orbits of the familiar banana-shape. Helically trapped particles are trapped in a small poloidal range and often have a superposed radial outwards drift. If the plasma temperature is high and the collision frequency is correspondingly low, they can quickly be lost. They are the reason for the unfavourable confinement regime of stellarators at high temperatures, the $1/\nu$ -regime. However, if there is a radial electric field the additional $E \times B$ -force leads to an additional poloidal drift that can compensate for the radial outward drift thus reducing the confinement degradation in the $1/\nu$ -regime.

Plasmas tend to expand such as to occupy the largest possible volume dV . If the plasma is collisionless then the flux $d\Phi$ through a given magnetic flux tube is conserved and the plasma moves to maximise $U=dV / d\Phi$ [19,20]. Thus stable plasma operation requires that the maximum of U is in the centre of the plasma and decreases outward. This is called the magnetic well configuration. In toroidal confinement this requirement can only be satisfied in an average sense. The specific volume U of a flux surface can be expressed as $U = \oint \frac{dl}{B}$ (the integration is

along the field line and extends to infinity if the surface is not a rational). If U decreases radially outward one has a magnetic well configuration. This is the typical situation in a tokamak.

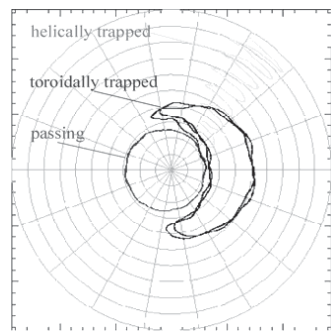


Figure 10 Poloidal cross-section with classes of particle orbits in W7-AS.

TJ-II has been designed to study a wide range of magnetic hill values, in particular it allows to experimentally change from a magnetic well to a magnetic hill configuration.

IV. PLASMA CURRENTS

The vacuum stellarator field confines charged particles. With increased density and temperature of the particles, thus with plasma beta, sizable currents flow in the plasma, that modify the applied magnetic field: They are the Pfirsch-Schlüter current and the bootstrap current. Additional currents can be induced, e.g. ohmically, by absorption of asymmetrically launched electro-magnetic waves or by unbalanced neutral beam injection.

As in a tokamak, plasma equilibrium is established by the force-balance equation: $\underline{j} \times \underline{B} = \nabla p$. This equilibrium also consists of flux surfaces, which are slightly different from the vacuum flux surfaces. They equally fulfil the requirement $\underline{B} \cdot \nabla \Psi = 0$ where Ψ is a function that is constant on the flux surface. The diamagnetic current, \underline{j}_\perp , component of \underline{j} balances the pressure gradient. Since this current is not divergence-free an additional current along the field lines is necessary, the Pfirsch-Schlüter current, $\underline{j}_{P.S.}$, such that $\nabla \cdot (\underline{j}_{P.S.} + \underline{j}_\perp) = 0$. These two components of the current are indicated in Figure 11.

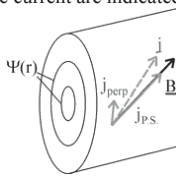


Figure 11 Schematic of the Pfirsch-Schlüter and diamagnetic current component.

In a net-current free stellarator the current filaments are poloidally closed. This can be seen in Figure 12.

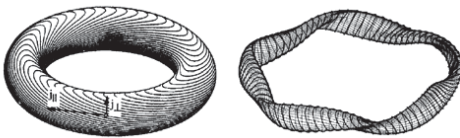


Figure 12 Current filaments on a flux surfaces of a tokamak (left) and of a stellarator (W7-X, right).

Since the Pfirsch-Schlüter current has a large vertical component, this leads to a plasma beta dependent horizontal displacement of the flux surfaces, called Shafranov-Shift Δ_{sh} approximately given by

$$\Delta_{sh} = 4\pi^2 \cdot R \cdot \beta / t^2$$

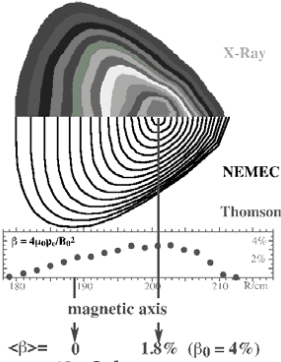


Figure 13 Soft x-ray reconstruction of the plasma temperature profile (upper half), calculated flux surfaces with NEMEC (lower half), plasma beta profile measured with Thomson scattering.

This leads to a limitation of the maximum achievable β since the maximal displacement of the plasma centre at most a (the plasma minor radius), thus $\beta_{max} = 4\pi^2 t^2 / A$ where A is the aspect ratio, $A = R/a$. This limit, however, can be increased by changing t or A accordingly or by changing the ratio of $\langle j_{||} \rangle / \langle j_\perp \rangle$ which is one of the goals in stellarator optimisation [21,22,23]. In the design of the stellarator W7-AS this current ratio was reduced by about a factor of 2 compared to the $l=2$ -stellarator W7-A. Experimentally, the resulting Shafranov-Shift can be inferred directly from the actual displacement of the hot plasma centres observed with soft X-ray tomography [23] as shown in Figure 13.

Figure 14 shows the measured plasma centre displacement for various values of the plasma beta as inferred from soft x-ray data for various values of plasma beta. The calculated values for a $l=2$ stellarator are shown for comparison. This demonstrates that the optimisation goal of reducing the Shafranov shift in W7-AS was achieved. The displacement of the plasma can also be deduced from measuring the vertical flux associated with the Pfirsch-Schlüter currents [25].

Similar to a tokamak plasma also a stellarator plasma generates a toroidal current as a result of the plasma density gradient and the friction between trapped and untrapped particles. Figure 15 sketches the orbit of a toroidally trapped particle. Superposed on the banana-orbit motion is a precession in toroidal direction (shown left). On the r.h.s. the orbit is shown in its poloidal projection. If there is a density gradient then there is a local toroidal flux of particles. Since they are trapped there no toroidal net current is associated with that. However, fractional drag with passing particles leads to a toroidal net current, the bootstrap current.

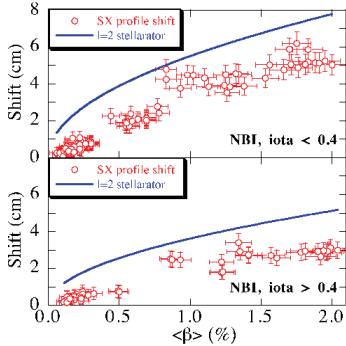


Figure 14 Measured Shafranov shift versus volume averaged plasma beta.

As was pointed out before in a stellarator particles can be helically trapped. Their drift direction is opposite to toroidally trapped particles due to the sign change of $\mathbf{B} \times \nabla B$. This is illustrated in Figure 16 for the special case of a true helical stellarator. Thus the associated bootstrap current has the opposite sign of the current caused by toroidally trapped particles.

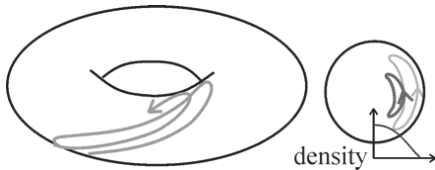


Figure 15 Perspective and poloidal projection of toroidally trapped particles. Density gradient causes a toroidal particle flux.

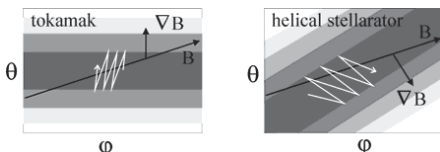


Figure 16 Drift motion of toroidally trapped particle in tokamak and helically trapped particle in a stellarator.

The bootstrap current reduces the externally applied rotational transform whereas the bootstrap current associated with toroidally trapped particles increases the rotational transform. Since it is undesirable to have the rotational transform being modified by the plasma pressure one can minimise the bootstrap current by an optimisation procedure: by balancing the toroidal and helical component of the field against each other. Any residual bootstrap current can be easily measured in a stellarator plasma since it is not necessary to separate out the (large) inductive plasma current as in a tokamak plasma. Figure 17 shows the measured and calculated values on ATF where by

Dirk Hartmann – Stellarator

changing the value of the quadrupole moment of the magnetic field one could change the ratio of helically and toroidally trapped particles [26] and thus the sign of the bootstrap current. The bootstrap current was measured with a Rogowski coil.

Perfect cancellation of the bootstrap current for all values of plasma beta and magnetic configurations is not possible. Therefore it is important to have means to compensate for the residual bootstrap current. This can be done by installing an Ohmic transformer (like in a tokamak) and inducing a compensation current in the plasma. But even if the total current is compensated it is locally not compensated since the ohmic current density profile peaks in the plasma center where the electron temperature is highest and the plasma resistivity is lowest whereas the bootstrap current peaks off-axis where the density gradient is highest. This can lead to different ι -profiles for constant edge $\iota(a)$ and might have degrading effects on plasma confinement. Another means is driving a current non-inductively by launching electromagnetic waves in preferentially one toroidal direction. For example, in electron cyclotron heating (ECH) the direction of the wave propagation can be steered with a mirror. Finally a current can also be driven in a plasma by heating with tangential, unbalanced neutral beam injection. For example, W7-X that is optimised for minimal the bootstrap current still requires up to 50 kA of externally driven toroidal plasma current driven by external means for compensation.

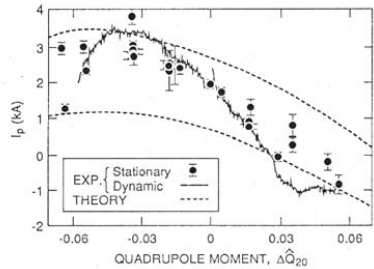


Figure 17 Bootstrap current in ATF.

V. PLASMA CONFINEMENT

This section describes how the different parameters of the vacuum magnetic field, such as the rotational transform, the shear and the magnetic well, influence plasma.

Off all magnetic flux surfaces those that have a rotational transform ι are singular. They are particular susceptible to small field perturbations in which case they form islands that short-circuit the inner plasma region with the outer region. Thus the plasma confinement is deteriorated. Strong shear inhibits the formation of islands. However, strong shear in a plasma also means that the ι -profile crosses a number of those "low order rational surfaces". Higher order rational surfaces are not important

since the large number of necessary toroidal and poloidal rotations renders other effects more important which prevent the creation of islands. The fractions made up of low integers are not equally densely spaced, rather regions around the simplest fractions, like $1/2$, are void of higher fractions. The low shear stellarators show the highest confinement times in these regions. This is shown in Figure 18 where the plasma energy is plotted versus $\iota(a)$ over a wide experimental range of the rotational transform on W7-AS [15]. Near the low order rationals the energy shows pronounced maxima. In contrast, high shear stellarators do not show such a dependence.

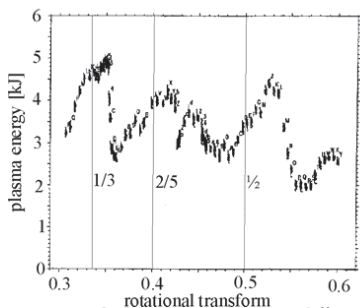
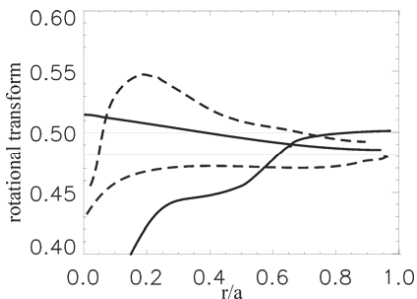


Figure 18 Stored plasma energy versus different values of the external rotational transform.

The dependence of the stored energy on the combination of ι and magnetic shear can be understood in more detail. By inducing a current in the plasma and changing the magnetic field configuration accordingly one can change the ι -profile while keeping the edge value $\iota(a)$ constant. In Figure 19 calculated ι -profiles are shown with approximately the same $\iota(a)$ but different profiles [27]. The horizontal lines indicate lower order rationals. The discharges with either a $\iota(r)$ -profile in the rational free zone or with strong shear (due to the induced current) have similar stored energies. Their ι -profiles are shown with solid lines. The stored energy belonging to the discharge that has a ι -profile neither in the rational-free zone nor with strong shear (shown with dashed lines) is only half as large than the others. Therefore in low shear devices like W7-AS and W7-X it is necessary to keep the iota-profile in a resonance-free region or add sufficient shear with an additional current to obtain optimal confinement.



Dirk Hartmann – Stellarator

Figure 19 iota profiles for good confinement (solid) and poor confinement (dashed).

The importance of the magnetic well is investigated in TJ-II. By changing the magnetic configuration from a magnetic well near the plasma edge to a magnetic hill the relative plasma density fluctuation level at the plasma edge doubled [28]. Whether this increased level of plasma density fluctuations is caused by pressure driven instabilities and whether this leads to a degraded plasma confinement is still under investigation.

VI. NEOCLASSICAL TRANSPORT

Neo-classical transport theory is the calculation of the transport coefficients (particle, energy, momentum) based on the particle drift orbits. The transport is calculated with a diffusion equation (assuming a random walk of the particles away from its flux surface) with a diffusion coefficient χ given by $\chi = \Delta r^2 / \tau_{coll}$, where Δr is the step size of the particle between two collisions and τ_{coll} is the time between two collisions. When collisions are important and the mean free path of the particles is short, the neo-classical predictions for stellarators and tokamaks are similar. Thus a stellarator exhibits a Pfirsch-Schlüter regime and a plateau regime corresponding to a tokamak. At even lower collision frequencies and thus longer mean free path lengths the transport coefficients show an increase inversely proportional to the collision frequency, called the $1/\nu$ -regime. This behavior is due to helically trapped particles. As was shown before helically trapped particles are localized in a small poloidal range. Their radial outward drift is fast. Therefore if the collision frequency is low, particles that are helically trapped increase the radial transport. This behavior is shown in Figure 20 for W7-AS.

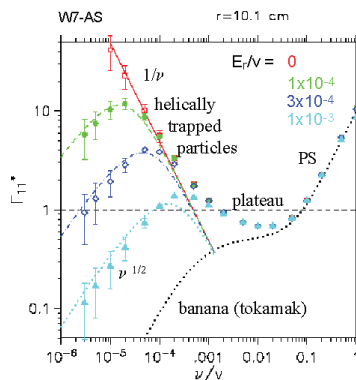


Figure 20 Particle transport coefficient versus normalised collision frequency.

With this $1/\nu$ -behaviour a stellarator would be unacceptable for a reactor because the energy and particle loss in the temperature regime where the reactor operates would be too large. An improvement of the neo-classical

confinement can be obtained either by optimising the magnetic field and limiting the number of helically trapped particles or by an additional radial electric field that limits the excursions of the helically trapped particles due to an additional $\underline{E} \times \underline{B}$ poloidal rotation [29]. With the radial electric field one obtains a region of a reduced transport coefficient that has a \sqrt{v} -dependence. Figure 20 shows the reduction for different values of the radial electric field, however, the values for W7-AS are still above those of an equivalent tokamak. In tokamaks there is no dependence of the transport coefficients on the radial electric field as long as the banana orbits still exist.

The electric field adjusts itself self-consistently according to the requirement of ambipolarity whereby the outward particle fluxes of electrons Γ_e and ions Γ_i are equal. Since the transport coefficients depend on E_r , even multiple solutions ("roots") of this condition are possible. In most discharges the "ion root" is observed with a rather small negative electric field and comparable electron and ion temperatures. With strong central electron heating it is also possible to obtain the "electron root" in the centre of the plasma with positive electric field and $T_e \gg T_i$. In Figure 21 l.h.s. the radial profile of the radial electric field is shown [27] for W7-AS. The lines are neo-classical calculations that at some locations have the two "roots". In Figure 21 r.h.s. the heat transport coefficient is calculated from the two roots and compared with the experimentally determined coefficient. Near the centre experimental and neo-classical values approximately agree with each other. Near the plasma edge the experimental values are much larger than the neo-classical values. Because of the small values of the transport coefficient these discharges have record electron temperatures [30]. The enhancement of the measured transport over the neo-classical transport is called anomalous transport and is particularly pronounced for electrons. Similar results are reported from CHS [31].

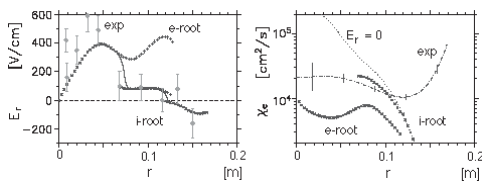


Figure 21 Calculated and measured electric field and calculated and measured electron heat transport coefficient.

The highest ion temperatures in W7-AS were obtained in discharges with a combination of electron cyclotron resonance heating and neutral beam injection [32,33]. These discharges were characterised by neo-classical electron and ion transport in the plasma centre up to 75% of the plasma radius and strong anomalous transport in the plasma edge region.

VII. TOWARDS A STELLARATOR REACTOR

In recent years the focus of stellarator research has become dominated by the demands of a fusion reactor. These studies include the investigation of

- parametric dependence of the plasma confinement on global quantities with the goal of extrapolating to the necessary size of a stellarator fusion reactor,
- high beta discharges and the search for instabilities that might limit the maximum achievable plasma beta,
- in-vessel components suitable to withstand high heat load and simultaneously causing little increase of impurity concentration in the plasma,
- long pulse discharges to verify the steady-state viability,
- non-inductive current drive to balance the internally generated plasma currents.

The plasma confinement properties of different helical devices are compared with one another by fitting the measured energy confinement time to a product of global quantities of minor radius a , major radius R , absorbed heating power P , on-axis magnetic field B , volume-averaged density n and edge rotational transform $t(a)$ with to be determined exponents. The energy confinement time τ_E is calculated from the measured stored plasma energy and heating power according to $\tau_E \equiv W/(P - dW/dt)$. This resulted in the International Stellarator Scaling ISS95 [34] given by

$$\tau_E \propto a^{2.21} \cdot R^{0.65} \cdot P^{-0.59} \cdot n^{0.51} \cdot B^{0.83} \cdot t^{0.4}$$

The scaling is well fitted by all helical devices. Note the positive dependence on minor and major axis. W7-AS and LHD have a proportionality factor that is between 1.5 and 2 higher than the scaling. This can be seen in Figure 22 where the measured energy confinement time is plotted versus the predicted value from ISS95.

In addition, values from tokamak L-mode discharges are shown that approximately follow the same scaling. The highest values belong to JET. In tokamaks, typically a factor of 2 improvement is obtained in H-mode discharges. The parametric dependence of tokamaks and stellarators is similar except that tokamaks do not show a positive dependence on density and stellarators do not show a dependence on particle mass of the plasma. Extrapolation based on this scaling is used in order to determine the required size of a reactor. Thus obtained dimensions ($R=20m$, $a=2m$) are considered feasible (see Section VIII).

An economically attractive reactor has to operate at the highest plasma beta possible since the magnetic field coils amount to about a third of the reactor investment costs. Therefore the optimisation process of the stellarator magnetic fields includes the plasma stability against pressure driven instabilities. For example, W7-X has been optimised for maximum average beta value of 5%. In W7-AS and LHD the maximum beta values were calculated to be about 2%. In both devices the predicted maximum beta

values have been surpassed in experiments and up to now the maximum achievable b has been limited by the available heating power and not by deleterious pressure driven instabilities [35,36,36].

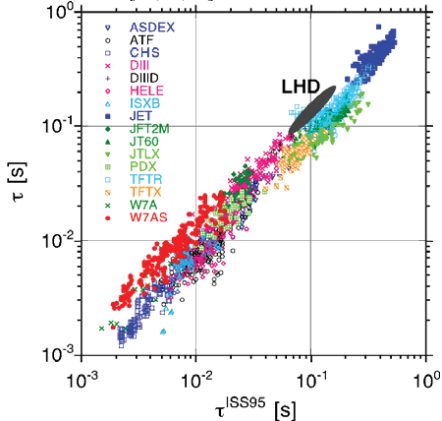


Figure 22 Measured energy confinement time of plasmas in helical devices and L-mode tokamak discharges versus international stellarator scaling ISS95.

Stellarators are inherently capable of steady-state operation since plasma confinement does not require a constantly driven toroidal plasma current LHD and W7-X are equipped with super-conducting coils. It also requires plasma heating methods capable of steady-state operation. Appropriate sources for neutral beam injection and electromagnetic wave generation are being developed at present. In ATF a one-hour discharge has been achieved at small power level with electron cyclotron heating and low values of magnetic field and plasma density [38]. In LHD plasma discharges at higher power levels and magnetic fields have reached a duration of several minutes. An example for a plasma shot over longer than a minute is shown in Figure 23 [39,39].

Stellarators and tokamaks need to keep impurities that are released by wall sputtering from entering the plasma and need to keep the heat load on any surface low. In a tokamak this is done adding additional coils to generate an X-point. Fanning out the plasma near there and directing it at acute angles on target plates, the divertor plates, it is possible to keep the core plasma well separated from the edge region. The magnetic surface that passes through the X-point becomes the last closed flux surface. Thus the magnetic field lines that intersect the target plates have no direct connection to the interior plasma. In a stellarator it is not possible to introduce additional X-points, however, the natural islands (compare Figure 24 l.h.s.) already provide such X-points. In an island divertor these islands are intersected with high heat load resilient target plates. Thus a similar separation of plasma-target interaction zone and main plasma as in a tokamak is achieved. It is also possible to intersect the helical islands that exist outside of a heliotron. This has been done on LHD where graphite tiles

have been installed that intersect the helical plasma fans (compare Figure 24 r.h.s.). This reduced the iron impurity influx and led to improved plasma performance [39].

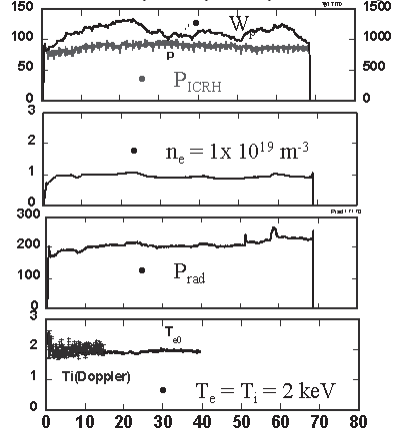


Figure 23 Long pulse discharge done with ion cyclotron resonance heating on LHD

On W7-AS an island divertor has recently been installed. In contrast to a tokamak it consists of 5×2 modules located at isomorphic positions in the vessel. Figure 24 shows a picture of one module before installation. Each module consists of two graphite target plates separated by a small pumping region that intersect the islands and baffles that shield the back side of the divertor module from the plasma region and allow for additional gas pumping.

The first results obtained with this divertor are encouraging [17,43]. It facilitated plasma operation at high densities (line-averaged density $>3 \times 10^{20} \text{ m}^{-3}$) under steady-state conditions for the longest plasma duration possible in the device. The plasma edge temperature in the vicinity of the target plates could be reduced to values of about 10 eV. At this temperature the plasma ions start to recombine and high radiation loss occurs due to partially ionised carbon (partial detachment). This isotropic radiation reduces the heat load on the target plates and therefore also the sputtering of target material. Thus the radiation profile of the plasma was dominated by the radiation from the plasma edge. In addition, it was found that the confinement time of artificially injected impurities (aluminum) decreased in these high density scenarios which is very encouraging for reactor operation. Finally, the density in these discharges was sufficiently high to heat the plasma centrally with electron cyclotron resonance heating overcoming the usual plasma density cut-off for wave propagation by invoking a mode conversion of the ordinary plasma wave into an electron Bernstein wave [30]. The same type of divertor will also be used for W7-X.

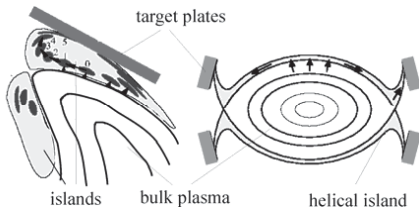


Figure 24 Schematic of the island divertor of W7-AS and of the helical divertor of LHD.

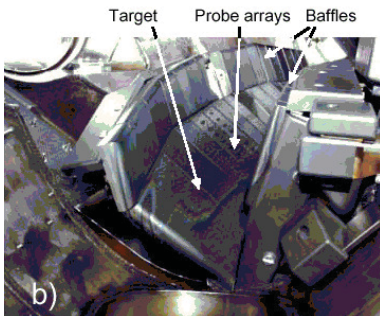


Figure 25 Picture of one module of the island divertor of W7-AS.

Studies investigate the stellarator reactor properties based on the concept of LHD and W7-X [19,41]. Based on the experimental confinement time scaling of W7-AS a helias reactor (optimisation similar to W7-X) that yields a fusion power of 3000 MW has a major radius of 18m and a minor radius of about 2m. The field at the coils is sufficiently low to allow the use of conventional NbTi super-conductors. The total weight of the super-conducting

Dirk Hartmann – Stellarator

coils will be less than half of that for ITER which will significantly reduce the costs of the device. However, the manufacturing costs of the non-planar coils will be higher. The larger aspect ratio than a tokamak and therefore the increased area of the vessel reduces the neutron wall loading such that blanket segments probably need to be replaced less often than in a comparable tokamak reactor.

VIII. PHYSICS CHALLENGES OF THE STELLARATOR CONCEPT

In order to feel confident about proposing the stellarator as a viable fusion reactor concept a number of physics challenges still have to be overcome or their proposed remedies have to be demonstrated. The neo-classical transport in the reactor regime has to be reduced to levels acceptable in a reactor. This can be done by further optimisation of the magnetic field in particular by generating magnetic fields that have quasi-symmetries (quasi-helical, quasi-axial, quasi-omnigeneous) from the particle point of view or by enhancing the radial particle flux of one species to drive a radial electric field. Experiments are in planning or have already been build that will test these approaches. The viability of the island divertor has to be experimentally demonstrated. The current profile control with ECH or tangential neutral beam for bootstrap current compensation has to be tested in high density situations. Whether there is an experimental limit to the maximum achievable plasma beta imposed by magnetohydrodynamic events still has to be investigated. Up to now no universal features have been identified that account for limitations of the maximum achievable energy. Central particle refuelling could be a problem [42] but might be accomplished with negative neutral beam injection. Finally high α -particle confinement at high energies and simultaneously low confinement at thermal energies for helium ash removal still have to be investigated.

IX BUILDING WENDELSTEIN 7-X

A number of the issues raised in the previous section are planned to be addressed in the stellarator experiment Wendelstein 7-X (W7-X). This experiment is presently being built at the Max-Planck Institute for Plasma Physics in Greifswald. Completion of assembly is planned for end of 2015 and start of commissioning for beginning of 2016.

The goals of W7-X have been chosen to be reactor relevant [45]. Thus it is to achieve quasi-steady state operation at temperatures in excess of 5 keV and densities on the order of 10^{20} m^{-3} , to reach plasma equilibrium with an average beta of 5%, to control plasma density and its impurity content. Ignition is not one of the goals, thus the device will not be operated with a tritium, deuterium mixture. Plasma experiments, therefore have to be done with external plasma heating.

The structure of the magnetic field is decisive for the

energy confinement time of stellarators even though also for these devices anomalous transport is a dominant factor. Therefore the structure of the magnetic field has been chosen such that simultaneously a number of criteria are met [45]:

- (1) Magnetic surfaces with a corresponding iota profile that avoid low order resonances to limit the effect of islands.
- (2) A small Shafranov shift to yield a high beta limit and to allow installation of an island divertor.
- (3) Good magneto hydrodynamic stability via a magnetic well to achieve a high plasma beta.
- (4) Reduced neoclassical transport in the $1/\nu$ regime.
- (5) Small bootstrap current to avoid changing the iota profile to create low resonance islands
- (6) Good modular coil feasibility (only modular coils allow generation of the magnetic field that meets the criteria (1)-(5)).

The magnetic field that meets these requirements is called to have a quasi-isodynamic property [46].

The basic parameters of W7-X to generate such a magnetic field and to achieve the experimental goals mentioned above are: Major average radius 5.5m, minor average radius 0.5 m, a magnetic field of up to 3 T on axis, 10 MW cw plasma heating with ECRH for up to 30 minutes, up to 20 MW of pulsed (10 sec) NBI heating.

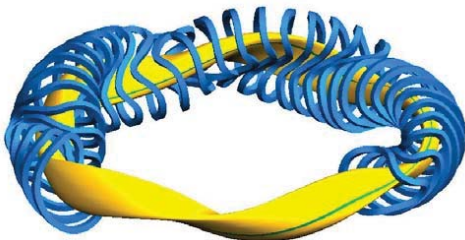


Figure 26 Simplified non-planar coils of 3.5 modules of W7-X and the lcfs of the plasma

The magnetic field is generated a set of 50 modular superconducting coils of 5 different types supplemented by a set of 20 superconducting planar coils of two types for added experimental flexibility arranged in a five-fold symmetry (Fig. 26). The coils are wound of NbTi strands in an aluminium cable with in-conduit He cooling that are placed in a stainless steel housing. Coils of the same type are electrically connected in series and powered by an independent power supply. All coils are bolted to a support structure that forms an inner ring in the torus. Additional support elements are added between neighbouring coils. All coils and coil housings are individually supplied with liquid helium.

All the magnets, the support structures and supply lines are lined in a toroidal, vacuum tight double shell structure, called the cryostat, whose inner wall is the plasma vessel. All inside surfaces of the cryostat are insulated against thermal radiation by multilayer
Dirk Hartmann – Stellarator

aluminium coated capton foils under a thermal shield helium cooled to 80 K.

The plasma vessel and its 254 ports have to be protected from convective, radiation and fast particle plasma losses while sources for plasma impurities have to be kept sufficiently small. A toroidally extended island divertor is installed at ten symmetric locations in the plasma vessel that is designed to withstand the convective losses of up to 10 MW/m². Its plasma facing elements consists of CFC material that is brazed on an actively water-cooled support structure. The area close to the divertor can be actively pumped with cryo pumps to reduce the effects of recycling and impurity generation on the plasma. Additional control coils that can be operated with a AC current can diffuse the magnetic field lines to reduce the heat load. Areas of the plasma with reduced convective losses of up to 500 kW/m² are covered with graphite tiles that are clamped onto a water-cooled support structure. Areas where no convective losses are expected including the inside walls of the 254 ports are covered with water cooled stainless steel sheets. The cooling circuits occupy about 120 of the 254 ports. The remainder is used for plasma heating and diagnostics. A schematic cut-open view of the basic device is shown in Fig. 27.

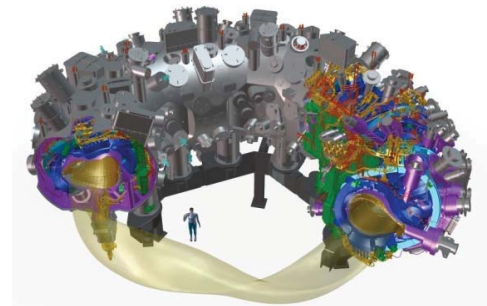


Figure 27 Schematic, cut-open view of the basic device of Wendelstein 7-X.

The plasma heating systems consists of 10 gyrotrons at 140 GHz with a nominal power of 1 MW each during steady-state operation for ECRH heating, predominately 2nd X mode heating. The power is transported into the torus hall with optical transmission and directed into the plasma using steerable mirrors thus facilitating current drive and also advanced heating methods. Further heating for high heat experiments and studies of particle confinement is provided by 2 NBI injectors with 4 sources each for pulsed 2.5 MW injection at up to 90 keV D. Eventually, also a 4 MW ICRH system will be installed for high beta experiments and further studies with fast hydrogen ions.

The diagnostic systems are being prepared to allow full characterization of the plasmas. A Thomson scattering system with 50 channels will measure electron temperature and density every 50 msec. A dispersion interferometer system with 5 channels will measure the line integrated

electron density continuously. An ECE radiometer will measure the electron temperature profiles at 24 different locations. A test neutral beam injector system will measure the ion temperature at three adaptable locations. A bolometer system to measure the 2 D shape of the flux surfaces at finite beta experiments. Magnetic diagnostics measure the diamagnetic energy, the plasma current profile and magneto-hydrodynamic fluctuations.

The assembly of the device is organized by identifying sub components that can be pre-assembled to reduce the number of required assembly steps in the torus hall. To that purpose all coils of one half module that corresponds to a 36° segment of the device were first mounted onto the appropriate sector of the plasma vessel and attached to the sector of the central support structure before mounted to the neighboring half module to form one complete module. Cryo lines and the bus lines for the electrical coil connections were installed if possible. This sub-assembly were then lowered into the lower half shell of the outer vessel, placed on the machine base into the torus hall, before one module was then completed by welding the upper shell of the outer vessel on top. Thus subsequently the five modules were placed onto the machine base in the torus hall where the attachments of the segments of the central support structure to its neighbours, the cryo and bus lines, the thermal insulation, plasma vessel and the outer vessel was done. Since the overall required accuracy of the location of the current paths of the coils has to be on the order of a few millimetres, great care was taken to ensure that during the subsequent assembly steps there was no accumulation of an intolerable large error. The 254 ports and the current leads that provide feed throughs for the coil current are installed then. The view of the experimental hall after four modules have been installed (2012) is shown in Fig. 28.



Figure 28 View of the basic device in the experimental hall when four of the five modules were installed.

The installation of the components inside the plasma vessel is done in two steps corresponding to two phases of operation. In the first phase when the total injected energy per plasma discharge will be limited to 50 MJ uncooled divertor units will be installed together with a subset of the wall panels and graphite protections. For a second phase of

operation these divertor units are replaced with the completely water cooled divertor units and all other protective elements and diagnostics will be installed. Presently, as of summer 2013, the plasma vessel components for the operational phase 1 are being installed.

In addition to the device itself, a number of additional components (e.g. diagnostics, heating systems, peripheral supply lines, support structures) have to be placed in the experimental hall. Due to the limited space and the need for simultaneous development the design and the layout of these components have to be done following the principles of concurrent engineering. To that purpose a reference CAD model set is updated daily that describes the present state and maturity of the design of the various components and configuration management tools are applied throughout. The present design of the torus hall is shown in Fig. 28.

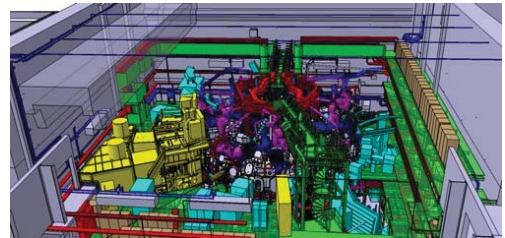


Figure 29: CAD view of the experimental hall with the basic device (grey), heating systems (yellow), cooling water lines (blue), cable trays (red), support structures (green), vacuum systems (magenta), cubicles (brown), diagnostics (light blue) diverse infrastructure elements (light grey).

At present plans are being developed to commission the about 50 main systems for operation. First each system needs to be provided with the required means for operation. Thus these supply systems have first to be commissioned on their own. Each system is then put into local operation. Then the complete system of W7-X is sequentially put into operation. In order to save time commissioning processes have been parallelized wherever possible, certain commissioning processes even run in parallel to remaining assembly processes. Care is been taken to check for all logical interdependencies that have to be taken into account. It is planned to put the cryostat under vacuum first before evacuating the plasma vessel. During the subsequent cool-down of the cryostat the deformation of the magnet system is being measured. After the coils have been successfully energized the accuracy of the magnetic field is then measured. Should magnetic field errors be detected that cannot be tolerated the trim coils will be put into operation to correct for them. A short experimental campaign to provide a first check of the ECRH heating system and principle diagnostics will then conclude this first operational phase in the beginning of 2015. After that campaign the assembly of remaining components of the plasma vessel will resume to then start the first experimental exploration of W7-X late in 2015.

REFERENCES

1. M. Van Schoor, "Fusion Machines", these proceedings.
2. Jaspers, "Thermonuclear Burn Criteria", these proceedings.
3. L. Spitzer, *Phys. Fluids* 1, 253 (1958).
4. A. Iiyoshi et al., *Nucl. Fusion* 39, 1245 (1999).
5. G. Grieger, *J. Plasma Fusion Res.*, (1998).
6. D.T. Anderson et al., *J. Plasma Fusion Res. SERIES*, Vol. 1 (1998).
7. B.A. Carreras et al., *Nuclear Fusion* 28, 1613 (1988).
8. G. Grieger et al., *Nuclear Fusion* 25, 1231 (1985).
9. J.I. Shohet in *Fusion* (Ed. E. Teller) Vol. I, 243, Academic Press, Cambridge 1980.
10. C. Alejaldre et al., *Plasma Physics Control. Fusion* 41, 539 (1999).
11. J. Nührenberg et al., *Phys. Lett. A* 129, 113 (1988).
12. D.A. Spong, 18th Fusion Energy Conf. Proc. 2000.
13. E. Ascasibar, *J. Plasma Fus. Res.*, 1, 183 (1998).
14. Komori, *Stell. News* 58, 1 (1998).
15. R. Jaenicke et al., *Nucl. Fusion* 33, 687 (1993).
16. De Blank, "Plasma Equilibrium in Tokamaks", these proceedings.
17. P. Grigull et al., *Plas. Phys. Contr. Fus.* 43, A175, (2001)
18. H.J. de Blank, "Guiding Center Motion", these proceedings.
19. M. Wakatani, "Stellarator and Heliotron Devices", Oxford University Press, 1998.
20. K. Miyamoto, "Plasma Physics for Nuclear Fusion", MIT Press, 1989.
21. J. Nührenberg et al., *Trans. Fusion Technology* 27, 71 (1995).
22. G. Grieger et al., *Physics of Fluids B* 4, 2081 (1992).
23. H. Wobig, *Plasma Physics and Contr. Fusion* 35, 903 (1993).
24. Weller et al., *Plasma Phys. And Contr. Fusion* 11, 1559 (1991).
25. H. Renner et al., *Controlled Fusion and Plasma Physics, Proc. 19th European Conf., Innsbruck, 1992*, Vol. 16C, Part I, 501.
26. M. Murakami, *Phys. Rev. Lett.* 66, 707 (1991).
27. R. Brakel et al., *Plasma Phys. Control. Fusion* 39, B273 (1997).
28. C. Alejaldre et al., 18th Fusion Energy Conf. Proc., 2000.
29. H. Maassberg et al., *Plas. Phys. Contr. Fus.* 35, B319 (1993).
30. H. Laqua et al., *Phys. Rev. Lett.* 78, 3467 (1997).
31. H. Idei et al., *Phys. Rev. Lett.* 71, 2220 (1993).
32. R. Jaenicke et al., *Plas. Phys Contr. Fus.* 37A, 163 (1995).
33. J. Baldzuhn et al., *Plasma Physics Control. Fusion* 40, 967 (1998).
34. U. Stroth et al., *Nucl. Fusion* 36, 106 (1996).
35. M. Fujiwara et al., 18th Fusion Energy Conf. Proc. 2000.
36. R. Jaenicke et al., 18th Fusion Energy Conf. Proc. 2000.
37. Weller et al, *Phys. Plas.*, 8, 931, (2001).
38. T.C. Jernigan et al., *Phys. Plas.*, 2, 2435, (1995).
39. R. Kumazawa et al., *Phys. Plas.*, 8, 2139 (2001). LHD, *Stell. News* 62 (1999).
40. Komori et al., *Phys. Plas.*, 8, 2002, (2001)
41. C.D. Beidler et al., 18th Fusion Energy Conf. Proc. 2000.
42. H. Maassberg et al., *Plasma Physics Control. Fusion* 41, 1135 (1999).
43. M. Hirsch et al., *Plasma Phys. Control. Fusion* 50 (2008)
44. H. Wobig et al., „Nuclear Energy“, Vol. 3B, chapter 7, Springer, Berlin, 2005, p. 418.
45. C. Beidler et al. *Fus. Tech.*, 17, 11, (1990)
46. C. Beidler et al., *Nucl. Fusion* 51, 1 (2011)

CONFINEMENT IN TOKAMAKS

J.ONGENA

Laboratoire de Physique des Plasmas-Laboratorium voor Plasmafysica
Association "Euratom-Etat belge"-Associatie "Euratom-Belgische Staat"
Ecole Royale Militaire-Koninklijke Militaire School
Brussels

I. INTRODUCTION

The total amount of heating power coupled to the plasma P_{tot} and the energy confinement time are determining parameters for realizing the plasma conditions suitable for the reactor. We recall that the ignition condition can be expressed by the following condition on the triple fusion product:

$$nT\tau = \frac{P_{tot}\tau^2}{3Vol} = \frac{3n^2T^2Vol}{P_{tot}} > (nT\tau)_{ignition} \quad (1)$$

where $\tau = E / P_{tot}$ is the energy confinement time, $E = 3nT Vol$ for an isothermal plasma with $T_i = T_e = T$ and a plasma volume Vol ; n is the plasma density. The value $T \approx 15 \text{ keV}$ corresponds to the minimum value of $(nT\tau)_{ignition}$ as a function T (see Fig. 1). In the present discussion for the sake of simplicity, we neglect density and temperature profile factors. The heating power in most of the present experiments is given by $P_{tot} = P_{OH} + P_{add}$ where P_{OH} is the ohmic power and P_{add} is the additional heating due to neutral beam injection or radiofrequency heating. At ignition, the additional heating power must come completely from the energetic α -particles produced by the fusion reactions and we must have $P_{tot} = P_\alpha$ if we neglect the residual P_{OH} and the plasma losses by Bremsstrahlung ($P_{Br} \propto n^2\sqrt{T}$).

Around $T \approx 15 \text{ keV}$ the fusion power P_f is approximately given by:

$$P_f = 5P_\alpha \propto n^2T^2 Vol \propto \beta^2 B_t^4 \quad (2)$$

This expression shows that for a given machine characterised by his volume and toroidal magnetic field B_t i.e. his cost, the achieved value of P_f depends on the plasma beta

$$\beta = 4 \mu_0 \frac{nT}{B_t^2} = 0.01 \beta_n \frac{I_p}{aB_t}$$

The value of β is generally normalised with respect to the ratio $\frac{I_p}{aB_t}$ expressed in MA/(m T) (where I_p is the

plasma current and a is the plasma minor radius) which is an important parameter to express the beta limit of the toroidal plasma due to MHD instabilities; the achieved beta performances of a given machine are then expressed by the factor β_N . The fusion power is limited by the maximum achievable value of β_N through the relation

$$P_{f,max} \propto \beta_n^2 \left(\frac{I_p}{aB_t} \right)^2 Vol B_t^4 \propto \left(\frac{\beta_n}{q} \right)^2 \left(\frac{a}{R} \right)^2 Vol B_t^4 \quad (3)$$

where q is the discharge safety factor at the edge

$$q = \frac{5a^2B_t}{RI_p} \quad (\text{m,T,MA}), \text{ and } R \text{ is the major radius.}$$

In the present machines with negligible fusion power production, β_N and τ are also determining the maximum heating power, given by the formula below, that the discharge can tolerate without disruption due to the β limit:

$$P_{tot,max} = 0.0375 \frac{\beta_{n,max}}{\mu_0\tau q} B_t^2 \left(\frac{a}{R} \right) Vol \quad (4)$$

Equ. (4) is generally a non-linear equation in P_{tot} because τ is a function of P_{tot} (e.g. $\tau \propto P_{tot}^{-0.5}$).

In a reactor operating at $T \approx 15 \text{ keV}$, the maximum beta and therefore the maximum fusion power can also be limited by the maximum achievable plasma density. For gas puff fuelled discharges it is found empirically that the maximum observed density in a tokamak is the so-called Greenwald limit [1] given by:

$$\bar{n}_{eo,GR} = \frac{I_p}{\pi a^2} = \frac{5B_t}{\pi R q} \quad (10^{20} \text{m}^{-3}, \text{MA}, \text{m}, \text{T}) \quad (5)$$

when expressed in the mentioned units, $\bar{n}_{eo,GR}$ being the central line averaged density. The ratio $\bar{n}_{eo} / \bar{n}_{eo,GR}$ is often called the Greenwald number and its value thus indicates how close a given plasma density is with respect to the Greenwald limiting density. Note that in the last 2 years several machines have overcome this limit to a large extent and have obtained Greenwald factors of up to 1.7 stationary and up to 2 transiently. In most of the cases these supra-Greenwald densities are accompanied by a strong reduction in confinement, even lower than L-Mode confinement (see § II.A for a discussion of the different confinement modes). Under RI-Mode conditions as obtained on TEXTOR (see § IV.B), this degradation in confinement can be overcome and discharges can be obtained with a Greenwald factor of 1.4 with simultaneously ELM-free H-Mode confinement.

In the original design of ITER (International Thermonuclear Experimental Reactor) as specified in the Final Design Report [2,15] the following values for the machine parameters are considered: $R = 8.14 \text{ m}$, $a = 2.8 \text{ m}$ (with elongation $\kappa \sim 1.6$), $B_t = 5.68 \text{ T}$, $I_p = 21 \text{ MA}$, $P_f = 1.5 \text{ GW}$, $n\tau T = 3.3 \times 10^{21} \text{ m}^{-3} \text{ keV s}$, $\bar{n}_{eo} = 1.3 \times \bar{n}_{eo,GR}$, $\beta_N = 2.4$, $\tau = 6 \text{ s}$, $E = 1.2 \text{ GJ}$. Note that the current design of ITER (2009) is one with reduced parameters, (caused by the withdrawal of the US as an ITER partner in 1996 for a mix of political and erroneous scientific reasons; they joined again in 2001). The current ITER design (2009) has a 50% reduced capital cost compared to the previous larger design and the main parameters are: $R = 6.2 \text{ m}$, $a = 2.0 \text{ m}$, $\kappa = 1.70\text{-}1.85$, $B_t = 5.3 \text{ T}$, $I_p = 15\text{-}17 \text{ MA}$, $P_f = 500\text{-}700 \text{ MW}$, $\bar{n}_{eo} = \bar{n}_{eo,GR}$, $\beta_N = 1.8\text{-}2.4$, $\tau = 3.6\text{-}3.9 \text{ s}$.

To reach ignition, the ohmic power alone is not sufficient and additional heating power is necessary. Additional heating of tokamak plasma is performed by neutral beam injection and radio-frequency heating. Various ranges of frequencies are used for the radio-frequency heating. Mainly (i) the ion cyclotron frequency range (ICRH ~ 10 to 150 MHz) where powerful tetrodes are used as power source and where electron and ion heating is possible; (ii) the lower hybrid frequency range (LH $\sim 1 \text{ GHz}$ to 10 GHz) which is used mainly for current drive (LHCD) and where the power is delivered by klystrons; (iii) the electron cyclotron frequency range (ECRH ~ 30 to 200 GHz) where electron heating is performed and which uses gyrotrons as power source. This last frequency band requires the simplest structures inside the tokamak achieving the highest RF power density but still requires the development of gyrotrons able to deliver long pulses in the MW range to compete with the ICRH method. ICRH together with neutral beam

injection are the most widely used methods for additional heating on large machines.

II. CONFINEMENT IN OHMIC AND ADDITIONALLY HEATED DISCHARGES WITHOUT INTERNAL TRANSPORT BARRIER

II.A. Scaling laws

Confinement in tokamak plasmas does not behave classically due to anomalous diffusion. There exist many theoretical models of anomalous diffusion linked to different types of turbulence which can be classified in two main categories: electrostatic and magnetic turbulence. Each theory leads to its own expression for the scaling of confinement. Up to now, the major mechanism(s) for anomalous diffusion have not been clearly identified. In practice, empirical scaling laws are derived by assuming that the global confinement scaling can be taken as a power law of so-called engineering quantities:

$$\begin{aligned} \tau &= C_1 I_p^r R^p a^\alpha B_t^\beta n^v P_{tot}^\pi \kappa^k M_i^\mu \\ &= C_2 a^{2+\alpha} B_t^{1+\beta} n^v P_{tot}^\pi R^{\rho-1} q^{-1} \kappa^k M_i^\mu \end{aligned} \quad (6)$$

(where M_i is the ion atomic mass and $\kappa = b/a$ the plasma elongation) and by fitting this expression to an as large as possible set of experimental data obtained on different tokamaks.

Note (i) that the engineering quantities can be replaced by a set of non-dimensional ones which are assumed to express the physics of confinement (e.g. ρ^* , β , v^* , a/R , κ , q , M_i) [3] and (ii) that other expressions can be considered to fit to the confinement database (as e.g. the linear offset scaling: see § II.B).

II.B. Confinement scaling of ohmically and additionally heated tokamaks

Following the presentation of B.B.Kadomtsev [4] the usual confinement of ohmic and additionally heated discharges can be summarised as following (see Fig. 2):

(A) In ohmically heated discharges, at low plasma densities, the energy confinement is proportional to the plasma density and can be expressed by the so-called Neo-Alcator or Linear Ohmic Confinement (LOC) scaling law (here given for the circular case i.e. $\kappa = 1$):

$$\tau_{NA} \propto \bar{n}_{eo} R^2 a q^\alpha M_i^{0.5} \quad (7)$$

where \bar{n}_{eo} is the central line-averaged density, R and a resp. the major and minor radius. We added a

dependence on the atomic mass M_i of the plasma ions which is often observed [5]; q is the safety factor at the edge with $0.5 < \alpha < 1.0$, depending on the machine. For TEXTOR it has been shown [6] that $0.5 < \alpha < 0.8$ and for the sake of simplicity, we take $\alpha = 0.5$. The Neo-Alcator scaling is considered as the experimental optimal mode for confinement in tokamaks [4]. Above a certain density n_s , a saturation of the ohmic confinement can occur. This Saturated Ohmic Confinement regime (also called SOC) has a low density dependence and can often be described by taking the L-mode scaling law for additional heated discharges (see equation (8) in the next section), where P_{tot} is substituted by the ohmic heating power, P_{OH} [7].

Using an adequate procedure for the conditioning of the wall [8] or pellet injection it is possible to restore a Neo-Alcator scaling for confinement at high densities. This regime, which has been called Improved Ohmic Confinement (IOC) is the prolongation of τ_{NA} above $\bar{n}_{e0} = n_s$ as shown in Fig. 2. Practically, on TEXTOR at high densities, the ohmic confinement lies between τ_{NA} and τ_{SOC} depending upon the machine condition.

	C_1	ν	ρ	α	β	γ	π	k	μ
GOLDSTON [9]	3.68×10^{-2}	1.00	1.75	-0.37	0.00	0.00	-0.50	0.50	0.50
KAYE-GOLDSTON [10]	3.02×10^{-2}	1.24	1.65	-0.49	-0.09	0.26	-0.58	0.28	0.50
ITERL-89P [11]	4.80×10^{-2}	0.85	1.20	0.30	0.20	0.10	-0.50	0.50	0.50
ITERL-97P [12]	3.40×10^{-2}	0.96	1.89	-0.06	0.03	0.40	-0.73	0.64	0.20
ITERH-92P(Y) [13]	3.40×10^{-2}	0.90	1.90	-0.20	0.05	0.30	-0.65	0.80	0.40
IPB98(y,2) [14]	3.65×10^{-2}	0.93	1.39	0.58	0.15	0.41	-0.69	0.78	0.19
ITERH-93P [15]	3.60×10^{-2}	1.06	1.90	-0.11	0.32	-0.17	-0.67	0.66	0.41
ITERH-97P [16]	3.10×10^{-2}	0.95	1.84	0.08	0.25	0.35	-0.67	0.63	0.42

Table 1: Coefficients for confinement scaling expressions of the form

$$\tau = C_1 I_p^\nu R^\rho a^\alpha B_t^\beta n^{\gamma} P_{tot}^\pi \kappa^k M_i^\mu$$

with units (s, MA, m, m, T, $10^{19}m^{-3}$, MW, -, -)

(B) When additional heating is applied, the basic mode of confinement is L-mode. If one looks at the values of the exponents for different empirical scalings (see Table 1), one observes that to a good approximation:

$\nu \approx 1$, $\beta \approx 0$, $\gamma \approx 0$, $\alpha \approx 0$, $\rho \approx 1.5$, $\pi \approx -0.5$, $k \approx 0.5$, $\mu \approx 0.5$
Therefore Equ. (6) can be approximated as :

$$\tau = f_H C_1 I_p R^{1.5} P_{tot}^{-0.5} (\kappa A_i)^{0.5} \quad (8)$$

where f_H is an enhancement factor with respect to the considered scaling. It is characterised by a low-density dependence, a linear increase with current and a degradation with the total applied heating power.

Illustrations of the low-density dependence and of the power degradation of the L-mode are given on Figs. 3a and 3b.

The L-mode scaling can also be described approximately by the T-10 scaling ([4], p.141):

$$\tau_{T-10} = \tau_{SOC} \sqrt{\frac{P_{OH}}{P_{tot}}} \approx \tau_L \quad (9)$$

Many improved confinement schemes have roughly the same parametric dependence, and can be characterised by their enhancement factor f_H with respect to L-mode scaling. The best known is the H-mode regime, for which $f_H = 1.5$ to 2 (see the ITERH-93P scaling of Table 1 for ELM-free H-mode discharges which has a parametric dependence similar to the L-mode scalings).

The H-mode is an improved confinement regime which is observed in divertor machines above a certain threshold for the additional heating power. The H-Mode is characterised by the following features: existence of a transition between the usual confinement regime (L-mode) and the H-mode with a reduction of the H_α light at the transition, formation of a density and/or temperature pedestal at the plasma edge and an improvement of the energy and particle confinement time. During the H-mode, MHD events called ELMs (Edge Localised Modes) can occur and the confinement improvement will depend on their repetition rate. Moreover, at high density a further degradation is often observed, and it is difficult to maintain the H-mode or even L-mode confinement up to the density limit of the machine (cfr. the discussion of the Greenwald limit in § 1).

The largest confinement is obtained in the absence of ELMs but this confinement regime leads to non-stationary discharges ending with the onset of MHD phenomena and with a tendency of impurity accumulation in the centre of the plasma (see Fig. 4a). Stationary conditions can be obtained in ELMy H-Mode discharges (see Fig. 4b). Confinement in such plasmas is somewhat lower than in ELM-free H-Modes and can be roughly characterised by:

$$\tau_{ELMy H-mode} = 0.85 \times \tau_{ITERH-93P} \quad (10)$$

The ELMy H-mode regime is presently considered as the favourite operational regime for ITER to reach ignition.

The extrapolation of ELMy H-Mode confinement, as given by equation (10), to the parameters of ITER is shown in Fig. 5.

Additionally heated discharges can also be described, especially for the transition from OH to predominantly additionally heated conditions, by the

linear offset scaling [6]:

$$\tau_{OL} = \frac{\tau_{OH}P_{OH} + \tau_{inc}(P_{tot} - P_{OH})}{P_{tot}} \quad (11)$$

with τ_{OH} being the ohmic confinement time and equal to τ_{NA} or τ_{SOC} , depending on the machine conditions. The incremental confinement time τ_{inc} is proportional to I_p [6] and is relatively insensitive to P_{tot} and \bar{n}_{e0} for not too high values of these quantities. At high values of P_{tot} , τ_{inc} decreases as given by Equ (8). Fig. 6a shows the evolution of $E = P_{tot}\tau_{OL}$ as a function of \bar{n}_{e0} compared to the behaviour of the ohmic energy $E_{OH} = P_{OH}\tau_{OH}$. For $\bar{n}_{e0} > n_s$ the increase in plasma energy, $\tau_{inc}(P_{tot} - P_{OH})$, can take place with respect to the Neo-Alcator scaling (or its extension above n_s , IOC) instead of the SOC. Starting from SOC, one would find an apparent large τ_{inc}^* (see Fig. 6a). In fact, the total increase of energy is not only due to the heating effect (as described by τ_{inc}) but also by the restoration of the non-saturated ohmic confinement regime by the additional heating (e.g. by its action on the plasma boundary) [6]. This is illustrated in Fig. 6b.

II.C. Triple fusion product scaling

From equations (8) and (1) one can derive an approximate expression for the triple fusion product:

$$nT\tau = C_2 \left(\frac{f_H}{q} \right)^2 (aB_i)^2 M_i = C_3 \left(\frac{R}{a} I_p \right)^2 f_H^2 M_i \quad (12)$$

where f_H is the enhancement factor of the considered discharge regime with respect to a standard L or H mode scaling. The constants C_2 and C_3 depend on the scaling chosen.

Expression (12) shows that the value of the triple fusion product required for ignition $(nT\tau)_{ignition}$ is more easily obtained at a large current and aspect ratio R/a , and with a large enhancement factor f_H . For a given value of aB_i (characterising the toroidal field coils) the ignition condition is strongly dependent on the ratio f_H/q which is considered as a figure of merit for ignition margin [8].

Equation (12) also shows that the usual power degradation observed for confinement $\propto P_{tot}^{-0.5}$ leads to a scaling of the triple fusion product independent of the additional heating power.

Fig. 1 shows the values obtained for $nT\tau$ versus T in different experiments. The 'parabolic' lines indicate the domains corresponding to ignition (reactor conditions) or breakeven (fusion power = additional power supplied to the plasma).

III. PLASMA THERMALISATION

For fusion reactions to occur, the kinetic energy of the ions has to be sufficiently large. The amount of energy transferred to ions and electrons depends on the heating method. Heating methods that deliver mainly energy to the plasma ions, can lead to the formation of energetic ion tails.

With neutral beam injection energetic ion beams are injected into the plasma. These beams have slowing down times proportional to $\frac{T_e^{1.5}}{n_e}$ [17]. An

equal amount of energy is transferred of from this energetic ion beam to the plasma ions and electrons if the beam energy E_b equals the so-called critical energy $E_c \propto T_e$ [17]. For $E_b > E_c$ the beam energy is predominantly delivered to the electrons. The α -particles produced in fusion reactions mainly heat the electrons because their large energy (3.5 MeV) is much higher than E_b . The various heating scenarios used for ICRH heating (minority heating, wave conversion, ion harmonic cyclotron damping) often lead to the formation of hot energetic ion tails, and depending on the conditions the heating power is shared differently between plasma electrons and ions [17]. The fusion reactions due to the presence of ion energetic tails or beams can generate an appreciable part of the total fusion power, due to head-on collisions of the fast ions with slower or counter circulating fast ions (originating from counter beam injection). This is the case for tritium or deuterium neutral beam injection in a D-T plasma. The fusion power is then due to thermal, beam-target, and beam-beam reactions (see also § IV.C).

The ratio of the ion and electron thermal energy E_i resp. E_e can be derived from the energy balance equation of

(i) the total energy $E = E_e + E_i$

$$\frac{dE}{dt} + \frac{E}{\tau} = P_{OH} + P_{add} = P_{tot} \quad (13)$$

where the global energy confinement time τ , takes into account the losses due to conduction, convection, radiation and charge exchange,

(ii) the electron energy

$$\frac{dE_e}{dt} + \frac{E_e}{\tau_e} = P_{OH} + P_{add,e} - P_{e,i} \quad (14)$$

and (iii) the ion energy

$$\frac{dE_i}{dt} + \frac{E_i}{\tau_i} = P_{add,i} + P_{e,i} \quad (15)$$

where τ_e and τ_i are respectively the electron and ion confinement time and $P_{e,i}$ is the power transferred from electrons to ions through Coulomb collisions. From (8) and (9) we have

$$\frac{1}{\tau} = \frac{1}{\tau_e} \frac{E_e}{E} + \frac{1}{\tau_i} \frac{E_i}{E} \quad (16)$$

In stationary conditions one can easily derive from Equations (14) and (15) the ratio between E_e and E_i . Taking into account that $P_{e,i}$ can be expressed as $\frac{(E_e - E_i)}{\tau_{equi}}$ where τ_{equi} is an effective equipartition

time between the electrons and ions due to Coulomb collisions, we have:

$$\frac{E_i}{E_e} = \frac{P_{OH} + P_{add,e} + P_{add,i}(1 + \frac{\tau_{equi}}{\tau_e})}{P_{add,i} + (P_{OH} + P_{add,e})(1 + \frac{\tau_{equi}}{\tau_i})} \quad (17)$$

τ_{equi} is proportional to $\frac{T_e^{1.5} M_i}{n_e Z_{eff}}$ where M_i is the ion atomic mass number and Z_{eff} is the effective charge of the ions of the plasma.

When τ_{equi} is small with respect to τ_e and τ_i (i.e. at sufficiently high plasma density), we have a thermal plasma with $E_e = E_i = \frac{1}{2} E$ and Equ. (16) becomes:

$$\tau = 2(\tau_e^{-1} + \tau_i^{-1})^{-1} \quad (18)$$

Note also that at high density the presence of energetic tails in the plasma becomes negligible and they thus contribute only to a small extent to the total plasma energy. Operational regimes with a (much) larger ion temperature than electron temperature are called "hot-ion modes".

IV. CONFINEMENT RESULTS IN PRESENT TOKAMAKS

In this section some recent some more details on recent confinement results are summarised. In Sect. 2.3 we indicated that a burning D-T fusion reactor, where the plasma heating is performed by the energetic α -particles produced in the fusion reactions, requires a sufficiently large confinement time (expressed by f_H/q and a sufficiently large β (expressed by β_N/q). A large β is achieved at a sufficiently large plasma density i.e. at a sufficiently large Greenwald number.

In addition, these requirements have to be fulfilled in stationary conditions with a low central pollution of the D-T plasma by impurities or ash (i.e. α -particles) from the fusion reactions. This last condition is equivalent with requiring a sufficiently low He particle confinement. The heating power delivered to the plasma by the α -particles will finally reach the walls of the machine and must then be evacuated. Without special precautions, this power will lead to a too large power flux in hot spots, resulting in large localised erosion or sputtering of the limiter or the divertor plates. Attempts are presently made to solve this problem by radiating homogeneously a large part of this power either in the plasma edge or in the divertor region, thus reducing to a serious extent the peak heat load values to the first wall.

In the next paragraphs a summary is given of different tokamak scenarii. They are presently under investigation to check their ability to simultaneously (i) reach high values for f_H and β_N (ii) solve the heat exhaust problem (iii) reach stationary conditions and (iv) to show evidence of plasma heating by α -particles in D-T plasmas.

IV.A. H-mode discharges

Confinement characteristics of the H-Mode regime are summarised in § II.B. Fig. 4a shows an ELM-free H-mode discharge in JET that has led to a record neutron yield in D-D plasmas. This mode of operation is non-stationary and is limited in time by the occurrence of MHD phenomena (specifically for the discharge shown in the last figure: onset of MHD turbulence followed by a giant ELM). The ELMy H-mode regime is the favoured operational scenario for ITER because of its stationarity and good confinement characteristics (i.e. a sufficiently large f_H). An example of such a discharge is shown in Fig. 4b [18]. Current investigations of this regime are related to its applicability to a reactor; more specifically (i) to reduce the uncertainty concerning the threshold heating power which has to exceeded in the reactor to obtain the transition from L to H mode (ii) to try to obtain this regime at sufficiently large densities (equal to or above the Greenwald density, without loss of the good confinement properties) (iii) to solve the problem of heat exhaust, particularly in the presence of large ELMs. A way to solve this last problem is to seed impurities to produce edge radiation.

Recent experiments at JET [28, 29] have shown that it is possible to reach the ITER operational data for density and confinement simultaneously with (a) increasing the triangularity of the plasma, (b) by impurity seeding in low and high triangular plasmas and (c) by an adapted pellet fuelling cycle. Triangularity of a plasma can be roughly described as the "pointedness" of the plasma, and one

distinguishes in principle an upper δ_U and lower δ_L triangularity (Fig. 4c). Very often only the average triangularity $\delta = (\delta_U + \delta_L)/2$ of the plasma is used. High triangularity is beneficial to increase confinement at high densities, as shown in Fig. 4d. These discharges are also quite robust to strong gas puffing (needed to reach the high density), provided sufficient heating power to keep Type I ELMs [30, 31]. The amount of power needed increased with decreasing triangularity. On the other hand, in low triangularity discharges high confinement and high density can be reached simultaneously by applying Ar seeding, as illustrated in Fig. 4e. This discharge shows a so-called "puff" and "after-puff" phase. In the puff phase strong gas puff is applied to raise the density to values around the Greenwald limit, but confinement degrades. This is restored in the afterpuff phase, i.e. when the strong gas puff is suddenly interrupted, and where only a gentle D and Ar puffing is continued, to keep density and radiation high. An adapted pellet fuelling cycle, where first a fast pellet train enters the plasma, followed by a second much slower pellet train (Fig. 4f), allows to reach high densities without degrading confinement too much. The philosophy here is much similar to the one applied in the low triangularity discharges with puff and afterpuff: first build up the density (irrespective of other quantities) and later on try to keep the high density without degradation of confinement, by a much gentler fuelling procedure.

IV.B. Discharges with edge radiation cooling and improved confinement

At a large radiated power fraction γ , it has been possible to achieve improved L-mode conditions with a confinement quality close to or even exceeding that of ELM-free H-mod [23]. In the next section examples of this regime are discussed.

A new confinement regime [24] has been established on TEXTOR-94, a tokamak with a circular cross-section and equipped with a toroidal pump limiter. This regime is obtained by appropriate impurity seeding during the heating phase of the discharge and has been called the Radiative I-mode (or RI-mode). It is characterised by its ability to simultaneously realise the following features, important for the extrapolation to a reactor: (i) quasi-stationarity of the plasma parameters, (ii) high confinement with a quality close to that of the ELM-free H-mode, (iii) high plasma density near or even above the Greenwald limit, (iv) high normalised beta (β_N up to 2), (v) strong edge radiation (

$\gamma = \frac{P_{rad}}{P_{tot}}$ up to 95 % where P_{rad} is the edge radiated power) (vi) the possibility to operate at low edge q values (down to 2.8), leading to reactor relevant values of the figure of merit for ignition f_H / q , (vii) no decrease of the plasma fusion reactivity due to the seeded impurity.

An example of the quasi-stationarity achieved in the RI-Mode is shown by the discharge in Fig. 7. which has

a high confinement phase of more than 7s, limited only by technical constraints of the machine. Remarkable in this figure is the evolution of the diamagnetic plasma energy E_{dia} and of the associated enhancement factor f_{H93} , which compares the experimentally obtained energy confinement time versus ELM-free H-mode confinement as given by the scaling law ITERH-93P (see Table I). Soon after the start of Ne seeding a confinement transition takes place, when $\gamma \approx 50\%$, resulting in a sudden increase of E_{dia} and f_{H93} . Note the long duration of the high confinement phase which is about 160 confinement times ($\tau_E \approx 50\text{ms}$) and equivalent to several skin resistive times. We remark in passing that the ratio of the burn time to the projected confinement time of ITER (Final Design Report [25]) is also equal to 160! Note also that improved confinement at these high densities is not due to fast particle contributions (because of the high density reached) confirmed by the comparison of the measurements of the MHD E_{MHD} and diamagnetic energy E_{dia} .

The energy confinement in the RI-Mode improves with density and thus shows a totally different density behaviour as the usual L- or H-mode. This is illustrated in Fig. 8, where the evolution of E_{dia} is plotted versus \bar{n}_{eo} for ohmic discharges and discharges heated by the combination of NBI-co-ICRH with $P_{tot} \approx 2.25$ MW at $I_p = 350$ kA. The diamagnetic energy in ohmic discharges follows the Neo-Alcator scaling E_{NA} until $\bar{n}_{eo} \approx 3.0 \times 10^{19} \text{ m}^{-3}$ where a saturation sets in. For additionally heated discharges at low densities, E_{dia} follows roughly the L-mode scaling, or can be described by a linear offset scaling $E_{OL} = E_{NA} + \tau_{inc}(P_{tot} - P_{OH})$ where P_{OH} is the ohmic heating power taken in a corresponding ohmic discharge and τ_{inc} is the incremental confinement time, which is roughly constant for not too high P_{tot} or \bar{n}_{eo} and for a given I_p . A clear confinement transition occurs at $\bar{n}_{eo} \approx 4.0 \times 10^{19} \text{ m}^{-3}$, where the E_{dia} values obtained differ substantially from L-mode scaling, resulting in a τ_{inc} which increases strongly with density for $\bar{n}_{eo} > 4.0 \times 10^{19} \text{ m}^{-3}$, as shown in Fig. 9. Discharges corresponding to these conditions belong to the RI-Mode, and are obtained as soon as γ exceeds about 50%. Furthermore, if f_{H93} values are plotted as a function of $\bar{n}_{eo} / \bar{n}_{eo,GR}$ (for different plasma currents and for a wide range of P_{tot} and γ) we find [24] not only that (i) f_{H93} increases approximately linearly with density but moreover that (ii) this result is independent of the plasma current. Therefore, the confinement time in RI-Mode discharges τ_{RI} is proportional to $(\bar{n}_{eo} / \bar{n}_{eo,GR}) \times \tau_{ITERH\ 93-P}$. A detailed analysis shows that the proportionality factor is close to 1 and we have thus to a very good approximation that:

$$\tau_{RI} = \frac{\bar{n}_{eo}}{\bar{n}_{eo,GR}} \times \tau_{ITERH93-P} \quad (19)$$

Striking in this formula is the linear density dependence (as for the ohmic Neo-Alcator scaling) and the absence of a current dependence, contrasting with the usual scalings for additionally heated discharges. The comparison of the global confinement time of the RI-mode with the L- and the ohmic LOC-regimes is shown in Fig. 2b. As low edge q operation ($q_a = 2.8$) presents no stability problems, this leads then in a natural way to high values for the figure of merit for ignition margin f_{L89}/q_a equal to 0.65 at high density which is the value requested for the reactor. One still has to demonstrate that this regime can maintain its interesting features on larger and reactor size machines without significant central plasma pollution by the seeded impurity.

Confinement of the RI-Mode can be conveniently compared with confinement in the L- and H-Mode regime, independent of heating power or plasma current, in a normalised confinement diagram. Instead of plotting the confinement time τ versus density (see e.g. Fig. 2a and 2b), one plots the quantity $\tau P^{1.5}/I_p$ versus the Greenwald factor $\bar{n}_{eo}/\bar{n}_{eo,GR}$. The effect of such a transformation of variables is graphically depicted in Fig. 10b. The resulting diagram for RI-Mode data is given in Fig. 10c. One sees very clearly the L- and RI-Mode part in the data. One also sees that at the highest densities, RI-Mode confinement supersedes H-Mode confinement.

Discharges with a radiative mantle have now also been obtained at JET, with good confinement and density values using Ar as seeding impurity, as indicated in the previous section. A summary of main latest results obtained on JET can be found in [26]. Non noble gas impurities have been used (N_2), leading to Type III discharges with rather small ELMs, but with degraded density (compared to the Greenwald density $\bar{n}_{eo}/\bar{n}_{eo,GR}$) and confinement ($f_{H93} \approx 0.7$).

IV.C. D-T operation

A preliminary D-T fusion experiment has been performed on JET in 1991 in plasmas with a mix of 10%D and 90%T [27] resulting in a fusion power output of about 1.7MW. In the period end 1993-beginning 1997, TFTR has been routinely operated with D-T discharges [28]. The operational regime in the high performance D-T discharges in TFTR was a (limiter) hot ion mode ($T_{i0} > T_{e0}$) and was obtained with NBI heating, consisting of a mix of tritium and deuterium injection (to provide the necessary tritium fuelling of the discharge), resulting in a maximum fusion output of 10.7 MW. A second D-T experimental campaign has been performed in JET in September-November 1997. ELM-free H-Mode hot-ion modes,

optimised shear regimes and steady-state ELMy H-modes were used, heated by NBI or NBI combined with ICRH [29], again with part of the injectors being operated with tritium in order to provide at the same time the T fuelling. These experiments have resulted in the demonstration of near-break-even conditions: $Q = P_{fusion}/P_{heating} = 0.62$ transiently, with an output power from fusion reactions of more than 16 MW; under quasi-stationary conditions $Q = 0.35$ was obtained with a fusion power of about 5 MW. Fig. 11a gives a summary of the JET high performance D-T results and compares them to the results obtained previously on TFTR. Fig. 11b shows the time traces of the electron and ion temperatures of the record D-T fusion shot of JET. Maximum temperatures obtained for ions and electrons are resp. 28 keV and 14 keV. Fig. 11c shows the time trace of the different contributions to the neutron production as modelled by TRANSP [30]. This shot was heated by 22.3MW NBI and 3.1MW of ICRH. The total heating power in this discharge is also in part (about 3MW or nearly 10%) delivered by the α particles generated in the fusion reactions. Note that the largest part of the fusion power output is due to reactions of thermal neutrons, with the rest mainly produced in beam-target reactions and only a small fraction due to beam-beam reactions. Due to their large energy the α particles deposit their energy mainly to the electrons. Most of the ion heating is produced by the NBI and the largest part of the electron heating is due to the equipartition power between the hotter ions and the electrons. Note that for an ignited reactor the total heating power must be produced by the fast α particles. These experiments have nevertheless demonstrated the effectiveness of α -particle heating without significant plasma micro-instabilities.

Combined NBI-ICRH heating of D-T plasmas has also been performed on TFTR (and also recently on JET [31]) with direct heating of T ions at the second harmonic frequency for tritium $2\omega_{CT}$. A small amount (2 %) of 3He was added to the discharge to increase the single pass absorption by 3He minority heating [18]. In these experiments T_{i0} was increased from 26 to 36 keV and T_{e0} from 8 to 10.5 keV by the addition to 23 MW NBI of 5.5 MW of ICRH.

IV.D. Improved confinement through the formation of an Internal Transport Barrier (ITB)

After the L- to H-mode transition, the improvement in confinement is due to the formation of a transport barrier at the edge of the plasma [32] attributed to a transport reduction through ExB velocity shear decorrelation of the turbulence [32]. The VH-mode regime is linked to the penetration of the transport barrier deeper into the plasma.

ExB shear decorrelation of micro-instabilities (as e.g. in ITG modes) is not the only mechanism

which decreases transport. A reduction of transport (e.g. by reduction of MHD modes) is also possible by choosing an adequate value of the magnetic shear

$$s = \frac{r}{q} \frac{dq}{dr}. \text{ Such confinement improvement schemes}$$

are obtained by tailoring the current density resulting in

(i) discharges with a high internal inductance I_i (obtained e.g. by realising a highly peaked current density profile)

(ii) discharges with negative central magnetic shear i.e. with $s = -\frac{r}{q} \frac{dq}{dr} < 0$ in the centre of the plasma

resulting in a non-monotonic q-profile. The q value on the magnetic axis in that case is not the minimum q value in the q(r) profile. Such reversed shear plasmas are obtained in the presence of large non-inductive currents (bootstrap current, non-inductive current drive by e.g. LH) or by heating the plasma during the initial current ramp of the discharge. The formation of the Internal Transport Barrier (ITB) is due to a synergetic effect of transport reduction through adequate magnetic shear and ExB shear.

An example of a discharge on DIII-D with an ITB inside the plasma obtained with this last technique is shown in Fig. 12a. The minimum q is off-axis and the value for the safety factor in the centre of the plasma q_0 is much larger than 1. A large confinement improvement is observed at the step in the neutral beam power, as evidenced by a large increase in the central T_i together with a peaking of the density profile. The effect of the formation of an ITB on the ion temperature profile of JET is shown in Fig. 12b.

The problem to extrapolate such these regimes to a reactor is to realise it in steady state and at sufficiently high density. An example of the achievement in TORE SUPRA [34] of a steady-state confinement improvement attributed to the presence of a large bootstrap current I_{BS} is shown in Fig. 13. The figure shows also the profile of the bootstrap current density profile and the obtained scaling of

$$I_{BS} \propto I_p \beta_p \sqrt{\frac{a}{R}} = q_a \beta_N I_p \sqrt{\frac{R}{a}} \quad (20)$$

REFERENCES

[1] M. Greenwald, J.L. Terry et al., Nucl. Fusion **28**, 2199 (1988).
 [2] "Technical basis for the ITER interim design report, cost review and safety analysis" ITER EDA documentation series n° 7, IAEA, Vienna, 1996.
 [3] J.G. Cordey, B. Balet et al., Plasma Physics

Control. Fusion **38**, A67-A75 (1996).

[4] B.B. Kadomtsev, "Tokamak Plasma : a complex physical system", Plasma Physics Series, IOP Publishing Ltd, Bristol and Philadelphia, 1992, pp 100-101.
 [5] F. Wagner, U. Stroth, Plasma Physics Control. Fusion **35**, 1321 (1993).
 [6] R.R. Weynants, Control. Fusion and Plasma Physics (Proc. 14th Eur. Conf. Madrid, 1987), **11D**, Part I, EPS, Geneva (1987) 197.
 [7] G. Bracco, K. Thomsen, Report JET-R(96)03 (1996).
 [8] M. Bessenroth-Weberpals, et al., Report MPI-IPP Garching 1/248 (1989).
 [9] R.J. Goldston, Plasma Physics and Control. Fusion **26** (1984) 87.
 [10] S.M. Kaye and R.J. Goldston, Nucl. Fusion **25** (1985) 65.
 [11] P.N. Yushmanov et al., Nucl. Fusion **30** (1990) 1999
 [12] S.M. Kaye and the ITER Confinement Database Working Group, Nucl. Fusion **37** (1997) 1303.
 [13] O.Kardaun and the ITER H-Mode Database Working Group, Plasma Physics and Controlled Nuclear Fusion Research (Proc 14th Int. Conf. Würzburg.1992) Vol 3 (Vienna:IAEA) 251.
 [14] ITER Expert Working Groups and the ITER JCT and Home Teams, *ITER Physics Basis Document*, Nucl. Fusion, **39**, 2137 (1999)
 [15] D.Schissel and the H-Mode Database Working Group (Proc. 20th EPS Conf. Lisbon (1993)) Vol 17C (1993), Part I, 103; K.Thomsen, Nucl. Fusion **34** (1994) 131.
 [16] Cordey J.G. and the ITER Confinement Database Working Group, Plasma Phys. Control. Fusion **39** (1997) B115.
 [17] See presentations by E.Lerche and D.Van Eester, these proceedings.
 [18] JET Team, in Plasma Physics and Control. Fusion, Nuclear Research 1997, IAEA Vienna, in print, paper IAEA-CN-64/O1-4
 [19] J.Ongena et al, Plasma Physics Control. Fusion, **43**, A11-A30 (2001)

- [20] W.Suttrop et al., Phys. Plasmas **9** 2103 (2002)
- [21] G.Saibene et al, Proc. EPS Conference Funchal (Madeira), 18-24 June 2001
- [22] R.Sartori et al., Proc. EPS Conference on Plasma Physics and Controlled Fusion, Funchal (Madeira) 18-24 June 2001.
- [23] J. Neuhauser et al., Plasma Physics Control. Fusion **37** (1995) A37.
- [24] A.M. Messiaen, J. Ongena et al., Phys. Plasmas **4**, 1690 (1997).
- [25] Technical Basis for the ITER Final Design Report, ITER Documentation Series 15 and 16 (IAEA, Vienna, 1998)
- [26] J.Ongena et al., Fusion Science and Technology, **53**, No 4, 891 (2008).
- [27] JET Team, Nuclear Fusion **32** (1992) 187.
- [28] D.W. Johnson et al., Plasma Physics Control. Fusion **37** (1995) A69.
- [29] J.Jacquinot and the JET team, Plasma Physics Control. Fusion, **41** (1999) A13
- [31] JET Team, in Control. Fusion and Plasma Physics (Proc. 24th Eur. Conf. Berchtesgaden 1997), **21A**, Part IV, EPS, Geneva (1997) 1865.
- [32] K.H. Burrell, Phys. Plasmas **4** (1997) 1499.
- [33] S. Allen and R.A. Moyer, private communication.
- [34] Tore Supra Team, Plasma Phys. Control. Fusion **38** (1996) A251.

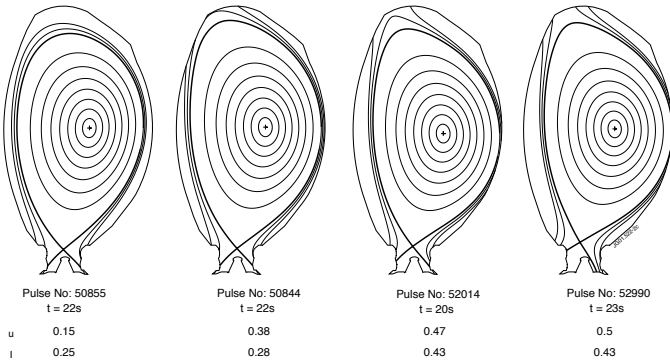


Fig 4c: Different shapes for the plasma cross section which can be realised in JET. From left to right the average triangularity is increasing.

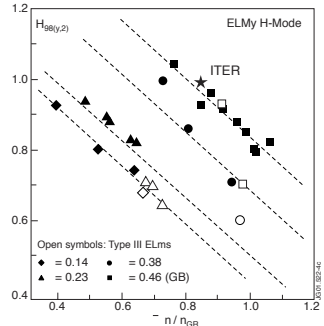


Fig 4d: Confinement ($H_{98(y,2)}$) versus the Greenwald factor (n/n_{GW}) for different triangularities. For each triangularity with increasing density confinement degrades. However, increasing triangularity helps to increase confinement for a given density. For the highest triangularities the ITER values are reached.

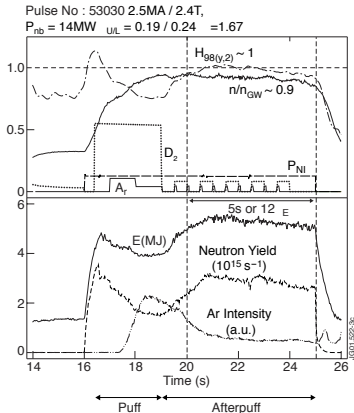


Fig 4e: Example of a discharge obtained at JET with impurity seeding in a plasma with triangularity. In the afterpuff phase high density ($n/n_{GW} = 0.9$) and high confinement ($H_{98(y,2)} = 1.0$) is realised.

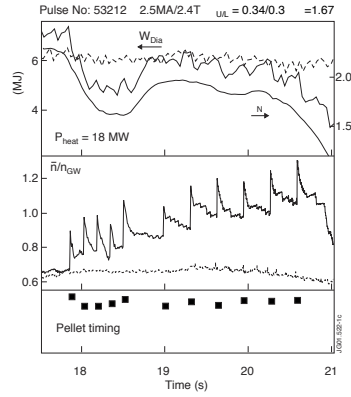


Fig 4f: Example of a discharge with an adapted pellet fuelling rate. The dashed lines correspond to a reference discharge without pellet fuelling (and without gas puffing). The black squares indicate the pellet timing. In the second part of the fuelling cycle (at an injection frequency of 6 Hz) high density is realised at the Greenwald limit with good confinement as seen from the diamagnetic energy and beta values.

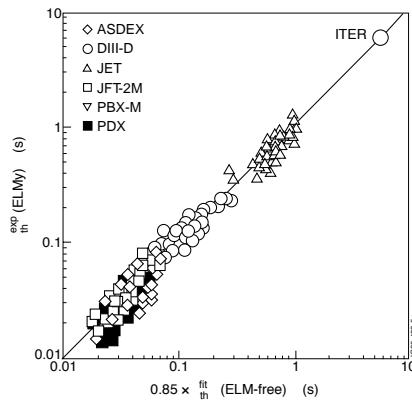


Fig. 5: Experimental confinement time (for thermal energy confinement) as a function of $0.85 \times \theta_{98}^{fit}$ for different divertor machines. The needed extrapolation to ITER is also shown (corresponding to $\tau_E = 6.1$ s and $n_{e0} = 1.3 \cdot 10^{20} m^{-3}$ and $P_{tot} = 190$ MW). Note that if τ_E is lower by 30%, no ignition takes place and $Q = 10$.

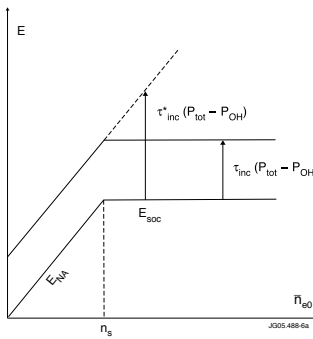


Fig. 6a: Schematic representation of the behaviour of the plasma energy content as a function of density, for discharges with ohmic and additional heating.

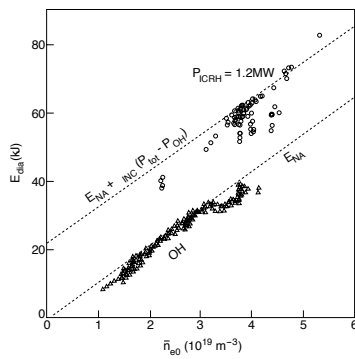


Fig. 6b: Corresponding experimental points of TEXTOR for ohmic discharges (where the start of the SOC regime appears) and for ICRH discharges in presence of Neon injection at $I_p = 350$ kA.

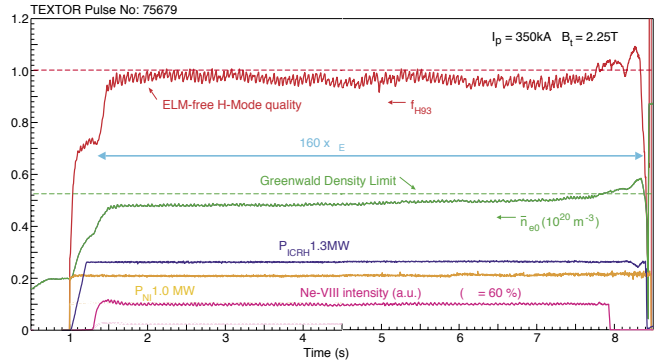


Fig. 7: Long stationary RI-mode discharge obtained with Ne seeding ($I_p = 350$ kA, $B_t = 2.25$ T). Shown are the diamagnetic energy measurement, line average density \bar{n}_0 , P_{NBI} (co-injection), P_{ICRH} , the Greenwald density limit and I_{H93} versus time.

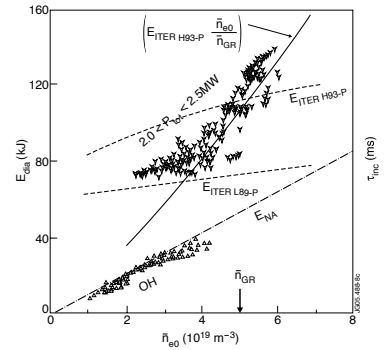


Fig. 8: Plasma energy as a function of the density \bar{n}_0 for ohmic discharges and for additionally heated ones (the latter in presence of Neon seeding and with $2 < P_{tot} < 2.5$ MW). The predictions of the Neo-Alcator, ITER L89-P and $(\bar{n}_0 / \bar{n}_{GR}) \times \text{ITER H93-P}$ scalings are also indicated together with the value of the Greenwald limit.

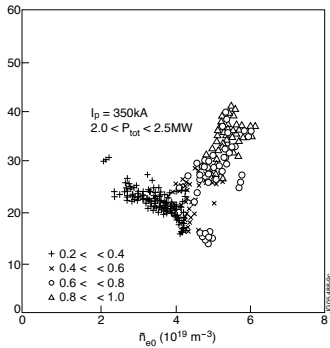
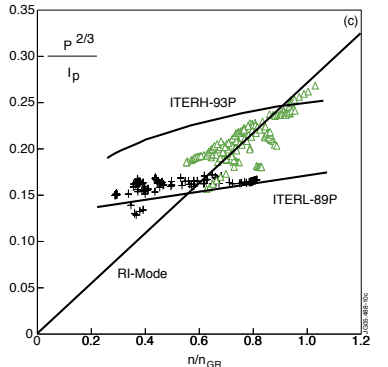
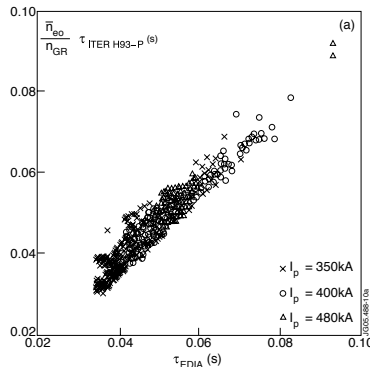
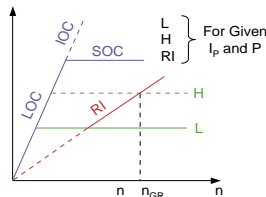


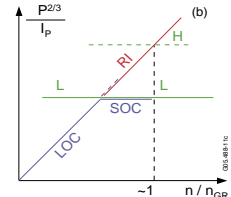
Fig. 9: Incremental confinement time versus \bar{n}_0 for the additionally heated discharges shown in Fig. 8. The corresponding values are indicated.



SCHEMATIC CONFINEMENT BEHAVIOUR IN TEXTOR



$$\begin{aligned} \text{LOC} & n f(I_p) \quad n P_{OH}^{-2/3} \\ \text{L} \quad \text{H} & I_p P^{-2/3} \\ \text{SOC} & L (P = P_{OH}) \end{aligned}$$



$$RI = \begin{cases} c' n P^{-2/3} \\ \frac{n}{n_{GR}} \text{ ITER H93-P} \end{cases}$$

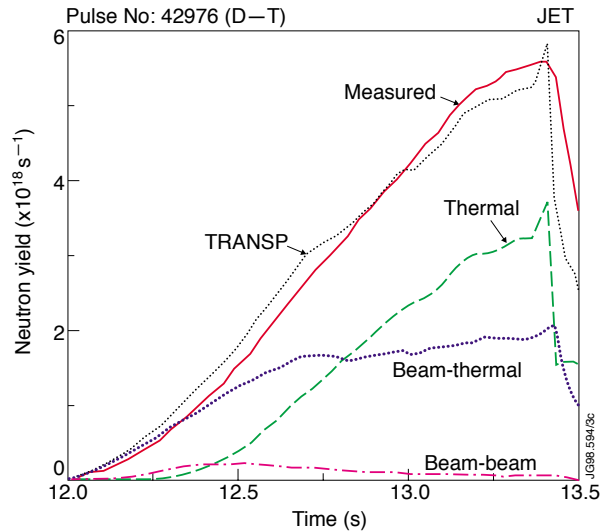
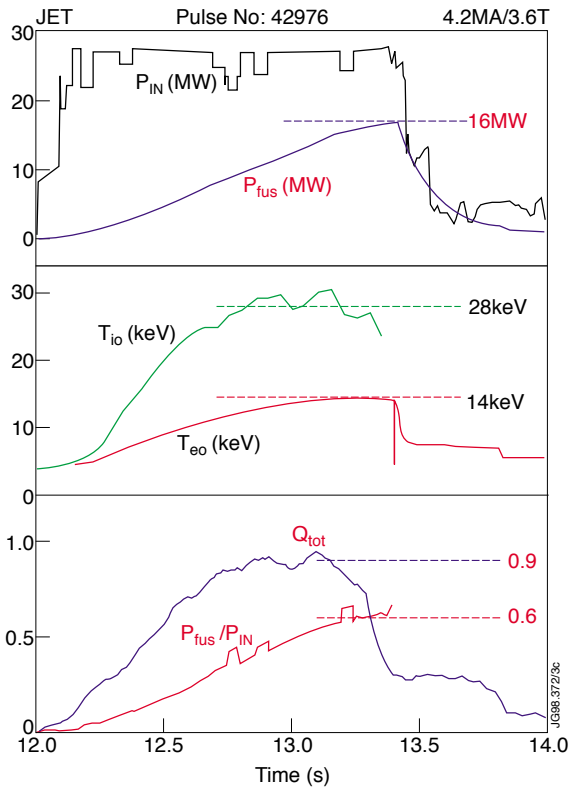
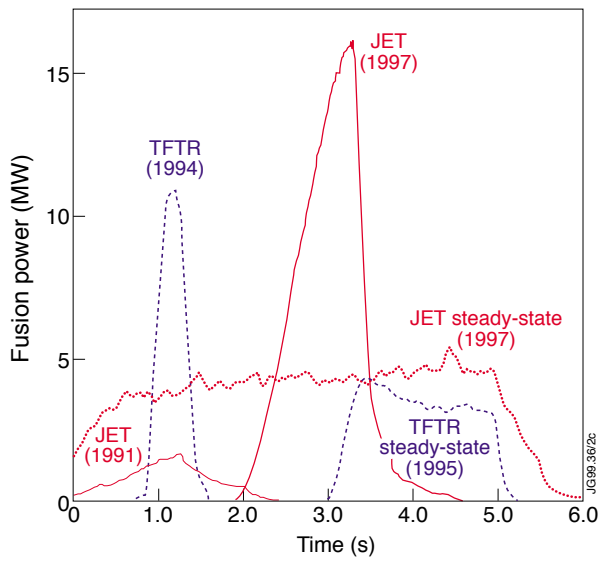


Fig. 11a): Fusion power development in the D-T campaigns of JET and TFTR. (I) Hot-ion modes, (II) Optimised shear and (III) steady-state ELMy H-Modes. b) Time traces of the highest performance JET D-T hot-ion H-Mode discharge producing a record fusion output of 16 MW and $Q = 0.62$. c) Time evolution of the observed total neutron yield compared with a simulation by the TRANSP code for the shot of Fig. 11b. Also shown are the thermal, beam-thermal and beam-beam contributions to the neutron yield as predicted by TRANSP.

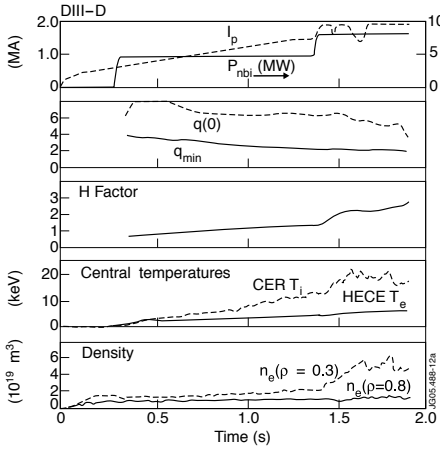


Fig. 12a: Discharge in DIII-D with early heating during the current ramping to the formation of an ITB. Shown versus time are I_p , P_{NBI} , $q(0)$ and the off-axis minimum q_{min} , the enhancement factor H with respect to the L-mode scaling (ITER L89P), the central ion and electron temperatures and the density at two locations of r/a . [24]

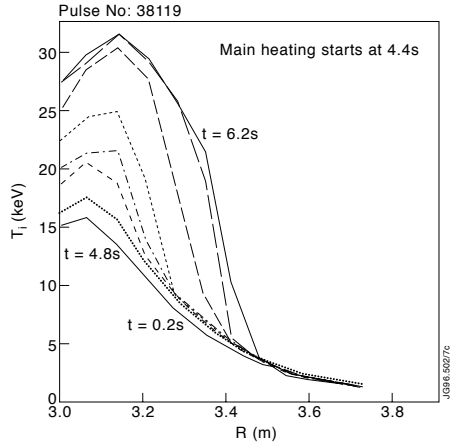


Fig. 12b: Evolution of the ion temperature profile in JET after the formation of an ITB (at $R = 3.5m$) due to an early heating scenario (of NBI + ICRH).

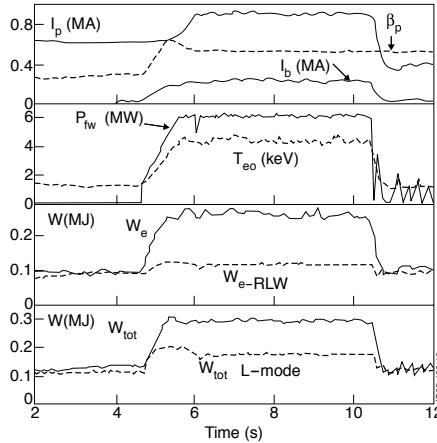
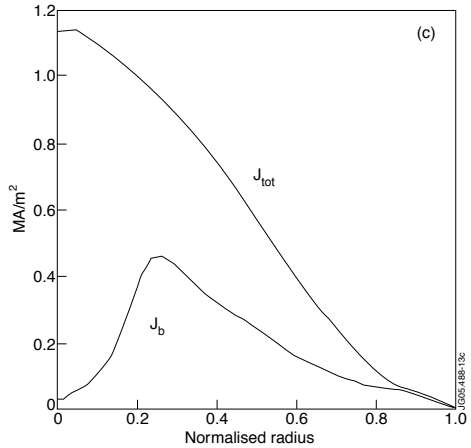
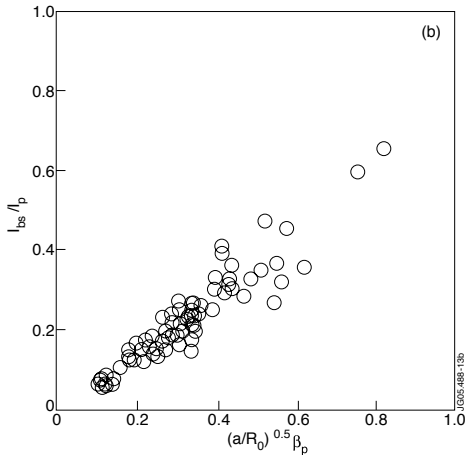


Fig. 13a: Stationary high bootstrap current discharge obtained by ICRH (fast wave electron heating scenario). I_b is the bootstrap current, P_{fw} the ICRH power, W_e and W_{tot} correspond to the electron and total plasma energies [25]. W_{e-RLW} and $W_{tot L-mode}$ are predictions of L-mode scalings



GUIDING CENTER MOTION

H.J. de Blank

FOM Institute DIFFER – Dutch Institute for Fundamental Energy Research,
Association EURATOM-FOM, P.O. Box 1207, 3430 BE Nieuwegein, The Netherlands, www.differ.nl.

ABSTRACT

The motion of charged particles in slowly varying electromagnetic fields is analyzed. The strength of the magnetic field is such that the gyro-period and the gyro-radius of the particle motion around field lines are the shortest time and length scales of the system. The particle motion is described as the sum of a fast gyro-motion and a slow drift velocity.

I. INTRODUCTION

The interparticle forces in ordinary gases are short-ranged, so that the constituent particles follow straight lines between collisions. At low densities where collisions become rare, the gas molecules bounce up and down between the walls of the containing vessel before experiencing a collision.

High-temperature plasmas, however, cannot be contained by a material vessel, but only by magnetic fields. The Lorentz forces that act on the particles tie them to the magnetic field and force them to follow the field lines. In order to confine the particles in a bounded volume, the magnetic field must be curved and inhomogeneous. In addition, it must be strong. So strong, that the Lorentz force dominates all other forces. Therefore, charged particles do not follow straight lines between collisions but follow strongly curved orbits under the influence of the magnetic field. In fact, many properties of a magnetically confined plasma are dominated by the motion of the particles subject to the Lorentz force $q\mathbf{v} \times \mathbf{B}$. Here \mathbf{B} is the macroscopic field, i.e., the sum of externally applied field and the fields generated by the plasma particles collectively, but excluding the microscopic variations of the fields due to the individual particles.

The particle motion in the macroscopic field is the subject of this lecture. The microscopic fields, i.e., the interactions between individual particles (“collisions”), cause deviations from these particle orbits. Collisions in a plasma are caused by Coulomb interactions between the particles, with properties that are very different from collisions in a gas.

Firstly, the cross-section of Coulomb collisions is a strongly decreasing function of the energies of the interacting particles. Hence, the mean free paths of charged particles in high-temperature fusion devices are very long and the particles will trace out their trajectories over distances that can be comparable to or even larger than the size of the device before they are swept out of their orbits by collisions.

Secondly, the Coulomb force is a long range interaction. In a well-ionized plasma, particles rarely suffer large-angle deflections in two-particle collisions. Rather, their orbits are deflected through weak interactions with many particles simultaneously. Hence, the effects of collisions can be best described statistically, in terms of distributions of particles. The kinetic equation for the particle distribution function will be discussed at the end of this chapter, with emphasis on the role of the particle orbits, not the collisions.

The equations of motion of a particle with mass m and charge q in electromagnetic fields $\mathbf{E}(\mathbf{x}, t)$ and $\mathbf{B}(\mathbf{x}, t)$ are,

$$\dot{\mathbf{x}} = \mathbf{v}, \quad \dot{\mathbf{v}} = \frac{q}{m}(\mathbf{E} + \mathbf{v} \times \mathbf{B}), \quad (1)$$

where the dot denotes the time derivative. Each of the N plasma particles satisfies such equations. The solutions to the $6N$ equations are the particle trajectories. These trajectories determine the local charge and current density which are the sources in Maxwell’s equations and which determine the electromagnetic fields \mathbf{E} and \mathbf{B} . In turn, these fields determine the particle trajectories. This self-consistent picture is extremely complex.

However, as illustrated above, in a weakly collisional plasma one can first study the behaviour of test particles in given fields $\mathbf{E}(\mathbf{x}, t)$ and $\mathbf{B}(\mathbf{x}, t)$. The role of the particles as sources of charge density and current in Maxwell’s equations is disregarded. The fields \mathbf{E} and \mathbf{B} of course obey the subset of Maxwell’s equations,

$$\nabla \times \mathbf{E} = -\partial \mathbf{B} / \partial t, \quad \nabla \cdot \mathbf{B} = 0. \quad (2)$$

II. GYRATION AND DRIFT

A. Motion in a Constant Magnetic Field

Let us first consider the motion of a charged particle in the presence of a constant magnetic field \mathbf{B} ,

$$m\dot{\mathbf{v}} = q(\mathbf{v} \times \mathbf{B}).$$

The kinetic particle energy remains constant because the Lorentz force is always perpendicular to the velocity and can thus change only its direction, but not its magnitude. The particle velocity can be decomposed into components parallel and perpendicular to the magnetic field, $\mathbf{v} = v_{\parallel} \mathbf{b} + \mathbf{v}_{\perp}$, where $\mathbf{b} \equiv \mathbf{B}/B$ is the unit vector in the direction of

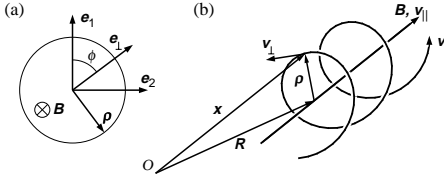


Figure 1: Definition of the gyro-angle ϕ (a) and guiding center (b).

B. The Lorentz force does not affect the parallel motion: $v_{\parallel} = \text{constant}$. Only v_{\perp} interacts with \mathbf{B} , leading to a circular motion perpendicular to \mathbf{B} . The centrifugal force mv_{\perp}^2/r balances the Lorentz force $qv_{\perp}B$ for a gyration radius r equal to the ‘‘Larmor radius’’

$$\rho \equiv \frac{mv_{\perp}}{|q|B}.$$

If we set $\frac{1}{2}mv_{\perp}^2 = kT$ for the two dimensional thermal motion $\perp \mathbf{B}$, we obtain $\rho = (2mkT)^{1/2}/|q|B$. In a typical fusion plasma ($kT = 10 \text{ keV}$, $B = 5 \text{ T}$) the electrons have a gyroradius of $67 \mu\text{m}$ and deuterons 4.1 mm .

The frequency of the gyration, called cyclotron frequency ω_c , follows from $v_{\perp} = \omega_c \rho$,

$$\omega_c = qB/m.$$

In fusion experiments the electron cyclotron frequency is of the same order of magnitude as the plasma frequency. Although the particle motion in a constant field is elementary, the following notation will also serve more complicated cases. Let $\mathbf{e}_1, \mathbf{e}_2$ be unit vectors perpendicular to each other and to \mathbf{b} , and define co-rotating unit vectors (Fig. 1(a)):

$$\begin{aligned} \mathbf{e}_{\perp}(t) &= \mathbf{e}_1 \cos \phi + \mathbf{e}_2 \sin \phi, \\ \mathbf{e}_{\rho}(t) &= \mathbf{e}_2 \cos \phi - \mathbf{e}_1 \sin \phi, \quad \phi = \phi_0 - \omega_c t. \end{aligned}$$

As illustrated in Fig. 1(b), the particle position \mathbf{x} can be decomposed into a **guiding center** position \mathbf{R} that moves with velocity $v_{\parallel} \mathbf{b}$, and a rotating gyration radius vector ρ ,

$$\mathbf{x} = \mathbf{R} + \rho, \quad (3a)$$

$$\rho = -\frac{m}{qB^2} \mathbf{v} \times \mathbf{B} = \rho \text{sgn}(q) \mathbf{e}_{\rho}, \quad (3b)$$

$$\mathbf{v}_{\perp} = \dot{\rho} = v_{\perp} \mathbf{e}_{\perp}. \quad (3c)$$

The particle trajectory is a helix around the guiding center magnetic field line (Fig. 2).

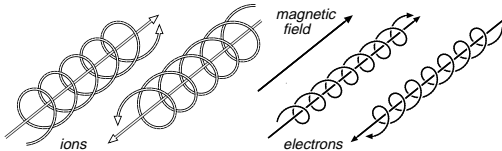


Figure 2: Orientation of the gyration orbits of electrons and ions in a magnetic field. The guiding center motion is also shown.

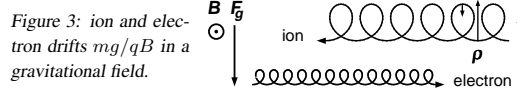


Figure 3: ion and electron drifts mg/qB in a gravitational field.

B. Drift due to an Additional Force

If, in addition to the Lorentz force, a constant force \mathbf{F} acts on the charged particle, the equation of motion is

$$m\dot{\mathbf{v}} = q(\mathbf{v} \times \mathbf{B}) + \mathbf{F}. \quad (4)$$

The motion of the particle due to \mathbf{F} can be separated from the gyration due to \mathbf{B} by using the guiding center as reference frame. Again the guiding center position \mathbf{R} , the position of the particle \mathbf{x} , and the gyration radius vector ρ are related as in Eq. (3). The velocity of the guiding center can be obtained by differentiating the equation $\mathbf{R} = \mathbf{x} - \rho$,

$$\begin{aligned} \mathbf{v}_g &\equiv \dot{\mathbf{R}} = \dot{\mathbf{x}} - \dot{\rho} \\ &= \mathbf{v} + \frac{m}{qB^2} \dot{\mathbf{v}} \times \mathbf{B} \\ &= \mathbf{v} + \frac{1}{qB^2} (q\mathbf{v} \times \mathbf{B} + \mathbf{F}) \times \mathbf{B}. \end{aligned}$$

Using $(\mathbf{v} \times \mathbf{B}) \times \mathbf{B} = -v_{\perp} B^2$ and $\mathbf{v} - v_{\parallel} \mathbf{b} = v_{\perp} \mathbf{b}$ we obtain

$$\mathbf{v}_g = v_{\parallel} \mathbf{b} + \frac{\mathbf{F} \times \mathbf{B}}{qB^2}.$$

Thus, one sees that any force with a component perpendicular to \mathbf{B} causes a particle to drift perpendicular to both \mathbf{F} and \mathbf{B} . The basic mechanism for a drift in this direction is a periodic variation of the gyro-radius. When a particle accelerates in a force field, the gyroradius increases and when it slows down its gyroradius decreases, leading to the non-closed trajectories shown in Fig. 3. The net effect is a drift perpendicular to the force and the magnetic field.

A force parallel to \mathbf{B} does not lead to a drift, but simply causes a parallel acceleration as can be seen from Eq. (4). Summarizing,

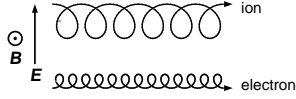
$$\mathbf{v}_{g,\perp} = \frac{\mathbf{F}_{\perp} \times \mathbf{B}}{qB^2}, \quad \frac{dv_{g,\parallel}}{dt} = \frac{F_{\parallel}}{m}. \quad (5)$$

An example is the drift due to a constant gravitational force $F_g = mg$ perpendicular to the magnetic field. The resulting drift velocity, $v_g = mg/qB$, is in opposite directions for electrons and ions (see Fig. 3). The net effect is a current density. However, in laboratory plasmas v_g is far to small to be of importance ($2 \times 10^{-8} \text{ m/s}$ in a magnetic field $B = 5 \text{ T}$).

C. $\mathbf{E} \times \mathbf{B}$ Drift

A different situation arises in the presence of a constant electric force $q\mathbf{E}$. Since the electric force is in opposite directions for electrons and ions, the resulting drift velocity,

Figure 4: $\mathbf{E} \times \mathbf{B}$ drift of ions and electrons.



$$\mathbf{v}_E = \frac{\mathbf{E} \times \mathbf{B}}{B^2}, \quad (6)$$

does not depend on the sign of the charge or the particles. It is also independent of the particle mass and therefore identical for ions and electrons. Hence, this drift leads to a net flow of the plasma, not to a current.

D. Polarization Drift

If the electric field is spatially constant but depends on time, $\partial \mathbf{E} / \partial t \neq 0$, the $\mathbf{E} \times \mathbf{B}$ drift (6) is not constant. Instead, there is an acceleration $\perp \mathbf{B}$ which can be thought of as being caused by a force

$$\mathbf{F} = m \frac{d\mathbf{v}_E}{dt} = \frac{m}{B^2} \frac{\partial \mathbf{E}}{\partial t} \times \mathbf{B}.$$

This force, according to Eq. (5), yields yet another drift,

$$\mathbf{v}_p = \frac{\mathbf{F} \times \mathbf{B}}{qB^2} = \frac{m}{qB^2} \frac{\partial \mathbf{E}}{\partial t}.$$

This secondary drift is the polarization drift, which depends on the charge and the mass of the particle. The associated current density is

$$\mathbf{j}_p = \frac{\rho_m}{B^2} \frac{\partial \mathbf{E}}{\partial t},$$

where $\rho_m = m_e n_e + m_i n_i$ is the mass density. The electron contribution to this current density is a factor $\mathcal{O}(m_e/m_i)$ smaller than the contribution from the ions.

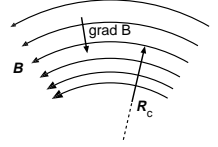
E. Particle Drift in Inhomogeneous Magnetic Fields

For spatially slowly varying magnetic fields, Eq. (5) can still be applied if the relative variation of \mathbf{B} along one gyration of the particle is small.

One type of field inhomogeneity that gives rise to a drift is curvature of the magnetic field lines. For a particle that moves along a curved magnetic field line the separation of its velocity into v_\perp and v_\parallel changes with its position. This effect will be taken into account systematically in Section IV. In the present section we will give an intuitive argument that shows how field line curvature can cause drift motion. The curvature is given by $\nabla_\parallel \mathbf{b} = -\mathbf{R}_c / R_c^2$, a vector $\perp \mathbf{B}$. Here $\nabla_\parallel \equiv \mathbf{b} \cdot \nabla$ is the gradient along \mathbf{B} and \mathbf{R}_c is the curvature radius shown in Fig. 5. A particle which follows the curved field line with velocity v_\parallel experiences a centrifugal force $\mathbf{F}_c = mv_\parallel^2 \mathbf{R}_c / R_c^2$, which is responsible for the drift velocity

$$\mathbf{v}_c = \frac{mv_\parallel^2}{qB^2} \mathbf{B} \times \nabla_\parallel \mathbf{b}. \quad (7)$$

Figure 5: Inhomogeneous magnetic field. Relation between the curvature radius and the field gradient in a force-free magnetic field ($\nabla \times \mathbf{B} \parallel \mathbf{B}$).



The other inhomogeneity that results in a drift is the transverse gradient of the magnetic field strength. The particle orbit has a smaller radius of curvature on that part of its orbit located in the stronger magnetic field. This leads to a drift perpendicular to both the magnetic field and its gradient. The drift is not the result of a constant force, and hence Eq. (5) cannot be applied directly.

Instead we discuss the averaged effect of ∇B on the gyro-orbit by considering the current $I = q\omega_c/2\pi$ associated with the gyro-motion of a charged particle. The magnetic moment is defined as the product of the current and the area which is surrounded by the current. Since the area encompassed by the gyro-orbit equals $\pi\rho^2$, the magnetic moment per unit particle mass is

$$\mu = \pi\rho^2 \frac{I}{m} = \pi\rho^2 \frac{q^2 B}{2\pi m^2} = \frac{v_\perp^2}{2B}. \quad (8)$$

The gyro-averaged force equals the force on a magnetic dipole in a magnetic field gradient,

$$\mathbf{F}_{\nabla B} = -m\mu \nabla B. \quad (9)$$

Application of Eq. (5) to this force yields the ∇B -drift,

$$\mathbf{v}_{\nabla B} = \frac{mv_\perp^2}{2qB^3} \mathbf{B} \times \nabla B. \quad (10)$$

The curvature and ∇B drifts are often comparable. In a plasma in equilibrium one has approximately $\nabla \times \mathbf{B} \parallel \mathbf{B}$. For a pressure gradient $\nabla p = 0$ this relation is exact. It implies a relation between the curvature vector and ∇B , illustrated in Fig. 5,

$$\nabla_\parallel \mathbf{b} = \frac{\nabla_\perp B}{B}. \quad (11)$$

Using this relation, the ∇B and curvature drifts (10) and (7) can be combined to

$$\mathbf{v}_c + \mathbf{v}_{\nabla B} = \frac{m}{qB^3} (v_\parallel^2 + \frac{1}{2}v_\perp^2) \mathbf{B} \times \nabla B. \quad (12)$$

Averaged over a thermal velocity distribution, this drift velocity equals $2T/qBR_c = 2v_{th}\rho_{th}/R_c$.

As a first example of these drifts, consider the electrons and protons captured in the earth's magnetic field (trapping in a magnetic field will be discussed in the next section). Due to the gradient and curvature of the earth's magnetic field, the electrons and protons captured in this field drift around the equator, the electrons from west to east and the protons in the opposite direction, producing the so-called 'electron current' shown in Fig. 6.

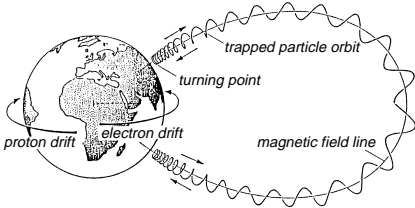


Figure 6: Electron and proton drifts in the Earth magnetic field.

F. Plasma Diamagnetism

The current of a gyrating particle generates a magnetic field in the direction opposite to the given field \mathbf{B} , so that a plasma is diamagnetic. The contributions to the current density of neighbouring gyrating particles cancel each other in a homogeneous plasma. The magnetization of the medium is found by summing over all particles, $\mathbf{M} = -n\langle m\boldsymbol{\mu} \rangle$. In a thermal plasma $\langle \frac{1}{2}mv^2 \rangle = T$ and therefore $\langle m\boldsymbol{\mu} \rangle = T/\mathbf{B}$ and $\mathbf{M} = -b\mathbf{p}/B$. Here n is the particle density and p the pressure. If the pressure is not constant, the magnetization causes a **diamagnetic current**

$$\mathbf{j}_D = \nabla \times \mathbf{M} = -\frac{\nabla p \times \mathbf{B}}{B^2}.$$

This current precisely agrees with the force balance in a conducting fluid, $\nabla p = \mathbf{j} \times \mathbf{B}$. Here, the force per unit volume $\mathbf{j} \times \mathbf{B}$ is the Lorentz force $q\mathbf{v} \times \mathbf{B}$ summed over all particles, making use of $\mathbf{j} = \sum nq\mathbf{v}$. If one views the electrons and ions in the plasma as separate fluids, the diamagnetism is found to give different contributions to the ion and electron fluid velocities, the **diamagnetic velocities**,

$$\mathbf{v}_{D,i} = -\frac{\nabla p_i \times \mathbf{B}}{q_i n B^2}, \quad \mathbf{v}_{D,e} = \frac{\nabla p_e \times \mathbf{B}}{en B^2},$$

which resemble drift velocities of the form (5). Their relation to the diamagnetic current is $\mathbf{j}_D = n_i q_i \mathbf{v}_{D,i} - n_e e \mathbf{v}_{D,e}$.

III. ADIABATIC INVARIANTS

When a system performs a periodic motion, the action integral $I = \oint P dQ$, taken over one period, is a constant of motion, where P is a generalized momentum and Q the corresponding coordinate. For slow changes of the system (compared with the characteristic time of the periodic motion) the integral I remains constant and is called an 'adiabatic invariant'. More precisely: if the system changes on a timescale τ , and the frequency of the periodic motion is ω , then changes to I of the order $\Delta I \sim e^{-\omega\tau}$ can be expected.

A. Magnetic Moment

The first adiabatic invariant is the magnetic moment $\mu = v_{\perp}^2/2B$ defined in Eq. (8), which is proportional to the magnetic flux $\pi\rho^2 B$ enclosed by the gyro-orbit. The periodic

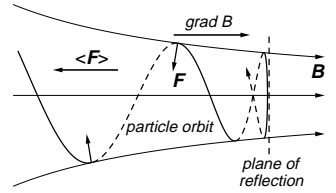


Figure 7: Reflected particle orbit in a magnetic mirror.

motion is the Larmor gyration, P is the angular momentum $mv_{\perp}\rho$ and the coordinate Q is the angle ϕ . We get

$$\oint P dQ = \oint mv_{\perp}\rho d\phi = 2\pi\rho mv_{\perp} = 4\pi\frac{m^2}{q}\mu.$$

Note that μ is no longer a constant of motion if the charge q changes, for instance due to ionization or charge exchange, which preferentially occurs at the edge of the plasma.

B. Particle Trapping

The invariance of μ plays a role in magnetic mirrors. The mirror effect occurs when a particle guiding center moves towards a region with a stronger magnetic field. As Fig. 7 shows, field lines encountered by the particle gyro-orbit converge. Hence the Lorentz force has a gyro-averaged component opposite to ∇B . This mirror force $\parallel \mathbf{B}$ is precisely the force on a magnetic dipole of strength μ in a gradient $\nabla_{\parallel} B$, given by Eq. (9). According to Eq. (5) this force causes a parallel deceleration

$$\dot{v}_{\parallel} = -\mu\nabla_{\parallel} B. \quad (13)$$

Since the particle experiences a magnetic field change $\dot{B} = v_{\parallel}\nabla_{\parallel} B$, Eq. (13) and the conservation of energy $\epsilon = \frac{1}{2}v_{\perp}^2 + \frac{1}{2}v_{\parallel}^2 = \mu B + \frac{1}{2}v_{\parallel}^2$ imply that the magnetic moment μ is constant. In general, the change of the parallel velocity of a particle in a (spatially or temporally) varying magnetic field can be determined from the constancy of μ and ϵ in

$$v_{\parallel}(B) = \pm\sqrt{2(\epsilon - \mu B)}.$$

Figure 8 shows the principle of particle confinement in a

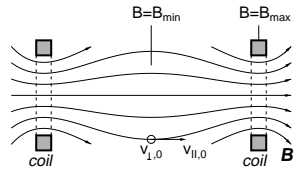


Figure 8: Magnetic field lines of a simple axisymmetric magnetic mirror.

mirror machine. The criterion for the particle passing the high field ends of the mirror machine ($v_{\parallel} > 0$) is

$$\epsilon = \frac{1}{2}v_{\perp,0}^2 + \mu B_{\min} > \mu B_{\max}, \quad (14)$$

where $v_{\perp,0}$ is the parallel velocity in the low field region. If we divide equation (14) by $\mu B_{\min} = \frac{1}{2}v_{\perp,0}^2$, we obtain

$$\frac{v_{\perp,0}}{v_{\perp,0}} > \sqrt{B_{\max}/B_{\min} - 1} \quad (15)$$

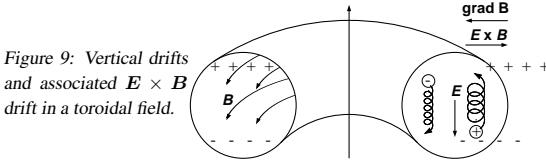


Figure 9: Vertical drifts and associated $\mathbf{E} \times \mathbf{B}$ drift in a toroidal field.

as the criterion for particle loss. In laboratory plasmas the mirror principle yields too large plasma losses at the open ends to be a promising candidate for fusion reactors. Coulomb collisions and certain instabilities cause a continuous transfer of trapped particles into the loss region (15).

The earth's magnetic field is also an example of a magnetic mirror. It forms two belts of confined charged particles originating from the solar wind (see Fig. 6).

A second adiabatic invariant, the longitudinal invariant $J = \oint m v_{\parallel} dl_{\parallel}$, is defined as the integral over the periodic orbit for trapped particles in mirror geometries. Defining the length L between two turning points and the average longitudinal velocity $\langle v_{\parallel} \rangle$, the constant of motion is $J = 2m \langle v_{\parallel} \rangle L$. When L decreases, $\langle v_{\parallel} \rangle$ increases. This is the basis of the Fermi acceleration principle of cosmic radiation.

C. Toroidal Systems: the Tokamak

The end losses inherent to mirror devices are avoided in the closed geometry of toroidal systems. It is important to realize that in a simple toroidal magnetic field (Fig. 9), the magnetic field curvature and gradient (Fig. 5) give rise to **vertical drifts** that are in opposite directions for ions and electrons. The resulting charge separation causes an outward $\mathbf{E} \times \mathbf{B}$ drift for electrons and ions alike. A plasma in a toroidal field alone will thus be unstable.

This conclusion can also be reached by considering the Lorentz force $\mathbf{j} \times \mathbf{B}$ on the plasma as a whole instead of the individual particle orbits. With the current density given by $\mathbf{j} = \nabla \times \mathbf{B} / \mu_0$, it can be shown that this force cannot “point inward” everywhere to confine a plasma in a purely toroidal field.

Therefore, in toroidal plasma devices additional magnetic field components are required in order to reach a steady state where the plasma pressure is balanced by magnetic forces ($\nabla p = \mathbf{j} \times \mathbf{B}$). The required twisted magnetic field is produced in tokamaks by the toroidal plasma current. As a consequence, particles approximately move on closed toroidal surfaces labelled by the poloidal magnetic flux ψ .

The vertical drifts average to zero over one poloidally closed particle orbit, as can be seen as follows. Because of the toroidal symmetry of \mathbf{B} , the canonical angular momentum associated to the toroidal angle is conserved exactly,

$$\begin{aligned} P_{\text{tor}} &= (m v_{\text{tor}} - q A_{\text{tor}}) R \\ &= m R v_{\text{tor}} - q \psi \\ &\simeq m R v_{\parallel} - q \psi = \text{constant}. \end{aligned} \quad (16)$$

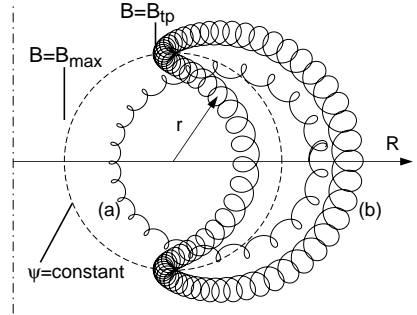


Figure 10: Projection of circulating (a) and trapped (b) particle orbits on the poloidal plane. R is the distance to the vertical axis.

Hence, because v_{\parallel} remains in the range determined by ϵ and μ , the particle remains in a bounded ψ zone and does not escape in the vertical direction.

In a tokamak, the field strength has its maximum value at the inside of the torus. A particle travelling along a field line feels a periodic mirror force. If the energy and magnetic moment of this particle have values such that $\epsilon > \mu B_{\text{max}}$, the particle is not reflected but continues its course and encircles the torus. These are circulating or transit particles.

On the other hand, if $\epsilon < \mu B_{\text{max}}$ the particle is reflected at the point where $\epsilon = \mu B_{\text{tp}}$ (see Fig. 10). The particle is trapped between magnetic mirrors and bounces between turning points. Thus, in leading order the particle executes a periodic motion along a field line.

The topology of the trajectories of trapped and circulating particles are quite different. While transit particles encircle the torus in the toroidal as well as in the poloidal direction, trapped particles may encircle the torus in the toroidal direction but be poloidally confined to the low field side of the torus. Due to this difference in topology, trapped and circulating particles often behave as different species.

Equation (16) shows that, because v_{\parallel} of a trapped particle changes sign, its orbit is more strongly affected by the vertical drift than is a transit particle orbit. The projection of a trapped particle orbit on the poloidal plane of an axisymmetric torus is sketched in Fig. 10. The flux surfaces are assumed to have circular cross-sections. The width of this orbit can easily be calculated from Eq. (16). It follows that the total width, $\Delta r = \Delta \psi / (\partial \psi / \partial r)$, of the orbit is

$$\Delta r = 2 \frac{m R v_{\parallel}}{q \partial \psi / \partial r} = 2 \frac{v_{\parallel} m}{q B_{p,m}}, \quad (17)$$

where r is the cylindrical radius and $v_{\parallel m}$ is the value of the parallel velocity at the midplane. Note that the denominator in (17) is the gyro-frequency in the poloidal field at the midplane $B_{p,m}$. More about the particle orbits in tokamaks can be found in Refs. [1,2,3].

ACKNOWLEDGMENT

This work, supported by the European Communities under the contract of Association between EURATOM/FOM, was carried out within the framework of the European Fusion Programme with financial support from NWO. The views and opinions expressed herein do not necessarily reflect those of the European Commission.

REFERENCES

1. G. Schmidt, "*Physics of High Temperature Plasmas*," Academic Press, New York (1979).
2. R.B. White, "*Theory of Tokamak Plasmas*," North-Holland, Amsterdam (1989).
3. J.A. Wesson, "*Tokamaks*," 2nd ed., Oxford University Press, Oxford (1997).
4. T.G. Northrop, "*The Adiabatic Motion of Charged Particles*," (1963), Interscience, New York.
5. R.J. Hastie, in "*Plasma Physics and Nuclear Fusion Research*," (1981), ed. R.D. Gill, Academic Press.
6. R.M. Kulsrud, in "*Handbook of Plasma Phys*" Vol. 1, edited by M.N. Rosenbluth and R.Z. Sagdeev, (1983) North-Holland Publ. Co.

KINETIC PLASMA THEORY (KT-1)

S. Poedts

Centre for mathematical Plasma Astrophysics, Dept. of Mathematics
KU Leuven, Celestijnenlaan 200 B, 3001 Leuven, Belgium

Abstract

First, the place of kinetic theory among other mathematical models to describe plasma physics is discussed. Next, some basic kinetic concepts are introduced and the kinetic plasma equations are described. The use of these equations is then demonstrated considering electron plasma oscillations, a simple example of collective behaviour, and deriving a fundamental plasma parameter, viz. the plasma frequency, a fundamental plasma parameter. The a surprising fundamental phenomenon Landau damping is briefly discussed.

1 Introduction: theoretical models in plasma physics

Different mathematical models exist for different kinds of plasma processes. The model to be used or applied depends on the kind of phenomenon to be studied. Three kinds of theoretical description can be distinguished on the basis of the chosen approach [1]:

1. the theory of the motion of *individual charged particles* in given magnetic and electric fields; e.g. the motion of a charged, non-relativistic particle is described by

$$m \frac{d\mathbf{v}}{dt} = q(\mathbf{E} + \mathbf{v} \times \mathbf{B}), \quad (1)$$

where $\mathbf{E}(\mathbf{r}, t)$ and $\mathbf{B}(\mathbf{r}, t)$ are given solutions of the Maxwell's equations, and one has to solve for the particle velocity $\mathbf{v}(\mathbf{r}, t)$. This model is useful to describe gyration of particles in a magnetic field and adiabatic invariants of this cyclotron motion, the

magnetic mirror effect, drifts, etc. But plasmas usually contain a lot of particles, e.g. a large Corona Mass Ejection on the Sun involves up to 10^{30} particles, requiring a different model approach;

2. the *kinetic theory* of a such collections of charged particles, describing plasma behavior on a *microscopic scale* by means of particle distribution functions $f_{e,i}(\mathbf{r}, \mathbf{v}, t)$, the evolution of which is most generally described by the Boltzmann dissipative equation (see below). There exists an alternative Particle-In-Cell (PIC) approach, however, in which the particles are modelled as 'super particles' or 'particle clouds' which are accelerated by the forces (Lorentz, gravitational, etc.). This alternative approach will be described in module KT-2;
3. the *fluid theory* (MHD), describing plasma behavior on a *macroscopic scale* in terms of averaged (over \mathbf{v}) functions of only \mathbf{r} and t . The three basic steps to get from kinetic theory to the plasma model are discussed in the last section of this contribution.

Clearly, this is a rough division of model approaches and there exist combinations, like hybrid models with one or more species described in the fluid theory and other species described in kinetic theory. Here, we will focus on the kinetic plasma theory.

Why kinetic theory?

In the single particle orbit theory mentioned above, the interactions between the particles is ignored. This is a valid assumption only when the density of the charged particles is low enough. Plasmas, however, exhibit *collective*

behaviour because of the large amount of *interacting* particles involved. As a result, a statistical approach can be used to analyse its dynamics and this is precisely what kinetic plasma theory does. In this sense, the kinetic description of plasma is fundamental. The position of particles is known in phase space, the space of all possible values of position and momentum variables, making even the electron scale accessible.

Of particular importance are kinetic or micro-instabilities. These are short wavelength - high frequency modes of the system that may grow in amplitude when the charged particle species in a collisionless plasma possess a non-maxwellian velocity distribution. In other words, these modes are driven unstable by the kinetic anisotropy of the plasma particles which provides a source of free energy. The velocity distributions (microstates) measured in-situ in space plasmas, for instance, often show departures from thermodynamic (Maxwellian) equilibrium in the form of temperature anisotropy, plasma flows or beams ('strahls'), suprathermal tails, etc. *These deviations from thermal equilibrium and the micro-instabilities they induce can be described only with a kinetic approach.*

Here, we will not elaborate on the derivation of the equation(s) describing the evolution of the plasma, which was introduced by Ludwig Boltzmann in 1872 and constitutes a vast amount of theoretical analysis (See, e.g. the comprehensive treatise by Balescu [2]), but merely exploit *the Boltzmann equation*, one of the end results of this work.

Closely following Goedbloed and Poedts [1], we will first introduce some basic kinetic concepts (Section 4) and consider a simple example of collective behaviour (Section 5), viz. electron plasma oscillations, and derive *the plasma frequency*, a fundamental plasma parameter. The (Landau) damping of these oscillations through kinetic effects is then discussed briefly in Section 5. It will also be discussed in modules KW-1 and KW-2 in this school. In module KT-2, numerical simulation models based on kinetic theory will be discussed and some of the impressive results will be demonstrated there.

2 Some basic plasma parameters

In Eq. (1) we did not specify the mass m and the charge q of the particles. Clearly, they correspond to either elec-

trons ($m = m_e, q = -e$) or ions with mass number A and charge number Z (i.e. multiples of the proton mass and charge: $m = m_i = Am_p, q = Ze$). When we consider such a charged particle in a constant magnetic field in the z -direction, in the absence of an electric field: $\mathbf{B} = B\mathbf{e}_z, \mathbf{E} = 0$, we can get some insight by performing two simple vector operations on Eq. (1). First project this equation \mathbf{B} and using vector identities, we get that $v_{\parallel} = \text{const}$ because

$$m \frac{dv_{\parallel}}{dt} = 0. \quad (2)$$

When we project the same equation on \mathbf{v} , we get

$$\frac{d}{dt}(\frac{1}{2}mv^2) = 0 \rightarrow \frac{1}{2}mv^2 = \text{const}, \quad (3)$$

which in combination with (2) yields that also $v_{\perp} = \text{const}$. because

$$\frac{1}{2}mv_{\perp}^2 = \text{const}. \quad (4)$$

Solving Eq. (1) more systematically, using $\mathbf{v} = dx/dt = (\dot{x}, \dot{y}, \dot{z})$, we get two coupled differential equations describing the motion in the perpendicular plane:

$$\begin{aligned} \ddot{x} - \Omega \dot{y} &= 0, \\ \ddot{y} + \Omega \dot{x} &= 0, \end{aligned} \quad (5)$$

where

$$\Omega \equiv \frac{|q|B}{m}, \quad (6)$$

is *the gyro- or cyclotron frequency*.

We here do not elaborate on the derivation (see [1]), but the helical orbit consists of gyration (a periodic circular motion) $\perp \mathbf{B}$ about a *the guiding centre* and with a *the gyro- or cyclotron radius*

$$R \equiv \frac{v_{\perp}}{\Omega} = \text{const}, \quad (7)$$

and inertial motion $\parallel \mathbf{B}$. The magnetic field \mathbf{B} thus determines the geometry of the plasma.

Remarks that electrons and ions gyrate in opposite directions (Fig. 1). Due to their mass difference, their gyro-frequencies and gyro-radii are quite different:

$$\begin{aligned} \Omega_e \equiv \frac{eB}{m_e} &\gg \Omega_i \equiv \frac{ZeB}{m_i}, \\ R_e \equiv \frac{v_{\perp,e}}{\Omega_e} &\ll R_i \equiv \frac{v_{\perp,i}}{\Omega_i} \quad (\text{assuming } T_e \sim T_i). \end{aligned} \quad (8)$$

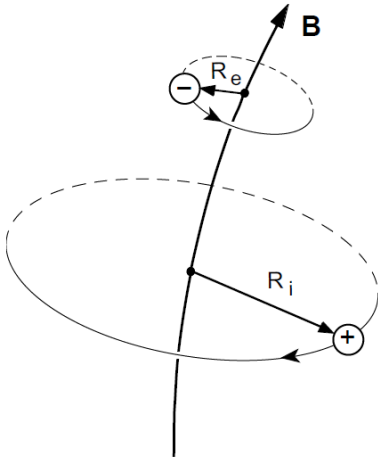


Figure 1: Gyration of electrons and ions in a magnetic field (source: [1]).

Inserting a magnetic field $B = 3 \text{ T} (= 30 \text{ kgauss})$, typical for tokamaks, and the values for e , m_e , and m_p , we find for the angular frequencies of protons and electrons

$$\begin{aligned} \Omega_e &= 5.3 \times 10^{11} \text{ rad s}^{-1} \quad (\text{i.e., a freq. of } 84 \text{ GHz}), \\ \Omega_i &= 2.9 \times 10^8 \text{ rad s}^{-1} \quad (\text{i.e., a freq. of } 46 \text{ MHz}). \end{aligned} \quad (9)$$

Considering particles with thermal speed $v_{\perp} = v_{\text{th}} \equiv \sqrt{2kT/m}$ we can estimate the gyro-radii. For electrons and protons at $\tilde{T} = 10 \text{ keV}$, i.e. $T_e = T_i = 1.16 \times 10^8 \text{ K}$, we obtain

$$\begin{aligned} v_{\text{th},e} &= 5.9 \times 10^7 \text{ m s}^{-1} \quad \Rightarrow \quad R_e \approx 0.1 \text{ mm}, \\ v_{\text{th},i} &= 1.4 \times 10^6 \text{ m s}^{-1} \quad \Rightarrow \quad R_i \approx 5 \text{ mm}. \end{aligned} \quad (10)$$

Adding a constant background electric field perpendicular to the magnetic field, i.e. $\mathbf{B} = B\mathbf{e}_z$, $\mathbf{E} = E\mathbf{e}_y$, only slightly complicates the analysis. However, in this case the gyration is superposed with a constant 'drift' in x -direction. Hence, the perpendicular electric field results in the so-called $\mathbf{E} \times \mathbf{B}$ drift (see [1]).

3 Kinetic model equations

The equations of the kinetic model consist of equations for the particle distribution functions combined with Maxwell's equations (13) which determine the electric and magnetic fields $\mathbf{E}(\mathbf{r}, t)$ and $\mathbf{B}(\mathbf{r}, t)$.

3.1 The Boltzmann equation

Let us consider a plasma that consists of electrons and one kind of ions. Clearly, the information on the individuality of the particles is lost in the statistical description. However, the time-dependent *distribution functions* $f_{\alpha}(\mathbf{r}, \mathbf{v}, t)$ for the electrons and ions ($\alpha = e, i$) contain relevant physical information on the plasma as a whole. The distribution functions express the density of the representation points of particles of type α in the six-dimensional *phase space* which is formed by the three position coordinates (x, y, z) and the three velocity coordinates (v_x, v_y, v_z) (see, e.g., Bittencourt [3]). In other words, $f_{\alpha}(\mathbf{r}, \mathbf{v}, t) d^3r d^3v$ represents the probable number of particles of type α in the six-dimensional volume element $d^3r d^3v$ centred at (\mathbf{r}, \mathbf{v}) . We here assume that the total number of particles, $N_{\alpha} \equiv \iint f_{\alpha} d^3r d^3v$, is constant. This is, of course, not valid for plasmas that are in thermal and/or chemical non-equilibrium, like the partially-ionized plasmas in the lower solar atmosphere (photosphere and lower chromosphere) and thermonuclear plasmas in which fusion reactions create and annihilate particles. In such cases, more than two distribution functions are needed, e.g. also one for neutrals in the case of the solar photosphere, and the respective total number of particles will not be constant.

We now make a distinction between the motion of individual particles and the motion of a collection of their representative points in phase space, which is somehow similar to the motion of a swarm of bees (versus the motion of a particular bee in the swarm). The 'swarm' of representative points is described by the distribution function $f_{\alpha}(\mathbf{r}, \mathbf{v}, t)$, and its motion is given the *total* time derivative of f_{α} , using the chain rule we get:

$$\begin{aligned} \frac{df_{\alpha}}{dt} &\equiv \frac{\partial f_{\alpha}}{\partial t} + \frac{\partial f_{\alpha}}{\partial \mathbf{r}} \cdot \frac{d\mathbf{r}}{dt} + \frac{\partial f_{\alpha}}{\partial \mathbf{v}} \cdot \frac{d\mathbf{v}}{dt} \\ &= \frac{\partial f_{\alpha}}{\partial t} + \mathbf{v} \cdot \frac{\partial f_{\alpha}}{\partial \mathbf{r}} + \frac{q_{\alpha}}{m_{\alpha}} (\mathbf{E} + \mathbf{v} \times \mathbf{B}) \cdot \frac{\partial f_{\alpha}}{\partial \mathbf{v}}, \end{aligned} \quad (11)$$

where Eq. (1) has been used inserted in the second line.

Here, the scalar products involving derivatives with respect to the vectors \mathbf{r} and \mathbf{v} simply denote sums over the products of the vector components, i.e. $\mathbf{v} \cdot \partial/\partial\mathbf{r} \equiv v_x \partial/\partial x + v_y \partial/\partial y + v_z \partial/\partial z$, and idem for the term with $\partial/\partial\mathbf{v}$. Notice also the subtle difference between d/dt for the total time derivative and d/dt for ordinary time derivatives. Liouville's theorem ([5]) states that, in the absence of binary interactions between particles, $df_\alpha/dt = 0$, i.e. the density of representative points in phase space remains constant.

Clearly, the behaviour of a collection of particles only becomes interesting when these particles collide with each other, i.e. interact. In 1872, Ludwig Boltzmann derived an equation describing the time variation of the distribution functions of electrons and ions. This kinetic equation, called *the Boltzmann equation* reads:

$$\frac{\partial f_\alpha}{\partial t} + \mathbf{v} \cdot \frac{\partial f_\alpha}{\partial \mathbf{r}} + \frac{q_\alpha}{m_\alpha} (\mathbf{E} + \mathbf{v} \times \mathbf{B}) \cdot \frac{\partial f_\alpha}{\partial \mathbf{v}} = \left(\frac{\partial f_\alpha}{\partial t} \right)_{\text{coll}}^{\text{coll}}. \quad (12)$$

Note that here $\mathbf{E}(\mathbf{r}, t)$ and $\mathbf{B}(\mathbf{r}, t)$ consist of the contributions of the external fields plus that of the averaged internal fields originating from the long-range inter-particle interactions. The right-hand side represents the effect of an unspecified collision term which should model the short-range inter-particle interactions, or 'collisions'. These are the large-angle Coulomb collisions resulting from the cumulation of the many small-angle velocity changes. A first important objective of kinetic theory is to distinguish between different (long- and short-range) interactions and binary collisions and to determine on what ranges they are valid, yielding different forms of this collision term. One choice leads to the Landau collision integral (1936) [7]. And when only the accumulated effects of the small-angle collisions are taken into account, the above equation leads to the *Fokker-Planck equation*; and neglecting all collisions, i.e. setting the RHS equal to zero, leads to the *Vlasov equation* (1938) [12]. Another choice leads to the Landau collision integral (1936) [7].

3.2 Maxwell's equations

In order to obtain a closed system of equations the Boltzmann equation (12) (or the Vlasov equation in case collisions can be ignored) for the distribution functions $f_\alpha(\mathbf{r}, \mathbf{v}, t)$, are combined with Maxwell's equations (13),

determining the electric and magnetic fields $\mathbf{E}(\mathbf{r}, t)$ and $\mathbf{B}(\mathbf{r}, t)$, and providing expressions (14) for the charge and current density source terms $\tau(\mathbf{r}, t)$ and $\mathbf{j}(\mathbf{r}, t)$. In mksA units these equations are given by:

$$\begin{cases} \nabla \times \mathbf{E} = -\frac{\partial \mathbf{B}}{\partial t} & \text{(Faraday)}, \\ \nabla \times \mathbf{B} = \mu_0 \mathbf{j} + \frac{1}{c^2} \frac{\partial \mathbf{E}}{\partial t} & \text{('Ampère'), } c^2 = (\epsilon_0 \mu_0)^{-1}, \\ \nabla \cdot \mathbf{E} = \frac{\tau}{\epsilon_0} & \text{(Poisson)}, \\ \nabla \cdot \mathbf{B} = 0 & \text{(no magnetic monopoles)}. \end{cases} \quad (13)$$

We have ignored polarisation and magnetisation effects, i.e. $\epsilon = \epsilon_0$ and $\mu = \mu_0$ so that $\mathbf{D} = \epsilon_0 \mathbf{E}$ and $\mathbf{H} = (\mu_0)^{-1} \mathbf{B}$, since these effects are absorbed in the definitions of charge and current density:

$$\begin{cases} \tau = \sum_\alpha q_\alpha n_\alpha \\ \mathbf{j} = \sum_\alpha q_\alpha n_\alpha \mathbf{u}_\alpha \end{cases} \quad (\alpha = e, i). \quad (14)$$

Here, n_α and \mathbf{u}_α are the particle density and the macroscopic velocity of particles of type α .

The charge and current density source terms $\tau(\mathbf{r}, t)$ and $\mathbf{j}(\mathbf{r}, t)$ are related to the particle densities and the average velocities:

$$\begin{aligned} n_\alpha(\mathbf{r}, t) &\equiv \int f_\alpha(\mathbf{r}, \mathbf{v}, t) d^3v, \\ \text{and } \tau(\mathbf{r}, t) &\equiv \sum q_\alpha n_\alpha, \\ \mathbf{u}_\alpha(\mathbf{r}, t) &\equiv \frac{1}{n_\alpha(\mathbf{r}, t)} \int \mathbf{v} f_\alpha(\mathbf{r}, \mathbf{v}, t) d^3v, \\ \text{and } \mathbf{j}(\mathbf{r}, t) &\equiv \sum q_\alpha n_\alpha \mathbf{u}_\alpha. \end{aligned} \quad (15) \quad (16)$$

This completes the microscopic equations.

Solving these kinetic equations in seven dimensions (with the details of the single particle motions entering the collision integrals) is a formidable task, even with the help of present-day supercomputers. Hence, whenever possible, i.e. when the physical phenomenon that is studied allows it, modelers will look for a macroscopic reduction. Here, however, we will stick to the kinetic equations and take up the challenge of solving them.

4 Moment reduction

Macroscopic equations, i.e. equations that do not involve details of velocity space any more can be obtained by expanding in a finite number of moments of the Boltzmann equation (12). These moments are obtained by first multiplying the equation with a function $\chi(\mathbf{v})$ and then integrating over velocity space. The function χ consists of powers of the velocity:

$$\chi(\mathbf{v}) = \begin{cases} 1, & \text{zerth moment;} \\ \mathbf{v}, & \text{first moment;} \\ v^2, & \text{second moment;} \\ \dots, & \end{cases} \quad (17)$$

and the procedure is truncated after a finite number (5, 10, 20...) of such moments. Clearly, taking moments of the Boltzmann equation involves the moments of the distribution function itself. For instance, the zeroth moment is associated with the particle density $n_\alpha(\mathbf{r}, t)$ and the first moment is associated with the average velocity $\langle \mathbf{v} \rangle_\alpha \equiv \mathbf{u}_\alpha(\mathbf{r}, t)$, defined above. This expansion in moments clearly needs to be truncated in order to be practical. A popular truncation occurs already after the five moments (one scalar + one vector + one scalar) indicated explicitly in Eq. (17). This truncation is justified in the transport theory. Macroscopic variables $\langle g \rangle_\alpha(\mathbf{r}, t)$ generally appear as averages of some phase space function $g(\mathbf{r}, \mathbf{v}, t)$ over the velocity space, i.e.

$$\langle g \rangle_\alpha(\mathbf{r}, t) \equiv \frac{1}{n_\alpha(\mathbf{r}, t)} \int g(\mathbf{r}, \mathbf{v}, t) f_\alpha(\mathbf{r}, \mathbf{v}, t) d^3v. \quad (18)$$

Clearly, this definition assumes or requires that the distribution functions f_α decrease fast enough with $v \rightarrow \infty$ in order to yield a finite answer.

The systematic procedure of taking moments of the Boltzmann equations also involves the determination of the different moments of the collision term in the RHS. The collision operator

$$\left(\frac{\partial f_\alpha}{\partial t} \right)_{\text{coll}} \equiv C_\alpha, \quad (19)$$

represents evolution of f_α due to local collisions. It can be decomposed in contributions $C_{\alpha\beta}$ due to collisions of particles α (e.g. electrons) with particles β (i.e. electrons

as well as ions):

$$C_\alpha = \sum_\beta C_{\alpha\beta}. \quad (20)$$

So, e.g. C_i is the sum of the intraspecies collision operator C_{ii} , which represents the effect of ion-ion collisions, and the interspecies collision operator C_{ie} , which represents the effect on the ions of ion-electron collisions. C_α is thus an operator which maps functions of velocity space, $f_i(\mathbf{v})$ and $f_e(\mathbf{v})$, to a function of velocity space, $C_\alpha(\mathbf{v})$.

The collision of course respect some constraints. For instance, in the absence of fusion reactions, there is *conservation of mass*, i.e. the total number of particles α at a certain position does not change by collisions with particles β :

$$\int C_{\alpha\beta} d^3v = 0. \quad (21)$$

In a similar way, *conservation of momentum* yields

$$\int \mathbf{v} C_{ii} d^3v = 0, \quad (22)$$

and

$$\int \|\mathbf{v}\|^2 (C_i + C_e) d^3v = 0; \quad (23)$$

while *conservation of energy* yields

$$\int \mathbf{v} C_{ii} d^3v = 0, \quad (24)$$

and

$$\int \|\mathbf{v}\|^2 (C_i + C_e) d^3v = 0. \quad (25)$$

More details of the derivation of these expressions and on the procedure in general can be found in Goedbloed and Poedts [1]. In order to give an idea of the procedure, we will here only derive the lowest moment equation, which describes mass conservation.

As mentioned above, the *zerth moment* is obtained by integrating the Boltzmann equation (Eq. (12)) over velocity space. Doing this term by term, we get subsequently:

$$\int \frac{\partial f_\alpha}{\partial t} d^3v = \frac{\partial n_\alpha}{\partial t} \quad (\text{def. (15)}),$$

$$\int \mathbf{v} \cdot \frac{\partial f_\alpha}{\partial \mathbf{r}} d^3v = \nabla \cdot (n_\alpha \mathbf{u}_\alpha) \quad (\text{def. (16)}),$$

$$\int \frac{q_\alpha}{m_\alpha} (\mathbf{E} + \mathbf{v} \times \mathbf{B}) \cdot \frac{\partial f_\alpha}{\partial \mathbf{v}} d^3v = 0 \quad (\text{int. by parts}),$$

$$\int C_{\alpha\beta} d^3v = 0 \quad (\text{summing Eq. (21)}).$$

The continuity equation for particles of species α is obtained by adding these four expressions, yielding

$$\frac{\partial n_\alpha}{\partial t} + \nabla \cdot (n_\alpha \mathbf{u}_\alpha) = 0. \quad (26)$$

Similarly, the first moment of the Boltzmann equation is obtained by multiplying it with $m_\alpha \mathbf{v}$ and integrating this expression over the velocities. This yields the momentum equation:

$$\frac{\partial}{\partial t} (n_\alpha m_\alpha \mathbf{u}_\alpha) + \nabla \cdot (n_\alpha m_\alpha \langle \mathbf{v} \mathbf{v} \rangle_\alpha) - q_\alpha n_\alpha (\mathbf{E} + \mathbf{u}_\alpha \times \mathbf{B}) = \int C_{\alpha\beta} m_\alpha \mathbf{v} d^3v. \quad (27)$$

The scalar second moment of Eq. (12) is then obtained by multiplying with $\frac{1}{2} m_\alpha v^2$ and integrating over velocity space. This yields the energy equation:

$$\frac{\partial}{\partial t} (n_\alpha \frac{1}{2} m_\alpha \langle v^2 \rangle_\alpha) + \nabla \cdot (n_\alpha \frac{1}{2} m_\alpha \langle v^2 \mathbf{v} \rangle_\alpha) - q_\alpha n_\alpha \mathbf{E} \cdot \mathbf{u}_\alpha = \int C_{\alpha\beta} \frac{1}{2} m_\alpha v^2 d^3v. \quad (28)$$

See [1] for the explicit steps in the derivation of these equations.

This chain of moment equations can be continued indefinitely. Notice that each moment introduces a new unknown whose temporal evolution is described by the next moment of the Boltzmann equation. However, the infinite chain must be truncated to be useful. In fluid theories truncation is just after the above five moments: the continuity equation (26) (scalar), the momentum equation (27) (vector), and the energy equation (28) (scalar), by making additional assumptions. In (very) broad outlines, the procedure can be summarized as follows:

(a) First, split the particle velocity \mathbf{v} into an average part \mathbf{u}_α and a random part $\tilde{\mathbf{v}}_\alpha$, i.e.

$$\tilde{\mathbf{v}}_\alpha \equiv \mathbf{v} - \mathbf{u}_\alpha, \quad \text{where } \langle \tilde{\mathbf{v}}_\alpha \rangle = 0. \quad (29)$$

In this way thermal quantities can be defined, like

$$T_\alpha(\mathbf{r}, t) \equiv \frac{m_\alpha}{3k} \langle \tilde{v}_\alpha^2 \rangle \quad (\text{temperature}), \quad (30)$$

$$\mathbf{P}_\alpha(\mathbf{r}, t) \equiv n_\alpha m_\alpha \langle \tilde{\mathbf{v}}_\alpha \tilde{\mathbf{v}}_\alpha \rangle = p_\alpha \mathbf{I} + \boldsymbol{\pi}_\alpha,$$

$$p_\alpha \equiv n_\alpha k T_\alpha \quad (\text{stress tensor}), \quad (31)$$

$$\mathbf{h}_\alpha(\mathbf{r}, t) \equiv \frac{1}{2} n_\alpha m_\alpha \langle \tilde{v}_\alpha^2 \tilde{\mathbf{v}}_\alpha \rangle \quad (\text{heat flow}), \quad (32)$$

$$\mathbf{R}_\alpha(\mathbf{r}, t) \equiv m_\alpha \int C_{\alpha\beta} \tilde{\mathbf{v}}_\alpha d^3v \quad (\text{momentum transfer}), \quad (33)$$

$$Q_\alpha(\mathbf{r}, t) \equiv \frac{1}{2} m_\alpha \int C_{\alpha\beta} \tilde{v}_\alpha^2 d^3v \quad (\text{heat transfer}). \quad (34)$$

Note that in this notation \mathbf{I} is the unit tensor, i.e. $\boldsymbol{\pi}_\alpha$ represents the off-diagonal terms of the pressure tensor \mathbf{P} . For instance, the Maxwell distribution for thermal equilibrium:

$$f_\alpha^0(\mathbf{r}, \mathbf{v}, t) = n_\alpha \left(\frac{m_\alpha}{2\pi k T_\alpha} \right)^{3/2} \exp \left(-\frac{m_\alpha \tilde{v}_\alpha^2}{2k T_\alpha} \right), \quad (35)$$

is consistent with these definitions and makes the LHS of the Boltzmann equation (12) vanish. This means that the collision term on the RHS should vanish too, i.e. when the two distributions have equal average velocities ($\mathbf{u}_e = \mathbf{u}_i$) and temperatures ($T_e = T_i$). The deviations from this thermal equilibrium and the way in which collisions cause relaxation to thermal equilibrium, is what plasma kinetic theory is concerned with (Braginskii [4]).

(b) The temperature evolution equation is then transformed into a pressure evolution equation by introducing the ratio of specific heats, $\gamma \equiv C_p/C_v = 5/3$. The resulting equations for n_α , \mathbf{u}_α , and p_α then appear rather macroscopic, but still hide unsolved kinetic dependences involving higher order moments and variables which involve the unspecified collision operator.

(c) The obtained truncated set of moment equations is then finally closed by exploiting the transport coefficients derived by transport theory (Braginskii [4], Balescu [2]), which concerns the deviations from local thermodynamic equilibrium, expressed by Eq. (35). In this theory the distribution functions are developed in powers of a small parameter measuring these deviations. This results in transport coefficients, determining relations between the thermal quantities defined in Eqs. (30)–(34) and the gradients of the macroscopic quantities. The second objective of kinetic theory is to provide these coefficients, which is again a formidable task.

Following [1], we will now present an application of the two-fluid description (Section 5). It will be highly simplified in the sense that most of the complicated terms discussed above do not occur. Yet, this simple application illustrates a very important basic physical mechanism at work, namely collective electrostatic oscillations. After that, we will return to the kinetic description in terms of distribution functions and discuss how velocity space effects lead to Landau damping, a surprising kinetic phenomenon (Section 6).

5 Collective phenomena: plasma oscillations

Chen [6] defines a plasma as *a quasi-neutral gas of charged and neutral particles which exhibits collective behaviour*. The typical size of a region in the plasma over which charge imbalance due to thermal fluctuations may occur, is the *Debye length*. In the present section, we will extend these electric field concepts. We will first study perturbations of quasi-neutrality in a cold plasma by typical *plasma oscillations* which are called Langmuir waves (1929)¹. We then study how these oscillations are affected by finite temperatures; first by including a finite pressure, next by taking into account velocity space effects by applying the kinetic equations, which will lead to the concept of *Landau damping*.

5.1 Cold plasma oscillations

We start by considering a highly simplified case, viz. that of a cold plasma in the absence of a magnetic field ($\mathbf{B} = 0$). In other words, all thermal effects are neglected (\mathbf{P}_α , \mathbf{h}_α , \mathbf{R}_α , and Q_α vanish). As a result, all the complicated terms in the equations of motion vanish and the energy equations can be dropped. For cold plasma oscillations we thus just need to consider the continuity equations,

$$\frac{\partial n_\alpha}{\partial t} + \nabla \cdot (n_\alpha \mathbf{u}_\alpha) = 0 \quad (\alpha = e, i), \quad (36)$$

and the simplified ($\mathbf{B} = 0$) momentum equations,

$$m_\alpha \left(\frac{\partial \mathbf{u}_\alpha}{\partial t} + \mathbf{u}_\alpha \cdot \nabla \mathbf{u}_\alpha \right) = q_\alpha \mathbf{E} \quad (\alpha = e, i). \quad (37)$$

¹named after the author who also introduced the term 'plasma' in 1923

The *Poisson equation* (13)(c) then enables us to determine the electric field in a self-consistent manner, where *the charge density* is obtained from Eq. (14)(a):

$$\nabla \cdot \mathbf{E} = \frac{\tau}{\epsilon_0} = \frac{e}{\epsilon_0} (Zn_i - n_e). \quad (38)$$

Remark that these equations form a complete set for the variables $n_{e,i}(\mathbf{r}, t)$, $\mathbf{u}_{e,i}(\mathbf{r}, t)$, and $\mathbf{E}(\mathbf{r}, t)$ which describe the problem of electrostatic oscillations.

One of the most fundamental properties of plasmas is that they maintain approximate charge neutrality. As a matter of fact, charge imbalances on a macroscopic scale L would create huge electric fields ($E \sim \tau L / \epsilon_0$) which would accelerate the electrons and thus neutralise these imbalances extremely fast. As a result, the plasma maintains almost perfect charge neutrality.

Charge imbalances do occur, however, on a finer time and length scale, viz. in the form of typical oscillations. For these plasma oscillations, we can consider the heavy ions ($m_i \gg m_e$) as a fixed ($\mathbf{u}_i = 0$) neutralising background in which only the light electrons move ($\mathbf{u}_e \neq 0$). When a small region inside the plasma is then perturbed, by displacing the electrons in that region, the charge neutrality is disturbed ($n_e \neq Zn_i$). The problem is then completely determined by the electron variables (the two ion equations (36) and (37) for $\alpha = i$ may be dropped):

$$\begin{aligned} n_e &\approx n_0 + n_1(\mathbf{r}, t), \\ \mathbf{u}_e &\approx \mathbf{u}_1(\mathbf{r}, t), \end{aligned} \quad (39)$$

whereas the ion variables simplify to

$$n_i \approx n_0 / Z = \text{const}, \quad \mathbf{u}_i \approx 0. \quad (40)$$

Here, the subscripts 0 and 1 refer to the constant background and the (small) perturbations, respectively. The small density perturbation $|n_1(\mathbf{r}, t)| \ll n_0$ occurs in a small region of the plasma. We can thus *linearize* the equations, i.e. we can neglect terms involving products of perturbations since these are much smaller than the linear terms. As a result, the small electric field \mathbf{E}_1 that is created is proportional to n_1 and creates a small electron flow velocity \mathbf{u}_1 , which is also proportional to n_1 .

A complete set of equations is thus obtained, consisting of the linearized electron density equation (36), the momentum equation (37) (both with $\alpha = e$), and the Poisson

equation (38):

$$\begin{aligned}\frac{\partial n_1}{\partial t} + n_0 \nabla \cdot \mathbf{u}_1 &= 0, \\ m_e \frac{\partial \mathbf{u}_1}{\partial t} &= -e \mathbf{E}_1, \\ \nabla \cdot \mathbf{E}_1 &= \frac{\tau_1}{\epsilon_0} = -\frac{e}{\epsilon_0} n_1.\end{aligned}\quad (41)$$

Eliminating \mathbf{u}_1 and \mathbf{E}_1 then yields a single wave equation for n_1 :

$$\frac{\partial^2 n_1}{\partial t^2} = -n_0 \nabla \cdot \frac{\partial \mathbf{u}_1}{\partial t} = \frac{n_0 e}{m_e} \nabla \cdot \mathbf{E}_1 = -\frac{n_0 e^2}{\epsilon_0 m_e} n_1. \quad (42)$$

5.2 Plasma frequency and Debye length

The solutions of the wave equation (42) can be written in the form $n_1(\mathbf{r}, t) = \hat{n}_1(\mathbf{r}) \exp(-i\omega t)$. They represent *plasma oscillations*, which are electron density oscillations with a characteristic frequency, called *the electron plasma frequency*:

$$\omega = \pm \omega_{pe}, \quad \omega_{pe} \equiv \sqrt{\frac{n_0 e^2}{\epsilon_0 m_e}}. \quad (43)$$

This frequency is one of the fundamental parameters of a plasma and is usually very high (because m_e is very small). It provides a diagnostic for the determination of the plasma density since it depends only the plasma density. In tokamak plasmas, a typical density $n_0 = 10^{20} \text{ m}^{-3}$ gives

$$\omega_{pe} = 5.7 \times 10^{11} \text{ rad s}^{-1} \quad (\text{i.e. } 91 \text{ GHz}),$$

which is of the same order of magnitude as the electron cyclotron frequency for tokamaks with very strong magnetic fields ($B \sim 3 \text{ T}$).

Remark that in cold plasma theory the spatial form of the amplitude $\hat{n}_1(\mathbf{r})$ of the plasma oscillations is not determined. This is different for ‘warm’ plasmas, where deviations from charge neutrality due to thermal fluctuations occur in small regions of a size of the order of the *Debye length*

$$\lambda_D \equiv \sqrt{\frac{\epsilon_0 k_B T_e}{n_0 e^2}} = \frac{v_{\text{th},e}}{\sqrt{2} \omega_{pe}}. \quad (44)$$

Note that we here indicate the Boltzmann constant with a subscript, k_B , to distinguish it from the wave number k of

the waves that now enters the analysis. For thermonuclear plasmas, with $\tilde{T} = 10 \text{ keV}$, $v_{\text{th},e} = 5.9 \times 10^7 \text{ m s}^{-1}$, $\omega_{pe} = 5.7 \times 10^{11} \text{ rad s}^{-1}$ gives

$$\lambda_D = 7.4 \times 10^{-5} \text{ m} \approx 0.07 \text{ mm},$$

i.e. the Debye length is of the order of the electron gyroradius R_e .

5.3 (Finite pressure) Plasma oscillations

In warm plasmas, the frequency of the plasma oscillations becomes dependent on the wavelength because of the above-mentioned thermal fluctuations. The thermal contributions may be computed by means of the two-fluid equations for an unmagnetised plasma ($\mathbf{B} = 0$), assuming an isotropic pressure and neglecting heat transport and collisions. Assuming immobile ions again and linearising these equations for the electrons, like we did before for a cold plasma, we now get a modified eigenvalue problem where the pressure $p_0 = n_0 k_B T_0$, i.e. the temperature, of the background plasma enters:

$$\frac{\partial n_1}{\partial t} + n_0 \nabla \cdot \mathbf{u}_1 = 0, \quad (45)$$

$$n_0 m_e \frac{\partial \mathbf{u}_1}{\partial t} + \nabla p_1 = -e n_0 \mathbf{E}_1, \quad (46)$$

$$\frac{\partial p_1}{\partial t} + \gamma p_0 \nabla \cdot \mathbf{u}_1 = 0, \quad (47)$$

$$\nabla \cdot \mathbf{E}_1 = -\frac{e}{\epsilon_0} n_1. \quad (48)$$

Assuming plane waves in the x -direction, and ignoring spatial dependencies in the y - and z -directions,

$$n_1(x, t) = \hat{n}_1 e^{i(kx - \omega t)}, \quad (49)$$

(and similar expressions for \mathbf{u}_1 , p_1 , \mathbf{E}_1), the gradients $\nabla \rightarrow i k \mathbf{e}_x$ and the time derivatives $\partial/\partial t \rightarrow -i\omega$, so that Eqs. (45)–(48) become an algebraic system of equations for the amplitudes \hat{n}_1 , $\hat{\mathbf{u}}_1$, \hat{p}_1 , and $\hat{\mathbf{E}}_1$. The dispersion equation is obtained from the determinant and reads

$$\omega^2 = \omega_{pe}^2 (1 + \gamma k^2 \lambda_D^2). \quad (50)$$

Notice that here, since the oscillations are one-dimensional, we should exploit the value $\gamma = 3$ (see Chen [6], Chapter 4). Remark that the (c)old result (43)

is recovered for long wavelengths, where $k^2\lambda_D^2 \ll 1$, but there is a large effect now on the oscillations for wavelengths of the order of or smaller than the Debye length. However, this thermal correction of the dependence of ω on k turns out to be incomplete as misses the damping obtained in the proper kinetic derivation. We will discuss this briefly in the next section.

6 Collective phenomena: Landau damping

Following Goedbloed and Poedts [1], we remark that a more refined analysis of longitudinal plasma oscillations for ‘warm’ plasmas should take velocity space effects into account, exploiting the Vlasov, or *collisionless* Boltzmann, equation (12) (with vanishing RHS) for the perturbations $f_1(\mathbf{r}, \mathbf{v}, t)$ of the electron distribution function. Considering again plane wave solutions $\sim \exp(i\mathbf{k} \cdot \mathbf{r} - \omega t)$, one immediately runs into a mathematical problem:

$$\frac{\partial f_1}{\partial t} + \mathbf{v} \cdot \frac{\partial f_1}{\partial \mathbf{r}} = -i(\omega - \mathbf{k} \cdot \mathbf{v}) f_1 = \frac{e}{m_e} \mathbf{E}_1 \cdot \frac{\partial f_0}{\partial \mathbf{v}}, \quad (51)$$

so that inversion of the operator $\partial/\partial t + \mathbf{v} \cdot \partial/\partial \mathbf{r}$, to express f_1 in terms of \mathbf{E}_1 , leads to singularities for every $\omega - \mathbf{k} \cdot \mathbf{v} = 0$. Landau (1946) [8] performed a proper treatment of the related initial value problem, and showed that these singularities give rise to damping of the plasma oscillations, now called *Landau damping*. Since there is no dissipation as we are considering a purely collisionless medium here, this is a surprising phenomenon! Twenty years later, Malmberg and Wharton [9] verified the phenomenon of Landau damping experimentally. In fact, later (1968) these authors also demonstrated that the information contained in the initial signal may be recovered by means of plasma wave echos, i.e. it is not lost.

Van Kampen (1955) [10, 11] considered a complementary approach to the electrostatic plasma oscillations by means of a normal mode analysis. In this approach, the singularities $\omega - \mathbf{k} \cdot \mathbf{v} = 0$ lead to a continuous spectrum of singular, δ -function type, modes (the Van Kampen modes), which constitute a complete set of ‘improper’ eigenmodes for this system. Damping occurs because of *phase mixing*, a package of those modes rapidly loses its spatial phase coherence.

6.1 Landau solution of the initial value problem

For a more careful analysis, which is beyond the level of this introductory chapter, we refer to Goedbloed and Poedts [1].

Landau’s careful study of the initial value problem of electrostatic plasma oscillations shows that there is an important contribution of the singularities $v = v_{\text{ph}} \equiv \omega/k$ where the particles are in resonance with the phase velocity of the waves. For a Maxwell distribution, the solution of the dispersion equation (obtained by Landau) for long wavelengths ($k\lambda_D \ll 1$) is given by

$$\omega \approx \omega_{pe} \left\{ 1 + \frac{3}{2} k^2 \lambda_D^2 - i \sqrt{\frac{\pi}{8}} (k\lambda_D)^{-3} e^{-\frac{1}{2}(k\lambda_D)^{-2} - \frac{3}{2}} \right\}, \quad (52)$$

where the imaginary part represents *damping of the waves*. For long wavelengths, this damping is exponentially small. For short wavelengths ($k\lambda_D \sim 1$), the damping becomes very strong so that wave motion with wavelengths smaller than the Debye length becomes impossible.

7 From kinetic theory to fluid description

In this section we come back to the text of Goedbloed and Poedts [1]. We have seen that kinetic theory involves the detailed evolution of the distribution functions on very short length and time scales, such as the Debye length λ_D and the plasma frequency ω_{pe} . The development of the fluid picture of plasmas from the kinetic theory involves three major steps, illustrated in Fig. 2:

(a) Collisionality The formulation of the lowest moments (26)–(28) of the Boltzmann equation in Section 4 and the transport closure relations mentioned there, was the first step, yielding a system of *two-fluid equations* in terms of the ten variables $n_{e,i}$, $\mathbf{u}_{e,i}$, $T_{e,i}$. To establish the two fluids, the electrons and ions must undergo frequent collisions:

$$\tau_H \gg \tau_i \left[\gg \tau_e \right], \quad (53)$$

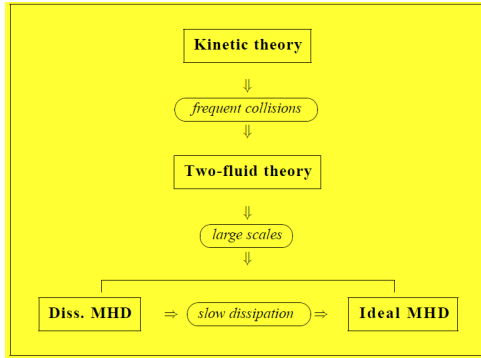


Figure 2: Different theoretical plasma models and their connections.

with τ_H the time scale on which the hydrodynamic description is valid, while τ_e and τ_i indicate the collisional relaxation times of the electrons and ions respectively.

(b) Macroscopic scales Since the two-fluid equations still involves the small length and time scales of the fundamental phenomena we have encountered, viz. the plasma frequency ω_{pe} , the cyclotron frequencies $\Omega_{e,i}$, the Debye length λ_D , and the cyclotron radii $R_{e,i}$, the essential second step towards the *magnetohydrodynamics* (MHD) description of plasmas is to consider *large length and time scales*:

$$\lambda_{\text{MHD}} \sim a \gg R_i, \quad \tau_{\text{MHD}} \sim a/v_A \gg \Omega_i^{-1}. \quad (54)$$

Hence, the larger the magnetic field strength, the more easy these conditions are satisfied. On these scales, the plasma is considered as a *single* conducting fluid without distinguishing its individual species.

(c) Ideal fluids The third and final step is to consider the plasma dynamics on time scales *faster* than the *slow dissipation* connected with the decay of the macroscopic variables, in particular the resistive decay of the magnetic field:

$$\tau_{\text{MHD}} \ll \tau_R \sim a^2/\eta. \quad (55)$$

This condition is well satisfied for the relatively small sizes of fusion machines, and very easily for the huge sizes of astrophysical plasmas, and leads to the model of *ideal MHD*.

References

- [1] J.P. Goedbloed and S. Poedts: "Principles of Magnetohydrodynamics: with applications to laboratory and astrophysical plasmas", Cambridge University Press, 2004.
- [2] R. Balescu, *Transport Processes in Plasmas; Vol. 1: Classical Transport Theory, Vol. 2: Neoclassical Transport* (Amsterdam, North Holland, 1988).
- [3] J. A. Bittencourt, *Fundamentals of Plasma Physics* (New York, Pergamon Press, 1986); 2nd edition (Brazil, Foundation of the State of São Paulo for the Support of Research, 1995).
- [4] S. I. Braginskii, 'Transport processes in a plasma', in *Reviews of Plasma Physics, Vol. 1*, ed. M. A. Leontovich (New York, Consultants Bureau, 1965), pp. 205–311.
- [5] H. Goldstein, *Classical Mechanics*, 2nd edition (Reading, Addison Wesley, 1980).
- [6] F. C. Chen, *Introduction to Plasma Physics and Controlled Fusion, Vol. 1: Plasma Physics*, 2nd edition (New York, Plenum Press, 1984).
- [7] L. D. Landau, 'The transport equation in the case of Coulomb interactions', *J. Exp. Theor. Phys. USSR* **7** (1937), 203. [Transl.: *Phys. Z. Sowjet.* **10** (1936), 154; or *Collected Papers of L. D. Landau*, ed. D. ter Haar (Oxford, Pergamon Press, 1965) pp. 163–170.]
- [8] L. D. Landau, 'On the vibrations of the electronic plasma', *J. Phys. USSR* **10** (1946), 25. [Transl.: *JETP* **16** (1946), 574; or *Collected Papers of L.D. Landau*, ed. D. ter Haar (Oxford, Pergamon Press, 1965) pp. 445–460.]
- [9] J. H. Malmberg and C. B. Wharton, 'Dispersion of electron plasma waves', *Phys. Rev. Lett.* **17** (1966), 175–178. J. H. Malmberg, C. B. Wharton, R. W. Gould and T. M. O'Neil, 'Observation of plasma wave echos', *Phys. Fluids* **11** (1968), 1147–1153.
- [10] N. G. van Kampen, 'On the theory of stationary waves in plasmas', *Physica* **21** (1955), 949–963.
- [11] N. G. van Kampen and B. U. Felderhof, *Theoretical Methods in Plasma Physics* (Amsterdam, North-Holland Publishing Company, 1967).
- [12] A. A. Vlasov, 'The oscillation properties of an electron gas', *Zhur. Eksp. Teor. Fiz.* **8** (1938), 291–318; 'Vibrational properties, crystal structure, non-dissipated counter-directed currents and spontaneous origin of these properties in a "gas"', *J. Phys. USSR* **9** (1945), 25–40.

Kinetic Plasma Simulation: Particle In Cell Method

Giovanni Lapenta Center for mathematical Plasma Astrophysics, KU Leuven, Belgium

The classical or relativistic description of the natural world is based on describing the interaction of elements of matter via force fields. The example that will guide the discussion is that of a plasma composed of charged particles but the discussion would be similar and easily replicated for the case of gravitational forces. In the case of a plasma, the system is composed by charged particles (for example negative electrons and positive ions) interacting via electric and magnetic fields.

If we identify each particle with a label p and their charge with q_p , position with \mathbf{x}_p , position with \mathbf{v}_p , the force acting on the particles is the combination of the electric and magnetic (Lorentz) force:

$$\mathbf{F}_p = q_p \mathbf{E}(\mathbf{x}_p) + \mathbf{v}_p \times \mathbf{B}_p(\mathbf{x}_p) \quad (1)$$

The force acting on the particles is computed from the electric and magnetic fields evaluated at the particle position.

The electric and magnetic fields are themselves created by the particles in the system and by additional sources outside the system (for example magnets around the plasma or external electrodes). The fields are computed by solving the Maxwell's equations:

$$\begin{aligned} \nabla \cdot \mathbf{E} &= \frac{\rho}{\epsilon_0} & \nabla \times \mathbf{E} &= -\frac{\partial \mathbf{B}}{\partial t} \\ \nabla \cdot \mathbf{B} &= 0 & \nabla \times \mathbf{B} &= \mu_0 \mathbf{J} + \mu_0 \epsilon_0 \frac{\partial \mathbf{E}}{\partial t} \end{aligned} \quad (2)$$

1 Types of interacting systems

A key point in the derivation of the particle in cell method is the consideration of how the sources in the Maxwell's equations ought to be computed. In principle since the system is made of a collection

of particles of infinitesimal size, the sources of the Maxwell's equations are distributions of contributions one for each particle.

Figure 1 summarises visually the situation. Let us consider a system made by a collection of particles, each carrying a charge situated in a box with the side of the Debye length, λ_D (the box is 3D but is depicted as 2D for convenience). We choose the Debye length because a basic property of plasmas is to shield the effects of localized charges over distances exceeding the Debye length. Of course the shielding is exponential and the effect is not totally cancelled over one Debye length, but such a length provides a conventional reasonable choice for the interaction range. The electric field in each point of the box is computed by the superposition of the contribution of each particle.

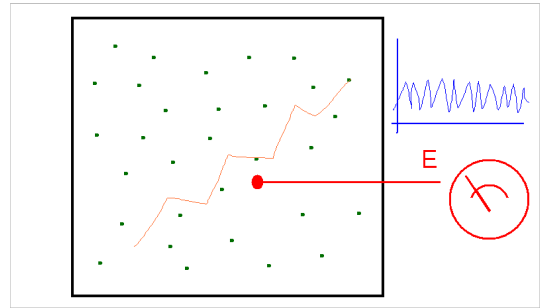


Figure 1: A strongly coupled system.

Let us conduct an ideal thought experiment based on using an experimental device able to detect the local electric field in one spatial position. Such an experimental device exists, but the determination of the local electric field remains a difficult but not impossible task. At any rate we try to conduct a thought experiment where in no step any law of physics is

violated but where the difficulties of experimental work are eliminated.

If we consider the configuration in Fig. 1, we note that within the domain there are few particles and the measurement obtained by our fantastic electric field meter would be very jumpy. The particles in the box move constantly, interacting with each other and agitated by their thermal motion. As a particle passes by the detector, the measurement detects a jump up and when a particle moves away it detects a jump down. On average at any given time very few particles are near the detector and their specific positions are key in determining the value measured. The effect of a given particle on the electric field at the location of measurement decays very rapidly with the distance and only when the particle is nearby the effect is strong.

The same effect is detected by each of the particles in the system. The electric field each particle feels is a the sum of the contributions of all others but only when another particle passes by the electric field would register a jump: in common term this event is called a collision. The particle trajectories would then be affected by a series of close encounters registered as jumps in the trajectory.

The system described goes in the language of kinetic theory as a *strongly coupled system*, a system where the evolution is determined by the close encounters and by the relative configuration of any two pairs of particles. The condition just described is characterised by the presence of few particles in the box: $N_D = n\lambda_D^3$ is small.

The opposite situation is that of a weakly coupled system. The corresponding configuration is described in Fig. 2.

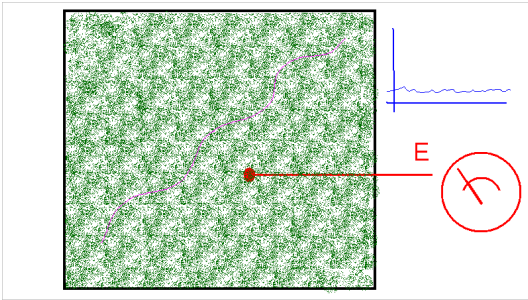


Figure 2: A weakly coupled system.

Now the system is characterised by being composed by an extremely large number of particles. In any given point, the number of particles contributing to the electric field is very large. Regardless of the

particle motion, the field is given by the superposition of many contributions. As a consequence, by simple averaging of the effects of all the particles contributing to the measurement, the measurement is smooth and does not jump in time. Similarly the trajectory of a particle is at any time affected by a large number of other particles. The trajectory is smooth and without jumps. These systems are called *weakly coupled*. If in the strongly coupled system, the characteristic feature was the presence of a succession of collisions, in the weakly coupled system, the characteristic feature is the mean field produced by the superposition of contributions from a large number of particles.

2 Description of interacting systems

The discriminant factor in the previous discussion was the number of particles present in the box under consideration. If we choose the conventional box with side equal to the Debye length, the number of particles present is

$$N_D = n\lambda_D^3 \quad (3)$$

where n is the plasma density.

A system is considered weakly coupled when N_D is large and strongly coupled when N_D is small.

This concept can be further elaborated by considering the energies of the particles in the system. The particles in the box are distributed in a non-uniform, random way, but on average, the volume associated with each particle is simply the volume of the box, λ_D^3 , divided by the number of particles in the box, N_D . This volume, $V_p = n^{-1}$, can be used to determine the average interparticle distance, $a = V_p^{1/3} \equiv n^{-1/3}$. This relation provides an average statistical distance. The particles are distributed randomly and their distances are also random, but on average the interparticle distance is a .

The electrostatic potential energy between two particles with separation a is

$$E_{pot} = \frac{q^2}{4\pi\epsilon_0 a} \quad (4)$$

where we have assumed equal charge q for the two particles. Conversely, from statistical physics, the kinetic energy of the particles can be computed to be of the order of

$$E_{th} = kT \quad (5)$$

where k is the Boltzmann constant.

A useful measure of the plasma coupling is given by the so-called *plasma coupling parameter*, Λ , defined as:

$$\Lambda = \frac{E_{th}}{E_{pot}} = \frac{4\pi\epsilon_0 a k T}{q^2} \quad (6)$$

Recalling the definition of Debye length ($\lambda_D = (\epsilon_0 k T / n e^2)^{1/2}$) and the value of a obtained above, it follows that:

$$\Lambda = \frac{4\pi\epsilon_0 k T}{q^2 n^{1/3}} \equiv 4\pi N_D^{2/3} \quad (7)$$

The plasma parameter gives a new physical meaning to the number of particles per Debye cube. When many particles are present in the Debye cube the thermal energy far exceeds the potential energy, making the trajectory of each particle little influenced by the interactions with the other particles: this is the condition outlined above for the weakly coupled systems. Conversely, when the coupling parameter is small, the potential energy dominates and the trajectories are strongly affected by the near neighbour interactions: this is the condition typical of strongly coupled systems.

3 Computer simulation

A computer simulation of a system of interacting particles can be conducted in principle by simply following each particle in the system. The so-called *particle-particle (PP)* approach describes the motion of N particles by evolving the equations of Newton for each of the N particles taking as a force acting on the particle the combined effect of all the other particles in the system.

The evolution is discretized in many temporal steps Δt , each chosen so that the particles move only a small distance, and after each move the force is recomputed and a new move is made for all the particles. If we identify the particle position and velocity as, respectively, \mathbf{x}_p and \mathbf{v}_p , the equations of motion can be written as:

$$\begin{aligned} \mathbf{x}_p^{new} &= \mathbf{x}_p^{old} + \Delta t \mathbf{v}_p^{old} \\ \mathbf{v}_p^{new} &= \mathbf{v}_p^{old} + \Delta t \mathbf{F}_p \end{aligned} \quad (8)$$

The main cost of the effort is the computation of the force which requires to sum over all the particles in the system,

$$\mathbf{F}_p = \sum_{p'} \mathbf{F}_{pp'} \quad (9)$$

where $F_{pp'}$ is the interaction force between two particles p and p' . For example in the case of the electrostatic force,

$$\mathbf{F}_{pp'} = \frac{q_p q_{p'}}{4\pi\epsilon_0 |\mathbf{x}_p - \mathbf{x}_{p'}|^2} \cdot \frac{\mathbf{x}_p - \mathbf{x}_{p'}}{|\mathbf{x}_p - \mathbf{x}_{p'}|} \quad (10)$$

where in practice all forces are computed with the old values of the particle positions available at a given time. Once the force is computed the new velocities can be computed. Then the new positions can be computed and the cycle can be repeated indefinitely.

For each particle, the number of terms to sum to compute the force is $N - 1$, and considering that there are N particles, but that each pair needs to be computed only once, the total number of force computations is $N(N - 1)/2$.

For strongly coupled systems, where the number of particles per Debye cube is small, the PP approach is feasible and forms the basis of the very successful molecular dynamics method used in condensed matter and in biomolecular studies. We refer the reader to a specific text on molecular dynamics to investigate the approach more in depth [FS02]. The approach is also used in the study of gravitational interactions, for example in the cosmological studies of the formation and distribution of galaxies. In that case, specifically the dark matter is studied with a PP approach. The PP approach can be made more efficient by using the *Barnes-Hut* or *tree algorithm* [BH86] that can reduce the cost (but not without loss of information) to $O(N \log N)$.

Even with the reduced cost of the tree algorithm, PP methods cannot be practical for weakly coupled systems where the number of particles is very large. As the number of particles increases, the cost scales quadratically (or as $N \log N$) and makes the computational effort unmanageable. In that case, one cannot simply describe every particles in the system and a method must be devised to reduce the description to just a statistical sample of the particles. This is the approach described in the next section.

4 Finite size particles

The key idea behind the simulation of weakly coupled systems is to use as building block of the model not single particles but rather collective clouds of them: each computational particle (referred to sometimes as superparticle) represents a group of particles and can be visualised as a small piece of phase space. The concept is visualized in Fig. 3.

The fundamental advantage of the finite-size particle approach is that the computational particles,

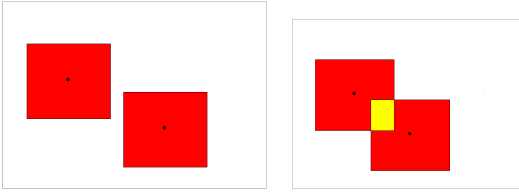


Figure 3: *Finite size particle.*

being of finite size, interact more weakly than point particles. When two point particles interact, for example via coulombian force, the repulsive or attractive force grows as the particles approach, reaching a singularity at zero separation. Finite size particles instead, behave as point particles until their respective surfaces start to overlap. Once overlap occurs the overlap area is neutralized, not contributing to the force between the particles. At zero distances when the particles fully overlap (assuming here that all particles have the same surface) the force become zero. Figure 4 shows the force between two spherical charged particles as a function of their distance. At large distances the force is identical to the Coulomb force, but as the distance becomes smaller than the particle diameter, the overlap occurs and the force starts to become weaker than the corresponding Coulomb force, until it becomes zero at zero separation.

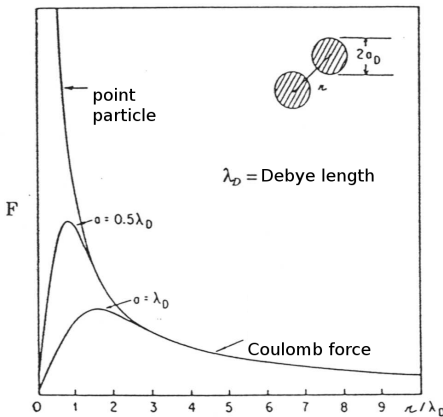


Figure 4: *Interactions between finite size particles. Reproduced from [Daw83].*

The use of finite-size computational particles allows to reduce the interaction among particles. Recalling the definition of plasma parameter, the use of finite-size particles results in reducing the potential

energy for the same kinetic energy. The beneficial consequence is that the correct plasma parameter can be achieved by using fewer particles than in the physical system. The conclusion is that the correct coupling parameter is achieved by fewer particles interacting more weakly. The realistic condition is recovered.

5 Particle in Cell Method

The idea of the particle in cell (PIC, also referred to as particle-mesh, PM) method is summarised in Fig. 5. The system is represented by a small number of finite-size particles all interacting via the correct potential at distances beyond the overlap distance, but correcting the effect of fewer particles at small distances by the reduced interaction potential.

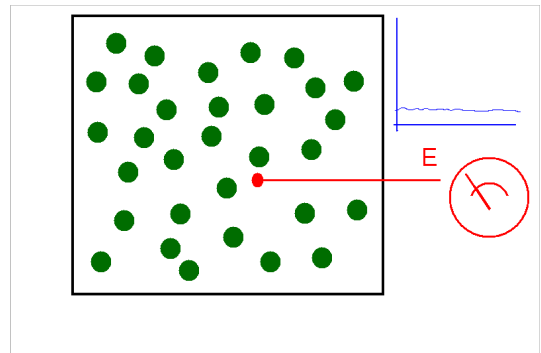


Figure 5: *A system of finite size particles.*

The end result is that the electric field fluctuations in the system are correctly smooth as they should be in a weakly coupled system. The reason now is not that at any time a very large number of particles average each other but rather that the effect of the few particles close to the measure point is weak.

Similarly the trajectory of particles are smooth as in the real system but not because each particle is surrounded by a very large number of near neighbours. Rather the few near neighbours produce weak interactions.

The collective effect is still correct as the long range interaction is unmodified and reproduces correctly the physical system.

6 Mathematical Derivation of the PIC method

We consider there the procedure for deriving the PIC method. Two classic textbooks [HE81, BL04] and a

review paper [Daw83] report a heuristic derivation based on the physical properties of a plasma. We consider here a different approach aimed at making a clear mathematical link between the mathematical model of the plasma and its numerical solution. To make the derivation as easy as possible, while retaining all its fundamental steps we consider the following 1D electrostatic and classical plasma. The extension to 3D electromagnetic plasmas is no more difficult but clouded by the more complicated notation.

The phase space distribution function $f_s(x, v, t)$ for a given species s (electrons or ions), defined as the number density per unit element of the phase space (or the probability of finding a particle in a dx and dv around a certain phase space point (x, v)), is governed by the Vlasov equation:

$$\frac{\partial f_s}{\partial t} + v \frac{\partial f_s}{\partial x} + \frac{q_s E}{m_s} \frac{\partial f_s}{\partial v} = 0 \quad (11)$$

where q_s and m_s are the charge and mass of the species, respectively.

The electric field in the electrostatic limit is described by the Poisson's equation for the scalar potential:

$$\epsilon_0 \frac{\partial^2 \varphi}{\partial x^2} = -\rho \quad (12)$$

where the net charge density is computed from the distribution functions as:

$$\rho(x, t) = \sum_s q_s \int f_s(x, v, t) dv \quad (13)$$

6.1 Numerical Approach

The PIC method can be regarded as a *finite element approach* but with finite elements that are themselves moving and overlapping. The mathematical formulation of the PIC method is obtained by assuming that the distribution function of each species is given by the superposition of several elements (called computational particles or superparticles):

$$f_s(x, v, t) = \sum_p f_p(x, v, t) \quad (14)$$

Each element represents a large number of physical particles that are near each other in the phase space. For this reason, the choice of the elements is made in order to be at the same time physically meaningful (i.e. to represent a bunch of particles near each other) and mathematically convenient (i.e. it allows the derivation of a manageable set of equations).

The PIC method is based upon assigning to each computational particle a specific functional form for

its distribution, a functional form with a number of free parameters whose time evolution will determine the numerical solution of the Vlasov equation. The choice is usually made to have two free parameters in the functional shape for each spatial dimension. The free parameters will acquire the physical meaning of position and velocity of the computational particle. The functional dependence is further assumed to be the tensor product of the shape in each direction of the phase space:

$$f_p(x, v, t) = N_p S_x(x - x_p(t)) S_v(v - v_p(t)) \quad (15)$$

where S_x and S_v are the *shape functions* for the computational particles and N_p is the number of physical particles that are present in the element of phase space represented by the computational particle.

A number of properties of the shape functions come from their definition:

1. The support of the shape functions is compact, to describe a small portion of phase space, (i.e. it is zero outside a small range).

2. Their integral is unitary:

$$\int_{-\infty}^{\infty} S_\xi(\xi - \xi_p) d\xi = 1 \quad (16)$$

where ξ stands for any coordinate of phase space.

3. While not strictly necessary, Occam's razor suggests to choose symmetric shapes:

$$S_\xi(\xi - \xi_p) = S_\xi(\xi_p - \xi) \quad (17)$$

While these definitions still leave very broad freedom in choosing the shape functions, traditionally the choices actually used in practice are very few.

6.2 Selection of the particle shape

The standard PIC method is essentially determined by the choice of S_v , the shape in the velocity direction as a Dirac's delta:

$$S_v(v - v_p) = \delta(v - v_p) \quad (18)$$

This choice has the fundamental advantage that if all particles within the element of phase space described by one computational particle have the same speed, they remain closer in phase space during the subsequent evolution.

The original PIC methods developed in the 50's were based on using a Dirac's delta also as the shape

function in space. But now for the spatial shape functions, all commonly used PIC methods are based on the use of the so-called b-splines. The b-spline functions are a series of consecutively higher order functions obtained from each other by integration. The first b-spline is the flat-top function $b_0(\xi)$ defined as:

$$b_0(\xi) = \begin{cases} 1 & \text{if } |\xi| < 1/2 \\ 0 & \text{otherwise} \end{cases} \quad (19)$$

The subsequent b-splines, b_l , are obtained by successive integration via the following generating formula:

$$b_l(\xi) = \int_{-\infty}^{\infty} d\xi' b_0(\xi - \xi') b_{l-1}(\xi') \quad (20)$$

Figure 6 shows the first three b-splines.

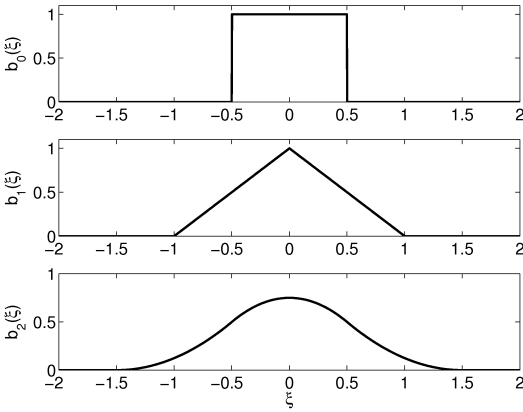


Figure 6: First three b-spline functions.

Based on the b-splines, the spatial shape function of PIC methods is chosen as:

$$S_x(x - x_p) = \frac{1}{\Delta_p} b_l\left(\frac{x - x_p}{\Delta_p}\right) \quad (21)$$

where Δ_p is the scale-length of the support of the computational particles (i.e. its size). A few PIC codes use splines of order 1 but the vast majority uses b-splines of order 0, a choice referred to as cloud in cell because the particle is a uniform square cloud in phase space with infinitesimal span in the velocity direction and a finite size in space.

7 Derivation of the equations of motion

To derive the evolution equations for the free parameters x_p and v_p , we require that the first moments of the Vlasov equation to be exactly satisfied by

the functional forms chosen for the elements. This procedure require some explanations:

1. The Vlasov equation is formally linear in f_s and the equation satisfied by each element is still the same Vlasov equation. The linear superposition of the elements gives the total distribution function and if each element satisfies the Vlasov equation, the superposition does too. A caveat, the electric field really depends on f_s making the Vlasov equation non-linear. As a consequence the electric field used in each Vlasov equation for each element must be the total electric field due to all elements, the same entering the complete Vlasov equation for f_s :

$$\frac{\partial f_p}{\partial t} + v \frac{\partial f_p}{\partial x} + \frac{q_s E}{m_s} \frac{\partial f_p}{\partial v} = 0 \quad (22)$$

2. The arbitrary functional form chosen for the elements does not satisfy exactly the Vlasov equation. The usual procedure of the finite element method is to require that the moments of the equations be satisfied.

We indicate the integration over the spatial and velocity domain by the symbol $\langle \dots \rangle \equiv \int dx \int dv$.

7.1 Moment 0

The zeroth order moment ($\langle Vlasov \rangle$) gives:

$$\frac{\partial \langle f_p \rangle}{\partial t} + \left\langle v \frac{\partial f_p}{\partial x} \right\rangle + \left\langle \frac{q_s E}{m_s} \frac{\partial f_p}{\partial v} \right\rangle = 0 \quad (23)$$

where we used the interchangeability of the integration in $dx dv$ and of the derivation over time. The second and third term are zero, as:

$$\int \frac{\partial f_p}{\partial x} dx = f_p(x = +\infty) - f_p(x = -\infty) = 0$$

where the last equality follows from the compact support of f_p , assumed in the definition of the elements. A similar calculation holds for the term with the derivative over v . Recalling that $\langle f_p \rangle = N_p$, it follows:

$$\frac{dN_p}{dt} = 0 \quad (24)$$

The application of the first zeroth order moment leads to the establishment of the conservation of the number of physical particles per computational particle.

7.2 Moment 1_x

The application of the first order moment in x , ($< x \cdot Vlasov >$) gives:

$$\frac{\partial \langle f_p x \rangle}{\partial t} + \left\langle v x \frac{\partial f_p}{\partial x} \right\rangle + \left\langle x \frac{q_s E}{m_s} \frac{\partial f_p}{\partial v} \right\rangle = 0 \quad (25)$$

The last term is still zero by virtue of integration over v , the other terms, instead, are new. The first term is:

$$\langle f_p x \rangle = N_p \int S_v(v - v_p) dv \int x S(x - x_p) dx$$

where the first integral is 1 by definition of S_v as a function of unitary integral and the second expresses the first order moment of S_x . Recalling the assumption of symmetry of S_x , that moment equals x_p :

$$\langle f_p x \rangle = N_p x_p$$

The third term requires the integration of:

$$\int v dv \int x \frac{\partial f_p}{\partial x} dx =$$

$$\int v [f_p(x = +\infty) - f_p(x = -\infty)] x dv - \int v f dx dv = - \langle f_p v \rangle$$

where integration by part has been used. The integral can be computed as above, reversing the roles of x and v :

$$\langle f_p v \rangle = N_p \int v S_v(v - v_p) dv \int S(x - x_p) dx = N_p v_p$$

using the parity of S_v . The end result of applying the first order moment in x is:

$$\frac{dx_p}{dt} = v_p \quad (26)$$

7.3 Moment 1_v

The application of the first order moment in v , ($< v \cdot Vlasov >$) gives:

$$\frac{\partial \langle f_p v \rangle}{\partial t} + \left\langle v^2 \frac{\partial f_p}{\partial x} \right\rangle + \left\langle v \frac{q_s E}{m_s} \frac{\partial f_p}{\partial v} \right\rangle = 0 \quad (27)$$

The second term is still zero by virtue of integration over x , as in the case of the zeroth order moment. The first term has already been computed above. The remaining term must be computed:

$$\int \frac{q_s E}{m_s} dx \int v \frac{\partial f_p}{\partial v} dv = - \int \frac{q_s E}{m_s} dx \int f_s dv = \left\langle \frac{q_s E}{m_s} f_s \right\rangle$$

using again integration by part and the finite support of the elements.

The remaining integral defines a new important quantity, the average electric field acting on a computational particle, E_p :

$$\left\langle \frac{q_s E}{m_s} f_s \right\rangle = -N_p \frac{q_s}{m_s} E_p$$

where the electric field on a computational particle is:

$$E_p = \int S_v(v - v_p) dv \int S_x(x - x_p) E(x) dx \quad (28)$$

Recalling the property of S_v , the formula for E_p simplifies to:

$$E_p = \int S_x(x - x_p) E(x) dx \quad (29)$$

The first order moment in v gives the final equation:

$$\frac{dv_p}{dt} = \frac{q_s}{m_s} E_p \quad (30)$$

7.4 Equations of motion for the computational particles

The equations above give the following complete set of evolution equations for the parameters defining the functional dependence of the distribution within each element:

$$\begin{aligned} \frac{dN_p}{dt} &= 0 \\ \frac{dx_p}{dt} &= v_p \\ \frac{dv_p}{dt} &= \frac{q_s}{m_s} E_p \end{aligned} \quad (31)$$

It is a crucial advantage of the PIC method that its evolution equations resemble the same Newton equation as followed by the regular physical particles. The key difference is that the field is computed as the average over the particles based on the definition of E_p .

Naturally, the electric field is itself given by Maxwell's equations which in turn need the charge density (and for complete models also the current density). The particle in cell approach described above provides immediately the charge density as the integral over the velocity variable of the distribution function:

$$\rho_s(x, t) = q_s \sum_p \int f_p(x, v, t) dv \quad (32)$$

Using the functional form for the distribution function of each computational element, the charge density becomes:

$$\rho_s(x, t) = \sum_p q_s N_p S_x(x - x_p) \quad (33)$$

The set of equations above provide a closed description for the Vlasov equation. Once accompanied by an algorithm to solve Maxwell's equations the full Vlasov-Maxwell system can be solved.

8 Field Equations

The solution of the field equations can be done with a wide variety of methods. The majority of the existing PIC methods relies on finite difference or finite volume, a choice we follow here to provide an example of the interfacing with the numerical solution of the Poisson and Vlasov equations.

Assuming the finite volume approach, a grid of equal cells of size Δx is introduced with cell centres x_i and cell vertices $x_{i+1/2}$. The scalar potential is discretized by introducing the cell-averaged values φ_i . The discrete form of the field equation is obtained by replacing the Laplacian operator (i.e. the simple second derivative in 1D) with a corresponding discretized operator.

In the simplest form, the Poisson's equation can be discretized in 1D using the classic three point formula:

$$\epsilon_0 \frac{\varphi_{i+1} - 2\varphi_i + \varphi_{i-1}}{\Delta x^2} = -\rho_i \quad (34)$$

where the densities ρ_i are similarly defined as average over the cells:

$$\rho_i = \frac{1}{x_{i+1/2} - x_{i-1/2}} \int_{x_{i-1/2}}^{x_{i+1/2}} \rho(x) dx \quad (35)$$

A most convenient formulation of the density averaged over each cell can be obtained recalling the definition of the b-spline of order 0

$$\int_{x_{i-1/2}}^{x_{i+1/2}} \rho(x) dx = \int_{-\infty}^{\infty} b_0 \left(\frac{x - x_i}{\Delta x} \right) \rho(x) dx \quad (36)$$

and recalling the expression of the density:

$$\int_{x_{i-1/2}}^{x_{i+1/2}} \rho(x) dx = \sum_p \int_{-\infty}^{\infty} b_0 \left(\frac{x - x_i}{\Delta x} \right) S(x - x_p) dx \quad (37)$$

The standard nomenclature of the PIC method defines the *interpolation function* as:

$$W(x_i - x_p) = \int S_x(x - x_p) b_0 \left(\frac{x - x_i}{\Delta x} \right) \quad (38)$$

It is crucial to remember the distinction between the shape function and the interpolation function. The interpolation function is the convolution of the shape function with the top hat function of span equal to the cell. The usefulness of the interpolation functions is that they allow a direct computation of the cell density without the need for integration. Defining the average cell density as, $\rho_i = \int_{x_{i-1/2}}^{x_{i+1/2}} \rho(x) dx / \Delta x$, it follows that:

$$\rho_i = \sum_p \frac{q_p}{\Delta x} W(x_i - x_p) \quad (39)$$

where $q_p = q_s N_p$.

From the definition of the shape functions based on the b-spline of order l , it follows that if the shape function $S_x = \frac{1}{\Delta_p} b_l \left(\frac{x - x_p}{\Delta_p} \right)$ a very simple expression can be derived when the particle size equals the cell size, $\Delta p = \Delta x$:

$$W(x_i - x_p) = b_{l+1} \left(\frac{x_i - x_p}{\Delta_p} \right) \quad (40)$$

that follows trivially from the generating definition of the b-splines.

The solution of the Poisson equation can be conducted with the Thomas algorithm given appropriate boundary conditions. Once the solution is obtained, the potential is known in each cell, but in the form of the discrete values of the cell-averaged potentials φ_i . To compute the fields acting on the particles, the field is needed in the continuum. A procedure is needed to reconstruct it.

First, the electric field is computed in the cell centres from the discrete potentials as:

$$E_i = -\frac{\varphi_{i+1} - \varphi_{i-1}}{2\Delta x} \quad (41)$$

where centred difference are used. Then the continuum electric field is reconstructed using the assumption that the field is constant in each cell and equal to its cell-averaged value

$$E(x) = \sum_i E_i b_0 \left(\frac{x - x_i}{\Delta x} \right) \quad (42)$$

From the definition of E_p it follows that:

$$E_p = \sum_i E_i \int b_0 \left(\frac{x - x_i}{\Delta x} \right) S_x(x - x_p) \quad (43)$$

and recalling the definition of interpolation function,

$$E_p = \sum_i E_i W(x_i - x_p) \quad (44)$$

9 Discretization of the equations of motion

The equations of motion derived in paragraph 1.3.4 are simple ordinary differential equations with the same form as the regular Newton equations. Of course, in the literature there are many algorithms to achieve the goal of solving the Newton equations. For the PIC algorithm a efficient choice is to use simple schemes: given the very large number of particles used (billions are now common in published works), the use of complex schemes may result in prohibitively long simulations. However, if more advanced schemes allow one to use large time steps, the additional cost per time step may be compensated by taking longer time steps.

The simplest algorithm and by far the most used in the so-called *leap-frog algorithm* based on staggering the time levels of the velocity and position by half time step: $x_p(t = n\Delta t) \equiv x_p^n$ and $v_p(t = (n + 1/2)\Delta t) \equiv v_p^{n+1/2}$. The advancement of position from time level n to time level $n + 1$ uses the velocity at mid-point $v_p^{n+1/2}$, and similarly the advancement of the velocity from time level $n - 1/2$ to $n + 1/2$ uses the mid point position x_p^n . This stepping of velocity over position and position over velocity recalled some of the early users of the children's game bearing also the name leap-frog (see Fig. 7).

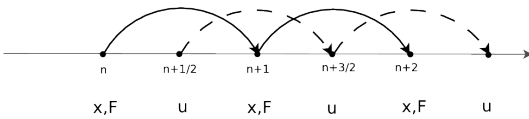


Figure 7: Visual representation of the leap-frog algorithm.

The scheme is summarised by:

$$\begin{aligned} x_p^{n+1} &= x_p^n + \Delta t v_p^{n+1/2} \\ v_p^{n+3/2} &= v_p^{n+1/2} + \Delta t \frac{q_s}{m_s} E_p(x_p^{n+1}) \end{aligned} \quad (45)$$

where E_p is computed solving the Poisson equation from the particle positions given at time level n .

Note that technically the leap-frog algorithm is second order accurate, when instead the regular explicit Euler-scheme is only first order. Nevertheless,

the two differ in practice only for the fact that the velocity is staggered by half time step. This staggering is achieved by moving the initial velocity of the first time cycle by half a time step using an explicit method:

$$v_p^{1/2} = v_p^0 + \Delta t \frac{q_s}{m_s} E_p(x_p^0)$$

10 Recapitulation

Collecting the steps gathered so far, the PIC algorithm is summarised by the series of operations depicted in Fig. 8.

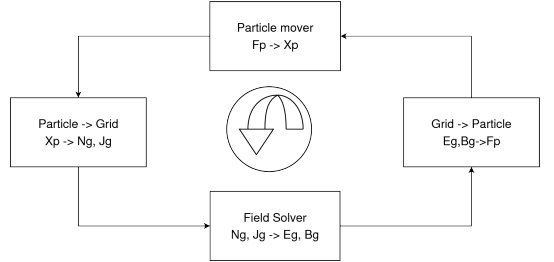


Figure 8: Summary of a computational cycle of the PIC method.

10.1 Algorithm of the PIC method, electrostatic case in 1D

- i The plasma is described by a number of computational particles having position x_p , velocity v_p and each representing a fixed number N_p of physical particles.
- ii The equations of motion for the particles are advanced by one time step using,

$$\begin{aligned} x_p^{n+1} &= x_p^n + \Delta t v_p^{n+1/2} \\ v_p^{n+3/2} &= v_p^{n+1/2} + \Delta t \frac{q_s}{m_s} E_p^{n+1} \end{aligned}$$

using the particle electric field from the previous time step.

- iii The charge densities are computed in each cell using:

$$\rho_i = \sum_p \frac{q_p}{\Delta x} W(x_i - x_p)$$

- iv The Poisson equation is solved:

$$\epsilon_0 \frac{\varphi_{i+1} - 2\varphi_i + \varphi_{i-1}}{\Delta x^2} = -\rho_i$$

and the electric field E_i in each cell is computed:

$$E_i = -\frac{\varphi_{i+1} - \varphi_{i-1}}{2\Delta x}$$

- v From the field known in the cells, the field acting on the particles is computed as

$$E_p^{n+1} = \sum_i E_i W(x_i - x_p^{n+1})$$

which is used in the next cycle

- vi The cycle restarts.

The algorithm above is implemented in the MATLAB code provided (see Lapenta's web site). The b-spline of order 0 is used for the shape functions and consequently of order 1 for the interpolation function.

References

- [BH86] J. Barnes and P. Hut. A hierarchical $O(N \log N)$ force-calculation algorithm. *Nature*, 324:4446–449, 1986.
- [BL04] C.K. Birdsall and A.B. Langdon. *Plasma Physics Via Computer Simulation*. CRC Press, Boca Raton, 2004.
- [Daw83] J. M. Dawson. Particle simulation of plasmas. *Rev. Mod. Phys.*, 55:403–447, 1983.
- [FS02] D. Frenkel and B. Smit. *Understanding Molecular Simulation*. Academic Press, San Diego, 2002.
- [HE81] R. W. Hockney and J. W. Eastwood. *Computer Simulation Using Particles*. McGraw-Hill, New York, 1981.
- [Lap12] Giovanni Lapenta. Particle simulations of space weather. *Journal of Computational Physics*, 231(3):795–821, 2012.
- [LBR06] G. Lapenta, J. U. Brackbill, and P. Ricci. Kinetic approach to microscopic-macroscopic coupling in space and laboratory plasmas. *Physics of Plasmas*, 13:5904, May 2006.

PLASMA EQUILIBRIUM IN TOKAMAKS

H.J. de Blank

FOM Institute DIFFER – Dutch Institute for Fundamental Energy Research,

Association EURATOM-FOM, P.O. Box 1207, 3430 BE Nieuwegein, The Netherlands, www.differ.nl.

ABSTRACT

This lecture treats the magnetohydrodynamic (MHD) equilibrium of axisymmetric plasmas, as given by the Grad-Shafranov equation. In a brief introduction, equilibrium parameters such as the q -profile, the internal inductance, and the poloidal beta are introduced. The properties of these quantities will be illustrated in the case of the tokamak, by applying the large aspect ratio tokamak approximation. The properties of a non-circular plasma cross-section and the role of the vertical field will also be discussed in this approximation. Some attention is given to the (numerical) problem of solving the equilibrium equation and of reconstructing a plasma equilibrium from external measurements. The numerical methods themselves are presented in [1].

I. INTRODUCTION

Magnetic confinement experiments in fusion research have a rich history in which a variety of magnetic configurations [2, 3] have been tried, like stellarators, mirror machines and pinch experiments. The first considerations were to confine a plasma with as high as possible pressure in a magnetic field that is limited in terms of required currents and external forces. The confinement properties in many of these ‘optimized’ plasmas were below expectations due to instabilities. As the theoretical understanding of plasma instabilities grew, magnetic confinement devices that avoided these instabilities were designed. More refined devices would often be plagued by slightly more subtle instabilities. The tokamak emerged relatively late on the scene. Tokamaks are characterized by a strong toroidal magnetic field. However, as we will see, the force exerted by a purely toroidal field is not pointed towards the plasma in all points. It cannot prevent a toroidal plasma from expanding its major radius. Therefore a poloidal field is required as well. The poloidal field does not have to be as large as the toroidal field and in a typical tokamak it is considerably smaller, by a factor which scales with the aspect ratio (ratio of major radius to minor radius) of the device. A poloidal field inside the plasma is required for local force balance, and an external vertical field has to be added to prevent the plasma as a whole from increasing its major radius. The internal poloidal field can only be created by a large toroidal plasma current. This current is primarily created inductively, by the flux change in a

transformer yoke through the torus. An important disadvantage of this scheme is that the flux can be changed only for a finite duration, so that stationary operation is not possible. A large research effort is presently being undertaken to drive a major fraction of the plasma current by means of injected radiofrequency waves and by the so-called bootstrap current, created during the rather complex loss processes that a high pressure tokamak plasma suffers. Another apparent flaw of the tokamak design is the wastefully large toroidal field, compared to the poloidal field and the plasma pressure it can confine. The important advantage of the tokamak is the inherent stability provided by both the strong toroidal field and the large plasma current. The immunity of a tokamak against some very fundamental and fast plasma instabilities can easily be shown, but it seems that many less straightforward plasma modes are naturally stabilized by the ‘robustness’ of this magnetic configuration.

In addition, some disruptive instabilities nowadays can be avoided thanks to the increased experimental experience with tokamak operation, and instabilities of the plasma position are tackled with improved magnetic control techniques, for instance. As a consequence, the most important instabilities that are persistent in modern tokamaks have a rather complicated spatial structure [2, 3, 4] and are likely to involve subtle interactions between the kinetics of individual particles and collective plasma motion.

On short timescales a tokamak plasmas show a variety of oscillations and turbulent phenomena. On sufficiently long timescales (which depend on the size of the machine, resistivity of the plasma, *etc.*) the plasma behaviour is governed by gradual changes in the magnetic configuration (internal or imposed by the coils) and by changes of the plasma heating, the diffusive losses, and the ratios between particle species. We will consider situations where there exists an intermediate timescale on which the tokamak plasma is in “equilibrium”. On this timescale, the plasma pressure and the magnetic forces must balance. The proper equations for this situation are provided by ideal MHD, which treats the plasma as an ideally conducting fluid, subject to the low-frequency Maxwell equations (no displacement current in Ampère’s law: $\mathbf{j} = \nabla \times \mathbf{B}$). Ideal MHD equilibria satisfy the force balance

$$\nabla p = \mathbf{j} \times \mathbf{B}. \quad (1)$$

Together with the constraints $\nabla \cdot \mathbf{B} = 0$ and $\nabla \cdot \mathbf{j} = 0$, this implies (according to a result from topology called Hopf’s

theorem) that in a volume where $\nabla p \neq 0$, the surfaces of constant pressure are tori (either simply nested or in braids), and one sees immediately from Eq. (1) that the field lines of \mathbf{B} and \mathbf{j} lie in these surfaces [5]. The field lines can either close in themselves after a finite number of revolutions, or fill a magnetic surface ergodically. The third possibility, that a field line fills a finite volume in space stochastically, can happen in ideal MHD only if $\nabla p = 0$ (and indeed, in a less idealized plasma model, such a volume exhibits fast losses of particles and energy). These results are applicable to all closed confined plasma configurations and can even be generalized to cases with stationary plasma flow (rotation) or an anisotropic pressure tensor. In the following, we will restrict ourselves to magnetic fields that form a single set of nested toroidal flux surfaces around a circular magnetic axis.

From the above we can conclude that closed flux surfaces are required to support a pressure gradient $\nabla p \neq 0$, *i.e.*, to confine the plasma. This is also what one expects after considering the microscopic picture, since individual particles stick to a given flux surface as long as they continue gyrating around the same field line.

The constraint $\nabla \cdot \mathbf{B} = 0$ implies that on a given magnetic surface field lines cannot cross each other. Therefore, if one follows a field line around the torus, the ratio between the numbers of toroidal and poloidal revolutions of the field line converges to a constant q for $n \rightarrow \infty$. The quantity q is called the safety factor because of its importance in stability criteria for a wide range of MHD modes. It is related to the average pitch of the helical field on a magnetic surface. Specifying the q values of all magnetic surfaces describes the complete topology of the magnetic field lines. In particular, the q value of a magnetic surface with closed field lines is a rational number, since each field line closes after integer numbers of toroidal and poloidal revolutions.

II. THE GRAD-SHAFRANOV EQUATION

In order to describe axisymmetric MHD equilibria we will initially use the right-handed cylinder coordinates (R, ϕ, Z) , where ϕ is the angle of symmetry and R measures the distance to the axis of symmetry (the major radius in a toroidal system). Using

$$0 = \nabla \cdot \mathbf{B} = \frac{1}{R} \frac{\partial}{\partial R} (RB_R) + \frac{1}{R} \frac{\partial B_\phi}{\partial \phi} + \frac{\partial B_Z}{\partial Z}, \quad (2)$$

and the symmetry ($\partial/\partial\phi = 0$ when acting on a scalar) one can write \mathbf{B} in terms of a stream function ψ ,

$$\mathbf{B} = \mathbf{B}_p + B_t \hat{\phi}; \quad \mathbf{B}_p = \nabla \psi \times \nabla \phi,$$

where $\hat{\phi} = R\nabla\phi$ and where B_t and ψ do not depend on ϕ . Whenever $\mathbf{B}_p \neq 0$, the magnetic field lines lie on surfaces of constant ψ . They are called flux surfaces because ψ is related to the poloidal flux ψ_p , for instance through an annulus in the equatorial plane defined by

$$S = \{Z = 0, R(\psi_1) < R < R(\psi_2)\}. \quad (3)$$

We write the poloidal field as $\mathbf{B}_p = \nabla \times (\psi \nabla \phi)$. The poloidal flux through the surface S is

$$\begin{aligned} \psi_p &= \int_S \mathbf{B}_p \cdot d\mathbf{A} = \int_S \nabla \times (\psi \nabla \phi) \cdot d\mathbf{A} \\ &= \oint_{\partial S} \psi \nabla \phi \cdot d\boldsymbol{\ell} = 2\pi(\psi_2 - \psi_1). \end{aligned} \quad (4)$$

The total poloidal flux (vacuum as well as plasma field) through the circular magnetic axis is found by taking for ψ_1 and ψ_2 the values on the magnetic axis and at $R = 0$, respectively.

The current density is given in terms of the magnetic field by Ampère's law,

$$\begin{aligned} \mathbf{j} &= \nabla \times \mathbf{B} = \nabla \times (\nabla \psi \times \nabla \phi + RB_t \nabla \phi) \\ &= -\Delta^* \psi \nabla \phi + \nabla (RB_t) \times \nabla \phi. \end{aligned} \quad (5)$$

where the elliptic, Laplacian-like Grad-Shafranov operator Δ^* is defined by

$$\Delta^* \psi = R^2 \nabla \cdot \left(\frac{\nabla \psi}{R^2} \right) = R \frac{\partial}{\partial R} \left(\frac{1}{R} \frac{\partial \psi}{\partial R} \right) + \frac{\partial^2 \psi}{\partial Z^2}. \quad (6)$$

(In the last step in (5) one can use the dyadic identity $R^2 \nabla \nabla \phi = -\nabla R \nabla \phi - \nabla \phi \nabla R$.) The final ingredient is the momentum balance equation (1). We will discuss its three vector components formed by taking the scalar products of Eq. (1) with \mathbf{B} , \mathbf{j} , and $\nabla \psi$, respectively. The first component, $\mathbf{B} \cdot \nabla p = 0$, implies that the flux surfaces are surfaces of constant $p(\psi)$ (" p is a flux function"). Using this result, the second component of the force balance, $\mathbf{j} \cdot \nabla p = 0$, tells that the current flows along the flux surfaces. For expression (5) it has the consequence that RB_t is a surface quantity as well. We write

$$RB_t = F(\psi). \quad (7)$$

This quantity $F(\psi)$ is related to the poloidal current through the surface S , given in Eq. (3). It follows from (7) that the poloidal current density, which is the second term in expression (5), can be written as $\mathbf{j}_p = \nabla \times (F \nabla \phi)$. Hence, the total current through S can be derived as an integral similar to the one for the poloidal flux (4), is

$$\begin{aligned} I_p &= \int_S \mathbf{j}_p \cdot d\mathbf{A} = \int_S \nabla \times (F \nabla \phi) \cdot d\mathbf{A} \\ &= \oint_{\partial S} F \nabla \phi \cdot d\boldsymbol{\ell} = 2\pi(F(\psi_2) - F(\psi_1)). \end{aligned}$$

If one takes $R(\psi_1) = 0$, I_p includes the current flowing in the toroidal field coils as well as the poloidal plasma current. Finally, in terms of the two flux functions $p(\psi)$ and $F(\psi)$, the force balance in the $\nabla \psi$ direction gives

$$\Delta^* \psi = -R^2 \frac{dp}{d\psi} - F \frac{dF}{d\psi}. \quad (8)$$

This 2-dimensional partial differential equation in ψ is called the Grad-Shafranov equation [6, 7, 8]. For given functions $p(\psi)$ and $F(\psi)$, it is an elliptic second order nonlinear differential equation for ψ . Sufficient boundary conditions would be to specify ψ everywhere on a closed contour, by specifying the shape of one flux surface, for instance. If a fixed outer surface of the plasma is specified, then in essence the plasma-vacuum boundary is replaced by the surface of a perfect conductor (on which ψ is necessarily constant). This is a fixed boundary condition, which defines ψ in the entire plasma. By specifying a flux surface in the vacuum region, one has a free boundary problem. Taking into account the currents in the coils leads to a somewhat different approach [9]. One can use the known currents in the coils and an *assumed* plasma current distribution to compute ψ on a boundary which is convenient for the computations, a rectangle, say. With these Dirichlet boundary conditions one then solves the Grad-Shafranov equation in the interior. This leads to a different plasma current distribution than originally assumed, and one iterates the procedure. As an alternative, or in addition to considering the coil currents and computing \mathbf{B} in the metal parts as well as the vacuum, poloidal field measurements can be available close to the coils or near the plasma. This makes the set of boundary conditions altogether more inhomogeneous and a very adaptable equilibrium solver is required. The system can even be overdetermined and to a certain extent the functions $p(\psi)$ and $F(\psi)$ can then be computed.

III. FLUX COORDINATES

Of great importance in equilibrium calculations, but also in the modelling of plasma transport and in stability analyses, are flux coordinates (r, θ, ϕ) . Here ϕ is the usual toroidal angle. The radial coordinate $r(\psi)$ labels the flux surfaces. It can be the flux itself, or the volume enclosed by each flux surface, or can be chosen to closely resemble the minor radius (distance to the magnetic axis). One possibility is the minor radius at $Z = 0$. Another definition takes the square root of the area of the cross section. The differences between such definitions are easy to account for and usually not very important. The various definitions [10, 11, 12] used for the poloidal angle θ , however, are convenient in very specific applications: (i) the proper geometrical angle can be used when the geometry is fixed, for instance in tomographic diagnostic methods, (ii) an orthogonal coordinate system ($\nabla r \cdot \nabla \theta = 0$) is convenient in ballooning stability analysis and in solving the Grad-Shafranov equation by means of the conformal mapping method [13], (iii) and most universally applied, especially in stability studies, are coordinates in which the field lines appear straight [14]. In these coordinates the pitch $d\phi/d\theta$ of the field lines is a constant on each flux surface. This constant, of course, is precisely $q(\psi)$.

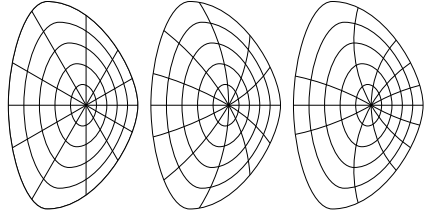


Figure 1: Flux coordinate systems. Left: proper poloidal angle; center: straight fieldline coordinates; right: orthogonal coordinates

For general flux coordinates (r, θ, ϕ) the Jacobian is

$$J \equiv |\nabla r \times \nabla \theta \cdot \nabla \phi|^{-1} = \frac{R}{|\nabla r|} \frac{d\ell}{d\theta}.$$

The general line element and the metric tensor are now given by

$$\begin{aligned} ds^2 &= g_{rr} dr^2 + 2g_{r\theta} dr d\theta + g_{\theta\theta} d\theta^2 + g_{\phi\phi} d\phi^2, \\ g_{rr} &= \frac{J^2}{R^2} |\nabla \theta|^2, \quad g_{r\theta} = -\frac{J^2}{R^2} \nabla \theta \cdot \nabla r, \\ g_{\theta\theta} &= \frac{J^2}{R^2} |\nabla r|^2, \quad g_{\phi\phi} = R^2. \end{aligned}$$

By applying the general operator identity

$$\begin{aligned} \nabla &= \nabla r \frac{\partial}{\partial r} + \nabla \theta \frac{\partial}{\partial \theta} + \nabla \phi \frac{\partial}{\partial \phi} \\ &= \frac{1}{J} \left(\frac{\partial}{\partial r} \nabla r + \frac{\partial}{\partial \theta} \nabla \theta + \frac{\partial}{\partial \phi} \nabla \phi \right) J \end{aligned}$$

to the operator Δ^* , we can derive the Grad-Shafranov equation in flux coordinates,

$$\frac{R^2}{J} \psi' \left[\frac{\partial}{\partial r} \left(\frac{g_{\theta\theta} \psi'}{J} \right) - \frac{\partial}{\partial \theta} \left(\frac{g_{r\theta}}{J} \right) \psi' \right] + R^2 p' + F F' = 0, \quad (9)$$

where a prime denotes d/dr . This expression can immediately be adapted to any particular flux coordinate system. In particular, we will use it in the next section, where we will employ approximate flux coordinates to describe flux surfaces with almost circular poloidal cross sections.

We will now use the coordinate system to express the safety factor $q(\psi)$ in terms of the magnetic field. Due to toroidal symmetry, the ratio between toroidal and poloidal revolutions of the field lines can be found with an integral of $d\phi/d\theta$ over just one poloidal revolution,

$$q(\psi) = \frac{1}{2\pi} \int_0^{2\pi} \frac{d\phi}{d\theta} d\theta = \frac{1}{2\pi} \oint \frac{B_t}{R B_p} d\ell.$$

Here we have used that the pitch of the field lines is locally given by the ratio between the toroidal and poloidal field

components. By writing $\mathbf{B} = \nabla\psi \times \nabla\phi + F(\psi)\nabla\phi$ the safety factor can be written as

$$q(\psi) = \frac{F}{2\pi} \oint \frac{d\ell}{R|\nabla\psi|} = \frac{F}{2\pi\psi'} \oint \frac{J}{R^2} d\theta. \quad (10)$$

The last definition we introduce here in general flux coordinates is the flux surface averaged value $\langle X \rangle$ of a given quantity X . In order to be compatible with volume integrals, $\int \langle X \rangle d^3x = \int X d^3x$, it is a suitably weighed integral over the flux surface,

$$\langle X \rangle = \lim_{\Delta V \rightarrow 0} \frac{1}{\Delta V} \int_{\psi}^{\psi+\Delta\psi} X dV = \frac{\oint X \frac{d\ell}{B_p}}{\oint \frac{d\ell}{B_p}} = \frac{\int_0^{2\pi} X J d\theta}{\int_0^{2\pi} J d\theta}.$$

Here, $V(\psi)$ is the volume enclosed by the flux surface given by ψ . The integral in (10) can be written as a flux average,

$$q = \frac{F}{4\pi^2} \left\langle \frac{1}{R^2} \right\rangle \frac{dV}{d\psi}.$$

IV. LARGE ASPECT RATIO EXPANSION

All tokamak equilibria have some global properties in common, which can be discussed either qualitatively or quantitatively, but in the latter case this generally requires numerical solutions of the Grad-Shafranov equation. Instead, we will restrict ourselves to a discussion of equilibria with almost circular poloidal cross sections and a small inverse aspect ratio ε , so that a purely analytic treatment is possible [2, 10, 11]. Thus we will discuss some properties of plasma shaping effects (deviations from circular cross sections) and the outward shift, called Shafranov shift), of the plasma centre under the influence of high plasma pressure.

Our flux coordinates will be θ , the geometric angle with respect to the Shafranov shifted [10] center of each flux surface $(R, Z) = (R_0 - \Delta(\psi), 0)$, and $r(\psi)$, the θ -averaged minor radius of the flux surface. The distance ρ to the centre of a flux surface will be subject to shaping functions $S_m(r)$ ($m \geq 2$),

$$\begin{aligned} R &= R_0 - \Delta(r) + \rho \cos \theta \\ Z &= \rho \sin \theta \\ \rho &= r - \sum_{m \geq 2} S_m(r) \cos m\theta. \end{aligned}$$

The relation to the generally used notation

$$\begin{aligned} R &= R_0 + a \cos(\theta - \delta \sin 2\theta) \\ Z &= \kappa a \sin \theta \end{aligned}$$

is that the elongation is $\kappa = 1 + 2S_2/r$ and the triangularity is $\delta = 4S_3/r$. Our approximation is $\varepsilon = a/R_0 \ll 1$; hence we use the ordering $r = \mathcal{O}(\varepsilon R)$. Deviations from centered circles are taken to be one order smaller, $\Delta = \mathcal{O}(\varepsilon^2 R)$, and

$S_m = \mathcal{O}(\varepsilon^2 R)$. We will neglect smaller terms, $\mathcal{O}(\varepsilon^3 R)$, throughout. In order to express the Grad-Shafranov equation in these coordinates we need

$$\begin{aligned} g_{r\theta} &= \frac{\partial Z}{\partial r} \frac{\partial Z}{\partial \theta} + \frac{\partial R}{\partial r} \frac{\partial R}{\partial \theta} \\ &= r\Delta' \sin \theta + \sum_m m S_m \sin m\theta + \mathcal{O}(\varepsilon^2 r), \\ g_{\theta\theta} &= \left(\frac{\partial Z}{\partial \theta}\right)^2 + \left(\frac{\partial R}{\partial \theta}\right)^2 \\ &= r^2 - 2r \sum_m S_m \cos m\theta + \mathcal{O}(\varepsilon^2 r^2), \\ J &= R \left(\frac{\partial R}{\partial \theta} \frac{\partial Z}{\partial r} - \frac{\partial R}{\partial r} \frac{\partial Z}{\partial \theta} \right) \\ &= -rR_0 \left[1 + \left(\frac{r}{R_0} - \Delta' \right) \cos \theta \right. \\ &\quad \left. - \sum_m \left(S_m' + \frac{S_m}{r} \right) \cos m\theta + \mathcal{O}(\varepsilon^2) \right]. \end{aligned}$$

Substituting these expressions in Eq. (9), and keeping only leading order and $\mathcal{O}(\varepsilon)$ terms in the result, we obtain

$$\begin{aligned} \frac{\psi'^2}{r} \left\{ 1 + \left(r\Delta'' + \Delta' - \frac{r}{R_0} \right) \cos \theta \right. \\ \left. + \sum_m \left[r^2 S_m'' + r S_m' + (1 - m^2) S_m \right] \cos m\theta \right\} \\ + \psi' \psi'' \left\{ 1 + 2\Delta' \cos \theta + 2r \sum_m S_m' \cos m\theta \right\} \\ + R_0^2 \left(1 + 2\frac{r}{R_0} \cos \theta \right) p' + FF' = 0. \end{aligned} \quad (11)$$

The leading order terms do not depend on θ and form the radial force balance,

$$\frac{1}{2r^2} (r^2 \psi'^2)' + R_0^2 p' + FF' = 0. \quad (12)$$

It is the balance between the forces exerted by the plasma pressure (∇p) and by the magnetic pressure ($\nabla \frac{1}{2} B^2$), and describes how the poloidal and toroidal magnetic fields prevent the plasma from expanding in the ∇r direction. It would be the exact force balance if the plasma column were a cylinder. We will define now the quantity poloidal beta, in an arbitrary flux surface enclosing a volume V_0 as

$$\beta_p(r_0) = \frac{2}{V_0} \frac{\int_0^{V_0} p dV}{(B_p^2)_0},$$

In the case of circular cross sections this becomes

$$\beta_p(r_0) = -2 \frac{R_0^4 q^2}{F^2 r_0^4} \int_0^{r_0} p' r^2 dr. \quad (13)$$

Multiplication of Eq. (12) by r^2 and integrating yields

$$\beta_p(r_0) = 1 + \frac{1}{r_0^2 \psi'^2} \int_0^{r_0} \frac{dF^2}{dr} r^2 dr.$$

One sees that if $\beta_p > 1$, then $dF^2/dr > 0$ and the toroidal field contributes to confinement of the pressure. If $\beta_p < 1$, however, the toroidal field counters confinement since then $dF^2/dr < 0$. However, due to the toroidal shape of the configuration, radial confinement is not sufficient, since θ -dependent terms unavoidably appear in the force balance equation. They are the factors R that appear in the Grad-Shafranov equation (10) and the operator (6). Consequently, Eq. (11) contains $\mathcal{O}(\varepsilon)$ terms proportional to $\cos \theta$. This component of the Grad-Shafranov equation yields a radial equation for the Shafranov shift [10],

$$\Delta'' + \left(2\frac{\psi''}{\psi'} + \frac{1}{r}\right)\Delta' - \frac{1}{R_0} + 2\frac{rR_0p'}{\psi'^2} = 0. \quad (14)$$

This equation expresses how the poloidal field prevents the flux surfaces from expanding in the ∇R direction. Since the shift Δ is always smaller than the plasma minor radius, this equation limits the pressure to values of the order of RB_p^2/a , which for $B_p \sim \varepsilon B_t$ implies that the pressure is $\mathcal{O}(\varepsilon)$ smaller than the magnetic pressure,

$$\beta = \frac{2p}{B^2} = \mathcal{O}(\varepsilon),$$

which is called the high- β tokamak ordering. In our ordering, $\Delta' = \mathcal{O}(\varepsilon r)$, which corresponds to the low- β tokamak ordering,

$$\beta = \frac{2p}{B^2} = \mathcal{O}(\varepsilon^2).$$

Equation (14) can be integrated after writing $\psi' = -rF/qR_0 + \mathcal{O}(\varepsilon^2)$ and multiplying by r^3/q^2 . This yields

$$\Delta' = \frac{r}{R_0} \left(\beta_p + \frac{1}{2}\ell_i\right), \quad (15)$$

where the normalized internal inductance at a flux surface with $r = r_0$ and enclosed volume V_0 is defined by

$$\ell_i(r_0) = \frac{2L_i}{R_0} = \frac{4}{I_p^2(r_0)R_0} \int_0^{V_0} \frac{1}{2} B_p^2 dV. \quad (16)$$

The plasma internal and external inductances are given by

$$\frac{1}{2}L_i I_p^2 = \int_{\text{plasma}} \frac{1}{2} B_p^2 dV, \quad \frac{1}{2}L_e I_p^2 = \int_{\text{plasma}} \frac{1}{2} B_p^2 dV.$$

In the case of a circular cross section Eq. (16) gives approximately

$$\ell_i(r_0) = 2\frac{q}{r_0^4} \int_0^{r_0} \frac{r^3}{q^2} dr.$$

Equation (15) describes force balance in the ∇R direction in the interior of the plasma. The first term to the right arises because the plasma pressure tries to increase the plasma volume. Since $V \approx 4\pi^2 r_0^2 R$, this can be done not only by increasing the minor radius of a flux surface (p' -term in Eq (12)) but also by increasing its major radius. The second

term on the right is due to the toroidal current. It is the hoop force due to the self-inductance of a current carrying circuit. The balancing term on the left is caused by the compression of the flux surfaces, *i.e.*, compression of the poloidal flux, at the low field side of the torus.

At the plasma surface $r = a$, the horizontal force balance is not automatically satisfied. At the plasma surface the poloidal field is

$$B_p = \frac{|\nabla\psi|}{R} = \frac{\psi' g_{\theta\theta}^{1/2}}{J} = -\frac{\psi'}{R_0} \left[1 + \frac{a}{R_0} (\beta_p + \frac{1}{2}\ell_i - 1) \cos \theta\right]. \quad (17)$$

These values of B_p on the surface should match the solution in the surrounding vacuum region. The vacuum field satisfies $\nabla \times \mathbf{B} = 0$, *i.e.*, $\Delta^* \psi = 0$. It is possible to integrate the vacuum equation outward starting with the initial values (17). The dominant contribution in (17), the poloidal field generated by the plasma current, vanishes for $R \rightarrow \infty$. The $\cos \theta$ terms in (17) and in Δ^* do not vanish at infinity, however. The asymptotic value of B_p is proportional to $\cos \theta$, *i.e.*, it is a vertical field. In other words, the surface poloidal field (17) cannot be generated by the plasma current alone. An external vertical field is required. This field can be provided by vertical field coils, but for short tokamak discharges a conducting shell sufficiently close to the plasma can provide the force balance. The poloidal flux is then compressed between the plasma and the conducting shell when the plasma shifts outward during heating. In practical situations the calculation of the external fields can be complicated, but by computing the integrated quantity $\langle B_p \cos \theta \rangle$ from Eq. (17) one can arrive after some manipulations at the following identity given by Freidberg [2],

$$2\pi R_0 I_p B_v = \frac{1}{2} I_p^2 \frac{\partial}{\partial R_0} (L_e + L_i) - 2\pi^2 \int dr r^2 (p' - \frac{FF'}{R_0^2}).$$

The term on the left-hand side is the inward force of the vertical field acting on the toroidal plasma current. It balances the four outward forces on the right. The first two of these represent the hoop force of the plasma current via the self-inductance, to which the poloidal fluxes inside and outside the plasma contribute. The third term is the tire tube force due to the pressure gradient, and the last term is the $(1/R)$ magnetic force, directed outward if $\beta_p < 1$ and inward if $\beta_p > 1$ (see comments below Eq. (13)).

Equation (17) also expresses that the quantity $\beta_p + \frac{1}{2}\ell_i$ of the entire plasma can be deduced from the external poloidal field, without knowing the pressure and current distribution in the plasma. However, this measurement alone does not provide the total plasma pressure (as expressed in β_p) separately.

More information can be extracted from the vacuum field if the plasma has a non-circular cross section. Equation (11) contains the higher poloidal harmonics due to shap-

ing coefficients. The $\cos m\theta$ terms are

$$S_m'' + \left(2\frac{\psi''}{\psi'} + \frac{1}{r}\right)S_m' + \frac{1-m^2}{r^2}S_m = 0. \quad (18)$$

Near the plasma centre, ψ' is approximately proportional to r so that this equation becomes

$$S_m'' + \frac{3}{r}S_m' + \frac{1-m^2}{r^2}S_m = 0,$$

which has solutions $S_m \sim r^{\pm m-1}$. Only the solution $\sim r^{m-1}$ is regular in $r = 0$. If one integrates Eq. (18) outward, starting with the regular solution at $r = 0$, one obtains S_m and S_m' at the plasma boundary. These values can be determined by external measurements. Since equation (18) involves $\psi' \sim r/q$, these measurements provide (crude) information about the $q(r)$ profile. This gives an estimate of ℓ_i . Concluding, β_p can be obtained directly from magnetic measurements if there is sufficient plasma shaping, especially elongation.

V. EQUILIBRIUM IDENTIFICATION

For several purposes it is required to know the equilibrium configurations of tokamak plasmas, *i.e.*, the current profile, the pressure profile, and the positions and shapes of the flux surfaces (or, alternatively, the direction and magnitude of the poloidal magnetic field). Primarily, this information has to be deduced from the known coil currents and magnetic measurements well outside the plasma, typically near the coils. The problem is to find a smooth solution of the Grad-Shafranov equation that best fits the measurements (Neumann conditions on a closed boundary) [9]. Smoothing, and the inclusion of assumptions on "reasonable" profiles is necessary because the reconstruction problem is inherently ill-posed: small changes (errors, inconsistencies) in the magnetic measurements outside the plasma cause changes in the solution that inflate dramatically further inward.

When accuracy rather than speed and automatic operation is the issue, a lot can be gained by using additional information: density and temperature measurements provide information on the pressure profile, motional Stark effect or Faraday rotation give poloidal field values inside the plasma, and hence information about the current density. In addition there can be discrete pieces of information: is the plasma touching the limiter? Do observed plasma oscillations give the radius of a specific rational- q surface?

Much depends on the specific purpose of the reconstruction. Here we list a few.

1. Fast reconstruction during the discharge. During a discharge, immediate knowledge about the plasma position is often required for control. This requires good modelling of the vacuum boundary conditions, the coils, and the iron around the machine. The modelling of the plasma equilibrium itself need not be as accurate as in other applications.

Therefore crude assumptions about the plasma current and pressure profiles may be used.

2. Interpretation of some plasma measurements. Some tokamak diagnostics measure quantities inside the plasma integrated over a line of sight. If the original quantity is a flux function (for instance the electron density as measured by an interferometer system), additional information is required to deduce this flux function from the set of line integrated measurements. This is required for instance if one has to combine different flux quantities (density and temperature in order to obtain the pressure). For such a profile reconstruction one needs to know both the positions of the lines of sight and the shapes and positions of the flux surfaces. Since the problem is entirely geometrical, accuracy of the pressure and current profiles in the Grad-Shafranov equation is only important insofar the shapes of the flux surfaces are concerned.

3. Plasma energy, heating and transport simulations. To study transport rates and local power balance in the plasma it is important to get optimal information about the plasma pressure from magnetic and other measurements. For correct interpretation of the data, the presence of impurity particle species and non-thermal particle populations may have to be accounted for.

4. Stability analysis. In order to analyze the stability of plasmas (planned or experimentally produced), knowledge of the current density (q -profile) and local pressure gradients is important. For many numerical stability calculations, a precise numerical solution of the Grad-Shafranov-equation is more important than an accurate fit to all available experimental data.

ACKNOWLEDGMENT

This work, supported by the European Communities under the contract of Association between EURATOM/FOM, was carried out within the framework of the European Fusion Programme with financial support from NWO. The views and opinions expressed herein do not necessarily reflect those of the European Commission.

REFERENCES

1. R. Keppens and J.W.S. Blokland, "Computing ideal magnetohydrodynamic equilibria", these proceedings.
2. J.P. Freidberg, "*Ideal Magnetohydrodynamics*", Plenum Press, New York (1987).
3. J.P. Freidberg, "Ideal magnetohydrodynamic theory of magnetic fusion systems," *Rev. Mod. Phys.* **54**, 801 (1982).
4. H.J. de Blank, "*MHD instabilities in tokamaks*", these proceedings.
5. M.D. Kruskal and R.M. Kulsrud, "Equilibrium of a magnetically confined plasma in a toroid," *Phys. Fluids* **1**, 265 (1958).

6. H. Grad and H. Rubin, "Hydromagnetic equilibria and force-free fields," in *Proceedings of the Second United Nations International Conference on the Peaceful Uses of Atomic Energy* United Nations, Geneva, Vol. 32, p. 42 (1958).
7. R. Lüster and A. Schlüter, "Axialsymmetrische magneto-hydrodynamische Gleichgewichtskonfigurationen", *Z. Naturforschung*. **12A**, 850 (1957).
8. V.D. Shafranov, "On magnetohydrodynamical equilibrium configurations," *Zhurnal Experimentalnoi i Teoreticheskoi Fiziki* **33** (1957) 710 [*Sov. Phys. J.E.T.P.* **6** (1958) 545].
9. T. Takeda and S. Tokuda, "Computation of MHD equilibrium of tokamak plasma" *Journ. Comp. Phys.* **93**, 1 (1991).
10. V.D. Shafranov, "Plasma equilibrium in a magnetic field," in *Reviews of Plasma Physics* (edited by M.A. Leontovich), Consultants Bureau, New York, Vol. 2, p. 103 (1966).
11. L.S. Solov'ev and V.D. Shafranov, "Plasma confinement in closed magnetic systems," in *Reviews of Plasma Physics* (edited by M.A. Leontovich), Consultants Bureau, New York, Vol. 5, p. 1 (1970).
12. L.E. Zakharov and V.D. Shafranov, "Equilibrium of current-carrying plasmas in toroidal configurations," in *Reviews of Plasma Physics* (edited by M.A. Leontovich), Consultants Bureau, New York, Vol. 11, p. 153 (1986).
13. J.P. Goedbloed, "Conformal mapping methods in two-dimensional magnetohydrodynamics," *Comput. Phys. Commun.* **24**, 311 (1981).
14. S. Hamada, "Hydromagnetic equilibria and their proper coordinates," *Nucl. Fusion* **1**, 23 (1962).

MHD INSTABILITIES IN TOKAMAKS

H.J. de Blank

FOM Institute DIFFER – Dutch Institute for Fundamental Energy Research,

Association EURATOM-FOM, P.O. Box 1207, 3430 BE Nieuwegein, The Netherlands, www.differ.nl.

ABSTRACT

A general introduction to ideal magnetohydrodynamic (MHD) stability of tokamak plasmas is given, using linear perturbations of the ideal MHD equations. Subsequently the Energy Principle for ideal MHD instabilities is derived. The specific instabilities which are then discussed are loosely divided into two categories. Under the name “current driven instabilities”, external and internal kink modes, which are modes with a large radial extent, are discussed. The internal $m = 1$ kink mode is responsible for sawtooth collapses and fishbone oscillations in tokamaks. Under the header “pressure driven instabilities”, more localized modes are presented. These modes may limit the pressure gradient in the plasma without causing sizeable disruptions. The ballooning limit and the Mercier criterion are presented. The Troyon limit is mentioned as a synthesis of several of these stability boundaries.

I. GENERAL THEORY OF MHD INSTABILITIES

A. The stability problem

In magnetically confined plasmas, the optimization of the plasma density and temperature for fusion energy production has lead to a wide range of plasma instabilities. The adaptation of current and pressure profiles to avoid one type of instability can lead to yet another type of instability. The fastest instabilities in magnetically confined plasmas are usually MHD instabilities, and part of this lecture describes how to avoid them.

The main question in MHD stability theory is to consider an MHD equilibrium (measured or computed), and to predict if it is stable or unstable. The obvious approach is to simulate the evolution of the plasma numerically. The simulation may show growing instabilities and their long-term fate: saturation, triggering of other instabilities, or turbulence. However, this essentially **nonlinear** modelling is computationally expensive, especially when a wide range of length or time scales are involved.

The present lecture focusses on **linear** instabilities instead. This approach is systematic and decides if infinitesimal perturbations of an equilibrium are stable (wave-like, oscillating) or unstable (exponentially growing).

However, many other (usually slower) instabilities have been discovered that depend on physics ingredients that are

not part of ideal MHD: electric resistivity, drift waves, and energetic (not thermalized) particles [1]. Yet, these instabilities often look very much like MHD instabilities if one considers the plasma motion, electric currents, and magnetic field perturbations. The second purpose of this lecture is therefore, to learn about the structure of MHD instabilities. In experiments, this helps to understand how a variety of instabilities show up in diagnostic signals.

B. Ideal MHD

Starting point is the set of equations of **resistive MHD**:

$$\begin{aligned}\frac{\partial \rho}{\partial t} &= -\nabla \cdot (\rho \mathbf{U}), \\ \frac{\partial p}{\partial t} &= -\mathbf{U} \cdot \nabla p - \gamma p \nabla \cdot \mathbf{U}, \quad \gamma = 5/3, \\ \rho \left(\frac{\partial \mathbf{U}}{\partial t} + \mathbf{U} \cdot \nabla \mathbf{U} \right) &= \mathbf{j} \times \mathbf{B} - \nabla p, \\ \frac{\partial \mathbf{B}}{\partial t} &= -\nabla \times \mathbf{E}, \\ \mathbf{E} &= \eta \mathbf{j} - \mathbf{U} \times \mathbf{B}, \\ \mathbf{j} &= \nabla \times \mathbf{B}.\end{aligned}$$

In addition there is Gauss’ law $\nabla \cdot \mathbf{B} = 0$ which, once satisfied, is conserved by Faraday’s law. In hot plasmas, the electric resistivity η is negligible for sufficiently fast plasma processes. Taking $\eta = 0$ in Ohm’s law, we obtain the **ideal MHD** model. Introducing the total time derivative $d/dt \equiv \partial/\partial t + \mathbf{U} \cdot \nabla$, the ideal MHD equations can be written as

$$\rho \frac{d\mathbf{U}}{dt} = \mathbf{B} \cdot \nabla \mathbf{B} - \nabla (s\rho^\gamma + \frac{1}{2}B^2), \quad (1)$$

$$\frac{d\rho}{dt} = -\rho \nabla \cdot \mathbf{U}, \quad (2)$$

$$\frac{ds}{dt} = 0, \quad s \equiv \frac{p}{\rho^\gamma}, \quad (3)$$

$$\frac{d\mathbf{B}}{dt} = \mathbf{B} \cdot \nabla \mathbf{U} - \mathbf{B} \nabla \cdot \mathbf{U}. \quad (4)$$

where s is the entropy density of the plasma. The momentum balance equation (1) is central to the MHD physics: it gives the evolution of the plasma flow \mathbf{U} in terms of the density ρ , the magnetic field \mathbf{B} , and the entropy s (or pressure $p = s\rho^\gamma$).

An important property of the MHD model is that the other three equations (the mass continuity equation (2), the

energy equation of state (3), and Faraday's law (4), give the evolution of ρ , s (or p), and \mathbf{B} due to the plasma flow as local conservation laws.

This is most easily seen for the energy equation (3), which merely states that the entropy density s is conserved in each point as it moves along with the plasma velocity \mathbf{U} . For the other conservation laws, we first specify how an infinitesimal line element $d\mathbf{x}$ moves with the plasma flow \mathbf{U} ,

$$\begin{aligned}\frac{d}{dt}d\mathbf{x} &= \frac{d}{dt}(\mathbf{x} + d\mathbf{x}) - \frac{d\mathbf{x}}{dt} \\ &= \mathbf{U}(\mathbf{x} + d\mathbf{x}) - \mathbf{U}(\mathbf{x}) \\ &= d\mathbf{x} \cdot \nabla \mathbf{U}.\end{aligned}$$

By constructing infinitesimal surface and volume elements out of line elements, $d^2\mathbf{x} = d\mathbf{x}_1 \times d\mathbf{x}_2$ and $d^3\mathbf{x} = d\mathbf{x}_1 \times d\mathbf{x}_2 \cdot d\mathbf{x}_3$, we obtain

$$\begin{aligned}\frac{d}{dt}d^2\mathbf{x} &= -(d^2\mathbf{x} \times \nabla) \times \mathbf{U} \\ &= d^2\mathbf{x} \nabla \cdot \mathbf{U} - (\nabla \mathbf{U}) \cdot d^2\mathbf{x},\end{aligned}\quad (5)$$

$$\frac{d}{dt}d^3\mathbf{x} = d^3\mathbf{x} \nabla \cdot \mathbf{U}.\quad (6)$$

Combining expression (6) with (2), one finds the mass conservation law in integral form,

$$\frac{d}{dt} \int \rho d^3\mathbf{x} = 0,\quad (7)$$

for any volume that moves with the plasma flow. In the same way we can combine Eqs. (4) and (5) to give

$$\frac{d}{dt} \int \mathbf{B} \cdot d^2\mathbf{x} = 0.\quad (8)$$

This equation states that the magnetic flux through an arbitrary surface that moves with the plasma is conserved.

To understand the consequences of this flux conservation law, consider the surface of a thin tube that surrounds a stretch of magnetic field line. By construction, there is zero magnetic flux crossing the surface. In addition, Gauss' law states that the flux that enters one end of the tube equals the flux that leaves the other end. Let this tube flow with the plasma velocity as time proceeds. The flux conservation law dictates that the flux that crosses the tube will remain zero and that the flux through the tube will remain the same. Hence, also at later times, the moving tube will precisely surround a magnetic field line. We can therefore say that *magnetic field lines move with the plasma flow* in ideal MHD. It follows that in an ideal MHD plasma, magnetic field lines cannot be created or annihilated, *nor can they break up and reconnect*. The magnetic topology is conserved, "frozen in the fluid", so to speak.

Strictly speaking, ideal MHD instabilities cannot change the magnetic topology of nested toroidal surfaces in a tokamak plasma. Thus, in a very hot (e.g. fusion-) plasma with negligible resistivity, ideal MHD instabilities may not

seem to be dangerous to plasma confinement. However, as we shall see later, MHD instabilities may involve "magnetic resonant surfaces" in the plasma, where the plasma motion induces a narrow layer with very high current density. In such a layer, even very low resistivity may be sufficient to cause magnetic reconnection. Although this reconnection of field lines is confined to a thin layer, these field lines may extend into regions where they are far apart. Therefore, localized reconnection may have global consequences for particle and energy confinement.

The topological constraints can prevent ideal MHD instabilities altogether, even if there is plenty of (magnetic and kinetic) free energy to drive instabilities, as is often the case in magnetically confined (fusion-) plasmas. In such cases there may be a much slower, resistive MHD-instability, for which magnetic reconnection (again, taking place in a thin resonant layer) is essential. One such instability is the *tearing mode*, presented in another lecture [2].

Another important property of the ideal MHD system is that it can be derived from Hamilton's principle: the plasma motion $\mathbf{U}(\mathbf{x}, t)$ that makes the action

$$S = \int_{t_0}^{t_1} L dt$$

stationary, where the Lagrangian is [3, 4]

$$L = \int d^3\mathbf{x} \left(\frac{1}{2} \rho U^2 - \frac{p}{\gamma - 1} - \frac{1}{2} B^2 \right),\quad (9)$$

is the true dynamical motion that satisfies the MHD equations. Here, it is understood that the plasma motion determines the evolution of ρ , p , and \mathbf{B} through Eqs. (2), (3), and (4), respectively.

In order to demonstrate that Hamilton's principle for the Lagrangian (9) indeed produces the MHD momentum equation (1), we investigate how the action S changes if the MHD fields are perturbed. Since all MHD quantities respond to the plasma motion, the primary perturbation is an arbitrary infinitesimal displacement $\boldsymbol{\xi}(\mathbf{x}, t)$ of the plasma fluid. We introduce the operator $\delta_\xi X$, the Lagrangian perturbation of a variable X , which is the change in the quantity while following the perturbed plasma motion. For instance, $\delta_\xi \mathbf{x} = \boldsymbol{\xi}$. It is helpful to introduce also the Eulerian perturbation $\delta_\xi^E \equiv \delta_\xi - \boldsymbol{\xi} \cdot \nabla$, which gives the perturbation at a fixed point in space, $\delta_\xi^E \mathbf{x} = 0$. It therefore commutes with partial space and time derivatives,

$$\delta_\xi^E \nabla = \nabla \delta_\xi^E, \quad \delta_\xi^E \frac{\partial}{\partial t} = \frac{\partial}{\partial t} \delta_\xi^E.$$

While the Lagrangian perturbation does not commute with ∇ and $\partial/\partial t$, it commutes with the total derivative instead,

$$\delta_\xi \frac{d}{dt} = \frac{d}{dt} \delta_\xi, \quad \text{since } \delta_\xi \mathbf{U} = \frac{d\boldsymbol{\xi}}{dt}.$$

An infinitesimal line element varies as $\delta_\xi d\mathbf{x} = d\mathbf{x} \cdot \nabla \boldsymbol{\xi}$. With these tools, one can obtain the perturbed density, pressure,

and magnetic field from Eqs. (7), (3), and (8) respectively,

$$\delta_\xi \rho = -\rho \nabla \cdot \boldsymbol{\xi}, \quad (10)$$

$$\delta_\xi p = -\gamma p \nabla \cdot \boldsymbol{\xi}, \quad (\delta_\xi s = 0) \quad (11)$$

$$\delta_\xi \mathbf{B} = \mathbf{B} \cdot \nabla \boldsymbol{\xi} - \mathbf{B} \nabla \cdot \boldsymbol{\xi}. \quad (12)$$

The perturbed volume element is given by $\delta_\xi d^3x = d^3x \nabla \cdot \boldsymbol{\xi}$. Now we can obtain the perturbed Lagrangian from Eq. (9),

$$\begin{aligned} \delta_\xi L &= \int d^3x \left[(\nabla \cdot \boldsymbol{\xi}) \left(\frac{1}{2} \rho U^2 - \frac{p}{\gamma-1} - \frac{1}{2} B^2 \right) \right. \\ &\quad \left. + \delta_\xi \left(\frac{1}{2} \rho U^2 - \frac{p}{\gamma-1} - \frac{1}{2} B^2 \right) \right] \\ &= \int d^3x \left[\rho \mathbf{U} \cdot \frac{d\boldsymbol{\xi}}{dt} + (p + \frac{1}{2} B^2) \nabla \cdot \boldsymbol{\xi} - \mathbf{B} \cdot (\mathbf{B} \cdot \nabla \boldsymbol{\xi}) \right] \\ &= \int d^2x \cdot \boldsymbol{\xi} \left(p + \frac{1}{2} B^2 \right) + \frac{d}{dt} \int d^3x \rho \mathbf{U} \cdot \boldsymbol{\xi} \\ &\quad - \int d^3x \boldsymbol{\xi} \cdot \left(\rho \frac{d\mathbf{U}}{dt} - \mathbf{j} \times \mathbf{B} + \nabla p \right). \end{aligned} \quad (13)$$

In the last step we have used the mass conservation equation (2). The first term in (13) vanishes upon integration if one considers only internal perturbations, *i.e.*, $\boldsymbol{\xi} \cdot \mathbf{n} = 0$ on the plasma boundary (also $\rho = 0$ and $\mathbf{B} \cdot \mathbf{n} = 0$ there). Hamilton's principle can be extended to free-boundary perturbations (with $\boldsymbol{\xi} \cdot \mathbf{n} \neq 0$) by adding to the Lagrangian the vacuum magnetic energy that surrounds the plasma. The second term in (13) does not contribute to the perturbed action $\delta_\xi S = \int \delta_\xi L dt$ if the perturbation is zero at $t = t_0$ and $t = t_1$. The term vanishes altogether if one considers perturbations of a static equilibrium. The third term vanishes for arbitrary $\boldsymbol{\xi}$ if and only if the momentum balance equation (1) is satisfied. In this way Eq. (1) follows from Hamilton's principle.

C. The linearized MHD equations

We now possess the tools to study MHD waves and instabilities. Perturbing the momentum equation (1) gives us the equation of motion for $\boldsymbol{\xi}$,

$$\begin{aligned} 0 &= \delta_\xi \left(\rho \frac{d\mathbf{U}}{dt} - \mathbf{j} \times \mathbf{B} + \nabla p \right) \\ &= \rho \frac{d^2 \boldsymbol{\xi}}{dt^2} - \mathbf{F}(\boldsymbol{\xi}), \end{aligned} \quad (14)$$

where the linear force operator \mathbf{F} is defined as

$$\begin{aligned} \mathbf{F}(\boldsymbol{\xi}) &= \delta_\xi (\mathbf{j} \times \mathbf{B} - \nabla p) + \rho \frac{d\mathbf{U}}{dt} \nabla \cdot \boldsymbol{\xi} \\ &= (\nabla \times \mathbf{Q}) \times \mathbf{B} + (\nabla \times \mathbf{B}) \times \mathbf{Q} + \\ &\quad \nabla (\boldsymbol{\xi} \cdot \nabla p + \gamma p \nabla \cdot \boldsymbol{\xi}) + \nabla \cdot \left(\rho \boldsymbol{\xi} \frac{d\mathbf{U}}{dt} \right), \end{aligned} \quad (15)$$

and where

$$\mathbf{Q} \equiv \delta_\xi^E \mathbf{B} = \nabla \times (\boldsymbol{\xi} \times \mathbf{B}).$$

Since Eq. (14) is linear in $\boldsymbol{\xi}$, it determines eigenfunctions $\boldsymbol{\xi}(\mathbf{x}, t) = \boldsymbol{\xi}(\mathbf{x}) e^{-i\omega t}$

The force operator \mathbf{F} possesses the important property that it is self-adjoint, *i.e.*, given any two vector fields $\boldsymbol{\xi}$ and $\boldsymbol{\zeta}$, the operator satisfies

$$\int \boldsymbol{\zeta} \cdot \mathbf{F}(\boldsymbol{\xi}) d^3x = \int \boldsymbol{\xi} \cdot \mathbf{F}(\boldsymbol{\zeta}) d^3x. \quad (16)$$

Direct proofs of the self-adjointness of \mathbf{F} can be found in many texts [5, 3, 6, 7, 8, 9]. Most proofs require lengthy vector manipulations that seem to lack direction. We will therefore take a more instructive approach.

The key element of our proof is that the Lagrangian perturbations form a Lie algebra. Consider the commutator of two perturbations, $(\delta_\zeta \delta_\xi - \delta_\xi \delta_\zeta) \mathbf{x} = \delta_\zeta \boldsymbol{\xi} - \delta_\xi \boldsymbol{\zeta} \equiv \boldsymbol{\eta}$. This is equal to another perturbation of the position, $\boldsymbol{\eta} = \delta_\eta \mathbf{x}$. Since the perturbations of all MHD quantities derive from the displacement vector, we have the general operator identity

$$\delta_\zeta \delta_\xi - \delta_\xi \delta_\zeta = \delta_\eta, \quad \boldsymbol{\eta} \equiv \delta_\zeta \boldsymbol{\xi} - \delta_\xi \boldsymbol{\zeta},$$

which defines the Lie algebra. Now consider the double variation of the Lagrangian (13) and use the boundary conditions,

$$\begin{aligned} \delta_\zeta \delta_\xi L &= \delta_\zeta \int d^3x \left[\frac{\partial}{\partial t} (\rho \mathbf{U} \cdot \boldsymbol{\xi}) - \boldsymbol{\xi} \cdot \left(\rho \frac{d\mathbf{U}}{dt} - \mathbf{j} \times \mathbf{B} + \nabla p \right) \right] \\ &= \int d^3x \left[\frac{\partial}{\partial t} \left(\rho \frac{d\boldsymbol{\zeta}}{dt} \cdot \boldsymbol{\xi} \right) - \boldsymbol{\xi} \cdot \left(\rho \frac{d^2 \boldsymbol{\zeta}}{dt^2} - \mathbf{F}(\boldsymbol{\zeta}) \right) \right] \\ &= 2K(\boldsymbol{\zeta}, \boldsymbol{\xi}) - 2\delta W(\boldsymbol{\zeta}, \boldsymbol{\xi}), \end{aligned} \quad (17)$$

where we have defined the kinetic and potential energy functionals [5],

$$\begin{aligned} K(\boldsymbol{\zeta}, \boldsymbol{\xi}) &= \frac{1}{2} \int \rho \frac{d\boldsymbol{\zeta}}{dt} \cdot \frac{d\boldsymbol{\xi}}{dt} d^3x, \\ \delta W(\boldsymbol{\zeta}, \boldsymbol{\xi}) &= -\frac{1}{2} \int \boldsymbol{\zeta} \cdot \mathbf{F}(\boldsymbol{\xi}) d^3x. \end{aligned}$$

According to the Lie algebra, $\delta_\zeta \delta_\xi L - \delta_\xi \delta_\zeta L = \delta_\eta L$. Moreover, $\delta_\eta L = 0$ because the unperturbed plasma satisfies the momentum equation (1). Therefore, $\delta_\zeta \delta_\xi L = \delta_\xi \delta_\zeta L$, and since the kinetic energy functional K is manifestly self-adjoint, it follows that the potential energy functional δW is symmetric,

$$\delta W(\boldsymbol{\zeta}, \boldsymbol{\xi}) = \delta W(\boldsymbol{\xi}, \boldsymbol{\zeta}).$$

This concludes the proof that the force operator (15) is self-adjoint.

D. The Energy Principle

The self-adjointness (16) of the force operator has several important consequences that are useful in the stability analysis of actual configurations. Here, we list four properties.

1. For a normal mode $\xi(\mathbf{x}, t) = \xi(\mathbf{x})e^{-i\omega t}$, ω^2 is always real. It is easy to see that $\omega^{*2} = \omega^2$ from

$$\begin{aligned}\omega^2 \int \rho \xi^* \cdot \xi d^3x &= - \int \xi^* \cdot \mathbf{F}(\xi) d^3x \\ &= - \int \xi \cdot \mathbf{F}(\xi^*) d^3x = \omega^{*2} \int \rho \xi^* \cdot \xi d^3x.\end{aligned}$$

The first step uses the eigenvalue equation for the mode, $-\rho\omega^2\xi = \mathbf{F}(\xi)$, the second step self-adjointness, and the third step the complex conjugate of (14). Because of 1, an eigenmode is either oscillating (ω real) or exponentially growing (ω imaginary). Overstable modes (growing oscillations) cannot occur. Hence if a mode is stable it cannot become unstable by a slight variation of the equilibrium which would add a small imaginary component to a real frequency ω . Instead, access to instability is only possible via marginal stability ($\omega = 0$), because ω^2 has to change sign.

2. Eigenmodes with different eigenvalues are orthogonal,

$$\int \rho \xi_m^* \cdot \xi_n d^3x = 0, \quad \text{if } \omega_m^2 \neq \omega_n^2.$$

3. The Energy Principle [5, 10] states that an equilibrium is stable if and only if

$$\delta W(\xi^*, \xi) \geq 0$$

for all possible displacements ξ , which satisfy appropriate boundary conditions and are bounded in energy. We will prove first the sufficiency and then the necessity of the stability condition.

Sufficiency of the Energy Principle follows simply from conservation of the total energy $H = K(t) + \delta W(t)$. If $\delta W > 0$ then $K(t)$ cannot grow beyond the initial total energy H , i.e., an exponentially growing instability is not possible. The necessity of the Energy Principle means that the equilibrium is unstable whenever we can find a trial function ξ_T (not necessarily an eigenmode) for which $\delta W < 0$. In order to see this we consider the positive integral

$$I(t) \equiv \frac{1}{2} \int \rho |\xi|^2 d^3x.$$

We now calculate d^2I/dt^2 . Using Eqs. (14) and (1) to remove $d^2\xi/dt^2$ terms we obtain

$$\frac{d^2I}{dt^2} = 2K - 2\delta W.$$

Now take as initial condition $\partial\xi_T/\partial t = 0$, so that initially the kinetic energy K is zero. Therefore the (conserved) total energy $H = K + \delta W$ is negative. Since at later times $K \geq 0$ we find

$$\frac{d^2I}{dt^2} = 4K - 2H > -2H > 0,$$

which proves that I grows at least as fast as t^2 as $t \rightarrow \infty$. This proves the Energy Principle [11, 7].

An advantage of the Energy Principle is that one can consider the sign of δW for a class of cleverly chosen trial functions ξ_T , which are however not eigenfunctions. (The eigenfunctions might be difficult to calculate). For such a limited class of trial functions the condition $\delta W > 0$ is necessary for stability, but not sufficient. One obtains a stability boundary beyond which the equilibrium is definitely unstable. On the “stable” side of such a boundary, however, there might still be unstable modes that have been “overlooked” because they are not in the set of trial functions. An example of such a necessary but insufficient criterion is the Mercier criterion which we will encounter in section III.

4. In order to find the precise stability limits one has to minimize δW for all allowed perturbations ξ . This can be done in a standard way by variational calculus. The resulting Euler equation is precisely equation (14) at marginal stability,

$$\mathbf{F}(\xi) = 0. \quad (18)$$

In other words, finding stability boundaries by minimizing δW and finding normal modes by solving Eq. (14) are equivalent. This fact will appear several times in the following sections.

E. The intuitive form of the energy functional

In this section and in the following one we consider the actual stability boundaries for tokamak configurations. Such stability limits are found by considering at marginal stability ($\omega = 0$) specific classes of modes that are expected to be the most unstable ones. Most of the following analysis will be done not on the basis of the marginal stability equation (18) but with the energy principle. Freidberg [6, 7] will be followed here in discussing the intuitive form of the energy functional,

$$\begin{aligned}\delta W &= \frac{1}{2} \int_P d^3x \left[\gamma p |\nabla \cdot \xi|^2 + |Q_\perp|^2 + B^2 |\nabla \cdot \xi_\perp + 2\xi_\perp \cdot \kappa|^2 \right. \\ &\quad \left. - j_\parallel (\xi^* \times \mathbf{b} \cdot Q_\perp) \right. \\ &\quad \left. - 2(\xi_\perp \cdot \nabla p)(\xi_\perp^* \cdot \kappa) \right], \quad (19)\end{aligned}$$

which can be obtained from expression (17) by putting $K = 0$ and by performing several integrations by parts. Here, $\mathbf{b} = \mathbf{B}/B$ is the unit vector parallel to the magnetic field. Its derivative along the field line $\kappa = \mathbf{b} \cdot \nabla \mathbf{b}$ is the field line curvature. Note that $\kappa \perp \mathbf{b}$. For the adjoint perturbation we have taken the complex conjugate, $\xi^A = \xi^*$. The Eulerian perturbation of the magnetic field Q is given after Eq. (15).

The first three terms in the integrand of (19) are always positive and stabilizing. The last two terms are potentially destabilizing.

The first stabilizing term represents plasma compression. It is an important stabilizing force in sound waves. At marginal stability, however, the kinetic energy being zero, it is the only term in which ξ_\parallel appears. All other terms depend on ξ_\perp only. One can minimize δW once and for all with

respect to ξ_{\parallel} . In a tokamak configuration ξ_{\parallel} can actually be chosen to make $\frac{1}{2} \int d^3x \gamma p |\nabla \cdot \xi|^2 = 0$, by making $\nabla \cdot \xi = 0$ in the entire plasma with the possible exception of some isolated surfaces. It is a fortunate situation that we can consider the plasma as being incompressible because the ideal gas equation of state (3) has a rather limited range of validity in tokamaks in the low collisionality regime, especially in the presence of non-thermal particles due to non-Ohmic heating or fusion reactions. The second term is caused by the perturbed magnetic field component perpendicular to the equilibrium field. It is the energy required to bend magnetic field lines. It is the dominant stabilizing term in shear Alfvén waves. The third term involves the parallel component of the perturbed magnetic field and therefore the perturbation of the magnetic field strength B . Since B can be viewed as the density of field lines, this term is caused by the compression of field lines, countered by the magnetic pressure. This term dominates compressional Alfvén waves.

The fourth term can be destabilizing. Because it is proportional to j_{\parallel} , modes driven unstable by it are called current driven instabilities. The fifth term is also a potential source of instabilities, called pressure driven modes because the term is proportional to the pressure gradient. We will consider both classes of instabilities in more detail.

II. CURRENT DRIVEN INSTABILITIES

A. Introduction

In this section we will consider instabilities which are driven by the energy stored in the current parallel to the magnetic field, *i.e.*, by the fourth term in the energy functional (19). The driving force is due to the tendency of two conducting wires (read: flux tubes) with parallel currents to repel each other. The destabilizing effect remains even if the plasma pressure is small. This justifies the distinction between current driven modes and pressure and driven instabilities such as the ballooning modes.

We shall see that the current-driven modes tend to have very small parallel wave numbers, $\mathbf{b} \cdot \nabla \ll \nabla$, so that these modes must have almost the same helical structure as the magnetic field lines. In a large aspect ratio tokamak plasma ($a \ll R$) with circular poloidal cross-section, the plasma locally has the approximate symmetry of a cylinder, and eigenmodes of the system can be approximated by a single poloidal harmonic [12, 13]. Modes dominated by such a helical displacement $e^{i(m\theta - n\phi)}$ are called kink modes.

The next subsection gives a general approach to internal MHD instabilities with low poloidal and toroidal mode numbers (m, n), *i.e.*, with a wavelength comparable to the machine minor radius. Associated with the large spatial extent of the linear mode is usually also a large nonlinear amplitude of the instability. Therefore such instabilities can lead to a disruptive loss of confinement in a significant fraction of the plasma.

Most current-driven modes are stable in ideal MHD (*i.e.* without resistivity), except free boundary modes, which are instabilities with a finite amplitude on the plasma surface and in the vacuum region. The vicinity of a conducting wall can be important in stabilizing these modes. They are discussed in the next subsection.

The final subsection discusses $m = 1, n = 1$ kink modes. These modes require a special treatment because they can also lead to internal instabilities, if a flux surface with $q = 1$ is present in the plasma. The internal kink mode is one of the mechanisms that in tokamaks drive internal disruptions or sawtooth collapses, so called because they occur in the hot plasma core repetitively, typically removing all the excess pressure from the center, leaving profiles with a flat or even hollow central part. The spatial extent of these modes is mainly determined by the plasma volume where the safety factor $q < 1$. This volume usually contains a considerable fraction of the plasma kinetic energy. Sawtooth collapses often show fast initial growth of the perturbation. In the language of linear stability, a large growth rate means that the plasma is far in the unstable region in configuration space. Therefore, the mode is not triggered when the slowly evolving equilibrium crosses the stability boundary. Rather, some essentially nonlinear trigger mechanism has to take place, which is at present not understood. Hence, we have to keep in mind that linear stability theory does not give a description of the temporal behaviour of a disruptive instability. It can, however, give a good indication whether an instability can indeed occur, and in addition it can provide the spatial structure and growth rate of the mode at low amplitudes.

B. Kink modes

The most important features of current driven instabilities can be studied in the low- β approximation, in which

$$\mathbf{j}_{\perp} = \frac{\mathbf{B} \times \nabla p}{B^2} = \mathcal{O}(\varepsilon^2), \quad \varepsilon = \frac{a}{R_0} \ll 1.$$

An immediate consequence of $\beta = \mathcal{O}(\varepsilon^2)$ is that the Shafranov shift of the flux surfaces is small, $\Delta = \mathcal{O}(\varepsilon^2 a)$. Therefore, if shaping effects such as elongation and triangularity are small, the flux surfaces have approximately centered circular cross sections [14]. In addition, since ε is small, the field line curvature is small and B ($\sim 1/R$) does not vary much over the plasma cross section. Therefore, we can approximate the plasma by a cylindrical column of radius $r = a$ and length $2\pi R_0$. Our cylindrical coordinates will be (r, θ, ϕ) , where θ is the poloidal angle and ϕ the longitudinal coordinate. Of course we impose periodic boundary conditions for $\phi \rightarrow \phi + 2\pi$. We will write vectors in column notation when they are given in terms of the orthonormal basis $\hat{r}, \hat{\theta}, \hat{\phi}$. The magnetic field and the current density are

$$\mathbf{B} = B \begin{pmatrix} 0 \\ \frac{r}{qR_0} \\ 1 \end{pmatrix} + \mathcal{O}(\varepsilon^2), \quad \mathbf{j} = \frac{B}{R} \begin{pmatrix} 0 \\ 0 \\ \frac{1}{r} \left(\frac{r^2}{q} \right)' \end{pmatrix} + \mathcal{O}(\varepsilon^2).$$

We will now look for the perturbations ξ that minimize δW (19). We do this in four steps.

1. Due to the symmetry in both θ and ϕ we can consider single poloidal and toroidal harmonics, with mode numbers (m, n) as normal modes,

$$\xi = \xi(r) e^{i(m\theta - n\phi - \omega t)}.$$

2. We write the vector ξ as

$$\xi = \xi_r \hat{r} + \xi_\theta \hat{\theta} + \xi_\parallel \hat{b}.$$

The component ξ_\parallel occurs in δW only in the plasma compression term $\int \gamma p |\nabla \cdot \xi|^2 d^3x$, which can be minimized to zero by choosing ξ_\parallel such that $\nabla \cdot \xi = 0$ in most of the volume. The remaining energy functional depends on ξ_r and ξ_θ only.

3. As a consequence of the low- β ordering, the stabilizing magnetic energy terms in δW are by far the largest: all other terms are $\mathcal{O}(\varepsilon^2)$ smaller. Hence, minimization of δW requires to leading order that $\frac{1}{2} \int |\mathbf{Q}|^2 d^3x$ is minimized. We will see that this minimization poses only one condition on the two functions $\xi_r(r)$ and $\xi_\theta(r)$. After this first minimization we will consider the remaining terms in the energy, which are $\mathcal{O}(\varepsilon^2)$, and derive a stability criterion from them. The (Eulerian) perturbation of the magnetic field is

$$\mathbf{Q} = \nabla \times (\xi \times \mathbf{B}) = \frac{B_0}{r} \begin{pmatrix} -i \left(\frac{m}{q} - n \right) \frac{r}{R_0} \xi_r \\ \frac{r}{R_0} \left[\left(\frac{r}{q} \xi_r \right)' + i n \xi_\theta \right] \\ - (r \xi_r)' - i m \xi_\theta \end{pmatrix},$$

One sees that the $\hat{\phi}$ component is dominant. The \hat{r} and $\hat{\theta}$ components are $\mathcal{O}(\varepsilon)$ smaller and give $\mathcal{O}(\varepsilon^2)$ smaller contributions to the energy. Hence, we arrive at the condition that the $\hat{\phi}$ component must be small, at most $\mathcal{O}(\varepsilon)$. At this point, we must be somewhat more careful. Our derivation so far is fine if we consider an unstable equilibrium and merely look for a trial function ξ_T that makes $\delta W(\xi_T) < 0$ in order to prove this. However, in order to obtain the actual stability criterion one needs to extend the expansion to higher order, $\mathcal{O}(\varepsilon^2)$, in the energy. Moreover, we want to find the actual eigenfunction ξ . We want to know the spatial structure of the mode. In principle, we have to solve the original Euler equation $\mathbf{F}(\xi) = 0$, all three components of it, in the three unknown components of ξ . Here, another nice property of the energy principle comes to the rescue. After all, we already have arrived at a one-dimensional system with only two unknowns,

$$\delta W(\xi_r, \xi_\theta) = 2\pi^2 B_0^2 \int \frac{R_0}{r} |(r \xi_r)' + i m \xi_\theta|^2 dr + \mathcal{O}(\varepsilon^2).$$

The usefulness of the energy approach is that we can readily extract Euler equations for ξ_r and ξ_θ from this expression,

$$\begin{aligned} r \frac{d}{dr} \left[\frac{1}{r} ((r \xi_r)' + i m \xi_\theta) \right] &= \mathcal{O}(\varepsilon^2) \\ - \frac{i m}{r} ((r \xi_r)' + i m \xi_\theta) &= \mathcal{O}(\varepsilon^2). \end{aligned} \quad (20)$$

To leading order, the two equations are not independent, and we will have to go to higher order in ε to find an independent second equation. We discuss Eq. (20) for the cases $m = 0$ and $m \neq 0$ separately. For $m = 0$ we have $(r \xi_r)' = 0$. The only solution that is regular in $r = 0$ is $\xi_r = 0$. This implies that ξ is always tangent to the flux surfaces and energy cannot be released: the $m = 0$ modes are stable. For $m \neq 0$ we obtain

$$\xi_\theta = \frac{i}{m} (r \xi_r)' + \mathcal{O}(\varepsilon^2). \quad (21)$$

Note that this equation does not merely reduce the dominant term, shown in Eq. (20), to the order of the other terms, $\mathcal{O}(\varepsilon^2)$. The term becomes much smaller than the rest of δW , $\mathcal{O}(\varepsilon^4)$. This is a general feature which occurs if one expands a bilinear energy functional in a small parameter. Another general pattern is that the orders of the energy terms are always even powers of the small parameters. It is also useful to note that the term that we have minimized is approximately the field line compression energy. Accordingly, Eq. (21) states that the plasma motion in the poloidal plane is to a good approximation incompressible, $\text{Div}(\xi_r, \xi_\theta) = 0$. 4. Using Eq. (21) we eliminate ξ_θ from $\delta W(\xi_r, \xi_\theta)$. This requires some integrations by parts and cancellation of q' -terms. The result is

$$\begin{aligned} \delta W_{\text{cyl}} &= \pi^2 \frac{B_0^2}{R_0} \int_0^a (|r \xi_r'|^2 + (m^2 - 1) |\xi_r|^2) \left(\frac{n}{m} - \frac{1}{q} \right)^2 r dr \\ &+ \mathcal{O}(\varepsilon^4), \end{aligned} \quad (22)$$

Since $m \neq 0$, the dominant terms in expression (22) are clearly positive definite and therefore do not give rise to instabilities. We will now discuss two ways in which unstable modes can arise that are described by Eq. (22). The first possibility involves the boundary conditions. If the mode has a non-zero amplitude at the plasma boundary, $\xi_r(a) \neq 0$, then extra terms should be added to δW_{cyl} corresponding to the energy of the vacuum region and of the plasma boundary itself. The additional terms can be negative and can give rise to external kink modes. These instabilities will be briefly discussed in the next subsection. The other possibility of instability is when δW_{cyl} vanishes to leading order, which is only possible if $m = 1$. Then the $\mathcal{O}(\varepsilon^4)$ terms become important, and these terms can be negative. This leads to the potentially unstable internal $m = 1$ kink mode, which will be treated in the final subsection.

C. External kink modes

The computation of external kink modes can be performed using an extended energy principle, which takes into account the energy in the plasma, in the vacuum region, and in general a contribution from the plasma-vacuum boundary surface. The boundary conditions between plasma and vacuum, and between vacuum and (conducting) wall, play a central role in the derivation of the extended energy functional. The

first two of these conditions are that at both boundaries the magnetic field is tangent to the boundary surface. The third condition is that at the plasma-vacuum interface the momentum balance requires that the quantity $p + \frac{1}{2}B^2$ is continuous. We will give here the resulting energy functional for the case of a circular plasma cross section with minor radius $r = a$ and a perfectly conducting wall at $r = b$, which can be obtained following the steps outlined in the previous subsection [15].

$$\delta W_{\text{external}} = \quad (23)$$

$$\pi^2 \frac{B_0^2}{R_0} \left\{ \int_0^a (|r\xi_r'|^2 + (m^2 - 1)|\xi_r|^2) \left(\frac{n}{m} - \frac{1}{q} \right)^2 r dr + \left[\frac{2}{q} \left(\frac{n}{m} - \frac{1}{q} \right) + (1 + m\lambda) \left(\frac{n}{m} - \frac{1}{q} \right)^2 \right] r^2 |\xi_r|^2 \Big|_{r=a} \right\},$$

where

$$\lambda = \frac{1 + (a/b)^{2m}}{1 - (a/b)^{2m}}.$$

The contribution of $\lambda > 0$ is the stabilizing effect of the wall. The first term in the second line of Eq. (C.) is destabilizing if $q(a) < m/n$. All other terms are positive. For fixed m/n , the mode with the lowest poloidal mode numbers has the lowest field line bending energy and is therefore the least stable one. Potentially the most unstable external kink modes are the $m = 2, n = 1$ mode and in particular the $m = 1, n = 1$ mode. They are also the most dangerous modes since they affect a large part of the plasma and can cause a violent disruption that terminates the discharge and can damage tokamak components. These modes require $q(a) < 2$ and $q(a) < 1$, respectively. As soon as $q(a)$ drops below 2, the $m = 2$ mode becomes unstable unless the current profile is extremely peaked or a conducting shell is close to the plasma. As a consequence, present day tokamaks normally need to operate with $q(a) > 2$ in order to avoid the $m = 2$ kink mode [16]. Note that the external $m = 1$ kink mode remains out of reach by a safe margin.

Whether a mode is actually unstable depends on the details of the current profile. In order to obtain a stability criterion the integral over the plasma interior in (C.) must be minimized. The minimizing function $\xi_r(r)$ is a solution of the Euler equation obtained from (C.),

$$\frac{d}{dr} \left[\left(\frac{n}{m} - \frac{1}{q} \right)^2 r^3 \frac{d\xi_r}{dr} \right] = (m^2 - 1) \left(\frac{n}{m} - \frac{1}{q} \right)^2 r \xi_r. \quad (24)$$

Note that for $n = 0$ this equation is identical to the radial equations for small equilibrium shaping effects, equation (18) in Ref. [14]. Equation (24) is singular in $r = 0$ and in $q = m/n$. In the vicinity of the magnetic axis $q(r)$ is approximately constant. Hence, for small r we can find exact solutions to Eq. (24), $\xi_r(r) \sim r^{-1 \pm m}$. The solution that is regular at $r = 0$ is

$$\xi_r \sim r^{m-1}, \quad \xi_\theta = i\xi_r. \quad (25)$$

One sees that for $m = 1$ the components ξ_r and ξ_θ are constant in the plasma centre, which corresponds to a rigid displacement of the plasma core. For $m > 1$, however, the mode amplitude vanishes in the plasma centre. Equation (24), together with (21), gives a good indication of how a global MHD eigenfunction with specific toroidal and poloidal mode numbers looks like in an approximately circular plasma cross section, even if one has to take into account additional effects before the stability criterion for such a mode can be found. An example of this is presented in the next subsection.

D. The internal $m=1$ kink mode

We will show in this subsection that for $m = 1$ one can also find an unstable mode with $\xi_r(a) = 0$, *i.e.*, an internal mode. It is clear from the energy functional (22) that the case $m = 1$ requires a special treatment. A general calculation shows that the $m = n = 1$ mode is in general more unstable than the $m = 1$ modes with higher toroidal mode numbers. For simplicity, we will restrict ourselves to the toroidal mode number $n = 1$ from the start. The leading order energy functional reduces to

$$\delta W_{m=1} = \pi^2 \frac{B_0^2}{R_0} \int_0^a r^3 |\xi_r'|^2 \left(1 - \frac{1}{q}\right)^2 dr. \quad (26)$$

Equation (25) implies that this functional is minimized by $\xi_r(r) = \text{constant}$. However, we are looking for an internal mode, $\xi_r(a) = 0$. Consider therefore a trial function which is constant in the plasma centre, shows a steep step at the radius $r = r_1$ where $q = 1$, and vanishes for $r > r_1$ [17]. Let us call the width of the layer where $\xi_r(r)$ changes from its central value to zero δ . We will show now that $\delta W_{m=1}$ vanishes for $\delta \rightarrow 0$. The radial derivative of ξ_r is of course large, $|\xi_r'|^2 = \mathcal{O}(1/\delta^2)$. On the other hand, $q \approx 1$ in this layer, so that $(1 - 1/q)^2 = \mathcal{O}(\delta^2)$. Therefore, small and large factors cancel in the integrand of (26). It follows that $\delta W_{m=1}$ vanishes because the integration interval itself has width δ .

The resulting eigenfunction $\xi(x)$ represents a rigid displacement of the plasma inside the $q = 1$ surface. It can be understood that the stabilizing magnetic energy terms in δW practically vanish by considering the three-dimensional structure of the mode $\xi(x) = \xi \exp i(\theta - \phi)$. In the $\phi = 0$ plane, the rigid displacement is pointed toward the low field side. At $\phi = \frac{\pi}{2}$ it is directed upward, at $\phi = \pi$ the motion is to the high field side, and at $\phi = \frac{3\pi}{2}$ it is downward. Summarizing, the motion of the plasma ring with $q < 1$ consists of a rigid shift in the horizontal $\phi = 0$ direction combined with a tilt with respect to the axis in that direction. In contrast with higher m, n modes, which cause a helical kink deformation, the $m = n = 1$ mode does not deform the flux surfaces, and therefore the field line compression and bending terms in δW vanish.

The $q \approx 1$ layer, where ξ_r' is large, requires a more careful discussion, however. Note that the poloidal displace-

ment, given by Eq. (21), becomes very large for $\delta \rightarrow 0$. This can be visualized as follows. The rigid displacement of the plasma inside the $q = 1$ surface pushes it against this surface and the outer plasma, which remains motionless. Since field lines cannot cross each other, and because of incompressibility, the plasma has to flow back at high speed in the thin $q \approx 1$ layer, thus creating extreme convection cells. The plasma motion in the singular layer does not require magnetic energy because the field lines with $q = 1$ are closed and have exactly the same helicity as the mode. Hence they can be interchanged freely.

Summarizing, we have minimized the energy functional to the point that $\delta W = \mathcal{O}(\varepsilon^4)$. First, we have chosen ξ_{\parallel} such that there is no plasma compression. Then we have chosen ξ_{ρ} such that there is no field line compression, and finally we have taken $m = n = 1$ and we have taken a step-function for ξ_r so that there is no field line bending. We have found the general shape of the displacement function, but not yet a stability criterion. In order to find the marginal stability criterion we have to solve the $\mathcal{O}(\varepsilon^4)$ equation $\delta W(\xi^*, \xi) = 0$. This requires that the eigenfunction ξ is computed to higher order in ε than we have done above. In $\mathcal{O}(\varepsilon^4)$, the energy functional contains the following new terms.

1. Terms due to ∇p and j_{\perp} , which are $\mathcal{O}(\beta \sim \varepsilon^2)$ smaller than the terms previously considered, enter the cylindrical model. Hence, the internal kink mode is not a purely current driven mode. In practice, the instability is mainly driven by large pressure gradients in the central plasma (within the $q = 1$ surface), while the current is somewhat stabilizing if it is peaked in the centre.
2. The toroidal curvature of the plasma has to be taken into account. This leads to corrections to the cylindrical approximation. An example of such a correction is the Shafranov-shift, which is of the order $\Delta(r) = \mathcal{O}(\varepsilon r)$ in the low- β ordering. This shift contains ‘‘toroidal’’ terms due to the pressure and the current.
3. Another consequence of the toroidal shape is that eigenmodes are not exact poloidal harmonics. In the case of the internal $m = 1$ kink instability, the mode is dominantly the $m = 1$ harmonic, as discussed in the cylindrical approximation. In addition, however, there are small sidebands. They have poloidal mode numbers $m = 0$ and $m = 2$, and are $\mathcal{O}(\varepsilon)$ smaller than the $m = 1$ harmonic of the instability. These two sideband harmonics as well avoid plasma compression and field line compression. In suitable coordinates they obey the cylindrical equation (24) with $m = 0$ and $m = 2$, respectively. They cannot avoid field line bending however (which only the $m = 1$ step-function can do). Hence these small harmonics contribute to $\mathcal{O}(\varepsilon^4)$ to the energy, *i.e.*, they are just as important for the stability criterion as the main $m = 1$ harmonic.
4. In subsection A. we concluded that the field compression energy was minimized to $\mathcal{O}(\varepsilon^4)$. Therefore we must presently take into account that the magnetic field is not entirely incompressible.

The derivation of the final stability criterion requires a lot of algebra and yields a rather complicated equation. The current profile enters in a non-trivial way, for instance, because the general solution of Eq. (24) for the $m = 2$ harmonic is not a closed form. The pressure plays a more straightforward role. The final form of δW is a quadratic function of

$$\beta_p(r_1) \equiv -2 \frac{R_0^2 q^2}{B_0^2 r_1^4} \int_0^{r_1} p' r^2 dr.$$

This quantity represents the total available kinetic energy within $r = r_1$. A simple form for δW can be obtained if we consider a parabolic current profile $j_{\phi}(r)$, and if we assume that $q(r)$ in the centre does not differ very much from unity,

$$|1 - q(0)| \ll 1, \quad q(0) < 1.$$

Then, the $m = 1$ internal kink mode is mainly pressure driven and the potential energy is approximately [18]

$$\delta W \approx 6\pi^2 \frac{B_0^2 r_1^4}{R_0^3} |\xi_r(0)|^2 [1 - q(0)] [\beta_{\text{crit}}^2 - \beta_p^2(r_1)], \quad (27)$$

where $\beta_{\text{crit}}^2 = \frac{13}{144}$. One sees that instability, $\delta W < 0$, occurs if the driving force β_p exceeds the threshold value $\beta_{\text{crit}} \approx 0.3$.

Equation (27) qualitatively matches the observations of sawtooth oscillations in tokamaks. Sawteeth generally occur when the central plasma temperature rises due to auxiliary plasma heating. When the central temperature reaches a certain level, the plasma core becomes unstable and quickly, typically within $100 \mu\text{s}$ in the hottest tokamak plasmas, loses all its excess energy. The temperature profile after the crash is usually completely flat in the central plasma, or even hollow. It has been observed that the instability initially is a fast $m = 1$, $n = 1$ displacement of the hot plasma core, and that the part of the plasma where this motion takes place and where eventually the temperature is reduced indeed matches the $q < 1$ region.

The application of the internal $m = 1$ kink model to sawtooth collapses has many limitations, though. Firstly, we have seen that the motion at the $q = 1$ surface is highly singular. The motion minimizes δW , but in the case of an unstable mode the fast motion near $r = r_1$ corresponds to a large kinetic energy, and hence the actual growth rate of the mode is limited. However, other processes can take place. The singular behaviour was due to the fact that flux surfaces with $q < 1$ were pushed against flux surfaces with $q > 1$. In ideal MHD this process cannot proceed, and the ideal $m = 1$ mode is expected to saturate nonlinearly at a very small amplitude. It is here that resistivity, however small in a hot plasma, becomes important [19]. In the singular layer it can cause pairs of approaching flux surfaces with $q < 1$ and $q > 1$ to coalesce and to form a topologically distinct magnetic island [20]. In the process the different temperatures of the two merging surfaces are of course averaged. In

Kadomtsev's model of the sawtooth relaxation [21], the reconnection process proceeds until the entire plasma core is replaced by the island and as a result $q = 1$ in the entire central region. Also the resulting temperature and density profiles are practically flat in this region. However, this model does not match all observations of sawteeth. For instance, sawtooth crash times much shorter than the prediction of the Kadomtsev model have been observed. In addition, measurements of the central q -profile have been made which indicate that sawteeth can occur with $q(0) < 0.8$ throughout the sawtooth cycle [22]. Ref. [28] gives a review of $m = 1$ mode theory.

III. PRESSURE DRIVEN INSTABILITIES

A. Introduction

In this section modes are considered that are mainly driven by the pressure gradient, *i.e.*, modes for which the fifth term in the intuitive form of the energy functional (19) is the dominant destabilizing contribution. One sees that this term can be destabilizing when $\xi \cdot \nabla p$ and $\xi \cdot \kappa$ have the same sign, and this effect is strongest when the vectors ∇p and κ are in the same direction (unfavourable curvature). To clarify this situation for tokamak equilibria, we rewrite the momentum balance equation $\nabla p = \mathbf{j} \times \mathbf{B}$ as

$$\nabla p = B^2 \kappa - \frac{1}{2} \nabla_{\perp} B^2, \quad (\nabla_{\perp} = \nabla - \mathbf{b}\mathbf{b} \cdot \nabla)$$

Suppose for a start that the plasma pressure is balanced by the magnetic pressure, the second term on the right. However, due to the toroidal geometry B has an overall $1/R$ dependence. Therefore, $\nabla_{\perp} B^2$ is necessarily directed outward at the low field side of the torus, *i.e.*, magnetic pressure cannot prevent a plasma column from expanding in the ∇R direction. Hence, at the low field side the magnetic curvature term (the pull of the field lines) must balance the pressure gradient. It is clear from Eq. (19) that this results in a region of bad curvature ($\kappa \cdot \nabla p > 0$).

In such a region a flux tube is pulled inward by its own tension and pushed outward by the pressure gradient. Thus, if a flux tube of higher pressure could interchange position with a flux tube of lower pressure, their changes of the magnetic energy would cancel while pressure energy would be released. If the motions of the flux tubes in a bad curvature region were not constrained in other ways, instabilities could occur on an arbitrarily small scale. The process would be analogous to the Rayleigh-Taylor instability.

Two effects prevent this process from happening universally. Firstly, field lines in a tokamak pass regions of favourable curvature (where the magnetic pressure confines the plasma) as well as bad curvature regions. Indeed, the bad curvature region in a tokamak plasma can be minimized by a suitable combination of outward pointing triangularity and vertical elongation. Secondly, in the presence of magnetic shear, field lines on neighbouring flux surfaces are not

perfectly aligned so that interchange of field lines requires some magnetic energy.

B. Ballooning stability

The pressure-driven modes that are generally the most unstable (and which give rise to the most stringent stability limits) are the so-called ballooning modes. These modes owe their name to their tendency to have a larger amplitude in parts of the plasma where the destabilization originates, in a tokamak usually the low field side. Such a spatial variation of the amplitude needs to be of a very particular nature in order to avoid the strong stabilizing effect of the magnetic field. In contrast, kink modes avoid this stabilizing effect by having an almost constant amplitude on a flux surface. Another contrast is that for ballooning modes, higher toroidal mode numbers n are more unstable. Ballooning modes have a rather complicated spatial structure because their stability depends on geometric details of the plasma, especially the curvature of the field lines. We shall avoid this complexity by focussing on the stability limit (usually a limit on the pressure gradient). Exactly at the stability boundary, which is found in the limit $n \rightarrow \infty$. The corresponding modes are highly localized in radius, so that we obtain stability criteria for each flux surface separately.

We shall find the marginally stable modes by minimizing $\delta W(\xi)$, which is equivalent to solving Eq. (18). In terms of the minimized value of the energy functional, the criterion for instability is then $\delta W_{\min} < 0$. Our approach will be to consider only a specific class of instabilities, with high poloidal and toroidal mode numbers m and n . As we will see, such modes tend to be rather localized in r . We are in effect considering the situation where a gradually evolving (intensively heated) plasma equilibrium, when it reaches stability limits, initially does so in a small volume. Therefore, we expect the first instability to occur to be a localized one. Though this is the most straightforward situation, we will see in the next section that some of the most common instabilities affect a rather large plasma volume, what makes them more dangerous for confinement.

Here, we will consider instabilities in the limit $n \rightarrow \infty$. Connor, Hastie, and Taylor [23] have treated this limit, neglecting $\mathcal{O}(1/n^2)$ but retaining $\mathcal{O}(1/n)$ terms. They have shown that the $\mathcal{O}(1/n)$ terms are always stabilizing. In this sense, the most unstable modes are the ones with $n = \infty$. Therefore, in this section we will take the limit $n \rightarrow \infty$ and neglect the $\mathcal{O}(1/n)$ terms right away. The minimization of δW proceeds in five steps [7], bringing us from the three-dimensional vector equation $\mathbf{F}(\xi) = 0$ to a one-dimensional equation for one scalar function.

1. The plasma compression term in (19) vanishes by minimization with respect to ξ_{\parallel} , which is chosen in such a way that $\nabla \cdot \xi = 0$ almost everywhere in the plasma.

2. One cannot take the limit $n \rightarrow \infty$ straight away. If one considers high mode numbers m and n , one quickly sees that the stabilizing contribution $|\mathbf{B} \cdot \nabla \xi_{\perp}|^2$ to the field line bend-

ing energy $\frac{1}{2} \int d^3x |\mathbf{Q}_\perp|^2$ is proportional to $(n - m/q)^2$ and is therefore much larger than the destabilizing terms in (19). Hence, the most unstable modes will tend to be aligned to the field lines, $m \approx nq$. In more general words, ξ_\perp will vary strongly only perpendicular to the field lines ($\mathbf{k}_\perp \gg 1/a$) while varying slowly, on the scale of the machine size, along the field lines ($k_\parallel \sim 1/a$). We implement this ordering by means of an eikonal representation for ξ_\perp [23, 24],

$$\xi_\perp(\psi, \theta, \phi) = \xi_\perp(\psi, \theta) e^{inS}, \quad \mathbf{B} \cdot \nabla S(\psi, \theta, \phi) = 0.$$

Since n is large, e^{inS} is a rapidly varying function, while $\xi_\perp(\psi, \theta)$ varies slowly.

$$|n \nabla S| \gg \frac{1}{a}, \quad |\nabla \xi_\perp| \sim \frac{|\xi_\perp|}{a}.$$

This formalism serves its purpose. The large quantity ∇S does not enter the field line bending energy as one can see by working out \mathbf{Q} in terms of ξe^{inS} ,

$$\mathbf{Q}_\perp = e^{inS} [\nabla \times (\xi_\perp \times \mathbf{B})]_\perp.$$

The energy functional becomes

$$\begin{aligned} \delta W = \frac{1}{2} \int d^3x & \left[|\mathbf{Q}_\perp|^2 + B^2 |in \nabla S \cdot \xi_\perp + \nabla \cdot \xi_\perp + 2\boldsymbol{\kappa} \cdot \xi_\perp|^2 \right. \\ & - 2(\xi_\perp \cdot \nabla p)(\xi_\perp^* \cdot \boldsymbol{\kappa}) \\ & \left. - j_\parallel \xi_\perp^* \times \mathbf{b} \cdot \mathbf{Q}_\perp e^{-inS} \right] \end{aligned} \quad (28)$$

3. At this stage the mode number n still appears in the field compression (second term) and leads to the large stabilizing energy contribution $\frac{1}{2} n^2 \int d^3x B^2 |\nabla S \xi_\perp|^2$. In order to keep this term finite, the perturbation ξ_\perp must have the general form

$$\xi_\perp = \xi_{\perp 0} + \frac{\xi_{\perp 1}}{n}, \quad \xi_{\perp 0} \equiv \frac{X}{B} \mathbf{b} \times \nabla S \quad (29)$$

where $X(\psi, \theta)$ is a new scalar function independent of $\xi_{\perp 1}$. One may verify that with ξ_\perp of the form (29), the term of concern in Eq. (28) is indeed finite,

$$in \nabla S \cdot \xi_\perp = i \nabla S \cdot \xi_{\perp 1}.$$

4. Now we can take the limit $n \rightarrow \infty$. In this limit

$$\begin{aligned} \mathbf{Q}_\perp &= \nabla \times [(X \mathbf{b} \times \nabla S) \times \mathbf{b}]_\perp \\ &= \nabla \times (X \nabla S)_\perp \\ &= \nabla \times (X \nabla S) - \mathbf{b} \mathbf{b} \cdot \nabla \times (X \nabla S) \\ &= (\mathbf{b} \cdot \nabla X) \mathbf{b} \times \nabla S. \end{aligned}$$

The j_\parallel -term vanishes because

$$(\xi_{\perp 0}^* \times \mathbf{b}) \cdot \mathbf{Q}_\perp = \frac{X^*}{B} \nabla S \cdot (\mathbf{b} \cdot \nabla X) \mathbf{b} \times \nabla S = 0.$$

Thus the energy becomes

$$\begin{aligned} \delta W = \frac{1}{2} \int d^3x & \left[|\nabla S|^2 |\mathbf{b} \cdot \nabla X|^2 \right. \\ & + B^2 |i \xi_{\perp 1} \cdot \nabla S + \nabla \cdot \xi_{\perp 0} + 2\boldsymbol{\kappa} \cdot \xi_{\perp 0}|^2 \\ & \left. - 2(\mathbf{B} \times \nabla S \cdot \nabla p)(\mathbf{B} \times \nabla S \cdot \boldsymbol{\kappa}) |X|^2 \right]. \end{aligned}$$

The variable $\xi_{\perp 1}$ appears only in the second term. Therefore, the energy can be minimized with respect to $\xi_{\perp 1}$ simply by choosing $i \xi_{\perp 1} \cdot \nabla S = -\nabla \cdot \xi_{\perp 0} - 2\boldsymbol{\kappa} \cdot \xi_{\perp 0}$, thus eliminating the field compression term altogether.

5. The remaining functional contains only one variable X and its derivative along the field lines, $\mathbf{b} \cdot \nabla X$. It is essentially one-dimensional since it does not contain the radial derivative of X . We can therefore consider a potential energy functional on each flux surface separately

$$\begin{aligned} \delta W = \int d\theta & J \left[|\nabla S|^2 |\mathbf{b} \cdot \nabla X|^2 - \right. \\ & \left. 2(\mathbf{B} \times \nabla S \cdot \nabla p)(\mathbf{B} \times \nabla S \cdot \boldsymbol{\kappa}) |X|^2 \right] \end{aligned} \quad (30)$$

where the Jacobian is $J(\psi, \theta, \phi) = (d\ell/d\theta)/B_p$. The derivative in the magnetic field direction can be rewritten as $\mathbf{b} \cdot \nabla X = (\partial X/\partial \theta)/JB$. Hence the Euler equation for X , associated with the functional (30) is given by

$$\frac{1}{J} \frac{\partial}{\partial \theta} \left(\frac{|\nabla S|^2}{JB^2} \frac{\partial X}{\partial \theta} \right) + 2(\mathbf{B} \times \nabla S \cdot \nabla p)(\mathbf{B} \times \nabla S \cdot \boldsymbol{\kappa}) X = 0. \quad (31)$$

It is a linear second order differential equation in the poloidal coordinate θ . Note that the combination $J^{-1} \partial/\partial \theta$ is independent of the definition of the poloidal coordinate.

How have we lost the radial dimension of our stability problem? It is not a straightforward matter of invariance, as is the case with the ϕ coordinate. The modes we consider have $\mathbf{b} \cdot \nabla = k_\parallel \ll |\mathbf{k}_\perp|$, which is a non-trivial situation in a tokamak because of the presence of magnetic shear: q varies with the radius. The answer is that we have hidden these difficulties in our assumption that we can find an eikonal function that satisfies $\mathbf{B} \cdot \nabla S = 0$. In the orthogonal flux coordinates this condition can be written as

$$\frac{F}{R^2} \frac{\partial S}{\partial \phi} + \frac{1}{J} \frac{\partial S}{\partial \theta} = 0. \quad (32)$$

We now consider a single toroidal harmonic, $S(\psi, \theta, \phi) = -\phi + S(\psi, \theta)$, and obtain solutions by integrating Eq. (C) with respect to θ ,

$$S = -\phi + F \int_{\theta_0}^{\theta} \frac{J}{R^2} d\theta. \quad (33)$$

The integration boundary θ_0 is a free parameter in our solution. The energy functional should be minimized with respect to θ_0 as well in order to find the most unstable mode. For up-down symmetric equilibria the minimizing

value often is $\theta_0 = 0$. We recognize in (33) an incomplete version of the integral that yields the safety factor, $q(\psi) = (F/2\pi) \oint d\theta J/R^2$. It is clear now that the function S satisfies

$$S(\psi, \theta + 2\pi, \phi) = S(\psi, \theta, \phi) + 2\pi q.$$

Let us consider the value of S on two neighbouring field lines with a small spatial separation. In the presence of magnetic shear these lines will differ slightly, by Δq . Then, since n is large, the values of e^{inS} on these field lines will diverge strongly from each other, at the rate $n\Delta q$, when θ increases. Therefore e^{inS} depends so strongly on the radial coordinate that almost all radial dependence of the vector ξ is contained in the factor e^{inS} .

It seems that we have treated complicated behaviour as a function of the radius in a compact way. There are, however, two problems with this approach. The most obvious problem is that the radial dependence of e^{inS} is strongly oscillatory and does not give rise to a radially localized eigenfunction ξ , although Eq. (31) applies to any individual flux surface. The second problem arises because for irrational values of q , the function e^{inS} is not periodic in θ , and neither is ∇S . Hence, the constraint (32) is incompatible with periodicity. Even if a periodic solution $X(\theta)$ can be found, the associated displacement vector $\xi(\psi, \theta, \phi)$ is not periodic in θ and hence not acceptable as a physical perturbation of the equilibrium. We will see that the two problems are related and that the solution of the second problem takes care of the first one as well.

A practical solution of these difficulties has been given by Connor, Hastie, and Taylor [24]. The basic idea is to give up the periodicity in θ in the energy functional (30), and allow the generalized angle θ run over the entire real axis $(-\infty, \infty)$. Also the Euler equation (31) should be considered as a differential equation over the real axis, with its boundary conditions in $\theta = \pm\infty$. With this Ansatz, we make four observations.

1. The linear second order equation (31) has in general two independent solutions, one of which vanishes for $\theta \rightarrow -\infty$, the other for $\theta \rightarrow \infty$. Marginal stability corresponds to special values of the equilibrium quantities for which the equation has a solution that vanishes for $\theta \rightarrow \pm\infty$ simultaneously. This we require since the eigenmode must have a finite energy content. Of course, away from marginal stability one still requires that the eigenfunction is finite, and a kinetic energy term with the proper value of ω^2 has to be added to Eq. (31) to make this possible.

2. Now consider the eigenfunction $\xi_Q(x)$ associated with a finite solution $X(\theta)$ of Eq. (31). This eigenfunction is not periodic in θ and hence not physical but it does satisfy the equation of motion at marginal stability (18), $F(\xi_Q) = 0$, everywhere in the extended (ψ, θ, ϕ) space. The function ξ_Q is called a quasi-mode. Note that the force operator itself is periodic, $F(\psi, \theta, \phi) = F(\psi, \theta + 2\pi, \phi)$. Hence, if the shifted quasimode $\xi_Q(\psi, \theta + 2\pi k, \phi)$ is a solution of the force balance equation as well.

3. The force operator F is a **linear** operator.
4. The infinite sum

$$\xi(\psi, \theta, \phi) = \sum_{k=-\infty}^{\infty} \xi_Q(\psi, \theta + 2\pi k). \quad (34)$$

is clearly periodic in θ if it converges. We have effectively wound the infinite θ -axis around the unit circle, summing the contributions to the eigenfunction on it in the process. It is clear that the proper boundary conditions for the generalized Euler equation have to include $X \rightarrow 0$ for $\theta \rightarrow \pm\infty$ in order to have a convergent sum.

We will now combine these four observations. According to observation 2, all terms in the sum (34) satisfy the equation of motion at marginal stability and point 3 (linearity) guarantees that the sum (34), if it exists, also satisfies this equation. Observation 1 states that the necessary boundary conditions for the existence of the sum, $X(\theta \rightarrow \pm\infty) = 0$, are satisfied in the case of marginal stability. Finally, according to point 4, expression (34) defines a periodic solution of the marginal stability equation (18).

Expression (34) is a sum over many terms that have different values of the non-periodic function e^{inS} , which contains the radial dependence of ξ . Note that the individual quasimodes are not bounded in the radial direction since the exponent vanishes nowhere. Fortunately, as pointed out by Pegoraro and Schep [25], the sum (34) is radially localized at the flux surface where we have solved Eq. (31). They show that one can make a Fourier transformation from an extended poloidal coordinate to an extended radial coordinate, and hence the poloidal and radial widths of the mode are inversely proportional. Loosely speaking, ballooning modes tend to be rather localized in the radial direction when they have an extended range in the poloidal coordinate.

Satisfied with the above picture, one can find the stability at a given flux surface by solving Eq. (31) for that particular value of ψ . The coefficients in the differential equation can be computed numerically from the q -profile, the pressure gradient, and the shape of the flux surface. One usually obtains such data from a numerical equilibrium solver (solver of the Grad-Shafranov equation) though in principle one does not need a solution in the entire plasma in order to find the stability of a single flux surface.

C. The Mercier criterion and β -limits

Straightforward integration of the ballooning equation (31) is often numerically demanding because the coefficients contain “slowly” and “quickly” varying functions of θ . The quantity $|\nabla S|$ is a steadily increasing function for $\theta \rightarrow \infty$. On the other hand, quantities κ , J , and B are periodic functions of θ . They can be considered rapidly oscillating functions of θ on the scale on which $|\nabla S|$ becomes large. One can find the asymptotic behaviour of solutions $X(\theta)$ by a procedure of averaging over the oscillating terms. For large

θ equation (31) takes the form

$$\frac{d}{d\theta} \left(\theta^2 \frac{dX}{d\theta} \right) + D_M X = 0, \quad (35)$$

where the so-called Mercier constant D_M is a complicated function of the equilibrium quantities on the flux surface. It follows that the general asymptotic form of $X(\theta)$, *i.e.*, the general solution of (35) is

$$X = c_+ \theta^{\lambda_+} + c_- \theta^{\lambda_-}, \quad \lambda_{\pm} \equiv -\frac{1}{2} \pm \sqrt{\frac{1}{4} - D_M}.$$

If $D_M < \frac{1}{4}$ there is a large solution $\sim \theta^{\lambda_+}$ and a small solution $\sim \theta^{\lambda_-}$. The large solution makes the integral (28) infinite, so only the small solution is allowed. The ballooning criterion is precisely the condition under which one solution of (31) is asymptotically small, $\sim \theta^{\lambda_-}$, for both $\theta \rightarrow -\infty$ and $\theta \rightarrow \infty$. The situation is different if $D_M > \frac{1}{4}$. In this case both exponents λ_{\pm} are complex and lead to oscillatory solutions with a finite energy content. In this case all solutions of Eq. (31) are allowed, *i.e.*, there is always instability and there is no ballooning stability boundary. It can be shown that this situation is unstable by constructing radially localized trial functions ξ_T for which $\delta W(\xi_T^*, \xi_T) < 0$, instead of constructing proper eigenfunctions as required for the ballooning stability criterion. The condition

$$D_M < \frac{1}{4}. \quad (36)$$

is the Mercier criterion [26]. It is a necessary condition for stability. If it is violated instability occurs. If it is satisfied, the plasma can still be unstable to ballooning modes. A simple closed form for D_M can be derived for large aspect-ratio circular flux surfaces. In this approximation the ballooning equation takes the form

$$\frac{d}{d\theta} \left((1 + P^2) \frac{dX}{d\theta} \right) + \alpha (\cos \theta + P \sin \theta + V) X = 0, \quad (37)$$

where the ‘‘shear integral’’ P originates from $|\nabla S|$ in Eq. (31) and the potential term V gives the effect of the ‘‘magnetic well’’ in the plasma centre. They are given by

$$P = s\theta - \alpha \sin \theta, \quad V = \varepsilon \left(1 - \frac{1}{q^2} \right).$$

The quantities

$$s = \frac{r}{q} \frac{dq}{dr}, \quad \alpha = -2 \frac{Rq^2}{B^2} \frac{dp}{dr}, \quad (38)$$

are the magnetic shear and the normalized pressure gradient. In this model the Mercier index is

$$D_M = \varepsilon \frac{\alpha}{s^2} \left(\frac{1}{q^2} - 1 \right). \quad (39)$$

Combining Eqs. (36) and (39) one sees that Mercier instability requires q below unity, low shear, and a large pressure gradient.

In the case that the Mercier criterion indicates stability, $D_M < \frac{1}{4}$, one can test Eq. (37) for ballooning instability. Also in the case of ballooning modes one finds that generally low shear is more unstable than high shear. This is understandable since instabilities tend to align with the magnetic field on a given flux surface. The rate at which the mode and the magnetic field become misaligned on neighbouring flux surfaces is proportional to the magnetic shear. The pressure gradient is destabilizing, and in general large α will lead to instability. Surprisingly, Eq. (37) also implies that for very large values of α and not too high shear a second regime of stability exists. For such high pressure the Shafranov shift gives rise to a very asymmetric plasma cross section, with flux surfaces tightly pushed together at the low field side. In that region the local magnetic shear (not the flux quantity s defined in (38)) becomes high and stabilizes ballooning modes. It turns that if the plasma cross section is strongly triangular, the second stability regime is also accessible for lower values of the pressure gradient, provided the magnetic shear is negative.

Perhaps the most powerful application of ballooning stability analysis is the numerical optimization of the total plasma β by varying the p and q profiles and the plasma shape, under the constraint that all flux surfaces be Mercier and ballooning stable. The best known of such studies has been carried out by Troyon *et al.* [27]. They have varied the p and q profiles as well as the plasma elongation and triangularity. Their stability criteria involve ballooning stability on every flux surface. In addition, there are the constraints $q(a) > 2$ in order to prevent $m = 2$ external kink modes and $q(0) > 1$ in order to satisfy the Mercier criterion and to avoid $m = 1$ internal kink modes. The resulting β -limit is

$$\beta = 0.028 \frac{I_0}{aB_0},$$

where the units are I_0 (MA), a (m), and B_0 (T). This result is called the Troyon limit. It can be of limited validity for instance when instabilities that are not listed above play a role. A positive aspect is that a tokamak discharge may exceed the Troyon limit if part of the plasma is in the second stability regime.

In experiments, ballooning limits are often ‘‘soft’’. This means that when attempts are made to increase the tokamak plasma pressure with intense heating, a certain pressure gradient cannot be exceeded. This is probably related to the fact that the instabilities near the ballooning stability limit are very localized. The small amplitudes of the instabilities are then seen as enhanced heat loss, not as a disruptive instability. However, ballooning modes have also been associated with some of the Edge Localized Modes (ELMs) observed in tokamaks. These modes appear repetitive as a sudden loss of the outer layer of plasma from the tokamak.

ACKNOWLEDGMENT

This work, supported by the European Communities under the contract of Association between EURATOM/FOM, was carried out within the framework of the European Fusion Programme with financial support from NWO. The views and opinions expressed herein do not necessarily reflect those of the European Commission.

REFERENCES

1. S. Sharapov "MHD and fast particle effects", *these proceedings*.
2. H. Wilson "Neo-classical tearing mode", *these proceedings*.
3. R.M. Kulsrud, "General stability theory in plasma physics," in "Proc. of the Int. School of Physics "Enrico Fermi", Course XXV, "Advanced Plasma Theory"" (edited by M.N. Rosenbluth), Academic Press, New York, (1964).
4. R.M. Kulsrud, "MHD description of plasma," in "Handbook of Plasma Physics" (edited by M.N. Rosenbluth and R.Z. Sagdeev), North-Holland, Amsterdam, Vol. 1, p. 115, (1983).
5. I.B. Bernstein, E.A. Frieman, M.D. Kruskal, and R.M. Kulsrud, "An energy principle for hydromagnetic stability problems," *Proc. Roy. Soc. A* **244**, 17, reprinted in "Magnetohydrodynamic Stability and Thermonuclear Confinement" (edited by A (1958). Jeffrey and T. Taniuti), Academic Press, New York (1966).
6. J.P. Freidberg, "Ideal magnetohydrodynamic theory of magnetic fusion systems," *Rev. Mod. Phys.* **54**, 801 (1982).
7. J.P. Freidberg, "Ideal Magnetohydrodynamics", Plenum Press, New York (1987).
8. J.P. Goedbloed and S. Poedts, "Principles of Magnetohydrodynamics", Cambridge University Press (2004).
9. I.B. Bernstein, "The variational principle for problems of ideal magnetohydrodynamic stability," in "Handbook of Plasma Physics" (edited by M.N. Rosenbluth and R.Z. Sagdeev), North-Holland, Amsterdam, Vol. 1, p. 421, (1983).
10. K. Hain, R. Lüst, and A. Schlüter, "Zur Stabilität eines Plasmas," *Z. Naturforschung*, **12**, 833 (1957).
11. G. Laval, C. Mercier, and R. Pellat, "Necessity of the energy principles for magnetostatic stability," *Nucl. Fusion* **5**, 156 (1965).
12. W.A. Newcomb, "Hydromagnetic stability of a diffuse linear pinch," *Ann. Phys. (NY)* **10**, 232 (1960).
13. V.D. Shafranov, "Hydromagnetic stability of a current carrying pinch in a Strong Longitudinal Field," *Zhurnal Tekhnicheskoi Fiziki* **40**, 241 (1970) [*Sov. Phys.-Techn. Phys.* **15**, 175 (1970)].
14. H.J. de Blank, "Plasma equilibrium in tokamaks," and references therein, *these proceedings*.
15. J.A. Wesson, "Hydromagnetic stability of tokamaks," *Nucl. Fusion* **18**, 87 (1978).
16. H.R. Koslowski, "Operational limits and limiting instabilities in tokamak machines," *these proceedings*.
17. M.N. Rosenbluth, R.Y. Dagazian, and P.H. Rutherford, "Non-linear properties of the internal kink instability in the cylindrical tokamak," *Phys. Fluids* **16**, 1894 (1973).
18. M.N. Bussac, R. Pellat, D. Edery, and J.L. Soule, "Internal kink modes in toroidal plasma with circular cross-section," *Phys. Rev. Lett.* **35**, 1638 (1975).
19. H.P. Furth, J. Killeen, and M.N. Rosenbluth, "Finite resistivity instabilities of a sheet pinch," *Phys. Fluids* **6**, 459 (1963).
20. R.B. White, "Resistive instabilities and field line reconnection," in "Handbook of Plasma Physics" (edited by M.N. Rosenbluth and R.Z. Sagdeev), North-Holland, Amsterdam, Vol. 1, p. 611, (1983).
21. B.B. Kadomtsev, "Disruptive instability in tokamaks," *Fizika Plazmy* **1** (1975) 710 [*Sov. J. Plasma Phys.* **1** (1976) 389].
22. H. Soltwisch et al., in *Plasma Physics and Controlled Nuclear Fusion Research 1986*, Proceedings of the 11th International Conference, Kyoto (IAEA, Vienna, 1987), Vol. 1, p. 263.
23. J.W. Connor, R.J. Hastie, and J.B. Taylor, "High mode number stability of axisymmetric toroidal plasmas," *Proc. Roy. Soc. A* **365**, 1 (1979).
24. J.W. Connor, R.J. Hastie, and J.B. Taylor, "Shear, periodicity, and plasma ballooning modes," *Phys. Rev. Lett.* **40**, 396 (1978).
25. F. Pegoraro and T.J. Schep, "Low-frequency modes with high toroidal mode numbers: A general formulation," *Phys. Fluids* **24**, 478 (1981).
26. C. Mercier, "Un critère nécessaire de stabilité hydro-magnétique pour un plasma en symétrie de révolution," *Nucl. Fusion* **1**, 47 (1960).
27. F. Troyon, R. Gruber, H. Sauremann, S. Semenzato, and S. Succi, "MHD limits to plasma confinement," *Plasma Phys. Controlled Fusion* **26**, 209 (1984).
28. S. Migliuolo, "Theory of ideal and resistive $m=1$ modes in tokamaks," *Nucl. Fusion* **33**, 1721 (1993).

OPERATIONAL LIMITS AND LIMITING INSTABILITIES IN TOKAMAK MACHINES

H. R. Koslowski

*Forschungszentrum Jülich GmbH, Institut für Energie- und Klimaforschung 4 – Plasmaphysik
D-52425 Jülich, Germany*

ABSTRACT

The optimisation of the fusion output power in a tokamak device of given size and magnetic field requires to maximise the fusion triple product $nT\tau_E$. The parameter space for safe, reliable, and stable operation of a tokamak is limited by various constraints. Operational limits of tokamak devices originate from violation of magnetohydrodynamic stability criteria or excessive radiation from impurity ions in the plasma. Exceeding the boundaries of stable operation may either result in a deterioration of plasma confinement, or even lead to the uncontrolled disruptive termination of the discharge.

I. INTRODUCTION

The need to optimise the tokamak operation in order to get a sufficient fusion yield is the main motivating force to explore and understand operational limits. As a starting point, a quite general 0-dimensional consideration of a fusion power generating machine will be presented. The thermonuclear power density (i.e. released power per volume) in a D-T plasma is

$$P_{DT} = n_D n_T \langle \sigma v \rangle \epsilon_{DT}, \quad (1)$$

where $n_{D,T}$ are the ion densities of D and T nuclei, $\langle \sigma v \rangle$ is the rate coefficient for the fusion reaction, and $\epsilon_{DT} = 17.6 \text{ MeV}$ is the released energy per fusion reaction. The fusion power density has a maximum when the concentrations of both, D and T ions, are each 50% of the total ion density. In the temperature range between 10 keV and 20 keV the rate coefficient scales within a few % proportional to the square of the temperature, $\langle \sigma v \rangle \propto T^2$. Using the definition of the plasma beta, the ratio between kinetic plasma pressure, p , and magnetic field pressure, $\beta = 2\mu_0 p / B^2$, substituting quantities in equation 1, and integrating over the plasma volume gives

$$P_{fus} \propto p^2 V \propto \beta^2 B^4 V. \quad (2)$$

This equation shows that the achievable fusion power of a tokamak device strongly depends on the magnetic field and the machine size, but there is a considerable dependence on the plasma pressure, i.e. the way the

machine is operated. One way to increase the fusion power output of a machine is to build a larger device with a higher magnetic field. Beside the fact that especially increasing the size of the machine will increase the cost, there are technological limits. The magnetic field can not be increased arbitrarily because the required superconducting coils only allow a maximum field because superconductivity gets lost at magnetic field strengths above a critical field H_c . Another route to performance optimisation is opened due to the dependence of the fusion power on the square of the plasma pressure. Appropriate means to tailor the discharge and increase the pressure at a given magnetic field are required.

The most common operational scenario of a tokamak machine nowadays (and foreseen as base operational mode on ITER) is the so-called ELMy H-mode (*high confinement mode*). This is a plasma regime (only observed in tokamaks with a poloidal divertor) where a transport barrier at the plasma edge builds up, steepens the plasma profiles, and leads to an increase of the stored energy in the plasma [1]. The energy confinement times of H-mode plasmas have been well documented in numerous experiments on many divertor tokamaks and a scaling law based on engineering quantities has been derived [2]:

$$\tau_{E,th} \propto I_p^{0.93} B_t^{0.15} P^{-0.69} n_e^{0.41} M^{0.19} R^{1.97} \epsilon^{0.58} \kappa^{0.78} \quad (3)$$

(I_p plasma current, B_t toroidal magnetic field, P heating power, n_e line averaged electron density, M isotope mass, R major tokamak radius, $\epsilon = a/R$ inverse aspect ratio, a minor tokamak radius, κ plasma elongation). Without going in too much detail¹, it can be seen again that increasing machine size, and increasing plasma current and density have a beneficial effect on the confinement. In addition, the plasma elongation has a strong influence on the confinement properties.

The equations above indicate which plasma parameters have to be increased in order to achieve best plasma performance in a tokamak machine of given size and magnetic field. However, there are only a few actuators for external control of plasma parameters. The density can be controlled by adjusting the gas

¹For a detailed discussion of this scaling law see J. Ongena "Heating, Confinement and Extrapolation to Reactors", these proceedings.

fuelling into the plasma. The plasma current is controlled by adjusting the loop voltage through the flux change in the primary winding of the transformer. The plasma temperature can be regulated by auxiliary heating systems, e.g. neutral beam heating or wave heating in the ion cyclotron, electron cyclotron, and lower hybrid range of frequencies. As a side effect (or in some situations deliberately wanted) the plasma heating methods can drive localised currents in the plasma. This is utilised to increase plasma stability or access a certain confinement mode of the plasma.

All actions and attempts to optimise the fusion power output are constraint by operational boundaries, i.e. the plasma density can't be increased infinitely but has to be kept below the so-called density limit. The plasma current cannot be increased above a critical value without excitation of magnetohydrodynamic (MHD) instabilities. In the worst case the violation of operational limits leads to a disruption of the discharge, which is a sudden breakdown of the plasma current and a release of the stored energy to the first wall of the tokamak. The severity of operational limits can be categorised into *soft limits* which result in a deterioration of confinement and a related reduction of fusion power, and *hard limits* which eventually lead to a disruption with potentially harmful impact on the integrity of the machine.

The mechanisms leading to a deterioration of confinement or initiating a plasma disruption have to be studied in detail in order to devise strategies to avoid touching an operational limit, stabilise an instability once it occurs, or completely prevent disruptions to happen.

II. OPERATIONAL PARAMETER SPACE OF A TOKAMAK: THE HUGILL DIAGRAM

An overview on the operational space of a specific tokamak machine is usually given in form of the so-called *Hugill diagram* [3]. Figure 1 shows such a plot for the TEXTOR tokamak² The Hugill diagram is a plot of the inverse safety factor at the plasma surface, $1/q_a$, versus the Murakami number, $n_e R/B_t$ [4]. Because in a cylindrical approximation the edge safety factor³ can be written as

$$q_a = 5a^2 B_t / (R I_p), \quad (4)$$

the inverse of the edge safety factor is proportional to the plasma current I_p . Therefore the Hugill diagram

²The TEXTOR tokamak was located in the Forschungszentrum Jülich and has been in operation for 30 years until 2013. See O. Neubauer et al., *Fusion Sci. Technol.* **47** 76 (2005) for a description of the machine.

³The edge safety factor is infinite in a poloidal X-point divertor configuration. In those cases the safety factor q_{95} of the flux surface encompassing 95% of poloidal flux is used synonymously.

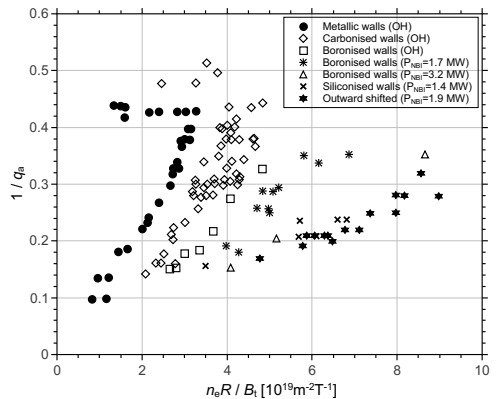


Figure 1: Hugill diagram for the TEXTOR tokamak.

can be seen as a plot of the plasma current versus the line averaged plasma density (scaled by machine size).

The operational space of the TEXTOR tokamak is shown in figure 1. The data have been collected during several years and cover various experimental campaigns with different methods of wall conditioning and ohmic as well as neutral beam injection heated scenarios [5, 6]. Careful inspection of this diagram reveals the existence of three operational boundaries.

At first one notices the absence of data points above an inverse edge safety factor of 0.5, i.e. $q_a < 2$. When the edge safety factor falls below 2 the $m = 2, n = 1$ external kink mode gets destabilised [7]. This mode grows to a large amplitude⁴. Eventually the plasma will end up in a disruption.

A second operational limit manifests itself by the absence of data points in the lower right of the diagram. For a given plasma current (which corresponds to a specific $1/q_a$ value) there exists a maximum electron density. This is an empirical boundary which is not as sharply defined as the $q_a > 2$ limit discussed before. The Hugill diagram shows that the maximum density depends on the first wall surface material of the tokamak, and on the applied heating power. Especially the improvement of wall conditioning techniques led to an increase of tokamak performance which can be attributed to cleaner plasmas with a lower effective charge, Z_{eff} [8]. There is obvious link of the achievable density with the purity of the plasma, or in other words, the plasma can sustain a higher density when there are less impurity ions in the plasma. Impurity ions lead to an increased energy loss of the plasma which increases with density up to the critical point when the radiated power

⁴Mode amplitude is the radial magnetic field component, but in this context the displacement of flux surfaces is used synonymously.

equals the heating power. It can be seen in figure 1 that discharges with neutral beam heating can be stable operated at higher density.

A third limit is not very obvious but results in a lack of data points at very low density, i.e. close to the left axis of figure 1. Due to the toroidal loop voltage the electrons in the plasma experience an accelerating force. Under normal conditions the electric force is balanced by the friction force resulting from collisions. Because friction scales $\propto n_e v^{-2}$ there is a critical velocity upon which an electron is continuously accelerated and *runs away*. The Maxwellian distribution function develops a non-thermal tail. The plasma operation under these conditions has to be avoided because runaway electrons (RE) will be accelerated up to several MeV of energy and the RE beams can carry a substantial amount of energy which, when released to the first wall, may cause serious damage to the machine.

III. RADIATION LIMITS

Tokamak plasmas always contain a certain amount of impurity ions. These ions originate either from the material of the surrounding walls and are released by sputtering, or impurities are deliberately introduced in the discharge for the purpose to cool the plasma edge or divertor region in order to control plasma surface interaction. The presence of these impurity ions results in an increase of the radiation from the plasma which brings about the possibility of radiation driven instabilities.

A. Radiation Mechanisms

In a tokamak plasma different sources for radiation losses are present. The power radiated by *bremstrahlung* due to electron-ion collisions (free-free) or recombination (free-bound) scales like

$$P_{br} \propto Z^2 n_e n_Z T_e^{1/2}, \quad (5)$$

where Z is the ion charge state⁵, n_e and n_Z are the densities of electrons and ions in charge state Z , and T_e denotes the electron temperature. For normal tokamak operational conditions this power loss can be easily supplied by the plasma heating systems.

A more substantial power loss is due to *electron cyclotron radiation*:

$$P_c = e^4 / (3\pi\epsilon_0 m_e^3 c^3) B^2 n_e T_e, \quad (6)$$

where e is the elementary charge, ϵ_0 the permeability of free space, m_e the electron mass, and c the velocity of light. The power radiated by electron cyclotron emission can become quite large, but it is not of concern because the plasma is optically thick at

⁵Due to the strong dependence on the effective charge number, the standard Z_{eff} diagnostic of a tokamak is the measurement of the visible bremsstrahlung.

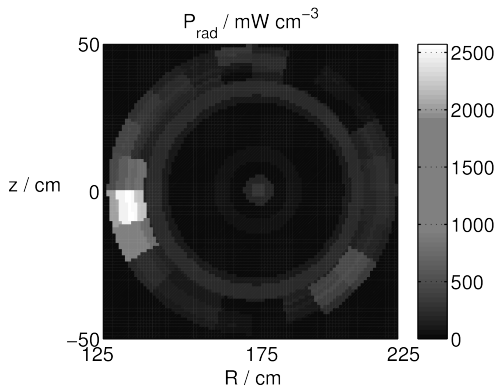


Figure 2: Asymmetric plasma radiation after onset of a MARFE in TEXTOR.

the fundamental frequency and the emitted power is immediately re-absorbed. Loss of a small fraction of radiated power can occur at the harmonic frequencies where the plasma is not optically thick.

Most important source of radiative power loss are impurity ions. They lead to an increase of bremsstrahlung losses (see equation 5) and additionally emit *line radiation* with a power density given by

$$P_R = L(T_e) n_e n_I, \quad (7)$$

where $L(T_e)$ is the cooling rate⁶ [9] for a specific impurity and n_I gives the impurity density. It is important to note that the cooling rates increase when the temperature drops, i.e. $dL_{T_e}/dT_e < 0$.

B. Density Limit

The density limit in tokamaks is actually a radiation limit. When the electron density is increased at constant pressure (i.e. without increasing the heating power), the electron temperature drops. This leads to an increase of the radiative power loss due to the above mentioned shape of the cooling rate curves. The density limit is reached when the radiative power equals the total heating power which is the sum of ohmic and auxiliary heating powers:

$$P_{rad} = P_{heat} = P_{OH} + P_{aux}. \quad (8)$$

The critical density scales like [10]

$$n_e^{crit} \propto (P_{heat}/(Z_{eff} - 1))^{1/2}. \quad (9)$$

Low effective charge and high heating power can effectively increase the density limit. This can be seen as well in the Hugill diagram figure 1 where with the progress in wall conditioning (carbonisation, boronisation) and with increased heating power larger densities were accessible.

⁶Other authors refer to this quantity as radiation parameter or radiation function.

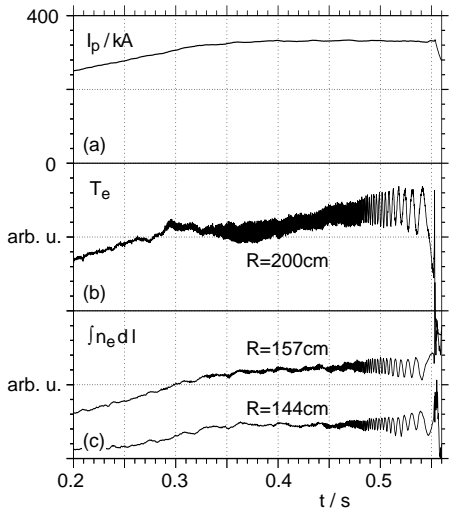


Figure 3: $m = 2, n = 1$ disruption precursor mode.

Present-day tokamaks with metal walls and/or state-of-the-art wall cleaning methods and sufficient heating power installed would allow for a rather high density limit. Unfortunately, it turns out that the radiative density limit is not dominated by a symmetric radiation belt following equation 9 but is determined by a variety of other mechanisms [11]. Particle transport at the edge, plasma detachment and recycling phenomena which plasma cooling being a key element of them all start to play a role. One important and rather common phenomenon in this context is the appearance of the so-called MARFE⁷ [12]. In a situation with local plasma cooling the characteristic shape of the cooling rate curves leads to a self-amplifying *condensation* process most often resulting in a radiation collapse. The requirement of pressure balance results in a local, cold and very dense plasma, the MARFE. Figure 2 shows a tomographic reconstruction of the poloidal radiation distribution during a MARFE. The appearance of the MARFE is strongly correlated with the recycling flux from the plasma edge [13]. Reducing this particle flux by moving the plasma away from the surrounding walls allows for higher densities (see points labelled *outward shifted* in figure 1). The data from many tokamaks has been analysed in detail [11] and a surprisingly simple scaling law could be derived:

$$\bar{n}_{e,G} = \kappa \bar{j}, \quad (10)$$

with $n_{e,G}$ the maximum line-averaged density in units of 10^{20} m^{-3} , κ the elongation of the poloidal plasma cross section, and \bar{j} the poloidal average of the current density in units of MAm^{-2} . Despite its simplicity

⁷The acronym MARFE stands for *Multifaceted Asymmetric Radiation From the Edge*.

this simple formula has been found to well approximate the density limit in a variety of tokamaks of different size.

C. Impurity Accumulation

Nowadays tokamak are more and more equipped with limiters and divertor tiles made of high-Z materials like tungsten due to their high melting temperatures and low sputtering rates. When off-normal events lead to increased thermal and particle loads high-Z material may be eroded and released to the plasma where it is transported toward the plasma centre. The strong radiation causes local cooling and flat or even hollow temperature profiles. Because the electrical conductivity scales $\sigma \propto f(Z_{eff})T_e^{3/2}$ with temperature a decrease of the central plasma current follows and enforces the temperature decay and further accumulation of the high-Z impurity on plasma axis.

IV. BETA LIMIT

In the introduction it has been shown that the increase of beta

$$\beta_t = 2\mu_0 \langle p \rangle / B_t^2, \quad (11)$$

where $\langle p \rangle$ is the volume averaged plasma pressure, is a rational way to increase fusion performance and make best use of the applied toroidal magnetic field B_t . This gives rise to the question, how large the plasma pressure can get before MHD instabilities become destabilised.

A. The Ideal Beta Limit

The maximum plasma pressure which can be confined by a given magnetic field has been calculated by Troyon [14]. In his calculations he considered stability against (i) the Mercier criterion [15], (ii) ballooning modes, and (iii) the $n = 1$ free-boundary kink mode. It has been found that the latter determines the upper limit on beta. For circular plasma cross section a simple scaling law for the poloidal beta⁸ has been found:

$$\beta_p^{max} = 0.14 (R/a) q_a. \quad (12)$$

More general, the maximum beta β_m for a given configuration⁹ can be written as

$$\beta_m = g \frac{I}{aB_t} \quad (13)$$

where g is named the *Troyon factor* and a value of $g = 2.8$ the Troyon limit. The quantity

$$\beta_N = \frac{\beta}{I/(aBt)} \quad (14)$$

⁸Same as toroidal beta in equation 11 but toroidal field is replaced by poloidal field B_p .

⁹Here configuration means plasma shape.

is called normalised beta. The stability limit can then be simply expressed as $\beta_N < g$. It turns out that the Troyon factor depends on the shape of the current density profile and can be approximated in many cases by $g = 4l_i$, where l_i is the internal inductance of the plasma.

B. Resistive Wall Modes

A certain operation mode of tokamaks, the so-called advanced scenario, makes use of an elevated q -profile, a broad current density distribution, and steep pressure gradients which lead to a large bootstrap current fraction. In this scenario the external kink mode plays the limiting role. The mode can be stabilised by a close fitting conducting wall. This will result in a somewhat higher maximum beta value. Due to the conducting wall the growth rate of the external kink is reduced to the inverse of the resistive time constant of the wall. Depending on the properties of the stabilising wall, the achievable beta is in the range

$$\beta^{no-wall} < \beta < \beta^{ideal-wall}. \quad (15)$$

In this context the beta limit is called the *resistive wall mode* (RWM) limit. Stabilisation of the RWM is proposed via two different mechanisms: (i) dissipation of the free energy of the mode by fast plasma rotation, and (ii) active feedback control to cancel the RWM field by a set of saddle coils mounted inside the vacuum vessel [16].

C. (Neoclassical) Tearing Modes¹⁰

In contrast to kink modes which are driven by the plasma pressure, a class of modes named *tearing modes* are driven by the radial gradient of the plasma current. These modes, when destabilised, form so-called magnetic islands which are radially and poloidally localised regions where reconnection of magnetic field lines occurs and the magnetic topology is changed. The growth of tearing modes depends on the tearing parameter Δ' defined as

$$\Delta'(w) = \frac{1}{B_r} \left. \frac{\partial B_r}{\partial r} \right|_{r_s+w/2}^{r_s-w/2}, \quad (16)$$

where w is the island width and r_s the radius of the rational surface where the mode grows [17]. A positive Δ' will destabilise the mode. The growth rate depends on the resistivity η of the plasma and is approximately given by

$$\frac{dw}{dt} \simeq \frac{\eta}{2\mu_0} \Delta'(w). \quad (17)$$

Tearing modes can grow to rather large size with a radial width of 10%-20% of the minor plasma radius.

¹⁰This section is just for completeness and kept rather concise, a much more detailed article by H. R. Wilson on "Neoclassical Tearing Modes" can be found elsewhere in these proceedings.

An example of a tearing mode is shown in figure 3. Here the plasma current (a), the electron temperature at about half radius (b), and two interferometer chords (c) are shown. The time traces of T_e and n_e measurements show a characteristic modulation which results from the flattening of the plasma profiles across the island¹¹ and the diamagnetic drift motion. It can be seen in the figure that the island rotation frequency slows down when the island size gets larger.

A common observation in almost all tokamaks is that the ideal beta limit can only be reached transiently but that the stationary achievable beta values are lower [18]. This behaviour has been found to be caused by the onset of a $m = 3, n = 2$ or $m = 2, n = 1$ tearing modes. Strangely, the Δ' parameter of these modes is negative, i.e. the modes should be stable. These modes have been named *neoclassical tearing modes* (NTM) and their growth can be described by a generalised Rutherford equation [18]. Additional to the tearing parameter this equation contains two pressure driven contributions. One term is destabilising and originates from the loss of bootstrap current due to the pressure profile flattening in the island. The second term is assumed to be stabilising and results from a polarisation current within the island. Neoclassical tearing modes are usually a soft limitation, i.e. the discharge does not disrupt but the confinement gets deteriorated. Plasma disruptions are possible in case the $m = 2, n = 1$ neoclassical tearing mode gets unstable. A widely investigated method for stabilisation of NTMs is to replace the missing bootstrap current in the island by non-inductively driven current using ECRH wave injection or lower hybrid current drive¹² [19, 20].

V. THE CURRENT LIMIT

The q_a -limit

$$q_a > 2 \quad (18)$$

has been already mentioned when discussing the Hugill diagram (figure 1). This is an hard limitation and falling below this value will unavoidably end up with a disruption. Because the density increases with plasma current, increasing the current is an easy way to achieve better confinement, as can be seen by the proportionality of the energy confinement time with plasma current (see equation 3). The main implication of the q_a -limit is that there is a maximum sustainable plasma current at a given toroidal magnetic field. But even at q_a values above 2 but close to 2 the plasma may be already affected by MHD stability issues due to the growth of the $m = 2, n = 1$ tearing

¹¹Magnetic islands are commonly referred as O-points of the mode, whereas the crossing of the island separatrix between O-points is labelled the X-point.

¹²See E. Westerhof's article on "Non-inductive Current Drive" in these proceedings.

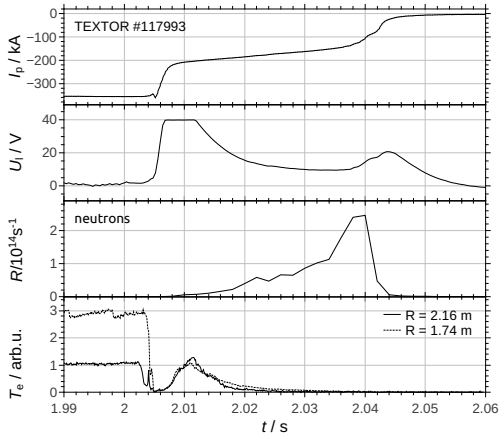


Figure 4: Plasma disruption with runaway electron plateau. Traces from top to bottom are (i) plasma current, (ii) loop voltage (measurement is saturated), (iii) neutron rate, and (iv) electron temperature (centre and edge).

mode. There is no simple criterion to decide whether this mode is unstable because the shape of the current density profile, the plasma pressure, plasma rotation, and the proximity to a conducting wall influence the stability. As a rule of thumb one can say that the excitation of the $m = 2, n = 1$ mode becomes more likely at lower edge safety factor q_a . Most plasma scenarios today use values of 3 or larger.

VI. LOCKED MODES AND ERROR FIELDS

An MHD perturbation like a kink or tearing modes are usually frozen in the plasma fluid according to Alfvén’s theorem. As a consequence modes rotate due to drifts or momentum input by neutral particle injection. A growing mode in the plasma will experience friction caused by induced eddy currents in the wall and slow down the plasma rotation. Eventually the mode can lock to the wall and the rotation in the tokamak frame stands still. The growth rate of the mode after locking is determined by the resistivity of the tokamak first wall and much larger than in the rotating state. In many cases mode locking is observed to be a precursor to a disruptions. The slowing down and locking leading to fast mode growth and disruption can be seen in figure 3. Here a disruption starts at $t = 0.552$ s shortly after the mode stopped and a fast growths (see T_e signal) set in.

A common source for the excitation of locked modes are intrinsic error fields. These fields can arise from small alignment errors of the coils systems. Already low error field amplitudes of the order

$B_r/B_t \approx 10^{-4}$ (B_r is the radial component of the error field) have been found sufficient to excite locked $n = 1$ modes. An error field of this size is expected on ITER due to small coil misalignments [21].

The critical mode amplitude for mode excitation has been investigated in a variety of tokamaks and a power law scaling expression has been derived [22]:

$$B_r/B_t \propto n_e^{\alpha_n} B_t^{\alpha_B} q_{95}^{\alpha_q} R^{\alpha_R}. \quad (19)$$

The exponents α_x show a rather large scatter between individual machines, good agreement has been found only for α_n which is about 1, i.e. the resistance against error field driven modes increases linearly with plasma density. α_B is always negative, meaning that acceptable error field levels become even smaller at larger machines.

Plasma rotation generally increases the threshold for mode excitation. Momentum input which adds to the diamagnetic drift will act stabilising, but when the fluid rotation is compensated by external momentum input the error field threshold shows a minimum [23].

VII. VERTICAL STABILITY

A circular shaped plasma is stable with respect to vertical displacements if the field index

$$n = -\frac{R}{B_v} \frac{dB_v}{dR} \quad (20)$$

is larger than zero [7]. However, vertical elongation κ has a positive effect on the confinement (see equation 3) and most of the tokamaks are operated with elongated plasma shape. A drawback is that the plasma column becomes unstable with respect to vertical displacements. The growth rate of this vertical displacement event (VDE) depends on plasma elongation and can become rather large. A loss of control will result in the plasma either touching on the divertor or armour tiles at the top. Large heat loads and halo currents¹³ arise before the plasma current eventually disrupts. The growth rate of the VDE can be decreased down by a close fitting conducting wall (similar to RWM stabilisation). Experiments on the Swiss tokamak TCV have shown that growth rates of several 1000 s^{-1} could be feedback stabilised [24].

VIII. DISRUPTIONS

A disruption is a fast decay of the plasma current as a consequence of a severe plasma instability, an operational limit, or a loss of plasma control. The evolution of a disruption can be divided into several stages

¹³Halo currents arise when the plasma column touches the wall and a fraction of the plasma current flows partly in the wall.

[10]. An initiating event causes an unstable state, often accompanied by changes of the current density distribution. Precursor like mode oscillations appear next before the actual disruption starts. There are two distinct phases: (i) the thermal quench (TQ) during which the temperature profile collapses and the stored plasma energy is released to the surrounding walls, and (ii) the current quench (CQ) during which the plasma current decays very fast and the magnetic energy is released. Energetic electrons with energies up to several MeV can be generated during the CQ because the tokamak loop voltage rises due to Lenz's law.

Disruptions pose a threat to the integrity of a tokamak because they could result in (i) radiative and convective heat loads on plasma facing components which may cause melting or evaporation, (ii) strong $j \times B$ forces on the vacuum vessel due to induced eddy currents and halo currents, and (iii) a beam of high energetic electrons which can carry a significant fraction of the plasma current and may cause severe damage when hitting plasma facing components.

Disruption studies are at high urgency for ITER [21] and methods for reliable early detection, avoidance, and mitigation need to be developed.

A. Runaway Electrons

Runaway electrons (RE) are generated when the friction force due to collisions gets smaller than the electric force due to the toroidal loop voltage. A relativistic calculation of the critical electric field required for electrons to run away yields

$$E_{crit} = \frac{n_e e^3 \ln \Lambda}{4\pi \epsilon_0^2 m_e c^2} \quad (21)$$

where $\ln \Lambda$ is the Coulomb logarithm, e and m_e charge and mass of an electron, and c the speed of light. For normal tokamak conditions the electric field is less than the critical electric field, so no runaway electrons are generated. At very low density the loop voltage is large enough to produce runaway electrons. These conditions are at the left edge of the Hugill diagram (figure 1). Although in a strict sense the generation of runaway electrons is no operational limit, tokamak operation at those conditions is usually avoided because of the potential damage they may cause.

Once there is a population of energetic electrons an avalanche-like process due to small angle collisions with thermal electrons sets in [25]. This secondary generation process will be dominant on large tokamaks.

B. Disruption Avoidance

The optimum approach to solve the disruption problem would be to avoid any disruption happening. This requires a reliable way to detect the very early stage of a disruption, e.g. a precursor, and some

actuators to rectify whatever went wrong and to regain plasma control. The application of neural networks for early detection of disruptions is under investigation and shows good progress [26]. For certain classes of disruptions a direct detection of a precursor mode and the use of neutral beam injection in order to enhance plasma rotation and stabilise the mode has proven to be successful [27].

C. Disruption Mitigation

The situation that a disruption cannot be avoided may arise. In this case a way to deliberately shut down the plasma discharge and to ameliorate the consequences of a disruption is required. The shutdown procedure has to be designed in a way which keeps $j \times B$ forces on vessel and coil systems within acceptable limits, dissipates the plasma stored thermal and magnetic energies in a way which does not lead to localised overheating of plasma facing components, and prevents that a part of the plasma current is transformed into REs. The energy balance for a shutdown procedure is as follows:

$$W_{th} + W_{mag} = W_{rad} + W_{coupled} + W_{conv} (+W_{RE}) \quad (22)$$

The thermal plasma energy W_{th} and the magnetic energy W_{mag} are converted in to radiated energy W_{rad} (this is preferred because radiation is distributed on a large wall surface), the energy $W_{coupled}$ which is coupled via the mutual inductances into the tokamak coil systems, the part of the energy which is connected by plasma wall contact W_{conv} , and the energy which is carried by RE electrons. Especially the latter two components result in small wetted areas and large local heat loads. Various disruption mitigation methods have been proposed: (i) A fast controlled ramp-down of the plasma current seems to be a good solution but is not always possible. It needs a rather large warning time, and the plasma density (and radiation) may not decrease with the required rate thus provoking a density limit disruption. (ii) Injection of so-called *killer pellets*¹⁴ or *shattered pellets*¹⁵ in order to force the plasma into a radiation limit disruption. (iii) *Massive gas injection* [28] using specially designed fast valves is another promising method to deliberately induce a radiation collapse. This method is presently under investigation on many tokamaks.

IX. SUMMARY

The operational limits of a tokamak machine arise from a variety of different physical mechanisms. The density limit is actually defined by the balance between plasma radiation and heating power. Clean

¹⁴Similar to frozen hydrogen fuelling pellets but made of neon or argon.

¹⁵Nobel gas pellets of large size which are shot against a solid target which disaggregates the pellet before entry into the plasma.

plasmas and good wall conditioning together with sufficient heating power can assure stable operation close to this limit. A limitation on the maximum plasma current at a given toroidal field results from the MHD stability properties of the $m = 2, n = 1$ mode. The generation of runaway electrons constrains the operation at low density. The ideal beta limit originates from pressure driven $n = 1$ kink instabilities. More of importance is the so-called *practical beta limit* which is due to the neoclassical tearing mode and is the most frequent limitation to plasma performance. Disruptions can cause damage to the machine pose the most severe problem on large tokamaks requiring an adequate mitigation method.

REFERENCES

1. F. Wagner et al., "Regime of Improved Confinement and High Beta in Neutral-Beam-Heated Divertor Discharges of the ASDEX Tokamak", *Phys. Rev. Lett.*, **49**, 1408 (1982).
2. ITER Physics Expert Groups on Confinement and Transport and Confinement Modelling and Database, "Chapter 2: Plasma confinement and transport", *Nucl. Fusion*, **39**, 2175-2249 (1999).
3. S. J. Fielding et al., "High-Density Discharges with Gettered Torus Walls in DITE", *Nucl. Fusion* **17** 1382 (1977).
4. M. Murakami et al., "Some Observations on Maximum Densities in Tokamak Experiments", *Nucl. Fusion* **16** 347 (1976).
5. G. Waidmann et al., "Density Limits and Evolution of Disruptions in Ohmic TEXTOR Plasmas", *Nucl. Fusion*, **32**, 645 (1992).
6. J. Rapp et al., "Scaling of Density Limits with Respect to Global and Edge Parameters in TEXTOR-94", in Proc. 26th EPS Conf. on Contr. Fusion and Plasma Physics, Maastricht, *ECA* **23J**, 665 (1999).
7. J. A. Wesson, "Hydrodynamic Stability of Tokamaks", *Nucl. Fusion*, **18**, 87 (1978).
8. J. Winter, "Wall conditioning in fusion devices and its influence on plasma performance", *Plasma Phys. Control. Fusion*, **38**, 1503 (1999).
9. D. E. Post et al., "Steady-state radiative cooling rates for low-density high-temperature plasmas", *At. Data Nucl. Data Tables*, **20**, 397 (1977).
10. F. C. Schüller, "Disruptions in Tokamaks", *Plasma Phys. Control. Fusion*, **37**, A135 (1995).
11. M. Greenwald, "Density Limits in Toroidal Plasmas", *Plasma Phys. Control. Fusion*, **44**, R27 (2002).
12. B. Lipschultz, "Review of MARFE Phenomena in Tokamaks", *J. Nucl. Mater.*, **145-147**, 15 (1987).
13. P. C. de Vries et al., "Influence of Recycling on the Density Limit in TEXTOR-94", *Phys. Rev. Lett.* **80**, 3519 (1998).
14. F. Troyon et al., "MHD-Limits to Plasma Confinement", *Plasma Phys. Control. Fusion*, **26**, 209 (1984).
15. C. Mercier, "A necessary condition for hydro-magnetic stability of plasma with axial symmetry", *Nucl. Fusion* **1** 47 (1960).
16. M. S. Chu and M. Okabayashi, "Stabilisation of the external kink and the resistive wall mode", *Plasma Phys. Control. Fusion*, **52**, 123001 (2010).
17. H. P. Furth et al., "Tearing mode in the cylindrical tokamak" *Phys. Fluids*, **16**, 1054 (1973).
18. O. Sauter et al., "Beta Limits in Long-Pulse Tokamak Discharges", *Phys. Plasmas*, **4**, 1654 (1997).
19. H. Zohm et al., "Experiments on Neoclassical Tearing Mode Stabilisation by ECCD in ASDEX-Upgrade", *Nucl. Fusion*, **39**, 577 (1999).
20. C. D. Warrick et al., "Complete Stabilisation of Neoclassical Tearing Modes with Lower Hybrid Current Drive on COMPASS-D", *Phys. Rev. Lett.*, **85**, 574 (2000).
21. T. Hender et al., "MHD Stability, Operational Limits and Disruptions" (Chapter 3 in "Progress in the ITER Physics Base"), *Nucl. Fusion*, **47**, S128 (2007).
22. R. J. Buttery et al., "Error field mode studies on JET, COMPASS-D and DIII-D, and implications for ITER", *Nucl. Fusion*, **39**, 1827 (1999).
23. H. R. Koslowski et al., "Dependence of the Threshold for Perturbation Field Generated $m/n = 2/1$ Tearing Modes on the Plasma Fluid Rotation", *Nucl. Fusion*, **46**, L1 (2006).
24. F. Hofmann et al., "Vertical Position Control in TCV: Comparison of Model Predictions with Experimental Results", *Nucl. Fusion*, **40**, 767 (2000).
25. R. Jaspers et al., "Disruption Generated Runaway Electrons in TEXTOR and ITER", *Nucl. Fusion*, **36**, 367 (1996).
26. G. Pautasso et al., "Prediction and mitigation of disruptions in ASDEX Upgrade", *J. Nucl. Mater.*, **290-293**, 1045 (2001).
27. A. Krämer-Flecken et al., "Heterodyne ECE Diagnostic in the Mode Detection and Disruption Avoidance at TEXTOR", *Nucl. Fusion*, **43**, 1437 (2003).
28. D. G. Whyte et al., "Disruption mitigation with high-pressure noble gas injection", *J. Nucl. Mater.*, **313-316**, 1239 (2003).

MHD AND FAST PARTICLES IN TOKAMAKS

S.E. Sharapov

*Euratom/CCFE Fusion Association, Culham Science Centre, Abingdon, Oxfordshire OX14 3DB, UK
Sergei.Sharapov@ccfe.ac.uk*

ABSTRACT

An introduction is given to ideal MHD waves and the problem of resonant interaction between such waves and energetic ions born in fusion reactions and/or produced by auxiliary plasma heating. Shear Alfvén waves are shown to form a discrete spectrum of Global Alfvén Eigenmodes in current-carrying cylindrical plasmas and Toroidal Alfvén Eigenmodes in toroidal plasmas. A comparison between theory and experiment is presented for the observed discrete spectra of Alfvén waves driven by energetic ions in Joint European Torus. The mechanism of excitation of Alfvén instabilities is qualitatively explained by considering particle-to-wave power transfer, and mechanisms of wave-induced re-distribution and losses of energetic ions are discussed.

I. INTRODUCTION

Instabilities of Alfvén Eigenmodes (AEs)^{1,2} are an important issue for burning plasma studies, with weakly-damped Toroidal Alfvén Eigenmode (TAE)³ representing the most dangerous mode that may limit the pressure of energetic ions and cause fast ion losses. Since 3.5 MeV alpha-particles are born in fusion deuterium-tritium (DT) plasmas at a speed exceeding the Alfvén velocity, these alpha-particles may excite TAE via Landau resonance $V_{\alpha} = V_A$ if the power transfer from the alphas to the wave exceeds the wave damping by thermal plasma⁴. The Alfvén instability is driven by radial gradient of energetic particle pressure if the fast particles have energy high enough to resonate with Alfvén waves, and this instability cause a radial re-distribution of the energetic particles giving non-optimal heating profiles and energetic particle losses damaging the first wall. Without the energetic particles the modes are stable ideal magneto-hydrodynamic (MHD) waves. The present lecture describes discrete weakly-damped AEs in cylindrical and toroidal plasmas and the fast particle drive and AE-induced transport of the fast particles.

I.A. Fast ions in fusion plasmas

In present day experiments, energetic particles produced with auxiliary heating systems have very high parameters well suitable for investigating AEs with further extrapolation to burning plasmas with significant

pressure of alpha-particles. On Joint European Torus (JET), energetic ions are produced with NBI and ICRH techniques capable of accelerating hydrogen isotopes H, D, T, and He³ up to the MeV energy range^{5,6}. It is also possible to accelerate a population of He⁴ ions up to the MeV energy range with NBI+ICRH technique in helium plasma which has no fusion products⁷. Table I presents typical values of energetic ion populations achieved in JET experiments with ICRH, the values for alpha-particles in JET deuterium-tritium (DT) plasmas, and expected alpha-particle values in burning ITER plasma.

Table I. Characteristics of ICRH-accelerated ions and alpha-particles in JET and ITER: slowing down time, τ_s , heating power per volume at the magnetic axis, $P_f(0)$, ratio of the on-axis fast ion density to electron density, $n_f(0) / n_e(0)$, on-axis fast ion beta, $\beta_f(0)$, volume-averaged fast ion beta, $\langle \beta_f \rangle$ (%), and normalised radial gradient of fast ion beta, $\max |R \nabla \beta_f|$.

Reference	JET ^{5,6}	JET ⁷	JET ⁸	ITER ⁹
Fast ions	H or He ³	He ⁴	Alpha	Alpha
Source	ICRH tail	ICRH tail	Fusion	Fusion
Mechanism	minority	3 rd harm. of NBI	DT nuclear	DT nuclear
τ_s (s)	1-0.9	0.4	1.0	0.8
$P_f(0)$ (MW/m ³)	0.8-1	0.5	0.12	0.55
$n_f(0) / n_e(0)$ (%)	1-1.5	1.5	0.44	0.85
$\beta_f(0)$ (%)	2	3	0.7	1.2
$\langle \beta_f \rangle$ (%)	≈0.3	0.3	0.12	0.3
$\max R \nabla \beta_f $ (%)	≈5	5	3.5	3.8

I.B. Measuring Alfvén perturbations

Alfvénic instabilities are observed as high-frequency perturbations, having a typical frequency in the plasma reference frame from 50 to 500 kHz. The observed spectrum of the instabilities is not continuous, but discrete, with TAE in the range of 100-200 kHz in the plasma reference frame. Elliptical Alfvén Eigenmodes¹⁰ are also seen sometimes at a frequency twice that of TAEs, and Alfvén Cascade eigenmodes¹¹ are seen in discharges with reversed magnetic shear at a frequency below the TAE frequency. The modes are detected by

external magnetic pick-up coils with a high sampling rate^{8,12}. They can be also detected using interferometry¹³, reflectometry¹⁴, and electron cyclotron emission¹¹. A typical magnetic spectrogram showing amplitude of magnetic perturbations as function of frequency and time is shown in Figure 1. Multiple TAE modes with different toroidal mode numbers are seen as a discrete spectrum in the frequency range 250-450 kHz in this plasma with high toroidal rotation that causes Doppler shift of frequency (to be described later). We'll try to understand why the spectrum of TAE is discrete and what limits the number of unstable TAE.

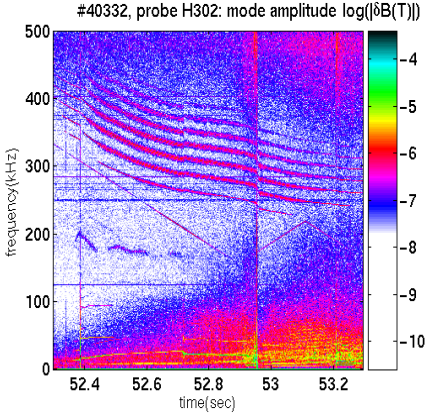


Fig.1. Magnetic spectrogram (Fourier decomposition as function of time) of a Mirnov coil signal.

II. MHD WAVES WITHOUT FAST PARTICLES

Plasma represents a self-consistent system of charged particles and perturbed electric and magnetic fields. For describing the plasma particles, we take into account the quasi-neutrality condition,

$$n_e = \sum_i Z_i \cdot n_i$$

and take velocity moments of kinetic Vlasov equations for electrons and ions and sum them to obtain

$$\begin{aligned} \frac{\partial \rho}{\partial t} + \nabla \cdot (\rho \mathbf{V}) &= 0; \\ \rho \frac{d\mathbf{V}}{dt} &= -\nabla p + \frac{1}{c} \mathbf{J} \times \mathbf{B}; \\ \frac{\partial p}{\partial t} + \mathbf{V} \cdot \nabla p + \Gamma p \nabla \cdot \mathbf{V} &= 0; \\ \mathbf{E} + \frac{1}{c} \mathbf{V} \times \mathbf{B} &= 0; \end{aligned}$$

where ρ and \mathbf{V} are mass density and mass velocity of the plasma, p is plasma pressure, and Γ is adiabaticity index. This set of equations has no resistivity or other

dissipative effects and described ideal magneto-hydrodynamics (MHD) evolution of plasma. For describing electromagnetic fields in the plasma, Maxwell's equations are used

$$\begin{aligned} \nabla \times \mathbf{B} &= \frac{4\pi}{c} \mathbf{J}; \\ \nabla \times \mathbf{E} &= -\frac{1}{c} \frac{\partial \mathbf{B}}{\partial t}; \\ \nabla \cdot \mathbf{B} &= 0. \end{aligned}$$

For considering small linear perturbations of plasma near the equilibrium, all the field and plasma variables are represented as sums of equilibrium (denoted by subscript 0) and perturbed (denoted by δ) quantities as follows:

$$\mathbf{J} = \mathbf{J}_0 + \delta \mathbf{J}, \quad \mathbf{B} = \mathbf{B}_0 + \delta \mathbf{B}, \quad \mathbf{V} = \delta \mathbf{V},$$

$$p = p_0 + \delta p, \quad \rho = \rho_0 + \delta \rho, \quad \mathbf{E} = \delta \mathbf{E}, \quad (1)$$

where all the perturbed quantities satisfy $\delta \ll 1$, i.e. $|\delta \mathbf{J} / \mathbf{J}_0| \ll 1$ etc. We assume the time-space dependence corresponding to waves, $\delta A \propto \exp(-i\omega t + ikr)$ in the limit $\omega \ll \omega_{Bi} \equiv e_i B_0 / mc$. One can now substitute the expressions (1) in the starting set of equations and obtain equations with terms: a) not having δ at all; b) having δ ; c) having δ^2 etc. The terms not having δ are balanced due to the plasma equilibrium

$$\nabla p_0 = \frac{1}{c} \mathbf{J}_0 \times \mathbf{B}_0 \quad (2)$$

and terms linear in δ describe ideal MHD perturbations:

$$\frac{\partial \delta \rho}{\partial t} + \nabla \cdot (\rho_0 \delta \mathbf{V}) = 0 \quad (3)$$

$$\rho_0 \frac{d\delta \mathbf{V}}{dt} = -\nabla \delta p + \frac{1}{4\pi} [\nabla \times \delta \mathbf{B}] \times \mathbf{B}_0 \quad (4)$$

$$\frac{\partial}{\partial t} \delta \mathbf{B} = \nabla \times [\delta \mathbf{V} \times \mathbf{B}_0] \quad (5)$$

$$\delta p = \Gamma \frac{p_0}{\rho_0} \delta \rho. \quad (6)$$

II.A. MHD waves in plasma

Introduce plasma displacement from the equilibrium, ξ , related to $\delta \mathbf{V}$ via $\delta \mathbf{V} = \partial \xi / \partial t$. From Eqs.(3), (5) we find

$$\delta \rho = -\text{div}(\rho_0 \xi)$$

$$\delta \mathbf{B} = \nabla \times [\xi \times \mathbf{B}_0] = -\mathbf{B}_0 \text{div} \xi_{\perp} + \mathbf{B}_0 \frac{\partial \xi_{\perp}}{\partial z}$$

where $\nabla \times [\mathbf{a} \times \mathbf{b}] = (\mathbf{b} \nabla) \mathbf{a} - (\mathbf{a} \nabla) \mathbf{b} + \mathbf{a} \text{div} \mathbf{b} - \mathbf{b} \text{div} \mathbf{a}$ and $\mathbf{B}_0 \uparrow \uparrow \mathbf{e}_z$ were used. Substitute the expressions for $\delta \rho$, $\delta \mathbf{B}$ in the remaining two equations and obtain

$$\frac{\partial^2 \xi}{\partial t^2} = c_s^2 \nabla \text{div} \xi + V_A^2 \nabla_{\perp} \text{div} \xi_{\perp} + V_A^2 \frac{\partial^2 \xi_{\perp}}{\partial z^2}, \quad (7)$$

where $c_s^2 = \gamma p_0 / \rho_0$ is the ion sound speed, and $V_A^2 = B_0^2 / (4\pi \rho_0)$ is the square of Alfvén velocity. This equation describes linear MHD perturbations of homogeneous ideally conducting plasma. Single vector equation gives three scalar equations for three types of waves: compressional Alfvén and slow magnetosonic waves, in which the “returning” force are the magnetic pressure and the kinetic pressure, correspondingly, and the shear Alfvén wave, in which the “returning” force is the tension of magnetic field lines (see Figure 2).

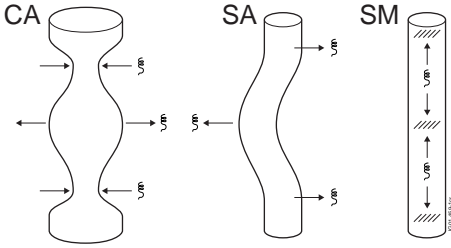


Fig.2. Plasma displacement ξ in three types of MHD waves¹⁵: Compressional Alfvén (CA), Shear Alfvén (SA), and Slow Magnetosonic (SM).

In contrast to the compressional waves, the shear Alfvén wave is incompressible:

$$\xi_z = 0, \\ \text{div} \xi_{\perp} = 0.$$

For such waves the main MHD equation becomes simply

$$\frac{\partial^2 \xi_{\perp}}{\partial t^2} = V_A^2 \frac{\partial^2 \xi_{\perp}}{\partial z^2}, \quad (8)$$

which coincides with equation for string oscillations. The “returning” force is the tension of magnetic field lines, which act similarly to the strings. In shear Alfvén wave the fluid displacement vector ξ and $\delta \mathbf{E}$ are perpendicular to the magnetic field \mathbf{B}_0 . The wave propagates along \mathbf{B}_0 :

$$\omega = \pm k_{\parallel} V_A; \quad k_{\parallel} = \mathbf{k} \cdot \mathbf{B}_0 / B_0, \quad (9)$$

and it has no parallel perturbed components, $\delta E_{\parallel} = 0$, $\delta B_{\parallel} = 0$. In comparison to CA wave, SA wave requires less energy for excitation, and in comparison to SM wave, SA wave experiences less significant damping due to thermal ions since for typical plasmas $V_{Ti} / V_A = \sqrt{\beta_i} \approx 0.1 \ll 1$. As a result, the SA

wave is easiest to excite, and this is why the SA wave constitutes the most significant part of the spectrum of MHD waves and is probably best studied.

The description of shear Alfvén waves above assumed homogeneous plasma. In spatially inhomogeneous plasmas with $V_A = V_A(r)$ and $k_{\parallel} = k_{\parallel}(r)$, the frequency of shear Alfvén waves, $\omega_A(r) = k_{\parallel}(r) \cdot V_A(r)$, varies with radius. A radially-extended packet of SA waves in such spatially inhomogeneous plasmas has a finite life time (which may be also interpreted as wave damping) since the radially different “slices” of the wave packet propagate at different velocities along different directions of $\mathbf{B}(r)$. As time increases, the “slices” of local Alfvén waves become thinner in radius and run into the short wavelength region, $k_r \rightarrow \infty$, where they are carried away due to the radial group velocity caused by finite Larmor radius (description of this effect goes beyond the scope of this lecture). The lifetime, τ , of the wave packet is inversely proportional to radial gradient of the local Alfvén frequency $\omega_A(r)$,

$$\tau \propto \left| \frac{d\omega_A(r)}{dr} \right|^{-1} \equiv \left| \frac{d}{dr} k_{\parallel}(r) \cdot V_A(r) \right|^{-1}.$$

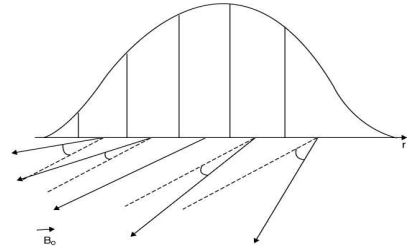


Fig.3. Schematic picture showing spread of a radially-extended wave-packet of shear Alfvén waves in inhomogeneous plasma.

The lifetime τ increases if the wave-packet is localised in vicinity of an extremum point of $\omega_A(r)$,

$$\left. \frac{d}{dr} \omega_A(r) \right|_{r=r_0} = 0. \quad (10)$$

It is of interest to investigate a possibility of existence of SA perturbations, which are localized in the vicinity of the Alfvén continuum extremum points and may be less damped and thus have a longer life-time.

II.B. Global Alfvén eigenmode (GAE) in cylindrical plasma with current

Investigations of Alfvén spectrum in cylindrical plasmas with plasma current and condition (10) fulfilled have

revealed that in cylindrical geometry, in addition to the continuous SA spectrum, $\omega^2 = \omega_A^2(r) \equiv k_{\parallel}^2(r) V_A^2(r)$, a discrete Global Alfvén Eigenmode (GAE) exists^{16,17}. The mode was found as an extremely high-quality, $Q \equiv \omega/\gamma \sim 10^3$, resonance excited in cylindrical plasma with co-directed equilibrium magnetic field and current by an external antenna. Figure 4 shows the plasma response seen as the antenna coil impedance as function of the frequency scanned in the antenna.

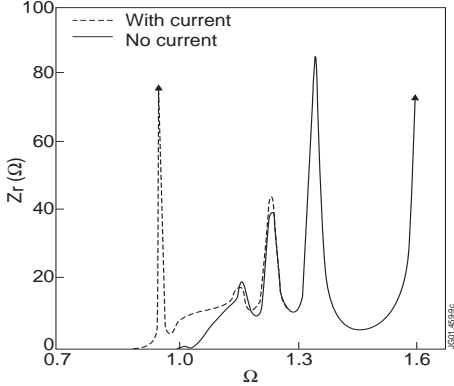


Fig.4. Real part of the coil impedance versus normalized frequency. GAE discrete eigenfrequency is shown with broken line as a high-quality narrow resonance peak below $\Omega = \omega / \omega_A^{\min} = 1$.

In cylindrical geometry, the length of the cylinder L determines the lowest parallel wave-vector as $k_{\parallel}^{\min} = 2\pi/L$ so that the lowest SA frequency is still above zero. The ideal MHD mode GAE with $0 < \omega_{GAE} < \omega_A^{\min}$ exists if the current profile provides a minimum in the Alfvén continuum via the condition:

$$\frac{1}{k_{\parallel}} \frac{dk_{\parallel}}{dr} = - \frac{1}{V_A} \frac{dV_A}{dr}.$$

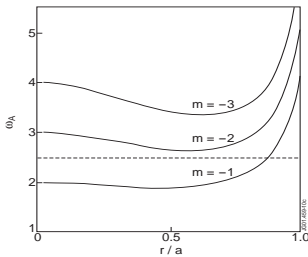


Fig.5. Structure of Alfvén continuum in cylindrical plasma with current and plasma density gradient.

It is important to note that the frequency of GAE is actually below the Alfvén continuum. This frequency shift is caused by the well-known property of electromagnetic waves (to which the SA wave belongs to) of forming a waveguide at the extremum of perpendicular refraction index. Indeed, the local minimum of the Alfvén continuum seen in Fig.5 provides a maximum of the perpendicular refraction index $N_r = ck_r/\omega$. Similarly to fiber optics, GAE propagating in a “wave-guide” surrounding the region of the extremum refraction index has most of the wave energy at the radial position of the extremum point. Figure 6 shows the radial structure of the GAE wave-fields.

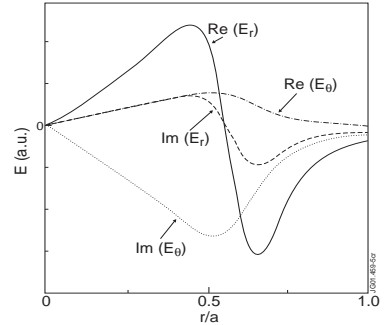


Fig.6. Radial structure of Global Alfvén Eigenmode with $m=-2$ in cylindrical plasma with current and density gradient.

Due to the frequency shift between GAE and ω_A^{\min} , the eigenfrequency of GAE does not satisfy the local Alfvén resonance condition, i.e.

$$\omega_{GAE} \neq \omega_A(r) \quad (11)$$

Therefore, although GAE has all the properties of the SA wave, it represents a coherent radially-extended wave-packet, to which the phase mixing effect shown in Figure 3 does not apply, so GAE has no continuum damping.

II.C. Toroidal Alfvén Eigenmode (TAE)

In a torus, the wave solutions are quantized in toroidal and poloidal directions:

$$\phi(r, \vartheta, \zeta, t) = \exp(-i\omega t + in\zeta) \sum_m \phi_m(r) \exp(-im\vartheta) + c.c.$$

n is the number of wavelengths in toroidal direction and m is the number of wavelengths in poloidal direction. The parallel wave-vector for the m -th harmonic of a mode with toroidal mode number n , is determined by the safety factor $q(r) = rB_z / RB_\theta$ as follows:

$$k_{\parallel m} = \frac{1}{R_0} \left(n - \frac{m}{q(r)} \right) \quad (12)$$

It was found³ that for a given $q(r)$ and n , but for different m two cylindrical SA branches become degenerate in toroidal geometry at radial positions

$$\omega = k_{\parallel m}(r)V_A(r) = -k_{\parallel m+1}(r)V_A(r), \quad (13)$$

and so-called toroidicity-induced gap of the width $\Delta\omega/\omega \propto r/R_0$ exists at the frequency satisfying (13), with extremum points (10) caused by the toroidal coupling of neighboring poloidal harmonics m and $m+1$. In addition to the SA continuum, a new Toroidal Alfvén Eigenmode (TAE) was shown to exist in the TAE-gap. Figure 7 shows computed radial structure of Alfvén and SM continuous spectra in one of JET discharges, together with a discrete eigenfrequency corresponding to $n=1$ TAE with eigenfrequency inside the TAE gap.

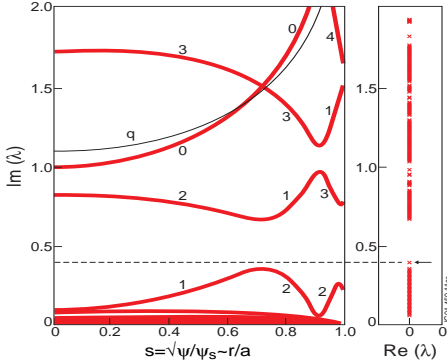


Fig.7. Radial structure of the Alfvén continuum in tokamak for toroidal mode number $n=1$.

Similarly to GAE in cylinder, TAE frequency does not satisfy the local Alfvén resonance condition in the region of TAE localization,

$$\omega_{TAE} \neq \omega_A(r)$$

so TAE does not experience strong continuum damping. Most of the wave energy of TAE with mode numbers n , m is localised at the position of the extremum where $k_{\parallel m}(r_{TAE}) = -k_{\parallel m+1}(r_{TAE})$, i.e.

$$q(r_{TAE}) = \frac{m+1/2}{n} \quad (14)$$

as Figure 8 shows.

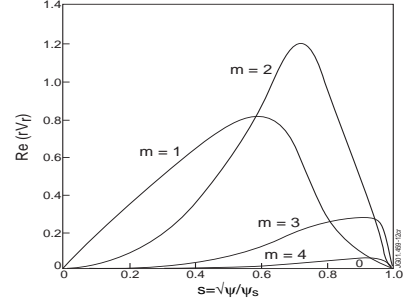


Fig.8. Radial structure of Toroidal Alfvén Eigenmode consisting of several coupled poloidal harmonics.

We substitute this value of safety factor in (13) to obtain characteristic frequency of TAE,

$$\omega_{TAE} \cong \frac{V_A(r_{TAE})}{2R_0 q(r_{TAE})}, \quad (15)$$

which does *not* depend on n or m . For typical plasma parameters on JET,

$$B_0 \cong 3 \text{ T}; \quad n_i = 5 \times 10^{19} \text{ m}^{-3}; \quad m_i = m_D;$$

one obtains $V_A \cong 6.6 \times 10^6 \text{ m/s}$, so that TAE frequency on JET ($R_0 = 3 \text{ m}$ and, e.g. $q \approx 1$) is:

$$\omega_{TAE} \cong 10^6 \text{ sec}^{-1}; \quad f_{TAE} \cong \omega_{TAE}/2\pi \cong 160 \text{ kHz}.$$

We also note that the radial width of poloidal harmonic of TAE is

$$\Delta_{TAE} \approx r_{TAE}/m \approx r_{TAE}/nq.$$

Figure 9 shows experimentally observed TAE and EAE modes driven by ICRH-accelerated ions in one of JET discharges, together with computed TAE and EAE frequency gaps. At a low speed of toroidal rotation of the plasma, the frequencies in the plasma and laboratory reference frames are nearly the same, and the modeling of AE can be directly applied to the observation without the Doppler shift correction.

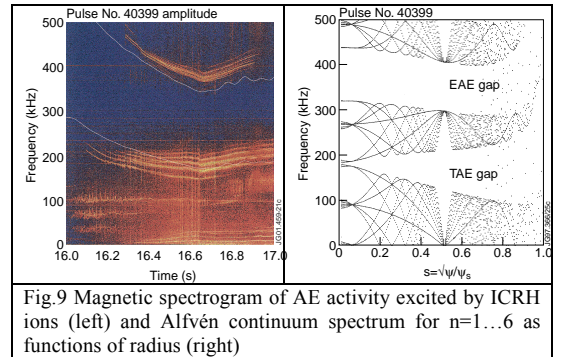


Fig.9 Magnetic spectrogram of AE activity excited by ICRH ions (left) and Alfvén continuum spectrum for $n=1\dots 6$ as functions of radius (right)

In JET discharges with high power NBI, the uni-directional NBI spins up the plasma and drives a significant toroidal plasma rotation (up to 40 kHz). Frequencies of waves with mode number n in laboratory reference frame, f_n^{LAB} , and in the plasma, f_n^0 , become different then and are related through the Doppler shift $nf_{rot}(r)$:

$$f_n^{LAB} = f_n^0 + nf_{rot}(r).$$

The Doppler shift proportional to the toroidal mode number explains why TAE are seen at much higher frequencies in Figure 1. Figure 10 shows an example of the observed and computed TAE modes in JET discharge with strong toroidal plasma rotation when the Doppler shift is included.

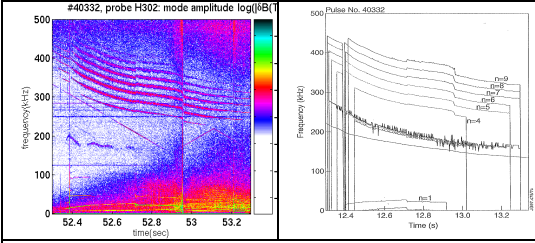


Fig.10 Discrete spectrum of TAE observed in JET discharge #40332. Plasma starts at $t=40$ sec (left) and eigenfrequencies of TAEs with $n=4..9$ computed for equilibrium in JET discharge #40332 (right).

III. TAE EXCITATION BY FAST PARTICLES

TAE modes have perturbed electric and magnetic field components, $\delta\mathbf{E}_\perp$, and $\delta\mathbf{B}_\perp$, perpendicular to the equilibrium magnetic field \mathbf{B}_0 , but no parallel electric or magnetic fields. It is important to understand how such modes could be excited by energetic particles in toroidal geometry.

III.A. Qualitative explanation of the particle-to-wave power transfer

If some energetic ions move along \mathbf{B}_0 with velocity close to the phase velocity of the wave \mathbf{V}_A , the wave exchanges energy with such ions. For the ideal MHD shear Alfvén wave, it is the perpendicular electric field $\delta\mathbf{E}_\perp$ of the wave that interacts with the ions since, in toroidal geometry, the ions undergo the magnetic field curvature and ∇B drifts across the magnetic field. The drift surfaces of the energetic ions deviate from the magnetic surfaces to which the TAE mode is attached as shown schematically in Fig.11 for passing and trapped energetic ions.

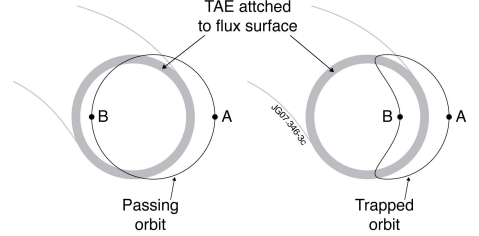


Fig.11 TAE modes are attached to magnetic flux surfaces, while energetic particles are not: they drift across the flux surfaces and TAE structure.

The exchange of energy between TAE and the ion occurs when the ion moves from, say, point A to point B across the radial structure of the mode and gains or loses energy $-e_h\Delta\phi$, where, $\phi(r)$ is electrostatic potential associated with the mode, and e_h is the charge of energetic ion labelled by subscript ‘‘h’’ (for hot ion). In the guiding centre approximation, the power transfer P_h from the ion to the mode is given by

$$P_h = -e_h \mathbf{v}_d \cdot \delta\mathbf{E}_\perp,$$

where \mathbf{v}_d is unperturbed guiding centre drift velocity.

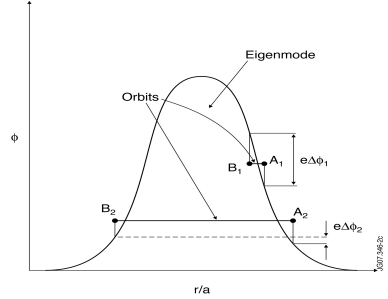


Fig.12 When charged particle moves radially across TAE from point A to point B, the mode and the particle exchange energy $e\Delta\phi$ as this Figure shows.

The particle-to-wave power transfer for the whole distribution function of energetic ions takes the form

$$P_h = \iint (-e_h \mathbf{v}_d \cdot \delta\mathbf{E}_\perp) f_h d^3v d^3x,$$

where f_h is the linear perturbed distribution function of hot ions. The most significant contribution to the power transfer comes from ions satisfying the wave-particle resonance, $\omega_0 - n\omega_\phi - l\omega_g = 0$, where ω_ϕ and ω_g are the toroidal and poloidal orbit frequencies of the energetic ions, and l is an integer.

Analytical estimates of the power transfer could be done in the reference frame of the energetic ion, which “sees” TAE electric field along its orbit as, e.g. a shifted circle in the simple case of the passing ions^{19,18}:

$$r = \bar{r} + \Delta_O \cos \bar{\vartheta},$$

$$\vartheta = \bar{\vartheta} - \frac{\Delta_O}{\bar{r}} \sin \bar{\vartheta} \approx \bar{\vartheta}.$$

The structure of TAE electrostatic potential $\phi_m(r)$ in the reference frame of the ion could be expanded as,

$$\phi_m(\bar{r} + \Delta_O \cos \vartheta) = \sum_{l=0}^{\infty} \phi_{m,l} \cos l \vartheta$$

This poloidal dependence gives resonance conditions:

$$V_{\parallel} = \frac{V_A}{|1 - 2l|} = 1, \frac{1}{3}, \frac{1}{5} \dots$$

showing that TAE can interact with sub-Alfvénic ions at satellite resonances^{2,18}. In the presence of gradients of the energetic particle distribution function, $\partial f_0 / \partial r$ and $\partial f_0 / \partial E$, and in the limit of the ion orbits smaller than the radial width of TAE, the expression for the normalized growth rate of TAE, γ , is given by

$$\frac{\gamma}{\omega_0} = \frac{P_h}{2W_{TAE}} \cong \beta_h \left(\frac{\omega_{sh}}{\omega_0} - 1 \right) F \left(\frac{V_A}{V_h} \right),$$

where

$$\omega_{sh} = -\frac{m}{r} \frac{T_h}{e_h B} \frac{d \ln p_h}{dr}$$

is the diamagnetic frequency of the energetic ions, β_h , p_h , and T_h are the beta value, pressure, and temperature of the energetic ions, W_{TAE} is the wave energy of the mode, and function $F(V_A/V_h)$ depends on the type of energetic particle distribution function.

It is clear from Fig.12 that the particle-to-wave power transfer determined by the value $-e_h \Delta \varphi$ has a non-monotonic behavior as function of the ratio between drift orbit width and TAE width, so the power transfer achieves a maximum at $\Delta_O / \Delta_{TAE} \approx 1$ ¹⁸ as Figure 13 shows

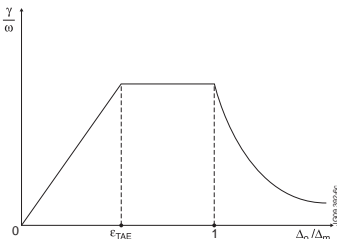


Fig.13. Qualitative graph showing how the power transfer depends on the ratio between fast particle drift orbit and radial width of TAE.

The net power transfer from energetic particles to the mode becomes positive if the radial gradient of the

energetic particles is high enough to satisfy $\omega_{sh} / \omega_0 > 1$. The amplitude of the mode increases if the growth rate due to energetic particles exceeds TAE damping rate.

III.B. Experimental validation of TAE instability zone

One can observe experimentally how TAE modes are excited one-by-one at increasing pressure of energetic ions. Figure 14 shows JET discharge with gradually increasing power of ICRH driving TAE.

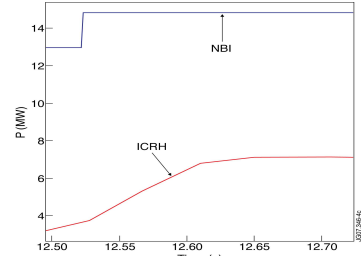


Fig.14. Power waveforms of ICRH and NBI in JET discharge # 40329.

As the population of ICRH-accelerated energetic ions increases, TAE modes with different toroidal mode numbers got excited one-by-one as Figure 15 shows. The instability starts from the most unstable TAE with $n = 8$ satisfying the maximum power transfer condition, $m \approx nq \approx r_{TAE} / \Delta_{orbit}$, and then involves more stable TAEs with other toroidal mode numbers at higher fast ion pressure.

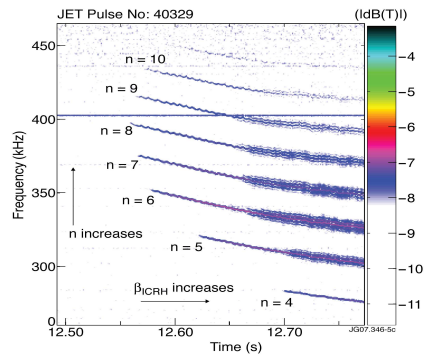


Fig.15. TAEs with different toroidal mode numbers appear one-by-one as fast ion pressure increases (JET discharge # 40329).

IV. TAE-INDUCED ENERGETIC PARTICLE TRANSPORT

Non-linearly the TAE instability leads to a radial flattening of the fast ion distribution function. However, losses of fusion born alphas must be minimized down to few percent (<5% on ITER⁹) for avoiding the first wall damage. Also, a radial redistribution of the alphas could give a non self-consistent alpha-heating profile and He ash profile and may affect the burn²¹.

IV.A. Qualitative estimates

The unperturbed orbit of a charged particle is determined by three invariants:

$$\mu \equiv \frac{Mv^2}{2}; \quad E \equiv \frac{Mv^2}{2}; \quad P_\phi \equiv -\frac{e}{c}\psi(r) + RMv_\phi$$

In the presence of a fixed amplitude TAE, neither E nor P_ϕ is conserved for the ion orbit, but their combination is still invariant:

$$E - \frac{\omega}{n} P_\phi = \text{const}$$

It is easy to see that a change in the ion energy is related to change in the ion radius induced by TAE as follows²²:

$$\Delta E = \frac{\omega}{n} \Delta P_\phi \cong \frac{\omega e}{nc} \psi' \Delta r.$$

We can see then that the interaction between TAE and fast ions causes radial transport of the ions at nearly constant energy.

IV.B. Two main types of TAE-induced redistribution and losses

In present-day machines, fast ion orbits are comparable to the machine radius, $\rho_\alpha/a \cong 10^{-1} + 1$. A single-mode 'convective' transport linearly proportional to TAE amplitude $\propto \delta B_{TAE}$ is important as Figure 16 shows.

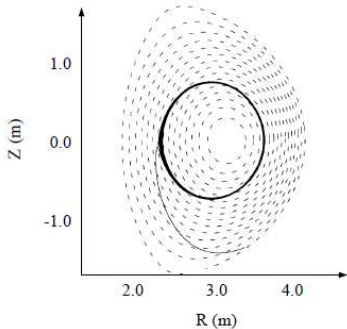


Fig. 16. TAE-induced conversion of passing confined to a trapped lost ion on JET.

However, for ITER with parameter $\rho_\alpha/a \cong 10^{-2}$ the dominant channel of alpha-particle transport will differ from present-day machines. On ITER, higher- n ($n > 10$) TAEs will be most unstable. Under these conditions, a transport of alpha-particles is due to the wave-particle resonance overlap leading to a global stochastic diffusion, with the transport $\propto \delta B_{TAE}^2$. Figure 17 shows an example of stochastization of drift orbit surfaces and the resulting transport of alpha-particles computed for JET²².

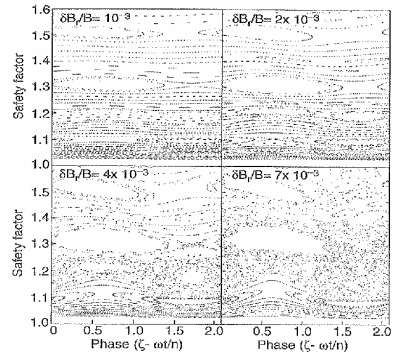


Fig. 17. Stochastization of drift surfaces of fusion alpha-particles at increasing TAE amplitude.

REFERENCES

1. J. WESSON, *Tokamaks*, Clarendon Press, Oxford, 2011.
2. A.B. MIKHAILOVSKII, *Sov. Zh.ETPh.* **41** 890 (1975).
3. C.Z. CHENG, L. CHEN, M.S. CHANCE *Ann. Phys.* **161** 21 (1985).
4. G.Y. FU, J.W. VAN DAM *Phys. Fluids B* **1** 1949 (1989).
5. D.F.H. START et al., *Nucl. Fusion* **39** 321 (1999).
6. L.-G. ERIKSSON et al., *Nucl. Fusion* **39** 337 (1999).
7. M. MANTSINEN, *Phys.Rev.Lett.* **88** 105002 (2002).
8. S.E. SHARAPOV et al., *Nucl. Fusion* **39** 373 (1999).
9. A.FASOLI et al., *Nucl. Fusion* **47** S264 (2007).
10. R.BETTI, J.P.FREIDBERG, *Phys.Fl.* **B3** 1865 (1991).
11. S.E. SHARAPOV et al., *Phys. of Plasmas* **9** 2027 (2002).
12. A. FASOLI et al., *PPCF* **44** B159 (2002).
13. S.E. SHARAPOV et al., *Phys.Rev.Lett.* **93** 165001 (2004).
14. S. HAQUIN et al., *PPCF* **49** 1371 (2007).
15. B.B. KADOMTSEV, *Collective phenomena in plasmas*, Moscow: Nauka, 1976 (in Russian).
16. D.W. ROSS et al. *Phys. Fluids* **25** 652 (1982).
17. K.APPERT et al. *PPCF* **24** 1147 (1982).
18. B.N. BREIZMAN, S.E. SHARAPOV, *PPCF* **37** 1057 (1995).
19. H.L. BERK et al., *Phys. Lett.* **162A** 475 (1992).
20. D.T. SIGMAR et al., *Phys. Fluids* **B4** 1506 (1992).
21. H.L. BERK et al., *Phys. Fluids* **B5** 3969 (1993).
22. L.C. APPEL et al., *Nucl. Fusion* **35** 1697 (1995).

NEOCLASSICAL TEARING MODES

H.R. Wilson

*York Plasma Institute, Department of Physics, University of York, Heslington, York, YO10 5DQ U.K.
howard.wilson@york.ac.uk*

ABSTRACT

Tearing modes often limit the performance of tokamak plasmas, because the magnetic islands which they generate lead to a loss of confinement, or even a disruption. A particularly dangerous instability is the neoclassical tearing mode, which can grow to a large amplitude because of the amplification effect that the bootstrap current has on an initial ‘seed’ magnetic island. This paper will address the mechanisms which dominate the neoclassical tearing mode evolution, and thereby identify possible control techniques.

I. INTRODUCTION

The good confinement of the tokamak is achieved because to leading order the ions and electrons follow the magnetic field lines, which in turn lie on toroidally symmetric, nested magnetic flux surfaces. However, there are a number of plasma instabilities which can modify the magnetic geometry and so lead to a reduction in confinement and a loss of plasma stored energy. In this paper we shall concentrate on a particular type of instability, the tearing mode, and explore its consequences for tokamak performance. One consequence of the tearing mode instability is that the plasma adopts a new, non-symmetric equilibrium (or, if the instability is particularly violent, the plasma can be lost altogether in a disruption). This new equilibrium is characterised by a chain of magnetic islands, and field lines can migrate radially around these over a distance comparable to the island width. The result is that the radial particle and energy flux is enhanced in the regions where the magnetic islands form, and the overall confinement is degraded (eg the central plasma temperature is reduced). For this reason, understanding the causes of tearing modes is an important part of tokamak physics research, and this paper provides a brief review of the progress made in our understanding, and the gaps that remain.

We shall begin in Section II with a brief summary of the basic properties of tearing modes, and provide a simple derivation of the ‘classical’ (Rutherford) tearing mode evolution equation¹. Then in Section III we shall address a number of other mechanisms which can contribute to the tearing mode evolution in toroidal plasmas to derive, heu-

ristically, the so-called modified Rutherford equation for neoclassical tearing modes (NTMs). In Section IV we shall explore the experimental evidence for neoclassical tearing modes and make comparisons with the theory. Finally, in Section V, we shall consider some of the control methods which have been proposed, largely motivated by our theoretical understanding of these instabilities.

II. CLASSICAL TEARING MODE PHYSICS

Let us begin by introducing some of the terminology associated with tearing mode physics, broadly following Ref [2]. To simplify the geometry, let us take an annulus of toroidal plasma with major radius R (say between minor radii $r=r_1$ and $r=r_2$), and cut this open in the toroidal and poloidal directions to form the plasma slab shown in Fig 1. We have placed an island chain at the radial position $r=r_s$ and indicated the positions of the so-called X-points and O-points of the island. It is conventional to define the mode structure in terms of the dominant Fourier components of the island; the case shown in Fig 1 has poloidal mode number $m=2$ and toroidal mode number $n=1$. Note that the dashed line connecting the island O-points is approximately a line of symmetry in the large aspect ratio approximation of the tokamak. Thus the island magnetic geometry can be defined in terms of three coordinates: the radial variable, r , the poloidal angle, θ , and a new helical angle, ξ , which is directed along a line perpendicular to

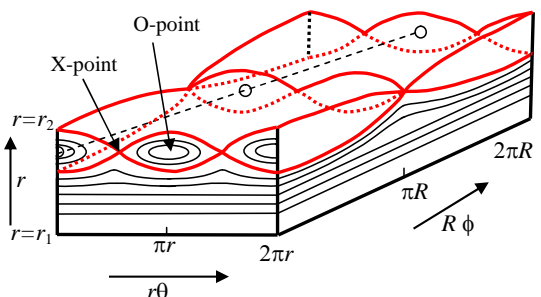


Fig. 1. A toroidal annulus of plasma showing flux surfaces forming magnetic islands. The annulus has been cut along the poloidal (θ) and toroidal (ϕ) directions and opened out.

that connecting the island O-points

$$\xi = \theta - \frac{n}{m} \phi \quad (1)$$

Again adopting a large aspect ratio approximation, we see that the component of magnetic field in the helical direction is given by

$$B_h = B_\theta \left(1 - \frac{n}{m} q(r) \right) \quad (2)$$

where B_θ is the poloidal component of the magnetic field and $q(r)$ is the safety factor. The role of the tearing mode instability is to provide the radial component of magnetic field required to generate a magnetic island. Denoting this by $\delta B = B_s \sin m\xi$, and noting that a field line will follow a trajectory given by

$$\frac{dr}{r_s d\xi} = \frac{\delta B}{B_h} \quad (3)$$

we see that the radial excursion of field lines is negligible unless B_h is small (we consider that the radial field generated by the tearing mode is typically much smaller than the equilibrium magnetic fields imposed in the tokamak by the machine operator). Thus the largest radial excursions are experienced at the radial position where $q=m/n$; that is, island chains form on rational surfaces. Taylor expanding q about the rational surface $r=r_s$, then we can use Eq (2) in Eq (3) to derive the following equation for the field lines:

$$\Omega = \frac{2x^2}{w^2} - \cos m\xi \quad (4)$$

where $x=r-r_s$, Ω is a flux surface label (a constant of the integration) and

$$w = 2 \left(\frac{rqB_r}{mB_\theta dq/dr} \right)^{1/2} \quad (5)$$

is the island half-width. Note that $\Omega=1$ defines the island separatrix, $-1<\Omega<1$ defines flux surfaces inside the island and $\Omega>1$ defines flux surfaces outside the island.

Having described the geometry and introduced the essential terminology, we are now in a position to describe some of the basic theoretical principles behind tearing modes. The theory can be broadly categorised into linear and non-linear theory. We shall be concerned with larger magnetic islands, so that the non-linear theory is the appropriate one to adopt here. Above, we characterised the

perturbation in terms of the radial magnetic field it produced; in fact we shall find it more convenient to instead use the flux function, ψ . Thus we define the perturbed flux

$$\psi = \tilde{\psi} \cos m\xi \quad B_r = \frac{m\tilde{\psi}}{rR} \quad (6)$$

where $\tilde{\psi}$ is related to B_r and is assumed to vary only slowly with radius over the island width length scale. In terms of ψ , the total magnetic field is given by

$$\mathbf{B} = f(r)\nabla\phi + \nabla\phi \times \nabla(\Psi + \psi) , \quad (7)$$

where $f(r)=RB_\theta$ and $\Psi(r)$ is the poloidal magnetic flux. Let us restrict consideration to small magnetic islands whose width is much less than the tokamak minor radius. Then the current perturbation is small, and we are justified in assuming that ψ varies only slowly with r . For islands whose width is much less than their length, Ampere's law relates ψ to the current density perturbation parallel to the magnetic field, J_\parallel :

$$\frac{1}{R} \frac{d^2\psi}{dr^2} = \mu_0 J_\parallel , \quad (8)$$

Another condition on the validity of this expression is that the perturbed current is localised about the island region so that, although $d\psi/dr$ is small, it changes rapidly in a narrow region in the vicinity of the island so that its second derivative need not be small. Making use of this we integrate across the island region from $r=-l$ to $r=l$, where $r_s \gg l \gg w$ is assumed. In addition we define a parameter which characterises the jump in $d\psi/dr$ across the island, conventionally denoted by the symbol Δ' :

$$\Delta' = \lim_{l \rightarrow \infty} \frac{1}{\psi} \left[\frac{d\psi}{dr} \Big|_{r=l} - \frac{d\psi}{dr} \Big|_{r=-l} \right] \quad (9)$$

As a result we arrive at the following basic equation for tearing mode evolution:

$$\Delta' \tilde{\psi} = 2\mu_0 R \int_{-\infty}^{\infty} dx \oint d\xi J_\parallel \cos m\xi \quad (10)$$

The next task is to determine the perturbed current. Note that it is only the current parallel to the magnetic field that contributes to the island evolution equation. The simplest model is that considered by Rutherford¹, in which the only contribution to J_\parallel comes from the induced current associated with island growth. Thus, for an island which is evolving, so that ψ has a time-dependence, an electric field proportional to $d\psi/dt$ is generated parallel to the magnetic field (note that ψ is proportional to the component of the

perturbed vector potential in the magnetic field direction). This gives rise to a current via Ohm's law:

$$\eta J_{\parallel} = \frac{\partial \tilde{\psi}}{\partial t} \cos m\xi - \nabla_{\parallel} \varphi \quad (11)$$

where η is the plasma resistivity, φ is the electrostatic potential and ∇_{\parallel} is the derivative along the perturbed magnetic field lines of the island.

It is worthwhile spending a little time considering the ∇_{\parallel} operator, which is defined as

$$\nabla_{\parallel} \equiv \frac{\mathbf{B} \cdot \nabla}{B} = \frac{1}{Rq} \frac{\partial}{\partial \theta} \Big|_{\Omega, \xi} + k_{\parallel} \frac{\partial}{\partial \xi} \Big|_{\theta, \Omega} \quad (12)$$

where $k_{\parallel} = -mx/rL_s$ and $L_s = Rq/s$, with $s = (r/q)(dq/dr)$ being the magnetic shear. A useful procedure is to define an average over the two angles, θ and ξ , which annihilates the ∇_{\parallel} operator. We shall indicate this averaging procedure by angled brackets, defined as

$$\langle \dots \rangle \equiv \begin{cases} \frac{\oint d\theta \oint d\xi \frac{\dots}{\sqrt{\Omega + \cos \xi}}}{\oint d\theta \oint d\xi \frac{1}{\sqrt{\Omega + \cos \xi}}} & \Omega > 1 \\ \sum_{\sigma} \sigma \frac{\oint d\theta \int_{-\xi_b}^{\xi_b} d\xi \frac{\dots}{\sqrt{\Omega + \cos \xi}}}{\oint d\theta \int_{-\xi_b}^{\xi_b} d\xi \frac{1}{\sqrt{\Omega + \cos \xi}}} & -1 < \Omega < 1 \end{cases} \quad (13)$$

where $\cos \xi_b = -\Omega$ and $\sigma = x/|x|$. We can now use this averaging operator to eliminate φ from Eq (11) as follows. First we note that we expect J_{\parallel} to be a function only of Ω , due to the fact that we neglect particle drifts perpendicular to the magnetic field for the present (so that perpendicular currents must also be absent), and therefore we must satisfy $\nabla \cdot \mathbf{J} = \nabla_{\parallel} J_{\parallel} = 0$. Thus, we arrive at the result

$$J_{\parallel} = \frac{1}{\eta} \frac{\partial \tilde{\psi}}{\partial t} \langle \cos m\xi \rangle \quad (14)$$

and substitution of this into Eq (10), together with Eq (5), yields the classical Rutherford tearing mode evolution equation:

$$a_1 \tau_r \frac{dw}{dt} = r_s^2 \Delta' \quad (15)$$

where $\tau_r = \mu_0 r_s^2 / \eta$ is the current diffusion time and $a_1 = 0.82$ is associated with the island geometry. Note that this equation predicts that an island will grow linearly in time provided $\Delta' > 0$, at least initially when the island is sufficiently

small that Δ' is independent of w . Clearly the parameter Δ' is important for the stability of tearing modes, and it is therefore useful to say a few more words about its physical significance, and how it is determined.

Recall that we have assumed that ψ is approximately independent of r in the vicinity of the island, and so far we have only solved for ψ , or equivalently w , in that region. Away from the island region, two simplifying approximations can be made: (1) the plasma response is linear, and (2) resistivity is unimportant. Thus, away from the island region the equations of linear ideal magnetohydrodynamics (MHD) can be used to evaluate $\psi(r)$ (note that over the longer length scales across the plasma minor radius, the r dependence of ψ cannot be neglected, and indeed is calculated from the ideal MHD equations). Applying appropriate boundary conditions at the plasma edge and centre, and integrating the MHD equations from the centre out to the rational surface, and from the edge into the rational surface, one can calculate $\psi(r)$ over the full plasma region, taking ψ to be continuous at the island rational surface. In general, one will find that this solution will have a discontinuous gradient at the rational surface, and from this one can calculate Δ' from the ideal region using Eq (9), but replacing $-l$ with the limit as $r \rightarrow r_s$ from below, and $+l$ with the limit as $r \rightarrow r_s$ from above. This is basically a matching condition between the solution for ψ in the ideal MHD region and that in the island region. Thus we see that Δ' is a property of the *global* plasma equilibrium, and in the limit of small islands ($w \ll r_s$) is not influenced by the presence of the island itself. Indeed, it can be shown that Δ' represents the free energy available in the plasma current density distribution to drive the tearing mode. In the following sections we will see how other effects can modify the evolution of tearing modes, but these are different from the Δ' drive in that they originate from the island region itself.

III. THE MODIFIED RUTHERFORD EQUATION

In the previous section we considered only the inductive contribution (due to island growth) to the perturbed current, J_{\parallel} . In this section we consider a number of other contributions, which together constitute the ingredients of the so-called neoclassical tearing mode (NTM).

Let us begin by considering the most important element: the perturbed bootstrap current^{3,4}. The bootstrap current is a current which flows along the tokamak magnetic field lines due to the combined effect of the trapped particles and the density and temperature gradients which exist. We do not go into the details of this current here, but it suffices to know that the bootstrap current is proportional to a linear combination of density and temperature gra-

dients, and requires the plasma to be in a low (so-called 'banana' or 'plateau') collisionality regime so that trapped particles can perform a complete orbit before being de-trapped by collisions. For our purposes it is sufficient to use a simple model for the bootstrap current, which we express in the form:

$$J_{bs} = -2.44 \frac{\sqrt{\varepsilon}}{B_0} \frac{dp}{dr} \quad (16)$$

This expression is accurate in the limit of small inverse aspect ratio, ε , and zero temperature gradient (p denotes the plasma pressure).

The main reason for a perturbation in the bootstrap current in the vicinity of the island is due to the island's effect on the plasma pressure there. Suppose that at some initial time there exists a magnetic island. There is rapid parallel transport along field lines so that the pressure is approximately a flux surface quantity; this means that in the absence of heat and particle sources inside the island, the pressure gradient tends to be removed from inside the island. From Eq (16) we therefore see that the bootstrap current is removed from inside the island, whilst outside (where a pressure gradient is still maintained across the flux surfaces) the bootstrap current remains. Thus there is a 'hole' in the bootstrap current which exists around the island O-points; ie there is an additional contribution to J_{\parallel} which has the required $\cos m\xi$ component to contribute to the island evolution in Eq (10). Thus, if we now combine this contribution with the inductive contribution, Eq (14), and substitute the total J_{\parallel} into Eq (10) (using Eq (5) for the island width in place of ψ), we find:

$$a_1 \frac{\tau_r}{r_s^2} \frac{dw}{dt} = \Delta' + a_2 \sqrt{\varepsilon} \frac{\beta_\theta}{w} \frac{L_q}{L_p} \quad (17)$$

We have introduced a new numerical factor a_2 , which originates from the integral over space, the poloidal beta, $\beta_0 = 2\mu_0 p/B_0^2$, $L_q^{-1} = d\ln q/dr$ and $L_p^{-1} = -d\ln p/dr$. Note that in normal tokamak situations $L_q/L_p > 0$ and therefore the bootstrap current term usually contributes a *drive* for the tearing mode (a notable exception is the case of reverse shear discharges, where $L_q < 0$). Indeed, for sufficiently small island widths the bootstrap term is the dominant one, so that even in situations when the plasma is stable to the classical tearing mode, the effect of the bootstrap current is to drive it unstable. In such cases the instability is called a *neoclassical tearing mode*.

Let us suppose that we are in this neoclassical tearing mode instability regime, so that $\Delta' < 0$. It is useful to plot dw/dt as a function of w , and this is shown in Fig 2. There

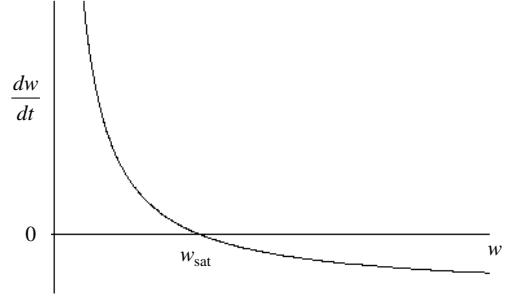


Fig. 2. The island growth as a function of the width, from Eq (17) indicating the saturated island width solution at $w=w_{sat}$.

is an important value of $w=w_{sat}$ for which $dw/dt=0$: for $w < w_{sat}$, $dw/dt > 0$, so the island will grow until $w=w_{sat}$; for $w > w_{sat}$, $dw/dt < 0$, so the island will shrink until $w=w_{sat}$. Thus we see that $w=w_{sat}$ is a stable point, corresponding to the saturated island width that the neoclassical tearing mode will evolve towards. We can use Eq (17) to derive:

$$\frac{w_{sat}}{r_s} = a_2 \sqrt{\varepsilon} \frac{\beta_\theta}{(-r_s \Delta')} \frac{L_q}{L_p} \quad (18)$$

In order to gain an order of magnitude estimate of the effect, let us further suppose that $L_q \sim L_p$ and that $r_s \Delta' \sim -2m$ (which is correct in the asymptotic limit of large m); then we find that

$$\frac{w_{sat}}{r_s} \sim \frac{\beta_\theta}{2m} \quad (19)$$

Equation (19) illustrates why these modes are so dangerous: as we increase β_θ the island will grow, leading to an ever increasing degradation in confinement; eventually a situation would be reached where all the heating power which is put into the plasma is immediately flushed out by the island, and it will be impossible to increase β_θ further. In this sense, the NTM provides a 'soft' β -limit. However, particularly for low m modes, we see that Eq (19) predicts that island sizes can become comparable to the minor radius of the tokamak: then we would expect the plasma to respond violently, and terminate in a disruption.

If Eq (17) represented the full story, then the future of the tokamak would be exceedingly bleak, and indeed it would not have enjoyed the success it has had, particularly in recent years. The point is that, according to Eq (17), all neoclassical tearing modes which have a rational surface in the plasma would be unstable and the confinement would be completely wrecked. This clearly is not the case,

and so there must be more to the story. Indeed there are additional effects which are important when the island size is very small. For such small islands the theory is seriously complicated by both finite particle orbit width effects and finite radial transport effects. To illustrate this, note that the theory used to calculate the bootstrap current expression given in Eq (16) is based on an expansion in the ratio of ion banana width to the equilibrium length scales, assumed small. Clearly, then, for islands whose width is of order the ion banana width, Eq (17) may be flawed. Indeed, all rigorous analytic calculations of the modified Rutherford equation to date rely on an expansion in the ratio of the ion banana width to the island width: this therefore sets the scale at which the theory must be questioned. Let us now look briefly at two additional effects which may be important for such small islands.

We begin with the effects of radial diffusion^{5,6}. Recall that we made the statement that the pressure gradients would be removed from inside the island region. This is a statement that the parallel transport effects dominate the radial diffusion. For arguments sake, let us consider a model for the electron heat transport (the particle transport is further complicated by the requirement that we expect quasi-neutrality to be maintained and the parallel transport would be dominated by sound waves). In steady state, and in the absence of any heat sources, we expect $\nabla \cdot \mathbf{Q} = 0$, where \mathbf{Q} is the heat flux. Suppose the heat flux parallel to the field lines is given by $Q_{\parallel} = -n\chi_{\parallel} \nabla_{\parallel} T$ and that perpendicular to the field lines is $Q_{\perp} = -n\chi_{\perp} \nabla_{\perp} T$ where χ_{\parallel} and χ_{\perp} are the thermal diffusivities parallel and perpendicular to the magnetic field, respectively, n is the density and T is the temperature. Taking these diffusivities to be approximately constant over the island width length scale of interest, we deduce

$$\nabla \cdot \mathbf{Q} = n\chi_{\parallel} \nabla_{\parallel}^2 T + n\chi_{\perp} \nabla_{\perp}^2 T = 0 \quad (20)$$

Now if the perpendicular transport can be neglected, then Eq (20) clearly provides the result that the temperature is constant on a field line (and it then follows that it must be constant inside the island). Suppose we now consider the conditions under which the perpendicular transport effects cannot be neglected. It is easiest to assume that T is independent of θ , ie $T = T(\Omega, \xi)$, and then the parallel operator can be taken to be of order $mw/(RqL_q)$ (see Eq (12) and note that the relevant length scale in k_{\parallel} is $x \sim w$). For the perpendicular gradients, the relevant length scale is again w , and so we deduce that the radial transport term will compete with the parallel transport term when

$$\frac{m^2 w^2}{R^2 q^2 L_q^2} \chi_{\parallel} \sim \frac{\chi_{\perp}}{w^2} \quad (21)$$

that is, for a sufficiently small magnetic island. Rearranging Eq (21) we can therefore deduce a critical island width, w_{χ} , below which the pressure is not flattened across the island, and therefore the drive for the NTM is reduced:

$$w_{\chi} = \sqrt{\frac{RqL_q}{m} \left(\frac{\chi_{\perp}}{\chi_{\parallel}} \right)^{1/4}} \quad (22)$$

[Note that in hot, collisionless plasmas, free streaming dominates the parallel transport, resulting in a balance $k_{\parallel} v_{\parallel} \sim \chi_{\perp} \nabla_{\perp}^2$, and a different scaling for w_{χ}]. To estimate the size of w_{χ} and how it scales with plasma parameters is difficult because this needs knowledge of the perpendicular heat diffusivity in the plasma, and this is not well-understood. If one puts in neoclassical heat diffusivity, then one obtains a very small value of the order 1mm: clearly the NTM model we have described is not appropriate at such small scale lengths, when finite Larmor radius effects will inevitably play a role. However, we know that in tokamaks the perpendicular heat flux is larger than the neoclassical prediction because of the plasma turbulence. As one possible model for this, let us assume that the transport has a gyro-Bohm scaling, ie $\chi_{\perp} \sim \rho_j^2 v_{thj}^2 / r$, where ρ_j is the Larmor radius and v_{thj} is the thermal velocity (j labels ions or electrons). Taking a collisional model for the parallel diffusivity, $\chi_{\parallel} \sim v_{the}^2 / \nu_e$, where ν_e is the electron collision frequency, we then have the estimate:

$$w_{\chi} \sim \sqrt{\frac{L_q \rho_i}{m} v_{*e}^{1/4} q^{1/4} \left(\frac{\epsilon m_e}{m_i} \right)^{1/8}} \quad (23)$$

where m_j and ν_{sj} are the mass and collisionality of species j , respectively. If we take typical tokamak parameters, then we find that this predicts a value in the region $w_{\chi} \sim 1\text{cm}$. This value puts us above the length scales where Larmor radius effects are important, but is typical of the ion banana width in a tokamak, and therefore we remain in a regime where finite orbit width effects need to be taken into account. [Note that the parallel transport of density and ion heat is slower than that of the electron heat, and thus w_{χ} would be somewhat larger for these quantities.]

Let us now consider finite orbit width effects. There is no simple model to describe these, and therefore we will not attempt to reproduce the analysis here, but instead restrict ourselves to a discussion of the origin of the effect. Interested readers can consult the reference list for the more detailed theory, which is an evolving subject⁷⁻¹⁴. For small magnetic islands with width comparable to the ion banana width, the ions and electrons respond differently to the perturbed magnetic surfaces. For the electrons, the

parallel streaming (ie the $v_{\parallel}\nabla_{\parallel}$ term in the kinetic equation) dominates their response, and the electron distribution function will adjust so that, to leading order, it will be constant along the perturbed field lines. In contrast, for the ions the $E\times B$ drift dominates their response. Clearly the ion density must be a flux surface quantity if the electron density is (to satisfy quasi-neutrality) and therefore the $E\times B$ drift must be strongest along the perturbed flux surfaces. This, in turn, means that an electrostatic potential must be generated which is constant on the island flux surfaces. Away from the island (ie a few island widths away) both the electron and ion distribution functions are unaffected by the island, and therefore this electrostatic potential is localised around the island.

Having established that an electrostatic potential is an essential feature of any small scale island, let us now consider the more detailed consequences of this. The trapped ions will execute their banana orbits, and in doing so will experience an average of the potential over these orbits. The electrons, on the other hand, have a much narrower banana orbit, and they will experience the local potential. The consequence of this is that the $E\times B$ drifts of the two species will differ, and therefore a current perpendicular to the magnetic field will be generated. This is the neoclassical polarisation current. We noted below Eq (10) that only a current parallel to the magnetic field can affect the island evolution. However, one finds that the divergence of this perpendicular current is not zero and therefore a small electric field is generated, directed along magnetic field lines. This accelerates the electrons to generate a parallel current (the sum of this parallel current and the perpendicular current is divergence-free), and this does contribute to the island evolution. An additional feature of the neoclassical polarisation current is that when the ion collision frequency is sufficiently high, ie $v_i/\varepsilon\omega > 1$ (ω is the island propagation frequency in the frame where the electric field far from the island is zero), the drift information carried by the trapped ions is communicated to the passing ions, leading to a large amplification of the polarisation current^{9,10}.

If one works through the algebra, one finds that this polarisation current contributes an additional term to the modified Rutherford equation, known as the polarisation term. A final point to note is that this polarisation term depends on the island propagation frequency ω , and can be either stabilising or destabilising. This complicates matters because additional, uncertain, physics related to plasma dissipation processes (eg viscosity or Landau damping) needs to be introduced in order to determine ω , and here the theory is as yet incomplete¹⁵. What is generally assumed, and this will suffice for our purpose, is that the mode frequency is such that the polarisation current provides a stabilising effect (without this assumption it is dif-

ficult to interpret the experimental data, which we come to in the next section). The result is our final expression for the modified Rutherford equation, which becomes:

$$a_1 \frac{\tau_r}{r_s^2} \frac{dw}{dt} = \Delta' + a_2 \sqrt{\varepsilon} \frac{\beta_\theta}{w} \frac{L_q}{L_p} \frac{w^2}{w^2 + w_\chi^2} - a_3 g(\varepsilon, v_i) \left(\frac{\rho_{bi}}{w}\right)^2 \left(\frac{L_q}{L_p}\right)^2 \frac{\beta_\theta}{w} \quad (24)$$

$$g(\varepsilon, v_i) = \begin{cases} 1.64\varepsilon^{1/2} & v_i/\varepsilon\omega \ll 1 \\ \varepsilon^{-1} & v_i/\varepsilon\omega \gg 1 \end{cases} \quad (25)$$

ρ_{bi} is the ion banana width and a_3 is a third numerical coefficient associated with the spatial integral (which appears in Eq (10)) and the value of ω . Equation (24) can be derived using drift-kinetic theory, provided the island width is larger than the ion banana width and $w_\chi \rightarrow 0^9$. We shall assume that the expression actually holds for island widths down to the ion banana width, but stress that as yet there is no theoretical justification for this assumption. Such a justification is a challenging task, which can probably only be addressed through large scale computational modelling¹².

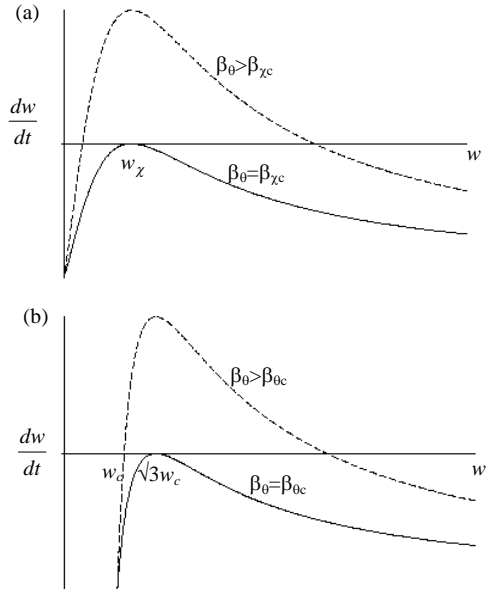


Fig. 3. Plots of dw/dt versus w for (a) the transport threshold model, and (b) the polarisation current model. Curves for β_θ equal to its critical value and exceeding this value are shown.

Note that we have taken account of the effect of the radial transport through a modification of the bootstrap current term: this modification is an interpolation formula, which reproduces Eq (17) for $w \gg w_\chi$ and also reproduces the results of linear theory in the opposite limit $w \ll w_\chi$. Equation (24) thus provides a model which includes all the essential ingredients of neoclassical tearing modes. [There is an additional, so-called ‘Glasser’ stabilising term^{16,17}, which we have not discussed here due to space limitations; this may be particularly important for spherical tokamaks¹⁸.]

Both the radial transport effects and the polarisation current can provide a threshold for NTMs. Let us first take $a_3=0$ and consider finite w_χ : this is shown in Fig 3a (to be compared with Fig 2, where no threshold effects were included). We see that for $\beta_0 < \beta_{\chi c}$ $dw/dt < 0$ for all w , so any initial ‘seed’ perturbation which led to a magnetic island would always decay away. However, for $\beta_0 > \beta_{\chi c}$ the situation is particularly interesting: there are now *two* values of w for which $dw/dt=0$. For $w < w_{\chi c}$, $dw/dt < 0$ and the island will tend to shrink, while for $w > w_{\chi c}$, $dw/dt > 0$ and the island will grow; indeed it will continue to grow until w reaches w_{sat} , when $dw/dt=0$ again. For $w > w_{\text{sat}}$, $dw/dt < 0$ and islands will decay. Thus we note that $w=w_{\text{sat}}$ again corresponds to a stable point, corresponding to a saturated island. On the other hand, the point $w=w_{\chi c}$ is an unstable point: it corresponds to a threshold in that an initial ‘seed’ island width must exceed this value for the island to grow to the large width $w=w_{\text{sat}}$. Thus, for this model, two conditions are required for growth of the NTM: both β_0 and the ‘seed’ island width must exceed critical values. These critical values, which can be deduced from Eq (24), are

$$\beta_{\chi c} = -\frac{2\Delta' w_\chi L_p}{a_2 \sqrt{\varepsilon} L_q} \quad w_{\chi c} = \frac{w_\chi \beta_{0c}}{2\beta_0} \quad (26)$$

where the expression for $w_{\chi c}$ is given for β_0 far above threshold (at threshold $w_{\chi c}=w_\chi$).

We turn to the polarisation term ($a_3 \neq 0$) and set $w_\chi=0$. Fig 3b shows dw/dt as a function of w ; we see that it is essentially of the same form as that obtained from the transport effects, described above. Again we see that thresholds in *both* β_0 and w need to be exceeded for island growth, and they can be deduced from Eq (24):

$$\beta_{0c} = \frac{3\sqrt{3}}{2a_2 \sqrt{\varepsilon}} \frac{L_p}{L_q} (-w_c \Delta') \quad (27)$$

$$w_c = \sqrt{\frac{a_3}{3a_2}} \frac{\sqrt{g(\varepsilon, V_i)}}{\varepsilon^{1/4}} \sqrt{\frac{L_p}{L_q}} \rho_{bi}$$

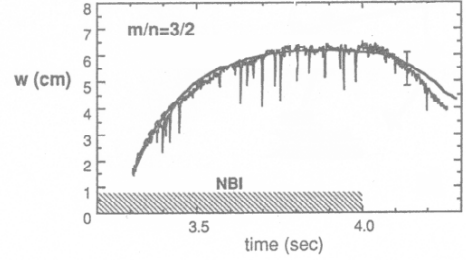


Fig. 4: Trace comparing the experimentally determined island width in TFTR with the result obtained by integrating Eq (17); ‘NBI’ indicates the time for which neutral beam injection heating was applied [Reprinted with permission from Z Chang et al, *Phys Rev Lett* **74** 4663 (1995). Copyright (1995) by the American Physical Society.].

The expression for w_c is given for β_0 far above threshold (at threshold w_c is simply a factor $\sqrt{3}$ larger). There are two important points to note about this result: (1) the threshold is predicted to be significantly larger in the collisional regime (through the variable g , see Eq (25)) and (2) the thresholds are proportional to the ion banana width.

IV. EXPERIMENTAL EVIDENCE

The first evidence for neoclassical tearing modes in a tokamak came from measurements on the TFTR tokamak¹⁹. In Fig 4 we show a comparison between the measured magnetic signal and the prediction of Eq (17), and we see that in general the comparison is rather encouraging. However, two features are evident: (1) at the beginning of the trace, we see that the mode is initiated at finite amplitude, suggesting that a threshold ~ 1 cm needs to be exceeded for island growth, and (2) the fit is not so good when the island starts to decay. Both of these point towards a

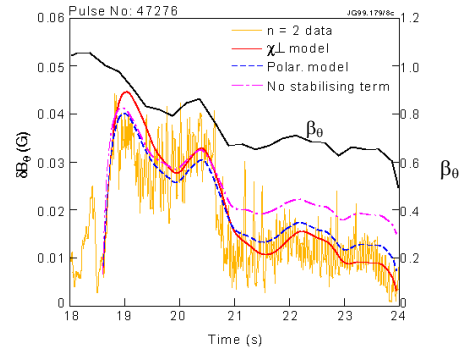


Fig. 5. Tracking the island evolution as the heating power is reduced on JET, we see that inclusion of either of the threshold effects improves the agreement with the measured amplitude of the magnetic perturbation, δB (from Ref 20)

threshold mechanism which is important for small island widths, but has little influence on the evolution of larger islands. Indeed, this is a property of both of the threshold effects we have discussed above. Careful experiments on JET have shown that the agreement between the data and experiment is much better when the threshold effects are taken into account²⁰, and this can be seen in Fig 5, where the predicted evolution is plotted (1) neglecting threshold effects, (2) including only the transport effect and (3) including only the polarisation effect. Recent high resolution temperature profile measurements in the vicinity of NTMs on MAST indicate that the transport effects are likely to play a role in the threshold physics²¹.

The theory we have described suggests that very small islands cannot grow (at least if $\Delta' < 0$); ie, island growth cannot occur unless an initial 'seed' island is generated by some other mechanism to excite it above the threshold. This does indeed seem to be the case experimentally, and in many cases NTM growth follows immediately after a sawtooth crash^{22,23,24}. One model is that the sawtooth is predominantly an instability associated with the $q=1$ surface, but that as this instability grows, it induces magnetic island chains at other rational surfaces through toroidal coupling, for example. If these so-called 'sideband' islands exceed the thresholds for NTM growth, then as the sawtooth crash occurs, and the associated $q=1$ instability disappears, the NTM is free to grow. Other types of instability have also been observed to seed NTMs²⁴.

Experiments have probed the conditions for NTM onset rather deeply^{21,25,26}. In particular, roles have been deduced for both collisionality and ρ_* (which is the ratio of ion Larmor radius to minor radius). While there seems no general consensus between the different devices for the dependence on collisionality, it is generally observed that NTMs are only observed at lower values of collisionality. One feature of the polarisation threshold model is that it is a much stronger effect at higher collisionality (through $g(\epsilon, \nu_i)$), and the transport model can also provide a collisionality dependence. In addition, experiments on ASDEX-Upgrade seemed to confirm a role for ρ_* in the threshold²⁵, as predicted by the polarisation model, but could also originate from the transport model if one adopts a gyro-Bohm scaling for the perpendicular diffusivity (see Eq(23)). A particular concern for ITER is that a multi-machine database appears to indicate that the threshold β_0 is linearly proportional to ρ_* , a parameter which is rather small on ITER^{20,26}. On the other hand, there is also some evidence that the seed island size reduces as ρ_* gets smaller²⁶, and then whether or not NTMs will be an issue on ITER will depend on which gets smaller faster: the threshold, or the seed islands from the sawteeth. So far we do not have sufficiently accurate data in the correct regimes to be

confident in the predictions, and therefore it is prudent to assume NTMs will be an issue for ITER, and we must guard against them.

The key to avoiding or controlling NTMs is current drive. One can envisage two schemes: (1) to reduce the free energy available in the equilibrium current profile so that Δ' becomes more negative, and (2) to drive current directly at the island O-point (to replace the missing bootstrap current). Both of these have been tried, with success. In COMPASS-D, radio-frequency waves in the lower hybrid frequency range have been used to drive current close to the rational surface where the island forms²³. In these experiments, the radial width of the current deposition was typically much wider than the island width, and then it can be shown that there is little contribution to the right hand side of Eq (10). However, calculations of Δ' showed that the additional current that was being driven by the lower hybrid waves did make Δ' more negative, and then both expressions (26) and (27) predict that the threshold for NTMs is increased. Fig 6 shows the experimental results.

The second technique is to drive current directly at the island O-point, highly localised within the magnetic island. Here the stabilisation is achieved through an additional contribution to J_{\parallel} on the right hand side of Eq (10). This has been achieved using radio-frequency waves at the electron-cyclotron resonance, which drives current in a much narrower radial region than the lower hybrid waves used on COMPASS-D. In particular, successful experiments have been performed on ASDEX-Upgrade²⁴ and DIII-D²⁵, and this is the method envisaged for ITER.

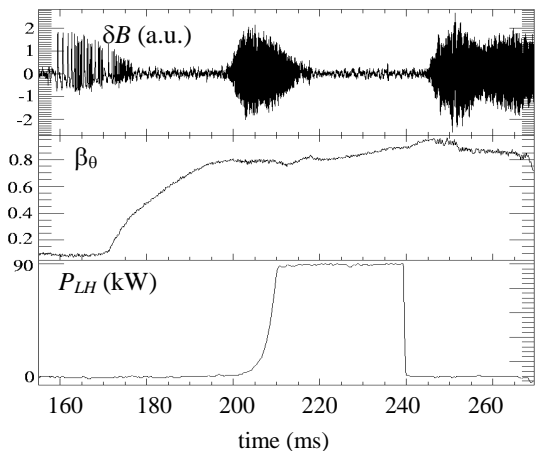


Fig. 6. The magnetic signal (δB) shows the growth of a NTM on COMPASS-D after 190ms, with a corresponding saturation in β_0 . 90kW of lower hybrid power (P_{LH}) is switched on just after 200ms, the NTM decays, and β_0 again rises.

V. SUMMARY

In summary, understanding the physics of the NTM is one of the success stories of fusion. The instability was predicted 10 years before it was identified experimentally, and since then theories have been refined, and broadly confirmed, by more detailed experiments. Nevertheless, the theory is still some way short of being truly predictive: it needs to address the seed island formation, as well as provide more accurate, quantitative models of the threshold effects, both of which require improved models to describe the relevant situation when the island width is comparable to the ion banana width. This will inevitably require the development of large scale numerical models for the situation. The neoclassical tearing mode is likely to be an issue for ITER, but the prospects for controlling them using radio-frequency waves to drive current close to the rational surface, or perhaps by controlling the seeding mechanism²⁶, look promising. This remains an evolving topic of research, both theoretically and experimentally.

ACKNOWLEDGMENTS

I should like to thank Richard Buttery, Jack Connor and Anthony Webster for their helpful comments.

REFERENCES

1. P H Rutherford "Nonlinear growth of the tearing mode", *Phys Fluids* **16** 1903 (1973)
2. J Wesson, *Tokamaks, first edition* (Clarendon Press, 1987), p168
3. R Carrera, R D Hazeltine and M Kotschenreuther "Island bootstrap current modification of the non-linear dynamics of the tearing mode", *Phys Fluids* **29** 899 (1986)
4. W X Qu and J D Callen "Nonlinear growth of a single neoclassical MHD tearing mode in a tokamak", University of Wisconsin report UWPR 85-5 (1985)
5. R Fitzpatrick "Helical temperature perturbations associated with tearing modes in tokamak plasmas", *Phys Plasmas* **2** 825 (1995)
6. R D Hazeltine, P Helander and P J Catto "Plasma transport near the separatrix of a magnetic island", *Phys Plasmas* **4** 2920 (1997)
7. A I Smolyakov "Nonlinear evolution of tearing modes in inhomogeneous plasmas" *Plasma Phys Control Fusion* **35** 657 (1993), and references therein.
8. J W Connor, F L Waelbroeck and H R Wilson "The role of polarization current in magnetic island evolution", *Phys Plasmas* **8** 2835 (2001), and references therein
9. H R Wilson, J W Connor, R J Hastie and C C Hegna "Threshold for neoclassical magnetic islands in a low collision frequency tokamak", *Phys Plasmas* **3** 248 (1996)
10. H R Wilson et al "The collisionality dependence of tokamak β -limits", *Plas Phys Control Fusion* **38** A149 (1996)
11. F L Waelbroeck, J W Connor and H R Wilson, "Finite Larmor radius theory of magnetic island evolution", *Phys Rev Lett* **87** (2001) 215003-1
12. A Bergman, E Poli and A G Peeters, "Collisionality dependence of the polarisation current", *Phys Plasmas* **12** 072501 (2005)
13. R. Fitzpatrick and F.L. Waelbroeck, "Drift-tearing magnetic islands in tokamak plasmas" *Phys Plasmas* **15** (2008) 012502
14. M James, H.R. Wilson and J.W. Connor "Modelling the effect of cross-field diffusion on tearing mode stability", *Plas. Phys. Cont. Fusion* **52** (2010) 075008
15. A B Mikhailovskii, et al "An approach to calculation of magnetic island rotation frequency", *Phys Plasmas* **7** 2530 (2000)
16. M Kotschenreuther, R D Hazeltine and P J Morrison "Nonlinear dynamics of magnetic islands with curvature and pressure", *Phys Fluids* **28** 294 (1985)
17. H.Lutjens, et al "Curvature effects on the dynamics of tearing modes in tokamaks", *Phys Plasmas* **8** (2001) 4267
18. C C Hegna "Nonlinear dynamics of pressure driven magnetic islands in low aspect ratio tokamaks", *Phys Plasmas* **6** 3980 (1999)
19. Z Chang et al, "Observation of nonlinear neoclassical pressure-gradient-driven tearing modes in TFTR", *Phys Rev Lett* **74** 4663 (1995)
20. R J Buttery et al "Neoclassical tearing modes", *Plasma Phys Control Fusion* **42** B61 (2000)
21. J. Snape, et al, "The influence of finite radial diffusion on the structure and evolution of m/n=2/1 neoclassical tearing modes on MAST", *Plas. Phys. Control. Fusion* **54** (2011) 085001
22. R J la Haye and O Sauter "Threshold for metastable tearing modes in DIII-D", *Nucl Fusion* **38** 987 (1998)
23. R J Buttery et al "Onset and control of neoclassical tearing modes on JET", *Proceedings of the 26th EPS Conference on Controlled Fusion and Plasma Physics (Maastricht)* 121 (1999)
24. A Gude et al "Seed island of neoclassical tearing modes at ASDEX Upgrade", *Nucl Fusion* **39** 127 (1999)
25. S Günter et al " β scaling for the onset of neoclassical tearing modes at ASDEX-Upgrade", *Nucl Fusion* **38** 1431 (1998)
26. R J la Haye et al "Dimensionless scaling of the critical beta for onset of a neoclassical tearing mode", *Phys Plasmas* **7** 3349 (2000)
27. C D Warrick et al "Complete stabilization of neoclassical tearing modes with lower hybrid current drive on COMPASS-D", *Phys Rev Lett* **85** 574 (2000)
28. H Zohm et al "Experiments on neoclassical tearing mode stabilization by ECCD in ASDEX Upgrade", *Nucl Fusion* **39** 577 (1999)
29. R J la Haye et al "Control of neoclassical tearing modes in DIII-D", *Phys Plasmas* **9** 2051 (2001)
30. O Sauter et al "Control of neoclassical tearing modes by sawtooth control", *Phys Rev Lett* **88** 105001-1 (2002)

EDGE LOCALIZED MODES IN TOKAMAKS

Howard Wilson

*York Plasma Institute, Department of Physics, University of York, Heslington, York YO10 5DQ UK
Email: howard.wilson@york.ac.uk*

ABSTRACT

As one increases the heating power in a tokamak beyond a threshold, the confinement undergoes a bifurcation, with a dramatic increase in the confinement time by a factor ~ 2 . This improved confinement regime, or H-mode, is primarily due to the formation of an insulating region at the plasma edge, where steep pressure gradients can form. A feature of H-mode operation is a series of explosive plasma eruptions, called Edge Localised Modes, or ELMs. They repeatedly expel large amounts of energy and particles from the plasma, with serious consequences for the heat loads that plasma facing components must be designed to handle. The present understanding of these ELMs in terms of ideal magneto-hydrodynamic instabilities will be reviewed in this paper.

I. INTRODUCTION

In the early 1980's an exciting new discovery was made in tokamaks: the H-mode¹. This mode of operation is achieved by increasing the plasma heating power above a threshold. The plasma then undergoes a bifurcation to a new state called the H-mode, in which the confinement is typically a factor of two greater than that in the standard L-mode discharges. The discovery of the H-mode is exceedingly important for fusion. In particular, ITER relies on achieving H-mode in order to meet its objectives.

There has been much activity to understand why the plasma suddenly jumps to this high confinement state. It is known, for example, that the reason for the high confinement is that a transport barrier forms at the plasma edge. A transport barrier is a region where heat and/or particle transport across the magnetic flux surfaces is suppressed. The pressure gradient is therefore typically high there. While this is good for confinement, instabilities called edge localized modes, or ELMs, can be triggered^{2,3,4} in this high pressure gradient region (which is also sometimes called the pedestal region). These ELMs are repetitive events, which eject a large amount of

heat and particles from the plasma. In a large tokamak, like ITER, the energy expelled could cause excessive erosion⁵. It is therefore essential that this phenomenon is understood so that steps can be taken to ameliorate the effect of ELMs, or perhaps eliminate them altogether. This paper describes the progress that has been made in our understanding of ELMs in terms of magneto-hydrodynamic (MHD) instabilities. In particular, we shall explore some of the characteristic features of ELMs, and how they can be understood in terms of this model. In Section 2, we discuss some of the experimental signatures for ELMs, before introducing the so-called peeling-ballooning model in Section 3. This linear ideal magneto-hydrodynamic (MHD) model is widely believed to explain at least the largest ELMs, and some of the experimental evidence for this is described in Section 4. In Section 5 we consider non-linear aspects of the model, and again compare with experimental observations. We conclude in Section 6, including a brief discussion on ELM control techniques.

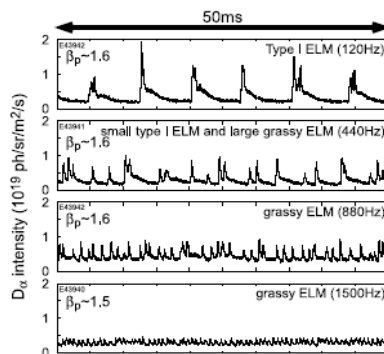


Fig. 1. D_α light emission, showing a sequence of ELMs on the JT-60U tokamak as bursts in the intensity; time traces for 4 discharges are shown giving examples of large, Type I ELMs (top) down to small, high frequency, “grassy” ELMs (bottom). [reproduced from Ref 6]

II. EXPERIMENTAL SIGNATURE OF ELMs

IIA. D_α light

An ELM is typically detected by observing the emission of D_α light near the divertor target plates, for example (see Fig 1). It is worthwhile considering the origin of the D_α light. The largest cross section for emission results from the interaction of electrons with neutral particles. Thus D_α light which is emitted from the divertor target plate region arises due to the electrons which are ejected from the core plasma during the ELM and then rapidly travel along the scrape-off layer towards the target plates where they interact with neutral particles. Ions are also ejected during the ELM, and these travel down to the target plate on a longer time-scale. They also increase the level of D_α light there by either (i) releasing more neutral particles from the target plate, which then interact with the electrons, or (ii) become neutralized themselves, again increasing the number of neutral particles for the electrons to interact with. After rapidly reaching a peak, the D_α light decays away more slowly as the ELM event finishes and the number of electrons arriving at the target plates decays to zero.

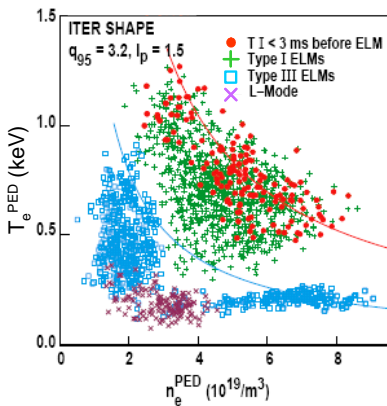


Fig. 2. Plot of temperature pedestal versus density pedestal for a range of different ELM types on DIII-D [figure reproduced from Ref 8]

IIB. ELM types

Experimentalists have managed to group the range of different ELM types into a number of different categories. Most ELMs fall into the category of Type I or Type III. The way these are typically distinguished is by measuring how the frequency of ELM events (ie the “ELM frequency”) varies with heating power. For Type I ELMs, the frequency increases with power, while for Type III ELMs the frequency decreases. Perhaps a more useful

distinction between the ELM types is obtained by comparing the temperatures and densities of discharges⁷. These are measured at the inner edge of the transport barrier: the so-called pedestal values. Figure 2 shows an example of how a set of discharges from DIII-D are distributed in the space of temperature pedestal, T_{ped} , versus density pedestal, n_{ped} ⁸. Note that the Type I ELMs are clustered around a line of constant pressure. This provides some evidence that these are instabilities that are driven by the plasma pressure. There are two clusters of Type III ELMs: one at high density, low temperature, and one at low density, high temperature. Both of these clusters are positioned at a pedestal pressure significantly below that where Type I ELMs occur. Note also that the Type III ELMs occur in a similar region to where the transition from the L-mode to the H-mode occurs.

It is found that regimes with Type I ELMs tend to have better confinement than those with Type III, but that the energy expelled in a Type I ELM event is much greater than for a Type III. Indeed, Type I ELMs would likely be too damaging on ITER, and therefore cannot be tolerated. The confinement degradation caused by Type III ELMs, on the other hand, is likely to be unacceptable. From Fig 2, it is clear that the pressure pedestal in Type III-ELMing discharges is significantly less than that in Type I discharges. This lower pedestal pressure is presumably the cause of the reduced confinement. This therefore raises the question “can we operate with a pressure pedestal characteristic of Type I ELM regimes, but with ELMs that release a much smaller amount of energy”? The answer is “yes”: but it is not easy and the parameter space required to achieve this is presently rather restrictive. Nevertheless, a range of small ELM regimes exist which seem to have good confinement⁹. These include Type II ELMs, grassy ELMs, Type V ELMs, etc. An example of grassy ELMs from the Japanese tokamak, JT-60U, is shown in the lower D_α trace of Fig 1, and compared to that for Type I ELMs. No clear definition of these regimes exists, and we will not attempt to refine our definition beyond that of small ELMs with good confinement. There is as yet no complete theoretical understanding for these ELM-types, but they do seem to be associated with strong plasma shaping and/or high edge safety factor. In addition, the grassy ELMs shown in Fig 1 appear to be associated with higher plasma rotation⁶. Without a rigorous understanding, it remains unclear whether ITER will be able to operate with any of these small ELMs. The subject therefore remains an active area of tokamak research.

III. PEELING-BALLOONING MODEL OF ELMs

Over the past decade the peeling-ballooning model^{10,11,12,13} has emerged as the strongest contender to explain the characteristics of the largest ELMs: Type I. In

addition, there is scope within the model to explain the origin of smaller ELM types, although the models here are much more qualitative and not universally accepted.

As the name suggests, the model derives from two particular instabilities: the ballooning mode and the peeling mode. The ballooning mode has a short wavelength perpendicular to the magnetic field lines, and a long wavelength parallel to them. It is destabilized when the pressure gradient exceeds a critical value, but tends to be stabilized by current density. In particular, sufficiently high current density completely stabilizes the ballooning mode, allowing the pressure gradient to be increased indefinitely (neglecting the effect of other types of instability). This is known as “second stability access”. These features are illustrated in Fig 3a. Actually, this second stability access strictly only occurs in the limit that the toroidal mode number, n , tends to infinity. As we shall see later, intermediate n modes (the peeling-ballooning modes) also have a drive due to the current density gradient, and these typically close off the second stability access. A final point to note is that the instability typically affects the whole of the plasma in the transport barrier region, and would therefore be expected to have a significant impact on it.

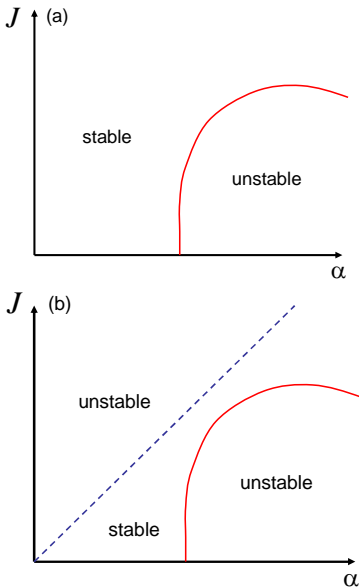


Fig. 3. Stability diagrams for (a) the ballooning mode and (b) the ballooning (full) and peeling mode (dashed). J is the current density at the plasma edge, α is the normalized pressure gradient.

The second type of instability, the peeling mode, is destabilized by the current density at the plasma edge, but stabilized by pressure gradient there. It is strongly related to the external kink instability, but is not limited to finite n . The schematic stability diagram for a limited plasma is illustrated in Fig 3b. This peeling mode is highly localized, and only affects a very small region of the transport barrier, exceedingly close to the plasma edge. At high pressure gradient, the peeling and ballooning modes couple^{10,14}, providing a strong instability with both current and pressure gradient drives that affects the whole transport barrier region. It is this coupled instability that is thought to be responsible for driving Type I ELMs.

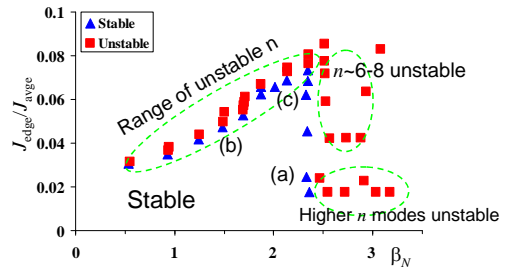


Fig. 4. Stability diagram for a JET-like plasma. The edge current density, J_{edge} , and normalized pressure, β_N , for each equilibrium are plotted as a square if unstable, and a triangle if stable.

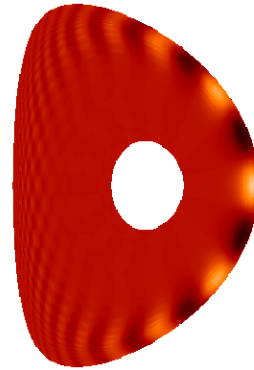


Fig. 5. ELITE calculation for the mode structure in the poloidal plane for a coupled peeling-ballooning mode. Orange represents zero perturbation, while dark and light colours correspond to positive and negative perturbations, respectively.

In Fig 4 we show the stability diagram for a (JET-like) model tokamak equilibrium. This has been produced using the ELITE code^{12,15}, which is a very efficient code for calculating the stability of the plasma edge to ideal MHD instabilities with intermediate to high toroidal mode numbers, n . For each point, the current density in the pedestal region is assumed to be a combination of the bootstrap current and Ohmic current. The stability boundary (between square and triangle symbols) is qualitatively similar to what one would expect, combining the peeling and ballooning stability boundaries of Figs 3b. Using ELITE, we can also evaluate the mode structures. Figure 5 shows the mode structure for a peeling-ballooning mode, which extends right across the pedestal region. Note that the amplitude is maximum on the outboard (low field) side. This characteristic is referred to as “ballooning”. The pure ballooning mode has a similar structure, but the pure peeling mode differs in two respects. First, the peeling mode has a similar amplitude on the inboard side to that on the outboard side (ie no ballooning nature). Second, it is extremely edge localized, typically well within the last 1% of poloidal flux (unless the toroidal mode number is low, ie $n \sim 1, 2$); we do not plot it here as it would not even be visible. The pure ballooning modes, from the region of Fig 4 labeled (a), have very high toroidal mode numbers (several 10’s); the pure peeling modes, from the region labeled (b) have a range of toroidal mode numbers, the most unstable having their external rational surface closest to the plasma edge; the peeling-ballooning modes, from the region labeled (c), have intermediate toroidal mode number $n \sim 10$.

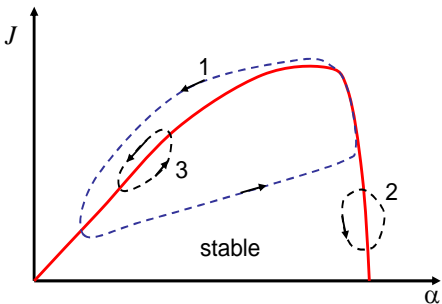


Fig. 6. Possible trajectories (dashed curves) of edge current density, J , and normalized pressure gradient, α , during ELMs. The stability boundary is indicated by the full curve. See text for descriptions and suggested links to ELM types.

Stability diagrams such as Fig. 4 are a simplification of the actual situation, as the stability diagram typically depends on the width of the pedestal region, as well as the pressure gradient within it (narrower pedestals tend to be more stable than wider ones at fixed pressure gradient).

The linear stability calculations shown in Figs 4 and 5 motivate the peeling-ballooning model for ELMs. Figure 6 shows a number of possible trajectories for the edge pressure gradient and current density in an ELMing discharge. These could correspond to different ELM types as follows. Starting with the trajectory labeled 1 in Fig 6, this is proposed as the trajectory of edge plasma parameters during a Type I ELM. Thus, while the plasma is stable between ELMs, the edge pressure gradient increases up to the ballooning boundary. The bootstrap current, which is proportional to the pressure gradient, would also increase until the peeling-ballooning mode is destabilized. Recall that this mode extends right across the transport barrier, so affects the whole pedestal region. As the instability develops, the expected increase of transport causes the pressure gradient to fall, further destabilizing the mode and triggering a large crash in the pressure (and consequent large energy loss). The discharge parameters eventually re-enter the stable region, and the cycle repeats. The trajectory labeled 2 is somewhat different. The plasma achieves a similar pressure gradient (and hence confinement) to the trajectory labeled 1, but now only the ballooning mode is destabilized. In this regime, which has reduced current compared to trajectory 1, the drop in pressure gradient stabilizes the ballooning mode, switching off the instability without a dramatic loss in pressure. This could provide an explanation of some of the small ELM regimes. Finally, the trajectory labeled 3 could provide a substantial loss of pressure gradient but, because the instability is so extremely edge-localized, the total loss of energy might be small (no rigorous theory for this speculative statement exists as yet). Note that the pressure gradient for this trajectory is significantly below that for trajectory 1, and this might therefore provide a model for Type III ELMs where the confinement is reduced (at least the class with low density and high temperature, where the edge current density is expected to be high).

Of the three models, the trajectory describing the Type I ELM behavior is the most accepted. The others are more speculative. Indeed, we shall see later that there is additional important physics that has been deduced from non-linear theories. This should be taken into account for a full understanding of ELM behavior. Before we address this non-linear physics, let us first consider some of the experimental evidence that supports some of the features predicted by this linear MHD model for Type I ELMs.

IV. EXPERIMENTAL EVIDENCE FOR THE PEELING-BALLOONING MODEL

The best way to test the peeling-ballooning model for ELMs is to carefully reconstruct the equilibrium using detailed measurements of the current density and pressure

actual experimental values of shear and α for this JET discharge (55937). The circle shows the parameters immediately (2ms) before an ELM, indicating that the discharge is indeed close to the stability boundary. It is therefore reasonable to assume that the instability is the cause of the ELM. Just after the ELM event (10ms after), the pressure gradient is lower, and the discharge moves away from the stability boundary. There are two points indicated at this later time, and these correspond to two assumptions about the plasma current which, as stated earlier, cannot be measured. The point at higher magnetic shear has a lower plasma current, given by the steady bootstrap current associated with the lower pressure gradient at this later time. The point at lower magnetic shear has a higher current density: in this case it is assumed that in the brief period between the ELM onset and the end of the ELM event, the current has not had time to relax. The current is therefore assumed to be the same as that immediately before the ELM (and given by the steady state bootstrap current at that time).

V. NON-LINEAR MODELS

VA. The theory

While linear models provide quantitative information about the onset of instability, they tell us relatively little about the consequences. In particular, it is unlikely that we shall be able to construct a predictive model for the energy ejected during an ELM on ITER based purely on linear theory. Having said that, we have already suggested that there might be a link between the radial extent of the linear eigenmode structure and the energy lost during the ELM. There is certainly some evidence to support this, at least qualitatively^{20,21}, but also quantitatively in some cases (eg from DIII-D¹²). However, in general there does not seem to be a one-to-one correspondence between the radial width of the linear eigenmode and the ELM-affected volume²². This does not exclude some form of correlation between the radial eigenmode width and the ELM-affected region, but the two do not appear to be the same in general.

Thus it seems unlikely that we can address the key question of how much energy is ejected during an ELM from a model based purely on the linear theory. This has motivated recent studies that address non-linear models. One of the first was an analytic calculation during the early non-linear phase of the ballooning mode in a tokamak plasma²³. This has recently been extended deeper into the non-linear regime²⁴. There were two key predictions from this first model²³: that the ballooning mode grows explosively during the non-linear phase, and that the instability would eject hot filaments of plasma. The explosive nature is an important point. One might expect from linear theory that a pure ballooning mode

would grow relatively slowly as the pressure gradient builds on a transport timescale through the marginally stable value. However, the non-linear theory suggests there is much more to the story. As the mode amplitude grows to a level where the non-linear terms first become important, the growth is accelerated much above the linear growth rate. In addition, the spatial structure of the mode is also altered during the non-linear phase to form filament-like structures that are predicted to be aligned with the magnetic field lines.

In Section 3 we described a model based on linear theory which suggests that the crash is a consequence of a coupling between the peeling and ballooning modes. The explosive growth predicted by the non-linear model suggests that it is possible to trigger a crash event just by considering the ballooning mode. However, there is another twist. The equation that describes the non-linear evolution of the ballooning mode has a key term that causes the explosive behavior. If the coefficient of this term is positive, the filaments erupt outwards towards the scrape-off layer, otherwise they erupt inwards towards the core. It has been found theoretically that filaments only erupt outwards when there is sufficient current density in the plasma edge²⁵. If one assumes that an outward-erupting filament is more dangerous than an inward one, then this could provide another reason why the ELM size might depend on the edge current density and provide an ingredient to understanding the differences between the mechanisms for large and small ELMs.

There are other types of models that predict filamentary structures. These are related to so-called ‘‘blob’’ theories, and predict that if a filament of plasma should break off from the core plasma, then it will propagate radially outwards due to an ExB drift^{26,27}. This is different to the non-linear ballooning mechanism, where the filament is only ejected from the outboard side, and remains connected into the core plasma on the inboard side. Thus the filaments due to a non-linear ballooning mode can continue to tap the free energy of the pressure gradient in the transport barrier, and accelerate rapidly away from the core plasma. In addition, because they remain connected to the core plasma, they can act as a conduit (or hose-pipe), linking the transport barrier region to the scrape-off layer, siphoning hot plasma from the barrier region into the exhaust region. If this is the mechanism, it raises a new concern: what if the filaments should strike the vessel wall on the outboard side while still connected to the core plasma on the inboard side? This would place very high heat loads on the vessel walls, where there is relatively little protection. If, on the other hand, the filaments break off from the core plasma before striking the wall they would have a reduced impact on it. If this is the case, there is scope for both mechanisms to play a role: the non-linear ballooning theory may be

relevant for the early phase of the ELM, while the “blob” theories may be relevant later, after the filament has detached.

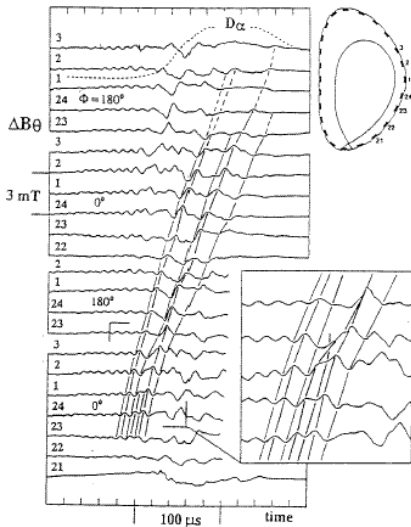


Fig. 9. Mirnov signals from a series of coils positioned at various toroidal and poloidal positions around the COMPASS-D tokamak²⁸.

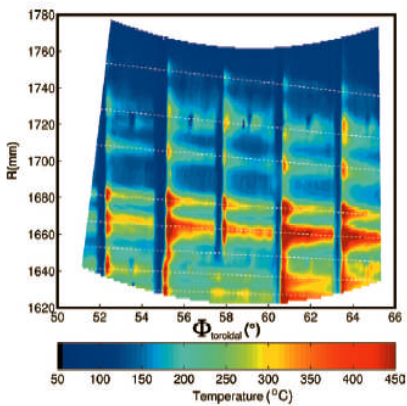


Fig. 10. Filamentary structures evident in the infra-red emission from the outer sections of the ASDEX-Upgrade divertor target [Figure reproduced from Ref 30]

VB. Experimental evidence for filaments

Some of the first data that suggested that filamentary structures might be associated with ELMs comes from COMPASS-D²⁸. A poloidal and toroidal array of Mirnov coils allowed the magnetic signal associated with the ELM to be tracked in time in the two directions. The results, reproduced in Fig 9, indicate a field-aligned structure. More recently, a series of stripes have been observed in the infra-red emission from the outer sections of the divertor in ASDEX-Upgrade (see Fig 10)^{29,30}. These stripes are also consistent with ELMs ejecting field-aligned filamentary structures. The most dramatic evidence, where the filaments were first observed directly, comes from the MAST tokamak^{31,32,33}. A unique feature of a spherical tokamak is that one can view the whole plasma surface through a port. Such a view is shown in Fig 11 where the filamentary structures are clearly visible. These filaments are aligned with the magnetic field lines, as theory would predict³³, and are ejected far into the scrape-off layer, and beyond. They are observed to accelerate radially, qualitatively consistent with the prediction of non-linear ballooning theory, and decelerate in the toroidal direction³³.

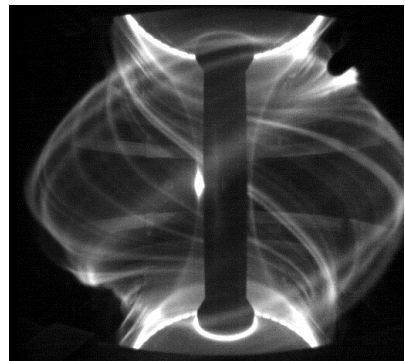


Fig. 11. Filamentary structures observed during ELMs on the MAST tokamak³²

Another interesting observation, made on both MAST and DIII-D, is that the rotation shear (that is the differential rotation between different flux surfaces) is eliminated during the ELM event^{34,35} (see Fig 12). Within the ideal MHD model of the non-linear ballooning mode, this must happen: the filament could not erupt out of the plasma if there is differential rotation. So again there is a nice consistency here. It does, however, raise an interesting question: Is the eruption of the filament causing a locking of the flow profile in the outer regions of the plasma, or is there some other event which removes

the flow shear, which then allows the filaments to erupt? In other words, is the filament a cause or consequence of the ELM? The consensus is that the filaments are the cause, but conclusive proof remains elusive.

VC. Heat loss mechanisms

Let us close this section with a discussion of the possible heat loss mechanisms. We simply state the possible mechanisms which might be operating here, and do not attempt to rule any of the models out or in. More details are provided in Ref 36.

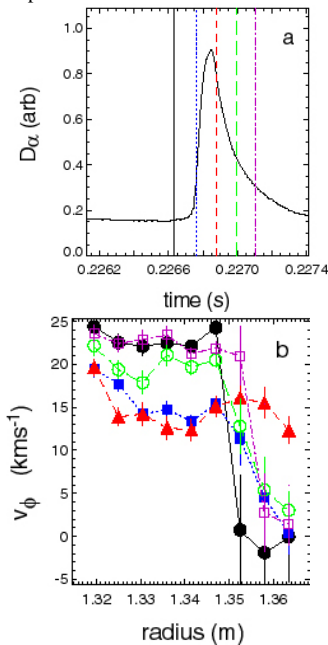


Fig. 12. Flow shear suppression during ELMs on the MAST tokamak. The full circles are the earliest time indicated by the vertical lines in the D_α trace of a single ELM (top), followed by the full squares, full triangles, open squares and open triangles. [Fig reproduced from Ref 34]

A key point to note is that within ideal MHD there can be no loss of heat or particles: everything that flows out along the filament into the scrape-off layer would flow back into the confinement region while the filament remained attached to the core plasma on the inboard side. It is necessary to introduce some additional physics. Three mechanisms are proposed for how the filaments might lead to enhanced transport. (1) The hot filaments “leak”, so that hot plasma flows across field lines from

the filament as it pushes out into the scrape-layer. (2) There is a reconnection process, probably in the vicinity of the X-point, in which the magnetic field lines contained in the hot filament break and then reconnect with the magnetic field lines of the scrape-off layer on the outboard side. Because the filament is relatively unperturbed on the inboard side, it remains inside the transport barrier there. Thus, following the reconnection event, there would be a continuous path along the filament from the pedestal region to the divertor target plates, and therefore a rapid loss of heat and particles. (3) The transport barrier is thought to be sustained by a sheared plasma flow within it. As the filament pushes out, it suppresses the flow shear and the barrier collapses with a significant, temporary confinement degradation. There is much experimental activity, and increasing efforts to simulate ELMs computationally, to identify the dominant mechanism. Both are exceedingly difficult, and are high priority areas of research for ITER.

VI. CONCLUSIONS

The importance of understanding ELMs and developing control scenarios for ITER is now well-established. Considerable progress has been made in our understanding, with the majority of the community accepting the peeling-ballooning model for at least the largest, Type I ELMs. There is also scope within the model to explain some of the other ELM regimes, but there is more uncertainty here. Non-linear theories have been developed and, together with experiment, have established that filamentary structures are likely to be an important part of the process of energy and particle loss during ELM events.

So, after all of this work, what are the consequences for ITER? ELMs remain one of the biggest concerns for ITER, which cannot operate for more than a few discharges at full power if large Type I ELMs are triggered. Small ELM regimes do exist, but the operating space for these is generally small, and it is not even clear that they will extrapolate to ITER. For this reason, there has been an increased focus on ELM control. We do not go into the details here, but instead refer the interested reader to the references. One method involves applying small magnetic perturbations to the plasma edge, thus degrading the confinement. The mechanism is not completely understood, but ELMs are then generally suppressed, probably because the pressure gradient in the transport barrier is maintained below the critical value for instability. Experiments on DIII-D validated and then perfected this form of ELM control^{37,38}, which has recently been repeated in ASDEX-Upgrade³⁹. A second technique, pioneered on ASDEX-Upgrade, is complementary to this. Rather than suppress ELMs, they are instead triggered more frequently by firing small

pellets of frozen deuterium into the transport barrier. Each time a pellet is fired into the plasma edge, an ELM is triggered⁴⁰. By triggering frequent ELMs, the energy released in a single event is smaller, and the impact on the divertor target is much reduced. A physical understanding of the mechanism is emerging from nonlinear MHD simulations⁴¹.

To summarize, there is still much to do for a complete understanding of the ELM event, although much progress has been made in the last decade. As well as being an issue that we must address for ITER, it is an area that is rich in physics. Here we have focused on the plasma physics issues, but there is also a range of issues related to plasma-surface interactions that must be brought into the model to develop a complete understanding of the ELM cycle: a formidable, but rewarding, task.

ACKNOWLEDGMENTS

I am grateful to Andrew Kirk, for many enlightening discussions regarding the experimental data and its interpretation.

REFERENCES

1. F. WAGNER, et al, *Phys Rev Lett* **53**, 1453 (1984)
2. H. ZOHM *Plasma Phys. Control. Fusion* **38**, 105 (1996)
3. J. W. CONNOR, *Plasma Phys. Control. Fusion* **40**, 531 (1998)
4. W. SUTTROP, *Plasma Phys. Control. Fusion* **42**, A1 (2000)
5. A. LOARTE, et al, *Phys Scri* **T128**, 222 (2007)
6. N. OYAMA, et al, *Nucl Fusion* **45**, 871 (2005)
7. W. SUTTROP, et al *Plasma Phys. Control. Fusion* **39**, 2051 (1997)
8. T. OSBORNE, et al, *Proceedings of the 24th EPS Conference on Controlled Fusion and Plasma Physics, Berchtesgaden Part III*, 1101 (1997)
9. N. OYAMA, et al, *Plasma Phys. Control. Fusion* **48**, (2006) A171
10. J.W. CONNOR, et al, *Phys. Plasmas* **5**, 2687 (1998)
11. H.R. WILSON, et al, *Phys. Plasmas* **6**, 1925 (1999)
12. P.B. SNYDER, et al, *Phys. Plasmas* **9**, 2037 (2002); Figure reprinted with permission from reference. Copyright (2002), American Institute of Physics.
13. P.B. SNYDER, et al, *Nucl Fusion* **44**, 320 (2004)
14. C.C. HEGNA, et al, *Phys Plasmas* **3**, 584 (1996)
15. H.R. WILSON et al, *Phys. Plasmas* **9**, 1277 (2002)
16. D. THOMAS, et al *Phys. Rev. Lett.* **93**, 065003 (2004)
17. S. SAARELMA, et al, *Plasma Phys. Control. Fusion* **47**, 713 (2005)
18. S SAARELMA et al, *Plasma Phys. Control. Fusion* **49**, 31 (2007)
19. C. KONZ, et al, to appear in *Proceedings of the 34th EPS Conference on Controlled Fusion and Plasma Physics, Warsaw* (2007)
20. L.L. LAO, et al, *Nucl. Fusion* **41**, 295 (2001)
21. S. SAARELMA et al, *Nucl. Fusion* **43**, 262 (2003)
22. A. LOARTE, et al *Plasma Phys. Control. Fusion* **44**, 1815 (2002)
23. H.R. WILSON and S.C. COWLEY, *Phys Rev Letts* **92** 175006 (2004)
24. P. ZHU, C.C. HEGNA and C.R. SOVINEC, *Phys Plasmas* **14**, 055903 (2007)
25. H.R. WILSON, et al *Proceedings of the 21st IAEA Fusion Energy Conference, Chengdu, on CD-ROM: IAEA-CN-149, paperTH/4-1Rb* (2006)
26. S.I. KRASHANNIKOV, *Phys Lett A* **283**, 368 (2001)
27. W. FUNDAMENSKI, et al *Plasma Phys. Control. Fusion* **48**, 109 (2006)
28. M. VALOVIC, et al, *Proceedings of 21st EPS Conference on Controlled Fusion and Plasma Physics, Montpellier Part I*, 318 (1994)
29. T. EICH, et al, *Phys Rev Lett* **91**, 195003 (2003)
30. T. EICH, et al, *Plasma Phys. Control. Fusion* **47**, 815 (2005)
31. A. KIRK, et al, *Phys Rev Lett* **92**, 245002 (2004)
32. A. KIRK, et al *Proceedings of the 21st IAEA Fusion Energy Conference, Chengdu, on CD-ROM: IAEA-CN-149, paper EX/9-1* (2006)
33. A. KIRK, et al *Plasma Phys. Control. Fusion* **48**, B433 (2006)
34. A. KIRK, et al *Plasma Phys. Control. Fusion* **47**, 315 (2005)
35. J.A. BOEDO, et al, *Phys. Plasmas* **12**, 072516 (2005)
36. H.R. WILSON, et al, *Plasma Phys. Control. Fusion* **48** A71 (2006)
37. R.A. MOYER, et al, *Phys. Plasmas* **12** (2005) 056119
38. T. E. EVANS, R.A. Moyer et al. *Phys. Rev. Lett.* **92** (2004) 235003
39. W. SUTTROP et al, *Phys. Rev. Lett.* **106** (2011) 225004
40. P.T. LANG, et al, *Nucl. Fusion* **44** 665 (2004)
41. G.T.A. HUYSMANS, et al, *Plasma Phys. Control. Fusion* **51** (2009) 124012

CLASSICAL AND NEOCLASSICAL TRANSPORT IN TOKAMAKS

P. Helander

Max Planck Institute for Plasma Physics
Wendelsteinstraße 1, 17491 Greifswald, Germany

ABSTRACT

These lecture notes provide a short overview of classical and neoclassical transport in tokamaks. The classical theory is widely applicable in laboratory and space plasma physics if the mean free path is shorter than the macroscopic scale length. The neoclassical theory predicts important phenomena in tokamaks such as the bootstrap current, electric conductivity, transport in the scrape-off layer, and cross-field transport in regions where the turbulence is suppressed.

I. INTRODUCTION

After Boltzmann had formulated his famous kinetic equation for dilute gases in the 1870's, an outstanding problem in theoretical physics was to calculate transport coefficients (heat conductivity and viscosity) from it. This problem remained open for over four decades until Chapman [1] and Enskog [2] independently found the correct asymptotic expansion. The extension of their technique to ionised gases is referred to as classical or neoclassical theory, depending on whether the geometry of the magnetic field plays a role. In either case, it is a rigorous theory, meaning that it provides an asymptotic solution of the kinetic equation

$$\frac{\partial f_a}{\partial t} + \mathbf{v} \cdot \nabla f_a + \frac{e_a}{m_a} (\mathbf{E} + \mathbf{v} \times \mathbf{B}) \cdot \frac{\partial f_a}{\partial \mathbf{v}} = C_a(f_a) \quad (1)$$

for each species a , under the assumption that the gyroradius parameter $\delta = \rho_a/L$ is small, where ρ_a is the gyroradius and L the macroscopic scale length. In classical transport theory, it is assumed that the collisional mean free path λ is short, $\lambda/L \ll 1$, whilst in neoclassical theory λ is arbitrary. The extension to long mean free path is possible because a transport ordering is adopted, meaning that the time derivative is considered small,

$$\partial/\partial t \sim \delta^2 v_{Ta}/L,$$

where $v_{Ta} = (2T_a/m_a)^{1/2}$ is the thermal speed. This ordering removes plasma waves from the equations.

There is one final assumption concerning the magnitude of the electric field. This can either be ordered large,

$$E/B \sim v_{Ta},$$

or small,

$$E/B \sim \delta v_{Ta},$$

and the resulting theory is somewhat different in the two cases. Most commonly, the first ordering is adopted in the classical theory and the second one in the neoclassical theory.

II. FLUID EQUATIONS

As is well known, the moments of (1) express the conservation of density, momentum and energy,

$$\frac{\partial n_a}{\partial t} + \nabla \cdot (n_a \mathbf{V}_a) = 0, \quad (2)$$

$$\frac{\partial (m_a n_a \mathbf{V}_a)}{\partial t} + \nabla \cdot \mathbf{\Pi}_a = n_a e_a (\mathbf{E}_a + \mathbf{V}_a \times \mathbf{B}) + \mathbf{F}_a, \quad (3)$$

$$\begin{aligned} & \frac{\partial}{\partial t} \left(\frac{3n_a T_a}{2} + \frac{m_a n_a V_a^2}{2} \right) + \nabla \cdot \mathbf{Q}_a \\ & = e_a n_a \mathbf{E} \cdot \mathbf{V}_a + \int \frac{m_a v^2}{2} C_a(f_a) d^3 v, \end{aligned} \quad (4)$$

and it is the task of the kinetic theory to calculate the friction force

$$\mathbf{F}_a = \int m_a \mathbf{v} C_a(f_a) d^3 v,$$

the pressure tensor

$$\mathbf{\Pi}_a = \int m_a \mathbf{v} \mathbf{v} f_a d^3 v,$$

the energy flux

$$\mathbf{Q}_a = \int \frac{1}{2} m_a v^2 \mathbf{v} f_a d^3 v,$$

and the collisional energy exchange on the right-hand side of (4). The viscosity tensor is defined as

$$\boldsymbol{\pi}_a = \mathbf{\Pi}_a - p_a \mathbf{I} - m_a n_a \mathbf{V}_a \mathbf{V}_a,$$

where \mathbf{I} is the unit tensor, and the heat flux is

$$\mathbf{q}_a = \mathbf{Q}_a - \frac{5p_a \mathbf{V}_a}{2} - \boldsymbol{\pi}_a \cdot \mathbf{V}_a - \frac{m_a n_a V_a^2 \mathbf{V}_a}{2}.$$

The collision operator

$$C_a = \sum_a C_{ab}(f_a, f_b) \quad (5)$$

is a sum of contributions from collisions with each particle species “ b ”, including $b = a$. Its detailed form will be of little concern to us, but it is important to know that it conserves particles,

$$\int C_{ab}(f_a, f_b) d^3v = 0,$$

which has been used in the derivation of the continuity equation (2), as well as momentum and energy,

$$\int m_a \mathbf{v} C_{ab}(f_a, f_b) d^3v = - \int m_b \mathbf{v} C_{ba}(f_b, f_a) d^3v, \quad (6)$$

$$\int \frac{m_a v^2}{2} C_{ab}(f_a, f_b) d^3v = - \int \frac{m_b v^2}{2} C_{ba}(f_b, f_a) d^3v. \quad (7)$$

It will also be useful to know that the operator contains pitch-angle scattering,

$$\text{a part of } C_{ab}(f_a) = \nu_{ab} \mathcal{L}(f_a),$$

where the scattering frequency ν_{ab} is of the order of the inverse collision time, and the scattering operator is defined by

$$\mathcal{L} = \frac{1}{2} \frac{\partial}{\partial \xi} (1 - \xi^2) \frac{\partial}{\partial \xi}, \quad (8)$$

with $\xi = v_{\parallel}/v$.

III. CLASSICAL TRANSPORT THEORY

This theory was developed independently by several authors, but the most well-known and pedagogic formulation is due to Braginskii [3]. It considers a plasma with a single ion species i , but can straightforwardly be extended to multiple ion species, and assumes the large-flow ordering, $E/B \sim v_{Ti}$. It is remarkable that the complete theory for the small-flow case was only worked out only half a century after Braginskii’s original work [4].

III.A. Chapman-Enskog expansion procedure

Since the flow is considered large, the first step is to transform the kinetic equation (1) to a coordinate frame moving with the flow velocity $\mathbf{V}_a(\mathbf{r}, t)$

$$\frac{df_a}{dt} + \mathbf{v}'_a \cdot \nabla f_a + \left[\frac{e_a}{m_a} (\mathbf{E}' + \mathbf{v}'_a \times \mathbf{B}) - \frac{d\mathbf{V}_a}{dt} \right] \cdot \frac{\partial f_a}{\partial \mathbf{v}'_a}$$

$$-v'_{aj} \frac{\partial V_{ak}}{\partial r_j} \frac{\partial f_a}{\partial v'_{ak}} = C_a(f_a),$$

where $\mathbf{v}'_a = \mathbf{v} - \mathbf{V}_a$, $\mathbf{E}' = \mathbf{E} + \mathbf{V}_a \times \mathbf{B}$ is the electric field measured in the moving frame, and

$$\frac{d}{dt} = \frac{\partial}{\partial t} + \mathbf{V}_a \cdot \nabla$$

is the convective derivative. The largest terms are those involving the collision operator and the magnetic field, and the equation can be solved perturbatively by expanding the distribution function accordingly, $f_a = f_{a0} + f_{a1} + \dots$. In lowest order, the large terms force the electron ($e_e = -e$) distribution function to be a Maxwellian at rest in the moving frame,

$$f_{e0} = n_e \left(\frac{m_e}{2\pi T_e} \right)^{3/2} e^{-x^2},$$

where $x^2 = m_e v_e'^2 / 2T_e$. In the next order, we obtain an equation for the correction f_{e1} to the Maxwellian

$$\begin{aligned} & C_{ee}(f_{e1}) + C_{ei}^0(f_{e1}) + \frac{e}{m_e} \mathbf{v} \times \mathbf{B} \cdot \frac{\partial f_{e1}}{\partial \mathbf{v}} \\ &= \left[\frac{d \ln n_e}{dt} + \left(x^2 - \frac{3}{2} \right) \frac{d \ln T_e}{dt} + \mathbf{v} \cdot \nabla \ln n_e \right. \\ &+ \left(x^2 - \frac{3}{2} \right) \mathbf{v} \cdot \nabla \ln T_e + \frac{m_e \mathbf{v}}{T_e} \cdot \left(\frac{e}{m_e} \mathbf{E}' + \frac{d\mathbf{V}_e}{dt} \right) \\ &\left. + \frac{m_e v_j v_k}{T_e} \frac{\partial V_{ek}}{\partial r_j} + \nu_{ei} \frac{m_e \mathbf{v} \cdot \mathbf{u}}{T_e} \right] f_{e0}, \quad (9) \end{aligned}$$

where we have now written \mathbf{v} instead of \mathbf{v}'_e and where $\mathbf{u} = \mathbf{V}_e - \mathbf{V}_i$ is the mean velocity of the electrons relative to the ions. $C_{ei}^0(f_{e1}) = \nu_{ei} \mathcal{L}(f_{e1})$ denotes the scattering part of the electron-ion collision operator.

A crucial insight by Chapman and Enskog was that the time derivatives on the right-hand side can be eliminated by taking moments of the equation. Indeed, integrating Eq (9) over velocity space gives the continuity equation (2), which implies that $d \ln n_e / dt$ can be replaced by $-\nabla \cdot \mathbf{V}_e$. The $m_e \mathbf{v}$ -moment gives the momentum equation (3), but without the viscosity term, and can be used to eliminate $d\mathbf{V}_e/dt$ and \mathbf{E}' by

$$\frac{d\mathbf{V}_e}{dt} + \frac{e\mathbf{E}'}{m_e} = \frac{\mathbf{F}_e - \nabla(n_e T_e)}{m_e n_e}.$$

The energy moment, finally, gives the energy equation (4), but without heat conduction and energy exchange,

$$\frac{3}{2} \frac{d \ln T_e}{dt} + \nabla \cdot \mathbf{V}_e = 0,$$

and this can be used to eliminate dT_e/dt in Eq (9). The reason why certain terms in the full fluid equations (2)-(4) do not appear in the moments of Eq (9) is that

they are small in the ordering assumed. Eliminating time derivatives from Eq (9) in this manner gives the following kinetic equation for f_{e1} in the electron rest frame,

$$\begin{aligned} & C_{ee}(f_{e1}) + C_{ei}^0(f_{e1}) + \frac{e}{m_e} \mathbf{v} \times \mathbf{B} \cdot \frac{\partial f_{e1}}{\partial \mathbf{v}} \\ &= \left[\left(x^2 - \frac{5}{2} \right) \mathbf{v} \cdot \nabla \ln T_e + \mathbf{v} \cdot \left(\frac{\mathbf{F}_e}{p_e} + \frac{m_e \nu_{ei} \mathbf{u}}{T_e} \right) \right. \\ & \quad \left. + \frac{m_e}{2T_e} \left(v_j v_k - \frac{v^2}{3} \delta_{jk} \right) W_{jk}^e \right] f_{e0}, \end{aligned} \quad (10)$$

where

$$W_{jk}^a \equiv \frac{\partial V_{aj}}{\partial r_k} + \frac{\partial V_{ak}}{\partial r_j} - \frac{2}{3} (\nabla \cdot \mathbf{V}_a) \delta_{jk}. \quad (11)$$

is the so-called rate-of-strain tensor. Note that there are three driving terms on the right: the temperature gradient, the term involving the friction force, and the tensor W_{jk} which measures how rapidly the flow velocity varies in space and gives rise to plasma viscosity.

The ion analysis is slightly simpler since the ion-electron collision operator can be regarded as small, which implies that the friction is negligible in the ion kinetic problem. The analogue of (10) for ions is thus

$$\begin{aligned} & C_{ii}(f_{i1}) - \frac{e}{m_i} \mathbf{v} \times \mathbf{B} \cdot \frac{\partial f_{i1}}{\partial \mathbf{v}} \\ &= \left[\left(x^2 - \frac{5}{2} \right) \mathbf{v} \cdot \nabla \ln T_i + \frac{m_i}{2T_i} \left(v_j v_k - \frac{v_i^2}{3} \delta_{jk} \right) W_{jk}^i \right] f_{i0}, \end{aligned} \quad (12)$$

The equations (10) and (12) are linear, integrodifferential equations involving the complicated (but linearised) Coulomb collision operator. They are traditionally solved by expanding the distribution function in a suitable set of orthogonal functions, which converts the problem to an infinite set of coupled linear algebraic equations. A sufficiently accurate solution can be found by truncating this system of equations after only a few terms.

III.B. Results

Following Braginskii, we display the results in the limit $\rho/\lambda = 1/\Omega_e \tau_e \rightarrow 0$, which is the most interesting case for most situations in fusion and astrophysics. Here $\Omega_e = -eB/m_e$ is the electron gyrofrequency and

$$\tau_e = \frac{12\pi^{3/2} m_e^{1/2} T_e^{3/2} \epsilon_0^2}{2^{1/2} n_i Z^2 e^4 \ln \Lambda}$$

the electron collision time, with $Z = 1$ the ion charge and $\ln \Lambda$ the Coulomb logarithm.

The force \mathbf{F}_e acting on the electrons consists of a drag force and a thermal force

$$\mathbf{F}_e = \mathbf{F}_u + \mathbf{F}_T, \quad (13)$$

$$\mathbf{F}_u = -\frac{m_e n_e}{\tau_e} (0.51 \mathbf{u}_{\parallel} + \mathbf{u}_{\perp}), \quad (14)$$

$$\mathbf{F}_T = -0.71 n_e \nabla_{\parallel} T_e + \frac{3n_e}{2\Omega_e \tau_e} \mathbf{b} \times \nabla T_e, \quad (15)$$

where $\mathbf{u} = \mathbf{V}_e - \mathbf{V}_i$ and $\mathbf{b} = \mathbf{B}/B$. Because of momentum conservation the force acting on the ions is equal and opposite, $\mathbf{F}_i = -\mathbf{F}_e$. The parallel friction coefficient in Eq (14) is seen to be smaller than the perpendicular one by a factor of 0.51, which has to do with the fact that the collision frequency decreases with velocity, ($\tau_e \sim v^3$), causing electrons with large parallel velocities to be more distorted from the Maxwellian distribution than slower ones. The fast electrons then contribute more to the relative velocity, and less to the friction. The parallel thermal force (15) is also a consequence of the circumstance that the collision frequency falls off with increasing energy, for consider a situation where the electron fluid is at rest with respect to the ion fluid, so that the drag force \mathbf{F}_u vanishes. A typical ion is bombarded by electrons streaming along the field with their respective peculiar velocities. If there is a temperature gradient along the field, those electrons that travel in the direction of the temperature gradient come from a slightly colder region and will be more collisional than those going in the opposite direction. They will therefore exert a larger friction force on the ions, on which a thermal force therefore acts in the direction of $\nabla_{\parallel} T_e$. The corresponding force on the electrons (15) is in the opposite direction. The second term is smaller than the first one by a factor of $1/\Omega_e \tau_e \ll 1$.

The electron heat flux also has two pieces

$$\mathbf{q}_e = \mathbf{q}_u^e + \mathbf{q}_T^e, \quad (16)$$

$$\mathbf{q}_u^e = 0.71 n_e T_e \mathbf{u}_{\parallel} - \frac{3n_e T_e}{2\Omega_e \tau_e} \mathbf{b} \times \mathbf{u}_{\perp}, \quad (17)$$

$$\mathbf{q}_T^e = -\kappa_{\parallel}^e \nabla_{\parallel} T_e - \kappa_{\perp}^e \mathbf{b} \times \nabla T_e - \kappa_{\perp}^e \nabla_{\perp} T_e, \quad (18)$$

where the heat conductivities are

$$\kappa_{\parallel}^e = 3.16 \frac{n_e T_e \tau_e}{m_e}, \quad (19)$$

$$\kappa_{\perp}^e = -\frac{5n_e T_e}{2m_e \Omega_e}, \quad (20)$$

$$\kappa_{\perp}^e = 4.66 \frac{n_e T_e}{m_e \Omega_e^2 \tau_e}, \quad (21)$$

Physically, the first term in Eq. (17) has to do with the distortion of the distribution of fast electrons from a Maxwellian. In a coordinate system where $\mathbf{V}_e = 0$, more fast electrons travel in the direction of \mathbf{u} and more slow electrons in the direction of $-\mathbf{u}$, which gives rise to a heat flux.

This effect does not arise for ions since the ion-electron collision frequency is independent of ion energy. The ion heat flux therefore only has terms related to ∇T_i ,

$$\mathbf{q}_i = -\kappa_{\parallel}^i \nabla_{\parallel} T_i + \kappa_{\perp}^i \mathbf{b} \times \nabla T_i - \kappa_{\perp}^i \nabla_{\perp} T_i, \quad (22)$$

where

$$\kappa_{\parallel}^i = 3.9 \frac{n_i T_i \tau_i}{m_i}, \quad (23)$$

$$\kappa_{\perp}^i = \frac{5n_i T_i}{2m_i \Omega_i}, \quad (24)$$

$$\kappa_{\perp}^i = 2 \frac{n_i T_i}{m_i \Omega_i^2 \tau_i} \quad (25)$$

with $\Omega_i = ZeB/m_i$ and

$$\tau_{ii} = \frac{12\pi^{3/2} m_i^{1/2} T_i^{3/2} \epsilon_0^2}{n_i Z^2 e^4 \ln \Lambda}.$$

Note that the conductivities κ_{\parallel} , κ_{\perp} and κ_{\perp} are consecutively separated by the large factor $\Omega\tau$ for both species. The first and third terms in the expressions for \mathbf{q}_T^e and \mathbf{q}_i are parallel to the gradients that drive them, and will therefore tend to relax these gradients. This relaxation occurs on very disparate time scales in the two directions. Perpendicular to the magnetic field, the ion contribution is dominant, since for both species the cross-field diffusion scales according as $\kappa_{\perp} \sim n\rho_i^2/\tau_i$, indicating a random walk with the step size ρ_i , which is much larger for the ions than for the electrons. Parallel to the field, on the other hand, the electron heat flux dominates, and scales as $\kappa_{\parallel} \sim n\lambda^2/\tau_e$ with a random-walk step size equal to the mean free path. The latter is roughly the same for electrons and ions, but the collision time is much shorter for the electrons. Of intermediate magnitude is the diamagnetic heat flux term $\mathbf{q}_{\perp} = \pm\kappa_{\perp} \mathbf{b} \times \nabla T$, carrying heat across the field perpendicular to the gradient. This flux is not affected by collisions in the limit $\Omega_i \tau_i \gg 1$.

The heat exchanged between the species,

$$Q_i = \int \frac{m_i v_i^2}{2} C_{ie}(f_i) d^3v = \frac{3n_e m_e}{m_i \tau_e} (T_e - T_i), \quad (26)$$

is a result of temperature equilibration on the slow time scale $m_i \tau_e / m_e$ and frictional generation of heat. The viscosity tensor is complicated and will not be treated here. Its form depends on whether the large- or small-flow ordering is adopted.

III.C. Applications

As already remarked, classical transport is relatively small across the magnetic field and is therefore usually of little concern. In most situations it is easily overwhelmed by neoclassical or turbulent transport. Along the field, however, the classical transport is very

rapid and usually dominates over turbulence. The most important prediction of the classical theory is probably the electric (so-called Spitzer) conductivity, σ regulating the current

$$J_{\parallel} = -n_e e u_{\parallel} = \sigma E_{\parallel},$$

that arises in response to an applied parallel electric field [5]. It is obtained from (14) as

$$\sigma = 1.96 \frac{n_e e^2 \tau_e}{m_e},$$

and is thus proportional to $T_e^{3/2}$ but independent of the density n_e .

The parallel electron heat conductivity (19) is very important in the tokamak edge, where it governs the heat flux to the divertor plates. This conductivity is proportional to $T_e^{5/2}$ but is independent of density. In situations where the heat flux is constant, it predicts a temperature profile $T_e(s) \sim s^{2/7}$ as a function of the arc length s along the magnetic field. Parallel electron heat conduction is also important in space physics and astrophysics. It governs, for instance, the heat flux along magnetic loops in the solar corona.

The thermal force, which was discovered by Enskog (then a student) in 1911, has been used for isotope separation and plays an important role in plasmas with multiple ion species. The point is that the kinetic equation for hydrogenic ions in a plasma that also contains much heavier impurity ions is identical to the equation for electrons in a pure plasma (with the lighter ions playing the role of the electrons in a pure plasma). Many of Braginskii's results therefore carry over to the situation of an impure plasma and, in particular, there is a thermal force on heavy impurity ions in the direction of $\nabla_{\parallel} T_i$. This force pulls impurity ions out of the divertor into the main scrape-off-layer in a tokamak. In the transition region between the solar photosphere and the corona, there is a very strong vertical temperature gradient pulling out heavy ions and making the chemical composition of the solar wind different from that of the Sun.

IV. NEOCLASSICAL TRANSPORT

Classical transport applies in all magnetic-field geometries as long as the mean free path is short. When it is, the transport is determined locally and does therefore not depend much on the macroscopic field structure. When the mean free path is long, however, the transport can become much stronger, which is the subject of neoclassical theory.

IV.A. Collisionality

The physics of neoclassical transport in a tokamak depends decisively on the relative magnitude of the collision frequency ν and the transit frequency $\omega_t = v_T/qR$, the so-called collisionality. Here $q = rB_\varphi/RB_\theta$ is the safety factor and R the major radius of the tokamak. We note that the mean free path $\lambda = v_T/\nu$ is similar for electrons and ions since $\nu_{ee}/\nu_{ii} \sim v_{Te}/v_{Ti}$, but may differ among ion species with very disparate masses. Highly charged impurities are more collisional than bulk ions and electrons. If the collisionality is large,

$$\frac{L}{\lambda} \sim \frac{\nu}{v_T/qR} \gg 1, \quad (27)$$

the mean free path is shorter than the parallel distance around a flux surface $L \sim qR$, and the Braginskii fluid equations may be applied for the analysis. The particle orbits are then not fully completed by a typical thermal particle since its motion is disturbed by collisions before an orbit has been completed. This high-collisionality regime is called the *Pfirsch-Schlüter* regime.

In the opposite limit,

$$\frac{\nu}{v_T/qR} \ll 1,$$

referred to as the *banana-plateau* regime, orbits are completed and short-mean-free-path closure of the fluid equations is inapplicable. The core of a tokamak is usually in this regime.

If the inverse aspect ratio is small, $\epsilon \ll 1$, the banana-plateau regime is subdivided into two regimes: the plateau regime

$$\epsilon^{3/2} \ll \frac{\nu}{v_T/qR} \ll 1, \quad (28)$$

and the banana regime

$$\frac{\nu}{v_T/qR} \ll \epsilon^{3/2}. \quad (29)$$

In the former, most circulating particle orbits are completed but trapped orbits are interrupted by collisions since the effective collision frequency, $\nu_{\text{eff}} = \nu/\epsilon$, required to scatter a trapped particle out of its magnetic well, $\Delta B/B \sim \epsilon$, is larger than the bounce frequency $\omega_b \sim \sqrt{\epsilon}v_T/qR$, i.e.,

$$\nu_* \equiv \frac{\nu/\epsilon}{\omega_b} = \frac{\nu/\epsilon^{3/2}}{v_T/qR} \gg 1.$$

It is important to note that the effective collision frequency for scattering the velocity vector by an angle $\Delta\vartheta$ is $\nu/(\Delta\vartheta)^2$, since the pitch-angle scattering operator (8) is of second order. Trapped particles occupy the region $v_{\parallel}/v \sim \sqrt{\epsilon}$ in velocity space, so it is appropriate to take $\Delta\vartheta = \sqrt{\epsilon}$. The effective trapped-particle scattering frequency is thus substantially greater than ν if

$\epsilon \ll 1$. Finally, in the banana regime, $\nu_* \ll 1$, the particle dynamics is virtually collisionless, and both types of orbits (trapped and circulating) can be completed.

The diffusivity of particles and heat is proportional to the collision frequency in the banana and Pfirsch-Schlüter regimes (with different proportionality constants) but is independent of collisionality (forms a ‘‘plateau’’) in the plateau regime, see Fig 1. While this is strictly true in the limit $\epsilon \rightarrow 0$, at realistic aspect ratios the distinction between the regimes is blurred, and the plateau is difficult to discern.

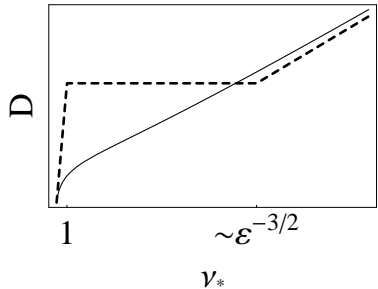


Figure 1: Dependence of neoclassical diffusion coefficient on collisionality at large aspect ratio. The dashed curve represents the asymptotic limit $\epsilon \rightarrow 0$, while the solid curve represents $\epsilon = 0.2$.

IV.B. Flows within the flux surface

The axisymmetric magnetic field of a tokamak has the form

$$\mathbf{B} = I(\psi)\nabla\varphi + \nabla\varphi \times \nabla\psi,$$

where φ is the toroidal angle measured in the direction of the plasma current and ψ the poloidal flux function. Since the pressure

$$p = \sum_a p_a = \sum_a n_a T_a$$

is a flux function when the rotation velocity is subsonic so that $\mathbf{J} \times \mathbf{B} = \nabla p$, the diamagnetic current beomes

$$\mathbf{J}_\perp = \frac{\mathbf{B} \times \nabla p}{B^2} = \left(\frac{I\mathbf{B}}{B^2} - R\hat{\varphi} \right) \frac{dp}{d\psi},$$

and is generally not divergence-free, $\nabla \cdot \mathbf{J}_\perp \neq 0$, necessitating a parallel, so-called Pfirsch-Schlüter, current. Since

$$0 = \nabla \cdot \left(\frac{J_{\parallel}\mathbf{B}}{B} + \mathbf{J}_\perp \right) = \mathbf{B} \cdot \nabla \left(\frac{J_{\parallel}}{B} + \frac{I}{B^2} \frac{dp}{d\psi} \right)$$

it follows that the quantity within the parentheses must be constant of flux surfaces, and the parallel current becomes

$$J_{\parallel} = -\frac{I}{B} \frac{dp}{d\psi} + K(\psi)B,$$

where $K(\psi)$ is an arbitrary integration constant. This is the “return current” necessary to close the diamagnetic current. A similar argument can be made for the flux $n_a \mathbf{V}_a$ for each species: its perpendicular component is given by the diamagnetic flux but is not divergence free, necessitating a parallel flux. The sum is equal to

$$n_a \mathbf{V}_a = \omega_a(\psi) n_a(\psi) R \hat{\varphi} + K_a(\psi) \mathbf{B}, \quad (30)$$

with

$$\omega_a(\psi) = -\frac{d\Phi}{d\psi} - \frac{1}{n_a e_a} \frac{dp_a}{d\psi}, \quad (31)$$

where Φ denotes the electrostatic potential. These relations hold in all collisionality regimes.

V. PFIRSCH-SCHLÜTER TRANSPORT

In the Pfirsch-Schlüter regime, the transport can mostly be calculated using Braginskii’s equations. Although these do not depend on the geometry of the magnetic field, there is nevertheless an enhancement of the transport level in the tokamak as compared with a plasma in a straight magnetic field. On the fluid level, it has to do with the fact that a parallel Pfirsch-Schlüter flow must arise, as we have just seen. In the particle picture, the transport enhancement can be understood in terms of a simple random-walk argument.

Since the collision frequency exceeds the transit frequency, parallel particle motion is diffusive, with a diffusion coefficient

$$D_{\parallel} \sim \lambda^2 / \tau \sim v_T^2 / \nu,$$

where $\lambda = v_T / \nu$ is the mean-free path. Thus, the time it takes for a particle to move around a flux surface is of the order

$$\Delta t \sim \frac{(qR)^2}{D_{\parallel}} \sim \nu \left(\frac{qR}{v_T} \right)^2,$$

since the parallel distance is of the order qR . The cross-field transport is caused by the guiding-centre drift,

$$\mathbf{v}_d \simeq -\frac{v^2 + v_{\parallel}^2}{2\Omega R} \hat{\mathbf{z}},$$

which is vertical and therefore directed radially outward (say) if the particle is above the midplane and inward if it is below the midplane. As the particle diffuses in the parallel direction, the cross-field drift is sometimes

outward and sometimes inward. This leads to a random walk in the radial direction, with a step length

$$\Delta r \sim v_d \Delta t \sim \frac{\rho v_T \Delta t}{R},$$

and a step time Δt . The resulting diffusion coefficient is thus

$$D_{\perp} \sim \frac{(\Delta r)^2}{\Delta t} \sim \nu q^2 \rho^2, \quad (32)$$

which is larger than the classical diffusion coefficient by a factor q^2 .

To derive the transport mathematically using the results from Section III.B, we consider the ion heat flux. When the plasma flow velocity is ordered small, $E/B \sim \delta v_{Ti}$, the ion energy equation (4) reduces to $\nabla \cdot \mathbf{q}_i = 0$. Recalling (22), we see that if we expand the temperature,

$$T_i = T_{i0} + T_{i1} + \dots,$$

in powers of $1/\Omega_i \tau_i$, then in lowest order, $\nabla_{\parallel} (\kappa_{\parallel}^i \nabla_{\parallel} T_{i0}) = 0$, so

$$T_{i0} = T_{i0}(\psi).$$

Thus, on the fastest time scale parallel heat conduction makes the temperature uniform on flux surfaces. In next order, we have

$$\nabla \cdot \left(\kappa_{\parallel}^i \nabla_{\parallel} T_{i1} - \kappa_{\perp}^i \mathbf{b} \times \nabla T_{i0} \right) = 0,$$

so that

$$\nabla_{\parallel} T_{i1} = \frac{I \kappa_{\perp}^i}{\kappa_{\parallel}^i} \frac{dT_{i0}}{d\psi} + L_i(\psi) B,$$

where the integration constant $L_i(\psi)$ can be determined from the relation $\langle B \nabla_{\parallel} T_{i1} \rangle = 0$. Here the angular brackets denote the so-called flux-surface average,

$$\langle Q \rangle(\psi) = \oint \frac{Q(\psi, \theta)}{\mathbf{B} \cdot \nabla \theta} d\theta / \oint \frac{d\theta}{\mathbf{B} \cdot \nabla \theta}$$

i.e., a volume average of the quantity Q between two neighbouring flux surfaces. Since $\kappa_{\perp}^i B$ is constant over the flux surface, it follows that

$$\nabla_{\parallel} T_{i1} = \frac{I \kappa_{\perp}^i}{\kappa_{\parallel}^i} \left(1 - \frac{B^2}{\langle B^2 \rangle} \right) \frac{dT_{i0}}{d\psi}. \quad (33)$$

We see that T_{i1} varies over the flux surface. The mechanism is the same as that giving rise to the Pfirsch-Schlüter current. The diamagnetic heat flux $\kappa_{\perp}^i \mathbf{b} \times \nabla T_{i0}$ is not divergence free, and must therefore be balanced by a parallel return flow, which, in turn, implies a small but important parallel temperature gradient. Since the latter (33) is positive on the inside of the torus and negative on the inside (assuming that $dT_{i0}/d\psi < 0$), the

temperature is up-down asymmetric. It is now straightforward to construct the heat flux across the flux surface from (22) and (33),

$$\begin{aligned} \mathbf{q}_i \cdot \nabla \psi &= (-\kappa_{\perp}^i \nabla_{\perp} T_{i0} + \kappa_{\parallel}^i \mathbf{b} \times \nabla T_{i1}) \cdot \nabla \psi \\ &= - \left[\kappa_{\perp}^i |\nabla \psi|^2 + \frac{(I \kappa_{\parallel}^i)^2}{\kappa_{\parallel}^i} \left(1 - \frac{B^2}{\langle B^2 \rangle} \right) \right] \frac{dT_{i0}}{d\psi}. \end{aligned} \quad (34)$$

The first term is the classical cross-field heat flux, and the second term is the neoclassical Pfirsch-Schlüter heat flux, which arises entirely because of toroidicity. Both heat fluxes are ultimately driven by the radial temperature gradient, but the neoclassical heat flux is also fundamentally associated with a parallel gradient. In a large-aspect-ratio tokamak with circular cross section, the total flux-surface averaged heat flux becomes

$$q_{ir} = \frac{\langle \mathbf{q}_i \cdot \nabla \psi \rangle}{|\nabla \psi|} = -\kappa_{\perp}^i (1 + 1.6q^2) \frac{dT_{i0}}{dr},$$

where the first term is the classical and the second term the Pfirsch-Schlüter contribution.

VI. TRANSPORT IN THE BANANA REGIME

When the mean free path is longer, the transport must be calculated kinetically, but since the gyroradius is supposed to be small, the full kinetic equation (1) can be reduced (by gyro-averaging) to the drift kinetic equation,

$$\frac{\partial f_a}{\partial t} + (v_{\parallel} \mathbf{b} + \mathbf{v}_{da}) \cdot \nabla f_a = C_a(f_a), \quad (35)$$

where \mathbf{v}_d is the drift velocity and the derivatives are taken at constant energy $H = m_a v^2/2 + e_a \Phi$ and magnetic moment $\mu = m_a v_{\perp}^2/2B$, so that the mirror force is contained in the parallel streaming term $v_{\parallel} \nabla_{\parallel} f_a$. In this equation, not all terms are equally large. As mentioned in the introduction, the first term on the left is ordered to be a factor δ^2 smaller than the second one, and the magnetic drift term is by definition a factor δ smaller than parallel streaming, $v_d/v \sim \delta$. We may thus expand $f_a = f_{a0} + f_{a1} + \dots$ and obtain

$$v_{\parallel} \nabla_{\parallel} f_{a0} = C_a(f_{a0}),$$

$$v_{\parallel} \nabla_{\parallel} f_{a1} + \mathbf{v}_{da} \cdot \nabla f_{a0} = C_a(f_{a1}),$$

in zeroth and first order, respectively. It can relatively easily be shown that the only solutions of the first equations are Maxwellians that are constant on flux surfaces. This conclusion is reached by multiplying the equation by $\ln f_{a0}$, integrating over velocity space, taking the flux-surface average, and using Boltzmann's H-theorem. It also follows from this argument that the electrostatic potential is approximately a flux function,

$$\Phi = \Phi_0(\psi) + \Phi_1(\psi, \theta),$$

with $\Phi_1/\Phi_0 \sim \delta$.

If an inductive electric field, $E_{\parallel}(A) = -\partial A_{\parallel}/\partial t$ is added to Eq (35), our remaining task is thus to solve the first-order equation

$$v_{\parallel} \nabla_{\parallel} f_{a1} - C_a(f_{a1}) = -(\mathbf{v}_d \cdot \nabla \psi) \frac{\partial f_{a0}}{\partial \psi} + \frac{e_a v_{\parallel} E_{\parallel}^{(A)}}{T_a} f_{a0}.$$

Since this equation is linear in f_{a1} and the driving terms on the right appear additively, we conclude that the radial density and temperature gradients in f_{a0} and the inductive electric field contribute separate and independent terms to f_{a1} . In this equation no assumption has yet been made about collisionality, i.e., on the relative magnitude of the terms on the left. If the equation is solved under the assumption that the collision term dominates, then Pfirsch-Schlüter transport is recovered. If the first term instead dominates, banana transport ensues. Mathematically, one makes a *subsidiary* expansion of f_{a1} in the smallness of the collision frequency,

$$f_{a1} = f_{a1}^{(0)} + f_{a1}^{(1)} + \dots,$$

which enables the equation to be solved analytically if the collision operator is simplified. The mathematics is somewhat complicated and will not be repeated here. The student who is interested in all the steps is encouraged to consult Ref [6].

VI.A. Radial transport

From the distribution function f_{a1} thus obtained, the radial particle and heat flux can be calculated. The results have been obtained in general axisymmetric geometry but are particularly simple in the case of a large-aspect-ratio tokamak with circular cross section. The largest flux is that of ion heat,

$$q_{ir} = -n_i \chi_i \frac{dT_i}{dr},$$

whose diffusivity is

$$\chi_i = \frac{1.35q^2}{\epsilon^{3/2}} \frac{T_i}{m_i \Omega_i^2 \tau_i}, \quad (36)$$

and thus scales as the classical diffusivity ρ_i^2/τ_i enhanced by the factor $1.35q^2/\epsilon^{3/2}$, which is usually in the range 10-100. The reason for this enhancement has to do with banana orbits. As already mentioned, particles with velocity vectors nearly perpendicular to the magnetic field, $|v_{\parallel}|/v_{\perp} \leq \epsilon^{1/2}$, are trapped in the relatively weak magnetic field on the outside of the torus and trace out banana orbits with a width

$$\delta r_b \sim q\rho/\sqrt{\epsilon},$$

cf Fig 2. The banana width δr_b is thus considerably

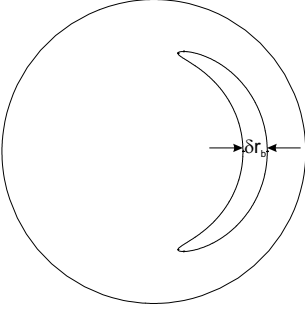


Figure 2: Banana orbit in a tokamak.

larger than the gyroradius, indicating a large random-walk step size for these particles. The diffusivity (36) is of order

$$\chi_i \sim f_t (\Delta x)^2 \nu_{\text{eff}},$$

where the trapped fraction of the particles $f_t \sim \epsilon^{1/2}$ is small, but the step size $\Delta x \sim \delta r_b$ is large, and so is the effective collision frequency $\nu_{\text{eff}} \sim \nu/\epsilon$ of events causing a trapped ion to take a step of order δr_b .

The electron heat flux is also enhanced by a similar factor over the classical result, but is insignificant as it is smaller than the corresponding ion flux by a factor $(m_e/m_i)^{1/2}$. The ion and electron particle fluxes are equal (ambipolarity) and are both on the level of the electron heat flux. The only neoclassical cross-field flux that is experimentally relevant is thus the ion heat flux. Even this flux is usually overwhelmed by the turbulent transport, but can be of importance in spherical tokamaks and in transport barriers. The H-mode pedestal seems to exhibit neoclassical ion energy confinement.

VI.B. Toroidal current

The parallel current is very well described by neoclassical theory, which predicts two important effects: a reduction in the conductivity due to trapped particles and the existence of the so-called bootstrap current. Both are of great experimental significance. When the drift kinetic equation is solved for f_{i1} and f_{e1} , and the parallel current is calculated, one finds

$$J_{\parallel} = -\frac{f_t q n_e T_e}{\epsilon B} \left[1.66 \left(1 + \frac{T_i}{T_e} \right) \frac{d \ln n_e}{dr} + 0.47 \frac{d \ln T_e}{dr} - \frac{0.29}{T_e} \frac{dT_i}{dr} \right] + (1 - 1.31 f_t) \sigma E_{\parallel}^{(A)},$$

for a large-aspect-ratio tokamak with circular cross section. The quantity $f_t \simeq 1.46 \epsilon^{1/2}$ denotes the “effective” fraction of trapped particles and appears in two places. It multiplies the entire first term, which constitutes the bootstrap current – a toroidal current that arises thanks

to density and temperature gradients in the plasma. It also appears in the second term as a reduction of the Spitzer conductivity σ caused by the fact that trapped particles cannot contribute to the parallel current.

Physically, the bootstrap current has its root in a diamagnetic effect of the banana orbits. Because of their width $\delta r_b \sim q\rho/\epsilon^{1/2}$, the co-current-moving, trapped population on a given flux surface is larger than the counter-moving one by an amount

$$-\epsilon^{1/2} \frac{dn}{dr} \delta r_b,$$

where $\epsilon^{1/2}$ is the approximate fraction of trapped particles. These are in collisional equilibrium with the passing ones, whose co-passing population therefore exceeds the counter-passing one by

$$-\frac{dn}{dr} \delta r_b.$$

The resulting current is of the order

$$J_{BS} \sim -v_{Te} a \frac{dn}{dr} \delta r_b \sim -\frac{q T_a}{\epsilon^{1/2} B} \frac{dn_a}{dr}.$$

Thus, at large aspect ratio the bootstrap current is mostly carried by the *passing* particles, although it is ultimately caused by the diamagnetic effect of the *trapped* ones.

The bootstrap current is thus of order

$$J_{BS} \sim \frac{\epsilon^{1/2} p}{r B_p},$$

where $B_p = \epsilon B/q$ is the poloidal field, and compares in the following way with the Ohmic current,

$$J_{BS}/J_{OH} \sim \epsilon^{1/2} \beta_p,$$

where $\beta_p = 2\mu_0 p/B_p^2$ is the poloidal beta. In the standard tokamak ordering $\beta \sim \epsilon^2 \Rightarrow \beta_p \sim 1$, the bootstrap current is thus formally smaller than the Ohmic current by a factor $\epsilon^{1/2}$. In practice, β and $\epsilon^{1/2}$ are sometimes not very small, and the bootstrap current is often comparable to, or even larger than, the Ohmic current. It is of great importance for the prospects of the tokamak to be an economic power source.

VI.C. Plasma rotation

We have already shown that the flow within the flux surface of each species is given by Eq (30), where the constant K_a must be calculated from kinetic theory. For ions this constant determines the poloidal plasma rotation, which is equal to

$$V_{i\theta} = \frac{1.17}{m_i \Omega_i} \frac{dT_i}{dr}$$

for a circular, large-aspect-ratio tokamak in the banana regime. Contrary to widespread belief, the poloidal rotation is independent of the radial electric field. In fact, this field only plays a minor role in neoclassical theory for axisymmetric plasmas. In the quasi-steady state described by the transport ordering, it does not affect cross-field transport or poloidal rotation. The only observable quantity where it shows up is the toroidal rotation frequency (31), where it appears in the same way for all species. Of course, there is a good reason for this. Suppose that we make a transformation from the laboratory frame to a frame rotating at the velocity

$$\mathbf{V} = -\dot{\varphi}R \frac{d\Phi_0}{d\psi}$$

of some flux surface ψ . The electric field measured in this frame vanishes on the flux surface in question since

$$\mathbf{E}' = \mathbf{E} + \mathbf{V} \times \mathbf{B} \simeq -\nabla\Phi_0 + \mathbf{V} \times \mathbf{B} = 0,$$

and the equation of motion for each species acquires new terms corresponding to the centrifugal force and the Coriolis force. These terms are, however, small if \mathbf{V} is smaller than the thermal speed, in which case the only consequence of the coordinate transformation is to eliminate the radial electric field. Thus, as long as the flow velocity is small, the radial electric field cannot affect neoclassical transport.

For this reason, the transport in a tokamak is *intrinsically ambipolar*, i.e., the radial electron and ion particle fluxes are always the same, regardless of the radial electric field, as long as the transport ordering is satisfied. The toroidal rotation frequency (31) can therefore attain any value: the plasma rotates freely in the toroidal direction. The situation is very different in non-axisymmetric systems such as stellarators, where ambipolarity is only attained at a certain value of the radial electric field. A stellarator plasma cannot rotate freely [7].

VII. DISCUSSION

Not only the neoclassical theory, but most of the theory of magnetically confined plasmas relies on an expansion in $\delta \ll 1$, and one can thus distinguish between plasma physics phenomena according to the order in which they first appear in the expansion. In zeroth order one finds, among other things, that the distribution function of each species must be Maxwellian, that flux surfaces should be isothermal, that an axisymmetric plasma is free to rotate toroidally, that its equilibrium and stability properties are predicted by MHD, and that the parallel electric conductivity is given by the Spitzer value with a reduction due to particle trapping. In first order, the bootstrap current and neoclassical poloidal rotation appear, and in second order

there is radial transport – either caused by collisions as in the neoclassical theory or by gyrokinetic turbulence. It is interesting to note that the robustness of the theoretical predictions decreases with increasing order in the expansion. The zeroth-order predictions are very robust in the sense that they are hardly affected by turbulence and are very well borne out in experiments. The first-order results are also broadly in line with observations, whilst the cross-field transport, which is of second order, is famously difficult to predict with confidence. The neoclassical cross-field transport is usually overwhelmed by turbulent transport, but this is (in gyrokinetics) also of second order in the gyroradius and therefore sensitive to details in the mathematical treatment and the physical conditions prevailing in the plasma.

VIII. FURTHER READING

A more complete exposition can be found in the author's book [6] and in the review by Hinton and Hazeltine [8]. Classical transport is very well described in the reviews by Braginskii [3] and Hinton [9].

REFERENCES

1. S. CHAPMAN, Phil. Trans. R. Soc. London Ser. A **98**, 1 (1916).
2. D. ENSKOG, *Kinetische Theorie der Vorgänge in mässig verdünnten Gasen* (Almqvist & Wiksell, Uppsala, 1917). Inaugural dissertation, Uppsala University; Arkiv för matematik, astronomi och fysik **16**, 16, 1 (1922).
3. S.I. BRAGINSKII, in *Reviews of Plasma Physics*, edited by M. A. Leontovich (Consultants Bureau, New York, 1965), Vol. 1, p. 205.
4. P.J. CATTO and A.N. SIMAKOV, Phys. Plasmas **11**, 90 (2004).
5. L. SPITZER and R. HÄRM, Phys. Rev. **89**, 977 (1953).
6. P. HELANDER and D.J. SIGMAR, *Collisional transport in magnetized plasmas* (Cambridge University Press, 2002).
7. P. HELANDER and A.N. SIMAKOV, Phys. Rev. Lett. **101**, 145003 (2008).
8. F.L. HINTON and R.D. HAZELTINE, Rev. Mod. Phys **48**, 239 (1976).
9. F.L. HINTON, in *Handbook of Plasma Physics*, edited by M.N. Rosenbluth and R.Z. Sagdeev, Vol. 1, p. 147 (North-Holland, Amsterdam, 1983).

DEGRADED CONFINEMENT AND TURBULENCE IN TOKAMAK EXPERIMENTS

G.M.D. Hogewij

FOM-Institute for Plasma Physics Rijnhuizen, Association EURATOM-FOM, Trilateral Euregio Cluster,
P.O.Box 1207, 3430 BE Nieuwegein, The Netherlands, www.rijnh.nl

ABSTRACT

After a review on the state of tokamak transport theory, the methodology to derive experimental results will be described. Examples of confinement in ohmic plasmas and the deterioration with additional heating will be given. Some examples of improved confinement modes will be discussed.

I. SUMMARY OF THEORETICAL EXPECTATIONS

In this section only a summary of theoretical expectations is given since in other lectures many aspects of transport theory will be treated, i.e. kinetic theory [1], classical and neoclassical transport in tokamaks [2], and the role of micro-instabilities in transport [3].

I.A. Collisional Transport Theory

Predictions of collisional transport theory in toroidal geometry, i.e. the so-called neoclassical transport (in the following denoted by subscript 'nc') can be described in short by:

- a Particle diffusion: from $D^{\text{ban}} = D_c q^2 (R/r)^{1.5}$ at low collisionality (Banana regime) to $D^{\text{PS}} = D_c (1 + q^2)$ at high collisionality (Pfirsich-Schlüter) with $D_c = \nu_e \rho_e^2$. This results in typically $D^{\text{nc}} \simeq 10^{-2}$ to 10^{-1} m/s.
- b Inward convection is predicted to have values $V_c^{\text{nc}} = -\epsilon^{0.5} E_{\text{tor}}/B_{\text{pol}}$, the so-called Ware-pinch, leading to values of typical 0.01 to 0.20 m/s. Also temperature gradients will drive an inward convection flux comparable to or smaller than the outward diffusive flux.
- c Impurity fluxes are dominated by the friction with the main ion population. This implies an accumulation of the impurities at the location of highest main ion density following: $n_Z/n_Z(0)(n_e/n_e(0))^2$.
- d The electron heat diffusivity, χ_e^{nc} , should be close to the particle diffusion coefficient D^{nc} .
- e The ion heat diffusivity, χ_i^{nc} , proportional to $\nu_i \rho_i^2$ is therefore $(m_i/m_e)^{0.5} = 43 - 76$ times larger than χ_e^{nc} and one can expect values up to 1 m²/s.
- f Parallel resistivity should be given by Spitzer's formula enhanced by the presence of trapped electrons with the factor $(1 - (r/R)^{0.5})^{-2}$.

g A part of the toroidal current is driven by the radial density and temperature gradients: the so-called bootstrap current, in first order given by $j_{\text{bc}} = -(r/R)^{0.5}(T/B_{\text{pol}})\nabla n$. Values around 10^5 A/m² can be expected.

h Viscosity for flows in the poloidal direction should be very high, effectively limiting poloidal velocities to typical 10^3 m/s.

i Viscosity for flows in the toroidal direction should be low with a momentum diffusivity $\chi_\phi \sim \chi_i^{\text{nc}}$.

I.B. Transport in Case of Electrostatic Turbulence

This subject will be treated extensively in this course [3]. The main idea is that fluctuations in the electrostatic potential due to instabilities cause particle drifts perpendicular to the further undisturbed magnetic surfaces. This enhances transport anomalously above the neoclassical level. Various instability models have been proposed each with their growth rate γ and typical wave number k_\perp .

I.C. Transport in Case of Magnetic Turbulence

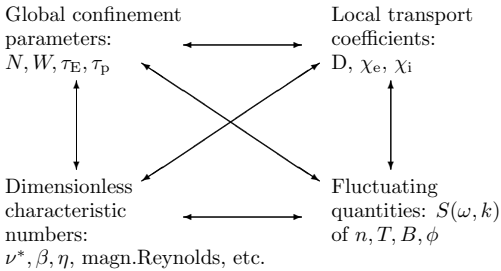
In case magnetic field lines cannot be described by closed magnetic surfaces one has to expect a stochastic meandering of field lines. Particles bound by these field lines have a finite chance that they reach the edge of the plasma. Since χ_\parallel is many orders of magnitude higher than χ_\perp this is a very effective loss mechanism especially for electrons. The predicted electron heat diffusivity is given by:

$$\chi_e^{\text{an}}(\perp) = (\tilde{B}/B)^2 \chi_e^{\text{c}}(\parallel) \quad (1)$$

From this we can conclude that a magnetic disturbance of $(\tilde{B}/B) = 10^{-5}$ is already enough to get $\chi_e > \chi_e^{\text{nc}}$. Particle diffusion is more complicated because a fast loss of electrons will only lead to strong electric fields withholding electrons and accelerating ions, i.e. lead to ambipolar flows.

II. EXPERIMENTAL METHODOLOGY

The experimental methodology to obtain insight in the possible transport mechanisms is to measure values belonging to the scheme of four categories shown below and compare the results of these categories:



Quantities like χ_e are derived from the so-called balance equations. These describe the plasma state as the result of balances between sources, sinks and fluxes. They can be derived by integrating various moments of the kinetic equation over velocity distributions. For practical experimental purposes one can limit oneself to three of these moments, resulting in the particle balance or continuity equation, the momentum balance, and the energy balance. As an example, the particle balance can be written as:

$$\partial n / \partial t + \text{div} \cdot \Gamma = \text{Sources} - \text{Sinks} \quad (2)$$

where the particle flux consists of a diffusive and a convective part:

$$\Gamma = -D \nabla n + n V_c \quad (3)$$

The balances are made up of numerous terms; usually a numerical transport code, with modules for the various source terms, is needed to solve the coupled balance equations - see the lecture on this subject [4].

II.A. Global Confinement Quantities

These are based on the plasma volume integral of density and energy, i.e. the total particle and energy content (N, W). The particle and energy losses can be written as N/τ_p and W/τ_E , respectively, in which τ_p and τ_E are the characteristic relaxation times for particle and energy confinement lumping all loss mechanisms together. The balance equations can be simplified to:

$$\tau_p^* = \tau_p / (1 - R) = N / (\Sigma \Phi_{\text{ext}} - \partial N / \partial t) \quad (4)$$

$$\tau_E = W / (\Sigma P_{\text{ext}} - \partial W / \partial t) \quad (5)$$

where Φ_{ext} and P_{ext} denote the external particle and heat sources, respectively, and where R is the recycling coefficient.

II.B. Local Transport Coefficients

Local transport coefficients are derived from experiments by calculating the fluxes crossing every magnetic surface Ψ and relating them to the local gradients at Ψ . From transport theory it follows that very probably every flux is driven by more than one gradient. Therefore,

one has to solve a matrix equation of the type:

$$\begin{pmatrix} \Gamma \\ q \end{pmatrix}_{\Psi} = - \begin{pmatrix} D & M_{12} \\ M_{21} & n\chi \end{pmatrix} \begin{pmatrix} \nabla n \\ \nabla T \end{pmatrix}_{\Psi} \quad (6)$$

in this example simplified to a two-by-two matrix. The fluxes crossing the magnetic surface Ψ can be calculated if one knows how large fraction of the external particle and heating sources are deposited within surface Ψ , i.e. $\Phi_{\text{ext}}(\Psi)$ and $P_{\text{ext}}(\Psi)$. This has to be corrected for the sinks integrated over the volume within Ψ and the change in particle and energy content within Ψ :

$$\begin{pmatrix} \Gamma \\ q \end{pmatrix}_{\Psi} = \frac{1}{\text{Area}} \begin{pmatrix} \Sigma \Phi_{\text{ext}}(\Psi) \\ \Sigma P_{\text{ext}}(\Psi) \end{pmatrix} - (\text{Sinks}) - \begin{pmatrix} \dot{N}(\Psi) \\ \dot{W}(\Psi) \end{pmatrix} \quad (7)$$

Special approaches to this scheme (see also Fig.1):

- Neglect off-diagonal transport matrix elements ($M_{ij} = 0$ for $i \neq j$); the resulting diagonal transport coefficients are called $D^{\text{eff}}, \chi^{\text{eff}}$, etc.
- One limits oneself to semi-stationary situations: $\partial N / \partial t = 0; \partial W / \partial t = 0$.
- One deliberately modulates N and W to derive dynamic values of D, χ from the propagation velocity of particle and heat waves: $D^{\text{dpp}}, \chi^{\text{hpp}}$, etc. [5].
- In case one finds a nonlinear relation between flux and gradient one replaces $D^{\text{eff}}, \chi^{\text{eff}}$ by the incremental values: $D^{\text{inc}} = \partial \text{flux} / \partial (\text{gradient})$. This approach is sketched in Fig.1. Nearly all experimental results show $D^{\text{inc}} = D^{\text{dpp}}; \chi^{\text{inc}} = \chi^{\text{hpp}}$, etc.

Deriving local transport coefficients from experimental profiles is based on two assumptions. First, these coefficients should not vary strongly on the length scale of the observation methods used. Second, the transport coefficients should be constant on surfaces of equal Ψ . The existence of Internal Transport Barriers (narrow regions of reduced transport) may falsify the first assumption. Since many kinds of turbulence have ballooning nature, i.e. they are localized on the outboard side, also the second assumption is questionable.

II.C. Dimensionless Parameters

Each of the various transport models depends on a different set of characteristic dimensionless numbers. For instance neoclassical transport depends critically on the so-called collisionality, i.e. the ratio of one banana orbit length and the collision free mean path of the averaged particle, etc. The reader is referred to the various lectures on transport theory of this summer school [1, 2, 3].

II.D. Fluctuations

Ideally one wants to know fluctuation levels of n, T, B and electrostatic potential Φ as well as their wavelength, frequency, growth rate and phase correlation between them. An overview of measurement techniques for these parameters is given in [6].

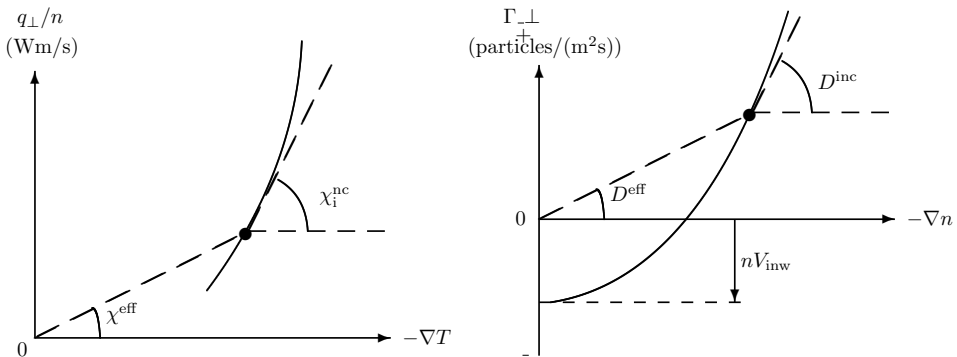


Figure 1: Schematic dependence of flux and gradient with the definitions of transport coefficients as given in the text. Anomalous inward particle and heat fluxes lead to an off-set crossing of the zero flux line and could be caused by other gradients than the prime one used for the horizontal axis. For instance in case of the particle flux a clear inward velocity has been observed presumably driven by the temperature gradient.

III. EXPERIMENTAL RESULTS WITH OHMICALLY HEATED PLASMAS

In tokamak experiments with only ohmic heating 3 types of confinement behaviour occur:

- a At low densities the plasma temperature stays nearly constant with increasing density, i.e. $\tau_E \sim n_e$. This is called **LOC** = 'Linear Ohmic Confinement'. Comparing experiments with different sizes, magnetic field and current the so-called **Neoclassical scaling** was established:

$$\tau_E = 7 \cdot 10^{-22} \langle n \rangle a R^2 q_a^{0.5} \quad (8)$$

This scaling is in stark contrast with neoclassical theory, which predicts τ_E^{nc} to fall with n_e . At low density τ_E^{nc} is at least one order of magnitude higher than the experimental value. Local transport analysis showed that this is mainly caused by the anomaly in the electron heat transport: χ_e is two orders of magnitude higher than χ_e^{nc} and this anomaly scales with $1/n_e$.

- b The standard regime at high n_e is **SOC** = 'Saturated Ohmic Confinement', characterized by τ_E being independent of n_e . In this regime $\chi_e \simeq \chi_i \simeq f \cdot \chi_i^{nc}$ with $f \simeq 1$ for small machines and $\simeq 3 - 10$ for large machines. The transition density between LOC and SOC appears to scale inversely proportional to the machine size.
- c The n_e profiles in both LOC and SOC always show a modest peaking, only weakly dependent on q_a with $n_e(0)/\langle n_e \rangle \simeq 1.5$. With a strong central particle source (by means of pellet injection) the peaking factor could be raised to more than 2 with the

surprising result that LOC was restored at SOC densities. This regime is called **IOC** = 'Improved Ohmic Confinement', see Fig.2.

The observations indicate that there are two or even more independent mechanisms each causing anomalous transport with different scaling. One mechanism, responsible for LOC behaviour, acts on electrons only and is damped linearly with density. A second mechanism, only slightly influenced by density, acts on both ions and electrons alike. This was confirmed by density fluctuation levels which dropped dramatically with increasing density in LOC but leveled off to a low, but still significant constant value of a few percent in SOC. See also Section VI. The IOC transition suggests that the latter mechanism is related with the density gradient.

IV. EXPERIMENTAL RESULTS WITH ADDITIONALLY HEATED PLASMAS

The standard regime with strong additional heating is the so-called **L-mode** = 'Low confinement mode', where confinement is degraded even more beyond SOC. Main observations:

- an increase of W with only $P_{tot}^{0.5}$ and therefore $\tau_E \sim P_{tot}^{-0.5}$;
- τ_E is nearly independent of density like SOC;
- a near linear increase in W and τ_E with current;
- the same profile consistency as with LOC and SOC.

A schematic behaviour of τ_E with density and power for ohmic and additionally heated plasmas is shown in Fig.2.

IV.A. Scaling Laws

Since L-mode behaviour is of crucial importance for the

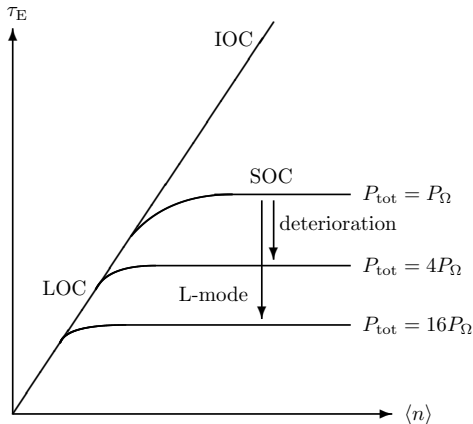


Figure 2: Scheme of the behaviour of τ_E with density for LOC, SOC, IOC and L-mode.

design of a thermonuclear reactor, the ITER confinement database working group constructed with great care a database of all existing tokamak results ranging of experiments with a typical size of 0.1 m to large ones with dimensions of meters and input powers ranging from 0.3 to 22 MW. Based on the subset of 1800 L-mode discharges (no ohmic discharges) the following scaling was found [7]:

$$\tau_E = 0.037 I_p^{0.74} B^{0.2} \kappa^{0.67} R^{1.38} a^{0.31} n^{0.24} M^{0.26} P^{-0.57} \quad (9)$$

This scaling predicts experimental results with an accuracy of 15% notwithstanding the huge span in conditions. This suggests that one mechanism is responsible for L-mode behaviour. It is comforting that also small tokamaks can study L-mode behaviour and still obtain reactor relevant results.

IV.B. Local Transport

The deterioration of confinement in L-mode plasmas is reflected in the local heat diffusivities. In general, χ_e , χ_i and χ_ϕ are close to each other. At high power χ_i can be more than one order of magnitude larger than χ_i^{pc} .

Dynamic measurements via perturbative methods, i.e. simultaneous heat- and particle pulse propagation show that off-diagonal elements in the transport matrix are important. For instance, the particle flux is strongly influenced by temperature gradients. See lecture on perturbative transport [5].

Off-axis heating has been used (JET) to study the dependence between the total heat flux and the electron temperature gradient. The result is as sketched in Fig.1a, i.e. without an inward heat pinch. However, in DIII-D one has made a distinction between ion and

electron heat flux for off-axis ECRH discharges. The authors claim that then a heat-pinch effect in the electron heat flux shows up which is not present in the total heat flux [8]. The dependence of q_e vs. ∇T_e is then similar to Fig.1b, rather than Fig.1a.

In TFTR one has compared pure deuterium and tritium plasmas. It has been found that χ_i decreases more than inversely proportional with ion mass whilst χ_e is independent of it. This explains why the global L-mode scaling of Eq.9, being a combination of both diffusivities shows an improvement of confinement with mass.

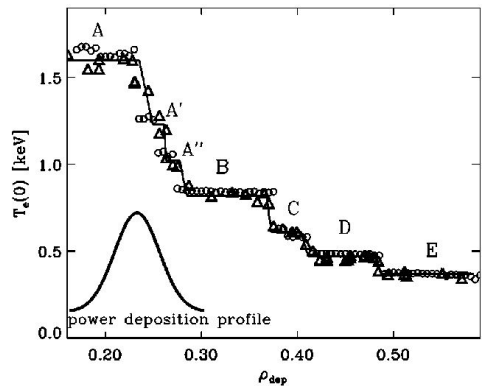


Figure 3: Central T_e as function of deposition radius of ECRH (ρ_{dep}) for a series of similar discharges of RTP (taken from [9]). The jumps in $T_e(0)$ indicate the crossing of an internal transport barrier by ρ_{dep} .

The sophisticated Thomson-scattering diagnostics at the RTP tokamak with a spatial resolution of 1% of the minor radius has resulted in the proof of existence of strong electron thermal barriers near radii with $q(r)$ close to an integer or half-integer value [9], see Fig.3. This suggests that L-mode confinement is in reality a global description of a very inhomogeneous and discontinuous plasma state with different ion- and electron transport mechanisms.

V. CONDITIONS WITH IMPROVED CONFINEMENT

Several methods were found to improve confinement albeit often only during a limited dynamic phase. These improved confinement modes are not only the starting point for creating more permanent and favourable conditions, they also contain clues what the problem with L-mode confinement is.

V.A. H-mode and influence of shear in plasma rotation

Already in the early eighties ASDEX showed that improvements in confinement could be obtained in a divertor machine [10].

Necessary condition: the heat flux over the last closed magnetic surface should be above a minimum level. The threshold value for the heat flux across the last closed magnetic surface increases with density and magnetic field, but decreases with ion mass.

Improvement reached: in standard divertor H-mode $\tau_E^H = 2\tau_E^L$. However, lately DIII-D has reached conditions for a VH-mode (Very High) which showed even an improvement of a factor 3.5. H-modes can be made semi-stationary by repetitive edge instabilities: ELMs. This causes a reduction in improvement to 1.75. This is the favoured mode for the plasma ignition device ITER. In limiter H-modes one normally reaches not more than a factor 1.5.

Observations: the onset of the H-mode is characterized by the sudden development of a barrier for particle, momentum and heat flux at the last closed magnetic surface (LCMS). Therefore, a sudden jump in density and temperature gradient across the LCMS occurs, creating an edge pedestal in the profiles. Simultaneously, the neutral density in scrape-off layer and divertor plasma falls, leading to the very characteristic drop in H_α emission. Probe and Doppler-shift measurement show a dramatic change in the radial electric field and poloidal rotation. Many authors postulate that this change is the essential one. This is confirmed by the observation during the VH-mode that the change in the shear of the radial electric field is extended further inwards than in H-mode [11]. Also the fact that limiter H-modes could be obtained in TEXTOR by forcing a change in rotation with a radial current introduced by electrodes [12], points in this direction. In the edge barrier all transport coefficients are reduced simultaneously.

V.B. Improvement by Peaked Density Profiles

In Ohmic discharges IOC was reached by creating more peaked density profiles than in SOC. The same result can be obtained in additionally heated plasmas.

Necessary condition: a strong particle source on axis. This can be done in a continuous way by massive neutral beam injection by which TFTR has reached its 'supershot' regime or in a more dynamic situation by pellet injection as Pellet-Enhanced Performance ('PEP') mode in JET [13], see Fig.4.

Improvement: the higher the value of $n_e(0)/\langle n_e \rangle$, the better. Empirical result of supershots: $\tau_E = 2\tau_E^L(n_e(0)/\langle n_e \rangle - 1)$. Improvement of a factor 3 above L-mode has been reached with a density peaking of 2.5.

Observations: also here all transport coefficients are reduced in a similar way. This means that also the impurity transport is reduced and an accumulation of impurities can occur. The large ∇n_e creates a large off-axis j_{bc} , which may maintain an inverted q profile and an inversion in magnetic shear. This magnetic con-

figuration leads to improved confinement as will be discussed in subsection V.C. This raises the question if the high peakedness of the density in itself is the reason for the improved confinement or that this peakedness is only instrumental to changing the magnetic configuration by a large j_{bc} .

V.C. Improvement by Shear Inversion

Normally the magnetic shear (s) in tokamaks is positive, i.e. the angle between the total magnetic field and the toroidal direction increases faster with increasing minor radius (r) than the ratio r/R itself, i.e. q increases from plasma centre to edge as a result of a monotonous decrease of the current density towards the edge.

Necessary conditions: In cases where the current density profile is hollow the value of q first decreases going from axis to edge but increases again from a certain radius onwards (see Fig.4). The inner part has then negative shear (NCS, C for Central), sometimes also called reversed shear (RS). This configuration can be obtained transiently by making use of the skin current effect, i.e. ramping the plasma current up faster than the magnetic diffusion allows penetration. In steady state the same can be reached by strong counter-current drive on axis and/or co-drive off-axis. The bootstrap current helps since it is largest there where the density gradient is strongest, i.e. off-axis.

Observations: The effect of such configuration on confinement is stunning and since about 1995 confirmed by many machines, ranging from small (RTP) to large (JET, TFTR, JT-60, DIII-D) [14, 15, 16, 17]. Within the radius where $s < 0$ all turbulence appears to be damped and confinement increases to neoclassical values. Record values of central plasma pressures have been reached. In some cases a local strong reduction of transport is observed only near the position of minimum q ; in other cases a more global transport reduction inside q_{min} is seen; the term internal transport barrier (ITB) is used in both cases. It should be noted that there appears to be a difference between electron and ion thermal transport: whereas for the electrons RS is sufficient to create an ITB [18], for the ions a combination of RS and high input power, i.e. strong flow shear, is needed.

V.D. Improvement by Impurity Injection

In TEXTOR [19] and later on also in large tokamaks like DIII-D and JET [20, 21], it was shown that impurity (neon, argon) injection could enhance the confinement: the so-called RI-mode. Appreciable enhancements of more than a factor 2 have been quoted. The transition from L-mode to RI-mode is believed to be caused by suppression of long wave length turbulence, in particular the Ion Temperature Gradient

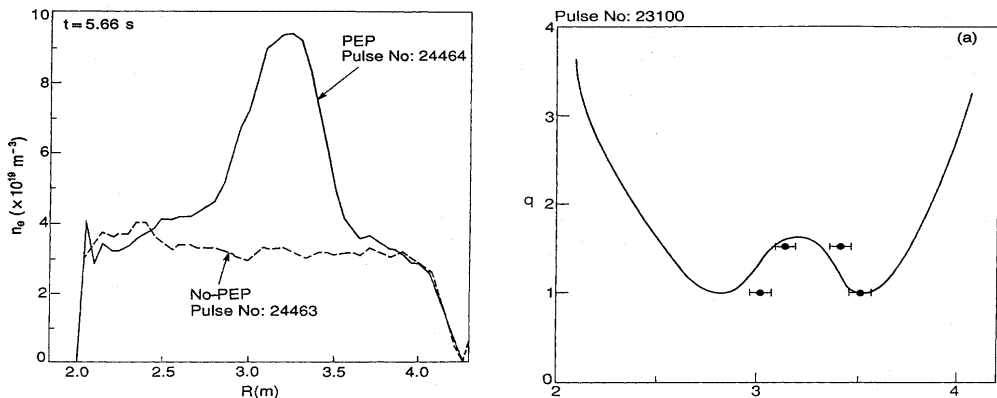


Figure 4: PEP mode in JET. Left panel: n_e profile for a PEP discharge, compared with a no-PEP one. Right panel: q profile, showing a region of reversed magnetic shear.

(ITG) mode [22]. The maximum growth rate of the ITG mode ($\gamma_{\text{ITG}}^{\text{max}}$) decreases with Z_{eff} and the peaking of the n_e profile. The suppression mechanism is supposed to be as follows: Z_{eff} is increased by impurity puffing; this decreases $\gamma_{\text{ITG}}^{\text{max}}$, which leads to peaking of n_e , which in turn further decreases $\gamma_{\text{ITG}}^{\text{max}}$. In the end this leads to full suppression of the ITG mode.

Apart from the improvement of confinement, the RI-mode is attractive because the radiative mantle evenly distributes the heat load over the vessel, instead of concentrating it on the limiter or in the divertor.

V.E. Outlook for ITER

Scenarios for ITER are developed along 2 lines: on one hand ELMy H-mode, on the other hand advanced scenarios based on NCS [23]. The latter have been vigorously pursued on JET; steady-state NCS operation appears possible with zero loop voltage, i.e. j_{bc} plus the current driven by the external heating sources are sufficient to sustain the desired plasma current [24]. Moreover, great progress has been made in JET towards real-time control of the plasma evolution [25].

VI. FLUCTUATIONS

Fluctuation measurements confirm that tokamak plasmas are a turbulent fluid. Measurements in TEXT and Tore Supra (Fig.5) show that there are at least two mechanisms acting at the same time in SOC and L-mode plasmas:

1. A broad band turbulence with large potential and density fluctuations exists at the edge. Levels are several tens of %. Electrostatic turbulence seems likely especially because the flux derived from n and E fluctuations are in good agreement with the local particle balance.

2. In the centre another broad band turbulence exists with high magnetic field fluctuations.

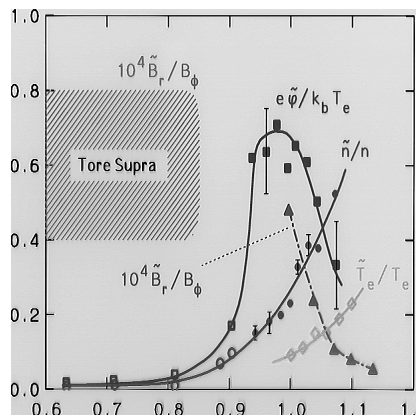


Figure 5: TEXT and Tore Supra results: relative level of various fluctuating quantities plotted against r/a .

The central density fluctuations are according to many experiments only on a few percent level but probably still significant, because the level is directly correlated with the anomaly in transport. The frequency spectrum is very similar to the magnetic fluctuations. High level temperature fluctuations can only be observed if their spatial dimension is equal or larger than the spatial resolution of the ECE equipment.

Interestingly, $\langle k_{\perp} \rangle$ decreases with increasing size of the device in contradiction with the electrostatic turbulence theory predicting $\langle k_{\perp} \rangle \cdot \rho_i \simeq 1$. Values below 0.1 have been reported. This suggests that τ_E should scale

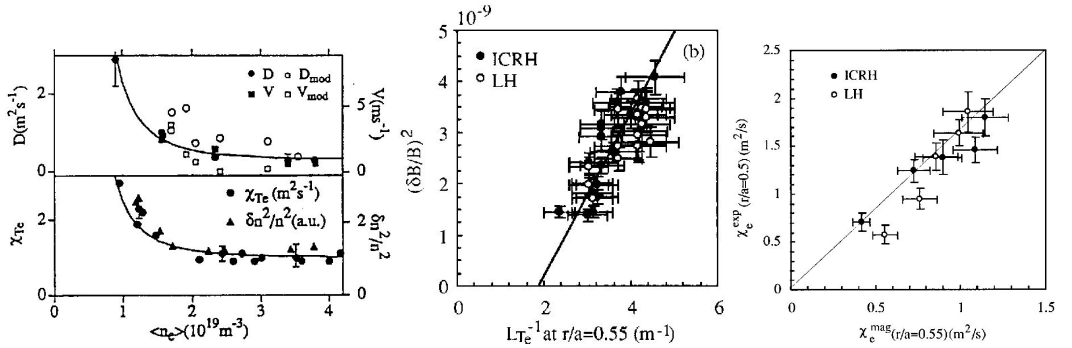


Figure 6: Relation between transport coefficients and fluctuation measurements in TORE SUPRA. Left: D and χ_e as function of n_e in ohmic plasmas together with the fluctuation level $(\delta n/n)^2$. Middle/right: Magnetic fluctuation levels as function of β_{pol} (middle), and χ_e calculated from this (right), taken from [26].

with a/ρ_i on a 'Bohm'-like way, whilst electrostatic turbulence theory predicts so-called 'gyro-Bohm' scaling.

It is still unclear how potential fluctuations in the core fit into the observations.

In Section III it was already mentioned that in LOC plasmas probably a third mechanism plays a dominant role since there density fluctuations are on a much higher level than in SOC plasmas. This high level is reduced with increasing density in the linear regime until it reaches SOC level at the transition to the SOC regime (see Fig.6).

VI.A. Connection with Transport

Ideally, one would like to see quantitative agreement between the measured fluctuation level and the observed heat or particle transport. One example of this is the measurement of magnetic turbulence in Tore Supra, which indicated fluctuation levels of typically $5 \cdot 10^{-5}$, inducing the right level of electron heat transport [26], see Fig.6. This is a strong argument in favour of magnetic turbulence as driving force of anomalous electron heat transport.

Another important quantitative observation of TFTR and TORE SUPRA is that if one derives the growth rate from the frequency spectra of the density fluctuations and the average perpendicular wavelength from the k -spectra and one plugs that in the expression for strong turbulence diffusivities ($D = \chi = \gamma / \langle k_{\perp} \rangle^2$) one finds very good agreement with local diffusivities for all kinds of confinement regimes.

Qualitative agreement is another way to prove the role of fluctuations. This can be either in time, i.e. a sudden drop of the turbulence level at the transition to an enhanced confinement regime, or in radial position, i.e. turbulence level and transport level have related radial dependences. Either of this is a strong indicator that indeed the fluctuations were driving the (locally

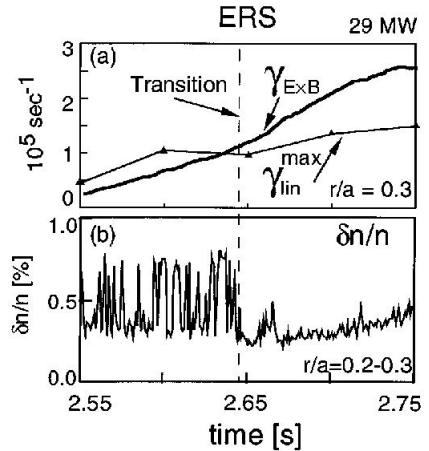


Figure 7: Transition from Reversed Shear to Enhanced Reversed Shear regime in TFTR (marked with dashed line), taken from [32]. Note the marked reduction of density fluctuation level at the transition.

or in time) quenched anomalous transport. There are many observations of this, e.g:

- The transition from RS to ERS in TFTR (E stands for Enhanced), see Fig.7.
- The observation that edge fluctuations in TEXTOR sharply drop at the transition to RI-mode [27].
- The electron ITB in electron heated JET discharges, where the fluctuation level sharply increases outside the ITB [28], see Fig.8.

VI.B. Theoretical Modelling

Modelling of turbulent transport can be done at different levels of detail, e.g. gyro-fluid vs. kinetic etc.

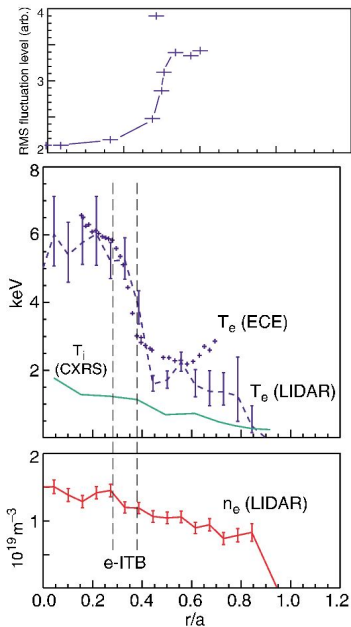


Figure 8: *JET* discharge with electron heating only. Upper panel: density turbulence level as measured with reflectometry; lower panel: T_e profile (taken from [28]).

See for example [29, 30]. Generally, turbulence is seen as 2D structures. This puts a strong request on diagnosticians to provide 2D measurements of fluctuations. Recent developments on TEXTOR promise to provide such 2D measurements of \tilde{n} and \tilde{T} by means of Microwave Imaging Reflectometry and ECE-Imaging.

Much of the turbulent transport modeling work does not take into account the magnetic structure of the plasma, although it is clear from the experimental results that the q and s profile are important. Some recent theoretical work, however, does reproduce the effect of rational q and shear reversal [31].

VII. CONCLUSIONS

- 1 Transport in tokamaks is of turbulent nature.
- 2 There are probably two or three mechanisms acting at the same time:
 - in the edge there is a broad band turbulence where strong electrostatic fluctuations play a dominant role;
 - in the centre there is at least one mechanism responsible for SOC- and L-mode behaviour with an important level of magnetic fluctuations and the q -related electron thermal barriers;
 - in LOC discharges a third mechanism may play

a role which nature is unknown but with rather strong central density fluctuations which are quenched at high density.

- 3 Turbulence causes particle, momentum and heat transport to vary simultaneously in a similar way.
- 4 There are strong non-diagonal elements in the transport matrix.
- 5 The effective diffusivities show a strong turbulence dependence: $D = \chi = (\gamma/(k_{\perp})^2)_{max}$
- 6 The turbulence level can be reduced under the following conditions:
 - steepening of the n_e (IOC, supershot, RI-mode);
 - change of the shear in radial electric field/poloidal rotation (H- and VH-mode);
 - magnetic shear inversion (NCS, PEP-mode).
- 7 With magnetic field fluctuations of 10^{-5} to 10^{-4} , it appears doubtful if the concept of unbroken magnetic surfaces is still useful for transport theory and if the distinction between electrostatic and magnetic turbulence can be held up. Probably a unified theory is necessary in which the magnetic field topology is broken in the presence of potential fluctuations such that fluctuations of B and potential mutually reinforce each other.

ACKNOWLEDGMENTS This work, supported by the European Communities under the contract of Association between EURATOM/FOM, was carried out within the framework of the European Fusion Programme with financial support from NWO. The views and opinions expressed herein do not necessarily reflect those of the European Commission.

REFERENCES

1. B. WEYSSOW, *these Proceedings*
2. P. HELANDER, *these Proceedings*
3. G. DIF-PRALADIER, *these Proceedings*
4. J. ONGENA, *these Proceedings*
5. G.M.D. HOGWEIJ, *these Proceedings*
6. A.J.H. DONNE et al, *Fus.Sc.Techn.* **49** (2T) (2006), 367
7. S.M. KAYE et al, *Nucl.Fus.* **37** (1997), 1303
8. C.C. PETTY et al, *Nucl.Fus.* **34** (1994), 121
9. M.R. de BAAR et al, *Phys.Plasmas* **6** (1999), 4645
10. F. WAGNER et al, *Phys.Rev.Let.* **49** (1982), 1408
11. K.H. BURRELL et al, *Phys.Plasmas* **1** (1994), 1536
12. S. JACHMICH, *Pl.Phys.Contr.Fus.* **40** (1998), 1105
13. P. SMEULDERS et al, *Nucl.Fus.* **35** (1995), 225
14. F.M. LEVINTON et al, *Phys.Rev.Let.* **75** (1995), 4417
15. E.J. STRAIT et al, *Phys.Rev.Let.* **75** (1995), 4421
16. S. ISHIDA et al, *Phys.Rev.Let.* **79** (1997), 3917
17. F.X. SÖLDNER et al, *Pl.Phys.Contr.Fus.* **39** (1997), B353
18. G.M.D. HOGWEIJ et al, *Pl.Phys.Contr.Fus.* **44** (2002), 1155
19. R.R. WEYNANTS et al, *Nucl.Fus.* **39** (1999), 1637
20. G.L. JACKSON, *Pl.Phys.Contr.Fus.* **44** (2002), 1893
21. P. DUMORTIER, *Pl.Phys.Contr.Fus.* **44** (2002), 1845
22. M.Z. TOKAR et al, *Phys.Rev.Let.* **84** (2000), 895
23. E.J. DOYLE et al, *Nucl.Fus.* **47** (2007), S18
24. X. LITAUDON, *Pl.Phys.Contr.Fus.* **44** (2002), 1057
25. D. MOREAU et al, *Nucl.Fus.* **48** (2008), 106001
26. L. COLAS et al, *Nucl.Fus.* **38** (1998), 903
27. L. BOEDO et al, *Nucl.Fus.* **40** (2000), 209
28. G. CONWAY, *Pl.Phys.Contr.Fus.* **44** (2002), 1167
29. C. ANGIONI et al, *Nucl.Fus.* **49** (2009), 055013
30. C. HOLLAND et al, *Phys.Plasmas* **18** (2011), 056113
31. X. GARBET et al, *Phys.Plasmas* **8** (2001), 2793
32. E.J. SYNAKOWSKI et al, *Phys.Plasmas* **4** (1997), 1736

INTRODUCTION TO DRIFT WAVE TURBULENCE MODELS

D. Reiser

*Forschungszentrum Jülich GmbH, Institut für Energie- und Klimaforschung – Plasmaphysik
EURATOM Association, 52425 Jülich, Germany*

ABSTRACT

This tutorial presents an introduction to the basic concepts of plasma turbulence models based on fluid theory. It is intended to elucidate basic features of drift fluid theory and drift wave turbulence. Theoretical methods widely used in tokamak transport and turbulence modelling are discussed briefly.

I. INTRODUCTION

The phenomenon of plasma turbulence is still an active field of research. It is accepted for years now that the turbulent transport is the main candidate to explain the degradation of plasma confinement known as the “anomalous” transport. Moreover, the theory of turbulent dynamics caused by the interplay of plasma transport and self-consistent electromagnetic fields, provides an explanation for the intermittent transport in the edge of tokamak plasmas, plasma oscillations and operational regimes found in experiments. In this tutorial we introduce a basic mathematical framework to study this kind of processes. Emphasis is put on illustrative examples of basic mechanisms driving turbulent processes in a plasma, e.g. linear instabilities, non-linear interaction and geometry effects. Of course, a comprehensive overview on all relevant aspects of turbulent transport and all varieties of theories would be too lengthy and confusing for this tutorial. Therefore, details on the physics of trapped particles, ITG and ETG modes [1], finite Larmor radius effects and elaborated kinetic theories have not been taken into account. However, the framework of fluid turbulence chosen here offers the opportunity to introduce systematically several terms and concepts relevant also for those methods and approaches not included here. The tutorial starts with a reminder of two-fluid plasma theory. By the use of the so-called drift approximation a very general set of model equations is established widely used in several variants in the literature to study a large number of plasma transport phenomena. By picking out certain ingredients of the general model presented basic processes like drift wave motion, drift wave coupling, linear instabilities and turbulent interaction are introduced. A second part is devoted to a discussion of

problems and details on the numerical simulation of tokamak turbulence.

II. DRIFT FLUID MODELS

In this section the basic equations of fluid theory of magnetized plasmas - known as Braginskii equations - are recapitulated. The problem of solving the perpendicular momentum equation is moved to the derivation of a vorticity equation to compute the self-consistent electric field and therefore the perpendicular velocity of the particles. It is shown that the so-called drift waves represent an elementary ingredient of the plasma dynamics of this kind of drift fluid model. In subsequent sections the possibility of linear instability drive due to resistivity and geometry effects, non-linear interactions and zonal flow oscillations are discussed.

A. Fluid Models

We start with the general fluid equations for the particle, momentum and energy balance for each plasma species [2, 3] neglecting external sources and sinks

$$\frac{dn}{dt} = -n \nabla \cdot \mathbf{V} \quad (1)$$

$$m n \frac{d\mathbf{V}}{dt} = -\nabla \cdot \mathbf{P} + \mathbf{R} + Z e n (\mathbf{E} + \mathbf{V} \times \mathbf{B}) \quad (2)$$

$$\frac{3}{2} n \frac{dT}{dt} = -\nabla \cdot \mathbf{q} - \mathbf{P} : \nabla \mathbf{V} - Q \quad (3)$$

where n denotes the density of the particular species, \mathbf{V} is the flow velocity and T the particular temperature. The pressure tensor is denoted by \mathbf{P} , m is the particle mass, Z is the charge number, \mathbf{q} is the heat flow and \mathbf{E} and \mathbf{B} are the electric and magnetic field vectors, respectively. External sources for particle, momentum and energy are neglected here. Finally the quantity Q and the vector \mathbf{R} denote the change of thermal energy and the force due to Coulomb collisions between the charged plasma particles. The total time derivative is defined by $d/dt = \partial/\partial t + \mathbf{V} \cdot \nabla$.

B. Drift Approximation

Using Eq. 2 one can write a formal solution for the perpendicular velocity \mathbf{V}_\perp as

$$\mathbf{V}_\perp = \frac{\mathbf{E} \times \mathbf{B}}{B^2} + \frac{\mathbf{B} \times \nabla p}{Z e n B^2} + \frac{m}{Z e B^2} \mathbf{B} \times \frac{d\mathbf{V}}{dt} \quad (4)$$

Here the pressure tensor is approximated by $\mathbf{P}=p\mathbf{1}$ and the perpendicular part of the friction \mathbf{R} has been neglected. The first term on the rhs of Eq. 4 defines the $E\times B$ -velocity \mathbf{V}_E , the second the diamagnetic drift \mathbf{V}_* and the third the polarization drift \mathbf{V}_p . Actually, Eq. 4 can be considered as an iteration scheme to find the perpendicular velocity \mathbf{V}_\perp . The iteration usually starts with the assumption that in zeroth order $\mathbf{V}_\perp^{(0)}=\mathbf{V}_E+\mathbf{V}_*$. Inserting this into Eq. 4 again gives in first order

$$\begin{aligned} \mathbf{V}_\perp^{(1)} &= \mathbf{V}_E + \mathbf{V}_* \\ &+ \frac{m}{ZeB^2} \mathbf{B} \times \left(\frac{\partial}{\partial t} + \mathbf{V}^{(1)} \cdot \nabla \right) (\mathbf{V}_E + \mathbf{V}_*) \end{aligned} \quad (5)$$

where $\mathbf{V}^{(1)}=\mathbf{V}_\parallel+\mathbf{V}_\perp^{(1)}$ denotes the total velocity of first order and \mathbf{V}_\parallel is the parallel velocity. Therefore, in first order a relation results between the perpendicular velocity $\mathbf{V}_\perp^{(1)}$ and the temporal evolution of the electric field $\mathbf{E}_\perp=-\nabla_\perp\phi$.

C. The Vorticity Equation

To compute the electric field an additional equation is needed. This is found by employing the quasineutrality condition $n_e=n_i\equiv n$ in the form

$$\nabla \cdot \mathbf{J} = \nabla \cdot (en\mathbf{u}_\perp - en\mathbf{v}_\perp) + \nabla_\parallel J_\parallel = 0 \quad (6)$$

with \mathbf{u}_\perp determined by

$$\begin{aligned} \mathbf{u}_\perp &= \mathbf{V}_E + \mathbf{u}_* \\ &+ \frac{m_i}{eB^2} \mathbf{B} \times \left(\frac{\partial}{\partial t} + \mathbf{u} \cdot \nabla \right) (\mathbf{V}_E + \mathbf{u}_*) \end{aligned} \quad (7)$$

and the electron drift approximated by

$$\mathbf{v}_\perp = \mathbf{V}_E + \mathbf{v}_* \quad (8)$$

i. e. due to their small mass the electron polarisation drift is neglected. This provides an equation - called vorticity equation or quasineutrality condition - for the time evolution of the electric potential ϕ and completes the model. Often the detailed vorticity equation is very difficult to derive, but as an example we will give an approximate expression widely used and valid for the case of cold ions, i. e. $T_i \approx 0$

$$\begin{aligned} \frac{m_i}{eB^2} \frac{\partial \nabla_\perp^2 \phi}{\partial t} + \frac{m_i}{eB^2} (\mathbf{u}_\parallel + \mathbf{V}_E) \cdot \nabla \nabla_\perp^2 \phi \\ = \frac{\nabla_\parallel J_\parallel}{en} + \frac{\nabla \cdot (n\mathbf{V}_E - n\mathbf{v}_\perp)}{n} \end{aligned} \quad (9)$$

This expression suffers from certain shortages concerning the energetic consistency of the entire model, this point has been discussed for cylindrical geometry in Ref. [4]. However, in practice, this is often a good approximation if $T_i \ll T_e$. This form also explains the name ‘‘vorticity equation’’, because the vorticity is

given by $\nabla_\perp^2 \phi = \mathbf{B} \cdot \nabla \times \mathbf{V}_E$ and is a measure for the local spinning of particles due to $E \times B$ motion. The vortices in plasmas are often called eddies. Now we have an equation for the perpendicular electric field $\mathbf{E}_\perp = -\nabla_\perp \phi$. For the parallel electric field it is assumed that $E_\parallel = -\nabla_\parallel \phi - \partial A_\parallel / \partial t$, where A_\parallel is the magnetic potential, which is related to a parallel current density via Ampère’s law $\mu_0 J_\parallel = -\nabla_\perp^2 A_\parallel$. Inserting the resulting drift velocities into the model equations Eqs. 1-3 and project the momentum equations on the direction parallel to the magnetic field lines leads to a set of model equations describing the temporal evolution of density, parallel momentum and temperatures. These are the particle conservation

$$\frac{\partial n}{\partial t} + \mathbf{v} \cdot \nabla n = -n \nabla \cdot \mathbf{v} \quad , \quad (10)$$

the conservation of parallel electron momentum (Ohm’s law)

$$\begin{aligned} m_e n \left(\frac{\partial v_\parallel}{\partial t} + \mathbf{v} \cdot \nabla v_\parallel \right) &= -\nabla_\parallel p_e + en \eta_\parallel J_\parallel \\ &- \alpha n \nabla_\parallel T_e + en \nabla_\parallel \phi + en \frac{\partial A_\parallel}{\partial t} \quad , \end{aligned} \quad (11)$$

the conservation of parallel ion momentum

$$\begin{aligned} m_i n \left(\frac{\partial u_\parallel}{\partial t} + \mathbf{u} \cdot \nabla u_\parallel \right) &= -\nabla_\parallel p_i - en \eta_\parallel J_\parallel \\ &+ \alpha n \nabla_\parallel T_e - en \nabla_\parallel \phi - en \frac{\partial A_\parallel}{\partial t} \quad , \end{aligned} \quad (12)$$

the heat transfer of electrons

$$\begin{aligned} \frac{3}{2} n \left(\frac{\partial T_e}{\partial t} + \mathbf{v} \cdot \nabla T_e \right) &= -\nabla \cdot \mathbf{q}_e \\ &- n T_e \nabla \cdot \mathbf{v} - \alpha \frac{J_\parallel}{e} \nabla_\parallel T_e + \eta_\parallel J_\parallel^2 \quad , \end{aligned} \quad (13)$$

and the heat transfer of ions

$$\begin{aligned} \frac{3}{2} n \left(\frac{\partial T_i}{\partial t} + \mathbf{u} \cdot \nabla T_i \right) &= -\nabla \cdot \mathbf{q}_i \\ &- n T_i \nabla \cdot \mathbf{u} \quad , \end{aligned} \quad (14)$$

where \mathbf{q}_e is the electron heat flux

$$\mathbf{q}_e = -\alpha T_e \mathbf{J}_\parallel / e + \kappa_\parallel^e \nabla_\parallel T_e - \kappa_\perp^e \nabla_\perp T_e \quad (15)$$

and \mathbf{q}_i is the ion heat flux

$$\mathbf{q}_i = \kappa_\parallel^i \nabla_\parallel T_i - \kappa_\perp^i \nabla_\perp T_i \quad (16)$$

and κ_\parallel and κ_\perp denote the classical heat conductivities. The thermal force coefficient is set to $\alpha=0.71$ [2, 3] and the parallel current density is defined by $\mathbf{J}_\parallel = en(\mathbf{u}_\parallel - \mathbf{v}_\parallel)$. The parallel derivative is defined by $\nabla_\parallel = \mathbf{b} \cdot \nabla$, where $\mathbf{B} = B\mathbf{b}$ denotes the total magnetic field (equilibrium field + fluctuations).

This forms the basis for the following discussions. Even though several physical effects are still missing (trapped particles, radiation, neutral physics etc.) this model contains a rich variety of physics such as the dynamics of drift waves, tearing modes, drift-Alfvén waves, ITG modes, sound waves, drift resistive ballooning modes etc. and it has been used as a starting point to study turbulent and intermittent plasma transport in the scrape-off-layer, the edge and the core plasma as well.

D. Drift Waves

To get an idea of the nature of drift waves we consider a subset of the model equations Eqs. 9-14 in cylindrical geometry. The cylinder geometry is not a severe restriction for the particular effects discussed here. We inspect the physical processes described by

$$\frac{\partial n}{\partial t} + \mathbf{V}_E \cdot \nabla n = 0 \quad (17)$$

$$\frac{T_e \nabla_{\parallel} n}{e n} - \nabla_{\parallel} \phi = 0 \quad (18)$$

This means that the particles are advected by the $E \times B$ -velocity and Ohm's law is reduced to a simple force balance between electron pressure and parallel electrostatic field. The temperature T_e is assumed to be constant and it follows $n = n_0 \exp(e\phi/T_e)$ along the magnetic field line. To study the interplay of a poloidal perturbation of mode number m and the symmetric profiles ("background") we split the density n and the electric potential ϕ according to

$$n = n_0(r) + n_m(r) e^{im\theta} + n_m^*(r) e^{-im\theta} \quad (19)$$

$$\phi = \phi_m(r) e^{im\theta} + \phi_m^*(r) e^{-im\theta} \quad (20)$$

This gives the evolution equations

$$\frac{\partial n_0}{\partial t} = \frac{2m}{rB} \frac{\partial}{\partial r} (\text{Im} \{n_m \phi_m^*\}) \quad (21)$$

$$\frac{\partial n_m}{\partial t} = \frac{im}{rB} \frac{\partial n_0}{\partial r} \phi_m \quad (22)$$

According to $n_m = e n_0 \phi_m / T_e$ the last equation gives

$$n_m(t) = n_m(0) \exp\left(i \frac{m}{rB} \frac{T_e}{e n_0} \frac{\partial n_0}{\partial r} t\right) \quad (23)$$

whereas $\partial n_0 / \partial t = 0$. This means for the simple system considered that the sinusoidal perturbation $n_m e^{im\theta}$ is traveling with the electron diamagnetic velocity in poloidal direction, i.e. $n_m(t) e^{im\theta}$ is moving with tangential velocity

$$r \frac{\partial \theta}{\partial t} = - \frac{T_e}{e n_0 B} \frac{\partial n_0}{\partial r} \quad (24)$$

Notice that the velocity is independent of the mode number m . A sketch of the geometry of the drift wave motion is shown in Fig. 1

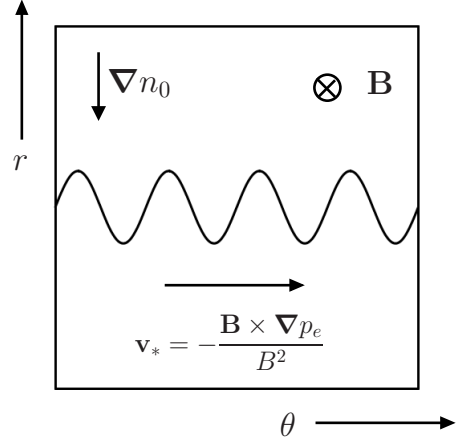


Figure 1: Geometry of a drift wave. The perturbation travels with the electron diamagnetic velocity.

E. "Anomalous" Transport in Drift Wave Models

Reconsidering Eq. 21 one finds that the homogeneous component n_0 will change in time if n_m and ϕ_m are not in phase anymore. This can be regarded as a transport mechanism because for the radial component v_m of the $E \times B$ velocity due to the perturbation ϕ_m one finds $v_m = -im \phi_m / rB$ and therefore a radial flux Γ_r shows up giving

$$\frac{\partial n_0}{\partial t} = -\nabla \cdot \Gamma \quad , \quad \Gamma = 2 \text{Re} \{n_m v_m^*\} \mathbf{e}_r \quad (25)$$

This relation is illustrated by Fig. 2 showing the effect on the net transport due to a phase shift σ between perturbations $\tilde{n} \sim \sin(m\theta)$ and $\tilde{\phi} \sim \sin(m\theta + \sigma)$. For $\sigma=0$, the net transport $\int \tilde{\Gamma} d\theta$ is zero and for $\sigma \neq 0$ the total particle transport is finite.

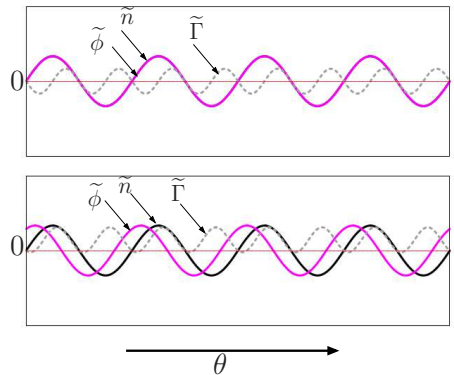


Figure 2: Effective transport $\tilde{\Gamma}$ for perturbations \tilde{n} and $\tilde{\phi}$ with $m=4$ with phase shift $\sigma=0$ (top) and $\sigma=\pi/3$ (bottom). The net flux is (dotted lines) is zero if \tilde{n} and $\tilde{\phi}$ are in phase.

F. Linear Instabilities

As has been shown in the last section a phase shift between perturbations in density and potential is able to modify the background profile of the density by means of an effective flux which can be much larger than the collisional diffusive flux [5]. On the other hand the Eq. 22 tells us that such a phase shift will also modify the profile of the perturbation density. Instead of a stable drift wave as before, when n_m and ϕ_m were in phase, it is then possible that the perturbation is damped or amplified. Of particular interest are of course the perturbations which grow in time and reach an amplitude level such that they might affect the global plasma profile. The question of possible candidates for a significant impact on plasma transport can be answered to a certain extent by a linear analysis. This approach is based on the linearization of the model equations and inspection of the temporal behaviour of Fourier decomposed perturbations. This will be illustrated by a simple example, the resistive instability. We start with a subset of model equations similar to the one of Section II. D but also including resistivity, parallel particle flow and a simplified vorticity equation.

$$\frac{\partial n}{\partial t} + \mathbf{V}_E \cdot \nabla n = -\nabla_{\parallel} (n v_{\parallel}) \quad (26)$$

$$\eta_{\parallel} J_{\parallel} = \frac{T_e \nabla_{\parallel} n}{e n} - \nabla_{\parallel} \phi \quad (27)$$

$$\frac{m_i}{e B^2} \left(\frac{\partial \nabla_{\perp}^2 \phi}{\partial t} + \mathbf{V}_E \cdot \nabla \nabla_{\perp}^2 \phi \right) = \frac{\nabla_{\parallel} J_{\parallel}}{e n} \quad (28)$$

Neglecting the parallel ion motion, i. e. $J_{\parallel} \approx -en v_{\parallel}$, and replace ∇_{\parallel}^2 by a constant $-k_{\parallel}^2$ leads to set of model equations known as the Hasegawa-Wakatani model or dissipative coupling model [6]. One finds for perturbations with mode number m as defined in Eqs. 19 and 20 the evolution equations

$$\frac{\partial n_m}{\partial t} = \frac{i m}{r B} \frac{\partial n_0}{\partial r} \phi_m + \frac{k_{\parallel}^2}{e \eta_{\parallel}} \phi_m - \frac{k_{\parallel}^2 T_e}{e^2 n_0 \eta_{\parallel}} n_m \quad (29)$$

$$\frac{m_i}{e B^2} \frac{\partial \nabla_{\perp}^2 \phi_m}{\partial t} = \frac{k_{\parallel}^2}{e n_0 \eta_{\parallel}} \phi_m - \frac{k_{\parallel}^2 T_e}{e^2 n_0^2 \eta_{\parallel}} n_m \quad (30)$$

Replacing now also $\partial/\partial t \rightarrow -i\omega$ and $\nabla_{\perp}^2 \rightarrow -k_{\perp}^2$ via Fourier decomposition one finds the algebraic equations

$$(D - i\omega) \frac{n_m}{n_0} - (D - i\omega_*) \frac{e \phi_m}{T_e} = 0 \quad (31)$$

$$D \frac{n_m}{n_0} - (D - i\omega k_{\perp}^2 \rho_s^2) \frac{e \phi_m}{T_e} = 0 \quad (32)$$

where the coupling parameter D and the diamagnetic frequency ω_* are defined by

$$D = \frac{k_{\parallel}^2 T_e}{e^2 n_0 \eta_{\parallel}}, \quad \omega_* = -\frac{m T_e}{e n_0 r B} \frac{\partial n_0}{\partial r} \quad (33)$$

and $\rho_s = c_s/\omega_i$, $c_s^2 = T_e/m_i$, $\omega_i = eB/m_i$, are the drift scale, the sound speed and the gyro-frequency, respectively. Finally, this leads to the dispersion relation for the frequency ω

$$\omega^2 + i \frac{1 + k_{\perp}^2 \rho_s^2}{k_{\perp}^2 \rho_s^2} D \omega - i \frac{D}{k_{\perp}^2 \rho_s^2} \omega_* = 0 \quad (34)$$

If $k_{\perp}^2 \rho_s^2 \ll 1$ this reduces to

$$\omega^2 + i \alpha (\omega - \omega_*) = 0, \quad \alpha = \frac{D}{k_{\perp}^2 \rho_s^2} \quad (35)$$

and for $\eta_{\parallel} \rightarrow 0$ the stable drift wave is recovered ($\omega = \omega_*$). For finite resistivity the frequency ω contains a non-zero imaginary part, which represents an unstable branch. If η_{\parallel} is small but finite, the solution can be expressed approximately by

$$\omega \approx \omega_* + i \frac{\omega_*^2}{\alpha} \quad (36)$$

Therefore it is possible that the drift wave perturbation becomes unstable, i. e. it starts to grow exponentially with a growth rate $\gamma \approx \omega_*^2/\alpha$.

G. Mixing Length Estimate

The linear instabilities discussed in the last section give important information on the plasma dynamics. Using the linear theory allows to draw conclusions on risky plasma configurations and typical time scales of plasma dynamics. However, it does not capture the important non-linear interaction in a plasma leading to non-linear saturation and the ‘‘anomalous’’ transport due to collective effects. To obtain more insight into this kind of effects requires substantial effort in development and analysis of non-linear models, theoretically and numerically as well. Nevertheless, many estimates widely used in theories on radial turbulent fluxes and plasma confinement use the so-called mixing length approach to draw conclusions just from linear growth rates of plasma instabilities. This is based on the idea that the linear instability with wave number k_{\perp} dominates the spatial structure of the turbulent field. On the other hand a rough estimate for the diffusion of particles is given by the ratio two basic statistical quantities describing the turbulent dynamics, i. e. $D \sim \lambda_c^2/\tau_c$, where λ_c denotes the correlation length and τ_c the correlation time. If one equates now the correlation length λ_c with the inverse wave number k_{\perp} (see Fig. 3 for an illustration) and considers the correlation time τ_c to be of the order of the inverse growth rate γ (the imaginary part of the frequency ω in the standard linear theory), one finds

$$D_{\perp} \sim \frac{\gamma}{k_{\perp}^2} \quad (37)$$

This is the standard mixing length diffusion coefficient used often in the literature. A refined version of this has been proposed by Connor and Pogutse [7].

However, it must be noted that this estimate can be quite useful for a qualitative analysis of trends, but very often the estimate is not useful for quantitative results.

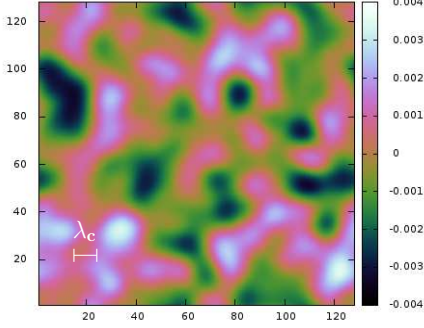


Figure 3: Snapshot of a turbulent structure of the electric potential ϕ . Lengths and amplitudes are given in a.u. The correlation length λ_c is indicated by the scale at the bottom left.

H. Non-Linear Interaction via $E \times B$ -Advection, Three-Wave-Coupling

So far we have considered the $E \times B$ advection just for the quasilinear model, where this mechanism leads to rotation and destabilization of perturbations and introduces an additional “anomalous” transport. If more perturbation modes are present another effect comes into play: the energy conserving interaction between modes leading to an energy cascade. To study this we reconsider the change in particle density due to the $E \times B$ -advection.

$$\frac{\partial n}{\partial t} = -\mathbf{V}_E \cdot \nabla n \quad (38)$$

Again a Fourier decomposition of the density n and the electric potential ϕ is useful.

$$n = \sum_{\mathbf{k}} n_{\mathbf{k}} e^{i\mathbf{k} \cdot \mathbf{x}} \quad , \quad \phi = \sum_{\mathbf{k}} \phi_{\mathbf{k}} e^{i\mathbf{k} \cdot \mathbf{x}} \quad (39)$$

Here \mathbf{x} is the three-dimensional position vector and \mathbf{k} the wave vector of the particular Fourier component. This gives

$$\mathbf{V}_E \cdot \nabla n = - \sum_{\mathbf{k}', \mathbf{k}''} \frac{\mathbf{B} \times \mathbf{k}'}{B^2} \cdot \mathbf{k}'' \phi_{\mathbf{k}'} n_{\mathbf{k}''} e^{i(\mathbf{k}' + \mathbf{k}'') \cdot \mathbf{x}} \quad (40)$$

$$\frac{\partial n_{\mathbf{k}}}{\partial t} = \frac{\mathbf{B}}{B^2} \cdot \sum_{\mathbf{k}'} (\mathbf{k}' \times \mathbf{k}) \phi_{\mathbf{k}'} n_{\mathbf{k} - \mathbf{k}'} \quad (41)$$

This means that the change of $n_{\mathbf{k}}$ can be considered as a (in general infinite) sum of interactions where three different wave vectors are involved, namely \mathbf{k} ,

\mathbf{k}' and their difference $\mathbf{k} - \mathbf{k}'$. Using this relation it can be proved that the following relation holds for a each triplet in Fourier space $\{\mathbf{k}_1, \mathbf{k}_2, \mathbf{k}_3\}$ which fulfills $\mathbf{k}_1 + \mathbf{k}_2 = \mathbf{k}_3$

$$\frac{\partial |n_{\mathbf{k}_1}|^2}{\partial t} \frac{1}{2} = \frac{\mathbf{B}}{B^2} \cdot (\mathbf{k}_3 \times \mathbf{k}_1) \operatorname{Re} \{ \phi_{\mathbf{k}_3} n_{\mathbf{k}_2}^* n_{\mathbf{k}_1}^* \} \quad (42)$$

$$+ \frac{\mathbf{B}}{B^2} \cdot (\mathbf{k}_1 \times \mathbf{k}_2) \operatorname{Re} \{ \phi_{\mathbf{k}_2}^* n_{\mathbf{k}_3} n_{\mathbf{k}_1}^* \}$$

$$\frac{\partial |n_{\mathbf{k}_2}|^2}{\partial t} \frac{1}{2} = \frac{\mathbf{B}}{B^2} \cdot (\mathbf{k}_2 \times \mathbf{k}_1) \operatorname{Re} \{ \phi_{\mathbf{k}_1}^* n_{\mathbf{k}_3} n_{\mathbf{k}_2}^* \} \quad (43)$$

$$+ \frac{\mathbf{B}}{B^2} \cdot (\mathbf{k}_3 \times \mathbf{k}_2) \operatorname{Re} \{ \phi_{\mathbf{k}_3} n_{\mathbf{k}_1}^* n_{\mathbf{k}_2}^* \}$$

$$\frac{\partial |n_{\mathbf{k}_3}|^2}{\partial t} \frac{1}{2} = \frac{\mathbf{B}}{B^2} \cdot (\mathbf{k}_1 \times \mathbf{k}_3) \operatorname{Re} \{ \phi_{\mathbf{k}_1} n_{\mathbf{k}_2} n_{\mathbf{k}_3}^* \} \quad (44)$$

$$+ \frac{\mathbf{B}}{B^2} \cdot (\mathbf{k}_2 \times \mathbf{k}_3) \operatorname{Re} \{ \phi_{\mathbf{k}_2} n_{\mathbf{k}_1} n_{\mathbf{k}_3}^* \}$$

Here the reality condition $n_{-\mathbf{k}} = n_{\mathbf{k}}^*$ has been used. Therefore, the sum of the three squared amplitudes is conserved

$$\frac{\partial}{\partial t} \left(\frac{|n_{\mathbf{k}_1}|^2}{2} + \frac{|n_{\mathbf{k}_2}|^2}{2} + \frac{|n_{\mathbf{k}_3}|^2}{2} \right) = 0 \quad (45)$$

This result allows the conclusion that any non-

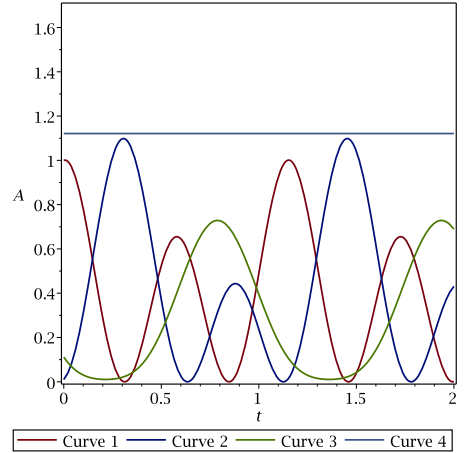


Figure 4: Example of the temporal evolution of three wave amplitudes $|n_{\mathbf{k}_1}|^2$, $|n_{\mathbf{k}_2}|^2$, $|n_{\mathbf{k}_3}|^2$ (curve 1, 2 and 3) interacting via $E \times B$ -advection. The sum of the three contributions is also shown (curve 4).

zero mode \mathbf{k}_1 in the system interacts with all pairs $\{\mathbf{k}_2, \mathbf{k}_3\}$ of modes fulfilling the relation $\mathbf{k}_1 + \mathbf{k}_2 = \mathbf{k}_3$ in a way that fluctuations are permanently exchanged and distributed in Fourier space, but always conserved. This is the non-linear mechanism behind the breaking of structures into smaller entities and vice versa.

I. Electromagnetic Effects, Shear Alfvén Waves, Tearing Modes

In this section the role of the electromagnetic pieces in the momentum equations are discussed. For this purpose we consider the following subset relating the electric potential ϕ and the magnetic potential A_{\parallel} .

$$\nabla_{\parallel}\phi + \frac{\partial A_{\parallel}}{\partial t} = 0 \quad (46)$$

$$\frac{m_i}{eB^2} \frac{\partial \nabla_{\perp}^2 \phi}{\partial t} = \frac{\nabla_{\parallel} J_{\parallel}}{en} \quad (47)$$

The first equation is a part of the parallel momentum balances and simply expresses that the parallel electric field is zero, i. e. $E_{\parallel}=0$. The second represents the response of the perpendicular electric field on a change in the parallel current to ensure quasineutrality. Now we consider small perturbations in the electric and magnetic field (labeled by a tilde) such that ∇_{\parallel} is undisturbed and governed by the dominant equilibrium field. Also the density n is assumed to be constant. Due to Ampère's law $\mu_0 J_{\parallel} = -\nabla_{\perp}^2 A_{\parallel}$ one obtains for the first equation Eq. 46

$$\mu_0 \frac{\partial \tilde{J}_{\parallel}}{\partial t} = \nabla_{\parallel} \nabla_{\perp}^2 \tilde{\phi} \quad (48)$$

and together with the second equation Eq. 47 it follows

$$\frac{\partial^2}{\partial t^2} \nabla_{\perp}^2 \tilde{\phi} = V_A^2 \nabla_{\parallel}^2 \nabla_{\perp}^2 \tilde{\phi} \quad (49)$$

$$\frac{\partial^2}{\partial t^2} \tilde{J}_{\parallel} = V_A^2 \nabla_{\parallel}^2 \tilde{J}_{\parallel} \quad (50)$$

where

$$V_A = \sqrt{\frac{B^2}{\mu_0 m_i n}} \quad (51)$$

These are wave equations for the perturbations in vorticity and current density, describing the traveling of the perturbations along the magnetic field with Alfvén speed V_A . If also a response of particle density via electron velocity is included and back-reaction via pressure gradient in the parallel electron momentum balance is taken into account, the resulting (linear) perturbations are called drift-Alfvén waves. It is also to be noted that by adding the resistive term in Eq. 46, i. e. considering $E_{\parallel} = -\eta_{\parallel} J_{\parallel}$ instead of $E_{\parallel}=0$, and taking into account the magnetic field fluctuations in the parallel gradient ∇_{\parallel} the two equations Eq. 46 and Eq. 47 describe a tearing mode, an important resistive instability [8]

J. Sound Waves

If one considers now a particular situation where the dynamics is governed by parallel motion

$$\frac{\partial n}{\partial t} = -\nabla_{\parallel}(nv_{\parallel}) \quad (52)$$

and - by neglect of electron mass - Ohm's law can be reduced to

$$\begin{aligned} -\nabla_{\parallel} p_e + e n \eta_{\parallel} J_{\parallel} - \alpha n \nabla_{\parallel} T_e \\ + e n \nabla_{\parallel} \phi + e n \frac{\partial A_{\parallel}}{\partial t} = 0 \end{aligned} \quad (53)$$

Then one finds for the linearized parallel ion momentum equation

$$m_i n \left(\frac{\partial u_{\parallel}}{\partial t} + u_{\parallel} \nabla_{\parallel} u_{\parallel} \right) = -\nabla_{\parallel} (p_i + p_e) \quad (54)$$

If one also assumes that the parallel current density is zero, i. e. $J_{\parallel} = en (u_{\parallel} - v_{\parallel}) = 0$, the continuity equation becomes

$$\frac{\partial n}{\partial t} = -\nabla_{\parallel}(nu_{\parallel}) \quad (55)$$

and linearizing the equations about a stationary equilibrium with constant temperatures T_e and T_i , i. e. $n = \bar{n} + \tilde{n}$ and $u_{\parallel} = \tilde{u}_{\parallel}$ gives

$$\frac{\partial \tilde{n}}{\partial t} = -\bar{n} \nabla_{\parallel} \tilde{u}_{\parallel}, \quad \frac{\partial \tilde{u}_{\parallel}}{\partial t} = -\frac{T_e + T_i}{m_i \bar{n}} \nabla_{\parallel} \tilde{n} \quad (56)$$

Therefore the perturbations \tilde{n} and \tilde{u}_{\parallel} fulfill

$$\frac{\partial^2 \tilde{n}}{\partial t^2} = c_s^2 \nabla_{\parallel}^2 \tilde{n}, \quad \frac{\partial^2 \tilde{u}_{\parallel}}{\partial t^2} = c_s^2 \nabla_{\parallel}^2 \tilde{u}_{\parallel} \quad (57)$$

where $c_s = \sqrt{(T_e + T_i)/m_i}$ is the sound speed. Like the Alfvén waves this is a wave like motion of perturbations along the magnetic field lines.

K. Curvature Effects

In the vorticity equation Eq. 9 and the continuity equation Eq. 10 terms containing the divergence of the perpendicular electron velocity \mathbf{v}_{\perp} appear. They can introduce an important kind of dynamics which we want to study by considering the subset

$$\frac{\partial n}{\partial t} = -n \nabla \cdot \mathbf{v}_{\perp} \quad (58)$$

$$\frac{m_i}{eB^2} \frac{\partial \nabla_{\perp}^2 \phi}{\partial t} = -\nabla \cdot \mathbf{v}_{\perp} + \nabla \cdot \mathbf{V}_E \quad (59)$$

According to the discussions above it is assumed that the dominant contributions in \mathbf{v}_{\perp} are given by the $E \times B$ -velocity and the diamagnetic velocity, i.e.

$$\mathbf{v}_{\perp} = \frac{\mathbf{B} \times \nabla \phi}{B^2} - \frac{T_e \mathbf{B} \times \nabla n}{enB^2} \quad (60)$$

Here $T_e = \text{const.}$ has been assumed, but this does not restrict the conclusions to be drawn from this illustrative example. It can be seen that for $\mathbf{B} = \text{const.}$, i. e. for a homogeneous magnetic field, the divergence $\nabla \cdot \mathbf{v}_{\perp}$ vanishes. This means that the perpendicular electron motion is incompressible for a homogeneous magnetic field. But in a curved magnetic field

the motion becomes compressible and a coupling between the density n and the vorticity $\nabla_{\perp}^2 \phi$ shows up. To continue the exercise we have to assume a concrete magnetic field structure. A reasonable choice is the standard magnetic field

$$\mathbf{B} = \frac{B_0}{qR} \mathbf{e}_{\theta} + \frac{B_0 R_0}{R^2} \mathbf{e}_{\varphi} \quad (61)$$

where θ is the poloidal angle, φ the toroidal angle, $R=R_0+r \cos \theta$, with major radius R_0 and minor radius r . The factor $q=q(r)$ is the so-called pitch parameter. This represents a twisted toroidal magnetic field with nested concentric circular flux surfaces and a magnetic field strength B_0 at the magnetic axes. Evaluating the divergences is now straightforward but cumbersome. We will just quote the result for the limit of high aspect ratio ($r/R_0 \rightarrow 0$) and define the curvature operator \mathcal{K} .

$$\begin{aligned} \mathcal{K}(f) &\equiv \nabla \cdot \left(\frac{\mathbf{B} \times \nabla f}{B^2} \right) \\ &\approx -\frac{2}{B_0 R_0} \left(\cos \theta \frac{1}{r} \frac{\partial f}{\partial \theta} + \sin \theta \frac{\partial f}{\partial r} \right) \end{aligned} \quad (62)$$

One obtains

$$\frac{\partial n}{\partial t} = -n \mathcal{K}(\phi) + \frac{T_e}{e} \mathcal{K}(n) \quad (63)$$

$$\frac{m_i}{e B^2} \frac{\partial \nabla_{\perp}^2 \phi}{\partial t} = \frac{T_e}{en} \mathcal{K}(n) \quad (64)$$

Now consider small perturbations of the form

$$\tilde{n} = \sum_m \tilde{n}_m e^{im\theta}, \quad \tilde{\phi} = \sum_m \tilde{\phi}_m e^{im\theta} \quad (65)$$

and linearize the equations (also the term $\sim \mathcal{K}(n)$ in the density equation is neglected here, because it is not relevant for our considerations)

$$\begin{aligned} \frac{\partial \tilde{n}_m}{\partial t} &= \frac{in}{R_0 B_0} \left(\frac{m-1}{r} \tilde{\phi}_{m-1} + \frac{m+1}{r} \tilde{\phi}_{m+1} \right. \\ &\quad \left. - \frac{\partial \tilde{\phi}_{m-1}}{\partial r} + \frac{\partial \tilde{\phi}_{m+1}}{\partial r} \right) \end{aligned} \quad (66)$$

$$\begin{aligned} \frac{\partial}{\partial t} \left(\frac{\partial^2 \tilde{\phi}_m}{\partial r^2} + \frac{1}{r} \frac{\partial \tilde{\phi}_m}{\partial r} - \frac{m^2}{r^2} \tilde{\phi}_m \right) \\ = -\frac{i T_e B_0}{m_i n R_0} \left(\frac{m-1}{r} \tilde{n}_{m-1} + \frac{m+1}{r} \tilde{n}_{m+1} \right. \\ \left. - \frac{\partial \tilde{n}_{m-1}}{\partial r} + \frac{\partial \tilde{n}_{m+1}}{\partial r} \right) \end{aligned} \quad (67)$$

The result is that the curvature of the magnetic field introduces an additional coupling between a mode \tilde{n}_m and the side bands $\tilde{\phi}_{m\pm 1}$ and vice versa. Actually this leads to the so-called ballooning instability [9]

which is located at the low field side of the tokamak, reflecting that a toroidal configuration is not symmetric anymore with respect to the poloidal angle. An important special case of this interaction is to be mentioned. If one assumes that the only perturbations present are

$$\tilde{n} = \tilde{n}_*(r) \sin \theta, \quad \tilde{\phi} = \tilde{\phi}_0(r) \quad (68)$$

one obtains for the sinusoidal density fluctuation

$$\frac{\partial \tilde{n}_*}{\partial t} = \frac{2n}{B_0 R_0} \frac{\partial \tilde{\phi}_0}{\partial r} \quad (69)$$

and for axisymmetric component of the electric potential

$$\frac{\partial}{\partial t} \left[\frac{1}{r} \frac{\partial}{\partial r} \left(r \frac{\partial \tilde{\phi}_0}{\partial r} \right) \right] = -\frac{T_e m_i B_0}{n R_0} \left[\frac{1}{r} \frac{\partial}{\partial r} (r \tilde{n}_*) \right] \quad (70)$$

Assuming $n \approx \text{const.}$ one can integrate the second equation with respect to r and it follows

$$\frac{\partial}{\partial t} \frac{\partial \tilde{\phi}_0}{\partial r} = -\frac{T_e B_0}{m_i n R_0} \tilde{n}_* \quad (71)$$

By inserting Eqs. 69 and 71 into each other one obtains

$$\frac{\partial^2 \tilde{n}_*}{\partial t^2} = -\omega_{\text{GAM}}^2 \tilde{n}_* \quad (72)$$

$$\frac{\partial^2}{\partial t^2} \frac{\partial \tilde{\phi}_0}{\partial r} = -\omega_{\text{GAM}}^2 \frac{\partial \tilde{\phi}_0}{\partial r} \quad (73)$$

The solutions are oscillations with frequency

$$\omega_{\text{GAM}} = \sqrt{\frac{2T_e}{m_i R_0^2}} \quad (74)$$

This oscillation of the sinusoidal component of the density and the radial derivative $\partial \phi_0 / \partial r$ is called the Geodesic Acoustic Mode (GAM) and has been observed in many tokamak experiments [10]. The derivative $\partial \phi_0 / \partial r$ actually represents a homogeneous poloidal flow in the plasma which is known as the Zonal Flow.

L. Résumé I

In the last sections we have paid attention to particular pieces of the basic set of model equations Eqs. 9-14. These pieces represent limiting cases of the full dynamics represented by the complete model. By this separation several isolated processes could be identified like drift waves (Sec. II. D), the dissipative instability (Sec. II. F), Alfvén waves (Sec. II. I), sound waves (Sec. II. J) and GAM oscillations (Sec. II. K). In the full model and in reality all these effects appear simultaneously and interact in a complicated way. Sometimes a single effect might be dominant,

but usually they have to be considered all together to obtain a consistent picture. Of course there are even more important effects hidden in the set of model equations or even more complete models not elucidated here. But the discussion of such effects can be conducted by similar reduction techniques presented here. We conclude this section by a rough estimate of the time scales related to the mechanisms mentioned above. For this purpose we compare the time scales of the drift wave motion $\tau_*^{-1} \sim k_{\perp} v_*$, the dissipative instability $\tau_{\alpha}^{-1} \sim \omega_*^2/\alpha$, the Alfvén waves $\tau_A^{-1} \sim k_{\parallel} V_A$, the sound waves $\tau_s^{-1} \sim k_{\parallel} c_s$ and the GAM oscillations $\tau_{\text{GAM}} \sim \sqrt{2} c_s/R_0$ and the diffusive time scale according to the mixing length estimate $\tau_D \sim k_{\perp}^2 a^2 \tau_{\alpha}$ for the dissipative instability. Using realistic estimates $k_{\perp} \rho_s \sim 1$, $k_{\parallel} R_0 \sim 1$, $\partial n_0/\partial r \sim n_0/a$, where a is the minor radius of the tokamak and R_0 its major radius this gives for $T_e=T_i=100$ eV, $n_0=10^{19}$ m⁻³, $a=0.5$ m, $R_0=1.75$ m, $m_i=2 m_p$ and $B=1$ T

$$\tau_* \sim 7.2 \cdot 10^{-6} \text{ s} \quad , \quad \tau_{\alpha} \sim 8.6 \cdot 10^{-4} \text{ s} \quad (75)$$

$$\tau_A \sim 3.6 \cdot 10^{-7} \text{ s} \quad , \quad \tau_s \sim 2.5 \cdot 10^{-5} \text{ s} \quad (76)$$

$$\tau_{\text{GAM}} \sim 1.7 \cdot 10^{-5} \text{ s} \quad , \quad \tau_D \sim 1.0 \cdot 10^2 \text{ s} \quad (77)$$

Of course these are rough estimates and the precise values can differ strongly for different plasma parameters. But it is typical that the Alfvén wave motion is the fastest process and that the time scales of the different effects cover a range of several orders of magnitude. The same can be concluded for the spatial scales hidden in the complete plasma transport model. This has important consequences for the practical computation of plasma transport and turbulence. The necessity to resolve very short and very large temporal and spatial in a single model scales makes it an enormous challenge to develop appropriate numerical methods for an efficient use of computers available.

III. TURBULENT TRANSPORT MODELLING

Even though the basic model defined by Eqs. 9-14 is not complete and misses certain important physical effects, it would be desirable to solve at least this reduced set in detail and without any approximation. Unfortunately the large range of temporal and spatial scales mentioned in the last section makes it very difficult to obtain results for realistic tokamak device parameters and operational regimes in an acceptable time. High resolution grids and a huge number of small enough time steps would be needed in a numerical computation. To make it worse, the implementation of complicated magnetic field geometries, e. g. including X-points, is an additional challenge for analytical and numerical methods. A first order workaround often used is the splitting of time scales and the restriction of the model to a certain range of

dynamics. Quite often it is useful to consider turbulent fluctuations only and to consider the large scale and slow dynamics as quasistationary. This reduces simulation run time because the slow processes do not have to taken into account. The need to cope with such requirements led to the derivation of several models with different content especially designed for particular scenarios, plasma devices and parameter regimes. It is not possible to compare them all in a short tutorial. But in the next sections we present an example of how a model reduction can be conducted and checked in a systematic way using a scale separation and an appropriate energy theorem.

A. The Problem of Setting up a Consistent Turbulence Model

In developing a model suitable for numerical solution we require that it is

- reasonably appropriate for the physics problem to be studied with respect to dominant transport mechanisms and geometry
- numerically tractable
- allowing a simulation in acceptable run time
- meeting the requirement of energetic consistency

In particular the last point is sometimes missed and model equations which might be reasonable and beautifully simple suffer from artificial effects due to inconsistencies. In the next section a practical example is presented. The four-field-model has been used often in turbulence studies and for this model the principles of energetic consistency can be illustrated by simple means.

B. Example: Four-Field-Model in Toroidal Geometry

In a first step we simplify the model Eqs. 9-14 by assuming $T_i=0$, $T_e=\text{const.}$, and by neglecting most of the parallel advection. Then one obtains for the continuity equation

$$\begin{aligned} \frac{\partial n}{\partial t} + \mathbf{V}_E \cdot \nabla n &= -\nabla_{\parallel} (n v_{\parallel}) \\ -n \nabla \cdot \mathbf{V}_E - n \nabla \cdot \mathbf{v}_* & \quad , \end{aligned} \quad (78)$$

and for Ohm's law

$$\frac{\partial A_{\parallel}}{\partial t} = \frac{T_e}{en} \nabla_{\parallel} n - \nabla_{\parallel} \phi - \eta_{\parallel} J_{\parallel} \quad (79)$$

The equation for the conservation of parallel ion momentum reduced by the use of Ohm's law Eq. 79 and reads

$$\frac{\partial u_{\parallel}}{\partial t} + \mathbf{V}_E \cdot \nabla u_{\parallel} = -\frac{T_e}{m_i n} \nabla_{\parallel} n \quad (80)$$

and the vorticity equation is

$$\begin{aligned} \frac{m_i}{eB^2} \left(\frac{\partial \nabla_{\perp}^2 \phi}{\partial t} + \mathbf{V}_E \cdot \nabla \nabla_{\perp}^2 \phi \right) \\ = \frac{\nabla_{\parallel} J_{\parallel}}{en} - \frac{\nabla \cdot (n \mathbf{v}_*)}{n} \end{aligned} \quad (81)$$

Now a partly linearization with respect to fluctuations is performed. Except for n the background pieces of ϕ , u_{\parallel} , and A_{\parallel} are assumed to be zero, i.e.

$$n = \bar{n} + \tilde{n}, \quad \phi = \tilde{\phi}, \quad u_{\parallel} = \tilde{u}_{\parallel}, \quad A_{\parallel} = \tilde{A}_{\parallel} \quad (82)$$

where \bar{n} is a constant density. This defines a four-field-model for fluctuations

$$\frac{d\tilde{n}}{dt} = -\tilde{\mathbf{V}}_E \cdot \nabla \tilde{n} + \frac{\nabla_{\parallel} \tilde{J}_{\parallel}}{e} - \bar{n} \nabla_{\parallel} \tilde{u}_{\parallel} \quad (83)$$

$$-\bar{n} \mathcal{K}(\tilde{\phi}) + \frac{T_e}{e} \mathcal{K}(\tilde{n})$$

$$\frac{\partial \tilde{A}_{\parallel}}{\partial t} = \frac{T_e}{e\bar{n}} \nabla_{\parallel} \tilde{n} - \nabla_{\parallel} \tilde{\phi} - \eta_{\parallel} \tilde{J}_{\parallel} \quad (84)$$

$$\frac{d\tilde{u}_{\parallel}}{dt} = -\frac{T_e}{m_i \bar{n}} \nabla_{\parallel} \tilde{n} \quad (85)$$

$$\frac{m_i \bar{n}}{B^2} \frac{d\tilde{w}}{dt} = \nabla_{\parallel} \tilde{J}_{\parallel} + T_e \mathcal{K}(\tilde{n}) \quad (86)$$

where

$$\frac{d}{dt} = \frac{\partial}{\partial t} + \tilde{\mathbf{V}}_E \cdot \nabla, \quad \nabla_{\parallel} = \frac{\mathbf{B} + \tilde{\mathbf{B}}}{B} \cdot \nabla \quad (87)$$

$$\tilde{w} = \nabla_{\perp}^2 \tilde{\phi}, \quad \mu_0 \tilde{J}_{\parallel} = -\nabla_{\perp}^2 \tilde{A}_{\parallel} \quad (88)$$

Notice that a radial derivative of \bar{n} is taken into account. This is a second parameter of the model in addition to the density \bar{n} itself. Both quantities are taken into account as constants to keep the framework as simple as possible (of course $\bar{n}=\text{const.}$ excludes a finite gradient $\partial \bar{n} / \partial r$ when taken accurately). Notice also that the parallel derivative contains the fluctuating magnetic field $\tilde{\mathbf{B}}$ related to the magnetic potential \tilde{A}_{\parallel} . This is approximately given by

$$\tilde{\mathbf{B}} = -\frac{\mathbf{B} \times \nabla \tilde{A}_{\parallel}}{B} \quad (89)$$

Despite the approximations needed to derive the four-field-model it still contains enough physics to describe reasonably the drift-Alfvén turbulence in the edge region of tokamak plasmas. Applications of this model and similar or even more reduced variants have been reported in Refs. [11–20], to mention only a few and without claiming to be exhaustive.

C. Energetics of the Four-Field-Model

The difficulties in the derivation of the four-field-model of the last section gives rise to the question to what extent the resulting model equations are still

realistic and appropriate for the problem to be studied. A very powerful and useful method to get some insight into the particular features of the simplified model found by certain manipulations is the analysis of an energy theorem. This means that the desirable property of energy conservation is still present in the simplified model. For this purpose an appropriate energy functional has to be found. For the example of the four-field-model this is the energy density

$$\tilde{U} = \frac{m_i \bar{n}}{2} \tilde{V}_E^2 + \frac{m_i \bar{n}}{2} \tilde{u}_{\parallel}^2 + \frac{\tilde{B}^2}{2\mu_0} + \frac{\bar{n} T_e}{2} \frac{\tilde{n}^2}{\bar{n}^2} \quad (90)$$

Using appropriate boundary conditions the temporal change of the different contributions integrated over the entire computational volume is given by

$$\frac{\partial}{\partial t} \int \frac{m_i \bar{n}}{2} \tilde{V}_E^2 dV = -\frac{m_i \bar{n}}{B^2} \int \tilde{\phi} \frac{\partial \nabla_{\perp}^2 \tilde{\phi}}{\partial t} dV \quad (91)$$

$$= -\int \tilde{\phi} \nabla_{\parallel} \tilde{J}_{\parallel} dV - \int T_e \tilde{\phi} \mathcal{K}(\tilde{n}) dV$$

$$\frac{\partial}{\partial t} \int \frac{m_i \bar{n}}{2} \tilde{u}_{\parallel}^2 dV = m_i \bar{n} \int \tilde{u}_{\parallel} \frac{\partial \tilde{u}_{\parallel}}{\partial t} dV \quad (92)$$

$$= -\int T_e \tilde{u}_{\parallel} \nabla_{\parallel} \tilde{n} dV$$

$$\begin{aligned} \frac{\partial}{\partial t} \int \frac{\tilde{B}^2}{2\mu_0} dV &= \int \tilde{J}_{\parallel} \frac{\partial \tilde{A}_{\parallel}}{\partial t} dV \\ &= \int \frac{T_e}{e\bar{n}} \tilde{J}_{\parallel} \nabla_{\parallel} \tilde{n} dV - \int \tilde{J}_{\parallel} \nabla_{\parallel} \tilde{\phi} dV \end{aligned} \quad (93)$$

$$- \int \eta_{\parallel} \tilde{J}_{\parallel}^2 dV$$

$$\begin{aligned} \frac{\partial}{\partial t} \int \frac{\bar{n} T_e}{2} \frac{\tilde{n}^2}{\bar{n}^2} dV &= \int \frac{T_e}{\bar{n}} \tilde{n} \frac{\partial \tilde{n}}{\partial t} dV \\ &= -\int T_e \tilde{n} \tilde{\mathbf{V}}_E \cdot \frac{\nabla \tilde{n}}{\bar{n}} dV + \int \frac{T_e}{e\bar{n}} \tilde{n} \nabla_{\parallel} \tilde{J}_{\parallel} dV \\ &\quad - \int T_e \tilde{n} \nabla_{\parallel} \tilde{u}_{\parallel} dV - \int T_e \tilde{n} \mathcal{K}(\tilde{\phi}) dV \end{aligned} \quad (94)$$

All contributions where the fluctuations are advected with the $E \times B$ -velocity \tilde{V}_E vanish. Strictly speaking, these contributions vanish exactly only if $\nabla \cdot \tilde{\mathbf{V}}_E = 0$, i. e. if \tilde{V}_E is incompressible. But one can consider the corrections due to compressibility for these terms to be small if the fluctuations are small. For the other contributions it can be proved that the following relations hold

$$\int \tilde{f} \nabla_{\parallel} \tilde{g} dV = -\int \tilde{g} \nabla_{\parallel} \tilde{f} dV \quad (95)$$

$$\int \tilde{f} \mathcal{K}(\tilde{g}) dV = -\int \tilde{g} \mathcal{K}(\tilde{f}) dV \quad (96)$$

Therefore, one gets for the temporal evolution of the total energy

$$\begin{aligned} \frac{\partial E}{\partial t} &= \int \frac{\partial U}{\partial t} dV \\ &= - \int \frac{T_e \tilde{n} \tilde{\mathbf{V}}_E \cdot \nabla \tilde{n}}{n} dV - \int \eta_{\parallel} \tilde{J}_{\parallel}^2 dV \end{aligned} \quad (97)$$

The second term in the second line is negative definite and represents a sink for the energy due to resistivity. The first term of the second line is usually positive and represents the source for the turbulence due to the gradient $\partial \tilde{n} / \partial r$ in the background density. All other contributions cancel each other and this represents an energy conserving exchange of energy. For example the piece $\int T_e \tilde{u}_{\parallel} \nabla_{\parallel} \tilde{n} dV$ gives the channel of energy exchange between \tilde{n} and \tilde{u}_{\parallel} due to sound waves. Such a kind of energy theorem helps to check if a certain set of model equations is consistent and to get some insight into its dynamics. Also it is obvious that any modifications in the model should preserve the energetic consistency. If, e. g., the curvature term $\sim \mathcal{K}(\tilde{\phi})$ in the continuity equation is removed from the model, the corresponding term $\sim \mathcal{K}(\tilde{n})$ should be removed too. Otherwise an artificial sink/source of energy disturbs the dynamics of the model and leads to unpredictable results. The same is valid if some manipulations are done to a single equation of the model. Usually this needs also modifications in other equations to keep it consistent.

D. Résumé II

It has been shown that even a simplified model with limited applicability needs a careful derivation and inspection of the consistencies of approximations used. This has to be kept in mind as long as one is restricted to simplified approaches due to the lack of computational power or appropriate numerical methods for more general problems. To overcome the limitations several activities are still ongoing to improve the physics content and the numerical treatment, e. g. the extension to gyro-fluid models and the development of gyro-kinetic models and simulations (see, e. g. , Refs. [21–24] and references therein). Also the increase of computational power available, in particular the use of parallel computers, offers the improvement of accuracy in the modelling of turbulent plasma dynamics. Nevertheless, the basic concepts presented in this tutorial remain of importance also in interpretation and analysis of improved models and techniques.

REFERENCES

1. J. Weiland, “Collective Modes in Inhomogeneous Plasmas”, IoP Publishing, 2000.
2. S. I. Braginskii, *Rev. Plasma Phys.*, **1**, 205 (1965).
3. K. Miyamoto, “Plasma Physics for Nuclear Fusion”, MIT Press, Cambridge 1980, p. 128-133.
4. D. Reiser, *Phys. Plasmas*, **19**, 072317 (2012).
5. F. F. Chen, “Introduction to Plasma Physics and Controlled Fusion”, Plenum Press, New York 1984, p. 186.
6. A. Hasegawa and M. Wakatani, *Phys. Rev. Lett.*, **50**, 682 (1983).
7. J. W. Connor and O. P. Pogutse, *Plasma Phys. Control. Fusion*, **43**, 155 (2001).
8. G. Schmidt, “Physics of High Temperature Plasmas”, 2nd edition, Academic Press, New York 1979, p. 146.
9. R. J. Hastie *et al.* *Phys. Plasmas*, **10**, 4405 (2003).
10. Y. Xu *et al.* *Phys. Rev. Lett.*, **97**, 165003 (2006).
11. M. Wakatani, A. Hasegawa, *Phys. Fluids* **27**, 611 (1984).
12. B. D. Scott, *Phys. Fluids B* **4**, 2468 (1992).
13. F. L. Hinton and C. W. Horton, Jr., *Phys. Fluids* **14**, 116 (1971).
14. B. D. Scott, *Plasma Phys. Contr. Fusion* **39**, 1635 (1997).
15. D. Reiser and B. Scott, *Phys. Plasmas* **12**, 122308 (2005).
16. D. Reiser, *Phys. Plasmas* **14**, 082314 (2007).
17. P. Beyer *et al.*, *Phys. Plasmas* **5**, 4271 (1998).
18. V. Naulin, *Phys. Plasmas* **10**, 4016 (2003).
19. B. D. Scott, *New J. Phys.* **4**, 52 (2002).
20. B. Scott, *Phys. Plasmas* **8**, 447 (2001).
21. F. Jenko *et al.*, *Phys. Plasmas*, **7**, 1904 (2000).
22. B. D. Scott, *Phys. Plasmas* **14**, 102318 (2007)
23. B. D. Scott, *Phys. Plasmas* **17**, 112302 (2010)
24. J. Madsen , *Phys. Plasmas* **20**, 072301 (2013)

RADIAL ELECTRIC FIELDS AND TRANSPORT BARRIERS

Maarten Vergote, Kristel Crombé

Laboratory for Plasma Physics, Association 'EURATOM-Belgian State'

Ecole Royale Militaire - Koninklijke Militaire School, Avenue de la Renaissance 30, B-1000 Brussels, Belgium

I. INTRODUCTION

The importance of radial (i.e. perpendicular to the magnetic surface) electric fields was already recognised early in the research on controlled thermonuclear fusion. An initial description of electric field effects in toroidal confinement was given by Budker[6]. Such a configuration with combined magnetic and electric confinement (“magnetolectric confinement”, where the electric field provides a toroidal equilibrium configuration without rotational transform) was studied by Stix[7], who suggested that a reactor-grade plasma under magnetolectric confinement (electric fields of order 1 MV/cm) may reach a quasi-steady-state with ambipolar loss of electrons and some suprathreshold ions (e.g. 3.5 MeV α -particles). Experiments such as on the Electric Field Bumpy Torus EFBT[8, 9] provided quite favourable scaling for particle confinement. The possible importance of radial electric fields for transport was in the past repeatedly established [10, 11, 12, 13]. Since the early days the plasma potential has been measured in tokamaks such as ST[14], TM-4[15] and ISX-B[16], but because no significant effects of the radial electric field E_r on plasma transport were observed under the machine conditions at that time, no further research was conducted in tokamaks.

However, a renaissance came after the transition from a low confinement mode (L-mode) to a high confinement mode (H-mode) was discovered in ASDEX[17]. The interest was suddenly refreshed and a flurry of activity started with the experimental[18, 19] and theoretical recognition[20, 21, 22] of a possible link between E_r and the H-mode phenomenon. Since then research on E_r has flourished and the H-mode has now been seen in a wide variety of magnetic confinement devices. Many theories have pointed to the possible decisive role of E_r in the creation of transport barriers (i.e. zones of finite radial extent where particle and/or heat diffusivity are depressed) and in the L-H bifurcation mechanism.

Typical features of an L-H transition could also be obtained by externally inducing a controlled radial electric field in the plasma (independently of other plasma parameters) in the tokamaks CCT[18] and TEXTOR[23, 24] and later in many other machines [see e.g. reviews[25, 26]]. These electrode biasing experiments (induced H-modes) have con-

tributed significantly to the understanding of the H-mode phenomenon and of the effects of E_r on plasma transport[27].

Besides an important theoretical activity, many experiments have since been performed in the plasma edge and the SOL of limiter or divertor devices[25, 26]. Imposing electric fields independently of other machine parameters allows to manipulate the edge and SOL profiles and flows, to control impurities and to affect particle and power exhaust[25].

Radial electric fields have been studied in a variety of devices: tokamaks, stellarators and other helical devices, reversed field pinches, mirrors, etc. In stellarators[28] where neoclassical transport dominates, the transport coefficients depend on E_r . A radial electric field limits the excursions of the helically trapped particles due to $\mathbf{E}\times\mathbf{B}$ poloidal rotation, whereby neoclassical transport can be reduced to such an extent that stellarators become viable for a fusion reactor. The present paper concentrates on tokamaks in which E_r itself without shear cannot contribute to confinement improvement because the ensuing rigid rotation which reduces orbit losses (“orbit squeezing”) and improves neoclassical transport has no effect on microturbulence which is regarded as the dominating cause of anomalous transport in auxiliary heated tokamaks. Effects of E_r on transport enter only through derivatives of E_r .

This paper is mainly based on a former version of this lecture [1], from which the main role of the radial electric field in a tokamak is taken. The underlying mechanism on how it suppresses the turbulent transport is still believed to happen in the way proposed by Burrell[27]. The development of this $\mathbf{E}\times\mathbf{B}$ velocity shear turbulence stabilisation model to explain the formation of transport barriers in magnetic confinement devices is exactly one of the scientific success stories of fusion research. This model has the universality needed to explain turbulence reduction and confinement improvement under a variety of conditions in limiter- and divertor tokamaks, stellarators, torsatrons, reversed field pinches, mirror machines, etc.

Further details on radial electric fields and their role in plasma confinement and exhaust can be found in review articles[29].

II. RADIAL ELECTRIC FIELDS AND ROTATION

The mechanism of a radial electric field as a transport barrier can be summarized through the link with the $\mathbf{E} \times \mathbf{B}$ drift velocity, creating steady state or oscillatory rotational flows in the poloidal and/or toroidal direction. The correct derivation of this link is described in the framework of neoclassical theory (see [2]). In the core plasma, this theory predicts a link between the radial electric field and (mostly) the toroidal rotation on the basis of ambipolarity, whereas the poloidal flow is strongly damped. In the edge of a tokamak, close to the separatrix, strong gradients in n (and to less extent T) make that the so-called ‘‘anomalous’’ transport overrules the ‘‘theoretical’’ one predicted by neoclassical theory [3]. In that region other mechanisms come into play; the neoclassical expression for the radial electric field is not valid and it should be replaced by numerical results from codes like ASCOT [4] or B2SOLPS [5].

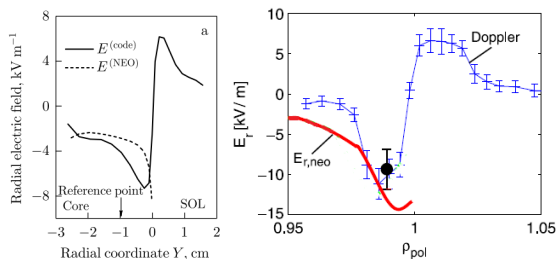


Figure 1: Left: E_r computed in the midplane by B2SOLPS and based on neoclassical theory (taken from [3]). Right: Comparison of E_r -measurement in ASDEX Upgrade with $E_{r,neo}$: Doppler reflectometry profile (#24812, 2.7 s) and single point (#24906, 2.3 s, circle), $E_{r,neo}$ (#24906, 2.3 s, red), taken from [42]

For every family of species individually, the radial electric field and plasma rotation are connected through the radial momentum balance. From an experimental point of view this opens quite some opportunities, because E_r can be determined from a single (impurity) ion radial force balance equation:

$$E_r = \frac{1}{n_i Z_i e} \nabla P_i - v_{\theta,i} B_\phi + v_{\phi,i} B_\theta \quad (1)$$

where n_i is the ion density, Z_i is the charge number of the ion, e is the electronic charge, P_i is the ion pressure, $v_{\theta,i}$ and $v_{\phi,i}$ are the poloidal and toroidal rotation velocities, respectively, of the ion species considered; and B_θ and B_ϕ are the poloidal and toroidal magnetic fields, respectively. This equation is valid at each point on any given flux surface, and the quantities involved are local quantities (E_r itself is not a flux function).

It follows from Eq. (1) that E_r is determined by three major driving forces: radial pressure gradient,

poloidal and toroidal rotation. Because E_r can be influenced by particle-, heat- and angular momentum input, and by changing the current profile (changing B_θ), various of these terms can be active in various machines with respect to $\mathbf{E} \times \mathbf{B}$ shear flow reduction of turbulence and transport, which occurs regardless of the plasma rotation direction. This provides the possibility of active control of transport; $\mathbf{E} \times \mathbf{B}$ shear as a control mechanism for turbulence and transport has the major advantage of flexibility, in that the shear can be generated or enhanced in several ways. Particle-, heat-, and momentum transport are not independent of each other, but have a complex coupling. Therefore, research on E_r can clarify complex plasma transport mechanisms.

III. $\mathbf{E} \times \mathbf{B}$ VELOCITY SHEAR REDUCTION OF TURBULENCE

$\mathbf{E} \times \mathbf{B}$ velocity shear reduction of turbulence in a plasma is a mechanism akin to the interaction between sheared velocity fields and turbulence in fluids. However, in a plasma $\mathbf{E} \times \mathbf{B}$ velocity and fluid velocity due to E_r can be quite different. The fundamental velocity is not the mass velocity, but rather the $\mathbf{E} \times \mathbf{B}$ velocity, the drift velocity at which all particles move – regardless of their charge or mass – and at which turbulent eddies are convected.

The fundamental physics involved in transport reduction is the effect of $\mathbf{E} \times \mathbf{B}$ shear on the growth, radial extent and phase decorrelation of the turbulent eddies. The identification of individual modes responsible for the observed turbulence may not be as important as the knowledge of turbulence drive suppression mechanisms, which provide a direct route to transport control.

Turbulence is stabilised by the shear rate $\omega_{E \times B}$ in the $\mathbf{E} \times \mathbf{B}$ flow velocity $\mathbf{v}_{E \times B}$ induced by E_r [30]

$$\omega_{E \times B} = \left| \frac{d\mathbf{v}_{E \times B}}{dr} \right| = \left| \frac{(RB_\theta)^2}{B} \frac{d}{d\psi} \left(\frac{E_r}{RB_\theta} \right) \right| \quad (2)$$

where R is the major radius, B_θ is the poloidal magnetic field and ψ is the poloidal flux.

The $\mathbf{E} \times \mathbf{B}$ shear rate enters quadratically into the various theories; accordingly, its sign is irrelevant. Indeed, H-mode edge barriers have been seen with both signs of E_r and its derivative [33]. Equation (2) shows that both E_r and B_θ contribute to the final result; E_r/RB_θ is the toroidal angular speed due to the equilibrium flow driven by E_r in standard neoclassical theory, suggesting that the basic shearing is in the toroidal direction.

Equation (2) also shows that the shear rate is not constant on a given magnetic flux surface, being significantly larger on the low toroidal field side, where the flux surfaces are more dense (the electric potential being constant on a flux surface). Experimental

data on H-modes have indeed demonstrated significant poloidal variation in the effect of $\mathbf{E} \times \mathbf{B}$ shear on turbulence.

Theoretically, there are two points of view[27]. The first (non-linear suppression) is that the turbulent eddies are distorted and the radial transport is reduced if the $\mathbf{E} \times \mathbf{B}$ shear rate exceeds the decorrelation rate of the ambient turbulence in the absence of $\mathbf{E} \times \mathbf{B}$ shear; this is valid for entire classes of turbulent modes. The second is linear stabilisation, which is mode specific, and therefore the details depend on the turbulence driving mechanisms. The fluctuation spectra are $\mathbf{E} \times \mathbf{B}$ Doppler-shifted, and the stabilisation is mainly due to shear in this Doppler shift.

An important point in plasmas is the synergistic effects between $\mathbf{E} \times \mathbf{B}$ velocity shear and magnetic shear. In neutral fluid dynamics sheared velocity is a source of free energy which can drive turbulence through Kelvin-Helmholtz instabilities. In a plasma shear in the magnetic field prevents coupling of the various modes across the velocity gradient so that they are unable to extract energy from the $\mathbf{E} \times \mathbf{B}$ velocity shear and grow[27].

IV. MEASUREMENT TECHNIQUES

Different methods exist for measuring the radial electric field in plasmas[34].

A. Spectroscopic measurements by charge exchange recombination spectroscopy (CXRS)[35]:

The different terms in eq. (1) can be measured on impurity ions. A beam of neutral particles (typical deuterium, hydrogen or helium atoms) is injected in the plasma. In some devices a special diagnostic beam is installed for this purpose or alternatively one of the heating beams can be used. Some of the injected neutral atoms transfer an electron to impurity ions. The emitted photons from the impurities in excited state are detected by a spectrometer. From the width, height and Doppler shift of the spectral line, the impurity temperature and density (and thus the pressure) can be calculated, as well as the rotation velocity. Careful attention is required to the correct interpretation of the measured line shape, moreover due to the energy dependence of the charge exchange cross-section and the gyro-orbit motion of the excited ions.

B. Measurements of the perpendicular fluctuation velocity by Doppler reflectometry:

A probing beam is launched at an oblique incidence with respect to the cut-off layer. The back-scattered field close to the cut-off layer is detected. Fluctuations whose wave-number (k_f) matches the Bragg rule $k_f = -2k_i$ where k_i is the probing wave-vector at the cut-off, are selected. Since they are

aligned with the magnetic field lines ($k_{\parallel} \ll k_{\perp}$) the signal frequency spectrum is Doppler shifted by $\Delta\omega = k_{\perp} v_{\perp}$, hence allowing the determination of the fluctuation rotation component in the perpendicular direction. A v_{\perp} profile is obtained by scanning the probing frequency. The measured velocity (v_{\perp}) is the sum of $\mathbf{E} \times \mathbf{B}$ velocity ($v_{E \times B}$) and turbulent phase velocity (v_{ph}). When v_{ph} is much smaller than $v_{E \times B}$ (which is the normal situation) a direct measurement of $v_{E \times B} = E_r \times B/B^2$ is obtained, and thus of the radial electric field when the B-field is known.

C. Plasma potential measurements with Heavy Ion Beam Probes (HIBP)[36]:

Single charged particles are generated in an ion source, accelerated in a tube and injected across the magnetic field into the plasma. As particles pass through the plasma they are further ionised to produce double charge exchange particles. The energy of the secondary beam is detected at the energy analyser. An advanced Heavy Ion Beam Probe can simultaneously measure the plasma electric potential ϕ (from the difference in energy between the secondary ions leaving the plasma and the primary ions), the electron density n_e (from the intensity of the secondary beam) and its fluctuations, the electron temperature T_e , and a poloidal magnetic field component B_{θ} at a point inside the plasma. This point can be scanned through the plasma cross-section by varying the deflection potentials (active beam control).

D. Measurements of the plasma potential in the edge region with Langmuir probes[37]:

Langmuir probes can provide radial profiles of n_e , T_e , plasma potential and phase velocity of density turbulent fluctuations. The radial electric field profile is computed from the first derivative of the plasma potential. Langmuir probe measurements are restricted to the plasma edge for high-temperature toroidal plasmas, but they have an excellent spatial resolution of less than 1mm, while the CXRS and HIBP measurements have typical resolutions above 5 mm.

E. Direct measurement of the radial electric field using Motional Stark Effect polarimetry (MSE)[39]:

MSE is a well established technique for measuring the magnetic field pitch angle in tokamaks. By viewing the Stark emission spectrum from two different angles, this technique can also provide local measurements of the plasma radial electric field (E_r).

V. TRANSPORT BARRIERS AND CONFINEMENT IMPROVEMENT

As outlined in the review paper of Burrell[26] (see also references therein) the $\mathbf{E} \times \mathbf{B}$ shear stabilisation

model was originally developed to explain the transport barrier formation at the plasma edge at the L to H transition. Later, it has been applied to explain the wider edge transport barrier at the H- to VH- (very high) mode transition moreover seen in DIII-D. Most recently, this model has been applied to the internal transport barriers (ITB) formed in plasmas with modified (negative or optimised) magnetic shear (DIII-D, TFTR, JT-60U, JET, ASDEX Upgrade, Tore Supra, etc), and to plasmas with transport reduction across the whole plasma radius (JT-60U and DIII-D).

A. $\mathbf{E} \times \mathbf{B}$ Shear Effects at the Plasma Edge

A large variety of studies related to the effect of radial electric fields on edge transport barriers (ETBs) exist. A review of H-mode studies over the past 25 years is given in [40]. The paper concentrates on a couple of the recent results on different tokamaks: ASDEX-Upgrade[41], JET[38], Alcator C-Mod[44] and the spherical tokamak MAST[46].

On *ASDEX-Upgrade*[41], radial electric field and shear measurements were performed using the Doppler reflectometer system as well as the recently installed toroidal and poloidal edge CXRS system following the B^{5+} ions.

The E_r profile has been measured in different confinement regimes. In L-mode, E_r is small in magnitude and exhibits little shear, while in the ETB of the H-mode a strong, negative E_r well and a localized minimum close to the separatrix ($\rho_{pol} > 0.99$) is found. The steepest gradients of the pressure profile are in the inner, negative shear region of the E_r well. The depth of the E_r well is observed to increase dramatically with the confinement of the discharge and the main ion pressure gradient term seems to be the dominant contribution to E_r (figure 2). The E_r profile undergoes a reversal at the plasma edge to become positive in the Scrape-Off-Layer, as is measured in Fig. 1.

Figure 3 shows the minimum of $E_{r,neo}$ for the different phases at varying densities. Error bars derived from shifting the T_i profile are given for the L-H transition points. At the L-H transition $E_{r,neo}$ shows no dependence on the electron density at the pedestal top, $n_{e,ped}$. Included in figure 3 are also E_r minimum values derived from Doppler reflectometry for a different set of discharges with comparable parameters. This shows a good agreement between CXRS and Doppler reflectometry for the different discharge mode regimes. The very weak variation of the L-H points in $E_{r,neo}$ is remarkable and underlines the possible key role of E_r in the L-H threshold.

Refurbishment of the *JET* edge CXRS diagnostic has resulted in higher quality impurity density profiles than previously, allowing analysis of the local C^{6+} impurity ion profiles across the L-H transition. Also with the JET-ITER-Like-Wall a shallow edge radial electric field well is observed at the L-H transi-

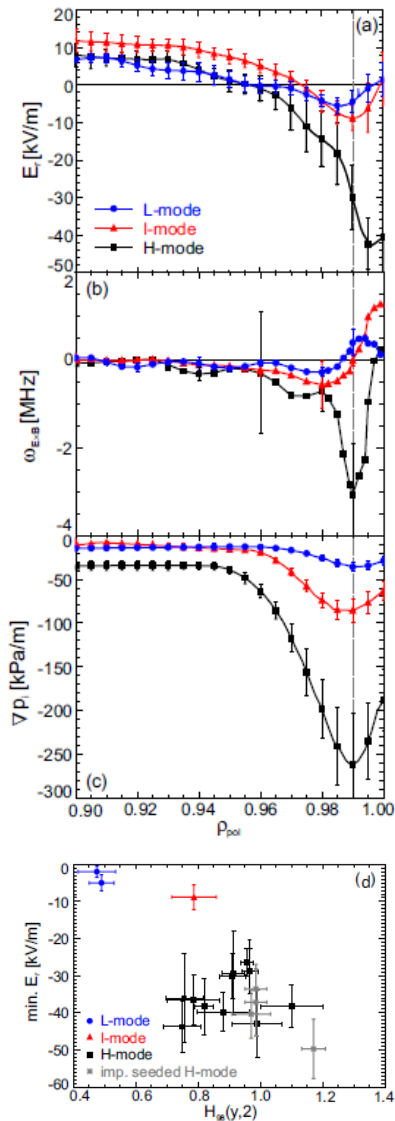


Figure 2: (a) E_r in L-, I- and H-mode and (b) resulting E_r shear. For better clarity the uncertainties are only shown for distinct radial positions. (c) Main ion pressure gradient, ∇p_i , in different confinement regimes. (d) Depth of E_r well as a function of the energy confinement factor $H_{98}(y,2)$ [41]

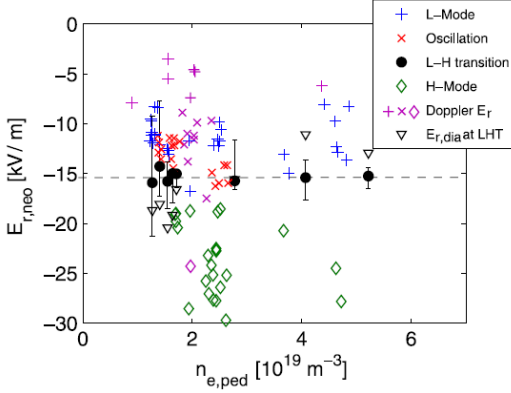


Figure 3: Minimum values in the profile of $E_{r,neo}$ versus $n_{e,ped}$, Doppler E_r and $E_{r,dia}$ for L-H transitions only. (figure taken from [42]).

tion. Consistent with previous poloidal velocity measurements in JET, but in contrast with results from other tokamaks, the edge impurity ion poloidal velocity remains low, close to its L-mode values ($0\text{--}5$ km/s \pm $2\text{--}3$ km/s), through the L-H transition and into the ELMy H-mode phase, with no measureable increase within the experimental uncertainties.

The experimental uncertainty in v_{pol} is dominated by poor photon statistics in the near-separatrix region, where the C^{6+} CX signal is very weak.

The large error bars in v_{pol} , coupled to its low values in JET, prevent the evaluation of the depth of the total E_r well and of the relative strength of diamagnetic versus poloidal velocity terms in the radial force balance of impurity ions (see fig.4). The diamagnetic term of the negative E_r well increases in magnitude across the L-H transition and into the H-mode phase in the radial region where the edge density and temperature transport barriers have formed and thus is likely to be correlated with the formation of the H-mode pedestal at the L-H transition. The edge toroidal rotation profile does not contribute to the depth of the negative E_r well and thus may not be correlated with the formation of the edge transport barrier in JET.

A new high-resolution CXRS system measuring B^{5+} ions has enabled the determination of the radial electric field in the *Alcator C-Mod* edge pedestal with high spatial and temporal resolution [44]. During H-mode operation, the radial electric field is positive in the core, but forms a negative well up to -30 kV/m deep in the region 10 mm inside of the LCFS. The well is consistently 5 ± 1.5 mm in width regardless of the type of H-mode or plasma parameters. This well is largely determined by the poloidal velocity and diamagnetic contributions in the B^{5+} radial force balance equation. The poloidal velocity contribution is

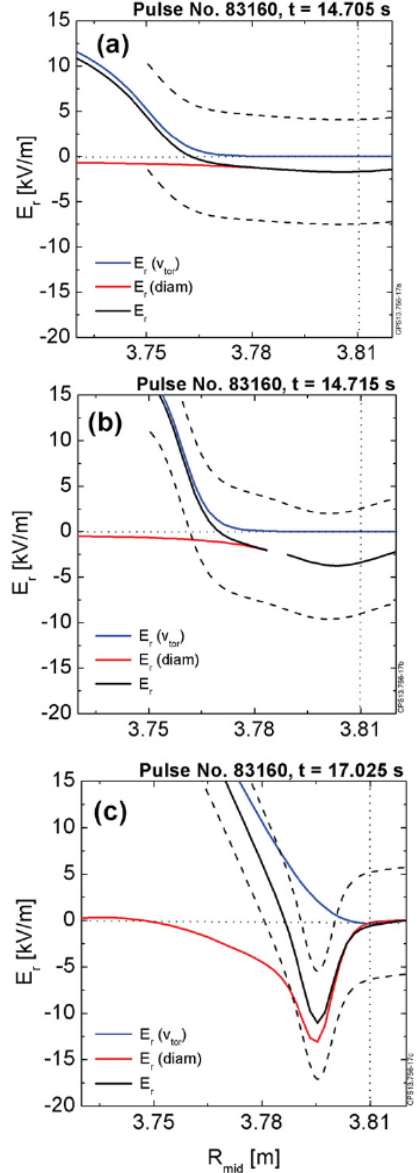


Figure 4: Edge E_r derived from the C^{6+} profiles, and assuming $v_{pol} = 0 \pm 2.5$ km/s due to the uncertainties. Solid black line: $E_r(v_{pol} = 0)$; dashed black lines: upper and lower bounds of E_r derived from the uncertainty in the v_{pol} measurement; solid red line: diamagnetic term; solid blue line: $v_{tor} \times B_{pol}$ term. (a) E_r at the L-H transition; (b) E_r 10 ms after the L-H transition and (c) E_r during the ELMy H-mode phase of the discharge. The vertical dashed lines mark the EFIT separatrix position, R_{mid} is the major radius at the magnetic axis, taken from [38]

typically the larger and narrower contribution of the two and dominates both the E_r well width and the $\mathbf{E} \times \mathbf{B}$ shear (see figure 5). The data show a clear correlation between deeper E_r wells, higher confinement plasmas, and higher electron temperature pedestal heights. However, improved L -mode (I -mode) plasmas exhibit energy confinement equivalent to that observed in similar H -mode discharges, but with significantly shallower E_r wells. I -mode plasmas are characterized by H -mode-like energy barriers, but with L -mode-like particle barriers. The decoupling of energy and particle barrier formation makes the I -mode an interesting regime for fusion research and provides for a low collisionality pedestal without edge localised modes.

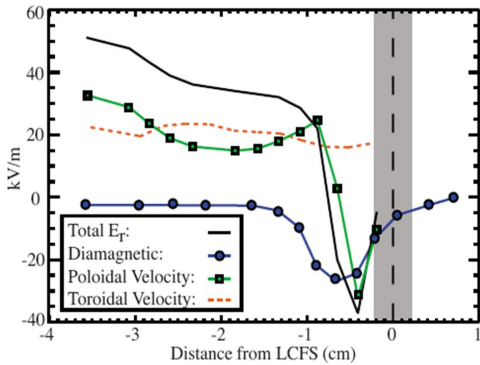


Figure 5: Contributions of the three components from Eq. (1) to the radial electric field in an EDA H -mode. The poloidal velocity contribution dominates the width of the E_r well (figure taken from [44]).

The first measurements of the structure of the edge radial electric field in a spherical tokamak (MAST) have been presented in [46]. Using active Doppler spectroscopy on He^+ with 120 lines of sight E_r profiles are calculated from the leading terms of the radial momentum balance equation. A spatial resolution up to 1.5 mm with a typical time resolution of 5 ms has been achieved. In L -mode the field is largely determined by the diamagnetic term of the force balance, and fields of only a few kV/m are observed. The measured impurity flow is mostly parallel to \mathbf{B} , and is greatly affected by MHD, such as sawteeth or mode locking of tearing modes, or error fields. In H -mode a strong perpendicular flow evolves with poloidal and toroidal velocities up to $v_{\phi,\theta}^{He^+} \approx -20$ km/s, and a deep negative electric field well $E_r^{min} \geq -15$ kV/m develops. The shape of the profile is dominated by the diamagnetic term.

The causal relationship between radial electric fields and improved confinement was demonstrated in biasing experiments [47]. By means of polariza-

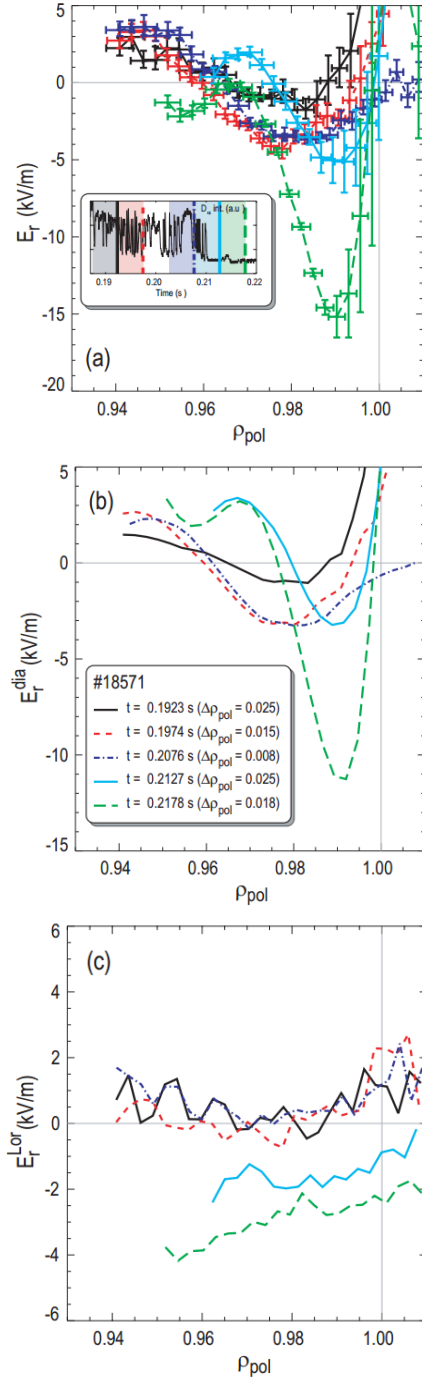


Figure 6: Evolution of E_r through a fast L/H transition, (a) total E_r , (b) diamagnetic part, (c) Lorentz part (figure taken from [46])

tion electrode at the plasma periphery, the edge radial electric field profile could be externally controlled and H-mode transitions could be triggered. Important results were contributed by the TEXTOR tokamak[48, 49].

B. $\mathbf{E} \times \mathbf{B}$ Shear Effects on internal transport barriers

Internal transport barriers (ITBs) have allowed the reduction of transport coefficients to close to neo-classical levels in a plasma region of finite radial extent, typically around mid-radius. ITBs have been produced on different tokamaks, moreover on DIII-D[50], JT-60U[51] and JET[52]. The formation of an ion ITB dramatically reduces ion heat and particle flux from the core (sub-neoclassical ion thermal diffusivity has been obtained). In as much as neoclassical transport is usually considered to be as the minimum transport possible in a tokamak, these results represent a dramatic improvement in confinement and performance. Furthermore, the strong pressure gradient associated with ITBs drives a bootstrap current which can substantially contribute to overcome the limited pulse length in tokamaks.

Most likely ITB dynamics is controlled by a combination of two or more of the following main mechanisms: (1) $\mathbf{E} \times \mathbf{B}$ flow shear; (2) magnetic shear $s=r/q \, dq/dr$ and low order rational q -surface, (3) the influence of the ratio T_i/T_e or strong electron density gradients (e.g. due to pellet injection) on instability growth rates; and (4) turbulence stabilisation by self-generated poloidal $\mathbf{E} \times \mathbf{B}$ zonal flows[53]. Numerous triggering mechanisms have been proposed: ion orbit losses[54], Stringer spin-up[55], critical gradients[56], magnetic shear[57, 58], Reynolds stress[59, 60, 61, 62].

Ion ITBs

JET plasmas are heated mainly by NBI and ICRH. The NBI is oriented in co-current direction and is an important source of toroidal momentum. In most cases ITBs on JET are clearly visible in the ion heat and toroidal momentum channels. During strong ITBs large excursions in poloidal rotation velocity have been observed[63]. Both toroidal and poloidal rotation terms contribute equally to the radial electric field in the region with reduced ion heat transport. The contribution from the diamagnetic term is an order of magnitude lower.

In dedicated experiments[64] the toroidal field (TF) ripple was modified, which changed the $\mathbf{E} \times \mathbf{B}$ rotation of the plasma. It was found that in plasmas with large TF ripple and small $\mathbf{E} \times \mathbf{B}$ rotation, ITBs could still be triggered, but did not develop into strong barriers. Also the poloidal rotation velocity seems to be related to the ITB strength, suggesting that it acts as a positive feedback mechanisms, which helps to sustain the region with reduced transport[65]. Figure 7 shows profiles of ITBs for different ripple amplitudes, shot no. 69670 has the standard TF ripple of $\delta=0.08\%$, shot no. 69665 has

$\delta=0.63\%$, shot no. 69684 has $\delta=0.82\%$ and shot no. 69690 has $\delta=1.00\%$. The T_i and ω_ϕ gradients are decreasing with increasing ripple, as is the excursion in V_θ .

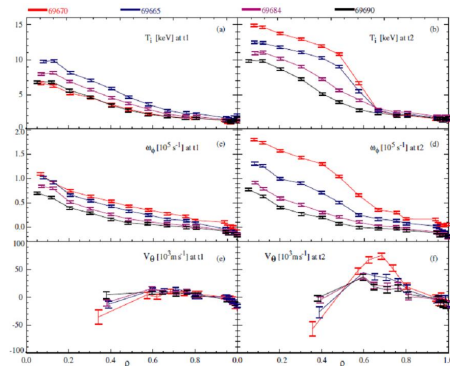


Figure 7: (a) and (b) Ion temperature, (c) and (d) toroidal angular frequency and (e) and (f) poloidal rotation velocity for four shots with different ripple amplitudes and reversed magnetic shear. Profiles on the left hand side are before the ITB. Profiles on the right hand side are during the ITB phase (figure taken from[65])

In recent *DIII-D* discharges with varying percentages of co- and counter-injected neutral beam fractions, differences in core barrier formation are observed. For fully co-injected discharges with high toroidal rotation and large $\mathbf{E} \times \mathbf{B}$ shear, either an enduring internal transport barrier (ITB) forms spontaneously or is triggered at the $q_{min}=2$ crossing. For balanced-injected discharges with low toroidal rotation and small $\mathbf{E} \times \mathbf{B}$ shear, no core barrier forms; however, transient improvements in transport are seen near integer q_{min} crossings (figure 8). In all cases reductions in fluctuation amplitudes occur near the rational q_{min} times as well as jumps in poloidal velocity. The observations support the model that zonal flow effects at integer q_{min} can act as an ITB trigger and sufficient background $\mathbf{E} \times \mathbf{B}$ shear is required for barrier sustainment[66].

Electron ITBs

In *DIII-D* ITB plasmas, large reductions in transport are observed in the ion (χ_i), angular momentum (χ_ϕ), and sometimes particle D diffusivities, but a similar large reduction in electron heat transport (χ_e) is often not observed. In low magnetic shear plasmas, χ_e shows little change, and remains well above χ_i . However, in some *DIII-D* discharges with strongly negative magnetic shear, large reductions in χ_e have been observed[67]. The electron temperature profile steepens just inside the ion ITB, indicating the formation of an electron ITB. In this region χ_e may decrease a factor of 3–10, but remains far above the neoclassical level (figure 9).

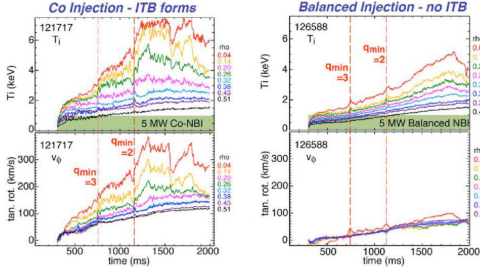


Figure 8: Time traces of ion temperature and toroidal rotation velocity in DIII-D plasmas with co- and balanced NBI-injection. When the $\mathbf{E} \times \mathbf{B}$ shearing rate is low only transient transport improvements are seen when q_{\min} crosses an integer value (figure taken from [66])

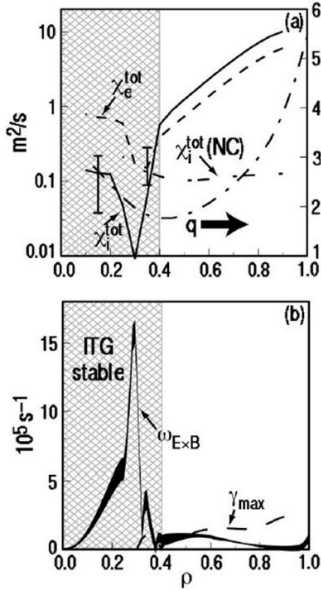


Figure 9: Ion stability in strong negative magnetic shear: (a) ion and electron diffusivity profiles, showing ion ITB, and q profile and (b) comparison of $\omega_{E \times B}$ flow shear rate and predicted γ_{\max} for the ITG mode (figure taken from [67]).

The formation of electron ITB was further studied using Electron Cyclotron (EC) heating in *JT-60U* plasmas with positive (PS) and reversed magnetic shear (RS)[68]. The NBI power was scanned. With no or small NBI power, a strong, box-type electron ITB was formed in RS plasmas while a peaked profile with no strong electron ITB was observed in PS plasmas. Comparison of Gyro Kinetic Simulation predictions with experiments, in low and strongly negative magnetic shear plasmas with an ITB, suggests that the region for improved ion transport seems well characterized by the condition $\omega_{E \times B} > \gamma_{\max}$, where $\omega_{E \times B}$ is the $\mathbf{E} \times \mathbf{B}$ flow shear rate, calculated from measured quantities, and γ_{\max} is the maximum calculated linear growth rate for ITG modes in the absence of flow shear. For the electrons, within a limited region just inside the point of ITG mode suppression, the ETG modes appear to dominate the electron thermal transport and, consequently, to provide a lower limit on electron thermal diffusivity. When the NBI power (and thus the shearing rate) was increased in EC-heated PS plasmas, the electron thermal diffusivity was reduced in conjunction with the increase in E_r gradient and reduction of ion thermal diffusivity, and strong electron and ion ITBs were formed. When the NBI power was increased in RS plasmas with high power EC heating, in which a strong electron ITB is already established, χ_e was not affected but χ_i decreased and a strong ion ITB was formed with the increase in E_r gradient. The dependences of χ_i and χ_e on the shearing rate are shown in figure 10. In this study, it is clearly shown that there is easier access to strong electron ITBs without a large E_r gradient in RS plasmas than in PS plasmas. Another new discovery is that electron transport in strong electron ITBs in RS plasmas is not affected by the increase in E_r gradient.

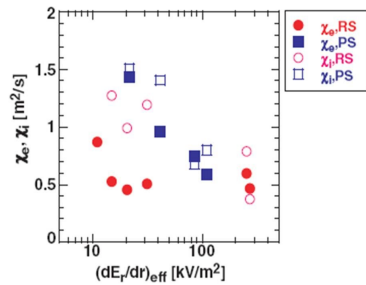


Figure 10: Dependence of minimum values of χ_e and χ_i on the shearing rate. Closed and open circles denote χ_e and χ_i in Reversed Shear plasmas and closed and open squares denote χ_e and χ_i in Positive Shear plasmas (figure taken from [68])

On the *National Spherical Torus Experiment (NSTX)* electron ITBs have been formed with no $\mathbf{E} \times \mathbf{B}$ shear, by heating only with High Harmonic Fast Wave

(HHFW) radio frequency heating[69]. It was found that in plasma with strongly negative magnetic shear (s) electron scale fluctuations were suppressed and the T_e profiles show a strong transport barrier around the region of minimum s (figure 11). Experiments have been conducted to investigate the interplay between the formation of electron ITBs and the maintenance of self-consistent plasma profiles under the action of Electron Cyclotron Resonance Heating and Current Drive ECRH/ECCD. A joint analysis of *T-10* and *TEXTOR* experimental results enabled to analyse effects bound with plasma self-organization. It was shown that the plasma pressure profiles obtained in different operational regimes and even in various tokamaks may be represented by a single typical curve, called the self-consistent pressure or canonical profile, also often referred to as profile resilience or profile stiffness[70].

Both phenomena, the self consistent profile and ITB, are connected with the density of rational magnetic surfaces, where the turbulent cells are situated. The distance between these cells determines the level of their interaction, and therefore the level of the turbulent transport. This process regulates the plasma pressure profile. If the distance is wide, the turbulent flux may be diminished and the ITB may be formed. In regions with rarefied surfaces the steeper pressure gradients are possible without instantaneously inducing pressure driven instabilities, which force the profiles back to their self-consistent shapes[71].

VI. CONCLUSIONS AND FUTURE STUDIES

The importance of radial electric fields is now widely recognized. It has been demonstrated in limiter- and divertor tokamaks, helical devices and mirror machines with a variety of discharge- and heating conditions as well as edge biasing schemes that improved confinement is often associated with strong $\mathbf{E} \times \mathbf{B}$ velocity shear. Turbulence stabilisation is a robust and universal mechanism which plays a major role in the formation and sustainment of transport barriers in magnetic confinement devices.

A negative well in the edge electric field profile has been measured in different tokamaks during improved confinement modes. The parameters that determine the shape of the E_r profile may differ from machine to machine, but the depth of the well (and thus the $\mathbf{E} \times \mathbf{B}$ shear) seems to be linked to the level of improved confinement.

Different mechanisms play a role in the triggering and sustainment of internal transport barriers. It has been demonstrated that synergistic effects exist between $\mathbf{E} \times \mathbf{B}$ velocity shear and magnetic shear. It has been found that a stable *ion* ITB can most easily be created in the vicinity of low order rational q -surfaces when a certain background $\mathbf{E} \times \mathbf{B}$ velocity shear is present[64, 65, 66]. Experiments are ongoing to

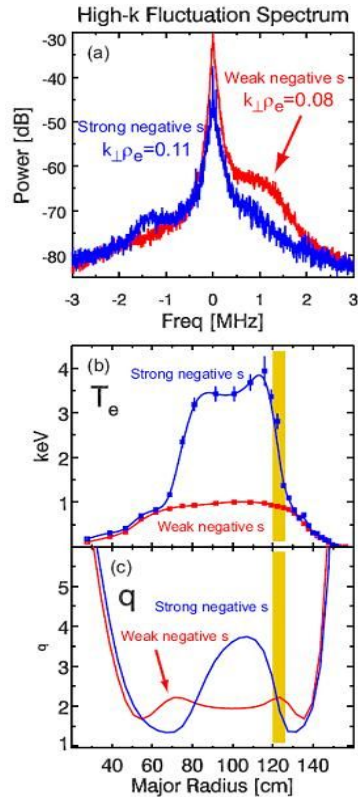


Figure 11: (a) High- k microwave scattering fluctuation power spectra comparison between a case with an e-ITB and strongly negative magnetic shear vs a weakly reversed shear case with lower electron temperature gradients. (b) Electron temperatures and (c) q -profiles for cases shown in (a), shaded region indicates the high- k measurement region (figure taken from [69])

study the formation of *electron ITBs*. The hypothesis is that the formation of an electron transport barrier is determined by the density of turbulent cells in the vicinity of low-order rational surfaces, a negative magnetic shear is favourable to a non-reversed q -profile.

Further improved comparison between experiment and theory requires the development or improvement of plasma diagnostics with higher spatial and temporal resolution.

REFERENCES

1. K. CROMBE and G. VAN OOST, Transactions of Fusion Science and Technology **61**, N^o 2T , (2012)
2. P. HELANDER, "Classical and neoclassical transport in tokamaks", Transactions of Fusion Science and Technology **61**, N^o 2T , (2012)
3. V. ROZHANSKY, Reviews of Plasma Physics **24**, p.1 , Springer (2008)
4. J. HEIKKINEN et al., Phys. Rev. Letters **84**, p.487 (2000)
5. V. ROZHANSKY et al., Contrib. Plasma Physics **40**, p.423 , Springer (2000)
6. T. BUDKER, in Plasma Physics and the Problem of Controlled Thermonuclear Reactions, edited by M.A. LEONTOVICH, Pergamon Press, New York, 1, p.78 (1951)
7. T. STIX, Phys. Fluids **14**, 692 (1971)
8. J.R. ROTH et al., Phys. Rev. Letters **22**, 1450 (1978)
9. J.R. ROTH, Proc. IAEA Technical Conference Meeting on Tokamak Plasma Biasing, Montreal (IAEA Vienna), p. 132 (1992)
10. J.G. GORMAN and L.H. RIETJENS, Phys. Fluids **9**, 2504 (1966)
11. E.J. STRAIT, Nucl. Fusion **21**, 943 (1981)
12. R.J. TAYLOR et al., Plasma Physics and Control. Thermonuclear Research **3** (IAEA Vienna), p. 251 (1982)
13. W7-A team et al., Proc. 3rd Joint Varenna-Grenoble , Int. Symp. Heating in Toroidal Plasma, Grenoble **2**, p.813 (1982)
14. J.C. HOSEA et al., Phys. Rev. Letters **30**, 839 (1973)
15. K.A. RAZUMOVA, Plasma Physics and Control. Fusion **26** (1984) 37
16. M. MURAKAMI et al., in Plasma Physics and Controlled Nuclear Fusion Research, **1** (IAEA Vienna), p. 87 (1984)
17. F. WAGNER et al., Phys. Rev. Letters **49**, 1408 (1982)
18. R.J. TAYLOR et al., Phys. Rev. Letters **63**, 2365 (1989)
19. R.J. GROEBNER, K.H. BURRELL and R.P. SERAYDARIAN, Phys. Letters **64**, 3015 (1990)
20. S.-I. ITOH and K. ITOH, Phys. Rev. Letters, **60**, p. 2276 (1988); K. ITOH, S.-I. ITOH, A. FUKUYAMA, " Transport and Structural Formation in Plasma", I.O.P. Publishing, Bristol (1999)
21. K.C. SHAINING, E.C. CRUME Jr. And W.A. HOULBERG, Phys. Rev. Letters **63**, 2369 (1989)
22. M. TENDLER, Plasma Physics and Controlled Fusion **39**, B371 (1997).
23. R.R. WEYNANTS et al, Proc. 17th Eur. Conf. On Controlled Fusion and Plasma Physics, Amsterdam, 1, (Europhysics Conf. Abstr. 14B), p. 287 (1990).
24. R.R. WEYNANTS et al, Nucl. Fusion **32**, p. 837 (1992).
25. R.R. WEYNANTS and G. VAN OOST, Plasma Physics and Controlled Fusion **35**, B177 (1993).
26. G. VAN OOST et al., Plasma Physics and Controlled Fusion **45**,621 (2003), and references therein.
27. K.H. BURRELL, Phys. Plasmas **4**, 1499 (1997)
28. D. HARTMANN, "Stellarators", Transactions of Fusion Science and Technology **61**, N^o 2T , (2012)
29. K. IDA, Plasma Physics and Controlled Fusion **40**, 1429 (1998).
30. Proceedings of the Technical Committee Meeting on H-mode Physics, Kloster Seeon, Germany, September 22-24, 1997, in Plasma Physics and Controlled Fusion **40**, Nr.5.
31. G. VAN OOST and M. TENDLER, Plasma Physics and Controlled Fusion **44**, 1761 (2002).
32. T.S. HAHM and K.H. BURRELL, Phys. Plasmas **2**, 1648 (1995).
33. K.H. BURRELL, Plasma Physics and Control Fusion **36**, A291 (1994).

34. A.J.H. DONNÉ, A.V. MELNIKOV, G. VAN OOST, Czechoslovak J. of Physics **52**, 1077(2002).
35. R. JASPERS, "Spectroscopy", Transactions of Fusion Science and Technology **61**, N° 2T , (2012).
36. Special issue on heavy ion beam probing, IEEE Trans. on Plasma Science **22**, Nr. 4 (1994).
37. G. VAN OOST, "Advanced probes for boundary plasma diagnosis in fusion devices", Transactions of Fusion Science and Technology **61**, N° 2T , (2012).
38. C. MAGGI et al., Nucl. Fusion **54** , p. 023007 (2014)
39. B.W. RICE et al., Phys. Rev.Letters Vol. 79, No. 14 (1997), 2694-2697
40. F. WAGNER et al., Plasma Phys. Control. Fusion **49** (2007) B1-B33
41. E. VIEZZER et al., Nucl. Fusion **53** , p. 053005 (2013)
42. P. SAUTER et al., Nucl. Fusion **52** , p. 012001 (2012)
43. Y. ANDREW et al., Europhysics Letters **83** (2008) 15003
44. R.M. MCDERMOTT et al., Physics of Plasmas **16** (2009) 056103
45. J. SCHIRMER et al., Nuclear Fusion **46** (2006) S780
46. H. MEYER et al., Journal of Physics, Conference Series **123** (2008) 012005
47. G. VAN OOST et al., Czech. J. Phys. **51** (2001) 957
48. R.R. WEYNANTS et al., Nuclear Fusion **32** (1992) 837
49. J. BOEDO et al., Nucl. Fusion **40** (2000) 1397
50. E. LAZARUS et al., Phys. Rev. Letters **77**, 2714 (1996).
51. K. USHIGUSA and the JT-60 team, Plasma Physics and Controlled Nuclear Fusion Research, 1 (IAEA Vienna) **37** (1996).
52. C. GORMEZANO, in Plasma Physics and Controlled Fusion **41**, B367 (1999).
53. Special issue on Experimental studies of zonal flow and turbulence, Plasma Phys. Control. Fusion **48**, 1181 (2006).
54. K.C. SHAING et al., Phys. Rev. Letters **63** (1989), 2369
55. A.B. HASSAM et al., Phys. Rev. Letters **66** (1991) 309
56. F.L. HINTON and G.M. STAEBLER Phys. Fluids B **5** (1993) 1281
57. C. KESSEL et al. Phys. Rev. Letter **72** (1994), 1212
58. E. SYNAKOWSKI Phys. Plasmas **4** (1994), 1736
59. P. DIAMOND, Y. KIM, Phys.Fluids B **3** (1991) 1626
60. B.A. CARRERAS et al Phys.Fluids B **3** (1991) 1438
61. P. DIAMOND et al Phys. Rev. Letters **72** (1994), 2565
62. C. HIDALGO et al., Plasma Phys. Control. Fusion **42** (2000) A153-A160
63. K. CROMBÉ et al., Phys.Rev.Lett. **95**,155003 (2005)
64. P.C. DE VRIES et al., Plasma Phys. Control. Fusion **50** (2008) 065008
65. K. CROMBÉ et al., Plasma Phys. Control. Fusion **51** (2009) 055005
66. M.E. AUSTIN et al. "The Effect of $E \times B$ Shear on Core Barrier Formation Near Low-Order Rational q Surfaces" presented at the joint EU-US Transport Taskforce Workshop: San Diego, California April 28-May 1, 2009
67. B.W. STALLARD et al., Phys. Plasmas **6** (1999)
68. T. FUJITA et al., Plasma Phys. Control. Fusion **46** (2004) A35-A43
69. H.Y. YUH et al., Phys. Plasmas **16** (2009), 056120
70. Y.N. DNESTROVSKI et al., Nuclear Fusion **46** 953 (2006) and references therein.
71. K.A. RAZUMOVA et al., Plasma Phys. Control. Fusion **48**, 1373 (2006).
72. A.V. MELNIKOV et al., Nuclear Fusion **51** (2011) 083043

PLASMA-WALL INTERACTIONS IN MAGNETICALLY CONFINED FUSION PLASMAS

U. Samm

*Institut für Energie- und Klimaforschung - Plasmaphysik
Forschungszentrum Jülich GmbH, Association EURATOM-FZJ, Jülich, Germany,
Member in the Trilateral Euregio Cluster*

ABSTRACT

The control of wall loads in fusion devices, in particular with respect to the life time limitations of wall components due to material erosion and migration, will be decisive for the realisation of a fusion power plant operating in steady state, whereas in a pulsed experiment like ITER the primary goal for plasma-wall interaction is the achievement of high availability of the device. The article describes the grand challenges of plasma-wall interactions research along the needs for ITER. Addressed are questions related to material limitations, erosion- and transport processes, tritium retention and transient heat loads.

I. INTRODUCTION

A fusion device cannot work without plasma-wall interactions. Two essential functions have to be provided via the interaction of the plasma with the wall:

- a) the exhaust of heating power to the plasma (mainly from alpha-particle heating) and
- b) the exhaust of alpha-particles (Helium ash) to avoid fuel dilution.

A large variety of processes is involved in plasma-wall interactions. They are determined by the properties of wall materials, plasma edge parameters (e.g. temperature, density, radiation), heat and particle transport and the plasma species (hydrogen and impurities). Thus the research field of plasma-wall interactions is interdisciplinary and comprises plasma physics, surface physics, physics of atoms and molecules, chemistry and materials sciences. The following describes the concepts for controlling plasma-wall interaction being developed in today's fusion devices.

II. PARTICLE AND HEAT EXHAUST IN ITER

In ITER the total heating power of $P_{\alpha} = 100$ MW plus an external heating of about $P_{\text{heat}} = 50$ MW has to be exhausted via radiation and plasma convection onto wall components. Linked to this is a production rate of Helium of about $2 \cdot 10^{20}$ particles per second (about 1 mg/s), which have to be pumped out continuously.

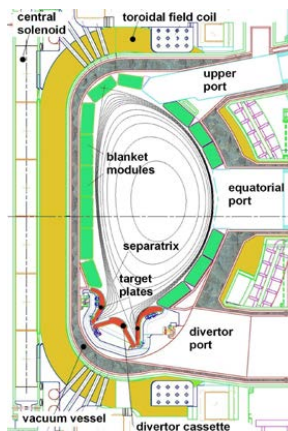


Fig. 1 Magnetic flux surfaces shown in a poloidal cross section of ITER; the highest loads are located at the target plates

Helium exhaust will be solved in ITER by pumping the neutral particles from the divertor chamber. The plasma flow into the divertor along the so called scrape-off layer (SOL) and the successive neutralisation of particles on the target plates provides a certain concentration of neutral particles inside the divertor (deuterium, tritium, helium and other impurities). The resulting gas pressure will be sufficient to achieve efficient pumping through channels below the divertor chamber. In ITER it is expected to achieve a characteristic exhaust time for helium of about 15 seconds which will lead in steady state to a helium concentration of about 4 %. This helium concentration in the plasma centre is low enough for providing a significant margin for other impurities, e.g. eroded particles or injected particles for the purpose of radiation cooling.

The required heat exhaust is more difficult to achieve because the radial extend of the SOL is only in the order of a centimetre and thus generates high heat load densities on a rather small area on the target plates. The heat load density on plasma wetted areas can be reduced by up to a factor of 6 by

inclining the target plates. Even then, the total area is only 6-8 m². In the reference scenario for ITER about half of the total heating power $P_{\alpha} + P_{\text{heat}}$ is convected to the target plates leading to a power density of up to 10 MW/m². Prototype modules for divertor plates which can take these loads under cycling conditions have already been manufactured and tested successfully (Fig. 2).



Fig. 2 (left) Monoblock from graphite (CFC) brazed on copper, as a water cooled element for the target plate, and (right) a prototype target plate module (vertical target) made from tungsten and CFC; these modules fulfill all requirements for heat exhaust under thermal cycling loads up to 23 MW/m² ¹

The other half of the heating power is radiated onto the whole inner wall on an area of 680 m² (radiation cooling). The corresponding power density of 0,11 MW/m² can be extracted rather easily via water cooled wall elements. A significant fraction of the radiation cooling is provided by electromagnetic radiation from excited impurity species in the plasma. Thus radiation cooling from impurities can be seen as a beneficial aspect of erosion of wall materials. This effect has to be taken into account when different wall materials are considered. It is important that the radiation from impurities is concentrated mainly on the plasma edge region, which is the case for light impurities. Normally the amount of eroded material is not sufficient to provide the necessary radiation level, in particular not in the case of heavy metals as wall material. By injecting additional impurities, preferably noble gases, we have the possibility to adjust the radiation level and thus to control the heat load to the target plates ².

With these concepts we can exhaust the average heat loads in ITER reliably. Much more critical are the transient loads. These loads are caused by plasma instabilities, like disruptions (e.g. at the density limit) or Edge Localized Modes (ELMs)³. Transient loads lead to enhanced erosion, possible excess loads (melting) or fatigue effects on thermo-mechanical properties.

Methods are developed to mitigate the peak loads caused by disruptions ⁴. ITER is in contrast to a fusion power plant, where disruptions should be avoided at all, an

experiment in which a certain number of disruptions are unavoidable when exploring the operational limits of the device.

Periodic events, like ELMs, are more difficult to cope with, since they are linked closely to the plasma scenario and the corresponding energy confinement. For ITER the standard scenario is the H-Mode plasma where ELM activity is always present. An example for ELM activity in JET ⁵ is shown in Fig. 3.

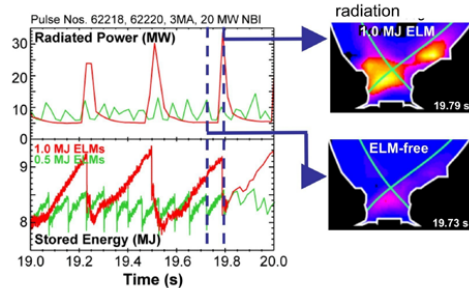


Fig. 3 Plasma discharges in JET with ELM-activity; comparison of two discharges with a) large low frequency ELMs (heat exhaust 1 MJ per ELM, dark line) and b) small and fast ELMs (0,5 MJ per ELM); the curves down left show the energy content (pressure) at the plasma boundary and the upper left curves show the corresponding radiation level; on the right the 2-dimensional view of the radiation pattern from carbon inside the divertor is shown during and before an ELM-crash ⁶

Large ELMs in JET can lead to a load on the target plate up to 0.5 MJ/m², causing a transient increase of the target temperature up to 2500 °C as observed for the operation with graphite target plates⁶. Extrapolations to ITER show that the transient loads due to ELMs must be limited in order to achieve a sufficient life time of the target plates. In ongoing research different strategies are pursued to achieve this goal.

There is a link between good energy confinement (and steep pressure gradients at the boundary) and ELM energy. A possible way for optimizing plasma-wall interactions with ELMs is to choose plasma-scenarios with an optimum balance between good energy confinement and ELM energy, with the consequence of accepting some decrease in energy confinement and thus energy amplification. In this respect, a possible way is the use of small type III ELMs induced by strong gas injection⁷.

Another attempt is the development of methods for ELM-mitigation: A pace-maker technique employing the injection of pellets or the recently developed technique of short vertical plasma displacements (kicks) can trigger ELMs before they acquire too much energy⁸. Another method is based on resonant magnetic perturbations (RMP) imposed by external

coils. By this method it has been shown that the magnetic field at the boundary is ergodized (chaotic field lines) leading to a change in transport and eventually to mitigation or even suppression of ELMs^{9,10}. This concept is also studied with the Dynamic Ergodic Divertor on the tokamak TEXTOR¹¹.

III: EROSION AND DEPOSITION

Plasma-Wall Interactions lead to significant erosion processes at plasma wetted areas. Some erosion mechanisms are caused directly by excess heat loads, like melting or sublimation. Normally the more important erosion mechanisms are linked to the particle fluxes to the wall: physical sputtering and chemical reactions.

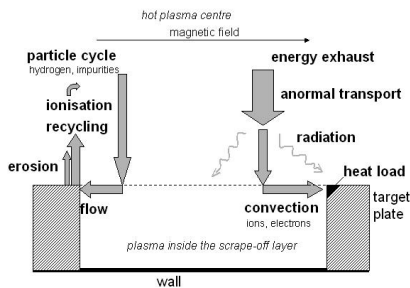


Fig. 4 Schematic 2-d view of particle recycling and heat exhaust; inside the SOL the plasma flows to both sides along the magnetic field lines towards the target plates

Erosion processes release particles from the wall, which are then ionized when entering the plasma or dissociated and ionized in the case of molecules. Transport processes in the plasma lead the impurity particles back to the wall - in most cases even to the place of their origin due to the specific guiding effect of the magnetic field lines. In contrast to the energy, the particles are cycling (Fig. 4). Hydrogen is neutralized at the target plate and is re-emitted as atom or molecule – this is called hydrogen-recycling. Impurities are eroded and deposited.

Physical sputtering of wall materials is caused by the bombardement of plasma ions. The sputtering yield depends on the energy of the ions, the mass ratio of projectile and target and the surface binding energy of the target particles. Fig. 5 shows some yields for deuterium on various materials as a function of the energy of the projectiles.

The energy with which the ions impinge on the target is primarily given by the plasma temperature. Typical values are between 2 and 100 eV. However, the sheath potential accelerates the ions proportional to their charge state

(typically about four times for singly charged ions). As a consequence, in relatively cold plasmas, typical e.g. for high density divertors, already rather small amounts of impurities can dominate the overall sputtering yield compared to the deuterium/tritium ions.

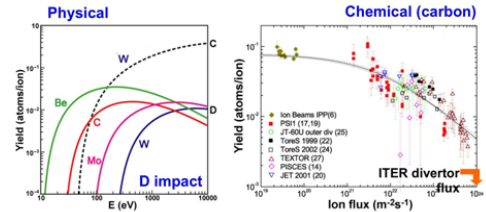


Fig. 5 Erosion yields of wall materials for physical sputtering by deuterium as a function of the energy of the projectiles (left)¹² and chemical erosion of graphite as a function of the flux density of deuterium (right)¹³; the dashed line shows the physical sputtering of tungsten by carbon

The effective yields for physical sputtering of carbon are in the range of 1-2 %. In case of tungsten the yields are much lower down to values of 0.01 to 0.001 % governed by impurities as carbon or injected impurities as neon for the purpose of radiation cooling¹⁴.

For some wall materials also chemical erosion processes are significant, as is the case for graphite, where chemical erosion is as important as physical sputtering. Particle flux density and surface temperature of the material are the most important parameters. The yield of chemical erosion shows a strong decay with high flux densities as was demonstrated in a multi-machine comparison (Fig. 5). The highest flux densities were provided by the tokamak TEXTOR, where special means (limiter locks) allow measurements with very high flux densities close to the conditions of ITER¹⁵.

Erosion in the divertor plays the main role for the life time of the target plates and contributes to the impurity contamination of the plasma. Also the erosion on the large main chamber contributes to the impurity contamination. Erosion on the main chamber wall can be caused by fast neutrals (via charge exchange processes) or by impinging ions due to enhanced radial transport. The latter may go mainly via convective cells which are formed due to instabilities in the edge plasma. This kind of turbulent transport is an important issue of ongoing research and is also the cause for some uncertainty in the extrapolations of global erosion results to ITER.

The eroded impurities can have a substantial influence on the plasma characteristics. The particles are ionized and excited by electron collisions, which can lead depending on the kind of impurities and their concentration to substantial radiation and thus cooling of the plasma. A lowered plasma temperature can have repercussion on the erosion yields. The choice of wall material and the characteristics of the plasma close to the

wall are therefore coupled nonlinearly.

The deposition of eroded wall material plays an important role for the extension of the life time of wall components. In some areas the deposition rates are smaller than the erosion rates (net-erosion zones), in other areas they are larger (net-deposition zones) and at the boundary of these areas there is even balance between erosion and deposition (Fig. 6).

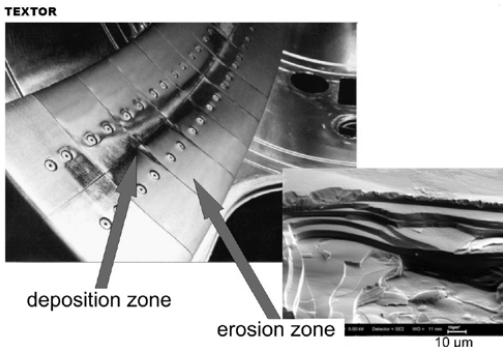


Fig. 6 Formation of layers by deposition of eroded carbon on limiters in the tokamak TEXTOR; the electron microscope image shows layers structures of about 4 μm thickness ¹⁶

Generally the local and global deposition processes lead to a strong reduction of net erosion - the deposition processes therefore represent an important self healing mechanism for highly loaded components, like divertor target plates or limiters.

In the zones with net deposition, however, accumulative layers develop. These can store deuterium and tritium by co-deposition. In fusion experiments, in particular at less loaded surfaces (remote areas), carbon layers with 100% hydrogen content have been observed. Based on these facts it is criticized using carbon at all for plasma facing components in ITER.

IV. WALL MATERIALS FOR ITER

A combination of different materials is intended for the plasma-loaded surfaces in ITER. A first design has foreseen the materials beryllium, tungsten and graphite, as they fulfill the requirements with their specific characteristics for the very different loads at different wall areas (Fig. 7).

This material choice was found on the basis of the following criteria:

Beryllium: Radiation by impurities in the plasma centre, as it can occur by heavy elements, is

unwanted. By the lining of the inner wall with as light an element as possible this condition can be fulfilled. Beryllium is the lightest metal, these wall components can be made of. Additionally, the property of beryllium as an oxygen getter, turned out to be advantageous for the vacuum characteristics and thus for the tokamak operation.

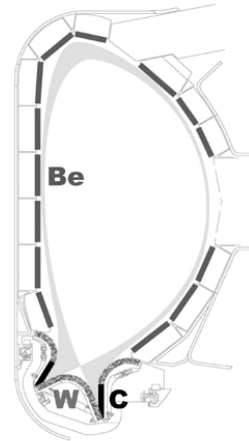


Fig. 7 Combination of wall materials for plasma-loaded surfaces in ITER according to the first design: Beryllium in the main chamber, graphite for the target plates in the divertor and tungsten for the remaining surfaces in the divertor

Graphite: With a melting point of only 1560 K beryllium cannot be used in the most loaded areas of the divertor. Here graphite is ideal a material. It is “forgiving”, because it does not melt with overloading but only sublimates (3825 K). This characteristics is in particular of high relevance in case of experiments like ITER, which will go to the operational limits. The largest disadvantage of graphite is its rather strong erosion, and associated to this the tritium retention by co-deposition. Therefore, the use of graphite should be restricted to a minimum area of high loads where the properties of graphite are required.

Tungsten: A combination of high melting point and very small sputtering yield is given by tungsten. The sputtering yield in the range of 10^{-5} to 10^{-4} for those particle energies as expected in ITER. Tungsten can be used for medium and high load areas instead of graphite, however, at the risk of melting in case of off-normal operation.

At present the risk of tungsten melting seems to less dangerous compared to the problem of tritium retention in connection with graphite as wall material, because an

accumulation of the mobilizable tritium inside the deposited layers could exceed the maximum allowed amount (at present 700 gr). In this case the machine would have to be shut-down for the period of cleaning or conditioning with possibly substantial disadvantages for the availability of the whole experiment¹⁷. Thus, graphite as a divertor material is still an option, but most likely the ITER divertor will be covered fully by tungsten.

In any case some wall components (e.g. the divertor plates) will have a limited life time and have to be exchanged occasionally. However, a too large replacing frequency would impair also the availability of the plant. The main uncertainties lie here in limited knowledge about the erosion by transient loads, like ELMs or disruptions. In ITER the exchange of the divertor after some years of operation is made possible by a cassette design for the divertor.

V. STRATEGIES FOR MINIMIZING THE RISKS

The risk of insufficient availability is to be minimized by a coordinated effort with experiments and calculations for plasma-wall interactions. This task is addressed worldwide with joint plasma-wall interaction experiments on many facilities facilities¹⁸. The strategy for minimizing the risk contains both the improvement of the wall concept with the selected materials (W/Be-wall in JET) and the parallel development of alternative material combinations (e.g. full metal wall in ASDEX-upgrade).

Carbon

The re-erosion of deposited carbon must still be understood better, in order to derive from it concepts for the minimization of hydrogen containing layers. We can forecast the net-erosion of the target plates in ITER based on our current knowledge by computer models. Fig. 8 shows such a calculation of the ERO code for the outer divertor¹⁹.

The main zones of net-erosion and net-deposition concentrate on a few centimeters in the proximity of the magnetic separatrix, which intersects the target plate. Eroded particles are transported preferentially in the direction of the magnetic field lines and are deposited with a small offset on the target plate again. Finally 94% of the eroded carbon particles are re-deposited locally. The remaining local loss rate amounts to maximally 3 nm/s. This means that more than 3000 ITER discharges of 8 minutes duration are possible until a 5 mm thick layer is eroded at the target plate. According to this calculation we do not have a life time problem.

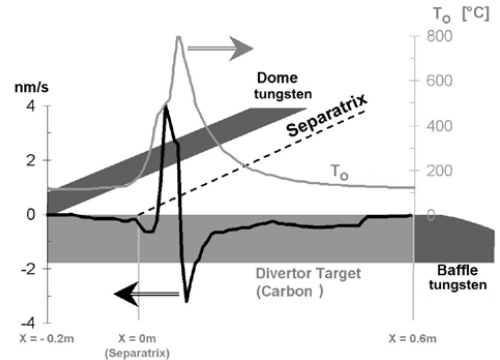


Fig. 8 Calculation of erosion, deposition and surface temperatur on an ITER target plate ITER with the computer code ERO; the direction of the magnetic field line is indicated by the separatrix

About 6 % of the eroded carbon particles leave the target region and deposit at other surfaces. These in such a way formed layers will be mainly responsible for the unwanted tritium retention, contrary to the deposited layers on the target plate, which can take up little tritium only because of the high surface temperatures.

The computations still suffer from uncertainties due to limited knowledge in our understanding of some processes:

- Control and effect of transient loads by ELMs and disruptions
- Effect of eroded beryllium from the main chamber on the erosion behavior of carbon in the divertor
- Data on the probability of re-erosion of deposited carbon and its migration behavior to remote or hidden surfaces
- Understanding of mixed material systems in tokamaks
- Retention of tritium by beryllium layers.

Tungsten - Beryllium

Recently the JET main chamber wall has been covered fully by beryllium and the divertor is now made fully of tungsten (the "ITER-like wall": ILW)^{20,21,22}. The main driver for the installation of the JET-ILW was the expected reduction in fuel retention. The expectations have been met: with the JET-ILW the long-term fuel retention has been reduced by more than one order of magnitude with respect to JET-C²³. The remaining retention mechanisms are now co-deposition with Be and, of less importance, hydrogen implantation in Be and W. A strong reduction of divertor radiation has been found with the ILW. This is a consequence of the absence of carbon radiation and the low radiation potential of beryllium and deuterium inside the divertor²⁴. With incident power densities of 5-10MW/m² or higher, divertor target plates of large tokamaks are driven close to the material limits. Moreover, the possible occurrence of thermo-mechanical fatigue cannot be ignored.

All High-Z metal wall

In view of the necessities for DEMO also the avoidance of Beryllium is an important matter. This could be achieved by using a full tungsten lining of the inner wall and the divertor. The Tokamak ASDEX-upgrade took the leading task developing an integral solution with main chamber wall and divertor covered fully with tungsten. (Fig. 9)²⁵.

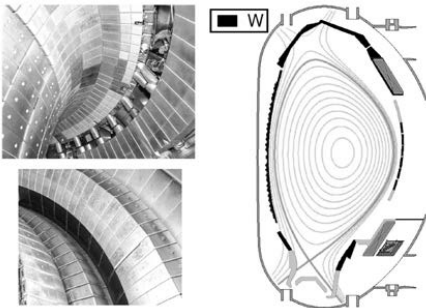


Fig. 9 Lining of the inner wall of ASDEX-Upgrade with tungsten

As a main result the transport of eroded material to remote areas has been reduced significantly. The deposited layers in the inner divertor were reduced by a factor of ten. The deposits are mainly B and C from boronization and residual C in the machine²⁶. The absence of carbon radiation requires external impurity seeding for achieving a sufficient power exhaust via radiation. This has been demonstrated successfully by feed-back controlled injection of different gas species²⁷.

VI. CONCLUSIONS

The primary goal of ITER - 500 MW fusion power for 8 minutes of pulse duration and significant alpha-particle heating - will be achieved with the available concepts for the control of plasma-wall interaction. The open questions of plasma-wall interactions refer to problems with the realization of a continuously operated fusion device. In ITER these questions have only relevance for the availability of the experiment.

A high availability is crucial for the economy of a fusion power plant. Fusion research enters now into a new era, in which the main question is not anymore whether we can produce a burning fusion plasma – this we know in principle based on the results of JET²⁸. Now the new goal is the demonstration of an economical long-term operation. The research field plasma-wall interaction is for this a key topic.

The current research in the area of plasma-wall interactions concentrates in the coming years on decisions related to the

construction of ITER. On the long run the research will contribute to the improvement of the ITER operation as well as on the preparatory work for the next step – the construction of the first fusion power station DEMO.

The stellarator development will play an important role for the plasma-wall interaction research regarding the development of concepts for steady state operation of fusion devices. Stellarators, like the Wendelstein 7-X, work contrary to tokamaks not in a pulsed manner. This makes stellarators particularly relevant for investigations of plasma-wall interactions during continuous operation. The concept of an island divertor will impose new questions about heat and particle exhaust. However, in general the problems of plasma-wall interactions are alike in stellarators and tokamaks.

Experiments with new wall concepts on a large scale are very important. However, the complex questions of plasma-wall interaction with its various aspects in plasma physics, surface physics, atomic and molecule physics, chemistry as well as material sciences cannot be solved alone on the large facilities, like JET or later ITER. Flexible smaller and medium sized plasma devices (tokamaks, stellarators, linear plasmas) as well as specialized laboratory equipment (e.g. test facilities for thermal loads, material laboratories) represent the actual backbone for the study of plasma-wall interaction.

REFERENCES

- ^{1/} G. Janeschitz et al., "Divertor design and its integration into ITER", Nucl. Fusion **42** (2002) 14-20
- ^{2/} U. Samm et al., "Radiative edges under control by impurity fluxes", Plasma Phys. Contr. Fusion **35** (1993) B167
- ^{3/} A Loarte et al., "Characteristics of type I ELM energy and particle losses in existing devices and their extrapolation to ITER", Plasma Phys. Control. Fusion **45** (2003) 1549-1569
- ^{4/} M. Lehnen et al., "Runaway generation during disruptions in JET and TEXTOR", J. Nucl. Mater. 390-391 (2009) 740 <http://www.jet.uk/>
- ^{5/} A. Huber et al., "Plasma radiation distribution and radiation loads onto the vessel during transient events in JET", J. Nucl. Mater. 390-391 (2009) 830
- ^{7/} J. Rapp et al., "Integrated scenario with type-III ELMy H-mode edge: extrapolation to ITER", 2009 Nucl. Fusion **49** 095012
- ^{8/} P.T. Lang et al., "ELM pace making and mitigation by pellet injection in ASDEX Upgrade", Nucl. Fusion **44** (2004) 665-677
- ^{9/} T.E. Evans et al., "Edge stability and transport control with resonant magnetic perturbations in collisionless tokamak plasmas", Nature Physics **2** (2006) 419
- ^{10/} Y. Liang et al., "Active Control of Type-I Edge-Localized Modes with n=1 perturbation fields in the JET tokamak", PRL **98** 265004 (2007)
- ^{11/} M. Lehnen et al., "Transport and divertor properties of the dynamic ergodic divertor", Plasma Phys. Control. Fusion **47** (2005) B237

-
- ^{/12/} W. Eckstein, „Computer simulation of ion-solid interaction“, Springer Verlag, Berlin (1991)
- ^{/13/} J. Roth et al., „Flux dependence of carbon erosion and implications for ITER“, J. Nucl. Mater. 337-339 (2005) 970
- ^{/14/} A. Kallenbach et al., „Tokamak operation with high-Z plasma facing components“, 32nd European Physical Society Conference on Plasma Physics (EPS) 2005 Tarragona, Spain, to be published in Plasma Phys. Contr. Fusion
- ^{/15/} A. Pospieszczyk et al., Phys. Scr. T 81 (1999) 48
- ^{/16/} P. Wienhold et al., „Short and long range transport of materials eroded from wall components“, J. Nucl. Mater. 313-316 (2003) 311
- ^{/17/} G. Counsell et al., „Tritium retention in next step devices and the requirements for mitigation and removal techniques“, Plasma Phys. Control. Fusion 48 No 12B (2006) B189
- ^{/18/} J. Roth et al., „Recent analysis of key plasma wall interactions issues for ITER“, J. Nucl. Mater. 390-391 (2009) 1-9
- ^{/19/} A. Kirschner et al., „Simulation of the plasma-wall interaction in a tokamak with the Monte-Carlo code ERO-TEXTOR“, Nucl. Fusion 40 5 (2000) 989
- ^{/20/} V. Philipps V. et al 2010 Fusion Eng. Des. 85 1581
- ^{/21/} S. Brezinsek S. et al 2011 J. Nucl. Mater. 415 S936
- ^{/22/} G. Matthews G.F. et al 2012 Phys. Scr. T145 014001
- ^{/23/} T. Loarer T. et al 2013 J. Nucl. Mater. 438 S108
- ^{/24/} A. Huber, A. et al. 2013 J. Nucl. Mater. 438 S139
- ^{/25/} A. Kallenbach et al., „Spectroscopic investigation of carbon migration with tungsten walls in ASDEX Upgrade“, J. Nucl. Mater. 363-365 (2007) 60
- ^{/26/} M. Mayer et al., „Carbon balance and deuterium inventory from a carbon dominated to a full tungsten Asdex Upgrade“, J.Nucl.Mater. 390-391 (2009) 538
- ^{/27/} A. Kallenbach, A et al. 2012 NF 52 122003
- ^{/28/} U. Samm, „Controlled Thermonuclear Fusion at the Beginning of a New Era“, Contemporary Physics 44 3 (2003) 203-217

TRANSPORT PROCESSES IN THE PLASMA EDGE

Bernhard Unterberg

Institut für Energieforschung - Plasmaphysik, Forschungszentrum Jülich GmbH* Association EURATOM-FZ Jülich
D-52425 Jülich, Germany, phone: +49 2461 61 4803, email: B.Unterberg@fz-juelich.de

ABSTRACT

Basic properties of the plasma edge in magnetically confined fusion plasmas are summarized. Starting from the magnetic topology of tokamaks we describe the transport of the scrape-off layer including drifts, the transition to high recycling and detached plasma regimes typical for divertors and the consequences of the electrostatic Debye sheath in front of the plasma facing components. The transport of the fuel neutrals (hydrogen atoms and molecules) is introduced.

I. INTRODUCTION

Processes at the edge plasma in general and plasma-wall interaction in particular play a crucial role for achieving a steady state burning fusion plasma. The first wall has to withstand and exhaust the α -particle heating power and the helium-ash must be removed (pumped) from the plasma. Wall erosion affects the lifetime of wall elements and releases impurities into the plasma, which then cause fuel dilution and energy loss due to radiation from the plasma centre. Moreover, also global confinement properties can be affected by edge processes. Therefore, understanding these processes and controlling the edge plasma by appropriate means is an important field of research (cf. also [1] for an introduction to the field of plasma-wall interaction).

The plasma in a tokamak or stellarator represents an open system. The wall is a perfect plasma sink and owing to the finite confinement times (energy and particle confinement times τ_E and τ_P) the plasma has to be renewed continuously. The energy content E is sustained by heating, $E = P_{heat} * \tau_E$, with the heating power P_{heat} . The number N of particles in the plasma is sustained by a permanent flow of D/T gas from the wall elements into the plasma, $N = \Gamma * \tau_P$. The alpha particles with a power density of $P_\alpha = 0.15 MW/m^3$ ($T=10$ keV, $n = 10^{20} m^{-3}$) lead to an average wall load of some $100 kW/m^2$, if we take into account a plasma volume of roughly $1000 m^3$ for self-sustained burn - a

moderate value. However, energy exhaust becomes a problem, because the magnetic field directs the convected heat load on rather small wall areas. This can lead to peak loads which could damage the wall.

Another important issue of edge physics is impurity generation and impurity exhaust. Any impurities in the plasma centre lead to fuel dilution reducing the fusion power. Their concentration has to stay below a certain level. E.g. the concentration of the unavoidable helium, which is generated at a rate of $R_{He} = 10^{18} s^{-1} m^{-3}$, should not exceed significantly a value of about 10%. This condition is fulfilled when the characteristic time $\tau_{p,He}^*$ for helium removal is sufficiently low [9], [10]. The experimental values found for $\tau_{p,He}^*$ are much larger (factor 10 or more) than the global confinement time of helium demonstrating that helium is recycling at the wall more than 10 times before it is removed by the pumps. The presence of other impurities in the plasma depends on the choice of wall materials, erosion processes and edge plasma properties, like temperature, density and particle transport (for a further description of impurity transport and radiation processes cf. [11]).

No unique definition exists for the term "plasma edge" or "plasma boundary". An important part of the edge plasma is the scrape-off layer (SOL) which is that region of the plasma where the magnetic field lines intersect wall elements. But significant processes occur also inside the confined plasma, like neutral particle penetration, ionization, charge exchange or impurity line radiation. These atomic processes have an impact on the properties of both, the edge plasma and the core plasma.

In this lecture plasma edge physics is introduced comprising the SOL as well as part of the confined plasma. The relevant processes are discussed following the transport cycle of the particles beginning with the boundary conditions which are given by the magnetic topology. After an illustration of the basic SOL properties, we discuss the penetration of neutrals into the plasma. Then a general description of the parallel transport in the SOL is given. Next, we introduce the Debye sheath in front of the plasma facing components,

*Partner in the Trilateral Euregio Cluster

before we finally discuss the properties of the simple limiter SOL and the complex divertor SOL. Overall, the physical processes in the plasma edge have important consequences for the interaction between plasma and wall and the resulting recycling and erosion mechanisms. This subject is discussed in a separate lecture [2].

An excellent introduction into the physics of the plasma boundary can be found in the book of P.C. Stangeby "The Plasma Boundary of Magnetic Fusion Devices" [3]. Further monographs used for this overview have been published by A.V. Nedospasov and M.Z. Tokar [4] and R. Schneider [5], a review article on experimental divertor physics by C.S. Pitcher and P.C. Stangeby is published in [6].

II. MAGNETIC TOPOLOGY

Wall elements which intersect the magnetic field serve as a perfect plasma sink and impose a flow directed along the field lines. The flux tubes generated at each wall element are filled with plasma by perpendicular transport (diffusion, drifts). This property helps to build up a particle density sufficient for helium exhaust. On the other hand the concentration of plasma flow on small areas is less beneficial for power exhaust, since a uniform plasma flow to the whole wall would avoid peak heat loads. The very details of particle and heat load on the wall are determined by the magnetic topology and the geometry of the plasma facing components. We have to distinguish two different concepts: divertor and limiter. The poloidal divertor shown in Fig. 1 is used in the performance oriented tokamak devices (JET, JT60-U, DIII-D, ASDEX-U) and is the preferred concept for the next step device. The simpler (and cheaper) limiter is explored e.g. in Tore Supra and TEXTOR (toroidal belt limiter), in particular, with respect to steady state technology, plasma-wall interaction and new concepts with ergodic boundaries. The subject of ergodic divertor physics is discussed in [7], for a review on divertor physics in stellarators the reader is referred to [8].

The projection of the flux tubes on the surface of the limiter/divertor plate is determined by two angles: the tilting angle α between toroidal and poloidal direction depends on the rotational transform (safety factor) q ; the angle Ψ in the poloidal plane between the magnetic field and the surface normal is given by the limiter shape or the orientation of the divertor plates. In torus geometry α varies along the poloidal coordinate depending on the aspect ratio and the plasma pressure.

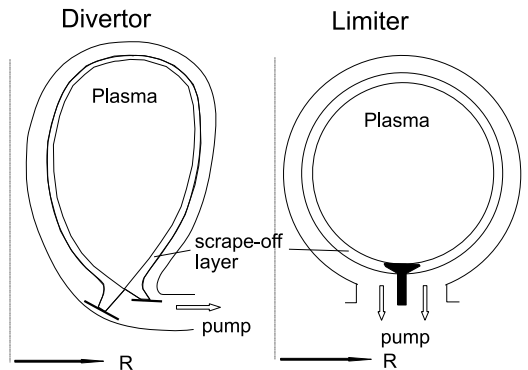


Figure 1: Poloidal divertor and toroidal limiter concept shown in the poloidal plane of a tokamak

III. BASIC CHARACTERISTICS OF THE SOL

Both concepts shown in fig. 1 are toroidally symmetric. This allows to discuss the main features by reducing the transport inside the SOL to a 2-dimensional problem: flow along the field line (coordinate z) and diffusion in radial direction (coordinate x) as shown in fig. 2. As we will see below, the radial extension of the SOL is small with respect to the minor radius of the plasma ($\lambda \ll a$), so that we can apply a plane geometry and straighten out the SOL as indicated in fig. 2, thereby neglecting toroidal effects.

The SOL begins at the last closed flux surface (LCFS). After the initiation of the plasma discharge and on a time scale of μs , electrons will rush ahead the ions as a consequence of their higher mobility and charge up the solid negatively. A thin sheath will form to shield the electrostatic potential with a characteristic length given by the so called Debye length

$$\lambda_D = \sqrt{\frac{\epsilon_0 k T_e}{n_e e^2}} \quad (1)$$

For $T_e = 20 eV$ and $n_e = 10^{19} m^{-3}$ we get $\lambda_D = 10^{-5} m$, which reflects the fact that the plasma maintains quasi-neutrality very well. Further properties of this sheath will be discussed in section VI.

However, the shielding is imperfect because of the thermal motion of the plasma particles and a small electric field penetrates the plasma (pre-sheath) which accelerates the ions towards the target. The electrons feel a corresponding retarding field. The plasma fluid as a whole is quasi-neutral, because of the plasma sink at the end of the field lines a pressure gradient develops and a symmetric flow towards both ends is driven. At the symmetry plane the parallel flow velocity $v_{||}$ and the

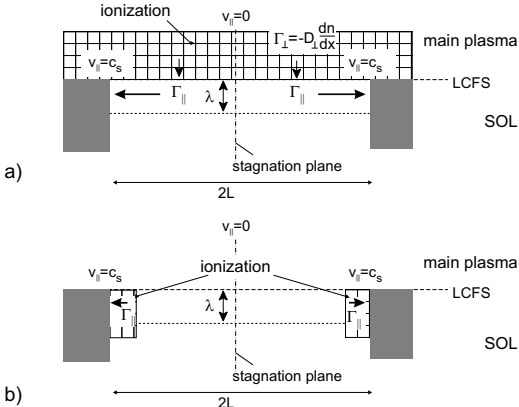


Figure 2: 2-d model of the SOL, a) simple SOL, b) complex SOL

parallel flux density Γ_{\parallel} must be zero (stagnation plane) and at both ends the flow velocity reaches sound speed, $v_{\parallel} = c_s$ (so called the "Bohm criterion").

At the material surfaces ions and electrons recombine and are released back into the plasma as neutrals, will be ionized by impact of electrons and form the plasma source to drive again plasma flow back to the material surfaces. This process which has a very short time scale compared to the duration of a plasma discharge (e.g. in TEXTOR several tens of ms compared to 10 s) is called *recycling*. The recycling process is strongly influenced by the fact how the neutrals are released into the plasma and where they get ionized. Some characteristics of the transport of neutrals in the plasma edge are summarized in section IV. Much more details, in particular on techniques how to prescribe the neutrals in realistic geometry are given in [9]. Two different situations can be distinguished with respect to the particle sources in the SOL. Under the simplified assumption that there are no ionization sources in the volume of the SOL but the sources are located inside the confined volume, the SOL is solely filled by a cross-field diffusion with a flux density $\Gamma = -D_{\perp} \partial n / \partial x$. This situation is generally named the "simple SOL", cf. fig. 2a). On the other hand, if all ionization sources are located inside the SOL, no perpendicular diffusion into the SOL develops, cf. fig. 2b). While the first situation is usually realized in limiter tokamaks and in divertor tokamaks with low plasma densities, the second situation can only be realized in divertor tokamaks at high plasma densities and is usually called the "complex SOL" for reasons which will become clear in the following.

Throughout this overview we will describe the edge

plasma in the fluid picture with equations for the average quantities rather than with a full kinetic analysis. Strictly, the requirement for such a procedure is that the self-collisional mean free paths of electrons and ions $\lambda_{ee} \approx \lambda_{ii} \approx 10^{16} T^2 / n$ (with T in eV and n in m^{-3} yielding $\lambda_{ee,ii}$ in m) are smaller than the extension of the plasma along the magnetic field (connection length L). In the medium size limiter tokamak TEXTOR with typical SOL parameters $L \approx 20m$, $n = 1 - 10 \cdot 10^{18} m^{-3}$ and $T = 10 - 100eV$ the mean free path is 0.1m (high density/ low temperature case) up to 100m (low density/ high temperature case) the situation can be marginal at SOL low densities.

With simple estimates we may now characterize some basic features of such a SOL as the SOL thickness and the radial density variation, assuming a simple SOL with perpendicular diffusion as particle source for the SOL. For this first estimate we may relate the length of the flux tube (connection length $2L$, where $L = \pi q_a R$ in a toroidal limiter / poloidal divertor configuration with q_a the safety factor at the edge and R the major radius) and the SOL thickness λ to the average transport velocities v_{\parallel} and v_{\perp} according to

$$\frac{v_{\perp}}{v_{\parallel}} = \frac{\lambda}{L}. \quad (2)$$

For the average velocities we take $v_{\parallel} = 0.5c_s$ and $v_{\perp} n = D_{\perp} \partial n / \partial x$. With the characteristic length $\lambda = (1/n) \partial n / \partial x$ we obtain for Eq. 2

$$\frac{D_{\perp} / \lambda}{0.5c_s} = \frac{\lambda}{L}. \quad (3)$$

From this relation we get the well known expression for the SOL thickness λ (i.e. the density decay length)

$$\lambda = \sqrt{\frac{D_{\perp} L}{0.5c_s}} \quad (4)$$

With typical values for an edge plasma $D_{\perp} = 1m^2/s$, $T = 50eV$, and $L=10$ m we obtain $\lambda = 30mm$. This is a remarkably small value compared to the dimensions of a fusion reactor. As a consequence, the surface area wetted by the plasma reduces by roughly two orders of magnitude with respect to the total wall area, leading to unacceptable high heat loads. We will see later that this simple calculation even overestimates the SOL thickness, in particular close to the plasma facing components.

The radial variation $f(x)$ of density inside the SOL can be derived from a simple 1d-calculation based on the conservation of mass along the flow channel z

$$\frac{\partial}{\partial x} D_{\perp} \frac{\partial n}{\partial x} = \frac{\partial}{\partial z} (n v_{\parallel}). \quad (5)$$

Assuming in a first step $D_{\perp} = \text{const}$ and $\partial n / \partial x = \text{const.}$ along z as well as a constant r.h.s of Eq. 5 represented by $\partial / \partial z (n v_{\parallel}) = n / \tau_{\parallel}$ with a characteristic particle residence time in the SOL given by τ_{\parallel} (parallel transport to the target is the only plasma sink, no particle sources caused by ionization of neutrals inside the SOL are considered) we obtain the solution of Eq. 5

$$n(x) = n(0) \exp(-x / \sqrt{D_{\perp} \tau_{\parallel}}) \quad (6)$$

The density shows an exponential decay inside the SOL with a characteristic length $\lambda = \sqrt{D_{\perp} \tau_{\parallel}}$ as given by Eq. 4, $n(0)$ denotes the density at the LCFS. Here, the typical time scale of parallel transport to the targets τ_{\parallel} is of the order of ms. However, one has to be careful when using these simple expressions, as particle sources inside the SOL and drifts will alter the result as discussed later on.

IV. NEUTRAL PARTICLE TRANSPORT

Hydrogen (deuterium or tritium) and impurity neutrals are released from the plasma facing components and penetrate into the edge plasma. Owing to the different release mechanisms as discussed in [2] we observe also different particle velocities. This has an important impact on the edge plasma.

Hydrogen may be released as a molecule H_2 or an atom H_0 . It has been found that in the recycling process the probability for molecule formation depends on the surface temperature, which determines the residence time in the surface. At low temperatures mainly molecules are desorbed while above about $T_s = 1200K$ the majority of particles is released as atoms [19] [20].

Some processes involved with the penetration of H_2 are illustrated in Fig. 3. Because of electron impact the molecule dissociates. Various dissociation channels compete, with cross sections depending on T_e . Some of them are given in table 1 together with the rate coefficients for $T_e = 50$ eV.

The reaction no.1, also illustrated in Fig. 3, is only dominant at or below $T_e = 10eV$, whereas at higher T_e the molecule is first ionized and then dissociated (reactions no.3 and no.4), as is obvious from the rate coefficients $\langle \sigma v \rangle_{dis}$ [21]. The atoms resulting from the dissociation of molecules in ground state gain energies in the range of $2.2eV$. Surprisingly, average energies significantly lower than these ($0.5eV$) have been measured in the vicinity of a limiter [22] [23]. It is assumed that this is caused by vibrationally excited molecules.

The probability that an atom has at least one charge exchange (CX) reaction before it is ionized is rather high because the rate coefficients for ionization

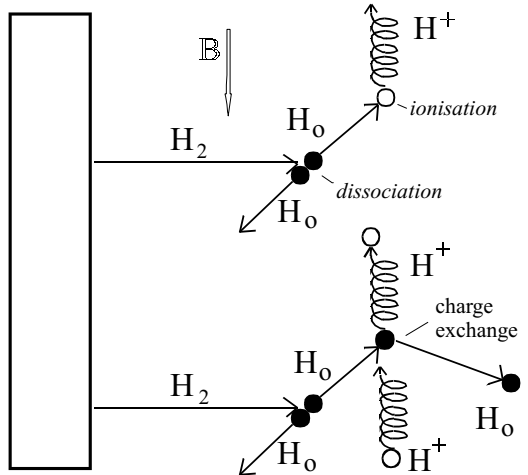


Figure 3: Molecule dissociation and charge exchange processes at the plasma boundary (solid circles: atoms, open circles: ions)

no.	dissociation reaction	$\langle \sigma v \rangle_{dis} / m^3/s$
1	$H_2 \rightarrow H_0 + H_0$	$6 \cdot 10^{-15}$
2	$H_2 \rightarrow H_0 + H^+$	$2 \cdot 10^{-15}$
3	$H_2 \rightarrow H_2^+$	$4 \cdot 10^{-14}$
4	$H_2^+ \rightarrow H_0 + H^+$	$3 \cdot 10^{-13}$
5	$H_2^+ \rightarrow H^+ + H^+$	$6 \cdot 10^{-15}$

Table 1: Dissociation reactions of hydrogen molecules and molecular ions[21].

$\langle \sigma v \rangle_i$ and CX $\langle \sigma v \rangle_{CX}$ are similar as is shown in the table 2 [21].

Using the atomic and molecular data the transport of neutral particles can be modelled with a rather high accuracy even for complicated 3d-geometries [24] [9].

The velocity of *impurity* atoms also depends on their release mechanisms. The fastest particles are reflected impurities (impurity ions from the plasma, neutralized and re-emitted). Among the erosion mechanisms, sputtering generates particles in the range of 5 eV. Atoms coming from molecules gain their velocity from the dissociation energy. Sublimated or evap-

$T_e = T_i$	10	100	eV
$\langle \sigma v \rangle_i$	$7 \cdot 10^{-15}$	$3 \cdot 10^{-14}$	$m^3 s^{-1}$
$\langle \sigma v \rangle_{CX}$	$2 \cdot 10^{-14}$	$5 \cdot 10^{-14}$	$m^3 s^{-1}$

Table 2: Rate coefficients for ionization and charge exchange [21].

orated atoms have only thermal energy, thus represent the slowest particles with the least impact on the edge plasma (cf. discussion in [2]).

Recombination processes are generally not important unless the plasma is very cold as in detached divertors, since in most cases the recombination times of ions are much longer than the average residence time of the particles in the plasma.

The ionization time of an atom can be calculated from the rate coefficient for ionization $\langle \sigma v \rangle_i (T_e)$ and the local electron density n_e . The time derivative of the neutral density n_0 owing to ionization is then given by

$$\frac{\partial n_0}{\partial t} = -n_e n_0 \langle \sigma v \rangle_i \quad (7)$$

leading to an exponential decay of the atom density

$$n_0(t) = n_0(t=0) \exp\left(-\frac{t}{\tau_i}\right). \quad (8)$$

The ionization time τ_i is given by

$$\tau_i = \frac{1}{n_e \langle \sigma v \rangle_i} \quad (9)$$

The penetration of neutral particles into a homogeneous plasma having a velocity v_0 is given by the ionization length

$$\lambda_i = \frac{v_0}{n_e \langle \sigma v \rangle_i} \quad (10)$$

In the presence of a radial profile of both the electron density and temperature the description of the ionization length can be generalized to

$$\int_0^{\lambda_i} \frac{n_e(r) \langle \sigma v \rangle_i (T_e(r))}{v_0} dr = 1 \quad (11)$$

We can define the ion source distribution $Q(r)$, which is given under steady- state conditions as

$$Q(r) = -\frac{\partial \Gamma_0}{\partial r} = n_0(r) n_e(r) \langle \sigma v \rangle_i (T_e(r)) \quad (12)$$

Here, $\Gamma_0 = n_0 v_0$ is the neutral flux density under the simplifying assumption of a mono-energetic neutral velocity distribution. The ionization length λ_i can be used to characterize the radial extent of the ion source distribution. As a consequence the impact of neutrals on the edge plasma is characterized both by their velocities as determined by the specific release mechanism and the edge plasma parameters n_e and T_e .

As stated before, for hydrogen atoms charge exchange processes are important in addition. This gives rise to a diffusion process of the atoms. The penetration depth is given by the geometric mean of the ionization

length λ_i as given by Eq. 10 and the mean free path for the CX process λ_{CX} [25] using for both (!) the thermal ion velocity $v_{th} = \sqrt{kT_i/m_i}$

$$\lambda_{pen} = \frac{v_{th}}{n_e \sqrt{\langle \sigma v \rangle_{CX} \langle \sigma v \rangle_i}}. \quad (13)$$

V. GENERAL DESCRIPTION OF PARALLEL TRANSPORT IN THE SOL

We start our general description of SOL transport parallel to the magnetic field (z direction) in the fluid picture with the conservation equations for particles, momentum and energy under steady- stated conditions (no partial time derivatives). The extension to 2D transport (parallel - radial) can be made by including "effective" cross field sources (cf. [3], chapter 13, and [4], section 1.1). We consider two species (electrons e and singly charged plasma ions i) under the assumption of quasi- neutrality ($n_e = n_i = n$).

$$\frac{\partial}{\partial z} (n_{i,e} v_{\parallel i,e}) = S_p \quad (14)$$

Here n denotes the particle density, v_{\parallel} the parallel fluid velocity and S_p the particle source which can be related to particle transport into the SOL, to ionization or recombination processes (the latter forming a particle sink in the SOL volume).

Next we introduce the momentum equations for plasma ions of mass m_i in its conservative form

$$\frac{\partial}{\partial z} (m_i n v_{i,\parallel}^2 + p_i) = enE + R_{ie} + R_n. \quad (15)$$

Here $p_i = kT_i n$ is the ion pressure with T_i the ion temperature, k the Boltzmann constant, e the elementary charge, E the parallel electric field, R_{ie} the friction force term owing to collisions with electrons and R_n the friction force term owing to collisions with neutrals. Both friction terms have two contributions,

$$R_{ie} = m_e (v_e - v_i) \nu_{ei} n + 0.71 n \frac{\partial kT_e}{\partial z} \quad (16)$$

with m_e the electron mass, ν_{ei} the electron ion collision frequency and T_e the electron temperature, and

$$R_n = -m_i (v_i - v_n) \langle \sigma v \rangle_{CX} n_n n + m_i v_n S_p \quad (17)$$

with v_n the velocity which with the neutrals with a Maxwellian distribution are drifting, $\langle \sigma v \rangle_{CX}$ the rate coefficient for charge exchange between ions and neutrals and n_n the neutral density.

For electrons the inertia term $\frac{\partial}{\partial z} (m_e n v_{e,\parallel}^2)$ can be neglected as well as electron momentum sources because of the small electron mass, and we are left with

$$\frac{\partial}{\partial z} p_e + enE = -m_e(v_e - v_i)\nu_{ei}n - 0.71n \frac{\partial kT_e}{\partial z} \quad (18)$$

If we solve equation 18 for the parallel electric field, we obtain Ohm's law as

$$E = \frac{j_{\parallel}}{\sigma_{\parallel}} - \frac{0.71}{e} \frac{\partial kT_e}{\partial z} - \frac{1}{en} \frac{\partial p_e}{\partial z} \quad (19)$$

where the parallel current density has been defined as $j_{\parallel} = en(v_i - v_e)$ and the parallel electric conductivity as derived assuming balance between electric and e-i friction force as $\sigma_{\parallel} = e^2 n / (m_e \nu_{ei})$. In most cases one assumes local ambipolarity, $j_{\parallel} = 0$ such that for a deuterium plasma $v_e = v_i = v$. Otherwise, a current continuity equation is needed e.g. to describe cases where external currents are driven in biasing experiments (cf. also the discussion in [3], chapter 17).

Next we proceed to the energy conservation equation for ions, which is given as

$$\begin{aligned} \frac{\partial q_{\parallel i}}{\partial z} &= \frac{\partial q_{\parallel i, conv}}{\partial z} + \frac{\partial q_{\parallel i, cond}}{\partial z} \\ &= \frac{\partial}{\partial z} \left[\left(\frac{5}{2} T_i + \frac{1}{2} m_i v_i^2 \right) n v_i - \kappa_{oi} T_i^{5/2} \frac{\partial T_i}{\partial z} \right] \\ &= env_i E + Q_{in} - Q_{eq}, \end{aligned} \quad (20)$$

where we have decomposed the parallel heat flux into its convective and conductive part. The heat conduction coefficient $K = \kappa_{oi} T_i^{5/2}$ has a very strong temperature dependence, for ions we have for deuterium ions $\kappa_{oi} = 60$ to get with T_i in eV and $\partial T_i / \partial z$ in eVm^{-1} the conductive heat flux in Wm^{-2} . The term Q_{in} denotes the energy exchange between ions and neutrals during charge exchange processes, Q_{eq} is the energy transport from ions to electrons in Coulomb collisions.

For electrons we get accordingly

$$\begin{aligned} \frac{\partial q_{\parallel e}}{\partial z} &= \frac{\partial q_{\parallel e, conv}}{\partial z} + \frac{\partial q_{\parallel e, cond}}{\partial z} \\ &= \frac{\partial}{\partial z} \left[\frac{5}{2} T_e n v_e - \kappa_{oe} T_e^{5/2} \frac{\partial T_e}{\partial z} \right] \\ &= -env_e E + Q_r - Q_{ei} + Q_{eq}, \end{aligned} \quad (21)$$

Again we have omitted the inertia term in the convective flux, Q_r denotes the Joule heating term (not present if $j_{\parallel} = 0$), Q_{ei} is the energy loss of electrons because of inelastic collisions which ionize or excite neutrals. The heat conduction by electrons is substantially larger than that of ions, $\kappa_{oe} = 2000$, because of the $m^{-1/2}$ dependence of the heat conductivity.

Now we are still missing *boundary conditions* for our fluid equations 6, 15, 18, 20 and 21. At the stagnation plane we request from symmetry considerations

$$v_{\parallel} = \frac{\partial n}{\partial z} = \frac{\partial T_i}{\partial z} = \frac{\partial T_e}{\partial z} = 0. \quad (22)$$

The boundary conditions at the limiter and target plate are defined by the existence of the Debye sheath mentioned before, which is the subject of the next section.

VI. THE SHEATH

Within the Debye sheath quasi - neutrality is no longer fulfilled and the electrostatic potential is given by Poisson's equation

$$\frac{\partial^2 V}{\partial z^2} = -\frac{e}{\epsilon_0} (n_i - n_e). \quad (23)$$

In this potential the electrons can be described by a Boltzmann equation

$$n_e(z) = n_{se} \exp(e(V - V_{se})/kT_e) \quad (24)$$

where $n_{se, e} = n_{se, i} = n_{se}$ is the density at the sheath entrance. This potential distribution constitutes a hill for the electrons ($V < 0$), as the limiter or diverter surface has initially been charged negatively by the electrons. At the sheath entrance we have the potential V_{se} which will be deduced from the parallel transport equations in section VII.

The ions will be accelerated in the sheath. If we assume now following the derivation in [3] that the parallel ion flux density remains constant within the very thin sheath, $n_i v_i = const.$, and for a moment that $T_i = 0$, we can use ion energy conservation $\frac{1}{2} m_i v_i^2 = -eV$ (no change of thermal energy) to obtain

$$n_i(z) = n_{se} (V_{se}/V)^{1/2}. \quad (25)$$

We use Eqns. 24 and 25 to transform 23 to

$$\frac{\partial^2 V}{\partial z^2} = -\frac{e}{\epsilon_0} n_{se} \left[\left(\frac{V_{se}}{V} \right)^{1/2} - \exp(e(V - V_{se})/kT_e) \right]. \quad (26)$$

Now we consider the region just inside the sheath where $\Delta V \equiv V_{se} - V > 0$ is small with respect to V and expand the two terms on the RHS of Eqn. 26

$$\left(\frac{V_{se}}{V} \right)^{1/2} \approx 1 + \frac{1}{2} \frac{\Delta V}{V_{se}} = 1 - \frac{1}{2} \frac{\Delta V}{|V_{se}|} \quad (27)$$

$$\exp(e(V - V_{se})/kT_e) \approx 1 - \frac{e\Delta V}{kT_e} \quad (28)$$

to get

$$\frac{\partial^2 \Delta V}{\partial z^2} = \frac{e \Delta V}{\varepsilon_0} n_{se} \left(\frac{e}{kT_e} - \frac{\Delta V}{|V_{se}|} \right). \quad (29)$$

From the condition that the electric potential in the Debye sheath has a monotonic distribution it follows that

$$\begin{aligned} \frac{e}{kT_e} &\geq \frac{\Delta V}{|V_{se}|} \\ m_i v_{se}^2 &\geq kT_e \\ v_{se} &\geq c_s \end{aligned} \quad (30)$$

where c_s is the sound velocity and Eqn. 30 defines the *Bohm criterion* for the "plasma exit velocity". It will be supplemented with a condition $v_{se} \leq c_s$ following from the calculation of the parallel velocity profile in the SOL as described in section VII to end with $v_{se} = c_s$ as boundary conditions for the parallel flow at the sheath entrance (valid as long no drifts are considered, cf. section VIII).

Using this Bohm criterion we can describe the ion flux density to the target as the parallel flux density at the sheath entrance (se) (neglecting additional sources in the very thin sheath)

$$\Gamma_{target}^i = n_{es} c_s = \frac{1}{2} n(0) \sqrt{\frac{k(T_i + T_e)}{m_i}}. \quad (31)$$

To preserve ambipolarity the ion flux (for an ion charge $Z=1$) must balance the electron flux which is influenced by the sheath potential drop V_s . The electron distribution remains Maxwellian in the retarding electric field. Thus, the electron flux to the target reads

$$\Gamma_{target}^e = \frac{1}{4} n_{es} \bar{c}_e = \frac{1}{4} n_{es} \exp\left(\frac{eV_s}{kT_e}\right) \sqrt{\frac{8kT_e}{\pi m_e}}. \quad (32)$$

Equating 31 and 32 yields

$$\frac{eV_s}{kT_e} = 0.5 \ln\left(2\pi \frac{m_e}{m_i}\right) \left(1 + \frac{T_i}{T_e}\right). \quad (33)$$

Typical values for the ratio given above are about 3. To quantify the total potential drop between stagnation plane and target surface one has to add the pre-sheath potential drop deduced in the next section VII (cf. Eqn. 48). Emission of electrons from the surface reduces the electrostatic potential. In some cases it can even lead to a breakdown of the sheath. The most important effect is the emission of secondary electrons, but also reflected electrons, photon induced emission and

thermal emission play a role. In particular, above certain temperatures thermal emission can dominate and is considered to be one reason for the formation of so called hot spots [18].

The ions gain energy in the sheath (at the expense of the electrons which are cooled because only the fast part of the electron population can leave the plasma while the slower ones are repelled by the sheath potential). The impact energy of ions to the target

$$E_{ion} = 2kT_i + 3ZkT_e \quad (34)$$

with Z the charge of the ions, is significantly increased by the acceleration in the sheath, especially for highly charged impurity ions, leading to enhanced physical sputtering (cf. discussion in [2]).

The heat flux density of ions and electrons from the plasma onto the surface can be related to the particle flux densities leaving the plasma with the help of the so called "sheath transmission coefficients" defined as

$$\gamma_{i,e} = \frac{q_{i,e}}{kT_e \Gamma_{target}} \quad (35)$$

For electrons we get $\gamma_e \approx 2 + 3 + 0.5$ from the thermal, sheath and pre-sheath contribution. The ions don't have a Maxwellian distribution, if they had, then $\gamma_i \approx 2.5T_i/T_e + 0.5 + 0.5T_i/T_e$. Numerical simulations allowing for non-Maxwellian ion distributions give somewhat smaller results $\gamma_i \approx 2 - 3$. The total sheath transmission coefficient is then around $\gamma = 8$. The heat flux density to the target can be expressed as

$$q_{target} = \gamma n_{es} c_s kT_e = n_{es} \sqrt{\frac{k(T_i + T_e)}{m_i}} kT_e. \quad (36)$$

We finally can include the power flow deposited on the target upon recombination of the ion-electron pairs and possibly formation of molecules. This potential energy flow density can be expressed as

$$q_p = n_{es} c_s k \varepsilon_p = n_{es} \sqrt{\frac{k(T_i + T_e)}{m_i}} \varepsilon_p. \quad (37)$$

with the potential energy ε_p composed of the ionization and dissociation energy of deuterium atoms and molecules, $\varepsilon_p \approx 16eV$.

The magnetic field \vec{B} has no influence on the sheath description as long as the surfaces are orthogonal to \vec{B} . In practice, however, surfaces are tilted to spread the power onto the target. By enlarging the angle Ψ between \vec{B} and the normal to the surface the power flux density normal to the target can be reduced to

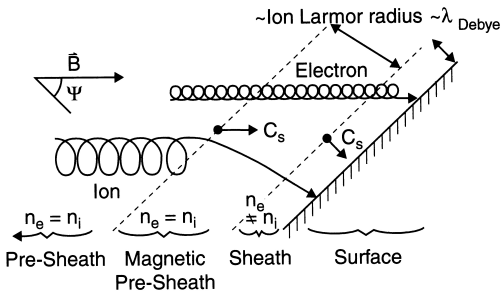


Figure 4: Near surface region for a target inclined to the magnetic field [13] (figure adapted from [3])

$$q_{dep} = q_{\parallel} \cos \Psi. \quad (38)$$

The parallel heat flux density in a fusion reactor can be in the order of $100 - 1000 MW m^{-2}$ so that a shallow inclination of the targets with Ψ up to 89° is envisaged. For these small angles of incidence a new feature, the *magnetic pre-sheath* [13] shows up, which extends from the electrostatic Debye sheath discussed before about one ion larmor radius ($\sim 10^{-3}m$) into the plasma. The reason for the formation of the magnetic pre-sheath is, that there is now an ExB drift of the ions perturbing the last gyro-orbits in front of the target, while the electrons will follow the magnetic field lines virtually all the way to the surface because of their much smaller gyro radius (cf. fig. 4). As a consequence, the Bohm criterion for the parallel flow now applies at the magnetic pre-sheath edge.

Equating the ion flux at the magnetic pre-sheath (mse) with the electron flux at the electrostatic sheath entrance (se), again assuming ambipolar flow and no sources in the pre-sheath and the Boltzmann relation for electrons)

$$n_{mse} c_s \cos \Psi = n_{se} c_s = n_{mse} \exp(eV_{mse}/(kT_e)) c_s \quad (39)$$

leads to

$$\frac{eV_{mse}}{kT_e} = \ln \cos \Psi. \quad (40)$$

The total potential drop in Debye V_{DS} and magnetic pre-sheath V_{mse} together is independent on Ψ to first order as found in numerical calculations [13], instead Ψ determines the split between V_{mse} and V_{DS} . Thus, to first order, the sink action of the solid surface acting on the plasma, with regard to both particle and power flows, is unaffected by the change from a normal

to an oblique target, as are the sheath voltage drop and the ion impact energy onto the target (Eqn. 34).

VII. PROPERTIES OF THE SIMPLE SOL

Now we return back to the description of the parallel flow in the SOL. First we will describe the case of the simple SOL (cf. fig. 2a), which is also called the *sheath-limited regime*. The model assumptions are the following:

- The 1D fluid flow is isothermal, $T_i = const.$ and $T_e = const.$, and there are no heat sinks or sources inside the SOL. Thus, we don't need the energy transport equations.
- There are no particle sources from ionization inside the SOL, the only source is diffusive cross field transport.
- The target is a perfect plasma sink, there are no volume sinks as recombination.
- The ions and electrons are fully decoupled.

The source term for the continuity equation along z is given by radial particle transport into the SOL (no ionization inside the SOL)

$$\frac{\partial}{\partial z}(nv_{\parallel}) = S_p = -\frac{\partial}{\partial x}(D_{\perp} \frac{\partial n}{\partial x}) = \frac{D_{\perp} n}{\lambda^2}. \quad (41)$$

For the ion momentum balance, we again neglect friction with neutrals (CX losses and ionization) and represent the electric field with the help of the Boltzmann relation Eq. 24 yielding

$$m_i n v_{\parallel} \frac{\partial v_{\parallel}}{\partial z} = -k(T_e + T_i) \frac{\partial n}{\partial z} + m_i v_{\parallel} S_p \quad (42)$$

with S_p as given by Eq. 41.

Defining a parallel Mach number $M_{\parallel} = v_{\parallel}/c_s$ and using the definition of the (isothermal) ion sound velocity $c_s = \sqrt{(k(T_e + T_i))/m_i}$ we can now use Eqs. 41 and 42 to deduce two coupled equations which describe the variation of the density and the Mach number along z

$$\frac{\partial n}{\partial z} = -\frac{n D_{\perp}}{c_s \lambda^2} \frac{2M_{\parallel}}{1 - M_{\parallel}^2} \quad (43)$$

$$\frac{\partial M_{\parallel}}{\partial z} = \frac{D_{\perp}}{c_s \lambda^2} \frac{1 + M_{\parallel}^2}{1 - M_{\parallel}^2} \quad (44)$$

The divergence of these two equations for $M_{\parallel} = \pm 1$ defines the boundary condition of the flow at the sheath

entrance (the Bohm criterion as mentioned before). Combining Eqs. 43 and 44 we get

$$\frac{\partial n}{\partial M_{\parallel}} = -n \frac{2M_{\parallel}}{1 + M_{\parallel}^2} \quad (45)$$

which can be integrated analytically:

$$\frac{n}{n_0} = \frac{1}{1 + M_{\parallel}^2} \quad (46)$$

with n_0 the density in the stagnation plane where $M_{\parallel}(z=0) = 0$. Therefore, the density drops from the stagnation point to the sheath entrance to half its value. As we assumed no variation of the particle source originating from cross field transport into the SOL and $|\partial n/\partial x| = n/\lambda = \text{const.}$, the SOL thickness λ reduces towards the target proportional to the density further aggravating the problem of the high target load as indicated before.

The equation describing the variation of the Mach number along z reads

$$M_{\parallel} - 2 \arctan M_{\parallel} = \left(\frac{\pi}{2} - 1\right) \frac{z}{L} \quad (47)$$

Finally, combining Eq. 46 and 24 we get an equation for the potential in the pre-sheath

$$V(z) = -\frac{kT_e}{e} \ln(1 + M_{\parallel}(z)^2) \quad (48)$$

Therefore, at $M_{\parallel} = 1$ the total pre-sheath drop is given by $V \approx -0.69kT_e/e$.

Fig. 5 depicts the variation of the plasma density, the Mach number and the electric potential as given by Eqs. 46, 47 and 48, respectively, from the stagnation plane $z/L=0$ to the sheath entrance $z/L=1$.

For the situation of a simple SOL the power flux density is determined by the power flow into the SOL and the power decay length together with the perpendicular extension of the target (i.e. the poloidal extension in case of a toroidal limiter), which is small as is the density decay length discussed in section III. At the same time the temperature at the target surface remains high, unless both the power flow into the SOL and the temperature at the LCFS are reduced by power loss mechanisms inside the confined volume (cf. [11]).

VIII. IMPACT OF DRIFTS ON THE SOL FLOW

Next we discuss briefly the influence of drift effects on the parallel particle transport in the SOL which have been identified as the cause of significant poloidal asymmetries in tokamaks ([14], [15], [16], [17], cf. also discussion in [3], chapter 18, and references therein).

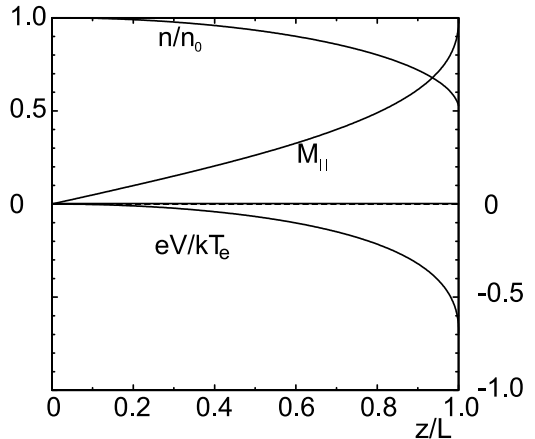


Figure 5: Variation of plasma density n normalized to $n(0)$, parallel Mach number and normalized potential drop in the pre-sheath along the magnetic field from the stagnation plane $z/L=0$ to the sheath entrance $z/L=1$

The model for the parallel transport discussed before can be extended to include a perpendicular drift component caused by ExB drift, diamagnetic drift and ∇B and curvature drift. We decompose the drift motion into a radial and a binormal component ($\vec{e}_r \perp \vec{e}_\perp \perp \vec{e}_\parallel$) which allows to express the poloidal velocity component v_θ as

$$v_\theta = v_{\parallel} \sin \alpha + v_{\perp} \cos \alpha \quad (49)$$

where α denotes the angle between the toroidal and poloidal magnetic field components as before ($\tan \alpha = B_\theta/B_\phi$).

As we will continue to investigate transport along the field line, we have to project the resulting poloidal velocity onto the parallel direction (cf. fig. 6)

$$\tilde{v}_{\parallel} = v_{\parallel} + \frac{1}{\tan \alpha} v_{\perp}. \quad (50)$$

As a consequence Eqs. 43 and 44 are modified to

$$\frac{\partial n}{\partial z} = \frac{nD_{\perp}}{c_s \lambda^2} \frac{2M_{\parallel} + M_{\perp}/\tan \alpha}{(M_{\parallel} + M_{\perp}/\tan \alpha)^2 - 1} \quad (51)$$

$$\frac{\partial M_{\parallel}}{\partial z} = \frac{D_{\perp}}{c_s \lambda^2} \frac{1 + (M_{\parallel} + M_{\perp}/\tan \alpha)^2}{1 - (M_{\parallel} + M_{\perp}/\tan \alpha)^2} \quad (52)$$

where M_{\perp} normalizes the perpendicular velocity to the sound speed. The boundary condition for the parallel Mach number at the sheath entrance reads

$$M_{\parallel}(z = \pm L) = \pm 1 - \frac{M_{\perp}}{\tan \alpha}. \quad (53)$$

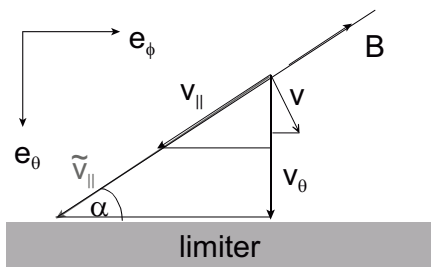


Figure 6: Projection of the perpendicular drift velocity onto the parallel direction.

Consequently, the flow towards both sides of the limiter or to the two divertor plates shown in Fig. 1 is asymmetric, resulting in an asymmetric density distribution along the field line and in poloidal direction. Eq. 46 is replaced by

$$\frac{n}{n_0} = \frac{1}{1 + M_{\parallel}(M_{\parallel} + M_{\perp}/\tan\alpha)}. \quad (54)$$

Within the simple model discussed above (still under the assumptions of no ionizations in the SOL) Fig. 7 illustrates the influence of a perpendicular Mach number $M_{\perp} = 0.05$ on the parallel Mach number along the field line from the electron drift side of the ALT- II limiter in TEXTOR (located 45° below the outer mid-plane) to the ion drift side. The toroidal magnetic field and plasma current are anti- parallel under standard conditions in TEXTOR. In that case $M_{\parallel} > 1$ on the ion drift side. The stagnation plane (as defined by $M_{\parallel} = 0$) is considerably shifted away from the geometrical symmetry plane (located at $z = 0.5$; here we normalize z to the total length of the flux tube $2L$).

In poloidal divertor tokamaks drifts are thought to be the cause of strong asymmetries in the power load of inner and outer divertor target plates, so that both divertor zones are often in different divertor regimes. These divertor regimes are the topic of the following section.

IX. PROPERTIES OF THE COMPLEX DIVERTOR SOL

At the end of section VII we have noted the problems of high power flux densities and high temperatures in limiter SOLs. While the high power flux densities

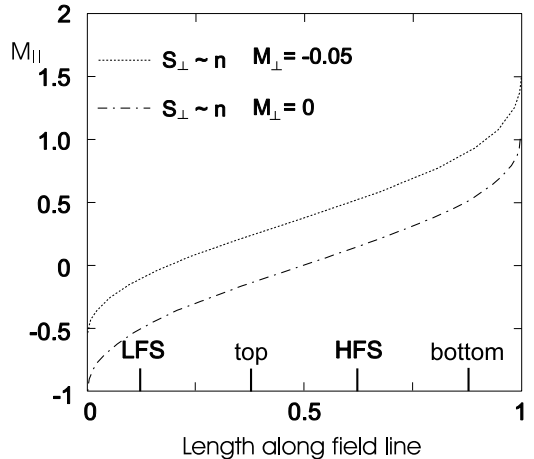


Figure 7: Influence of a perpendicular drift on the parallel Mach number ($\tan\alpha = 0.1$, no ionization in the SOL)

lead to large temperatures of the surfaces of plasma facing components, high temperatures give rise to large energies of particles impinging onto the material surface (cf. Eqn. 34). Both effects will pose huge problems with the plasma-wall interaction in fusion devices (see [1] [2]). Therefore, the formation of a plasma regime with reduced power flow to and a cold plasma in front of the targets (*conduction limited and high recycling regime*) is an important issue in plasma edge physics.

The possibility to reduce the plasma temperature in front of the plasma facing components by establishing a temperature gradient along the magnetic field lines is closely related to the necessity to localize the ionization of neutrals close to the target. As it is depicted in fig. 2b) the parallel plasma flow is then only developing in the ionization (or recycling) region close to the target, most of the SOL is stagnant. In particular, there is no particle flux into the SOL from the confined volume. In practise, such a situation cannot be reached to a full extent because there will be also interaction of the plasma with the main chamber walls, leading to ionization sources remote from the divertor target or limiter inside the SOL or even sources in the confined plasma, if the neutrals recycling at the main chamber walls penetrate across the LCFS. Nevertheless, the particle flux from the core and into the SOL remote from the targets may be rather small with respect to the recycling flux at the targets. While the particle sources are close to the targets, the heat fluxes remain in the core of the confined plasma. Therefore, there is still the power flow out of the confined volume into the SOL and along the magnetic field towards the targets which constitute the heat sink. Without particle flow this heat

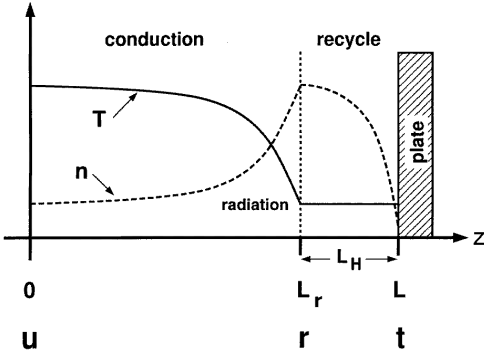


Figure 8: Schematic illustration of the two point model (figure adapted from [6])

flux cannot be convective but will be conductive and a temperature gradient *must* develop.

We can quantify the effects in the complex SOL of a divertor using a simple analytical model (the so called "two point model", cf. [3], chapters 4 and 5, and [6]). For simplicity we assume equal ion and electron temperatures, $T_i = T_e$. Fig. 8 illustrates the typical plasma profiles along the magnetic field for such a situation. We have two different regions, the conduction region consisting of most of the SOL where there are no sources or sinks, and the recycling region where we have the strong ionization sources and possibly a sink for energy and momentum. The two point model relates the conditions upstream of the target (position u) to those at the target (position t) in the case where the fraction f_{cond} of the power is conducted along the parallel temperature gradient as

$$q_{||,cond} = f_{cond} P_{SOL} / A_{q||} = -\kappa_0 T^{5/2} dT/dz, \quad (55)$$

where κ_0 is taken for electrons because of their higher heat conductivity (cf. Eqns. 20 and 21), P_{SOL} is the power flow into the SOL and $A_{q||}$ the total cross-sectional area of the SOL for power flow perpendicular to \vec{B} (all power enters the SOL upstream of the target). We include possible volumetric power sinks characterized by the factor $f_{loss} > 0$ in the balance between power flux into the SOL and power flux at the sheath entrance as

$$(1 - f_{loss}) P_{SOL} / A_{q||} = \gamma n_t c_s k T_t \quad (56)$$

We further introduce a factor $f_{fric} < 1$ into the pressure balance to take pressure losses because of momentum sinks and friction into account

$$n_u T_u f_{fric} = 2 n_t T_t. \quad (57)$$

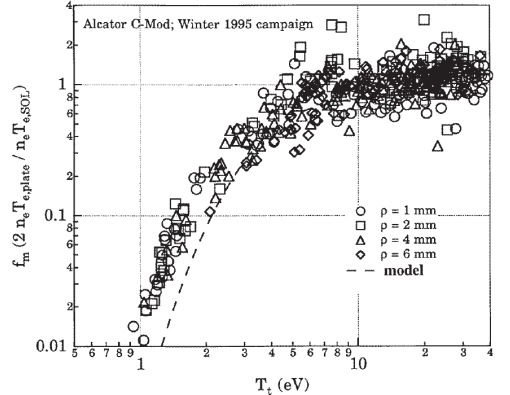


Figure 9: Pressure loss factor from ohmic discharges in C-Mod as a function of the electron temperature at the target T_t and factor calculated from Eqn. 59 (figure adapted from [6]).

Momentum losses induced by CX processes between ions and neutrals in a high density divertor play a major role in in poloidal divertors and occur for very low temperatures below 7 eV, and we will come back later to an assessment of the factor f_{fric} . On the other hand, in the island divertor of helical devices detachment processes at higher temperatures have been observed, which have been related to friction losses caused by counter streaming flux tubes in the complicated 3D geometry of such an island divertor [30] [8]. An expression for $f_{fric,CX}$ has been given in [6] following an 1D analytical solution for the momentum balance in [31]. Here it is assumed that the temperature in the recycling region shown in fig. 8 is constant and the momentum loss reduces the density only. The density ratio between the entrance of the recycle region (r) and the target is given as

$$\frac{n_r}{n_t} = \left(\frac{\alpha + 1}{\alpha} \right)^{(\alpha+1)/2} \quad (58)$$

where the coefficient α is linked to the rate coefficients for ionization and charge exchange (cf. section IV) as $\alpha \equiv \langle \sigma v \rangle_i / (\langle \sigma v \rangle_{CX} + \langle \sigma v \rangle_i)$. Using the pressure balance equation 57 we obtain

$$f_{fric} = 2 \left(\frac{\alpha}{\alpha + 1} \right)^{(\alpha+1)/2} \quad (59)$$

This Equation fairly well describes the experimentally determined pressure drop in the high density Alcator - CMOD tokamak [6] as shown in fig. 9.

Returning back to the two point model we now integrate Eqn. 55 over the distance L between the upstream region u and the target region t to obtain

$$T_u^{\tau/2} = T_t^{\tau/2} - \frac{7 P_{SOL} L}{2 A_{q\parallel} \kappa_0} f_{cond}. \quad (60)$$

Because $T_t^{\tau/2} \ll T_u^{\tau/2}$ as soon as a temperature gradient exists the upstream temperature is given as

$$T_u = \left(\frac{7 P_{SOL} L}{2 A_{q\parallel} \kappa_0} f_{cond} \right)^{2/7} \quad (61)$$

showing a very weak dependence on all parameters.

If we now take n_u and $P_{SOL}/A_{q\parallel}$ as given, we can derive from Eqs. 56, 57 and 61 an expression for the temperature at the target

$$T_t = \frac{m_i}{2e} \frac{4(P_{SOL}/A_{q\parallel})^2 \left(\frac{7 P_{SOL} L}{2 A_{q\parallel} \kappa_0} \right)^{-4/7}}{\gamma^2 e^2 n_u^2} \cdot \frac{(1 - f_{loss})^2}{f_{fric}^2 f_{cond}^{4/7}}. \quad (62)$$

Correspondingly we get for the density n_t at the target

$$n_t = \frac{n_u^3}{(P_{SOL}/A_{q\parallel})^2} \left(\frac{7 P_{SOL} L}{2 A_{q\parallel} \kappa_0} \right)^{6/7} \frac{\gamma e^2}{2m_i} \cdot \frac{f_{fric}^3 f_{cond}^{6/7}}{(1 - f_{loss})^2}. \quad (63)$$

High upstream densities n_u are very efficient to realize a cold and dense high recycling divertor with high n_t and low T_t . We further note that the plasma conditions at the target depend very sensitively on the loss parameters f_{loss} , f_{cond} and f_{fric} . A consistent picture of these parameters can only be obtained from sophisticated modelling (cf. the discussion in [5]).

Nevertheless, we will give some further considerations on the balance between convective and conductive heat flux density, which determines the desired temperature drop along the field lines.

As a first step we can deduce the ratio between upstream and target temperature from Eqn. 61 and 62 which scales as

$$\frac{T_u}{T_t} \propto n_u \left(\frac{7 P_{SOL} L}{2 A_{q\parallel} \kappa_0} \right)^{6/7} \frac{f_{fric}^2 f_{cond}^{6/7}}{(1 - f_{loss})^2}. \quad (64)$$

Naturally, the existence of conductive heat transport ($f_{cond} > 0$) and the resulting temperature ratio is directly linked, and any contributing heat convective heat transport will reduce T_u/T_t . Volumetric power losses close to the target strongly drive the temperature drop but momentum losses impede it. But what is now the ratio between convective and conductive heat

flux and how to control it? Why we observe high recycling regimes in divertor configuration but not in limiter machines? This difference is of course strongly linked to the possibility to retain the ionization sources inside of the SOL. To quantify this statement we have integrated the balance equation for the total energy (sum of Eqns. 20 and 21) retaining both conductive and convective heat flux densities. We used the power flux density as well as the particle flux density to the target as a boundary condition. The convective heat flux is driven by the particle sources inside the confined plasma $f_{SOL} \Gamma_0$ where we assume complete recycling at the target, $\Gamma_{t,\parallel} = \Gamma_0$. We obtain

$$\begin{aligned} \frac{\partial q_{\parallel}}{\partial z} &= \frac{q_{\parallel,t}}{L} \\ &= \frac{\partial}{\partial z} q_{\parallel,cond} + \frac{\partial}{\partial z} q_{\parallel,conv}. \end{aligned} \quad (65)$$

Here we have the parallel heat flux to the target given by the power P_{SOL} entering the SOL all along the connection length L , the cross section of the heat flux channel $A_{q\parallel} = 4\pi R \lambda_{q\parallel} a / (q_a R)$ and the energy loss by ionization and excitation $E_i = 30eV$ [4] given as

$$q_{\parallel,t} = \frac{P_{SOL}}{A_{q\parallel}} - f_{SOL} \Gamma_0 E_i = \gamma \Gamma_{t,\parallel} k T_t \quad (66)$$

and the rate of change of the conductive and convective heat flux density given as

$$\begin{aligned} \frac{\partial}{\partial z} q_{\parallel,cond} &= -\kappa_{e0} \left[T^{5/2} \frac{\partial^2 T}{\partial z^2} + \frac{5}{2} T^{3/2} \left(\frac{\partial T}{\partial z} \right)^2 \right] \\ \frac{\partial}{\partial z} q_{\parallel,conv} &= (1 - f_{SOL}) k \frac{\Gamma_0}{L} \left(5T + z \frac{\partial T}{\partial z} \right). \end{aligned} \quad (67)$$

The second order differential equation 65 is solved for T numerically after transformation into two first order equations

$$\begin{aligned} \frac{\partial T}{\partial z} &= \tilde{T} \\ \frac{\partial \tilde{T}}{\partial z} &= -(\kappa_{e0} L)^{-1} T^{-5/2} \left[q_{\parallel,t} - \frac{\Gamma_0}{(1 - f_{SOL}) k} (5T + z \tilde{T}) \right] \\ &\quad - \frac{5}{2} \tilde{T}^2 T^{-1} \end{aligned} \quad (68)$$

The boundary conditions are

$$\frac{\partial T}{\partial z} \Big|_{z=0} = 0 \quad \text{and} \quad T \Big|_{z=L} = T_t. \quad (69)$$

The target temperature is defined by the inferred heat flux density to the target Eqn. 66. The target density follows from the particle flux to the target, and target temperature and the upstream densities and temperatures are determined by the pressure balance Eqn. 57 where no momentum losses are considered.

We use typical parameters for the limiter tokamak TEXTOR, major radius $R = 1.75m$, minor radius $a = 0.46m$, connection length $L = 20m$, edge safety factor $q_a = 3$, power entering into the SOL $P_{SOL} = 1MW$, power decay length $\lambda_{q\parallel} = 0.02m$ and vary then the particle flux density onto the target. We use the fraction of ionizations inside the SOL f_{SOL} as a parameter. The results are shown in fig. 10.

We scanned the collisionality $\nu_* = L/\lambda_{ee}$ as the ratio between the connection length and the mean free path of electrons (or ions) in a wide range and calculated the ratio of upstream and target temperature T_u/T_t , absolute values of upstream and target temperatures, T_u and T_t as well as fraction of power lost on ionization and excitation of neutrals in the SOL f_{loss} . The calculation is stopped as soon as the target temperature approaches a value of $7eV$ because at these temperatures momentum dissipation by CX processes will become significant. We clearly see that the fraction of ionizations in the SOL has to be 0.6 and higher to allow for a significant temperature drop along the magnetic field. Such large neutral screening is, however, inaccessible in a limiter device because neutrals recycling at the limiter penetrate into the confined zone even at highest densities when the temperature falls below the ionization threshold for hydrogen.

Our result is consistent with [32] where an improved two point model including both convective and conductive heat transport as well as a realistic description of the neutrals and the resulting particle sources had been developed for a limiter SOL and compared to full numerical simulations with a fluid code coupled to a Monte-Carlo code for the neutrals (both codes use full 3D geometry). Here the numerical code shows that at maximum 50% of the neutrals can be ionized in the SOL of TEXTOR. As a consequence, the ratio T_u/T_t saturates at high collisionality. Higher neutral screening is only possible in a divertor tokamak where the targets are positioned remote from the confined volume inside. Closed divertor configurations which suppress leakage of neutrals out of the divertor chamber are best in this respect (cf. also the discussion in [5]).

As we see from fig. 10 under conditions of good neutral screening from the divertor we quickly approach a situation, where the temperatures in the recycling region are small enough to allow for large momentum losses, leading to a *detached* divertor state. Then the particle and power flux to the divertor plate is strongly reduced. Such a regime is envisaged for fusion devices. However, stability of a detached divertor is an issue as we can expect from the complicated and non-linear interplay of the various loss channels. Also the need for additional losses by radiation from impurities is a subject of current research. In present days experiments

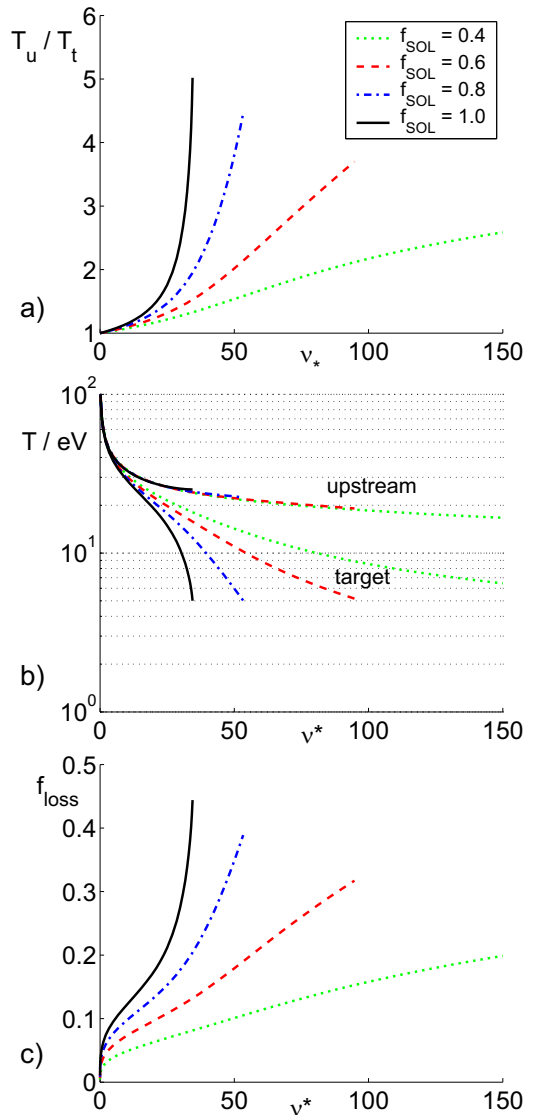


Figure 10: Variation of SOL parameters as a function of the upstream collisionality for typical TEXTOR conditions using the fraction of ionizations inside the SOL as parameter: a) ratio of upstream and target temperature, b) absolute values of upstream and target temperatures, b) fraction of power lost on ionization and excitation of neutrals in the SOL

the high heat load areas of the divertors are mostly made of carbon, an effective intrinsic radiator at the low temperatures close to detachment (see the extensive discussion in [5]).

ACKNOWLEDGMENTS

I wish to thank Michael Lehnen for Figs. 6 and 7 and for the model to calculate the parallel heat flux in the TEXTOR SOL.

REFERENCES

1. U. Samm, "Plasma- wall interaction in magnetically confined fusion plasmas", these proceedings.
2. A. Kirschner, "Erosion and deposition mechanisms in fusion plasmas", these proceedings.
3. P.C. Stangeby, "The Plasma Boundary of Magnetic Fusion Devices", Plasma Physics Series, IoP Publishing Ltd, Bristol, UK (2000).
4. A.V. Nedospasov and M.Z. Tokar', "Wall plasma in tokamaks", in Reviews of plasma physics, B.B. Kadomtsev (ed.), Vol. 18, Consultants Bureau, New York (1993).
5. R. Schneider, "Plasma edge physics for tokamaks", Laborbericht IPP Garching, IPP 12/1, February 2001
6. C.S. Pitcher and P.C. Stangeby, Plasma Phys. Control. Fusion **39** (1997) 779-930.
7. M.Z. Tokar, "Stochastic boundary plasmas", these proceedings.
8. R. König et al., Plasma Phys. Control. Fusion **44** (2002), 2365.
9. D. Reiter, "Recycling and transport of neutrals", these proceedings.
10. D. Reiter, G.H. Wolf and H. Kever, Nucl. Fusion **30** (10) 2141 (1990).
11. M.Z. Tokar, "Impurity transport and radiation at the edge", these proceedings.
12. S.I. Braginskii, "Transport processes in a Plasma", in Reviews of Plasma Physics, M. Leontovich (ed.), Consultants Bureau, New York (1965), 205.
13. R. Chodura, "Plasma flow in the Sheath and Presheath of a Scrape-off Layer", "Physics of Plasma-Wall Interaction in Controlled Fusion Devices", ed D.E. Post and R. Behrisch, Plenum Press, New York (1986), p. 99.
14. H. Gerhauser and H.A. Claassen, J. Nucl. Mater. **176-177**, 721 (1990).
15. M. Baelmans, D. Reiter and R.R. Weynants, Contrib. Plasma Phys., **36** 117 (1996).
16. M. Lehnen, M. Brix, U. Samm, B. Schweer, B. Unterberg and the TEXTOR- team, Nucl. Fusion **43** 168. (2003).
17. M. Lehnen, M. Brix, H. Gerhauser, B. Schweer and R. Zagorski, J. Nucl. Mater. **290-293** (3) 663 (2001).
18. V. Philipps et al., Nucl. Fusion **33** (6), 953 (1993).
19. P. Franzen and E. Vietzke, J. Vac. Sci. Technol. **A12** 820 (1994).
20. A. Pospieszczyk et al., J. Nucl. Mater. **266-269** 138 (1999).
21. M.F.A. Harrison in "Applied Atomic Collision Physics", Vol.2, Academic Press 1984, Eds. C.F. Barnett and M.F.A. Harrison (1984).
22. J.D. Hey et al., Contrib. Plasma Phys. **36** 583 (1996).
23. A. Pospieszczyk and Ph. Mertens, J. Nucl. Mater. **266-269** 884 (1999).
24. D. Reiter, J. Nucl. Mater. **196-198** 80 (1992).
25. B. Lehnert, Nucl. Fusion **8** 173 (1968).
26. H.P. Summers and M. von Hellermann, "Atomic and molecular data exploitation for spectroscopic diagnostics of fusion plasmas", in "Atomic and plasma- material processes in controlled thermonuclear fusion", Edt. by R.K. Janev and H.W. Darwin, Elsevier, Amsterdam (1993), 87., <http://adas.phys.strath.ac.uk/>
27. H.R. Griem, "Plasma Spectroscopy", Mc Graw-Hill Book Company, New York (1964)
28. H.P. Summers and R.W.P. McWhirter, J. Phys. B **12** (1979), 2387.
29. R.W.P. Mc Whirter and H.P. Summers, "Atomic Radiation from Low Density Plasma" in Applied Atomic Collision Physics, Vol. 2, ed. C.F. Barnett and M.F.A. Harrison, Academic Press, Orlando (1984).
30. P. Grigull et al, Plasma Phys. Control. Fusion **43** (2001), A175.
31. S.A. Self and H.N. Ewald, Phys. Fluids **9** (1966), 2486.
32. M.Z. Tokar', M. Kobayashi and Y. Feng, Phys. of Plasmas **11** 2004, 4610.

IMPURITY TRANSPORT AND RADIATION

M.Z. Tokar and M. Koltunov

Institute for Energy and Climate Research – Plasma Physics, Forschungszentrum Jülich GmbH,
EURATOM Association, Trilateral Euregio Cluster, D-52425 Jülich, Germany

ABSTRACT

The role of impurity radiation at the plasma edge in fusion devices is considered. Conditions critical for radiative instabilities, provoking the development of detachment and MARFE, are analyzed. Requirements necessary for the creation of a stable radiating edge, that would allow to protect the wall from intensive heat loads, are formulated.

I. INTRODUCTION

From the very beginning of nuclear fusion research an uncontrollable pollution of the plasma core with impurities released through the interaction of hot particles with the wall was a subject of deep concerns. It was early recognized that radiation losses from such impurities can hinder the plasma heating to thermonuclear temperatures and the concentrations, being “lethal” for fusion, have been estimated for different impurity species [1, 2].

Experiments on earlier tokamak devices with wall elements of heavy metals, e.g., stainless steel, molybdenum, tungsten, have demonstrated that instead of a gradual increase of radiation e.g., with increasing plasma density, the losses can start to grow explosively when the density exceeds a certain critical level (see, e.g., [3, 4]). This behavior is caused by a sudden accumulation of heavy impurity particles of high charges near the plasma axis. This fact forced researchers to switch to light elements like carbon, beryllium, boron in fabricating the wall facing components. The ions of these elements radiate most intensively at relatively low temperatures, i.e., in the edge region close to the plasma boundary [5]. This edge radiation can play a positive role reducing heat loads concentrated mostly on particular wall elements, such as limiters and divertor target plates [6, 7]. Nevertheless, also in this case the plasma behavior does not obey simple laws. The radiating edge layer attached to the plasma boundary can become unstable when the plasma density is ramped up above a threshold value [3]. Under some conditions this manifests itself in a radial contraction of the plasma column that preserves its poloidal and toroidal homogeneity [3, 9, 10]. By such a detachment the power launched

into the plasma is completely lost with impurity radiation from a thin toroidal shell at the edge. Often a detachment terminates the discharge through disruption [11] but may also lead to the formation of a quasi-stationary “detached plasma”. In other cases a toroidal plasma loop of very high density and low temperature, named the Multi-Faceted Radiation From the Edge (MARFE), arises at the high field side of the device and later can disappear or smear out into a “detached plasma” [12, 13, 14]. In divertor machines the processes of MARFE formation is initiated often by a plasma detachment from neutralizing plates and MARFE locates near the X-point [15].

A compromise has been found by deliberate seeding into the plasma of impurities of intermediate atomic numbers like neon, silicon, argon [6, 7]. On the one hand, their characteristics allow to increase the edge radiation to a level of 95% of the power transported from the plasma core without formation of MARFE or “detached plasmas” [7]. On the other hand, their electric charge is still low enough to avoid accumulation in the plasma core. Such a “radiating edge” allows to reduce significantly the heat flows to the wall elements.

Further exploration of the “radiating edge” concept has resulted in one of the most unexpected findings in controlled fusion research: under definite condition impurity seeding results in a reduction of anomalous heat and particle losses from the plasma [16, 17]. These discovery has shown that impurities are essentially involved not only in the global plasma behavior but also in the mechanisms of anomalous transport induced by micro-instabilities developing at very small spatial scales. The Radiation Improved (RI) mode, a regime with the energy confinement increased by the presence of impurities, is now considered as an attractive scenario for a fusion reactor. This mode combines the benefits both from the reduction of head loads on material surfaces and from improved energy confinement in the plasma core.

This brief introduction gives an idea about the broadness of the spectrum of impurity impacts on hot plasmas in fusion devices. These impacts extend from the negative phenomenon of radiation instability leading to MARFE and “detached plasma” to a desirable improvement of confinement in the RI-mode. Investigations of mechanisms underlying impurity influence pursue both academic and practical aims: (i)

deeper insight into radiative phenomena, (ii) better understanding of impurity involvement in transport processes and (iii) outgrowth of a coherent understanding of the impurity behavior in hot plasmas in order to optimize this in future reactors.

In the present contribution only the processes important from the point of view of radiation losses from impurities and their impact on the thermal stability at the plasma edge in fusion plasmas are considered.

II. POWER DENSITY OF RADIATION LOSSES

Normally, impurity enters the plasma as neutral particles, generated in erosion processes of the wall elements [18, 19] or deliberately seeded [7, 8]. In the process of ionization by electrons these neutrals are converted into ions of different electric charges Z . The power density of radiation losses from all impurity charge states can be calculated as follows:

$$Q_{\text{rad}} = \sum_{Z=0}^{Z_{\text{max}}} n n_Z L_Z \quad (1)$$

Here n is the density of plasma electrons which lose their energy either by exciting electrons bounded in impurity ions or due to Bremsstrahlung radiation by Coulomb scattering; n_Z the density of impurity ions of the charge Z ; L_Z the so called cooling rate, i.e., the power lost from a unit volume if one electron and one impurity ion are present there. To determine n_Z and L_Z , one has to consider the processes responsible for the transport of impurity particles and radiation from them.

If the exact spreading of each impurity charge state is non-relevant, one can express Q_{rad} through the effective impurity cooling rate $L_I = \sum_Z \zeta_Z L_Z$ and the total impurity ion density $n_I = \sum_Z n_Z$:

$$Q_{\text{rad}} = n n_I L_I \quad (2)$$

where $\zeta_Z = n_Z/n_I$ are the relative concentrations of different impurity charge states.

A. Impurity ion density

The densities of ions of different charges are described by the continuity equations:

$$\partial_t n_Z + \nabla_{\parallel} (n_Z V_{\parallel}^Z) + \nabla_{\perp} \Gamma_{\perp}^Z = S_Z - \nu_Z n_Z \quad (3)$$

where V_{\parallel}^Z is the ion velocity along magnetic field, Γ_{\perp}^Z the density of their flux in the perpendicular direction, S_Z and ν_Z are the source density and the frequency of ion disintegration, respectively. The latter include diverse processes [20], e.g., ionization by electrons, capture of free electrons by radiative and dielectronic recombination, and of electrons bounded in hydrogen atoms by charge-exchange, etc.

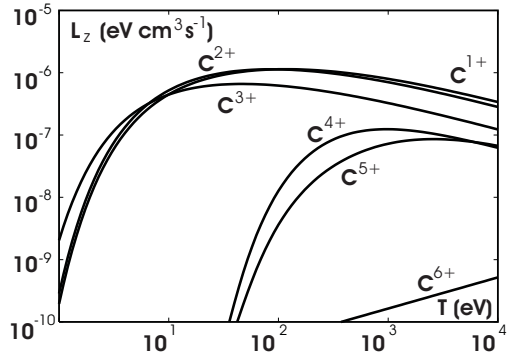


Figure 1: The temperature dependence of the cooling rates for different carbon charge states.

The parallel motion of impurity ions is of the most importance close to the sources where impurity particles are released into the plasma and obeys the momentum transfer equation:

$$\begin{aligned} & \partial_t (n_Z V_{\parallel}^Z) + \nabla_{\perp} (\Gamma_{\perp}^Z V_{\parallel}^Z) \\ & + \nabla_{\parallel} \left[n_Z (V_{\parallel}^Z)^2 + n_Z T_Z / m_Z \right] \\ & = M_Z - \nu_Z n_Z V_{\parallel}^Z + Z e E_{\parallel} / m_Z \\ & + \nu_{Zi} (V_{\parallel} - V_{\parallel}^Z) + \xi_Z \nabla_{\parallel} T / m_Z \end{aligned} \quad (4)$$

The first term on the right hand side, M_Z , is the momentum assimilated from the ion source and the second one is the loss by the ion disintegration; the third term is the acceleration due to the parallel electric field; the fourth one term is due to friction of impurities with the background ions moving with the mass parallel velocity V_{\parallel} , and ν_{Zi} is the friction coefficient [21]; the last term is the so called thermal force arising also due to collisions with the background plasma particles if their temperature T has a parallel gradient; this force exists because the collision frequency decreases with increasing temperature and for the impurity ion mass m_Z significantly larger than that of the background ions, m_i , $\xi_Z \approx 3.3Z^2$ [22]. Normally, the electric field arises because light electrons escape from the plasma to the limiter or divertor plate faster than ions. In such a case both electric and friction forces drag the impurity ions back to the material surface but the thermal force pulls them in the opposite direction, towards the region of higher temperature.

The perpendicular flux of impurities, averaged over the magnetic surfaces, is normally decomposed into diffusive and convective terms:

$$\Gamma_{Z\perp} = -D_{\perp} \nabla_{\perp} n_Z + V_{\perp} n_Z \quad (5)$$

In the diffusivity D_{\perp} and convection velocity V_{\perp} usually neoclassical and anomalous contributions are

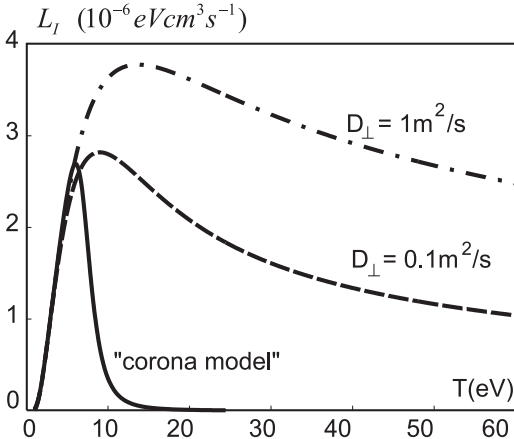


Figure 2: The effect of perpendicular diffusion of impurity ions on the effective cooling rate of carbon.

taken into account:

$$D_{\perp}(V_{\perp}) = D_{\perp}^{\text{neo}}(V_{\perp}^{\text{neo}}) + D_{\perp}^{\text{an}}(V_{\perp}^{\text{an}}) \quad (6)$$

The former one is due to collisions with the main ions [23] and the latter one – due to drift micro-instabilities in the plasma [24]. Normally $D_{\perp}^{\text{neo}} \ll D_{\perp}^{\text{an}}$ and $V_{\perp}^{\text{neo}} \lesssim V_{\perp}^{\text{an}}$. The convection velocities are controlled by the radial gradients of plasma parameters such as density, temperature, safety factor, etc.

The temperature T_Z of impurity species in the parallel pressure gradient on the left hand side of Eq. (4) is changing through the Coulomb collisions with the background plasma particles and is governed by the heat transfer equation:

$$\begin{aligned} & \partial_t (1.5n_Z T_Z) + \nabla_{\perp} (1.5\Gamma_{\perp}^Z T_Z) \\ & + \nabla_{\parallel} (2.5n_Z V_{\parallel}^Z T_Z) \\ & = Q_Z - 1.5\nu_Z n_Z T_Z + 3\nu_{Zi} n_Z (T - T_Z) \end{aligned} \quad (7)$$

where Q_Z is the density of heat assimilated from the ion source. It is worth to note that different impurity charge states are heated by the plasma particles to different temperatures and in the vicinity of local sources of impurity the effect of heating on its parallel transport can be comparable or even higher than that from the electric field arising by impurity ionization.

B. Impurity cooling rate

There are two the most important radiation processes through which plasma electrons lose their energy in interactions with impurity particles. The first one is the line radiation arising when impurity is excited by electron impacts [5]. In hot fusion plasmas the excited particles are normally de-excited spontaneously by radiating photons. Since

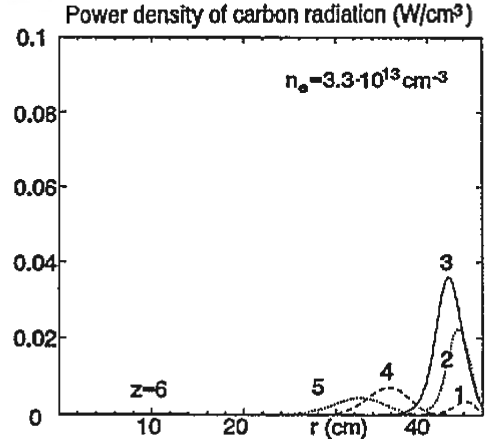


Figure 3: The radial profiles of the radiation loss density for different charge states of carbon impurity entering the plasma through the LCMS located at the minor radius $r = 46 \text{ cm}$, computed with the code RITM for an Ohmic discharge in the tokamak TEXTOR [27].

tokamak plasmas are normally transparent to impurity radiation, this leads to plasma cooling. The second one is Bremsstrahlung arising due to change of electron velocity caused by the attraction towards the impurity nuclei. Normally at the plasma edge the line radiation is the main contribution to the radiation from impurities. The cross-section of the Bremsstrahlung process increases, however, as Z^2 and in the hot central plasma, where impurity particles are strongly ionized, it dominates radiation losses. The temperature dependence of the cooling rate for carbon ions of all charges is shown in Fig. 1. The low ionized B, Be, Li-like charge states with $Z = 1, 2, 3$ are easy to excite since their typical excitation energy E_{ex} is of $5 - 10 \text{ eV}$; the He, H-like ions C^{4+} and C^{5+} with $E_{\text{ex}} \sim E_{\text{ion}} \gtrsim 300 \text{ eV}$ can be excited only at high temperatures; the nuclei C^{6+} contribute to Bremsstrahlung only.

Often, e.g. in the hot central plasma, the effective impurity cooling rate L_I is assessed in the so called corona approximation [5]. It has been developed for the description of Sun corona where the processes of ionization and recombination dominate the particle balances for different charge states and their densities are governed by the relations:

$$k_{Z-1}^{\text{ion}} n_{Z-1} + k_{Z+1}^{\text{rec}} n_{Z+1} = (k_Z^{\text{ion}} + k_Z^{\text{rec}}) n_Z \quad (8)$$

Here $k_{Z,Z\pm 1}^{\text{ion}}$ and $k_{Z,Z\pm 1}^{\text{rec}}$ are the ionization and recombination rate coefficients depending only on the electron temperature. In this case the relative concentrations of different impurity charge states, ζ_Z , and, thus, the effective impurity cooling rate L_I depend also on the local electron temperature only. This de-

pendence is shown for carbon by the solid curve in Fig. 2. The increase of L_I with the temperature at low T is due to temperature behavior of L_Z for impurity ions of low charges with small excitation energies, see Fig. 1. The sharp drop of L_I at high temperatures is due to ionization of impurity particles into dim high- Z states.

At the plasma edge in fusion devices the anomalous transport can be very intensive. Low- Z impurity ions, which are generated from neutrals entering the plasma, have enough time to diffuse into hot plasma regions before they are ionized into dim high- Z states. Therefore, transport processes increase effective cooling rate and make it less temperature sensitive compared to the corona approximation without transport effects; see Fig. 2 where L_I is shown by dashed and dash-dotted curves for different values of the impurity diffusivity D_\perp [25]. Similarly the charge-exchange of impurity ions with hydrogen neutrals affects L_I [26]. The effects of elementary and transport processes on the density, radiation losses and ion heat exchange from impurity are taken firmly into account in transport codes. Figure 3 shows the radial profiles of the radiation loss density for different charge states of carbon computed by the code RITM (Radiation of Impurity and Transport Model) for an Ohmic discharge in the tokamak TEXTOR [27]. One can see that the Li-like ions C^{3+} are the main contributors to the radiation losses. This is explained by the fact that, on the one hand, the characteristic excitation energy of these ions is relatively low, of 8 eV , and, on the other hand due to high enough ionization energy of 64 eV they live long and penetrate deeply into the plasma.

In the vicinity of intense localized impurity sources, e.g. diagnostic beams, injection valves or suddenly melted parts of the wall, one has to take into account the essential time-dependence and three-dimensionality of the impurity spreading process. During the life time $\tau_{\text{ion}}^Z \equiv 1/(k_Z^{\text{ion}}n)$ impurity ions of the charge state Z move along the magnetic field and diffuse in the direction y perpendicular to the field at distances $l_Z \approx V_\parallel^Z \tau_{\text{ion}}^Z$ and $\delta_Z \approx \sqrt{D_\perp \tau_{\text{ion}}^Z}$, respectively. On the one hand the area $A_Z = \delta_Z l_Z$ occupied by ions of low Z ions with very large k_Z^{ion} and small τ_{ion}^Z is negligible compared with the total area A_S of the magnetic surface. On the other hand, k_Z^{ion} decreases with increasing Z and, thus, A_Z grows up also. Therefore, the Z -state serves as an intensive but localized source for the next charge state. All together the regions on the magnetic surface occupied by charge states with $A_Z < A_S$ form a set of nested shells evolving in time. By using this ‘‘shell’’ approximation [28] one can complement transport codes, modeling the radial profiles of impurity ion densities, e.g., RITM, with a description of non-stationary spreading of impurity on magnetic surfaces.

III. THERMAL INSTABILITIES DUE TO RADIATION AND COULOMB COLLISIONS WITH IMPURITY

Presence of impurity can make a significant effect on the plasma parameters. In turn, this changes impurity transfer in such a perturbed plasma. The plasma can be significantly disturbed by: (i) the production of additional electrons by impurity ionization, (ii) electron heat losses on impurity excitation and ionization, (iii) heat transfer from the main ions to impurity ones by Coulomb collisions. The influence on the temperatures of electron and the main ion, T_e and T_i , respectively, is governed by the heat transport equations:

$$1.5n\partial_t T_e - \kappa_\parallel^e \Delta_\parallel T_e - \kappa_\perp^e \Delta_\perp T_e = -Q_{\text{rad}} \quad (9)$$

$$1.5n\partial_t T_i - \kappa_\parallel^i \Delta_\parallel T_i - \kappa_\perp^i \Delta_\perp T_i = -Q_{\text{coll}} \quad (10)$$

where $\kappa_\parallel^e \gg \kappa_\parallel^i \gg \kappa_\perp^e > \kappa_\perp^i$ are the components of the electron and ion heat conduction parallel and perpendicular to the magnetic field and $Q_{\text{coll}} = 3\nu_{Zi}n_Z(T_i - T_Z)$ is the power density of heat losses due to Coulomb collisions [21]. Consider the plasma region inside the last closed magnetic surface (LCMS) in a limiter tokamak or inside the separatrix in a divertor device. Initially the temperatures $T_e = T_i = T_0$ are assumed constant on a magnetic surface and impurity ions are cold, $T_Z \ll T_0$. Consider a spontaneous fluctuation in the temperature periodic in the direction l of the magnetic field:

$$T_{e,i} = T_0 + \delta T_{e,i} \times \exp(ikl + \gamma t)$$

where $k = 2\pi/\lambda$ with λ being the perturbation wave length, and γ is the growth rate of the perturbation which has to be determined. The plasma pressure $P = n(T_e + T_i)$ is equilibrated along field lines very fast and the temperature change leads to the perturbation in the plasma density:

$$\frac{\delta n}{n_0} = -\frac{\delta T_e + \delta T_i}{T_0} \quad (11)$$

Thus, at the position where the temperature is reduced the density is increased. We on purpose omit here the finiteness of the time required for movement of the main ions to cooled area as it allows us to exclude acoustic waves inessential for this consideration. By using the latter relation and linearizing Eqs. (9) and (10) for small perturbations, we get a system of equations for the perturbation amplitudes $\delta T_{e,i}$:

$$\begin{aligned} & \gamma(2\delta T_e + 0.5\delta T_i) + \frac{k^2 \kappa_\parallel^e}{n} \delta T_e \\ & = n_I \left[\frac{L_I}{2T_0} \delta T_i + \left(\frac{L_I}{2T_0} - \frac{dL_I}{dT_0} \right) \delta T_e \right] \quad (12) \end{aligned}$$

$$\begin{aligned} & \gamma(2\delta T_i + 0.5\delta T_e) + \frac{k^2 \kappa_\parallel^i}{n} \delta T_i \\ & = \frac{Q_{\text{coll}}}{T_0} (\delta T_i + 0.5\delta T_e) \quad (13) \end{aligned}$$

which nontrivial solution provides an equation for perturbation growth rate. Consider two limit cases. If radiative electron cooling prevails, $\delta T_e \gg \delta T_i$, it reduces to:

$$\gamma = \frac{n_I}{2} \left(\frac{L_I}{2T_0} - \frac{dL_I}{dT_0} \right) - \frac{k^2 \kappa_{\parallel}^e}{2n} \quad (14)$$

In the limit case of dominant Coulomb ion cooling, $\delta T_i \gg \delta T_e$, it provides:

$$\gamma = \frac{Q_{\text{coll}}}{T_0} - \frac{k^2 \kappa_{\parallel}^i}{n} \quad (15)$$

Small spontaneous reduction of plasma component temperatures provokes an increase in plasma density, n , caused by the pressure equilibration. This increases the heat losses both from electrons through the rising radiation and from the main ions due to heat exchange with impurity ions in Coulomb collisions. As it is seen from Eqs. (14) and (15), in both cases plasma heat conduction reduces the growth rate of perturbation and plays a stabilizing role. An instability develops, i.e. $\gamma \geq 0$ and initial spontaneous perturbations grow exponentially with time, if with increasing either plasma density or impurity content the heat losses from the main plasma components exceed the critical level which can not be compensated by the heat fluxes coming to impurity cloud with heat conduction. This level can be described by the parameter $\eta = n_I n / k^2$. For electron radiation instability this threshold value is equal to:

$$\eta_{\text{rad}} = \frac{\kappa_{\parallel}^e}{0.5L_I/T_0 - dL_I/dT_0} \quad (16)$$

and for cooling instability induced by heat exchange with impurity ions by Coulomb collisions:

$$\eta_{\text{coll}} = \frac{\kappa_{\parallel}^i T_0}{Q_{\text{coll}}} \quad (17)$$

This provides a hint for understanding why the MARFE, considered often as the non-linear stage of the radiation instability, develops in the inner plasma edge at the high field side (HFS). Due to the Shafranov shift of the plasma axis the distance between magnetic surfaces is larger at the HFS than at the low field side (LFS). Therefore, the radial temperature gradient and heat flux from the plasma core are weaker at the HFS. Already in the stationary state before plasma becomes unstable there is an inhomogeneity along the magnetic field so that the plasma temperature is somewhat lower and density is larger at the HFS than at the LFS. Therefore, the critical heat losses are reached first at the HFS and the radiation instability, leading to the MARFE formation, develops first there. One has to mention that also other mechanisms for the energy loss are of importance for the MARFE formation. In particular the perpendicular convection of charged particle from the MARFE

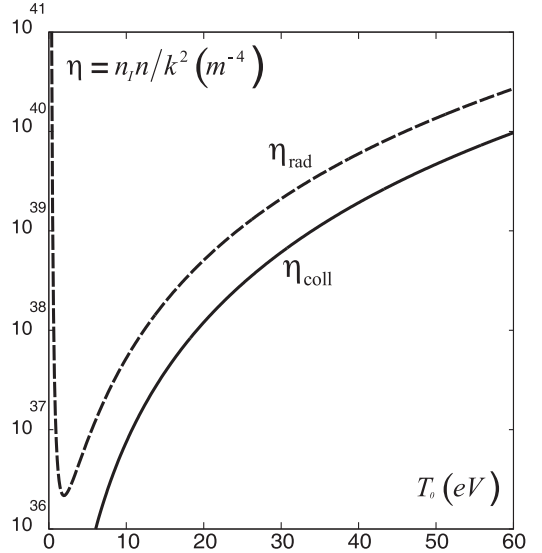


Figure 4: Critical parameter η for the development of thermal instabilities due electron cooling with carbon radiation and cooling of the main ions by Coulomb collisions with impurities.

region with increased density to the inner wall is considered now as an important one [25, 30].

For particular plasma conditions and impurity species η_{rad} and η_{coll} are functions of initial plasma temperature T_0 only. Figure 4 demonstrates this dependences for typical parameters of deuterium plasma with carbon impurities [29]. One can see that for the conditions usual for MARFE development, with the edge temperature below 50 eV, ion collision instability can develop at the product of the plasma and impurity densities several times smaller, than that required for development of electron radiation instability. For higher charge states this difference even stronger since $Q_{\text{coll}} \sim \nu_{Zi} \sim Z^2$. Thus, by studying the MARFE development one has to take ion-ion collisions into account.

IV. STABLE RADIATING LAYER AT THE PLASMA EDGE

Up to now we have neglected the fact that in fusion devices the temperature is inhomogeneous in the radial direction: since the heat is deposited into the plasma core and is transferred to the plasma edge with perpendicular plasma heat conduction a strong radial temperature gradient exists. This is, however, of very importance for the creation of a stable radiating layer at the edge. Such a layer would be very beneficial for the protection of wall elements from intensive heat loads and has been successfully realized in

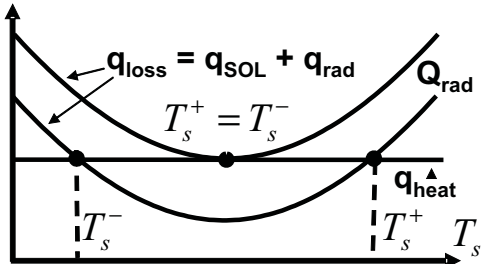


Figure 5: Dependence of the total losses from the plasma with the heat conduction to the SOL and edge radiation from impurity on the plasma temperature at the LCMS. Two stationary states can exist and that with the lower temperature is unstable. These states are merging, $T_s^+ = T_s^-$, when the maximum radiation level is achieved. No stationary states exist when q_{heat} is smaller than the minimum q_{loss} .

additionally heated discharges in TEXTOR by puffing of neon. Under these conditions up to 85–90% of the input power is radiated from the plasma edge inside the LCMS without MARFE formation or shrinking of the plasma column. To understand why it is possible, we proceed from the stationary heat balance at the edge homogeneous along magnetic field, i.e., from Eq. (9) with the first and second terms on the left hand side neglected:

$$-\kappa_{\perp} d^2T/dx^2 = -Q_{\text{rad}} \quad (18)$$

where x is the distance from the LCMS toward the plasma axis and $T_e = T_i = T$ is assumed henceforth. Moreover, we take into account that with a realistic level of the impurity particle diffusion of $1 \text{ m}^2/\text{s}$ the effective cooling rate L_I is nearly constant for the temperatures lower than a certain level T_{max} being close to the ionization energy of the impurity Li-like ions, see Fig. 2. For the sake of an analytical treatment we assume $Q_{\text{rad}}(T) = Q_0 = \text{const}$ for $T \leq T_{\text{max}}$ and $Q_{\text{rad}} = 0$ for $T > T_{\text{max}}$. The boundary condition at the LCMS, $x = 0$, is given by $dT/dx = T/\delta_T$ with the e-folding length δ_T prescribed by transport processes in the scrape-off layer (SOL) beyond the LCMS. At the interface of the radiating layer with the plasma core, $x = \Delta_{\text{rad}}$, $T = T_{\text{max}}$ and $\kappa_{\perp} dT/dx = q_{\text{heat}}$ where the latter is determined by the heating power in the plasma core. Thus, we have three boundary conditions for the second order ordinary differential equation (18). All of them are needed because Δ_{rad} is unknown *a priori*.

As a result of the integration of Eq. (18) one gets the following relation for the plasma temperature at LCMS, T_s :

$$T_s^{\pm} = \left(Q_0 \delta_T \pm \sqrt{Q_0^2 \delta_T^2 + q_{\text{heat}}^2} \right) \frac{\delta_T}{\kappa_{\perp}} \quad (19)$$

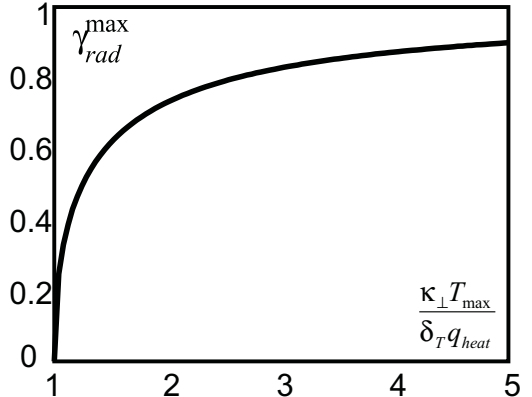


Figure 6: The variation of the maximum radiation level in stable steady states with the parameter characterizing transport, heating and impurity radiation ability.

The solution T_s^- is unstable. This can be seen by determining T_s from the edge power balance

$$q_{\text{heat}} = q_{\text{loss}} \equiv q_{\text{SOL}} + q_{\text{rad}} \quad (20)$$

where the first term in q_{loss} is the heat flux $q_{\text{SOL}} = \kappa_{\perp} T/\delta_T$ conducted by the plasma through the LCMS into the SOL and the second one, $q_{\text{rad}} = \Delta_{\text{rad}} Q_0$, is lost with the impurity radiation. The dependence q_{loss} on T_s is shown in Fig. 5 for two different magnitudes of Q_0 . Two stationary solutions exist if Q_0 is not too small and not too large. In the stationary state with $T_s = T_s^-$ a spontaneous reduction of T_s would lead to an increase of the energy losses due to widening of the radiating edge layer. Therefore T_s would decrease further, i.e., an instability takes place. A similar analysis shows that the solution T_s^+ is stable. The maximally achievable radiation level $\gamma_{\text{rad}} \equiv \Delta_{\text{rad}} Q_0 / q_{\text{heat}}$ in this state corresponds to the case where T_s^+ merges with T_s^- when Q_0 increases up to the critical level. This provides:

$$\gamma_{\text{rad}}^{\text{max}} = 1 - \frac{\kappa_{\perp} T_{\text{max}}}{q_{\text{heat}} \delta_T} + \sqrt{\left(\frac{\kappa_{\perp} T_{\text{max}}}{q_{\text{heat}} \delta_T} \right)^2 - 1} \quad (21)$$

Figure 6 displays the dependence of $\gamma_{\text{rad}}^{\text{max}}$ on the parameter combination $\kappa_{\perp} T_{\text{max}} / (q_{\text{heat}} \delta_T)$. One can see that with passing from Ohmic plasmas with relatively low transport (small κ_{\perp}) and intrinsic carbon impurity ($T_{\text{max}} \approx 60 \text{ eV}$) to additionally heated discharges with high transport (large κ_{\perp}) and seeding of neon ($T_{\text{max}} \approx 200 \text{ eV}$) the maximally achievable radiation level γ_{rad} without instability increases, as it takes place in the experiment [7].

When the critical level of Q_0 is exceeded, there is no anymore stationary states in the framework of the model considered above. This leads to the steadily cooling of the plasma edge. When T_s decreases below the excitation energy of low-Z impurity ions of

5 – 10 eV, the radiating layer develops in a radiating toroidal shell which shrinks towards the plasma axis [31]. This processes can, however, be terminated: the heat flux density from the core increases because the plasma current, that is maintained constant, flows in a narrower channel. Thus, the current density and ohmic heating in the core increase. As a result a “detached plasma” state develops [27].

V. DIVERTOR DETACHMENT CAUSED BY IMPURITY RADIATION

In a divertor configuration the radiation of impurities can be localized in the divertor volume, see Fig. 7, where the plasma state is essentially controlled by the recycling of charged particles and energy loss to the target plate [32]. Normally neutrals of the working gas of hydrogen isotopes are ionized very close to the plate in the “recycling zone”. In that zone heat is transported by the convection of plasma particles towards the plate. By going deeper into the plasma, at a distance larger than neutrals penetrate, the intensity of the charged particle source and, thus, the plasma flux drop and in the “conduction zone” the heat is transported predominantly by the heat conduction[33].

Consider an impurity particle eroded from the divertor target and entering the SOL plasma as a neutral. Because of the difference in masses the impurity atom is ionized at a shorter distance than hydrogen ones, i.e. still in the recycling region where the plasma flows to the plate with a velocity close to the sound speed. Huge friction between the plasma flow and newly born impurity ion will drag the latter in a short time back to the plate so that it will not have any opportunity to be excited and radiate. Does it mean that there is no any chance for impurity particles to “sneak away” and enter the conduction region where the thermal force overcomes the friction? This is not the case for impurity neutrals produced sufficiently close to the lateral side of the SOL. They can escape from the plasma layer into the gas volume and return back in the conduction region of the SOL. Let us estimate the probability of such a process, ω_{cond} . A neutral which has been produced at the plate at a distance y from the SOL side and moves towards it with a velocity v_0 will be not ionized in the SOL with a probability of $\exp(-y/l_0)$, where $l_0 = v_0/(k_0 n_p)$ is the penetration depth with k_0^{ion} being the ionization rate coefficient for impurity neutrals computed at the plasma temperature near the plate, T_p , and n_p is the plasma density there. By averaging this value over the SOL width Δ , we obtain:

$$\omega_{\text{cond}} = \frac{l_0}{\Delta} \left[1 - \exp\left(-\frac{\Delta}{l_0}\right) \right]$$

For typical plasma parameters in Div-I divertor in ASDEX-U [32], $T_p \approx 10$ eV, $n_p \approx 10^{20} \text{ m}^{-3}$, $\Delta \approx$

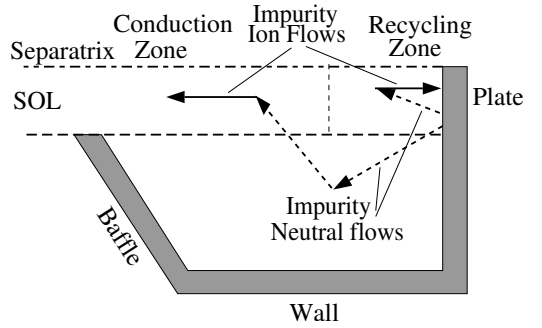


Figure 7: Geometry of the divertor volume, “recycling” and “conduction” zones in the plasma and flows of impurity neutrals and ions.

5 cm, one gets $\omega_{\text{cond}} \approx 0.1$ for carbon neutrals with $v_0 \approx 10^6 \text{ cm/s}$. This value is by several orders of magnitude larger than the probability of direct neutral penetration into the conduction zone of the SOL.

Another important parameter is the plasma temperature T_c at the interface between “recycling” and “conduction” zones. This value defines the actual range of temperatures, $T_c < T < T_{\text{max}}$, in which impurities radiate in the divertor SOL. To find T_c one should consider the particle and energy transport in the recycling region. We do this in a simple one-dimensional approximation by taking into account transport processes along magnetic field (l -direction) only. The density of recycling hydrogen neutrals, n_a , and the plasma density are determined from the continuity equations:

$$d(-D_a dn_a/dz)/dz = -k_{\text{ion}} n n_a \quad (22)$$

$$d(nV_{\parallel})/dl = k_{\text{ion}} n n_a \quad (23)$$

where $z = -l \sin \psi$ is the distance from the plate, $\psi \approx 0.1$ the angle between the plate and magnetic field; the transport of neutrals is described in a diffusive approximation by taking into account that neutral velocities change chaotically by charge-exchanges and $D_a = T/[nm_i(k_{\text{cx}} + k_{\text{ion}})]$ is the neutral diffusivity with k_{cx} and k_{ion} being the rate coefficients of charge-exchange and ionization of hydrogen atoms, respectively. At the plate, $l = z = 0$, full recycling takes place, i.e.,

$$-D_a \frac{dn_a}{dx} = -nV_{\parallel} \sin \psi$$

The plasma parallel velocity V_{\parallel} is governed by the conservation of the parallel momentum:

$$m_i n V_{\parallel}^2 + 2nT = 4n_p T_p \quad (24)$$

where it is taken into account that at the target the Bohm criterion, see, e.g., Ref. [20], has to be satisfied, i.e. V_{\parallel} is equal to the ion sound velocity

$c_s \equiv \sqrt{2T_p/m_i}$. In the recycling zone the radiation losses can be neglected and the plasma temperature here is governed by the conservation of the energy flux:

$$-\kappa_{\parallel} dT/dl + 5nV_{\parallel}T = \gamma c_s T_p \quad (25)$$

with $\gamma \approx 7.5$ being the so called heat transmission factor [20].

The plasma temperature at the plate, T_p , is taken as a parameter and the transport equations above are integrated numerically that gives their values as at larger $|l|$ and z . At a certain position with the temperature T_c the balance of the friction and thermal forces applied to impurities from the background particles is met:

$$m_z \nu z_i V_{\parallel} \approx -\xi_Z dT/dl \quad (26)$$

Calculations show that $T_c \approx T_p$ if T_p exceeds 30-40 eV and exceeds T_p by a factor of 3 if this is below 10eV.

Consider now the conduction zone. Here the thermal force accelerates impurity ions away from the plate up to a velocity at which the friction force with background particles, being nearly at rest, is in balance with the thermal force. Thus, also in this case the balance of forces applied to impurity ions can be described by Eq. (26) but with $-V_{\parallel}^Z$ instead of V_{\parallel} . This determines the impurity velocity and density:

$$V_{\parallel}^Z \approx \frac{\xi_Z}{\nu z_i m_z} \frac{dT}{dl}, \quad n_I \approx \frac{\Gamma_I^c}{V_{\parallel}^Z} \quad (27)$$

where Γ_I^c is the influx density of impurity neutrals into the conduction region averaged over the SOL width. This value is governed both by the impurity source due to erosion of the plate and by the conductance of the recycling region for neutrals. The former one is determined by the density of the plasma flux to the plate and the erosion coefficient Y_I . As a result we get:

$$\Gamma_I^c \approx n_p c_s \cdot Y_I \cdot \omega_{\text{cond}} \quad (28)$$

In the conduction part of the SOL the heat balance equation should take into account the energy losses with radiation,

$$\frac{d}{dl} \left(-\kappa_{\parallel} \frac{dT}{dl} \right) = -n n_I L_I \quad (29)$$

Since the plasma velocity here is much smaller than the ion sound speed, Eq. (24) results in the pressure balance $nT = 2n_p T_p = P_s$ with P_s being the plasma pressure at the separatrix. With the definitions of νz_i and κ_{\parallel} [21] and the n_I found above, we obtain:

$$\frac{d}{dl} \left(\kappa_{\parallel} \frac{dT}{dl} \right) \approx \sqrt{\frac{m_i}{m_e}} P_s^2 L_I \Gamma_I^c \left(T \kappa_{\parallel} \frac{dT}{dl} \right)^{-1} \quad (30)$$

This equation, multiplied by $3\kappa_{\parallel}^2 \frac{dT}{dl}$ and integrated over T from T_c to T_{max} , provides an equation for the plasma temperature at the target plate:

$$F_p + F_r \approx R \quad (31)$$

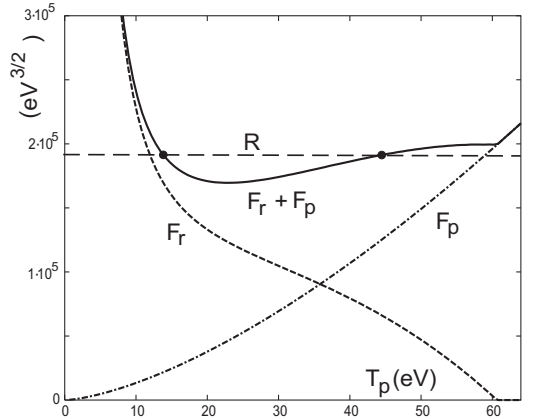


Figure 8: Functions $F_p(T_p)$ and $F_r(T_p)$ and their sum vs the plasma temperature at the target plate.

where $F_p = \gamma^3 T_p^{1.5}$ and

$$F_r = 2.4 Y_I \omega_{\text{cond}} \sqrt{\frac{m_i}{m_e}} m_i L_0 \frac{\kappa_{\parallel}(T_{\text{max}}) - \kappa_{\parallel}(T_c)}{\sqrt{T_p}}$$

and their sum are displayed in Fig. 8 as functions of T_p for deuterium SOL plasma in contact with divertor plates of carbon. The erosion coefficient $Y_I = 0.02$ was assumed independent of T_p since at low temperatures physical sputtering [18] of carbon is replaced by chemical erosion with roughly constant Y_I [19].

The right hand side of Eq. (31),

$$R \equiv \left(q_{\text{heat}}^{\parallel} \sqrt{2m_i/P_s} \right)^3$$

with $q_{\text{heat}}^{\parallel}$ being the density of the parallel heat flux into the divertor, is independent of T_p but controlled by global plasma parameters such as the heating power W_{heat} and the mean density $\langle n \rangle$. For a Bohm-like perpendicular transport in the SOL [20]:

$$R \sim W_{\text{heat}}^{2.7} / \langle n \rangle^{4.7}$$

Thus, as in the case of the edge radiating layer in the confinement region with perpendicular energy transport, see section IV and Fig. 5, stationary states in divertor exist if R is large enough, i.e. for sufficiently strong heating and not too high plasma density. If the former is fixed and the density increases above the critical level there are no steady state, the plasma near the target plate cools down due to impurity radiation, detachment from the plate and X-point MARFE should develop. The used system of transport equations fails to describe this evolution because many processes important at low temperatures are not taken into consideration. In particular, when T_p becomes noticeably less than the ionization potential of hydrogen, neutrals recycling from the plate freely

escape into the gas surrounding the plasma layer. These particles return later into the SOL through its lateral side and contribute significantly to momentum and heat dissipation [33]. Additionally, diverse channels for recombination of charged particles can influence all balances and govern the plasma state in a detached divertor.

REFERENCES

1. D.M. MEADE, Nucl. Fusion **14**, 289 (1974).
2. R.V. JENSEN, et al., Nucl. Fusion **17**, 1187 (1977).
3. V.A. VERSHKOV and S.V. MIRNOV, Nucl. Fusion **14**, 383 (1974).
4. R.J. HAWRYLUK, et al., Nucl. Fusion **19**, 1307 (1979).
5. D.E. POST, et al., Atomic Data and Nuclear Data Tables **20**, 397 (1977).
6. Y. SHIMOMURA, Nucl. Fusion **17**, 626 (1977).
7. U. SAMM, et al., Plasma Phys. Contr. Fusion **35**, B167 (1993).
8. R.S. GRANETZ, et al., Nucl. Fusion **47**, 1086 (2007).
9. G.M. MCCRACKEN, et al., J. Nucl. Mater. **145-147**, 181 (1987).
10. U. SAMM, et al., J. Nucl. Mater. **176-177**, 273 (1990).
11. J. WESSON, *Tokamaks, third Edition*, Clarendon Press, Oxford (2004).
12. J.L. TERRY, et al., Bul. Am. Phys. Soc. **26**, 886 (1981).
13. F. ALLADIO, et al., Phys. Lett. **90A**, 405 (1982).
14. D.R. BAKER, et al., Nucl. Fusion **22**, 807 (1982).
15. A. LOARTE, et al., Nucl. Fusion **38**, 331 (1998).
16. E.A. LASARUS, et al., J. Nucl. Mater. **121**, 61 (1984).
17. J. ONGENA, et al., Physica Scripta **52**, 449 (1995).
18. W. ECKSTEIN, et al., *Atomic and Plasma-Material interaction data for fusion (Suppl. to Nucl.Fusion)* **1**, 51 (1991).
19. A.A. HAASZ, et al., *Atomic and Plasma-Material interaction data for fusion (Suppl. to Nucl.Fusion)* **7A**, 9 (1998).
20. P.C. STANGEBY *The Plasma Boundary of Magnetic Fusion Devices*, IoP Publishing, Bristol, (2000).
21. S.I. BRAGINSKII in *Reviews of Plasma Physics* edited by Leontovich M A, New York, Consultants Bureau, **1**, 205 (1965).
22. S. CHAPMAN Proc. Phys. Soc., London, Sect. A, **72**, 353 (1958).
23. S.P. HIRSHMAN and D.J. SIGMAR, Nucl. Fusion **21**, 1079 (1981).
24. J. WEILAND *Collective Modes in Inhomogeneous Plasmas, Kinetic and Advanced Fluid Theory*, IOP Publishing, Bristol (2000)
25. M.Z. TOKAR and F.A. KELLY, Phys. Plasmas **10**, 4378 (2003).
26. D.E. POST, J. Nucl. Mater. **220-222**, 143 (1995).
27. M.Z. TOKAR, Plasma Phys. Control. Fusion **36**, 1819 (1994).
28. M. KOLTUNOV and M.Z. TOKAR *Plasma Phys. Control. Fusion* **54**, 025003 (2012).
29. M.Z. TOKAR and M. KOLTUNOV, Phys. Rev. E **85**, 046412 (2012).
30. M.Z. TOKAR, et al., J. Nucl. Mater **266-269**, 958 (1999).
31. U. SAMM, et al., Properties of “detached” plasmas, IPP Rep. Jül-2123, 1987.
32. U. WENZEL, et al., Plasma Phys. Control. Fusion, **41**, 801 (1999).
33. A.V. NEDOSPASOV and M.Z. TOKAR, in *Reviews of Plasma Physics*, edited by Kadomtsev B.B., Consultants Bureau **18**, 77 (1993).

STOCHASTIC BOUNDARY PLASMA IN TOKAMAKS WITH RESONANT MAGNETIC PERTURBATIONS

Y. Liang

Forschungszentrum Jülich GmbH, Institut für Energie- und Klimaforschung - Plasmaphysik, 52425 Jülich, Germany

August 10, 2015

ABSTRACT

Experimental results from different devices demonstrate that magnetic topology plays a key role in plasma confinement, edge MHD stability, and interactions between the plasma and the first wall, particularly with the divertor. Recently, three-dimensional (3D) magnetic topology effects, which are associated with stochastic boundary plasma physics, form one of the hottest topics in fusion research today, and understanding them is essential for the success of future fusion devices. In this paper, an overview of the physics understanding of the formation first of 3D magnetic topology and then of a stochastic layer, and its effects on the edge and divertor transport and on MHD stability in tokamak plasmas will be presented. In addition, comparing the advantages and disadvantages of 2D and 3D magnetic topology effects in magnetic confinement fusion will be discussed.

I. INTRODUCTION

On the basis of the fusion research achievements of the past half century, it is foreseen that a steady state operation of ITER [1] and future fusion power plants, e.g. DEMO, will require the resolution of plasma wall interaction, in which a tolerable plasma exhaust, including steady state and transient heat and particle fluxes on plasma-facing components, is controlled reliably by one or more mechanisms at high power densities.

A. Problem of transient plasma wall interaction

The standard tokamak H-mode [2] is foreseen as the baseline operating scenario of a future fusion machine, e.g. ITER. However, the steep plasma pressure gradient and associated increased current density at the edge pedestal could exceed a threshold value for driving magnetohydrodynamic (MHD) instabilities referred to as Edge Localized Modes (ELMs). Using results from various current devices, an extrapolation of the heat and particles deposited on the wall components has been carried out for ITER. Since the exact physics and scaling is unknown, the predicted

ELM energy loss ranges from ~ 5 to $22MJ$ [4]. It is expected that approximately half of this energy will reach the wall and be deposited over a region of $\sim 1m^2$, known as the wetted area. Thus, the surface energy density is suggested to be 2.5 to $11MJm^{-2}$ which is ~ 5 to 20 times higher than acceptable for the planned first wall components, primarily made of tungsten or carbon fibre composites, which can receive a maximum of $0.5MJm^{-2}$. Therefore, it is important to find mitigation/suppression solutions for ELMs.

B. Problem of stationary plasma-wall interaction

In a fusion reactor, a significant amount of heating power, which is mainly from auxiliary heating and energetic α particles produced in the D-T burning plasmas, has to be continuously exhausted through radiation or deposited directly on the plasma facing components during long-pulse or steady-state operation. Since the transport along field lines is several orders of magnitude higher than the cross field transport, this results a very rapid decay of the profiles inside the scrape-off layer (SOL) which causes a thin power deposition width, λ_q .

$$\lambda_q \approx \pi q R \sqrt{\frac{\chi_{\parallel}}{\chi_{\perp}}}, \quad (1)$$

Here, R is the major radius of the tokamak, q is the safety factor at the edge, χ_{\parallel} and χ_{\perp} are the energy diffusion coefficients in the direction parallel and perpendicular to the field lines, respectively.

Based on the present experimental scaling[3], λ_q is expected to be less than $1mm$, and then the parallel heat flux may approach $1GWm^{-2}$ for ITER. This obviously exceeds the engineering capability for any plasma-facing component. Therefore, it is necessary both to decrease the power conducted and convected to the edge by enhancing exhaust through non-magnetically confined particles (neutral atoms or photons) and also to increase the λ_q by controlling the edge plasma transport.

C. Stochasticity in Fusion Plasmas

The success of the *stochastic ansatz* goes back to 1905, when Einstein published three fundamental papers, one of which was on Brownian motion

[5, 6], a simple continuous-time stochastic process in natural science. Nowadays, the term stochastic occurs in a wide variety of professional or academic fields to describe events or systems that are unpredictable due to the influence of a random variable. The theory of stochasticity has been further developed [7, 8, 9, 10, 11]. Recently, *stochastic transport* theory was developed for plasmas [12].

In a magnetically confined fusion device, resonant magnetic perturbations (RMPs) can tear the nested flux surfaces and generate magnetic islands. The width of the magnetic island is proportional to the square root of the perturbation field. By simply increasing the perturbation field, the island width can be increased. Due to the fixed distance between neighbouring islands, the island chains will grow and further overlap. Then, the field lines start to behave in a chaotic way and all closed flux surfaces between the two surfaces will be destroyed. A standard criterion of stochastization is the Chirikov parameter, σ_{ch} , which is the ratio of the island width to the radial distance between the neighbouring island-chains. When $\sigma_{ch} \geq 1$, the criterion indicates island overlapping [8]. The magnetic fields between these two surfaces are now called *stochastic* or *ergodic*. These two terms are used with almost the same meaning in the fusion community although there is some difference in their mathematical meanings. If the overlapping of island chains exists, the transport (radial) will be greatly enhanced and the pedestal gradient could be reduced.

Very recently, structure formation and transport in stochastic plasmas has been a topic of growing importance in many fields of plasma physics from astrophysics to fusion research. In particular, the investigation of the possibility of controlling the particle and heat transport by the formation of a stochastic boundary layer has been investigated on most large and medium-sized magnetic confinement fusion devices across the world [13]. A major result was discovering that large type-I ELMs in H-mode tokamak plasmas can be mitigated [14] or even suppressed [15] by RMPs. This discovery opens up a possible mechanism for suppressing large type-I ELMs in future fusion devices such as ITER. However, it is widely recognized that a more basic understanding of the plasma response to the RMPs is needed to extrapolate the results obtained in present experiments to future fusion devices.

D. Scope of this lecture

This lecture will address the topic of stochastic boundaries and focus on three-dimensional (3D) edge physics and applications of RMPs in tokamaks. However, this topic itself is not specific to the tokamak magnetic configuration. In both tokamaks and stellarators, stochastic magnetic fields can arise and influence the interplay between 3D magnetic topology and plasma confinement. Stellarator devices repre-

sent an inherent 3D challenge. They make use of the island divertor concept, and stochasticity and magnetic topology therefore play a fundamental role in their operation. With the extended operational regimes pioneered on the Large Helical Device (LHD), and with W7-X, attention has been directed towards the challenge of 3D plasma equilibria, transport and plasma-surface interactions.

In this lecture, the fundamental physics of the formation of a stochastic boundary layer by the application of RMPs will be described. The physics of stochastic boundary plasmas including the rotational screening effect, the plasma equilibrium effect on the magnetic topology, and stochastic plasma transport and its effects on plasma-wall interactions will be discussed. Finally, the application of RMPs for controlling pedestal profiles and stability will be presented.

II. FORMATION OF A STOCHASTIC BOUNDARY LAYER IN MAGNETICALLY CONFINED FUSION PLASMAS

A. Resonant magnetic perturbations

Magnetic perturbations which are resonant with field lines in the plasma are known as RMPs. The resonance condition is fulfilled when the inverse winding number of the field lines, in tokamak physics known as the safety-factor

$$q = \frac{1}{2\pi} \oint \frac{B_t}{RB_p} ds, \quad (2)$$

corresponds to the ratio of the applied poloidal m and toroidal n perturbation mode numbers: $q = \frac{m}{n}$. Here, R is the major radius of the torus, B_t and B_p the toroidal and poloidal magnetic field components, and ds the line element in the poloidal plane. The term RMP is mostly used if the perturbation is deliberately applied. In a magnetic confinement device, several resonance conditions are usually fulfilled due to the continuous q -profile. As will be seen below, the key resonant perturbations are those in the plasma boundary.

B. Methods of producing RMPs

A standard technique for producing such RMPs is the usage of either in-vessel or external coil systems with a certain geometry to apply the required poloidal and toroidal mode numbers. The main focus is often on low toroidal mode numbers, usually in the range of 1 to 4. Although the general idea is always the same, the design of such RMP coil systems differs greatly from device to device.

On JET, the error field correction coils (EFCCs), which are located outside of the vacuum vessel, as seen in figure 1, are used to apply RMPs. They were originally designed to correct the intrinsic error field of misaligned toroidal field coils. As a consequence of

the large distance between the coils and the plasma edge, a strong current of several tens of kA is required to achieve an adequate perturbation of the plasma edge using such EFCCs.

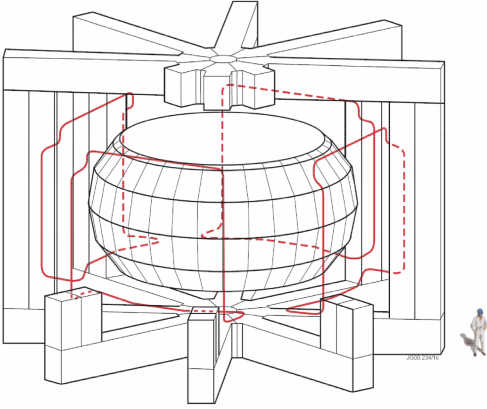


Figure 1: Perspective view of JET showing the 4 large error field correction coils mounted between the transformer limbs.

Depending on the wiring of the EFCCs, either $n = 1$ or $n = 2$ fields can be created [17]. The effective radial resonant magnetic perturbation amplitude, $|b_{res}^{r,eff}| = |B_{res}^{r,eff}/B_0|$, where $B_{res}^{r,eff}$ and B_0 are the radial resonant magnetic perturbation field and the on-axis toroidal magnetic field, respectively, calculated for $I_{EFCC} = 1kAt$ in $n = 2$ configuration, is shown in figure 2. $|b_{n=2}^{r,eff}|$ is the $n = 2$ effective radial resonant magnetic perturbation amplitude.

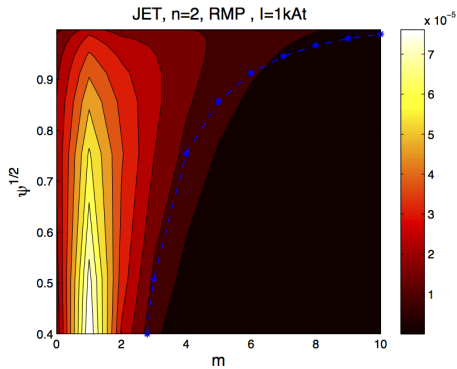


Figure 2: Radial component of the $n = 2$ helical mode spectrum with $I_{EFCC} = 1kAt$ using vacuum fields. Here, the x-axis is the poloidal mode number, m . The calculation is based on an equilibrium reconstruction for JET pulse #69557 at 20s. Pitch resonant modes with $m = nq(\Psi)$ are shown by the blue dashed line.

Recently, the formation of helical current fila-

ments flowing along field lines has been observed in the SOL during the application of lower hybrid waves (LHWs) on the Experimental Advanced Superconducting Tokamak (EAST) [18]. Magnetic perturbations induced by the currents flowing in these edge helical filament structures have been measured by a set of Mirnov coils during the modulation of LHWs. Because of the geometric effect of the LHW antenna, the perturbation fields induced by the HCFs are dominated by the $n = 1$ component. The magnetic perturbation spectrum calculated based on the experimental parameters indicates a good resonant feature, whereby the plasma edge resonant surfaces are well aligned on the ridge of the spectrum as seen in figure 3.

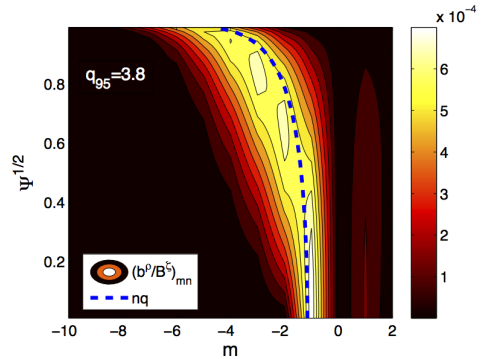


Figure 3: Radial component of the $n = 1$ helical mode spectrum calculated with $1kA$ HCF current. The calculation is based on an equilibrium reconstruction for a EAST pulse. Pitch resonant modes with $m = nq(\Psi)$ are shown by the blue dashed line.

C. 3D magnetic topology in tokamaks with RMPs

The application of RMPs results in the reorganization of the magnetic topology into a new equilibrium state. Resonances outside the plasma (in the SOL) cause an external kinking of the plasma; resonances inside the plasma lead to internal kinking and magnetic reconnection processes, also known as tearing. Due to this reconnection, magnetic islands are created on surfaces at locations where q is resonant. On these flux surfaces, groups of islands form which correspond in the number of islands in the poloidal and toroidal directions with the poloidal and toroidal mode numbers of the resonance at that location.

One method of visualizing the changes in the magnetic topology is by using a Poincaré plot. The simplest approach to modelling the effects of RMPs on the plasma is to superpose the axisymmetric equilibrium field with the additional perturbation field. This is a vacuum approach as no plasma is considered, although the field produced by the toroidal plasma current is included. Knowing the total magnetic field

$\vec{B} = (B_R, B_\phi, B_Z)$, the field lines can be traced based on the equations

$$\frac{dR}{d\Phi} = R \frac{B_R}{B_\phi}, \quad \frac{dZ}{d\Phi} = R \frac{B_Z}{B_\phi}. \quad (3)$$

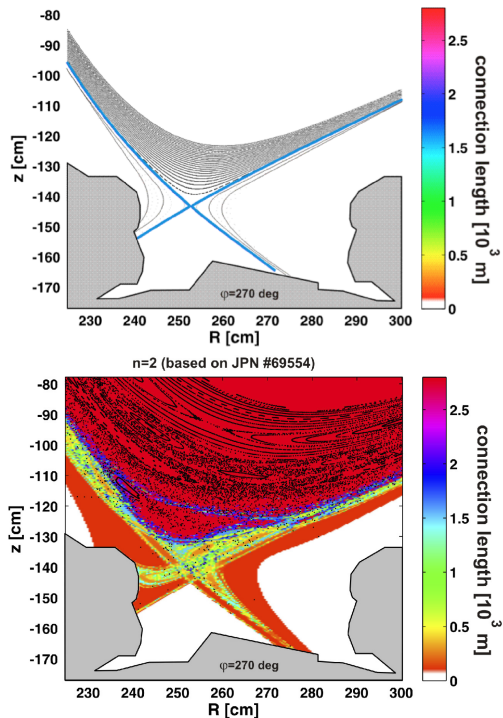


Figure 4: Poincaré plots of the separatrix topology combined with the contour plots of the connection length of the field lines with (upper) and without (lower) $n = 2$ EFCC perturbations with $I_{EFCC} = 32kAt$.

The crossing points of the field lines with the poloidal cross-section at a fixed toroidal angle Φ generate the Poincaré plot. Figure 4 (upper and lower) shows the modification of the magnetic topology when an $n = 2$ EFCC field was applied to a 2D poloidal divertor equilibrium. Here, the combined Poincaré plots of the stochastic magnetic field structures and the connection length of the perturbed field lines are calculated by the GOURDON field line tracing code [16] for an $n = 2$ EFCC configuration on JET. The calculation is based on an equilibrium reconstruction used for the calculation of the spectrum in figure 2 with the perturbation field superposed according to the vacuum approach [17]. Screening effects due to plasma rotation have been neglected. However, these initial results clearly exhibit the stochastic nature of the field line behaviour in the region around the X-point where the plasma rotation

is low. The lobes of the manifolds step out, seen as a splitting of the strike point. The connection length of the perturbed field lines slightly inside the separatrix is a few $100m$, which is less than ~ 20 toroidal turns.

The plasma edge of magnetic confinement devices is of great interest in RMP physics. In that region, the effective perturbation (the perturbation field normalized to the toroidal field), is aimed to be highest in order to achieve a strong stochasticization. Within the stochastic region, the radial transport is enhanced, which changes the plasma parameters [19, 20, 21, 22] and may explain experimental observations like the heat redistribution [23], modification of the edge electric field [24, 25], and the control of edge instabilities [15, 26, 27].

III. 3D BOUNDARY PLASMA PHYSICS

Within the last decade, it has become clear that the magnetic topology of a plasma in a tokamak cannot be fully described by the simple vacuum approach. In particular, during plasma operation in H-mode, additional currents exist in the plasma or are created as a response of the plasma to the applied external RMP fields. Many studies [28, 29, 30, 31, 32] have shown that this plasma response needs to be considered in order to understand the ongoing processes in a tokamak plasma in the presence of RMPs. The two main effects discussed are RMP field screening and the 3D equilibrium effect in low- or moderate-beta plasmas. Resonant field amplification has to be considered in high-beta plasmas, in which the external kink mode naturally becomes unstable. In addition, particle drifts in H-mode operation appear to have a strong influence [33]. Different ideas for improving the vacuum approach are discussed [33, 34, 35] and new methods based on kinetic [36] and fluid modelling used [37, 38, 39]. All these improved modelling approaches show an impact on the magnetic topology in the edge and core regions leading to modified plasma transport.

A. Plasma rotation screening effect on the RMPs

Depending on the plasma parameters and RMP spectrum, the actual RMP field could be very different in rotating plasmas, where the generation of current perturbations on rational surfaces could prevent reconnection and island formation, leading to the effective screening of RMPs [36, 40]. The equilibrium radial electric field produces $\vec{E} \times \vec{B}$ rotation which, together with the diamagnetic electron rotation, is particularly important for RMP screening in the pedestal region [38, 41].

Generally, the screening effect increases for lower resistivity, stronger rotation and smaller RMP amplitude. For an H-mode plasma with a steep pressure gradient at the edge pedestal, RMP penetration typically only occurs in the narrow region near

the separatrix due to the higher resistivity. However, at certain plasma parameters and/or because of the non-linear evolution of the radial electric field due to RMPs, $\vec{E} \times \vec{B}$ perpendicular rotation can be compensated by the electron diamagnetic rotation, i.e. $(V_{\theta, \vec{E} \times \vec{B}} + V_{\theta, e}^* \sim 0)$. In this case, the RMP harmonic (n, m) penetrates locally and forms islands on the corresponding resonant surface $q = m/n$ [42].

B. 3D equilibrium with a stochastic boundary

Tokamaks are often considered to be two-dimensional and consequently, their equilibrium is treated by solving the Grad-Shafranov equation. In real devices, the toroidal field ripple, error fields due to coil misalignments and the deliberate application of RMPs lead to a three-dimensional problem. The addition of RMPs to an axisymmetric equilibrium perturbs the force balance

$$\nabla p \neq \vec{J} \times (\vec{B} + \vec{B}_{pert,vac}). \quad (4)$$

Here, p , \vec{J} and \vec{B} are the plasma pressure, current density and magnetic field in an axisymmetric equilibrium, and $\vec{B}_{pert,vac}$ is the 3D vacuum perturbation field. To study the effect of the deviations from axisymmetry on the equilibrium the application of complex numerical tools is necessary. To re-establish the force balance, a 3D equilibrium including an equilibrium response to the 3D perturbation fields is needed.

$$\nabla p + \nabla p_{res} = (\vec{J} + \vec{J}_{res}) \times (\vec{B} + \vec{B}_{pert,vac} + \vec{B}_{res}). \quad (5)$$

Here, p_{res} , \vec{J}_{res} and \vec{B}_{res} are the 3D plasma responses of pressure, current density and magnetic field to the applied perturbation fields.

Nowadays, a number of numerical codes for the calculation of 3D MHD equilibria are available (VMEC, PIES, HINT2, IPEC). Some assume nested flux surfaces (VMEC, IPEC), while others allow for magnetic islands (PIES, HINT2). On TEXTOR, the HINT2 code [43] is used to compute numerical 3D equilibria. The converged 3D equilibria are compared with the simple vacuum superposition assumption for the case with a DED current of $7.5kA/coil$. While the major structures are conserved in the HINT2 calculation, an additional ergodisation around the X-points of the major islands (e.g. the $3/2$ island) appears. Furthermore, secondary structures appear in the islands, a feature already observed experimentally for $2/1$ islands with the DED in $3/1$ configuration [44]. This effect is caused by the modified Pfirsch-Schlüter current density distribution driven by the pressure gradient around the island. In figure 5 (a) and (b), connection length plots for an enlarged edge area are shown and indicate an increased island size in the HINT2 case. Furthermore, a statistical analysis shows an increase in short ($\leq 1000m$) and very long ($\approx 16000m$) field lines (see figure 5 (c)) in the HINT2 case. This indicates a shaper transition from the confined core to the vacuum region. It should be noted

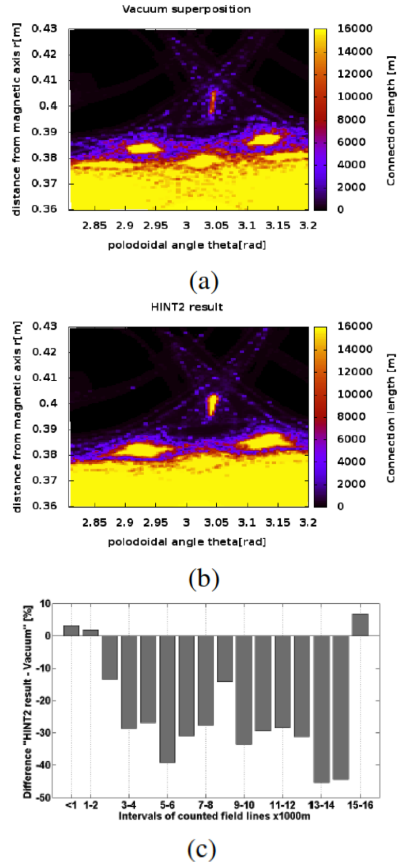


Figure 5: Connection length plots: (a) vacuum, (b) HINT2. (c) Difference in the number of field lines in specified length intervals: HINT2 result minus vacuum superposition in percent.

that the screening of the RMPs due to plasma rotation is not taken into account in the present HINT2 calculation.

C. Plasma transport in the stochastic boundary

A strong effect on the electron and thus heat transport is expected in a deep stochastic boundary layer ($\sigma_{ch} \gg 1$). The field line diffusion coefficient D_{FL} , and the electron heat diffusion coefficient can be described as :

$$\chi_e = D_{FL} \nu_{th}, D_{FL} = \sum_{m,n} \pi q R_0 \left| \frac{\delta B_{m,n}}{B_0} \right|^2. \quad (6)$$

Here, ν_{th} is the electron thermal velocity, $\delta B_{m,n}$ is the resonant component of the magnetic perturbation field. The electron heat transport in a stochastic boundary layer can be of the order of $10 - 100m^2s^{-1}$ over the perturbed edge and largely exceeds the usual anomalous transport $\sim 1m^2s^{-1}$ at the plasma edge.

Spin-up of the edge plasma rotation in the co-current direction and a change of the plasma edge electric field to a more positive value in the stochastic boundary layer have been observed in experiment [45]. This is due to the much larger electron mobility compared to the ion mobility implying an electron-retarding electric field in the plasma edge, which was previously dominated by ion losses due to their larger Larmor radius.

The effect of an additional radial diffusion on particle transport is difficult to analyse due to the coupling of the complicated transport regime to that of the physics of particle sources, namely neutral penetration. On JET, in a low- or a moderate-collisionality regime (electron collisionality at the pedestal, $\nu_{ped,e}^* \leq 1$), the electron density at the pedestal top decreased by $\sim 20\%$, the so-called density pump-out [46], during the application of an $n = 1$ field, while the pedestal electron temperature increased, keeping the pedestal pressure almost constant. However, the pedestal pressure gradient obtained from the derivative of the fitted curve shows that the maximum pressure gradient in the profile is decreased by 20% during the application of the $n = 1$ field, and the edge pressure barrier is 20% wider [47]. This is an effect mostly ascribable to the strong decrease in the n_e pedestal height with an almost unvaried width. In a high-collisionality regime ($\nu_{ped,e}^* > 1$), the effect of RMPs on the pedestal particle and heat transport is not clearly observed. [51].

Compensation of the density pump-out has been also investigated on JET using either gas fuelling or pellet injection in low-triangularity H-mode plasmas [17, 49, 50]. Although the ELM frequency stays high with $n = 1$ fields, no recovery of stored energy is observed. An optimized fuelling rate for compensating the density pump-out effect has been identified, and it depends on the plasma configuration.

D. Effects of a stochastic boundary layer on plasma-wall interaction

In the edge transport model, the transport of power in the stochastic layer has been treated as a diffusive process [55], which gives a significantly enlarged effective cross-field transport for the electron energy. As a result, a widening of the contact zone between plasma and wall has been predicted[56]. Experimental results from different devices [23, 57] have proved that the heat and particle deposition patterns are strongly structured.

The resulting heat deposition pattern reflects the complicated structure of the perturbed volume. It has been shown in [52] that the connection length and the radial penetration of the magnetic field lines defines the amount of power deposited on the target structures. The maximum of the heat flux density corresponds to the field lines with long connection length; however, those with shallow penetration seem to be strongly affected by the collisionality, in contrast to

the field lines with deep penetration, which connect the outermost existing island chain to the divertor surface. For a proper analysis of such a complicated topology, inevitably one needs 3D transport codes, which could describe such a variety of magnetic field lines.

As an example, splitting of the outer strike point (SP), appearing as multiple peaks in the ELM heat flux profile along the outer divertor plate, has been measured by a fast IR camera during the application of $n = 2$ fields on JET with the ITER-like wall (ILW) as shown in figure 6. These multiple peaks in the heat flux profile are observed only during a mitigated ELM crash when a certain I_{EFCC} threshold is reached. The preliminary results indicate that this I_{EFCC} threshold for the appearance of splitting of the outer SP during the ELM crash is at a similar level to that occurring for the saturation effect of the plasma response. Similar findings of strike point splitting have been reported on DIII-D in the presence of $n = 3$ RMP fields [53].

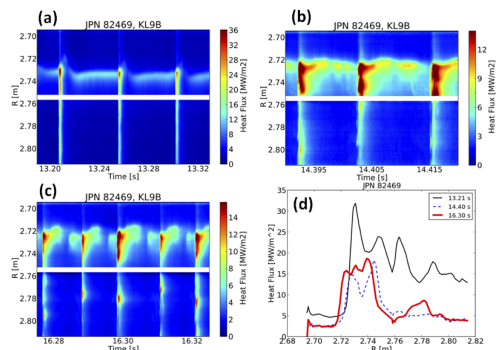


Figure 6: Extended time traces of the heat flux distribution on the outer divertor plate in the phases (upper left) without $n = 2$ field, (upper right) with $I_{EFCC} = 44$ kA and (lower left) with $I_{EFCC} = 88$ kA. (Lower right) ELM peak heat flux profiles along the outer divertor. From reference [51]

IV. ELM CONTROL USING RMP

Active control of ELMs by RMP fields offers an attractive method for next-generation tokamaks, e.g. ITER. The results obtained from the DIII-D, JET, MAST, KSTAR, AUG and NSTX tokamaks have shown that magnetic field perturbations can either completely suppress ELMs [15], trigger small ELMs during ELM-free periods, or affect the frequency and size of the type-I ELMs in a controllable way, preserving good global energy confinement [14].

A. Type-I ELM suppression with RMPs

The first successful demonstration of the ELM suppression technique was reported from DIII-D [15], where the in-vessel coils (I-coils) were employed. The I-coils consist of 12 single-turn loops, six above and six below the midplane (up-down symmetric) mounted on the low-field side of the vessel. For the ELM suppression experiments, the upper and lower loops are operated with either the same current polarities (even parity) or opposite current polarities (odd parity), and induce a static perturbation field with a toroidal mode number $n = 3$.

On DIII-D, the experimental results show that the effectiveness of ELM suppression with $n = 3$ fields depends on q_{95} . In low collisionality ($\nu_{ped,e}^* \leq 0.2$) H-mode plasmas, ELM suppression without small intermittent events is obtained in a narrow q_{95} window ranging from 3.5 to 3.9 with an even parity $n = 3$ field and ~ 7.2 with an odd parity $n = 3$ field. Outside this q_{95} range, type-I ELMs are mitigated (ELM frequency increased and ELM size decreased) by the applied $n = 3$ fields. These results indicate a resonant condition on the amplitude of RMPs for ELM suppression.

B. Type-I ELM mitigation with RMPs

Active control of type-I ELMs by the application of static $n = 1$ or 2 perturbation fields has been developed for more ITER-relevant configurations and parameters in a wide operational space of plasma triangularity (δ_U up to 0.45), q_{95} (4.8 – 3.0) and beta (β_N up to 3.0) on JET [14, 48, 49, 17]. The first results of ELM mitigation with $n = 2$ fields on JET demonstrate that the frequency of ELMs can be increased by a factor of $\sim 4-5$, limited by the available EFCC coil current. A wide operational window of q_{95} has also been obtained for ELM mitigation with $n = 2$ fields. During the application of the $n = 1, 2$ fields, a reduction in the ELM size (ΔW_{ELM}) and ELM peak heat flux on the divertor target by roughly the same factor as the increase in the ELM frequency has been observed. The reduction in heat flux is mainly due to the drop of particle flux rather than a change of the electron temperature. A modest drop (a few per cent) in the total stored energy has been observed during the ELM control phase with the EFCCs. However, when normalized to the $IPB98(y, 2)$ scaling, the confinement time shows almost no reduction.

Recently, mitigation of type-I ELMs was observed with an $n = 2$ field on JET with the ITER-like wall (ILW) [51]. A strong mitigation of type-I ELMs was observed when an $n = 2$ field was applied in high-collisionality ($\nu_{ped,e}^* = 2.0$) H-mode plasmas. No density pump-out effect was observed in the high-collisionality case, but was observed in the low-collisionality case. In the moderate-collisionality type-I ELMy H-mode plasmas with the ILW wall, a saturation effect of ELM mitigation and clear pre-ELM structures were observed on the outer divertor plate during the application of $n = 2$ fields, depend-

ing on q_{95} [51, 54].

V. SUMMARY AND OPEN QUESTIONS

Regarding on the control of plasma transport in the boundary zones, two conflicting issues have to be balanced. On one hand, to achieve a homogenization of the power deposition on target plates and reduce the peak heat flux on the divertor or the limiter, a high cross field transport level is required in the SOL. On the other hand, to keep a high fusion gain, good confinement with the edge plasma transport barrier (H-mode), is required. One attractive idea for broadening the SOL and distributing the particle and heat fluxes more evenly and over a larger surface is to soften the edge of the magnetic cage by the formation of a stochastic boundary with the application of external magnetic perturbations.

In tokamaks, non-axisymmetric magnetic perturbations, which change the magnetic topology, have been applied on the majority of contemporary large-scale tokamaks to control plasma edge stability and transport. Recent research has highlighted the significance of the role that stochasticity and 3D magnetic topology also play in this fundamentally 2D concept. Their influence can be seen in transport and energy confinement, in the control of various MHD instabilities, most notably ELMs, which expel considerable amounts of energy from the plasma and pose a risk of damaging plasma-facing components in ITER and other next-generation fusion devices.

RMP ELM suppression/control has shown very promising results up to now, although the physics mechanism is not well understood as yet. Future joint experiments from different devices (DIII-D, JET, MAST, NSTX, AUG, TCV, KSTAR and EAST) will help us to understand ELM suppression physics and provide support for ITER.

To date, many attempts to explain ELM suppression have focused on the idea that the edge thermal and particle losses are enhanced due to the formation of an outer ‘ergodic’ zone with RMP fields. This ‘ergodic’ boundary would reduce the edge pressure gradients, and thus stabilize the peeling-ballooning modes thought to underlie ELM formation [15], [37]. This mechanism is mainly supported by two experimental results from DIII-D: *i*) splitting of the inner strike-point observed during the RMP ELM suppression phase; and *ii*) spin-up of the edge plasma rotation in the co-current direction and a change of the plasma edge electric field to a more positive value due to larger losses of electrons than ions with an ergodic boundary. However, either bulk plasma or diamagnetic rotation can screen the RMP fields from the resonant magnetic flux surfaces. Many calculations of the Chirikov parameter or overlapping of resonant magnetic islands employ a vacuum assumption, which

neglects the plasma response (rotational screening effect and equilibrium effect).

Although the mechanism of ELM control with RMPs is not yet fully understood, it has been examined in a wide operational window in many different devices. Further optimisation of the magnetic perturbation with less reduction of the plasma performance, and an understanding of the underlying physics are essential for future investigations.

In addition, the existence of these stochastic and 3D magnetic topology effects brings tokamak and stellarator physics closer together, and a holistic approach to studying them provides the most promising path to making good progress. Understanding these effects is essential for the success of future fusion devices, and they represent a hot topic in current fusion research. Furthermore, reversed field pinches offer access to these topics with unique features such as the bifurcation into self-generated 3D equilibria and multi-mode unstable plasma conditions with a high degree of magnetic field stochasticity.

REFERENCES

1. "ITER Physics Basis", *Nucl. Fusion* **39** 2137 (1999)
2. F. Wagner et al., "Regime of Improved Confinement and High Beta in Neutral-Beam-Heated Divertor Discharges of the ASDEX Tokamak", *Phys. Rev. Lett.*, **49**, 1408 (1982).
3. T. Eich, et al., "Inter-ELM Power Decay Length for JET and ASDEX Upgrade: Measurement and Comparison with Heuristic Drift-Based Model", *Phys. Rev. Lett.*, **107**, 215001 (2011).
4. Loarte A, et al., "ELM energy and particle losses and their extrapolation to burning plasma experiments", *J. Nucl. Mater.*, **313-316** 962 (2003)
5. A. Einstein, "Über die von der molekularkinetischen Theorie der Wärme geforderte Bewegung von in ruhenden Flüssigkeiten suspendierten Teilchen", *Ann. Phys.*, **17** 549-560 (1905).
6. J. Klafter and M. Sokolov, "Anomalous diffusion spreads its wings", *Physics World*, **18** 29-32 (2005).
7. R. Kubo, "Statistical-mechanical theory of irreversible processes: I. General theory and simple applications to magnetic and conduction problems", *J. Phys. Soc. Japan*, **12** 570 (1957).
8. B. V. Chirikov, "A universal instability of many-dimensional oscillator systems", *Phys. Rep.* **52** 263?379 (1979).
9. G. M. Zaslavsky, "Chaos, fractional kinetics, and anomalous transport", *Phys. Rep.* **371** 461?580 (2002).
10. G. M. Zaslavsky, "Hamiltonian Chaos and Fractional Dynamics", *Oxford: Oxford University Press* (2005)
11. S. Chandrasekhar, "Stochastic problems in physics and astronomy", *Rev. Mod. Phys.* **15** 1?89 (1943)
12. R. Balescu, "Aspects of Anomalous Transport in Plasmas" *Bristol: Institute of Physics Publishing* (2005)
13. Y. Liang, "Overview of edge-localized mode control in tokamak plasmas", *Fusion Science and Technology* **59**, 586 (2011).
14. Y. Liang, et al., "Active control of type-I edge-localized modes with n=1 perturbation fields in the JET tokamak", *Phys. Rev. Lett.*, **98** 265004 (2007)
15. T. E. Evans, et al., "Edge stability and transport control with resonant magnetic perturbations in collisionless tokamak plasmas", *Nature Phys.*, **2** 419 (2006)
16. C. Gourdon, "Programme optimise de calculs numeriques dans les configurations magnetiques toroidales", *CEN Fontenay aux Roses* (1970)
17. Y. Liang, et al., "Active control of type-I edge localized modes with n = 1 and n = 2 fields on JET", *Nuclear Fusion* **50**, 025013 (2010).
18. Y. Liang, et al., "Magnetic Topology Changes Induced by Lower Hybrid Waves and their Profound Effect on Edge-Localized Modes in the EAST Tokamak", *Phys. Rev. Lett.*, **110** 235002 (2013)
19. T. Stix. "Plasma transport across a braided magnetic field", *Nuclear Fusion*, **18**, 353?358 (1978).
20. H. Wobig and R. H. Fowler, "The effect of magnetic surface destruction on test particle diffusion in the Wendelstein VII-A stellarator", *Plasma Physics and Controlled Fusion* **30**, 721 (1988).
21. T. Eich, D. Reiser and K. Finken, "Two dimensional modelling approach to transport properties of the TEXTOR-DED laminar zone", *Nuclear Fusion* **40**, 1757 (2000).
22. A. Wingen, S. Abdullaev, K. Finken, M. Jakubowski and K. Spatschek, "Influence of stochastic magnetic fields on relativistic electrons", *Nuclear Fusion* **46**, 941 (2006).
23. M. W. Jakubowski, S. Abdullaev, K. Finken and the TEXTOR Team, "Modelling of the magnetic field structures and first measurements of heat fluxes for TEXTOR-DED operation", *Nuclear Fusion* **44**, S1 (2004).

24. S. Jachmich, P. Peleman, M. Van Schoor, Y. Xu, M. Jakubowski, M. Lehnen, B. Schweer and R. Weynants, "First Mach probe measurements of rotation, electric field and particle transport in the DED-ergodized edge plasma of TEXTOR", In: *Proceeding of the 33rd EPS Conference on Plasma Physics*, **03.014** (2006)
25. A. Wingen and K. Spatschek, "Influence of different DED base mode configurations on the radial electric field at the plasma edge of TEXTOR", *Nuclear Fusion* **50**, 034009 (2010).
26. O. Schmitz et al., "Aspects of three dimensional transport for ELM control experiments in ITER-similar shape plasmas at low collisionality in DIII-D", *Plasma Physics and Controlled Fusion* **50**, 124029 (2008).
27. Y. Liang, C. G. Gimblett, P. K. Browning, P. Devoy, H. R. Koslowski, S. Jachmich, Y. Sun and C. Wiegmann, "Multiresonance Effect in Type-I Edge-Localized Mode Control With Low n Fields on JET", *Physical Review Letters* **105**, 065001 (2010).
28. T. E. Evans, I. Joseph, R. Moyer, M. Fenstermacher, C. Lasnier and L. Yan. "Experimental and numerical studies of separatrix splitting and magnetic footprints in DIII-D", *Journal of Nuclear Materials* **363-365**, 570-574 (2007).
29. E. Nardon et al. "Strike-point splitting induced by external magnetic perturbations: Observations on JET and MAST and associated modelling", *Journal of Nuclear Materials* **415**, S914-S917 (2011).
30. A. Kirk et al. "Magnetic perturbation experiments on MAST L- and H-mode plasmas using internal coils", *Plasma Physics and Controlled Fusion* **53**, 065011 (2011).
31. Y. Yang, Y. Liang, Y. Sun, T. Zhang, J. Pearson, Y. Xu and TEXTOR Team. "Experimental observations of plasma edge magnetic field response to resonant magnetic perturbation on the TEXTOR Tokamak." *Nuclear Fusion* **52**, 074014 (2012).
32. P. Denner, Y. Liang, Y. Yang, M. Rack, L. Zeng, J. Pearson, Y. Xu and the TEXTOR team. "Local measurements of screening currents driven by applied RMPs on TEXTOR". *Nuclear Fusion* **54** (2014).
33. A. Wingen, O. Schmitz, T. E. Evans and K. H. Spatschek. "Heat flux modeling using ion drift effects in DIII-D H-mode plasmas with resonant magnetic perturbations", *Physics of Plasmas*, **21**, 012509 (2014).
34. P. Cahyna and E. Nardon. "Model for screening of resonant magnetic perturbations by plasma in a realistic tokamak geometry and its impact on divertor strike points", *Journal of Nuclear Materials* **415**, S927 ?S931 (2011).
35. H. Frerichs, D. Reiter, O. Schmitz, P. Cahyna, T. E. Evans, Y. Feng and E. Nardon. "Impact of screening of resonant magnetic perturbations in three dimensional edge plasma transport simulations for DIII-D", *Physics of Plasmas* **19**, 052507 (2012).
36. M. F. Heyn, I. B. Ivanov, S. V. Kasilov, W. Kernbichler, I. Joseph, R. A. Moyer and A. M. Runov. "Kinetic estimate of the shielding of resonant magnetic field perturbations by the plasma in DIII-D", *Nuclear Fusion*, **48**, 024005 (2008).
37. M. Bécoulet et al. "Physics of penetration of resonant magnetic perturbations used for Type I edge localized modes suppression in tokamaks.", *Nuclear Fusion* **49**, 085011 (2009).
38. E. Nardon, P. Tamain, M. Bcoulet, G. Huysmans and F. Waelbroeck. "Quasi-linear MHD modelling of H-mode plasma response to resonant magnetic perturbations", *Nuclear Fusion* **50**, 034002 (2010).
39. A. Wingen, N. M. Ferraro, M. W. Shafer, E. A. Unterberg, T. E. Evens, D. L. Hillis and P. B. Snyder. "Impact of plasma response on plasma displacements in DIII-D during application of external 3D perturbations", *Nuclear Fusion* **54** (2014).
40. R. Fitzpatrick, "Bifurcated states of a rotating tokamak plasma in the presence of a static error-field", *Phys. Plasmas* **5** 3325 (1998)
41. D. Reiser D. and D. Chandra, "Plasma currents induced by resonant magnetic field perturbations in tokamaks", *Phys. Plasmas* **16** 042317 (2009)
42. M. Bécoulet, et al., "Screening of resonant magnetic perturbations by flows in tokamaks", *Nuclear Fusion*, **52** 054003 (2012)
43. Y. Suzuki, et al., "Development and application of HINT2 to helical system plasmas", *Nuclear Fusion*, **46** L19-L24 (2006)
44. Y. Liang, et al., "Observations of secondary structures after collapse events occurring at the q = 2 magnetic surface in the TEXTOR tokamak", *Nuclear Fusion*, **47** L21-L25 (2007)
45. K. H. Finken, et al., "Toroidal plasma rotation induced by the Dynamic Ergodic Divertor in the TEXTOR tokamak", *Phys. Rev. Lett.* **94** 015003 (2005)

46. J. C. Vallet et al., "Stabilization of tokamak Ohmic discharges at the density limit by means of the ergodic divertor", *Phys. Rev. Lett.* **67** 2662 (1991)
47. A. Alfier et al., "Edge T-e and n(e) profiles during type-I ELM mitigation experiments with perturbation fields on JET" *Nucl. Fusion* **48** 115006 (2008)
48. Y. Liang, et al., "Active control of type-I edge localized modes on JET", *Plasma Phys. Control. Fusion* **49** B581 (2007)
49. Y. Liang, et al., "Active control of edge localized modes with a low n perturbation fields in the JET tokamak", *J. Nucl. Mater.* **390-91** 733-739 (2009)
50. Y. Liang, et al., "Overview of ELM Control by Low n Magnetic Perturbations on JET", *Plasma and Fusion Research*, **5**, S2018 (2010)
51. Y. Liang, et al., "Mitigation of type-I ELMs with n=2 fields on JET with ITER-like wall", *Nucl. Fusion* **48** 115006 (2013)
52. M. W. Jakubowski, et al., "Observation of the heteroclinic tangles in the heat flux pattern of the ergodic divertor at TEXTOR", *J. Nucl. Mater.* **363** 371-376 (2007)
53. M. W. Jakubowski et al., "Overview of the results on divertor heat loads in RMP controlled H-mode plasmas on DIII-D", *Nucl. Fusion* **49**, 095013 (2009).
54. M. Rack, et al., "Findings of pre-ELM structures through the observation of divertor heat load patterns at JET with applied n=2 perturbation fields", *Nucl. Fusion* **54**, 072004 (2014).
55. A. B. Rechester and M.N. Rosenbluth, "Electron Heat Transport in a Tokamak with Destroyed Magnetic Surfaces", *Phys. Rev. Lett.* **40** 38 (1978)
56. A. V. Nedospasov and M.Z. Tokar, "Conception of divertorless tokamak reactor with turbulent plasma blanket", *J. Nucl. Mater.* **93-94** 248 (1980)
57. A. Grosman, P. Ghendrih, B. Meslin and D. Guilhem, "Power and particle flux to the neutraliser plates of the Tore Supra ergodic divertor modules", *J. Nucl. Mater.* **241-243** 532 (1997)

EROSION AND DEPOSITION MECHANISMS IN FUSION PLASMAS

A. Kirschner

*Institut für Energie- und Klimaforschung - Plasmaphysik, Forschungszentrum Jülich GmbH,
Association EURATOM-FZJ, Trilateral Euregio Cluster, 52425 Jülich, Germany*

ABSTRACT

An overview of erosion and deposition processes in fusion machines is presented. The underlying physical and chemical mechanisms are explained. The impact of erosion and deposition on wall lifetime and tritium retention, which define the availability of future fusion machines such as ITER, is discussed. Also, examples of erosion and deposition observed in present fusion experiments are presented.

I. INTRODUCTION

The next major step on the way to a fusion reactor is the international experimental reactor ITER¹. In long-pulse (about 400s) or even steady-state operation, which both are foreseen for ITER, erosion and deposition processes become more crucial than in current fusion experiments. Erosion of wall material leads to limitation of the lifetime of the wall components. Whereas on the one hand deposition of eroded material can eventually reduce net erosion, it will lead to formation of deposited layers on the other hand. Main concern of deposited material is its ability to retain large amounts of fuel, which in ITER will consist of 50% deuterium and 50% tritium within the active phase of operation. The in-vessel retention of radioactive tritium will be limited due to safety regulations. Current estimations of wall lifetime and tritium retention for ITER are based on extrapolations from present experiments or modeling calculations and imply relatively large uncertainties^{2,3}. Nevertheless, they indicate that the number of pulses before reaching the tritium retention limit or the maximum allowed erosion of wall components could be unacceptably low for an economical operation. From this, it is obvious that both erosion and deposition of wall material will strongly determine the availability of ITER. It is therefore necessary to understand the involved mechanisms and to find possibilities to minimize erosion and deposition.

The erosion and deposition properties naturally depend on the material choice. In ITER there are currently three different materials under discussion for the use as wall cladding. Beryllium (Be) is planned to cover the first wall in the main chamber. Compared to elements of high atomic number (Z) eroded Be ($Z = 4$) entering the plasma leads to lower plasma cooling due to radiation. With respect to the large area of the first wall

the use of low- Z Be is therefore more beneficial although in general the sputtering of low- Z elements is larger than that of high- Z ones. In addition, Be has the advantage of being a good oxygen getter. For the so-called baffles, which cover the region between the main wall and the divertor plates, tungsten is intended to be used. Here, larger ion fluxes (compared to the main wall) and a significant flux of charge exchange neutrals will reach the surface such that the sputtering should be minimized by using a high- Z material. Tungsten in addition has a relatively high melting point of about 3400°C. Finally, the divertor plates, on which the maximum particle and heat fluxes will occur, were originally planned to be made of carbon fiber composites (CFC). Carbon-based materials can withstand highest heat loads without melting (sublimation at a temperature of about 3800°C). Therefore problems caused by melt layer loss do not occur. However, carbon-based materials suffer from chemical erosion/sputtering by means of formation of volatile hydrocarbons C_xI_y , where "I" represents hydrogen H or its isotopes deuterium D and tritium T. The deposition of such species leads to formation of tritium-containing layers inducing the problems as addressed above. It was planned to use CFC divertor plates at the beginning of ITER operation in the non-active phase without tritium. For further operation in the active phase it was foreseen to exchange the CFC plates with tungsten ones to minimize tritium retention by co-deposition. At the moment discussions are ongoing to start already in the non-active phase with a tungsten divertor to reduce the overall costs of the ITER project.

Besides erosion of these "pure" elements also mixed layers, which are formed after erosion and re-deposition processes, have to be taken into account. In the mixture of materials currently foreseen for ITER one can expect the formation of carbides (Be_2C , WC) and also alloys with erosion and other physical properties (e.g. melting point) different from the pure elements.

II. EROSION MECHANISMS

The erosion yield Y

To characterize the strength of erosion the yield Y is defined as ratio of the averaged number of eroded particles and number of incoming projectiles. It is important that not a single projectile is considered but a large amount of projectiles such that the erosion yield represents the erosion probability. The yield can be determined by the flux of eroded particles Γ_{ero} divided by the flux of incoming projectiles Γ_{in} :

$$\Gamma_{in} = \frac{\text{number of incoming particles}}{\text{area} \times \text{time}} \quad (1a)$$

$$\Gamma_{ero} = \frac{\text{number of eroded particles}}{\text{area} \times \text{time}} \quad (1b)$$

$$Y = \frac{\Gamma_{ero}}{\Gamma_{in}} \quad (1c)$$

A. Physical sputtering

A.1. Basic features

Within the process of physical sputtering, the momentum of incoming projectiles (energetic ions or neutrals) is transferred to surface atoms of the target material via nuclear collisions. If the transferred energy is large enough to overcome the surface binding energy (which is only known for a few materials, therefore it is common to use the heat of sublimation as an estimate), the surface atom can leave the solid and is physically sputtered. Although the first momentum transfer from projectile to target atoms is directed into the surface, subsequent collisions can lead to a momentum transfer which is directed out of the solid surface. Different regimes of collision can be distinguished mainly depending on the projectile energy and mass:

i) Single collision regime

After one single collision of the projectile with a target atom, the projectile hits a surface target atom. This process particularly occurs for light projectile ions with low impact energies.

ii) Linear cascade regime

With medium projectile energies (larger than several 10 eV) a collision cascade is developing in the solid including also the generation of recoil atoms. However, collisions between two moving atoms are rare.

iii) Spike regime

At high impact energies (keV – MeV) and high projectile masses the densities of recoils of the collision cascade is increasing. Inside the spike region most atoms are moving, whereby collisions between simultaneously moving particles become important.

Figure 1 illustrates these different regimes. The first two regimes can be described with the binary collision approximation (BCA), which will be discussed in chapter II.A.2. In the spike regime many-body processes have to be taken into account and the heat spike can lead

to a local melting of the solid. However, under the conditions of wall materials in fusion experiments the spike regime is less important than the other two regimes.

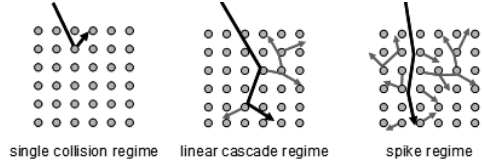


Figure 1: Collision regimes inside a solid induced by impact of a projectile atom.

In general, physical sputtering occurs for all combinations of projectile and target materials. The sputtered species are mostly neutral atoms or small clusters of the target material. Due to the nature of physical sputtering there exists a threshold energy for projectile particles below which the sputtering yield is zero. A surface atom at least has to receive the surface binding energy to be sputtered from the solid.

Besides the impact energy the sputtering yield also depends on the impact angle of projectiles. Also the combination of projectile and substrate material influences the sputter yield. This can be easily understood in terms of the maximum energy transfer factor γ for head-on collisions

$$\gamma = \frac{4 \cdot M_1 \cdot M_2}{(M_1 + M_2)^2} \quad (2)$$

where M_1 and M_2 are the masses of projectile and target material respectively. The factor γ is maximal ($= 1$) for identical masses of projectile and substrate, $M_1 = M_2$. Physical sputtering does not significantly depend on the surface temperature but is dominated by the kinetics of collisions.

The basics of physical sputtering of single-ion targets, covering theoretical aspects as well as experimental results, are described in ⁴. In the following the main dependencies of the sputtering yield are discussed in more detail.

Energy dependence of Y_{phys}

Below the threshold energy E_{th} the sputter yield is zero. The threshold energy can be estimated for light projectile ions when only two collisions between projectile and solid atoms are involved as shown in figure 1, left part. In the extreme case of head-on collisions the projectile of impact energy E_0 has the energy $(1 - \gamma) \cdot E_0$ after reflection at the solid atom. The reflected projectile then can transfer maximum energy of $\gamma \cdot (1 - \gamma) \cdot E_0$ to surface atoms of the solid. The sputtered atom finally has an energy of $E_{spu} = \gamma \cdot (1 - \gamma) \cdot E_0 - E_B$, where E_B is the surface binding energy. From this, the threshold energy follows by setting $E_{spu} = 0$, thus:

$$E_{th} = \frac{E_B}{\gamma \cdot (1 - \gamma)} \quad (3)$$

Table 1 summarizes threshold energies for sputtering of beryllium, carbon (low-Z) and tungsten (high-Z) due to deuterium (D) and oxygen (O) as calculated with Eq. (3). As can be seen for sputtering caused by deuterium bombardment, the threshold energy for high-Z materials is significantly larger than for low-Z ones. In addition, the sputtering of high-Z materials due to impurities such as oxygen starts at lower energies than the sputtering due to deuterium. However, Eq. (3) cannot be used universally for calculating threshold energies of physical sputtering. If the masses of projectile and target atoms are similar, wrong threshold energies are delivered (as shown in table 1 for sputtering of beryllium and carbon due to oxygen). This can be easily seen for the extreme case of $M_1 = M_2$ which gives $\gamma = 1$ and E_{th} in Eq. (3) would be infinity. Though, with $M_1 = M_2$ one faces the situation of so-called “self-sputtering”, which is a very effective mechanism and cannot be explained with the simple two-collisions model. For the case of $M_1/M_2 > 0.2$ a fit of experimental data⁵ results in

$$E_{th} = 8E_B \cdot \left(\frac{M_1}{M_2}\right)^{2/5} \quad (4)$$

For $M_1/M_2 < 0.2$ Eq. (3) still is a good approximation of experimental data. The threshold energies according to Eq. (4) for the material combinations discussed so far with $M_1/M_2 > 0.2$ are added in table 1 in brackets.

Table 1: Threshold energies (eV) for physical sputtering calculated acc. to Eq. (3) and Eq. (4) in brackets.

	D	O
Be ($E_B = 3.38$ eV)	14 (15)	47 (34)
C ($E_B = 7.42$ eV)	30 (—)	373 (67)
W ($E_B = 8.8$ eV)	214 (—)	42 (—)

For impact energies above the threshold energy physical sputtering occurs with the sputter yield increasing monotonically until reaching a maximum value at a certain impact energy: more energy can be transferred to surface atoms, which increases the probability for sputtering. Further increase of the impact energy leads to continuous decrease of the sputter yield: the impinging projectiles and therefore also the collision cascades penetrate deeper into the solid and therefore less energy is transferred to surface atoms.

Figure 2 shows as an example the energy dependence of physical sputtering of beryllium due to deuterium at normal incidence calculated with the TRIM⁶ code. More details about the TRIM code will be given in subsection A.2 when discussing the calculation of sputtering yields.

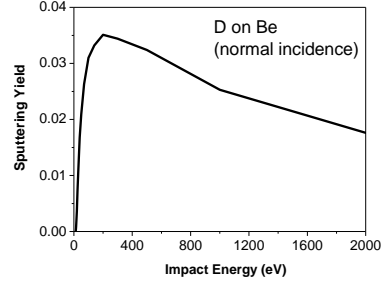


Figure 2: Calculated sputtering yield for D on Be in dependence on the impact energy.

It is important to mention that in a plasma, and therefore also in fusion experiments, the impact energy of ions hitting a surface is determined by the ion and electron temperature (T_i and T_e), where in many cases

$$E_{in} \sim 3 \cdot Q \cdot T_e + 2 \cdot T_i \quad (5)$$

with Q the charge state of the projectile⁷. The first part of Eq. (5) originates from the acceleration of the ions in the sheath potential and the second part reflects the Maxwell-distributed thermal velocity of the ions and the energy gain in the pre-sheath electric field.

Angular dependence of Y_{phys}

The angle of incidence α_0 of impinging projectiles is defined as angle between the velocity vector of the projectile and the surface normal vector. With this definition $\alpha_0 = 0^\circ$ represents normal and $\alpha_0 = 90^\circ$ grazing incidence. Figure 3 shows the calculated sputtering yield again for deuterium on beryllium but now with a fixed impact energy $E_0 = 200$ eV in dependence on the angle of incidence (data from TRIM calculations).

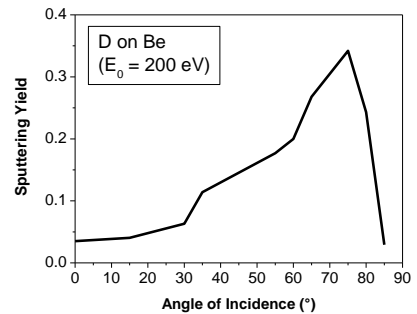


Figure 3: Calculated (TRIM) sputtering yield for D on Be in dependence on the impact angle.

Starting at normal incidence the sputter yield increases with increasing angle of incidence. With more grazing incidence of the projectiles more energy is deposited near the surface. After reaching a maximum yield (in the example of figure 3 at about 75°) the sputtering yield strongly decreases. At these shallow

angles reflection of projectiles becomes more important resulting in less energy available at the surface for sputtering. The described angular dependence of physical sputtering assumes smooth (on an atomistic scale) target surfaces. Unpolished surfaces normally exhibit a certain roughness.

Figure 4 demonstrates the effect of surface roughness on the sputter yield on the example of beryllium sputtering due to 300 eV deuterium ions⁸. TRIM simulation assume smooth surface and deviate from measurements at a rough surface especially showing a more pronounced increase with nominal angle of incidence. At rough surfaces two processes have to be taken into account: First, the local angle of incidence differs from the nominal one. Dependent on the nominal angle of incidence one has to consider a distribution of local angles of incidence instead of one fixed angle. Taking e.g. a nominal angle of incidence of 0°, leads to contributions of larger angles in the distribution of local angles of incidence. Thus, at a rough surface the sputter yield will be larger than at a smooth surface taking into account the angular dependence of figure 3. Similarly, at high nominal angles the sputter yield for rough surfaces will be smaller than for smooth ones – especially the maximum yield for a rough surface will be smaller than for a smooth surface. Secondly, sputtered particles can be re-deposited at side walls of valleys on the rough surface. This effect decreases the sputtering yield. Obviously the importance of re-deposition increases with surface roughness and is less important at glancing nominal angles of incidence. Both effects, the distribution of local angles of incidence and re-deposition of sputtered particles, are included in the simulation of figure 4 for rough surfaces demonstrating a good agreement with the measured data.

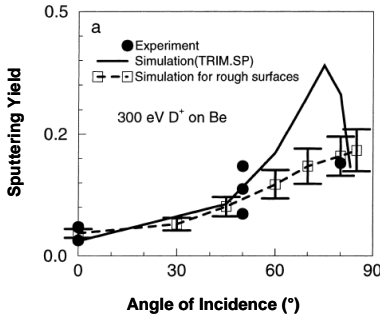


Figure 4: Measured and calculated sputter yields of D on Be in dependence on the nominal angle of incidence for a rough surface⁸.

Energy and angular distribution of sputtered particles

In many cases the energy distribution of sputtered particles can be described with a Thompson distribution:

$$N(E_{\text{sputt}}) \propto \frac{E_{\text{sputt}}}{(E_{\text{sputt}} + E_B)^3} \quad (6)$$

At $E_{\text{sputt}} = E_B/2$ the energy distribution has a maximum. At higher energies the probability for sputtered particles with the given energy decreases with $1/E^2$. The maximal energy, which can be transferred to sputtered particles equals $E_{\text{sputt}}^{\text{max}} = \gamma \cdot (1 - \gamma) \cdot E_0 - E_B$ and therefore has to be included in Eq. (6) as cut-off. Measurements of the energy distribution of sputtered particles agree fairly well with Eq. (6) for heavy-ion sputtering at normal incidence in the range of 1 keV⁹, whereas deviations occur for light impact ions and/or non-normal incidence.

The angular distribution of sputtered particles for normal incidence by medium and heavy ions can be approximated with a cosine distribution. This follows from the theory of cascade sputtering with the assumption of an isotropic collision cascade. Deviations to an over-cosine distribution, which peaks towards the surface normal, arise for light-ion bombardment. This deviation tends to be stronger with low impact energies and/or metals with high surface binding energy¹⁰. In practice surfaces are rough and data of angle distributions are rare, thus a cosine distribution is a good approximation.

A.2. Calculating of physical sputtering yields

Experimental data on physical sputtering yields are mainly obtained by means of ion beam irradiation were energetic ions are focused to a target. The sputter yield can then be determined by weight loss measuring of the target probe after bombardment. However, at low bombarding energies – especially near the threshold energy of physical sputtering – ion beam intensities become very low. Therefore measured data at low impact energies are rare and more uncertain. Modeling can help to close this gap.

To calculate the physical sputtering yield in dependence on the impact energy and angle fit formulae have been developed. Mostly the Bohdansky formula and its revised version are used, which give the yield for normal incidence in dependent on the impact energy⁵. The overall accuracy of this formula is about a factor of 2 – 3. Meanwhile several improvements of this analytic formula have been provided. New attempts have been done for a unified representation of the physical sputtering yield in dependent on the impact energy¹¹. The dependence on the impact angle is described by the Yamamura formula¹². Again the accuracy is not better than a factor of two.

A more detailed approach to calculate sputtering yields is based on the modeling of the transport of the impinging projectile inside the solid. The TRIM¹³ (TRansport of Ions in Matter) code and its derivative SDTrimSP¹⁴ follow the projectiles through a randomized target in the binary collision approximation (BCA) and calculate the collision cascade including recoils. The critical parameter is the potential describing the interaction between projectile and target atoms. Various potentials are in use, such as the screened Coulomb potential for Kr-C¹⁵, which is a good approximation for many projectile-solid atom

combinations. Within the BCA the interaction between the projectile and the target atoms is treated by successive two-body interactions. This approximation breaks down at low impact energies ($< \sim 10$ eV) where many-body and quantum mechanical effects become important. More suitable for the situation of low impact energies (< 10 eV) are molecular dynamic (MD) simulations. Within MD calculations the motion is followed by the numerical solution of Newton's equations. For this, the many-body interaction potentials have to be known, which is a main constraint of MD calculations. Several methods exist to calculate these interaction potentials: the empirical approach ignores any quantum-mechanical effects or includes them by empirical methods. Semi-empirical potentials use the matrix representation from quantum mechanics, whereas the matrix elements themselves come from empirical formulae. Finally, ab-initio methods make use of full quantum-mechanical formulae. However, currently not all potentials necessary for plasma-wall interaction in fusion research are available – especially there is still a lack of data where beryllium is involved.

A.3. Sputtering of layered systems and mixed materials

So far only physical sputtering of pure elements has been described. The mixing of different materials caused by deposition or implantation of impurities at the solid, leads to additional processes. One example is the sputtering of a carbon layer on top of a tungsten substrate due to deuterium ion impact, a situation which can occur at the tungsten baffles in ITER.

Figure 5 shows the calculated (SDTrimSP) carbon sputtering yields in dependence on the deuterium ion impact energy for various thicknesses of a carbon layer on top of a tungsten substrate. As seen in figure 5, for thin carbon layers carbon sputtering becomes more effective compared with a pure carbon target. This can be explained by an increased reflection of incoming deuterium ions at the heavy tungsten substrate atoms compared to reflection on carbon atoms.

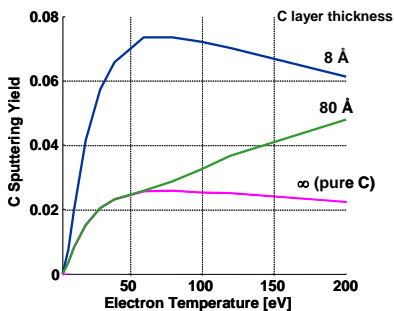


Figure 5: Physical sputtering yield of a carbon layer of varying thickness on top of a tungsten substrate (calculated with SDTrimSP). The impact energy E_{in} of impinging D^+ ions is given as electron temperature T_e ($E_{in} \sim 5T_e$).

Thus, more of the penetrating deuterium ions are reflected back to the surface where sputtering of carbon takes place. The enhanced sputtering occurs especially for thin layers and high projectiles impact energies.

In a more realistic situation the particles are implanted with a certain depth profile leading to different concentrations, which also depends on exposure time. However, the basic processes influencing the sputter yield are the same but the effects can be less pronounced than shown in figure 5. In nearly all cases of multi-element systems preferential sputtering of one of the components occurs, which can be reproduced with the TRIM and SDTrimSP code¹⁶. Under multi-species conditions, further effects can occur like an oscillating of the partial sputtering yield in the case of heavy-ion bombardment of light targets (e.g. W ions on carbon target)¹⁷. This effect is explained with fluence-dependent depth profiles of the implanted species. In addition to these collision-induced mechanisms, diffusion and segregation will influence the physical sputtering in mixed material systems.

B. Chemical erosion and sputtering

Chemical erosion involves thermal projectiles (in contrast to energetic ones in the process of chemical sputtering) initiating chemical reactions with surface atoms. In contrast to physical sputtering chemical erosion only occurs for specific combinations of projectile and target atoms. In fusion research chemical erosion of beryllium and carbon-based materials due to hydrogen (and its isotopes) are of main importance. Chemical erosion of carbon has been studied in great detail whereas the chemical erosion of beryllium is still subject of intense research.

Figure 6 summarizes the atomistic mechanisms leading to chemical erosion of carbon due to impact of thermal hydrogen atoms. Basic description of chemical erosion includes following processes: C atoms, bound in a sp^2 configuration (bottom of figure 6) of the solid, are hydrogenised to sp^3 complexes (top of figure 6) via an intermediate radical state sp^x (left-hand side, figure 6).

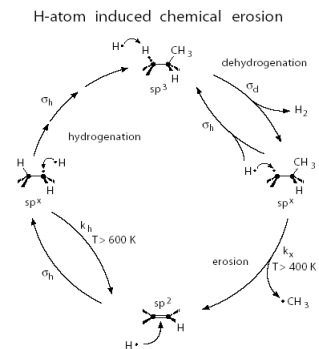


Figure 6: Atomistic processes involved in chemical erosion of carbon due to thermal hydrogen impact¹⁸.

Further impinging hydrogen atoms will lead to formation of hydrogen molecules H_2 , which are desorbed and thus leaving a radical state sp^x with a broken bond (right-hand side of figure 6). If the surface temperature is high enough (larger than $\sim 400K$), chemical erosion can occur via desorption of hydrocarbon complexes. At higher surface temperatures (above about $600K$) the intermediate radical state sp^x can recombine with adsorbed atoms with a certain rate. This reduces the sp^3 concentration and therefore leads to a decrease of chemical erosion. Altogether the chemical erosion can be described by the cross sections of hydrogenation σ_H and dehydrogenation σ_D and the surface temperature-dependant rate coefficients of desorption of hydrocarbon complexes k_x and recombination of incoming H atoms with adsorbed ones k_h . The chemical erosion rate in steady state is given by the product of k_x and the concentration c_{sp^x} of sp^x states, the latter one given as:

$$c_{sp^x} = c_{sp^3} \frac{\sigma_d \Gamma_H}{\sigma_h \Gamma_H + k_x} \quad (7)$$

with Γ_H as the impinging hydrogen atom flux. From this, the chemical erosion yield Y_{therm} , which is the erosion rate divided by the flux, follows to:

$$Y_{therm} = \frac{c_{sp^3}}{\Gamma_H} \cdot \frac{\sigma_d \Gamma_H}{\sigma_h \Gamma_H + k_x} \cdot k_x \quad (8)$$

In figure 7, measured chemical erosion yields for bombardment of different carbon-based materials with deuterium or hydrogen atoms are presented in dependence on the surface temperature. In agreement with the above-described model the yield has a maximum at around $600K$ and decreases with higher surface temperatures. In addition, the measurements show a strong dependence on the carbon material.

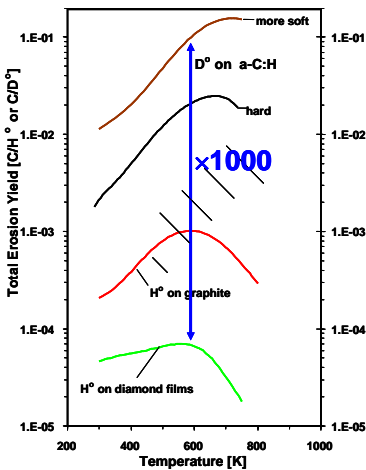


Figure 7: Chemical erosion yield for bombardment of different carbon-based materials with thermal hydrogen/ deuterium atoms ¹⁹.

Amorphous a-C:H carbon films (in the figure marked as “soft” and “hard”) suffer from much larger chemical erosion than graphite or pure diamond films. This can be explained in the model with the concentration of sp^x states, which strongly depends on the material structure.

A wide range of hydrocarbon species can be formed chemically. With thermal hydrogen atom impact CH_3 is formed, while CH_4 dominates at higher ion impact energies. In addition, a large family of higher hydrocarbons C_2H_x and C_3H_x is observed. Normally the energy spectrum of eroded species can be described with a Maxwell distribution around the surface temperature:

$$N(E_{therm}) \propto E_{therm} \cdot e^{-E_{therm}/kT_{surf}} \quad (9)$$

Similar to physical sputtering the angular distribution can be approximated with a cosine function.

Chemical sputtering is defined as process where due to ion bombardment a chemical reaction occurs, which produces a particle weakly bound to the surface which then can be desorbed into the gas phase. The ion bombardment promotes the chemical reaction whereas the release of the particle itself is mainly thermally driven. Chemical sputtering depends on the kinetic energy and the chemical reactivity of the impinging species. The eroded species are molecules formed out of projectile and target atoms. In contrast to physical sputtering but similar to chemical erosion, chemical sputtering occurs only for certain combinations of projectile and target material. The following discussion will focus on the chemical sputtering of carbon-based materials. The threshold energy for chemical sputtering is significantly smaller than for physical sputtering and the chemical sputtering yield shows a clear dependence on the surface temperature of the substrate. As for chemical erosion also chemical sputtering leads to a wide range of sputtered hydrocarbon species. In addition to the surface temperature dependence the distribution of sputtered species also depends on the ion impact energy.

The energetic hydrogen ions penetrate into the solid and as long as they have enough energy the interaction with the solid atoms is determined by collision effects (leading to displacement of target atoms or physical sputtering). At the end of the projectile’s trajectory, after thermalisation, chemical effects become important. This can be described by the model of chemical erosion as presented in the previous chapter – a hydrocarbon complex can be formed with a yield Y_{therm} . The hydrocarbon at the end of the ion range can then diffuse to the surface where it finally can leave the solid. However, in case of chemical sputtering the yield is enhanced compared to chemical erosion due to the effect of radiation damage of the penetrating energetic ion. The radiation damage in form of broken C-C bonds provides additional reaction sites for incoming H atoms and thus increases the probability of hydrocarbon formation. The yield for the enhanced thermal reaction can be written as

$$Y_{therm}^{damage} = Y_{therm} \cdot (1 + D \cdot Y_{dam}) \quad (10)$$

Here Y_{dam} is the radiation damage yield, D a fit parameter to match experimental results. For Y_{dam} one usually uses the physical sputtering yield but with a lower threshold energy. In addition to this damage-induced effect a process at the surface comes into play. It is observed experimentally that the hydrocarbon release under energetic ion bombardment starts at smaller surface temperatures than with thermal atom bombardment. This is explained by means of physical sputtering of weakly bound sp^3 CH_x groups from the surface and described with a yield Y_{surf} . The chemical sputtering yield can then be written as

$$Y_{chem}^{sputter} = Y_{therm} \cdot (1 + D \cdot Y_{dam}) + Y_{surf} \quad (11)$$

The yield according to Eq. (11) depends on surface temperature, energy and flux of impinging hydrogen ions. By means of comparison with experimental data this has been used to formulate a semi-empirical formula to describe these dependencies in detail ²⁰.

Energy dependence of $Y_{chem}^{sputter}$

The chemical sputtering yield calculated according to the formula in ²⁰ is plotted in figure 8 in dependence on the impact energy for two surface temperatures and a hydrogen flux of $1 \cdot 10^{22} \text{ m}^{-2} \text{ s}^{-1}$. At energies below $\sim 2 \text{ eV}$ only the thermal erosion process is active. At higher impact energies the yield is determined by the damage-induced (Y_{dam}) and the surface erosion (Y_{surf}) effect. The qualitative energy dependence is therefore similar to the one of physical sputtering (see figure 2).

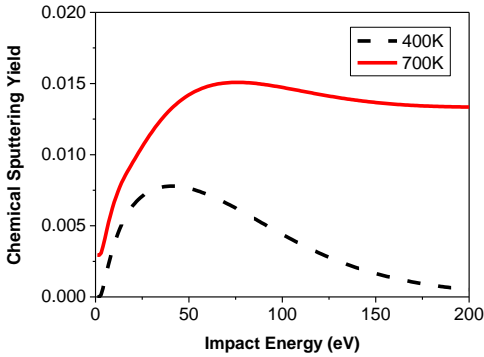


Figure 8: Calculated chemical sputtering yield in dependence on hydrogen impact energy for surface temperatures of 400 and 700K (for $\Gamma_H = 1 \cdot 10^{22} \text{ m}^{-2} \text{ s}^{-1}$).

Surface temperature dependence of $Y_{chem}^{sputter}$

Similar to chemical erosion also chemical sputtering shows a dependence on surface temperature. The common observation is a maximum of the sputtering yield about 900K. However, as will be discussed next, the surface temperature at which this maximum occurs also depends on the impinging hydrogen flux.

Flux dependence of $Y_{chem}^{sputter}$

A compilation of data from various experiments (ion beam devices, linear plasma machines as well as tokamaks) indicates a strong flux dependence of the chemical sputtering yield: with increasing incoming hydrogen flux the yield decreases. Figure 9 shows experimental data together with the graph according to the semi-empirical formula (black line) for chemical sputtering. For comparison the experimental data are normalized to an impact energy of 30 eV and the surface temperature of maximum yield. The flux dependence of the chemical sputtering yield can be understood in terms of the thermal reaction cycle. This predicts an increase of the temperature, where the maximum of chemical sputtering occurs, with flux. At these high surface temperatures the thermodynamic equilibrium of the H/C system shifts from hydrocarbon formation to H_2 release. Therefore, the chemical sputtering yield decreases with increasing flux.

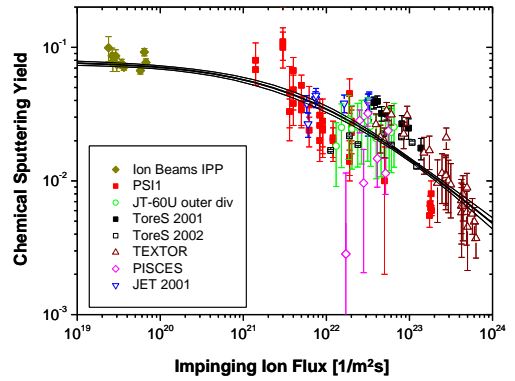


Figure 9: Chemical sputtering yield in dependence on impinging hydrogen ion flux ²¹.

Synergistic effects

Simultaneous bombardment of a carbon surface with thermal hydrogen and energetic ions (e.g. Ar) shows an enhanced carbon erosion compared to bombardment with hydrogen atoms only ²². This can be explained with the above-described model of chemical sputtering: the energetic ions produce broken bonds, which serve as reaction sites for the impinging hydrogen atoms. In addition, the energetic ions can sputter hydrocarbon complexes from the surface.

Also pre-irradiated graphite surfaces suffer from larger carbon erosion than untreated surfaces ²³. Again, the ions produce dangling bonds during the pre-irradiation procedure, which then lead to an increased chemical sputtering and erosion.

C. Other erosion mechanisms

C.1. Blistering

In laboratory experiments it is seen that high fluences (the fluence is the time-integrated flux) of light ions, such as hydrogen and its isotopes or helium, can cause blistering on metal surfaces like tungsten²⁴. This process is caused by trapping of gas atoms inside bubbles at the surface of the metal, which leads to very high pressures inside the bubble. Blistering can lead to enhanced erosion due to flaking of surface material, grain ejection or evaporation of thin blister caps. For helium impact on tungsten the critical fluence at which blistering starts is about 10^{21} to 10^{22} He atoms/m². In case of H isotopes it is about two orders of magnitude higher – on tungsten blistering starts at about 10^{24} D/m². The surface temperature range for H blistering on tungsten is <600°C whereas it goes to higher temperatures for helium.

The influence on blistering of carbon impurity impinging on a tungsten surface has been investigated in²⁵. It is seen that hydrogen blistering occurs at a target temperature of 650K and a carbon concentration of 0.95% whereas with lower carbon concentrations (0.11%) or higher surface temperatures no significant blistering is found. One possible explanation could be the formation of a carbide layer at top of the surface, which enhances hydrogen diffusion beyond the ion range and the carbide layer into the bulk (the solubility of hydrogen in WC is low). Then voids could be created in the bulk, which can develop to blisters. The decrease of blistering at higher surface temperatures could result from the higher thermal energy of hydrogen at which traps triggering the blistering are not active anymore.

Whereas in existing fusion experiments significant blistering has not yet been observed this could be different in ITER and next-step fusion machines. Especially the effect of alpha particles (He⁺) – which are a product of fusion reactions – has to be taken into account.

C.2. Radiation enhanced sublimation (RES)

In case of carbon-based materials anomalously enhanced erosion has been observed at elevated surface temperatures in laboratory experiments²⁶. Figure 10 shows the total erosion yield as result of argon ion bombardment (5 keV) on graphite in dependence on the surface temperature. Whereas the erosion yield is constant up to about 1000K and can be explained with physical sputtering it increases with higher surface temperatures. The increase starts clearly below the sublimation temperature of graphite (about 3200K) and can be described with an exponential function:

$$Y = Y_0 \cdot \exp(-E_{RES}/kT) \quad (12)$$

In Eq. (12) E_{RES} is the activation energy for radiation enhanced sublimation (0.6 – 0.9 eV) and Y_0 a pre-factor. RES is explained by the production of radiation defects (interstitials and vacancies) due to the

energetic ions. The diffusion of the interstitials to the surface then competes with the annihilation with vacancies. Interstitials, which survive annihilation with vacancies, can arrive at the surface and desorb into the gas phase. However, up to now RES has not been observed clearly under tokamak particle impact conditions as e.g. shown in²⁷. This might be due to the high fluxes in combination with low energies.

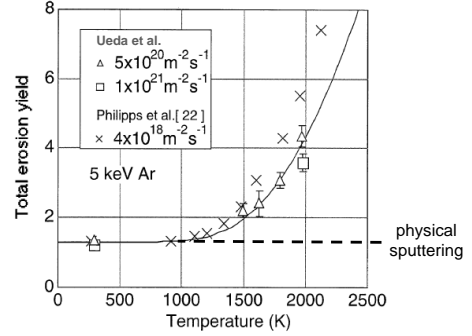


Figure 10: Total erosion yield of graphite due to Ar⁺ ion bombardment in dependence on surface temperature²⁶.

III. DEPOSITION MECHANISMS

A. Reflection & deposition

A projectile hitting a surface can be reflected (backscattered) from the surface with a certain probability which is expressed by the reflection coefficient R ($0 \leq R \leq 1$). Thus, the probability for a projectile of being deposited is $1-R$. The reflected particles are in most cases neutrals. Similar to erosion yields reflection coefficients of atoms can be measured under well-defined conditions in ion beam experiments. In case of molecular species other methods are in use as discussed later. Reflection data at fusion relevant low impact energies are rare. For calculation of reflection coefficients the same tools used for sputtering yield calculations can be applied (BCA based calculations such as TRIM, or MD simulations).

A.1. Atomic species

At first it is assumed that the projectile atoms interact with a smooth surface. Since reflection is governed by collisions between projectile and target atoms, the reflection coefficient depends on projectile and target masses (M_1, M_2) and impact energy and angle (E_0, α_0). Generally, the reflection coefficient increases with increasing mass ratio M_2/M_1 – the reflection of light projectiles at heavy substrate atoms is very effective.

As example, the energy dependence of the reflection coefficient for carbon on carbon at an impact angle of 45° calculated with TRIM is shown in figure 11.

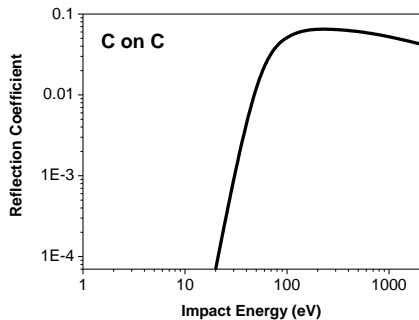


Figure 11: Energy dependence of the reflection coefficient R for carbon on carbon at impact angle of 45° (TRIM).

At impact energies larger than ~200 eV the reflection coefficient decreases monotonically – the projectiles penetrate deeper into the solid and the probability of implantation increases. The TRIM calculations show a steep decrease of reflection going to smaller impact energies. At $E_0 < 20$ eV the calculated reflection coefficient (figure 11) equals zero. However, as discussed in the previous chapter, the BCA method is not valid at such small impact energies below about 10 eV. MD calculations must be used under those conditions showing in contrast non-zero reflection coefficients even at impact energies less than 10 eV^{28,29}.

The dependence of reflection on the impact angle is presented in figure 12 based on TRIM calculations for C on C at impact energy of 200 eV. With increasing angle of incidence the reflection probability increases: with more grazing incidence the projectile penetrates less deep into the solid which decreases the implantation probability.

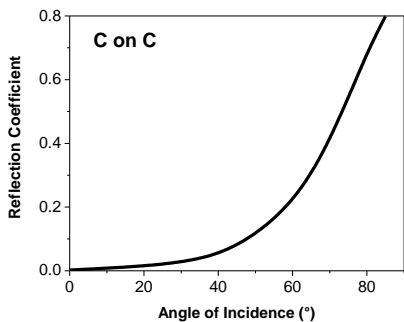


Figure 12: Angle dependence of reflection coefficient R for carbon on carbon at impact energy of 200 eV (TRIM).

The energy distribution of reflected particles depends on projectile – solid combination, impact energy and angle of projectile. For Maxwell-distributed projectiles the energy distribution of reflected particles can be described with an exponential decrease³⁰.

Significant deviations from this occur only for impact energies smaller than 200 eV.

At energies not too large (reduced energy $\varepsilon < \sim 10$, where $\varepsilon = \frac{M_1}{M_1 + M_2} \cdot \frac{a_s}{Z_1 Z_2 e^2} \cdot E_0$ with a_s the screening length and e the electron charge) and normal incidence the reflected particles have a cosine distribution, but deviations occur for different conditions. Nevertheless, for isotropic bombardment a cosine distribution is still a good approximation.

Reflection at rough surfaces

As discussed in the previous chapter II.A. surface roughness will change the local angle of incidence of projectiles compared to the nominal one. In³¹ the case of carbon bombardment onto a rough tungsten surface is discussed. For a nominal angle of incidence of 0° the carbon reflection is increased compared to a smooth surface. The measured reflection on the rough surface can be explained with a mean local angle of incidence of 38° instead of 0°. Similar results are obtained for a nominal angle of incidence of 60° (mean local angle of about 70°).

Prompt deposition

In fusion experiments magnetic fields are applied to ensure confinement³². Eroded and sputtered particles normally start as neutrals from the surface but are ionized at some distance (ionization length λ_{ion}) depending on the local plasma parameters. The magnetic field then leads to a gyration movement of the charged particle with a certain Larmor radius r_L . As can be seen from figure 13, there is some probability for the particle to return to the surface (where it then can be deposited with a probability of 1-R) within the first gyration if the Larmor radius is larger than the ionization length.

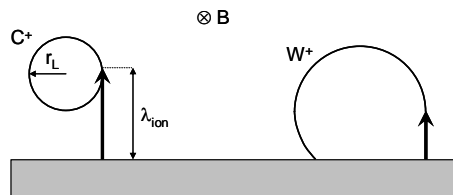


Figure 13: Schematic view of prompt deposition for tungsten W^+ ions.

From this a criterion for prompt deposition can be derived based on the following formulae:

$$\lambda_{ion} = \frac{v_{\perp}}{\langle \sigma v \rangle_{ion} n_e} \quad (13a)$$

where $\langle \sigma v \rangle_{ion}$ in [m³/s] is the ionization probability,

$$r_L = \frac{M \cdot v_{\perp}}{Q \cdot B} \quad (13b)$$

$$P_{prompt} = \frac{\lambda_{ion}}{r_L} = \frac{B}{\langle \sigma v \rangle_{ion} \cdot n_e \cdot M} \quad \text{for } Q = 1 \quad (13c)$$

If $P_{\text{prompt}} < 1$ prompt deposition becomes possible. From Eq. (13c) follows that prompt deposition especially occurs for high-Z materials of high mass M and in case of large ionization probability $\langle \sigma v \rangle_{\text{ion}}$. This is also illustrated schematically in figure 13 for tungsten (high-Z) in comparison to carbon (low-Z).

A.2. Sticking of hydrocarbons

As discussed in chapter II., chemical erosion/sputtering of graphite walls leads to the formation of hydrocarbons C_xH_y (here H represents hydrogen and its isotopes D and T), which are released into the plasma. These species can also return to wall elements and stick to the surface and form hydrocarbon layers. Direct measurements of sticking coefficients of hydrocarbons are rare since quantified radical sources for the species of interest are needed, which requires significant experimental efforts. As alternative to the sticking coefficient the surface loss probability can be measured by means of the cavity technique³⁵, which is more practicable. The surface loss probability β of a hydrocarbon equals the sum of the sticking probability S and the probability γ of the hydrocarbon to react to a non-reactive volatile product via surface reactions. The surface loss probability is thus an upper limiter for the sticking probability.

$$\beta = S + \gamma, \quad \text{with } S + \gamma + R = 1 \quad (14)$$

The cavity technique uses a closed volume with a small entrance slit and hydrocarbons entering this cavity will lead to deposition on the inside walls. With the measured deposition profiles and applying a transport model for hydrocarbons inside the cavity, the surface loss probabilities for the various species are obtained. It is seen that the surface loss probability significantly depends on the hybridization of the radical: $\beta(\text{sp}^1) \sim 0.8$, $\beta(\text{sp}^2) \sim 0.35$ and $\beta(\text{sp}^3) \sim 10^{-3}$. Therefore, especially unsaturated hydrocarbons contribute to film growth. These β values have been obtained with the cavity surface at room temperature. At higher surface temperatures erosion effects become important such that the surface loss probability can become negative (at T_{surf} around 600K)³⁴. At even higher surface temperatures (> 700K) graphitization can take place, which then results in positive loss probabilities associated with film growth. Further experimental data on surface loss probabilities can be found in³⁵.

Molecular dynamics modeling can be applied to calculate sticking coefficients (or surface loss probabilities) for hydrocarbon species. Compared to the experiments, modeling can more easily study the influence of incident energy, angle and surface conditions. As example, figure 14 shows modeled and measured data for CH_2 and CH_3 ³⁶. The experimental data, taken from^{37,38}, are obtained at thermal energies for incoming species. The films were growing under direct plasma contact. Therefore it can be assumed that hard, saturated graphite films did develop.

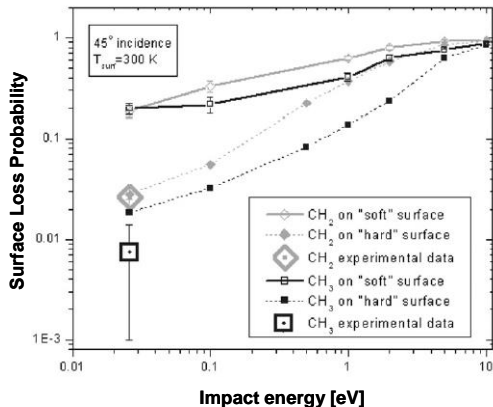


Figure 14: Measured and modeled (Molecular Dynamics) surface loss probabilities for CH_2 and CH_3 ³⁶.

As can be seen in figure 14, only the assumption of a hard surface results in a fair agreement between modeled and measured value of the surface loss probability.

More molecular dynamic modeling results of surface loss probabilities can be found e.g. in^{39,40}.

B. Adsorption

Up to now the deposition has been discussed by implantation of energetic particles into a solid or layer formation on top of it. The impinging particle is thermalized either inside the solid at a certain depth where it forms a binding with the solid atoms at the location where it comes to rest or in the near surface layer of a growing deposition film. Apart from these processes, thermal particles can also be adsorbed at the solid surface. Especially gaseous species (like O_2 or H_2) can form adsorbat layers. Adsorption is possible because the surface atoms of a solid have unsaturated bindings. Therefore it is energetically beneficial to form bindings with other atoms or molecules. Adsorption can be realized via two mechanisms: in case of physisorption the binding between the adsorbat and the solid surface atom is realized via van der Waals forces – which involve no change of the chemical structure of adsorbat and solid surface atom. The binding energy through van der Waals forces is less than about 0.5 eV. In case of chemisorption the binding between adsorbat and solid surface atom happens through the exchange or sharing of electrons resulting in binding energies of about several eV. The rate of adsorption depends on the material combination, the surface structure and temperature. Adsorbed species can be released from the surface via thermal desorption, ion induced collisions and also photons. With increasing surface temperature the rate of desorption increases. In fusion experiments the ion-induced desorption is the most important desorption process.

C. Mechanisms of fuel retention

Retention of the radioactive fuel tritium in the walls of fusion devices is a major concern for future fusion devices since the in-vessel amount of tritium is limited from safety aspects. If a certain limit is reached, plasma operation has to be stopped and the wall has to be cleaned. This limits the availability of the device and demonstrates the need to develop effective cleaning methods, which presently are only marginally developed.

Adsorption

Tritium can be adsorbed at the surface. This mechanism saturates – e.g. in case of a carbon when the surfaces of open porosity are filled. Due to the weak bonding between the adsorbed fuel and the surface atoms this retention mechanism is transient.

Implantation

Energetic tritium particles are trapped by chemical bonding in the material at a certain depth where they come to rest. This mechanism is permanent because of the strong binding between T and the solid atoms. However, it saturates when the maximum possible tritium density is reached.

Bulk diffusion

At higher surface temperatures diffusion into the bulk becomes important. This mechanism is permanent and does not saturate but depends on the diffusion coefficient and also on the density of traps at which the diffusing T can be bound quasi permanently. This process can become important for high Z plasma facing materials (e.g. W) under long-pulse operation and under high fluxes as in ITER and next step devices.

Co-deposition

Eroded material will be deposited somewhere and can thus lead to formation of layers if the deposition does not occur on the location of the material erosion. These layers will contain a certain amount of tritium due to co-deposition with the wall material. The tritium content of co-deposited layers shows a complicated parameter dependence on the layer composition, layer microstructure (density or porosity) and surface temperature. Tritium retention due to co-deposition is permanent and not saturating. This mechanism dominates the overall long-term tritium retention in devices with low-Z walls, which have comparably large erosion rates. If deposited layers become instable, flaking can occur and leading to dust formation inside the device.

Transmutation

In addition, neutrons (as result from fusion reactions) impinging on a beryllium surface will lead to the production of tritium via nuclear reactions, called neutron transmutation. The energetic neutrons produce also damages inside the wall materials, which then can serve as trapping sites for tritium and therefore increase the tritium retention.

IV. EROSION AND DEPOSITION IN FUSION EXPERIMENTS

Wall elements in fusion experiments have contact with the edge plasma and therefore a certain plasma ion flux will hit the wall. An edge plasma with electron temperature T_e , ion temperature T_i and electron density n_e leads in case of a hydrogen plasma to an hydrogen ion flux Γ_{H^+} of

$$\Gamma_{H^+} = c_S \cdot n_e \quad \text{with} \quad c_S = \sqrt{\frac{T_e + T_i}{M_H}} \quad (15)$$

where c_S is the acoustic sound speed and M_H the mass of hydrogen atoms. In addition to plasma ions also impurity ions strike the wall elements. According to the wall materials in use in present experiments these are mainly carbon, tungsten and beryllium. Besides this, there is always a certain oxygen impurity influx. Depending on the experimental conditions additional impurity fluxes can be important such as argon or neon, which are injected into the edge plasma for cooling issues. The local plasma parameters also define the amount of neutrals hitting the wall. Finally, in case of a fusion experiment with a significant amount of fusion reactions also helium ions and neutrons will hit the surrounding walls. Obviously, compared to a laboratory experiment the situation in a tokamak is much more complex: instead of one projectile species there is a whole bunch of impinging projectiles, which in addition are not mono-energetic but have a certain energy distribution.

In the following some selected examples of erosion, transport and deposition experiments will be described. Possible implications for future fusion experiments, especially ITER, will be discussed. Methods of erosion and deposition measurements are described in ⁴¹.

A. Erosion and deposition experiments in TEXTOR

TEXTOR (Torus EXperiment for Technology Oriented Research, sited in Jülich, Germany) is a medium size limiter tokamak with a large plasma radius of 1.75 m and a small plasma radius of 0.48m ⁴². The limiter configuration of tokamaks is described in ³². TEXTOR is an overall carbon machine. It is equipped with two limiter locks, which enable well diagnosed experiments under well-defined plasma conditions.

A.1. Measurement of chemical sputtering in TEXTOR

A spherically shaped graphite test limiter is exposed to the edge plasma of TEXTOR, which has been heated externally to study the dependence of chemical sputtering on surface temperature in detail. The chemical sputtering yield is measured by observing the CD emission near the limiter surface, which is a dissociation decay product of methane CD_4 , which itself is chemically sputtered. To obtain the eroded CD_4 flux from the measured CD light one needs the so-called D/XB value, which is the ratio of CD_4 particles and corresponding CD emission. D/XB values have to be determined independently. The best procedure is to

inject under the same conditions a defined amount of CD_4 and measuring the resulting CD emission. Figure 15 presents methane formation yields from test limiters in TEXTOR at a deuterium flux of about $2 \cdot 10^{22} \text{ m}^{-2} \text{ s}^{-1}$. More details of this experiment can be found in ⁴³. The surface temperature dependence of chemical sputtering yield corresponds well with the one described in chapter II. After a maximum yield at a certain temperature a significant decrease arises at higher temperatures. Maximum yield of about 4% occurs at a surface temperature of $\sim 950\text{K}$.

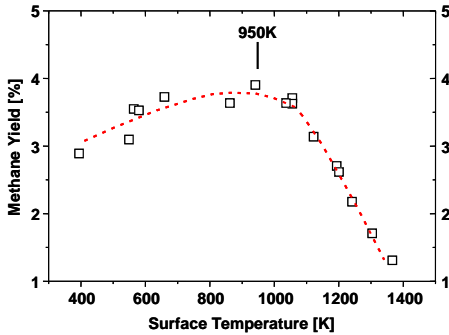


Figure 15: Methane formation yield (left y-axis) in dependent on surface temperature measured at a graphite test limiter exposed to the edge plasma of TEXTOR ⁴³.

A.2. Methane injection experiments in TEXTOR

Deposition of impurities is an important issue for ITER, mainly due to tritium retention by co-deposition in such layers. In TEXTOR this has been investigated in detail by injecting ^{13}C marked methane CH_4 through test limiters of different shape (spherical or roof-like) and material (graphite, tungsten and molybdenum) ^{44,45}. The ^{13}C marked methane has been chosen to distinguish natural ^{12}C deposition caused by background plasma from the deposition caused by local injection. Figure 16 shows exemplarily the tungsten limiters (roof-like and spherical shape) after local $^{13}\text{CH}_4$ injection demonstrating deposition near the injection hole. The broader dark region on the bottom part of the spherical limiter results from carbon ^{12}C deposition.



Figure 16: Tungsten test limiters after plasma exposure in TEXTOR with local methane $^{13}\text{CH}_4$ injection.

In all these experiments the local ^{13}C deposition efficiency (ratio of locally deposited ^{13}C on the test limiter surface and injected ^{13}C) was very small: for spherical limiters 0.3% on tungsten and 4% on graphite and for roof-like limiters 0.17% on molybdenum, 0.11% on tungsten and 0.17% on graphite. The substrate dependence of the ^{13}C deposition can be reproduced by SDTrimSP and is explained by a more effective erosion of thin carbon layers if the underlying substrate has a higher atom mass, see also figure 5. The larger deposition efficiency on spherical limiters can be explained with a flux dilution due to grazing incidence of the magnetic field at top of these limiters, leading to decreased erosion of deposited material.

The described experiments have been modeled with the impurity transport code ERO ⁴⁶. The low ^{13}C deposition efficiencies can be reproduced only if an enhanced erosion of deposited carbon compared to graphite at plasma-wetted areas is assumed ^{47,48}. Using “standard” values for hydrocarbon sticking and re-erosion of deposited carbon, the modeled ^{13}C deposition efficiency is typically in the 50% range. A possible explanation for this enhanced erosion is an ion-induced desorption of loosely bound hydrocarbons that are freshly deposited on the surface. It has to be noted that also from injection experiments with WF_6 and SiH_4 similar conclusions have been drawn concerning the in-situ enhanced erosion of deposits. Thus, this effect can have direct influence on ITER since it provides a process for impurity transport at plasma-wetted areas triggered by successive re-deposition and re-erosion until finally layer formation (and tritium retention) takes place at plasma-shadowed regions.

Experiments with varying surface roughness show an increase of ^{13}C deposition with roughness. Particles deposited inside the valleys of a rough surface are obviously more protected from the incident flux, which in the overall decreases the erosion of deposited ^{13}C . This is in agreement with the effect of surface roughness on physical sputtering as discussed in chapter II.A.

A.3. High-Z test limiter experiments in TEXTOR

The sputtering of high-Z materials has been investigated on test limiters by in-situ by spectroscopy. It is seen that the effective sputtering yield normalized to the impinging deuterium ion flux varies between 0.5 % at high edge density and 3% at low density ⁴⁹. These yields cannot arise from deuterium sputtering alone but actually are dominated by carbon and oxygen impurity sputtering. Comparison with calculated sputtering yields lead to good agreement if also prompt deposition of sputtered tungsten is taken into account. The erosion of tungsten from these limiters at elevated surface temperatures up to melting of W (3700K) does not show an enhanced yield compared to the expected physical sputtering ⁵⁰.

B. ELM-induced enhanced erosion in JET

JET (Joint European Torus, located in Culham, UK) is presently the largest fusion research experiment in the world and therefore the most ITER-relevant device with respect to size and magnetic field configuration. The major plasma radius is 2.96 m and the minor radius of the D-shaped plasma is 2.1 m in vertical and 1.25 m in horizontal direction. As ITER, it is a divertor machine, in which the magnetic field lines are diverted by means of special coils into the divertor chamber. At the divertor plates the main plasma-wall interaction takes place. Details of the divertor concept can be found in³². Main wall and divertor tiles of JET are made out of graphite.

Deposition in the divertor of JET can be measured shot-resolved with Quartz Micro Balances (QMB)⁴¹. One QMB is mounted in the inner divertor of JET (see figure 17.). With the magnetic configuration as indicated in figure 17, deposition at this QMB represents erosion on tile #4, where the strike point (SP) is located. The right part of figure 17 shows the carbon deposition on the QMB for high confinement discharges (H-mode) in dependent on ELM energy to the divertor – ELMs are periodic energy bursts typical for H-mode discharges and are seen as danger for ITER. The observed carbon deposition on the QMB (and thus erosion at the SP) in dependent on ELM energy cannot be explained with physical sputtering – the observed erosion at ELM energies larger than ~50 kJ is much larger and can be described with an Arrhenius-type fit⁵¹. Also chemical erosion should be smaller than ~0.1% according to large surface temperatures expected during an ELM. Possible explanation is a decomposition of formerly deposited carbon layers under ELM impact. This is in line with the observation, that bare graphite material does not suffer from enhanced erosion, as observed in the outer divertor of JET where no layers are formed.

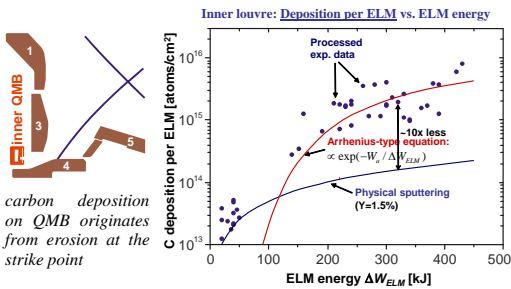


Figure 17: Influence of ELM energy on erosion of carbon layers in the inner divertor of JET⁵¹.

C. Erosion of activated materials

In contrast to present fusion experiments, ITER will produce significant fluxes of high energetic neutrons to the first wall elements during D-T operation, leading to material damages. Whereas physical and chemical sputtering of non-irradiated materials has been

investigated intensively, plasma-wall interaction at neutron damaged materials has been analyzed in much less detail. Main effects of fusion neutron (14.1 MeV) irradiation in fusion devices are the production of radiation-induced defects (such as vacancies, interstitials or traps), changes of the microstructure and change of chemical composition due to transmutation. These processes can lead to degradation of the irradiated materials. For instance, thermal conductivity and ductility can decrease. Moreover, swelling and He embrittlement can occur. Hydrogen diffusion, trapping and recycling will be influenced by radiation damages and thus finally strongly determine bulk retention of fuel. However, in the following only possible influence of radiation damage on erosion properties of materials is discussed.

The effect of radiation damage on sputtering has been investigated in the linear plasma simulator LENTA⁵². Instead of radiation damage due to fusion neutrons, energetic ions have been used to produce radiation damages in the materials. *Carbon-based materials* have been bombarded with 5 MeV C⁺ ions. Average produced damage is calculated (SRIM, a BCA code similar to TRIM) to be $\langle D \rangle = 9.7$ dpa with maximum damage of $D = 60$ dpa at 5 μm inside the sample. Various types of graphite have been irradiated and then exposed to the linear plasma device LENTA with D⁺ impact energy of 100 eV and surface temperature less than 40°C. Erosion has been measured by means of weight loss. Enhanced erosion of irradiated samples compared to non-irradiated ones has been observed as following:

- $Y_{\text{SEP irr}} / Y_{\text{SEP}} = 2.6$
- $Y_{\text{pyro irr}} / Y_{\text{pyro}} = 4.8$
- $Y_{\text{MPG irr}} / Y_{\text{MPG}} = 1.6$

Tungsten has been bombarded with 3-4 MeV He²⁺ ions to create radiation damages. SRIM calculations reveal maximum damage of $D = 5$ dpa at a depth of 6 μm , $\langle D \rangle = 0.3$ dpa. Exposure of irradiated tungsten samples to the LENTA plasma did show – in contrast to carbon – no clear effect of radiation damage on the erosion.

However, experiments with fusion relevant plasma-facing materials (including also beryllium) having neutron-induced damages are missing. Damage profiles induced by fast neutrons from fusion may be different from ion-induced ones (e.g. due to broader energy spectrum compared to monoenergetic ions) and thus leading to different effects.

V. SUMMARY & CONCLUSIONS

The most important sputtering and erosion mechanisms occurring in fusion experiments have been described. Physical sputtering occurs for all combinations of projectile and target but disappears at low impact energies below a threshold (around several eV). Eroded species are mainly neutral atoms or small clusters from the substrate material. Under most

conditions physical sputtering can be described by collision cascades inside the solid initiated by the impinging projectile using the binary collision approximation. However, at low impact energies ($< \sim 10$ eV) molecular dynamics methods have to be used to take into account chemical effects. The sputtering yield for high-Z materials is in general smaller than for low-Z materials. Chemical erosion and sputtering occurs only for special combinations of projectile and target material. In fusion research chemical erosion/sputtering due to hydrogen (and its isotopes) is of main importance for carbon-based materials and beryllium. For carbon also the erosion due to oxygen is relevant. Eroded species are molecules formed out of projectile and carbon – thus hydrocarbons C_xH_y , BeH and BeH_2 and CO_x . In contrast to physical sputtering no threshold energy exists. At large surface temperatures and high incoming fluxes the yield of chemical erosion/sputtering for carbon decreases significantly. A model, which describes the thermodynamical and kinetic processes involved in chemical erosion and sputtering for carbon has been presented.

Main features of backscattering of atomic species have been described. As for physical sputtering, the underlying physics can be described with the binary collision approximation or molecular dynamic simulations depending on the impact energy. Sticking of hydrocarbons is rather complex. Experimental data and also molecular dynamics simulations exist for various hydrocarbons species. It is seen that particularly unsaturated hydrocarbons contribute to layer growth.

Fuel retention, which is a major concern in future fusion devices, takes place by means of adsorption, implantation, bulk diffusion and co-deposition. From present experiments it is concluded that long-term retention in devices with low Z first walls (e.g. C or Be) will be dominated by co-deposition of fuel in deposited layers. It is thus important to understand the involved processes of erosion, material transport and deposition.

Examples of erosion and deposition experiments in fusion devices and plasma simulators have been given. The main dependencies of physical sputtering, chemical erosion and sputtering are confirmed by experimental observations. However, in fusion experiments the situation is more complicated due to the presence of various species, which leads to material mixing.

REFERENCES

- ¹ Progress in the ITER Physics Basis, *Nucl. Fusion* **47** (2007).
- ² G. COUNSELL et al., "Tritium retention in next step devices and the requirements for mitigation and removal techniques," *Plasma Phys. Control. Fusion*, **48**, No. 12 B, B189-B199 (2006).
- ³ A. KIRSCHNER et al., "Estimations of erosion fluxes, material deposition and tritium retention in the divertor of ITER," *J. Nucl. Mat.*, **390-391**, 152 (2009).

- ⁴ R. BEHRISCH (ed.), "Sputtering by particle bombardment. I. Physical sputtering of single-element solids," *Topics in applied physics*, **Vol. 47**, Berlin/Heidelberg/New York, Springer 1981.
- ⁵ J. BOHDANSKY, "A universal relation for the sputtering yield of monoatomic solids at normal ion incidence," *Nucl. Instr. Meth.*, **B2**, 587 (1984) and C. GARCIA-ROSALES et al., "Revised formulae for sputtering data," *J. Nucl. Mat.*, **218**, 8 (1994).
- ⁶ W. ECKSTEIN, "Calculated sputtering, reflection and range values," *Report IPP*, **9/132** (2002).
- ⁷ B. UNTERBERG, theses proceedings.
- ⁸ M. KÜSTNER, W. ECKSTEIN, E. HECHTL, J. ROTH, "Angular dependence of the sputtering yield of rough beryllium surfaces," *J. Nucl. Mat.*, **265**, 22 (1999).
- ⁹ H.L. BAY, W. BERRES, E. HINTZ, "Surface normal velocity distribution of sputtered Zr-atoms for light-ion irradiation," *Nucl. Instr. Meth.*, **194**, 555 (1982).
- ¹⁰ J. BOHDANSKY, "Sputtering," in Data compendium for plasma-surface interactions, *Nucl. Fusion, Special Issue*, eds. R.A. Langley et al. (1984).
- ¹¹ R.K. JANEV, Yu.V. RALCHENKO, T. KENMOTSU, K. HOSAKA, "Unified analytic representation of physical sputtering yield," *J. Nucl. Mat.*, **290-293**, 104 (2001).
- ¹² Y. YAMAMURA, Y. ITIKAWA, N. ITOH, "Angular dependence of sputtering yields of monoatomic solids," *Japan Report, IPPJ-AM-26*, Nagoya University (1983).
- ¹³ W. ECKSTEIN, *Computer simulation of ion-solid interaction*, Springer, Berlin (1991).
- ¹⁴ W. ECKSTEIN, R. DOHMEN, A. MUTZKE, R. SCHNEIDER, "SDTrimSP: A Monte-Carlo code for calculating collision phenomena in randomized targets," *Report IPP*, **12/3** (2007).
- ¹⁵ W.D. WILSON, L.G. HAGGMARK, J.P. BIRSACK, "Calculations of nuclear stopping, ranges, and straggling in the low-energy region," *Phys. Rev.*, **B 15**, 2458 (1977).
- ¹⁶ W. ECKSTEIN, W. MÖLLER, "Computer simulation of preferential sputtering," *Nucl. Instr. Meth. Phys. Research*, **B7/8**, 727 (1985).
- ¹⁷ W. ECKSTEIN, "Oscillations of sputtering yield," *Nucl. Instr. Meth. Phys. Research*, **B171**, 435 (2000).
- ¹⁸ J. KÜPPERS, "The hydrogen surface chemistry of carbon as a plasma facing material," *Surf. Sci. Rep.*, **22**, 249 (1995).
- ¹⁹ E. VIETZKE et al., "Chemical erosion of amorphous hydrogenated carbon films by atomic and energetic hydrogen," *J. Nucl. Mat.*, **145-147**, 443 (1987).
- ²⁰ J. ROTH, "Chemical erosion of carbon based materials in fusion devices," *J. Nucl. Mat.*, **266-269**, 51 (1999).

- 21 J. ROTH et al., "Flux dependence of carbon chemical erosion by deuterium ions," *Nucl. Fusion*, **44**, L21-L25 (2004).
- 22 E. VIETZKE, K. FLASKAMP, V. PHILIPPS, "Hydrocarbon formation in the reaction of atomic hydrogen with pyrolytic graphite and the synergistic effect of argon ion bombardment," *J. Nucl. Mat.*, **111+112**, 763 (1982).
- 23 E. VIETZKE, V. PHILIPPS, K. FLASKAMP, "Chemical reactivity of atomic hydrogen on graphite pre-irradiated by hydrogen and argon ions," *J. Nucl. Mat.*, **162-164**, 898 (1989).
- 24 Y. UEDA, K. TOBITA, Y. KATOH, "PSI issues at plasma facing surfaces of blankets in fusion reactors," *J. Nucl. Mat.*, **313-316**, 32 (2003).
- 25 T. SHIMIDA et al., "Blister formation on tungsten surface by irradiating hydrogen and carbon mixed ion beam," *J. Plasma and Fus. Research*, **78**, 289 (2002).
- 26 V. PHILIPPS, K. FLASKAMP, E. VIETZKE, "Enhancement of the sputtering yield of pyrolytic graphite at elevated temperatures," *J. Nucl. Mat.*, **111&112**, 781 (1982).
- 27 V. PHILIPPS et al., "Investigation of radiation enhanced sublimation of graphite test-limiters in TEXTOR," *J. Nucl. Mat.*, **220-222**, 467 (1995).
- 28 D.A. ALMAN, D.N. RUZIC, "Molecular dynamics simulation of carbon/hydrocarbon reflection coefficients on a hydrogenated graphite surface," *J. Nucl. Mat.*, **313-316**, 182 (2003).
- 29 K. OHYA et al., "Simulation of hydrocarbon reflection from carbon and tungsten surfaces and its impact on codeposition patterns on plasma facing components," *J. Nucl. Mat.*, **390-391**, 72 (2009).
- 30 W. ECKSTEIN, H. VERBEEK, "Data on light ion reflection," *Report IPP*, **9/32** (1979).
- 31 I. BIZYUKOV et al., "Relevance of surface roughness to tungsten sputtering and carbon implantation," *J. Appl. Phys.*, **100**, 113302 (2006).
- 32 M. VAN SCHOOR, these proceedings.
- 33 C. HOPF et al., "Surface loss probabilities of hydrocarbon radicals on amorphous hydrogenated carbon film surfaces," *J. Appl. Phys.*, **87**, 2719 (2000).
- 34 M. MEIER, A. VON KEUDELL, W. JACOB, "Consequences of the temperature and flux dependent sticking coefficient of methyl radicals for nuclear fusion experiments," *Nucl. Fus.*, **43**, 25 (2003).
- 35 A. VON KEUDELL, W. JACOB, "Elementary processes in plasma-surface interaction: H-atom and ion-induced chemisorption of methyl on hydrocarbon film surfaces," *Progress in Surf. Science*, **76**, 21 (2004).
- 36 D. A. ALMAN, D. N. RUZIC, "Molecular dynamics simulation of hydrocarbon reflection and dissociation coefficients from fusion-relevant carbon surfaces," *Phys. Scri.*, **T111**, 145 (2004).
- 37 H. TOYODA, H. KOJIMA, H. SUGAI, "Mass spectroscopic investigation of the CH₃ radicals in a methane rf discharge," *Appl. Phys. Lett.*, **54**, 1507 (1989).
- 38 M. SHIRATANI et al., "Surface reaction kinetics of CH₃ in CH₄ rf discharge studied by time-resolved threshold ionization mass spectrometry," *Jap. J. Appl. Phys.*, **36**, 4752 (1997).
- 39 P. TRÄSKELIN et al., "Molecular dynamics simulations of CH₃ sticking on carbon first wall structures," *J. Nucl. Mat.*, **313-316**, 52 (2003).
- 40 E. NEYTS et al., "Unraveling the deposition mechanism in a-C:H thin-film growth: A molecular-dynamics study for the reaction behavior of C₃ and C₃H radicals with a-C:H surfaces," *L. Appl. Phys.*, **99**, 014902 (2006).
- 41 A. KRETER, these proceedings.
- 42 U. SAMM, "TEXTOR: A pioneering device for new concepts in plasma-wall interaction, exhaust, and confinement," in Special Issue on TEXTOR, *Fusion Science Techn.*, **47**, 73 (2005).
- 43 A. POSPIESZCZYK et al., "Chemical erosion measurements from various carbon based limiters and coatings from TEXTOR-94," *J. Nucl. Mat.*, **241-243**, 833 (1997).
- 44 A. KRETER et al., "Investigation of carbon transport by ¹³CH₄ injection through graphite and tungsten test limiters in TEXTOR," *Plasma Phys. Control. Fus.*, **48**, 1401 (2006).
- 45 A. KRETER et al., "Study of local carbon transport on graphite, tungsten and molybdenum test limiters in TEXTOR by ¹³CH₄ tracer injection," *J. Nucl. Mat.*, **363-365**, 179 (2007).
- 46 A. KIRSCHNER et al., "Simulation of the plasma-wall interaction in a tokamak with the Monte-Carlo code ERO-TEXTOR," *Nucl. Fus.*, **40**, 989 (2000).
- 47 A. KIRSCHNER et al., "Modelling of carbon transport in fusion devices: evidence of enhanced re-erosion of in-situ re-deposited carbon," *J. Nucl. Mat.*, **328**, 62 (2004).
- 48 S. DROSTE et al., "Modelling of ¹³CH₄ injection experiments with graphite and tungsten test limiters in TEXTOR using the coupled code ERO-SDTrimSP," *Plasma Phys. Control. Fus.*, **50**, 015006 (2008).
- 49 V. PHILIPPS et al., "Experiments with tungsten limiters in TEXTOR-94," *J. Nucl. Mat.*, **258**, 858 (1998).
- 50 G. SERGIENKO et al., "Erosion of a tungsten limiter under high heat flux in TEXTOR," *J. Nucl. Mat.*, **363-365**, 96 (2007).
- 51 A. KRETER et al., "Nonlinear impact of edge localized modes on carbon erosion in the divertor of the JET tokamak," *PRL*, **102**, 045007 (2009).
- 52 B.I. KHRIPUNOV et al., "Evidence of radiation damage impact on material erosion in plasma environment," *J. Nucl. Mat.*, **390-391**, 921 (2009).

RECYCLING AND TRANSPORT OF NEUTRALS

D.Reiter

Institut für Energie- und Klimaforschung, Forschungszentrum Jülich GmbH,
 EURATOM Association, Trilateral Euregio Cluster
 D-52425 Jülich, Germany

ABSTRACT

Removal of helium, the ash from the D-T-fusion reaction, from a burning plasma flame, is one of the critical issues for future thermonuclear burning plasma. Even in plasmas driven by additional heating to large Q-values this is a severe problem. Recombination of fuel and ash ions at plasma exposed surfaces, re-emission as neutral particles and subsequent pumping (“recycling”) provides, at least in principle, the mechanism to flush the plasma from its ash. However, plasma surface interaction has to be limited in order to protect vessel components from excessive thermal load, often a conflicting requirement.

I. INTRODUCTION

This lecture deals with two, on first sight only loosely related topics. Firstly with the issue of helium removal from a stationary burning D-T fusion device, and secondly with the so called “recycling process” in the plasma near exposed first wall components. The strong interrelation of these two issues will be a major point in the following discussion.

Any kind of steady burning process depends upon both sufficient thermal insulation (to keep the temperature in the flame above a critical value) and, at the same time, sufficient particle throughput (re-fuelling, and ash removal). In the flame of a usual fire, this temperature is of the order of 1000 Kelvin, and the buoyancy driven flow of hot (used) air out of the flame provides the particle throughput. (For example a simple candle flame is choked within seconds by its own ash, if gravity is absent, as has for example been shown in demonstration experiments carried out during space flights).

For a D-T fusion plasma flame, these considerations can be translated into the terse statement, that the quality of thermal insulation (quantified by an energy confinement time) must exceed one tenth of the particle lifetime in the flame.

II. BURN CONDITION IN THE PRESENCE OF HELIUM ASH

To see this, we first consider the power balance equation, as it is often discussed for thermonuclear burn criteria (see the lecture by E.Rebhan and G. Van Oost, this issue, reference [1]). We replace the quasi-neutrality assumption $n_e = n_i$ (the electron density and ion density, respectively) made there now by the more general expression $n_e = n_i + 2 \cdot n_{He}$ (because the helium ion is fully ionized under reactor conditions). Introducing the fractional densities $f_i = n_i/n_e$, $f_{He} = n_{He}/n_e$ and $f_{tot} = n_{tot}/n_e$ for the fuel ions, the helium ash ions and the total particle content (electrons, fuel ions and ash) respectively, the equation for the fusion product $p\tau_{E2}$ (loc. cit.) becomes:

$$p\tau_E = \frac{(f_{tot}/2)^2}{f_i^2 \frac{\langle\sigma v\rangle}{(kT)^2} \cdot \frac{E_\alpha}{24} - \frac{2}{3} C' T^{-3/2}} \quad (1)$$

The new factors $f_{tot}(\geq 1)$ and $f_i(\leq 1)$ describe the contribution of the helium ash to the total plasma pressure and the fuel dilution effects, respectively. $E_\alpha = 3.5$ MeV, i.e., we assume complete thermalization of the helium ion, before it is lost, and C is a constant in the expression for radiation losses, which, in this particular form of ignition condition, have not been included in the definition of τ_E .

A similar consideration, balancing the helium particle production rate with the losses of helium particles due to their finite lifetime in the system (τ_α^*), yields ([2])

$$p\tau_E = \frac{f_{He} \cdot (f_{tot}/2)}{\rho \cdot f_i^2 \frac{\langle\sigma v\rangle}{kT} \cdot \frac{1}{8}} \left(from \frac{n_{He}}{\tau_\alpha^*} = \frac{1}{4} n_i^2 \langle\sigma v\rangle \right) \quad (2)$$

ρ denotes, as in [2], the confinement time ratio τ_α^*/τ_E . We will, further on, take this ratio as a constant parameter, i.e., independent of density and temperature. One might relax that choice, e.g. by employing empirical scaling laws for τ_E and τ_α^* . But this might be already well beyond the power of such simple zero-dimensional considerations, in particular due to the possibly very

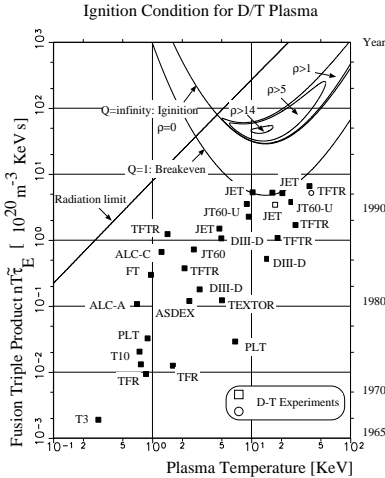


Figure 1: Fusion triple product vs. plasma temperature. Experiments, break-even ($Q=1$) and boundaries for ignition. Parameter $\rho = \tau_{\alpha}^*/\tau_E = 0, 1, 5, 14$

different spatial distributions of energy sources and recycling particle sources (see below).

Expressing f_i and f_{tot} in terms of f_{He} , and equating the expressions for $p\tau_E$ from Eqs. (1) and (2), one arrives at a cubic algebraic equation for f_{He} : $g(f_{He}) = 0$. The four coefficients are functions of temperature and ρ . Including one further free parameter f_Z for a fractional density of impurities of charge Z (which contaminate the plasma due to wall erosion processes or are introduced on purpose for plasma edge temperature control) is straightforward (*loc.cit.*). See again refs. [1] and [2] and Figure 2.

Clearly, f_{He} must lie in the interval $(0, 0.5)$.

Inspecting the cubic polynomial for f_{He} , one finds one (unphysical) root outside this range, and two other roots. These are negative at temperatures significantly below the critical ignition temperature and they turn conjugate complex with increasing temperature near the critical temperature. In these two regions no steady self-sustaining plasma burn is possible. The two roots become positive then at larger temperatures, in the region between 5 and 100 KeV (depending upon the value of ρ) and they lie in the physically accessible range between 0 and 0.5. Beyond this region the two roots turn complex again, due to the fact that radiation losses and fuel dilution prohibit steady burning at these even higher plasma temperatures.

If one inserts the physically relevant fractional helium densities obtained in this way (the algebraic closed form expressions for the roots of cubic polynomials) in either Eq. (1) or Eq. (2), the closed burn contours shown in Figure 1 (labelled $\rho = const$) result. Note that for convenience the ordinate has been re-scaled from $nT\tau_E$ to $nT\tilde{\tau}_E$, with $\tilde{\tau}_E$ denoting the “global confinement time”, which, in contrast to τ_E also contains radiation losses. In the definition of the parameter ρ , however, we have retained the energy confinement time τ_E . Otherwise the second (upper) branch would disappear, and the more familiar open burn-curves would result. Whether or not the ignition curves are open or closed (one or two solutions for f_{He}) depends upon the definition of ρ , not upon the definition of τ_E in the ordinate (e.g. in the fusion triple product).

If one uses the global confinement time $\tilde{\tau}_E$ to derive ignition conditions, (as it seems to be common practise) rather than τ_E as defined in Equation (1), and if one excludes the helium ash from consideration (i.e., if one sets $\rho = 0$) then one has to add a further constraint (called “radiation limit”, see Figure 1) to prevent unphysical ignition parameters $nT\tilde{\tau}_E$ resulting from negative transport losses (i.e., gains) balancing radiation losses.

The fact that the closed contours shrink in size and disappear beyond a certain critical ratio ρ_{crit} ($\rho_{crit} \approx 15$ for a pure D-T plasma) translates into the statements made above concerning the often conflicting requirements of good thermal insulation and poor particle confinement.

If one specifies a fixed relative impurity concentration $f_Z = n_Z/n_e$ for one (effective) impurity of charge Z and modifies f_{tot} and the radiation term in Equation (1) accordingly, then one finds that the contours shrink in size even faster with increasing Z and f_Z . For each confinement parameter ρ a maximum tolerable impurity concentration results, and, vice versa, for each impurity concentration one finds a critical maximum $\rho = \rho_{crit}(Z, f_Z)$. See Figure 2 and note the difference for light and heavy impurities (the abscissa has a log-scale).

Note that the need for poorer particle confinement (i.e., larger particle fluxes onto limiter and divertor targets, hence smaller values of ρ) may result in incomplete thermalization of the supra-thermal 3.5 MeV helium ash (we have assumed complete thermalization in the discussions above) and/or in increased surface erosion and hence impurity concentration. Whether nature provides an operational window to fulfill both requirements in an economic fusion power plant is still an open question.

Various further aspects may readily be included in this simple “point reactor analysis” without changing

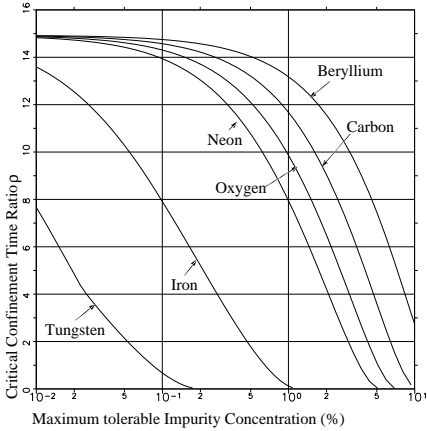


Figure 2: Critical confinement time ratio versus maximum tolerable impurity concentration, for Beryllium, Carbon, Neon, Oxygen, Iron and Tungsten (note: log-scale on abscissa)

the qualitative picture. For example the assumption of flat temperature and density profiles may be weakened by introducing profile shape factors in the balance Eqs. (1) and (2) (see e.g. ref. [3]). So called “advanced fuel” reactors based upon different fusion processes (such as D-D fusion, D-³He fusion, even including secondary fusion reactions between fusion products and the fuel particles) can be studied within the same framework.

In the case of more than one type of fusion product (say m different types, e.g. ⁴He, ³He, and p, and even if all parasitic fusion processes are accounted for) simply one particle balance equation for each type of ash particle has to be written. This results in a coupled set of m cubic polynomials for the m fractional ash densities, and again in the same type of closed ignition contours. For the cases studied so far, the critical confinement time in advanced fusion concepts ratio was found to be even smaller than in case of the D-T fusion reactor (ref. [2]).

III. THE PARTICLE LIFETIME τ_{α}^*

The energy confinement time τ_E in tokamak plasmas is an experimentally well characterized quantity. Various empirical scaling laws derived from large databases exist. Much less well defined is the particle confinement time τ_{α}^* entering the above formulae. A simple relation between τ_E and the heat diffusivity χ is frequently used: $\tau_E \propto \frac{1}{\chi}$. In a similar manner the lifetime of an ash particle, born in the burning core of a

fusion plasma and with a spatial source profile identical to the fusion energy source profile, can be related to a particle diffusion coefficient: $\tau_{\alpha 1} \propto \frac{1}{D}$. Both confinement times should also scale with a^2 (a denoting the small plasma radius).

This can be seen as follows:

If one assumes the particle and power input on axis, no inward pinches, spatially constant diffusivities D and χ , then one finds triangular profiles, from integrating

$$\Gamma = D \, dn/dr, \quad Q = n(0) \, \chi \, dT/dr \quad (3)$$

and consequently

$$T(r) \propto \frac{a}{\chi}(1-r/a), \quad n(r) \propto \frac{a}{D}(1-r/a). \quad (4)$$

This is based upon the assumption that the dominant plasma particle source (not the helium source) is still located in the edge plasma (not in the core) and hence convected power flux is negligible for most of the plasma region.

Hence the resulting confinement time ratio ρ would be determined (excluding convective fluxes) by the ratio $\frac{\chi}{D}$.

Since one can expect $\tau_{\alpha 1}$ to scale with a^2 but a much weaker dependence of τ_E on a is found experimentally, this would lead to extremely pessimistic predictions for the larger future fusion devices.

When a plasma particle finally reaches a wall, it is neutralized there and re-emitted into the plasma as neutral atom or molecule.

A fraction ϵ may be pumped away, the remaining fraction $R = 1 - \epsilon$ will be re-ionized in the plasma. R is generally referred to as “recycling coefficient”, ϵ is the pumping efficiency.

If the spatial distribution of the primary source helium ions (i.e., of the fusion alpha particles) and of the recycling source (i.e., of the re-ionized helium particles) would be approximately the same, then, as a result of non-perfect pumping, the particle confinement time $\tau_{\alpha 1}$ would simply be enhanced by the factor $\frac{1}{1-R}$.

$$\tau_{\alpha}^* = \frac{\tau_{\alpha}}{(1-R)} \quad (5)$$

with typical values of R close to one. Hence: again very pessimistic prospects.

Fortunately for the helium ash (as for the fuel particles) this similarity of source profiles for energy and particles is not the case, and a slightly more detailed consideration is necessary, carefully trying not to “overcharge” our simple model. Strictly: only transport analysis codes can provide a somewhat realistic picture. A modified expression for τ_{α}^*

$$\tau_{\alpha}^* = \tau_{\alpha 1} + \frac{R}{1-R} \tau_{\alpha 2} \quad (6)$$

has been derived in [2] from an analytical solution of a somewhat more refined (as compared to Eq. (2) above) but still 0-dimensional particle conservation equation.

We may consider re-ionization of recycling helium particles as a second source. This source, however, is located in the edge. Let us assume that all neutral helium particles are ionized at $r = a - \lambda_{iz}$. Hence:

$$-D \, dn/dr = 0 \text{ for } r < a - \lambda_{iz}, \quad (7)$$

i.e., $n(r) = n(0) = \text{constant}$ in the core region for this contribution and n decreases linearly in the ionization zone (the boundary plasma)

$$a - \lambda_{iz} < r < a.$$

(If a pinch $v_{pinch} = -2 D r/a^2$ is included, then a Gaussian $n(r)$ profile is added on top of the density-plateau).

For this recycling source contribution one then finds a particle confinement time

$$\tau_{\alpha 2} = \frac{a \lambda_{iz}}{D} \quad (8)$$

This $\tau_{\alpha 2}$, in contrast to τ_E and $\tau_{\alpha 1}$, is, essentially, a plasma edge quantity, since the ionization length depends upon T_e and n_e in the edge, and only the value of D (if it is not radially constant) within the ionization zone $a - \lambda_{iz} < r < a$ matters. Inserting for the ionization length λ_{iz}

$$\lambda_{iz} \approx \frac{v_0}{0.5 n_e < \sigma v >_{iz}} \quad (9)$$

with $v_0 \approx \text{some } 10^4 m/s$ the radial velocity of recycling atoms, we see that $\tau_{\alpha 2} \propto n_e^{-1}$. This scaling is often found in limiter-tokamaks, but not in divertor-tokamaks (see the lectures on edge plasma physics, and on divertors). In divertor experiments a significant fraction of re-ionization takes place within the scrape off layer, and that wrecks (amongst others) any simple relation between n_e , the flux Γ , the edge plasma density and particle confinement times τ_p .

We may conclude, that the decisive confinement parameter ρ is given as:

$$\rho = \rho_{core} + C_{edge}/n_e \quad (10)$$

One may not be able to do much about the core plasma transport parameter ρ_{core} , in particular size may not help. However, C_{edge} can probably strongly be influenced by appropriate divertor or limiter design. This is the second reason, in addition to the target surface loading problem (loc. cit.), why plasma edge physics has gained so much relevance in fusion research in the last few years.

IV. A RANDOM WALK MODEL FOR N_{HE}

The same result as in Equation (6) can be obtained using stochastic arguments: We consider a random walk (of the helium particle) in a system of only two states: the plasma core (birth point of the particle by fusion reaction), P1 and the limiter or divertor target, P2. All particles start at point P1, and travel (with probability one) to point P2, in a time $\tau_{\alpha 1}$. At point P2 they are either absorbed with probability ϵ (instantaneous transition into a final “limbo” state P3, if one wishes to look at it that way). With probability $(1-\epsilon)$ the particle returns to P2. This single return trip takes $\tau_{\alpha 2}$ seconds, the lifetime of recycled particles in the plasma core.

This recycling lifetime $\tau_{\alpha 2}$ should scale weaker with the plasma size a than $\tau_{\alpha 1}$, but instead scale with the relative re-penetration depth for neutral particles. Thus: the more relevant this second time $\tau_{\alpha 2}$ for the overall mean particle lifetime τ_{α}^* , the less severe becomes the helium removal problem for larger fusion devices.

The mean lifetime of the random walking particle is given as:

$$\tau_{\alpha}^* = \sum_{i=0}^{\infty} \tau_i \cdot p_i, \quad (11)$$

where p_i is the probability of exactly i recycling events before pumping, and τ_i is time spend in the core by a particle, which is absorbed after precisely i recycling events. Clearly: $p_i = \epsilon \cdot (1 - \epsilon)^i$, and $\tau_i = \tau_{\alpha 1} + i \cdot \tau_{\alpha 2}$. The infinite series can readily be shown to converge to:

$$\begin{aligned} \tau_{\alpha}^* &= \tau_{\alpha 1} + \frac{1 - \epsilon}{\epsilon} \cdot \tau_{\alpha 2} \\ &= \tau_{\alpha 1} + \frac{R}{1 - R} \tau_{\alpha 2} \end{aligned} \quad (12)$$

Rather than evaluating the infinite series equation (11) analytically, one could instead have used a pocket calculator with a random number generator. Generating a few thousand histories, each starting in point P1 and terminating in point P3 and accumulating the mean lifetime of the “test particles” would confirm (then only within statistical precision) the relation (12) above.

From this and Equation (2) we note, that the density of particles in a certain volume is given by the mean lifetime spend in that volume by random walking particles, multiplied by the source strength and divided by the volume. This stochastic procedure becomes far more handy than the analytical arguments from ref. [2], if more details are to be considered. For example the number of states can be increased to simulate the effects of several pumping stations with different pumping rates each (e.g., the effect of un-pumped divertor legs, etc.). Or the volume of interest can be subdivided

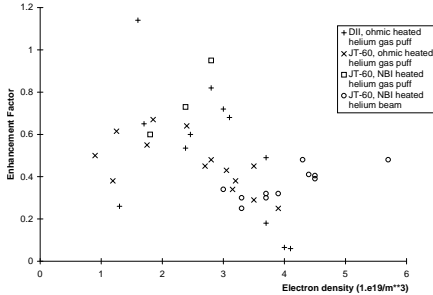


Figure 3: Helium enrichment near pumping stations from various Tokamak experiments, showing both (small) enrichment in some cases but also significant (unfavorable) de-enrichment.

into smaller volumes and the averaged density in each such cell can be computed.

We will return to this point later, but then for a very detailed random walk model with the number of possible states increased to infinity. The Chapman-Kolmogoroff equation of the resulting Markoff process in that case will directly be related to the linear transport equation (in integral form) for recycling neutral particles. But the method for obtaining particle densities from estimating the mean time spend by random walkers in specified volumes will essentially remain the same.

In closing this section we note that the ϵ in Equation (12) is the (effective) probability for a particle to be pumped, once it leaves the burning plasma core. One can (see again ref. [2]) reformulate Equation (12) in terms of a true surface pumping efficiency ϵ_r and a screening efficiency ϵ_S of the plasma edge region between wall and burning core. $\gamma_S = 1 - \epsilon_S$ is then the probability for an un-pumped particle to return to the core before it hits the wall for the next time.

One finds:

$$\tau_{\alpha}^* = \tau_{\alpha 1} + \frac{(1 - \epsilon_S)(1 - \epsilon_r)}{\epsilon_r} \tau_{\alpha 2} \approx \tau_{\alpha 1} + \frac{\gamma_S}{\epsilon_S} \tau_{\alpha 2} \quad (13)$$

The decisive factor $\frac{\gamma_S}{\epsilon_S}$ describes the recycling process and is often the ratio of two small numbers. It is hard to estimate, and has to be investigated on a case to case basis, usually resorting to complex Monte Carlo simulation models.

In particular the issue of “helium enrichment” near pumping stations (i.e. the relative decrease or increase of the fractional helium pressure near pumps due to configurational and/or atomic physics effects) remains rather unpredictable for this reason. No clear trends on whether the relative abundance of helium increases or

decreases in divertors or near limiters, as compared to upstream conditions, are found experimentally either. This depends upon configurational details, in particular upon the position of the pump relative to the strike point and the plasma. See Figure 3.

V. EXPERIMENTAL RESULTS

Since the particle lifetime τ_{α}^* has two components with a different scaling on machine size, it is rather difficult to extrapolate from the present database to next generation fusion devices such as ITER or even to a reactor. However, keeping in mind that roughly $\rho \approx \frac{\chi}{1-R}$ in present experiments might still characterize global confinement, one may get an idea of the experimental situation firstly by assuming a realistic value of R , (say: $R = 0.9$), and secondly by inspecting experimental data for the ratio $\frac{\chi}{D}$ (see [4], and references therein). Heat and density pulse propagation analysis (after sawtooth crashes) have shown $5 < \frac{\chi}{D} < 12$ in JET, and $\frac{\chi}{D} \approx 3-6$ in JT-60. Smaller values of $\frac{\chi}{D} \approx 2-3$ have been reported from JET from profile analysis, and $\frac{\chi}{D} \approx 4$ for L-mode and $\frac{\chi}{D} \approx 1$ for super-shot conditions in TFTR. A ratio of 5 is predicted from theory for “advanced stellarator” concepts.

Note that in case of an inward pinch, i.e. a non-diffusive inward flow of particles, the confinement time ratio is underestimated by $\frac{\chi}{D}$ even in case of perfect pumping $R = 0$. The existence of such pinch effects is often indirectly concluded from the experimentally observed peaking of density profiles even inside the region of particle sources. In this source free region and for roughly constant diffusion coefficients D , the profiles would have to be flat otherwise.

Direct experimental results for $\frac{\tau_{\alpha 1}}{\tau_E}$ are reported from TEXTOR and TFTR, with values in the range $\sim 2-3$ in both cases. Together with about 10% particle removal efficiency provided by the ALT-II pump-limiter at TEXTOR, the critical confinement time ratio mentioned above is presently just marginally within reach in medium sized tokamak experiments. This and taking the arguments from the previous section into account may indeed provide some optimism with regard to the ash removal issue.

VI. RECYCLING

As illustrated above, the mechanism of recycling of neutral particles back into the plasma plays a crucial role, and, since ratios of small numbers are involved, seemingly small details of this process can have large effects. Experimentally the neutral particle densities are found to be rather low in tokamak plasma edge regions, of the order 10^8 to 10^{12} ($\#/cm^3$). They are negligible further into the discharge, at least for the present tokamak generation such as TEXTOR, ASDEX-Upgrade and all larger devices. The only exception, occasionally, is a small region of highly localized recycling in the vicinity of the limiter strike point or near the “foot-print” of the plasma on a divertor target (neutral particle densities of up to 10^{14} ($\#/cm^3$) there).

Neutral molecules dissociate, usually in an even narrower layer at that location in the plasma where the electron temperature reaches the dissociation threshold energy (10 to 15 eV).

Neutral Franck-Condon atoms are formed there, with typically a few eV kinetic energy. Together with the other atoms, which are directly reflected from the surfaces, they penetrate the plasma.

The three figures in the right column show typical trajectories of neutral particles recycled at the divertor targets of ASDEX-Upgrade, JET and ITER divertor targets. In the first two cases they fill the divertor plasma (a smaller fraction in case of the JET divertor) and the vacuum region, but do not significantly (not at all in case of JET) penetrate the plasma core. The similar picture for ITER typical conditions shows an effective screening already of the divertor plasma against neutral particle penetration. (This causes one of the major uncertainties with regard to the ability of neutral particles to disperse power and momentum from an ITER-sized divertor in a “high recycling” regime, and has led to a revision of divertor concepts, away from high recycling divertors towards “detached” or “gas-target” divertors, see, again, the lectures on edge physics and divertors).

The trajectories in these figures are computed from a particle simulation program using the plasma density and temperature as input, and simulating the various elementary collision processes between neutral particles, the surface structures and the plasma electrons and ions.

The most dominant collision process considered here is charge exchange (CX): in the resonant case the neutral atom and the plasma ion exchange identity (scattering angle $\theta = \pi$ in the center of mass frame). As pointed out first by Sacharov back in 1961, it is in this way that low energy neutrals near the wall can gain energy through frequent CX scattering and penetrate

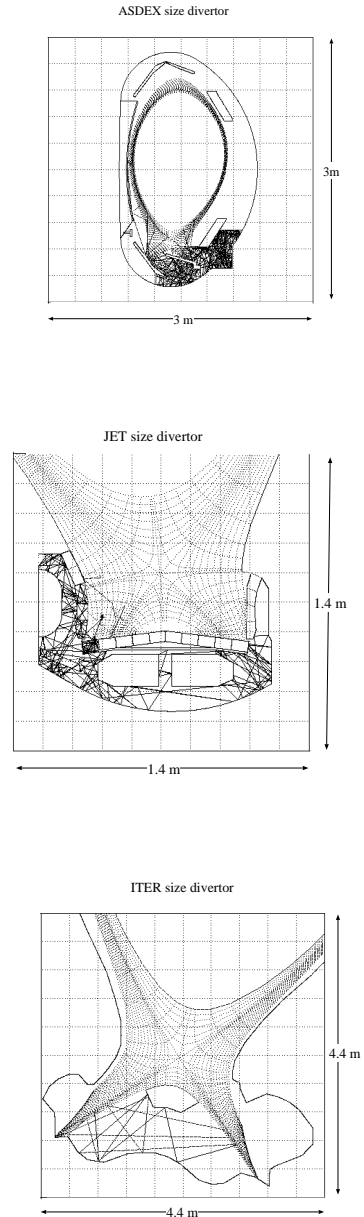


Figure 4: Neutral particle trajectories in Divertors, showing reduced penetration (compared to size) in larger divertors.

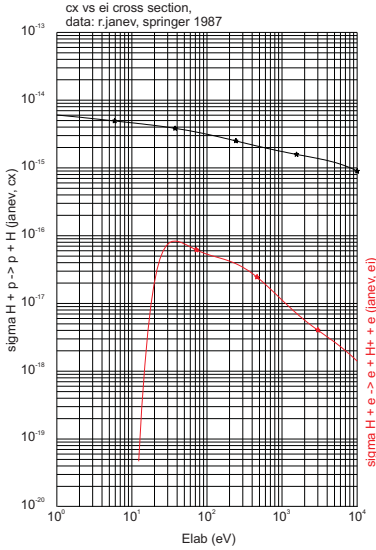


Figure 5: charge exchange cross section for hydrogen, in cm^2 (upper curve) and electron impact ionization cross section (lower curve)

into the plasma interior. Typically, in present limiter-tokamaks the cloud of neutral atoms reaches about 10 cm radially into the discharge. Using simple 1D diffusion equations, a diffusion coefficient for neutral atom penetration $D_n = (\delta x)^2/\delta t$ with δx the mean free path for CX and δt the mean time between CX events, one finds an effective penetration length for neutral particles into the plasma given as the harmonic mean of the charge exchange- and the ionization mean free path, both taken at the ion thermal speed. This is far in excess of the ionization mean free path alone, taken at a speed of thermal wall atoms or 3 eV Franck-Condon dissociation products.

This dominant resonant charge exchange (i.e.: $H + p \rightarrow p + H$) happens if the two particles, p and H , approach each other, then, for a short time, the one electron belongs to both (an intermediate H_2^+ molecule is formed) and, after separation, the electron stays with the former ion, and leaves the former neutral now in the ionized state. Since collision partners have changed their internal energy, this would be an in-elastic process. However, quantum-mechanically, it cannot be distinguished from ordinary elastic scattering between the two partners, i.e., from the event in which the electron happens to stay with the same particle after the event.

Therefore, quantum-mechanically, there is only **one** process, usually termed “elastic”, but including

both types of “events”. One must carefully avoid double counting charge exchange. I.e., one must never add an quantum mechanically derived “elastic” collision rate to a charge exchange rate taken from another source. The reader can find bad examples of neutral gas transport calculations, with this severe error in the dominant reaction rates, even in a recent issue of the “Journal of Nuclear Fusion” from the year 2000 (despite a correct treatment of this issue since about 40 years in most applications in fusion research). Needless to mention: these authors find “much better agreement with experiment” after having included, erroneously, the “new elastic effect”....

The terminating event in the lifetime of a neutral particle may either be the entry into a pump, or re-ionization by electron impact collisions.

Usually this re-ionization process is a step-process, with various intermediate excitations, radiative decays, etc. of the neutral atom before ionization. These processes are most conveniently described in terms of so called collisional-radiative ionization models, see, e.g., the “atomic and molecular data section” in [8]. They lead to an enhancement of the mean energy dissipated from the electrons from 13.6 eV per ionization to typically 25 eV per ionization and even larger values at electron temperatures below 20 eV. Similar concepts apply for dissociation of molecules, dissociative recombination of molecular ions, etc... For H_2 molecules, colliding with protons, there is also a (“non-diagonal”) charge exchange process, which can be resonant if the molecule is sufficiently high vibrationally excited. This leads to an atom and H_2^+ . If this molecular ion then decays (after electron impact) into two ground state atoms, this entire chain of events is, effectively, a recombination (accompanied by a dissociation of the molecule), and is therefore referred to as MAR (molecular assisted recombination). If the final products of the H_2^+ are one atom and one ion, however, then, effectively, this entire chain starting from the charge exchange is nothing but one effective dissociation (then termed MAD, molecular assisted dissociation, by abuse of language).

The competing rate coefficients for these two reaction chains are shown in Fig. 6. These coefficients must be multiplied by the local neutral molecule density and the proton density to turn them into a volumetric rate.

Clearly, for increasing plasma density, the dissociative channel grossly outweighs the recombinative channel. Despite the fact that the MAR rate may be large by itself (this having triggered quite optimistic predictions for the operational window for detached divertors initially, see e.g., the ITER physics basis studies, Nuclear Fusion, special issue, Dec. 2000) it has turned out to be a fairly irrelevant recombination process, after a more detailed computer modelling of dense edge

molecule assisted recombination, ion conversion channel

molecule assisted recombination, ion conversion channel

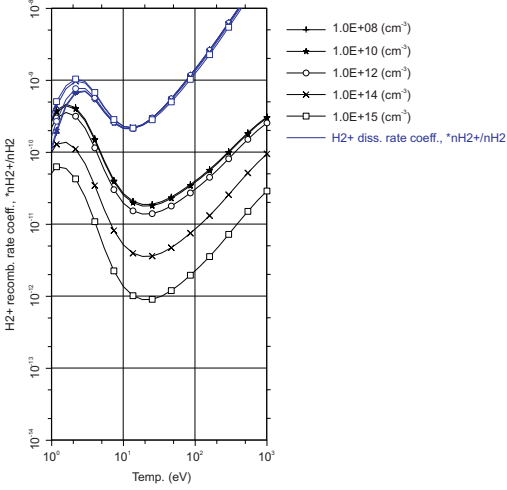


Figure 6: Rate coefficients for destruction of H_2 by proton impact leading to three neutral atoms (lower set of curves, MAR), and leading to one ion and two atoms (upper set of curves, MAD). The curves are labelled by the electron density.

plasma conditions (e.g. detached divertors) had been carried out. This is because the competitive process (MAD) is even much stronger and molecules are dissociated long before they can “assist recombination”, in current fusion edge plasma conditions.

In general: neutral particle recycling (atoms or molecules) is of crucial importance for the present concepts of plasma edge control: the neutral particles must be kept in the discharge long enough (i.e. the pump must not be too strong) to provide significant plasma cooling: presently 10 to 20% of the total power flowing into the edge plasma is dissipated via the neutral particle channel in high density divertor experiments.

This fraction must, according to more recent design considerations, be further increased for save reactor divertor concepts. On first sight this seems to conflict directly with the earlier discussed requirements of strong pumping and efficient particle removal. An intensive search for possible solutions out of this dilemma is presently carried out in many laboratories in the world, largely based on computer simulation experiments.

With regard to such computer models for the recycling process in particular (see again: ref. [8]) one has to note that the ratio of the charge exchange rate to the ionization rate is larger than one (typically three

to five, depending upon the electron temperature and only very weakly on the ion temperature), but not very large. The neutral gas cloud is re-ionized after a few CX mean free paths into the plasma. Furthermore the density in this cloud is usually too small in order to permit neutral-neutral elastic collisions to contribute significantly to the entropy production for the neutral component. A more precise quantification of this statement is provided by a “generalized Knudsen number” for the neutral particles, which relates entropy producing processes (resonant charge exchange with Maxwellian background ions, elastic collisions) to characteristic free flight and absorption lengths:

$$\overline{Kn}_{eff}(\vec{r}) = \frac{\overline{\lambda}_{sc}(\vec{r})}{\overline{l}_{eff}(\vec{r})} \quad (14)$$

with

$$\overline{\lambda}_{sc}(\vec{r}) = \frac{1}{n_0(\vec{r})} \int d\vec{v} \lambda_{sc}(\vec{v}, \vec{r}) f_0(\vec{v}, \vec{r}) \quad (15)$$

and

$$\overline{l}_{eff} = \frac{\overline{\lambda}_{absorption} \cdot \overline{l}_{freeflight}}{\overline{\lambda}_{absorption} + \overline{l}_{freeflight}} \quad (16)$$

Here f_0 denotes the neutral particle distribution function, λ_{sc} the mean free path for scattering (charge exchange and elastic), $\lambda_{absorption}$ is the mean free path for ionization (averaged over f_0 similarly), and $\overline{l}_{freeflight}$ is the averaged and also spatially dependent distance to the nearest boundary. Values of \overline{Kn}_{eff} below 0.1 indicate fluid like (diffusive) behavior of neutral particles. Unfortunately, typical profiles of \overline{Kn}_{eff} in divertors and near limiters are found to be about one or larger in those regions, in which the dominant neutral particle plasma interaction takes place.

This has two computationally important consequences:

1. the neutral gas transport has to be described on a kinetic rather than on a fluid level
2. the kinetic (Boltzmann-) equation is linear.

A large literature exists on the linear transport theory and the methods of solution. Analytical methods are e.g. discussed in [5], an extensive review of particle simulation (“Monte Carlo”-) techniques can be found in [6].

The linear kinetic transport equation can be written most conveniently for the collision density Ψ , with $\Psi = \frac{1}{\lambda} v f_0$ (loc. cit.) as:

$$\Psi(x) = S(x) + \int dx' \Psi(x') \cdot K(x' \rightarrow x) \quad (17)$$

Here x' and x are the states $(\underline{r}', \underline{v}', i')$ and $(\underline{r}, \underline{v}, i)$, respectively, in phase space, at two successive collisions. i and i' are species indices. S is the once collided contribution from sources Q , and the kernel K is usually decomposed into a collision- and a transport kernel, i.e. C and T , where

$$K(\underline{r}', \underline{v}', i' \rightarrow \underline{r}, \underline{v}, i) = \quad (18)$$

$$C(\underline{r}'; \underline{v}', i' \rightarrow \underline{v}, i) \cdot T(\underline{v}, i; \underline{r}' \rightarrow \underline{r}).$$

The kernel C is (excluding normalization) the conditional distribution for new co-ordinates (\underline{v}, i) given a collision at position \underline{r}' and can be decomposed further into:

$$C(\underline{r}'; \underline{v}', i' \rightarrow \underline{v}, i) = \sum_k p_k C_k(\underline{r}'; \underline{v}', i' \rightarrow \underline{v}, i), \quad (19)$$

with

$$p_k = \frac{\sigma_k}{\sum_k \sigma_k} \quad (20)$$

with summation over the index k for the different types of collision processes under consideration and p_k defined as the (conditional) probability for a collision to be of type k . σ_k is the total inverse local mean free path (dimension: 1/length) for each collision type. The normalizing factor

$$c_k(x') = \sum_i \int d\underline{v} C_k(\underline{r}', \underline{v}', i' \rightarrow \underline{v}, i), \quad \hat{C}_k = \frac{1}{c_k} C_k \quad (21)$$

gives the mean number of secondaries for this collision process. The function \hat{C}_k then is a conditional probability density.

The kernel T describes the free streaming motion of the particles between the collision events, and basically is determined by the total mean free path (or, equivalently, by the total macroscopic cross-section). T can be interpreted as the distribution density for the distance l for a free flight starting from \underline{r}' to the next point of collision $\underline{r} = \underline{r}' + l \cdot \underline{v}/|\underline{v}|$

Despite its simple physical content (namely: expressing particle conservation in phase space) this linear kinetic equation is algebraically extremely complex, and can be solved analytically or numerically only under often pathologically simplified assumption. A statistical simulation, however, accounting for the full complexity without any restriction, is straight forward.

With a procedure similar to the one explained above for the mean lifetime of an ash particle in the reactor burning core, a Markoff chain can again be constructed from the terms in this transport equation. One may for example use S as initial (birth) distribution and the kernel K as transition probability from

Particle sources near ALT2 Limiter (TEXTOR)

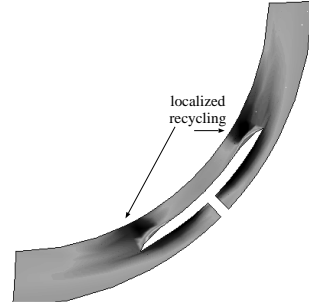


Figure 7: Re-ionization source distribution around ALT2 limiter (TEXTOR). Note: the main fraction is ionized within the confined plasma region (distinct from divertors)

one event to the next. Termination of a history can again be formulated in terms of the pumping probability, but in addition the ionization process provides a further, physically motivated, absorption probability. (Strictly speaking, the absorption probability used in the Markoff process needs not be related to a physical particle absorption process, but it facilitates interpretation of histories generated from the Markoff process, as e.g. in figures shown above.

Distinct from the simple Markoff chain discussed above, now the relevant macroscopic quantities (densities, re-ionization rates, pumped fluxes etc.) cannot be computed directly. Instead random number generators are employed to generate a large set (a few 10.000) of random walks. These are then processed into profiles of the required quantities by statistical averaging.

As outlined above the mean value of the time spend by all histories in any particular region of the plasma can directly be scaled into an estimate of the neutral particle density. Likewise, the spatially resolved re-ionization rate can be obtained by proper scaling of the statistical mean (over the random walks) of the ratio of path length to the ionization mean free path in any particular cell of the computational volume.

Note that this and related profiles enter as source terms in the fluid equations which are generally used for describing tokamak edge plasmas

Figure 7 shows one such re-ionization profile in the vicinity of the ALT-II pump-limiter in TEXTOR. Plasma and neutral gas transport are computed consis-

tently by iteration a finite element plasma fluid code with a kinetic neutral particle (“Monte-Carlo-”) code until overall convergence [7]. Even under such rather open limiter conditions (compared with high recycling divertors, in which the neutral particle cloud usually is much more localized, the neutral particle recycling terms are the dominant terms in the plasma fluid equations near the target surfaces and determine the plasma flow there. Typically the radial plasma flow near limiters is driven by localized neutral particle recycling. On top of the limiter, often the radial plasma flow is found to be reversed (back into the plasma core).

This feature is characteristic for limiters and one of the main arguments in favor of the technologically much more demanding divertor configuration. Given that collisional friction is the dominant force acting on surface released impurities and recycling helium particles, the risk of plasma poisoning and insufficient helium removal is obvious. A major effort in limiter tokamak studies, therefore, is devoted to this issue.

In principle, divertors do not suffer from such problems. Since the plasma flow is channelled outside (or at least far away from) the plasma core, direct contamination by surface released impurities is less likely. In particular the strong parallel plasma flow towards the target surface provides the impurity and helium retention mechanism.

However, as recent computer studies and also a few experiments have revealed, also these concepts can suffer from a certain kind of flow reversal: if the accumulated recycling sources within one flow channel are larger than the parallel plasma flow to the divertor target in this channel, the plasma flow in this channel has to reverse (as a simple consequence of particle conservation).

Such excess re-ionization can occur in some flow channels (at the expense of other flow channels) due to the unhindered cross field motion (via CX) of the neutral particles. The onset of this flow reversal depends sensitively on details of pumping and baffling in the divertor. If pumping is too inefficient, (either because of physical and engineering constraints, or on purpose because of the beneficial effects of large neutral gas densities in divertor plasma for heat dissipation), in some parts of the divertor plasma the plasma flow can reverse (away from the target, along the field-lines, back into the confined discharge). And, depending on the location of their sources, impurities and helium particles might be dragged back into the main discharge (“the divertor throws up”).

VII. CONCLUSIONS

The issue of helium removal for steady plasma burn

is apparently very closely connected with the details of plasma recycling via the neutral particle channel. Firstly because only neutral ash particles can be channelled into pumping stations, but secondly also because of the effects of neutral particle recycling on the edge plasma flow, and thus on the forces acting on the ionized helium particles. Various conflicting requirements have to be met simultaneously such as:

- good confinement (for energy balance)
- poor confinement (for particle throughput)
- strong pumping (for ash removal)
- weak pumping (for the favorable high recycling conditions)

The search for a plasma edge configuration compatible with all these constraints, both experimentally and by computer simulations, is one of the key design issues to be solved before a reliable plasma surface interaction concept for ITER (and a future reactor) can be developed.

REFERENCES

1. E. REBHAN and G. VAN OOST, “Thermonuclear burn criteria for DT-plasmas”, this volume.
2. D. REITER, G.H. WOLF, H. KEVER, “Burn Condition, Helium Particle Confinement and Exhaust Efficiency”, Nucl. Fusion, 30 (1990), p2141
3. D. REITER, G.H. WOLF, H. KEVER, “Stationary burning: Analysis of profile effects”, J. Nucl.Mater.,176&177, (1990), p756
4. D. REITER et al., “Helium Removal from Tokamaks”, Plasma Physics and Controlled Fusion, 33, 13, (1991), p1579
5. K.M. CASE, P.F. ZWEIFEL, “Linear transport theory”, Addison Wesley Pub. Comp., (1967)
6. J. SPANIER, E.M. GELBARD, “Monte-Carlo principles and neutron transport problems”, Addison Wesley Pub. Comp., (1969)
7. D. REITER, “Neutral Gas Transport in Fusion Devices” in: Atomic and Plasma-Material Interaction Processes in Controlled Thermonuclear Fusion, R.K. JANEV and H.W. DRAWIN (eds.), Elsevier Science Publishers B.V., (1993)
8. D. REITER, “The EIRENE code users manual”, <http://www.eirene.de> (2006)

LABORATORY EXPERIMENTS AND DEVICES TO STUDY PLASMA SURFACE INTERACTION

G.J. van Rooij

FOM-Institute for Plasma Physics Rijnhuizen, Association EURATOM-FOM
Edisonbaan 14, 3439 MN Nieuwegein, The Netherlands; www.rijnh.nl

ABSTRACT

Laboratory experiments are widely used to study plasma surface interaction issues for fusion research. In this paper it is described why dedicated experiments for PSI are advantageous and what the requirements are to reach the parameter regime relevant for ITER. An overview is given of some typical devices, particularly PISCES-B, PSI-2 (nowadays JULE-PSI), Nagdis, Pilot-PSI, and Magnum-PSI, along with selected results to illustrate their capabilities.

I. INTRODUCTION

The interaction between plasma and the material wall of a fusion device has become a discipline in its own right within fusion research (eg. [1]). In earlier days it was merely a matter of optimization of confinement of the core plasma by minimizing the inflow of impurities that are generated at the walls. This has led to the application of low z wall materials and the development of the divertor configuration. Nowadays, the challenges lie down in the development of a material wall in combination with plasma scenarios that ensure prolonged operation of ITER [2] and fusion reactors beyond ITER such as DEMO. The issues are retention of the fuel (a safety issue for ITER and a problem for the fuel cycle for future fusion energy plants), life time of the wall, and formation of dust (again merely a safety issue).

The proximity of a plasma to a surface results in a wide variety of processes that well may interfere. These include chemical erosion and physical sputtering, association and recombination, formation of clusters of molecules, redeposition, hydrogen retention. Together, these form the complex 'plasma surface interaction' (PSI). It is obvious that it is difficult to diagnose, understand, and predict the outcome of these processes. This becomes even worse if the plasma conditions that are encountered are as diverse as all the PSI processes that are involved, as is inevitably the case in a fusion experiment.

It is difficult to study the PSI physics in present day fusion devices, especially if it concerns the conditions that are expected for ITER. Especially the exposure times relevant for ITER are not met and certainly not in combination with the expected extreme particle and power loads. Also a critical aspect is the inaccessibility of the wall and in particular the divertor in fusion devices. Firstly, this means that it is not easy to change (parts of) the wall material to quickly test different candidate targets. It also means that targets studied post mortem have faced a wide range of different experimental conditions so that it will be very hard to correlate them with the observed damage. Similarly, diagnostic access for *in situ* studies limited.

Several linear plasma generators are operational in the world. Table 1 lists the main operational parameters of a few that are especially active on plasma-surface interactions: PISCES (Plasma Interaction with Surface and Components Experimental Simulator) at the University of California, San-Diego [3], NAGDIS (Nagoya University Divertor Simulator) [4], PSI in Berlin [5, 6], which has been moved to Juelich and is nowadays called JULE-PSI[7] and LENTA [8] at Kurchatov Institute in Moscow. Studies at these devices have led to a progress in understanding of processes relevant for a tokamak divertor. Some phenomena were even first discovered at linear plasma generators and later observed in tokamaks. For example, a detached regime in helium and hydrogen plasma as well as appearance of plasma flow reversal were discovered and investigated at PISCES-A [9]. A series of PSI studies at moderate flux densities was carried out at these linear apparatuses. To give an impression of the wide range of investigated subjects, we mention several of them. Measurements of erosion mechanisms from solid (carbon, tungsten) and liquid materials (gallium and lithium) were performed at the PISCES-B apparatus [10]. Experiments with hydrogen plasma at NAGDIS-II were devoted to the role of molecular activated recombination in the plasma detachment [11, 12]. A series of experiments on the interaction of helium plasma with tungsten surfaces was conducted at the NAGDIS-I set-up [4, 13]. Studies at PSI-1 fo-

Table 1: Parameters of various experiments for PSI in the world. PIG = Penning Ionisation gauge; CA = Cascaded Arc; Magnum-PSI data are specifications.

	NAGDIS-II	PSI-2	PISCES-B	LENTA	Pilot-PSI	Magnum-PSI
Type source	PIG	PIG	PIG	e-Beam	CA	CA
Power [kW]	10.5	50	85	7.5	45	270
Pressure source [Pa]	10	0.1-1	0.1-1		10^4	10^4
Pressure target [Pa]	0.1	0.01-0.1	$10^{-3} - 1$	0.2-7	1-10	< 10
T_i target [eV]	50	< 15	10-500	5	0.1 - 5	0.1 -10
T_e target [eV]	10	< 30	3-50	0.5-20	0.1 - 5	0.1 -10
n_i target [m^{-3}]	$6 \cdot 10^{19}$	10^{19}	$10^{17} - 10^{19}$	10^{19}	10^{21}	10^{20}
Ion flux target [$m^{-2}s^{-1}$]	10^{22}	10^{22}	$10^{21} - 10^{23}$	$5 \cdot 10^{21}$	$2 \cdot 10^{25}$	10^{24}
$B[T]$	0.25	0.1	0.04	0.2	1.6	3
Beam diameter target [cm]	2	6-15	3-20	2.5	1.5	10
Distance to target [m]	2.8	2.5	1.5	2	0.5 - 1	1.0-1.5

cused on chemical sputtering of carbon based materials at high ion flux densities of deuterium plasma [14, 15]. Investigations on high-frequency and microwave radiation from the zone of interaction of hydrogen and helium plasma streams with neutral background gas targets were performed at LENTA linear plasma generator [16]. Also the development of a liquid lithium surface as a candidate for a reactor first wall [17] and imitation of deuterium plasma interaction with tungsten surfaces [18] and carbon materials [19] were carried out at this device.

All of the above mentioned plasma generators can produce hydrogen, deuterium and helium plasma with electron densities $10^{18} - 5 \cdot 10^{20} m^{-3}$, flux densities in the range of $10^{21} - 10^{23} m^{-2} \cdot s^{-1}$, and operate in a magnetic field of 0.1 - 0.3 T. Unfortunately, this does not cover the conditions that are expected for ITER (these will be estimated in the next paragraph) at least by an order of magnitude in the flux density. To bridge this gap, FOM-Rijnhuizen is constructing a new linear plasma generator, Magnum-PSI [21]. It aims at providing a 10 cm diameter plasma beam with hydrogen plasma flux density $10^{24} m^{-2} s^{-1}$ at a temperature of 1-5 eV, in a magnetic field of 3 T. Design issues for Magnum-PSI, in particular the development of a plasma source that produces the required plasma fluxes, are investigated in a smaller device that is presently operational, Pilot-PSI. In the mean time, Pilot-PSI has demonstrated to be capable of producing these fluxes, albeit in a smaller beam diameter and in pulsed magnetic fields of 1.6 T. This makes the device already a unique tool for PSI studies in the extreme flux regime.

In this paper the emphasis will be on Pilot-PSI results to illustrate the capability of linear machines for PSI research. In addition, some important results of other machines are mentioned and cited to give a complete picture. But first the requirements with respect

to particle and power fluxes that are expected for the ITER divertor will be estimated to set the framework for the recent developments at the FOM Institute Rijnhuizen.

II. PARTICLE AND POWER FLUXES EXPECTED IN THE ITER DIVERTOR

The starting point for these rough estimations is the ITER objectives and capabilities: 500 MW of fusion power, produced with ~ 50 MW of heating power. Power that is exhausted from the core plasma of ITER will be directed to the target of the divertor. A large part will be radiated away, but still 25% will reach the divertor. The power losses P_{loss} are estimated as one fifth of the fusion power (i.e. the fusion energy ending up in helium) plus the ignition power:

$$P_{loss} = 150 MW. \quad (1)$$

So, a quarter of this power is transported in the scrape off layer (SOL) to the target over a connection length $L_{\parallel} \sim 100m$. The width of the SOL follows from the ratio between the parallel and cross field heat conduction, which is classically equal to:

$$\frac{\kappa_{\parallel}}{\kappa_{\perp}} \propto (\omega_{ce} \tau_{ei})^2 \approx 10^4. \quad (2)$$

This yields for the width of the SOL:

$$L_{\perp} = L_{\parallel} \left(\frac{\kappa_{\parallel}}{\kappa_{\perp}} \right)^{-1} \propto 100m \times 10^{-4} \approx 10^{-2}m. \quad (3)$$

The power fall-off length in present day devices, which is also expected for ITER, is indeed close to this value: 5 cm. With the main radius of ITER being $R = 6.2m$, the

parallel power density reaching the target is estimated as:

$$q_{\parallel} \approx \frac{P_{loss}}{4\pi RL_{\perp}} \approx 50 \frac{MW}{m^2}. \quad (4)$$

This power is directed onto the target under an angle (the angle of the field line to the target in the poloidal plane). A typical value for this so-called flux expansion is 10.

$$q_{target} = q_{\parallel}/10 \approx 5 \frac{MW}{m^2}. \quad (5)$$

To put this number in perspective: it is a tenth of the power at the surface of the sun. The particle flux density follows from the sheath voltage, which is typically assumed to be five times the electron temperature T_e . For ITER it is imperative that T_e is below ~ 10 eV because otherwise the acceleration of light impurities over the sheath voltage leads to physical sputtering of the wall material. This yields for the particle flux:

$$\Gamma_{ion} = \frac{q_{target}}{eV_{sheath}} = \frac{q_{target}}{5eT_e} \approx 10^{24} m^{-2} s^{-1}. \quad (6)$$

III. PRODUCTION OF LOW TEMPERATURE PLASMA

A common concept to produce the low temperature plasma in a linear experiment is acceleration of electrons that are emitted from a heated LaB_6 cathode to a ring anode. This geometry is very similar to that of a Penning Ionization gauge. It is for example in use at the PISCES and PSI experiments. In order to produce electron currents up to $40 A/cm^2$, the cathode is indirectly heated to $\sim 1800^{\circ}C$ with tungsten filaments. Total cathode currents of 500-1000 A are common. The pressure inside the source is low, typically at most several Pa. A more detailed description of this source type is given by Goebel et al. [22]. An important advantage of this type of source is that its pressure is compatible with high vacuum conditions.

In order to make a large step in flux densities (and total fluxes), the Pilot-PSI relies on a high pressure source: the cascaded arc [23, 24]. Figure 1 shows a schematic overview of the source, which consists of tungsten cathodes in an ionization chamber, a stack of water-cooled copper plates and a nozzle. A central bore in the plates forms the discharge channel, presently 4-7 mm diameter and 3 cm length. Gas is introduced into the cathode chamber at a pressure of typically 10^4 Pa. It is heated by the electron current emitted from the cathode tips, thus creating a plasma. In turn, these cathode tips are heated by the impact of ions that are accelerated upstream over the negative potential of the cathodes. The large pressure difference with the vacuum vessel downstream makes the plasma to expand

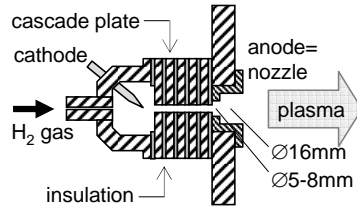


Figure 1: Schematic of the cascaded arc as it is used to produce hydrogen plasma in Pilot-PSI. A central bore of 4 mm diameter in 5 electrically insulated water-cooled plates forms the 30 mm length plasma channel. Hydrogen flows at several slm ($2.5 \text{ slm} = 1.0 \times 10^{21} \text{ H}_2/\text{s}$) into the cathode chamber at 10^4 Pa, the discharge current is stabilized to $\sim 10^2$ A.

into the vessel. Due to the large pressure inside the ionization channel, the electrons and ions are well coupled in temperature via Coulomb collisions [25]. These temperatures are typically 1-3 eV as the plasma is at the lower end of the Saha equilibrium [24]. Fig. 2 shows as a function of the magnetic field the plasma conditions that are routinely produced in Pilot-PSI with this cascaded arc. It is seen that the magnetic field plays a crucial role for the plasma density. If it would be absent, the densities would be orders of magnitude lower. In that case, the plasma would freely expand and drop in temperature. At temperatures below ~ 1 eV, recombination via molecular processes becomes efficient and at the relatively high pressures at which the Pilot-PSI is operated ($\sim 1 \text{ Pa}$, due to the large gas inflow from the source)

IV. ON THERMAL EQUILIBRIUM AND POWER TRANSPORT

The characteristics of the plasma produced by these two different types of plasma sources differ significantly. Firstly, the equilibrium between the electron and ion temperature is dependent on the source pressure. This is illustrated by Fig. 3 The high pressure cascaded arc operates at typically $10^3 - 10^4$ Pa, which is in the region where the electron temperature T_e and the heavy particle temperature T_h are close to equilibrium and are of order 1 eV. The low pressure sources operate at a pressure that is typically 2 orders of magnitude lower. The graph shows that this uncouples the two temperatures and increases the electron temperature towards 10 eV.

The pressure difference has also an impact on the plasma convection speed. In the low pressure sources, this speed is typically of the order of 100 m/s, whereas in the cascaded arc the plasma is accelerated to sound

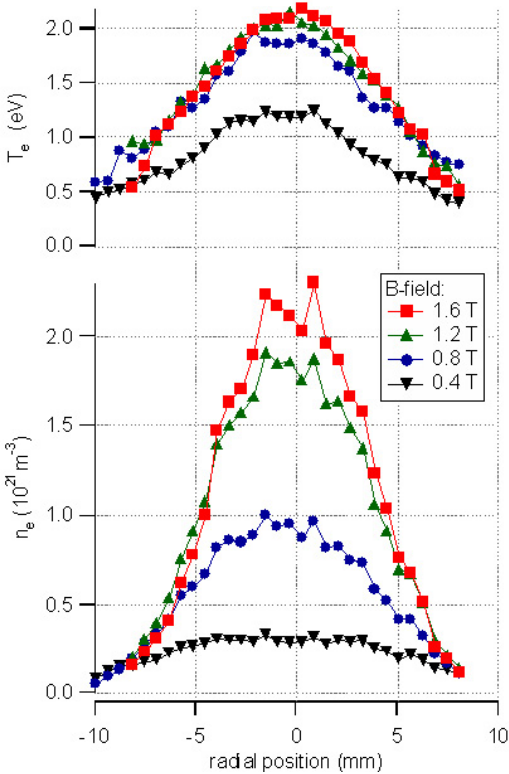


Figure 2: Hydrogen plasma conditions measured with Thomson scattering [26] in Pilot-PSI.

speed, i.e. 10^4 m/s. The consequence is that in the former case power conduction is dominant, whereas in the latter case plasma convection is the main transport mechanism. Let's calculate the power convection and conduction for the two source types to illustrate this difference. The heat conductivity parallel to the magnetic field is $\kappa_{\parallel} = 10^3 T_e^{5/2}$, i.e. $\sim 2 \times 10^3$ W/m/eV at 1 eV and $\sim 6 \times 10^5$ W/m/eV at 10 eV. Assuming a temperature difference of 1 eV over a length of 1 m, this gives the same numbers in W/m². The parallel thermal heat convection is $5/2k(T_e + T_i)n_e v_{plasma}$, which is $\sim 5 \times 10^5$ W/m² and $\sim 5 \times 10^4$ W/m² for the high and low pressure source example, respectively.

V. SELECTION OF RESULTS OBTAINED AT LINEAR PLASMA GENERATORS

In the introduction already a wide range of applications were indicated with references to relevant liter-

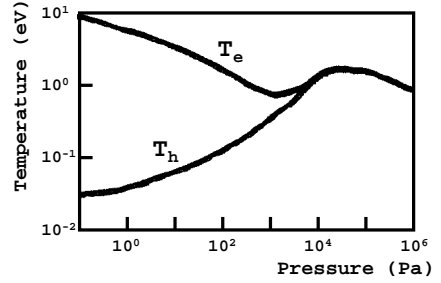


Figure 3: Schematic of the behavior of the electron temperature T_e and heavy particle temperature T_h in a discharge as a function of the pressure.

ature. Here only a small selection is discussed and an emphasis is put on recent results of Pilot-PSI.

An issue that has and is being intensively being studied with linear plasma generators is the erosion of carbon, remaining one of the concerns for the design of ITER. Recently, first experiments have been performed on carbon erosion in Pilot-PSI. This was the first time that the extreme flux density regime was entered. Until then, the record flux density in a linear plasma generator for erosion experiments had been $10^{23} D^+ / m^2 s$, realized in PSI-2 [14]. The measurements discussed here served predominantly to manifest the high fluxes and operation conditions that we can cover. The fine grain carbon targets (R 6650, SGL Carbon Group; $\varnothing 26 \times 2.4$ mm) were clamped on a water cooled copper heat sink at 0.56 m from the nozzle of the plasma source. A series of over 10 exposures was carried out to a single target with the following experimental parameters: 7 mm bore discharge channel, $B = 0.4$ T, 100 s exposure time, discharge current 100 A to 200 A, gas flow 0.2 slm to 0.5 slm (setting the neutral pressure in the vessel to 0.35 and 1.6 Pa, respectively). The target was grounded and a net electron current of up to $I_{t,target} = 59$ A (depending on the discharge current and the gas flow) was measured to the target (where higher neutral pressures led to a lower net current to the target). The erosion was characterized by analyzing the target surface *ex situ* with a profilometer. The result is shown in Fig. 4 It is very likely that during the different exposures different mechanisms (e.g., chemical erosion, sublimation, radiation enhanced sublimation, localized heating due to anode spot formation) were important. So the material loss cannot be interpreted in terms of a chemical erosion yield. However, what can be concluded is that significant redeposition occurred. In volume more than half of the eroded material is found back at the sides of the crater. It is very striking that this redeposition zone is within the plasma wetted area. It is

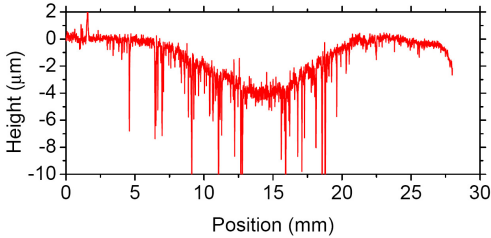


Figure 4: Erosion crater of a fine grain carbon target exposed to ITER relevant plasma fluxes in Pilot-PSI measured *ex situ* with a profilometer.

presently the challenge to understand this in terms of plasma conditions and to benchmark these experimental results with numerical transport codes.

Molecular spectroscopy was performed on the CH band to quantify the chemical erosion [27]. In this approach, the intensity of the CH band is compared with the H_γ line to determine the erosion yield. The plasma flux density was determined from Thomson scattering measurements at 18 mm in front of the target by calculating the sheath flux from the measured density and temperature. In this way, the famous Roth curve (the flux dependence of the carbon chemical erosion yield) [28] was extended with a data point at a flux density of $2 \cdot 10^{24} m^{-2} s^{-1}$.

The PISCES-B machine is unique in the sense that it is capable of studying the effect of Be impurities in the plasma on the interaction with the target. This is generally referred to as "mixed materials" studies. A good example is the erosion of carbon and the hydrogen retention by tungsten being influenced by Be impurities. A recent paper by Doerner et al. [29] gives a good overview of the present understanding. For mixed Be/C surfaces this is summarized as:

- Be ions are accelerated over the sheath potential and gain enough energy to be implanted. This will lead to the formation of beryllium carbide (Be_2C).
- The formation of the beryllium carbide in the carbon surface will reduce chemical erosion and physical sputtering.
- The layer of beryllium carbide will reach a maximum thickness and subsequently arriving Be will not bond as a carbide and will be more easily eroded.
- Beryllium is the main species that is eroded from a carbon surface with a Be_2C layer.

VI. DESIGN OF MAGNUM-PSI

The Magnum-PSI device is presently operated with conventional coils similarly to Pilot-PSI[30]. The device will be upgraded to a super conducting magnet system. A schematic of the device is shown in Figure 5[31]. The cascaded arc source used in Pilot-PSI is being scaled up to produce the plasma in Magnum-PSI. Scaling studies predict power efficiencies in excess of 10%. Like in Pilot-PSI, the plasma will be additionally heated by Ohmic dissipation (of current to the target or to a ring electrode in front of the target) and RF heating. Pressure control is essential for efficient plasma transport to the target as well as ITER relevant neutral densities at the target. Three stage differential pumping based on roots pumps compatible with the large influx of neutral hydrogen will maintain pressures of ~ 1 Pa in the exposure chamber as is confirmed by modelling and experiments on Pilot-PSI. The superconducting magnet has been pre-designed and will have a bore of 1.3 m and a length of 2.5 m, with 2×8 room temperature diagnostic ports. It will be placed on rails so that it can be moved for access to the vacuum vessel. This vessel consists of three elements (the source-, heating-, and target chamber) that can be modified if necessary. The target chamber has been designed for optimal diagnostic access. Magnum-PSI will allow targets with a width of < 10 cm and a length of < 60 cm. The sample manipulator allows tilting to grazing incidence, rotation and axial translation, and will have 100 kW cooling capacity. Targets are exchanged in the target analysis chamber, where also first surface analysis can be performed.

ACKNOWLEDGMENTS

This work, supported by the European Communities under the contract of Association between EURATOM/FOM, was carried out within the framework of the European Fusion Programme with financial support from NWO.

REFERENCES

1. G. FEDERICI, C.H. SKINNER, J.N. BROOKS, J.P. COAD, C. GRISOLIA, A.A. HAASZ, A. HASSANEIN, V. PHILIPPS, C.S. PITCHER, J. ROTH, W.R. WAMPLER, D.G. WHYTE, Nucl. Fusion **41**, 1967 (2001).
2. ITER PHYSICS BASIS EDITORS, Nucl. Fusion **47**, (2007).
3. D. GOEBEL, G. CAMPBELL, AND R.W. CONN, J. Nucl. Mater. **121**, 27 (1984).
4. M.Y. YE, S. TAKAMURA, N. OHNO, J. Nucl. Mater. **241-243**, 1243 (1997).

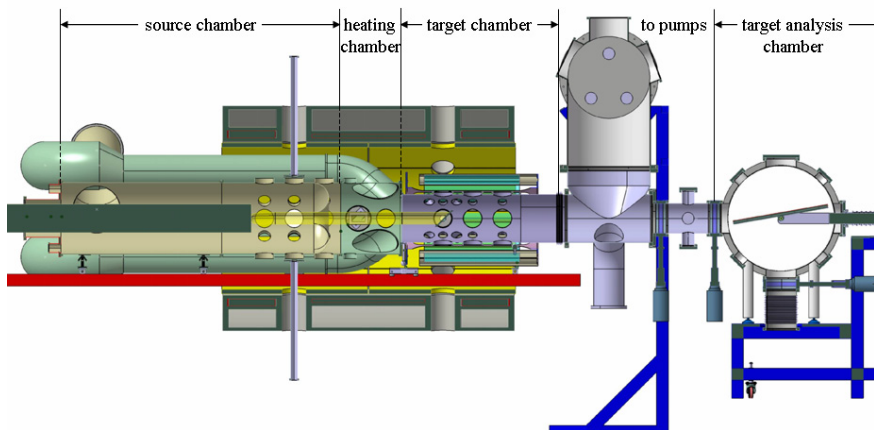


Figure 5: Total overview of the Magnum-PSI experiment with target station and target manipulator. Shown are (from left to right) the source-, heating- and target chamber with pump ducts. Next to these, the pumping station for the third stage is shown. On the right hand side, the target station with target and target manipulator are visible. In the target analysis station, the targets can be analyzed in detail with surface analysis equipment.

5. H. MEYER, S. KLOSE, E. PASCH, G. FUSSMANN, *Phys. Rev. E* **61**, 4347 (2000).
6. T. LUNT, G. FUSSMANN, O. WALDMANN, *Phys. Rev. Lett.* **100**, 175004 (2008).
7. B. UNTERBERG et al., *Fusion Eng. Des.* **86**, 1797 (2011).
8. A.M. LITNOVSKY. Ph.D. thesis. Moscow Engineering Physics Institute (2001) (in Russian).
9. L. SCHMITZ, B.MERRIMAN, L. BLUSH, R. LEHMER, R.W. CONN, R. DOERNER, A. GROSSMAN, F. NAJMABADI, *Phys. Plasmas* **2**(8), 3081 (1995)
10. R.P. DOERNER, M.J. BALDWIN, R.W. CONN, A.A. GROSSMAN, S.C. LUCKHARDT, R. SERAYDARIAN, G.R. TYNAN, D.G. WHYTE, *J. Nucl. Mater.* **290-293**, 166-172 (2001)
11. N. OHNO, N. EZUMI, S. TAKAMURA, S.I. KRASHENINNIKOV, A. YU. PIGAROV, *Phys. Rev. Lett.*, **81** 818 (1998)
12. N. EZUMI, D. NISHIJIMA, H KOJIMA, *J. Nucl. Mater.* **266-269**, 337, (1999)
13. M.Y. YE, K.KUDOSE, T. KUWABARA, N. OHNO, S. TAKAMURA, *J. Nucl. Mater.* **266-269**, 742 (1999)
14. P. KORNEJEV, W. BOHMEYER, H.-D. REINER, C.H. WU, *Phys. Scr.* **T91** 29, (2001).
15. H. GROTE, W. BOHMEYER, P. KORNEJEV, H.-D. REINER, G. FUSSMANN, R. SCHLOGL, G. WEINBERG, C. H. WU, *Chemical Sputtering Yields of Carbon Based Materials at High Ion Flux Densities.* *J. Nucl. Mater.* **266-269**, 1059-1064 (1999)
16. A.M. LITNOVSKY, B.I. KHRIPUNOV, G.V. SHOLIN, V.B. PETROV, V.V. SHAPKIN, N.V. ANTONOV, *J. Nucl. Mater.* **290-293**, 1107 (2001)
17. B.I. KHRIPUNOV, V.B. PETROV, V.V. SHAPKIN, A.S. PLESHAKOV, A.S. RUPYSHEV, N.V. ANTONOV, A.M. LITNOVSKY, D.YU. PROKHOROV, YU. S. SHPANSKY, V.A. EVTIKHIN, I.E. LYUBLINSKY, A.V. VERTKOV, *J. Nucl. Mater.* **313-316**, 619-624 (2003)

18. M.I. GUSEVA, V.I. VASILIEV, V.M. GUREEV, L.S. DANELYAN, B.I. KHRIPUNOV, S.N. KORSHUNOV, V.S. KULIKAUSKAS, YU.V. MARTYNENKO, V.B. PETROV, V.N. STRUNNIKOV, V.G. STOLYAROVA V.V. ZATEKIN, A.M. LITNOVSKY, *J. Nucl. Mater.* **290-293**, 1069 (2001)
19. S.N. KORSHUNOV, M.I. GUSEVA, V.M. GUREEV, L.S. DANELYAN, B.I. KHRIPUNOV, B.N. KOLBASOV, V.S. KULIKAUSKAS, A.M. LITNOVSKY, YU.V. MARTYNENKO, V.B. PETROV, V.V. ZATEKIN, *J. Nucl. Mater.* **313-316**, 87-91 (2003)
20. S. KLOSE, W. BOHMEYER, M. LAUX, H. MEYER, G. FUSSMANN, AND THE PSI-TEAM, *Contrib. Plasma Phys.*, **41**, 467-472 (2001)
21. J. WESTERHOUT, W.R. KOPPERS, W.A.J. VIJVERS, R.S. AL, S. BREZINSEK, S. BRONS, H.J.N. VAN ECK, R. ENGELN, B. DE GROOT, R. KOCH, H.J. VAN DER MEIDEN, M.P. NUIJTEN, V. PHILIPPS, M.J. VAN DE POL, P.R. PRINS, U. SAMM, J. SCHOLTEN, D.C. SCHRAM, B. SCHWEER, P.H.M. SMEETS, D.G. WHYTE, E. ZOETHOUT, A.W. KLEYN, W.J. GOEDHEER, N.J. LOPES CARDOZO, G.J. VAN ROOIJ, *Phys. Scr.* **T128** 35 (2007).
22. D.M. GOEBEL Y. HIROOKA, T.A. SKETCHLEY, *Rev. Sci. Instrum.* **56** 1717 (1985)
23. G.J. VAN ROOIJ, V.P. VEREMIYENKO, W.J. GOEDHEER, B. DE GROOT, A.W. KLEYN, P.H.M. SMEETS, T.W. VERSLOOT, D.G. WHYTE, R. ENGELN, D.C. SCHRAM, AND N.J. LOPES CARDOZO, *Appl. Phys. Lett.* **90**, 121501 (2007).
24. W.A.J. VIJVERS, D.C. SCHRAM, A.E. SHUMACK, N.J. LOPES CARDOZO, J. RAPP, G.J. VAN ROOIJ, *Plasma Sources Sci. Technol.* **19**, 065016 (2010).
25. A.E. SHUMACK, V.P. VEREMIYENKO, D.C. SCHRAM, H.J. DE BLANK, W.J. GOEDHEER, H.J. VAN DER MEIDEN, W.A.J. VIJVERS, J. WESTERHOUT, N.J. LOPES CARDOZO, G.J. VAN ROOIJ, *Phys. Rev. E* **78**, 046405 (2008).
26. G.J. VAN ROOIJ, H.J. VAN DER MEIDEN, M.H.J. 'T HOEN, W.R. KOPPERS, A.E. SHUMACK, W.A.J. VIJVERS, J. WESTERHOUT, G.M. WRIGHT, J. RAPP, *Plasma Phys. Controlled Fusion* **51** 124037 (2009).
27. J. WESTERHOUT, N.J. LOPES CARDOZO, J. RAPP, G.J. VAN ROOIJ, *Appl. Phys. Lett.* **95** 151501 (2009).
28. J. ROTH *et al*, *J. Nucl. Mater.* **337-339** 971 (2004).
29. R.P. DOERNER, M. BALDWIN, J. HANNA, CH. LINSMEIER, D. NISHIJIMA, R. PUGNO, J. ROTH, K. SCHMID, A. WILTNER, *Phys. Scr.* **T128** 115 (2007).
30. H.J.N. VAN ECK, A.W. KLEYN, A. LOF, H.J. VAN DER MEIDEN, G.J. VAN ROOIJ, J. SCHOLTEN, P.A.Z. VAN EMMICHOVEN, *Appl. Phys. Lett.* **101**, 224107 (2012).
31. H.J.N. VAN ECK, W.R. KOPPERS, G.J. VAN ROOIJ, W.J. GOEDHEER, B. DE GROOT, P. SMEETS, J. SCHOLTEN, M. VAN DE POL, S. BRONS, R. KOCH, B. SCHWEER, U. SAMM, V. PHILIPPS, R.A.H. ENGELN, D.C. SCHRAM, N.J. LOPES CARDOZO, A.W. KLEYN, *Fusion Eng. Des.* **82** 1878 (2007).

TUNGSTEN AS A PLASMA FACING COMPONENT AND DEVELOPMENT OF ADVANCED MATERIALS FOR FUSION

J.W.Coenen

*Forschungszentrum Jülich GmbH, Institut für Energie- und Klimaforschung - Plasmaphysik
52425 Juelich, Germany*

ABSTRACT

For the realization of fusion energy especially materials questions pose a significant challenge already today. Heat, particle and neutron loads pose a significant problem to material lifetime when extrapolating to DEMO [1, 2] the first stage prototype fusion reactor [3, 4, 5] considered to be the next step after ITER towards realizing fusion [6]. For many of the issues faced tungsten was considered the solution. Recent progress has however shown that new advanced tungsten or material grades maybe required. In particular safety relevant components such as the first wall and the divertor of the reactor can benefit from introducing new approaches such as composites or new alloys into the discussion. Cracking, oxidation as well as fuel management are driving safety issues when deciding for new materials. Considering in all this also the neutron induced effects such as transmutation, embrittlement and after-heat and activation is essential. A component approach taking into account all aspects is required.

When considering a future fusion power-plant multiple interlinked issues need to be evaluated (fig. 1). Some of the main problems a future reactor is faced with are linked to the materials exposed to the fusion environment and their lifetime considerations. Already from fig. 1 one can see that at the far branches of the tree multiple times the following issues arise, cooling media, neutron flux and neutron damage, ion impact and sputtering as well as heat loads and transient events.

In the following a subset of those conditions can be evaluated only and so far only for the relatively well known conditions of the next step devices e.g. DEMO [2].

The devices called DEMO is so far considered to be the nearest-term reactor design that has the capability to produce electricity and is viewed as single step between ITER and a commercial fusion plant. Currently, no conceptual design exists apart from early studies [3, 5]. A design has not been formally selected, and detailed operational requirements are not yet available [7]. For discussion purposes it is simple to assume a reactor with the fusion power of 2GW and a wall area of $1200m^2$.

I. BOUNDARY CONDITIONS



Figure 1: Materials Issues for fusion - incomplete

$$P_{exhaust} = P_H + P_\alpha \sim 450MW \quad (1)$$

$$P_n = 1600MW/1200m^2 (\sim 40dpa/5fpy[8]) \quad (2)$$

$$P_R = 225MW/1200m^2 \quad (3)$$

$$P_P = 225MW/1200m^2 \quad (4)$$

This means an average of $1.5MW/m^2$ on the first wall with $\sim 1.3MW$ coming from neutrons, typically $10 - 20MW/m^2$ on the divertor and not yet any transient loads taken into account. This machine is already significantly different in size and performance from the next step device, ITER. Main differences include significant power and hence neutron production ($1dpa \sim 5 \times 10^{25}n/m^2$), Tritium self sufficiency, high availability and duty cycle as well as a pulse length of hours rather than minutes. In addition, safety regulation will be more stringent both for operation and also for maintainability and component exchange [7]. A reactor might even go beyond, e.g. steady state operation.

II. PWI CONSIDERATIONS

Several issues related to materials used in its construction of a future fusion reactor need still to be tackled. Among those are the issues related to the first wall and divertor surfaces, their power handling capabilities and lifetime. For the next generation device, ITER, a solution based on actively cooled tungsten (W) components has been developed for the divertor, while beryllium will be used on the first wall [9]. The cooling medium will be water as is also considered for high heat load components in DEMO [7]. In contrast to a reactor where high wall temperature ($> 300^\circ\text{C}$) facilitate energy production ITER W components are only operated at 70°C and hence in the brittle regime.

For the first wall of a fusion reactor unique challenges on materials in extreme environments require advanced features in areas ranging from mechanical strength to thermal properties. The main challenges include wall lifetime, erosion, fuel management and overall safety. For the lifetime of the wall material, considerations of erosion, thermal fatigue as well as transient heat loading are crucial as typically 10^9 (30Hz) transients, so called ELMs, are to be expected during one full power year of operation.

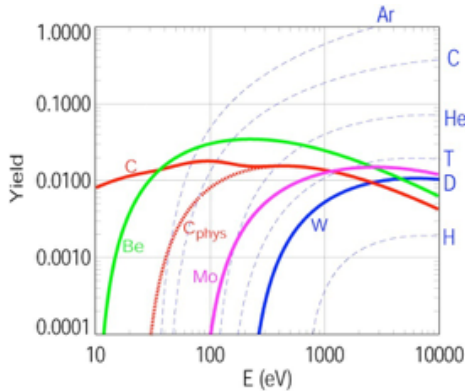


Figure 2: Sputtering yields for C, Mo, Be and W bombarded with D ions [10]. For C, chemical erosion enhances the yield at low energies and yields. For W, impurity sputtering, such as Ar ions, dominates. Based on [11, 10]

Tungsten is the main candidate material for the first wall of a fusion reactor as it is resilient against erosion (Fig. 2), has the highest melting point of any metal and shows rather benign behavior under neutron irradiation as well as low tritium retention. Erosion of the first wall and the divertor will require a significant armor thickness or short exchange intervals, while high-power transients need strong mitigation efficiency to prevent damage to the plasma facing components (PFCs) [12].

One issue that is related to the wall erosion is the fusion performance of the fusion device and hence the

amount of tolerable impurities. For tungsten only minute amounts can be tolerated when considering the burn conditions of the plasma and cooling provide by tungsten radiating in the plasma. In [13] the analysis given for only helium as one of the impurities shows that 10^{-4} W atoms per deuterium atom can be enough to extinguish the fusion performance.

For the next step devices, e.g. DEMO, or a future fusion reactor the limits on power-exhaust, availability and lifetime are quite stringent. Radiation effects including neutron embrittlement may limit actively cooled W components in DEMO to about $3\text{--}5\text{ MW/m}^2$ due to the diminished thermal conductivity or the need to replace CuCrZr with Steels [14]. Quite extensive studies and materials programs [15, 16, 17, 1] have already been performed hence it is assumed that the boundary conditions [14] be fulfilled for the materials are in many cases above the technical feasibility limits as they are understood today.

- High divertor power handling, i.e., ability to withstand power loads larger than 10 MW/m^2 . here especially the choice of coolant is critical. Water cooling will be required to allow sufficient exhaust efficiency
- The radiation damage for the divertor is predicted to be close to 3 dpa/fpy . For copper if chosen the value varies between 3 and 5 dpa/fpy (full power year)
- It is assumed that despite the radiation damage erosion is the dominant lifetime determining factor.
- Even when starting up DEMO in phases a final blanket should be capable of lasting up to 50 dpa.

In the following we will however try to concentrate on three groups of issues [14, 7]

- Power exhaust and energy production: The first wall blanket exhausts the power and hence must be operated at elevated temperatures to allow for efficient energy conversion. Here a material must be chosen with a suitable operational window and sufficient exhaust capability. The cooling medium for high temperature operation can be crucial.
- Mitigate material degradation due to neutrons and reduce radioactive waste: One can select materials that allow high temperature operation, mitigate effect of operational degradation such as embrittlement and neutron effects linked to transmutation.
- Tritium self-sufficiency and safety: 22 kg/year of tritium are required for a 2GW plasma operated at 20% availability, this means $\sim 85\%$ [14] of the

in-vessel surface must be covered by a breeding blanket and the loss of tritium without ability to recover needs to be minimized. Accident scenarios need to be considered e.g. loss of coolant and air ingress are among the possible scenarios.

Tritium retention in plasma-facing components (PFCs) due to plasma wall interactions is one of the most critical safety issues for ITER and future fusion devices. For carbon based PFCs the co-deposition of fuel with re-deposited carbon has been identified as the main retention mechanism (fig. 3).

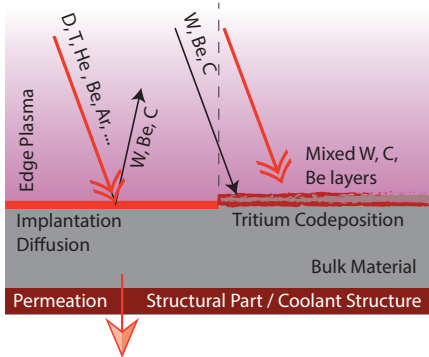


Figure 3: Fuel retention and permeation issues under plasma exposure conditions

This retention grows linearly with particle fluence and can reach such large amounts that carbon is omitted in the activated phase of ITER and future reactors [11]. Instead, tungsten is foreseen as PFC material in the divertor of ITER and is the most promising candidate for PFCs in future reactors. Fuel retention behavior of tungsten is subject to present studies. It was shown that by replacing CFC with W in the Joint European Torus (JET) the retention e.g. can be significantly reduced [18] as predicted (Fig. 4). An issue that however remains is the potential for diffusion of hydrogen into the material. In the breeding blankets especially the interaction of tritium with Reduced Activation Ferritic Martensitic (RAFM) steels, e.g. EUROFER-97, can be crucial to minimize fuel retention or loss.

III. MATERIAL ISSUES FOR TUNGSTEN

In the following sections several issues are described that arise from the above depicted boundary conditions. As an example the divertor lifetime is considered as the desired parameter. Typically there are three main avenues of damage to the material of the divertor. Either high heat-loads cause melting, cracking or recrystallization or neutrons impact the actual microstructure of the material. Surfaces

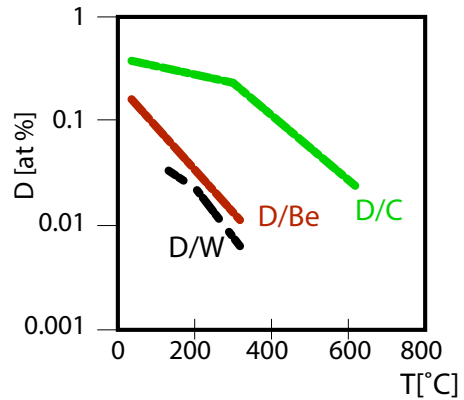


Figure 4: Estimate of retained deuterium concentration in C, Be and W deposits under codeposition conditions. (Sketch based on [11])

are damaged by ions impacting and causing both surface morphology changes or erosion. Fig. 5 depicts hence one approach to solving at least some of the problems. Choosing Tungsten (W) as the main wall material suppresses sputtering due to the high atomic mass in contrast to the sputtering ions. Tungsten also has a rather high thermal conductivity (Cu: ~ 390 W/(mK) W: ~ 173 W/(mK) Mo: ~ 138 W/(mK) Steel: ~ 17 W/(mK) and can hence facilitate higher heat exhaust than e.g. steel, for tungsten also the high melting point is beneficial. Thermal properties however are intrinsically linked to potential transmutation and irradiation processes. In addition it is known that tungsten has a rather low hydrogen solubility and hence facilitates low retention under fusion conditions [18]. Tungsten is however inherently brittle and does show catastrophic oxidation behavior at elevated temperatures.

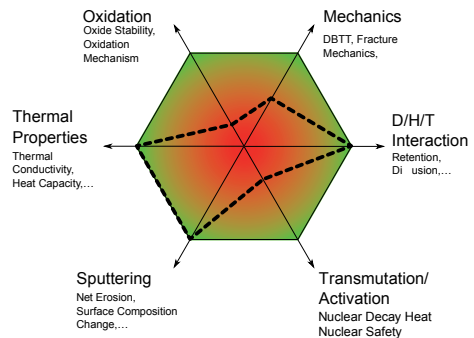


Figure 5: Tungsten as a first wall material

Not always all material properties can be optimized at once. After an optimization step a material might be developed that in its entirety fulfills all criteria by interaction between individual criteria as displayed in fig. 6

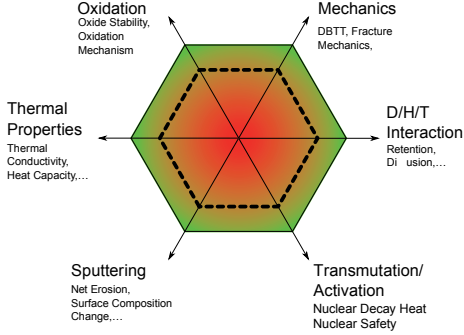


Figure 6: A Compromise 1st Wall Material

A. Operational Window

Based on the assumption that W is the option so far to be used as the surface layer the reactor PFCs already quite basic assumptions can be made when picking the operational window and thickness of such components.

The lower operating temperature limit in metal alloys is mainly determined by radiation embrittlement (decrease in fracture toughness), which is generally most pronounced for irradiation temperatures below $\sim 0.3T_{melt}$, where T_{melt} is the melting temperature (Tungsten $\sim 3300K$) [19]. The upper operating temperature limit is determined by one of four factors, all of which become more pronounced with increasing exposure time such as thermal creep (grain boundary sliding or matrix diffusional creep), high temperature helium embrittlement of grain boundaries, cavity swelling (particularly important for Cu alloys), and coolant compatibility such as corrosion issues.

If the PFCs surface is operated at $1100^\circ C$ as optimal for W [20] and copper is chosen together with water as part of the coolant solution the thickness is automatically determined (5) with κ the heat conductivity)

$$q = \frac{T_{surface} - T_{cool}}{d_1/\kappa_1 + d_2/\kappa_2} \quad (5)$$

This means that the maximum heat-exhaust is determined by the heat conduction, the potential for recrystallization and the ductile to brittle transition behavior of the material. Here new material options are required to allow a larger operational window, by overcoming the limiting factor, keeping in mind that a maximized heat conduction is crucial (e.g. Steel).

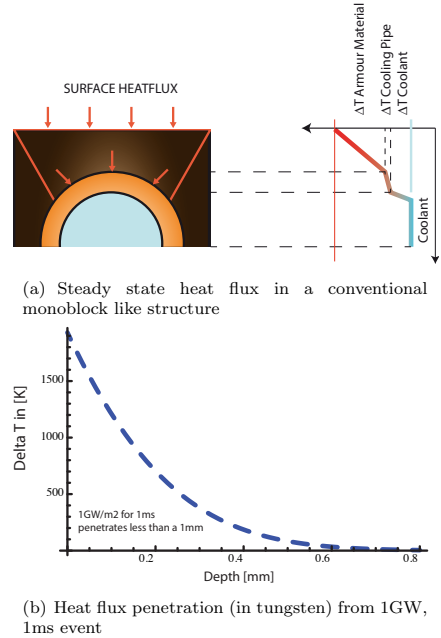


Figure 7: Power-exhaust - Issues arising from steady state and transients

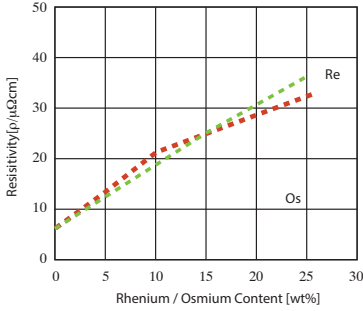
For transient events the limits can even be more stringent when considering the limited penetration depth of a given heat-pulse fig. 7(b) and its maximum surface temperature rise (eg. (6)) with κ the heat conductivity, ρ the density and c the heat capacity). Active cooling for fast transients is meaningless because of the small penetration depth.

$$\Delta T_{surface}^{\infty}(t) = \frac{q_s}{\sqrt{\kappa\rho c} \cdot \sqrt{\pi}} \sqrt{\Delta t} \quad (6)$$

From assumptions related to unmitigated ELMs at $1 GW/m^2$ for 1ms [12] already a temperature rise of $1500K$ is achieved in only the top 1 mm. Cracking or melting is difficult to prevent here. Irreparable damage has to be avoided at any cost. Even higher thermal wall loads caused by so called disruptions, sudden and uncontrolled loss of the plasma with deposition of the energy on the wall. Assuming that 50% of the thermal energy are radiated during thermal quench of the plasma and with a limited inhomogeneity in toroidal and poloidal direction respectively the thermal disruption loads are always much above the crack limit [21] even though below the melt limit. Variation of the torus geometry (aspect ratio) provides only moderate reduction of loads.

B. Evolution of Thermal Properties

In addition to the above mentioned issues fig. 8 shows that the fusion environment can also drastically



(a) Electrical resistivity of W containing various amounts of Re or Os. The red line and green line stand for W-xRe and W-xOs respectively [22]

Figure 8: Change of electrical and thermal properties of tungsten under neutron irradiation and transmutation

change some of the set assumptions. Already a small amount of transmutation can have a significant influence on the power-exhaust. When calculating the thermal conductivity based on $\kappa \cdot \rho = L \cdot T$ with κ the thermal conductivity, ρ the resistivity and L the Lorentz number with a value of $3.2 \times 10^{-8} W\Omega K^{-2}$ for tungsten one can estimate that κ drops 60% already at 5wt% or Re or Os. From previous work [23] one can determine that especially at lower temperatures κ drops significantly (30%). In any case one does depend on stable and predictable material properties even under radiation - or a detailed knowledge of the time dependent evolution to determine lifetime and performance of components.

C. Embrittlement

Conventional high performance materials offer high strength and stiffness combined with low density hence weight. However, a fundamental limitation of the current approach is the inherent brittleness of tungsten. As seen above cracking hence brittle behavior can be a limiting factor when operating any PFC in a tokamak [21]. For the fusion environment the additional problem becomes operational embrittlement. An issue related to embrittlement is certainly the recrystallization of tungsten. at temperatures of 1400K only mere hours are required to complete recrystallize the material [24].

Fig. 9 shows that already at moderate neutron fluence corresponding to 1 dpa the DBTT of tungsten moves up to almost 900° C. If in addition recrystallization takes place (fig. 9) almost no structural load can be given to the tungsten component at temperatures of a few hundred degrees. For a typical monoblock [12, 23] a tungsten thickness of 6mm on top of the CuCrZr cooling pipe would mean, based on sim-

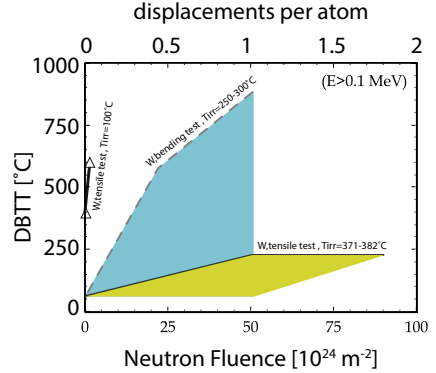


Figure 9: DBTT dependence after neutron irradiation based on [25]

ple estimations (eg. 5) that only the top part of an exposed mono-block would be in the allowed temperature range [20]. This means for a water-cooled solution tungsten is normally a brittle hence only a functional part, suppressing e.g. erosion and allowing for high operational temperatures. Failure is usually sudden and catastrophic, with no significant damage or warning and little residual load-carrying capacity if any. Structures that satisfy a visual inspection may fail suddenly at loads much lower than expected. Cracking is usually avoided for PFCs and certainly for structural components.

D. Activation & Transmutation

An issue that especially for complex components with multiple material and alloying components can be quite crucial is the recyclability and activation under neutron irradiation. As fusion is typically considered a technology with minimal or now longterm nuclear waste [25] tungsten and e.g. special steel grades [26] have optimized radiation performance with respect to low activation, e.g. molybdenum and aluminium are avoided as they produce long term activation products [8, 25]

Based on a study provided in [5, 8] with a neutron flux at the first wall of $\sim 1.0^{15} ncm^{-2}s^{-1}$ one can estimate the activation of materials after a 5 year period. For materials exposed in the divertor a factor 10 lower neutron rate is expected in the area of the high heat flux exposure due to geometrical reasons [7].

Fig. 10 shows the values of an assumed component containing W, Cr, Cu and Er, representing e.g. a typical mono-block with small interlayers and a copper cooling structure. Already here it is clear that the shielded hands on radiation level can not be achieved after 100 years when using copper cooling at the first wall. Mitigation of these effects need to be consid-

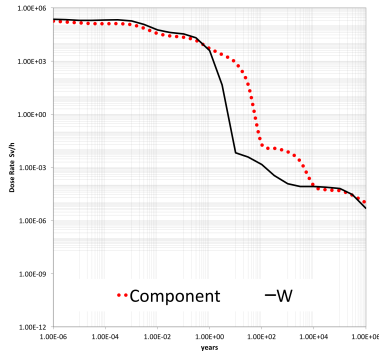


Figure 10: The activation of tungsten (first wall) is shown in comparison to a component (W 79.7wt%, Er 0.6wt%, Cr 12.1wt%, Cu 7.5%) for the first wall can be estimated as an upper bound (based on [8]). Divertor components in general are less prone to activation. Shielded hands-on level: $2 mSv/h$, Hands-On Level: $10 \mu Sv/h$

ered by utilizing non or low activation materials. e.g. replacing copper for the first wall and removing Er or Al oxides in favor of Ytria.

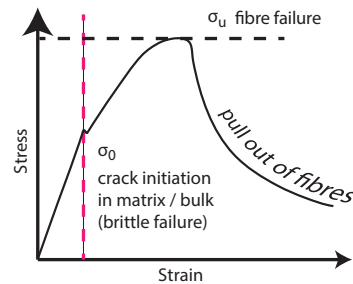
IV. NEW MATERIAL OPTIONS

For all the above described issues or boundary condition potential solutions need to be developed. We are faced with a multilayer approach for the Plasma-Facing-Components (PFCs) including armor, fuel barriers, cooling structures & breeding elements and hence we have to consider a multitude of interacting materials. From the plasma toward the cooling structure we consider tungsten or tungsten alloys on either a copper or steel structure with functional layers e.g. permeation barriers or compliance layers. A generally new components concepts to circumvent classical definitions of limits is required with damage resilient materials such as composites followed by a much better definition what can be tolerated before a component needs to be exchanged. We need to define lifetime with more parameters than erosion and cracking for PFCs. Composite approaches to enhance material parameters and mitigate damage modes by utilizing mixed properties will be ideal including safety features like passivating alloys etc. Not yet developed ideas on self-healing or damage tolerant materials similar to aerospace applications might be a future field of research including e.g. liquid metals [27]. Already today smart materials, fiber composites and alloys which adapt to the operational scenario are possible. In some cases detrimental effects such as erosion are actually used to facilitate material functions (sec.). If W as a 1st wall material

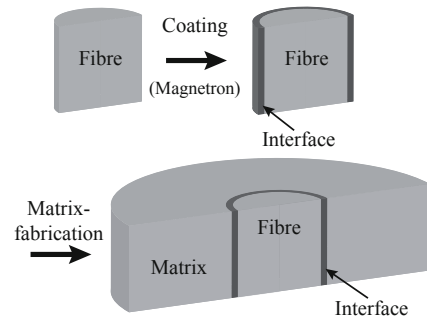
is required to suppress erosion even preferential sputtering can turn the top layer of alloys or steel into a thin layer of erosion suppressing tungsten [28, 29, 30].

A. Composites for High Loads

A basic strategy to achieve pseudo-ductility is the incorporation of new ductile matrices and fibres, which needs extensive development and validation [31]. To overcome brittleness issues when using W, a W-fiber enhanced W-composite material (Wf/W) incorporating extrinsic toughening mechanisms can be used. The composite approach enables energy dissipation and thus stress peaks can be released at crack tips and cracks can be stopped. Another option is a composite laminates made of commercially available raw materials [32, 17].



(a) Strain-Stress-Curve for a typical Composite Material



(b) fibre enhanced composite and interface layer

Figure 11: Composite approaches based on pseudo-ductilisation.

Accordingly, even in the brittle regime this material allows for a certain tolerance towards cracking and damage in general. In comparison conventional tungsten would fail immediately. From fig. 11(a) the principle of composite strengthening behavior can be seen. Even when a crack has been initiated inside the material the energy dissipation mechanisms allow further load to be put towards the component until at a later stage also the fiber and hence the overall material fails.

First W_f/W samples have been produced, showing extrinsic toughening mechanisms similar to those of ceramic materials [33, 34]. These mechanisms will also help to mitigate effects of operational embrittlement due to neutrons and high operational temperatures. A component based on W_f/W can be developed with both chemical infiltration (CVI), utilizing a newly installed CVI-setup and a powder metallurgical path through hot-isostatic-pressing [35, 36]. Crucial in both cases is the interface between fiber and matrix. The interface is a thin layer which provides a relatively weak bond between the fiber [37] and the matrix for enabling pseudo-ductile fracture in the inherently brittle material, similar to e.g. SiC ceramics [38].

Keeping in mind the above mentioned boundary conditions one can consider that brittleness from either neutron irradiation or elevated temperatures can be mitigated as the pseudo-ductilisation does not rely on any part of the material being ductile, crack resilience can be established [33, 34]. Facilities to produce both CVI as well as powder metallurgical W_f/W are now available. It now needs to be shown that for those components equally good behavior in terms of thermal conductivity, erosion and retention can be established. As part of the development especially the choice of the fiber and interface material can be crucial. A sag-stabilized potassium doped fibre can even retain some ductility in addition strengthening the material. For the interface a non activating choice is necessary hence one can move from the so far considered erbia [37, 33] potentially towards yttria.

In addition to conventional composites also fine grain tungsten is an option to strengthen and ductilize tungsten [39] similar to other metals [40] an option to achieve this for W & DEMO applications is Powder Injection Molding (PIM) [41, 42]. Powder Injection Molding (PIM) as production method enables the mass fabrication of low cost, high performance components with complex geometries. The range in dimension of the produced parts reach from a micro-gearwheel ($d = 3mm, 0.050g$) up to a heavy plate ((60x60x20)mm, 1400 g). Furthermore, PIM as special process allows the joining of tungsten and doped tungsten materials without brazing and the development of composite and prototype materials. Therefore, it is an ideal tool for divertor R&D as well as material science.

B. Tungsten smart alloys

Addressing the safety issue, a loss-of-coolant accident in a fusion reactor could lead to a temperature rise of 1400 K after $\sim 30 - 60$ days due to neutron induced afterheat of the in-vessel components [5].

Thereby, a potential problem with the use of W in a fusion reactor is the formation of radioactive and highly volatile WO_3 compounds. In order to suppress the release of W-oxides tungsten-based alloys containing vitrifying components seem feasible, as they can

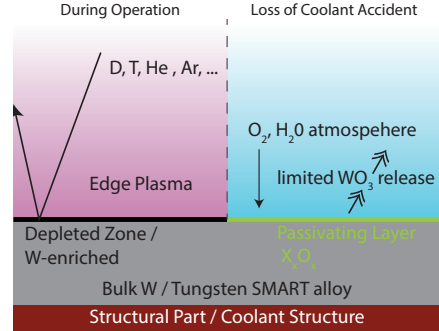


Figure 12: Working principle of a smart alloys based PFC with both the operational and accident mechanisms shown.

be processed to thick protective coatings with reasonable thermal conductivity, e.g. by plasma spraying with subsequent densification. Enhanced erosion of light elements during normal reactor operation is not expected to be a concern. Preferential sputtering of alloying elements leads to rapid depletion of the first atomic layers of light alloying elements and leaves a pure W-surface facing the plasma [43]. This mechanism is similar to the above mentioned EUROFER-97 surface enrichment. Fig. 12 displays the basic mechanism. During operation plasma ions erode the light constituents of the alloy leaving behind a thin depleted zone with only tungsten remaining. Subsequently the tungsten layer suppresses further erosion hence utilizing the beneficial properties of tungsten. In case of a loss of coolant and air or water ingress the tungsten layer oxides releasing a minima amount of WO_3 and then passivating the alloy due to the chromium content. W-Cr-Y with up to 780 at% of W content already shows 10^4 -fold suppression of tungsten oxidation due to self-passivation [44]. Test systems are being produced via magnetron sputtering and evaluated with respect to their oxidation behavior. Production of bulk samples is ongoing. Rigorous testing of oxidation behavior, high heat flux testing and plasma loads as well as mass production for candidate materials is under preparation. The material can be considered for both first wall and divertor applications especially when combined with the strengthening properties of the W_f/W composite approach. The PWI behavior and potential neutron or temperature embrittlement need to be quantified.

C. Functionally Graded Materials

Having discussed tungsten as the main candidate for the PFMs of a fusion reactor the joint to the cooling structure or wall structure in general is crucial. From the values of thermal expansion for the different materials (copper $\sim 16.5\mu m/(mK)$, tungsten: $\sim 4.5\mu m/(mK)$ molybdenum: $\sim 4.8\mu m/(mK)$,

stainless steel: $\sim 12\mu\text{m}/(\text{mK})$ it is clear that a mature solution of joining them needs to be established.

As one of the example systems the development of Functionally Graded Materials (FGMs) between W as the PFM with the structural material EUROFER-97 can be considered. As depicted in [45] FGMs are a candidate especially when considering applications such as the blanket modules of a DEMO [7] or even a helium cooled tungsten divertor with low to medium heat-flux ($1 - 5\text{MW}/\text{m}^2$) for which the heat conductivity of EUROFER-97 maybe sufficient.

Similar ideas are developed for the transition between copper and W [46, 47] potentially being used as solution for a water-cooled high heat-flux divertor [7, 14]

D. Tritium Management

Moving towards the actual structural part of the reactor tritium management is an issue especially for the breeding blankets. In order to prevent tritium loss and radiological hazards it is important to suppress permeation through the reactor walls. Research on permeation barriers ranges over a variety of materials [48, 49, 50, 51] including erbia and alumina. Permeation barriers require high permeation reduction factors, high thermal stability and corrosion resistance as well as similar thermal expansion coefficients compared to those of the substrate. Establishing the permeation mitigation requires controlled experiment. A new gas-driven permeation setup is established at FZJ to investigate deuterium permeation through different ceramic coatings on EUROFER-97, which significantly reduce the deuterium permeation. Several techniques to apply the coatings can be considered e.g. Arc Deposition, Chemical Routes, Magnetron Sputtering. A mitigation factor of 50-100 is essential to allow safe operation and allow a reasonable tritium breeding ratio.

In addition to permeation mitigation and mechanical feasibility, compatibility with neutron irradiation needs to be enforced. Here especially erbia and alumina but also zirconia [52] do have issues. Permeation barriers from Ytria [53] may be a potential low activation element element (fig. 10) and in addition is quite similar in terms of thermal expansion when considering EUROFER-97 as the substrate.

V. SUMMARY AND OUTLOOK

Considering all the above mentioned issues when using materials in a fusion reactor environment a highly integrated approach is required. The lifetime of PFCs and joints due to erosion, creep, thermal cycling, embrittlement needs to be compatible with steady state operation and short maintenance intervals. Thermal properties of composites and components have to be at least similar to bulk materials when enhanced properties in terms of strength are

not to hinder the maximization of operational performance. Damage resilient materials can here facilitate small, thin components and hence higher exhaust capabilities. The components need to be compatible with the aim of tritium breeding and self-sufficiency and hence mitigate tritium retention and loss.

Despite using various alloying components, interlayers or coatings maintainability and recycling of used materials is required to make fusion viable and publicly acceptable. Last but not least, large scale production of advanced materials is crucial. We hence propose to utilize the composite approach together with alloying concepts to maximize the potential of the tungsten part of a potential PFC. Together with W/Cu composites at the coolant level and W/EUROFER joints high-performance components can be developed. Rigorous testing with respect to PWI and high heat-flux performance are planned for all concepts to have prototype components available within 5 years for application in existing fusion devices.

VI. ACKNOWLEDGEMENTS

In particular I would like to thank all people involved in preparing this manuscript: S.Antusch⁴, M.Aumann¹, W.Biel^{1,3}, J.Du¹, J.Engels¹, S.Heuer¹, A.Houben¹, T.Hoeschen², B.Jasper¹, F.Koch², J.Linke¹, A.Litnovsky¹, Y.Mao¹, R.Neu^{2,5}, G.Pintsuk¹, J.Riesch², M.Rasinski¹, J.Reiser⁴, M.Rieth⁴, A.Terra¹, B.Unterberg¹, Th.Weber¹, T.Wegener¹, J-H.You² and Ch.Linsmeier¹

¹Forschungszentrum Jülich GmbH, Institut für Energie- und Klimaforschung, Jülich, Germany ²Max-Planck-Institut für Plasmaphysik, Garching Germany ³Department of Applied Physics, Ghent University, Ghent, Belgium ⁴Karlsruhe Institute of Technology, Institute for Applied Materials, Eggenstein-Leopoldshafen, Germany ⁵ Technische Universität München, Boltzmannstrasse 15, 85748 Garching, Germany⁷

REFERENCES

1. Stork et al, D. Assessment of the eu r&d programme on demo structural and high-heat flux materials, final report of the materials assessment group., Technical Report EFDA(12)52/7.2, EFDA (December 2012).
2. Wenninger, R. et al. *Nuclear Fusion*, **54** (2014), 11. Cited By 0.
3. Maisonnier, D. et al. *Nuclear Fusion*, **47** (2007), 11, 1524.
4. Maisonnier, D. et al. *Fusion Engineering and Design*, **81** (2006), 814, 1123 – 1130. Proceedings of the Seventh International Symposium on Fusion Nuclear Technology ISFNT-7 Part B Proceedings of the Seventh International Symposium on Fusion Nuclear Technology.

5. Maisonnier, D. et al. A conceptual study of commercial fusion power plants. Final Report of the European Fusion Power Plant Conceptual Study (PPCS) EFDA(05)-27/4.10, EFDA (2005). EFDA(05)-27/4.10.
6. Romanelli, F. Fusion Electricity A roadmap to the realisation of fusion energy. European Fusion Development Agreement, EFDA (2012). ISBN 978-3-00-040720-8.
7. Federici, G. et al. In Fusion Engineering (SOFE), 2013 IEEE 25th Symposium on, pages 1–8 (June 2013).
8. Forrest, R. et al. Handbook of activation data calculated using easy-2007. UKAEA FUS 552, EURATOM/UKAEA Fusion Association (March 2009).
9. Pitts, R. et al. *Journal of Nuclear Materials*, **415** (2011), 1 SUPPL, S957S964.
10. Eckstein, W. et al. Sputtering data. Technical Report IPP 9/82, Max-Planck-Institut fuer Plasmaphysik (1993).
11. Roth, J. et al. *Journal of Nuclear Materials*, **390391** (2009), 0, 1 – 9. Proceedings of the 18th International Conference on Plasma-Surface Interactions in Controlled Fusion Device Proceedings of the 18th International Conference on Plasma-Surface Interactions in Controlled Fusion Device.
12. Pitts, R. et al. *Journal of Nuclear Materials*, (2013), 438, S48.
13. Puetterich, T. et al. *Nuclear Fusion*, **50** (2010), 2, 025012.
14. Bachmann, C. In <http://www.soft2014.eu>. <http://www.soft2014.eu> (2014).
15. Stork, D. et al. *Journal of Nuclear Materials*, **455** (2014), 1-3, 277–291. Cited By 1.
16. Rieth, M. et al. *Journal of Nuclear Materials*, **442** (2013), 1-3 SUPPL.1, S173–S180. Cited By 2.
17. Reiser, J. and Rieth, M. *Fusion Engineering and Design*, **87** (2012), 56, 718 – 721. [jce:title;Tenth International Symposium on Fusion Nuclear Technology \(ISFNT-10\)|/ce:title.j](#).
18. Brezinsek, S. et al. *Nuclear Fusion*, **53** (2013), 8, 083023.
19. Igitkhanov, Y.; Bazylev, B. and Fetzer, R. The quantification of the key physics parameters for the demo fusion power reactor and analysis of the reactor relevant physics issues. KIT Scientific Reports 7661, KIT (2015).
20. Zinkle, S. and Ghoniem, N. *Fusion Engineering and Design*, **5152** (2000), 0, 55 – 71.
21. Linke, J. et al. *Nuclear Fusion*, **51** (2011), 7, 073017.
22. Tanno, T. et al. *Journal of Nuclear Materials*, **386388** (2009), 0, 218 – 221. Fusion Reactor Materials Proceedings of the Thirteenth International Conference on Fusion Reactor Materials.
23. Linke, J. *Fusion Science And Technology*, **53** (2008), 2T, 278–287.
24. Goodwin, F. et al. In Martienssen, W. and Warlimont, H., editors, Springer Handbook of Condensed Matter and Materials Data, pages 161–430. Springer Berlin Heidelberg (2005). ISBN 978-3-540-44376-6.
25. Bolt, H. et al. *Journal of Nuclear Materials*, **307311, Part 1** (2002), 0, 43 – 52.
26. Lindau, R. et al. *Fusion Engineering and Design*, **7579** (2005), 0, 989 – 996. Proceedings of the 23rd Symposium of Fusion Technology {SOFT} 203.
27. Coenen et al, J. *Physica Scripta*, **2014** (2014), T159, 014037.
28. Rasinski et al, M. In PFMC-2015 (2015). Poster at this conference.
29. Sugiyama, K. et al. *Journal of Nuclear Materials*, (2014). Cited By 0; Article in Press.
30. Roth, J. et al. *Journal of Nuclear Materials*, **454** (2014), 13, 1 – 6.
31. Czel, G. and Wisnom, M. *Composites Part A: Applied Science and Manufacturing*, **52** (2013), 0, 23 – 30.
32. Reiser, J. et al. *Advanced Engineering Materials*, **17** (2014), 4, 491–501. Cited By 0.
33. Riesch, J. et al. *Physica Scripta*, **2014** (2014), T159, 014031.
34. Riesch, J. et al. *Acta Materialia*, **61** (2013), 19, 7060 – 7071.
35. Riesch et al, J. In PFMC-2015 (2015). Article at this conference.
36. Hoeschen et al, T. In PFMC-2015 (2015). Poster at this conference.
37. Du, J.; You, J.-H. and Hschen, T. *Journal of Materials Science*, **47** (2012), 11, 4706–4715.
38. Shimoda, K. et al. *Composites Science and Technology*, **68** (2008), 1, 98 – 105.

39. Nemeth, A. A. et al. *International Journal of Refractory Metals and Hard Materials*, **50** (2015), 0, 9 – 15.
40. Hohenwarter, A. and Pippan, R. *Philosophical Transactions of the Royal Society of London A: Mathematical, Physical and Engineering Sciences*, **373** (2015), 2038.
41. Antusch, S. et al. *Fusion Engineering and Design*, **88** (2013), 9-10, 2461–2465. Cited By 1.
42. Antusch et al., S. *Nuclear Materials and Energy*, (2015). Accepted for publication.
43. Eckstein et al, W. *IAEA*, (2001), 7b, pp. 76. Vienna.
44. Wegener et al, T. In PFMC-2015 (2015). Poster at this conference.
45. Aktaa, J. et al. *Fusion Engineering and Design*, **89** (2014), 78, 913 – 920. Proceedings of the 11th International Symposium on Fusion Nuclear Technology-11 (ISFNT-11) Barcelona, Spain, 15-20 September, 2013.
46. Greuner, H. et al. *Fusion Engineering and Design*, (2015), 0, –.
47. You, J.-H. et al. *Journal of Nuclear Materials*, **438** (2013), 13, 1 – 6.
48. Hollenberg, G. et al. *Fusion Engineering and Design*, **28** (1995), 0, 190 – 208. Proceedings of the Third International Symposium on Fusion Nuclear Technology.
49. Levchuk, D. et al. *Physica Scripta*, **2004** (2004), T108, 119.
50. Chikada, T. et al. *Fusion Engineering and Design*, **84** (2009), 26, 590 – 592. Proceeding of the 25th Symposium on Fusion Technology (SOFT-25).
51. Chikada, T. et al. *Fusion Engineering and Design*, **85** (2010), 79, 1537 – 1541. Proceedings of the Ninth International Symposium on Fusion Nuclear Technology.
52. Zhang, K. and Hatano, Y. *Journal of Nuclear Materials*, **417** (2011), 1-3, 1229–1232. Cited By 3.
53. Wu, Y. et al. *Fusion Engineering and Design*, **90** (2015), 0, 105 – 109.

HIGH HEAT FLUX PERFORMANCE OF PLASMA FACING MATERIALS AND COMPONENTS UNDER SERVICE CONDITIONS IN FUTURE FUSION REACTORS

Jochen Linke

Forschungszentrum Jülich GmbH, IEK-2, EURATOM Association, D-52425 Jülich, Germany, j.linke@fz-juelich.de

ABSTRACT

The first wall and the divertor in present-day or next step thermonuclear fusion devices are exposed to intense fluxes of charged and neutral particles, in addition the plasma facing materials and components are subjected to radiation in a wide spectral range. These processes, in general referred to as 'plasma wall interaction' will have strong influence on the plasma performance, and moreover, they have major impact on the degradation and on the lifetime of the plasma facing armour and the joining interface between the plasma facing material and the heat sink. Beside physical and chemical sputtering processes, thermal fatigue damage due to cyclic heat fluxes during normal operation and intense thermal shocks caused by severe thermal transients are of serious concern for the engineers which develop reliable wall components. In addition, the material and component degradation due to high fluxes of energetic neutrons is another critical issue in D-T-burning fusion devices which requires further extensive research activities. This paper represents a tutorial focussed on the development and characterization of plasma facing components for thermonuclear fusion devices [1].

I. INTRODUCTION

The plasma facing components in magnetic confinement experiments, i.e. the first wall (FW), the limiters and the divertor will be exposed to intense thermal loads during plasma operation. In existing and next step devices the resulting thermal loads to the first wall will in general remain below 1 MWm^{-2} . However, special attention has to be paid to high heat flux components, i.e. to the limiter and the divertor with power densities up to approximately 10 MWm^{-2} for next step tokamaks (such as ITER) or stellarators (e.g. Wendelstein 7-X) during normal plasma operation. These requirements make high demands on the selection of qualified materials and reliable fabrication processes for actively cooled plasma facing components [2 - 3].

Beside the above mentioned quasi-stationary heat loads, short transient thermal pulses with deposited energy densities in the order of several ten MJm^{-2} are a serious concern for next step tokamak devices, in particular for ITER. The most serious of these events are plasma disruptions. Here a considerable fraction of the plasma energy is deposited on a localized surface area in the

divertor strike zone region; the time scale of these events is typically in the order of milliseconds. In spite of the fact that a dense cloud of ablation vapour will form above the strike zone, only partial shielding of the divertor armour from incident plasma particles will occur. As a consequence, thermal shock induced crack formation, vaporization, surface melting, melt layer ejection, and particle emission induced by brittle destruction processes will limit the lifetime of the components. In addition, dust particles (neutron activated or toxic metals or tritium enriched carbon) are a serious concern from a safety point of view. Instabilities in the plasma positioning (vertical displacement events, VDE) also may cause irreversible damage to plasma facing components, particularly to metallic wall armour.

Furthermore, irradiation induced material degradation due to the impact with 14 MeV neutrons in D-T-burning plasma devices is another critical issue, both, from a safety point of view, but also under the aspect of the component lifetime. Next step thermonuclear confinement devices such as ITER with an integrated neutron fluence in the order of 1 dpa (displacements per atom; for low-Z materials 1dpa corresponds to approx. $10^{25} \text{ n} \cdot \text{m}^{-2}$) do not pose any unsolvable material problems. However, in future devices such as DEMO or in commercial fusion reactors with integrated neutron wall loads of 80 to 150 dpa new radiation resistant materials have to be developed and tested under realistic conditions. Due to the lack of an intense 14 MeV neutron source, complex neutron irradiation experiments are been performed in material test reactors to quantify the n-induced material damage. These tests provide the required data base on the degradation of thermal and mechanical parameters; in addition the thermal fatigue and thermal shock performance of irradiated high heat flux components is another important issue for the engineering design, the licensing and the safe operation of future fusion reactors.

II. DEVELOPMENT AND MANUFACTURING OF PLASMA FACING COMPONENTS

The applicability of a future energy generating fusion reactors is, among others, based on the feasibilities of plasma facing components which can guarantee a reasonable lifetime from a safety and economical point of view. This lifetime is limited mainly by thermal fatigue due to cyclic thermal loads and by thermally induced mechanical stresses to these components [4]. Transient

thermal loads, in particular tokamak specific plasma disruptions can deposit energy densities of several ten MJm⁻². These events have pulse durations in the order of 1 millisecond and will damage and/or erode the divertor, especially in the separatrix strike zone region. Further transient events which deposit a large fraction of the plasma energy on relatively small wall areas are the vertical displacement events (VDE).

The quasi-continuous plasma operation in large future confinement experiments is associated with another transient heat load event, namely energy deposition by type-I ELMs (edge localized modes) which will deposit another non-negligible amount of energy during each event; the expected power deposition is in the order of GW per square metre on a sub-millisecond time scale. Up to now only limited information is available on the material performance under these events. However, there is a serious concern that high cycle fatigue damage and thermal erosion combined with brittle destruction (BD) might be another lifetime limiting event.

The expected loading scenarios for the above mentioned thermal fatigue and thermal shock loads are strongly design dependent. The expected thermal loads are shown schematically in table 1 for the stellarator W 7-X, for the ITER design, and for a future thermo-nuclear fusion reactor. It should be noted that the intense flux of 14 MeV-neutrons will additionally degrade all (plasma facing and structural) materials in D-T burning devices such as ITER or the reactor; this is subject of an extensive long-term materials test programme.

TABLE I. Wall loading in Wendelstein 7-X, in ITER and in a thermonuclear fusion reactor

	W7-X	ITER	reactor
heat flux FW / MWm ⁻²	< 0.2	< 1	< 1
heat flux divertor / MWm ⁻²	10	5 - 20	≈ 5 - 20
VDEs / MJm ⁻²	?	60	-
disruptions / MJm ⁻²	-	≈10	-
ELMs / MJm ⁻²	?	1	?
neutron fluence / dpa	-	< 1	< 150

The technical design solutions which are considered today for the plasma facing components in the ITER divertor (cf. Fig. 1) are mainly based on carbon or refractory metals as plasma facing materials (PFM) and copper alloys for the heat sink. The selection of these materials [5] was based on a number of criteria; the most critical requirements are summarized in Fig. 2.

The prime candidate for the first wall region is the low-Z material beryllium. Due to its affinity to oxygen it is an excellent getter material which guarantees plasma discharges with low impurity levels; compared to carbon, it also exhibits better erosion resistance and hence, a reduced material transport during plasma operation of the fusion device. In addition, Be is characterized by a rather good

thermal conductivity ($\approx 190 \text{ Wm}^{-1}\text{K}^{-1}$ at RT) to remove the surface heat flux and to avoid overheating of the wall structures. This is most essential, in particular for a first wall made from beryllium tiles or beryllium coatings which exhibit only a moderate melting point of about 1285°C (see Fig. 3).

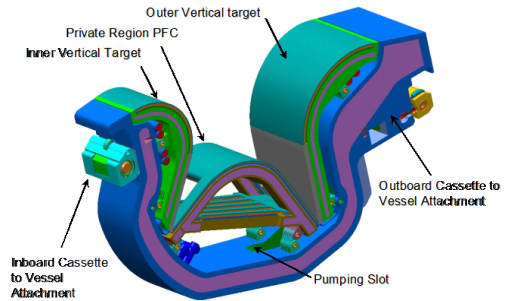


Fig. 1 Divertor cassette for ITER

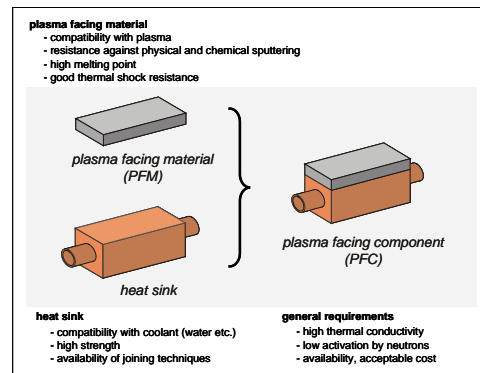


Fig. 2 Requirements for plasma facing and heat sink materials [10]

The divertor region and the baffle components in ITER will be manufactured from tungsten and/or carbon-fibre-composites (CFC) with integrated coolant structures. Compared to beryllium, tungsten is a refractory metal with an extremely high melting point (3410°C) and an adequate room temperature thermal conductivity of approx. $140 \text{ Wm}^{-1}\text{K}^{-1}$; hence from a thermo-physical point of view tungsten appears to be the most attractive material candidate for high heat flux component. A drawback however is its brittle nature; tungsten is ductile and easily machinable only above the so-called ductile-brittle-transition-temperature

(DBTT) of about 400°C. In addition tungsten shows a strong tendency to recrystallize at high temperatures well below the melting point. Compared to the other PFM candidates (Be or C) tungsten is significantly activated during neutron irradiation.

	Be	CFC	W
atomic number Z	4	6	74
max. allowable concentration in the plasma	15 %	12 %	1 ppm
thermal conductivity λ [W/mK]	190	200 ... 500	140
melting point [°C]	1285	3500 (subl.)	3410
coefficient of thermal expansion [10^{-6} K^{-1}]*	11.5	- 0 **	4.5
n-irradiation behaviour	swelling	decrease in λ	activation

* CTE copper = $16 \cdot 10^{-6} \text{ K}^{-1}$ ** NB31 in pitch fiber direction

Fig. 3 Thermo-physical properties of metallic and carbon based plasma facing materials.

The third candidate material, carbon, is of special importance since it does not melt. This special feature makes carbon an attractive candidate for the strike zone of the so-called separatrix on the divertor. Here it can withstand very high heat loads without the risk of forming any liquid phase; however, sublimation of carbon at elevated temperatures ($T \geq 2200^\circ\text{C}$) is becoming essential and an enhanced material erosion due to brittle destruction (cf. chapter 5) is also of serious concern. On the other hand, the thermo physical properties are excellent, in particular if fibre-reinforced grades are taken into consideration. Depending on the selected fibre type and the weave geometry, these carbon-fibre reinforced carbons can be manufacture to day with thermal conductivities equal or even better compared to copper (up to $\approx 500 \text{ Wm}^{-1}\text{K}^{-1}$). However, this excellent thermal conductivity will be degraded rapidly under the influence of thermal or fast neutrons (cf. chapter 6). The fibre reinforcement will also improve the strength of the composite in comparison to conventional isotropic fine grain graphites which are frequently used as plasma facing armour in present-day tokamaks or stellarators.

Different design options for the attachment of the plasma facing material to the heat sink (cf. Fig. 4) have been developed, manufactured and tested [6, 7, 9]. The heat sink, in general a precipitation hardened or a dispersion strengthened copper-alloy with an integrated high pressure coolant tube has now become the standard technology for ITER or other existing medium- and long-pulse fusion devices. To reduce stresses which might affect the integrity of the plasma facing material or the joint (stresses due to the mismatch between the plasma facing and the heat sink material, as well as thermally induced stresses due to the

thermal gradient during plasma exposure), a segmentation of the PFM using thin slots perpendicular to the surface down to the heat sink (so-called castellations, or ‘macro-brush’) is frequently used. To guarantee a non-detachable contact between the PFM and the heat sink a number of joining techniques such as brazing, hot isostatic pressing (HIPing), electron beam welding or diffusion bonding have been developed and applied successfully [8 – 10].



Fig. 4 Design options for actively cooled plasma facing components for divertor applications [9]

The interface between the PFM and the heat sink does not necessarily require a flat geometry; the so-called monoblock design (also: ‘tube in block’ solution) consists of cube-shaped monolithic tiles which are equipped with a cylindrical hole which allows the joining to the water cooled copper tube directly. This design option has an unrivalled advantage since the loss of the PFM-tile under thermal excursions which might be associated with a major failure of the whole component (cascade failure [11]) is excluded.

III. CHARACTERIZATION OF PLASMA FACING MATERIAL AND COMPONENTS

To select among different commercially available plasma-facing and heat sink materials a reliable characterization is necessary. An extensive data base is essential to choose the best suitable material candidates and the applied treatments (alloying, thermo-mechanical treatments such as heat exposure, rolling or forging, sintering etc.). In addition, a number of promising new materials have been developed and improved in a laboratory scale and are now ready for an upgrading for an industrial production. To identify the most promising candidates and later, to guarantee the material parameters during the serial production, an extensive set of different characterization techniques is prerequisite for the successful development and manufacturing of reliable high heat flux components. This material characterization must cover the full temperature range for the particular application; in addition, a number of material properties are also required in the neutron irradiated state to predict the material and component performance during nuclear operation of a thermonuclear facility such as ITER. This characterization is not limited to the materials; the integrity of joints has to be evaluated and demonstrated by reliable techniques (X-

ray methods, ultrasonic inspection, infra-red techniques to identify imperfections or thermal barriers in the interface layer [17].

Material characterization also includes the testing of actively cooled components under fusion specific loading conditions. A number of test facilities suitable to provide thermal loads with power densities ranging from the MW/m² to several GW/m², and pulse durations ranging from a few hundred microseconds to almost continuous power loading have been developed in several laboratories world wide [12]. Most of these test devices (so-called high heat flux (HHF) test facilities) are based on intense electron or hydrogen ion beams which are used in pulsed and/or scanned modes to simulate the thermal loads which are expected during normal operation scenarios; short thermal pulses are applied to characterize the material or component performance under normal (ELMs) or off-normal events (VDEs, disruptions). For the latter type of HHF-experiment also plasma accelerators [18] and ion beam facilities play an important role.

IV. THERMAL FATIGUE BEHAVIOUR OF PLASMA FACING COMPONENTS

To evaluate the thermo mechanical performance of various divertor designs, a significant number of small scale divertor components have been manufactured by industry or research laboratories. These cover different design options (flat tile, monoblock) and different joining techniques for both, CFC and tungsten armour [4]. In the following a survey of selected plasma facing component with CFC and tungsten armour for the divertor and with beryllium coatings/tiles for first wall applications are summarized; the major characteristics of carbon and tungsten armoured modules and the results for medium term thermal fatigue tests are listed in Fig. 5.

The heat flux limits which have been obtained so far in electron beam experiments on small scale mock-ups with typical cycle number of $n = 1000$ can be summarized as follows:

- CFC flat tiles withstood cyclic thermal loads up to 19 MWm⁻²,
- CFC monoblocks have been tested up to 25 MWm⁻²,
- tungsten flat tiles (macrobrush design) didn't show any failure up to 18 MWm⁻²,
- tungsten monoblocks (drilled W-tiles and W-lamellae) withstood up to 20 MWm⁻².

These data show very clearly that technical solutions for the divertor targets are feasible which meet or even exceeded the HHF requirements for ITER.

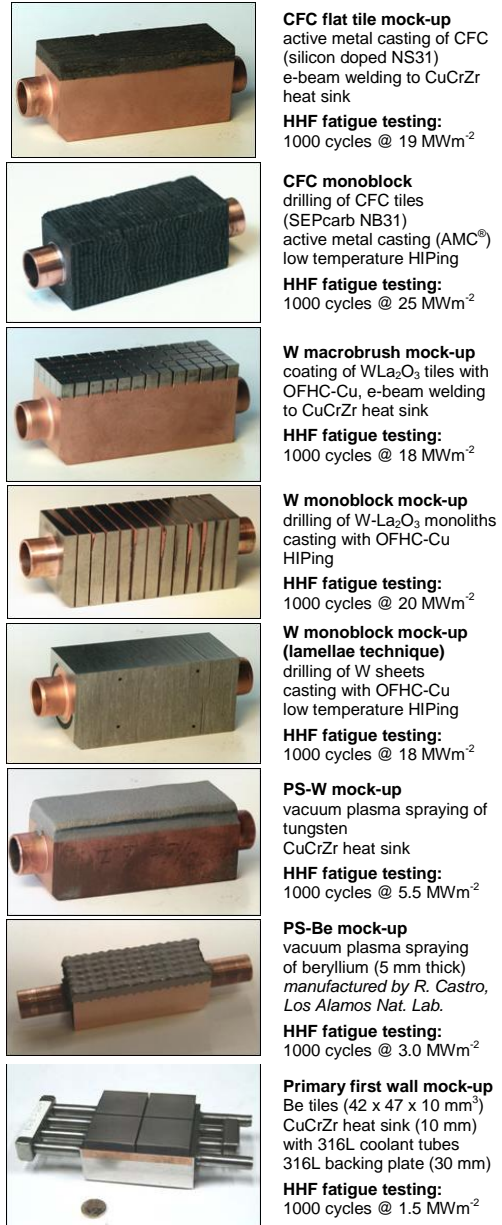


Fig. 5. Survey of small scale mock-ups with different plasma facing armour (CFC, tungsten, beryllium) and different design options (flat tile components, monoblock design and plasma sprayed modules) [8]

Similar to the divertor applications, precipitation hardened copper (CuCrZr) has also become a promising candidate for the heat sink in first wall components. Hence, additional efforts have been allocated to the development and thermo-mechanical testing of beryllium/CuCrZr-joints. Best performances obtained so far with HHF tests in the electron beam test facility JUDITH on a variety of components produced with different joining parameters have shown detachments of the Be tiles after cyclic operation only for heat fluxes $> 2.75 \text{ MW/m}^2$.

HHF testing has also been performed on flat CuCrZr heat sink modules which were coated in a plasma spray process with tungsten (see Fig. 5). These modules have shown a favourable thermal fatigue performance with peak heat loads of 5.5 MWm^{-2} without detectable failure. Be-coated component which have also been produced by plasma spray techniques didn't show any degradation of the heat removal efficiency up to 3 MWm^{-2} ; however, some cracks developed perpendicular to the component's surface (i.e. parallel to the heat flux direction). These findings were predictable since both types of plasma sprayed components have not been castellated so far.

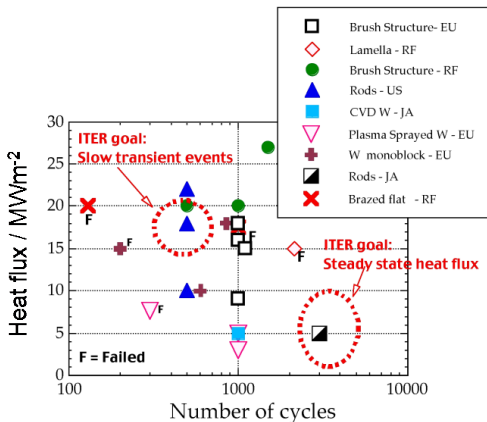


Fig. 6 Damage limits for plasma facing components with tungsten armour [cf. ITER web-page]

To compare the results from different thermal fatigue tests on plasma facing components with carbon armour which have been performed so in different laboratories in Europe, Russia and Japan, the maximum acceptable heat flux for a given pulse number is plotted in Fig. 6. This diagram also shows the ITER target values (dotted circles) for steady state operation (approx. 5 MWm^{-2}) and for slow thermal transients (up to 20 MWm^{-2}). Although HHF tests with high cycle number ($n > 1000$) are scarce (mainly because they are rather time and cost consuming), the diagram clearly proves the existence of technically mature

design solutions for the high heat flux components in large scale fusion devices such as ITER.

Most of the thermal load tests so far have been performed on small-scale modules [12 – 13]. These components typically have cross-sectional geometries which are identical with the proposed design solutions for PFCs in ITER or other large fusion devices; however, to minimize the manufacturing cost and to facilitate the testing procedure, in general short single-tube mock-ups with a length of about 5 to 20 cm have been tested. To benchmark the performance real scale modules with the actual length and assembly of the ITER divertor, medium and full scale prototypes (Fig. 7) have been manufactured and tested successfully under cyclic thermal loads in a powerful high heat flux test facility in France (FE 200) [14]. In a similar way full scale tests on a first wall panel ($L \approx 1\text{m}$) with beryllium tiles brazed to a dispersion strengthened heat sink are on the way [15].

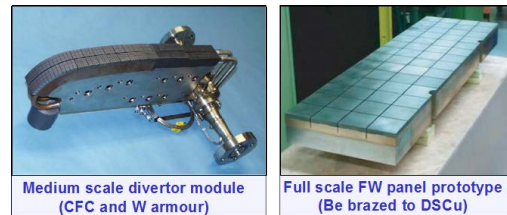


Fig. 7 Medium scale mock-up for the divertor and the first wall of ITER

V. THERMAL SHOCK LOADING

Beside the normal operation scenarios, transient loading conditions also have been taken into consideration [16, 18]. Among these events (cf. table I) the so-called vertical displacement events (i.e. the malfunction of the plasma positioning system) may result in severe surface damage due to short term (100 – 300 ms) thermal loads to plasma facing components. Such an event with a deposited energy density of about 60 MJm^{-2} (ITER) will mainly affect the surface of components with metallic PFMs (beryllium or tungsten). The material performance during these short term events is shown schematically in Fig. 8, both for metallic (e.g. tungsten or beryllium) and carbon based materials (e.g. graphites or CFC). The energy density during plasma disruptions or VDEs in general exceeds the melting threshold, not only for beryllium but also for tungsten. Depending on the energy density of the incident beam pulse, the liquefied material will either remain in the position where it is formed and recrystallize after a short period, or it will be ejected due to the high vapour pressure at the surface of the melt pool. A further increase of the incident power density may also result in a boiling and

bubble formation of the melt layer. These processes are a major source for the formation of metallic droplets, particularly if additional (e.g. magnetic) forces are acting on the melt layer. These droplets might contaminate the plasma. Metallic dust originating from recrystallized melt droplets has been identified as a critical safety issue in future fusion devices.

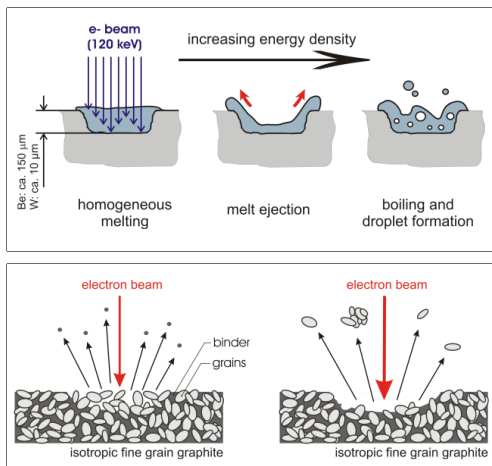


Fig. 8 Metals (top) and graphite (bottom) under intense thermal loads in an electron beam device [10].

The melt layer thickness under these events was determined experimentally in electron beam tests and was found to be in the order of a few millimetres (depending on the pulse duration), see Fig. 9. Mock-ups with un-doped CFC armour are more resistant under identical thermal loads since pure carbon does not form any liquid phase; however, some thermal erosion by sublimation and brittle destruction (see below) has been detected.

More serious material damage is expected during plasma disruptions which occur on a millisecond timescale. For ITER about 10% of the discharges are supposed to be terminated in a plasma disruption. The published data about the expected amount of deposited energy density show some scatter; furthermore, part of the incident plasma energy is absorbed by a dense cloud of ablation vapour which forms above the heat affected surface area. Nevertheless, an absorbed energy density of several MJm^{-2} will be deposited on the PFC surface. Due to the rather short pulse duration ($\Delta t \approx 1 \text{ ms}$) heat conduction into deeper parts of the PFM does not play any important role and the mayor damage is restricted to a thin surface layer with a thickness of several ten microns. Under these conditions metallic plasma facing materials such as beryllium or tungsten will melt instantaneously; this mechanism is

associated with the formation of bubbles in the melt layer and with the ejection of metallic droplets which finally will contaminate the plasma boundary layer or will be deposited in the form of metallic dust or layers in gaps behind the PFCs. From a safety point of view this process may generate non negligible amounts of toxic beryllium particles or highly activated tungsten dust which might need periodical removal to avoid the accumulation of critical dust concentrations.

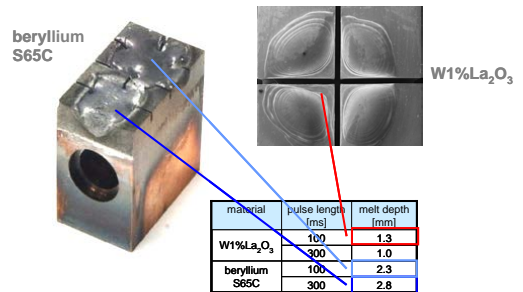


Fig. 9 Electron beam simulation of vertical displacement events with a deposited energy density of 60 MJm^{-2} [10]

The short pulse duration of disruption events will generate steep thermal gradients in the surface of the plasma facing material; this will induce severe thermal stresses which may generate cracks with a depth of several hundred microns and beyond. This effect is of special importance if the temperature of the heat effected material is below DBTT (ductile brittle transient temperature), i.e. at below $\approx 400^\circ\text{C}$ for un-irradiated sintered tungsten.

In contrast to metallic PFMs carbon based materials such as graphites or CFCs do not melt; hence, the formation of dust particles via the above mentioned mechanism does not occur. However, brittle destruction (BD) [19], i.e. generation of thermally induced microcracks in the surface of these materials during intense thermal loads will result in the formation of carbon dust particles, if a critical threshold value of the incident beam power is exceeded (see Fig. 8, bottom). The brittle destruction mechanism has been detected in electron beam simulation experiments; a typical example is shown in Fig. 10 for an absorbed power density of $\geq 3.3 \text{ GWm}^{-2}$ ($\Delta t = 2 \text{ ms}$). Here the trajectories of the hot carbon particles are clearly visible; particle velocities $\geq 150 \text{ ms}^{-1}$ have been determined by optical time-of-flight measurements [20]. Below a critical threshold value ($< 3 \text{ GWm}^{-2}$) no particle emission has been observed. Up to a 2nd threshold value mainly small and medium sized particles are ejected from the surface of the plasma facing material. In fine grain graphite this process is characterized by the release of the binder phase between the graphitic grains (cf. Fig. 8, bottom). If the 2nd threshold value is

exceeded large dust particles (grains or grain clusters) are emitted from the surface. Major concern of the carbon dust is the co-deposition together with tritium in gaps or in remote areas behind the divertor structure. In particular the large particle emission results in a substantial erosion of the graphite surface; this has been clearly demonstrated by weight loss and SEM analyses [19].

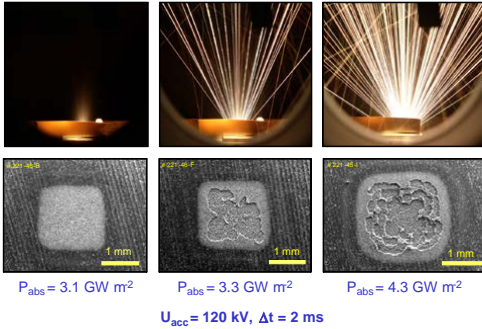


Fig. 10 Brittle destruction of isotropic fine grain graphite (power density $P_{\text{abs}} = 3.2 \dots 4.3 \text{ GW m}^{-2}$, $\Delta t = 2 \text{ ms}$).

The threshold values for the onset of brittle destruction have been determined for graphites and CFCs both for disruption and VDE specific pulse durations, i.e. for 1 to 5 and for 100 ms; similar studies for the ELM regime are on the way. The thermal loads during plasma disruptions and VDEs in ITER are clearly above the threshold values for brittle destruction, while the ELM regime seems to remain in a safe operation regime. Nevertheless, brittle destruction may also play an important role for ELM specific loads because of the high frequency of these events (1 Hz) and an integrated number of several million incidents during the lifetime of the divertor target in ITER.

Carbon dust particles have been collected and analysed by different methods. The size of these objects covers a rather wide range from a few nanometers to a maximum of about $100 \mu\text{m}$, i.e. their dimensions are ranging from nanotubes to graphitic grains or even grain clusters. Simulation tests with carbon fibre composites show a rather similar behaviour compared to fine grain graphites, however, the threshold values are slightly shifted to higher energy densities; this is due to the improved thermal conductivity of this material. The material erosion strongly depends on the architecture of the CFC composite and on the type and orientation of the fibres used.

VI. NEUTRON INDUCED MATERIAL DEGRADATION

The irradiation induced degradation of mechanical and thermal properties has been performed on selected plasma facing materials which have been subjected to ITER relevant neutron fluxes in fission type material test reactors, such as the high flux materials test reactor (HFR in Petten, The Netherlands). Furthermore, modifications in the high heat flux performance have been investigated in electron beam tests on neutron irradiated small scale components with CFC, tungsten and beryllium armour.

The heat removal efficiency of actively cooled components mainly depends on the thermal conductivity λ of the materials. This parameter was determined in laser flash experiments which allows a direct measurement of the thermal diffusivity α in combination with additional recordings of the material density ρ and the temperature dependent specific heat c_p ($\lambda(T) = \alpha(T)\rho(T)c_p(T)$).

Carbon based materials show a rather strong decrease in thermal conductivity even after relatively low neutron fluences [21, 22]. The ITER candidate CFC armour material NB31 for example exhibits excellent thermal conductivities before neutron irradiation. Fig. 11 shows laser flash data measured in the high thermal conductivity direction (i.e. parallel to the pitch fibre reinforcement) with RT values exceeding $300 \text{ W m}^{-1}\text{K}^{-1}$. Even low neutron fluences have a strong effect on the thermal conductivity with values below $50 \text{ W m}^{-1}\text{K}^{-1}$ at room temperature. n-irradiation to 1.0 dpa finally results in a reduction of λ by one order of magnitude. Due to annealing effects the thermal conductivity reduction diminishes at elevated temperatures.

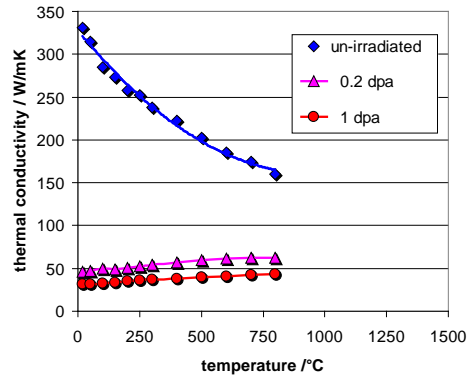


Fig. 11 Thermal conductivity of NB31 before and after neutron irradiation (0.2 and 1.0 dpa, $T_{\text{irr}} = 200^\circ\text{C}$, pitch fibre orientation) [8]

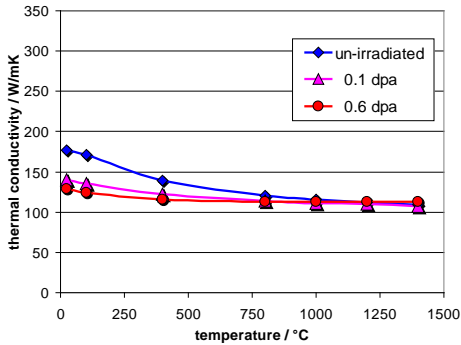


Fig. 12 Thermal conductivity of W before and after neutron irradiation (0.1 and 0.6 dpa, $T_{\text{irr}} = 200^\circ\text{C}$) [8]

The room temperature thermal conductivity of sintered tungsten is significantly smaller compared to NB31 (cf. Fig. 12); however, there is only a marginal reduction at elevated temperatures. For irradiated tungsten the neutron induced degradation of the thermal conductivity λ is also less pronounced; in a temperature range $T \leq 1400^\circ\text{C}$ and up to the ITER specific fluence of approx. 0.6 dpa λ remains well above $100 \text{ Wm}^{-1}\text{K}^{-1}$. For $T \geq 1000^\circ\text{C}$ the difference between irradiated and un-irradiated material is negligible.

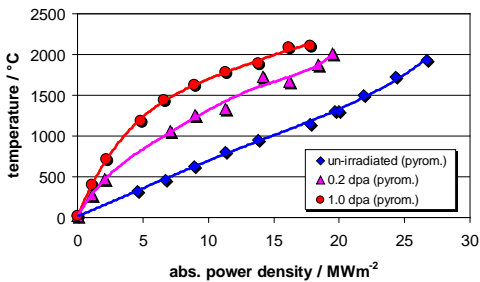


Fig. 13 Surface temperature of flat-tile divertor components with CFC armour as a function of the applied thermal load (unirradiated and neutron irradiated at 200°C , 0.2 and 1.0 dpa) [8].

Actively cooled divertor components with CFC and tungsten armour (flat tile and monoblock design) have been exposed to similar neutron doses in the HFR reactor. The thermal fatigue behaviour of all mock-ups has been evaluated without and after neutron irradiation. Typical results for CFC flat tile components at different neutron fluences of 0.2 and 1.0 dpa @ 200°C are plotted in Fig. 13. To avoid excessive carbon vaporization these experiments

were limited to surface temperatures of above 2000°C . In compliance with these restrictions the un-irradiated components have been exposed to heat loads of more than 25 MWm^{-2} (screening tests); after neutron irradiation these limits were achieved already below 20 MWm^{-2} . For temperatures below approx. 1000°C the slope of the plotted curves in Fig. 13 shows the neutron irradiation induced changes in the heat removal efficiency. For higher thermal loads, i.e. when the surface temperature exceeded values of approx. 1000°C , part of the neutron induced defects recover.

Beside screening tests with small cycle numbers, thermal fatigue experiments have been performed with $n = 1000$ cycles [8] in agreement with the experiments on un-irradiated components in chapter 4. The results which have been obtained so far can be summarized as follows [21, 23]:

- CFC flat tiles have been exposed to cyclic thermal loads up to 15 MWm^{-2} (at 0.2 dpa and 1.0 dpa) and for 1000 thermal cycles without any failure,
- CFC monoblocks have been tested up to 12 MWm^{-2} for 1000 cycles; screening tests performed at 14 MWm^{-2} have been terminated caused by vaporization losses due to high surface temperatures,
- tungsten monoblock modules did not show any failure up to 18 Wm^{-2} (0.1 and 0.6 dpa).
- tungsten flat tiles (macrobrush) withstood 1000 cycles at 10 MWm^{-2} (0.1 and 0.6 dpa); the fatigue tests were characterized by a non-negligible increase of the surface temperature.

Neutron irradiation experiments with beryllium armoured primary first wall mock-ups (low temperature irradiation at 0.6 dpa) are in preparation.

VII. SUMMARY

The design activities for the divertor and the primary first wall modules follow roughly the same general pattern which is shown schematically in Fig. 14. The major steps of the R&D activities include the design selection, the qualification of the materials for the plasma facing armour and for the heat sink, the development and improvement of reliable joining techniques. Step-by-step iterations resulted in the production of numerous small scale mock-ups which were subjected to non-destructive qualification tests and to extensive high heat flux testing, preferably in electron beam test devices. In a further step, selected material samples and small-scale modules were irradiated in material test reactors to ITER specific fluences. Finally, medium and full-scale components have been manufactured mainly by industry, but also by research laboratories. These prototype components have been exposed to cyclic thermal loads (divertor) or are now ready for fatigue performance testing (blanket modules).

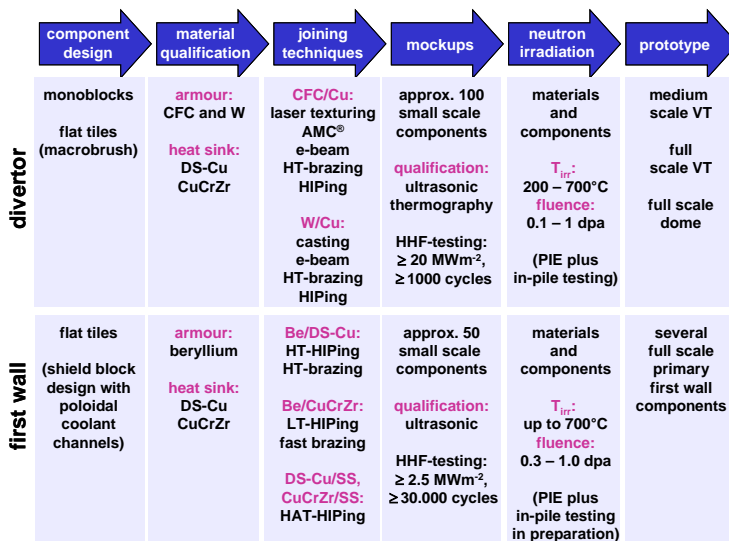


Fig. 14 Schematic presentation of the step-by-step development of first wall and divertor targets [8]

During the past few years the present design of the ITER divertor has received a well-engineered, technically mature status; this has largely been achieved by an intense collaboration within the European associations, with other international partners and with industry. In the frame of this study the relevant armour and heat sink materials have been qualified; the development and qualification of two different design options, the monoblock and the flat tile geometry have been pursued in parallel approaches. In addition, a wide spectrum of different joining methods such as e-beam welding, high temperature brazing or hot isostatic pressing (HIP) have been applied to the most promising material candidates. The quality of the bond has been benchmarked by non-destructive analyses or extensive high heat flux experiments (thermal fatigue testing and simulation of transient events). Finally medium and full scale components with tungsten and CFC armour have been evaluated successfully under ITER specific thermal loads. Today, fatigue resistant high heat flux components for thermal loads up to 20 MWm⁻² are technical feasible. A similar approach has been applied to develop thermal fatigue and radiation resistant first wall components. Here the low-Z material beryllium is the first choice for ITER; other existing or next step fusion devices also utilize or suggest carbon based materials (isotropic fine-grain graphites) and/or plasma sprayed boron carbide or tungsten coatings. Qualified heat sink materials are precipitation

hardened or dispersion strengthened copper alloys; stainless steel, in particular low activation grades, may also play an important role in the longer run.

Finally, neutron irradiation experiments have been performed in material test reactors to characterise the materials degradation. Here mainly thermal and mechanical properties have been investigated under ITER specific conditions, i.e. for neutron wall loads up to 1 dpa. Under these conditions rather serious degradation effects has been identified for carbon based materials; here the thermal conductivity shows a significant decrease up to one order of magnitude, even for neutron doses as low as 0.2 dpa. A number of qualification tests have been done to evaluate the HHF performance of actively cooled high heat flux components, mainly with carbon and tungsten armour. The results of these tests clearly indicate that technically mature solutions for high heat flux components in next step thermonuclear fusion devices are feasible.

REFERENCES

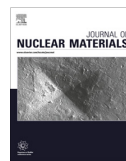
- [1] J. Linke: "Plasma facing materials and components for future fusion devices - development, characterization and performance under fusion specific loading conditions" to be published in Physica Scripta, 2005

- [2] R. Aymar and International Team: "ITER status, design, and material objectives", *J. Nucl. Mater.* 307 – 311, 1 (2002)
- [3] H. Bolt et al.: "Plasma facing and high heat flux materials – needs for ITER and beyond", *J. Nucl. Mater.* 307 – 311, 43 (2002)
- [4] M. Merola, M. Akiba, V. Barabash, I. Mazul, "Overview on fabrication and joining of plasma facing and high heat flux materials for ITER", *J. Nucl. Mater.* 307 – 311, 1525 (2002)
- [5] H. Bolt, V. Barabash, W. Krauss, J. Linke, R. Neu, S. Suzuki, N. Yoshida, ASDEX Upgrade team, "Materials for the plasma facing components of fusion reactors", *J. Nucl. Mater.* 329 – 333, 66 (2004)
- [6] R. Tivey et al, "ITER divertor, design issues and research and development", *Fusion Eng. Design* 46, 207 (1999)
- [7] M. Scheerer, H. Bolt, A. Gervash, J. Linke, I. Smid: "The design of actively cooled plasma-facing components", *Physica Scripta T91*, 98 (2001)
- [8] J. Linke, P. Lorenzetto, P. Majerus, M. Merola, D. Pitzer, M. Rödig: "EU Development of High Heat Flux Components", *Proc. ANS 16th Topical Meeting on the Technology of Fusion Energy*, Madison, Wisconsin, 14. – 16.09.2004
- [9] I. Smid, "Material Processing and Testing of Plasma-Interactive Components for Fusion Energy Systems", *Material Science Forum Vols. 475 – 479*, 1355 (2005)
- [10] J.M. Linke, T. Hirai, M. Rödig, L.A. Singheiser, "Performance of plasma-facing materials under intense thermal loads in tokamaks and stellarators", *Fus. Sci. Tech.*, 46, 142 (2004)
- [11] J. Schlosser et al.: "Technologies for ITER divertor vertical target plasma facing components", *Nucl. Fusion* 45, 512 (2005)
- [12] T. Hirai, K. Ezato, P. Majerus: "ITER Relevant High Heat Flux Testing on Plasmas Facing Surfaces", *Materials Transactions*, Vol. 46, No.3, 412 (2005)
- [13] H. Greuner, B. Böswirth, J. Boscary, G. Hofmann, B. Mendelevitch, H. Renner, R. Rieck: "Final design of W7-X divertor plasma facing components – tests and thermo-mechanical analysis of baffle prototypes", *Fus. Eng. Design* 66 – 68, 447 (2003)
- [14] M. Merola, J. Palmer and the EU ITER Participating Team: 'EU Activities in Preparation of the Procurement of the ITER Divertor', *Proc. Intern. Symposium on Fusion Nuclear Technology*, Tokyo, 22. – 27.05.2005
- [15] P. Lorenzetto, B. Boireau, C. Boudot, Ph. Bucci, A. Furmanek, K. Ioki, J. Liimatainene, A. Peacock, P. Sherlock, S. Tähtinen, "Manufacture of Blanket Shield Modules for ITER", *Proc. SOFT-23*, Venice, Italy (2004), to be published
- [16] G. Federici et al.: "Key ITER plasma edge and plasma-material interaction issues", *J. Nucl. Mater.* 313 -316, 11 (2003)
- [17] J. Jacquinet al.: "Recent developments in steady-state physics and technology of tokamaks in Cadarache", *Nucl. Fusion* 43, 1583 (2003)
- [18] A. Zhitlukhin, et al: "Effect of ELMs and disruptions on ITER divertor armour materials" *J. Nucl. Mater.* 337 – 339, 684 (2005)
- [19] J. Linke, S. Amouroux, E. Berthe, W. Kühnlein, M. Rödig: "Brittle destruction of carbon based materials in transient heat load tests", *Proc. 22nd Symposium on Fusion Technology*, Helsinki, 08. – 13.09.2002
- [20] T. Hirai, J. Linke, W. Kühnlein, G. Sergienko, S. Brezinsek, "Light emission from carbon-based materials under ITER relevant thermal shock loads", *J. Nucl. Mater.* 321, 110 (2003)
- [21] M. Roedig, W. Kuehnlein, J. Linke, D. Pitzer, M. Merola, E. Rigal, B. Schedler, E. Visca: "Post irradiation testing of samples from the irradiation experiments PARIDE 3 and PARIDE 4", *J. Nucl. Mater.* 329 - 333, 766 (2004)
- [22] V. Barabash, G. Federici, J. Linke, C.H. Wu: "Material/plasma surface interaction issues following neutron damage", *J. Nucl. Mater.* 313 – 316, 42 – 51 (2003)
- [23] M. Rödig et al.: "High Heat Flux Performance of Neutron Irradiated Plasma Facing Components", *J. Nucl. Mater.* 307 – 311, 53 (2002)



Contents lists available at ScienceDirect

Journal of Nuclear Materials

journal homepage: www.elsevier.com/locate/jnucmat

Plasma-surface interaction in the Be/W environment: Conclusions drawn from the JET-ILW for ITER

S. Brezinsek^{a,b,*}, JET-EFDA contributors²^aJET-EFDA, Culham Science Centre, OX14 3DB, Abingdon, UK^bForschungszentrum Jülich, Institut für Energie- und Klimaforschung - Plasmaphysik, 52425 Jülich, Germany

ARTICLE INFO

Article history:

Available online 23 December 2014

ABSTRACT

The JET ITER-Like Wall experiment (JET-ILW) provides an ideal test bed to investigate plasma-surface interaction (PSI) and plasma operation with the ITER plasma-facing material selection employing beryllium in the main chamber and tungsten in the divertor. The main PSI processes: material erosion and migration, (b) fuel recycling and retention, (c) impurity concentration and radiation have been studied and compared between JET-C and JET-ILW. The current physics understanding of these key processes in the JET-ILW revealed that both interpretation of previously obtained carbon results (JET-C) and predictions to ITER need to be revisited. The impact of the first-wall material on the plasma was underestimated.

Main observations are: (a) low primary erosion source in H-mode plasmas and reduction of the material migration from the main chamber to the divertor (*factor* 7) as well as within the divertor from plasma-facing to remote areas (*factor* 30 – 50). The energetic threshold for beryllium sputtering minimises the primary erosion source and inhibits multi-step re-erosion in the divertor. The physical sputtering yield of tungsten is low as 10^{-5} and determined by beryllium ions. (b) Reduction of the long-term fuel retention (*factor* 10 – 20) in JET-ILW with respect to JET-C. The remaining retention is caused by implantation and co-deposition with beryllium and residual impurities. Outgassing has gained importance and impacts on the recycling properties of beryllium and tungsten. (c) The low effective plasma charge ($Z_{eff} = 1.2$) and low radiation capability of beryllium reveal the bare deuterium plasma physics. Moderate nitrogen seeding, reaching $Z_{eff} = 1.6$, restores in particular the confinement and the L-H threshold behaviour. ITER-compatible divertor conditions with stable semi-detachment were obtained owing to a higher density limit with ILW. Overall JET demonstrated successful plasma operation in the Be/W material combination and confirms its advantageous PSI behaviour and gives strong support to the ITER material selection.

© 2014 The Authors. Published by Elsevier B.V. This is an open access article under the CC BY-NC-ND license (<http://creativecommons.org/licenses/by-nc-nd/3.0/>).

1. Introduction

A coherent approach of good plasma performance with full first-wall compatibility is required to ensure safe and reliable plasma performance in future fusion devices such as ITER [1]. The use of Plasma-Facing Components (PFCs) made of carbon-based materials with their good power-handling capabilities decoupled to a certain extent the plasma-scenario development – with good confinement and intrinsic carbon radiation in the divertor [2] – from critical Plasma-Surface Interaction (PSI) processes related to lifetime and safety aspects. But unacceptable high steady-state first-wall erosion

[3] and unfavourable co-deposition of fuel [4] – causing high tritium retention and a non-sustainable tritium cycle in ITER and beyond – revealed the limitations in the usage of carbon-based PFCs and the need to operate with the only currently available alternative – metallic PFCs. Metallic PFCs were already in use prior to the carbon era, but suffered in tokamaks with limiter configuration and high oxygen content in the plasma from strong high-Z sources, poor screening, and accumulation [5]. The introduction of the divertor in combination with the development of wall-conditioning techniques lead to a renaissance of metallic PFCs. Experience has been gained in CMOD, equipped with molybdenum PFCs [6], and ASDEX Upgrade, equipped with a full tungsten first wall [7]. TEXTOR with tungsten limiter PFCs [8] contributed with dedicated experiments to pursue and explore plasma operation at and above the operational limitations. Up to the start of the JET ITER-Like Wall experiment (JET-ILW), no tokamak experience existed in the wall combination proposed for ITER.

* Corresponding author at: Forschungszentrum Jülich, Institut für Energie- und Klimaforschung - Plasmaphysik, 52425 Jülich, Germany.

E-mail addresses: sebastijan.brezinsek@jet.efda.org, s.brezinsek@fz-juelich.de

¹ Presenting author.

² See annex of F. Romanelli et al., Fusion Energy 2012 (Proc. 24th Int. Conf. San Diego, 2012) IAEA, (2012).

ITER employs a full metallic wall consisting of beryllium in the main chamber and, as recently decided, full tungsten divertor from the first day of operation [9]. On the one hand beryllium is selected as low Z-material, tolerable from the point of view of impurity concentration, with excellent potential to getter oxygen in the absence of chemical reactivity with hydrogen. Though beryllium forms layers which are capable to co-deposit fuel, PISCES-B experiments demonstrated lower fuel content in these layers [10] in comparison to carbon. This lower long-term fuel retention in beryllium leads ultimately to the ITER predictions [4], forecasting a significant increase of plasma-operation time without active fuel-removal requirement before the fuel-inventory limit is reached. On the other hand tungsten has been selected owing to the good power-handling capabilities with an extreme high melting point, the low physical sputtering yield, and the low fuel retention. However, in ITER and a reactor, low tungsten concentrations in the order of 10^{-5} are required [11] to avoid excessive core radiation which relies on high tungsten divertor retention and high-density divertor operation. The material choice represents the best currently available compromise to demonstrate fusion power with metallic walls.

The JET tokamak has been transformed from an all-carbon device to a metallic device with the described ITER-like wall combination [12,22]. The JET-ILW provides a unique opportunity to document both the changes from an all-carbon to a Be/W device after PFC replacement and to characterise plasma operation, plasma-edge physics and plasma-wall interaction in the ITER-relevant material mix [13,14]. The JET-ILW is with this respect a test-bed and demonstrated low long-term fuel retention [15] and fully plasma-facing material compatible plasma scenarios [16] in the absence of carbon as intrinsic radiator [17]. A vessel intervention concluded the first year of operation in order to retrieve a selection of PFCs for post-mortem analysis [18]. Plasma operation resumed with emphasis on dedicated tungsten melting studies to give timely input to the first divertor decision in ITER [19], and on confinement studies with the aim to recover the loss in plasma performance [20] in particular with nitrogen seeding [21].

Here, the different experimental findings made with JET-ILW are reviewed and connected to the main PSI processes in the tokamak environment: (a) material erosion and migration, (b) fuel recycling and retention, (c) impurity concentration and radiation. The current physics understanding of these key processes in the JET-ILW revealed that both interpretation of previously obtained JET-C results and predictions to ITER need to be revisited. The impact of first wall materials on the plasma performance was underestimated. This review is structured as follows: Section 2 describes briefly the PFC installation, power-handling qualification, and deals with the residual carbon and oxygen content in the plasma after start of operation. Section 3 is addressing the sputtering processes of beryllium in the main chamber and tungsten in the divertor as well as the associated material migration. The impact of the metallic wall on the global long-term fuel retention, recycling, and outgassing is presented in Section 4. Section 5 reveals the differences in the radiation pattern and plasma purity between JET-ILW and JET-C as well as introduces the beneficial impact of impurity seeding with nitrogen on the confinement. A summary of the physics processes driving the plasma-surface interaction in the Be/W mix and their impact on ITER is given in Section 6.

2. JET-ILW installation, conditioning and first plasma

In JET all PFCs made of carbon-fibre composites (CFC) had been replaced by metallic components in a single shutdown of 18 months duration by the remote-handling system [22]. 15,828 PFCs made of beryllium for the first-wall cladding and limiter as well as tungsten for the divertor and protection tiles in the main chamber were installed, resulting in sum to 2 tons of beryllium

in form of bulk Be or Be-coated inconel tiles and 2 tons of tungsten as bulk W or W-coated CFC tiles. The choice between bulk material or coating depends on the requirements concerning erosion/lifetime and power loads. The total amount of installed PFCs and the required installation sequencing underlines the logistic challenge of the project and serves as example for ITER. Fig. 1 shows a comparison of JET-C with JET-ILW: on the left-hand side the previously installed all-carbon wall before extraction of PFCs and on the right-hand side the ILW after the first year of operation. The absence of a distinctive deposition pattern with ILW is striking and indicates drastic changes in material migration.

Despite the same choice of materials, the absence of active cooling forces limitations on the power handling and a much more cautious operation in JET in comparison with ITER equipped with actively cooled PFCs. JET relies purely on inertial cooling, this requires on the one hand maximisation of the power-handling capabilities of the components by design optimisation [23] and on the other hand strict limits on power loads to avoid melting [24]. Dedicated experiments were performed to verify the design of both main PFCs, bulk Be limiters and bulk W divertor, as well as – in view of similar ITER applications – to verify the tools and procedures themselves [25]. The operation in ohmic inner-wall limited discharges and a nominal power load of $P_{in} = 1 \text{ MW m}^{-2}$ at the contact point revealed two power-decay lengths on the limiter surface with an unexpected narrow feature at the apex. This experimental finding has been included in a cross-machine comparison of power-decay lengths, resulting in a scaling law used to predict the power-decay length in ITER [26] and to verify the ITER main chamber PFC design. The narrow power-decay length in connection with a minor toroidal misalignment ($\approx 1 \text{ mm}$) of half of the ten protruding inner wall limiters led in auxiliary heated limiter discharges (JPN83620, $I_p = 1.7 \text{ MA}$, $B_t = 2.3 \text{ T}$, $P_{NBW} = 5 \text{ MW}$ for 8 s) to peak power loads of $P_{in} = 6 \text{ MW m}^{-2}$ and beryllium melting. However, this slight damage did not prevail further operation in limiter configuration, but demonstrated that the assumption of symmetric toroidal power distribution is critical [25].

Though the PFC exchange was carried out in one shutdown – in contrast to ASDEX-Upgrade with the sequential PFC replacement over several years [7] – both experiments share common, crucial questions with respect to the residual carbon content: by how much is the carbon content in the plasma reduced and how much effects the residual carbon the plasma operation and impacts on PSI processes? In JET, no active cleaning of the inconel vessel took place, thus a natural reservoir of carbon was present after pump down and the initial conditioning. The conditioning cycle itself consisted of pumping at a vessel temperature of 473 K, baking at 593 K, and a series of glow discharges in deuterium accumulating 200 h of

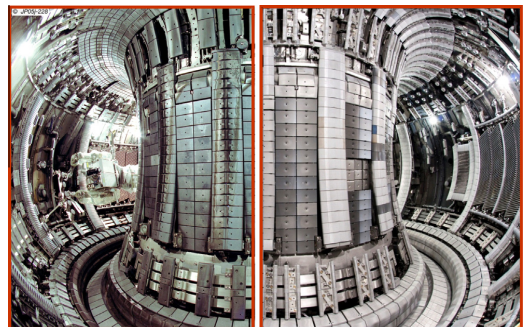


Fig. 1. Transformation of JET: From an all-carbon (JET-C) to an ITER-like device (JET-ILW) with Be main chamber and W divertor.

low temperature plasma and ion bombardment of the freshly installed components [27]. Be-head evaporations were not required in contrast to a conditioning cycle in JET-C. After a major shutdown in JET-C, the first plasmas lasted typically a few hundreds of milliseconds and conditioning by repetitive plasma operation was required to prolong the plasma duration. The behaviour with JET-ILW is with this respect different and allowed an easier plasma access with sustainable breakdown and long lasting plasma in the first attempt which can be attributed to the good oxygen gettering properties of beryllium [13]. All subsequent plasma breakdowns have been, apart from technical set-up failures, successful and no further plasma conditioning was required over the whole initial campaign. This is in strong contrast to JET-C operation where hydrogen-rich carbon co-deposits impacted the plasma breakdown by outgassing [28]; the controlled breakdown with the JET-ILW is in-line with the reduction of radiation by impurities and fuel. In an analogue manner, the averaged carbon and oxygen impurity levels in the plasma-edge layer during the plasma current flat-top phase dropped strongly with ILW in comparison with JET-C. Fig. 2a shows the reduction by more than one order of magnitude of the carbon edge content visualised by *CIII* emission normalised to the edge density. In the initial phase of plasma operation, a short clean-up period in carbon can be identified before almost steady-state conditions set in [17] with a slight increase in the period of high auxiliary power operation at the end of the first year. The carbon content remained low and almost constant in the second campaign executed after the tile intervention confirming an intact metallic first wall. The visual inspection during the intervention corroborated the spectroscopic observations – no significant damage of W-coated PFCs. The JET-ILW represents for the whole collection of studies presented here a valid test bed for a tokamak with beryllium first wall and tungsten divertor as envisaged in ITER.

The initial phase of plasma operation was affected by an air leak (leak rate: 1×10^{-3} mbar \cdot s $^{-1}$), nevertheless, the oxygen edge concentration in JET-ILW plasmas (Fig. 2b) was about one order of magnitude below a typical concentration in JET-C plasmas after vessel opening and substantial exchange of PFCs [27]. Beryllium PFCs in the main chamber which are not directly exposed during the limiter start-up phase to deuterium or beryllium ions are likely oxidised forming thin BeO-layer. The oxygen gettering capability of beryllium saturates in time which might explain that during normal plasma operation, oxygen levels are less pronounced suppressed than carbon levels.

3. Material erosion, transport and deposition

As demonstrated in the previous section, the PFC exchange led to a suppression of residual oxygen and carbon in the plasma

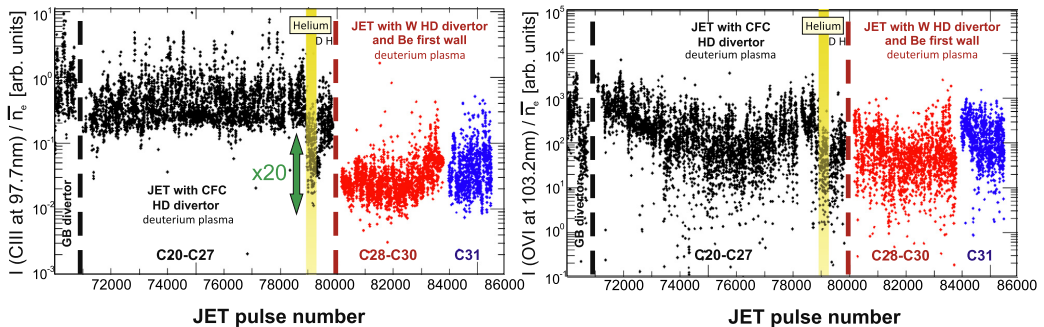


Fig. 2. From JET-C to JET ILW: C (*CIII*/ n_e) and O edge plasma content (*OVI*/ n_e) during the divertor phase as function of discharge number.

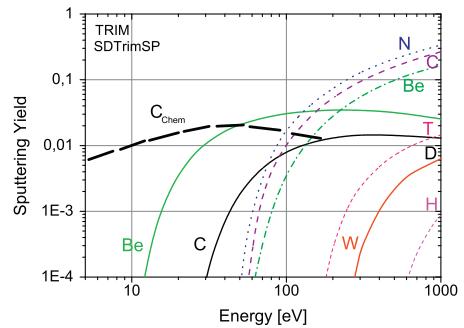


Fig. 3. Predicted physical sputtering yield of Be, C, W by D, and W by Be, C, N in binary-collision approximation. The sputtering yield for chemical erosion of carbon by deuterium at lowest impact energies is supplementary added.

leaving beryllium to be the main intrinsic impurity. A key issue is the source strength determination of beryllium in the JET-ILW and the comparison with carbon in JET-C in the absence of chemical erosion of beryllium at low impact energies as predicted by literature. Calculations by TRIM [29] in the binary-collision approximation predict slightly higher physical sputtering yields for beryllium (Fig. 3) at impact energies above the energy threshold which are usually present in limiter conditions for deuterons and charge-exchange neutrals in diverted plasmas. Previous ITER predictions assumed a comparable primary impurity source in an all-C and a Be/W device [4] that had fundamental consequences on material transport, deposition and fuel retention. The determination of the impurity composition is also essential to describe the tungsten source strength in the divertor where physical sputtering of tungsten will not be determined by fuel ions owing to their low mass, but due to plasma impurities. Fig. 3 shows the corresponding predicted physical sputtering yields and impact energy thresholds for tungsten sputtering by C, N, Be which needs to be compared with actual measurements.

In order to interpret the campaign-integrated footprint of erosion and deposition in the JET vessel, it is useful to distinguish between the operational time in limiter configuration with pure Be interaction and divertor configuration with Be/W interaction. The total operational time in the first year of JET-ILW operation (2011–2012) amounts 19 h of which 12 h were executed in divertor configuration. This needs to be compared with the last JET-C campaign (2008–2009) and 33 h total operational time of which 12 h were in limiter configuration. The separation allows to distinguish between material migration paths in these two configura-

tions. Note that in contrast to ITER, where long-pulse operation under steady-state conditions for several hundred seconds is foreseen, the plasma duration in JET-ILW is limited to tens of seconds with a factor 5 larger ratio of limiter-to-divertor time.

3.1. Beryllium erosion and migration in limiter plasmas

Dedicated discharges in limiter configuration were performed to assess the erosion of the beryllium first wall. The local plasma conditions at the inboard limiters and within the deuterium impact energies varied in the range of $E_{in} = 35\text{--}200\text{ eV}$ under an impact angle of about 60° . The effective Be sputtering yield $Y_{Be}^{tot} = \frac{\Gamma_{Be}}{\Gamma_D}$ at the limiter contact point was in-situ determined by optical emission spectroscopy observing $BeII$ (527 nm), representative for Be^+ resulting from beryllium erosion, and D_β , representative for the recycling flux or impinging deuteron flux under ionising conditions. In Fig. 4a is this gross erosion yield depicted as function of the local electron temperature (T_e) averaged over the observation spot. Y_{Be}^{tot} increases with T_e from 4% to more than 100% due to beryllium self-sputtering at the highest T_e or impact energies E_{in} [30]. The beryllium sputtering measurements in JET are currently applied to benchmark the Monte-Carlo code ERO taking into account the local geometry, the impact angles, impact energies and two sets of Be sputtering yields obtained from MD calculations, TRIM calculations and laboratory experiments [31]. Current modelling results (Fig. 4a) show an overestimation of the effective sputtering yield by a factor two for the best match between experiment and modelling. ERO has been previously applied to predict the lifetime of ITER first wall modules [32] which would be prolonged by the same factor two assuming the beryllium sputtering data applied in ERO is responsible for the discrepancy.

The measured Y_{Be}^{tot} is at high impact energies about a factor two larger than the corresponding Y_{Be}^{tot} in JET-C; the impact of self-sputtering at these energies is still minor with carbon. In contrast, at the accessible lowest impact energies in limiter discharges Y_{Be}^{tot} is lower than the corresponding Y_{Be}^{tot} in JET-C. However, though no temperature assisted chemical erosion exists with beryllium, chemical assisted physical sputtering (CAPS) of Be via BeD has been identified by optical spectroscopy and contributes additionally to Y_{Be}^{tot} . At an impact energy of e.g. $E_{in} = 75\text{ eV}$ CAPS contributes to about 1/3 of the effective beryllium sputtering yield which needs therefore be written as $Y_{Be}^{tot} = Y_{Be}^{phys} + Y_{Be}^{chem}$ [30]. The appearance of Y_{Be}^{chem} is likely caused by the supersaturation of the beryllium surface by the impinging deuteron flux density, which

induces a transient deuterium surface coverage of more than 50%, leading to both (a) the appearance of CAPS as additional channel with the release of BeD_x with $x = 1 \dots 3$ and (b) at higher concentrations potentially to dilution of beryllium at the surface and reduction of Y_{Be}^{tot} . Indeed Fig. 4b reveals the dependence of Y_{Be}^{tot} on the surface temperature in a series of identical limiter discharges with gradual increase of the tile temperature until equilibrium between heat-up during plasma exposure and cool-down between discharges occurred. The value at highest surface temperatures represents the surface-temperature independent bare Y_{Be}^{phys} without any measured CAPS as well as low deuterium content in the interaction layer due to outgassing. Further details about CAPS in the JET-ILW, MD modelling, and PISCES-B are described in [30,33,34]. However, it needs to be stressed that both, physical and chemical assisted physical sputtering, have an energetic threshold that inhibits erosion at lowest impact energies. This is in contrast to chemical erosion of carbon and carbon layers which can also be eroded by low energetic neutrals at room temperature.

A gross erosion yield of 10% is representative for the campaign-averaged beryllium erosion in limiter configuration in the first JET-ILW campaign. This translates to a gross erosion rate of $4.1 \times 10^{18}\text{ Be/s}$ or an integral of 1.5 g Be sputtered from one centred inner-limiter tile ($A_{tile} = 0.025\text{ m}^2$) in the view of the spectroscopic system ($A_{spot} = 0.011\text{ m}^2$). This can be compared with a net erosion of 0.8 g Be deduced from post-mortem tile profiling for a comparable beryllium tile or a net erosion rate of $2.3 \times 10^{18}\text{ Be/s}$ considering the total exposure time in limiter configuration during the campaign [18]. The comparison of spectroscopy and post-mortem analysis reveals a factor two between gross and net beryllium erosion with JET-ILW. The net carbon erosion rate of a corresponding tile in JET-C is twice as high as the net beryllium erosion rate in JET-ILW, however, taking into consideration the different number of interacting limiters in JET-C (#16) and JET-ILW (#10), the discrepancy of the primary impurity source in limiter configuration reduces to 25%. For the complete beryllium source estimation both, spectroscopy and post-mortem analysis, must extrapolate the local information to the total limiter-interaction area which represents a fraction of the total inner wall protruding limiters ($A_{lim} = 4.5\text{ m}^2$), but have less interaction area due to shadowing effects [35]. The main fraction of beryllium eroded at the limiters stays within the main chamber, deposited in recessed areas like the limiter wings, and only a small fraction of eroded beryllium neutrals escapes geometrically from the main chamber into the divertor. Indeed the initial experiment in diverted configuration identified only moderate tungsten surface

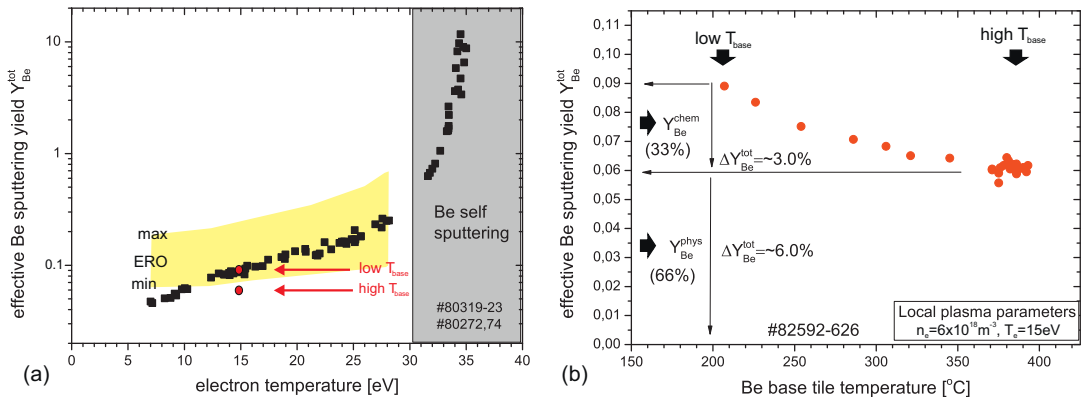


Fig. 4. (a) The effective Be sputtering yield as function of T_e measured in JET-ILW and associated ERO modelling. (b) Composition of the effective Be sputtering yield at $E_{in} = 75\text{ eV}$ as function of the Be tile temperature [30].

coverage by beryllium after about 625 s in limiter configuration with dominant beryllium self-sputtering [36]. However, the amount of beryllium entering the divertor in limiter configuration is insignificant in comparison with the amount in divertor configuration.

3.2. Beryllium erosion and migration in diverted plasmas

The present understanding on material migration is predominantly based on tokamaks with carbon-based PFCs and information obtained from optical spectroscopy during plasmas and post-mortem analysis after PFC extraction. The main chamber is identified as primary erosion source and material is transported via scrape-off layer (SOL) flows in normal magnetic field configuration mainly towards the inner divertor where finite deposition occurs [37]. In a subsequent multi-step process, material transport to remote and inaccessible areas takes place, leading to co-deposition and high fuel retention. The later ultimately led to the abandoning of carbon PFCs in ITER due to safety aspects [4]. Despite being a net source, the outer divertor plays only a minor role in the overall migration.

In the JET-ILW, no main chamber plasma-facing material (beryllium) is installed in the divertor, thus, all Be ions flowing into the tungsten divertor are originated from the main chamber during diverted plasma operation. Homogenous Be and BeD light emission in toroidal and poloidal direction at the inner wall can be measured by spectroscopy in divertor configuration resulting from erosion processes in these recessed areas in the SOL. The origin of these processes is twofold: (i) energetic charge exchange neutrals (CXN) are impinging the recessed inner-wall area ($A_{wall} = 18.5 \text{ m}^2$) equipped primarily with cladding tiles ($A_{clad} = 11.2 \text{ m}^2$) of which 2/3 are made of Be-coated inconel and 1/3 of tungsten tiles located between adjacent poloidal limiters and positioned typically 6–10 cm behind the separatrix. (ii) Residual plasma flux is reaching the recessed wall and limiters. The variation of the distance between separatrix and beryllium surface, is causing changes in the Be and BeD particle flux indicating that the residual deuterium ion flux contributes to the beryllium erosion. Though no Be-cladding exists at the outer wall, CXN and residual plasma flux interact with the outer-poloidal limiters and contribute to the Be main chamber source; the degree depends on plasma conditions and distance of the separatrix to these PFCs.

Beryllium material probes installed between cladding tiles show at different locations measurable erosion after the initial JET-ILW campaign [38] confirming that this area is a zone of net erosion. The beryllium source from the inner wall was quantified ex-situ by RBS to 12.2 g in the integrated divertor time. The corresponding erosion rate during divertor operation amounts to $0.78 \times 10^{18} \text{ Be m}^{-2} \text{ s}^{-1}$. The rate can be compared with the erosion

rate of $3.14 \times 10^{19} \text{ C m}^{-2} \text{ s}^{-1}$ in JET-C (2005–2009) where similar long-term carbon samples were installed and analysed [39]. The erosion rates differ by a factor of 4.0 which reflects essentially the strong reduction of the primary erosion source with the JET-ILW. The global source is even stronger reduced by a factor 5.3 when the different total area of CFC cladding in JET-C to Be cladding in JET-ILW is considered. A difference in the erosion processes is required to explain the discrepancy in the primary source as (a) the CXN flux and the residual plasma flux impinging on the first wall are similar in both wall configurations and (b) the bare physical sputtering of beryllium is larger than carbon (Fig. 3). Indeed this discrepancy can only be explained by chemical erosion of carbon at the lowest, even thermal energies of impinging deuterium ions and atoms solely present in JET-C.

The beryllium migration path in the JET-ILW can be described as follows: (i) neutral Be and BeD from physical sputtering and chemical assisted physical sputtering at the recessed wall enter the plasma, (ii) BeD dissociates and neutral Be is ionised and transported by SOL-flows towards the inner divertor (Fig. 5a) where (iii) significant deposition takes place on top of the inner vertical-target plate (Fig. 5b). Post-mortem analysis confirms almost pure, hydrogen-poor beryllium layers with minor oxygen content at this location as shown in Fig. 5c. The integral beryllium source in the main chamber during divertor operation and the amount of beryllium deposited in the inner divertor is comparable according to initial global balance studies [35]. The comparison with corresponding carbon deposition in the JET-C divertor reveals a factor seven reduction in beryllium divertor deposition with JET-ILW induced by the lower main chamber source.

Within the divertor (Fig. 5b), beryllium performs much less re-erosion/deposition cycles than carbon due to the energetic threshold for physical sputtering of beryllium which inhibits the multi-step transport to the divertor floor, and even further, to the remote areas at the pump-duct entrance. Post-mortem analysis [18] demonstrated that the inner vertical target is only partially covered by beryllium and indeed intact bare tungsten surfaces can be detected. This is confirmed by optical spectroscopy and W emission in the plasma throughout the campaign. The measured effective deposition thickness is in the order of 1/5 of the surface roughness of the W-coatings which makes the analysis challenging. In contrast, the balance between erosion and deposition at the inner-target plate of JET-C was moved strongly towards deposition leading up to thick carbon co-deposits with more than a factor 50 times thicker deposition.

Detailed ERO modelling was applied to compare the transport of beryllium in the JET-ILW once entering the inner divertor leg with the transport of carbon in JET-C [40]. Indeed it is only possible

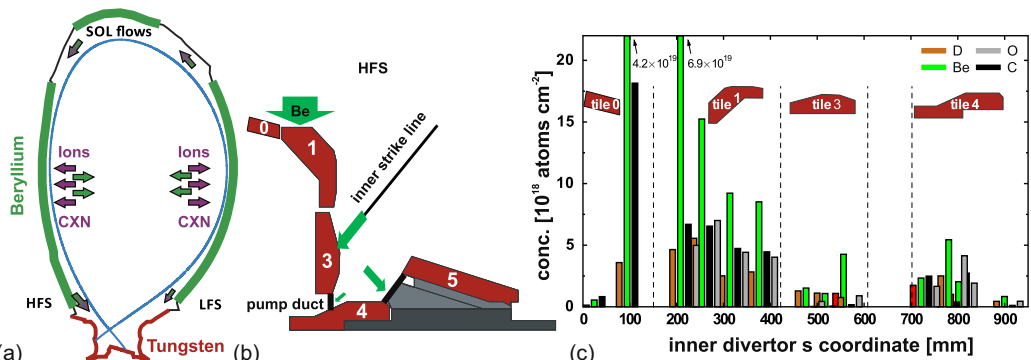


Fig. 5. Global (a) and inner divertor (b) material (beryllium) migration paths with the JET-ILW. (c) Deposition of Be, C, O and D along the inner divertor target plates deduced from post-mortem analysis [42].

to describe the measured beryllium deposition pattern in the inner divertor of the JET-ILW if a factor 5–10 lower initial impurity ion flux (Be^{2+}) in comparison with the carbon flux (C^{4+}) in JET-C is considered which is consistent with spectroscopic observations and the fact that the tungsten divertor plate is not buried by beryllium. This impinging Be ion flux is neutralised at the target, reflected and transported line-of-sight towards the side protection of tile 5. Different deposition monitors [cf. [40] and references within] showed low net deposition with a reduction of about a factor 15 in comparison with JET-C references. The reduction in the material transport towards the inner pump-duct entrance is even more pronounced; a factor 30–50 reduction in deposited material [41] was found. Indeed the thin deposits ($\approx 1 \mu\text{m}$) on the sloping part of the horizontal-target plate (Fig. 5c) are rich with impurities such as oxygen (from air leaks) and carbon (residual content) [43,44] which reduces effectively the net transport of beryllium by another factor two. This leads to the conclusion that beryllium is only performing line-of-sight transport after physical sputtering processes (about 2 steps) whereas the residual carbon still performs the multi-step transport (about 10 steps) caused mainly by chemical erosion leading to enrichment of carbon in the remote and inaccessible divertor areas. It should be stressed that the overall integral deposition in these remote areas is about two orders of magnitude lower with the JET-ILW than with JET-C. The majority of deposited Be in the divertor remains on top of tile 1 and only a minor fraction is participating in further transport within the divertor.

3.3. Tungsten sputtering and transport in diverted configuration

The tungsten sputtering yield was quantified in-situ by optical emission spectroscopy [45] in L-mode discharges with density ramps reaching partially divertor detachment and impact energies of ions and deuterons around the energetic sputter threshold. Optimised diagnostic access for W spectroscopy is only available at the bulk-tungsten target plate which represents an almost pristine tungsten surface as situated in a net-erosion zone throughout the campaign. It should be noted that this also true for the lower vertical-target plates as post-mortem analysis confirmed, but the spectroscopic view is vignettted and observation of neutral tungsten with penetration depths of a few mm is challenging. The physical sputtering of tungsten is in general determined by impurities and their composition, energy, and flux assuming that the energy overcomes the threshold. Deuterons play only a role at impact energies above $\approx 250 \text{ eV}$ due to their low mass (Fig. 3).

In JET, the physical sputtering of tungsten can for a wide range of plasma conditions be described by beryllium ion Be^{2+}

bombardment with a concentration of about 0.5% with respect to the impinging deuteron flux. Though the fraction of beryllium in the impinging ion flux varies with plasma conditions, the concentration of 0.5% is in very good agreement with the described low primary beryllium source and the beryllium transport into the divertor. Fig. 6a shows the effective sputtering yield as function of T_e at the target plate for comparable experiments in JET-ILW, ASDEX Upgrade and TEXTOR; T_e acts here as proxy for $E_{in} = 3 \times k_B Z_x T_e + 2 \times k_B T_i \approx 5 \times k_B T_e$ assuming locally $T_e \approx T_i$. The lines represent TRIM calculations for different impinging species and concentrations as described in Fig. 3. The JET-ILW confirms the expected threshold behaviour for Be^{2+} at low T_e achieved by plasma cooling by deuterium fuelling or impurity seeding. The effective tungsten sputtering yield is above 6×10^{-5} for $T_e > 20 \text{ eV}$, reflecting fully attached divertor conditions, and more than one order of magnitude below yields determined in ASDEX Upgrade [11] and TEXTOR [46]. In ASDEX Upgrade and TEXTOR, the dominant impurity species is C which has a higher mass and higher charge state than Be and is therefore more effective to sputter W. In ASDEX Upgrade the best fit is achieved assuming an effective impinging impurity species C^{4+} of 1% to 2%; C^{4+} includes effectively N, O, and F ions which are present in discharges without boronisation. The lower effective W sputtering yield in JET is a consequence of the low concentration of plasma impurities or, in other words, the high plasma purity owing to the use of Be PFCs as explained in Section 2. The prompt re-deposition of tungsten has been estimated to $\approx 50\%$ at a magnetic field of 2.5 T by comparing WI and WII-lines resulting in the deposition of eroded tungsten within one Larmour radius [45] which is in agreement with ASDEX Upgrade [11] and TEXTOR [46]. The divertor retention of tungsten was determined by the comparison of the W concentration in the plasma core and the W source in the divertor and estimated to be about 100 for the open divertor geometry in JET [47].

The operation with inertially cooled PFCs requires mitigation of steady-state power loads to the divertor-target plates in H-mode plasmas with high auxiliary power and energy content. This can be achieved by impurity seeding (N_2) which induces (semi-) detachment at the target plates and mitigates the W sputtering simultaneously as the impact energy of deuterons and impurity ions fall below the physical sputtering threshold as depicted in Fig. 6b. However, Edge Localised Modes (ELMs), filaments which carry energetic deuterons and impurity ions from the hot pedestal region down to target plate, interrupt regularly the quiet (inter-ELM) phase. These particles with energies above the physical sputtering threshold induce tungsten sputtering and can even represent the sole tungsten source as it is shown in Fig. 6b where tungsten sputtering is

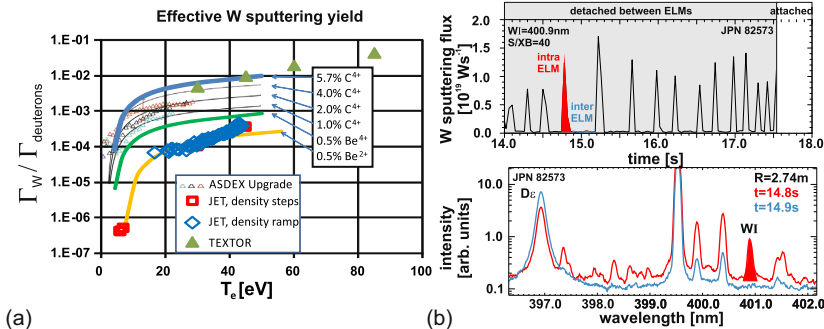


Fig. 6. (a) Physical sputtering yield of W in JET, TEXTOR and ASDEX Upgrade. (b) Top: W sputtering during ELM excursions and detached divertor conditions between ELMs in nitrogen seeded JET-ILW discharges. Bottom: Emission spectrum in the outer divertor covering WI at 400.9 nm recorded in the intra and inter-ELM phase.

fully mitigated in the detached inter-ELM phase. The tungsten source can be distributed in different portions between ELM and inter-ELM phase depending on the electron temperature between ELMs and the ELM frequency. These observations are in agreement with observations made in ASDEX Upgrade [11].

Though ELMs are responsible for at least a fraction of the W production in H-mode plasmas, ELMs are also required to remove W from the confined region by flushing as otherwise W accumulation can occur. A set of W control tools have been developed in JET in order to ensure plasma operation without W accumulation, thus, steadiness over the achievable flat-top phase of more than 10s. From the point of view of the source and transport, it is mandatory to keep the inter-ELM source low which requires a minimum deuterium injection rate or significant impurity seeding (to overcome the seeding impurity-induced W sputtering) and sustain a minimum ELM frequency as described in [47]. This restricts the operational window with W in comparison with C divertor in JET-C where no limitations with respect to plasma fuelling existed [16]. H-mode plasmas with sole deuterium fuelling from first wall outgassing – so-called unfuelled plasmas – are in general not stable with the JET-ILW. However, ITER will require semi-detached plasma operation [1] and ELM pacing which will secure both safe operation with respect to the power loads at the target plates as well as will provide quasi-intrinsic W control.

4. Fuel recycling, retention and removal

Implantation and co-deposition of fuel are the main mechanisms for retention in tokamaks. Implantation saturates in principle with impinging ion flux or fluence and co-deposition can increase linearly with ion flux and operational time [4], thus, the dominant mechanism for long-term retention remains the co-deposition of fuel with the main impurity, i.e. Be in JET-ILW as C in JET-C. The change in the fuel content in co-deposits can be, according to fuel-content scalings in Be and C co-deposits deduced in PISCES [10], responsible for about a factor ten of the reduction at the nominal vessel temperature at JET (473 K) assuming otherwise comparable plasmas, i.e. ion flux and impurity concentration, and surface conditions. Co-deposition with tungsten is negligible in comparison with beryllium.

4.1. Long-term retention and fuel removal

Global gas balances, measured as an integral through multiple discharges [48], have been executed in different plasma conditions and confinement regimes in JET-ILW and compared with JET-C ref-

erence experiments [49,15]. The long-term retention rate of deuterium normalised to the operational time in diverted configuration phase drops substantially by more than one order of magnitude with introduction of the JET-ILW in all performed experiments to values below $1.5 \times 10^{20} \text{ D s}^{-1}$ which represents the absolute upper limit [15]. The drop of a factor 10 to 20, depending in detail on the plasma regime and to a certain extent on the ion flux to the PFCs, is shown in Fig. 7a. The retention rate falls below $1.0 \times 10^{20} \text{ D s}^{-1}$ in H-mode plasmas if the 50% longer outgassing period between discharges in JET-ILW in comparison with JET-C is considered, indicating the prominent role of short-term retention. Though the short-term retention, potentially by transient supersaturation of Be and W surfaces, and post-plasma outgassing is in absolute magnitude comparable between JET-ILW and JET-C [50], the relative importance is increased as the underlying long-term retention is dramatically reduced. The outgassing behaviour with a power law of $t^{-0.7}$ had been already observed in JET with toroidal circumferential beryllium belt limiter [51]. The accessible fuel inventory with the JET-ILW was determined in isotope exchange experiments including gas balances with isotope quantification. The exchange by tokamak discharges revealed an inventory of $3 \times 10^{22} \text{ D s}^{-1}$ which is ten times lower than in JET-C [52], but during the exchange re-capturing of released fuel in co-deposits in the divertor takes place. Fuel exchange by ion-cyclotron wall conditioning plasmas demonstrated a higher recovery of $5 \times 10^{22} \text{ D s}^{-1}$ in absence of co-deposition in the divertor [53] which offers a better perspective as tritium removal techniques in ITER in connection with the accessibility of co-deposits on plasma-facing sides.

The high reproducibility of retention rates deduced in H-mode plasmas in the middle and the end of first year of ILW operation [15] underlines that the dominant mechanism for the residual long-term retention remains unchanged in this period. This points to co-deposition of fuel with Be as dominant process as implantation into the bulk material shall be in principle saturated owing to the large fluence in the main chamber and divertor to the PFCs. But these plasma-specific gas balances can neither provide detailed information on the types of co-deposits nor their exact location. However, supportive spectroscopy suggests that co-deposition by beryllium occurs mainly in the inner divertor and that the contribution of other impurities in these experiments is low which is confirmed by residual-gas analysis and gas chromatography [54]. Post-mortem analysis of PFCs provides complementary information though campaign integrated over all limited and diverted plasmas, resulting in a 15 times lower fuel inventory with JET-ILW in comparison with JET-C [42] and confirming the gas-balance

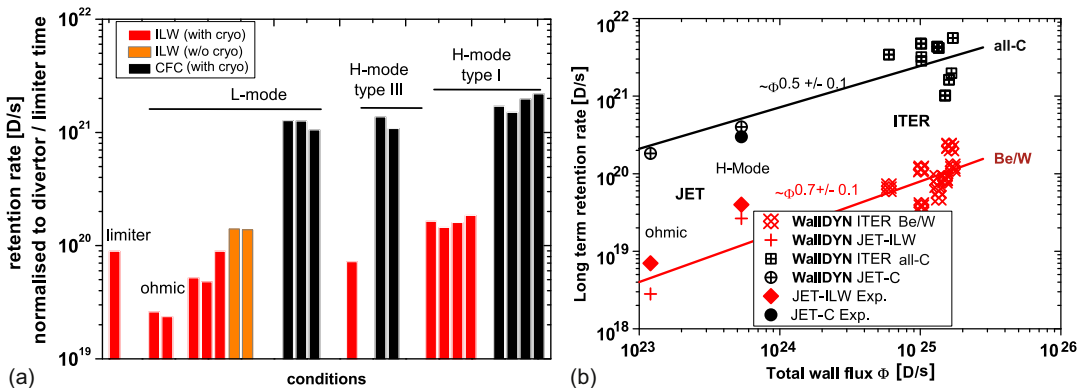


Fig. 7. (a) Long-term fuel retention rates in the JET-ILW measured by global gas balances. (b) Long-term retention rate predictions for ITER made by WallDYN [57] and JET-ILW benchmarks from global gas balances.

measurements. A difference in absolute retention rates exist as the long outgassing phase between the last experiment and the actual tile analysis of about one year impacts strongly on the absolute fuel content in comparison with gas-balance studies and an outgassing period of 1.5 h [30]. The distribution of the fuel can under the assumption of toroidal symmetry be described as follows: one third of the retained fuel is found in the main chamber PFCs (5.7×10^{22} D on the low-field side, 2.8×10^{22} D on the high-field side, 2.1×10^{22} D on the upper wall PFCs) and two third are in the divertor (2.9×10^{23} D in the inner divertor Fig. 5b and 8.6×10^{22} D in the outer divertor) – further details are given in [42]. The retention distribution is largely consistent with the observed migration pattern of beryllium in limiter (Be migration within the main chamber) and divertor operation (Be migration into the divertor) and the corresponding operational time as described before. The observed retention in the limiter phase is consistent with gas-balance measurements (Fig. 7a) in ohmic limiter discharges [15]. The normalisation of the retention to the time in divertor configuration overestimates the retention rate by a about 15% due to the inclusion of the retention which takes place in the limiter start-up phase (3 : 1 ratio between divertor and limiter-configuration duration) [15]. In summary the reduction in the ITER-relevant long-term fuel retention in divertor configuration can be attributed to following processes: (i) The primary impurity source in the main chamber during divertor operation, C in JET-C and Be in JET-ILW, is reduced with JET-ILW leading to less beryllium co-deposition. (ii) Reduced deuterium content in pure beryllium co-deposits in comparison with carbon co-deposits at the JET wall temperatures. The initial prediction was the absolute dominance of the second process, but a fraction of co-deposits are found in divertor areas which have lower surface temperatures than the nominal vessel temperature, and the difference between carbon and beryllium co-deposits shrinks at e.g. 473 K to a factor 5 [55]. Moreover, co-deposition of fuel with beryllium and residual impurities (C,O) occurs in particular on the horizontal-target plates and the fraction of fuel in this mixed layer is higher than in pure beryllium co-deposits [42]. Though the fuel fraction in these layers is high, the overall contribution to the total retention is very low in comparison with the main, pure beryllium deposition area on top of tile 1.

An improved way to predict the tritium retention in ITER is the usage of the WallDYN code [56], verified with JET-ILW gas-balance experiments and applied to predicted ITER plasma backgrounds, instead of simplified experimental scalings of wall fluxes from the same experiments [15]. WallDYN is based on a set of rate equations for a number of pre-defined plasma-surface interaction processes and calculates the global erosion and deposition pattern with the help of a set of discrete interaction points in the poloidal circumference and a redistribution matrix for a given static plasma background. The code provides therefore not only the integral fuel retention, but also the primary impurity sources, the migration path and the final co-deposition areas where the scaling laws for the fuel content are applied [10]. WallDYN has been benchmarked against a set of JET-ILW and JET-C gas balance experiments in ohmic and H-mode conditions [57,15] but adapted to the total outgassing from PFCs according to [50] in order to predict the long-term retention comparable to post-mortem analysis data. WallDYN can reproduce for limiter and divertor plasma conditions qualitatively the observed beryllium migration pattern including the primary erosion sources at the first wall and the deposition of beryllium on top of the upper vertical target in the JET-ILW. In contrast, the co-deposition in the whole carbon divertor, as observed in the JET-C experiments, can be reproduced which essentially confirms the previously described multi-step transport of carbon caused by chemical erosion. This the key difference between JET-C and JET-ILW in modelling and experiment. Fig. 7b shows the

good agreement of the deuterium retention rate in the divertor phase as function of the total ion flux to the wall in the experiment and modelling. Extrapolation of the verified code to different ITER background plasmas provides the wide range of long-term fuel-retention rates in ITER which finally results in 3000 to 20,000 full power DT discharges with 400 s duration before the tritium inventory limit is reached [57]. Therefore, the JET-ILW experiment and the WallDYN code confirm the low long-term fuel retention in the Be/W material mix and justified the selection of the ITER-material mix with respect to this safety issue.

4.2. Fuel recycling

The outgassing properties of both beryllium and tungsten PFCs are impacting on the recycling behaviour at the main PFCs. Fig. 8 shows the fuel retention in the limiter phase, plasma contact to the beryllium limiters, and in the divertor phase, plasma contact to the tungsten target plates, for a series of identical discharges in L-mode (JPN#81937 – 81973, $I_p = 2.5$ MA, $B_t = 2.4$ T, $P_{aux} = 0.5$ MW) with low fuelling and solely turbo-molecular pumping [15]. Each of the 35 discharges (averaged repetition rate 20 min) remains for about 20 s in the divertor configuration with a typical ion flux to the target plates of 3×10^{22} D s⁻¹. The integral retention drops in the first ten discharges until an equilibrium between short-term retention in the discharges and outgassing during and after the discharge occurs. The inertially cooled tungsten target plates are heated-up by the impinging power load in the first ten discharges until a thermal equilibrium between plasma impact and cool-down phase is reached. Longer breaks between discharges, as indicated in Fig. 8, are causing more outgassing and more retention in the subsequent discharge. As the ion flux to the target plates remains the same in these discharge series, the difference in retention can only be explained by a change of the local recycling connected to the surface temperature increase. The tungsten divertor shows a dynamic behaviour of the deuterium recycling with a recycling coefficient $R < 1$ in these first low fuelled L-mode discharges. Note, that the outer-strike line is located on the pristine bulk-tungsten surface and the inner-strike line on the vertical target which is only partially covered by a thin layer and has intact tungsten areas as discussed in Section 3.

The deuterium recycling is even more dynamic in H-mode plasmas when ELMs are present. An ELM is induced by the crash of the H-mode pedestal and releases hot plasma to the SOL and to the tungsten-target plate. ELMs are conducting on a timescale of 1 ms [58] additional power to the target plate and heat it up in addition to the surface temperature induced by the steady-state heat load reaching 1570 K in regular operation on the bulk-W target plate. Each ELM desorbs deuterium from the tungsten PFCs depending on the actual temperature increase per ELM and its duration. The desorption peaks in the W-coated PFCs are already

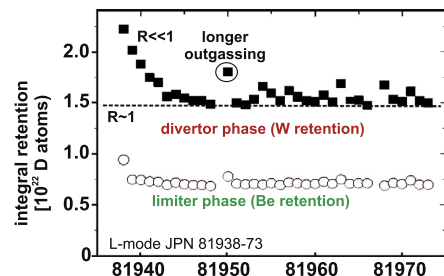


Fig. 8. Active pumping of deuterium by the tungsten divertor in a series of identical JET-ILW L-mode plasmas.

reached at 570 K and 690 K [42] which are exceeded routinely in H-mode due to the inertial cooling. Thus, the accessible deuterium reservoir is partially emptied considering the actual temperature footprint of the ELM on the tungsten target plate. The desorbed deuterium needs to be refilled to reach equilibrium, therefore, the recycling coefficient changes for a short time from $R \approx 1$ to $R < 1$ after the ELM crash. The deuteron flux to the target plate is used to refill the partially emptied reservoir as externally injected deuterium or deuterium reabsorption cannot provide the required amount in the order of 10^{20} D within a few ms which a typical ion flux of $\sim 10^{23}$ D s $^{-1}$ m $^{-2}$ to the target can do. The tungsten target plate effectively represents an additional particle sink for a few ms which can be defined as required *refill-time*. According to EDGE2D-EIRENE studies of the ELM-cycle [59] of a moderate additional heated H-mode plasma in the JET-ILW (#83621-83791, $B_t = 2.0$ T, $I_p = 2.0$ MA, $P_{aux} = 12$ MW, $\Delta W_{ELM} = 160$ kJ, $\Delta T_{ELM} = 150$ K and further details in [15]), a transient particle sink after an ELM-crash can be the cause for a delayed recovery of the pedestal density and a longer lasting ELM of up to 8 ms though the time scale of the MHD ELM-crash remains almost identical between JET-C and JET-ILW as described in [58]. However, it should be noted that the physical particle reservoir to be desorbed is limited whereas the ion flux to the target can increase e.g. with the plasma current and auxiliary power in H-mode discharges. Therefore, the transient phase with $R < 1$ at the target plate, effectively the refill-time, gets shorter with larger impinging ion flux and plasma current. Indeed such a behaviour has been seen in H-mode plasmas with plasma current increase [58]. Such an effect has not been observed for comparable moderate heated deuterium plasmas in JET-C which is likely caused by the large reservoir of fuel in co-deposits compensating quasi instantaneously the out-gassing. Contrary, it can explain the different ELM-behaviour in helium in JET-C where no fuel reservoir exists in carbon PFCs.

5. Impurity content, radiation pattern and seeding

5.1. Impact of the impurity content on the plasma-edge behaviour

The exchange of carbon ($Z = 6$) by beryllium ($Z = 4$) and the reduction of the primary impurity source is reflected in the impurity concentration and the effective charge of the plasma (Z_{eff}). In JET-C, the line-averaged Z_{eff} deduced from Bremsstrahlung amounts 2.0 in the divertor phase with an averaged carbon concentration of about 3.0% in the plasma; variations depend on the plasma conditions [60]. With JET-ILW Z_{eff} shows typical values of 1.2 in deuterium fuelled H-mode plasmas and the averaged impurity composition can be described by a beryllium concentration of about $c_{Be} \approx 1.1\%$ and a residual carbon contribution of about $c_C \approx 0.1\%$ taken from spectroscopy. Fig. 9a shows typical Z_{eff} -profiles from charge-exchange recombination spectroscopy (CXRS) for a set of high triangularity plasmas in H-mode [21] at same

current and magnetic field: Z_{eff} is for the pure deuterium JET-ILW plasma about $Z_{eff} = 1.1$ and the profile is absolute flat. This is in contrast to the carbon-dominated Z_{eff} -profile in JET-C which is about an order of magnitude higher and slightly hollow. Moderate nitrogen seeding recovers the Z_{eff} -profile shape and magnitude which is likely related to the comparable radiation capabilities of nitrogen and carbon. In ASDEX Upgrade Z_{eff} , amounts typically to 1.4 in discharges shortly after a boronisation and 1.7 in discharges long after a boronisation [61], thus, Z_{eff} is even without impurity seeding close to values obtained in JET-ILW with nitrogen seeding. Responsible are residual levels of low-Z impurities (C, O and F) in the ASDEX Upgrade plasma. The impact of boron on the plasma purity in ASDEX Upgrade can be compared to beryllium in JET-ILW with the difference that beryllium is acting permanently and boron only for a short period after a boronisation.

However, not only the Z_{eff} -profile recovers with seeding of nitrogen, also a number of plasma edge, respectively, pedestal properties are restored in comparison with changes observed in bare JET-ILW and JET-C discharges: (a) In unseeded plasmas, a reduction of the threshold power for the L-H transition in the low density branch was observed with the JET-ILW [62]. Nitrogen seeding inducing $Z_{eff} \approx 2.0$ increases the L-H power threshold and restores almost the behaviour observed in JET-C [63]. (b) The loss of confinement in high triangularity discharges with deuterium fuelling of about 30% of the H-factor in the JET-ILW in comparison with JET-C reference discharges was reported before [20]. This loss in confinement has primarily been correlated to a reduction of the pedestal temperature (Fig. 9b) and partial recovery was observed with nitrogen seeding [64] and with increase of normalised plasma pressure β_N [20]. Indeed in the set of available discharges a correlation between the averaged Z_{eff} and the pedestal temperature was observed (Fig. 9b). Though in both cases a correlation with Z_{eff} is observed, the physics mechanisms and to which degree the impurity content and/or the impurity profile is responsible for the recovery is not known and subject of current intensive studies. However, similar correlations have been observed in ASDEX Upgrade with the installation of the all-W first wall and the usage of nitrogen seeding [7].

5.2. Divertor characterisation and density limit

A direct consequence of the practical absence of carbon is the loss of significant impurity-induced radiation cooling in the divertor plasma, which leads to an increase of the local T_e as well as impact energies of ions impinging on the target plate. This is caused by (a) the much lower cooling potential of beryllium in contrast to carbon under typical divertor temperatures of $T_e \approx 30$ eV [65], and (b) the fact that also less beryllium (JET-ILW) as carbon (JET-C) is present in the divertor due to the lower primary source and the change of the migration pattern discussed before. Moreover, carbon in the carbon divertor of JET-C performed multiple

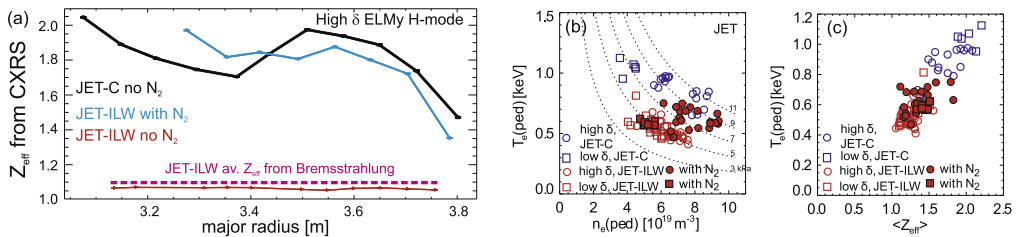


Fig. 9. (a) Radial profiles of Z_{eff} calculated from charge-exchange recombination spectroscopy for three conditions: deuterium fuelled JET-C, JET-ILW and N-seeded JET-ILW discharge. (b) Variation of the T_e^{ped} as function of n_e^{ped} and Z_{eff} for the three conditions and two plasma triangularities (high $\delta = 0.4$ and low $\delta = 0.2$) [20].

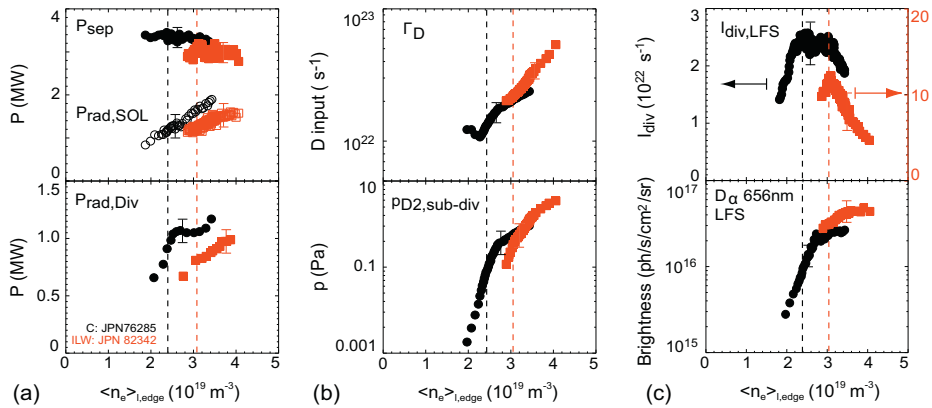


Fig. 10. Pair of comparable JET-ILW and JET-C L-mode density-ramp discharges: (a) radiated power, (b) deuterium throughput and divertor pressure, and (c) ion flux to and recycling flux at the outer-target plate. Complete ion-flux roll over and increase of the density limit with the JET-ILW.

erosion/deposition steps (≈ 10) before reaching the inaccessible pump-duct area [3] which enhances effectively the radiation capability of a single carbon by the same factor. In contrast, the incoming beryllium from the main chamber performs in the tungsten divertor only about two steps, caused by re-erosion owing to physical sputtering or reflection, before it sticks to the target material. The migration pattern and the chemical sputtering of carbon in the case of JET-C had vital impact on the divertor and SOL conditions whereas the (unseeded) JET-ILW case reveals almost the bare deuterium plasma. A series of experiments with density ramp-up discharges in different magnetic configurations have been applied to verify the T_e increase, the loss of divertor radiation, and to characterise the divertor plasma in the JET-ILW [66]. These purely deuterium fuelled experiments confirmed indeed a moderate increase of T_e in the W divertor in comparison with JET-C reference cases. The increase was moderate due to the fact that in the JET-C reference case in L-mode, impurity radiation contributed only about 20–30% of the total radiation (Fig. 10a); the vast amount was determined by deuterium radiation (Fig. 10b). However, the difference in residual impurity radiation has vital impact on the accessibility of the completely detached and recombining divertor regime as well as on the density limit (Fig. 10c).

Complete divertor detachment has been achieved in both legs providing even a window for stable MARFE operation with full recombining divertor, thus, full detachment and radiation at the x -point region [67]. Moreover, the density limit is increased by 20–30% revealing that in JET-C the limit was determined in-fact by a radiation limit caused by carbon before the empirical Greenwald density limit n_{CW} was achieved. The density limit in JET-C and JET-ILW takes still place at the same total radiation, but as beryllium is not significantly contributing to the divertor radiation, more deuterium is required to compensate and radiates in the divertor. As the deuterium gas throughput is further increased, the maximum achievable density overcomes finally the empirical Greenwald limit with $n_{ILW}/n_{CW} = 1.05$ before a disruption occurs. Minor variations in the absolute numbers depend on the actual magnetic configuration. The available data set of well diagnosed discharges in different magnetic configurations is applied to benchmark the plasma boundary code SOLPS [68], also used for ITER predictions [69], and EDGED2D-EIRENE [70] reproducing the general behaviour [71], but still cannot match the exact in-out asymmetry of the radiation pattern in the divertor. Nevertheless, the JET-ILW experiments widen the operational window with

semi- or even completely-detached divertor operation with respect to earlier studies in JET-C.

6. Summary and conclusion

The JET ITER-Like Wall experiment provides for the first time an insight in the coupling between tokamak-plasma operation and plasma-surface interaction in the Be/W material environment and acts as test-bed to verify physics models and modelling tools for ITER. The cross-correlation of the main plasma-surface interaction processes employing a beryllium wall and a tungsten divertor: (a) material erosion and migration, (b) fuel recycling and retention, (c) impurity concentration and radiation, were established and the newly gained physics understanding compared with earlier observations and physics interpretation in JET with all-carbon first wall as well as in other metallic tokamaks. The inter-connection of plasma-surface interaction with plasma-edge physics such as pedestal or divertor properties revealed that both interpretation of previously obtained JET-C results and predictions to ITER need to be revisited. The impact of the first wall material on the plasma performance as well as the prominent role of chemical erosion of carbon were underestimated: carbon in the plasma, eroded from the plasma-facing components, masked partially the plasma behaviour and properties which were attributed solely to the deuterium plasma.

(a) The change in the material migration with the JET-ILW in divertor configuration is one key result as it impacts directly or indirectly on the majority of PSI processes mentioned above and corrects partially the migration pattern predictions made in [4] for Be/W PFCs: the primary beryllium source in JET-ILW is lower than the carbon source in JET-C. As consequence of the lower initial source is the inner divertor not covered by beryllium, but intact tungsten surfaces exist, and the absence of beryllium sputtering at low impact energies inhibits the cycle of multiple erosion/deposition within the divertor. Instead beryllium remains deposited at the positions where it lands or performs one more step by reflection/physical sputtering above the energetic threshold. However, it should be noted that the JET-ILW migration pattern might not yet be in full equilibrium due to limited operational time and could therefore represent an intermediate state with respect to long-pulse operation.

(b) The second key result is the reduction in long-term fuel retention with the JET-ILW confirmed by gas balances, post-mor-

tem analysis and WallDYN modelling. The remaining long-term retention is caused by implantation and co-deposition with beryllium and residual impurities. Short-term retention gained relative importance with respect to the low level of long-term retention and impacts on the recycling properties of both beryllium and tungsten and local plasma conditions. Predictions to ITER with WallDYN indicate more than 3000 DT-discharges before the fuel-inventory limit is reached, thus, the need to apply very often fuel removal techniques is no longer given.

(c) The low effective charge of the plasma ($Z_{\text{eff}} = 1.2$) and the low radiation capability of beryllium reveals the bare deuterium plasma physics in the tokamak. Moderate impurity seeding with nitrogen, reaching $Z_{\text{eff}} = 1.6$ close to the ITER-reference value, restores in particular the confinement and the L-H threshold behaviour. ITER-compatible divertor conditions with stable semi-detachment have been achieved widening the operational window before density limit disruptions occur. The reduction of the impurity concentration in the plasma edge and the primary erosion source is similar to the situation observed in helium plasmas in JET-C. In both cases, the JET-ILW case with deuterium and the JET-C case with helium plasma, the fundamental process of chemical erosion at low impact energies is absent and can explain the drop in the impurity content which is then reflected in the corresponding values of Z_{eff} in the plasma core: $Z_{\text{eff}} = 1.2$ in JET-ILW deuterium plasmas, $Z_{\text{eff}} = 2.5$ in JET-C helium plasmas, and $Z_{\text{eff}} = 2.0$ in JET-C deuterium plasmas.

Overall JET demonstrated successful plasma operation in the Be/W material combination and confirms its advantageous behaviour with respect to material migration and fuel retention and gives strong support to the ITER material selection. Moreover, the recovery of the pedestal with changes in the recycling behaviour and the effective plasma charge with nitrogen indicates that plasma properties obtained in JET-C can be partially recovered at ITER-relevant effective plasma charge, but still using the benefit of the metallic wall with respect to the majority of plasma-interaction processes.

References

- [1] A. Loarte et al., Nucl. Fus. 47 (2007) S203.
- [2] G. Saibene et al., Plasma Phys. Contr. Fus. 44 (2002) 1769.
- [3] G.F. Matthews et al., J. Nucl. Mater. 337–339 (2005) 1.
- [4] J. Roth et al., J. Nucl. Mater. 390–391 (2009) 1.
- [5] V. Arunasalam et al., Recent Results from the PLT tokamak, in: Proc. 8th Conf. EPS, Prague, vol. 2, 1977, pp. 17–28.
- [6] B. Lipschultz et al., J. Nucl. Mater. 363 (2007) 1110.
- [7] R. Neu et al., J. Nucl. Mater. 438 (2013) S34.
- [8] A. Pospieszyczyk et al., J. Nucl. Mater. 290–293 (2001) 947.
- [9] R.A. Pitts et al., 55th APS Meeting (2014), Denver, CO, USA, paper WE1.00001.
- [10] G. de Temmerman et al., Nucl. Fus. 48 (2008) 075008.
- [11] R. Dux et al., J. Nucl. Mater. 390–391 (2009) 858.
- [12] V. Philipps et al., Fus. Eng. Des. 85 (2010) 1581–1586.
- [13] G.F. Matthews et al., J. Nucl. Mater. 438 (2013) S2.
- [14] S. Brezinsek et al., J. Nucl. Mater. 415 (2011) S936.
- [15] S. Brezinsek et al., Nucl. Fus. 53 (2013) 083023.
- [16] E. Joffrin et al., Nucl. Fus. 54 (2014) 013011.
- [17] S. Brezinsek et al., J. Nucl. Mater. 438 (2013) S303.
- [18] A. Widdowson et al., Phys. Scr. T159 (2014) 014010.
- [19] J.W. Coenen et al., J. Nucl. Mater. 463 (2015) 78–84.
- [20] M.N.A. Beurskens et al., Plasma Phys. Control. Fus. 55 (2013) 124043.
- [21] C. Giroud et al., Plasma Phys. Control. Fus. 57 (2015) 14039.
- [22] G.F. Matthews et al., Phys. Scr. T145 (2011) 014001.
- [23] I. Nunes et al., Fus. Eng. Des. 82 (2007) 1846.
- [24] V. Riccardo et al., Phys. Scr. T38 (2009) 014033.
- [25] G. Arnoux et al., Phys. Scr. T159 (2014) 014009.
- [26] J. Horacek et al., J. Nucl. Mater. 463 (2015) 385–388.
- [27] D. Douai et al., J. Nucl. Mater. 438 (2013) S1172.
- [28] P. de Vries et al., Nucl. Fus. 53 (2013) 053003.
- [29] W. Eckstein et al., Report IPP 9/132, 2002.
- [30] S. Brezinsek et al., Nucl. Fusion 54 (2014) 103001.
- [31] D. Borodin et al., J. Nucl. Mater. 438 (2013) S267.
- [32] D. Borodin et al., Phys. Scr. T145 (2011) 014008.
- [33] C. Björkas et al., New J. Phys. 11 (2009) 123017.
- [34] R.P. Doerner et al., J. Nucl. Mater. 438 (2013) S272.
- [35] A. Baron-Wiechec et al., this conference.
- [36] K. Krieger et al., J. Nucl. Mater. 438 (2013) S262.
- [37] R.A. Pitts et al., Plasma Phys. Control. Fus. 47 (2005) B303.
- [38] S. Krat et al., J. Nucl. Mater. 456 (2015) 106.
- [39] M. Mayer et al., J. Nucl. Mater. 438 (2013) S780.
- [40] A. Kirschner et al., J. Nucl. Mater. 463 (2015) 116–122.
- [41] H.G. Esser et al., this conference.
- [42] K. Heinola et al., this conference.
- [43] P. Petersson et al., J. Nucl. Mater. 463 (2015) 814–817.
- [44] D. Ivanova et al., Phys. Scr. T159 (2014) 014011.
- [45] G. van Rooij et al., J. Nucl. Mater. 438 (2013) S42.
- [46] S. Brezinsek et al., Phys. Scr. T145 (2011) 014016.
- [47] T. Pütterich et al., Plasma Phys. Control. Fus. 55 (2013) 124036.
- [48] T. Loarer et al., J. Nucl. Mater. 390–391 (2009) 20.
- [49] T. Loarer et al., J. Nucl. Mater. 438 (2013) S108.
- [50] V. Philipps et al., J. Nucl. Mater. 438 (2013) S1067.
- [51] V. Philipps et al., J. Vac. Sci. Technol. 11 (1993) 437.
- [52] T. Loarer et al., J. Nucl. Mater. 463 (2015) 1117–1121.
- [53] T. Wauters et al., J. Nucl. Mater. 463 (2015) 1104–1108.
- [54] S. Romanelli-Grünhagen et al., Phys. Scr. T159 (2014) 014068.
- [55] R.P. Doerner et al., Nucl. Fus. 49 (2009) 035002.
- [56] K. Schmid et al., J. Nucl. Mater. 415 (2011) S284.
- [57] K. Schmid et al., J. Nucl. Mater. 463 (2015) 66–72.
- [58] B. Sieglin et al., Plasma Phys. Control. Fus. 55 (2013) 124039.
- [59] D. Harting et al., J. Nucl. Mater. 463 (2015) 493–497.
- [60] J.W. Coenen et al., Nucl. Fus. 53 (2013) 073043.
- [61] A. Kallenbach et al., Nucl. Fus. 49 (2009) 045007.
- [62] C.F. Maggi et al., Nucl. Fus. 54 (2014) 023007.
- [63] C.F. Maggi et al., presented at the EPS 2014.
- [64] C. Giroud et al., Nucl. Fus. 53 (2013) 113025.
- [65] A. Kallenbach et al., J. Nucl. Mater. 415 (2011) S19.
- [66] M. Groth et al., Nucl. Fus. 53 (2013) 083032.
- [67] A. Huber et al., J. Nucl. Mater. 438 (2013) S139.
- [68] L. Aho-Mantila et al., J. Nucl. Mater. 463 (2015) 546–550.
- [69] A. Kukushkin et al., Fus. Eng. Des. 86 (2011) 2865.
- [70] S. Wiesen et al., EDGE2D-EIRENE coupling, JET-ITC project report, 2006, <<http://www.eirene.de>>.
- [71] C. Guillemaut et al., Nucl. Fusion 54 (2014) 093012.

STRUCTURE MATERIALS IN FUSION REACTORS: ISSUES RELATED TO TRITIUM, RADIOACTIVITY AND RADIATION-INDUCED EFFECTS

M. Rubel

Royal Institute of Technology (KTH), Dept. of Fusion Plasma Physics, Teknikringen 31, 100 44 Stockholm, Sweden

ABSTRACT

A concise overview is given on materials applied in fusion technology. The influence of plasma operation on the behaviour of reactor components and diagnostic systems is discussed with emphasis on effects caused by fast particles reaching the reactor wall. Issues related to primary and induced radioactivity are reviewed: tritium inventory and transmutation. Tritium breeding in the reactor blanket, separation of hydrogen isotopes and safety aspects in handling radioactively contaminated components are also included.

I. INTRODUCTION

The ultimate goal of fusion research is to construct and operate an energy generating system. In a controlled fusion reactor the temperature gradients between the plasma and the surrounding wall will probably be the greatest in the Universe and the operation will be associated with intense nuclear radiation. Therefore, the technology for next-step devices presents challenges not encountered in present-day machines. This includes development and construction of components capable of reliable performance in highly radioactive environment.

The assessment of radioactivity level and lifetime of materials and components (multi-material structures) are the driving forces in studies of plasma-material interactions in controlled fusion devices [1,2]. They are essential for economy and safety of a reactor-class machine operated with a 50:50 mixture of deuterium and tritium. Secondly, radioactivity-related effects and power handling by plasma-facing components (PFC) are universal for all confinement schemes, either magnetic or inertial, realised for energy generating systems. A broad overview of power handling by the reactor first wall has been presented by Loarte [3] and Linke [4]. This paper deals with radioactivity aspects of the fusion process and its influence on reactor structure and plasma-facing materials and components. The paper is organised in such a way, that first basic requirements for plasma facing and reactor materials are presented. This is followed by a description of radioactivity sources in a fusion reactor. Afterwards tritium inventory, tritium breeding and radiation effects are discussed. The work is concluded with remarks on safety issues associated with handling components in radioactive environment. Finally, crucial topics to be tackled in future research of fusion reactor materials (FRM) are addressed.

II. REACTOR STRUCTURE AND MATERIALS

The next-step fusion machine is the International Thermonuclear Experimental Reactor (ITER) being under construction in Cadarache, France. The objectives of ITER science and technology programme include: (a) extended burn time; (b) achievement of a self-sustained thermonuclear burn; (c) safe operation of a reactor-like device; (d) testing of components under reactor-like conditions and (e) testing of tritium breeding blanket modules [5,6]. These are essential steps towards construction of power-generating systems in the future. In brief, a reactor will be composed of a support structure, a cryostat with super-conducting magnets, a vacuum vessel and the first wall being an integrated blanket. The blanket includes structural materials, a neutron absorber and high-heat flux components, i.e. plasma-facing armour and heat sink.

Energy leaves plasma in the form of electromagnetic radiation and kinetic energy of particles. Plasma-surrounding wall is irradiated by ions, charge-exchange neutrals, electrons, neutrons and photons originating from nuclear (γ) and electronic processes (X, UV). All of them modify material properties, from the very surface to the bulk. Therefore, blanket materials must be compatible with ultra-high vacuum, cryogenics (cryopumps), magneto-hydro dynamics, neutron irradiation and handling of high heat loads. As a consequence, there are stringent requirements regarding properties of plasma-facing materials (PFM): high thermal conductivity, good thermo-mechanical properties and resilience to thermal shocks, low activation by neutrons and resistance to radiation damage, low accumulation of hydrogen isotopes accompanied by low chemical affinity to hydrogen in order to avoid chemical erosion leading to the formation of volatile compounds. High affinity to oxygen towards formation of stable and non-volatile oxides is also important for gettering oxygen impurity species in a reactor. Properties of no single element, compound or alloy can satisfy all points from that list. Only a few candidate materials for the plasma-facing components are seriously considered: carbon fibre composites (CFC), beryllium and tungsten. Behaviour of these elements under plasma conditions, i.e. particle bombardment and high heat flux deposition, is very different [1-4]. Therefore, their planned distribution on the ITER wall is not accidental: beryllium on the main chamber wall; tungsten on the divertor dome and upper vertical target and CFC on the lower vertical target where the greatest power is deposited. A detailed distribution of W and

CFC in the divertor has been discussed by Samm [7]. An option of a full tungsten divertor (without CFC) is currently considered [8]. The operation with such set of wall materials (Be, W and CFC or Be and W) requires a large-scale test. In year 2004 it was decided to restructure wall components in the JET tokamak in order to operate the machine with a metal wall: ITER-Like Wall (ILW) Project with components of the main chamber wall made of beryllium and plasma-facing material in the divertor made of tungsten: bulk metal and W-coated CFC. The operation of JET with the carbon wall was finished in October 2009. The installation of the metal wall was completed in May 2011. Soon later plasma operation was successfully started. Photographs in Fig. 1 show in-vessel components and distribution of wall materials (a) and a section of the bulk tungsten divertor (b). Scientific objectives of the ILW project and challenges in the design and construction of components have been presented by Matthews [9,10] and Mertens [11], while plasma-wall interactions in a full metal machine have been reviewed by Matthews in [12].

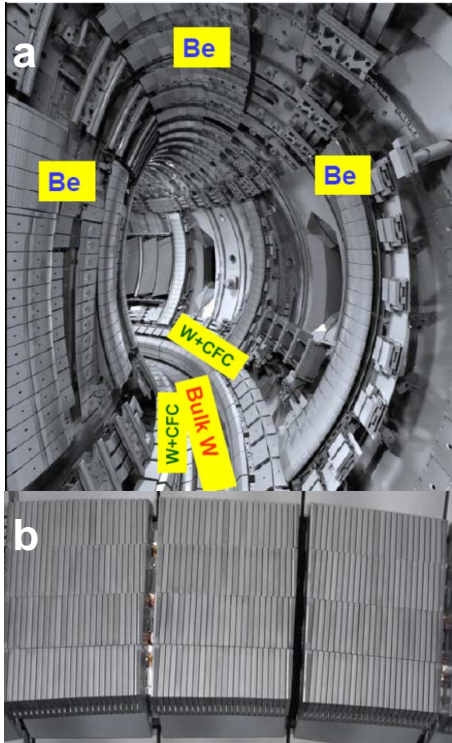


Figure 1: Toroidal view inside the JET vessel with the ITER-Like Wall (a) and a toroidal section of the tungsten load bearing plate in the divertor.

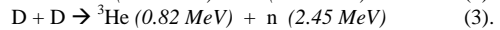
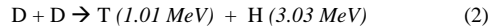
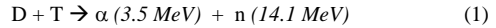
The list of candidate structural materials for the blanket comprises mainly steel (e.g. 316L), Eurofer alloy, vanadium-titanium alloys (V-Ti, V-Ti-Si, V-Ti-Cr) and silicon carbide composites [13]. Major

requirements emphasise mechanical strength and low activation by neutrons. Low activation and increased resistance to radiation damage are also crucial for ceramic insulators and components of in-vessel diagnostic such as optical fibres, cables, mirrors and windows [14,15].

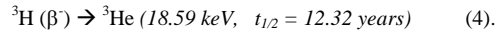
The intention of this paper is to highlight the field of FRM and physics underlying their behaviour in radioactive environment, but not to give an extensive account on all ever-considered candidate materials and all kinds of radiation-induced effects. Only the most important processes affecting material properties will be discussed in more detail in Chapter V.

III. SOURCES OF RADIOACTIVITY

All primary and induced radioactivity in controlled fusion devices is associated with the substrates and products of the fusion process: tritium in the D – T fuel and a consequent production of high energy neutrons:



The branching ratio of reactions (2) and (3) is around one. Tritium (symbol: T or ${}^3\text{H}$) is a low-energy β^- emitter:



Resulting radioactivity of 1 g of tritium equals to 9652 Ci (3.571×10^{14} Bq). Safety requirements limit the in-vessel inventory to the total of 700 g T. If this level would be overcome, a clean-up of the vessel would become necessary in order to reduce the radioactivity. Processes leading to the accumulation of tritium and methods of tritium removal will be discussed in the next chapter. *In-situ* induced radioactivity attributed to nuclear transmutation by fast neutrons passing the plasma-facing and structural materials of the blanket will be presented in Chapter V.

IV. IMPACT OF EROSION & RE-DEPOSITION ON FUEL INVENTORY AND DUST GENERATION

The term “fuel inventory” denotes accumulation and long-term retention of fuel in all in-vessel components, either those facing the plasma directly or located in remote (shadowed) areas such as water cooled louvers in the divertor structure [1,16,17] or other parts of pumping ducts. This applies to all hydrogen isotopes and has several detrimental effects on the reactor operation. There are several pathways leading to the accumulation of fuel in reactor components:

- i. direct implantation in the PFC surface region,
- ii. T production by neutron-induced transmutation,
- iii. diffusion and migration into the bulk,
- iv. co-deposition process.

Neutron-assisted production of T will be treated in the next chapter. The process of in-depth fuel migration into CFC materials is still under investigation in order to assess its impact on the overall inventory [18-20]. At present, there is a consensus that the process of co-deposition is decisive for the in-vessel fuel accumulation.

Co-deposition is defined as re-deposition of eroded and then transported material (i.e. plasma impurities) together with fuel species. Material eroded from one place of the reactor wall is re-deposited in another location, unless it is pumped-out [8,21]. The most serious consequence of co-deposition is the formation of mixed-material layers which may contain vast amounts of fuel. The process that has been studied most extensively in devices with carbon walls is directly related to the pronounced erosion (physical and chemical) of carbon by hydrogen plasma and the resultant formation of various hydrocarbon species. They are characterised by different sticking coefficients to solid surfaces [22]. Those of a high sticking co-efficient are easily deposited and form amorphous carbonaceous (a:C-H) films retaining from a few to about 50 % atomic percent of hydrogen isotopes [16,23]. As measured in various tokamaks, the growth rate of such films is usually between 1.5 and 12 nm/s. When this number is scaled-up to a full year of plasma operation co-deposited layer of a thickness from 4.7 cm to 38 cm would be formed, respectively. This indicates the scale of the problem arising from the carbon erosion, its re-deposition and fuel inventory. The retention of radioactive tritium causes the most severe problems because methods must still be developed to accomplish the efficient release of fuel and/or decomposition and removal of co-deposits in order to ensure safe and economical reactor operation. A range of concepts has been proposed and tested in laboratories [24-27] and also inside tokamaks [28-30].

Fig. 2 shows a limiter tile exposed to the tokamak plasma for a few operation hours. One can distinguish two regions: a shiny and smoothly looking erosion zone and a deposition zone covered with a peeling-off (flaking) deposit. Images in Fig. 3 and 4 show two basic micro-structures of co-deposited films: granular and stratified (laminar), respectively [31,32]. The layers shown here are 30-50 micrometers thick, but the formation of much thicker deposits (1 mm) has been also observed on the neutraliser plates of the belt pump limiter at TEXTOR [31]. Thick deposits are very brittle, easily disintegrate and thus fuel-rich dust is produced. The amount of dust in the reactor must be strictly controlled as it poses danger of ignition and steam reaction in case of accidental massive air or cooling water leak into the vacuum vessel. Dust generation mechanism, motion in plasma and morphology of particulates has been intensively studied [32-35]. In JET with full metal fuel accumulation has been reduced by a factor of 10 in comparison to that measured with carbon walls [12].

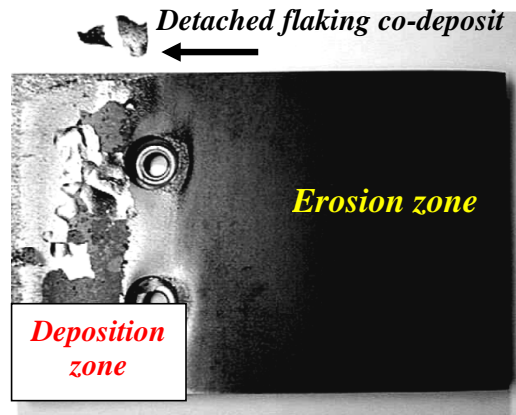


Figure 2: Limiter tile exposed for several hours to the plasma operation at the TEXTOR tokamak.

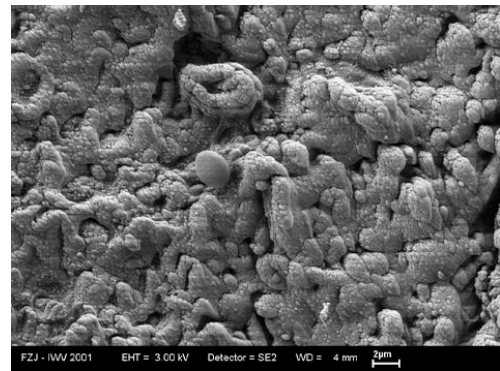


Figure 3: Granular structure of a co-deposit on the scoop of the toroidal belt pump limiter at TEXTOR.

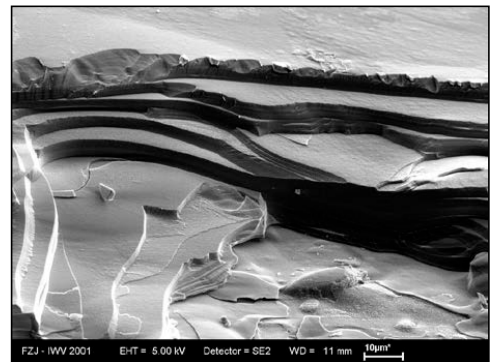


Figure 4: Stratified co-deposit on the limiter tile from TEXTOR. The tile is shown in Figure 2.

The estimated fuelling rate of the ITER plasma is around 54 g of T per 400 s pulse. From this amount approximately only 1 g will be burnt in the D-T fusion, whereas the remaining majority must be pumped out and returned to the tritium plant (the plant is discussed in

Chapter VII). However, the pumped-out fraction will depend on the long-term tritium retention in co-deposits. Predictions have been made for the cumulative tritium retention in co-deposited carbon films until the safety limit for in-vessel inventory (700 g) is reached and a clean-up must be performed [1]. The predictions have been based on the experience gathered after the full D-T operation in JET and on scenarios modelled by computer codes for erosion and re-deposition. One could conclude that the clean-up would be necessary after 30-40 (JET equivalent at full carbon wall) to 350-400 ITER pulses (inventory 2 g/pulse with carbon tiles only in the strike zone in the divertor). Whichever inventory scenario might take place in the reactor, frequent breaks in the operation must not happen because it would have a serious impact on the economy of operation. It would also severely hinder efficient realisation of the scientific and technical programme. Therefore, either carbon PFC should be eliminated and replaced by tungsten (see [8]) or/and efficient methods for tritium removal must be fully developed. Both approaches are complex but they are under intense experimental scrutiny. A comprehensive test of materials and their impact on fuel accumulation is one major goal of JET-ILW.

Several methods of T removal and vessel clean-up were tested at TFTR and JET following full D-T campaigns [24,28]: tokamak discharges in D₂ fuelled plasma, H and He glow discharge cleaning, venting with oxygen. Tokamak discharges and hydrogen glow aim at the D-T and H-T isotope exchange. Helium glow sputters away isotopes from the surface layer. Ventilation with air leads to the formation of tritiated water. While the T removal from the main chamber (PFC) could be deemed reasonable effective, the removal rate from remote areas, where the thickest tritiated co-deposits were formed, was poor. Peeled-off flakes were removed by vacuum cleaning. Several other methods for tritium and co-deposit removal have been proposed and tested under laboratory conditions. They are based on chemical decomposition (H and He glow plasma with water vapour [25], O₂-He glow [29]), pulsed irradiation [26,27] or mechanical treatment of surfaces with co-deposits [36]. Irradiation with a laser [27] or flash light [29] stimulates desorption of H isotopes and disintegration of co-deposits. However, the side effect of the deposit removal and disintegration is the formation of dust particulates. Another challenge is related to development of an efficient method to remove co-deposits from gaps between tiles and grooves of castellation [37]. The issue is important because all plasma-facing components in ITER will be castellated and the number of narrow grooves will be over one million. Full scale *in-situ* tests are still to be done in a tokamak environment. Taking into account a variety of co-deposit structures and their location in the reactor, a combination of techniques must be applied. An overview of methods has been presented by Counsell [38]. Full metal wall can mitigate the retention. As mentioned above, the fuel inventory in JET-ILW has been vastly reduced [12].

V. RADIATION-INDUCED EFFECTS

Properties of reactor materials and components are modified by fast neutrons and ionising radiation: γ , X and UV. The neutron flux to the wall of ITER will be of the order of $5 \times 10^{17} \text{ m}^{-2} \text{ s}^{-1}$. Energy carried by 14 MeV neutrons must be converted in the blanket into heat and tritium breeding. The blanket acts as a neutron absorber and T-breeder. Its additional important role is the protection of the vacuum vessel and super-conducting coils from neutron irradiation. Neutrons, on their way through the armour and structural components of the blanket, cause volumetric radiation damage and chemical modification leading to the change and deterioration of material properties. The major neutron-induced effects in solids are: structural damage (displacement damage) [39,40] and nuclear transmutation [41]. These are very closely inter-related processes and they affect all types of materials. Some specific effects are induced by fast photons in ceramic insulators.

The measure of damage to a crystalline matter caused by bombardment with energetic particles is expressed in terms of "displacement per atom" (dpa), i.e. the number of times each atom is dislodged by radiation from its place in the crystal. In other words, 1 dpa is equivalent to displacing all atoms once from their lattice sites. The cross-section for processes of neutron displacement damage is generally in the range from 1 to 10 barns ($1 \text{ b} = 10^{-28} \text{ m}^2$). Damage depends on the fluence (total dose) and, in some cases, also on the neutron flux. For instance, in carbon, beryllium or ceramic materials 1 dpa is produced by a neutron dose of around $1 \times 10^{25} \text{ m}^{-2}$. Volumetric damage leads to the formation of dislocations, interstitials, voids and vacancies in the crystal lattice. This results from the direct knock-on of atoms and/or ions from their sites. Knock-on atoms of sufficiently high energy may produce further displacements by cascades. Dislocation is defined as a line, plane or region in which there is a discontinuity in the regularity of the lattice. Voids and vacancies are the empty spaces formed by shifting the atoms from their original sites. In the end effect materials volume is changed due to swelling (metals, ceramics) or shrinkage (CFC). 1 dpa typically results in 1 % volume change. This in turn, leads to the significant drop in thermal conductivity, even by 70% from the original value [42]. Swelling of a metal crystal changes drastically its mechanical properties causing hardening and resultant increased brittleness (embrittlement). The extent of the damage is reduced at elevated temperatures due to annealing. However, it is obvious that the temperature of materials and components cannot be increased indefinitely. Therefore, efforts in irradiation tests are focused on the definition of operation limits, i.e. dose and temperature.

The processes described above apply also to all insulating ceramics applied as important components of heating and current drive and diagnostic systems

exposed directly to neutron fluxes: feed-through assemblies, magnetic pick-up coils, mineral insulated cables, bolometers, pressure gauges, thermocouples, other temperature sensors, optical fibres, laser diodes, detectors, windows, mirrors, etc [15,43]. For insulators the requirements are more stringent than for metallic materials because it is necessary to maintain not only their mechanical performance but also sensitive physical properties such as electrical insulation and optical transmission. These properties are influenced by neutrons and photons due to radiation-induced or radiation-enhanced:

- i. conductivity (excitation of electrons into a conduction band),
- ii. electrical degradation (increased electrical conductivity),
- iii. absorption (light transmission loss),
- iv. electromotive force (induced voltage between the centre and outer conductors of a mineral insulated cable),
- v. radiation-enhanced diffusion (for instance increased tritium mobility in ceramic windows).

To ensure reliable performance of insulated devices further testing and development of radiation-hard materials must be carried out. The list of examined ceramic materials include Al, Mg, Si, Be oxides, nitrides (Si_3N_4), natural and CVD-diamonds, mica and ferroelectrics.

The second fundamental radiation-induced effect is transmutation defined as the change in a nucleus structure leading to the formation of different isotope(s) or element(s) induced by bombarding the nucleus with particles or photons. In case of photons the process goes *via* the Compton effect. The efficiency of transmutation, as for all nuclear reactions, depends on the cross-section of a given nuclear process. Basically, neutron-induced transmutation can be divided into three categories dependent on the reaction products:

- i. formation of gaseous species such as hydrogen isotopes and helium: (n,p) , (n,np) , (n,d) , (n,t) , (n,α) , $(n,n\alpha)$,
- ii. gamma radiation: (n,γ) , $(n,n'\gamma)$
- iii. neutron breeding: $(n,2n)$, $(n,3n)$.

One may easily notice that the first-group processes lead to the formation of hydrogen isotopes (H,D,T) or helium. Gases accumulated in the crystal lattice form bubbles and blisters. Bubbles are formed not only in the surface layer but also in the bulk. This increases brittleness. When the pressure of the accumulated gas overcomes a certain limit, blisters explode leading to the exfoliation (example is shown in Fig. 5).

An important consequence of nuclear reactions is simultaneous formation of other (than H and He) transmutation products modifying material properties. The problem associated with such impurities becomes particularly serious following high-dose irradiation. Secondly, some of those transmutation products are

radioactive isotopes. Basic physics underlying the transmutation cannot be overcome and the only way to minimize its effects is to use low-activation materials, i.e. materials containing elements of low cross-section for transmutation or elements whose transmutation products are either non-radioactive or isotopes of short lifetime. It is clear that products and related radioactivity (i.e. energy spectrum and lifetime) strongly depend on the initial composition of the irradiated material. It also implies that not only major constituents must undergo low activation but also the quantity and quality of admixtures and impurities must be strictly controlled. For instance, while major constituents of a low activation vanadium alloys (V-3Ti-1Si) transmute to isotopes of short lifetime, the presence of nickel impurities transmuted to ^{60}Co leads to a long-term activation ($t_{1/2}^{60\text{Co}} = 5.27$ years). In conclusion, fabrication of low activation and high purity FRM is essential.

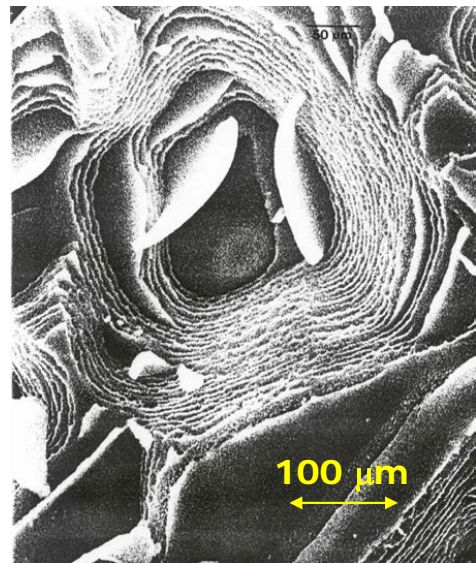


Figure 5: Exfoliation of metal following high dose irradiation.

VI. TRITIUM BREEDING IN THE BLANKET

As already pointed out, the conversion of neutron energy to heat and T-breeding takes place in the absorber part of the blanket. The role of blanket is also to shield superconducting magnets (niobium tin Nb_3Sn and/or niobium-titanium Nb-Ti) against neutrons and gamma radiation [44]. Three test tritium breeding blanket modules (TBM) are planned to be installed in ITER. The aim of TBM implementation in ITER is to test their performance and verify technology for DEMO, i.e. for a prototype of a power-generating fusion reactor. The modules are composed of structural (i.e. containment and coolant loop made of EUROFER) and functional materials (i.e. breeder). Two basic coolants have been

considered: water and high-pressure helium [45]. Figure 6 shows a scheme of helium-cooled blanket being developed for DEMO.

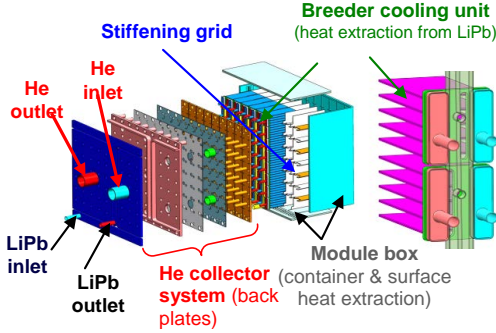
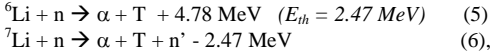
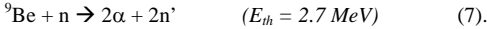


Figure 6: Schematic view of a helium-cooled blanket module to be operated with liquid lithium-lead developed for DEMO. Source: EFDA.

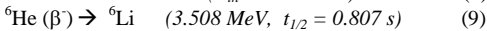
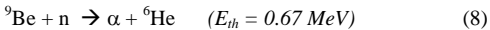
Lithium is an efficient breeder. Therefore, it is a constituent of all candidate materials considered for the absorber. Lithium has two stable isotopes ${}^6\text{Li}$ and ${}^7\text{Li}$ with natural abundance of 7.5% and 92.5%, respectively:



where E_{th} denotes the threshold energy of the process. These reactions are essential for tritium production because that isotope must be produced on site. Several ceramics have been tested: Li_2ZrO_3 , Li_8ZrO_6 , Li_2TiO_3 , LiAlO_2 , Li_2SiO_3 and Li_4SiO_4 ⁴⁶. The other candidates are lithium oxide (Li_2O), Li17-Pb liquid alloy (eutectic) and 2LiF-BeF₄ mixture called Flibe, Li_2BeF_4 . To increase the amount of neutrons for T breeding, beryllium is added as a neutron multiplier:



However, other side reactions with low cross-sections also occur thus leading to the production of tritium and helium and, eventually, to accumulation of tritium in He bubbles in Be:



Then, ${}^6\text{Li}$ and ${}^7\text{Li}$ are transmuted to tritium in processes (5) and (6), respectively. Taking into account all these pathways of T generation from lithium, the overall fusion process reads:



showing that the energy production cycle is based on easily achievable reactants found in nature in inexhaustible supply: deuterium extracted from sea water ($\sim 33.3 \text{ g D/m}^3$) and lithium extracted from sea water or obtained from common minerals such as lepidolite, petalite, spodumene and amblygonite.

VII. TRITIUM PLANT

Tritium bred in the blanket and that pumped-out from the torus (non-used fuel and released from the wall by cleaning methods) must be handled in the tritium plant before it can be used for plasma fuelling. Tritiated species occur in the form of gas molecules (I_2 , where I denotes a mixture of hydrogen isotopes), hydrocarbons (C_xI_y) and water (I_2O). The separation methods comprise cryogenic distillation, condensation, electrolysis, diffusion via Pd membranes, catalytic processes: oxidation of C_xI_y , decomposition of I_2O and C_xI_y and vapour stage exchange:

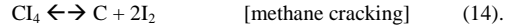
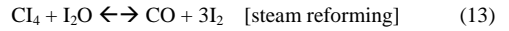
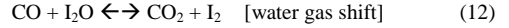


Fig. 7 shows a schematic flow diagram in an isotope separation facility [47]. This example is based on the Tritium Separation Test Assembly, TSTA, operated until 1997 in Los Alamos NL, New Mexico, USA. Details of the ITER fuel cycle have been recently presented by Mardoch [48].

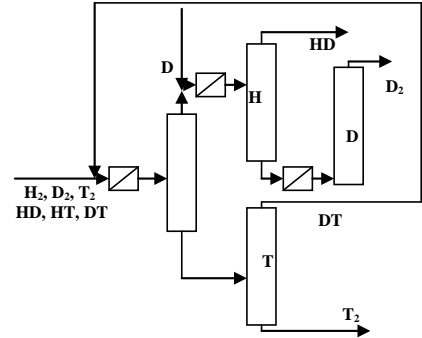


Figure 7: A schematic flow diagram of tritiated gases in an isotope separation station (ISS).

All tritium for introduction to the torus (freshly supplied to the reactor site and that leaving the ISS) must be stored in uranium or Co-Zr beds at low temperature. This is to ensure precise dosing and to avoid uncontrolled release of the radioactive gas. Also deuterium for the gas introduction system is stored in U-beds. The discharge of pure gases from the beds is realised at elevated temperature of about 450 °C [28].

VIII. SAFETY ASPECTS AND HANDLING OF REACTOR COMPONENTS

Already the D-D phase of the ITER operation will activate components to the level unacceptable for manned intervention in the reactor vessel. Radioactivity will be significantly increased in the D - T phase. Additionally, the use of beryllium (health hazard) on the entire wall of the main chamber imposes strict

precautions for in-vessel operation during shut-down periods. Therefore, like in other branches of nuclear industry, the design and construction of all in-vessel components of a fusion reactor is fully compatible with remote handling by robotic arms. The major role of these programmed (trained) devices is in installation, exchange and repair of PFC, blanket, divertor modules and in-vessel diagnostics. Fig. 8 shows a robotic arm used in the JET tokamak. The technology was developed for handling components following the full D-T campaign [28,49]. All replacements of the JET divertor structure and installation of diagnostic tools are performed by these means. Remote handling technology at JET has been further developed to meet requirements in installation of beryllium and tungsten components for the ILW project. This has comprised a design and construction of a new robot capable of handling components of up to 100 kg [9,10].

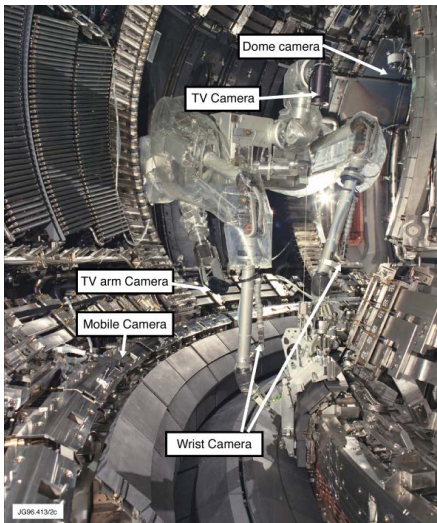


Figure 8: A remotely controlled robotic arm at JET: restructuring of the divertor configuration (1998).

IX. FUTURE STUDIES OF FUSION REACTOR MATERIALS

The list of most important issues to be tackled on the way towards the reactor construction includes:

- i) further development of low-activation and radiation-hard materials and components of high purity,
- ii) development of efficient techniques for tritium removal or elimination of carbon as material for PFC in order to reduce inventory related to the co-deposition,
- iii) testing of materials and components under high-flux irradiation with 14 MeV neutrons.

The last point requires a construction of an efficient test facility capable of simulating the neutron energy spectrum of a D-T fusion reactor. Sufficient intensity of

the n-flux and the irradiation volume of at least 500 cm^3 are indispensable for testing samples of candidate materials up to a full lifetime of anticipated use in a reactor (e.g. DEMO), i.e. over 80 dpa. A conceptual design of the facility has been completed. Engineering validation and engineering design activity (EVEDA) phase will soon begin and it should be followed by decisions regarding the site for the facility and work schedule. The project is called IFMIF: International Fusion Material Irradiation Facility [50]. The facility shown schematically in Fig. 9 is an intense neutron source based on an accelerator-driven generation of neutrons by deuterium-lithium reactions: ${}^7\text{Li}(d,2n){}^7\text{Be}$, ${}^6\text{Li}(d,n){}^7\text{Be}$. Deuterons in the range of 30 - 40 MeV are to be produced by means of two continuous-wave linear accelerators. Interaction of deuterons in a flowing lithium target would lead to production of neutrons with the energy spectrum peaking at around 14 MeV. The neutron generation rate of some 10^{17} n s^{-1} would result in a flux of some $10^{19} \text{ m}^{-2} \text{ s}^{-1}$ at the rear side of the target. Therefore, displacement damage and transmutation products (He) in the irradiated material would match the neutron-induced effects anticipated in the fusion reactor environment. Fig. 10 shows a scheme of the IFMIF test assembly and target chambers.

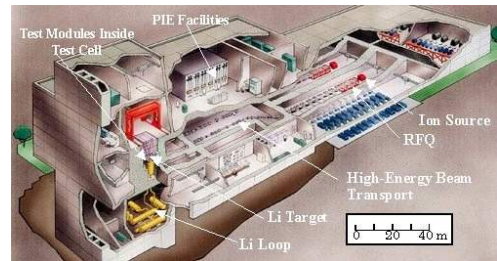


Figure 9: A schematic view of IFMIF.
(Source:http://insdell.tokai.jaeri.go.jp/IFMIFHOME/ifmif_home_e.html)

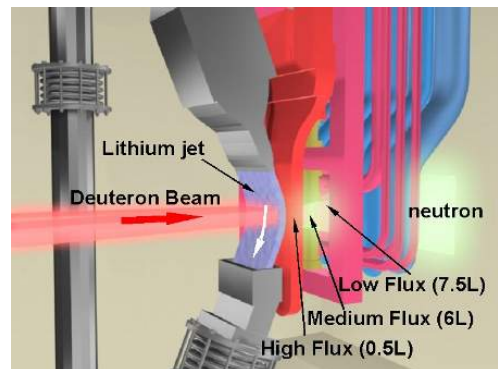


Figure 10: IFMIF: liquid lithium target and characteristics of target chambers.
(Source:http://insdell.tokai.jaeri.go.jp/IFMIFHOME/ifmif_home_e.html)

X. CONCLUDING REMARKS

The above mentioned aspects of material science are necessary and important to accomplish the ultimate goal of fusion research, i.e. the construction of a power generating system. Development and intense testing of materials and components, will play a crucial role in and for the operation of ITER and DEMO machines. Having in mind scientific and technical challenges associated with the project, all efforts are to be made to ensure the best possible material selection for a reactor-class machine. Fusion, if realised under terrestrial conditions, offers inexhaustible energy supply free of CO₂ emission. However, a reactor is a nuclear device and radioactive aspects of fusion will undergo intense public scrutiny. For that reason, proper testing and validation of material and component performance is essential. Based on the best of our present knowledge [51,52] we have to use and to develop tools, methods and materials best fitted for the steady-steady reactor operation. International co-operation established around ITER is an important step on the way towards commercial fusion.

The lecture has addressed not only problems and future challenges but also achievements in technology of FRM. With the present-day experience and background from many fields of science and technology we know “*what*” and “*why*” may happen with materials in a hostile fusion environment. This, in turn, allows definition of actions “*how*” to deal with problems and reach solutions. It certainly still requires substantial funding but also a lot of invention. In that sense, fusion-related material research is an attractive and long-term field for a generation of young scientists and nuclear engineers.

REFERENCES

1. G. Federici et al., “Plasma-Material Interactions in Current Tokamaks and their Implications for Next Step Fusion Reactors”, *Nucl. Fusion*, **41**, 1967 (2001).
2. W. O. Hofer and J. Roth (Eds), *Physical Processes of the Interaction of Fusion Plasmas with Solids*, Academic Press, New York (1996).
3. A. Loarte, “Implications of the Use of Carbon-Based Plasma Facing Components in Next Step Fusion Devices”, *Phys. Scr.*, **T111**, 13 (2004).
4. J. Linke, “Plasma Facing Materials and Components Future Fusion Devices: Development, Characterisation and Performance under Fusion Specific Loading Conditions”, *Phys. Scr.*, **T123**, 45 (2006) and *These proceedings*.
5. Progress in the ITER Physics Basis, *Nucl. Fusion*, **47** (2007) (also: www.iter.org).
6. R.A. Pitts et al., “Status and Physics Basis of the ITER Divertor”, *Phys. Scr.* **T138**, 014001 (2010).
7. U. Samm, “Plasma – Wall Interaction”, *These proceedings*.
8. R.A. Pitts, “A Full Tungsten Divertor for ITER: Physics Issues and Design Status”, *J. Nucl. Mater.*, **438**, S48 (2013).
9. G. F. Matthews et al. “Overview of the ITER-Like Wall Project”, *Phys. Scr.*, **T128**, 137 (2007).
10. G.F. Matthews et al., “The JET ITER-Like Wall – Status and Experimental programme”, *Phys. Scr.*, **T145**, 014001 (2011).
11. Ph. Mertens et al., “Detailed Design of a Solid Tungsten Divertor at JET”, *Phys. Scr.*, **T145**, 014002 (2011).
12. G.F. Matthews, “Plasma Operation with an All Metal First Wall: Comparison of an ITER-Like Wall and a Carbon Wall in JET”, *J. Nucl. Mater.*, **438**, S2 (2013).
13. E. E. Bloom, “The Challenge of Developing Structural Materials for Fusion Power Systems”, *J. Nucl. Mater.*, **258-263**, 7 (1998).
14. T. Yano et al. “Physical Property Change of Neutron Irradiated CVD-diamond, Silicon and Silicon Carbide”, *J. Nucl. Mater.*, **307-311**, 1102 (2002).
15. M. Decréton, T. Shikama and E. Hodgson, “Performance of Functional Materials and Components in a Fusion Reactor: the Issue of Radiation Effects in Ceramics and Glass Materials for Diagnostics”, *J. Nucl. Mater.*, **329-333**, 125 (2004).
16. J. P. Coad et al., “The Amount and Distribution of Deuterium Retained in the JET Divertor after the C and Be Phases”, *J. Nucl. Mater.*, **241-243**, 408 (1997).
17. M. Rubel et al., “Beryllium and Carbon Films in JET following D-T Operation”, *J. Nucl. Mater.*, **313-316**, 323 (2003).
18. B. Emmoth, M. Rubel and E. Franconi, “Deep Penetration of Deuterium in Carbon-Based Substrates”, *Nucl. Fusion*, **30**, 1140 (1990).
19. V. K. Alimov and J. Roth, “Hydrogen isotope retention in plasma-facing materials: review of recent experimental results”, *Phys. Scr.*, **T128**, 6 (2007).
20. A. Kreter et al., “Deuterium Retention in Different Carbon Materials Exposed at TEXTOR”, *J. Physics Conf. Series*, **100**, 062024 (2008).
21. V. Philipps et al., “Erosion and Re-deposition of Wall Material in Controlled Fusion Devices”, *Vacuum*, **67**, 399 (2002).
22. A. von Keudell et al., “Surface Loss Probabilities of Hydrocarbon Radicals on Amorphous Hydrogenated Carbon Film Surfaces”, *Nucl. Fusion*, **39**, 1451 (1999).
23. M. Rubel et al., “Analysis and Oxidation of Thick Deposits on TEXTOR Plasma Facing Components”, *J. Nucl. Mater.*, **266-269**, 1185 (1999).

24. C.H. Skinner et al., "Plasma Wall Interaction and Tritium Retention in TFTR", *J. Nucl. Mater.*, **241-243**, 214 (1997).
25. B. Landkammer et al., "Erosion of Thin Hydrogenated Carbon Films in Oxygen, Oxygen/Hydrogen and Water Plasmas", *J. Nucl. Mater.* **264**, 148 (1999).
26. C. H. Skinner et al., "Thermal Response of Tritiated Co-deposits from JET and TFTR to Transient Heat Pulses", *Phys. Scr.*, **T103**, 34 (2003).
27. D. Ivanova et al., "Laser-based and Thermal Methods for Fuel Removal and Cleaning of Plasma-Facing Components", *J. Nucl. Mater.*, **415**, S801 (2011).
28. D. Stork (Ed.), *Technical Aspects of Deuterium-Tritium Operation at JET*, (special issue) *Fusion Eng. Des.*, **47**, (1999).
29. M. Rubel et al., "Fuel Removal from Plasma-Facing Components by Oxidation-Assisted Technique. An Overview of surface morphology after oxidation", *J. Nucl. Mater.*, **363-365**, 877 (2007).
30. A. Widdowson et al., "Efficacy of photon cleaning of JET divertor tiles" *J. Nucl. Mater.*, **363-365**, 341 (2007).
31. M. Rubel et al., "Thick Co-Deposits and Dust in Controlled Fusion Devices with Carbon Walls: Fuel Inventory and Growth Rate of Co-Deposited Layers", *Phys. Scr.*, **T103**, 20 (2003).
32. M. Rubel et al., "Dust Particles in Controlled Fusion Devices", *Nucl. Fusion*, **41**, 1087 (2001).
33. J. Winter and G. Gebauer, "Dust in Magnetic Confinement Devices and its Impact on Plasma Operation", *J. Nucl. Mater.*, **266-269**, 228 (1999).
34. V. Rohde et al., "Dust Investigations at ASDEX Upgrade" *Phys. Scr.*, **T138**, 014024 (2009).
35. D. Ivanova et al., "Survey of Dust Formed in the TEXTOR Tokamak: Structure and Fuel Retention", *Phys. Scr.*, **T138**, 014025 (2009).
36. G. Counsell and C.H. Wu, "In-situ Detection and Removal of Carbon Debris – a Challenge for the Next Step Fusion Device", *Phys. Scr.*, **T91**, 70 (2001).
37. M. Rubel et al., "Overview of Co-deposition and Fuel Inventory in Castellated Divertor Structures at JET", *J. Nucl. Mater.*, **367-370**, 1432 (2007).
38. G. Counsell et al., "Tritium Retention in Next Step Devices and Requirement for Mitigation and Tritium Removal Techniques", *Plasma Phys. Control. Fusion*, **48**, B189 (2006).
39. R. A. Johnson and A. N. Orlov (Eds), *Physics of Radiation Effects in Crystals, Modern Problems in Condensed Matter Sciences*, Vol. 13, North-Holland, Amsterdam (1986).
40. H. Ullmaier, *Contributions to High-Temperature Plasma Physics*, K. H. Spatschek and J. Ulenbusch (Eds), Chap. 3, p. 201, Akademie Verlag, Berlin (1994).
41. H. S. Plendl (Ed.), *Nuclear Transmutation Methods and Technologies*, North-Holland, Amsterdam 1998. (also : www.chemistrycoach.com/nuclearchem.htm)
42. T. D. Burchell, "Radiation Damage in Carbon-Carbon Composites", *Phys. Scr.*, **T64**, 17 (1996).
43. *Proc. 8th Int. Conf. on Fusion Reactor Materials (ICFRM-8)*, Sendai, Japan, October, 1997, *J. Nucl. Mater.*, **258-263** (1998), Section 7, pp. 1798-1919.
44. L. Giancarli et al., "Breeding Blanket Modules Testing in ITER: An International Programme on the Way to DEMO", *Fusion Eng. Des.*, **81**, 393 (2006).
45. Y. Poitevin et al., "The Test Blanket Modules Project in Europe", *Fusion Eng. Des.*, **82**, 2164 (2007).
46. A. R. Raffray et al., "Breeding Blanket Concepts for Fusion and Material Requirements", *J. Nucl. Mater.*, **307-311**, 21(2002).
47. J. L. Anderson and P. LaMarche, "Tritium Activities in the United States", *Fusion Technol.*, **28**, 479 (1995).
48. D.K. Murdoch et al., "ITER Fuel Cycle Development", *Fusion Sci. Technol.*, **48**, 3 (2005).
49. A. Rolfe, "Remote handling on fusion experiments", *Fusion Eng. Des.*, **36**, 91 (1997).
50. A. Möslang et al., "Suitability and Feasibility of the International Fusion Materials Irradiation Facility (IFMIF) for Fusion Materials Studies", *Nucl. Fusion*, **40**, 619 (2000) 619 (also: www.fzk.de and http://insdell.tokai.jaeri.go.jp/IFMIFHOME/ifmif_home_e.html).
51. *Proc. Int. Conf. on Fusion Reactor Materials (ICFRM)*, *J. Nucl. Mater.*, **133-134** (1985), **141-143** (1986), **155-157** (1988), **179-181** (1991), **212-215** (1994), **258-263** (1998), **283-287** (2000), **307-311** (2002), **329-333** (2004), **367-370** (2007), **386-399** (2009).
52. *Proc. 15th Int. Conference on Fusion Reactor Materials (ICFRM-15)*, *Fusion Sci. Technol.*, **62**, (2012).

PLASMA HEATING IN PRESENT-DAY AND FUTURE FUSION MACHINES

Yevgen Kazakov, Dirk Van Eester, and Jef Ongena

*Laboratory for Plasma Physics, LPP-ERM/KMS,
EUROfusion Consortium Member, Brussels, Belgium*

ABSTRACT

A fusion reactor requires plasma pre-heating before the rate of deuterium-tritium fusion reactions becomes significant. Ohmic heating due to the toroidal plasma current that flows in tokamak plasmas allows to reach temperatures of several keV only. In this lecture we provide a short overview of the two main auxiliary heating systems relevant for fusion machines: an injection of high-energy neutral particles and radiofrequency plasma heating.

I. INTRODUCTION

The energy balance for a fusion reactor implies that the energy losses are compensated by the plasma heating due to fusion-born alpha particles. The fusion rate is a strong function of plasma temperature and at low temperatures is negligible. Hence, plasma pre-heating is required before a positive power balance can be reached in a fusion machine.

A fusion triple product, which characterizes the performance of a fusion device, is minimized at plasma temperature $T \approx 15$ keV. The initial heating in tokamaks comes from the ohmic heating: likewise an electric current flowing through a metal wire heats it up, the toroidal plasma current, which is used in tokamaks for plasma confinement, dissipates its energy and heats the plasma. However, ohmic heating allows to reach plasma temperature of a few keV only [1, 2]. As the plasma temperature increases, the collisional frequency and the plasma resistivity, being proportional to $\propto 1/T^{3/2}$, decrease. The limitations of ohmic heating are discussed in more detail in a separate lecture by R. Koch and D. Van Eester [3]. There, it is also shown that raising the plasma current to increase the ohmic power $P_{\Omega} = RI_{\text{pl}}^2$ is limited by the necessity to keep the edge safety factor $q_{\text{edge}} > 2$ for MHD stability of the plasma. Note that for stellarators the confining magnetic field is solely produced by the external magnetic coils and the plasma current is so low that ohmic heating is negligible.

There are two main methods for heating fusion plasmas. The first technique is based on injecting the beam of high-energy neutral particles to the plasma (NBI). As the beam particles are ionized in the

plasma, they transfer their energy to bulk ions and electrons via Coulomb collisions. The second method relies on launching electromagnetic waves into the plasma and providing proper conditions for strong localized wave damping by ions and/or electrons. Due to the inhomogeneity of the confining magnetic field in toroidal plasmas, the position of the power deposition for radiofrequency (RF) heating can be controlled externally, e.g., by a choice of the wave frequency. The supported by plasmas resonant wave frequencies will be identified below, using a simplified – yet, good as a first approximation – cold-plasma approach.

There are numerous applications of NBI and RF systems beyond heating itself. Tokamaks are inherently pulsed machines, and driving non-inductive current with auxiliary heating systems is essential for maximizing the plasma pulse duration, a prerequisite condition for economic viability of tokamaks as fusion reactors. Heating systems are also routinely used for diagnostics purposes, controlling impurities and plasma instabilities, optimizing particle and energy transport, for plasma start-up and landing, etc.

II. NEUTRAL BEAM INJECTION HEATING

Neutral beam injection has been used as a working horse for plasma heating in most of fusion machines. For instance, the world highest fusion power 16 MW was obtained on JET tokamak by injecting 22 MW of NBI and 3 MW of ICRF heating. A strong magnetic field is used for plasma confinement in magnetic fusion devices, and this prohibits a direct injection of energetic ions into the plasma. Whereas injected energetic ions will be deflected by the magnetic field and can not penetrate deep into the plasma, neutral particles do not feel the Lorentz force and will travel along straight-line trajectories until their ionization by collisions with the background plasma. The penetration length for a beam in the plasma – before most of its power is deposited due to ionization – depends essentially on the injection beam energy E_{NBI} . As will be discussed in this section, most of present-day tokamaks and stellarators operate with beam energies $E_{\text{NBI}} \simeq 100$ keV, and the application of NBI to

ITER and next-step devices requires a fundamental change and an increase of the beam energy by an order of magnitude up to $E_{\text{NBI}} \approx 1$ MeV. E_{NBI} also determines whether a collisional ion or electron heating dominates due to the slowing down of the NBI-generated fast ions. Present-day NBI systems usually provide a high fraction of ion heating, while for the future machines most of the injected beam power will be transferred to electrons.

A schematic diagram of NBI system is shown in Fig. 1. There is no direct way of accelerating neutral particles to high energies, and one still has to start with accelerating electrically charged ions, and then set a dedicated system to convert energetic ions into energetic neutral particles. Low-energy ion source is a first step of the NBI system. Beam energies of about 100 keV are sufficient for the machine's and plasma parameters of the existing fusion devices, and this allows using well-established techniques for producing positive ions. However, ion sources based on a plasma discharge produce not only the required atomic ions (e.g., D^+), but also a significant fraction of molecular ions (D_2^+ and D_3^+). The molecular ions will ultimately dissociate into atoms with one-half and one-third NBI energies. Such $E_{\text{NBI}}/2$ and $E_{\text{NBI}}/3$ atoms will have a lower penetration to the plasma and deposit more heating at the plasma edge, which is not desirable. In future fusion machines, including ITER, a different technology for the ion source has to be adopted, and NBI systems will be based on using negative ion beams (N-NBI).

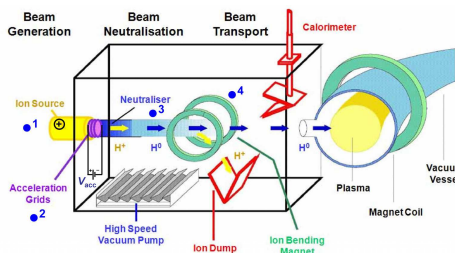


Figure 1: Layout of neutral beam injection system (Courtesy: Ursel Fantz, IPP-Garching).

At the second stage, the ions are accelerated to the required energy by applying a high DC voltage. Because a positive electrostatic voltage will be applied to extract negative ions in N-NBI systems, there will be no one-half and one-third beam components present after the extraction. The accelerated beam current is usually about 50 A, and one can easily compute the consumed input electrical power for this part of NBI system by multiplying the acceleration voltage by the beam current.

After this stage a directed beam of high-energy ions is formed and it enters the neutralization chamber, where the conversion of energetic ions into

energetic neutrals occurs. The neutralizer consists of a simple gas cell, filled with the molecular gas and open at each end, through which the beam passes. Normally the gas species for the neutralizer is chosen the same as for the ion source. The density of the neutralizing gas is varied to achieve the maximum efficiency of ion-to-neutral conversion. Figure 2 depicts the maximum neutralization efficiency, $\eta_{\text{neutr.}}^{(\text{max})}$ computed for atomic D and H ion beams as a function of beam energy. For the same NBI acceleration energy, the neutralization efficiency of H beams is lower than for D beams because of the larger energy per nucleon. As follows from this figure, the neutralization efficiency for D^+ ions at $E_{\text{NBI}} \approx 100$ keV is reasonably good, $\approx 50\%$, but at higher beam energies decreases to unacceptably low levels. In contrast, for negative beams (both for D^- and H^-) the neutralization efficiency is much higher, $\eta_{\text{neutr.}}^{(\text{max})} \approx 60\%$. This is the reason why using negative ions is the inevitable choice for neutral beam systems of ITER and future fusion machines, which will operate at MeV level.

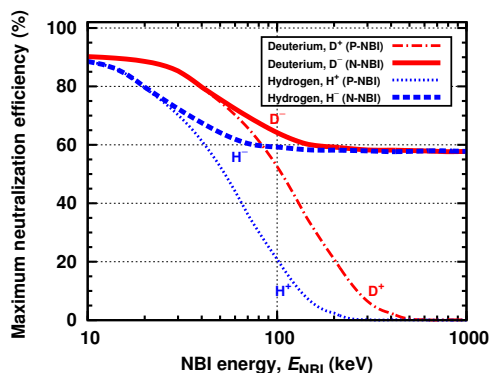


Figure 2: Maximum neutralization efficiency for D and H atomic ion beams as a function of beam energy.

It is quite easy to compute quantitatively the maximum value of $\eta_{\text{neutr.}}$ for N-NBI systems. At high beam energies 200 – 1000 keV/amu, the two most important reactions occurring in the neutralizer are: 1) a stripping reaction $\text{D}^- + \text{D}_2 \rightarrow \text{D}_0 + \text{D}_2 + e$ (cross-section σ_{-10}), which converts a negative ion to an energetic neutral; and 2) a competing loss process due to a re-ionization of the formed neutral by a collision with background neutrals, $\text{D}_0 + \text{D}_2 \rightarrow \text{D}^+ + \text{D}_2 + e$ (σ_{01}). Also negative ions can be directly converted to positive ions via a reaction $\text{D}^- + \text{D}_2 \rightarrow \text{D}^+ + \text{D}_2 + 2e$ (cross-section σ_{-11}). Then, the maximum neutralization efficiency, when the gas density of the neutralizer is optimized for D^0 generation, is connected to the cross-sections as follows

$$\eta_{\text{neutr.}}^{(\text{max})} = \frac{\sigma_{-10}}{\sigma_{-10} + \sigma_{-11}} p^{p/(1-p)} \approx 58\%. \quad (1)$$

Here, $p = \sigma_{01}/(\sigma_{-10} + \sigma_{-11}) \approx 0.28$ and the first term $\sigma_{-10}/(\sigma_{-10} + \sigma_{-11}) \approx 0.95$. The tabulated data for the cross-sections can be found in [4]. For negative ions the neutralization efficiency at high beam energies remains nearly constant. At the exit of the neutralizer, the beam consists of 58% of high-energy neutrals, and 25% and 17% of positive and negative ions, respectively.

One should note here that for present-day NBI systems based on positive ions, the acceleration energy, beam current and beam power fractions depend significantly on the ion species used for injection. Table 1 illustrates this for the NBI system of the tokamak JET, which consists of two neutral injector boxes equipped each with up to eight positive ion neutral injectors (PINIs) [5]. The system was recently upgraded to increase the total injected deuterium neutral beam power to at least 34 MW and to increase the beam pulse length. If operating with deuterium, the full-energy beam component carries about 50% of the total NBI power, and for the hydrogen mode of operation a half-energy component is the dominant.

Table 1: Measured (D₂) and predicted (H₂ and T₂) parameters of the JET NBI system after the completion of recent upgrade [5]. The total power is computed for two neutral injector boxes equipped with up to eight PINIs each.

Parameter \ Gas species	H ₂	D ₂	T ₂
Max. beam energy (keV)	90	125	118
Max. beam current (A)	50	65	45
Max. power per PINI (MW)	1.0	2.16	2.2
Max. total power (MW)	16.0	34.6	35.2
Predicted beam power			
fractions, $E_0 : E_0/2 : E_0/3$	28:44:28	52:39:9	63:26:11

Since one should avoid of injecting high-energy positive/negative ions from NBI system to the plasma (after entering the plasma they will likely deposit their energy on the neutral beam entrance port), the next stage of the NBI system is the residual ion dump. Here, the charged beam components are filtered out by using the deflection magnets or the electrostatic field. To increase the wall-plug efficiency of NBI systems (in present-day machines it is $\approx 20 - 30\%$ only), for devices following ITER a possibility of energy recovery (recirculating the residual negative ions) is explored [6]. In addition, utilizing photo-detachment or plasma neutralizers to improve the neutralization efficiency beyond 58% – maximum for the standard gas neutralizers – is being actively studied in the context of DEMO development. The wall-plug efficiency of NBI systems has to be improved by a factor of two to become reactor-relevant [6].

After passing the neutralization stage, the remaining neutral beam either impinges onto the calorimeter or continues into the duct leading to a plasma. Adopting a movable calorimeter allows an off-line commissioning and optimization of the beam system without plasma operation. Combined with measurements of the losses in the neutral beam duct, this also allows the injected NBI power to be determined independently of the plasma device.

Estimating the required NBI energy

In this subsection, we estimate the required beam energies as a function of machine’s size and operational plasma densities, and show why NBI system for ITER has to provide beams with the energy of about 1 MeV.

When the neutral beam particles enter the plasma, there are several processes causing an ionization of a high-energy neutral in a plasma: charge exchange, electron and ion impact ionization in collisions with plasma electrons, ions and impurities. As the neutral beam penetrates and is absorbed in the plasma, its flux exponentially decays with the propagation distance, $I(\Delta l) = I_0 \exp[-\int_0^{\Delta l} dl n(\vec{r})\sigma(\vec{r})]$, where Δl is a distance along the beam propagation path. Assuming a constant density profile $n \approx \text{const}$, one can write

$$I(\Delta l) = I_0 e^{-\Delta l/L_{\text{NBI}}}. \quad (2)$$

A characteristic distance, at which the initial beam intensity is attenuated by a factor of $e \approx 2.7$ – further referred to as the beam decay length – is then $L_{\text{NBI}} = 1/(n\sigma)$. For simplicity, we neglect an ionization due to electron impact. For $E/A_{\text{NBI}} \geq 40$ keV/amu, the total cross-section for charge exchange and ion impact is inversely proportional to the beam energy and can be approximated as $\sigma_{i+\text{CX}}(\text{m}^2) \approx 1.8 \times 10^{-18} / [E_{\text{NBI}}(\text{keV})/A_{\text{NBI}}]$. Then, the beam decay length is given by

$$L_{\text{NBI}}(\text{m})|_{\sigma=\sigma_{\text{CX}}+\sigma_i} \simeq \frac{E_{\text{NBI}}(\text{keV})/A_{\text{NBI}}}{180n_{e,20}}, \quad (3)$$

where $n_{e,20}$ is the plasma density expressed in the units 10^{20} m^{-3} .

Let us consider an updated JET NBI system with 125 keV D⁰ beams as an example. Using a typical plasma density of $n_e = 5 \times 10^{19} \text{ m}^{-3}$, Eq. (3) predicts $L_{\text{NBI}} \approx 0.7$ m, which is comparable to the minor radius of the machine $a \approx 0.9$ m. However, such NBI energies are too low for heating ITER plasmas ($a = 2$ m, $n_e = 1 \times 10^{20} \text{ m}^{-3}$): according to Eq. (3), at $E_{\text{NBI}} = 125$ keV a decay length will be $L_{\text{NBI}} \approx 0.35$ m (taking into account charge-exchange and ion impact ionization mechanisms only). A short decay length (i.e., $L_{\text{NBI}} \ll a$) is undesirable since most of the energy is deposited at the outer part of the plasma volume. As a result, the beam energy has to be significantly increased for ITER and future

larger, higher-density fusion machines in order to allow neutrals to penetrate deeper into the plasma.

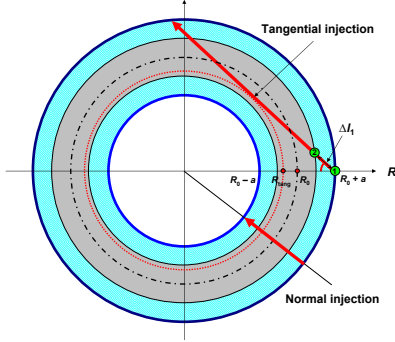


Figure 3: Plan view illustrating a very different beam propagation length for normal and tangential NBI injection.

The required NBI energy for ITER can be estimated as follows (see Fig. 3). In ITER, the two heating neutral beams will inject beams tangentially with a tangency radius $R_{\text{tang}} = 5.28$ m ($R_{\text{tang}} \approx R_0 - a/2$), and the third diagnostic beam is designed for a normal injection [7]. The full path of the tangential beam through the plasma is $\Delta l_2 = 2\sqrt{(R_0 + a)^2 - R_{\text{tang}}^2} \approx 12.5$ m, and because of the very long geometrical distance the shintthrough fraction (amount of NBI power arriving at the wall) is very small. However, a significant fraction of beam power is deposited in the outer shell of the plasma during a relatively short path of the beam since its entrance to the plasma (point '1' in Fig. 3) to the point, when it intersects the flux surface $r/a = 0.5$ (point '2'). This distance is given by $\Delta l_1 = \sqrt{(R_0 + a)^2 - R_{\text{tang}}^2} - \sqrt{(R_0 + a/2)^2 - R_{\text{tang}}^2} \approx 1.4$ m. The fraction of beam power deposited along this path is $p_{\text{abs}} \approx 1 - e^{-\Delta l_1/L_{\text{NBI}}}$, and this sets a limitation on the acceptable NBI decay length and, hence, required beam energies. L_{NBI} should be comparable to Δl_1 or even less in order to reduce the beam power deposition at the edge. In fact, already at $\Delta l_1/L_{\text{NBI}} = 0.7$, $> 50\%$ of the incident beam power is deposited within $r/a \geq 0.5$ region. For a fusion device with the ITER-like aspect ratio, Δl_1 can be approximated as $\sqrt{aR_0}/3$, and one can derive an estimate for the required NBI energy ($L_{\text{NBI}} \gtrsim 0.5\sqrt{aR_0}$)

$$E_{\text{NBI}}(\text{keV})|_{\sigma=\sigma_{\text{CX}}+\sigma_i} \gtrsim 90 \sqrt{aR_0} n_{e,20} A_{\text{NBI}}. \quad (4)$$

In Eq. (4), the beam energy is given in keV, and the machine's minor and major radii are in meters.

For ITER operating with deuterium beams, Eq. (4) yields an estimate of $E_{\text{NBI}} \approx 600$ keV. Why are then heating NBI systems of ITER designed for 1 MeV D_0 beams? In fact, at high beam energies (of several hundreds keV or higher) an additional mechanism – multistep ionization – produces a substantial increase of the beam stopping cross-section and this reduces the beam penetration. As discussed in [8, 9], the multistep ionization arises from excitation of the beams and the subsequent ionization of already excited neutral atoms. The enhancement factor of the ionization against the single step-processes considered above, $\sigma_{\text{eff}} = \sigma(1 + \delta)$ is theoretically predicted to increase with the beam energy and the electron density, $\delta = \delta(E_{\text{NBI}}, n_e, \dots)$. While an effect of the multistep ionization is relatively small for present-day beam systems, an enhancement of the stopping cross-section by a factor of two was measured for 350 keV hydrogen beam in JT-60U tokamak ($\delta \approx 0.8 - 1.05$), in accordance with theoretical predictions. A similar enhancement factor is expected for high-energy deuterium beams in ITER. Then, Eq. (3) for estimating the beam decay length in a plasma has to be adopted accordingly to include the multistep ionization

$$L_{\text{NBI}}(\text{m}) \approx \frac{E_{\text{NBI}}(\text{keV})/A_{\text{NBI}}}{180(1 + \delta)n_{e,20}}. \quad (5)$$

The same multiplication factor $(1 + \delta)$ has to be included to Eq. (4), when estimating the required beam energies and this correction yields $E_{\text{NBI}} \approx 1$ MeV for ITER.

Initially ITER will use two neutral beams for plasma heating that are designed to inject each 16.5 MW of power to the plasma. Operation with deuterium (1 MeV/40 A) and hydrogen (870 keV/46 A) will be supported. Note that whereas tritium has been used with positive ion based injectors during the D-T experiments on JET and TFTR tokamaks, a current status of the ITER NBI design does not consider using tritium due to the regulations on tritium handling. The third NBI port in ITER is reserved for the diagnostics neutral beam that will be installed to support the charge exchange recombination spectroscopy, which is an essential diagnostic for the measurement of the helium-ash density in the core of D-T plasmas. The diagnostics neutral beam in ITER will use a normal injection of the hydrogen beam with a much smaller energy (H^- , 100 keV/60 A).

Critical energy

After the ionization of the injected neutral particles in the plasma, the resulting fast ions are slowed down by Coulomb collisions with bulk plasma ions and electrons. A Fokker-Planck description of the test-particle slowing down is normally adopted to compute the resulting power deposition. The

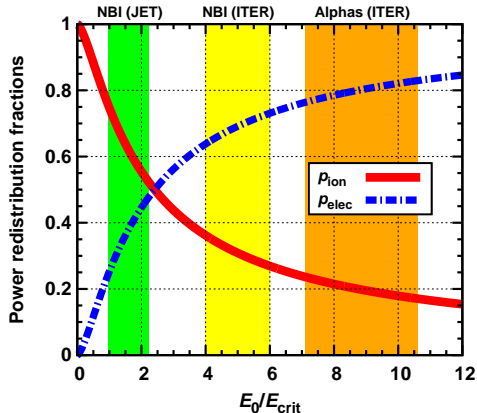


Figure 4: Fraction of the fast ion energy transferred to bulk ions and to electrons as a function of E_0/E_{crit} . The shaded areas highlight regimes relevant for JET NBI system ($E_0^{(\text{D})}=125$ keV, $T = 3 - 7$ keV), ITER N-NBI system ($E_0^{(\text{D})} = 1$ MeV, $T = 10 - 15$ keV), and for fusion-born alpha particles ($E_0^{(\alpha)} = 3.5$ MeV).

corresponding derivation one can find in a lecture [3]. For our discussion it is sufficient to note that whether the resultant dominant bulk ion or electron heating occurs, depends on the ratio of the fast-particle energy to the so-called critical energy, E_{crit} defined as

$$E_{\text{crit}} = 14.8 A_{\text{fast}} T_e \left(\sum_i X_i Z_i^2 / A_i \right)^{2/3}, \quad (6)$$

where $X_i = n_i/n_e$ are the concentrations of various ion species in a plasma. A fast ion with the energy $E = E_{\text{crit}}$, transfers instantaneously the same amount of power to ions and electrons via collisions.

If we consider a slowing down of fast particles with the initial (birth) energy E_0 to thermal velocities, then the average fraction of the total energy given up by the fast particles, which goes into the thermal bulk ions of the plasma, is

$$p_i(E_0) = \frac{E_{\text{crit}}}{E_0} \int_0^{E_0/E_{\text{crit}}} \frac{dy}{1 + y^{3/2}}. \quad (7)$$

The fraction of power flowing to electrons is then

$$p_e(E_0) = 1 - p_i(E_0). \quad (8)$$

A plot of p_i and p_e as a function of E_0/E_{crit} is shown in Fig. 4. Note that at $E_0 = E_{\text{crit}}$ about 75% of the fast ion energy is transferred to the plasma ions, and an equal total energy transfer to ions and electrons is reached at $E_0/E_{\text{crit}} \approx 2.4$.

It is instructive to illustrate these results with a few examples. For $E_{\text{NBI}}^{(\text{D})} = 125$ keV beam particles injected to 5 keV deuterium plasma, $E_0/E_{\text{crit}} \approx 1.3$ and $p_i:p_e \approx 2:1$. For NBI system relevant for ITER

a much higher beam energy has to be adopted, as discussed in the previous subsection, and the ratio E_0/E_{crit} will be significantly larger than for the present-day NBI systems. As a result, N-NBI systems with $E_{\text{NBI}} \approx 1$ MeV will provide a dominant electron heating. A similar test-particle slowing down reasoning applies for fusion-born alpha particles. Since the birth energy of alpha particles is 3.5 MeV, this means that their energy loss is mainly due to collisions with plasma electrons.

III. RADIOFREQUENCY HEATING

Radiofrequency heating is another very efficient method for increasing fusion plasma temperatures. Magnetized plasmas have several ‘natural’ resonant frequencies and support the variety of wave modes. This results in the existence of many different RF heating and current drive scenarios. Though RF heating involves a much more complicated physics of electromagnetic wave propagation in plasmas and wave-particle interaction, this, in turn, makes RF heating much more flexible in terms of external control of the heating region than for neutral beams. For example, if the RF heating in the ion cyclotron range of frequencies (ICRF) is applied, changing power deposition from dominant ion to dominant electron can be done by varying the chosen operational wave frequency or selecting a proper plasma composition. Furthermore, ICRF is the only heating method in future fusion machines capable of providing a significant fraction of bulk ion heating. On the other hand, heating in the electron cyclotron range of frequencies (ECRF) is characterized with a very localized power deposition, and this allows also to use ECRF as a tool to control the plasma pressure and current density profiles for the MHD plasma stability [10]. Lower hybrid (LH) heating has been actively exploited on different present-day machines as a very efficient method of non-inductive current drive.

For ITER, in addition to 33 MW of NBI power, installing two RF heating systems (ECRH and ICRH) each providing 20 MW of auxiliary power is foreseen. A further 40 MW upgrade of the ITER heating mix, with a possibility of installing lower hybrid heating, is also considered.

The principle of wave heating is similar for all RF scenarios. A generator (the type of utilized source is very different depending on the operating frequency) sends waves along the transmission line to a launching structure located at the plasma edge [11]. Then, in contrast to NBI heating which has no problem of injecting neutral particles to the plasma, a special care has to be taken to optimize coupling of RF power from the launcher to the plasma [12]. Once the required electromagnetic wave starts its propagation in the plasma, the focus of the discussion shifts

towards understanding how to make RF power to be absorbed at a desired part of the plasma volume, often preferably close to the plasma center.

It is impossible to cover all aspects of plasma waves physics in a short lecture note. An interested reader is referred to lectures [13, 14] for the further reading, and to books [15, 16] for an in-depth discussion on plasma waves in magnetized plasmas. In this lecture note, we will focus only on a single issue of RF plasma heating: determining resonant wave frequencies suitable for efficient heating and current drive.

Cold plasma dielectric tensor

The propagation of electromagnetic waves in an arbitrary medium is described by Maxwell's equations (cgs system is adopted here)

$$\begin{cases} \text{rot}\vec{E} = -\frac{1}{c}\frac{\partial\vec{B}}{\partial t} \\ \text{rot}\vec{B} = \frac{1}{c}\frac{\partial\vec{E}}{\partial t} + \frac{4\pi}{c}\vec{j}. \end{cases} \quad (9)$$

Plasma consists of charged particles, ions and electrons, and it influences the wave propagation characteristics via the wave induced current density \vec{j} . Depending on the level of complexity of describing the system, different plasma models can be adopted. We consider the simplest case, when a cold plasma is immersed in a constant equilibrium magnetic field $\vec{B} = B_0\vec{e}_z$ and the wave amplitude is small such that wave propagation can be treated as a linearized perturbation for every individual mode $\vec{B}_\sim, \vec{E}_\sim \propto e^{i(\vec{k}\vec{r}-\omega t)}$ (ω is the wave frequency and \vec{k} is the wave number). Under these assumptions, the time derivative and curl operator in Eqs. (9) can be replaced with $\partial/\partial t \rightarrow -i\omega$ and $\text{rot} = i\vec{k}\times$, respectively.

Cold plasma description allows to use a simple equation of motion for an ion/electron, $d\vec{v}/dt = q\vec{E}/m + (qB_0/mc)\vec{v}\times\vec{e}_z$, to characterize its response to the electromagnetic field. This equation for the simplified case considered here can be easily solved, and the individual velocity components as a function of RF electric field are given by

$$\begin{cases} v_x = \frac{iq}{m}\frac{\omega}{\omega^2 - \omega_c^2}E_x - \frac{q}{m}\frac{\omega_c}{\omega^2 - \omega_c^2}E_y, \\ v_y = \frac{iq}{m}\frac{\omega}{\omega^2 - \omega_c^2}E_y + \frac{q}{m}\frac{\omega_c}{\omega^2 - \omega_c^2}E_x, \\ v_z = \frac{iq}{m\omega}E_z, \end{cases} \quad (10)$$

and the cyclotron frequency $\omega_c = qB_0/mc$ has been introduced. The cyclotron frequency depends on q/m ratio of a particle, and therefore for electrons it is about 2000 times larger than for ions. In addition, ω_c includes the sign of a particle's charge, which reflects the fact that ions and electrons rotate in the opposite directions around the confining magnetic field. As

follows from Eq. (10), if $B_0 \neq 0$ plasma behaves as a gyrotropic medium: e.g., v_x component is not only proportional to E_x , but depends also on E_y .

If v_i as a function of \vec{E} are known, the current density can be easily computed $\vec{j} = \sum_{s=e,i} q_s n_s \vec{v}_s$ and formally written as $\vec{j} = \overline{\sigma}\vec{E}$ ($\overline{\sigma}$ is defined as the conductivity tensor). The second equation (9) is often re-written in a simpler form, by combining the two terms at the right-hand side

$$\text{rot}\vec{B} = \frac{1}{c}\frac{\partial\vec{E}}{\partial t} + \frac{4\pi}{c}\vec{j} = \frac{1}{c}\frac{\partial(\vec{\epsilon}\vec{E})}{\partial t}, \quad (11)$$

and introducing a quantity $\vec{\epsilon}$, which is called as the plasma dielectric tensor. The plasma dielectric and the conductivity tensors are related via $\vec{\epsilon} = \vec{I} + (4\pi i/\omega)\overline{\sigma}$.

Then, by introducing the wave refractive index $\vec{n} = c\vec{k}/\omega$, Eqs. (9) and (11) can be merged into a single equation for the RF electric field \vec{E}

$$\vec{n}\times(\vec{n}\times\vec{E}) + \vec{\epsilon}\vec{E} = 0. \quad (12)$$

In the cold plasma limit, the plasma dielectric tensor is a function of the imposed wave frequency (see Eqs. (10)), but is independent of the wave number. The Stix's notation for $\vec{\epsilon}$ is commonly adopted [15]

$$\vec{\epsilon} = \vec{\epsilon}(\omega) = \begin{pmatrix} S & -iD & 0 \\ +iD & S & 0 \\ 0 & 0 & P \end{pmatrix}, \quad (13)$$

where $S(\omega) = 1 - \sum_s \omega_{ps}^2/(\omega^2 - \omega_{cs}^2)$, $D(\omega) = \sum_s (\omega_{cs}/\omega)(\omega_{ps}^2/(\omega^2 - \omega_{cs}^2))$, $P(\omega) = 1 - \sum_s \omega_{ps}^2/\omega^2$, and $\omega_{ps}^2 = 4\pi n_s q_s^2/m_s$ is the square of the plasma frequency.

Equation (12) is a set of three coupled, linear, homogeneous equations for the three components of the RF electric field. Requiring non-trivial solutions to exist, the determinant of these equations must vanish, and one can obtain the wave dispersion relation, which defines the refractive index n as a function of wave frequency ω :

$$A(\omega, \theta)n^4 - B(\omega, \theta)n^2 + C(\omega, \theta) = 0, \quad (14)$$

where θ is an angle between the wave vector and the confining magnetic field ($k_y = 0$), and the functions $A(\omega, \theta)$, $B(\omega, \theta)$ and $C(\omega, \theta)$ can be easily derived (see, e.g., [15]).

Equation (14) is a bi-quadratic, and hence for any ω there are two – generally different – solutions $n^2 = n_{1,2}^2(\omega)$. This means that within the cold plasma approximation for any wave frequency plasma supports two different wave modes (with a different dispersion relation). In hot plasmas, the dielectric tensor is also a function of the wave number \vec{k} , which leads to the appearance of extra new modes and solutions, and makes wave physics more complicated.

For heating fusion plasmas, the electromagnetic waves are usually excited to propagate predominantly perpendicular to the confining magnetic field. For a simplified limiting case of purely perpendicular propagation $\theta = \pi/2$, the wave resonances are determined by the condition

$$A(\omega, \theta = \pi/2) = S(\omega) = 1 - \sum_{s=e,i} \frac{\omega_{ps}^2}{\omega^2 - \omega_{cs}^2} = 0. \quad (15)$$

This is a desired equation for computing the resonant wave frequencies (for a perpendicular, cold plasma resonance). The solutions of Eq. (15) define the range of electromagnetic frequencies used for efficient plasma heating and current drive in fusion plasmas.

Resonant wave frequencies

Before we proceed to finding solutions of Eq. (15), it is helpful to note that the electron plasma and electron cyclotron frequencies are comparable in the core of fusion plasmas ($\omega_{pe}/\omega_{ce} \approx 3\sqrt{n_{e,20}}/B_T$; B_T is the confining magnetic field in Tesla), and the relation $\omega_{pi}^2/\omega_{ci}^2 \gg 1$ holds for bulk ions. Another useful identity is $\omega_{pe}^2/|\omega_{ce}| = \sum_i \omega_{pi}^2/\omega_{ci}$ – this is just the charge quasi-neutrality re-written in a different way.

1) ECRF (electron cyclotron range of frequencies), $f \simeq f_{ce} \gg f_{ci}$.

For this frequency range ions are immobile and Eq. (15) can be simplified by neglecting the ion contribution term ($\simeq \omega_{pi}^2/\omega_{ce}^2 \propto m_e/m_i \ll 1$)

$$S(\omega) = 1 - \sum_i \frac{\omega_{pi}^2}{\omega^2 - \omega_{ci}^2} - \frac{\omega_{pe}^2}{\omega^2 - \omega_{ce}^2} = 0. \quad (16)$$

This defines the resonant frequency known as the upper hybrid (UH) resonance

$$\omega_{UH}^2 = \omega_{ce}^2 + \omega_{pe}^2. \quad (17)$$

The word ‘hybrid’ refers here that the resonant frequency involves both ω_{ce} and ω_{pe} . The upper hybrid frequency is somewhat above ω_{ce} . Since $f_{ce} \approx 28 \times 10^9 B_T$, ECRF heating requires sources in the range 100–200 GHz. Note that gyrotrons – sources for ECRF heating – can deliver one or a few wave frequencies only. For ITER, $f = 170$ GHz is selected and the radiofrequency sources for the ECRF system will be composed of 24 gyrotrons (with 1 MW unit output).

2) ICRF (ion cyclotron range of frequencies), $f \simeq f_{ci} \ll f_{ce}$.

For this frequency range, a resonant frequency occurs when there are two or more ion species present in a plasma

$$S(\omega) = 1 - \frac{\omega_{p1}^2}{\omega^2 - \omega_{c1}^2} - \frac{\omega_{p2}^2}{\omega^2 - \omega_{c2}^2} - \frac{\omega_{pe}^2}{\omega^2 - \omega_{ce}^2} = 0. \quad (18)$$

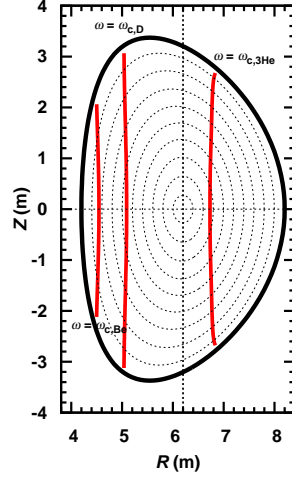


Figure 5: Location of ion cyclotron resonance layers in ITER-like plasma for $f = 50$ MHz ($B_0 = 5.3$ T).

Then, the vacuum and electron contributions are negligible in comparison with the contributions due to ion species, which balance each other.

The solution of Eq. (18) is referred to as the ion-ion hybrid (or Buchsbaum) resonance

$$\omega_{IIH}^2 = \frac{\omega_{p1}^2 \omega_{c2}^2 + \omega_{p2}^2 \omega_{c1}^2}{\omega_{p1}^2 + \omega_{p2}^2}. \quad (19)$$

One can show that the ion-ion hybrid resonant frequency is bounded between the two ion cyclotron frequencies, $\min(\omega_{c1}, \omega_{c2}) < \omega_{IIH} < \max(\omega_{c1}, \omega_{c2})$. The most successful ICRF heating scenario – minority ion heating – relies on wave absorption by a small fraction of resonant minority ions (e.g, H) in deuterium majority plasmas (minority and majority ions should have different q/m). If the concentration of minority ions is much less than the concentration of majority ions, then $\omega_{IIH} \approx \omega_{c, \text{minor}}$.

Wave absorption by ions occurs in the vicinity of the ion cyclotron fundamental resonance ($\omega = \omega_{ci}$) and harmonic ($\omega = N\omega_{ci}$, $N \geq 2$) layers. The latter is a finite-Larmor-radius effect and usually requires significant plasma beta and pre-heating to become efficient. Since the magnetic field in tokamaks is inversely proportional to the distance to the torus axis, $B(R) \simeq B_0 R_0/R$, the lines of the ion cyclotron resonance are (almost) vertical lines in (R, Z) plane and can be determined from the following simple equation:

$$R_{IC} \Big|_{\omega=N\omega_{ci}} \approx R_0 (N \times Z_i/A_i) \frac{15.2 B_0(\text{T})}{f(\text{MHz})} \quad (20)$$

($N = 1$ for the fundamental resonance, and $N \geq 2$ for harmonic resonances). Figure 5 shows the location of the ion cyclotron resonances in ITER-like plasma

for the wave frequency $f = 50$ MHz ($B_0 = 5.3$ T, $R_0 = 6.2$ T). Note that the cyclotron resonance of ${}^3\text{He}^{2+}$ ions is located at $R \approx 6.8$ m. It can be easily shifted to the plasma center for core ion heating by adopting a different wave frequency $f = 54$ MHz.

Frequencies used for ICRF heating in present-day fusion devices usually vary from 20 MHz to about 100 MHz, depending on the central magnetic field and ion species used for plasma heating. Note that – unlike gyrotrons – ICRF generators are much more flexible in varying wave frequency, and at every device a number of different wave frequencies are normally available for plasma heating. For instance, A2 ICRF antennas on JET have been designed to operate within the frequency range $f = 23 - 55$ MHz. For ITER, the bandwidth $f = 40 - 55$ MHz has been chosen.

iii) LH (lower hybrid), $f = f_{\text{LH}}$, $f_{ci} \ll f_{\text{LH}} \ll f_{ce}$.

In the intermediate frequency range between the ion and electron cyclotron frequencies, $\omega_{ci} \ll \omega \ll \omega_{ce}$, there exists another solution of Eq. (15):

$$S(\omega) = 1 - \sum_i \frac{\omega_{pi}^2}{\omega^2 - \omega_{ci}^2} - \frac{\omega_{pe}^2}{\omega^2 - \omega_{ce}^2} = 0. \quad (21)$$

For this frequency range, one can neglect ω_{ci}^2 in the denominator of the second term and ω^2 in the denominator of the third term. The corresponding solution of Eq. (21) is known as the lower hybrid resonance

$$\omega_{\text{LH}}^2 = \frac{\sum_i \omega_{pi}^2}{1 + \omega_{pe}^2/\omega_{ce}^2}. \quad (22)$$

If the second term in the denominator of Eq. (22) is much larger than one (case often relevant for astrophysical plasmas), then $\omega_{\text{LH}} \approx \sqrt{\omega_{ci}\omega_{ce}}$. The LH heating utilizes the frequency range $f \approx 1 - 8$ GHz and is mainly used for non-inductive current-drive.

Another important factor, which influences the wave damping strength, is the wave polarization. For cyclotron resonance heating, a strong wave absorption requires a presence of the wave electric field component, which rotates in the same sense as ions for ICRF heating, and as electrons for ECRF heating. In inhomogeneous plasmas (which is the case for toroidal plasmas since B and n_e vary with the radial coordinate) – in addition to resonant frequencies – there can be cutoff frequencies (defined as $n(\omega_{\text{cutoff}}) = 0$), where the incoming wave is partially reflected. Furthermore, plasmas support at least two different modes at the same wave frequency, and there are special cases, when one wave mode can be transformed into another mode with a different dispersion relation. This phenomenon is called as mode conversion and has been also actively exploited for efficient RF heating.

IV. FURTHER READING

This note is complementary to the more detailed lectures on NBI and fast-particle heating [3], and RF heating [10, 13] of the CMSS12. A comprehensive introduction to the physics of plasma heating can be found in books [1, 2]. Articles [9] and [17, 18] are focused on a discussion of heating systems of ITER and JET tokamaks. For an in-depth discussion on plasma waves, books [15, 16] are recommended.

REFERENCES

1. J. Wesson, “Tokamaks” (Oxford: Clarendon) (2004).
2. J. Freidberg, “Plasma Physics and Fusion Energy” (Cambridge University Press) (2007).
3. R. Koch and D. Van Eester, “Fast particle heating”, these proceedings.
4. C.F. Barnett, “Atomic Data for Fusion, vol. 1, Collisions of H, H₂, He and Li Atoms and Ions with Atoms and Molecules”, Report ORNL-6086 (1990).
5. D. Ćirić et al., *Fusion Engineering and Design* **86**, 509–512 (2011).
6. R. McAdams, “Beyond ITER: Neutral beams for a demonstration fusion reactor (DEMO)”, *Review of Scientific Instruments* **85**, 02B319 (2014).
7. R. Hemsworth et al., “Status of the ITER heating neutral beam system”, *Nuclear Fusion* **49**, 045006 (2009).
8. R.K. Janev, C.D. Boley and D.E. Post, “Penetration of Energetic Neutral Beams into Fusion Plasmas”, *Nuclear Fusion* **29**, 2125–2140 (1989).
9. ITER Physics Expert Group on Energetic Particles, Heating and Current Drive, *Nuclear Fusion* **39**, 2495–2539 (1999).
10. E. Westerhof, “Electron cyclotron waves”, these proceedings.
11. P. Dumortier and A.M. Messiaen, “ICRH Antenna Design and Matching”, these proceedings.
12. F. Louche and R. Koch, “The Coupling of Electromagnetic Power to Plasmas”, these proceedings.
13. R. Koch, “The ion cyclotron, lower hybrid and Alfvén wave heating methods”, these proceedings.
14. D. Van Esster and E. Lerche, “Kinetic Theory of Plasma Waves”, these proceedings.
15. T.H. Stix, “Waves in Plasmas” (New York: AIP) (1992).
16. M. Brambilla, “Kinetic Theory of Plasma Waves – Homogeneous Plasmas” (Oxford: Clarendon) (1998).
17. J.-M. Noterdaeme et al., *Fusion Science and Technology* **53**, 1103–1151 (2008).
18. M.-L. Mayoral et al., *Nuclear Fusion* **54**, 033002 (2014).

THE COUPLING OF ELECTROMAGNETIC POWER TO PLASMAS

F. Louche & R. Koch

*Plasma Physics Laboratory
Ecole Royale Militaire - Koninklijke Militaire School
1000 Brussels - BELGIUM; EURATOM-Belgian State Association*

ABSTRACT

This lecture addresses, on the basis of elementary and intuitive treatment, the process of coupling of electromagnetic power to plasma. Coupling is here meant in a broad sense. It consists of four different steps. (i) The first one is the coupling of vacuum electromagnetic power to plasma waves. An elementary antenna coupling theory is given. The state of the art in coupling models and status of comparisons with experiments are briefly discussed. (ii) The second is the transfer of plasma wave energy to particle energy. The resonant processes leading to this transfer are described in a heuristic way. (iii) The third one is the build-up of fast particle populations. It will be outlined through a sketch of quasilinear diffusion for the simple case of Landau damping. (iv) The last step is the conversion of power through the resonant particle population to bulk plasma heating by collisions, which will be briefly addressed.

I. INTRODUCTION

The principle of wave heating is similar for all schemes and is sketched in Fig.1. The electromagnetic energy is produced by a generator and sent to the machine area via transmission lines constituted of coaxial lines at low frequency and waveguides at higher frequency. At very high frequency optical transmission is also possible. Some matching circuitry has to be incorporated in the transmission system in order to prevent the reflected power to come back to the generator. The transmission line is connected to some launching structure (antenna, waveguide,) that will couple the power inside the machines vacuum chamber. The vacuum wave that exists inside the launching structure and at the very edge of the plasma is then converted to a plasma wave that transports electromagnetic energy to some region inside the plasma where it will be absorbed. This is the region where the resonant process occurs. This process accelerates the population of particles that is in resonance with the wave, usually a small fraction of the plasma particles. A slightly or strongly non-maxwellian resonant population builds up against the restoring force of collisions between this population and the remainder of

the plasma. It is through the latter collisional process that the bulk of the plasma is heated up. In this paper, we shall not describe the technical parts of the launching systems, i.e. generators, transmission lines, matching systems (see lecture by Dumortier [2]), but shall focus on the physics of power coupling. Let us first start with the elementary wave theory.

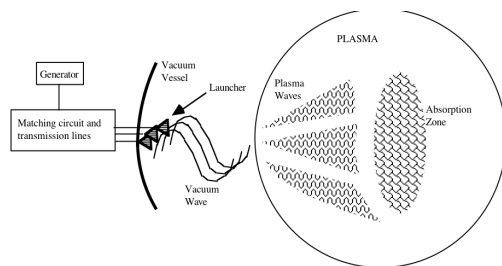


Figure 1: Principle of heating by plasma waves

II. WAVE PROPAGATION IN A PLASMA

The study of plasma waves is a very broad subject and we will limit ourselves to the cold-plasma approximation [1] which is mostly sufficient to describe the basic propagation properties of the waves used in plasma heating. Interested readers should consult references [8, 9] for an exhaustive description of plasma waves.

We consider a plasma immersed in a static magnetic induction field \vec{B}_0 . If the wave is considered as a first-order perturbation with a harmonic space-time dependence $\sim \exp[-i(\omega t - \vec{k} \cdot \vec{x})]$ then the cold-plasma dispersion relation can be written[8]:

$$\mathbf{D} \cdot \vec{E} = \vec{k} \times (\vec{k} \times \vec{E}) + \frac{\omega^2}{c^2} \epsilon \cdot \vec{E} = 0 \quad (1)$$

where \vec{k} is the wave vector, \vec{E} is the wave electric field, ω is the generator angular frequency and c is the speed of light. It is sometimes useful to work instead with the refractive index vector $\vec{n} = \vec{k}/k_0$ where $k_0 = \omega/c$

is the vacuum wave vector. The components of the cold-plasma dielectric tensor ϵ are given by [8]:

$$\epsilon = \begin{pmatrix} \epsilon_{\perp} & i\epsilon_{xy} & 0 \\ -i\epsilon_{xy} & \epsilon_{\perp} & 0 \\ 0 & 0 & \epsilon_{\parallel} \end{pmatrix} \text{ with } \begin{cases} \epsilon_{\perp} = 1 - \sum_s \frac{\omega_{ps}^2}{\omega^2 - \omega_{cs}^2} \\ \epsilon_{xy} = \sum_s \frac{\omega_{ps}^2 \Omega_{cs}}{(\Omega_{cs}^2 - \omega^2)\omega} \\ \epsilon_{\parallel} = 1 - \sum_s \frac{\omega_{ps}^2}{\omega^2} \end{cases} \quad (2)$$

The wave equation is an algebraic homogeneous system of 3 equations for the 3 cartesian components of the electric field. It will have a non vanishing solution if and only if the determinant of \mathbf{D} is zero. This defines the dispersion relation, an implicit relation between the generator frequency, the parallel and perpendicular components of the refractive index vector n_{\perp} and n_{\parallel} , and the plasma properties (encoded in the dielectric tensor). The dispersion equation solution determines all the wave modes which can propagate in the plasma for a given plasma model. If the static magnetic induction \vec{B}_0 is taken along the z -direction of a cartesian frame, then, because of the isotropy in the plane parallel to \vec{B}_0 , the direction of the perpendicular component of the wave vector k_{\perp} is irrelevant and can be arbitrarily chosen as x -direction. The dispersion equation is then expressed as a bi-quadratic equation in $n_{\perp} = |n_{\perp}|$:

$$\begin{vmatrix} \epsilon_{\perp} - n_{\parallel}^2 & i\epsilon_{xy} & n_{\perp} n_{\parallel} \\ -i\epsilon_{xy} & \epsilon_{\perp} - n_{\perp}^2 - n_{\parallel}^2 & 0 \\ n_{\perp} n_{\parallel} & 0 & \epsilon_{\parallel} - n_{\perp}^2 \end{vmatrix} = 0 \quad (3)$$

We shall generally express its solution as $k_{\perp}^2 = \kappa(k_{\parallel}, \omega)$ because k_{\parallel} is generally fixed by the launcher structure. The two roots are often called fast (or magnetosonic) and slow waves. Their behaviour will be studied in details in [3, 4] for the various range of frequencies. For our purpose we simply need to underline that at some frequencies (corresponding to specific locations in the plasma) "something can happen" ! First, the dielectric tensor becomes singular each time $\omega = \omega_{cs}$. This means that the particle current becomes infinite for a finite electric field (*wave-particle resonances* discussed in sections IV-C, D, E). The other special frequencies are those for which $k_{\perp}^2 \rightarrow \infty$ and appear when $\epsilon_{\perp} = 0$. We speak about *wave resonances* and they will be discussed in section IV-B. In addition, at low frequencies -ion cyclotron range of frequencies or below- ϵ_{\parallel} is much larger than the other elements such that the dispersion equation reduces to the top left 2X2 determinant (3). This approximation corresponds to the zero electron mass limit and leaves only one wave (the fast wave) in the dispersion. In the ICRH the slow wave is evanescent almost everywhere in the plasma bulk, and practically the zero electron mass limit is equivalent to neglecting the parallel component of the electric field. This can be forced by setting up a screen in front of the launcher.

III. ELEMENTARY WAVE COUPLING THEORY

A. Types of launcher and coupling

The simplest case is that of electron cyclotron waves in large machines. In this case, the wavelength of the vacuum wave $\lambda = 2\pi/k_0$ is very small as compared to the plasma cross-section. The wave is launched as a propagating wave pencil that will progressively convert to a plasma wave. Because of the smallness of the wavelength, the boundary conditions at the conducting wall of the machine, as well as on the launching structure, play no explicit role. The wave can be accurately described in the geometric optics limit and the only boundary conditions that matter are the initial launching angle and reflections at the wall, if any.

If the vacuum wavelength becomes comparable to the antenna structure, the scale length of variations of edge plasma parameters or the plasma radius, the launcher environment and the plasma will affect the coupling process and a full boundary-value problem has to be solved to describe it. Such is usually the case of Alfvén wave, ion cyclotron, or lower hybrid wave launchers in medium or large-size machines. But this may also be the case of electron cyclotron launchers in low-field, small machines.

We shall now introduce coupling theory, on the basis of the simplest model. More sophisticated theories rest on similar principles but include more of a realistic geometry.

B. Coupling model

We consider the simplest case of an antenna facing a large plasma such that the plasma looks nearly uniform in the toroidal (z) and poloidal (y) directions (Fig.2). In the radial direction x the plasma is usually non-uniform, and this is taken into account in standard coupling models, but here, in order to simplify the algebra, we consider a step model. The density is zero for $x < 0$ and constant density for x positive. The influence of a realistic density profile was studied in [30]: the cut-off position and the density gradient were shown to have a primary importance in the assessment of an antenna coupling capabilities, but these considerations are out of the scope of the present introduction. We assume that the absorption is good and hence, there is no reflected wave. This is the so-called single-pass approximation. In addition, we shall also assume that the system is invariant in the y -direction (which implies in particular that the antenna is infinite) and neglect propagation in the y -direction ($k_y = 0$). Next, we have to choose a model for the plasma waves. To be specific, we choose the case of coupling in the ion cyclotron frequency range (ICRF). The slow wave being evanescent in the plasma bulk, we shall consider only coupling to the fast magnetosonic wave (FW). As the FW equations will be

needed later on, we first derive them, starting from the cold wave theory.

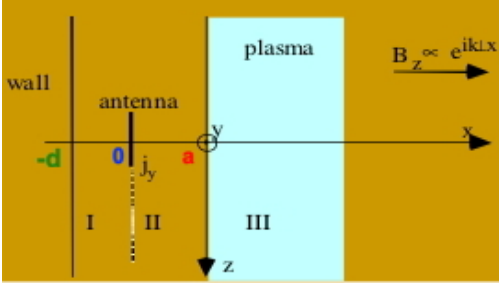


Figure 2: 2-D slab coupling model. The plasma is uniform in the y (poloidal) and z (toroidal) directions. The width of the antenna is $2w_z$, the distance between the antenna and the plasma is a and the distance between the antenna and the wall is d .

C. The fast magnetosonic wave equation

We write the full cold-plasma dispersion relation in terms of the parallel ($n_{\parallel} = n \sin \theta$) and perpendicular ($n_{\perp} = N \cos \theta$) components of the refractive index

$$n_{\parallel} = \frac{k_{\parallel}}{k_0}; n_{\perp} = \frac{-i}{k_0} \frac{d}{dx} \quad (4)$$

We keep to n_{\perp} its operator meaning because x is the direction of inhomogeneity. In the parallel direction, the plasma is homogeneous and we use the Fourier transformed form. The dispersion equation (3) derived previously can be used and we take the zero electron mass limit to uncoupling the FW. This limit implies that the parallel electric field cannot penetrate the plasma, i.e. that the evanescence length of the slow wave is zero. Eq. (1) can be recast to

$$k_{\perp,FW}^2 E_y = -i \left(\frac{d}{dx} + \mu k_y \right) (\omega B_z) \quad (5a)$$

$$k_{\perp,FW}^2 E_x = - \left(k_y + \mu \frac{d}{dx} \right) (\omega B_z) \quad (5b)$$

$$i\omega B_z = \frac{d}{dx} E_y - ik_y E_x \quad (5c)$$

with $\mu = \epsilon_{xy} k_0^2 / u$, $u = k_0^2 \epsilon_{\perp} - k_{\parallel}^2$ and $k_{\perp,FW}^2 = u(1 - \mu^2)$. The other components of the FW field follow from Maxwell's equation $i\omega \vec{B} = \vec{\nabla} \times \vec{E}$ (with $E_z = 0$):

$$B_x = \frac{-k_{\parallel}}{\omega} E_y; \quad B_y = \frac{k_{\parallel}}{\omega} E_x \quad (6)$$

Finally, taking the limit $k_y \rightarrow 0$ and eliminating B_z from (5a)-(5c), we obtain the FW equation:

$$\frac{d^2 E_y}{dx^2} + k_{\perp,FW}^2 E_y = 0 \quad (7)$$

D. The Plasma surface impedance

For a uniform plasma, the wave equation (7) has constant coefficient and the solutions are simply exponential. The single-pass approximation allows us to impose at $z \rightarrow \infty$ a *radiating boundary condition* and the wave solution in the plasma can be written:

$$E_y = C_{III} \exp(ik_{\perp,FW} x) \quad (8)$$

where C_{III} is a constant (relative to region III in Fig. 2) to be determined. Eq. (6) then gives the H_z component:

$$B_z = \frac{k_{\perp,FW}}{\omega} E_y \quad (9)$$

The field in the plasma is thus known up to a multiplicative constant. Tangential field components being continuous at the plasma-vacuum interface (II-III), their ratio is also continuous. This quantity is known as the *surface impedance* of the plasma Z_S

$$Z_S = \frac{E_y}{\omega B_z} = \frac{1}{k_{\perp,FW}} \quad (10)$$

We express the continuity of this quantity at $x = 0$ as

$$[[Z_S]]_0 = Z_S(0_+) - Z_S(0_-) = 0 \quad (11)$$

In the general case where all field components are to be considered, the equivalent of (10) is a vector relation and \mathbf{Z}_S is the surface impedance matrix:

$$\begin{pmatrix} E_y \\ E_z \end{pmatrix} = \mathbf{Z}_S \begin{pmatrix} \omega B_y \\ \omega B_z \end{pmatrix} \quad (12)$$

E. Fields in the vacuum region I-II

Equipped with this boundary condition, the vacuum problem can be solved on its own. The plasma properties will enter its solution only via the quantity Z_S and the vacuum solution is therefore formally independent of the particular plasma model considered. The general electromagnetic field in vacuum can be decomposed into its TE (transverse electric) and TM (transverse magnetic) parts with respect to a given direction, here z . Maxwell's equations then appear in the form:

$$\begin{pmatrix} B_x \\ E_y \end{pmatrix} = \frac{1}{k_0^2 - k_{\parallel}^2} \begin{pmatrix} -i\omega/c^2 & ik_{\parallel} \\ ik_{\parallel} & -i\omega \end{pmatrix} \begin{pmatrix} ik_y E_z \\ dB_z/dx \end{pmatrix} \quad (13a)$$

$$\begin{pmatrix} E_x \\ B_y \end{pmatrix} = \frac{1}{k_0^2 - k_{\parallel}^2} \begin{pmatrix} -i\omega & ik_{\parallel} \\ -ik_{\parallel} & i\omega/c^2 \end{pmatrix} \begin{pmatrix} -ik_y B_z \\ dE_z/dx \end{pmatrix} \quad (13b)$$

$$\frac{d^2}{dx^2} \begin{pmatrix} E_z \\ B_z \end{pmatrix} = (k_y^2 + k_{\parallel}^2 - k_0^2) \begin{pmatrix} E_z \\ B_z \end{pmatrix} \quad (14)$$

From this it can be seen that the problem can be solved independently for E_z and B_z . The TM part

of the field, which has a longitudinal (along z) \vec{E} component does not couple to the plasma waves because $E_z = 0$ in the plasma (see section II). Therefore, for the simplified problem considered here, we can retain the TE mode alone and ignore the field components deriving from E_z . The solution for the two vacuum regions is elementary:

$$\text{Region I: } B_z = A_I \cosh k_{\parallel} x + B_I \sinh k_{\parallel} x \quad (15a)$$

$$\text{Region II: } B_z = A_{II} \cosh k_{\parallel} x + B_{II} \sinh k_{\parallel} x \quad (15b)$$

where the A 's and the B 's are constants to be determined by the following boundary conditions:

- At the metallic wall $x = -d$: $E_y = 0$ (16a)

- The antenna is represented by an infinitely thin current sheet of finite width w and infinite length. This gives rise to a jump condition on the tangential magnetic field: $[[B_z]]_0 = -\mu_0 j_y$ (16b)

- and a continuity condition $[[E_y]]_0 = 0$ (16c)

- At the plasma surface, $x = 0$: $[[Z_s]]_a = 0$ (16d)

These conditions are sufficient to determine the 4 constants in (15a) and (15b). In particular, this gives the relation between all field components and their source, the current density at the antenna j_y [12].

There is one additional condition, the continuity of E_y (or B_z) at $x = a$ that was not necessary to solve the vacuum problem. It can be used to determine C_{III} in Eq. (8) as all field quantities in the vacuum region are now known.

F. Poynting's theorem and antenna radiation

Let us consider in the vacuum region I-II an arbitrary volume containing the antenna. Starting from Maxwells equations, one can easily write down Poynting's theorem [7] from which we get the complex radiated power in region II for an antenna current \vec{j}_A :

$$P = -\frac{1}{2} \int_V \vec{E} \cdot \vec{j}_A dV \quad (17)$$

On the r.h.s. appears the work done by the electric field on the antenna current. Strictly speaking, it should be zero because the antenna is a metallic conductor on which the tangential electric field should vanish. It is non-zero because the current distribution on the antenna has been *assumed* rather than self-consistently computed. This is known as the *induced e.m.f. method*. Though it may appear rough, this method usually gives good results if the assumed current is a reasonable guess of the exact one. In more sophisticated computations[16, 22], the current distribution on the antenna is self-consistently determined. A theory completely similar to the above one can be done for waveguide[16] or aperture launchers. In these cases, the incoming wave field distribution on the aperture is given and the field reflected by the plasma

and surrounding structures is the result of the computation. Alternatively, the above formalism can be applied without changes if the aperture boundary condition is expressed as an equivalent current density[25]. It is to be observed that the quantity on the r.h.s. of Eq.(17) has both a real and an imaginary part. The real part is the power radiated by the antenna, while the imaginary part is related to the reactive properties of the antenna, as we will see. We can compute the former for our simplified model. First we rewrite Poyntings theorem (17) in terms of the k_{\parallel} field spectrum using Parseval's relation:

$$P = -\frac{1}{2} \int_V E_y j_y^* dV = -\frac{1}{4\pi} \int_{-\infty}^{\infty} E_y(k_{\parallel}) j_y(k_{\parallel}) dk_{\parallel} \quad (18)$$

The Fourier spectrum of the electric field $E_y(k_{\parallel})$ is evaluated in region II, in front of the strap ($x = 0$) and is given by:

$$E_y(k_{\parallel}) = \omega \mu_0 (g_2 - i h_2) j_y(k_{\parallel}) \quad (19a)$$

with

$$g_2 - i h_2 = \frac{i \sinh k_{\parallel} d}{k_{\parallel}} \frac{\sinh k_{\parallel} a - i Z_S \cosh k_{\parallel} a}{\sinh k_{\parallel} (a + d) - i Z_S \cosh k_{\parallel} (a + d)} \quad (19b)$$

The antenna radiation spectrum can be obtained from the Poynting theorem and taking the real part of it

$$\Re(P) = -\frac{\omega \mu_0}{4\pi} \int_V g_2 |j_y|^2 dk_{\parallel} \quad (20)$$

If we take the limit $d \rightarrow \infty$

$$\Re(P) \sim -\frac{\omega \mu_0}{4\pi} \int_V \frac{k_{\perp}}{k_{\perp}^2 + k_{\parallel}^2} e^{-2|k_{\parallel}|a} |j_y|^2 dk_{\parallel} \quad (21)$$

This expression highlights one of the fundamental challenges of low frequency wave heating, namely the fact that ingoing waves undergo a strong *evanescence* in the vacuum layer between the antenna and the plasma and are furthermore confronted on their path to the plasma bulk with brutal *refractive index change*, leading to a strong reflection at plasma vacuum interface. The k_{\parallel} spectrum of a given launcher is mostly determined by the geometry of the launcher. For a simple radiating strap of width w it is given by $k_{\parallel} \sim \pi/w$. Therefore the radiated power will decay as $\exp(-2\pi a/w)$. This provides a simple rule to estimate the evanescence of the field launched by the antenna in vacuum. If the launcher is made of an array of identical elements spaced by $L_z < w$ in the toroidal direction and excited with a phase difference $\Delta\Phi$, then the typical parallel wave vector must be taken as $k_{\parallel} a = \Delta\Phi/L_z$. Evanescence will then be stronger than in the previous case of an unphased structure. One could think that working with an antenna spectrum peaking at $k_{\parallel} = 0$ (monopole phasing) could solve this problem. Actually realistic plasma surface spectra displays large contributions occurring

for $k_{\parallel} < k_0$, but they are due to coaxial & surface modes[14]. The coaxial modes correspond to TEM/ z or TE/ z electromagnetic waves propagating between the tokamak wall and the plasma column, which plays the role of a lossy metal wall. These modes lead to power deposition in the SOL and wall region.

G. Antenna coupling properties

The structure of the antenna modelled in the present exercise is basically that of a strip-line, i.e. a conductor running above an infinite conducting plane. The field in such a strip line is known to have a TEM (transverse electro-magnetic) structure, like a coaxial transmission line. A TEM field has the property that the electric and magnetic field structure in the transmission line cross-section is the same as that respectively of the electrostatic and magnetostatic field it can sustain. Therefore, the antenna properties can be computed in the electrostatic and magnetostatic limits and used as in transmission line theory. We shall recast the results obtained above in terms of strip line characteristics. This formalism is often used in practice to represent properties of real ICRF antennas, which structure is indeed close to that of strip lines. The radiation impedance Z_A of the antenna can be obtained by equating the power flow to the same expression for a transmission line:

$$-\frac{1}{2} \int_V \vec{E} \cdot \vec{j}_A dV = \frac{1}{2} (R + iX) I^2 \quad (22)$$

where I is the total current flowing on the antenna, R and $X = -\omega L$ being respectively the specific input resistance and reactance of the line, and L being the specific inductance. From the spectral form of Poynting's theorem (17) we obtain:

$$\frac{1}{2} (R - i\omega L) I^2 = -\frac{1}{4\pi} \int_{-\infty}^{\infty} E_y(k_{\parallel}) j_A(k_{\parallel}) dk_{\parallel} \quad (23)$$

The previous equality constitutes the definition of the two quantities R and L in the present antenna model. The plasma enters their definition only through the functions g_2 and h_2 (19b). No equivalent capacitance C appears in Eq.(23) because we have dropped the TM part of the field. It can however easily be obtained by solving the TM vacuum field equations with the boundary condition $E_y = 0$ at the plasma $x = 0$. The three constants R , L , C completely determine the properties of the transmission-line equivalent to the antenna[11, 12] and are of primary interest for the design of the transmission and matching system[2].

H. Radiated field

Using the additional boundary condition at the plasma-vacuum interface, i.e. continuity of E_y , the field in the plasma can also be computed and used to determine the properties of the radiated far field [15]. In Fig. 3, the far field Poynting flux distribution over constant phase surfaces is shown for a phased antenna

array in an ITER-like plasma. As the Poynting flux is the RF power flux, this shows how phasing, by sending the power at different parallel wave numbers sends it in different spatial directions as well.

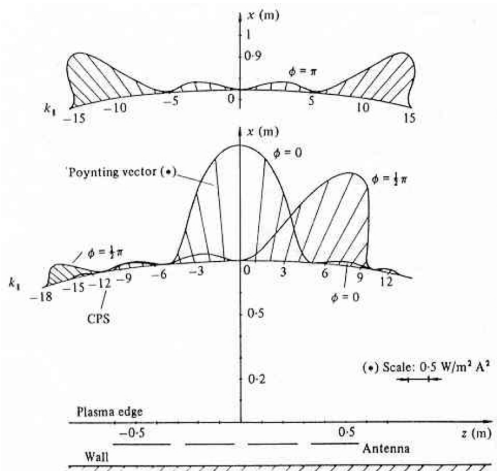


Figure 3: Distribution of the Poynting vector in the far-field region for three different phase differences Φ between successive straps of a 4-strap antenna array. From[15].

I. State of the art

The theory presented in the previous sections is as we said simple: it neglects feeders, poloidal antenna inhomogeneity and plasma density profile. These limitations were assessed in [12, 13] notably, and it appears that such a simple model can fairly reproduce most of the coupling properties of more realistic antenna models. Nevertheless the rigorous self-consistent solution of the full boundary-values problem is a formidable task that can only be tackled with numerical codes. A review of the early development of sophisticated coupling codes can be found in the review[21] to which one must add reference to the RANT-3D code[20] describing coupling of recessed antennas to plasma. Both in ICANT[22] and in TOPICA[25] detailed current distributions are now computed over all antenna parts. In parallel to the development of these plasma coupling codes, sophisticated commercial codes have been used to compute and optimise the reactive properties of antennas in vacuum or in the presence of a dielectric[23, 26, 29]. In this process, it was shown that an adequately chosen dielectric can to some extent simulate coupling to a plasma[26]. Antenna models have been compared with success to experimental results in a number of cases, both in the ICRF[20, 25, 17, 18, 27] and Lower Hybrid range[19] and are used to predict the performance of ITER antennas[28, 29].

IV. POWER COUPLING FROM WAVES TO PARTICLES

A. Absorption mechanisms

Once the wave has been launched in the plasma, one could think that it can be damped simply because the accelerated particles experience a drag due to collisions. This is in general not the case. In the bulk of a hot plasma, e.g. $T_e \simeq T_i = 5 \text{ keV}$, $n = 5 \cdot 10^{19} \text{ m}^{-3}$ the collision frequency is

$$\nu = 2.9 \cdot 10^{-12} n \ln \Lambda T^{-3/2} = 20 \text{ kHz} \quad (24)$$

In electromagnetic theory the ratio ν/ω , ($\omega = 2\pi f$) is characteristic of the importance of dissipative effects due to collisions with respect to reactive, i.e. wave oscillation, energy. For small values of ν/ω , the motion is almost dissipation-less and huge fields and large perturbations in the particle motion are necessary if any significant amount of energy is to be damped in the plasma. Equation (24) implies that, at frequencies in the MHz range or higher, direct dissipation of the wave by collisions will be negligible. In order to magnify collisional absorption one has recourse to *resonances*. Under resonance conditions, a small excitation will create either a huge response in the particle's motion (*wave-particle* resonance) or large wave-field build-up (*wave* resonance). In Fig.1 the "absorption zone" is the region where such a resonance takes place (the shape is of course only symbolic).

B. Wave resonances

Assuming that k_{\parallel} is for the essential determined by the antenna system, and thus fixed, we shall characterise the resonance by $k_{\perp} \rightarrow \infty$. An example of wave resonance is that of the fast wave, Eq.(7), when $u = k_0^2 \varepsilon_{\perp} - k_{\parallel}^2 = 0$. We notice that, as we proceed from the plasma edge to the plasma inside, e.g. along the major radius direction (x), ε_{\perp} will vary because both the magnetic field and the plasma density vary. If the resonance is isolated from the cut-off, the wave is absorbed at resonance [8]. Typically we have both a cut-off and a resonance in the plasma, with a region between them where the wave is evanescent. If the distance between cut-off and resonance is not too large, it is possible for part of the wave energy to tunnel through the evanescent region. This *back-to-back resonance and cut-off* (assumed located at $x = 0$) can be described by a simple wavenumber dependence of the form

$$k_{\perp,FW} = k_{\infty}^2 - \frac{\alpha}{x} \equiv K^2(x) \quad (25)$$

with α a positive constant. Eq.(25) is often called *Budden* equation [10, 8]. Except in the vicinity of $x = 0$, the wave is propagating with constant $k_{\perp} \simeq \pm k_{\infty}$. If the wave approaches the resonance from the left, it will slow-down more and more (its group velocity

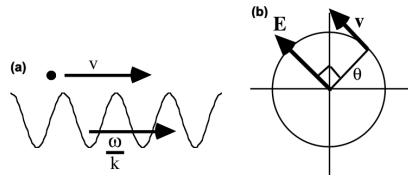


Figure 4: Wave-particle resonances: (a) Landau interaction; (b) cyclotron resonance

goes to zero) and come to rest at $x = 0$. In this simple WKB picture, all wave fronts coming from the left pile-up at the resonance leading to a large increase in wave amplitude. In addition, as the wave field oscillates a large number of times before propagating any significant amount of distance toward the resonance, it is obvious that the effects of any damping mechanism will be considerably magnified in the vicinity of the resonance. A detailed integration of (25) in the complex plane shows that the power is constant for $x \neq 0$ and jumps abruptly at the crossing of the resonance. In the case of a cold or maxwellian plasma the jump correspond to a decrease in power, i.e. to wave energy absorption (by the plasma). This will be shown explicitly for the case of the ion-ion hybrid in a subsequent lecture [3]. Power is thus absorbed at the resonance notwithstanding the fact that no absorption mechanism was explicitly considered in the original equation (7).

C. Wave-particle resonances - Landau damping

Wave-particle resonances appear as resonant denominators in the integrand of the expression of the kinetic dielectric tensor[5]. Physically, they result from the fact that, in their reference frame, particles see a constant electric field and are therefore uniformly accelerated. Such a singular phenomenon can appear only in an approximate treatment of the problem, namely in the linearised approximation. For example let us consider, as in Fig.4-(a), a particle moving at the constant velocity v in an electric field directed along v and propagating at the phase velocity ω/k . The equations of motion of this particle are

$$m \frac{dv}{dt} = ZeE \cos(kv - \omega t); \quad \frac{dx}{dt} = v \quad (26)$$

When we linearise the problem ($v \simeq v_0 + v_1$) we arrive at the equation of motion

$$\frac{dv_1}{dt} = \frac{ZeE}{m} \cos[(kv_0 - \omega)t + kx_0] \quad (27)$$

where we have used in the expression for the field the unperturbed particle motion $x = x_0 + v_0 t$. The perturbed velocity v_1 is oscillatory and there is no energy exchange between the particles and the wave as long as they have a different zero-order velocity $v \neq \omega/k$. But if they have the same velocity, the particle sees a

constant electric field and is uniformly accelerated:

$$v_1 = \frac{ZeE}{m} \cos(kx_0)t \quad (28)$$

An alternative way of looking at the same phenomenon is the Fourier transform approach, which here reduces to looking only at the periodic solutions of the problem:

$$v_1 = \frac{ZeE}{m} \frac{e^{i(kv_0 - \omega)t}}{i(kv_0 - \omega)} \quad (29)$$

It can be seen that the singularity in the spectrum appearing at the resonance corresponds to the secularity ($\sim t$) in the time-representation. The corresponding absorption is known as *Landau damping* and the condition $v = \omega/k$ is called the *resonance condition*. Whether the particle will be continuously accelerated or decelerated depends on the phase of the wave at the initial particles position kx_0 . To see if globally the power will go from the wave to the particles or vice versa, we have to make an average of the energy increment over initial phases and over the initial particle distribution function[24], which leads to the classical Landau's formula:

$$\frac{dW}{dt} \approx -\frac{\pi\omega Z^2 e^2 E^2}{2mk|k|} f'(\frac{\omega}{k}) \quad (30)$$

We see that damping rate is proportional to the slope of the unperturbed velocity distribution function at the phase velocity of the wave. Landau's formula (30) shows that power is transferred from the waves to the particles if there are more particles slower than the waves than faster ones. This is the case for a maxwellian. In the other case energy will go from the particles to the wave, which will be amplified, leading to instability (this process is sometimes called "inverse Landau damping"). A distribution function monotonous and decreasing constitutes therefore a dissipative medium in the absence of collisions.

D. Wave-particle resonances - Transit time magnetic pumping

Another frequently quoted non-collisional absorption mechanism is *transit time magnetic pumping* or TTMP. It is similar to Landau damping, except that it is due to a propagating magnetic rather than electric-wave modulation $B_1 = \delta B \cos(kx - \omega t)$ superposed on the static field B_0 . This modulation gives rise to the perpendicular force $\mu \nabla B$ acting on the particles magnetic moment μ , according to the equation for the motion along the magnetic field lines:

$$m \frac{dv}{dt} = -\mu \nabla B \quad (31)$$

which is similar to Eq.(26).

E. Wave-particle resonances - Cyclotron damping

Another type of wave-particle resonance is the cyclotron resonance (Fig.4-(b)). Assume that the particle is rotating at the cyclotron frequency $\theta = \omega_c t$ and that we apply a rotating electric field at the same frequency $\omega = \omega_c$ with a component along the particle velocity v : the particles perpendicular energy will increase linearly with time. This mechanism will be discussed in details in [3].

This very sketchy analysis puts into light a weakness of the linearised approach. Indeed what will happen in reality is not that uniform acceleration will take place indefinitely but rather that the accelerated particle will escape the resonant condition and thence terminate the resonant process. Resonant absorption can only continue if, once this particle has left the interaction area, it is replaced by a fresh one that can continue the resonant interaction. In terms of distribution functions, this means that the wave will produce velocity diffusion such as to empty the interaction region from particles, which in practice means a flattening of the distribution function in the interaction zone. Once the distribution is flat the interaction has stopped. Collisions or other processes like stochasticity counteract this tendency by restoring the gradients. If the latter processes are strong, the distribution function can remain maxwellian, however, generally speaking, the distribution function of a particle population heated by a resonance process is not maxwellian.

V. QUASILINEAR DIFFUSION AND TAILS

In the previous sections, we have seen that the RF power could be absorbed by the plasma via wave-particle or wave resonances. In both cases, the wave equation tells us that the wave will be damped while travelling in the plasma but leaves open the question: where is this power going to ?

A wave resonance corresponds to infinity in physical variables. At resonance, not only the wave vector goes to infinity but field components as well, as is clear from the solution of the wave Eq.(7), which can be expressed analytically in terms of Bessel functions[8]. Such infinities are the sign that some smallness hypothesis is violated and that additional terms should have been retained in the wave equation. Retaining these terms changes the resonance into a mode conversion[9] whereby the initial low- k_{\perp} wave is converted into high- k_{\perp} branch. Ultimately, the latter can only be absorbed through collisional or non-collisional (i.e. wave-particle resonance) processes.

The existence of absorption through wave-particle resonance manifests itself by the presence of an anti-hermitian part of the magnetised hot-plasma dielectric tensor[5]. The classical expression of the dielectric tensor is obtained by assuming that the unperturbed distribution function is a maxwellian. We shall see

that this is only an approximation and that the heating process only takes place with a sub-class of plasma particles and necessarily leads to some deformation of the distribution function of the heated population.

The corresponding theory is called *quasilinear theory* and we will here derive the equations for the simplest case, that of Landau damping in unmagnetised plasma. We start with Vlasov's equation in one dimension:

$$\frac{\partial f}{\partial t} + v \frac{\partial f}{\partial z} + \frac{ZeE}{m} \frac{\partial f}{\partial v} = 0 \quad (32)$$

where $E = E_1$ is the perturbed electric field (there is no equilibrium electric field). We decompose the distribution function into a slowly varying part (f_0), both in time and space, and a perturbed part (f_1), $f = f_0 + f_1$, and insert this expression in Eq.(32). In order to isolate the slowly varying part of the distribution function, we average this equation over time (many wave periods) and space (many wavelengths). Denoting by $\langle . \rangle$ this averaging operation, we obtain:

$$\frac{\partial f_0}{\partial t} + v \langle \frac{\partial f_0}{\partial z} \rangle + \frac{Ze}{m} \langle E \frac{\partial f_1}{\partial v} \rangle = 0 \quad (33)$$

where we have used the fact that $\langle E \rangle = \langle f_1 \rangle = 0$. The second term in this equation is zero for uniform plasma and we are left with an equation that determines the evolution of the equilibrium distribution function under the action of the first-order perturbations:

$$\frac{\partial f_0}{\partial t} = -\frac{Ze}{m} \langle E \frac{\partial f_1}{\partial v} \rangle \quad (34)$$

The second term in this equation is the *quasilinear* term. In order to write it down explicitly, we must solve the equation for the perturbation of the distribution function f_1 which we obtain by subtracting Eq.(34) from Eq.(32):

$$\frac{\partial f_1}{\partial t} + v \frac{\partial f_1}{\partial z} + \frac{ZeE}{m} \frac{\partial f_0}{\partial v} = 0 \quad (35)$$

Fourier-transforming in space and Laplace-transforming in time ($f \sim \exp[i(kz - \omega t)]$), we easily obtain the solution of this equation:

$$f_1 = -\frac{iZeE}{m(\omega - kv)} \frac{\partial f_0}{\partial v} \quad (36)$$

Inserting this expression into Eq.(34), we obtain, noting that the average of two oscillating quantities $u(t)$ and $v(t)$ is $\langle u(t)v(t) \rangle = (1/2)\Re(uv^*)$:

$$\frac{\partial f_0}{\partial t} = -\frac{Z^2 e^2 |E|^2}{2m^2} \frac{\partial}{\partial v} \Im \left[\frac{1}{\omega - kv} \right] \frac{\partial f_0}{\partial v} \quad (37)$$

This equation can be given a Fokker-Planck type form:

$$\frac{\partial f_0}{\partial t} = \frac{\partial}{\partial v} \left(D \frac{\partial f_0}{\partial v} \right); \quad D = -\frac{Z^2 e^2 |E|^2}{2m^2} \Im \left[\frac{1}{\omega - kv} \right] \quad (38)$$

where D is the *quasilinear diffusion coefficient*. Note that the imaginary part appearing in the expression for D is nothing else than $\delta(\omega - kv)$. This implies that only the particles which are in resonance will be pushed in velocity space by the heating process. If the wave is directional, i.e. if the k_{\parallel} spectrum is asymmetric, the deformation of the distribution function will also be asymmetric, leading to the generation of current by the waves, like in LH current drive.

VI. THERMALISATION

If Eq.(38) is solved as it is, it can lead to a time-asymptotic stationary solution only if the energy transferred by the wave to the particle is zero. Therefore the stationary solution of Eq.(38) must exhibit a quasilinear plateau, i.e. a zones around the resonant velocity where f_0 is flat ($\partial f_0 / \partial v = 0$). This ensures that the heating power vanishes.

In a situation where there is stationary power transfer to the plasma, the evolution equation for the particles distribution functions, Eq.(38) is thus lacking a loss term. This is the collision term, which we denote by $C(f_0)$. It includes collisions on all particle species, including the heated ones. It also implies that the distribution function of the heated species will tend to relax to a maxwellian. From the different contributions to $C(f_0)$, one can then compute the power transfer to the different plasma components and the resulting temperature increases. The complete equation for the evolution of f_0 should thus be written

$$\frac{\partial f_0}{\partial t} = \frac{\partial}{\partial v} \left(D \frac{\partial f_0}{\partial v} \right) + C(f_0) \quad (39)$$

This collisional thermalisation process is in close relation with the slowing down of fast NBI ions discussed in [6].

REFERENCES

1. Y. Kazakov, "Heating the Plasma", *These Proc.*
2. P. Dumortier, "Antenna Design and Matching Issues", *These Proc.*
3. E. Lerche, "Ion cyclotron, lower hybrid and Alfvén wave heating", *These Proc.*
4. E. Westerhof, "Electron Cyclotron Resonance Heating", *These Proc.*
5. D. Van Eester & E. Lerche, "Kinetic Theory of Plasma Waves", *These Proc.*
6. D. Van Eester, "Fast Particle Heating (NBI) & Modelling particle heating and current drive in tokamaks", *These Proc.*
7. J.D. Jackson, "Classical Electrodynamics" 2nd Ed., J. Wiley & Sons (1975)

8. T.H. Stix, *Waves in plasmas*, AIP New York (1992).
9. D.G. Swanson, *Plasmas Waves*, American Institute of Physics (1989).
10. K.G. Budden, "The Propagation of Radio Waves", Cambridge U.P. (1985)
11. R.R. Weynants *et al.*, "ICRH antenna design and coupling optimisation studies", in "Heating in toroidal plasmas", Commission of the European Communities, Vol. I (1980), 487
12. A. M. Messiaen *et al.*, "Theoretical aspects of the coupling properties of ICRH antennae", in "Heating in toroidal plasmas", Commission of the European Communities, Vol. I (1982), 243
13. V.P. Bhatnagar *et al.*, "A 3-D Analysis of the Coupling Characteristics of ICRH Antennae", *Nucl. Fusion* **22** (1982) 280
14. A. M. Messiaen *et al.*, "Analysis of the plasma edge radiation by ICRH antenna", Proc. 4th International Symp. on Heating in Toroidal Plasmas, Vol. I (1984), 315
15. R. Koch *et al.*, "An asymptotic analysis of the radiation pattern of ion cyclotron resonance heating antennas", *J. Plasma Phys.* **32** (1984), 291
16. R. Koch, "A global solution of the ICRH problem based on the combined use of a planar coupling model and hot-plasma ray-tracing in tokamak geometry", *Computer Phys. Comm.*, **40** (1986), 1
17. R. Koch *et al.*, "A Comparison Between ICRF Theory and Experiment", *Plasma Phys. Contr. Fus.*, **30** (1988), 1559
18. P. Descamps *et al.*, "Global Modes Excitation in TEXTOR and Comparison with Theory", *Plasma Phys. Contr. Fus.*, **33** (1991), 1109
19. C. Gormezano, "High power lower hybrid current drive on JET: results and prospects", Report JET-P(93)65 (1993)
20. M.D. Carter *et al.*, "Three Dimensional Modelling of ICRF Launchers for Fusion Devices", *Nucl. Fusion* **36** (1996), 209,
21. R. Koch *et al.*, "Progress in RF Theory: a sketch of recent evolution in selected areas", *J. Plasma Phys.* **40** (1998), A141
22. S. Pecoul *et al.*, "Numerical modeling of the coupling of an ICRH antenna with a plasma with self-consistent antenna currents", *Computer Phys. Comm.*, **146** (2002)166-187
23. D. Hartmann *et al.*, "Measurements and calculations of electrical properties of ICRF antennas", in *Radio Frequency Power in Plasmas*, AIP Conf. Proc. **694** (2003), 106
24. R. Koch, "Wave-particle interactions in plasmas", *Plasma Phys. Contr. Fus.*, **48**(2006), B329
25. V. Lancellotti *et al.*, "TOPICA: an accurate and efficient numerical tool for analysis and design of ICRH antennas", *Nucl. Fusion* **46** (2006), S476
26. P. Lamalle *et al.*, "Recent developments in ICRF antenna modelling", *Nucl. Fusion*, **46** (2006), 432-443
27. D. Milanesio *et al.*, "Analysis of the Tore Supra ICRF antenna in TOPICA RF antenna code", *Plasma Phys. Contr. Fus.*, **39** (2009), 405-419
28. D. Milanesio & R. Maggiora, "ITER ICRF antenna analysis and optimisation using the TOPICA code", *Nucl. Fusion* **50** (2010), 025007
29. F. Louche *et al.*, "3D electromagnetic optimization of the front face of the ITER ICRF antenna", *Nucl. Fusion* **51** (2011), 103002
30. A. Messiaen & R. Weynants, "ICRH antenna coupling physics and optimum plasma edge density profile. Application to ITER", *Plasma Phys. Contr. Fus.* **53** (2010) 085020

THE ION CYCLOTRON, LOWER HYBRID AND ALFVEN WAVE HEATING METHODS

R. Koch

*Laboratory for Plasma Physics
Ecole Royale Militaire - Koninklijke Militaire School
B-1000 Brussels, Belgium*

ABSTRACT

This lecture covers the practical features and experimental results of the three heating methods. The emphasis is on ion cyclotron heating. First, we briefly come back to the main non-collisional heating mechanisms and to the particular features of the quasilinear coefficient in the ion cyclotron range of frequencies (ICRF). The specific case of the ion-ion hybrid resonance is treated, as well as the polarisation issue and minority heating scheme. The various ICRF scenarios are reviewed. The experimental applications of ion cyclotron resonance heating (ICRH) systems are outlined. Then, the lower hybrid and Alfvén wave heating and current drive experimental results are covered more briefly. Where applicable, the prospects for ITER are commented.

I. ION CYCLOTRON HEATING

I.A. Introduction

Before going in further details of heating mechanisms, it is important to recapitulate the order of magnitude of the different quantities characterising the plasma and the RF. A table of plasma parameters (Table 1), typical of moderate plasma performance in a machine like JET, was given earlier¹. Two important parameters that characterise the collisionality of the plasma are to be added to complete the picture: the ion and electron collision frequencies: $\nu_e \approx 10\text{kHz}$, $\nu_i \approx 100\text{Hz}$. A JET-type machine is characterised by the following parameters:

$$R_0 = 3\text{m}, 2\pi R_0 \approx 20\text{m}; a_p = 1.5\text{m}, 2\pi a_p = 10\text{m}.$$

In the light of these numbers, one sees that the time for a cyclotron gyration is extremely short: 10ps for an electron, 40ns for an ion. During this single gyration, the electron travels 0.4mm in the toroidal direction and the ion 2cm. It takes 1 μs to an electron to complete a toroidal turn around the machine, 40 μs to an ion. During this turn, an electron has performed 50,000 cyclotron gyrations, an ion 1,000. This means that gyro motion is an extremely fast process

as compared to transit times across any macroscopic area. Equivalently, the gyro radii of electrons (0.05mm) and of ions (3mm) are small as compared to plasma size. The plasma is nearly non-collisional: the electron mean free path is 3km and the ion one 5km, or, respectively, 150 and 250 toroidal revolutions.

The following parameters are typical of an ICRF system:

- frequency: $f \approx 10\text{-}100\text{ MHz}$
- Power: 2 MW/antenna strap
- Voltage: 10-50 kV at the antenna
- Antenna current: $I_A \approx 1\text{ kA}$
- Central conductor: width $\approx 0.2\text{m}$, length $\approx 1\text{m}$, distance to the plasma 5cm, to the wall 20cm
- Typical RF electric field: 20kV/m
- Typical RF magnetic induction: 10^{-3}T

ICRF antennas are quite often built as boxes enclosing one or several *central conductors* to whom the high voltage is applied. Such a central conductor is also called a *strap*. The maximum voltage that could be applied to an antenna operating in a tokamak, in the presence of plasma, lies around 45kV. The ratio of voltage to current and the power coupling capability of an antenna are determined by the geometry of the antenna and the plasma edge properties¹. The electric field at the antenna is easily evaluated by dividing the input voltage by the antenna length. This is valid for the field component polarised along the antenna; other field components can be much higher in the vicinity of the antenna feeding point. Except for possible focusing effects, the field inside the plasma is lower than at the antenna, because $k_{\perp}|E|^2$ is nearly constant and k_{\perp} is roughly proportional to \sqrt{n} . The typical RF magnetic field is easily computed using ampere's law: $2\pi dH = I_A$ where d is typical of the distance over which the magnetic field can spread. These electrostatic- and magnetostatic-type estimates have a meaning due to the fact that the vacuum wavelength is large as compared to the antenna dimensions:

$$\lambda_0 = c/f \approx 10 \text{ m (30 MHz)}.$$

I.B. Linearity

These numbers show that the RF causes only a small perturbation of the particle trajectory. First, the RF magnetic field is much smaller than the static one:

$$B_{\text{RF}} \approx 10^{-3} \text{ T} \ll B_0 \approx 3 \text{ T}.$$

Second, the RF electric field $\approx 20 \text{ kV/m}$ is also much smaller than the $\mathbf{v} \times \mathbf{B}$ field associated with the ion's (and even more electron's) thermal motion: $V_{\text{th}} \times B_0 \approx 1.5 \text{ MV/m}$. Third, we shall show below that the perturbation of the parallel motion is also small. Let us write the equation of motion of a particle in the RF field, decomposing the motion into an unperturbed (thermal) part labelled 0 and a perturbed part: $\mathbf{v} \rightarrow \mathbf{v}_0 + \mathbf{v}$

$$m \left(\frac{d\mathbf{v}_0}{dt} + \frac{d\mathbf{v}}{dt} \right) = Ze(\mathbf{E} + \mathbf{v}_0 \times \mathbf{B}_0 + \mathbf{v}_0 \times \mathbf{B} + \mathbf{v} \times \mathbf{B}_0 + \mathbf{v} \times \mathbf{B}) \quad (1)$$

Subtracting the unperturbed part of this equation

$$m \frac{d\mathbf{v}}{dt} = Ze \mathbf{v}_0 \times \mathbf{B}_0 \quad (2)$$

which describes the unperturbed cyclotron motion leaves us with the perturbed part of the equation of motion.

$$m \frac{d\mathbf{v}}{dt} = Ze(\mathbf{E} + \mathbf{v}_0 \times \mathbf{B} + \mathbf{v} \times \mathbf{B}_0 + \mathbf{v} \times \mathbf{B}) \quad (3)$$

In the r.h.s parenthesis the last term is clearly negligible as compared to the 3rd one. We thus arrive at the following equation, which is linear in the perturbed field amplitude:

$$m \frac{d\mathbf{v}}{dt} = Ze(\mathbf{E} + \mathbf{v}_0 \times \mathbf{B} + \mathbf{v} \times \mathbf{B}_0) \quad (4)$$

Finally, we can estimate the correction to the parallel uniform motion due to the RF field. Taking the parallel component of Eq.(3) and $d/dt \approx \omega_{ci}$, we get for an ion

$$m \omega_c v_{\parallel} = Ze[E_{\parallel} + (\mathbf{v}_0 \times \mathbf{B})_{\parallel}] \quad (5)$$

or, in order of magnitude

$$v_{\parallel} \approx \left| \frac{E_{\parallel}}{B_0} \right| \quad \text{or} \quad \approx V_{\text{th}} \left| \frac{B_{\text{RF}}}{B_0} \right| \quad (6)$$

Thus, in any case the RF-induced particle quiver velocity is small as compared to the thermal (unperturbed) ion velocity. In summary, the corrections to the particle's trajectory due to the RF field are indeed small, and the linearisation is justified.

Although Eq.(4) is linear in the fields, it is not at all linear for the unknowns \mathbf{r} and \mathbf{v} . Indeed, the electric field depends non-linearly on the particle position \mathbf{r} . However, we have seen that the RF fields only cause small perturbations to the particle trajectories. Therefore, we can neglect these small deviations in the evaluation of the electromagnetic field at the particle location and write

$$\mathbf{E}(\mathbf{r}) \approx \mathbf{E}(\mathbf{r}_0); \quad \mathbf{B}(\mathbf{r}) \approx \mathbf{B}(\mathbf{r}_0) \quad (7)$$

with $d\mathbf{r}_0/dt = \mathbf{v}_0$ and \mathbf{v}_0 is the solution of the unperturbed equation of motion Eq.(2). Then the equation determining the velocity perturbation is

$$m \frac{d\mathbf{v}}{dt} = Ze[\mathbf{v} \times \mathbf{B}_0 + \mathbf{E}(\mathbf{r}_0) + \mathbf{v}_0 \times \mathbf{B}(\mathbf{r}_0)] \quad (8)$$

This is now a linear equation that can be solved explicitly if the unperturbed trajectories $(\mathbf{r}_0, \mathbf{v}_0)$ are known explicitly. The next step in the solution of the problem is to decompose the zero-th order motion into a guiding centre motion \mathbf{r}_G and a gyromotion $\boldsymbol{\rho}$:

$$\mathbf{r}_0 = \mathbf{r}_G + \boldsymbol{\rho} \quad (9)$$

and to expand around the guiding centre motion:

$$\mathbf{E}(\mathbf{r}_0) = \sum_{n=0}^{\infty} \frac{[(\boldsymbol{\rho} \cdot \nabla)^n \mathbf{E}]_{\mathbf{r}_0 = \mathbf{r}_G}}{n!} \quad (10)$$

This procedure is known as the *small Larmor radius expansion*. In general geometry this development can become quite heavy², but in straight geometry, it can be performed explicitly. In the latter case (uniform plasma), the decomposition of the motion, Eq.(9) is exact and the expansion Eq.(10) can be expressed in terms of Bessel functions, see Eq.(13, 16) of ref.³. Like in the case of Landau damping¹, the explicit integration of the linearised equation of motion Eq.(8) can, in some cases, lead to secular solutions, corresponding to resonant denominators in Fourier space⁴. The same denominators are found back under the velocity integral in the expression of the full hot conductivity tensor³, leading to the general resonance condition

$$\omega - n\omega_c - k_{\parallel} v_{\parallel} = 0; \quad n = 0, \pm 1, \pm 2, \dots \quad (11)$$

I.C. The cyclotron absorption mechanisms

I.C.1 Resonances due to non-rotating fields

If we look at the $n=0$ contribution to the conductivity tensor Eq.(20) in ref.³, we see that only the lower right 2×2 part of the S_n matrix is non-zero. For a uniform electric field ($k_{\perp} \mathbf{E} = \partial \mathbf{E} / \partial x = 0$), only the zz term survives. It correspond to resonant parallel acceleration by the parallel electric field, i.e. to Landau damping. The three other terms require, at least, a gradient of the electric field ($\partial \mathbf{E} / \partial x \neq 0$). By computing the expression $\mathbf{E}^* \cdot \boldsymbol{\sigma} \cdot \mathbf{E}$, (proportional to the absorbed wave power) for the case where only E_y is present, it is easy to see that this quantity is proportional to

$$(k_{\perp} E_y)^2 = (\omega B_z)^2$$

If we assume E_y to be linear, we thus have a case of acceleration by a uniform B_z field propagating in the z direction with $\omega = k_{\parallel} v_{\parallel}$. We have seen¹ that the resonance mechanism in this case is *transit time magnetic pumping* (TTMP). More detail about this and about the interplay between Landau damping and TTMP in the case both E_y and E_z differ from zero, can be found in the book of Stix⁵.

Landau damping and TTMP are not important mechanisms for the ions in the ICRF because $k_{\parallel}V_{th}$ is usually much smaller than $\omega \approx \omega_{ci}$, as can be seen from Table 1 and k_{\parallel} estimates¹. For the electrons, on the contrary, they are the only damping mechanisms in this frequency range. As they correspond to parallel acceleration, they are of primary importance for the fast wave *current drive* applications.

I.C.2. Resonances due to the left-handed component of the field.

This is the case where the wave has the same handedness as the ions and the resonances correspond to $n > 0$ in Eq.(11). If $n=1$, we have the case of the fundamental cyclotron resonance, which was discussed already¹:

$$\omega = \omega_c + k_{\parallel}v_{\parallel} \quad (12)$$

Because of the Doppler shift $k_{\parallel}v_{\parallel}$ is small, this requires that the operating frequency be rather close to the ion cyclotron frequency. Looking at the expression of S_n in ref.³, we see that such a resonance can be caused by a uniform field ($k_{\perp}E = \partial E / \partial x = 0$). On the contrary, for second harmonic damping ($n=2$) to exist, the same expression shows that a gradient of the electric field is required. Similarly, higher harmonic damping requires the existence of non-vanishing higher derivatives of the electric field.

While it is easy to imagine how the fundamental cyclotron resonance works, it is much harder to visualise the reason why a particle rotating at the frequency ω_c can resonate with a wave that is rotating at twice this frequency! In order to understand how this happens it is useful to come back first to the fundamental resonance and look at the simpler situation where the wave propagates (or is non-uniform) in the x -direction while the E -field is polarised in the y -direction. The principle is shown on top of Fig.1. The particle travels from left to right and at the initial moment $t=0$, I assume that the electric force is in phase with the particle velocity. After a quarter period, if the field oscillates at the cyclotron frequency, $\omega = \omega_c$, the field is zero, after half a period it is negative, etc. Therefore, either the force is in phase with the particle motion, or it is zero and over one cyclotron period, the particle experiences a net acceleration in the direction of its motion. If, with the same uniform field distribution, the field varies at twice the cyclotron frequency $\omega = 2\omega_c$, after a quarter period, it has changed sign, points in the negative y direction and is perpendicular to the particle's velocity. After half a cyclotron period, its phase has varied of 2π , it is again positive, points out of the paper in the direction opposite to the particle's velocity and so on. Hence, over a cyclotron period, the average force exerted on the particle is zero, there is no net acceleration and no resonance.

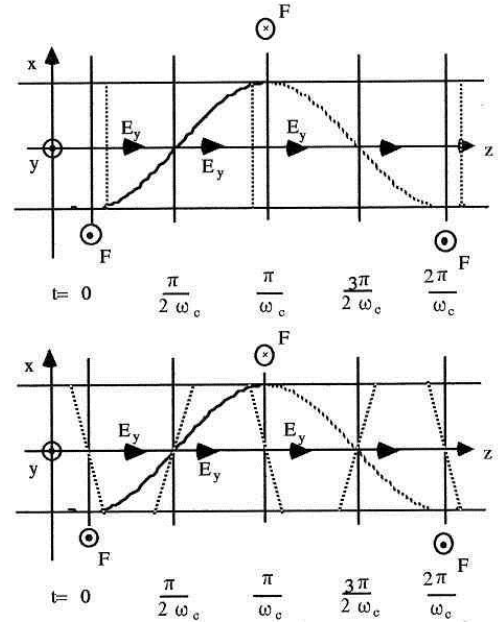


Fig. 1. Mechanism of the fundamental (top) and second harmonic (bottom) resonance. The ion moves in the z -direction and the projection of its helical motion on the (x,z) plane is shown: solid line, above the plane; dotted line, below. The electric field distribution along x is shown at quarter periods of the cyclotron frequency. The direction of the electric force F at the particle's position is also indicated.

However, if the field varies linearly in space, as shown on the bottom of Fig.1, at the same time as it alternates sign, the particle moves from one side of the gradient to the other, therefore keeping in phase with the electric force and experiencing a net acceleration over one period, as shown. It is therefore the interplay between the field periodicity and the sampling of the field non-uniformity by the particle that allows resonance at the cyclotron harmonics.

I.C.3. Resonances due to the right-handed component of the field.

This type of resonance, corresponding to $n < 0$, is somewhat counter-intuitive as the field rotates in the direction opposite to the particle. However the resonance condition shows that, in order to come into resonance, the particle must have a very large velocity:

$$v_{\parallel} = \frac{\omega + |n|\omega_c}{k_{\parallel}} \gg V_{ti} \quad (13)$$

One can then understand the resonance process as follows. Let us start with a particle with zero parallel velocity and a right-hand polarised field at frequency ω slightly larger than ω_{ci} and positive phase velocity $\omega k_{\parallel} > 0$. The particle sees the field rotating slightly faster than itself, in the opposite direction. Then if the particle starts to move at a speed $v_{\parallel} > 0$, in the reference frame moving at the same velocity, the field is now rotating at the slightly lower frequency $\omega' = \omega k_{\parallel} v_{\parallel}$. If v_{\parallel} is large enough, this frequency may equal ω_{ci} but the ion and the field are rotating in opposite directions. Then, if the particle's velocity becomes much larger, the field may become stationary $\omega k_{\parallel} v_{\parallel} = 0$: the particle is gyrating in a stationary field. This cannot give rise to a resonance. If v_{\parallel} is still increased, $\omega k_{\parallel} v_{\parallel} < 0$ and the wave field will start to rotate in the left-handed direction. Still increasing the particle's velocity, we can come to the situation where $\omega k_{\parallel} v_{\parallel} = -\omega_{ci}$ which means that the field is left-hand polarised and rotating at the cyclotron frequency, thereby causing resonant acceleration. This absorption mechanism is generally negligible for particles belonging to the thermal population in the plasma. However, for the much faster particles belonging to a high-energy tail, either created by the RF itself, or by NBI or for α -particles, this mechanism may not be negligible at all. Even more so, as we shall see, as the right-hand field component tends to dominate in the fast wave, in the vicinity of resonances.

I.C.4. Quasilinear diffusion coefficient

Ion cyclotron heating tends to create high-energy tails in the distribution function of the heated particles. For heating at the n -th cyclotron harmonic, the diffusion coefficient is of the form:

$$D \propto |J_{n-1} E_+ + J_{n+1} E_-|^2 \approx \left| J_{n-1} \left(\frac{k_{\parallel} v_{\parallel}}{\omega_c} \right) \right|^2 |E_+|^2 \quad (14)$$

where E_+ and E_- are, respectively, the left-hand and right-hand components of the electric field:

$$E_+ = \frac{1}{2}(E_x + iE_y); \quad E_- = \frac{1}{2}(E_x - iE_y) \quad (15)$$

One notices the presence of a right hand component contribution in the diffusion coefficient. For not too fast particles in the FW field, this contribution is negligible because the argument of the Bessel functions is small. This is not necessarily the case for fast ions. In the case of the thermal population, one can take only the first term of the power series expansion of the Bessel functions, and we get:

- Fundamental: $D \propto K |E_+|^2$ with K a constant (16.1)

- Second harmonic: $D \propto \left| \frac{k_{\parallel} v_{\parallel}}{\omega_c} \right|^2 |E_+|^2$ (16.2)

- n -th harmonic: $D \propto \left| \frac{k_{\parallel} v_{\parallel}}{\omega_c} \right|^{2(n-1)} |E_+|^2$ (16.3)

A first conclusion to be drawn from these expressions is that, as $k_{\perp} r_L$ is a small quantity, the diffusion coefficient (hence the strength of the heating) strongly decreases with the harmonic number. Second, fundamental heating pushes all particles with the same strength irrespective of their velocity: the diffusion coefficient is independent of velocity. On the contrary, harmonic heating tends to accelerate more the faster particles. A consequence of this last observation is that harmonic heating tends to create tails at higher energy than fundamental heating. In the same vein, harmonic heating tends to interact more with faster particles like beams or alphas.

I.D. The FW dispersion and polarisation

The FW equation was given in section II.C of ref.¹. We shall now specialise the expressions of the dielectric tensor components³ to the ICRF where

$$\omega \approx \omega_{ci} \ll \omega_{pi} \ll \omega_{pe}, \omega_{ce}. \quad (17)$$

We obtain

$$S = 1 - \frac{\omega_{pe}^2}{\omega^2 - \omega_{ce}^2} - \sum_i \frac{\omega_{pi}^2}{\omega^2 - \omega_{ci}^2} \approx - \sum_i \frac{\omega_{pi}^2}{\omega^2 - \omega_{ci}^2} \quad (18)$$

$$D = \frac{\omega_{ce}}{\omega} \frac{\omega_{pe}^2}{\omega^2 - \omega_{ce}^2} + \sum_i \frac{\omega_{ci}}{\omega} \frac{\omega_{pi}^2}{\omega^2 - \omega_{ci}^2} \quad (19)$$

$$\approx \frac{\omega_{pe}^2}{-\omega \omega_{ce}} + \sum_i \frac{\omega_{ci}}{\omega} \frac{\omega_{pi}^2}{\omega^2 - \omega_{ci}^2} = \sum_i \frac{\omega}{\omega_{ci}} \frac{\omega_{pi}^2}{\omega^2 - \omega_{ci}^2}$$

The first line of Eq.(12) of ref.¹ gives the relation linking E_x and E_y and can be used to compute the ratio of the left-to-right-hand components of the electric field:

$$\left| \frac{E_x + iE_y}{E_x - iE_y} \right| = \left| \frac{D + (S - N_{\parallel}^2)}{D - (S - N_{\parallel}^2)} \right| \quad (20)$$

Let us now consider the case of a single ion species. Eqs.(18-19) become

$$S \approx - \frac{\omega_{pi}^2}{\omega^2 - \omega_{ci}^2}; \quad D \approx - \frac{\omega}{\omega_{ci}} S \quad (21)$$

and

$$\left| \frac{E_x + iE_y}{E_x - iE_y} \right| \approx \left| \frac{1 - \frac{\omega}{\omega_{ci}} - N_{\parallel}^2 / S}{1 + \frac{\omega}{\omega_{ci}} - N_{\parallel}^2 / S} \right| \approx \left| \frac{\omega - \omega_{ci}}{\omega + \omega_{ci}} \right| \quad (22)$$

The last approximate equality follows from

$$N_{\parallel}^2 / S \approx \frac{N_{\parallel}^2 (\omega_{ci}^2 - \omega^2)}{\omega_{pi}^2} \ll 1 \quad (23)$$

The striking feature of the result Eq.(22) is that, at cyclotron resonance $\omega = \omega_{ci}$, in a plasma with only one ion species i , the left-hand polarised component of the wave vanishes. Thus the cyclotron resonance mechanism cannot

work because the resonant wave component is absent! Incidentally, this shows explicitly why there is no singularity of the fast wave propagation at the cyclotron frequency³: the resonant wave component is blocked by the resonance and all the power is transferred to the other component. This dramatic result can be avoided by heating a small amount of ions of one species in a plasma with ions of another species. This is called the *minority heating* scenario. Consider, for example a plasma of deuterium with a minority of hydrogen. Then the wave polarisation is determined by the majority component while the wave frequency is the cyclotron frequency of hydrogen. Inserting $\omega = \omega_{cH} = 2\omega_{cD}$ in Eq.(22) yields

$$\frac{E_x + iE_y}{E_x - iE_y} \approx \left| \frac{\omega - \omega_{cD}}{\omega + \omega_{cD}} \right| = \frac{2\omega_{cD} - \omega_{cD}}{2\omega_{cD} + \omega_{cD}} = \frac{1}{3} \quad (24.1)$$

This is the most widely used minority heating scenario, denoted D-(H) to indicate that a minority of H is heated in a majority D plasma. This concept of heating a given species in a mixture can be extended to other mixtures. For example in a reactor, one can heat D at the fundamental in a D-T mixture. Then, for not too large D concentration, the ratio of polarisations is:

$$\frac{E_x + iE_y}{E_x - iE_y} \approx \left| \frac{\omega_{cD} - \omega_{cT}}{\omega_{cD} + \omega_{cT}} \right| = \frac{1}{5} \quad (24.2)$$

This explanation has the advantage of simplicity and to some extent gives a good picture of reality. The shrewd reader would however notice by working out himself the complete polarisation expression for a mixture of ions that even in this case the left-handed polarisation vanishes at each cyclotron harmonic! The final explanation can only be obtained by taking hot-plasma (absorption) effects³ into consideration and noting that in a mixture the wave left-handed component has a significant magnitude over a much wider region around the cyclotron harmonic than in the single-ion case. This is of course particularly evident when only a small minority is considered. This allows non-collisional damping at Doppler-shifted frequencies to remain efficient over a much wider range as compared to the single-ion case.

Another way to avoid the polarisation problem is to work at harmonics of the cyclotron frequency. Then

$$\frac{E_x + iE_y}{E_x - iE_y} \approx \left| \frac{n\omega_{ci} - \omega_{ci}}{n\omega_{ci} + \omega_{ci}} \right| = \frac{n-1}{n+1} \quad (24.3)$$

however, as we saw in Eq.(16.3), the damping strength strongly decreases with harmonic number.

I.E. The ion-ion hybrid resonance

Let us now consider, like in ref.³, the case of a 50%-50% mixture of D and T.

$$n_D = n_T = n_c/2 \quad (25)$$

Then, taking into account the fact that $\omega_{cD} = \omega_{cH}/2$ and $\omega_{cT} = \omega_{cH}/3$, and defining

$$\omega_{pH} = \sqrt{2}\omega_{pD} = \sqrt{3}\omega_{pT} \quad (26)$$

we can recast the expressions for S and D , Eq.(18-19) as

$$S = \frac{2\omega_{pH}^2}{\omega_{cH}^2 - 4\omega^2} + \frac{3\omega_{pH}^2}{\omega_{cH}^2 - 9\omega^2} = \frac{5\omega_{pH}^2(\omega_{cH}^2 - 6\omega^2)}{(\omega_{cH}^2 - 4\omega^2)(\omega_{cH}^2 - 9\omega^2)} \quad (26.1)$$

$$D = \frac{\omega}{\omega_{cH}} \left[\frac{4\omega_{pH}^2}{\omega_{cH}^2 - 4\omega^2} + \frac{9\omega_{pH}^2}{\omega_{cH}^2 - 9\omega^2} \right] \quad (26.2)$$

Eq.(26.1) clearly shows that S will vanish -which is the condition of wave resonance for perpendicular propagation³- when $\omega_{cH} = \sqrt{6}\omega$. This is the ion-ion hybrid resonance condition for a 50%-50% D-T plasma. One can likewise obtain this resonance condition from the FW wavevector Eq.(14.2) of ref.¹, for the case of purely perpendicular propagation ($k_{\parallel}=0$):

$$k_{\perp FW}^2 = k_0^2 S - \frac{(k_0^2 D)^2}{k_0^2 S} = k_0^2 \frac{5\omega_{pH}^2(\omega_{cH}^2 - 5.76\omega^2)}{\omega_{cH}^2(\omega_{cH}^2 - 6\omega^2)} \quad (27)$$

Note that the general ($k_{\parallel} \neq 0$) resonance condition of the FW is

$$k_0^2 S - k_{\parallel}^2 = 0 \quad (28)$$

and is *not* one of the general resonances $A=0$ discussed in ref.³. In fact, it does not exist in the full cold-plasma dispersion relation, where a conversion between the FW and the slow wave (Eq.(62) of ref.³) takes place instead of a resonance. The FW resonance Eq.(28) arises because of the neglect of the slow wave.

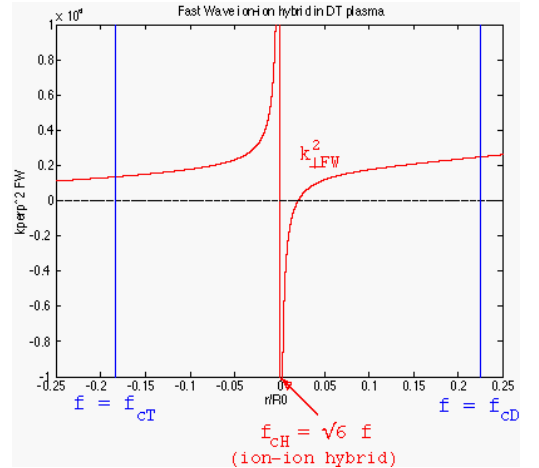


Fig. 2. Variation of the FW's wavevector(squared) over the plasma cross-section. The plasma density is assumed uniform. The ion-ion hybrid is located in the centre $x=0$.

We are now in a position to show that the model equation Eq.(38) of ref.¹ is a reasonable simplified resonance model. For the specific case of the ion-ion hybrid, and using Eq.(27) for simplicity, we shall also be able to show how to determine which sign to use in Eq.(43) of ref.¹. In a tokamak, the toroidal magnetic field decreases as $1/R$, R the major radius. Accordingly, the FW's wavevector varies across the plasma. Such a variation is shown in Fig.2, in the vicinity of the ion-ion hybrid resonance and assuming that the plasma density is constant for simplicity. Let us define the resonance location as $R=R_0$ and

$$\omega_{cH0}^2 = 6\omega^2; \quad \omega_{cH} = \frac{\omega_{cH0} R_0}{R} = \frac{\omega_{cH0} R_0}{R_0 + x} \quad (29)$$

With these definitions, we can re-write the resonant denominator

$$\omega_{cH}^2 - 6\omega^2 = \frac{\omega_{cH0}^2 R_0^2}{(R_0 + x)^2} - 6(\omega + i\nu)^2 \quad (30)$$

where we have introduced a small imaginary part to the frequency, in agreement with the causality rule³. In the vicinity of the resonance ($x/R_0 \ll 1$),

$$\omega_{cH}^2 - 6\omega^2 \approx -\frac{12\omega^2}{R_0} \left(x + \frac{i\nu}{\omega} R_0 \right) \quad (31.1)$$

$$k_{\perp FW}^2 \approx -\frac{k_0^2 \omega_{pH}^2}{60\omega^2} \frac{R_0}{(x + i\frac{\nu}{\omega} R_0)} \quad (31.2)$$

This proves our statements, as the singularity is indeed $1/x$ and the pole is slightly *below* the real x -axis. It is thus circled clockwise while performing the x -integration in Eq.(42) of ref.¹, which implies that the negative sign has to be taken in Eq.(43) of ref.¹, and that, given the sign in the r.h.s. of Eq.(31.2), the wave energy is indeed absorbed – rather than emitted- at the crossing of the resonance.

I.F. Scenarios

In present-day machines, the most usual scenario is fundamental heating of a hydrogen minority in a D plasma, or D-(H). Other mixtures have been tried successfully, like D-(³He), or even *heavy minority scenarios* like H-(D), H-(³He). Second and third harmonic heating, like $f=2f_{cH}$ or $f=3f_{cD}$, have been used, either as a majority or as a minority scenario. Mode conversion heating was proven to heat efficiently electrons, and FW current drive based on Landau-TTMP damping has been shown to follow theoretical expectations. In D-T plasmas, nearly all possible scenarios have been tested, T-(D), D-(T), second harmonic T, mixed $f=2f_{cT}$ and fundamental minority ³He, D-T-(³He) and even mode conversion. Finally, let us note that direct ion Bernstein wave launch experiments have also been performed, with limited success in terms of power coupling, but inducing in some cases poloidal rotation and transport barrier formation. A

good survey of these experiments, together with a large number of references is given in ref.⁶.

I.G. Database and applications

High power ICRH systems have been installed in a large number of machines. A maximum power of 22MW was coupled to the plasma in JET⁷. ICRH power was injected in various sorts of plasmas, including L-mode, ELM-free and ELMy H-mode, RI-mode⁸. In D-T, a record steady-state fusion Q performance ($Q=0.22$) was achieved with ICRH alone in JET⁹. At the occasion of the compilation of transport databases for ITER, it was noted that no significant differences in heating efficiency can be observed between the RF (ICRH and ECRH) subset and the rest of the database¹⁰. Although it is generally the case that the heating efficiency is equivalent for all auxiliary heating methods, there are cases where differences are observed. They are usually interpreted as resulting either from differences in power deposition profile or from a different impact on confinement. As an example of the latter, the choice of heating method – H/D co/counter NBI / ICRH- D-injection, can have definite impact on the achievement and quality of the RI-mode on TEXTOR¹¹.

Like in the case of NBI, the neutron production rate furnishes an indirect measurement of the tail created by the RF. Comparisons with theoretical predictions indicate that the tail formation process is fairly well understood¹². Fast ion energy content¹³ and direct tail measurements¹⁴ provide similar indications. Other comparisons have addressed the question of ion/electron power partition and power deposition profile^{15,16}. The interaction of ICRH with beam-injected fast-ions was also investigated, in particular in relation with third harmonic heating and RF-induced fast particle diffusion¹⁷. Good agreement with theoretical predictions was observed. FW electron current drive has been tested in DIII-D and Tore-Supra, showing good agreement with the expected T_e -scaling⁶. Minority-ion current drive, by flattening or steeping the current density profile allowed control of the sawtooth frequency¹⁸. ICRF systems have recently found new applications in the field of plasma production in presence of a static magnetic field. The plasmas produced in this way could be used for efficient wall conditioning or for start-up assistance^{11,19,20}.

An ICRF system has been designed for ITER⁶, which would couple 50MW through three ports. A rather large voltage is required (42kV) because the coupling is relatively low due to the large distance between the antenna and the plasma.

II. LOWER HYBRID HEATING

In the lower hybrid (LH) heating domain, two waves coexist: the fast and the slow wave. For $N_{||} = 0$, they are uncoupled and evanescent and only the FW exhibits a resonance at the LH. If $N_{||}$ is increased (up to $N_{||} \approx 1$), both waves become propagating at the edge but merge some distance inside the plasma (confluence). Further in, both are evanescent (complex conjugate k_{\perp}^2) and the central part of the plasma is not accessible to the waves from the edge. It is only when the *accessibility condition* Eq.(65) of ref.³, is satisfied that the two waves uncouple and propagate both inside the plasma. The accessibility condition implies that the launcher must be designed such as to launch waves with a parallel wavelength shorter than $\lambda_{||} = c/(N_{c}f)$ (32) This is obtained by using an array of phased waveguides called the *grill*²¹.

The original concept of LH heating is to launch the slow wave (SW) at a frequency below the central value of the LH resonance. The SW then propagates up to the LH resonance and is absorbed there. It however became apparent from experiments that usually the wave tended to be absorbed by electron Landau damping before having reached the resonance. This is largely due to the cone propagation effect³. Indeed, the wave rays tend align to the magnetic field as the wave propagates inwards, eventually becoming exactly parallel at the LH resonance. Accordingly, the waves tend to circle around the plasma centre and to damp there. This efficient electron absorption is now exploited and recent LH heating experiments operate at frequencies above the central LH frequency, so that there is no longer a wave resonance inside the plasma and all the power goes to electrons. With an asymmetric $N_{||}$ spectrum, LH heating is used as a current drive method. The cone behaviour is responsible for the main problem in applying LH to reactor-size machines, namely that the LH wave energy tends to propagate peripherally around the plasma and to deposit its energy away from the plasma centre. More precise information about the location where the power is deposited in toroidal geometry can be obtained using ray-tracing techniques²².

LH was first used as a heating method. The corresponding experimental results have been nicely summarised in a plot showing the different heating regimes in FT²³. At low density, LH waves heat electrons. As the density is increased, electron heating fades away and ion heating sets in, creating ion tails. At still higher density, ion heating also decreases and disappears while parametric decay activity sets in. The different damping mechanisms of LH waves and the interpretation problems

of experimental results, such as the spectral gap problem, are described in the book by Cairns²⁴. Presently, the main application of LH is non-inductive current drive; it constitutes today the best, experimentally proven, current drive method. In large hot plasmas like ITER or reactors, the LH waves can usually not reach the centre. Accordingly, LH in ITER²⁵ is mainly seen as a tool for controlling the current profile by off-axis current drive in advanced scenarios²⁶. It can also be used for saving volt-seconds in the ramp-up phase of the plasma current.

III. ALFVEN WAVE HEATING

In the Alfvén wave domain, two types of cold-plasma waves can propagate³,

$$\omega = k_{||} c_A \quad \text{the shear Alfvén wave (SW)} \quad (33.1)$$

$$\omega = k c_A \quad \text{the compressional Alfvén wave (FW)} \quad (33.2)$$

The first of these relations implies that the shear Alfvén wave can propagate only along the field lines.

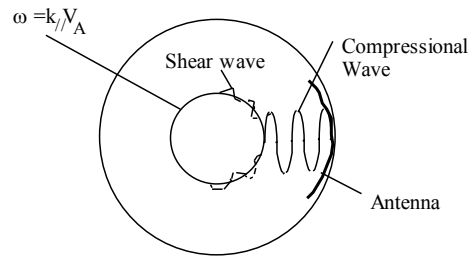


Fig. 3. The principle of Alfvén wave heating. Poloidal cross-section of the tokamak.

In an inhomogeneous plasma there is only one surface, close to a magnetic surface, where for a given $N_{||}$ the shear wave dispersion relation Eq.(33.1) is satisfied. So, the shear Alfvén wave can propagate only on that surface, as shown on Fig.3: it is trapped on that surface. Therefore, the idea is to launch from the outside the compressional Alfvén wave, which can propagate in all directions and reach the Alfvén resonance. Once the power is coupled to the shear wave, it stays on the magnetic surface and dissipates there. Note that the wavelength of the compressional wave is of the order of 1m. This means that, for 1m wide or narrower antennas, most of the wave spectrum will be evanescent with an evanescence length of the order of the antenna size¹.

From the experimental point of view the most extensive experiments and analysis of Alfvén wave heating have been performed on the TCA tokamak²⁷ ($R_0=0.6m$). Although antenna coupling and general wave behaviour appeared to be in agreement with the theory, generally speaking little plasma heating was observed

while the main effect of the RF was a large density increase, sometimes interpreted as an increase in the particle confinement time. In view of these disappointing results there have been few attempts to apply Alfvén wave heating to large tokamaks and this method is usually not mentioned for the heating of ITER or reactors. However, there has been some renewed interest in this field as the conversion to the kinetic Alfvén wave may induce poloidal shear flows, and possibly generate transport barriers²⁸.

IV. FURTHER READING

An excellent introductory overview of the different wave heating methods is given by Cairns²⁴. A very complete work on plasma waves is that of Stix⁵. Brambilla²⁹ reviews the same subject with finer detail and a more direct view toward practical applications. In particular, many dispersion relation features are discussed in detail.

REFERENCES

1. R. KOCH, "The coupling of electromagnetic power to plasmas" *These Proc.*
2. P. LAMALLE, "Kinetic theory of plasma waves: Part III Inhomogeneous plasma" *These Proc.*
3. E. WESTERHOF, "Kinetic theory of plasma waves: Part II Homogeneous plasma" *These Proc.*
4. R. KOCH, "Heating by Waves in the Ion Cyclotron Frequency Range", *Transactions of Fusion Technology*, 33, 227, (1998)
5. T.H. STIX, "Waves in plasmas", AIP New York (1992).
6. ITER team, *et al.*, "ITER Physics basis", *Nucl. Fus.* 39(1999)
7. V.P.BHATNAGAR, *et al.*, "ICRF Heating and Synergistic LH and Fast-Wave current Drive in JET", *9th Top. Conf. on Radio Freq. Power in Plasmas, Charleston* 115, (1991)
8. J.P.H.E. ONGENA, "Extrapolation to reactors", *These Proc*
9. J. JACQUINOT & The JET Team, "Deuterium-tritium operation in magnetic confinement experiment: results and underlying physics", *Plasma Phys. Contr. Fus.* 41, A13,(1999)
10. K. THOMSEN, *et al.*, "ITER H-mode confinement database update", *Nucl. Fus.* 34, 131, (1994).
11. R. KOCH, *et al.*, "Progress on TEXTOR-94: Radiative-Improved-Mode and Radio-Frequency plasma production in the Ion Cyclotron Range", Proc. VI Ukrainian Conf. and School on Plasma Phys. and Contr. Fus., Alushta 1, 70,(1998)
12. L.-G. ERIKSSON, *et al.*, "Theoretical analysis of ICRF heating in JET DT plasmas", ICPP & 25th EPS Conf. on Contr. Fus. and Plasma Phys., Prague, Europhysics Conf. Abstracts 22C, 1186, (1998)
13. L.-G. ERIKSSON, *et al.*, "Comparison of Time Dependent Simulations with Experiments in Ion Cyclotron Heated Plasmas", *Nucl. Fus.*, 33, 1037, (1993)
14. D.F.H. START, *et al.*, "ICRF Results in D-T Plasmas in JET and TFTR and Implications for ITER", *Plasma Phys. Contr. Fus.*, 40, A87, (1998)
15. R. KOCH *et al.*, "A Comparison Between ICRF Theory and Experiment", *Plasma Phys. Contr. Fus.*, 30, 1559, (1988).
16. M.PORKOLAB, *et al.*, "Recent Progress in ICRF Physics", *Plasma Phys. Contr. Fus.*, 40, A35,(1998)
17. R. KOCH *et al.*, "Interaction of ICRF Waves with Fast Particles on TEXTOR", *Plasma Phys. Contr. Fus.*, 37, A291, (1995).
18. V.P.BHATNAGAR, *et al.*, "Local Magnetic Shear Control in a Tokamak via Fast Wave Minority Ion Current Drive: Theory and Experiments in JET", *Nucl. Fus.*, 34, 1579, (1994)
19. R. KOCH *et al.*, "Low loop voltage start-up of the TEXTOR-94 plasma with ICRF and/or NBI assistance", 26th EPS Conf. on Contr. Fus. & Plasma Phys., Maastricht, (1999)
20. A. LYSSOIVAN *et al.*, "ICRF Plasma Production in TORE SUPRA: Analysis of Antenna Coupling and Plasma Properties", *ibid.*
21. A. EKEDAHL, *et al.*, "Conditioning and high power operation of the lower hybrid current drive launcher in JET" *Report JET- P(97)19* (1997)
22. M. BRAMBILLA, "Ray tracing of lower hybrid and ion cyclotron waves", *Computer Phys. Reports* 4, 71 (1986).
23. F. ALLADIO *et al.*, "Lower hybrid heating experiments on FT", in Proc. *4th Int. Symp. Heating in Toroidal Plasmas, (Roma)*, Ed. Knoepfel H., Sindoni E. 1, 546 (1984).
24. R.A. CAIRNS, "Radiofrequency heating of plasmas", Adam Hilger, IOP (1991).
25. P. FROISSARD, *et al.*, "Lower hybrid wave injection system", NET report EUR FU/XII-218/113/98 (1998)
26. D. MOREAU *et al.*, "ITER operation scenarios involving current profile control", NET report EUR FU/XII-218/112/98 (1998)
27. G. BESSON *et al.*, "A review of Alfvén waves heating", *Plasma Phys Contr. Fus.* 28, 1291 (1986).
28. G. AMARANTE SECUNDO, *et al.*, " Calculation of Alfvén wave driving forces, plasma flow, and current drive in the TCABR tokamak", *26th EPS Conf. on Contr. Fus. Plasma Phys., Maastricht*, (1999)P3.092
29. M. BRAMBILLA, "Kinetic Theory of Plasma Waves – Homogeneous Plasmas", *Clarendon Press Oxford* (1998).

ELECTRON CYCLOTRON WAVES*

Egbert Westerhof

FOM Institute DIFFER, Dutch Institute for Fundamental Energy Research,
PO Box 6336, 5600 HH Eindhoven, The Netherlands, www.differ.nl

* These lecture notes form an update of those appearing under the same title in the proceedings of the 10th Carolus Magnus Summer School

ABSTRACT

This lecture gives an overview of heating and current drive with electron cyclotron waves. We present the main theoretical aspects of wave propagation, wave absorption, and non-inductive current drive, as well as important technical aspects for the application of high power electron cyclotron waves, and the major achievements in their experimental application.

I. INTRODUCTION

Electron cyclotron waves are electromagnetic waves with a frequency in the range of the electron cyclotron frequency. For a given magnetic field the electron cyclotron frequency is 28 B [T] GHz. This means that for a typical field of 4 T or in case of second harmonic resonance and a field of 2 T, we are dealing with frequencies of the order of 100 GHz and, consequently, wavelengths of a few mm. In this frequency range, the waves can be injected from vacuum in the form of well-focused beams with higher power densities than achieved by any of the other additional heating methods (like neutral beams, ion cyclotron or lower hybrid waves). Moreover, these beams can be injected from steerable mirrors towards different parts of the plasma. Because the coupling of the power to the plasma is the result of a resonant interaction with the electrons, the power deposition in the plasma is localized. This combination of narrow, steerable beams and localized power deposition is unique for electron cyclotron resonance heating (ECRH) and current drive (ECCD). It is also what has given ECRH and ECCD its unique tasks among the other additional heating systems, in particular, for the control of instabilities. Excellent reviews of ECRH and ECCD can be found in Refs [1-4].

II. THEORETICAL ASPECTS

II.A. Wave Propagation.

A basic impression of wave propagation in the electron cyclotron range of frequencies is obtained by analysis of the cold plasma dispersion. The relevant dispersion relation is known as the Appleton-Hartree dispersion relation and is given by

$$N^2 = 1 - \frac{\omega_p^2}{\omega^2} \frac{2(\omega^2 - \omega_p^2)}{2(\omega^2 - \omega_p^2) - \omega_c^2 (\sin^2 \theta \pm \rho)} \quad (1)$$

with

$$\rho^2 = \sin^4 \theta + 4 \cos^2 \theta \left(\frac{\omega^2 - \omega_p^2}{\omega - \omega_c} \right)^2,$$

where ω is the wave frequency, $\omega_p \equiv (4\pi n_e e^2 / m_e)^{1/2}$ the electron plasma frequency, $\omega_c \equiv eB / m_e c$ the electron cyclotron frequency (defined positive here) and θ is the angle between the wave vector and the magnetic field. The + and - signs refer to the two possible modes of propagation which are known as the extraordinary or X-mode and ordinary or O-mode, respectively.

Because of toroidal symmetry, RN_ϕ is a conserved quantity along the trajectory of wave propagation. This means that the parallel refractive index, N_{\parallel} , is an approximate constant as well, such that the accessibility of the plasma to electron cyclotron waves can be gleaned from inspection of dispersion curves for the perpendicular wave vector at constant N_{\parallel} (see Figure 1). Wave cut-offs and resonances can be conveniently defined as cut-offs and resonances of the perpendicular refractive index, i.e. $N_{\perp} = 0$ and $N_{\perp} = \infty$, respectively. The O-mode is seen to have a single branch with a cut-off at the plasma frequency ω_p . The X-mode has a right hand, ω^+ , and a left hand cut-off, ω^- , and is split into two branches by an evanescent region between the right hand cut-off and the Upper-Hybrid resonance, ω_{UH} . The right hand and left hand cut-offs are given by

$$\omega^{\pm} \equiv \pm \frac{1}{2} \omega_c + \sqrt{\left(\frac{1}{2} \omega_c\right)^2 + \omega_p^2 / (1 - N_{\parallel}^2)}, \quad (2)$$

while the Upper Hybrid resonance is

$$\omega_{UH} \equiv \sqrt{\omega_c^2 + \omega_p^2}. \quad (3)$$

The upper X-mode branch $\omega > \omega^+$, which is characterized by faster-than-light phase velocities, is known as the fast X-mode branch, while the other branch limited from above by the Upper Hybrid resonance and from below by the left hand cut-off, ω^- , is the slow X-mode.

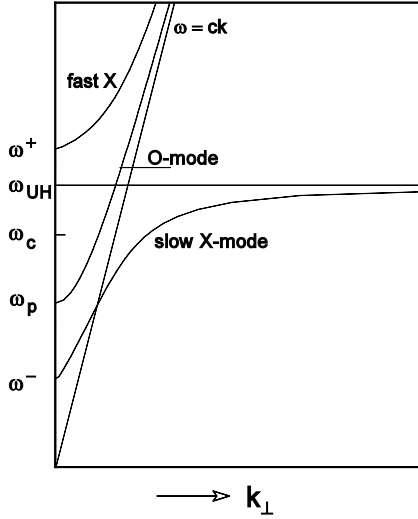


Figure 1: The dispersion diagram of high frequency electromagnetic waves is sketched for an under dense plasma, i.e. $\omega_p < \omega_c$. The O-mode is seen to propagate for $\omega > \omega_p$, while the X-mode has two cut-offs ω^{\pm} and a resonance at ω_{UH} .

These wave modes are characterized by their polarization. For perpendicular propagation, the electric field of the O-mode is parallel to the equilibrium magnetic field, and X-mode polarization is perpendicular to the magnetic field. Near the cyclotron resonance, the X-mode attains a large electrostatic contribution, which minimizes the interaction with the right handedly gyrating electrons, i.e. the perpendicular X-mode becomes left handed. Efficient absorption of X-mode at the fundamental resonance requires oblique injection of the waves or a very high plasma temperature.

Wave accessibility

In a tokamak the magnetic field is approximately inversely proportional to the major radius, $B \propto 1/R$, and the density usually rises monotonically from the edge to the magnetic axis. This leads to a picture of the wave cut-offs and resonances inside the plasma as sketched in Fig. 2. For the X-mode two cases are shown with either the fundamental or second harmonic resonance inside the plasma. The former case is characterized by the presence of an evanescent layer in between the right hand cut-off and the Upper-hybrid resonance, which shields the fundamental resonance from waves injected from the low field side. Fundamental X-mode heating is only possible with high field side (HFS) launch. The accessibility for second harmonic X-mode and fundamental O-mode is similar. They are in cut-off when either the right hand cut-off ($2X$) or plasma frequency (O), exceeds the wave frequency. Thus, waves injected from any direction can reach the resonance as long as the

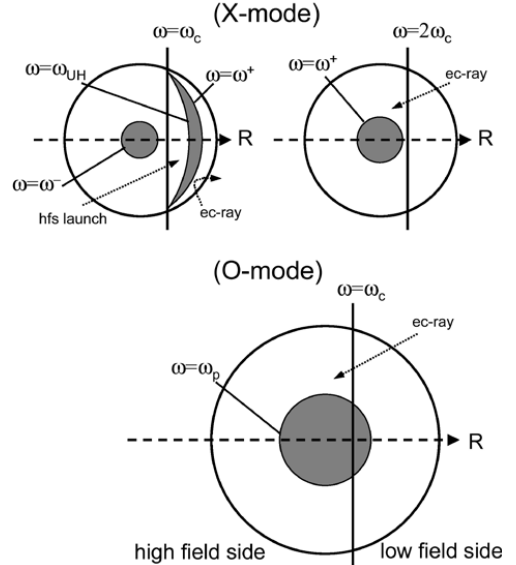


Figure 2: Wave cut-offs and resonances in a poloidal cross section of a tokamak plasma. The upper figure shows two X-mode cases with either the fundamental or second harmonic resonance inside the plasma. The lower figure shows the fundamental O-mode. A high central density is assumed in all cases such that all relevant cut-offs are in the plasma. Gray regions are evanescent. Dotted curves sketch possible wave trajectories. The dashed line indicates the major radius, R .

resonance itself is not inside a cut-off region. As densities come close to cut-off, wave refraction will play an important role. Evaluation of actual wave trajectories requires detailed ray-tracing calculations.

II.B. Wave Absorption

It is straightforward to see how a right handed gyrating electron, satisfying the resonance condition

$$\omega = \omega_c / \gamma + k_{\parallel} v_{\parallel} \quad (4)$$

is continuously accelerated in the vertical direction by a right handed polarized electric field. At the same time one easily sees that for other harmonics or a parallel electric field the interaction always averages to zero unless the wave has a finite perpendicular wave number and the electron a finite Larmor radius ρ_e . We will illustrate this by the example of the equation of motion of an electron in a perpendicularly propagating O-mode, $E_{\parallel} \cos(k_{\perp} x - \omega t)$,

$$\dot{p}_{\parallel} = -e E_{\parallel} \cos(k_{\perp} \rho_e \sin(\omega_c t / \gamma) - \omega t + \phi). \quad (5)$$

With the help of the Bessel function identity

$$\cos z \sin \phi = \sum_{n=-\infty}^{n=\infty} \cos(n\phi) J_n(z)$$

this is rewritten in terms of an infinite sum of cyclotron harmonics $n\omega_c$. One obtains,

$$\dot{p}_{\parallel} = -eE_{\parallel} \sum_{n=-\infty}^{n=\infty} \cos(n\omega_c t / \gamma - \omega t + \phi) J_n(k_{\perp} \rho_e), \quad (6)$$

which shows the possibility of resonant acceleration of electrons satisfying a (harmonic) resonance condition $n\omega_c / \gamma = \omega$. Individual particles either gain or lose energy, subject to their phase relative to the wave. Net exchange of energy between wave and plasma depends on the ensemble average over all particles. Just as in the case of Landau damping this depends on the gradient of the distribution function at the cyclotron resonance.

At this stage a side remark must be made as it may appear as if the O-mode leads to an increase of the parallel energy, whereas the wave itself carries no parallel momentum. This is because in our discussion above we have completely neglected the action of the magnetic field that is also associated with the wave. Although it cannot provide a net energy gain it does rotate the momentum vector in such a way, that the net energy gain will be in the perpendicular direction: *electron cyclotron absorption leads primarily to an increase in the perpendicular energy of resonant electrons.*

A useful quantity is the optical depth τ , which is defined as the integral of the absorption coefficient α along the trajectory s of the wave, $\tau \equiv \int \alpha ds$. The total absorbed power P_{abs} in the plasma is

$$P_{\text{abs}} = P_{\text{inj}} (1 - \exp(-\tau)). \quad (7)$$

Optical depths of a plasma slab in which the magnetic field varies as $B \sim 1/R$ are given in Table I. For the O-mode, the optical depth is given for perpendicular propagation and harmonics $n = 1, 2, \dots$. Similarly for the X-mode and harmonics $n = 2, 3, \dots$. The optical depth for the fundamental harmonic $n = 1$ of the X-mode is given for oblique propagation. In the table, N_O and N_X refer to the refractive indices of the O- and X-mode, while $v_t = (kT_e/m_e)^{1/2}$ is the thermal electron velocity. Currently, in most ECRH experiments either the fundamental O-mode or second harmonic X-mode is employed. Except near the plasma edge, optical depths of order of one or higher are generally achieved for both fundamental O- as well as second harmonic X-mode resulting in complete single pass absorption.

II.C. Non-inductive Current Drive

As described above, EC wave absorption leads mainly to an increase in perpendicular energy of resonant electrons. Nevertheless efficient non-inductive current drive by EC waves is possible. The basic mechanism is best understood as follows. Take an electron with given parallel and perpendicular momentum. This electron will lose its parallel

$\tau_{n \geq 1}^O(\perp)$	$\frac{\pi^2 n^2 (n-1)}{2^{n-1} (n-1)!} N_O^{2n-1} \left(\frac{\omega_p}{\omega_c}\right)^2 \left(\frac{v_t}{c}\right)^{2n} \frac{R}{\lambda}$
$\tau_{n \geq 2}^X(\perp)$	$\frac{\pi^2 n^2 (n-1)}{2^{n-1} (n-1)!} A_n \left(\frac{\omega_p}{\omega_c}\right)^2 \left(\frac{v_t}{c}\right)^{2(n-1)} \frac{R}{\lambda}$ with $A_n = N_X^{2n-3} \left(1 + \frac{\omega_p^2/\omega_c^2}{n(n^2-1-\omega_p^2/\omega_c^2)}\right)^2$
$\tau_{n=1}^X(\angle)$	$\pi^2 N_X^5 \left(1 + \frac{\omega_p^2}{\omega_c^2}\right)^2 \left(\frac{\omega_c}{\omega_p}\right)^2 \left(\frac{v_t}{c}\right)^2 \cos^2 \theta \frac{R}{\lambda}$

momentum in a typical momentum loss time defined by the collision frequency ν_m . Now, assume that after interaction with EC waves its perpendicular momentum is increased by a small amount. Again it will lose its parallel momentum in a collision time, but the collision frequency is now decreased since it is proportional to $\sim 1/v^3$. Oblique injection leads to a Doppler shifted resonance and selectively heats electrons moving in one direction, thus generating a net current.

This picture has been formalized by Fisch and Boozer to obtain the current drive efficiency [5]. Suppose an electron is moved from a position \mathbf{v}_1 in velocity space to a position \mathbf{v}_2 . As a consequence it contributes an additional amount of current during its subsequent slowing down, which is estimated as

$$J \equiv \frac{1}{\Delta t} \int^{\Delta t} \mathcal{J}(t) dt \approx \frac{-e}{\Delta t} \left(\frac{v_{\parallel 2}}{v_2} - \frac{v_{\parallel 1}}{v_1} \right) \quad (8)$$

where v_i are the appropriate collision frequencies for momentum slowing down. The power that has been spent to create this current is $(E_2 - E_1)/\Delta t$. Substituting differentials for the finite differences, this leads to the current drive efficiency defined as [4,5]

$$\frac{J}{P} = -e \frac{\hat{\mathbf{s}} \cdot \nabla_{\mathbf{p}} v_{\parallel} / \nu_m}{\hat{\mathbf{s}} \cdot \nabla_{\mathbf{p}} p^2 / 2m_e} \quad (9)$$

where $\hat{\mathbf{s}}$ is the unit vector in the direction of EC wave driven momentum displacement. In case of ECCD, the nominator and denominator must be integrated along the electron cyclotron resonance curve with appropriate weighting for the local (in momentum space) power absorption.

This picture is further complicated by the presence of trapped electrons. During slowing down, an electron may become trapped and, thereby, lose its remaining parallel momentum. This effect can be incorporated in the current drive efficiency (9) by substituting the correction due to trapping in the response function v_{\parallel}/ν_m . EC waves can also directly push passing electrons over the trapping boundary thereby destroying their momentum and driving a reversed current, known as the Ohkawa current [6].

The highest current drive efficiencies are expected for deposition of the wave power on fast particles. A large Doppler shift is called for to selectively heat particles with high parallel velocities. Such a Doppler

shift, of course, requires a corresponding up- or down-shift of the wave frequency with respect to the local cyclotron frequency. On this basis, two ECCD scenarios are discerned: the down-shifted scenario with waves injected from the high-field side, and the up-shifted scenario using low-field side injection. In the down shifted scenario, the X-mode is the natural mode of choice, since it has the highest possible absorption for oblique injection. For the up-shifted scenario, either the fundamental O- or second harmonic X-mode can be used.

The down-shifted scenario is the scenario of choice in smaller tokamaks, where it is difficult to obtain sufficient absorption in the fundamental O- or second harmonic X-mode. However, in large hot tokamaks the highest ECCD efficiencies are found with up-shifted scenarios. In such devices the optical depth of the fundamental O- or second harmonic X-mode is sufficient to deposit all power in energetic particles on one side of the resonance.

II.D. Numerical Tools

Ray- and Beam-tracing codes

At higher densities and, in particular near cut-off, wave refraction plays an important role and will have to be taken into account in calculations of the power deposition profiles. This is commonly done using ray-tracing codes in which a wave beam is represented by a large set of individual rays. Each of these rays is then traced through the plasma using the geometric optics approximation [7]. The power absorbed along the ray is evaluated and linear estimates of the non-inductively driven current may be obtained as well.

In many present day experiments focused beams are being used. Near the beam focus simple ray-tracing breaks down. For these conditions, beam tracing-codes have been developed. An example of such a code is the TORBEAM code [8], which describes the propagation through the plasma of a Gaussian wave beam in terms of its central ray trajectory and the evolution of its beam width and curvature.

Most ray- and beam-tracing codes evaluate the trajectories on the basis of cold plasma dispersion only using the full warm plasma dispersion relation to evaluate the power absorbed along these trajectories. However, near electron cyclotron resonance, the warm plasma dispersion and absorption are strongly inhomogeneous in both real and wave vector space. This has important consequences for the wave beam propagation both in terms of its direction [9] as well as for the beam width. Apart from full wave analyses, a proper description of these effects requires new, quasi-optical techniques [10].

Density and magnetic field perturbations due to plasma turbulence also affect wave propagation. As the turbulence is slow compared to the time scale of wave propagation, at any instant in time the wave propagation is determined by the instantaneous plasma state. Averaged over time the net effect of the turbulence can then be obtained from an ensemble average of the

different beam realizations. This idea is embodied in a recent in the WKBeam code [11]. In particular, edge turbulence in larger tokamaks like ITER has been found to result in a significant broadening of the wave power deposition profile [12].

Fokker-Planck codes

When the absorbed power density exceeds the limit of $p_{\text{abs}}[\text{MW}/\text{m}^3]/n_e^2[10^{19}/\text{m}^3] > 0.5$, EC waves will modify the electron momentum distribution function significantly [13]. This has consequences for the local power absorption as well as the non-inductively driven current. The kinetic evolution of the electron momentum distribution function can be described by the bounce-averaged quasi-linear Fokker-Planck equation, which symbolically can be written as [14]

$$\frac{\partial f_e}{\partial t} = \frac{\partial f_e}{\partial t} \Big|_{\text{collisions}} + \frac{\partial f_e}{\partial t} \Big|_{\text{ECRH}} + \frac{\partial f_e}{\partial t} \Big|_{E_{\parallel}}, \quad (10)$$

where the distribution function is averaged over the fast gyro and bounce motion of the electrons. This gives an equation for the distribution function on each magnetic surface that is 2D in momentum space (p_{\parallel}, p_{\perp}). The Fokker-Planck equation describes the balance between collisions, driving the distribution function back to Maxwellian, the diffusion of resonant particles driven by the waves, as well as the convection caused by a parallel electric field. An additional term can be added to model the anomalous radial transport of electrons. This makes the model 3D and becomes necessary, when the relevant collisional timescale on which a steady state is reached, becomes similar to the time scale for radial transport. Several numerical 3D Fokker-Planck codes are available and have been used to model non-thermal electron generation and current drive under conditions of high power ECRH [14].

III. TECHNICAL ASPECTS

III.A. Wave Sources

The high power required for ECRH and ECCD experiments is provided by gyrotrons [15]. In a gyrotron the waves are generated by leading a weakly relativistic electron beam (typically ~ 80 kV) through a resonant cavity in a magnetic field. A magnetic field slightly in excess of $v(\text{GHz})/28$ T is required for efficient fundamental interaction. The field must be very stable and is usually generated by a superconducting magnet. The specific (wave guide) mode that is generated in the cavity depends on the magnetic field, the position in the cavity of the electron beam and the size of the cavity. Modern gyrotrons use high order modes (for example, $\text{TE}_{22,6}$) to limit dissipation in the cavity. An internal quasi optical mode converter is used to convert the radiation into a Gaussian beam, which is coupled out of the gyrotron.

One of the most critical issues for high power, long pulse gyrotrons is the handling of the power dissipation

in the various components: in particular, inside the cavity, on the collector where the power of the spent electron beam is being dumped, and in the vacuum window through which the radiation is transmitted. In the latest generation of gyrotrons the dissipation in the collector is reduced by using a depressed collector. This also improves the overall efficiency of the gyrotron to well over 50% as required by ITER specifications. The material of choice for the vacuum window these days is CVD (Chemical Vapor Deposition) diamond, which combines a very low loss for mm waves with very high heat conductivity. Long pulse, 1 MW gyrotrons in the 100 to 170 GHz range are now available and 2 MW coaxial gyrotrons are being developed. In addition, multi-frequency gyrotrons are now becoming available providing even further flexibility to future ECRH systems.

III.B. Wave Transmission and injection

Wave transmission from the source to the plasma is commonly achieved by oversized waveguides, quasi-optical lines, or a mixture of both. Modern waveguides are now generally corrugated and employ the low loss HE₁₁ mode (hybrid TE₁₁/TM₁₁). This mode couples well to a Gaussian beam and vice versa. The coupling efficiency has a sharp maximum at the appropriate waveguide diameter. Also optical techniques like miter (mirror) bends can be used. In such cases transmission is very efficient with the losses being determined mainly by the bends (0.25% to 0.5% per bend). In case of high power wave transmission or small diameter waveguides, arcing can pose serious problems. In order to avoid arcing, evacuated waveguides have been employed.

In quasi-optical (QO) lines the free space Gaussian beam is transported between mirrors. Though achieving equally high transmission efficiency, QO systems require significantly more space to allow for the expansion of the Gaussian beam between mirrors.



Figure 3: Picture of the launching mirror of the TEXTOR ECRH system. The focusing mirror and the push and pull rods for actuation of horizontal and vertical rotation are visible.

Typical losses on individual copper mirrors are 0.2 %. On most tokamaks, a focused wave beam is finally launched quasi-optically from a steerable mirror. An example of the latter is given in Fig. 3, which shows the launching mirror of the former TEXTOR ECRH system. The TEXTOR ECRH launcher, which was steerable in both the horizontal and vertical planes. Up to date descriptions of modern ECRH systems in use on various tokamaks can be found in Refs [16–20].

IV. EXPERIMENTAL RESULTS

IV.A. Validation of Propagation and Absorption

A first step in the experimental verification of theoretical predictions regarding wave propagation and absorption is the measurement of transmitted power. Such measurements have been performed in the electron cyclotron range of frequencies both at low power for diagnostic purposes as well as at high power (see Ref. [2] and references therein). Measurements generally agree well with predictions from ray-tracing as long as refraction is not too strong. It is likely that at high densities, close to cut-off, fluctuations in the plasma can give rise to time varying refraction, which on average leads to a broadening of the wave beam.

The absorption profile can be determined by the initial plasma response following switch-on of ECRH (assuming a steady state at the time of switch on):

$$p_{\text{ECRH}}(r) = \frac{\partial}{\partial t} \left(\frac{3}{2} n_e k T_e \right)_{t=t+} \quad (11)$$

Alternatively, it can be determined by the plasma response at switch-off or by the plasma response to modulated ECRH [21]. The location of the power deposition is generally observed to coincide well with predictions from ray- or beam-tracing [3,22]. Several experiments report total amounts of measured power significantly below the amount of power absorbed from the beam according to transmission measurements or calculations. The ‘missing power’ has been ascribed to fast changes in electron transport or hidden energy reservoirs [2]. In more recent power deposition studies on ASDEX-Upgrade, the full absorbed power could be accounted for in the deposition measurements [22].

IV.B. Validation of Current Drive Predictions

Measurements of the EC driven current are usually complicated by the presence of other currents like the bootstrap current and, in most cases, the inductive current. The presence of a residual loop voltage also affects the current drive efficiency. Bounce averaged Fokker-Planck code calculations predict significant synergy between ECCD and the loop Voltage in agreement with experiments [23]. Large differences are predicted between co- and counter current drive [24]. The most detailed comparison between experiments and simulations comes from DIII-D. In the analysis of these experiments measurements of the Motional Stark Effect

are used to determine the internal poloidal magnetic field and from there the current density distribution. Comparing discharges with and without ECCD the driven current is obtained. A series of equilibrium reconstructions is required to obtain the loop voltage at the position of ECCD. That information has been used in a bounce averaged Fokker-Planck code (CQL3D [25]) to simulate the experiments. Such a complete simulation is shown to provide a good fit to the experimental results [26]. Simulations either neglecting the parallel electric field or based on a linear calculation of the driven current lead to unsatisfactory fits. The data set covers co- as well as counter-drive, and a large range of minor radii. In addition, the data covers a wide range in the non-linearity parameter $p_{\text{abs}}[\text{MW}/\text{m}^3]/n_e^2[10^{19}/\text{m}^3]$ with many points near or over the threshold [3,26]. The good correspondence of the data and the simulations provides a critical test of the bounce averaged quasi-linear Fokker-Planck model including, in particular, trapped particle effects.

Fully non-inductive current drive with ECCD has only been obtained in a limited number of tokamaks. This generally requires special conditions like low density and or low plasma current to maximize on the one hand the EC driven current and on the other hand the bootstrap current fraction. One such example comes from the T-10 tokamak [27]. However, in this case the ECCD pulse was relatively short and a steady state was not reached. More recently, fully non-inductive current drive with ECCD has been obtained in TCV. The discharge could be maintained stable over several current redistribution times provided a sufficiently broad current profile was driven by ECCD [28]. This was achieved by aiming three ECCD beams at different positions in the poloidal cross section.

IV.C. Plasma Heating and Confinement

In terms of confinement, plasmas heated by ECRH behave in very much the same way as plasmas heated by other additional heating methods such as NBI and ICRH [2]: ECR heated plasmas roughly follow the L-mode scaling. The transition to H-mode is observed at the expected power level or even below. Differences in confinement scaling can be attributed to the strong (central) localization of the ECRH power deposition and the fact that ECRH heats only electrons. The latter two effects also have consequences for the particle transport: the central density some times displays a strong pump-out during ECRH.

In several experiments, very high central electron temperatures of the order of 10 keV have been achieved with central power deposition. In particular, in the presence of an internal transport barrier created by a region of negative or reduced magnetic shear. For example, on TCV [29] this has been achieved by using ECCD to drive some counter-current on axis to establish the negative shear, while on ASDEX Upgrade [30] ECRH has been applied during a preexisting internal transport barrier, established through a programmed current ramp.

The localized nature of the ECRH power deposition makes it an ideal tool for detailed studies of electron transport. One such study has been performed on the RTP tokamak, where a scan of the power deposition over the minor radius revealed a complex response of the plasma with multiple internal transport barriers [31]. Modulation of the ECRH power has become a standard tool for the study of the electron heat diffusivity [21].

IV.D. MHD Stability Control

The localization of the power deposition also makes ECRH and ECCD ideal tools to control the plasma pressure or current density profiles, which determine the MHD stability of the plasma. Several instabilities are affected by ECRH: sawteeth, tearing modes, ELMs, etc..

Most tokamaks equipped with ECRH report a lengthening of the sawtooth period or complete sawtooth stabilization by ECRH near the sawtooth inversion radius (see, e.g. the early experiments on T-10 [32] or the more recent and more detailed results from TCV [33] and ASDEX Upgrade [34]). The sawtooth crash is triggered when the $m=1$, $n=1$ internal kink mode is destabilized [35]. The stability threshold of this mode is seen to depend on the shear at the $q=1$ surface. Consequently, changes to the shear at $q=1$ affected by localized current drive such as ECCD can strongly change the sawtooth period. This has been observed in various experiments and has been modeled in detail for TCV [36]. The dependence of the internal kink stability threshold on the local shear can also be used to derive a simple criterion for the required EC driven current to have a significant effect on the sawtooth period [37]:

$$I_{cd} \geq 2I_{q=1}(\Delta r_{cd} / r_{q=1})^2 \quad (12)$$

where I_{cd} is the non-inductively driven current with a Gaussian width of Δr_{cd} , and $I_{q=1}$ is the plasma current inside the $q=1$ surface, $r_{q=1}$. Co-current drive just inside the $q=1$ surface is found to shorten the sawtooth period, whereas co-current driven just outside the $q=1$ surface will lengthen the sawtooth period. Counter-current drive will have just the opposite effect. A comprehensive review of sawtooth control is provided in Ref. [38].

The control of tearing modes by ECRH and ECCD has received a lot of attention over the years. This stems from the potential threat that these modes pose to tokamak reactors: large tearing modes not only lead to a substantial degradation of plasma confinement, they may also lead to disruption of the plasma [39]. In particular, control of neoclassical tearing modes (NTM) occurring in high β tokamak plasmas has been studied [40]. The stability of an (N)TM can be affected in two ways. First, through control of the equilibrium profiles which determine the stability parameter Δ' [41]. Second, by generating additional current, the failing current inside the magnetic island, responsible for its instability, can be replaced resulting in stabilization of the mode [40]. The additional current inside the island can either be generated inductively by heating the island, or driven non-inductively, for example, by ECCD [42]. The

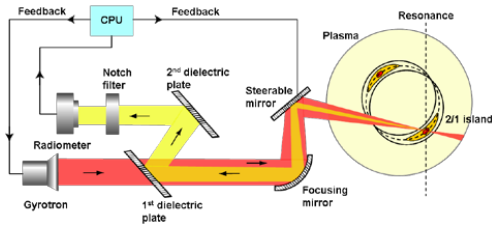


Figure 4: The principle of inline ECE as sensor for feedback controlled EC power deposition. The dielectric plates stand for frequency selective couplers that transmit the high power ECRH waves but reflect the low power ECE at desired frequencies. When the steering mirror is adjusted such that a feature like a 2/1 magnetic island is localized in the sensor spectrum at the actuator (gyrotron) frequency, the power deposition exactly on that feature is ensured.

suppression of NTMs by ECCD has been demonstrated in several experiments [43-46].

In several experiments the NTM suppression was achieved by operation of the ECRH systems under full feedback control [45,46]. EC emission (ECE) is used as sensor to detect the location of the NTM with the help of the oscillations due to the mode on the ECE signals, and this knowledge is then used to steer the actuator, i.e. the ECRH launcher, in the proper direction. This requires accurate real-time knowledge of the equilibrium and real-time ray tracing to link the sensor derived location to the reference frame of the actuator. To circumvent these latter steps, inline ECE (see Figure 4) has been proposed [47]. In this case the sensing occurs along the reference frame of the actuator, i.e. the gyrotron wave beam. A proof-of-principle inline ECE system was implemented on TEXTOR [48] and used successfully to demonstration tracking and suppression of tearing modes [49].

V. THE ITER ECRH SYSTEMS

The international experimental fusion reactor ITER will be equipped with an advanced ECRH system [50-52]. According to the ITER design requirements and guidelines this system must have the capability to perform or assist in a number of tasks: (1) heating in order to access H-mode and reach conditions for $Q > 10$ operation, (2) on and off-axis current drive for steady state operation (achieving a current density on axis of $> 20 \text{ MA/m}^2$ and a total driven current inside $\rho = 0.6$ in excess of 1 MA), (3) stabilization of NTMs by current drive at the $q=3/2$ and $q=2$ surfaces, (4) wall conditioning, and (5) start-up assist. To (3) should be added the control of sawteeth by current drive at the $q=1$ surface. To perform these tasks an ECRH system has been designed consisting of a total of 24, 170 GHz gyrotrons each capable of delivering a power of 1 MW, CW. The power will be transferred to the tokamak

through evacuated HE_{11} wave guide using wave guide switches to switch between the alternate upper-port or mid-plane launchers. Due to limited steering capabilities of these launchers, each of them will be used to perform specific tasks. The mid plane launcher is optimized for central heating and current drive, whereas the upper port launcher design is optimized towards the control of NTMs (cf. Fig. 5) and sawteeth. The design work is supported by extensive simulations for the various tasks and by extrapolation from current experiments to ITER [53-55]. Still uncertainties remain. For example, edge density fluctuations have been shown to potentially result in a doubling of the ECCD power deposition profile width near the $q=1.5$ or 2 rational surfaces, which would correspond to an equivalent increase in the required ECCD power for NTM suppression [12].

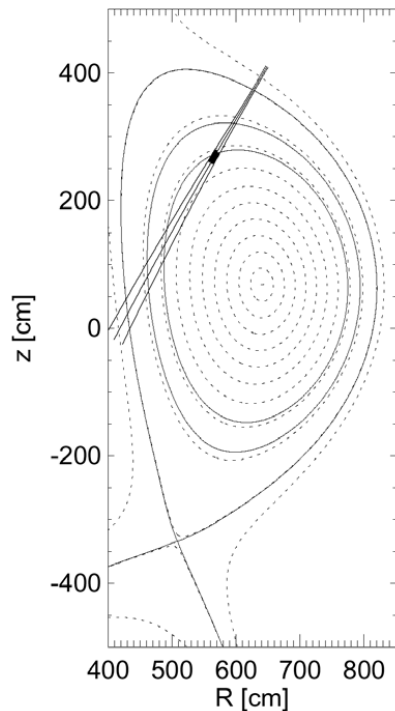


Figure 5: Example of results from of a beam tracing calculation with the TORRBEAM code for a single wave beam coming from an upper launcher, aiming at the $q=3/2$ surface. The black region shows the well localized area of power deposition. The dotted curves indicate flux surfaces with some special surfaces indicated by full lines, from the outside going in: the separatrix, the $q=2$, and $q=3/2$ surface, respectively.

ACKNOWLEDGMENTS

This work was carried out with financial support from NWO.

REFERENCES

- [1] M. BORNATICI, et al. Nucl. Fusion, **23**, 1153 (1983).
- [2] V. ERCKMANN, and U. GASPARINO, Plasma Phys. Contr. Fusion, **36**, 1869 (1994).
- [3] R. PRATER, Phys. Plasmas, **11**, 2349 (2004).
- [4] N.J. FISCH, Rev. Modern Phys. **59** 175 (1987)
- [5] N.J. FISCH, A.H. BOOZER, Phys. Rev. Lett. **45** 720 (1980).
- [6] T. OHKAWA, Steady state operation of tokamaks by rf heating, General Atomics Report GA-A13847 (1976).
- [7] R. PRATER, et al., Nucl. Fusion **48** 035006 (2008).
- [8] E. POLI, A.G. PEETERS, G.V. PEREVERZEV, Comput. Phys. Commun. **136**, 90 (2001).
- [9] M.D. TOKMAN, et al., Nucl. Fusion **43**, 1295 (2003).
- [10] A.A. BALAKIN, et al., Nuclear Fusion **48**, 065003 (2008).
- [11] H. WEBER, et al., EPJ Web of Conferences **87**, 01002 (2015).
- [12] E. POLI, et al., Nucl. Fusion **55** (2015) 013023.
- [13] R.W. HARVEY, et al., Phys. Rev. Lett. **62**, 426 (1989).
- [14] E. WESTERHOF, *Proc. of 9th Joint Workshop on ECE and ECH, Borrego Springs, California, 1995*, Ed. J. Lohr, World Scientific, Singapore, p. 3 (1995).
- [15] G.S. NUSINOVICH, M.K.A. THUMM, M.I. PETELIN, J. Infrared Milli Terahz Waves **35** (2014) 325.
- [16] T.P. GOODMAN, et al., Proc. 19th Symp. Fusion Technology, Lisbon, 16-20 September 1996, Ed. C. Varandas, F. Serra (North-Holland, Amsterdam, 1997), Vol. 1 pp. 565 (1996).
- [17] F. LEUTERER, et al., Nucl. Fusion **43**, 1329 (2003).
- [18] R.W. CALLIS, et al., Nucl. Fusion **43**, 1501 (2003).
- [19] Y. IKEDA, et al., Fus. Eng. Design **53**, 351 (2001).
- [20] E. WESTERHOF, et al., Nucl. Fusion **43**, 1371 (2003).
- [21] G.M.D. HOGWEIJ, Transport studies using perturbative experiments, these proc. (2012).
- [22] K.K. KIROV, et al., Plasma Phys. Controlled Fusion **44**, 2583 (2002).
- [23] R.A. JAMES, et al., Phys. Rev. A **88**, 8783 (1992).
- [24] A. MERKULOV, et al., Phys. Plasmas **14**, 052508 (2007).
- [25] R.W. HARVEY, M.G. McCOY, *Proc. IAEA TCM Advances in simulations and modeling of thermonuclear plasmas*, Montreal, Canada, 1992 (IAEA, Vienna, 1993) p.498.
- [26] C.C. PETTY, et al., Nucl. Fusion **42**, 1366 (2002).
- [27] V.V. ALIKAEV, et al., Nucl. Fusion **32**, 1811 (1992).
- [28] O. SAUTER, et al., Phys. Rev. Lett. **84**, 3322 (2000).
- [29] Z.A. PIETRZYK, et al., Phys. Rev. Lett. **86**, 1530 (2001).
- [30] S. GÜNTER, et al., Phys. Rev. Lett. **84**, 3097 (2000).
- [31] N.J. LOPES CARDOZO, et al., Plasma Phys. Control. Fusion **39** B303 (1997)
- [32] R.M.J. SILLEN, et al., Nucl. Fusion **26**, 303 (1986).
- [33] Z.A. PIETRZYK, et al., Nucl. Fusion **39**, 587 (1999).
- [34] A. MÜCK, et al., Plasma Phys. Control. Fusion **47** 1633 (2005).
- [35] F. PORCELLI, et al., Plasma Phys. Control. Fusion **38**, 2163 (1996).
- [36] C. ANGIONI, et al., Nucl. Fusion **43**, 455 (2003)
- [37] A. MERKULOV, et al., *Theory of Fusion Plasmas, Proc. Joint Varenna-Lausanne Int. Workshop, Varenna, Italy, August 30 – September 3 2004*, J.W. Connor, O. Sauter, and E. Sindoni (Editors), Societa Italiana di Fisica, Bologna, 2004, p. 279.
- [38] I.T. CHAPMAN, et al., Plasma Phys. Control. Fusion **49** (2007) B385–B394.
- [39] H.R. KOSLOWSKI, Operational limits and limiting instabilities in tokamak machines, these proceedings (2015)
- [40] R.J. LA HAYE, Phys. Plasmas **13**, 055501 (2006).
- [41] E. WESTERHOF, Nucl. Fusion **30** 1143 (1990)
- [42] C.C. HEGNA, J.D. CALLEN, Phys. Plasmas **4**, 2940 (1997).
- [43] G. GANTENBEIN, et al., Phys. Rev. Lett. **85**, 1242 (2000).
- [44] C.C. PETTY, et al., Nucl. Fusion **44**, 243 (2004).
- [45] A. ISAYAMA, et al., Nucl. Fusion **43**, 1272 (2003).
- [46] F. FELICI, et al., Nucl. Fusion **52** (2012) 074001.
- [47] E. WESTERHOF, et al., 13th Joint Workshop on ECE & ECRH (17–20 May 2004), ed. A. Litvak (Nizhny Novgorod, Russia: IAP/RAS) p. 357 (2005).
- [48] J.W. OOSTERBEEK, et al., Rev. Sci. Instruments **79**, 093503 (2008).
- [49] B.A. HENNEN, et al., Plasma Phys. Controlled Fusion **52**, 104006 (2010)
- [50] M.A. HENDERSON, et al., Nucl. Fusion **48**, 054013 (2008).
- [51] K. TAKAHASHI, et al., Fusion Sci. Technol. **47**, 1 (2005)
- [52] M. HENDERSON, et al., Phys. Plasmas **22**, 021808 (2015).
- [53] D. FARINA, et al., Phys. Plasmas **21**, 061504 (2014).
- [54] R.J. LA HAYE, et al., Nucl. Fusion **46**, 451 (2006).
- [55] I.T. CHAPMAN, et al., Nucl. Fusion **53** (2013) 066001.

NON-INDUCTIVE CURRENT DRIVE*

Egbert Westerhof

FOM Institute DIFFER, Dutch Institute for Fundamental Energy Research,
PO Box 6336, 5600 HH Eindhoven, The Netherlands, www.differ.nl

* These lecture notes are identical (except for minor corrections) to the lecture notes appearing in the proceedings of the 10th Carolus Magnus Summer School

ABSTRACT

This lecture addresses the various ways of non-inductive current generation. In particular, the topics covered include the bootstrap current, RF current drive, neutral beam current drive, alternative methods, and possible synergies between different ways of non-inductive current generation.

I. INTRODUCTION

Earlier lectures [1,2] have stressed the requirement of a finite poloidal magnetic field in addition to the toroidal magnetic field in order to confine charged particles in a toroidal configuration. Whereas in a stellarator the poloidal field is supplied by external coils [3], the tokamak relies on a toroidal plasma current for the generation of the poloidal field. Generally, the toroidal current in a tokamak is generated inductively by means of a transformer, in which the plasma acts as the secondary winding [1]. This immediately leads to a major limitation of tokamak operation: the finite flux swing of the transformer in combination with the finite resistivity of the plasma results in a finite pulse length of a tokamak discharge and necessarily pulsed reactor operation. For many reasons steady state operation of a fusion reactor is highly desirable. This has motivated the development of alternate ways for the generation of the toroidal plasma current. Such methods are classified as ‘non-inductive current drive’. A second advantage offered by non-inductive current drive, is that it decouples the current density profile from the temperature profile, which determines the plasma conductivity and consequently defines the inductive current density profile. The freedom to shape the current density profile is particularly important for the control of plasma stability [4, 5].

An important measure is the efficiency of current drive which can be defined as the ratio of the driven current density, j , over the spent power density, p : $\eta_{CD} \equiv j/p$. Since the total current generated scales as $I_{CD} \sim \pi a^2 j$, while the total spent power scales as $P \sim 2\pi R \pi a^2 p$, a more practical measure for the current drive efficiency is $\eta_{CD} \equiv n_e R I_{CD} / P$. Here, a and R are the minor and major radius of the tokamak, respectively. The factor n_e accounts for the fact that in many cases the non-inductively driven current is inversely proportional to the

density such that the current drive efficiency η_{CD} becomes a constant which can be compared across different experiments and used for extrapolation to future devices.

Subsequent sections treat various methods of non-inductive current generation. First, the so-called bootstrap current is discussed, which in a toroidal device comes entirely for free. It is a parallel (with respect to the magnetic field) plasma current which is driven by finite pressure gradients in toroidal geometry. Next, the various methods of non-inductive current generation by radio frequency (RF) waves are treated. This is followed by a discussion of the current generated by injection of neutral particle beams and a brief overview of various alternate concepts for non-inductive current generation.

For further reading we advise the excellent early review by N.J. Fisch [6], and for later updates the relevant chapters of the ITER Physics Basis [7] and its update [8]. Very instructive is also the book by J. Wesson [9].

II. BOOTSTRAP CURRENT

Neoclassical, collisional transport [10] in high pressure toroidal plasma generates a finite parallel plasma current. This current is known as the bootstrap current and is entirely self generated by the plasma [9, 11]. Its origin can be best understood as follows. In toroidal plasma the particles do not follow the magnetic field lines exactly, but exhibit a finite drift as a consequence of the magnetic field curvature and inhomogeneity. For the trapped particles this results in banana shaped orbits with a finite width [4]

$$w_b = 2 \frac{mv_{\parallel,m}}{qB_{p,m}}, \quad (1)$$

where q is the charge of the particle, m its mass, and $v_{\parallel,m}$ and $B_{p,m}$ are the parallel velocity and poloidal magnetic field at the mid plane (i.e. the position of minimum magnetic field along the orbit). In the presence of a finite density gradient, this results at any given point on the mid plane in an imbalance between the trapped particles moving in co- and counter-current direction. This constitutes the banana current. The bootstrap current finally is generated through collisional coupling of the trapped and passing particles. Formulated in terms of the velocity distribution function at a given position on the

low field side of the mid plane, one notices that a finite density gradient results in an asymmetry in the trapped particle region. Collisions will extend this asymmetry across the trapped passing boundary into the passing particle region resulting in the bootstrap current.

In a more complete theory, not only the density gradient, but also the temperature gradient is seen to contribute to the bootstrap current. For large aspect ratio $\epsilon^{-1} \equiv R/a$, the expression for the bootstrap current is [10]

$$j_{BS} = -\frac{\sqrt{\epsilon} n}{B_p} \left(2.44(T_e + T_i) \frac{dn}{n dr} + 0.69 \frac{dT_e}{dr} - 0.42 \frac{dT_i}{dr} \right), \quad (2)$$

while for $\epsilon \rightarrow 1$ it reduces to [10]

$$j_{BS} = -\frac{1}{B_p} \frac{dp}{dr}, \quad (3)$$

where p is the total plasma pressure.

III. PRINCIPLES OF RF CURRENT DRIVE [6]

Intuitively, the generation of a non-inductive current appears to require some method to directly impart parallel momentum to electrons. This could be done for example by means of neutral beams (see Section IV) or through resonant interaction with RF waves. In the latter case, the wave can impart its energy and momentum to electrons satisfying either the Landau resonance, $\omega - \mathbf{k} \cdot \mathbf{v} = 0$, or, in the case of strongly magnetized plasmas, the cyclotron resonance, $\omega - k_{\parallel} v_{\parallel} - n\Omega_e/\gamma = 0$ ($n = \pm 1, \pm 2, \dots$).

An estimate of the theoretical current drive efficiency is obtained from the following arguments. Suppose the parallel momentum imparted to an electron is $m\Delta v_{\parallel}$. The incremental current carried by this electron is $\Delta j = -e\Delta v_{\parallel}$, while its incremental energy is $\Delta \epsilon = m v_{\parallel} \Delta v_{\parallel}$. The fact that $\Delta \epsilon/\Delta j$ is proportional to v_{\parallel} , shows that it is energetically favorable to accelerate low parallel velocity electrons and, consequently, first studies of RF current drive focused on waves with low phase velocity $\omega/k \ll v_{te}$ such as Alfvén waves. However, the incremental current will decay with the collision frequency $\nu(v) \sim 1/v^3$ and the power required to sustain this current consequently is $P_{RF} = \nu(v)\Delta \epsilon$. Using the notation $J = \Delta j$, and combining the expressions for Δj , $\Delta \epsilon$ and P_{RF} , one obtains the theoretical steady state current drive efficiency as

$$\frac{J}{P_{RF}} = \frac{-e}{m v_{\parallel} \nu(v)}. \quad (4)$$

Thus, maximizing the current drive efficiency requires minimizing the expression $v_{\parallel} \nu(v)$. Optimization is obtained in two opposite limits (see also Fig. 1): for $v_{\parallel} \rightarrow 0$, but $v_{\perp} \approx v_{te}$, one has $\nu(v) \approx$ constant; while for $v_{\parallel} \gg v_{te}$, $\nu(v) \sim 1/v_{\parallel}^3$. The second limit calls for the use of waves with high parallel phase velocity such as Lower Hybrid (LH) waves (lower hybrid current drive, LHCD).

It can be shown that the direct transfer of parallel momentum is not even a strict requirement for current drive. This was first realized by N.J. Fisch and A.H.

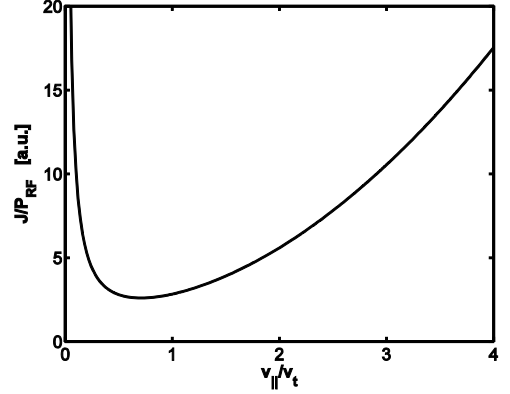


Figure 1: The theoretical current drive efficiency (in arbitrary units) for direct momentum transfer as a function of the parallel velocity.

Boozer [12]. The basic argument runs as follows. Take an electron with given parallel and perpendicular momentum, $m v_1$. This electron would lose its parallel momentum in a typical momentum loss time defined by the collision frequency ν_1 . As its parallel momentum decays, it would contribute a parallel current which averaged over the time Δt can be approximated by $J_1 \approx -e v_{\parallel 1}/\Delta t \nu_1$. Now, assume that after interaction with EC waves its momentum is changed by a small amount to $m v_2$. Again it will lose its parallel momentum in a collision time, but the collision frequency is now changed since it is proportional to $1/v^3$. As a result a net current is generated, which can be equated to

$$J \equiv J_2 - J_1 \approx \frac{-e}{\Delta t} \left(\frac{v_{\parallel 2}}{\nu_2} - \frac{v_{\parallel 1}}{\nu_1} \right). \quad (5)$$

The power that has been spent to create this current is $(E_2 - E_1)/\Delta t$. Substituting differentials for the finite differences, this leads to the Fisch-Boozer current drive efficiency given by [6, 12]

$$\frac{J}{P_{RF}} = -e \frac{\hat{s} \cdot \nabla_{\mathbf{p}} (v_{\parallel}/\nu)}{\hat{s} \cdot \nabla_{\mathbf{p}} (p^2/2m_e)} \quad (6)$$

where \hat{s} is the unit vector in the direction of RF driven momentum displacement. As parallel momentum transfer between waves and particles no longer is a requirement, also waves which carry little or no parallel momentum can be used for effective current drive. In fact, the theoretical efficiency for current drive by perpendicular pushing of electrons reaches up to 3/4 of the efficiency for direct parallel pushing of electrons [13]. This holds, in particular, for electron cyclotron current drive (ECCD).

It has subsequently been found that ‘adjoint techniques’ allow to find a more precise expression for the ‘current response function’, $\chi = -e v_{\parallel}/\nu$. Starting from the steady state Fokker-Planck equation,

$$C(f_e(\mathbf{v})) = \nabla_{\mathbf{p}} \cdot \mathcal{S}_w, \quad (7)$$

where \mathcal{S}_w is the quasi-linear wave driven momentum space flux, an adjoint equation for the current response function can be written as [6, 14]

$$C(f_{em}(v)\chi(v)) = ev_{\parallel}f_{em}(v), \quad (8)$$

where $f_{em}(v)$ is the Maxwellian distribution function, and $f_{em}(v)\chi(v)$ is required to have zero density and energy. Now, writing the current from the solution to the steady state Fokker-Planck equation as

$$J = -\int ev_{\parallel}f_e(v) d^3v = -\int (f_e/f_{em}) C(f_{em}\chi) d^3v, \quad (9)$$

and using the self-adjointness of the collision operator,

$$\int \psi C(f_{em}\chi) d^3v = \int \chi C(f_{em}\psi) d^3v, \quad (10)$$

it is easily shown that

$$J = \int \mathcal{S}_w \cdot \nabla_p \chi d^3v. \quad (11)$$

The current drive efficiency then becomes

$$\frac{J}{P_{RF}} = -e \frac{\int \hat{s} \cdot \nabla_p \chi d^3v}{\int \hat{s} \cdot \nabla_p (p^2/2m_e) d^3v} \quad (12)$$

generalizing the Fisch-Boozer efficiency (6). These adjoint techniques are limited to the regime in which the plasma response to the RF waves is almost linear. When significant quasi-linear modifications of the distribution function are induced, a proper estimate of the driven current can only be obtained from solution of the full Fokker-Planck equation.

The presence of trapped electrons further complicates the picture: in a tokamak or stellarator, all particles in the cone in velocity space given by $|v_{\parallel 0}/v_{\perp 0}| < (B_{\max}/B_{\min}-1)^{0.5}$ are trapped between the magnetic field maxima along a field line [2]. Trapped particles have zero average parallel velocity and cannot contribute to the parallel current. Consequently, when a passing particle crosses the trapped/ passing boundary during its slowing down, it no longer contributes any parallel current. This will reduce the current drive efficiency. As a passing particle is pushed across the trapped/passing boundary by the resonant interaction with RF waves, its contribution to the parallel current is lost and a net current is driven in the opposite direction, which is known as the Ohkawa current [15]. Furthermore, increasing a particle's perpendicular energy near the maximum in the magnetic field will increase its parallel velocity on the remainder of its trajectory. This should favor current drive by pushing particles in the perpendicular direction (in particular, ECCD) on the high field side. All these effects can be included in an adjoint calculation of the current drive efficiency by calculating the appropriate current response function for the bounce-averaged Fokker-Planck equation [16, 17, 18].

III.A. Lower Hybrid Current Drive (LHCD)

LHCD has proven to be the most successful non-inductive current drive method in tokamaks to date [19]. It makes use of the slow wave in the intermediate frequency regime between the ion and electron cyclotron frequencies: $\Omega_{ci} \ll \omega \ll |\Omega_{ce}|$. This is the realm of the lower hybrid resonance,

$$\omega_{LH} = \frac{\omega_{pi}^2}{1 + \omega_{pe}^2/\Omega_{ce}^2} = \frac{|\Omega_{ci}\Omega_{ce}|}{1 + \Omega_{ce}^2/\omega_{pe}^2}. \quad (13)$$

For the slow wave to have access to the high density part of the plasma in this frequency range, the parallel refractive index must satisfy the accessibility condition [20]

$$N_{\parallel} > N_c \equiv \frac{1}{1 - \omega^2/|\Omega_{ci}\Omega_{ce}|}. \quad (14)$$

As a result, the waves are evanescent at the plasma edge and efficient coupling of the waves requires a close proximity of the LH wave antenna to the plasma edge. A particular property of lower hybrid waves is that the group velocity is perpendicular to the wave vector. Since also typically $k_{\perp} \gg k_{\parallel}$, the group velocity is almost parallel to the magnetic field and the wave propagates in a narrow ‘‘resonance cone’’ along the magnetic field. This means that the waves can only reach the centre of the plasma after traveling a number of times around the torus.

For efficient current drive, one should avoid parasitic damping of the waves by ions and, in case of a reactor, by fusion alpha particles. This requires the use of sufficiently high frequencies in order to avoid the presence of the lower hybrid resonance inside the plasma. In addition, efficient current drive is favored by high phase velocities, i.e. small N_{\parallel} . While one would expect such high phase velocities with $v_{ph} \gg v_{te}$ to be ill absorbed as a consequence of exponentially small numbers of resonant electrons, early experiments nevertheless showed good absorption. The reason for this is the generation of an extended tail of energetic electrons by quasi-linear interaction with lower phase velocity components not originally present in the launched wave spectrum. The generation in the plasma of these lower phase velocity components is known as the ‘‘spectral gap’’ problem. It is generally assumed that the multi-pass ray trajectories in these experiments are responsible for the required N_{\parallel} upshift [21]. Several alternative explanations have been proposed to fill the spectral gap, including spectral broadening due to scattering off density fluctuations, wave diffraction, magnetic ripple, and parametric instabilities in the scrape-off layer in front of the launching antenna [22]. State of the art modeling employs coupled 3D ray-tracing and (2D in velocity space) Fokker-Planck codes with self-consistent absorption from the quasi-linearly modified electron distribution function [23]. This standard model of LHCD has proven very successful in explaining present experimental results [24].

LHCD has been the main tool for bulk current drive and for current profile tailoring in reversed central shear or low shear, hybrid tokamak scenarios. A record 3 hour discharge sustained by LHCD has been demonstrated on TRIAM-1M albeit at low current and density. On larger devices like JET and JT-60 fully non-inductive discharges have been sustained by LHCD at 3.0 and 3.6 MA, respectively. Current drive efficiencies obtained to date have reached values of $\eta_{LHCD} = 0.3 \times 10^{20}$ A/Wm²

(JT-60U and JET), and across different experiments are found to scale roughly as $\eta_{\text{LHCD}} \approx 1.2 \times 10^{20} \langle T_c [\text{keV}] \rangle / (5 + Z_{\text{eff}}) \text{ A/Wm}^2$ [8].

In ITER, the penetration of LH waves is limited to the outer parts as very efficient Landau damping occurs at plasma temperatures in the range of ~ 10 keV. Simulations confirm this limitation of LHCD to the colder outer part of the plasma. Typical efficiencies predicted for ITER are in the range of $\eta_{\text{LHCD}} = 0.2 \times 10^{20} \text{ A/Wm}^2$ [23]. The major aim of a possible LHCD system for ITER would be the achievement and sustainment of reversed shear or hybrid tokamak scenarios and the generation of discharges with fully non-inductive current drive.

Typical frequencies used for LHCD are in the range of 1 to 10 GHz, and in this frequency range fundamental wave guides can be used for an efficient transport of the waves. To generate the required spectrum grill antennae existing of multiple, appropriately phased fundamental wave guides are being used [20]. Also high power sources in this frequency range, especially klystrons, are readily available.

III.B. Electron Cyclotron Current Drive (ECCD)

Electron cyclotron waves generally carry little or no momentum, and current drive by these waves is based on the Fisch-Boozer mechanism in which electrons moving in one direction are selectively heated [25, 26]. This selective heating can be achieved by proper tailoring of the EC resonance condition,

$$\omega = n |\Omega_{ce}| / \gamma + k_{\parallel} v_{\parallel} \quad (15)$$

in the region of power deposition. It generally requires a finite parallel refractive index, $N_{\parallel} = k_{\parallel} c / \omega$, and sufficient optical depth in order to guarantee almost complete absorption on one side of the resonance. One then distinguishes ECCD at downshifted ($\omega < |\Omega_{ce}|$) and at upshifted frequencies ($\omega > |\Omega_{ce}|$) as illustrated in Fig. 2. Efficient downshifted ECCD can be obtained by oblique injection of slow X-mode waves at the fundamental resonance from the high field side. However, most experiments currently affect ECCD at upshifted frequencies by low field side oblique injection of either fundamental O-mode or second harmonic fast X-mode waves. State of the art modeling of ECCD employs ray- or beam tracing codes employing adjoint techniques for the calculation of the driven current [27]. Quasi-linear modifications of the electron distribution become significant for power levels exceeding the threshold value $p_{\text{ECCD}} [\text{MW/m}^2] / n_e^2 [10^{19}/\text{m}^3] > 0.5$ [28]. In such cases proper predictions of the EC driven current can only be obtained from (2D in velocity space) bounce averaged quasi-linear Fokker-Planck codes [29].

The current drive figures of merit achieved to date are typically in the range of $\eta_{\text{ECCD}} = 1 - 4 \times 10^{18} \text{ A/Wm}^2$, where the largest values have been achieved in high temperature discharges on JT-60U [30]. Extensive studies on DIII-D have shown that the experimentally measured EC driven current is in good agreement with predictions from combined ray-tracing and Fokker-

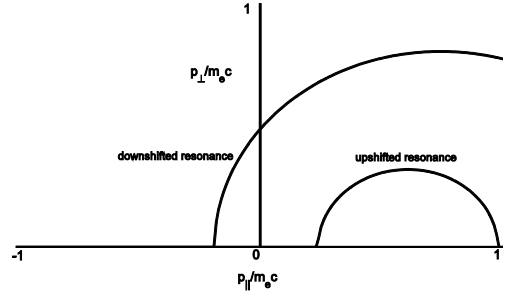


Figure 2: Illustration of the down and up shifted EC resonance in momentum space. The parallel refractive index is $N_{\parallel} = 0.5$, and the wave frequencies are chosen as $\omega / |\Omega_{ce}| = 0.9$ and 1.1 for the down- and upshifted case, respectively.

Planck code calculations provided the synergy between the ECCD and a residual parallel electric field is properly accounted for [31]. Full non-inductive current drive over several current diffusion times has been demonstrated on TCV [32]. In these discharges, the EC driven current density profile had to be carefully tailored in order to avoid driving too much current near the centre of the discharge and the resulting instabilities. This is due to the very localized EC power absorption and current drive as a consequence of the use of well focused wave beams and the cyclotron resonant character of the wave-plasma interaction. This localized character of the ECCD is in fact its main attractive feature: it allows the localized manipulation of the current density profile as required for the control of MHD instabilities like sawteeth and neoclassical tearing modes [25, 26].

Calculations of the expected ECCD efficiency in ITER predict a value of $\eta_{\text{ECCD}} = 0.2 \times 10^{20} \text{ A/Wm}^2$ in the high temperature centre of the discharge. Off-axis ECCD efficiencies will be significantly lower as a consequence of both trapped particle effects and lower local temperatures. Still the predicted driven current densities for the total available power of 20 MW are more than sufficient for the control of sawteeth and tearing modes [33], one of the major tasks of the ITER ECRH system.

III.C. Ion cyclotron resonance frequency (ICRF)

Current drive by ICRF waves (ICCD) is possible in a variety of scenarios [7, 8]. The wave to be injected in this range of frequencies is the fast magnetosonic wave (or fast wave FW), which has a dominant perpendicular electric field polarization [34]. Avoiding significant damping on the ions or mode conversion to ion Bernstein waves, most of the power can be deposited on electrons through multi pass absorption by electron Landau-damping and transit time magnetic pumping (TTMP). In case of the injection of an asymmetric wave spectrum, these result in fast wave current drive (FWCD). FWCD has been demonstrated on JFT-2M, DIII-D [35], and Tore-Supra [36]. Current drive efficiencies obtained scale with the central electron

temperature and have reached values up to $\eta_{\text{FWCD}} = 4 \times 10^{18}$ A/Wm² in agreement with theoretical modeling [7, 37]. Typical driven current density profiles are very peaked on axis due to both central peaking of the power deposition and trapped particle effects. Extrapolation of these results to ITER yield an expected current drive efficiency of $\eta_{\text{FWCD}} = 0.2 \times 10^{20}$ A/Wm² with a centrally peaked driven current density profile.

Alternative scenarios of ICCD make use of the generation of extended energetic ion tails, for example, through ion minority heating. In the case of asymmetric wave particle interaction, these can result in a sizeable driven ion current, which can be calculated from a trivial generalization of the Fisch-Boozer efficiency (6). As in the case of Neutral Beam current drive (see section IV) this energetic ion current J_m (with minority ion charge Z_m) results in a net plasma current $J = J_m (1 - Z_m/Z_i)$ where Z_i is the majority ion charge. The final equation for the ion minority current drive efficiency then becomes [6]

$$\frac{J}{P_{\text{ICCD}}} = eZ_m(1 - Z_m/Z_i) \frac{\hat{s} \cdot \nabla_{\mathbf{p}} v_{\parallel} / v}{\hat{s} \cdot \nabla_{\mathbf{p}} p^2 / 2m_e}. \quad (16)$$

Additional energetic ion currents can arise from finite orbit widths of (trapped) resonant ions [38]. These latter currents are highly localized and due to their diamagnetic origin typically of bipolar shape. This makes these currents well suited for MHD instability control. Successful control of sawteeth has been demonstrated by ICCD on JET resulting in possible avoidance of NTM [39].

III.D. Alfvén wave Current Drive (AWCD)

At first glance, current drive by low frequency $\omega < \Omega_{ci}$, low phase velocity $v_{\text{ph}} < v_{\text{te}}$ Alfvén waves appears very attractive as the current drive efficiency increases dramatically for low phase velocities (see Fig. 1). However, as the wave momentum is imparted to electrons with very small parallel velocity, most of these electrons are likely to be trapped. For this reason efficiencies for AWCD are expected to be very low. In one of the few experiments an efficiency of $\eta_{\text{AWCD}} = 0.4 \times 10^{18}$ A/Wm² was achieved. However, the favorable regime with very low phase velocity $v_{\text{ph}} < v_{\text{te}}$ could not be accessed [40].

IV. NEUTRAL BEAM CURRENT DRIVE (NBCD)

The possibility of current drive by the injection of energetic beams of neutral particles was already realized in the early stages of tokamak research [41]. Following the discussion as given in Ref. [6], the principle of NBCD can be understood as follows. Consider a homogeneous, neutral plasma with two groups of counter streaming ions. It is then always possible to choose the frame of reference such that their currents cancel exactly and the net ion current vanishes. When one of the two ion populations, say the left moving bulk ions, can now be made to collide more efficiently with the electrons then the right moving beam ions, the

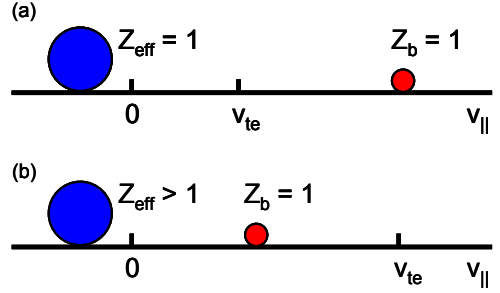


Figure 3: Illustration of the principle of neutral beam current drive. A difference in the momentum transfer rate from bulk (left) and beam (right) ions to the electrons is due to (a) a beam velocity well in excess of the electron thermal velocity or (b) a difference in charge state between bulk and beam ions.

electrons will be displaced in the direction of this left moving bulk ions and a net plasma current in the opposite direction would result. Finally, note that in neutral plasma the current is a Lorentz invariant, such that it is independent of the frame of reference in which it is derived.

Two possible ways to realize such a situation with different momentum transfer rates from the bulk and beam ion populations to the electrons are sketched in Fig. 3 (after Ref. [6]). In the first example (Fig. 3a), a beam of highly energetic ions is moving to the right at velocities v_b well above the electron thermal velocity (i.e. $v_b \gg v_{\text{te}}$). Due to the velocity dependence of the Coulomb collision frequency, the electrons would then collide much more frequently with the left moving bulk ion population, and a net current to the right would result. As said, this requires neutral beam injection with beam velocity far exceeding the electron thermal velocity, which in high temperature fusion plasmas is unpractical.

In the second example (Fig. 3b), the beam velocity maybe smaller than the electron thermal velocity (i.e. $v_b < v_{\text{te}}$). A difference in momentum transfer rates is now obtained by exploiting the dependence of the Coulomb collision frequency on the square of the ion charge state Z_i , while the current carried is only linear in Z_i . When the effective charge state of the bulk ions Z_{eff} now exceeds that of the energetic ion beam Z_b (or vice versa), the electrons again will collide more frequently with the left moving bulk ions (the beam ions), and a net current to the right (left) will arise. Neglecting trapped electron effects, this results in a current

$$J = \left(1 - \frac{Z_b}{Z_{\text{eff}}}\right) J_b, \quad (17)$$

where J_b is the current carried by the energetic ion beam. Trapped electron effects further restrain the electron motion, resulting in a further reduction of the cancelling electron current. In the large aspect ratio approximation the net result is [9,42]

$$J = \left(1 - \frac{Z_b}{Z_{eff}} \left(1 - 1.46\sqrt{\varepsilon} A(Z_{eff}) \right) \right) J_b, \quad (18)$$

where $A(Z_{eff})$ is a function whose values vary from 1.67 for $Z_{eff} = 1$ to 1.18 for $Z_{eff} = 4$.

A calculation of the beam current J_b , requires a Fokker-Planck solution of the beam ion distribution. In the absence of trapping an analytical solution for this ‘slowing down distribution’ has been found in the form [9]

$$J_b = p_{NBCD} \frac{2\tau_s e Z_b}{m_b v_b (1 + u_c^2)} \int_0^1 f_1(u) u^3 du \quad (19)$$

where p_{NBCD} is the local density of neutral beam power deposition, m_b the mass of the beam ions, τ_s is the energetic ion slowing down time, and u is the energetic ion velocity normalized to the injection velocity v_b . The function f_1 is the first order Legendre harmonic of the energetic ion distribution function, and is given by

$$f_1(u) = u^{2\beta} \left(\frac{1 + u_c^3}{u^3 + u_c^3} \right)^{1+2\beta/3}, \quad (20)$$

where

$$\beta = \frac{m_i Z_{eff}}{2m_b Z}, \quad u_c^3 = \frac{3\sqrt{\pi} m_e \bar{Z} v_{ie}^3}{4m_b v_b^3}$$

and

$$\bar{Z} = \sum_i \frac{m_b n_i Z_i^2}{m_i n_e}$$

where the subscript i refers to the different bulk ion species.

NBCD has been applied successfully in a number of tokamaks. The maximum driven currents are in agreement with the theoretical expectations according to the model outlined above [8]. Typical beam energies in current experiments range from several 10’s of keV in the smaller tokamaks up to 350 keV in the larger JT-60U tokamak. For efficient penetration into the high density ITER core, beam energies of 0.5 to 1 MeV will be required. The efficient neutralization of the accelerated beam ions before injection into the plasma at these high energies is only possible using negative ion sources. Due to the nature of the NB power deposition the NBCD profile can be relatively broad, and is most useful for driving bulk plasma current rather than current density profile tailoring. A record NBCD efficiency of $\eta_{NBCD} = 0.15 \times 10^{20}$ A/Wm² has been achieved on JT-60U using negative ion based NBCD at beam energies of 350 keV in $T_e(0) = 14$ keV, high beta plasmas with fully non-inductive plasma current sustainment [43]. Calculations for ITER conditions predict NBCD efficiencies up to $\eta_{NBCD} = 0.4 \times 10^{20}$ A/Wm² [7] for an optimized system.

V. ALTERNATIVE METHODS

Many alternative methods have been considered in the literature. However, none of these methods has achieved the experimental maturity of the RF and neutral

beam based current drive methods discussed above. We will provide only a cursory sketch of these alternatives.

V.A. Helicity injection

Helicity is defined as the inner product of the vector potential and the magnetic field, $K \equiv \mathbf{A} \cdot \mathbf{B}$, where the vector potential \mathbf{A} satisfies $\mathbf{B} = \nabla \times \mathbf{A}$. A transport equation for helicity can be written using Ohm’s law as [44]

$$\frac{\partial K}{\partial t} + \nabla \cdot \mathbf{Q} = -2\eta \mathbf{J} \cdot \mathbf{B}, \quad (21)$$

where the helicity flux is

$$\mathbf{Q} = \mathbf{B} \phi + \mathbf{E} \times \mathbf{A} = 2\mathbf{B} \phi + \mathbf{A} \times \partial \mathbf{A} / \partial t \quad (22)$$

with ϕ being the electrostatic potential, and the total electric field $\mathbf{E} = -\nabla \phi - \partial \mathbf{A} / \partial t$. The evolution of the total magnetic helicity $K_{tot} \equiv \int \mathbf{A} \cdot \mathbf{B} dV$, where the integration is over a plasma volume bounded by a magnetic surface, then is given by

$$\frac{\partial K_{tot}}{\partial t} = 2V_{loop} \Phi_T - \int 2\eta \mathbf{J} \cdot \mathbf{B} dV. \quad (23)$$

Here, the first term on the right hand side represents the helicity injection at the edge of the plasma given by the product of the toroidal loop voltage and the toroidal magnetic flux. The second term represents the volume integrated helicity dissipation. In the case of inductive current drive the dissipation of helicity is canceled by a DC loop voltage, which is limited by the flux swing of the primary transformer. In the concept of oscillating field current drive (OFCD) (or AC helicity injection) very low frequency, oscillating toroidal and poloidal electric fields are applied at the plasma edge, with relative phasing such that net time averaged helicity injection is obtained [45, 46]. The current generated in this way is located at the plasma surface and penetration to the plasma core must rely on Taylor relaxation: the conjecture that magnetically confined plasmas tend to relax to states with minimum magnetic energy while conserving total helicity [47]. An experimental demonstration is given in Ref. [48].

Electrostatic (or DC) helicity injection makes use of the term $2\mathbf{B} \phi$ in the helicity flux (22). This is only possible in case of open field lines exciting and entering the plasma volume. A simple prescription for electrostatic helicity injection then would be to cut an electric gap dividing the bounding surface into two areas where magnetic flux either enters or leaves the volume and to apply a voltage V over this electric gap. This results in an amount of helicity injection given by [44]

$$\left. \frac{\partial K_{tot}}{\partial t} \right|_{inj} = 2V \Phi_M, \quad (24)$$

where

$$\Phi_M = \frac{1}{2} \int |\mathbf{B} \cdot \mathbf{n}| dS$$

is the net flux entering/leaving the volume. The method has been applied successfully in a number of experiments using different geometries for the applied magnetic fields and voltages [49–52], and appears

particularly useful for current start-up in solenoid-free spherical tokamaks [53].

V.B. Alpha power channeling

The basic idea of ‘alpha power channeling’ is to transfer energy from the energetic fusion alpha particles into waves, which may then be put to practical use. The transfer of energy from particles to waves requires the inversion of the alpha particle distribution along the wave diffusion trajectory. In the original proposal, the alpha particle energy is channeled through interaction with Lower Hybrid waves into current drive [54]. Later, alpha particle interaction with Ion Bernstein waves has been envisaged to channel alpha particle energy into heating of fuel ions with the potential of increasing the plasma reactivity [55]. A review of the main concepts and of some partial experimental tests is given in Ref. [56].

V.C. Synchrotron radiation

Fusion plasmas are a powerful source of synchrotron radiation. As the tokamak vessel walls are generally highly reflective for these waves, the radiation is continuously emitted and reabsorbed. Whereas the emitted radiation is isotropic, it has been suggested that by proper shaping of the vessel walls the reflected spectrum can be made anisotropic such that the reflected waves could effectively drive plasma current [57]. The anisotropic reflection is achieved by means of a sawtoothed or fish-scale wall in which the vertical sections are made absorbing while the slanted sections are made reflecting. Further investigations seem to indicate that only part of the current can be driven in this way in a realistic fusion reactor [58, 59].

VI. SYNERGY

So far, the different current drive schemes have been treated individually. Synergy could be expected from combinations of any of these. For example, combining LHCD and ECCD has been shown to significantly increase the ECCD efficiency as the EC waves can interact with the LHCD produced high energy tail electrons [60]. In another experiment the combination of LHCD and ion Bernstein waves (IBW) has been shown to lead to a locally increased LHCD current, which is due to the local generation of a broadened electron velocity distribution by the IBW on which the LHCD wave are damped more efficiently [61]. On JET a synergy between LHCD and the FWCD was noted [62]. An increased NBCD efficiency could be expected from ion cyclotron resonance heating of the energetic beam ions: the increase of the perpendicular velocity of the beam ions increases their slowing down time and the resulting beam current [63]. Finally, radial gradients in RF driven quasi-linear populations will affect the bootstrap current [64].

VII. PROSPECTS FOR A STEADY STATE TOKAMAK REACTOR

Even with the highest predicted current drive efficiencies quoted above, full non-inductive drive of the total plasma current in a standard high performance H-mode discharge in ITER would require a prohibitively large amount of power. As we can foresee now, the fully non-inductive, steady state operation of ITER and future tokamak fusion reactors will have to rely on the bootstrap current for supplying the major part of the plasma current. Other methods, like NBCD or ECCD, need than be used to supply sufficient core current to fill in the hollow bootstrap current profile $\sim \sqrt{\epsilon} dp/dr$ [8]. Maximizing simultaneously bootstrap current fraction and performance is one of the goals of advanced tokamak scenario development. Integrated modeling of such scenarios illustrates the possibilities for steady state discharges in ITER [65].

ACKNOWLEDGMENTS

This work was carried out with financial support from NWO.

REFERENCES

- [1] M. VAN SCHOOR, ‘Fusion Machines’, these proceedings.
- [2] H.J. DE BLANK, ‘Guiding centre orbits’, these proceedings.
- [3] D.A. HARTMANN, ‘Stellarators’, these proceedings.
- [4] H.J. DE BLANK, ‘MHD instabilities in tokamaks’, these proceedings.
- [5] H.R. KOSLOWSKI, ‘Operational limits and limiting instabilities in tokamak machines’, these proceedings.
- [6] N.J. FISCH, *Rev. Modern Phys.* **59** 175 (1987).
- [7] ITER Physics Basis, Chapter 6: *Nucl. Fusion* **39** 2495 (1999).
- [8] C. GORMEZANO, et al, *Nucl. Fusion* **47** S285 (2007).
- [9] J. WESSON, ‘Tokamaks’ Third Edition, (2004).
- [10] P. HELANDER, ‘Neoclassical transport in plasmas’, these proceedings.
- [11] A.G. PEETERS, *Plasma Phys. Control. Fusion* **42** B231 (2000).
- [12] N.J. FISCH, A.H. BOOZER, *Phys. Rev. Lett.* **45** 720 (1980).
- [13] C.F.F. KARNEY, N.J. FISCH, *Nucl. Fusion* **21**, 1549 (1981).
- [14] C.F.F. KARNEY, *Comp. Phys. Reports* **4**, 183 (1986).
- [15] T. OHKAWA, General Atomics Report GA-A13847 (1976).
- [16] R.H. COHEN, *Phys. Fluids* **30**, 2442 (1987)
- [17] Y.R. LIN-LIU, et al, *Phys. Plasmas* **10**, 4064 (2003).

- [18] N.B. MARUSHCHENKO, et al, Nucl. Fusion **48**, 054002 (2008).
- [19] Y. PEYSSON, in Radio Frequency Power in Plasmas, AIP Conf. Proc. **485**, 183 (1999).
- [20] R.A. CAIRNS, Radiofrequency heating of plasmas, IOP Publishing, Bristol (1991).
- [21] P.T. BONOLI, R.C. ENGLADE, Phys. Fluids **29**, 2937 (1986).
- [22] R. CESARIO, et al, Nucl. Fusion **46**, 462 (2006).
- [23] P.T. BONOLI, et al, in Radio Frequency Power in Plasmas, AIP Conf. Proc. **694**, 24 (2003).
- [24] P.T. BONOLI, et al, Phys. Plasmas **15**, 056117 (2008).
- [25] E. WESTERHOF, 'Electron Cyclotron Waves', these proceedings.
- [26] R. PRATER, Phys. Plasmas **11**, 2349 (2004).
- [27] R. PRATER, et al, Nucl. Fusion **48** 035006 (2008).
- [28] R.W. HARVEY, et al, Phys. Rev. Lett. **62**, 426 (1989).
- [29] E. WESTERHOF, 9th Joint Workshop on ECE and ECH, Borrego Springs, California, 1995, Ed. J. Lohr, World Scientific, Singapore, p. 3 (1995).
- [30] T. SUZUKI, et al, Nucl. Fusion **44**, 699 (2004).
- [31] C.C. PETTY, et al, Nucl. Fusion **42**, 1366 (2002).
- [32] O. SAUTER, et al, Phys. Rev. Lett. **84**, 3322 (2000).
- [33] G. RAMPONI, et al, Fusion Sci. Technol. **52** 193 (2007).
- [34] F. LOUCHE, 'Coupling of EM waves to the plasma', these proceedings.
- [35] R. PRATER, et al, Plasma Phys. Control. Fusion **35**, A53 (1993).
- [36] EQUIPE TORE SUPRA, presented by B. Saoutic, Plasma Phys. Control. Fusion **36** B123 (1994).
- [37] C.C. PETTY, et al, Plasma Phys. Control. Fusion **43** 1747 (2001).
- [38] T. HELLSTEN, et al, Phys. Rev. Lett. **74** 3612 (1995).
- [39] O. SAUTER, et al, Phys. Rev. Letters **88**, 105001 (2002).
- [40] T. INTRATOR, et al, Phys. Plasmas **2**, 2263 (1995).
- [41] T. OHKAWA, Nucl. Fusion **10**, 185 (1970).
- [42] J.W. CONNER, J.G. CORDEY, Nucl. Fusion **14**, 185 (1974).
- [43] T. OIKAWA, et al, Nucl. Fusion **41**, 1575 (2001).
- [44] T.H. JENSSSEN, M.S. CHU, Phys. Fluids **27**, 2881 (1984).
- [45] P.M. BELLAN, Phys. Rev. Letters **54**, 1381 (1985).
- [46] A.H. BOOZER, Phys. Fluids **29**, 4123 (1986).
- [47] J.B. TAYLOR, Phys. Rev. Letters **33**, 1139 (1974).
- [48] K.J. MCCOLLAM, et al, Phys. Rev. Letters **96**, 035003 (2006).
- [49] M. Ono, et al, Phys. Rev. Letters **59**, 2165 (1987).
- [50] B.A. NELSON, et al, Phys. Plasmas **2**, 2337 (1995).
- [51] A.J. REDD, et al, Phys. Plasmas **9**, 2006 (2002).
- [52] R. RAMAN, et al, Nucl. Fusion **41**, 1081 (2001).
- [53] R. RAMAN, et al, Nucl. Fusion **47**, 792 (2007).
- [54] N.J. FISCH, J.M. RAX, Phys. Rev. Letters **69**, 612 (1992).
- [55] N.J. FISCH, et al, Nucl. Fusion **34**, 1541 (1994).
- [56] N.J. FISCH, Nucl. Fusion **40**, 1095 (200).
- [57] J.M. DAWSON, P.K. KAW, Phys. Rev. Letters **48**, 1730 (1982).
- [58] I. FIDONE, et al, Phys. Fluids **31**, 2300 (1988).
- [59] W. KERNBICHLER, S.V. KASILOV, Phys. Plasmas **3**, 4128 (1996).
- [60] G. GIRUZZI, et al, Phys. Rev. Letters **93**, 255002 (2004).
- [61] F. PAOLETTI, et al, Phys. Plasmas **6**, 863 (1999).
- [62] J. JACQUINOT, Plasma Phys. Control. Fusion **35**, A35 (1993).
- [63] K. OKANO, et al, Nucl. Fusion **23**, 235 (1983).
- [64] R.W. HARVEY, and G. Taylor, Phys. Plasmas **12**, 052509 (2005).
- [65] W.A. HOULBERG, et al, Nucl. Fusion **45**, 1309 (2005).

ICRH ANTENNA DESIGN AND MATCHING

P. Dumortier, A.M. Messiaen

*Laboratory for Plasma Physics —Ecole Royale Militaire/Koninklijke Militaire School
EURATOM-Belgian State Association, Trilateral Euregio Cluster
avenue de la Renaissance 30, B-1000 Brussels, Belgium
Tel.: (32 2) 742 65 77, Fax.: (32 2) 735 24 21, e-mail: pierre.dumortier@rma.ac.be*

ABSTRACT

RF heating and current drive in the ion cyclotron frequency range is widely used on existing machines and is planned on ITER. After a brief reminder of transmission line theory concepts the paper illustrates the process of antenna design by explaining some key design choices made for the ITER ICRH antenna. Finally the most common matching schemes are reviewed.

I. INTRODUCTION

The principle of heating and current drive by plasma waves has been addressed in several other lectures [1, 2, 3, 4]. In particular it has been seen [2] that the antenna current strap can be described as a strip-line with equivalent transmission line distributed parameters. The matching circuit is composed of transmission line components and hence its response can also be described by transmission line theory. Basic transmission line concepts are therefore reminded before going to antenna design and matching.

It is important to note that the time dependence of the various quantities is in $e^{+i\omega t}$ in this lecture, which is the “engineering” transmission line convention whereas the “physical” convention generally used to describe the wave propagation is time dependence in $e^{-i\omega t}$. As the $e^{+i\omega t}$ factor appears on all time-dependent terms it is customary to suppress it on all terms in the different expressions.

II. TRANSMISSION LINE MODELING

Transmission line theory can be approached either from an extension of circuit theory or from a specialization of the Maxwell’s equations. The first approach is favored here. The main difference with circuit theory lays in the physical size of the electrical circuit: the transmission line size is of the order of magnitude of the wavelength whereas it is much smaller in circuit theory. A transmission line is a distributed parameter network along which voltage

and current vary in amplitude and phase. Excellent overview of transmission line theory can be found in [5, 6].

A. The telegraphers equations

The voltage V and current I on the line vary due to the presence of the following distributed parameters:

- the series impedance per unit length $Z = R + iX = R + i\omega L$ (Ω/m), where R (Ω/m) is the series resistance per unit length and accounts for the conductor losses, X (Ω/m) and L (H/m) are the series reactance and inductance per unit length.
- the shunt admittance per unit length $Y = G + iB = G + i\omega C$ (S/m), where G (S/m) is the shunt conductance per unit length and accounts for the dielectric losses, B (S/m) and C (F/m) are the shunt susceptance and capacitance per unit length.

The evolution of the voltage and current along the line is described by two second-order differential equations known as the telegraphers’ equations:

$$\frac{d^2V}{dz^2} = -ZYV; \quad \frac{d^2I}{dz^2} = -ZYI \quad (1)$$

The solutions to these equations are the superposition of two traveling waves:

$$V(z) = V_0^+ e^{-\gamma z} + V_0^- e^{+\gamma z} = V^+ + V^- \quad (2)$$

$$I(z) = \frac{1}{Z_0} (V_0^+ e^{-\gamma z} - V_0^- e^{+\gamma z}) = I^+ + I^- \quad (3)$$

where the $e^{-\gamma z}$ term represents a wave propagating in the positive z direction and the term $e^{+\gamma z}$ represents a wave traveling in the negative z direction.

The time dependent solution for the voltage (it has a similar form for the current) is:

$$V(z, t) = V_0^+ e^{-\alpha z} e^{i(\omega t - \beta z)} + V_0^- e^{+\alpha z} e^{i(\omega t + \beta z)} \quad (4)$$

The complex propagation constant is :

$$\gamma = \alpha + i\beta = \sqrt{ZY} = \sqrt{(R + i\omega L)(G + i\omega C)}, \quad (5)$$

where α is the attenuation constant and β is the phase constant or wave number; $\alpha = 0$ for a lossless line.

$$Z_0 = \sqrt{\frac{Z}{Y}} = \sqrt{\frac{R + i\omega L}{G + i\omega C}} \quad (6)$$

is the characteristic impedance of the line. Note that γ and Z_0 are functions of the frequency.

B. Transfer matrix and Z transformation

If we know the voltage V_{out} and current I_{out} at one point in the line, chosen to be at $z = 0$, Eqs. 2 and 3 allow us to determine the constants V_0^+ and V_0^- . Knowing the characteristics of the line (γ and Z_0) and making use of Eqs. 2 and 3 we relate the voltage V_{in} and current I_{in} in $z = -l$ to V_{out} and I_{out} in $z = 0$ by the transfer matrix:

$$\begin{pmatrix} V_{in} \\ I_{in} \end{pmatrix} = \begin{pmatrix} \cosh(\gamma l) & Z_0 \sinh(\gamma l) \\ \frac{\sinh(\gamma l)}{Z_0} & \cosh(\gamma l) \end{pmatrix} \begin{pmatrix} V_{out} \\ I_{out} \end{pmatrix} \quad (7)$$

Also, the impedance at any point ($z = -l$), defined as the ratio of the voltage to the current at this point, is defined if we know the impedance at another point ($z = 0$):

$$Z_{in} = Z_0 \frac{Z_{out} + Z_0 \tanh(\gamma l)}{Z_0 + Z_{out} \tanh(\gamma l)} \quad (8)$$

C. Reflection coefficient and VSWR

The (voltage) reflection coefficient at one point in the line ($z = -l$) is expressed as the ratio of the reflected voltage to the incident voltage at this point and is linked to the reflection coefficient at another point in the line ($z = 0$) by:

$$\Gamma = \frac{V^-}{V^+} = \Gamma_0 e^{-2\gamma l} \quad (9)$$

Note the factor 2 appearing in the exponential term. It comes from the fact that the combined wave is the superposition of two waves, the incident and reflected waves, traveling in opposite direction at the same phase velocity.

The reflection coefficient at any point is linked to the impedance at the same point by:

$$\Gamma = \frac{Z - Z_0}{Z + Z_0} \quad (10)$$

The Voltage Standing Wave Ratio (or VSWR) is defined as the ratio of the amplitudes of the maximum and of the minimum voltages at a given point and is linked to the modulus of the reflection coefficient at this point by:

$$S = \frac{V_{max}}{V_{min}} = \frac{1 + |\Gamma|}{1 - |\Gamma|} \quad (11)$$

For a matched line $|\Gamma| = 0$ and $S = 1$.

III. ICRH ANTENNA DESIGN

A. Antenna components

An example of ICRH antenna is shown in figure 1. It is one of the two 2-straps antennas of TEXTOR, where each antenna is powered by a 2MW generator. The current strap is generally a strip-line that

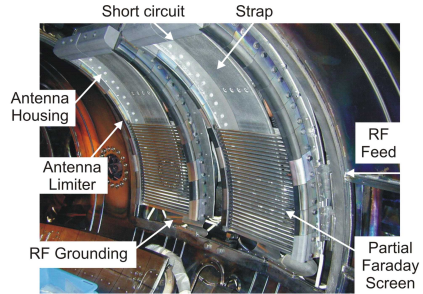


Figure 1: Two-strap TEXTOR ICRH antenna.

is short-circuited at one end to produce the magnetic field exciting the fast magnetosonic wave [2, 3]. Most recent antennas are arrays of poloidally and toroidally spaced straps. The phase and amplitude of the currents flowing in the different straps of the array need to be controlled to excite the required wave spectrum corresponding to the requested physics scenario (see last section on matching).

The strap is enclosed in the antenna box, part of the antenna housing, which is protected from the plasma by side limiters. It is not only a mechanical structure onto which the current straps, the screen bars and the feeding transmission lines are mounted but it also acts as a return conductor for the RF currents.

The geometry of the straps and antenna box will be subject to an optimization, constrained to the available physical space, to maximize the coupling while remaining below the current, voltage and electric field limits.

The antenna is generally mounted on the outboard equatorial plane of the machine. It is either mounted in the gap between the vessel and the plasma (TEXTOR, ASDEX-U, JET) or built as a whole assembly inside a port plug that is mounted onto the vessel (Tore-Supra, JT-60U, ITER). The first option requires smaller openings in the vessel as the components can be brought inside the machine by an access hole and possibly allows the deployment of larger radiating areas but the available depth can be reduced, impacting on the coupling. The advantages of the plug antenna are easier maintenance and remote handling. It generally has smaller radiating areas, partly compensated by the larger available depth.

RF grounding of the antenna avoids the excitation of unwanted modes (e.g. in the cavity formed by

the liner and the vessel on TEXTOR).

A Faraday shield or screen consisting in a slotted frame or a series of bars is generally placed in front of the straps. Its main role is to filter out the electric field parallel to the static magnetic field. For this reason it is preferably oriented parallel to the static magnetic field (what will only occur for a chosen rotational transform).

The antenna is fed by Vacuum Transmission Lines (or VTLs). They connect the antenna inside the machine to the pressurized transmission lines outside the machine and may contain some pre-matching elements.

The vacuum windows or vacuum feedthroughs are critical elements of the ICRH systems. Their primary goal is to enter the RF into the vacuum vessel without breaking the vacuum. They see the machine vacuum on the antenna side and either a private vacuum or pressurized lines on the generator side. They also act as a mechanical support for the inner conductors of the feeding lines and as tritium barriers, when necessary. As they are generally located in sections with high VSWR they must be able to cope with high voltages, of the order of $40-50kV$. They generally are constituted of cylindrical or conical ceramics (usually Al_2O_3) brazed onto the inner and outer metallic conductors of the cylindrical coaxial transmission line. ICRH technology is further discussed in [7].

B. Key design choices for the ITER ICRH antenna

The ITER ICRF antenna [8, 9]

The main functional requirements for the ITER ICRH system are heating, current drive and wall conditioning. The key specifications are the following:

- Nominal power per antenna (2 antennae are foreseen at the moment): $20MW$;
- Frequency range: $40 - 55MHz$;
- Quasi-CW operation;
- Phased antenna array (6 poloidal by 4 toroidal array of straps);
- Location: equatorial port plug.

The control of the currents (amplitude and phase) in the different columns of straps combined to the broad frequency range allows covering all requested physics scenarios to fulfill the functional specifications.

The ITER ICRH port plug (figure 2) contains 4 RF modules and is cantilevered from the port plug flange, where it is connected to the vacuum vessel. Its inside acts as a neutron shield, reducing the level of radiation at the back flange below a level permitting hands-on operation after some time for maintenance. The port plug is put in place by remote handling.

One RF module consists of two columns of three short current straps. Each strap is connected to a 15Ω characteristic impedance cylindrical coaxial feeder. Three poloidal straps with their feeders are connected in parallel by a 4-port junction (4PJ) to form a triplet

of straps. The 4PJ is connected to one 20Ω characteristic impedance RF feeding line containing a vacuum window acting as a mechanical support for the inner conductors, a vacuum and a tritium barrier.

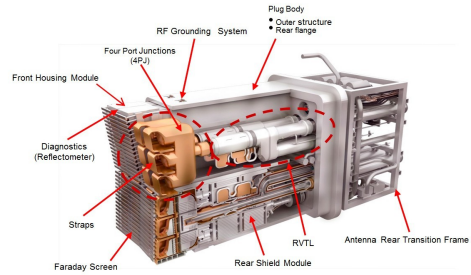


Figure 2: ITER ICRH antenna.

FEM approach vs. transmission line approach

Finite Element Modeling (FEM) codes with a plasma model as Topica [10] allow calculating the antenna input impedance and determine the distributions of electric and magnetic fields in the whole antenna with as input the plasma and Scrape-Off Layer (SOL) information (density and temperature profiles, composition), the static magnetic field information (amplitude and angle) and the antenna geometry. Plasma and SOL information can be used to create an equivalent dielectric load [11] if the FEM code doesn't have a plasma model, as it is the case for commercially available codes like CST MicroWave Studio [12] and ANSOFT HFSS [13]. The gyrotropy of the plasma is in this case not taken into account.

The FEM simulations indeed give a full RF characterization of the antenna but they require making use of very intensive computational resources. Hence the interest of the transmission line approach linked to a semi-analytical coupling code: it is very fast, requires limited computational resources and gives a very good approximation of the results. It also allows having a better understanding of the physical processes at hand.

Strap input impedance

As described in another lecture [2] the current strap can be described as a short-circuited strip-line with its distributed parameters R_A , L_A , C_A , which are determined by a semi-analytical coupling code, and length l_A . Using the $e^{+i\omega t}$ convention for the time dependence the strap input impedance, complex propagation constant and characteristic impedance are given by:

$$Z_F = R_F + iX_F = Z_{0A} \tanh(\gamma_A l_A) \quad (12)$$

$$\gamma_A = \sqrt{(R_A + i\omega L_A)i\omega C_A} \quad (13)$$

$$Z_{0A} = \sqrt{\frac{Z_A}{Y_A}} = \sqrt{\frac{R_A + i\omega L_A}{i\omega C_A}} \quad (14)$$

Choice of short straps

The power radiated by the antenna is given by:

$$P_{rad} = \int_0^{l_A} \frac{R_A |I(y)|^2}{2} dy, \quad (15)$$

where R_A is the radiation resistance as given by the coupling codes. If R_A is determined experimentally one has to subtract the losses in the antenna (determined from tests on vacuum) from the experimentally measured loading resistance.

The current and voltage along the strap are given by:

$$I(y) = I_{max} \cosh(\gamma y) \quad (16)$$

$$V(y) = Z_{0A} I_{max} \sinh(\gamma y) \quad (17)$$

A comparison of the radiated power pattern, voltage and current along one long strap and three short straps is given in figure 3. As the radiated power is proportional to $|\cosh(\gamma y)|^2$ the power is very effectively radiated near the short circuit (where $y = 0$ thus $\cosh(\gamma y) \approx 1$) and much less effectively when moving away from the short-circuit. The radiation efficiency is thus improved when going from one long strap to several short straps and for a given total power to be radiated the maximum current (at the short-circuit) will be lower. But the main advantage is the significant voltage reduction on the strap (about a factor 3 in the example of figure 3). The choice of short straps will lead to the design of high power density antennas.

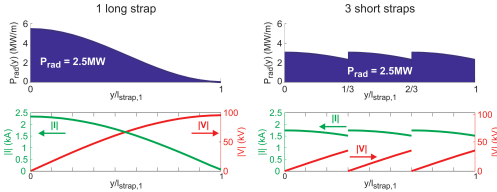


Figure 3: Radiated power pattern, voltage and current evolution along one long strap (left) and three shorter straps (right).

Choice of the feeder characteristic impedance

The main operating limit on current antennas is the maximum voltage in the system V_{max} . We can express the transferred power by:

$$P = \frac{G|V|^2}{2} = \frac{G_{min}|V_{max}|^2}{2} \quad (18)$$

G_{min} is the minimum conductance, which will occur where $V = V_{max}$ and represents the coupling to the plasma. The antenna optimization will consist in maximizing G_{min} , meaning maximizing the transferred power for a given allowed V_{max} on the system

(or minimizing the maximum voltage on the system for a given power to transfer).

We have seen that by choosing short straps we could decrease the voltage on the straps. As the straps are shorter than a quarter wavelength ($l_A < \lambda/4$) V_{max} will not occur on the strap and we need to include the next part, which is the strap feeder, into the system to be able to optimize the antenna.

The strap feeder is a cylindrical coaxial transmission line. The characteristic impedance of such a line with an inner radius a and outer radius b is:

$$Z_0 = \frac{1}{2\pi} \sqrt{\frac{\mu}{\epsilon}} \ln \frac{b}{a} \approx 60 \ln \frac{b}{a} \quad (19)$$

The maximum electric field will occur at the inner radius a and is equal to:

$$E_{max} = E(a) = \frac{V}{a \ln(\frac{b}{a})} \quad (20)$$

Figure 4 shows G_{min1} and E_{max} in the feeder as a function of its characteristic impedance (Z_{0F}). To improve the performance of the system (i.e. maximize G_{min1}) one has to choose Z_{0F} as small as possible. But this reduces the gap between inner and outer radii of the feeder and E_{max} is dramatically increasing, finally exceeding the limit of 2kV/mm (parallel to B_t), for small Z_{0F} . The strap input impedance chosen to estimate the performance and electric field in figure 4 is taken from Topica calculations with reference ITER plasma and SOL profiles and for $0\pi\pi 0$ toroidal phasing. $Z_{0F} = 15\Omega$ is chosen as a good compromise between voltage stand-off and performance.

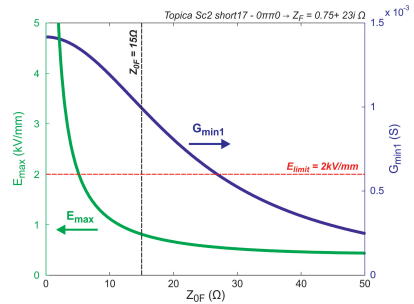


Figure 4: Minimum conductance (G_{min1}) and maximum electric field (E_{max}) in the feeder in function of its characteristic impedance (Z_{0F}).

Antenna segmentation

Short straps were chosen to limit the voltage on the straps and have high power density. But why were three straps chosen as optimal for ITER ?

Let's consider the ITER antenna box and split it into N segments. In the case of short straps—but not too short—the strap input impedance, mainly inductive, is roughly proportional to the length of the strap

($Z_{F,N} \approx Z_{F,1}/N$). The power of $2.5MW$ per feeding line is divided amongst the N segments. The feeder outer radius is constrained by the physical dimensions of the ITER antenna box ($320mm$ wide, $945mm$ high and $30mm$ thick strap). $Z_{0F} = 15\Omega$.

V_{max} , E_{max} and $\langle P_{loss} \rangle$ on the feeder section are shown in figure 5 in function of the number of segments N . E_{max} and $\langle P_{loss} \rangle$ are increasing with N but because of the constraints on the physical dimensions they also increase when going towards $N = 1$ or 2 . V_{max} is decreasing with N as the power is divided among more straps. Again the choice is a matter of trade-off and $N = 3$ is a good compromise between E_{max} and V_{max} on the feeder.

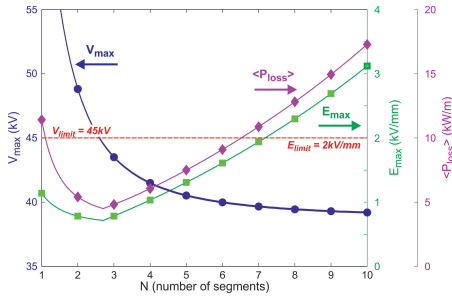


Figure 5: Maximum voltage V_{max} , maximum electric field E_{max} and average power loss $\langle P_{loss} \rangle$ in the feeder as a function of the segmentation of the antenna.

Passive power distribution: the 4-port junction

From the plasma point of view (or coupling) three short straps will be roughly equivalent to one long strap only if the currents flow in phase in the three straps. This can be achieved either actively or passively. An active control requires a large number of matching components to ensure the correct phase on the three straps, which in turn will lead to space issues and a very complex matching (the 24 straps are mutually coupled). This leads to the choice of a passive power distribution by the use of a multi-port junction: 3 straps are connected in parallel by a 4-port junction (4PJ). In this case the currents will be in phase if the 4-port junction is located around V_{max} .

This has consequences on the frequency response of the antenna. Let's note G_{min1} the minimum conductance in the strap feeder section (antenna side of the 4PJ) and G_{min2} the minimum conductance in the feeding line of one strap triplet (generator side of the 4PJ). For a given antenna geometry and loading conditions G_{min1} is evaluated by a coupling code. If the junction is located at the voltage anti-node (V_{max}) for all frequencies then $G_{min2} = G_{min2,max} = 3G_{min1}$. But in practice the junction is physically located at a fixed position and will be at V_{max} for a single frequency. Moving away from this point in frequency will lead to a $G_{min2} < G_{min2,max}$ (see figure 6). The

4-port junction acts as a frequency filter. The position of the maximum of G_{min2} can be moved towards lower/higher frequency by increasing/reducing the feeder or 4PJ length.

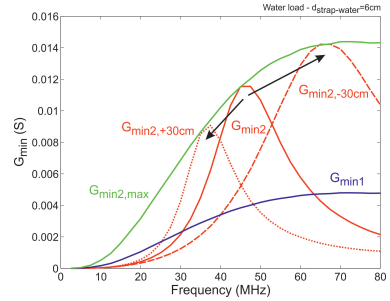


Figure 6: G_{min1} , $G_{min2,max}$ and G_{min2} (to have V_{max} at mid-band) vs. frequency. $G_{min2,-30cm}$ and $G_{min2,+30cm}$ when removing or adding $30cm$ of feeder length.

Antenna optimization [14, 15]

The main operating limit on current antennas being V_{max} the RF antenna design will strive to:

- improve the achievable V_{max} by design;
- maximize G_{min2} , i.e. maximize the transferred power for a given V_{max} .

Increasing G_{min2} can be obtained by increasing G_{min1} , i.e. by acting on the antenna front face geometry (strap width, box depth, septum recess). As the strap input impedance is mostly reactive ($R_F^2 \ll X_F^2$) we have:

$$G_{min1} \approx \frac{R_F}{X_F^2 + Z_{0F}^2} \quad (21)$$

The resistive part, R_F , is determined partly by the antenna box geometry and partly by the external medium (mainly plasma and SOL density profiles). The reactive term, X_F , depends mainly on the antenna box geometry and only weakly depends on the external medium.

Maximizing G_{min1} often leads to a reduction of X_F accompanied by a reduction in R_F . The current in the antenna then increases as $|I_F| = |V_F|/|Z_F| \approx |V_F|/|X_F|$. The ITER ICRF antenna being a long pulse antenna it needs active cooling. This sets a limit on the maximum allowed RF losses, thus the maximum allowed current (a.o. in the RF contacts). The RF optimization has to proceed together with the thermo-mechanical calculations in order to find the best trade-off between the limits on maximum current, electric field and voltage.

G_{min2} can also be maximized by the choice of the 4PJ geometry, which response should be as close as possible to the one of an ideal transmission line [14].

Finally it was shown [14] that broad-banding of the system response in the main transmission line

could be obtained by introduction of a quarter-wave stub at a quarter-wavelength of the 4PJ.

IV. MATCHING

The matching has three essential goals:

- maximizing the power transfer to the antenna and minimizing the power loss in the feed line;
- controlling the antenna array current spectrum;
- avoiding tripping the generator.

When a generator is delivering its power through a transmission line to a load the maximum power transfer occurs when the input impedance looking into the transmission line terminated by the load from the generator end is the complex conjugate of the output impedance of the generator [6].

In practice, the generator output impedance is real and equal to $Z_{0G} = 30\Omega$ or 50Ω . The strap input impedance is complex and essentially reactive. To maximize the transferred power we need to transform Z_F into Z_{0G} . This is the first role of the matching circuit.

Secondly the different heating and current drive scenarios require different antenna array current spectra: the phase and amplitude of the currents of the different poloidal columns of straps need to be controlled.

Finally the generators are protected against too high power reflection to avoid any damage (they are typically limited to $VSWR < 1.5$, i.e. $|\Gamma_G| < 0.2$). Above this limit the generator is tripped (no power is delivered any more).

A. Classical Matching

The principle of classical matching is shown in figure 7. A generator delivers incident power (P_{in}) to the system. Its output impedance is real (e.g. $Z_{0G} = 50\Omega$). The antenna has a complex input impedance $Z_F = R_F + iX_F$, with $R_F^2 \ll X_F^2$. The transmission line is generally matched to the generator ($Z_{0TL} = Z_{0G}$). Because of the impedance mismatch ($Z_F \neq Z_{0TL}$) most of the delivered power is reflected at the antenna and can cause tripping of the generator. To fully radiate P_{in} a matching circuit is inserted to constitute a resonant circuit, in which VSWR is high, with the antenna. It increases the antenna current to the value needed to radiate P_{in} and low (no in case of perfect match) power is reflected back to the generator. The generator side of the matching circuit is a matched section where $VSWR \approx 1$. The load of the antenna is not constant: varying plasma and SOL conditions (confinement regime transition, distance plasma-antenna, switching on of NBI) lead to changes in the strap input impedance: mainly in the resistive part (R_F) but also to a lesser extent in the reactive part (X_F). Consequently the elements constituting the matching circuit need to be adjustable. The most widely used matching components are:

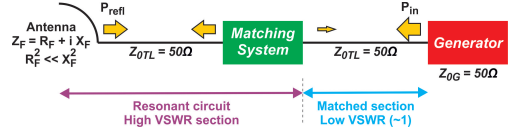


Figure 7: Principle of classical matching.

- reactive components such as capacitors or shunt short-circuited line sections called stubs;
- phase shifters or line stretchers.

The admittance of a capacitor is purely capacitive: $Y = iX$, with $X = \omega C$.

The impedance of a lossless short-circuited line section (or stub) is: $Z_{st} = iZ_0 \tan(\beta l_{St})$. The stub can be either capacitive or inductive depending on its length l_{St} .

The phase shifter is a section of transmission line of variable electrical length: it changes the phase angle of the reflection coefficient. This length can be changed mechanically by using trombones or electrically as on JET by a slight frequency shift on very long lines [16].

Other techniques are employed as modifying the electrical properties of the transmission line (e.g. liquid tuners [17]) or its magnetic properties (e.g. ferrite tuners [18]).

The single-stub tuner

The single stub tuner is a matching circuit composed of a line stretcher and a shunt stub, whose lengths are the two adjustable parameters.

The length of the line stretcher is chosen such that the input admittance looking towards the load at the stub insertion position is of the form $Y = Y_{0G} + iB$ (where $Y_{0G} = 1/Z_{0G}$). The length of the stub is then chosen such that its susceptance is equal to $-iB$ resulting in a matched condition.

There are two solutions: one inductive and one capacitive. All loads can be matched provided the available lengths are sufficient.

The double-stub tuner

This matching circuit is composed of two shunt stubs, whose lengths constitute the two adjustable parameters, distant by typically $\lambda/8$ for the mid-band frequency.

The first stub (antenna side) is set such that the input admittance looking towards the load at the position of the insertion of the second stub (generator side) is of the form $Y = Y_{0G} + iB$. Again the length of the second stub is chosen to neutralize the remaining susceptance.

This scheme doesn't allow matching all loads: there's an inaccessible region that depends on the distance between the two stubs. Adding a line stretcher however allows to move outside the inaccessible region.

B. ELM-resilient matching [19, 20]

The classical matching components are too slow to cope with the very fast load changes due to ELMs (Edge Localized Modes); they appeared with the discovery of the H-mode). The resistive load during ELMs is typically increased by a factor 2 to 4 while the inductive load typically decreases less dramatically by about 2 to 15%.

Two ELM-resilient schemes were developed and tested on several machines: the Conjugate-T (TEXTOR [21], Tore-Supra [22], JET [23, 24]), which is presently the ITER back-up option, and the hybrid coupler [25] (DIII-D [26], ASDEX-U [27], JET [28]), which is presently the ITER reference one [8].

The Conjugate-T

In this scheme two straps (two poloidal triplets for the ITER ICRH antenna) are connected to a single feeding line by a T-junction (see figure 8). A reactive element —generally a capacitor or a shunt stub—is added in each line between the strap and the T-junction. Its susceptance is chosen such that one branch is inductive with an admittance at the T-junction equal to $Y_1 = 1/(R + i|X|)$ and the other is capacitive with the complex conjugate admittance of the first branch at the T-junction: $Y_2 = Y_1^* = 1/(R - i|X|)$. The admittance in the feeding line at the T-junction is then $Y_T = Y_1 + Y_1^* = 1/Z_{0G}$.

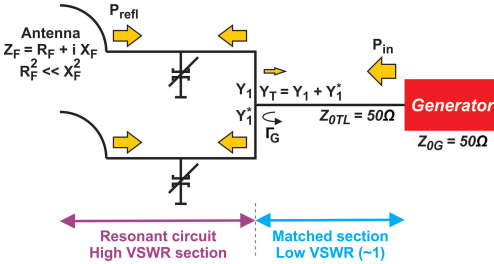


Figure 8: Conjugate-T circuit.

If only the resistive part of the load varies during an ELM then we can express the reflection coefficient at the T-junction towards the generator in function of the normalized variables $r = R/Z_{0G}$ and $x = X/Z_{0G}$ as:

$$\Gamma_G = \frac{(r - r_1)(r - r_2)}{(r + r_1)(r + r_2)} \quad (22)$$

with $r_1 r_2 = x^2$ and $r_1 + r_2 = 2$.

The evolution of $|\Gamma_G|$ in function of r is shown on figure 9. Perfect match occurs for $r = r_1$ and $r = r_2$. For $r_1 < r < r_2$ the curve presents a maximum at $r = r_s$ corresponding to a VSWR of $S = S_{max} = 1/x$. We can see that there is a large load-resilient domain ($[r_{b1}, r_{b2}]$), where $S < S_{max}$.

The price to pay for the load resilience is a change in phase angle between the currents flowing in the two branches, given by $\Delta\Phi = 2 \arctan(\sqrt{r_1 r_2}/r)$.

A second stage matching circuit (or impedance transformer) can be implanted between the generator and the T-junction in order to change the impedance on which one has to match at the T-junction. In this case one can improve the load resilience by lowering the impedance to match at the T-junction. This is especially useful for low loadings where the matching is more difficult to achieve. This also allows imposing a complex impedance on which to match at the T-junction, what can be useful in case of strong mutual coupling between different Conjugate-T circuits.

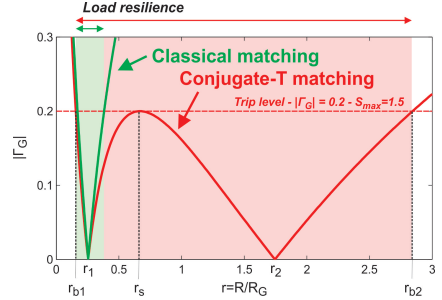


Figure 9: Reflection coefficient vs. normalized loading resistance for CT matching and classical matching. Load resilience domain is much larger for CT matching.

The Conjugate-T matching requires symmetric R and X variations and has limited resilience to X variations.

One of its most remarkable features is that it continues to deliver the power through the ELMs. The debate on whether this is an advantage or a drawback (it could favor arcing in this phase where plasma is expelled towards the antenna) is still open.

The Hybrid Coupler

In this case the power is delivered through a hybrid coupler to two straps (two poloidal triplet of straps for the ITER ICRH antenna). The last port of the hybrid coupler is connected to a dummy load (see figure 10).

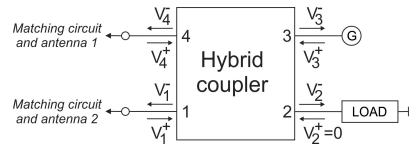


Figure 10: Hybrid coupler circuit.

The scattering matrix of the hybrid coupler is:

$$S = - \begin{pmatrix} 0 & i\delta & \alpha & 0 \\ i\delta & 0 & 0 & \alpha \\ \alpha & 0 & 0 & i\delta \\ 0 & \alpha & i\delta & 0 \end{pmatrix}, \quad \text{where } V_i^- = \sum_j S_{ij} V_j^+ \quad (23)$$

For the 3dB hybrid coupler $\alpha = \delta = 1/\sqrt{2}$ giving:

$$V_1^- = \frac{-1}{\sqrt{2}}V_3^+; V_4^- = \frac{-i}{\sqrt{2}}V_3^+ \quad (24)$$

In this case the power is split into two equal parts to the two branches but with a phase difference of $\pi/2$.

The matching is done by a classical matching circuit placed between the antenna current straps and the 3dB hybrid coupler. For perfectly matched conditions, no power is reflected back to the hybrid coupler. But when an ELM occurs the system is not matched any more and a high fraction of power is reflected towards the hybrid.

The reflection to the generator and transfer coefficient to the dummy load are given by:

$$\Gamma_3 = \frac{V_3^-}{V_3^+} = \frac{\Gamma_1 - \Gamma_4}{2}; T_{LG} = \frac{V_2^-}{V_3^+} = i\frac{\Gamma_1 + \Gamma_4}{2} \quad (25)$$

No reflection to the generator and full dump of the reflected power will happen when Γ_1 and Γ_4 are equal in phase and amplitude. This needs complete symmetry in the load variation (R and X) and of the matching circuit.

In the 3dB hybrid coupler scheme the generator continues to deliver power during the ELMs but most of this power is dumped into the dummy load. The generator is isolated from the load changes.

Decouplers

The ELM-resilient schemes not only require that the load variations on the two branches are symmetric but also that the level of mutual coupling is kept sufficiently low.

This last condition pleads in favor of the use of decouplers when possible (it is difficult to implement them with internal matching for instance).

A decoupler consists of two $\lambda/4$ lines of characteristic impedance Z_{0dec} connected to an adjustable reactance X_{dec} (see figure 11) [20].

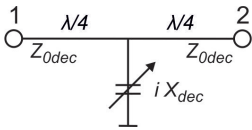


Figure 11: Decoupler circuit.

All the terms of the 2×2 admittance matrix Y_{dec} of this two-port network are equal to iX_{dec}/Z_{0dec}^2 . This circuit connected in parallel to a two-port network with admittance Y allows to cancel the reactive part of the coupling terms if $Y_{12} = Y_{21}$ or to reduce it in case of a non-symmetric matrix ($Y_{12} \neq Y_{21}$), which is the case on plasma. The decoupler adds an additional contribution to the diagonal terms (Y_{11} and Y_{22}) that has to be taken care of by the matching circuit.

REFERENCES

1. E. Lerche and D. Van Eester, Kinetic theory of plasma waves, *These Proc.*
2. F. Louche and R. Koch, The coupling of electromagnetic power to plasmas, *These Proc.*
3. R. Koch, The ion cyclotron, lower hybrid and Alfvén wave heating methods, *These Proc.*
4. E. Westerhof, Current drive, *These Proc.*
5. M.I.T. Radiation Laboratory Series: 28 Volumes on 2 CD-Roms, *ARTECH House* (1999)
6. D.M. Pozar, Microwave Engineering, *John Wiley & Sons, Inc.* (2004)
7. F. Durodié, *Transactions of Fusion Technology*, **25(2T)**:Part 2, 284-288 (1994)
8. P. Lamalle et al., *Fusion Engineering and Design*, In Press, doi:10.1016/j.fusengdes.2012.11.027 (2013)
9. D. Hancock et al., *AIP Conference Proceedings*, **1406**, 57-60 (2011)
10. V. Lancellotti et al., *Nucl. Fusion*, **46**, S476 (2006).
11. A. Messiaen et al., *Fusion Engineering and Design*, **86**, 855-859 (2011)
12. CST GmbH, CST Microwave Studio User Manual (2009), <http://www.cst.com>
13. "High Frequency Structure Simulator (TM)", Ansoft Corp., <http://www.ansoft.com>
14. P. Dumortier et al., *Fusion Engineering and Design*, **84**, 707711 (2009)
15. F. Durodié et al., "Performance Assessment of the ITER ICRF Antenna", *Proc. of the 24th IAEA Fusion Energy Conference* (2012)
16. T.J. Wade et al., *Fusion Engineering and Design*, **24**, 23-46 (1994)
17. R. Kumazawa et al., *AIP Conference Proceedings*, **485**, 441-444 (1999)
18. S. Martin et al., *AIP Conference Proceedings*, **244**, 318-321 (1992)
19. J.M. Noterdaeme et al., *Fusion Engineering and Design*, **74**, 191-198 (2005)
20. A. Messiaen et al., *Nuclear Fusion*, **49**, 055004 (2009)
21. F. Durodié et al., *Fusion Engineering and Design*, **66-68**, 509-513 (2003)
22. K. Vulliez et al., *Fusion Engineering and Design*, **66-68**, 531-535 (2003)
23. F. Durodié et al., *AIP Conference Proceedings*, **595**, 122-125 (2001)
24. F. Durodié et al., *Fusion Engineering and Design*, **84**, 279-283 (2009)
25. R. Goulding et al., *AIP Conference Proceedings*, **355**, 397-400 (1995)
26. R.I. Pinsker et al., *Plasma Physics and Controlled Fusion*, **40**, A215-A229 (1998)
27. J.M. Noterdaeme et al., *16th IAEA Conf. on Fusion Energy*, **3**, 335-342 (1996)
28. M. Vrancken et al., *Fusion Engineering and Design*, **82**, 873-880 (2007)

KINETIC THEORY OF PLASMA WAVES

D. Van Eester and E. Lerche

Laboratorium voor Plasmafysica - Laboratoire de Physique des Plasmas

EUROfusion Consortium member

Koninklijke Militaire School - Ecole Royale Militaire

Trilateral Euregio Cluster, Renaissanceaan 30 - B1000 Brussels - Belgium

Tel.: (32 2) 44 14 134, Fax.: (32 2) 735 24 21, e-mail: d.van.eester@fz-juelich.de & e.lerche@msn.com

ABSTRACT

In the present paper a very brief introduction is provided to the theory of kinetic waves relevant to the description of wave heating in fusion machines and focussing mostly on radio frequency or ion cyclotron resonance frequency waves in tokamaks. The text starts by sketching the basic philosophy underlying the standardly adopted methods, describing the interaction of a single particle with a given wave and the assumptions typically made to arrive at a trustworthy description of the energy exchange, and ends by discussing some of the subtleties of the modeling of wave-particle interaction in inhomogeneous magnetized plasmas. None of the topics will be treated in full detail. Hence, by no means, this text is meant to be all-inclusive. Rather, it aims at providing a framework that should allow understanding what are the difficulties involved, leaving out the detailed derivation of the expressions as well as subtleties such as relativistic corrections. The interested reader is referred to the provided references - and the references given therein - for more in depth information.

I. INTRODUCTION

The interaction between charged particles and electromagnetic waves can be looked at from 2 vantage points: From the point of view of the waves 'plasma heating' is a process by which they lose energy. The relevant equation to describe this is the wave equation, derived from Maxwell's equations. From the point of view of the particles the same process is viewed as a gain of energy. The relevant equation to describe this second interpretation of the same physical phenomenon is the Fokker-Planck equation, derived starting from the kinetic equation of state. A proper description of the phenomena requires that these 2 aspects are described on the same footing, which is not at all straightforward and which only starts to be done now that powerful computers are increasingly available.

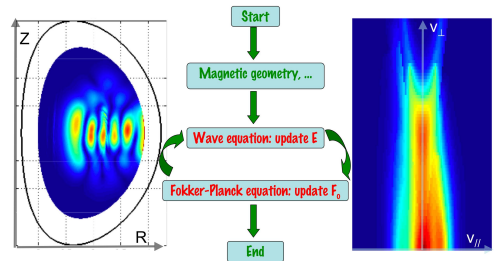


Figure 1: Wave-particle interaction: wave point of view (left: fast dynamics) vs. particle point of view (right: slow - net - dynamics) and scheme for modeling both aspects self-consistently. The wave field (left) is plotted in a toroidal cut of a tokamak, the RF heated ion distribution (right) is plotted in terms of the velocity components at the low field side crossing of the equatorial plane for a prescribed radial position.

The kinetic description of waves in plasmas typically starts from the equation

$$\frac{df}{dt} = C + S - L \quad (1)$$

in which f is the distribution function of the charged particles being studied, and the right hand side describes how the distribution equation evolves under the influence of collisions the particles undergo, and of particle injection (S =source) and particle loss (L). In the high frequency domain and for a sufficiently strong magnetic field, the left hand side is dominated by processes on a vastly different time scale than that of the net effect of collisional interaction and particle loss or gain. Hence on the fastest time scale of the problem the right hand side is negligibly small and can be neglected to a first approximation. The above equation then simply states that the number of particles is conserved in phase space: Particles can move about and gain or lose energy - which causes a stretching or squeezing of

volume in which a given number of particles resided at a given initial time - but the number of particles in the stretched phase-space volume is always conserved.

II. BASIC PHILOSOPHY [1-11]

II.A. General Formulation

In general, the orbits of particles immersed in electromagnetic fields are not integrable i.e. their motion cannot be described in terms of constants of the motion but is stochastic and thus ergodically covering parts of phase space. On top of that, charged particles in motion constitute a current themselves and thus influence the electromagnetic fields in the fusion machine. Hence, the RF plasma current needs to be carefully accounted for when solving Maxwell's equations. Describing the impact of the charged particles on the fields and the back reaction of the fields on the particles involves the challenging task of solving a set of coupled nonlinear equations in 6 independent variables in phase space. As the temporal and spatial scales cover a range of many orders of magnitude (ion cyclotron motion involves frequencies in the radio frequency - megaHertz - domain while net collisional interaction occurs on a time scale of hundreds of milliseconds in a tokamak such as JET, or seconds in ITER; the macroscopic dimensions of such fusion machines is several meters, while the ion Larmor radius ρ is of the order of a few millimeters) making simplifications is a necessity. The drawback of the wide range of scales is thereby turned into an advantage, allowing to set apart phenomena and tackling processes happening on drastically different scales separately.

It is instructive to have an idea of the relative magnitudes of various relevant quantities to understand why the 'quasi-linear' approach and other commonly made approximations make sense. For typical JET parameters in a D majority plasma (temperature of $5keV$, density of $5 \times 10^{19}m^{-3}$, magnetic field $3T$, major radius of $3m$ and minor radius of $1m$), the ion cyclotron frequency of the D ions is $23MHz$ and the electron cyclotron frequency is $80GHz$, the ion thermal velocity is $5 \times 10^5 m/s$ so the typical ion Larmor radius is $3mm$, the electron thermal velocity $3 \times 10^7 m/s$ so the electron gyroradius is $0.05mm$, the ion collision frequency is $100Hz$ and the electron collision frequency is $10kHz$. For typical RF waves of several MW with electric field values of $50kV/m$ close to the antennas, the RF magnetic field is $5 \times 10^{-3}T$ and the RF magnetic contribution to the Lorentz acceleration $|\vec{v} \times \vec{B}_{RF}| = 2.5kV/m$.

Hence the ions travel around the torus in about $4 \times 10^{-5}s$, the cyclotron ('gyro') period τ_g being much shorter than the transit ('bounce' & 'drift') time $\tau_{b,d}$, which itself is much smaller than the collision time τ_c ,

making it sensible to describe the cyclotron motion as much faster than the bounce/transit motion, itself typically much faster than the collision time and rendering a collisionless description sensible. The scaling $\tau_g \ll \tau_{b,d} \ll \tau_c$ is crucial for the customary models. In particular, the 'slower' phenomena are assumed to be constant on the faster time scale while the faster - oscillatory - phenomena are treated as being beyond their transient state, all quantities merely varying as a function of time as $exp[i\omega t]$, where ω is the frequency at which the external wave launchers are operated. The particle motion is essentially imposed by the confining magnetic field, the RF field being a small - be it fast - perturbation and the RF electric field effect dominating that of the magnetic field. Finally, the Larmor radius is commonly much smaller than the equilibrium quantity gradients, this giving rise to the so-called drift approximation and locally making a quasi-homogeneous description sensible. In particular $\rho/L_{B_o} \ll 1$ where ρ is the Larmor radius and L_{B_o} is a typical scalelength of the variation of the confining magnetic field.

To understand the basic physics of the impact of the RF electric field on a test particle, we locally solve the equation of motion and then use the result to evaluate the net energy a charged particle can gain or lose in a rapidly varying electric field along the trajectory it is forced to follow by the fusion machine's static confining magnetic field. We start from a homogeneous plasma, straight magnetic field line analysis and gradually include other effects.

Because the magnetic field is imposing a clear asymmetry in the dynamics along as opposed to perpendicular to the magnetic field lines, the discussion of the wave-particle interaction is most easily described with reference to the direction along $\vec{e}_{//} = \vec{B}_o/B_o$ and 2 independent directions perpendicular to the static magnetic field \vec{B}_o . Neglecting the equilibrium electric field related to the ohmic circuit, the solution of the equation of motion of a charged particle immersed in a homogeneous, static magnetic field can be written as $v_{\perp,1} = v_{\perp} \cos\phi$, $v_{\perp,2} = v_{\perp} \sin\phi$ where $\phi = \phi_o - \Omega(t - t_o)$ while $v_{//} = ct$, with $\Omega = qB_o/m$ (B_o the confining field, q the charge and m the mass of the species) the cyclotron frequency, which can further be integrated to get the particle position: $x_{\perp,1} = x_{\perp,1,GC} - \rho \sin\phi$, $x_{\perp,2} = x_{\perp,2,GC} + \rho \cos\phi$ in which the Larmor radius is given by $\rho = v_{\perp}/\Omega$ and 'GC' refers to the guiding centre position. Assuming the electric field is a plane wave characterized by a wave vector \vec{k} , defining ψ as the angle between \vec{k} and $\vec{e}_{\perp,1}$ ($k_{\perp,1} = k_{\perp} \cos\psi$, $k_{\perp,2} = k_{\perp} \sin\psi$), the work the electric field does on a particle can be written

$$q\vec{E} \cdot \vec{v} = q \sum_{N=-\infty}^{N=+\infty} L_N exp[-N\phi] \quad (2)$$

in which

$$L_N = \left[\frac{v_{\perp}}{2} (E_- J_{N+1} e^{i\psi} + E_+ J_{N-1} e^{-i\psi}) + E_{//} v_{//} J_N \right] e^{iN\psi}$$

is the Kennel-Engelmann operator [17] and where the electric field is evaluated at the guiding center $\vec{x}_{GC} = [x_{\perp,1} + \rho \sin\phi] \vec{e}_{\perp,1} + [x_{\perp,2} - \rho \cos\phi] \vec{e}_{\perp,2} + [v_{//}(t - t_o)] \vec{e}_{//}$ rather than at the particle position and in which the argument of the Bessel functions is $k_{\perp} \rho$. In doing so the most rapidly varying contribution (the cyclotron oscillation) is isolated from all slower contributions. Figure 2 illustrates that using the guiding center position rather than the particle position as the reference position makes the bookkeeping much simpler when studying heating: In the particle frame, integration over a reference volume entails integrating over all orbits with various speeds and guiding centers that are intersecting the reference volume. When particles are in coherent motion with a wave and are periodically exchanging energy with it, this exchange is not considered to be 'heating' although the energy streaming into the reference volume in \vec{x} will increase at some times and decrease at others. In the guiding center \vec{x}_{GC} frame the picture is much clearer, simpler and more symmetrical, as there is no leaking of particles into or out of reference volumes. On top of that, the fastest evolution has been separated out, a non-negligible advantage when searching for equations that will need to be solved numerically as it implies a significant speed-up of the computations. Finally, as will be seen later, expressing the fields in terms of guiding center coordinates allows interfacing to the Fokker-Planck equation describing the net impact of the fields on the particles (rather than the impact of the particle motion on the fields) in a natural way, allowing to make wave and particle equations more easily compatible. From the equation of motion one readily finds that the change of the particle energy is $\dot{\epsilon} = \frac{d\epsilon}{dt} = q \vec{E} \cdot \vec{v}$ which, using the above found expression, can be written more explicitly as

$$\dot{\epsilon} = q \sum_{N=-\infty}^{+\infty} L_N(\vec{E}_{GC}(t_o)) \exp[i(N\Omega + k_{//} v_{//} - \omega)(t - t_o)].$$

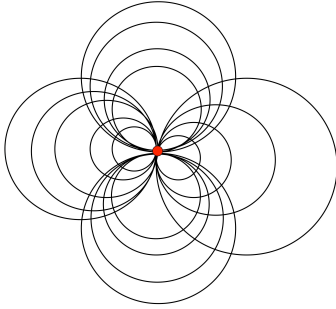
For most frequencies ω the right hand side is periodic and hence the energy transfer between the electric field and the particles is merely oscillating around an average value but no net acceleration is taking place. At the Doppler shifted cyclotron resonances $\omega = N\Omega + k_{//} v_{//}$ the exponential time dependent factor associated to a specific cyclotron harmonic N on the right hand side is constant and hence - in spite of all other terms still oscillating as a function of time - there is a net energy transfer.

Net heating takes place when $N\Omega + k_{//} v_{//} = \omega$, in which the Doppler shift term $k_{//} v_{//}$ is usually a correction to $N\Omega$, except when $N = 0$ in which case it is crucial. In the radio frequency domain (tens of MHz) and for typical magnetic field strengths of current-day magnetic fusion machines (a few Tesla), the resonance condition for the ions can easily be satisfied for $N \neq 0$ i.e. they undergo cyclotron heating, while that of the electrons requires $N = 0$ i.e. they feel the Cerenkov effect. As a consequence, ions and electrons react very differently to waves driven at frequencies in the ion cyclotron frequency range: For not too energetic particles, the argument $k_{\perp} \rho$ of the Bessel function is small so that $J_0 \approx 1$ and $J_M \ll 1$ when $M \neq 0$. Hence, the ions are mainly accelerated in the *perpendicular* direction by the perpendicular components of the electric field while the contribution of the parallel electric field has a minor impact on them; on the other hand, the parallel electric field gives the electrons a net pull in the *parallel* direction (Landau damping). Cerenkov interaction equally involves the perpendicular electric field components, an effect known as transit time magnetic pumping (TTMP). Whereas Landau damping causes parallel acceleration and is present even when the electric field is spatially uniform, TTMP affects the perpendicular energy and requires inhomogeneity of the field. An elegant discussion of the wave-particle interaction can be found in [12].

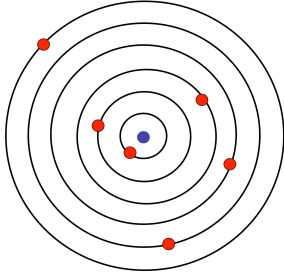
Since collisions are infrequent but non-absent, it is customary to interpret the frequency ω in the resonant denominator as a complex quantity with a very small, positive imaginary part $i\nu$, ν loosely being interpreted as the collision frequency that would appear in the particle equation of motion if collisions would be accounted for in a simple way. This gives a recipe for how to encircle the poles at the resonances to ensure causality. The contribution of the energy from events in the far past ($t_o \rightarrow -\infty$) is then absent and only the end contribution of the time integral at time t survives. The need for the elimination of the far past history is of particular interest to ensure there is net heating. It will be discussed separately later.

II.B. The Quasilinear Approach: The RF Perturbed Distribution and the Quasilinear Diffusion Operator

The time evolution equation (1) is rewritten making use of the fact the confining magnetic field is much larger than the fastly varying purely oscillatory electromagnetic perturbation, driven at the antenna frequency ω i.e. proportional to $\propto \exp[i\omega t]$: Both the distribution itself and the Lorentz force are separated into a large term only involving slowly varying quantities (referred to with a subscript 'o'), and a small but rapidly varying



Particle position as reference position:
all orbits crossing through a given
point ●



Guiding center position as reference position:
all orbits sharing the same guiding center ●

Figure 2: Cyclotron motion as seen in the particle (top) and guiding centre (bottom) reference frame.

contribution (related to the driven RF fields):

$$\frac{df}{dt} = \frac{df}{dt}|_o + \frac{df}{dt}|_{RF} =$$

$$\frac{dF_o}{dt}|_o + \frac{dF_o}{dt}|_{RF} + \frac{df_{RF}}{dt}|_o + \frac{df_{RF}}{dt}|_{RF} = C + S - L$$

with $\frac{d}{dt}|_o = \frac{\partial}{\partial t} + \vec{v} \cdot \nabla_{\vec{x}} + \frac{q}{m}[\vec{E}_o + \vec{v} \times \vec{B}_o] \cdot \nabla_{\vec{v}}$ and $\frac{d}{dt}|_{RF} = \vec{a}_{RF} \cdot \nabla_{\vec{v}} = \frac{q}{m}[\vec{E}_{RF} + \vec{v} \times \vec{B}_{RF}] \cdot \nabla_{\vec{v}}$, F_o the slowly varying and f_{RF} the rapidly varying distribution function. The first, zero order term in the above only varies on the slowest time scale, the next 2 terms are first order corrections which oscillate at frequency ω , while the most rapidly varying terms in the last, second order term contains factors that oscillate at frequency 2ω . Since F_o only depends on the constants of the motion, $\frac{dF_o}{dt}|_o$ can be simplified to $\frac{\partial F_o}{\partial t}$. The 2 linear terms yield an expression for the RF perturbed distribution i.e. for the evolution on the fast time scale, known as the Vlasov equation:

$$\vec{a}_{RF} \cdot \nabla_{\vec{v}} F_o + \frac{df_{RF}}{dt}|_o = 0$$

i.e.

$$f_{RF} = - \int_{orbit}^t dt' \vec{a}_{RF} \cdot \nabla_{\vec{v}} F_o \quad (3)$$

which can be inserted in the fourth term of the evolution equation. Averaging $\langle \dots \rangle$ the 4 terms over a full oscillation period for all oscillatory aspects of the motion and the driven response, yields an equation for the slow time variation, known as the Fokker-Planck equation. The first term stays untouched, the second and third term as well as the oscillatory parts of the fourth term vanish while a constant, second order contribution survives. This yields

$$\frac{\partial F_o}{\partial t} = \langle C \rangle + \langle S \rangle - \langle L \rangle + \langle Q \rangle \quad (4)$$

in which $\langle Q \rangle = \langle \nabla_{\vec{v}} \cdot \vec{a}_{RF}^* \int_{orbit}^t dt' \vec{a}_{RF} \cdot \nabla_{\vec{v}} F_o \rangle$ is the quasi-linear diffusion operator, acting on the slowly varying distribution function.

II.C. The Wave Equation & The Conductivity Tensor

Combining Maxwell's equations for the evolution of the electric field and the magnetic field, and assuming the waves are driven at a frequency ω , the wave equation can be written in terms of the electric field \vec{E} only,

$$\nabla \times \nabla \times \vec{E} - k_o^2 \vec{E} = i\omega\mu_o[\vec{J}_{antenna} + \vec{J}_{plasma}], \quad (5)$$

in which $k_o = \omega/c$ with c the speed of light. The fields are excited by the current density $\vec{J}_{antenna}$ flowing on the antennas typically located close to the edge of the plasma. The plasma current \vec{J}_{plasma} is composed of the contributions from the various plasma constituents s , $\vec{J}_{plasma} = \sum_s q_s \int d\vec{v} \vec{v} f_{RF,s}$, and is fully defined when the perturbed distributions of all species are known. Strictly, the plasma current contains an ohmic contribution ($\vec{J}_{plasma} = \vec{J}_{ohmic} + \vec{J}_{RF}$) aside from the fast-varying RF contribution. It has been neglected in the present text.

An elegant way to solve the wave equation is relying on variational techniques, by multiplying the equation with a test function vector and integrating over the volume of interest. Performing partial integration to remove the highest order derivatives from \vec{E} not only allows to choose lower order base functions for a given desired numerical accuracy when solving the equation, it also allows to obtain a more symmetrical formulation in which the test function vector \vec{F} and the electric field \vec{E} play a similar role. The resulting equation is

$$\int d\vec{x} [k_o^2 \vec{F}^* \cdot \vec{E} - (\nabla \times \vec{F})^* \cdot (\nabla \times \vec{E})] + W = - \left[\int_{surface} d\vec{S} \cdot \vec{F}^* \times \nabla \times \vec{E} + i\omega\mu_o \int d\vec{x} \vec{F}^* \cdot \vec{J}_{antenna} \right]$$

with $W/[i\omega\mu_o] = \int d\vec{x}\vec{F}^* \cdot \vec{J}_{RF} = q \int d\vec{x}d\vec{v}\vec{F}^* \cdot \vec{v}f_{RF}$. The surface term needs to vanish at the metallic wall to ensure no electromagnetic flux leaks away. A supplementary advantage of this formulation is that it readily yields the associated energy conservation theorem when substituting the test function vector by the electric field (see further for the expression for the absorbed power density shared by the wave and particle descriptions). The perturbed current density \vec{J}_{plasma} and the electric field \vec{E} are related by the conductivity tensor $\vec{\sigma}$: In Fourier space $\vec{J}_{plasma,\vec{k}'} = \vec{\sigma}_{\vec{k}',\vec{k}} \cdot \vec{E}_{\vec{k}}$ which is closely related to the dielectric tensor $\vec{K} = \vec{1} + i\omega\mu_o\vec{\sigma}$.

For a plasma in thermal equilibrium, the term $q\vec{F}^* \cdot \vec{v}f_{RF}$ can be written more explicitly as $-q\vec{F}^* \cdot \vec{v} \int^t dt' q\vec{E} \cdot \vec{v} \frac{F_o}{kT}$ in which the last factor can be shifted in front of the particle history integral since the slowly varying distribution only depends on the constants of the motion. One gets

$$W = \omega\mu_o q^2 2\pi \int d\vec{x}dv_{\perp}dv_{\parallel}v_{\perp} \frac{F_o}{kT} \sum_N \frac{L_N(\vec{F})^* L_N(\vec{E})}{N\Omega + k_{\parallel}v_{\parallel} - \omega} \quad (6)$$

Isolating the various contributions from the test function vector and the electric field in this expression yields an expression for the conductivity tensor.

The velocity space integrals in Eq. (6) can be performed to yield a compact expression for the dielectric response in a Maxwellian plasma. The integral over the *parallel* velocity yields the Fried-Conte plasma dispersion function $Z(\zeta)$, which - aside from the hot plasma corrections to the wave propagation - describes the process of collisionless damping. The argument of the Fried-Conte function is $\zeta = \frac{\omega - N\Omega}{k_{\parallel}v_{th}}$. Figure 3 depicts this function for $Im(\zeta) \rightarrow 0^+$. The real part asymptotically approaches the cold plasma limit $Re[Z] \approx -1/\zeta$, but bends the resonant crossing from $+\infty$ to $-\infty$ at $\zeta = 0$ into a smooth transition behaving like $Re[Z] \approx -2\zeta$. The imaginary part is a Gaussian. Physically its width is determined by the scalelength over which the cyclotron frequency Ω varies, and the factors contributing to the Doppler shift, namely the parallel wave number k_{\parallel} and the thermal velocity v_{th} . Away from the cold plasma resonance damping fades away quickly while the reactive part stays significant much further from $\zeta = 0$.

As long as $k_{\perp}\rho \ll 1$ is satisfied, the Bessel functions can easily be approached by their truncated Taylor series expansion and the perpendicular integrals can easily be integrated. Retaining *all* finite Larmor radius effects yields modified Bessel functions (see e.g. [3]). Although the perpendicular (cyclotron gyration) dynamics seems more daunting than the parallel dynamics, it is the latter that is most challenging: In strong

magnetic fields, the cyclotron motion moves the particle only a small distance - the Larmor radius ρ - away from the guiding center, hence equilibrium quantities typically vary little between the particle and the guiding center positions. But the guiding centers themselves often sample large regions of the machine since their motion is only restricted by the magnetic field topology. Taylor series expansions are routinely used for the perpendicular dynamics but have to be used with care for the parallel dynamics.

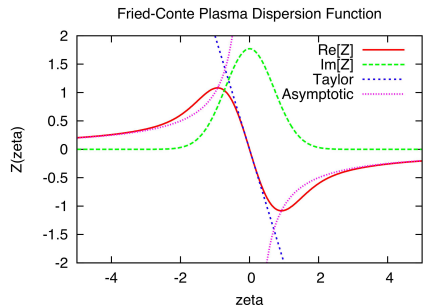


Figure 3: The Fried-Conte plasma dispersion function and its leading order Taylor and asymptotic series representation.

Expressions have also been derived to account for arbitrary F_o (see e.g.[7]). The Fried-Conte function is now replaced by other (in general numerically evaluated) functions. For a sufficiently refined velocity grid, the distribution function can locally be approximated with bi-linear functions and the partial integral can be evaluated analytically, yielding a logarithmic contribution. Upon crossing the resonance, the logarithm picks up a 'switch-on kick' imaginary contribution: It is the delta function contribution at the pole of the original integrand that represents the discontinuous Heaviside step energy 'kick' when picking up the energy due to crossing the resonance. The kick shows up in the uniform plasma description as a resonance crossing in velocity space. In non-uniform plasmas the kick can just as well be described by integrating along the orbit.

II.D. The Cold Plasma Limit

To get a feeling of how drastically a plasma changes the wave characteristics of the electromagnetic waves that exist in vacuum, it is already sufficient to simply consider the cold plasma limit. This may seem a drastic oversimplification but since $k_{\perp}\rho$ is small when the temperature is low, the cold plasma limit yields a reasonable description of the fate of the waves launched from RF antennas, to the obvious exception of the collisionless damping processes themselves which are an

inherently kinetic - as opposed to fluid - effect.

Although it is sufficient to take the asymptotic limit $Z(\zeta) \rightarrow -1/\zeta$ and $J_0(k_\perp \rho) \rightarrow 1$, while $J_M \rightarrow 0$ for Bessel function with order $M > 1$ to retrieve the cold plasma limit, it is much easier to directly rederive the conductivity tensor starting from the solutions of the equation of motion. Using the Stix notation [3], the cold plasma dielectric tensor can be written

$$\vec{K} \cdot \vec{E} = \begin{pmatrix} S & -iD & 0 \\ iD & S & 0 \\ 0 & 0 & P \end{pmatrix} \cdot \begin{pmatrix} E_{\perp,1} \\ E_{\perp,2} \\ E_{\parallel} \end{pmatrix}$$

in which $S = (R + L)/2$, $D = (R - L)/2$, with

$$R = 1 - \sum_s \omega_{p,s}^2 / \omega(\omega + \Omega_s),$$

$$L = 1 - \sum_s \omega_{p,s}^2 / \omega(\omega - \Omega_s)$$

$$P = 1 - \sum_s \omega_{p,s}^2 / \omega^2$$

where the sum is on the various types of species s the plasma is constituted of and ω_p is the plasma frequency.

II.E. Dispersion Equation Roots

Waves in a cold plasma are electromagnetic in character i.e. their energy is carried purely by the Poynting flux. When the plasma density goes to zero, their dispersion roots join the vacuum roots $k_\perp^2 = k_o^2 - k_\parallel^2$. With respect to \vec{B}_o , one of the 2 cold plasma roots is essentially transverse electric, and the other essentially transverse magnetic in character. Referring to the group (energy propagation) velocity, the former is known as a 'fast' wave while the other is a 'slow' wave. The former allows to carry wave power across magnetic surfaces and is the preferred candidate to heat the plasma core in the ion cyclotron domain, while the latter tends to propagate along magnetic surfaces. Finite temperature effects add kinetic corrections to these modes, and introduce supplementary wave branches. For not too energetic particles, the dielectric tensor is usually truncated at second order effects in the Larmor radius. This results in a supplementary mode appearing in the dispersion equation: the (first) Bernstein wave. This wave is essentially electrostatic in nature i.e. its energy is carried by particles in coherent motion with the wave, while its Poynting flux is negligible. Figure 4 shows a dispersion plot of the fast wave exciting the Bernstein wave at the place where the decoupled cold plasma fast wave has a resonance ($S = k_\parallel^2$). This being very close to the ion-ion hybrid layer ($S = 0$) since $k_\parallel^2 \ll |S|$ in sufficiently dense plasmas, the mode conversion layer is often labeled as the ion-ion hybrid layer.

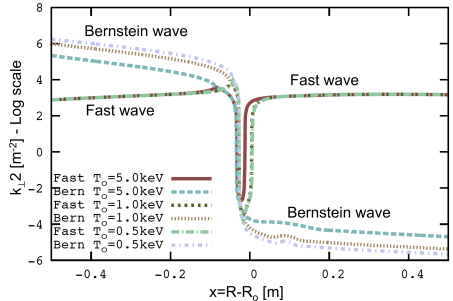


Figure 4: Fast and (first) ion Bernstein wave dispersion equation roots for 3 different central temperatures using a dielectric description retaining all finite Larmor radius corrections. Note that the fast wave root hardly changes while the Bernstein wave root - a root absent in a cold plasma description - depends sensitively on the temperature.

Strictly speaking, the Bernstein wave cannot be described by a dispersion resulting from a truncated Taylor series expansion in $k_\perp \rho$ since $k_\perp \rho$ is of order 1, although such a model does correctly locate the places where the fast wave excites it for up to second cyclotron harmonic terms. At higher frequencies and/or for more energetic particles, the customary truncation of the dielectric tensor is not even rigorous for the fast wave anymore. Hence, higher order finite Larmor radius terms have to be retained. A hot plasma supports an infinity of hot plasma modes, adding supplementary Bernstein modes. Whether they actually play a role depends on whether or not they are excited. Increasing the frequency while keeping the magnetic field fixed brings higher harmonics into the plasma. Higher Bernstein wave modes can be excited but the fast and Bernstein waves are gradually more decoupled at higher frequencies.

II.F. The Fokker-Planck Equation [17-23]

Electromagnetic waves cannot directly be observed experimentally so their behavior is indirectly studied through e.g. the response of temperature and density to sudden changes in the externally launched power level (see e.g. [22]). On the other hand, multiple diagnostics exist to monitor aspects of fast particle populations present in the plasma and to cross-check against theoretical predictions.

As briefly discussed before, when all fast scale dynamics are removed from the description by averaging over all oscillatory aspects of the motion and driven response, the Fokker-Planck equation (4) results. Whereas the wave equation is commonly tackled by integrating

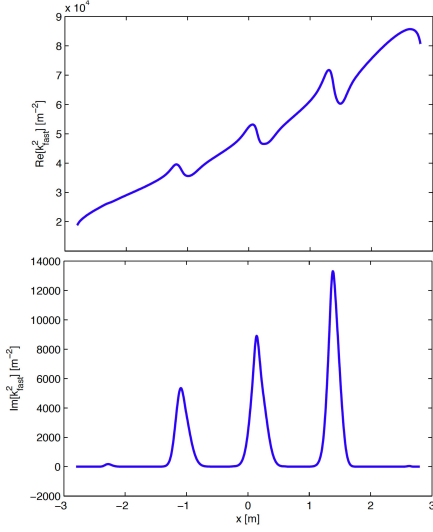


Figure 5: Fast wave dispersion root at $f = 300\text{MHz}$ and $k_{//,o} = 5/m$ in a $D - T - (\alpha) - (D_{NBI})$ DEMO plasma; $B_o = 5.74T$. The top curve shows the real part of the fast wave root; the bottom plot depicts the imaginary part in which ion cyclotron heating at the 6th, 7th and 8th harmonic is observed.

over velocity space so that the independent variables are spatial coordinates, the Fokker-Planck equation is necessarily solved in terms of constants of the motion. The distribution function of a given plasma species represented in terms of the constants of the motion (e.g. energy, magnetic moment) is, by definition, the same along the trajectory. However, because of the magnetic field inhomogeneity, the same distribution expressed in terms of its local velocity components ($v_{\perp}, v_{//}$) looks different depending on the location one looks at it (see Fig.6). Hence, interpretation of experimental data requires careful analysis: As diagnostics focus on different aspects of a same distribution, they may seemingly contradict but in truth corroborate one another.

The Coulomb collision operator for a uniform plasma is known. A convenient, symmetrical form is due to Landau (see e.g. [1, 2, 18]):

$$\sum_s C(F_{oa}, F_{os}) = \nabla \vec{v} \cdot \sum_s \vec{S}_C^{a/s}$$

$$\vec{S}_C^{a/s} = \frac{q_a^2 q_s^2 \ln \Gamma^{a/s}}{8\pi \epsilon_0^2 m_a} \int d\vec{v}' \frac{u^2 \vec{1} - \vec{u}\vec{u}}{u^3} \left[\frac{F_{oa}}{m_s} \frac{\partial F_{os}}{\partial \vec{v}'} - \frac{F_{os}}{m_a} \frac{\partial F_{oa}}{\partial \vec{v}} \right]$$

in which 'a' refers to the species under examination and the sum is over all species 's' in the plasma; \vec{u} is the relative velocity $\vec{v} - \vec{v}'$. Since the species of type 'a' is one

of the species in the sum, the collision operator is a non-linear integro-differential operator. If the species 'a' is a small minority, its selfcollisions can be neglected and the Fokker-Planck equation becomes a linear equation in F_{oa} , but if it is one of the main constituents the nonlinear collision operator has to be retained.

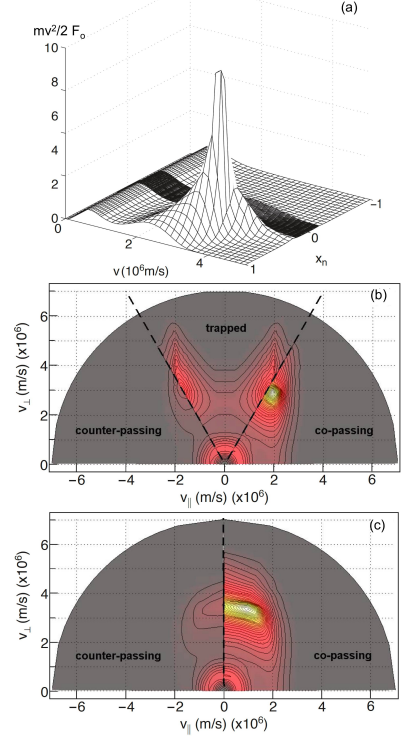


Figure 6: 3 representations of the *same* RF heated beam distribution energy density $\frac{mv^2}{2} F_o$: (a) as a function of the constants of the motion velocity v and (normalized) magnetic moment x_n , and as a function of ($v_{\perp}, v_{//}$) at (b) the low field side midplane and (c) the high field side midplane (see [23]).

Again, analytical expressions are available for the case the distribution function of the species 's' is Maxwellian, in which case the collision operator can be written in terms of the error function. In case F_{os} is isotropical, the integrals that need to be evaluated reduce to 1-dimensional integrals and in the fully anisotropical case the operator acting on F_{oa} can be written in terms of the Rosenbluth potentials. The step from the uniform plasma collision operator C to the operator $\langle C \rangle$ averaged over all fast aspects of the motion is a nontrivial step, the fully rigorous treat-

ment of which is still awaited.

In view of the fact that the various species interact with each other collisionally, and that several types of species can simultaneously be heated by electromagnetic waves, a series of coupled Fokker-Planck equations rather than a single one should be solved. This can be done iteratively, taking the distributions obtained in the previous iteration to compute the collision operator in the current step. Provided convergence is reached, this allows accounting for the non-linear collision operator without making use of a non-linear system solver. Figure 7 shows a simplified 1-dimensional case in which it was assumed that all distributions are isotropic. It depicts an ITER example for the conditions foreseen for wave heating of the $D-T$ plasma during the activated phase of operation of the machine: the majority of T ions is heated at its second harmonic cyclotron layer, while a minority of ${}^3\text{He}$ is simultaneously heated at its fundamental cyclotron resonance to help cranking up the fusion reactivity; unavoidably, the electrons are heated by Landau and TTMP damping.

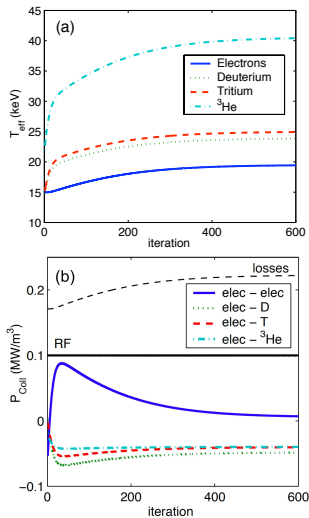


Figure 7: ITER $D-T-({}^3\text{He})$ heating: (a) Effective temperatures and (b) electron power balance.

II.G. A Note on Selfconsistency

A rigorous treatment requires that the Fokker-Planck (FP) and wave (W) equations are solved simultaneously and on the same footing. Their intimate connection is exemplified by the 2 expressions of the absorbed power density:

$$P_{abs,FP} = \frac{\partial}{\partial t} \left[\int d\vec{v} d\vec{x} \epsilon |F_o| \right]_{RF} = \int d\vec{v} d\vec{x} \epsilon \frac{\partial F_o}{\partial t} \Big|_{RF} =$$

$$\begin{aligned} & \frac{1}{2} Re \int d\vec{v} d\vec{x} \epsilon \nabla_{\vec{v}} \cdot \vec{a}_{RF}^* \int_{-\infty}^t dt' \vec{a}_{RF} \cdot \nabla_{\vec{v}} F_o \\ & = \frac{q}{2} Re \int d\vec{v} d\vec{x} \vec{E}^* \cdot \vec{v} f_{RF} = \frac{q}{2} Re \int d\vec{x} \vec{E}^* \cdot \vec{J}_{RF} = P_{abs,W} \end{aligned}$$

in which $P_{abs,FP}$ is the RF power density written in the way it is used in the Fokker-Planck equation (with ϵ the energy, and $\frac{\partial F_o}{\partial t} \Big|_{RF}$ the RF diffusion operator, and $P_{abs,W}$ the RF power density as written in the wave equation, involving the RF perturbed current density \vec{J}_{RF} and f_{RF} the perturbed distribution function; $\vec{a}_{RF} = \frac{q}{m} [\vec{E}_{RF} + \vec{v} \times \vec{B}_{RF}]$ is the Lorentz force acceleration/deceleration caused by the small but rapidly varying electromagnetic field driven at frequency ω . Formally writing down the above expression is immediate. To come up with practical expressions for the coefficients to be used in the wave and Fokker-Planck equations is less trivial, at least when the equations are truly treated on the same footing i.e. when the 2 problems posed in 6-dimensional phase space are solved removing 3 of the 6 independent variables to arrive at an equation in the remaining 3 variables using the *same* approximations for both equations. Getting the proper coefficients requires integrating (a) on the velocity space variables to obtain the dielectric response coefficients needed in the wave equation and (b) on the gyro, bounce and drift motions to find an expression for the quasi-linear diffusion operator. Ideally, the same elementary 'building blocks' are used and the relevant integrations are performed on them.

III. SOME ASPECTS OF NONUNIFORM PLASMA MODELING

III.A. Mode Coupling [38-51]

Before commenting on the particular issues brought about by the impact of the plasma inhomogeneities on the orbits of the particles and the challenges this leads to when trying to write down a rigorous expression for the dielectric response, a simplified problem is looked at first, namely that of the wave propagation in a tokamak in absence of a poloidal field i.e. where the guiding center orbits are assumed to simply being given by $\varphi(t) = \varphi(t_o) + v_{\parallel}(t - t_o)$. Starting from Eq. (6), but retaining the full wave spectrum and toroidal curvature while assuming that the various species are Maxwellian and that the toroidal angle as well as the distance from midplane are ignorable variables (allowing to isolate individual n toroidal modes and k_z) yields

$$\begin{aligned} W &= \omega \mu_o (2\pi)^3 \int dR R dv_{\perp} dv_{\parallel} v_{\perp} \frac{F_o}{kT} \\ & \sum_N \frac{[\int k_{R'} L_N(\vec{F})]^* [\int k_R L_N(\vec{E})]}{N\Omega + k_{\parallel} v_{\parallel} - \omega} \end{aligned}$$

which is fully symmetrical w.r.t. the test function vector \vec{F} and the electric field \vec{E} , guaranteeing a positive definite power density for a plasma in thermal equilibrium. To arrive at a practical expression one of the following 2 approaches is used:

- Assuming that $k_{\perp}\rho \ll 1$ so that the Bessel functions in the Kennel-Engelmann expressions can be approximated by a truncated Taylor series expansion around the origin, which upon realizing that

$$\frac{d^m}{dR^m} \vec{E}(R) = \int dk_R (ik_R)^m \exp[ik_R R] \vec{E}_{k_R}$$

allows to write down an expression for the dielectric response W and the purely electromagnetic (curl) term to be used in the Galerkin form of the wave equation; it is customary to truncate the Taylor series at terms of second order in $k_{\perp}\rho$. Removing the differential operators from the test function vector components \vec{F} by partial integrations allows to find the corresponding expression for the dielectric tensor, and the so obtained surface terms immediately provide the expression for the kinetic flux [38].

- In reality, $k_{\perp}\rho \ll 1$ is not satisfied for all modes that the plasma supports and thus that assumption should not be made if such modes are excited. Bernstein modes are finite temperature modes for which $k_{\perp}\rho \approx 1$ and even the cold plasma slow mode violates the smallness condition. Hence *if* short wavelength branches are excited - either directly at the plasma edge or at ion-ion hybrid layers [3] - a more rigorous treatment is needed to ensure the predicted fate of the shorter wavelength modes is correctly described. The easiest way to do this is to rewrite the Fourier integrals as discrete sums and to use locally constant base functions $[H(k_R - k_{R,i})][H(k_{R,i+1} - k_R)]$. The Galerkin form of the wave equation is hereby transformed into a system of linear equations allowing to find the electric field Fourier components in the discretized Fourier space.

Figure 8 shows an example of the integration of the 1D integrodifferential wave equation. The top figure depicts the perpendicular wave components. An incoming fast wave carries energy into the region of interest from the right. At the ion-ion hybrid layer at $R \approx 3m$ mode conversion to the Bernstein wave takes place, although part of the fast wave energy simply tunnels through the confluence layers and makes it to the high field side (left on the plot) as a fast wave. Note that the Bernstein wave is efficiently absorbed, its amplitude having shrunk again to zero about $0.3m$ towards the high field side. The bottom figure shows the corresponding

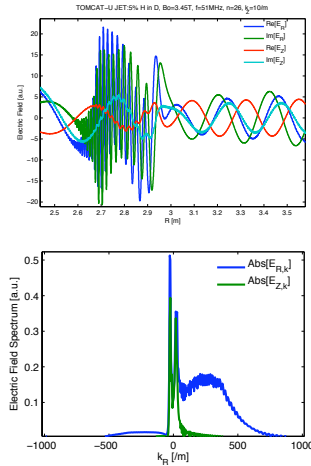


Figure 8: Bernstein wave excitation by the fast magnetosonic wave at the ion-ion hybrid layer: electric field components (top) and Fourier spectrum (bottom).

k_R Fourier spectrum of the perpendicular electric field. The Bernstein wave is a backward, electrostatic wave: Its main field component is the component in the direction of the background gradient, and for a leftward propagating wave that carries energy from the confluence layer towards the high field side it is the $k_R > 0$ spectrum that is significantly non-zero. The 2 peaks in the low k_R part of the spectrum correspond to the incoming fast wave (highest amplitude for $k_R < 0$ as the fast wave is a forward wave carrying energy in the same direction as the phase velocity) and the reflected wave (somewhat smaller peak, and in the $k_R > 0$ region since the reflected wave necessarily carries less energy than the incoming wave).

In two dimensions poloidal as well as radial mode coupling occurs. Figure 9 gives an example of 2D wave equation modeling in which the geometry and the poloidal magnetic field has been accounted for. In this ITER example the short wavelength modes are not excited.

III.B. Orbit topology [24-32]

The motion of a charged particle in an axisymmetrical tokamak is characterized by 3 constants of the motion and by 3 periodic aspects of the motion. The 3 constants of the motion often used are the energy $\epsilon = \frac{mv^2}{2}$, the magnetic moment $\mu = \frac{mv_{\perp}^2}{2B_{\phi}}$ and the toroidal angular momentum $P_{\varphi} = mRv_{\varphi} - q\Psi/2\pi$ (φ is the toroidal angle, q the charge and Ψ the poloidal magnetic flux) but suitable other sets of 3 independent functions of the customary 3 can equally well be used. In order of de-

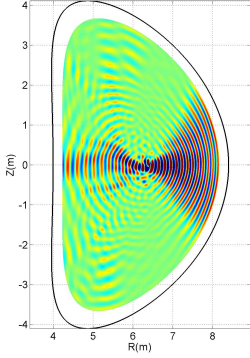


Figure 9: Poloidal electric field component for the RF heating scenario foreseen for the activated ITER phase; 3% ^3He in a balanced $D - T$ plasma, $f=53\text{MHz}$ and $B_o = 5.3T$.

creasing oscillation frequency, the 3 oscillatory aspects are the cyclotron motion, the bounce motion and the toroidal drift motion. Figure 10 gives a schematic view of the various oscillatory aspects of the motion for a trapped particle in a tokamak.

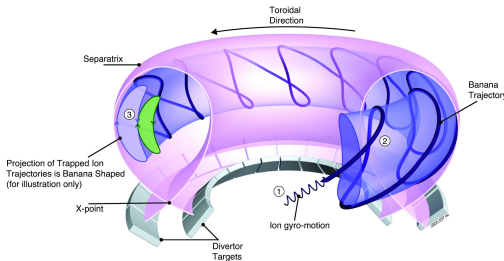


Figure 10: Schematic representation of the particle orbits in a tokamak (JET-EFDA figure JG05.537-4).

Even on a single particle level, adding the poloidal field to the description vastly changes the complexity of the wave-particle interaction problem since the guiding center orbits are now no longer on $R = ct$ surfaces but have become poloidally closed loops. Rather than sampling a unique value of the confining magnetic field, the guiding centers sample regions of varying toroidal field strength. Whereas in a uniform plasma a particle either is 'in resonance' or 'out of resonance' at all times, the resonances in inhomogeneous plasmas are localized i.e. the resonance condition is satisfied only locally at some positions along the orbit. The phase factor $\exp[i(N\Omega + k_{\parallel}v_{\parallel} - \omega)(t - t_o)]$ in the earlier men-

tioned evolution equation for the particle energy is now generalized to an integral over \vec{k} space of terms of the form $\exp[i\Theta(t)]$ in which $\Theta = -N\phi + \vec{k}(t) \cdot \vec{x}_{GC}(t) - \omega t$. In the neighbourhood of the resonance the phase in the exponential can be approximated by a truncated Taylor series expansion, $\Theta(t) \approx \Theta(t_o) + \dot{\Theta}(t_o)(t - t_o) + \frac{1}{2}\ddot{\Theta}(t_o)(t - t_o)^2 + \frac{1}{3!}\ddot{\ddot{\Theta}}(t_o)(t - t_o)^3$. The corresponding exponential factor generally oscillates very quickly so that its integral does not accumulate a net contribution. Close to stationary phase points ($\dot{\Theta} = 0$) the phase variation slows down and the integral picks up a finite contribution. Figure 11 depicts the relevant integral for a regular stationary phase point ($\dot{\Theta} \neq 0$) and for a higher order stationary phase point ($\dot{\Theta} = 0$). The former is representative for a standard resonance crossing while the latter is representative for a resonance at a turning point of the orbit, where 2 resonances merge (strictly, the higher order stationary phase point is a bit separated from the turning point: $v_{\parallel} = 0$ does not coincide with $v_{\theta} = 0$). The linear line corresponding to the uniform plasma case for which the particle always stays in resonance is indicated as well.

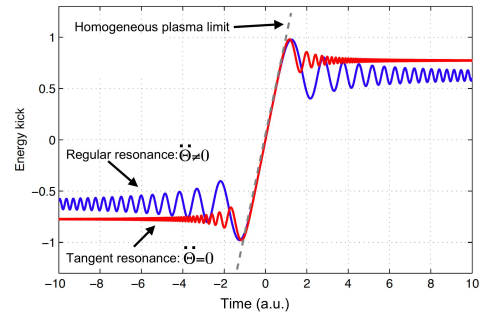


Figure 11: The energy kick felt by the particle along the orbit for resonance at a regular point ($\dot{\Theta} \neq 0$) and at a tangent resonance point ($\dot{\Theta} = 0$).

In spite of the fact that energetic ions have guiding center orbits that deviate significantly from magnetic surfaces, the difference between the toroidal angular momentum P_{φ} and the poloidal flux function Ψ is often neglected ('zero drift' or 'zero banana width' approximation). Aside from the fact that this is an acceptable approximation in large enough machines or for low enough temperatures, the main motivation for this approximation is that it hugely simplifies the equations while keeping poloidal mode coupling and particle trapping/detrapping, two of the most important inhomogeneity effects, intact. Since the dielectric response written earlier was using the electric field at the guiding center rather than the particle position and since guiding centers stay on magnetic surfaces in the zero drift

approximation, the parallel gradient can be written as an *algebraic* rather than as a differential operator when expressing the various quantities in terms of their (discrete) toroidal and poloidal Fourier series expansions:

$$\begin{aligned}\nabla_{//} &= \frac{\cos\alpha}{|\partial\bar{x}/\partial\varphi|} \frac{\partial}{\partial\varphi} + \frac{\sin\alpha}{|\partial\bar{x}/\partial\theta|} \frac{\partial}{\partial\theta} \\ &= \cos\alpha \frac{in_{tor}}{R} + \sin\alpha \frac{im_{pol}}{|\partial\bar{x}/\partial\theta|} = ik_{//}\end{aligned}$$

for each individual poloidal mode m_{pol} and toroidal mode n_{tor} ; α is the angle between the total magnetic field and the toroidal direction. The denominator resulting from the particle history integral is now no longer a constant and net resonant interaction only takes place at the poloidal angle that satisfies $N\Omega + k_{//}v_{//} = \omega$ in which the cyclotron frequency, the parallel wave number and the parallel velocity now all vary along the orbit. Although the density and temperature are constant along the zero-drift guiding center trajectory, poloidal mode coupling takes place because of the magnetic field and geometrical inhomogeneity the guiding center experiences along its orbit. This has one mild and one more important consequence:

- The mild consequence is that the perpendicular differential operator in the expression L_N due to Kennel-Engelmann requires retaining the differential character in both independent perpendicular directions. The resulting expressions yield a double sum over poloidal modes, and differential operators in the direction perpendicular to the magnetic surfaces. For heating scenarios in which short wavelength branches are excited, a proper description of the poloidal coupling requires accounting for a very large number of poloidal modes and couplings, and a large number of radial grid points. In an axisymmetrical tokamak there is no toroidal coupling and thus a single sum on the toroidal mode spectrum remains; in a real tokamak - in which magnetic ripple occurs since a discrete number of toroidal magnetic field coils are installed - and in a stellarator, also the toroidal modes are coupled. Even in the zero drift limit, solving the wave equation in 2 or 3 dimensions requires powerful computers.
- Whereas the previous section involves supplementary bookkeeping but is not truly posing a problem, the fact that the parallel mode number appears in the resonant denominator gives rise to a fundamental problem: Whereas expression (6) is fully symmetrical in the test function vector \vec{F} and the electric field \vec{E} and guarantees positive definite and purely resonant absorption for Maxwellian distributions, which is what is physically expected, the now obtained expressions are symmetrical for

what concerns the perpendicular operator but are asymmetrical for what concerns the parallel dynamics. As long as $k_{//}$ is modest (as is typically the case for the fast wave), this is of little consequence. But for short wavelength branches, positive definite absorption for Maxwellian distributions is no longer guaranteed. A rigorous cure for that flaw requires a much more sophisticated model, as will be discussed in the next section.

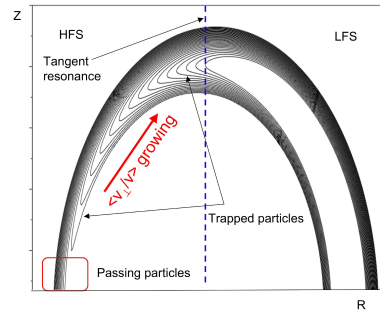


Figure 12: Schematic representation of the impact of cyclotron heating on a charged particle in a tokamak: The perpendicular energy of the particle gradually increases. Initially passing particles become trapped, their banana tip shifting towards the low field side when v_{\perp} gradually grows. The interaction of the particle with the wave stops when the orbit no longer cuts the resonance. Just prior to that happening, 2 resonances merge, giving rise to efficient heating at the tangent resonance.

It was mentioned earlier that for not too energetic ions the Doppler shift term $k_{//}v_{//}$ in the resonance condition $N\Omega + k_{//}v_{//} = \omega$ is a small correction to the cyclotron term. As the corresponding distribution is only significant in a restricted region of velocity space, it implies that the region where cyclotron interaction takes place is restricted in space as well: $\delta R/R \approx \delta(k_{//}v_{//})/\omega$. Although the electrons are equally resonantly interacting with the field, the resonance condition is much less stringent on them since $k_{//}v_{//} = \omega$ is commonly satisfied in a wide region because of the modest steepness of the temperature profile. Consequently, it is fairly straightforward in the ion cyclotron frequency domain to ensure ion heating can only take places at a predetermined location but it is less evident to avoid the often unwanted electron heating. In big, hot and dense machines such as ITER RF waves have already lost a non-negligible fraction of their energy by electron Landau and TTMP damping before arriving at the cyclotron layer.

III.C. Bounce Motion, Tangent Resonance, ...

Two approaches are commonly used to derive the wave equation (and in particular to find a suitable expression for the RF perturbed distribution function f_{RF}) and the Fokker-Planck equation (and in particular the quasilinear diffusion operator $\langle Q \rangle$). One is the very intuitive approach in which the governing Lorentz force can readily be recognized in the expressions and for which the link with straight magnetic field line uniform plasm theory is direct (see e.g. [26, 44, 43]). The other is more formal but more general and allows to benefit from the action-angle (Hamiltonian) formalism (see e.g. [33, 35, 36, 30]).

Practical expressions proposed by various authors tend to differ somewhat since different variables are chosen and different approximations are made. For wave equation studies (focussing on the fast dynamics), the trajectory integral is most intuitive and therefore most frequently adopted but for Fokker-Planck equation, the details of the fast dynamics are only indirectly relevant and all has to be expressed in terms of constants of the motion, hence tending to be closer to the action-angle technique which elegantly allows to retain the slow time scale physics while integrating away the fast phenomena by suitable averages over the various relevant oscillation periods. Kaufman showed, however, that the Hamiltonian description can equally be used to describe the fast scale physics. More importantly still, he stressed that a rigorous description of both aspects of the wave-particle interaction requires making the *same* approximations in both equations if one wants to describe the physics self-consistently. If applied rigorously, the path integral and action-angle methods are fully equivalent; for a somewhat more detailed discussion, see [34]. However, and in spite of Kaufman's visionary paper and presently available powerful computers, a fully rigorous description of the plasma heating process by electromagnetic waves is still awaited and a fully selfconsistent description based on a sufficiently rigorous footing is a project still to be tackled ...

The drift approximation and quasilinear approach make sense because of the vastly different time and spatial scales to describe the wave-particle interaction by first computing the zero order motion in absence of the rapid but small perturbation, and to account for the corrections relying on perturbation theory. In an axisymmetric tokamak in absence of perturbations, the particle motion can be described in terms of 3 constants of the motion $\vec{\Lambda}$ and 3 angles $\vec{\Phi}$ that describe the periodic aspects of the particle motion. Kaufman proposed to rely on action-angle variables but in the literature a wide variety of constants of the motion was successfully used. In contrast, the choice of the angles as used in the Hamiltonian theory is much more appealing than any other choice since these angles vary *lin-*

early with time and thus time history integrals become trivial: Formally, the integrals are like those appearing in the uniform plasma case since - once functions only involving constants of the motion have been pulled out of time history integrals (since $\frac{d}{dt}|_o = \frac{\partial}{\partial t} + \vec{\omega} \cdot \frac{\partial}{\partial \vec{\Phi}}$ e.g. $f_{RF} = - \int dt' \vec{a}_{RF} \cdot \nabla_{\vec{v}} F_o$ can simply be written as $f_{RF} = - \frac{\partial F_o}{\partial \vec{\Lambda}} \cdot \int dt' \dot{\vec{\Lambda}}$), the rapidly varying phase factor denoting all 4 oscillatory aspects of the driven response and particle motion is of the form $\vec{m} \cdot \vec{\Phi}(t) - \omega t$ in which $\vec{\Phi}(t) = \vec{\Phi}(t_o) + \vec{\omega}(t - t_o)$ and the gyro, bounce and toroidal drift frequencies $\vec{\omega} = (\omega_g, \omega_b, \omega_d)$ are only depending on the constants of the motion $\vec{\Lambda}$; the corresponding mode numbers are $\vec{m} = (m_g = -N, m_b, m_d = n_{tor})$ in which the bounce mode number m_b should not be confused with the poloidal mode number m_{pol} but the other 2 mode numbers correspond to the cyclotron mode and the toroidal mode numbers. And so time history integrals simply yield factors of the form $\dots / [\vec{m} \cdot \vec{\omega} - \omega]$ i.e. prescribe that waves and particles resonantly interact when the resonance condition $\vec{m} \cdot \vec{\omega} = \omega$ (ω being the generator frequency) is satisfied.

A major simplification of the algebra comes from the identity $\vec{a}_{RF} = \frac{i}{\omega m} [\frac{d}{dt} \nabla_{\vec{v}} - \nabla_{\vec{x}}] q \vec{E} \cdot \vec{v}$ (see e.g. [5]) since it allows to write the various contributions of which the time history integrals needs to be found to come up with an appropriate expression for the dielectric response of the plasma to a rapidly oscillating electromagnetic wave in terms of $\dot{\epsilon} = q \vec{E} \cdot \vec{v}$. For example

$$f_{RF} = \sum_{j=1}^3 \frac{i}{\omega m} \frac{\partial F_o}{\partial \Lambda_j} [-q \vec{E} \cdot \nabla_{\vec{v}} \Lambda_j + \int^t dt' D_{\Lambda_j} \dot{\epsilon}]$$

in which $D_G \dots = \frac{d}{dt} [\nabla_{\vec{v}} G \cdot \nabla_{\vec{v}} \dots] + \nabla_{\vec{v}} G \cdot \nabla_{\vec{x}} \dots$, hereby essentially reducing the algebraic work to be done to describe the impact of an arbitrary distribution function $F_o(\vec{\Lambda})$ to the work needed for the case of an isotropic distribution. For a Maxwellian distribution, it can easily be shown that the net absorption of wave energy by a particle population is positive definite and that the interaction is resonant in nature:

$$\sum_{\vec{m}, \vec{m}'} \langle q \vec{E} \cdot \vec{v} |_{\vec{m}}^* |_{\vec{m}'} \int_{-\infty}^t dt' q \vec{E} \cdot \vec{v} |_{\vec{m}} \rangle = \sum_{\vec{m}} \frac{|q \vec{E} \cdot \vec{v} |_{\vec{m}}|^2}{i [\vec{m} \cdot \vec{\omega} - \omega]}.$$

Making use of generating functions for the transformation between canonical variables and applying them to the action-angle $(\vec{J}, \vec{\Phi})$ variables proposed by Kaufman, one finds $D_{J_i} = m \frac{\partial}{\partial \Phi_i}$ where m is the mass of the examined type of particles [34]. Whereas the toroidal angular momentum P_φ and the magnetic moment μ are natural variables to use in the computations, the third Kaufman action - related to the surface enclosed by the poloidal closed drift orbit - is not very practical. Replacing it by the energy ϵ allows to find a compact operator to generalize the expression found for a

Maxwellian distribution to that for an arbitrary distribution $F_o(\vec{\Lambda})$: $\frac{\partial F_o}{\partial \Lambda_1} \rightarrow \frac{\partial}{\partial \Lambda_1} + N \frac{\partial}{\partial \Lambda_2} + n_{tor} \frac{\partial}{\partial \Lambda_3}$ when $\vec{\Lambda} = (\frac{e}{\omega}, -\frac{mv^2}{2\Omega}, P_\varphi = mRv_\varphi - \frac{q\Psi}{2\pi})$ where Ψ is the poloidal magnetic flux.

Of course, although the Hamiltonian method offers an elegant framework to do the required evaluations, its simplicity is somewhat misleading:

- The Fourier transformation of the work $q\vec{E} \cdot \vec{v}$ done by the electric field on the particles, written down only formally in Kaufman's paper is where the full complexity of the acceleration and deceleration of particles on their orbits through an inhomogeneous static magnetic field will show up. Happily, the vast difference in time response time of the various aspects of the motion allows to rely on asymptotic techniques to perform this step. First, the Fourier analysis is performed *at a fixed time*, and then the integrals along the orbits are evaluated. The Fourier transform of $q\vec{E} \cdot \vec{v}$ is

$$q\vec{E} \cdot \vec{v}|_{\vec{m}}(\vec{\Lambda}) = \frac{1}{(2\pi)^3} \int d\vec{\Phi} q\vec{E} \cdot \vec{v} \exp[-i\vec{m} \cdot \vec{\Phi}].$$

Formally writing the electric field in terms of its \vec{k} spectrum so that, analogously to the uniform plasma Eq. (2), the phase of $q\vec{E} \cdot \vec{v}$ is $\vec{k} \cdot \vec{x}_{GC} - N\phi - \omega t$ (GC=guiding center), it can readily be seen that the stationary phase points of the \vec{m} Fourier component are given by the condition $\vec{k} \cdot \vec{v}_{GC} + N\Omega = \vec{m} \cdot \vec{\omega}$ so that the global resonance condition $\vec{m} \cdot \vec{\omega} = \omega$ can be rewritten as $\vec{k} \cdot \vec{v}_{GC} + N\Omega = \omega$, which reduces to the familiar resonance condition $k_{||}v_{||} + N\Omega = \omega$ of the uniform plasma (and more in particular $\rho/L_{B_o} = 0$ i.e. driftless) limit. It is not a trivial task to rigorously account for the drift orbit effects since perpendicular corrections not only have to be added to the generalized Kennel-Engelmann operator but they now enter the resonance condition as well.

- A supplementary difficulty comes from the fact that there are many thousands of bounce modes that need to be evaluated to describe wave-particle interaction accounting for the plasma inhomogeneity rigorously. This amounts to a significant increase of the computation time required to solve the equations.

III.D. Decorrelation, Superadiabaticity [33-37,52-55]

It was discussed earlier that the work $q\vec{E} \cdot \vec{v}$ the electric field does on a charged particle is an oscillatory function of time i.e. can be written as a sum of terms proportional to a phase factor $\exp[i\Theta(t)]$. As the guiding center orbits in the drift approximation are closed

poloidally, the particles cross every poloidal position many times every second (bounce frequency). Most of the contributions to the work are oscillatory in nature and cancel out when integrated over all fast time scales (gyro-, poloidal bounce and toroidal drift motion), yielding a zero net effect. Only the resonant contributions possibly give rise to a finite effect. That even these do not cancel on average, is not as evident as it may seem at first sight: In general, the number of cycles the work goes through in between 2 successive transits is not an integer number and thus the phase change is not a multiple of 2π so the average work done over a longer period of time is the sum of 'energy kicks' with the same amplitude *but* at different phase. Assuming that the phase difference between 2 successive transits modulo 2π is $\Delta\Theta$, it can readily be seen that for every particular phase at a given crossing, there is another crossing in a not too distant past that more or less cancels out the present contribution since $\Delta\Theta$ attains any value between 0 and 2π with equal probability. And so, even if the particle gets an energy kick every time it crosses the resonance, the net effect of many crossings (typically a few thousand per second for standard ion temperatures in typical working conditions) is still zero ... *Unless* something breaks the pure periodicity and makes the particles somehow 'forget' about their encounters in the far past so that rather than a very large number of crossings being relevant, only the most recent ones are. Collisionality does exactly that.

Let us consider the simplest possible 'Krook' collision operator $C(f) = \nu f$, where ν is the dominant collision frequency for the species considered, to discuss the principle: Whereas the fast dynamics of the wave-particle interaction is typically described by the Vlasov equation, a somewhat more careful examination of the evolution equation we started from shows that collisionality can strictly *not* be omitted when describing the fast time scale: the collision operator C in that original equation acts on the full distribution $f = F_o + f_{RF}$ and not only on the slowly varying part F_o . Hence the Vlasov equation should be extended to contain a small but nonzero contribution, reflecting the rare but non-absent collisions the particles undergo along their unperturbed orbits: $\frac{d}{dt}|_o f_{RF} + \vec{a}_{RF} \cdot \nabla F_o = C(f_{RF})$. Writing the time derivative along the trajectory in terms of the constants of the motion $\vec{\Lambda}$ and the angles $\vec{\Phi}$ and assuming that the perturbed distribution can be written as the product of a term *only* involving slow dynamics and a term involving fast dynamics i.e. $f_{RF} = H(\vec{\Lambda}, t) \tilde{f}(\vec{\Lambda}, \vec{\Phi}, t)$, the fast and slow dynamics can be isolated: $[H \frac{d}{dt}|_o \tilde{f} + \vec{a}_{RF} \cdot \nabla_{\vec{v}} F_o] / \tilde{f} = [-\frac{\partial}{\partial t} H + \nu H]$. Since the right hand side of this expression only contains slow dynamics (no fast period response), one can formally write that both sides of this equation independently have to be equal to a slowly varying function,

$G = G(\vec{\Lambda}, t)$ which is negligibly small on the fast dynamics time scale, $G \approx 0$. It follows that the factor H can to good approximation be evaluated explicitly: $H \propto \exp(\nu t)$. And so the Vlasov equation is supplemented with a 'switch-off' or 'phase memory loss' factor: $f = - \int_{-\infty}^t dt' H^{-1} \vec{a}_{RF} \cdot \nabla F_0$ which - in view of the result found for H consistent with the Krook collision operator - is simply equivalent to the 'causality rule' which prescribes the frequency ω in the driven time response factor $\exp(i\omega t)$ and the resonant denominator ($N\Omega + k_{\parallel} v_{\parallel} - \omega$ in the uniform plasma expression, or $\vec{\omega} \cdot \vec{m} - \omega$ in its drift approximation generalisation) to be replaced by $\omega + i\nu$. Whereas the collisional contribution is very small, it plays a crucial role in the evaluation of the time history integral when integrating over many crossings through a given point on the closed bounce orbit: It constitutes the 'memory loss' factor ensuring that a finite net contribution is obtained for the resonant contributions to the work done by the driven electric field on the particles.

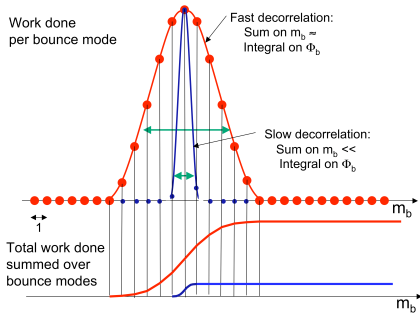


Figure 13: Schematic representation of the importance of decorrelation.

Why this is crucial and how it works can readily be seen in Fig. 13: due to the periodic nature of the bounce motion, the sum of the contributions over all bounce modes is only equivalent to the corresponding integral over (the stationary phase position) bounce angles *if* the collisional broadening of the resonance is wide enough. This brings out a subtle point in the analysis of the wave-particle interaction: Because of the large difference between the bounce and the gyro-frequency ($\omega_b \ll \omega_g$), it takes thousands of bounce modes to rigorously account for the magnetic field inhomogeneity i.e. the corresponding stationary phase points where the resonant interaction predominantly takes place ($\Theta=0$) are very closely spaced. Yet the discrete sum on the bounce modes *cannot* justifiably be replaced by a bounce integral unless the decorrelation time is short enough i.e. the collision frequency

large enough. And so the very different time scale on which the gyro and bounce motions occur is crucial to restore the 'quasi-homogeneous' nature of localized resonances, while the decorrelation needs to be sufficiently *fast* to ensure that a net interaction takes place at these resonance locations when averaging over all the faster processes. In view of the typical collision frequencies in hot plasmas, collisions at first sight cannot cause a fast enough decorrelation to guarantee RF heating to have a net effect.

Fully accounting for the actual collision operator in the right hand side of the 'generalised' Vlasov equation is not at all a trivial task. Kasilov [53] did the exercise of examining more realistic collision operators and found that the 'switch-off' factor H can to first approximation be taken to be $H = \exp[(t/\tau)^n]$ where $n = 3$ for Cerenkov interaction (Landau damping and transit time magnetic pumping) and $n = 5$ for cyclotron damping. He found that the decorrelation times τ are significantly *shorter* than the collision times $1/\nu$, implying that particles 'lose' memory of their phase quickly enough for RF heating to be efficient in magnetic fusion devices. Although the details of the impact of the various decorrelation functions differs, the net effect is the same: the 'kick' particles receive when crossing the resonance is similar (see Fig. 14).

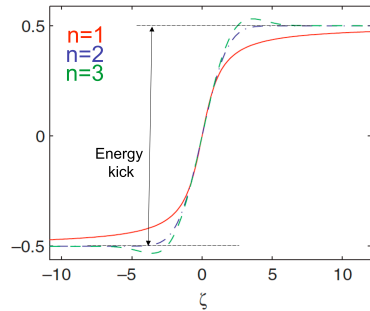


Figure 14: Integrated decorrelation functions for $n = 1, 2, 3$; $\zeta = \tau(\vec{m} \cdot \vec{\omega} - \omega)$ with τ the decorrelation time.

While for thermal particles it is thought that the details of the actual decorrelation are not too relevant (to the important exception of what happens near tangent resonance points where two closely spaced resonance points merge into a single one), for too energetic particles, however, the collisions may still be too infrequent so that their net effective absorption is reduced. This regime is known as 'superadiabaticity'.

Not only collisions cause a randomization of the phase. Because of the non-integrability of the orbits and the non-linearity of the problem, stochastization

takes place even if collisions would be absent when launching RF waves of a few MW in fusion relevant plasmas. The rich spectrum of modes, each contributing to the full wave-particle interaction and giving rise to fast phase variations of the total work done on the particles, is likely to trigger sufficient decorrelation.

IV. END NOTE

With the dawn of powerful parallel computers, the degree of realism that can be reached when modeling the interaction of particles and waves in hot, magnetized, inhomogeneous plasmas contained in magnetic fusion experimental reactors is gradually increasing. Various techniques are available to highlight the study of specific aspects of the interaction. Even so, the problem to be tackled is challenging and a number of aspects are only starting to be touched upon.

One aspect of importance in the context of wave-particle interaction is the description of the opposite of wave heating, namely the onset of instabilities triggered by particle distributions: In present-day wave and Fokker-Planck descriptions, it is implicitly assumed that the RF fields are never powerful enough to make the factor $\frac{\partial F_0}{\partial \Lambda_1} + N \frac{\partial F_0}{\partial \Lambda_2} + n \frac{\partial F_0}{\partial \Lambda_3}$ that appears in the perturbed distribution f_{RF} and hence in the expression for $\langle Q \rangle$ change sign, while experimentally it is well known that MHD modes can be triggered when RF heating is efficient.

Another - even more essential - aspect is the rigorous accounting of the bounce spectrum ensuring that the dielectric response is properly described, without artificially giving rise to damping that has to be rejected on physical grounds: While only the rigorous application of the procedure proposed by Kaufman guarantees the causality to be respected for all modes the plasma supports, no models based on this procedure are yet available.

V. A COMMENT ON THE LIST OF REFERENCES

Although most authors in the reference list comment on various subtopics treated in this text - making a clean separation impossible - the papers most relevant to read up on the general treatment have references [1-11], the wave equation is somewhat more the focus in [12-16] while the Fokker-Planck aspects are the main subject in [17-23]. Details on the orbit topology and its role in describing the wave-particle interaction can be found in [24-32]. The action-angle formalism is discussed in [33-37]. Comments on how to solve the relevant set of equations - with a focus on accounting for the realistic geometry - are given in [38-51] while the role of decorrelation is the key subject in [52-55].

VI. ACKNOWLEDGMENT

The authors gladly thank Dr. P.U. Lamalle for the material he provided for this lecture.

REFERENCES

1. B. WEYSSOW, *Kinetic Theory*, these summer school proceedings
2. R. BALESCU, *Transport Processes in Plasmas*, North-Holland, Amsterdam (1988)
3. T.H. STIX, *Waves in Plasmas*, AIP, New York (1992)
4. B.D. FRIED and S.D. CONTE, *The Plasma Dispersion Function*, Academic, New York (1961)
5. L.D. LANDAU & E.M. LIFSHITZ, *Course of Theoretical Physics*, Pergamon, Oxford (1960)
6. R. KOCH, Phys. Lett. A **157**, 399 (1991)
7. D. VAN EESTER, Plasma Phys. Contr. Fusion **35**, 1309-1319 (1993)
8. D. VAN EESTER, Journal Plasma Phys. **54** 1, pp. 31-58 (1995)
9. D. VAN EESTER, Journal Plasma Phys. **60** 3, pp. 627-671 (1998)
10. D. VAN EESTER, Journal Plasma Phys. **65** 5, pp. 407-452 (2001)
11. D. VAN EESTER, Plasma Phys. Contr. Fusion **47** 5, pp. 459-481 (2005)
12. R. KOCH, *Ion cyclotron, lower hybrid and Alfvén wave heating*, these summer school proceedings
13. E. WESTERHOF, *Electron cyclotron waves*, these summer school proceedings
14. P.U. LAMALLE, Phys. Lett. A **175**, pp. 45-52 (1993)
15. P.U. LAMALLE, *Non-local theoretical generalisation and tridimensional numerical study of the coupling of an ICRH antenna to a tokamak plasmas*, LPP-ERM/KMS Laboratory Report 101, Brussels (1994)
16. P.U. LAMALLE, Plasma Phys. Contr. Fusion **39**, 1409 (1997)
17. C.F. KENNEL and F. ENGELMANN, Phys. Fluids **9**, 2377 (1966)

18. C.F.F. KARNEY, Computer Physics Reports 4, North-Holland, Amsterdam, 1986 pp 183-244
19. J.D. GAFFEY, J. Plasma Phys. **16** 149 (1976)
20. R. KOCH, *Fast particle heating*, these summer school proceedings
21. E. WESTERHOF, *Current Drive*, these summer school proceedings
22. E. LERCHE et al., Plasma Phys. Contr. Fusion **50** 035003 (2008)
23. E. LERCHE et al., Plasma Phys. Contr. Fusion **51** 044006 (2009)
24. H. DE BLANK, *Guiding center motion*, these summer school proceedings
25. H. DE BLANK, *Plasma equilibrium in tokamaks*, these summer school proceedings
26. I.B. BERNSTEIN et al., Phys. Fluids **24**, 108 (1981)
27. V.S. BELIKOV and Y. I. KOLESNICHENKO, Plasma Phys. **24** 61 (1982)
28. V.S. BELIKOV and Y. I. KOLESNICHENKO, Plasma Phys. Contr. Fusion **36** 1703 (1994)
29. J. HEDIN, *Ion Cyclotron Heating in Toroidal Plasmas*, Ph.D. thesis, Royal Institute of Technology, Stockholm (2001)
30. J. HEDIN et al., Nucl. Fusion **42**, pp. 527-540 (2002)
31. P.U. LAMALLE, Plasma Phys. Contr. Fusion **40**, 465-479 (1998)
32. P.U. LAMALLE, Plasma Phys. Contr. Fusion **48**, 433-477 (2006)
33. A.N. KAUFMAN, Phys. Fluids **15** pp. 1063-1069 (1972)
34. D. VAN EESTER, Plasma Phys. Contr. Fusion **41**, L23 (1999)
35. A. BECOULET et al., Phys. Fluids B **3**, pp. 137-150 (1991)
36. A. BECOULET et al., Phys. Plasmas **1**, pp. 2908-2925 (1994)
37. H.E. MYNICK, Nucl. Fusion **30** 357 (1990)
38. D. VAN EESTER et al., Plasma Phys. Contr. Fusion **40**, 19491975 (1998)
39. L. VILLARD et al., Comput. Phys. Rep. **4**, 95 (1986)
40. D. SMITHE et al., Phys. Rev. Lett. **60** 801 (1988)
41. O. SAUTER, *Nonlocal Analyses of Electrostatic and Electromagnetic Waves in Hot, Magnetized, Nonuniform, Bounded Plasmas*, LRP-457/92, Ecole Polytechnique Fédérale de Lausanne (1992)
42. M. BRAMBILLA, Nucl. Fusion **34**, 1121 (1994)
43. M. BRAMBILLA, Plasma Phys. Contr. Fusion **41**, 1 (1999)
44. E.F. JAEGER et al., Phys. Plasmas **8** 1573 (2001)
45. E.F. JAEGER et al., Phys. Plasmas **13**, 056101 (2006)
46. J.C. WRIGHT et al., Phys. Plasmas **11**, 2473 (2004)
47. D.B. BATCHELOR, *Integrated Simulation of Fusion Plasmas*, Physics Today, **02/05**, 35 (2005)
48. J. CARLSSON et al., Nucl. Fusion **37**, 719 (1997)
49. J. CARLSON, *ICRH Heating and Current Drive in Tokamaks*, Ph.D. thesis, Royal Institute of Technology ISBN 97-7107-237-7 (1998)
50. T. HELLSTEN et al., Nucl. Fusion **44**, pp. 892-908 (2004)
51. M. DIRICKX and B. WEYSSOW, J. Plasma Phys. **59** 211 (1998)
52. D. FAULCONER and R. LIBOFF, Phys. Fluids **15** 1831 (1972)
53. S.V. KASILOV et al., Nucl. Fusion **30** 2467 (1990)
54. D. VAN EESTER et al., Phys. Letters A, **218**, pp. 70-79 (1996)
55. Y. LOUIS, *Etude analytique et numérique de la réponse diélectrique non-locale d'un plasma de tokamak à une perturbation radiofréquence, tenant compte de la toroidicité et de la décorrelation*, PhD thesis, Université Libre de Bruxelles, LPP-ERM/KMS Report 103 (1995)

FAST PARTICLE HEATING

R. Koch, D. Van Eester

*Laboratory for Plasma Physics, ERM/KMS,
EUROfusion Consortium member, B-1000, Brussels, Belgium*

ABSTRACT

The heating of plasmas by fast ions, with a focus on Neutral Beam Injection (NBI), is reviewed. First, the need of auxiliary heating and current drive systems in fusion machines is outlined. For the particular case of tokamaks, the limitations of Ohmic heating are discussed. The different ways of generating fast particles in plasmas are presented. The principle of operation of neutral beam injectors is explained. Positive-ion (PNBI) and negative-ion (NNBI) based concepts are discussed. Next, the physical processes by which the beam transfers energy to the plasma, namely ionization and slowing-down are described. For both, an elementary theory is given, whereby simple approximations to the distribution functions of beam injected ions and of alpha particles in reactors are obtained. Applications of NBI to heating, current drive and rotation drive are reviewed and the prospects of NBI for ITER are commented.

I. INTRODUCTION

The plasma of a tokamak cannot be heated to ignition using Ohmic heating only because the Joule heating efficiency decreases with the plasma temperature and because the maximum value of the plasma current is limited by the onset of magnetohydrodynamic instabilities that kill the discharge (disruption). These limitations of Ohmic heating will be briefly discussed in the next section. This is the first reason why auxiliary heating systems are required in tokamaks. For steady-state tokamak operation, also the plasma current needs to be sustained by external means, because the inductive current generation is by essence a non-stationary phenomenon. Because the momentum transfer required to generate a current is necessarily accompanied by energy transfer, any non-inductive current-drive method is also a heating method. Specific current-drive aspects will be treated in a subsequent lecture in these proceedings [1]. In other fusion reactor concepts like stellarators, the plasma must be both created and heated by external means. Therefore in all cases, additional heating systems are required. They can also be used for the production of plasma for wall cleaning and conditioning, ramping-up of the plasma current at the beginning of the discharge, tailoring of the plasma current

profile in the stationary current phase and inducing toroidal rotation. Some more exotic applications are: inducing a poloidal rotation, influencing fast particle transport or stabilizing MHD modes. The methods allowing doing this are termed "additional heating" methods, although in some cases they constitute in fact the primary or only source of plasma heating.

There are basically two ways of increasing the energy content of the plasma: one can inject either highly energetic particles or electromagnetic energy into the plasma. In both cases the energy must eventually be transferred to the bulk of the plasma and, ultimately to the fuel-ion component to generate the fusion reactions. The thermalization of the externally injected energy usually takes place through collisional processes: the injected fast particle or the particle accelerated by the electromagnetic field transfers its energy to the plasma background by collisions. In a reactor, the alpha particles generated by the fusion reactions also constitute a fast particle population that will heat the plasma by collisions. Therefore heating by fast particles is generic in fusion machines.

II. LIMITATIONS OF OHMIC HEATING

The power dissipated by the current flowing in a tokamak plasma is called "Ohmic Heating" power or "OH" power. It could also be called "Joule heating" as it is due to the dissipation associated with the electrical resistance of the plasma. The plasma current is an electron current and the resistivity is due to the collisions of the conduction electrons with the -essentially immobile- background ions. The resistance of the plasma loop is [2]

$$R_p = \frac{10^{-3} R_o Z_{eff}}{a_p^2 \kappa \gamma_E (Z_{eff})} \left[1 + \left(\frac{a_p}{R_o} \right)^{1/2} \right] T_{e,av}^{-3/2} \quad (1)$$

where R_o and a_p are the plasma major and minor radii, κ is the elongation, Z_{eff} is the effective ion charge and γ_E is a function of Z_{eff} that can be approximated by

$$\gamma(Z_{eff}) \approx 1 - 0.98/Z_{eff} + 0.56/Z_{eff}^2. \quad (2)$$

Note that this function takes a value close to 1/2 for clean plasmas. In Eq.1, the factor in square brackets accounts for the trapped particle corrections,

and $T_{e,av}$ is the volume-averaged electron temperature expressed in eV's. Unless explicitly stated otherwise, like above for temperatures, SI units are used throughout the paper. The $T^{-3/2}$ dependence reflects the fact that the strength of the collisions decreases as the cube of the relative velocity between the colliding species. This dependence also implies that the plasma resistance quickly drops as the plasma becomes hotter. The Ohmic power is also proportional to the square of the plasma current (I_p):

$$P_{OH} = R_p I_p^2. \quad (3)$$

So, although the resistance falls down when the current is increased as a result of the plasma heating, it is not clear from the above equations whether the Ohmic power increases or decreases with current. In order to investigate further the consequences of the fall in resistivity, we need a relation linking T_e to I_p . This is available from the so-called scaling laws for tokamaks [3] that provide an expression for the total energy content of the plasma W as a function of the various plasma parameters. In the Ohmic regime, the so-called ITER89 scaling is:

$$W_{OH} = 64 \times 10^3 M^{0.2} I_p^{0.8} R_o^{1.6} a_p^{0.6} \kappa^{0.5} N_{e,LA}^{0.6} B_T^{0.35} \quad (4)$$

where the new parameters introduced are the isotopic mass M and the line-averaged density $N_{e,LA}$. In the above, $N_{e,LA}$ is expressed in $10^{20} m^{-3}$ while the plasma current I_p is expressed in MA . Equating this expression to the definition of the total plasma energy content,

$$W_{OH} = (\kappa \pi a_p^2) (2\pi R_o) 3N k_B T_{av}$$

in which k_B is the Boltzmann constant, one gets

$$T_{av} = 68 M^{0.2} I_p^{0.8} R_o^{0.6} a_p^{-1.4} \kappa^{-0.5} N_{e,LA}^{-0.4} B_T^{0.35} \quad (5)$$

where T_{av} is in eV. It is amazing to note that because

$$T_{av} \propto I_p^{0.8} \quad (6)$$

the energy confinement time $\tau_E = W_{OH}/P_{OH}$ is independent of the current and the (Ohmic heating) power. This situation, which is characteristic of the good Ohmic confinement, is in strong contrast with the confinement degradation observed in auxiliary heated discharges where

$$\tau_E \propto P_{tot}^{-0.5} \quad (7)$$

However good the Ohmic confinement, Ohmic heating nevertheless is insufficient to bring a large machine to ignition. Using ITER-FDR-type parameters ($R_o = 7.75m$, $a_p = 2.8m$, $\kappa = 1.6$, $I_p = 25MA$, $B_T = 6T$), Eq.(5) implies $T_{av} \approx 1.3keV$. Even taking into account that the temperature profile is peaked, this means that it is difficult to get a central temperature that is high enough to ignite the plasma in

Ohmic operation. At first sight, rising the current above 25MA seems to be a solution. However, the plasma becomes magneto-hydrodynamically unstable and disrupts when a too high current flows through it (see [4]). The limiting condition ($q_{edge} > 2$) can be written as

$$I_p[MA] = \frac{5a_p \kappa B_T}{2R_o}. \quad (8)$$

Hence, 25MA is about the maximum current that can be obtained in a machine of this size and additional heating is required to bridge the gap to ignition. These conclusions, resting here on very simple considerations, are corroborated by more sophisticated simulations [5].

III. HEATING BY FAST PARTICLES

The basic heat source in a reactor will be the alpha-particles (4He nuclei) produced by the $D - T$ reaction:



Because of the strong dependence of the fusion reactivity on the ion temperature ($< \sigma_{fv} > \propto T_i^2$), the fast α -particles are mostly produced in the plasma core. Two additional heating methods are available for producing fast ion populations: NBI and ion cyclotron heating (ICRH). NBI directly injects fast neutrals in the plasma. The injected energy of the electrons is negligible because of their very small mass, so in the end only fast ions matter. ICRH directly accelerates ions inside the plasma at the ion-cyclotron resonance layer. Fast electrons cannot play a role similar to that of ions in heating because their collisionality is very low. In electron cyclotron heating, for example, the perpendicular distribution function remains nearly Maxwellian and the heating power goes through this nearly thermal population. On the other hand, electron cyclotron heating, like lower hybrid heating, can produce a substantial parallel velocity, making it a key player for non-inductive current drive.

IV. NEUTRAL BEAM INJECTION

Because of the strong toroidal magnetic field, there is no possibility to directly inject energetic charged particles inside the plasma. Instead, one injects fast neutrals at the expense of going through the sequence schematically described in Fig.1. The ions are produced in the source and accelerated to a high energy, usually electrostatically, before crossing a charge exchange cell where they are neutralised. The neutralisation is only partial and the remaining ions are deflected magnetically and sent to a dump. Usually, their energy is lost but it is conceivable to recover it by biasing the dump. The neutrals can

then cross the machines magnetic field and reach the plasma where they get ionized, transferring afterwards their energy to the plasma bulk by collisions. The beam source is a plasma discharge from which the ions are extracted by an electrostatic potential. A hydrogenic plasma discharge -for example in deuterium- not only produces atomic ions, D^+ and D^- , but also molecular ions D_2^+ , D_3^+ . After acceleration at high energy, these ions are neutralized with very different efficiencies. Figure 2 shows that the maximum neutralization efficiency of a gas cell becomes very small for atomic D^+ ions with energies above $200keV$. This is why high energy beam injectors are based on *negative* ion technology. At lower energy, it is more appropriate to use positive-ion based injectors as the production of positive ions is much easier than that of negative ions.

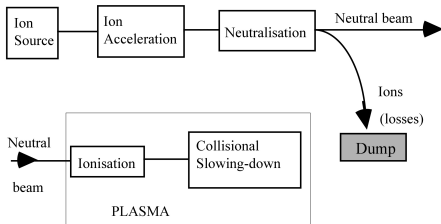


Figure 1: *Sketch of the principle of neutral beam heating. On top, generation of the neutral beam in the injector. Bottom, capture of the neutral beam energy in the plasma.*

A. Neutral beam injectors based on positive ions

All present-day injectors, except one discussed in next section, are based on positive ion (H^+ , D^+ , ...) technology. Nowadays, neutral beam injectors able to deliver 1–2MW of neutrals at energies up to $150keV$ exist. We shall now briefly describe some characteristic features of these injectors. As noted above, the plasma source generates various ion species. After extraction by a negative potential, the negative ions are eliminated but the molecular ions (D_2^+ , D_3^+ , ...) remain present in the beam. After acceleration and having the same charge, all ions have the same energy, E_o . But, as molecular ions contain several atoms, the final beam of neutrals delivered to the plasma will - after dissociation of molecules and ionization - provide ions at energy $E_o/2$ and $E_o/3$ in addition to the full energy (atomic) beam ions at E_o energy. Some 30% of the total beam power can be carried by these less energetic components that deposit their energy more at the outside of the plasma, as compared to the full energy component. This is a feature that has to be taken into account for computing power deposition profiles. When crossing the neutralization cell, each ion has a neutralization probability that first in-

creases with the length of its path in the cell. Afterwards, neutralized ions can be re-ionized again and the neutralization efficiency decreases [6]. Each ion thus has a maximum neutralization probability for a given thickness of the cell, different for each type of ion. Figure 2 shows this maximum neutralization efficiency. It indicates that for beams with energy below $150keV$, the molecular composition of the beam is that of the source. It also points to the limited efficiency of positive-ion based injectors, which falls below 50% around $100keV$.

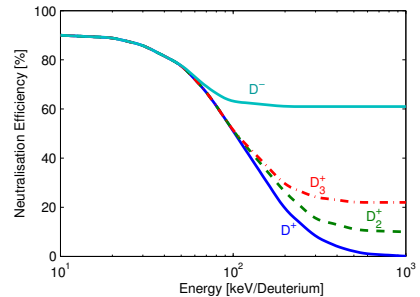


Figure 2: *Maximum neutralisation efficiency in D vs beam energy (see Berkner et al. [6]).*

B. Negative-ion-based injectors

The energy that can be reached -at reasonable efficiency- with positive-ion based technology is insufficient for the next generation of machines. For the heating of the ITER plasma $0.5MeV$ beams are required. If the beams are to be used to non-inductively generate the plasma current, energies of 1–2MeV are required. This is clearly out of reach of any positive-ion based neutral beam and efforts are presently devoted to the development of neutral beams based on a negative-ion source.

In their principle, negative-ion beam injectors are identical to the positive-ion based ones, as sketched in Fig. 1. The differences are that (i) the source must preferentially produce negative ions, (ii) negative-ion based beams can operate at much higher energy (0.5 - 1 MeV). The electron captured in the negative ion has a very low binding energy -called affinity- of $0.75eV$. It is therefore very easy to lose, and this feature explains why high neutralization efficiency can be achieved with negative ions (Fig.2). The reverse side of the medal is that these ions are hard to produce. In order to increase their rate of production, one incorporates cesium in the source, an element which has very low ionization potential ($E_1 = 3.894eV$), and which therefore easily liberates electrons. Two production mechanisms are exploited: surface and volume production. In *surface production* the ions are produced when atoms bounce off walls coated with cesium. As intense wall bombardment is required to

get a large negative ion yield, high power densities are required and the initial energy of the negative ions is rather large. Hence the difficulty to operate these sources for long pulses and to produce well focalized ion beams. Volume production rests on a process called dissociative attachment whereby a hydrogen molecule in a high vibrational state breaks up at the time it captures an electron. The efficiency of this mechanism was experimentally found to be unexpectedly large. Nevertheless, the ion yield remained limited, the high gas pressure required leading to early dissociation of the negative ions and high stray electron current. The presently most efficient sources combine both mechanisms through cesium seeding of volume sources. This increases the negative ion yield, minimizes the stray electron current and reduces the isotopic effect. (The production of D^- is only about half that of H^- in volume sources. This is raised to 80% in Cs seeded sources). Standard arc discharge sources have achieved the performances required for ITER [7]. However, they remain complicated and require regular maintenance of the filaments generating the arcs. Therefore a new type of source, the radio-frequency (RF) source, simpler and requiring no maintenance is under development. The status of NBI injector development is described in [8].

Negative ion sources are equipped with extractors that suppress the stray electron current by superposing the field of permanent magnets to the extracting electrostatic field. The stray electrons hit the extractor grid while the negative ion trajectories are nearly unaffected. These ions are then accelerated electrostatically up to energies of the order of the MeV and neutralized. Two types of accelerators are presently under development. The MAMuG (for Multi-Aperture Multi-Gap) accelerates in parallel a number of beamlets in steps of typically $200keV$. On the contrary, the SINGAP combines all beamlets into one single broad beam and provides the acceleration over a single gap. Like for positive ion beams, the simplest neutralization cell is a box filled with gas. At high energy, the maximum efficiency of such a gas neutralizer is about 60% (Fig.2). The adverse mechanism is re-ionization of fast neutrals (producing D^+ or H^+). Theoretically, plasma neutralizers could reach an efficiency of up to 85% if the plasma in the cell is fully ionized. (The efficiency decreases if the plasma is only partially ionized). However the realization of a reliable cell with fully ionized plasma is much more delicate than the gas cell technology.

The target of negative-ion based beam technology is to develop D^0 injectors with, typically, energy of $1MeV$ and a current of $40A$ in order to couple $50MW$ in ITER with three units. The best results have been achieved with the $JT - 60U$ injector. This injector was designed for pulses of $10MW$ for $10s$ at $0.5MeV$ [9]. The highest parameters reached up to now with this injector are [10]: $400keV$, $5.2MW$, pulse dura-

tion $1.9s$, for D injection; longer pulses have been achieved at reduced power [11]. The neutralization efficiency of 60% has been achieved, in agreement with predictions. More details about the physics of negative-ion beams can be found in a review paper by Pamela [12].

C. Penetration, ionization, losses

Neutral beams are usually injected close to the plasma equatorial plane as this provides the longest path through the densest part of the plasma in front of the beam. With respect to the toroidal direction, beams are usually injected either dominantly parallel or nearly perpendicular. This last solution is technologically easiest but the path through the plasma is rather small and the fast ions are created with large perpendicular energies and therefore a substantial fraction of them can be immediately trapped into banana orbits (see Fig.3). This can lead to significantly larger prompt ion-loss than in the case of parallel injection. Parallel injection beam lines are harder to design because of the limited amount of space available in between the toroidal field coils. However they provide a much longer path for the ionization of the beam and most of the ions are created along passing trajectories. In the parallel injection case, neutrals can be injected in the same direction as the plasma current (co-injection) or in the opposite direction (counter-injection). Due to the asymmetry created by the poloidal field, these two parallel injection schemes are not equivalent. As shown in Fig.3 the orbits of the co-current injected ions drift further outside the magnetic surface on which they were injected than the counter-injected ions. This leads to a somewhat broader power deposition profile in the counter-injection case.

There are two dominant loss mechanisms involved in the energy transfer from the neutral beam to the plasma. (i) Some neutrals cross the plasma without being ionized and are lost on the wall opposite to the injection point. These are called shine-through losses. (ii) Fast ions can get neutralized shortly after their ionization. The so created neutrals will either leave the plasma or be re-ionized at an arbitrary radius. This leads to direct losses and broadening of the power deposition profile. Because the neutralization process is mainly due to charge-exchange (see below), the corresponding losses are called charge-exchange (CX) losses. In the analysis of beam-heated discharges, these losses are usually subtracted from the injected beam power to yield the net power delivered to the plasma taken into account in confinement (power-balance) evaluations. Other losses can occur, especially for non-parallel injection, due to superbanana losses, i.e. loss of banana particles trapped in the ripples of the toroidal magnetic field. Finally if the ions are injected at a velocity faster than the local Alfvén velocity, they can excite global modes - e.g the toroidal Alfvén eigenmodes (TAE) - and be ejected

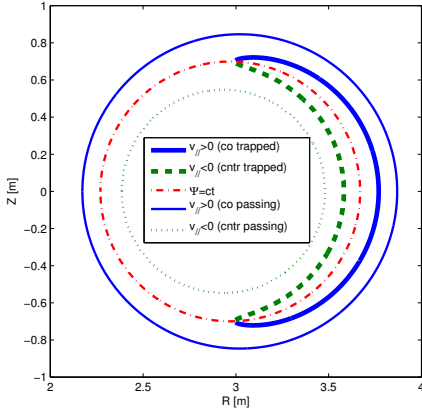


Figure 3: *Poloidal projection of the drift trajectories of beam ions for perpendicular injection (trapped trajectory) and for parallel co- and counter-injection for common toroidal angular momentum and energy; 'co' and 'counter' are defined w.r.t. the plasma current. Also the magnetic surface on which the banana tips lie is depicted.*

out of the plasma by interaction with the TAE's electromagnetic fields.

The ionization of the beam is due to several processes: ionization by impact on electrons and ions (both hydrogenic and impurities), charge exchange and multistep ionization. The dominant process for the lower energy range (e.g. $W_{b0} \leq 80 \text{keV}$ for deuterons) is charge exchange. The cross-section for charge-exchange with protons was given by Riviere [13] :

$$\sigma_{CX} = 0.6937 \times 10^{-18} \frac{(1 - 0.155 \log_{10} E)^2}{1 + 0.1112 \times 10^{-14} E^{3.3}} \quad (9)$$

Here, $E = W_{b0}/M_b$ (in eV/amu) and W_{b0} is the energy of the beam neutral; M_b its isotopic mass number of the beam particles. At higher energy, proton and electron impact ionization become dominant. The cross-section for proton impact is [13]

$$\log_{10} \sigma_p = -0.8712 (\log_{10} E)^2 + 8.156 \log_{10} E - 38.833 \quad (10)$$

or

$$\sigma_p = 3.6 \times 10^{-16} \log_{10}(0.1666E)/E \quad (11)$$

if $E < 150 \text{keV}$ or $E > 150 \text{keV}$, respectively. The cross section for electron impact is [14]

$$\bar{\sigma}_e = \langle \sigma v_e \rangle / v_{b0} \quad (12)$$

where

$$v_{b0} = 1.3715 \times 10^4 E^{1/2} \quad (13)$$

is the velocity of the neutral and $\langle \sigma_e v_e \rangle$ is the ionization rate averaged over the electron distribution, which is a function of the electron temperature T_e only. These three cross-sections are represented in Fig.4. If the plasma contains impurities, these can cause additional ionization. The cross-section for ionization by impurities with atomic number Z can be written in terms of a scaled-to-charge cross-section [15]:

$$\sigma_Z = Z \tilde{\sigma}_Z(E/Z) \quad (14)$$

$$\tilde{\sigma}_Z(w) = 7.457 \times 10^{-10} \times \left[\frac{1}{1 + 0.08095w} + \frac{2.754 \ln(1 + 1.27w)}{64.58 + w} \right] \quad (15)$$

where w is the energy divided by the atomic number expressed in keV. The scaled cross-section $\tilde{\sigma}_Z$ is also represented in Fig.4. In total, the ionization rate per unit length will be

$$-\frac{1}{I_b} \frac{dI_b}{dl} = N_e \sigma_e + N_H \sigma_p + N_H \sigma_{CX} + N_Z \sigma_Z \quad (16)$$

for a H plasma with a single impurity and where we have denoted by I_b the beam intensity and dl the elementary path length along the neutral's trajectory. We define the total or beam-stopping cross-section as:

$$\begin{aligned} \sigma_0 &= \sigma_e + \frac{N_H}{N_e} (\sigma_p + \sigma_{CX}) + \frac{N_Z}{N_e} \sigma_Z \\ &\approx \sigma_e + \sigma_p + \sigma_{CX} + \frac{N_Z}{N_e} \sigma_Z. \end{aligned} \quad (17)$$

Note, in particular, that the effect of the impurities is proportional to their concentration.

This cross-section was deemed satisfactory for the range of energies typical of early P_{NBI} injection in not too dense plasmas ($N_e \approx 10^{19} \text{m}^{-3}$, $E \approx 30 - 40 \text{keV}$). However, when the injection energy becomes larger, which is typically the case with NNBI, and/or for larger densities, this formula underestimates the cross-section because it ignores multi-step ionization. This is the process by which a neutral first gets into excited states due to successive collisions before being ionized. This process is negligible for a (relatively) slow neutral in low density plasma because the lifetime in the excited state is much shorter than the time between two successive collisions. If the speed of the neutral or the number of particles per unit volume increases sufficiently, this is no longer the case. Multi-step ionization can be taken into account by introducing the beam stopping increment δ_{ms} into the complete cross-section σ

$$\sigma = (1 + \delta_{ms}) \sigma_0. \quad (18)$$

The complete cross-sections have been computed by Janev et al. [15], and more recently by Suzuki et al. [16]. These authors also provide analytic fits to the data. The correction due to multi-step ionisation can go to 100% or more for NNBI [17]. For P_{NBI} , the

correction is usually less than 20%. The mean-free path of the neutrals in a plasma of density N is

$$\lambda = 1/(N\sigma) \quad (19)$$

and the evolution of the neutral density $I_b(l)$ for a narrow beam follows from Eq.16:

$$I_b(l) = I_{b0} \exp\left[-\int_0^l d\sigma(\vec{x})N(\vec{x})\right] \quad (20)$$

where the integration is along the path $\vec{x}(t)$ of the neutral in the plasma.

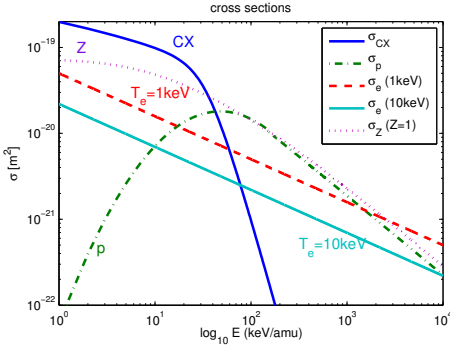


Figure 4: Cross sections for ionization of fast neutrals by charge-exchange (CX), electron impact (for two different electron temperatures $T_e = 1\text{keV}$ and 10keV), and by proton impact (p). The curve Z is the normalized $\bar{\sigma}$ for impurities.

Once created, the ion will follow a trapped or passing orbit, as already discussed. If the confinement of fast particles in the machine is sufficiently good, the ion can be assumed to stay on its magnetic surface and to slow down there by collisions. In a first approximation it is thus sufficient to study the slowing-down process as if it was taking place in an infinite homogeneous plasma having the same parameters as those of the magnetic surface. Neoclassical effects can be taken into account by the so-called bounce-averaging [18] procedure over the real drift-trajectories of particles but this topic will be left out in the present elementary presentation.

V. FAST ION HEATING AND SLOWING DOWN

Given a fast ion content in the plasma, and irrespective of the way it was generated, the transfer of its energy to the plasma bulk can be described in a first approximation as a slowing-down process in homogeneous plasma. This can be examined through two complementary approaches: the test-particle and the Fokker-Planck ones. The latter allows computing the fast-ion distribution function.

A. Slowing down; test particle approach

Starting from the theory of binary Coulomb collisions Sivukhin [19] has shown that the energy decrease of a particle due to the background species s with Maxwellian distribution

$$f_s(v) = \frac{1}{[(2\pi)^{1/2}v_{th,s}]^3} \exp\left[-\frac{v^2}{2v_{th,s}^2}\right] \quad (21)$$

where $v_{th,s} = (k_B T_s/m_s)^{1/2}$ is

$$\frac{dW_b}{dt} = -\frac{4\pi Z_b^2 e^2}{v_b} \sum_s N_s Z_s^2 e^2 \ln \Lambda \left[\frac{\text{Erf}(w_s)}{m_s} - \frac{2w_s(m_s + m_b)}{m_s m_b \pi^{1/2}} e^{-w_s^2} \right] \quad (22)$$

with $w_s = v_b/2^{1/2}v_{th,s}$ and the index 'b' refers to the beam ions. Consider a background plasma with ions ($s = i$) and electrons ($s = e$). For a 5keV plasma, for example, the thermal electron velocity $v_{th,e}$ is in the range of $3 \times 10^7 \text{m/s}$ while $v_{th,i} = 5 \times 10^5 \text{m/s}$. A 100keV ion has a velocity of $3 \times 10^6 \text{m/s}$. Therefore it is usually justified to make the assumption that the injected ions are much slower than the average electron ($w_e \ll 1$) and much faster than the average ion ($1 \ll w_i$). This simplifies considerably Eq.22 as $\text{Erf}(x) \approx 2x/\pi^{1/2}$ for $x \ll 1$ and $\text{Erf}(x) \approx 1$ for $1 \ll x$. One gets

$$\frac{dW_b}{dt} \approx -\frac{2W_b}{\tau_s} \left[1 + \left(\frac{W_c}{W_b}\right)^{3/2} \right] \quad (23)$$

where the first term in the square brackets corresponds to energy transfer to the electrons and the second one to the background ions. When $W_c = W_b$ an equal amount of power is transferred to electrons and ions. W_c is the critical energy $m_b v_c^2/2$; the critical velocity v_c is given by

$$v_c = (2k_B T_e/m_e)^{1/2} \left[\frac{3\pi^{1/2}}{4} \sum_i \frac{N_i Z_i^2 m_e}{N_e m_i} \right]^{1/3} \quad (24)$$

yielding

$$W_c = \frac{1}{2} m_b v_c^2 = 14.8 T_e [\text{keV}] m_b \left(\sum_i \frac{N_i Z_i^2}{N_e m_i} \right)^{2/3}. \quad (25)$$

When the beam ion velocity is much larger than the critical velocity ($W_c \ll W_b$), Eq.(19) is even simpler,

$$\frac{dW_b}{dt} \approx -\frac{2W_b}{\tau_s} \quad (26)$$

which describes a simple exponential decay. In this case all the energy is transferred to the electrons. Note that for the α particles ($M_\alpha = 4$, $Z_\alpha = 2$, $W_{\alpha 0} = 3.5\text{MeV}$) generated in a thermonuclear plasma ($T_e \approx 10\text{keV}$) one has

$$(W_c/W_\alpha)^{3/2} \approx 10^{-2} \quad (27)$$

implying that α -particles, in a reactor, will heat the electrons rather than the ions. In the case of dominant electron slowing-down the characteristic energy decay time is $\tau_S/2$. τ_S is called the slowing-down time on electrons and is given by the expression

$$\tau_S = \frac{3(2\pi)^{3/2} m_e m_b \epsilon_0 v_{th,e}^3}{N_e Z_b^2 e^4 \ln \Lambda} \approx 0.012 \frac{(T_e [keV])^{3/2} M_b}{N_e [10^{20} m^{-3}] Z_b^2} \quad (28)$$

when assuming $\ln \Lambda = 16.5$. Rather than being a constant, the latter quantity is a weak function of density, temperature charge and mass. For a $40keV$ deuteron in a $1keV$, $5 \times 10^{19} m^{-3}$ TEXTOR plasma, this gives $\tau_S \approx 50ms$. For an α particle in a $10keV$, $10^{20} m^{-3}$ plasma $\tau_S \approx 400ms$. At this point it should be noted that these values are not far from the energy confinement time values. Therefore, transport can play a role on the same time-scale as slowing-down in the process of energy transfer from the beam to the plasma (or from the α -particle to a reactor plasma).

The above equations describe the instantaneous slowing down of an ion in the plasma. Two other important quantities that describe the whole slowing-down process, from birth velocity to thermal velocity, are the fraction of the total energy that has gone to electrons (F_e) and to the ions (F_i) after complete slowing-down. This is easily evaluated from Eq.23. The instantaneous power transferred to the ions is:

$$P_i = \frac{2W_b}{\tau_S} \left(\frac{W_c}{W_b}\right)^{3/2} \quad (29)$$

and the energy transferred to the ions during the whole slowing-down process is

$$W_i = \int_0^\infty P_i dt. \quad (30)$$

Noting that one can re-write Eq.23 as

$$-\frac{2}{\tau_S} dt = \frac{dy}{y(1+y^{-3/2})} \quad (31)$$

with $y = W_b/W_c$, one finds

$$\begin{aligned} F_i &= -\frac{1}{W_{b0}} \int_0^\infty W_b \left(\frac{W_c}{W_b}\right)^{3/2} \left(-\frac{2}{\tau_S}\right) \\ &= \frac{W_c}{W_{b0}} \int_0^{W_{b0}/W_c} \frac{dy}{1+y^{3/2}} \end{aligned} \quad (32)$$

for the ratio $F_i = W_i/W_{b0}$ of the energy W_i collisionally lost to the ions to W_{b0} , the energy at which the beam is injected. The fraction flowing to the electrons then is

$$F_e = 1 - F_i. \quad (33)$$

A plot of these fractions is given in Fig.5.

B. The beam distribution function

The starting point of a computation of the distribution function is the Fokker-Planck equation. Its

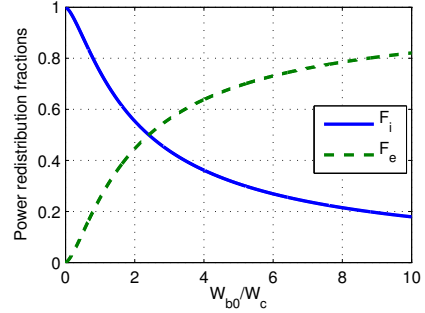


Figure 5: Fractions F_e and F_i of the beam ions energy going respectively to electrons and to ions during the slowing down process.

derivation can be found in Sivukhin [19]. This equation can be written:

$$\frac{\partial f_\alpha}{\partial t} = \sum_{\beta \neq \alpha} C(f_\alpha, f_\beta) + C(f_\alpha, f_\alpha) + S - L \quad (34)$$

where $C(f_\alpha, f_\beta)$ is the collision integral for particles of type α and β . The first sum is over all the background plasma species and the 2nd term accounts for collisions among the beam particles themselves. Usually one uses the Landau form of the collision integral [20],

$$\begin{aligned} C(f_\alpha, f_\beta) &= \frac{Z_\alpha^2 Z_\beta^2 e^4 \ln \Lambda_{\alpha\beta}}{8\pi \epsilon_0^2 m_\alpha} \\ \nabla_{\vec{v}} \cdot \int d\vec{w} \frac{u^2 \bar{1} - \vec{u}\vec{u}}{u^3} \left[\frac{f_\beta}{m_\alpha} \nabla_{\vec{v}} f_\alpha - \frac{f_\alpha}{m_\beta} \nabla_{\vec{w}} f_\beta \right], \end{aligned} \quad (35)$$

as starting point. Here $\vec{u} = \vec{v} - \vec{w}$ and $\bar{1}$ is the identity matrix. S is the source of fast ions (beam ions or α -particles; fast ions generated by ICRH do not appear as a source term in Eq.34, but are generated by an additional RF-induced diffusion term, as we shall see in a subsequent lecture). Because the collision operator conserves the number of particles, a loss-term L has to be included, otherwise, there could be no stationary solution to Eq.34. The simplest particle loss-term is

$$L = \frac{f_\alpha}{\tau} \quad (36)$$

which corresponds to both particle and energy loss. With a τ independent of velocity, it constitutes a good representation of charge-exchange losses. A more sophisticated loss term distinguishing particle and energy loss is

$$L = \frac{f_\alpha}{\tau_p} - \frac{1}{v^2} \frac{\partial}{\partial v} \left[\left(\frac{1}{\tau_E} - \frac{1}{\tau_p} \right) \frac{v^3}{2} f_\alpha \right] \quad (37)$$

where τ_E and τ_p are the energy and particle confinement times, which can be functions of the velocity. Solving Eq.34 is a complex problem because it involves three-dimensional collision integrals

that, even numerically, are heavy to evaluate [20]. In addition, this equation is non-linear because of the beam self-collision term $C(f_\alpha, f_\alpha)$. In order to simplify the problem one can assume (i) that self-collisions are negligible when the beam component is not a too large fraction of the plasma population (ii) that the beam distribution function is independent of the gyro-angle, (iii) that all background species are isotropic Maxwellians. In this case, all the collision integrals can be performed analytically and one arrives at the linear collision operator

$$C(f) = -\frac{1}{v^2} \frac{\partial}{\partial v} (A(v)v^2 f) + \frac{1}{2v^2} \frac{\partial^2}{\partial v^2} (B(v)v^2 f) + \frac{1}{4v^2} \frac{\partial}{\partial \mu} \left[G(v)(1 - \mu^2) \frac{\partial f}{\partial \mu} \right] \quad (38)$$

expressed in terms of the particle velocity v and of $\mu = v_{\parallel}/v$, the cosine of the pitch-angle. A , B and G are analytic expressions involving the error function [21]. These expressions can be further simplified by assuming, as was done above in the test-particle approach, that $v_{th,i} \ll v_\alpha \ll v_{th,e}$. One then arrives at the limits:

$$-Av^2 + \frac{1}{2} \frac{\partial}{\partial v} (Bv^2) \approx \frac{1}{\tau_S} (v^3 + v_c^3) \quad (39)$$

$$B \approx \frac{2T_e}{m_\alpha \tau_S} \left(1 + \frac{v_B^3}{v^3} \right) \quad (40)$$

$$G \approx \frac{v_G^3}{\tau_S v} \quad (41)$$

where one recognizes the earlier defined slowing-down-time τ_S and the critical velocity v_c . The additional expressions for v_B and v_G are [21]:

$$v_B^3 = \frac{3\pi^{1/2}}{4} \left(\frac{2k_B T_e}{m_2} \right)^{1/2} \sum_i \frac{N_i}{N_e} Z_i^2 \frac{2k_B T_i}{m_i} \quad (42)$$

$$v_G^3 = \frac{3\pi^{1/2}}{4} \frac{m_e}{m_\alpha} \left(\frac{2k_B T_e}{m_2} \right)^{1/2} \sum_i \frac{N_i}{N_e} Z_i^2 \quad (43)$$

Finally, retaining only the dominant terms one arrives at the standard form of the collision operator used for the investigation of fast-ion distribution functions:

$$C_1(f) = \frac{1}{\tau_S v^3} \left[v \frac{\partial}{\partial v} [(v^3 + v_c^3) f_\alpha] \right] + Z_2 \frac{\partial}{\partial \mu} \left[(1 - \mu^2) \frac{\partial f_\alpha}{\partial \mu} \right] \quad (44)$$

with

$$Z_2 = \frac{\sum_i N_i Z_i^2 / m_\alpha}{\sum_i N_i Z_i^2 / m_i} \quad (45)$$

It is important to note that while the original Landau form Eq.35 and the linearized form for Maxwellian background Eq.38 conserve the number of particles, the collision operator Eq.44 does not. Therefore the classical Fokker-Planck equation for fast ions can be written omitting a loss term:

$$\frac{\partial f_\alpha}{\partial t} = C_1(f_\alpha) + S. \quad (46)$$

The origin of the loss can be investigated by computing the evolution of the particle density

$$N_\alpha = \int d\vec{v} f_\alpha \quad (47)$$

due to the collision operator C_1 for an isotropic distribution function $f_\alpha(v)$:

$$\left. \frac{\partial N_\alpha}{\partial t} \right|_{Coll} = 2\pi \int_{-1}^{+1} d\mu \int_0^\infty dv v^2 \left. \frac{\partial f_\alpha}{\partial t} \right|_{Coll} = -\frac{4\pi v_c^3}{\tau_S} f_\alpha(0) \quad (48)$$

This result states that the origin of velocity space constitutes a particle sink when the C_1 collision operator is adopted.

Equation 46 with $S = 0$ is separable and the eigenfunctions of the pitch-angle operator (the last term in Eq.44) are Legendre polynomials. Therefore an analytic solution of the stationary version of Eq.46 can be obtained for a delta function source [22]

$$S(v, \mu) = \frac{S_0}{v^2} \delta(v - v_{\alpha,0}) \delta(\mu - \mu_{\alpha,0}) \quad (49)$$

where S_0 is the rate of injection of the beam particles. The index ' $\alpha, 0$ ' refers to the initial properties of the injected ions. The distribution function can be written:

$$f_\alpha(v, \mu) = \frac{\tau_S S_0}{v^3 + v_c^3} \sum_{l=0}^{\infty} \frac{2l+1}{2} P_l(\mu_{\alpha,0}) P_l(\mu) \left[\frac{v^3 + v_{\alpha,0}^3 + v_c^3}{v_{\alpha,0}^3 + v_c^3} \right]^{(l+1)Z_2/6} H(v_{\alpha,0} - v) \quad (50)$$

where H is the step function. One notes that this distribution function is abruptly cut off at the injection velocity $v = v_{\alpha,0}$ whereas, in reality, some beam ions will be diffusing to velocities in excess of $v_{\alpha,0}$. This is a consequence of the neglect of diffusion by thermal electrons. The characteristics of beam distribution functions have been illustrated in [23].

This obtained distribution function takes a particularly simple form when the source is *isotropic*,

$$S(v) = \frac{S_0}{v^2} \delta(v - v_{\alpha,0}). \quad (51)$$

Whereas this is usually not very realistic for neutral beam injection [23], it is quite appropriate for computing the distribution function of fusion-generated α -particles. For $\partial\mu/\partial\mu = 0$, Eq.46 is particularly easy to solve and one obtains

$$f(v) = \frac{\tau_S S_0}{v^3 + v_c^3} H(v_{\alpha,0} - v). \quad (52)$$

This is a good approximation of the α -particle distribution function and one should note that this function is very different from a Maxwellian. At large velocity, it decays like $1/v^3$ rather than exponentially, and becomes flat below the critical velocity v_c . Although insufficient for modeling the full distribution

function of a beam, the isotropic part of Eq.50 can be used to study quantities only involving the isotropic component.

In the general case of non-isotropic beam injection the beam component of the plasma will contribute to the parallel (W_{\parallel}) and perpendicular (W_{\perp}) energy content of the plasma differently from the background species for which $W_{\perp} = 2W_{\parallel}$. This has an impact on the interpretation of the diamagnetic and equilibrium energy signals. At the lower densities the beam component can be an appreciable fraction of the total plasma energy content. Similarly, in the reactor, the fast fusion products can contribute significantly to the total plasma beta.

VI. NBI: COMPARISONS WITH EXPERIMENTS

The experimental verification of the two basic processes of beam heating, namely ionization and slowing-down, is not trivial because both processes depend on a number of plasma parameters and profiles. In all what precedes, we have considered the beam as a thin mono-energetic pencil of neutrals. This is not quite the case as the beam cross-section may be a substantial fraction of the poloidal cross-section of the plasma itself. Therefore, a realistic beam can be conceived as a number of parallel thin beamlets, each making its own path through the density, temperature and impurity concentration profiles. Ionization is the easiest to check, by measuring the shine-through of the beam.

A. Ionization

In the already quoted ITER work [17], the theoretical increment in stopping cross-section, due to multi-step ionization is compared with experimental results for both positive and negative NBI in TFTR and JT-60, showing satisfactory agreement. Additional beam shine-through comparisons made in JT-60 can be found in Suzuki [16] and Oikawa [10].

B. Slowing down

Obviously, checks of slowing-down are more indirect as the slowing down computation must start from the result of the ionization computation, i.e. the beam-ion birth profile. For P_{NBI} , the analysis of fast-ion tails is further complicated by the presence of half and third energy beam components (section IV.A). On the experimental side, the direct measurement of fast ion distribution functions inside the plasma is presently not available. One can look at the distribution of the charge-exchange neutrals coming out of the plasma. However, this signal has a simple interpretation only in the case of rather small plasmas of low density, otherwise too few fast neutrals generated in the plasma bulk reach the plasma outside, all others being re-ionized. Comparisons based on charge-exchange spectra were made on PLT, showing

good agreement between theory and experiment [24]. Another way of looking at tails is by measuring the neutron rate from $D - D$ reactions (or from other fusion reactions, e.g. $D - T$ if tritium is present). The fusion reaction rate is indeed very sensitive to tails as it peaks in the hundreds of keV range. It is however even more indirect than CX neutrals measurement as the deuterium density and temperature profiles enter once more the computation of the reaction rate. After an abrupt switch-off of the NBI, the fast ion tail remains for a while, decaying at the slowing-down time rate (appropriately averaged over the plasma volume) and so does the neutron production rate. The decay rate of the fusion neutrons is thus an indirect measurement of the slowing-down time. Comparisons have been made in several machines [9, 24, 25], always giving good agreement with predictions.

An even more global way of making comparisons, which has become more or less standard, is to run a transport code equipped with a beam simulation package and to predict the total neutron flux from beam-target (the subject of the comparisons discussed just above), beam-beam and thermal fusion reactions and compare it with the experimentally measured flux [26].

VII. PHYSICS RESULTS WITH NBI

A. Heating

NBI has been used in all major tokamaks in the world and has produced high temperature and high performance plasmas [27, 28]. Shots with NBI heating constitute a large fraction of the ITER database [29]. NBI has also been used with success in $D - T$ experiments [30]. Both D and T have been injected in a $D - T$ target plasma. The highest fusion power output (16.1MW) shot in JET was obtained with 3.1MW of ICRH power and 22.3MW of beam power (with injection of 155keV T and 80keV D). It must be noted that most shots of this database are P_{NBI} shots with a large fraction of the power coupled to bulk ions because of the relatively low injection energy. For a 1MeV NNBI in ITER, the fraction coupled to ions will be much smaller. One should note also that injection energies are often close to the optimum energy for the $D - T$ reaction. For example, for the record JET shot cited above, close to 40% of the reaction rate was due to beam-target reactions. This will no longer be the case in ITER.

B. Current drive

Efficient current drive has also been achieved with NBI [1]. For central current drive, the results with NNBI on JT-60U showed good agreement with the predicted driven current deposition profile [17, 31] and a current drive efficiency somewhat higher than

PNBI [10]. However, recent high power off-axis NNBI did not produce the expected current and q profile changes [32]. This question remains under investigation.

C. Toroidal rotation drive

When a fast neutral particle with speed $\vec{v}_{\alpha,b}$ is ionized, it adds its toroidal angular momentum

$$\Delta L_T = m_\alpha R_b \vec{v}_{\alpha,b} \cdot \vec{e}_{tor} \quad (53)$$

to the plasma. Here \vec{e}_{tor} is the unit vector in the toroidal direction and R_b is the birth radius of the ion; recall that the toroidal angular momentum $L_T = mRv_\varphi - q\Psi/2\pi$ (Ψ being the poloidal flux) is a constant of the motion of a charged particle in an axisymmetric tokamak in absence of collisions. As shown experimentally in JET [33], this addition to the angular momentum will be transferred to the bulk plasma on three different time scales: (i) The ion that is born on a trapped trajectory, loses its momentum on a bounce time-scale. This momentum is transferred to the bulk plasma on the same time-scale by a $\vec{j} \times \vec{B}$ force due to the radial current associated with the displacement of the ion between its birth radius and the average radius of its banana orbit. (ii) The ion that is born on a passing trajectory will transfer its momentum by slowing down on the bulk plasma on a slowing down time scale. (iii) When the passing ion becomes part of the thermal population after full slowing down, it carries its residual toroidal momentum. The associated torques are balanced by toroidal momentum damping, which has been found to be anomalous. It is indeed much larger than the neoclassical estimates, and is usually close to the energy confinement time.

NBI can be used in ITER to induce toroidal rotation in addition to its obvious role of heating and current drive system. However, for high energy injection, the injected momentum per unit power ($\propto 1/v_{\alpha,0}$) is much less than for present experiments with PNBI.

VIII. PHYSICS OF BURNING PLASMAS

With the advent of ITER, a topic that is gathering importance is that of burning plasmas. These are plasmas containing a substantial fraction of fast α particles and in which a significant part of the heating is provided by these ions. As the burning plasma behaves in a more or less self-organized way, its control becomes more difficult, in particular with respect to pressure- or q-profiles. The inhomogeneous and non-Maxwellian fast ion distributions may also feed instabilities, like toroidal Alfvén eigenmodes (TAE). When the amplitude of the latter becomes sufficient, the fast particles can get trapped in the wave wells and increased diffusion or loss of fast particles may result. In the strongly nonlinear regimes, coherent

wave-particle structures known as energetic particle modes (EPM) can move through the plasma and lead to further fast ion losses [31]. In ITER or in a reactor these phenomena may lead to reduction of the efficiency of α -particle heating and decrease in reactivity. Burning plasma phenomena can to some extent be simulated in present machines using NBI, ICRH or a combination of both. New γ ray and neutron tomography diagnostics have allowed unprecedented measurements of fast ion distributions in the plasma [34, 35].

IX. FURTHER READING

A good introduction to Coulomb relaxation and to the analysis of beam heating of plasmas can be found in the book by Dnestrovskii & Kostamarov [36]. Detailed analysis of Coulomb collisions can be found in the works by Sivukhin [19] and Karney [20]. A technology-oriented description of NBI is given by Kunkel [37]. All the physics that is involved in tokamaks, reactors and ITER can be found in the rather complete ITER Physics Basis [17] and its recent complement Progress in the ITER physics basis [31].

REFERENCES

1. E. WESTERHOF, Current Drive: NBI & RF, these proc.
2. Koch R., Messiaen A.M. and Weynants R.R., LPP-ERM/KMS Brussels Report no 69 (1980)
3. P.N.YUSHMANOV et al., Scalings for tokamak energy confinement, Nucl. Fus. 30, 1999 (1990)
4. R. KOSLOWSKI, Operational limits in tokamak machines and limiting instabilities, these proc.
5. R. KOCH & D. VAN EESTER, Enhancement of reactivity by RF, Plasma Phys. and Contr. Fus. 35A, A211 (1993), F. LOUCHE, R. KOCH, Final Report on ITER subtask D350.1: Modelling of ICRH system heating performances with PION/PRETOR package, LPP-ERM/KMS Brussels Report n115 (1999)
6. K.H. BERKNER et al., Intense, mixed-energy hydrogen beams for CTR injection, Nucl. Fus. 15, 249, (1975)
7. ITER Final Design Report (July 2001)
8. T. INOUE et al., R&D on a high energy accelerator and a large negative ion source for ITER, Nucl. Fus. 45, 790 (2005); V. ANTONI et al., Technological aspects of the different schemes for accelerator and ion source for the ITER neutral beam injector, 21st IAEA Fusion Energy Conference, Chengdu, (2006)IT/2-3Rb; [Older ref:

- H.D. Falter et al., Status and plans for the development of an RF negative ion source for ITER NBI, 20th Fusion Energy Conference, Vilamoura (2004) IAEA-CN-116 /FT /12Rc]
9. K. USHIGUSA & JT-60 TEAM, Steady state operation research in JT-60U, Proc. 16-th IAEA Fus. Energy Conf., Montral, IAEA Vienna, Vol.1, 37 (1996)
 10. T. OIKAWA, et al., Heating and non-inductive current drive by negative-ion based NBI in JT-60U, Proc. 17-th IAEA Fusion Energy Conference, Yokohama, IAEA Vienna, paper IAEA-F1-CN-69/CD1/1 (1998)
 11. <http://www-jt60.naka.jaea.go.jp/english/annual/04/html/contents.html>
 12. J. PAMELA, The physics of production, acceleration and neutralisation of large negative ion beams, Plasma Phys. and Contr. Fusion, 37, 325 (1995)
 13. A.C.RIVIERE, Penetration of fast hydrogen atoms into a fusion reactor plasma, Nucl. Fus. 11, 363 (1971)
 14. D.R. SWEETMAN Ignition condition in tokamak experiments and role of neutral injection heating, Nucl. Fus. 13, 157 (1973)
 15. R.K. JANEV et al., Penetration of energetic neutral beams into fusion plasmas, Nucl. Fus. 29, 2125 (1989)
 16. S.SUZUKI et al. Attenuation of high-energy neutral hydrogen beams in high-density plasmas, Plasma Phys. Contr. Fus., 40, 2097 (1998)
 17. ITER team, et al., ITER Physics basis, Nucl. Fus. 39 (1999)
 18. J.G. CORDEY, The neutral injection heating of toroidal plasmas to ignition, in Physics of Plasmas Close to Thermonuclear Conditions , EUR FU BRU/XII/476/80, Ed. CEC Brussels, I, 359 (1979)
 19. D.V. SIVUKHIN, Coulomb collisions in a fully ionized plasma in Reviews of Plasma Physics, Ed. M.A. Leontovich, Consultants Bureau New York 4, 93 (1966)
 20. C.F.F. KARNEY, Fokker-Planck and quasilinear codes, Computer Physics Reports 4, 183 (1986)
 21. D. ANDERSON, Distortion of the distribution function of weakly RF heated minority ions in a tokamak plasma, J. Plasma Phys. 29, 317 (1983)
 22. J.D.Jr. GAFFEY, Energetic ion distribution resulting from neutral beam injection in tokamaks, J. Plasma Phys. 16, 149 (1976)
 23. D. VAN EESTER, Plasma heating and current drive: numerical methods, Second Carolus Magnus Summer School on Plasma Physics, Aachen 1995, Transactions of Fusion Technology, 29(1996) 258
 24. R.J. GOLDSTON, Neutral beam injection experiments, Physics of Plasmas Close to Thermonuclear Conditions, EUR FU BRU/XII/476/80, Ed. CEC Brussels, II, 535 (1979)
 25. W.W. HEIDBRINK et al., Comparison of experimental and theoretical fast ion slowing down times in DIII-D, Nucl. Fus. 28, 1897 (1988)
 26. JET Team, Fusion energy production from a deuterium-tritium plasma in the JET tokamak, Nucl. Fus. 32, 187 (1992)
 27. K. TOBITA, JT-60 Team, Latest plasma performance and experiments on JT-60U, Plasma Phys. and Contr. Fus., 41(1999) A333.
 28. E. THOMPSON, et al., "The use of neutral beam heating to produce high performance fusion plasmas, including the injection of tritium beams into the Joint European torus (JET)", Phys. Fluids B, 5(1993) 2468
 29. K. THOMSEN et al., ITER H mode confinement database update, Nucl. Fus. 34, 131, (1994)
 30. J. JACQUINOT, JET Team, Deuterium-tritium operation in magnetic confinement experiments: results and underlying physics, Plasma Phys. and Contr. Fus., 41(1999)A13
 31. K. IKEDA et al., Progress in the ITER physics basis, Nucl. Fus., 47, S1(2007)
 32. S. GENTER, Overview of ASDEX Upgrade Results, et al., 20th Fusion Energy Conference, Vilamoura (2004) IAEA-CN-116 /OV/1-5
 33. K. D. ZASTROW et al., Transfer rates of toroidal angular momentum during neutral beam injection, Nucl. Fus. 38, 257 (1998)
 34. V.G. KIPTILY , et al., γ -ray diagnostics of energetic ions in JET, Nucl. Fus., 42, 999 (2002)
 35. P.U. LAMALLE et al., Expanding the operating space of ICRF on JET with a view to ITER, Nucl. Fus., 46, 391, (2006) 391-400
 36. Y.N. DNESTROWSKII & D.P. KOSTAMAROV, Numerical simulation of plasmas, Springer-Verlag (1986)
 37. W.B. KUNKEL, Neutral beam injection, in Fusion Ed. E. Teller , Academic press 1B (1981)

MODELING PARTICLE HEATING AND CURRENT DRIVE IN FUSION MACHINES:
BRIEF OVERVIEW OF ADOPTED TECHNIQUES

D. Van Eester

Laboratorium voor Plasmafysica - Laboratoire de Physique des Plasmas

EUROfusion Consortium member

Koninklijke Militaire School - Ecole Royale Militaire

Trilateral Euregio Cluster, Renaissancelaan 30 - B1000 Brussels - Belgium

Tel.: (32 2) 44 14 134, fax.: (32 2) 735 24 21, e-mail: d.van.eester@fz-juelich.de

ABSTRACT

A brief overview is given of the techniques adopted for modeling plasma heating and current drive as well as the associated particle diffusion. Weaknesses and strengths of each method are highlighted; references are provided for those seeking further information.

I. INTRODUCTION: THE BASIC EQUATIONS

Plasma heating by virtue of RF (radio frequency) waves can be looked at from two complementary points of view. From the wave's viewpoint plasma heating is a loss process. Solving the relevant wave equation, $\nabla \times \nabla \times \vec{E}/k_o^2 = \mathbf{K} \cdot \vec{E} + i\vec{J}_a/\omega\epsilon_o = \vec{E} + i[\vec{J}_a + \vec{J}_p]/\omega\epsilon_o$ reveals where and to which particles the wave energy is lost. Here, \vec{E} is the electric field, \mathbf{K} is the dielectric tensor, ω is the driver frequency, and \vec{J}_a and \vec{J}_p are the antenna and plasma current densities. From the particle's point of view, plasma heating is the process of being accelerated or decelerated by an electric field. The net diffusion of particles resulting from this is described by the Fokker-Planck equation, $\frac{\partial F_o}{\partial t} = Q + C + S - L$ in which F_o is the distribution function, Q is the RF quasilinear diffusion term, C represents the effect of the Coulomb collisions, S is a source and L a loss term. Solving the coupled wave + Fokker-Planck equations involves tackling a 6-dimensional problem. Two - equivalent - approaches have been proposed to achieve this: the trajectory integral technique and the Hamiltonian formalism [1]. The key is to rewrite both equations in terms of shared building blocks describing the interaction of a particular wave component with a guiding center orbit. In absence of an external electric field, the orbits can be expressed in terms of 3 independent constants of the motion $\vec{\Lambda}$ and 3 angles $\vec{\Phi}$ (which - think of Hamiltonian action-angle variables - vary linearly with time and describe the rapid oscillatory aspects of the motion i.e. the poloidal bounce, the toroidal drift and

the cyclotron motions). When wave power is injected, the $\vec{\Lambda}$ are no longer constant as a function of time. The coefficients of the Fokker-Planck equation require removing all fast time scale effects i.e. filtering out all oscillatory motion. Evaluating the dielectric response in the wave equation involves integrating over the velocity space coordinates. This can either be done recasting the wave equation in a form directly amenable for non-local treatment [2] or it can be done by writing down a local expression for the dielectric tensor (see e.g. [3, 4]). Since the wave and Fokker-Planck equations describe 2 aspects of the same physics, they should be solved as a coupled system of equations (see e.g. [5] and the references therein). Because of the complexity involved, they are, however, solved separately in most applications.

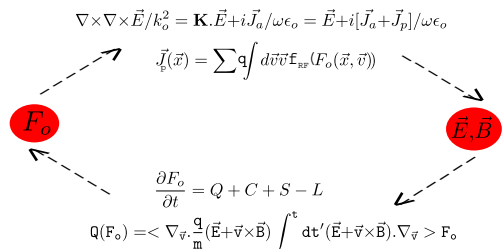


Figure 1: Schematic representation of self-consistent treatment of particle heating by electromagnetic waves.

II. WAVE DYNAMICS AND RAY TRACING

Lacking powerful computers allowing to solve the underlying equations truthfully, plasma heating was historically studied by making simplifications. The geometric optics or ray tracing method is a typical example. Its appealing simplicity results from the fact that

it decouples the coexisting branches of the dispersion equation and traces their characteristics independently. As it traces the evolution of a wave, it is a powerful technique for getting insight in the details of the wave-particle interaction. Ray tracing is based on the WKB assumption that the electric field can be written in the form

$$\vec{E} \propto \exp\left[\sum_{n=0}^{\infty} \delta^{n-1} S_n(\vec{x})\right] \quad (1)$$

where δ is a small parameter and the S_n vary slowly as a function of \vec{x} . Consider the simple 1-dimensional equation

$$E'' + k^2(x)E = 0 \quad (2)$$

where E is some electric field component and $' = d/dx$. When k^2 is constant, E describes plane waves propagating in the x -direction: $E = E_0 \exp[\pm ikx]$. When k varies slowly as a function of x , a solution of the above wave equation in the form of the proposed WKB expression can be sought. Assuming k is of order $1/\delta$ and grouping the terms of like order in δ results in a system of equations for the S_n [6]:

$$(S'_0/\delta)^2 + k^2(x) = 0; 2S'_0 S'_1 + S_0'' = 0 \quad (3)$$

$$2S'_0 S'_n + S_{n-1}'' + \sum_{j=1}^{n-1} S'_j S'_{n-j} = 0; n \geq 2 \quad (4)$$

Solving the first 2 equations above yields $E_{\pm} \propto \exp[\pm i \int dx k(x)]/k^{1/2}$. The WKB version of the conservation law associated with Eq.(1) can be written $(\ln P)' = -2\text{Im}(k)$ where $P = \text{Im}(E * E') = \text{Re}(k)|E|^2$.

Reinserting Eqs.(3-5) into Eq.(1) shows that the WKB solution is a good approximation if $|3/4(k'/k)^2 - 1/2k''/k| \ll |k^2|$ i.e. that the WKB ordering is justified when short wavelength waves are studied but that it breaks down near cutoffs ($k = 0$) and resonances or confluences ($k' = \infty$).

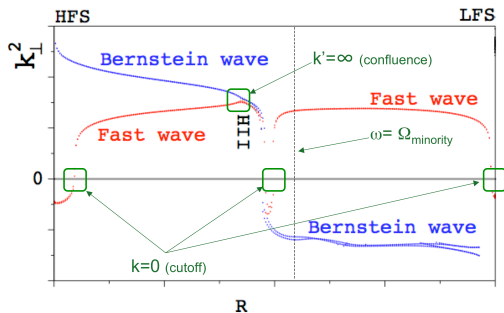


Figure 2: Dispersion plot with locations at which WKB breaks down.

Ray tracing is the multidimensional equivalent of the above scheme. Using the geometric optics definition $\vec{k} = \nabla\psi$ of the wave vector (ψ being the wave phase), the lowest order equation is the Fourier transformed wave equation for a homogeneous medium,

$$\mathbf{G} \cdot \vec{E}_o = \vec{k} \times \vec{k} \times \vec{E}_o + k_o^2 \mathbf{K} \cdot \vec{E}_o = \vec{0}. \quad (5)$$

Nontrivial solutions exist when the dispersion equation $D = \det(\mathbf{G}) = 0$ is satisfied. The different dispersion equation roots and their eigenvectors correspond to the different decoupled waves the plasma supports. The evolution of these waves is visualized via the method of characteristics. The characteristics or rays, by definition, are given by the equations

$$d\vec{x}/d\tau = -\partial D/\partial \vec{k}; d\vec{k}/d\tau = +\partial D/\partial \vec{x} \quad (6)$$

where τ is a variable that changes monotonically along the rays. When the dispersion is satisfied in one point on a ray, it is satisfied in all others ($\delta D = 0$). The variable τ can be linked to the physical time t through the transformation $dt = \partial D/\partial \omega d\tau$. The ray equations then become

$$d\vec{x}/dt = \partial \omega/\partial \vec{k}; d\vec{k}/dt = +[\partial D/\partial \vec{x}]/[\partial D/\partial \omega] \quad (7)$$

The first equation states that the ray's velocity is the energy propagation or group velocity $\vec{v}_g = \partial \omega/\partial \vec{k}$ and the second shows how the wave vector changes as a result of the background variations sensed by the ray. The ray equations can, strictly spoken, only be adopted when the plasma is lossless: as soon as dissipation is present, D is complex so the ray path is no longer a real trajectory. To overcome this problem the damping is assumed to be weak such that the anti-Hermitian part \mathbf{K}^A of the dielectric tensor is of order δ compared to the Hermitian part \mathbf{K}^H which allows to replace D by D^H in the above equation. A power transport equation, $d\ln P/dt = [d\ln P/d\vec{x}][d\vec{x}/dt] = -2\text{Im}(\vec{k}) \cdot \vec{v}_g$, generalization of the earlier mentioned conservation law, is added to the system (see e.g. [7]).

The WKB approximation is very useful when the wavelength of the waves is short w.r.t. the machine size. The fact that it breaks down near cutoffs, confluences and resonances is, however, a drawback limiting the ray tracing method's applicability. To overcome such problems one can try to solve the wave equation without making any a-priori assumptions on the dependence of \vec{E} on \vec{x} . In the next two sections we discuss how differential equations or partial differential equations can be solved by transforming them into algebraic ones.

III. THE FINITE DIFFERENCE METHOD

Of all methods to tackle partial differential equations, the finite difference approach is probably the one

that is most easily implemented. It is frequently used, both for studying wave and particle dynamics. It consists in replacing the partial differential operators in the equation and the boundary conditions by their finite difference counterparts. Doing so at each of the inner grid points and imposing the boundary conditions at the edge points, the differential problem is hereby reduced to an algebraic one that can be solved using standard matrix algebra techniques. Because the finite difference formulae only involve a small number of values of the unknown function(s) at neighbouring points, the matrices of the algebraic system are sparse. Dedicated algorithms accounting for this allow to save CPU time. Finite difference expressions for the various operators can be taken off the shelf (see e.g. [8]) or be auto-constructed from the truncated Taylor series expansion

$$G \approx \sum_{n=0}^N \frac{\hat{G}_n(x-x_o)^n}{n!} = \sum_{j=0}^N \alpha_j G(x_j) \quad (8)$$

where x_o is the point for which the N-point difference scheme is constructed, and the coefficient \hat{G}_n can be identified with the n-th derivative of G at x_o if $n \rightarrow \infty$ and if x is sufficiently close to x_o . The values of the function at x_o and at N neighboring grid points are used to write down a linear system of $N+1$ equations for finite difference approximations of up to the first N derivatives at x_o . Non-uniform grids are automatically accommodated for but the best performance for a given number of points is obtained using a uniform grid centered on x_o . Invoking more neighbors allows eliminating lower order contributions in the expansion: The 2-point forward scheme for the first derivative is of first order. Including the backward contribution allows to compensate the first order contribution and results in a second order accurate scheme. Doing the same for the next neighbors yields the third order scheme $(G_{-2} - 8G_{-1} + 8G_{+1} - G_{+2})/12\Delta x$ for the first derivative, etc.

III.A. Stability of finite difference schemes

Lacking sufficiently general theorems, stability analysis of a numerical scheme is often done by trial and error. The diffusion equation $\Delta\psi(\vec{x}, t) = \partial\psi/\partial t$ can be solved analytically and is sufficiently simple to perform the stability analysis for various finite difference schemes. Let us start from the 1-D version and impose Dirichlet conditions $\psi = 0$ at $x = 0$ and $x = 1$, and $\psi = \psi_o(x)$ at $t = 0$. Through Fourier analysis one finds $\psi = \sum_{k=1}^{\infty} \alpha_k \exp[-k^2 t] \sin[kx]$, the Fourier coefficients α_k in which are those of ψ_o . Note that high k-modes disappear fast from the exact solution when time advances. Morton and Mayers [9] examined the numerical stability of various finite difference schemes

for this equation by adopting a uniform grid in both $x = j\Delta x$ and $t = n\Delta t$, and introducing the amplification factor λ to study the evolution of the numerically obtained k th Fourier mode, $\psi_j^n = \lambda^n \exp[ikj\Delta x]$. For the explicit forward scheme $\psi_j^{n+1} = \psi_j^n + \nu \delta_x^2 \psi^n$ in which $\nu = \Delta t/\Delta x^2$ and $\delta_x^2 \psi^n = \psi_{j+1}^n - 2\psi_j^n + \psi_{j-1}^n$, one finds $\lambda = 1 - 4\nu \sin^2 k\Delta x/2$. Hence, when $\nu > 0.5$ this solution numerically grows in time, although the true solution does not! The fastest growing mode is characterized by a phase jump of π in between successive grid points. It eventually dominates the numerical solution. As the spatial grid scale is determined by the spatially fastest varying modes in the differential system, one is forced to make sufficiently small steps in time to avoid these unphysically growing solutions. To avoid having to take too small time steps, implicit rather than explicit schemes are adopted. Replacing the forward difference by a backward difference in the above we obtain the scheme

$$-\nu \psi_{j-1}^{n+1} + (1 + 2\nu) \psi_j^{n+1} - \nu \psi_{j+1}^{n+1} = \psi_j^n \quad (9)$$

In contrast to the forward scheme, time stepping now requires the inversion of a matrix. This extra amount of work pays off, however: one finds that λ is now of the form $\lambda = 1/[1 + 4\nu \sin^2 k\Delta x/2]$. Since $0 \leq |\lambda| \leq 1$ for any ν , this scheme is unconditionally stable.

The above two schemes either use 3 points at the previous time level, or 3 at the new time level. A straightforward generalisation consists in using all 6 of these points i.e. in adopting the scheme $\psi_j^{n+1} - \psi_j^n = \nu[\theta \delta_x^2 \psi^{n+1} + (1 - \theta) \delta_x^2 \psi^n]$ which is known as the θ -method. This scheme is conditionally stable if $\theta < 1/2$ and unconditionally stable if $1/2 \leq \theta < 1$. The first regime imposes that $\nu \leq 0.5/(1 - 2\theta)$ while ν is unconstrained for the second. Whereas the difference scheme is usually of first order in time, the scheme is second order accurate both in position and time when $\theta = 1/2$. This particular scheme is due to Crank and Nicolson.

III.B. Practical example

Applying a finite difference scheme to the time dependent Fokker-Planck equation yields a system of the form

$$\partial \vec{X} / \partial t = \mathbf{A} \cdot \vec{X} - \vec{b} \quad (10)$$

in which the contributions not involving F_o are grouped in the source term \vec{b} and the values of F_o at the grid points are stored in \vec{X} . When adopting the Crank-Nicolson method, the algebraic system takes the form

$$\vec{X}(t + \Delta t/2) = \mathbf{C}^{-1} \cdot \vec{d}; \mathbf{C} = \mathbf{1} - \Delta t/2 \mathbf{A}; \quad (11)$$

$$\vec{d} = [\mathbf{1} + \Delta t/2 \mathbf{A}] \cdot \vec{X}(t - \Delta t/2) - \Delta t \vec{b} \quad (12)$$

If \mathbf{A} is time independent, the \mathbf{C} matrix can be inverted once and for all. The source \vec{d} has to be updated at

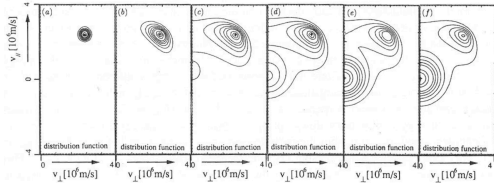


Figure 3: Time evolution of a beam population from the moment the particle source is switched on up to when the stationary state is reached, at which time the beam consists of a Maxwellian sub-population and a non-thermal sub-population centered on the source.

each time step, independent of the actual source term \vec{b} being independent of time or not.

IV. THE FINITE ELEMENT METHOD

IV.A. Variational techniques

Requiring somewhat more preparation and book-keeping than the finite difference method but allowing a better control on the overall numerical error, the finite element method is probably the most robust numerical technique for solving differential or integro-differential problems. To discuss this technique, we will again focus on Eq.(2). The finite element technique relies on a variational principle [10, 11]. Consider the functional

$$I(\mathbf{E}) = \int_{x_1}^{x_2} dx [-\mathbf{E}^2 + k^2 \mathbf{E}^2] + \hat{S} \quad (13)$$

$$\hat{S} = A_2 \mathbf{E}^2(x_2) + B_2 \mathbf{E}(x_2) - A_1 \mathbf{E}^2(x_1) - B_1 \mathbf{E}(x_1) \quad (14)$$

Allowing for a small variation of \mathbf{E} , one observes that the linear perturbation of the functional is stationary for the function \mathbf{E} obeying Eq.(2) and satisfying the boundary conditions $\mathbf{E}'(x_{1,2}) = A_{1,2} \mathbf{E}(x_{1,2}) + B_{1,2}/2$.

The Ritz approach to solve the equation consists in writing \mathbf{E} in terms of a set of base functions $\mathbf{E}(x) = \sum_{j=1}^J c_j \Theta_j(x)$ and imposing I to be stationary for all j : $\partial I / \partial c_j = 0$. Provided the integrals involving the base functions can be evaluated, this reduces the problem of integrating the wave equation to solving the (linear) system for the c_j . Although base functions allowing to evaluate the integrals over the full domain exist (see section V), one often prefers to subdivide the interval $[x_1, x_2]$ into a large number N of sub-regions and to use low order polynomials with restricted range such that the integrals can be approximated e.g. using the integration method of Gauss [8]. When J base functions are considered in each interval, a total of NJ linear equations for the NJ unknown coefficients is obtained

by imposing all stationarity conditions. In case the grid is so dense that coefficients of the original equation hardly vary in a single finite element, their variation can be omitted altogether and the integrals only involving base functions can then be done once and for all.

The Ritz approach seems cumbersome as prior to actually solving the equation, one first needs to find the functional I and derive the stationarity conditions. These 2 steps can be omitted when adopting the Galerkin approach, which consists of multiplying the differential equation with each of the base functions Θ_j , and integrating over the domain of interest. The resulting system is again a linear system that can be solved to find the c_j . The disadvantage of this strong approach is that the Θ_j need to have meaningful n th derivatives for an n th order equation. Lower order polynomial base functions can be chosen when tackling the problem in its weak form i.e. after removal of the highest order E-derivative terms from the integrand by performing partial integrations. Imposing the boundary conditions via the surface term, one readily finds that the weak Galerkin approach is equivalent to the Ritz approach.

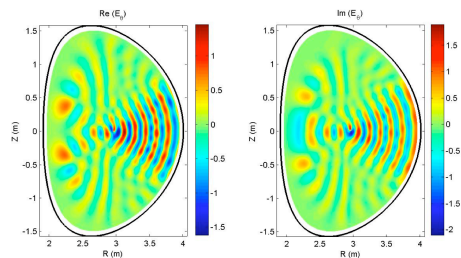


Figure 4: RF wave pattern for (H)-D heating at 3.45T and 51MHZ in JET, computed using finite elements on a 2-D mesh of triangles. The RF field propagates from the antenna on the low field side to the core, where it is damped near the central H cyclotron layer.

IV.B. Natural vs. essential boundary conditions

Natural boundary conditions can directly be derived from the weak variational form of the equation. The strong form is obtained by multiplying the equation by a sufficiently smooth test function G and integrating it over a finite interval. Partial integration is used to remove higher order derivatives from the unknown function and "transfer" them to derivatives of the test function. For a 1D differential equation of order n , $n/2$ derivatives can be removed from the unknown. The surface terms arising from these partial integrations involve the test function itself as well as its higher order derivatives up to $n/2 - 1$. Choosing a test function

with only 1 nonzero m th derivative ($0 \leq m \leq n/2 - 1$) at one of the two edges provides a set of $n/2$ natural boundary conditions at each edge, corresponding to "fluxes" entering or leaving the domain of interest. Imposing these at the two edges provides the exact number n of boundary conditions to uniquely define the solution (see e.g. [12]). Natural boundary conditions are intimately connected with the equation. Deriving the natural boundary conditions of the Laplace equation in the domain ($x_1 \leq x \leq x_2, y_1 \leq y \leq y_2, z_1 \leq z \leq z_2$) by multiplying the equation by a test function G , integrating over the volume, performing a partial integration and identifying $G = 1$, one finds

$$\int dydz \frac{\partial \psi}{\partial x} \Big|_{x_1}^{x_2} + \int dx dz \frac{\partial \psi}{\partial y} \Big|_{y_1}^{y_2} + \int dx dy \frac{\partial \psi}{\partial z} \Big|_{z_1}^{z_2} = 0 \quad (15)$$

imposing that the imposed Neumann boundary conditions should be consistent with the equations i.e. that they must guarantee that the net influx balances the net outflux, no damping being present.

Boundary conditions imposed on lower order ($< n/2$) derivatives cannot be derived from the equation itself, and cannot be imposed via the surface term. To impose such conditions another procedure is required. One common solution is to choose the base functions in such a way that the conditions in question are automatically fulfilled. Because of their more basic nature, the second type of boundary conditions is known as essential conditions.

To solve a differential equation, we transformed it into a linear system. When the original equation is an integro-differential instead of a differential equation, exactly the same method can be used, the only difference being that also integrals of products of base functions and not just derivatives appear inside the variational integral. In that case, the linear system is generally not sparse.

IV.C. Numerical pollution

The finite element technique relies on the local approximation of the solution of an equation by a sum of simple base functions. Aside from truncation errors which automatically creep into the system, such approximations can lead to numerical pollution i.e. to the excitation of modes lacking a physical counterpart. The vacuum wave equation

$$(k_{\parallel}^2 - k_o^2)E_x + ik_{\parallel}E'_z = 0 \quad (16)$$

$$(k_{\parallel}^2 - k_o^2)E_y - E_y'' = 0 \quad (17)$$

$$ik_{\parallel}E'_x - k_o^2E_z - E_z'' = 0 \quad (18)$$

suffices to demonstrate this effect [13]. In the above, it can be noted that E_x plays a different role than E_y or E_z : the highest order derivative of E_x appearing

in the system is one order lower than that for E_y and E_z . Knowing that the exact solutions of the vacuum wave equation are proportional to $\exp[ik_x x]$ where $k_x^2 = k_o^2 - k_{\parallel}^2$ we make the ansatz $\vec{E}(\vec{x}) = \sum_j \exp[ik_x x_j] \vec{\eta}_j$ where the x_j are the grid points and $\vec{\eta}_j$ the vectors of base functions. The discretized dispersion equation is the condition for having nontrivial solutions. Adopting the obtained equation for linear base functions, Sauter demonstrated that the physical root is well approximated by two of the numerical dispersion roots when the grid is sufficiently refined (small enough $k_x \Delta x$) but that the agreement is less good when $k_x \Delta x$ well exceeds 1. A third, purely numerical, root further spoils the solution. Reminding that E_x is differentiated one time less in the wave equation, Sauter subsequently considered constants for E_x while using linear functions for E_y and E_z . Although one expects intuitively that such cruder procedure would lead to less accurate results, he demonstrated that - quite on the contrary - the solution is now no longer polluted. One might hope that the spectral pollution problem automatically resolves itself when a more refined description (higher order polynomials as base functions) is used. It turns out that this is not the case. One finds exactly the same problem when using higher order polynomials for all components. Again, pollution can be removed choosing polynomials for E_x which have 1 degree of freedom less than those taken for E_y and E_z . Adding finite Larmor radius (temperature) effects to the wave equation destroys the special role E_x plays and eliminates this particular problem of pollution.

IV.D. Grid refinement techniques

One of the peculiarities of finite elements is that it allows squeezing and stretching local finite elements, which enables describing phenomena with vastly different length scales accurately by merely reshuffling the adopted grid but without touching the structure of the local equations. Hence, rather than opting for a more complete set of base functions enabling to capture more dynamics on a fixed grid but increasing the number of local 'projection' equations, code developers often prefer to refine the grid at locations where it is needed while keeping the base functions as simple as possible. This guarantees that CPU memory is optimally used: at every location the adopted grid is just fine enough to reach the desired accuracy level, but regions not requiring a fine grid are not densely populated with grid points. Various grid refinement techniques are available in the literature, and more often than not grid generating software can be found on the www. One of the classical techniques of grid refinement is the so-called 'red-triangle/green-triangle' technique [14] adopted when subdividing the domain of interest for a 2-D problem into a set of triangles. When local

gradients are too steep inside a triangle (red triangle), it is subdivided into 4 child-triangles born when dividing each of the 3 sides of the parent-triangle in 2 and connecting these 3 midpoints. If refinement in a neighboring triangle is required as well, the same technique is applied there while if no refinement is needed, the midpoint of the side is just connected to the opposite triangle corner (green triangle) to ensure the topology of the mesh is not changed.

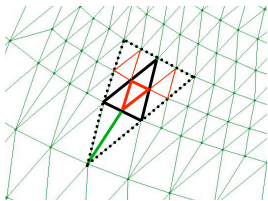


Figure 5: 'Red-green triangle' grid refinement scheme. Thick solid line: 'parent' triangle, subdivided into 4 child-triangles. Dotted lines: neighbor triangles with 'red' or 'green' subdivisions.

V. SPECTRAL METHODS: DIRECT FOURIER REPRESENTATION

As the set of exponential functions $exp(ikx)$ is complete, any (sufficiently continuous) function of the variable x can uniquely be represented by its k -spectrum. In a finite domain $[x_o, x_o + L_x]$, the coordinate x can then be related to the angular variable $\theta = 2\pi x/L_x$ and the spectrum of modes m is discrete. Although any function can be represented using the exponential set with a global error that is arbitrarily small, the spectrum of non-periodic functions decays so slowly as a function of m that one can wonder if the spectral method is the appropriate tool for tackling problems involving such functions. At the edge discontinuities, the series will never converge, although taking enough terms allows to find the correct value up to very close to the edge (Gibbs phenomenon). When all functions are periodic, the Gibbs phenomenon is absent and spectral representation is more appropriate. Consider again Eq.(2), $d^2\psi/d\theta^2 + M^2(\theta)\psi = 0$, for convenience rewritten in terms of the angular variable θ . Finding the Fourier spectrum of M^2 , $M^2(\theta) = \sum_{l=-\infty}^{+\infty} M_l^2 exp[im\theta]$, and projecting on the exponential base yields

$$-m^2\psi_m + \sum_{l=-\infty}^{+\infty} M_l^2\psi_{m-l} = 0 \quad (19)$$

for each m in the spectrum. Truncating the spectrum of the coefficient M^2 yields a sparse but infinite set of non-trivial equations to be solved simultaneously. For large $|m|$ ($m^2 \gg M_l^2$), the first term dominates the others, guaranteeing the Fourier series of ψ is convergent and justifying to truncate the spectrum. Through M^2 , the physics of the problem dictates the minimal number of modes to be retained in the truncated spectrum: For the simple case of a constant M^2 , the above equation prescribes that ψ_m must be zero unless $m^2 = M^2$. More generally, this filtering makes that part of the physics is not captured by the model if the spectrum is truncated at a too low m -value (see also in the next section). A practical example is the treatment of electron (Landau + TTMP) damping in the ion cyclotron range of frequencies: the damping strength being proportional to the square of the local perpendicular wave number k_{\perp} , this damping is underestimated by a model that does not properly resolve the Bernstein wave mode, a mode for which k_{\perp} is of the order of the inverse of the ion Larmor radius.

The spectral representation is commonly used for numerical applications posed in finite domains but is, by its nature, best suited to be adopted in wave problems. A spectral method in periodic variables is often combined with a finite element representation in the non-periodic variables.

The SciDAC project [15] gave a major thrust to RF modeling in the USA. Thanks to powerful computers and the adoption of Fourier techniques, wave problems have been solved that were off-limits before: Brambilla's TORIC has been upgraded to enable accounting for up to 10^4 poloidal modes simultaneously so that the fate of short wavelength branches can now be examined in detail (see e.g. [16]), and Jaeger's integro-differential AORSA code now solves the wave equation both for Maxwellian as for non-Maxwellian populations (see e.g. [17]).

VI. FAST FOURIER TRANSFORM & ALIASING

The spectral method relies on the fact that the Fourier spectra of the coefficients of the equation are known. In general the coefficients are known locally, but the spectrum is not. Finding the poloidal spectrum of functions needed to solve the 2-D or 3-D wave equation in tokamak geometry can be done relying on the smallness of the minor radius a_p w.r.t. to the major radius R_o , by writing out the various terms explicitly up to a given order in the inverse aspect ratio a_p/R_o . This procedure soon becomes cumbersome, however, and since a_p is not so small w.r.t. R_o , many terms in the development should be retained for a reasonable approximation. In practice, the Fourier components

$F_m = \frac{1}{2\pi} \int_0^{2\pi} d\theta \exp[-im\theta] f(\theta)$ of any needed quantity f are most often evaluated numerically. Adopting a uniform grid, the Fourier integral is approximated by the sum $F_m \approx \frac{1}{J} \sum_{j=1}^J \exp[-imj\Delta\theta] f(j\Delta\theta)$; $\Delta\theta = \frac{2\pi}{J}$. This technique is known as the fast Fourier transform (FFT). Note that the predicted value for the m th Fourier component is identical to that of $m - nJ$ where n is any integer. This means that the above procedure artificially misrepresents high m -modes by their lower mode number spectrum counterparts for which $J/2 < m - nJ \leq J/2$, an effect known as aliasing (see also [18]). To avoid aliasing, the whole spectrum should fall inside the interval $]-J/2, J/2]$. The corresponding grid has at least 2 mesh points per wavelength for the shortest wavelength mode in the system.

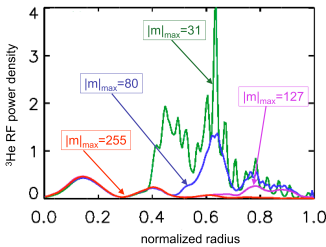


Figure 6: The importance of ensuring the full wave spectrum is sampled: power deposition profiles obtained truncating the poloidal mode spectrum at $|m| = 31$, $|m| = 80$, $|m| = 127$ and $|m| = 255$ (TORIC, Courtesy P. Bonoli).

VII. MONTE CARLO AND PARTICLE-IN-CELL TECHNIQUES

Integration in multidimensional space can be done efficiently relying on the Monte Carlo technique, which in contrast to adopting a regular grid uses a set of uniformly distributed random points. Adopting this procedure, the integral of a function in hyperspace is predicted up to errors of order $N^{-1/2}$, where N is the number of randomly generated positions, irrespective of the number of dimensions (while the accuracy of the prediction made on a uniform grid scales as $1/N^{1/d}$, where d is the number of dimensions). In order to simultaneously solve the wave and the Fokker-Planck equations, Hedin developed the SELFO code. He upgraded the LION wave code [15] to account for the actual drift orbits of the particles and for non-Maxwellian distribution functions by locally approximating the dielectric tensor using a series of hat functions [16], and interfaced the resulting code with the FIDO Monte Carlo code [17].

The FIDO Monte Carlo method advances a large number of test particles in time $\vec{\Lambda}(t_{n+1}) = \vec{\Lambda}(t_n) + \Delta\vec{\Lambda}$ and accounts for wave-particle interaction and for Coulomb collisions assuming the $\vec{\Lambda}$ are stochastic variables whose expectations E and co-variances C can be inferred from the orbit-averaged Fokker-Planck equation:

$$E[\Delta\Lambda_i] = \frac{d\mu_i}{dt} \Delta t; C[\Delta\Lambda_i, \Delta\Lambda_j] = \frac{d\sigma_{ij}}{dt} \Delta t \quad (20)$$

in which $\langle \dots \rangle = \int d\vec{\Lambda} F_0 \dots$ is the ensemble average, $\mu_i = \langle \Lambda_i \rangle$ and $\sigma_{ij} = \langle (\Lambda_i - \mu_i)(\Lambda_j - \mu_j) \rangle$. The Monte-Carlo operator becomes

$$\Delta\Lambda_i = \frac{d\Lambda_i}{dt} \Delta t + \sum_k A^{ik} \xi_k (\Delta t)^{1/2} \quad (21)$$

in which $\sum_k A^{ik} A^{jk} = d\sigma_{ij}/dt$ and where ξ_k are uncorrelated stochastic variables with zero expectation value and unity variance.

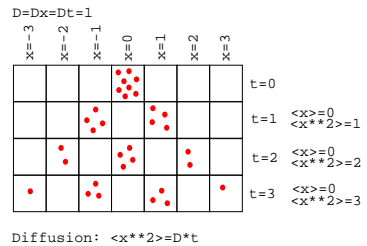


Figure 7: The principle of random walk / diffusion.

VIII. CONSERVATION LAWS

Conservation laws are often helpful when checking the precision of a computation. For Eq.(2) one readily sees that $S = \text{Im}[E * dE/dx]$ is conserved when k^2 is real i.e. in absence of damping. When damping is present the drop in flux S across the considered interval equals the integrated absorbed power $P_{abs} = \text{Im}(k^2)|E|^2$. In differential form the thus obtained conservation law is of the form $\nabla \cdot \vec{S} + P_{abs} = 0$. Adopting a variational approach one can formulate the wave equation in such a conservative form i.e. in a form which readily yields this conservation law upon substituting the sufficiently smooth test function vector by the electric field (see e.g. [18]). The Fokker-Planck equation is written in the above conservative form from the start: rewriting it in variational form (see e.g. [23]), one can express the conservation of the total number of particles (test function $G = 1$) or of the energy ($G = mv^2/2$). When the wave and Fokker-Planck models are consistent one with the other, the

conservation laws of the 2 equations share the expression for the absorbed wave power (see e.g. [1]).

Of course, conservation laws merely allow to check the numerical accuracy of a model, but do in themselves *not* constitute a check on the correctness or on the applicability of the model *itself*. Aside from performing convergence tests to ensure the shortest scale lengths are well captured, a-posteriori checks of the assumptions underlying the derivation of an equation should be performed: it is e.g. common to adopt a truncated finite Larmor radius (FLR) expansion to include temperature effects but one rarely discards the predictions on the fate of the power carried by the short wavelength (Bernstein) modes away from the (confluence) region, notwithstanding the fact that the wave violates the starting FLR assumption ...

IX. DECIDING ON A NUMERICAL STRATEGY

The speed and memory size of present day computers allow to pursue a high degree of realism in plasma physics models. Because of this high level of sophistication, it is crucial to be able to distinguish between actual physics and numerical artefacts. Jaun and collaborators have developed a very didactic, interactive and flexible tool to highlight the perspectives and drawbacks of various numerical schemes [18]. Existing commercial or freeware software libraries such as IMSL, HSL, NAG and NetLib allow to concentrate on physics instead of on numerics. In case no ready-made subroutines can be pulled off the shelf, softwares such as OCTAVE, MATLAB and MATHEMATICA are of great help in constructing ones own numerical schemes.

REFERENCES

1. D. VAN EESTER, Plasma Phys. Contr. Fusion **41**, L23 (1999)
2. P.U. LAMALLE Plasma Phys. Contr. Fusion **39**, 1409 (1997)
3. R. KOCH, Phys.Lett.A **157**, 399 (1991)
4. D. VAN EESTER, Plasma Phys. Contr. Fusion **35** 1309 (1993)
5. D. VAN EESTER, Journal of Plasma Physics **65** 407 (2001) and the references therein
6. C. BENDER and S. ORSZAG, Advanced mathematical methods for scientists and engineers, Mc Graw Hill, New York (1978).
7. V.P. BHATNAGAR et al., Nuclear Fusion **24**, 955 (1984)
8. M. ABRAMOWITZ, I.A. STEGUN, Handbook of Mathematical Functions, Dover, New York (1972)
9. K.W. MORTON, D.F. MAYERS, Numerical Solution of Partial Differential Equations, CUP, Cambridge (1994)
10. G. STRANG and G.J. FIX, An Analysis of the Finite Element Method, Prentice Hall, Englewood Cliffs (1973).
11. R. GRUBER and J. RAPPAPZ, Finite Element Methods in Linear Ideal Magnetohydrodynamics, Springer-Verlag, New York (1985).
12. D. VAN EESTER, R. KOCH, Plasma Phys. Contr. Fusion **43**, 1 (2001)
13. O. SAUTER, Nonlocal Analyses of Electrostatic and Electromagnetic Waves in Hot, Magnetized, Nonuniform, Bounded Plasmas, LRP-457/92, Ecole Polytechnique Fédérale de Lausanne (1992).
14. G. HEBER, R. BISWAS, G.R. GAO, Self-Avoiding Walks over Two-Dimensional Adaptive Unstructured Grids, CAPSL Technical Memo 21, University of Delaware (1998)
15. D.B. BATCHELOR, Integrated Simulation of Fusion Plasmas, Physics Today, **02/05**, 35 (2005)
16. J.C. WRIGHT et al., Phys. Plasmas **11**, 2473 (2004)
17. E.F. JAEGER et al., Phys. Plasmas **13**, 056101 (2006)
18. O. JAUN, J. HEDIN, T. JOHNSON, Numerical methods for partial differential equations: an overview and applications, Report TRITA-ALF-1999-05, Royal Institute of Technology, Stockholm (1999-2000); downloadable from <http://www.lifelong-learners.com/pde>
19. L. VILLARD et al., Comput. Phys. Rep. **4**, 95 (1986)
20. J. HEDIN, Ion Cyclotron Heating in Toroidal Plasmas, Ph.D. thesis, Royal Institute of Technology, Stockholm (2001)
21. J. CARLSSON, ICRH Heating and Current Drive in Tokamaks, Ph.D. thesis, Royal Institute of Technology ISBN 97-7107-237-7 (1998)
22. D. VAN EESTER, R. KOCH, Plasma Phys. Contr. Fusion **40**, 1949 (1998)
23. D. VAN EESTER Proc. 7th Eur. Fus. Theory Conf., Julich **1**, 283 (1997)

PLASMA DIAGNOSTICS IN VIEW OF ITER

A.J.H. Donné

FOM-Institute DIFFER, Dutch Institute for Fundamental Energy Research, Association EURATOM-FOM,
Partner in the Trilateral Euregio Cluster, P.O. Box 1207, 3430 BE Nieuwegein, The Netherlands, www.differ.nl
Tel. +31 30 60 96 960, Fax +31 30 60 31 204, e-mail: a.j.h.donne@differ.nl

Also Eindhoven University of Technology, Dept. of Applied Physics, PO Box 513, 5600 MB Eindhoven, The Netherlands

ABSTRACT

The ITER environment imposes many challenges for the various diagnostic systems. At the one hand diagnostic functionalities are required that go well beyond those at present devices. This is because there is a need to actively control (the profiles of) multiple plasma parameters, implying that measurement systems should be accurate and reliable. At the other hand the application of diagnostics at ITER is strongly hampered by constraints arising from the relatively harsh environmental conditions that give rise to phenomena that are new to the diagnostic designs. The nuclear environment puts stringent demands on the engineering and robustness of diagnostics, while the long pulse lengths require high stability of all systems. This paper will present an overview of the diagnostics for ITER with an additional glance in the further future.

I. INTRODUCTION

The step to ITER diagnostics is the most substantial challenge ever encountered in the development of diagnostics for high temperature plasmas:¹

- The measurement requirements on ITER are much more stringent than in present devices. Many diagnostics are incorporated in real-time feedback loops (e.g. for the stabilization of magnetohydrodynamic modes, for controlling the current profile, for controlling the presence and properties of internal transport barriers), requiring a high level of reliability and availability.
- The diagnostics have to cope with a much harsher environment than in present devices. Radiation-induced effects strongly restrict the use of insulators and of reflective components close to the plasma. Diagnostics need to be robust, such that they can survive during the complete ITER operational life time, or if that is not possible, such that they only need rather infrequent replacements or maintenance.
- The long ITER pulses put severe constraints on the stability and reliability of the diagnostics.
- Multiple diagnostics have to share a single diagnostic port, which creates many interfaces between different diagnostics which require well organized project teams and a high degree of quality assurance.

In this paper a brief overview will be given of the challenges in the design and manufacturing of the diagnostics for ITER, using Fig. 1 as a guideline. The most comprehensive paper that has been published thus far on ITER diagnostics,¹ as part of the ITER Physics Basis, contains a wealth of information on all aspects that will be covered in this paper. Instead of repeating that information here, the reader will be in several cases referred to tables in that paper.

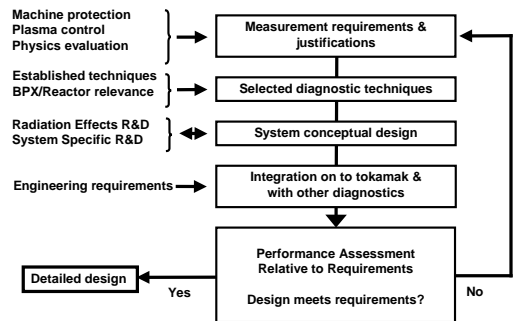


Figure 1: Simple flow diagram of the diagnostic design process.²

II. MEASUREMENT REQUIREMENTS

The implementation of diagnostics on ITER must be carefully optimized. There is only limited space available for diagnostics and moreover, diagnostic systems add cost and complexity. Therefore priorities must be established with the obvious logic that systems that provide measurements for machine protection are given the highest priority, followed by those for basic plasma control and then advanced plasma control. In many cases performance evaluation and physics studies can be done with the data from the same systems, albeit that some times the diagnostic performance (resolution, number of channels) needs to be boosted. In some cases dedicated measurements are needed specifically for physics studies. These systems have the lowest priority on ITER.

In order to meet all the measurement needs (machine protection, basic and advanced plasma control, physics evaluation) it is expected that about 45 – 50 different parameters will have to be measured.^{1,3} Table 1 in ref. [1] gives an overview of all measurements needed in various ITER operational scenarios (H phase, D phase, D/T phase, high power D/T phase, hybrid and steady state operation) and also specifies which of these measurements are needed for control purposes.

For each of the parameters, detailed measurement requirements need to be developed that specify the spatial and temporal resolution and accuracy that are required for the measurement of the plasma parameter under various conditions. It is important in this process to aim for the minimum requirements that still support the measurement needs, and to not over specify (which would enhance cost and complexity). Therefore each of the measurement requirements needs to be accompanied by a detailed justification that states for what purposes specific accuracies, spatial and temporal resolutions are needed.

The development of the measurement requirements has been an on-going process since the start of the ITER Engineering Design Activity in 1992. ITER is the first magnetic confinement device for which the measurement requirements have been systematically developed during the machine design phase. This coherent approach has been taken in order to achieve an optimised, fully integrated, measurement system with a capability closely matched to the requirements. In case a specific requirement cannot be met for whatever reason, one can directly conclude from the justifications what part of the ITER research programme or machine operation will be affected. The development and fine-tuning of the measurement requirements (to keep track of developments in the field) has been, and still is, a substantial challenge on its own. A large fraction of the measurement requirements is based on experience at present devices and extrapolations towards ITER. However, ITER will be the first device operating in unexploited physics regimes with dominant heating by alpha particles. This implies that part of the measurement requirements had to be developed on the basis of modelling – where possible supported by experiments (e.g. alpha-particle simulation experiments⁴).

The full list of detailed measurement requirements is too long to be reproduced here. The reader is instead referred to Table 2 in ref. [1]. Since the publication of that table in 2007, some further changes have been made in the measurement requirements. The latest version of the table is contained in the ITER Project Integration Document, which is continuously updated, and can be found in the ITER Document Management System.

III. SELECTION OF DIAGNOSTIC TECHNIQUES

The second step in the design process (see Fig. 1) is to select the diagnostic techniques to perform all measurements.

Most techniques that are used in present devices can also be used on ITER, but their application is not always straightforward since the environment is much harsher. Additionally, many diagnostic functionalities are required that go the beyond the scope of those at present devices; e.g. in ITER even profiles of various parameters such as plasma rotation, electron temperature, current density are needed for control purposes of the more advanced plasma scenarios. So, it is important to carefully assess whether diagnostic techniques established at present fusion devices can be made more robust to operate in the harsh ITER environment and whether – if applicable – their scope can be expanded. Table 1 gives an overview of the diagnostic techniques that are presently foreseen for ITER.

Magnetic Diagnostics	Spectroscopic and NPA Systems
Vessel Magnetics	CXRS Active Spectroscopy (+DNB)
In-vessel magnetics	H Alpha Spectroscopy
Divertor Coils	VUV Impurity Monitoring (Main Plasma)
Continuous Rogowski Coils	Visible & UV Impurity Monitoring (Divertor)
Diamagnetic Loop	X-Ray Crystal Spectrometers
Halo Current Sensors	Visible Continuum Array
Neutron Diagnostics	Soft X-Ray Array
Radial Neutron Camera	Neutral Particle Analyzers
Vertical Neutron Camera	Laser Induced Fluorescence
Microfission chambers (in-vessel)	MSE based on Heating Beam
Neutron Flux Monitors (ex-vessel)	Microwave Diagnostics
Gamma-Ray Spectrometers	ECE Diagnostics for Main Plasma
Neutron Activation Systems	Reflectometers for Main Plasma
Lost Alpha Detectors	Reflectometers for Plasma Position
Knock-on Tail Neutron Spectrometer	Reflectometers for Divertor Plasma
Optical/IR Systems	ECA for Divertor Plasma
Thomson Scattering (Core)	Microwave Scattering (Main Plasma)
Thomson Scattering (Edge)	Fast Wave Reflectometry
Thomson Scattering (X-point)	Plasma-Facing Component & Operational Diagnostics
Thomson Scattering (Divertor)	IR Cameras, visible/IR TV
Toroidal interferometer/Polarimeter	Thermocouples
Poloidal Polarimeter	Pressure Gauges
Collective Thomson scattering	Residual Gas Analyzers
Bolometric Systems	IR Thermography Divertor
Bolometric Array (Main Plasma)	Langmuir Probes
Bolometric Array (Divertor)	

Table 1: Overview of the diagnostics foreseen at ITER

ITER will be the first fusion device with dominant alpha heating. Because this is a new and unexploited regime,⁵ a range of new measurements is needed (e.g. the measurement of confined and escaping alpha particles,

alpha-particle driven instabilities) for which novel techniques need to be developed. Whenever possible these should be tested on present devices. Specific examples of such diagnostics are fast ion collective Thomson scattering for studying fast particles including alphas,⁶ fast-wave reflectometry for measuring the fuel ion ratio,⁷ and techniques to measure escaping alpha particles.⁸

IV. ENVIRONMENTAL EFFECTS

The third step in the diagnostics design process (see Fig. 1) is the system specific and radiation effects research and development. Diagnostics in ITER have to cope with an extremely harsh environment.^{1,9,10} Compared to the discharge of JET with the highest fusion performance thus far of 16 MW during 1 second,⁴ ITER will have:

- neutral particle fluxes emerging from charge exchange reactions that are about a factor of 5 higher;
- neutron and gamma fluxes that are both an order of magnitude higher;
- plasma discharges that are about three orders of magnitude longer;
- neutron fluences that are at least $>10^5$ times higher;
- nuclear heating up to 1 MW/m^3 (at JET essentially zero).

Especially the copious amounts of neutrons and gammas give rise to a range of phenomena that are new to the diagnostics and that should be incorporated in the system designs. Many of these phenomena deteriorate the proper functioning of electrical components:

- radiation-induced conductivity (RIC);
- radiation-induced electrical degradation (RIED);
- radiation-induced electromotive force (RIEMF);
- radiation-induced thermo-electric sensitivity (RITES);
- thermal-induced electromotive force (TIEMF).

Some of these effects depend on the irradiation dose whereas others depend on the dose-rate. Even straightforward components such as mineral insulated cables used to transmit signals from in-vessel detectors to data acquisition equipment outside the tokamak hall, and coils to measure magnetic fields in the vacuum vessel, suffer from these effects. The challenge is to develop cables, coils, diagnostic components, etc., in which the combined action of all effects does not deteriorate the proper functioning of the diagnostic.

Refractive materials (lenses, fibers, windows) are subject to:

- radiation-induced absorption (RIA) and
- radio-luminescence or radiation-induced emission (RL or RIE; see Fig. 2).

Therefore, refractive materials can in general not be used at close proximity to the plasma, even though these effects can be reduced to some extent by hydrogen hardening and/or annealing at elevated temperatures (see Fig. 3). For most optical diagnostics this implies that it safe to use re-

fractive components from the end of the port plug onwards. Inside the port plug only mirrors and/or waveguides can be used to transmit the radiation to and from the plasma.

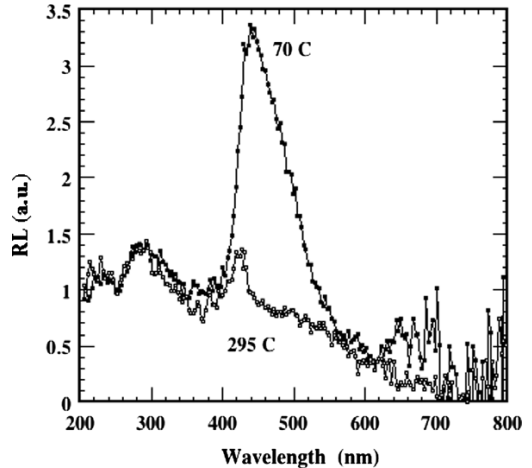


Figure 2: Low dose radio-luminescence (RL) spectra of KS-4V (a Russian-made quartz fibre) at 700 Gy/s and at temperatures of 70 and 295 °C.¹¹

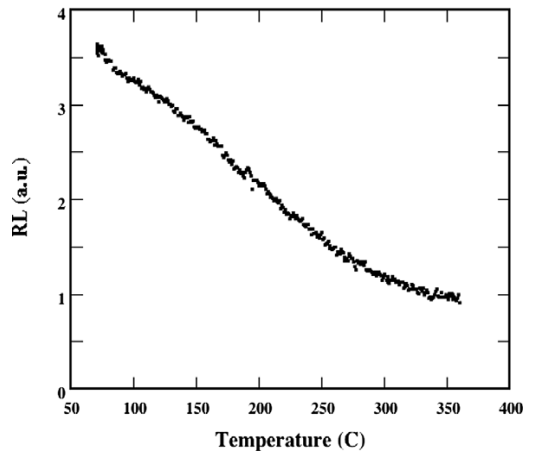


Figure 3: Thermal quenching of the 440 nm radio-luminescence line at 700 Gy/s.¹¹

Other effects caused by the high radiation levels are nuclear heating and changes in material properties such as swelling, transmutation¹² and activation. All these effects can strongly affect the proper operation of diagnostics and diagnostic components. The challenge is to either use ma-

materials that are robust to these effects or – in case this is impossible – to use alternative diagnostic techniques for measuring certain plasma parameters.

The nuclear environment sets also stringent demands on the engineering of the diagnostic systems.⁹ The diagnostics should be designed in such a way that neutrons are prevented from streaming out of the vessel. For many optical and microwave diagnostics this can be achieved by

avoiding straight viewing lines; instead the viewing lines can be folded by using mirrors or waveguide bends, respectively. All diagnostics should have a double tritium barrier with a monitored volume in between (see Fig. 4). A further complication is that all components inside the vacuum vessel and inside the port plugs must be capable of being repaired or replaced with remote handling tools. (see Fig. 5).

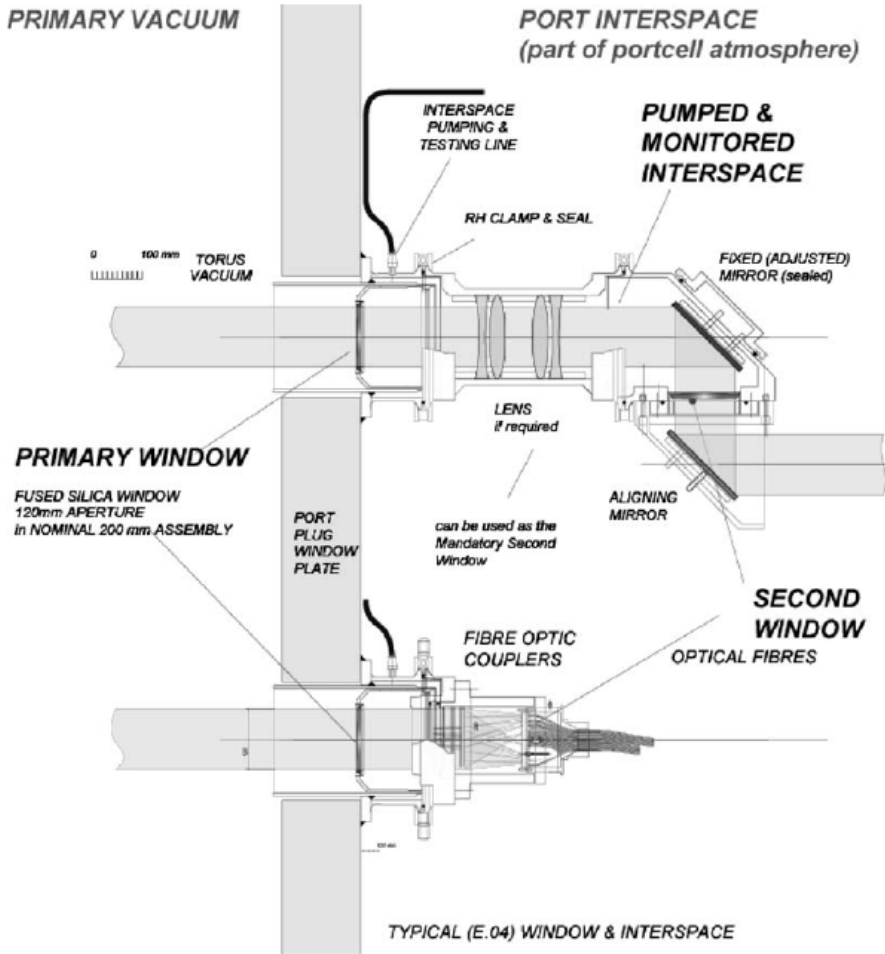


Figure 4: Typical example of two diagnostic window arrangements in ITER.⁹

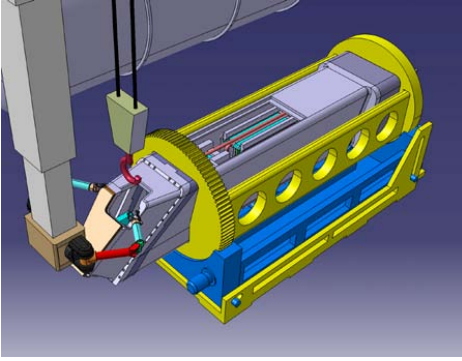


Figure 5: Remote Handling Operation on one of the ITER Port Plugs in the Hot Cell. Courtesy B.S.Q. Elzendoorn.

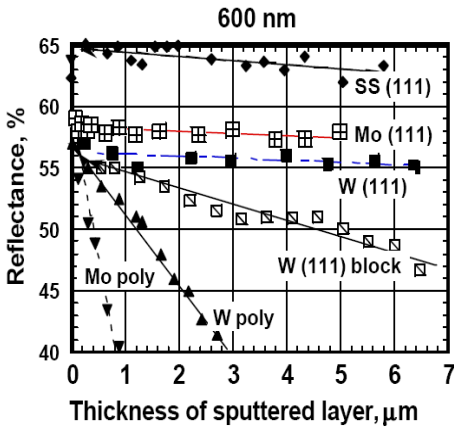


Figure 6: Reflectance of stainless steel (SS), W and Mo mirrors of different structures (polycrystalline, block single crystalline and single crystalline with (111) planes of orientation) at 600 nm depending on the thickness of the layer eroded due to bombardment by ions of deuterium plasma. (Adapted from [13]).

So mirrors seem to be the ‘magic’ solution. At the one hand they can be applied instead of refractive components that suffer from RIA and RIE, while at the other hand they make it possible to fold the optics path into a labyrinth to suppress the neutron streaming. However, nothing comes for free: The high neutral particle fluxes emerging from charge exchange reactions lead to erosion and redeposition elsewhere. Both of these effects can strongly affect the polarization dependent reflectivity of the mirrors, and thereby deteriorate the proper functioning of the diagnostics.¹⁴ Erosion is the least of the two problems, since in erosion dominated regions it is possible to use single crystalline mirrors of materials like tungsten, molybdenum, and stainless steel that are rather resistant to erosion. Moreover, the reflectivity of these single

crystalline mirrors does not strongly depend on the thickness of the eroded layer (see Fig. 6).

In contrast, deposition has in almost all cases a strong deleterious effect on the reflective properties of the mirrors (see Fig. 7). Much work is done in order to find the optimum mirror materials and also the best geometries for especially the first mirror, which is least vulnerable to erosion and especially deposition. Furthermore, attention is devoted to develop means for mirror protection (e.g. shutters, gas flow in front of the mirrors) or to mitigate deposition (e.g. operating the mirrors at elevated temperatures). In DIII-D it has been demonstrated that mirrors in the divertor heated to 200-300 °C suffer much less from deposits than mirrors at the same place, operated at room temperature (see Fig. 8).¹⁵

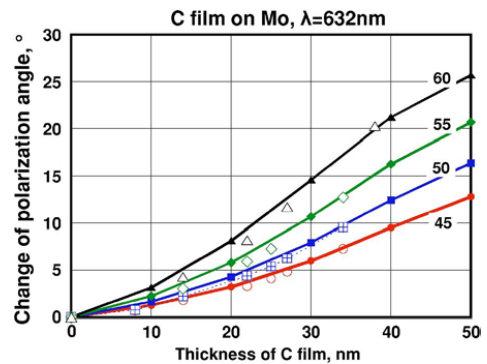


Figure 7: Calculated (lines and solid points) and experimental values (open points) for the change of the polarization angle of light at 632 nm reflecting from a Mo mirror coated with different thicknesses of C film. The angle of incidence is shown near every curve.¹⁶

Another diagnostic challenge arises from the long duration of the ITER discharges. These give rise to problems for traditional techniques such as inductive magnetic pick-up coils for measuring magnetic fields. Especially the integrators are vulnerable to drift. The combination of the long pulse and the high levels of radiation constitute a rather difficult measurement problem. In addition to trying to make these techniques more robust and radiation hard, research is on-going to develop radiation-hard steady state magnetic field sensors based on the Hall effect,¹⁷ and to develop alternative techniques such as position reflectometry¹⁸ to measure the gap between the density at the separatrix and the first wall.

A final challenge for diagnostics that will be mentioned in this paper is caused by the high temperatures in ITER, which can reach values up to about 40 keV. This gives rise to strong relativistic effects, which have a large effect on microwave diagnostics because of the downshifted electron cyclotron emission (ECE). The result is that in contrast to

present devices, ECE using the 2nd harmonic X-mode cannot be used for determining the electron temperature T_e in the plasma core, due to overlap by relativistically downshifted 3rd harmonic emission (see Fig. 9). Instead the 1st harmonic O-mode needs to be utilized. The downshifted emission also strongly limits the operational ranges of reflectometers to measure the density profile. The core density profile can only be measured by reflectometry via the lower cutoff from the high field side. Reflectometry on the plasma frequency from the low field side only can yield the density profile in the vicinity of the separatrix.

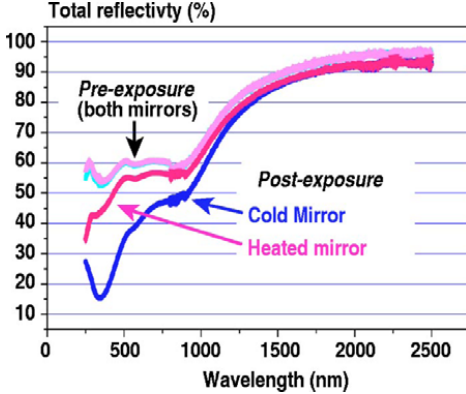


Figure 8: Total reflectivity of heated and non-heated mirrors before and after exposures in the DIII-D divertor.¹⁵

V. INTEGRATION OF DIAGNOSTICS

The fourth step in the diagnostic design process (see Fig. 1) is the engineering design and integration of all diagnostics on the tokamak. ITER will have five diagnostic ports at the equatorial level and twelve at the upper level. Additionally, a number of special instrumented cassettes are foreseen in the divertor. In contrast to present-day machines where each diagnostic is implemented on its own diagnostic port, there is a need to install several diagnostics in a single diagnostic port (see Fig. 10).^{9,19} This puts of course high demands on the integration of all systems. In most cases the various diagnostics will be developed by different teams in the ITER parties. Effects such as the neutron shielding, the total mechanical strength of the port plug and deformations under ITER operation have to be assessed for the full port plug, and these assessments must be redone if changes are made to the design of the individual diagnostics. Due to the multitude of interfaces between the various diagnostics and between the parties working on them, this is far from being an easy task.

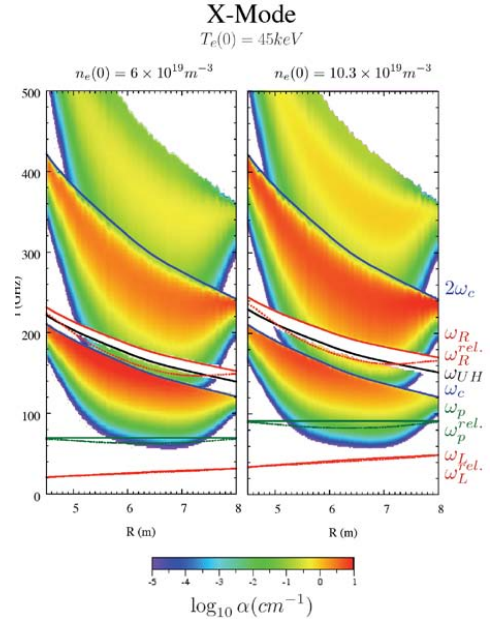
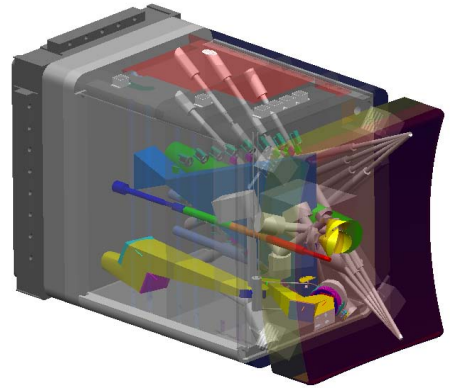


Figure 9: Local absorption contours for X-mode propagation at perpendicular incidence for two densities, at high temperature (T_e on axis is 45 keV) representing an extreme case of what might occur in an



ITER steady-state scenario Adapted from [20].

Figure 10: Cut-away view of equatorial port number 1 providing access for the radial neutron camera, high resolution neutron spectrometer, a visible IR-TV camera, gamma ray spectrometers, bolometry, one of the divertor impurity monitors, and one of the viewing systems for Motional Stark Effect diagnostic (courtesy C.I. Walker, ITER IO).

VI. DIAGNOSTIC ASSESSMENT

The final step in the diagnostic design process (see Fig. 1) is the assessment of the diagnostic capability with respect to the measurement requirements. This

is done rather frequently. Although there have been more recent assessments, Table 7 in ref. [1] is still actual. For roughly 50% of the plasma parameters it is expected that the measurement requirements can be met, for about the same number of other plasma parameters it is expected that the measurement requirements can be partly met. For three parameters it is expected that the measurement requirements can not be met. These are the measurements of alpha particle losses (escaping alpha particles), the ion temperature in the divertor and the plasma flow in the divertor. For these parameters it is necessary to go back to the measurement requirements (see Fig. 1) to judge whether they can be somewhat relaxed without harming the operation of the machine or the intended physics programme. If this is not possible it is necessary to try to improve the diagnostic design and/or to develop novel techniques in order to meet the requirements.

VII. DIAGNOSTIC FOR NEXT STEP DEVICES

The diagnostic design process for next step devices as DEMO²¹ will be in principle similar to the one sketched in Fig. 1. But DEMO will have higher levels of neutron flux, fluence, nuclear heating, gamma irradiation and plasma irradiation than ITER. In particular the neutron fluence will be ~50 times higher than in ITER, while the neutron flux is a few times higher. This implies that techniques or diagnostic components that marginally work in the ITER environment are likely to be inappropriate in DEMO. This applies to many in-vessel diagnostic components (e.g. cables, magnetic coils and bolometry), for which there seems little prospect for improvements that would make it possible to use them in DEMO in a similar way as in ITER.^{22,23}

The particle flux in DEMO is expected to be ~2 times higher with respect to ITER. Even this 'small' increase may make optical systems with large-aperture mirrors problematic, given the very difficult situation already in ITER. Small apertures and mirrors recessed far into the shielding, and use of exchangeable optical fibres, could make optical diagnosis possible, but with very limited views of the DEMO plasma. Techniques that still seem feasible without large modifications from the present practice are microwave techniques and direct line-of-sight techniques (e.g. neutrons and x-rays). As mainly the neutron fluence (and not the flux) in DEMO is larger than in ITER, i.e. effects in relation to lifetime, there may be prospects for use of in-vessel diagnostic components such as magnetic coils and bolometers if provisions are made that they can be replaced regularly. The same is true for larger mirrors. If such in-vessel diagnostics and optical diagnostics with large-aperture mirrors are deemed essential for DEMO, schemes must be enabled for regular replacement, which may significantly impact on the DEMO design.

These considerations lead to the following needs for R&D for DEMO diagnostics. New diagnostic techniques need to be developed that are suitable for the DEMO environment, in particular to replace the established diagnostic techniques that will be problematic in DEMO. For in-vessel components, there may be little prospect other than ensuring they can be replaced frequently as discussed above. For ex-vessel components the situation may be less critical. Nevertheless, this is an area that needs intensive study, requiring testing and qualification on fission reactors, ITER (full-power DT phase) and the International Fusion Materials Irradiation Facility.²⁴ It should be noted that irradiation testing, even at ITER-relevant levels, is time consuming and costly. The fission-reactor time needed to reach DEMO-relevant fluences may therefore be problematic. Work on ITER needs to guide the selection of techniques that can best cope with the harsh environment. During the ITER life time, experience should be gained with real-time data handling and validation to process large quantities of data, in-pulse calibration, etc.

ITER will routinely have DT plasmas and the alpha heating effect will be significant. Alpha particle physics and alpha induced instabilities can therefore be studied in full detail and the impact of those on DEMO can be assessed (along with a selection of the optimum diagnostics techniques).

Unlike ITER, DEMO will not be designed as a flexible research tool, since it needs to demonstrate the economics of the fusion reactor. It is expected that DEMO will have only 1 - 2 different (advanced) plasma operating scenarios. The selection of these scenarios needs to be done during the full power DT phase in ITER. The limited number of operating scenarios implies that likely a smaller number of measurements/diagnostics are required. Once the DEMO scenarios have been selected in ITER, a high number of essentially identical high performance pulses are needed in order to determine the minimum set of diagnostics that fully supports the DEMO scenarios. One should realize, however, that the lack of suitable diagnostic techniques may affect the options for controlling the DEMO plasma, in particular the ability to run "advanced" scenarios. This lack of diagnostics, and thus the reduced set of plasma parameters that can be measured, will make modelling more important in DEMO to derive the other parameters. Advanced predictive/analysis codes need to be developed to combine data from various diagnostics in an intelligent way in order to reduce the number of required diagnostics. A successful strategy is to use so-called "dynamic state observers", which is in essence a real-time simulation of a theoretical model of the plasma,²⁵ running parallel to the physical evolution of the plasma in the tokamak. The model predictions are continuously compared to the available diagnostic measurements, yielding improved estimates and/or leading to slight adaptations in the model. The actual control then uses the state estimate from the

observer, on a timescale independent from (and often faster than) the diagnostic measurements.

ACKNOWLEDGMENT

This paper is largely based on the experience of the author as chair of the ITER Expert Group on Diagnostics, the ITPA and the EFDA Topical Group on Diagnostics. He would like to thank all colleagues that have contributed to the work of these groups thus forming the basis of this paper. The paper is a slightly revised version of the paper that has been written for the 2009 and 2011 Carolus Magnus Summer Schools. The author is indebted to Ben Elzendoorn, Eric Hodgson, Dmitry Rudakov, George Vayakis and Chris Walker for giving permission to use their figures. This work, supported by the European Communities under the contract of Association between EURATOM/FOM, was carried out within the framework of the European Fusion Programme with financial support from NWO and ITER-NL. The views and opinions expressed herein do not necessarily reflect those of the European Commission.

REFERENCES

- ¹ A.J.H. DONNÉ, *et al.*, “Progress in ITER Physics Basis, Chapter 7 : Diagnostics”, *Nucl. Fusion* **47**, S337 (2007)
- ² A.J.H. DONNÉ and A.E. COSTLEY, “Key Issues in Diagnostics for Burning Plasma Experiments”, *IEEE Transact. Plasma Sci.* **32** (2004) 177.
- ³ K. EBISAWA *et al.*, “Plasma Diagnostics for ITER-FEAT”, *Rev. Sci. Instrum.* **72**, 545 (2001).
- ⁴ P.R. THOMAS *et al.*, “Overview of Alpha Heating in JET DT Plasmas”, *Phys. Rev. Lett.* **80**, 5548 (1998).
- ⁵ S.E. SHARAPOV *et al.*, “Burning Plasma Studies at JET”, *Fusion Sci. Techn.* **53**, 989 (2008).
- ⁶ E. TSAKADZE *et al.*, “Fast Ion Collective Thomson Scattering for ITER: Design Elements”, *Fusion Sci. Techn.* **53**, 69 (2008).
- ⁷ L. CUPIDO *et al.*, “High Resolution Fast Wave Reflectometry: JET Design and Implications for ITER”, *Rev. Sci. Instrum.* **79**, 10F106 (2008).
- ⁸ M. SASAO *et al.*, “Fusion Product Diagnostics”, *Fusion Sci. Techn.* **53**, 604 (2008).
- ⁹ G. VAYAKIS *et al.*, “Generic Diagnostic Issues for a Burning Plasma”, *Fus. Sci. Techn.* **53**, 699 (2008).
- ¹⁰ A.E. COSTLEY *et al.*, “ITER R&D: Auxiliary Systems: Plasma Diagnostics”, *Fusion Eng. Design* **55**, 331 (2001).
- ¹¹ A. MOROÑO and E.R. HODGSON, “Radio-luminescence Behaviour for Electron Irradiated KS-4V”, *J. Nucl. Mat.* **367-370**, 1107 (2007).
- ¹² M. GONZALEZ and E.R. HODGSON, “Radiation Resistant Bolometers using Platinum on Al₂O₃ and AlN”, *Fusion Eng. Design* **74**, 875 (2005).
- ¹³ A.E. COSTLEY *et al.*, “ITER R&D: Auxiliary Systems: Plasma Diagnostics”, *Fusion Eng. Design* **55**, 331 (2001).
- ¹⁴ A. LITNOVSKY *et al.*, “Progress in Research and Development of Mirrors for ITER Diagnostics”, *Nucl. Fusion* **49**, 075014 (2009).
- ¹⁵ D. RUDAKOV *et al.*, “First Tests of Molybdenum Mirrors for ITER Diagnostics in DIII-D Divertor”, *Rev. Sci. Instrum.* **77**, 10F126 (2006).
- ¹⁶ V. VOITSENYA *et al.*, “Simulation of Environmental Effects on Retroreflectors in ITER”, *Rev. Sci. Instrum.* **76**, 083502 (2005).
- ¹⁷ I. BOLSHAKOVA *et al.*, “Performance of Hall Sensor-based Devices for Magnetic Field Diagnosis at Fusion Reactors”, *Sensor Lett.* **5**, 283 (2007).
- ¹⁸ F. DA SILVA, *et al.*, “Developments of Reflectometry Simulations for Fusion Plasmas: Application to ITER Position Reflectometers”, *J. Plasma Phys.* **72**, 1205 (2006).
- ¹⁹ C.I. WALKER *et al.*, “ITER Diagnostics: Integration and Engineering Aspects”, *Rev. Sci. Instrum.* **75**, 4243 (2004).
- ²⁰ G. VAYAKIS *et al.*, “Status and Prospects for mm-Wave Reflectometry in ITER”, *Nucl. Fusion* **46**, S386 (2006).
- ²¹ D. MAISONNIER, “European DEMO Design and Maintenance Strategy”, *Fusion Eng. Design* **83**, 858 (2008).
- ²² A.J.H. DONNÉ *et al.*, “Diagnostics for plasma control on DEMO: challenges of implementation”, *Nucl. Fusion* **52**, 074015 (2012).
- ²³ A.J.H. DONNÉ, “From present Fusion Devices to DEMO: a changing Role between Diagnostics and Modeling”, accepted for publication in *Plasma Fusion Res.* **8**, 2102084 (2013).
- ²⁴ P. GARIN and M. SUGIMOTO, “Main Baseline of IFMIF/EVEDA Project”, *Fusion Eng. Design* **84**, 259 (2009).
- ²⁵ F. FELICI *et al.*, “Real-time physics-model-based simulation of the current density profile in tokamak plasmas”, *Nucl. Fusion* **51**, 083052 (2011).

A new approach to the formulation and validation of scaling expressions for plasma confinement in tokamaks

A. Murari¹, E. Peluso², M. Gelfusa², I. Lupelli^{2,3} and P. Gaudio²

¹ Consorzio RFX (CNR, ENEA, INFN, Università di Padova, Acciaierie Venete SpA),
Corso Stati Uniti 4, 35127 Padova, Italy

² Department of Industrial Engineering, University of Rome 'Tor Vergata', via del
Politecnico 1, Roma, Italy

³ CCFE, Culham Science Centre, Abingdon, Oxon, OX14 3DB, UK

E-mail: andrea.murari@euro-fusion.org

Received 3 June 2014, revised 25 April 2015

Accepted for publication 15 May 2015

Published 5 June 2015



Abstract

The extrapolation of the energy confinement time to the next generation of devices has been investigated both theoretically and experimentally for several decades in the tokamak community. Various scaling expressions have been proposed using dimensional and dimensionless quantities. They are all based on the assumption that the scalings are in power law form. In this paper, an innovative methodology is proposed to extract the scaling expressions for the energy confinement time in tokamaks directly from experimental databases, without any previous assumption about the mathematical form of the scalings. The approach to obtain the scaling expressions is based on genetic programming and symbolic regression. These techniques have been applied to the ITPA database of H-mode discharges and the results have been validated with a series of established statistical tools. The soundest results, using dimensional variables, are not in the form of power laws but contain a multiplicative saturation term. Also the scalings, expressed in terms of the traditional dimensionless quantities, are not in power law form and contain additive saturation terms. The extrapolation to ITER of both dimensional and dimensionless quantities indicate that the saturation effects are quite significant and could imply a non-negligible reduction in the confinement time to be expected in the next generation of devices. The results obtained with the proposed techniques therefore motivate a systematic revisiting of the scaling expressions for plasma confinement in tokamaks.

Keywords: scaling laws, confinement time, tokamaks, nuclear fusion, genetic programming, symbolic regression, power laws

(Some figures may appear in colour only in the online journal)

1. The extrapolation of the energy confinement time to future devices

The problem of extrapolating the energy confinement time from present devices to the future generation of machines is a long standing issue in the tokamak community. For several decades various approaches have been pursued, both theoretically and experimentally. Theoretically, the main theories typically make one of two quite extreme assumptions. Either the transport is dominated by short wavelength turbulence (drift waves), to be scaled to intrinsic plasma parameters, or the cross field transport is due to long wavelength turbulence (MHD), scaled to the main dimensions of the devices. The first family comprises the so called gyro-Bohm scalings and the second is indicated with the name Bohm scalings [1]. Unfortunately, even if substantial progress has been made in characterizing the transport mechanisms in tokamaks, the physics is not

sufficiently established to allow performing first principle calculations to interpret the results of the present devices. In any case, even if the mechanisms dominating transport were well understood, modelling them in sufficient detail to obtain realistic values of the global confinement time would remain a quite challenging task. Therefore, since many decades, the theoretical studies have been complemented by experimental efforts aimed at collecting enough data to derive data-driven scaling expressions for the confinement time, sufficiently robust to be extrapolated to the next generation of devices. The obtained databases have typically been analysed using traditional log regression. The resulting scaling expressions are therefore in the form of power law monomials:

$$A = \frac{B^\beta C^\alpha \dots D^\delta}{G^\gamma H^\lambda \dots K^\mu}, \quad (1)$$

where the capital letters represent physical quantities [2]. This assumption on the form of these scaling equations is not

justified neither on theoretical nor on experimental ground. Indeed theoretically there is no justification to limit the analysis to scalings obeying power law expressions. Experimentally, the vast majority of the used databases do not present statistical distributions compatible only with power laws.

In general, it must be considered that the formulation of the scaling expressions as power laws can be unsatisfactory for several reasons. In power law scalings, there is no saturation of the effects even when the independent variables grow to infinity or decay to zero. These scalings are also monotonic and tend to overestimate the relevance of the variables with the longest tails. The interaction of all the variables is also assumed to be multiplicative, which normally results in non-integer exponents of the independent variables not always easy to reconcile with theory. It is also important to appreciate that there are many dynamical interactions which can give rise to power laws and therefore this statistics is not very informative about the underlying physics. These inadequacies of power laws have become evident recently and are motivating efforts to extract more sophisticated scaling expressions from the data [3]. In the case of tokamak physics, the limitations of the power law scalings have clearly been shown in [4, 5]. The rigidities' of power laws can be particularly problematic in case of significant extrapolations, as it is the case of trying to model ITER on the basis of present day machines.

In order to alleviate this problem of uncertainties in the extrapolation and to obtain a more reliable physical basis for the results, the scaling expressions of the confinement time have also been formulated in terms of dimensionless variables [6]. In this case, the main idea consists of the observation that, if the basic equations governing the plasma behaviour are invariant under a certain class of transformations, also the scaling expressions for these plasmas must show the same invariances. In the literature, the plasma behaviour has been assumed to obey the Vlasov equation in various approximations and limits. These assumptions allow on the one hand to identify the dimensionless variables to be used in the scalings and, on the other hand, they provide constraints on the exponents of the various terms [7]. Again the scaling expressions are assumed '*a priori*' to be power law monomials. All the mathematical limitations of the power laws as scaling functions apply to the case of dimensionless variables. Again in practice, the databases expressed in terms of dimensionless variables do not support the assumption of distributions of the power law form.

In this paper advanced techniques of symbolic regression via genetic programming are applied to the problem of deriving scaling expressions for the confinement time from large databases without practically any assumption about their mathematical form. The proposed methods allow identifying the most appropriate mathematical expression for the regression equations. Moreover, the versatility and robustness of these techniques is such that they allow regressing also the non-dimensional quantities; it is worth pointing out that this can be problematic for the databases analysed in this paper using log regression. In any case, independently from the choice of the variables, dimensional or dimensionless, the best scaling identified by symbolic regression, in the case of the studied ITPA H-mode database, are not power law monomials. This has been confirmed

by a series of statistical methods deployed to assess how well the candidate scaling expressions interpret the available experimental evidence. A combination of non-linear fitting tools and statistical criteria will be shown to address this aspect of the analysis in a quite reliable manner. The extrapolation of the identified scaling expressions indicate that the confinement time in ITER could be about 20% lower than predicted by the traditional power law scalings (but the various estimates agree within their respective confidence intervals).

With regard to the structure of the paper, section 2 provides an overview of the main methodology developed. In particular, symbolic regression via genetic programming, the main tool for the exploration of the databases, is introduced. The main mathematical details about the methodology are provided in appendix A1. In section 3 the ITPA database is reviewed. The obtained scaling expressions in non-power law form and expressed in terms of dimensional quantities are reported and discussed in section 4. Section 5 contains the same analysis for the scalings expressed in terms of dimensionless variables. The conclusions and prospects of future activities are discussed in the last section 6 of the paper.

2. The statistical tools for the exploration of the databases, the extraction of the scaling expressions and their selection

As mentioned in the introduction, this paper describes the application of advanced statistical techniques to the problem of deriving scaling expressions for the confinement time from large databases. The main advantage of the proposed approach consists of practically eliminating any assumption about the form of the scaling expressions. The methods developed indeed allow identifying the most appropriate mathematical expression for the regression equations and to demonstrate that it has the potential to better interpret the present experimental data for the confinement time in comparison with power laws (PLs). This section describes briefly the mathematical basis of the tools implemented to perform the analysis used in the rest of the work. All the details can be found in the references and are summarized in appendix A1.

The objective of the method consists of testing various mathematical expressions to interpret a given database. The main stages to perform such a task are reported in figure 1. First of all, the various candidate formulas are expressed as trees, composed of functions and terminal nodes. The function nodes can be standard arithmetic operations and/or any mathematical functions, squashing terms as well as user-defined operators [8, 9]. The terminal nodes can be independent variables or constants (integer or real). This representation of the formulas allows an easy implementation of the next step, symbolic regression with genetic programming. Genetic programs (GPs) are computational methods able to solve complex and non-linear optimization problems [8, 9]. They have been inspired by the genetic processes of living organisms. In nature, individuals of a population compete for basic resources such as water, food and shelter. Those individuals that achieve better surviving capabilities have higher probabilities to generate descendants. As consequence, best adapted individuals' genes have a higher probability to be passed on to the next generations.

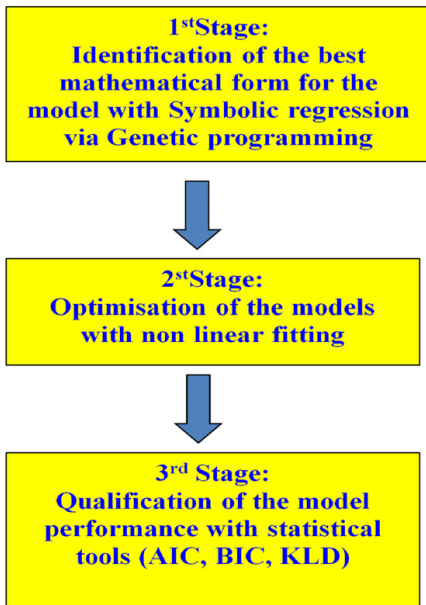


Figure 1. The main steps of the proposed methodology to identify the best scaling laws without assumption on their mathematical form.

GPs emulate this behaviour. They work with a population of individuals, e.g. mathematical expressions in our case. Each individual represents a possible solution of a problem. A fitness function (FF) is used to measure how good an individual is with respect to the environment. A higher probability to have descendants is assigned to those individuals with better FF. Therefore, the better the adaptation (the value of the FF) of an individual to a problem, the higher is the probability that its genes can be propagated. The line of reasoning of the standard procedure of GP, to solve a specific optimization problem, is the one summarized below.

- (1) Generate a random population of individuals.
- (2) Evaluate each individual of the population with a fitness function.
- (3) Select individuals (parents) to create a new population; the better their fitness function, the more likely they are chosen for this parental role.
- (4) Pass the genes of the chosen parents, obtaining 'children', forming the new generation.
- (5) Repeat the steps 2 to 4 till an ending condition is fulfilled.

In our application, the role of the genes is played by the basis functions used to build the trees. The list of basis functions used to obtain the results described in the rest of the paper is reported in table 1. Evolution is achieved by using operators that perform genetic like operations such as reproduction, crossover and mutation. Reproduction involves selecting an individual from the current population and allowing it to survive by copying it into the new population. The crossover operation involves choosing nodes in two parent

Table 1. Types of function nodes included in the symbolic regression used to derive the results presented in this paper, x_i and x_j are the generic independent variables.

Function class	List
Arithmetic	c (real and integer constants), $+$, $-$, $*$, $/$
Exponential	$\exp(x_i)$, $\log(x_i)$, $\text{power}(x_i, x_j)$, $\text{power}(x_i, c)$
Squashing	$\text{logistic}(x_i)$, $\text{step}(x_i)$, $\text{sign}(x_i)$, $\text{gauss}(x_i)$, $\text{tanh}(x_i)$, $\text{erf}(x_i)$, $\text{erfc}(x_i)$

trees and swapping the respective branches thus creating two new offspring. Mutations are random modifications of parts of the trees.

To derive the results presented in this paper, the Akaike Information [Criterion (AIC) has been adopted [10] for the FF. The AIC, is a well-known model selection criterion that is widely used in statistics, to identify the best models and avoid overfitting. The AIC form used in the present work is:

$$\text{AIC} = 2k + n \cdot \ln(\text{RMSE}), \quad (2)$$

where RMSE is the root mean square error, k is the number of nodes used for the model and n the number of y_{data} provided, so the number of entries in the database (DB). The AIC allows rewarding the goodness of the models, by minimizing their residuals, and at the same time penalizing the model complexity by the dependence on the number of nodes. The better a model, the smaller its AIC. All the mathematical justification for its adoption can be found in the references and in appendix A1.

At this stage, the best mathematical expression for the scaling expression has been identified. In order to improve the model, the parameters of the equation are adjusted with traditional tools of non-linear regression [11]. This has proved to be important not only to improve the quality of the models but also to provide confidence intervals in their parameters. It is worth pointing out that our methodology tends to provide more reliable confidence interval than log regression, since its hypotheses are not satisfied by the available databases [4, 5]. All these aspects, together with the techniques for non-linear fitting, are discussed in more detail in appendix A1.

Having optimized the models with non-linear fitting, now what remains is the qualification of the statistical quality of the obtained scaling expressions. To this end a series of statistical indicators have been implemented. They range from model selection criteria, such as the Bayesian information criterion (BIC), to statistical indicators, such as the Kullback–Leibler divergence (KLD) [12, 13]. These are nowadays quite standard indicators and in our case they all agree that the new proposed scaling expressions are better than the previous power laws. In any case, for the benefit of the interest readers, they are described in some detail in appendix A1.

3. The ITPA database and weight selection

3.1. The main characteristics of the ITPA database DB3v13f

To maximize the generality of the results obtained with the methodology described in the previous sections, an international database has been considered [14]. This database was explicitly conceived to support advanced studies of the

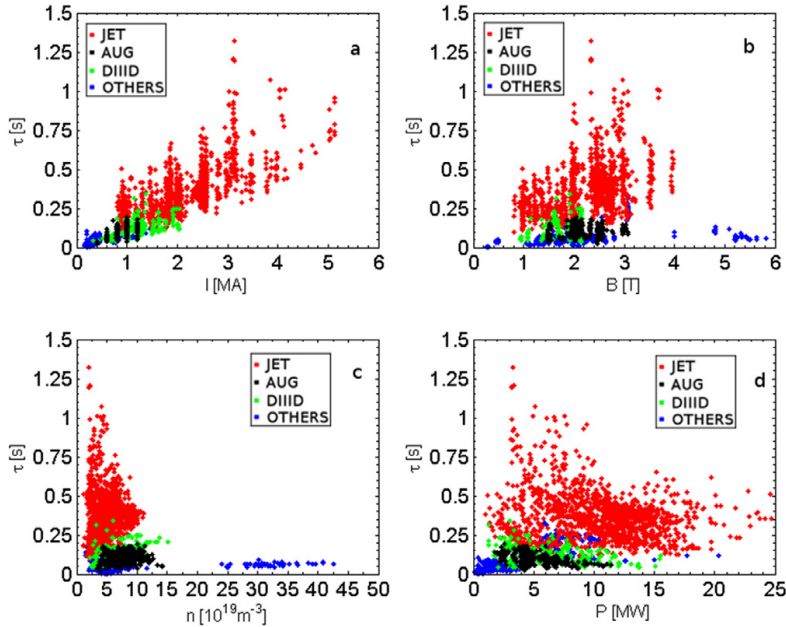


Figure 2. Trend of the confinement time with four physical quantities considered in the pools of selected data: (a) (I (MA)); (b) (B (T)); (c) (n (10^{19} m^{-3})); (d) (P (MW)).

confinement time and includes validated signals from the vast majority of the most relevant tokamak machines ever operated in the world. In line with the previous literature on the subject, the following quantities have been considered good candidate regressors in the present work.

- Dimensionless variables: ρ^* , β , v^* , k_a , ϵ , q_{95} , M
- Dimensional variables: B (T), I (MA), n (10^{19} m^{-3}), R (m), M , ϵ , k_a ; P (MW).

In the previous lists, ρ^* indicates the normalized ion Larmor radius, β the normalized plasma pressure, v^* the normalized collision frequency, k_a the volume elongation measurement, ϵ the inverse aspect ratio, q_{95} the plasma safety factor evaluated at the flux surface enclosing the 95% of the poloidal flux, M the effective atomic mass in a.m.u, n the central line average plasma density, B the toroidal magnetic field, R the plasma major radius, I the plasma current and finally P the estimated power loss [15]. In agreement with previous works [15], in the case of regressions in terms of dimensionless variables, the dependent quantity considered is the product of the ion cyclotron frequency, conveniently rescaled, times the confinement time, $y = \tau \omega_{ci}$. The definitions of the other dimensionless quantities are the same normally used to interpret the experiments and reported in the literature [15]:

$$\rho^* = \left(\frac{2m_p}{3e^2}\right)^{\frac{1}{2}} \cdot \left(\frac{MW}{Vn}\right)^{\frac{1}{2}} \cdot \frac{1}{Ba} \quad \beta = \frac{4\mu_0}{3} \cdot \frac{W}{VB^2},$$

$$k_a = \frac{V}{2\pi^2 a^2 R} \quad \epsilon = \frac{a}{R} \quad q = q(a) = \frac{2\pi a^2 Bk}{\mu_0 IR},$$

$$v^* = \left(\frac{15e^4 \ln(\Lambda_i)}{4\pi^{\frac{3}{2}} \epsilon_0^2 \mu_0}\right) \cdot \frac{V^2 R^2 B \epsilon^{\frac{1}{2}} n^3 k}{W^2 I}.$$

The entries of the database have been selected adopting exactly the same criteria used in [15] to build the database DB3, from which the reference scalings in power law form were derived. This choice has been motivated by the main goal of the paper, which consists of demonstrating the higher potential of the new data analysis tools compared to the traditional log regression. In this perspective, it is only appropriate to apply the new tools exactly to the same database DB3, used to obtain the reference power law scalings [15]. The final database analysed consists therefore of 3093 entries for the dimensional scalings and a total of 2806 examples for the dimensionless set. Figure 2 shows the trend of the confinement time versus four dimensional physical quantities, while figure 3 shows the behaviour of the non-dimensional product $\tau \cdot \omega_{ci}$ with four non-dimensional quantities.

All the quantities selected as regressors are routinely available in all the major tokamaks, providing enough data for a sound statistical analysis. The uncertainties in the dimensional quantities can be derived from [15] and the information provided in the database. These errors are summarized in table 2.

From the information about the dimensional variables, the uncertainties in the dimensionless quantities can be estimated with traditional error propagation. The results are reported in table 3. It is worth mentioning that it has been checked numerically that SR via GP can handle this level of uncertainties. First, a series of systematic numerical tests, with hundreds of models of the widest mathematical form and noise level up to 50%, have been performed. Given enough data and computational time, the proposed method can certainly handle level of uncertainties of 40% and performs always better than

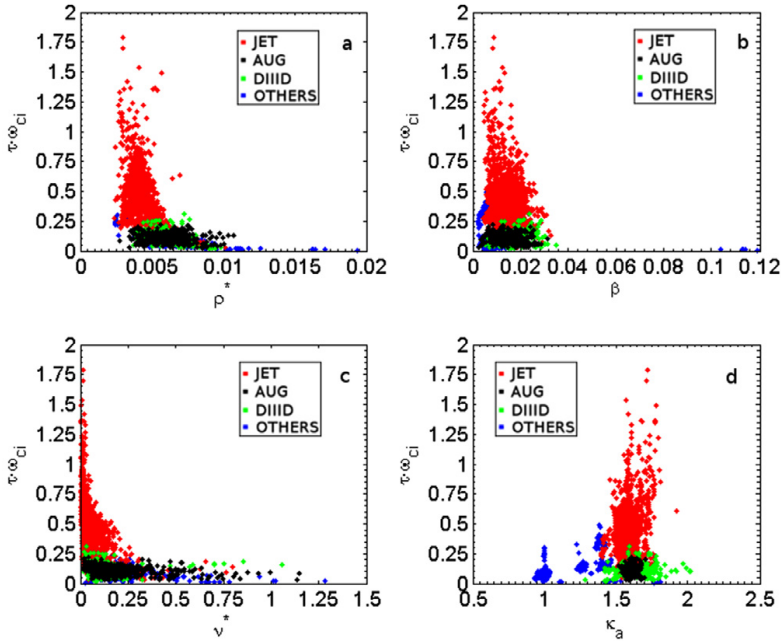


Figure 3. Trend of the confinement time with four physical quantities considered in the pools of selected data: (a) $\tau \cdot \omega_{ci}(\rho^*)$; (b) $\tau \cdot \omega_{ci}(\beta)$; (c) $\tau \cdot \omega_{ci}(v^*)$; (d) $\tau \cdot \omega_{ci}(\kappa_a)$.

Table 2. Uncertainties in the dimensional variables in the ITPA Database.

	ϵ_I	ϵ_B	ϵ_R	ϵ_n	ϵ_a	ϵ_M	ϵ_W	ϵ_P	ϵ_k	ϵ_V	ϵ_{q95}	ϵ_τ
Error %	1.3	1.5	1.3	5	0.9	8.4	14.1	14.2	3.7	4.6	8.1	28.3

Table 3. Errors in the non-dimensional variables, computed using table 2.

	ϵ_ρ	ϵ_β	ϵ_v	ϵ_ϵ	ϵ_{κ_a}	$\epsilon_{\tau \cdot \omega_{ci}}$
Error %	34.5	20.2	33.7	2.2	6.8	38.2

log regression, particularly against collinearities and outliers. Second, our methodology, thanks to the non-linear fitting step, provides robust estimates of the uncertainties in all the derived quantities as reported in the rest of the paper.

3.2. The selection of the weights

For all the results reported in the rest of the paper, the weights have been chosen with the method of the percentiles. This technique allows weighting data depending on their distribution. The objective consists in fact of weighting more the data falling in the tails of their distributions, since those data carry more relevant information for the determination of scaling expressions. For instance high plasma current values ($I > 2.5$ (MA)) of JET are extremely valuable since they are the closest to ITER operational region of 15 MA. Even if statistically they could be considered as outliers, physically they are the most relevant points.

For each physical quantity, five percentiles have been computed in order to divide the distribution function in six partitions, which can be independently weighted. In our case we have chosen the inverse of the cumulative probability, defining the percentiles themselves, as the weight for data falling in each different partition. This can be repeated for all the selected physical quantities to obtain a final weight for each entry of the DB. These weights have been used consistently in all the various steps of the data analysis method reported in figure 1. More sophisticated methods are under study but it is worth mentioning that, for this database, the traditional choice of the weights, using the number of entries per machine [15], does not change qualitatively the results obtained in the paper. A sensitivity study has indeed been performed showing that small variations in the weights do not alter significantly the final results. Therefore the qualitative difference between the scaling expressions found with symbolic regression and the ones in the literature remain valid independently from the choice of the weights.

4. Results in terms of dimensional quantities

The best models found with symbolic regression via genetic programming in general are not in power law form but they present additional terms. In particular, in the case of scalings

Table 4. Power laws (PLs) and non-power law model (NPL). PL1 is the IPB98(y,2) scaling while PL2 is (EIV) [15]. The term $h(n,B)$ is:

$$h(n, B) = n^{0.448 \frac{0.460}{0.436}} \cdot (1 + e^{-9.403 \frac{0.912}{-9.694} (\frac{B}{T})^{-1.365 \frac{-1.318}{-1.412}}} y^{-1}).$$

PL1	$5.62 \times 10^{-2} I^{0.93} B^{0.15} n^{0.41} M^{0.19} R^{1.97} \epsilon^{0.58} \kappa_2^{0.78} P^{-0.69}$
PL2	$5.55 \times 10^{-2} I^{0.75} B^{0.32} n^{0.35} M^{0.06} R^{2.0} \epsilon^{0.76} \kappa_a^{1.14} P^{-0.62}$
NPL	$0.0367 \frac{0.0369}{0.0366} \cdot I^{1.0061 \frac{0.016}{0.996}} R^{1.731 \frac{1.751}{1.712}} \kappa_a^{1.450 \frac{1.489}{1.411}} P^{-0.735 \frac{-0.727}{-0.744}} h(n, B)$

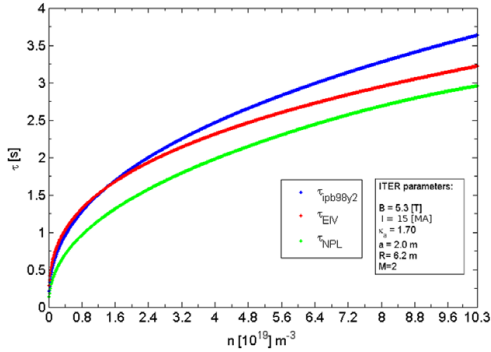


Figure 4. Comparison of the PLs and NPLs scaling expression behaviour with the plasma density at the parameters of ITER.

with dimensional quantities, the most performing models include one or more multiplicative saturation/squashing terms in the plasma current, plasma density or magnetic field. It is interesting to note that the method by itself selects these three quantities as the ones responsible for the saturation of the confinement time. However, the plasma volume, represented by the major radius R , is not found to cause any saturation as intuitively expected, since there is no physical reason for the confinement to present non-linear saturation terms scaling with volume.

Among the best scalings found by symbolic regression, the statistically most performing functional form for the confinement time, in terms of dimensional quantities, is reported in table 4. Also the power laws (PL1 and PL2) typically used as reference by the community are reported: PL1 is IPB98(y,2) and PL2 is EIV of [15]. The most important aspect of the non-power law (NPL) functional form is the presence of a single saturation term depending only on the ratio between density and magnetic field. Since the various physical quantities appear as products in this NPL expression, their multiplicative constants can be considered to have the right units to obtain the appropriate dimensionality as discussed in [15]. The scaling with density of the models in table 4 can be seen in figure 4, once the other physical quantities have been set to their values at ITER. To obtain the right dimensionality for NPL, it must be assumed that the multiplicative constant in front of the expression presents the dimensions: $[I]^{-1.00} [I]^{-0.2} [P]^{0.74} [t]$ (where l indicates the unit of length, t the unit of time, etc). The multiplicative constant in the exponent of the squashing term $h(n,B)$ has dimensions of $[B]^{-1.37} [I]^{4.1}$.

The equations of the scaling expressions have been used to generate their estimate corresponding to the values of the database and their pdfs have been compared with the

Table 5. Statistical estimators used to qualify the scaling reported in table 2. The KLD has been computed in a range of $\pm 6\sigma$ around the mean value of the data. MSE is the mean square error in units of second².

	k	AIC	BIC	MSE (s ²)	KLD
PL1	10	-19 416.86	-19 362.86	1.866×10^{-3}	0.0337
PL2	10	-19 084.36	-19 203.68	2.077×10^{-3}	0.0802
NPL	10	-19 660.03	-19 599.04	1.724×10^{-3}	0.0254

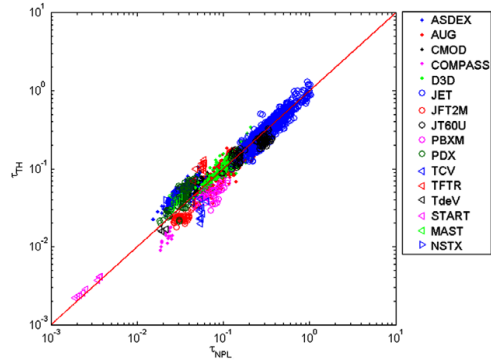


Figure 5. Log-Log plot of the energy confinement time of the proposed NPL model versus the experimental values.

experimental ones. The Kullback–Leibler divergence, the MSE and the BIC and AIC criteria all show that the NPL scaling is better than the PLs in interpreting the experimental data available. The comparison between the traditional PL and the NPL scalings, in terms of statistical indicators, is summarized in table 5, proving the best quality of the NPL regression. The good fit of the experimental data obtained with the NPL model is illustrated also graphically in figure 5.

In some cases, particularly in comparison with the scaling PL1, the improvement in the statistical indicators is not dramatic. On the other hand, all the indicators show consistently that the NPL is the best model, which gives a quite high degree of confidence in this scaling. Moreover, the improvement in the quality of the NPL expression in terms of KLD, which takes into account the probability distribution of the residuals, is quite significant. In any case, even if the superior properties of the NPL scaling are quite consolidated in statistical terms, its extrapolation capability could still be questioned. In reality, the better quality of the NPL expression in this respect is in a certain sense proved by its best performance in terms of AIC and BIC. These two indicators, being model selection criteria, already take into account the complexity of the equations and therefore tend to avoid overfitting (see appendix A1).

On the other hand, extrapolation is always a delicate matter, particularly when the gap from existing examples to new devices is as large as in the case of ITER. Therefore, to assess the potential of NPL also in this respect, a first extrapolation test has been performed consisting of fitting the NPL model on the database for currents below 2.5 MA and then extrapolating this fitted model to higher current data. The NPL scaling, once fitted and extrapolated, shows similar

Table 6. Power laws (PLs) and Non-Power Law model (NPL) fitted on the subset of data without the JET’s entries. The term $h(n, B)$ is:

$$h(n, B) = n^{0.279^{0.290}_{0.269}} \cdot (1 + e^{-13.645^{-12.328 - \frac{1}{B}} - 0.802 - \frac{0.728}{0.877}})^{-1}$$

PLs	$5.355^{5.39}_{5.30} \times 10^{-2} I^{0.670^{0.73}_{0.63}} B^{0.12^{0.17}_{0.07} H^{0.38^{0.41}_{0.35}} M^{0.43^{0.51}_{0.35}} R^{1.691^{0.78}_{1.59}} \epsilon^{0.53^{0.63}_{0.44}} \kappa_a^{0.39^{0.48}_{0.29}} P^{-0.54^{-0.52}}$
NPL	$0.0647^{0.0651}_{0.0643} \cdot I^{0.950^{0.972}_{0.937}} R^{1.216^{1.233}_{1.199}} \kappa_a^{0.280^{0.316}_{0.244}} P^{-0.503^{-0.516}_{-0.490}} h(n, B)$

Table 7. Statistical estimators used to qualify the scaling extrapolated on JET data.

	k	AIC	BIC	MSE (s^2)	KLD
PLs	10	-5842.20	-6720.79	1.578×10^{-2}	5.895
NPL	10	-6005.91	-6975.85	1.406×10^{-2}	3.829

statistical values respect to the PLs, but improves clearly the reconstruction of the high current data distribution ($KLD_{NPL} = 0.1258$, while $KLD_{PL1} = 0.3210$ and $KLD_{PL2} = 0.7478$). A second and more relevant test has been performed, by non-linearly fitting the various models using data of smaller devices and testing the results with JET data. Since the PL1,2 models have the same variables, only one fit has been performed and labelled as PLs. The non-linear fits for the PLs and the NPL have been performed using the weights obtained by the percentiles method described above. The PLs perform slightly better on the small machines ($MSE_{PLs} = 3.322 \times 10^{-4} s^2$ and $KLD_{PLs} = 0.0516$; while $MSE_{NPL} = 3.531 \times 10^{-4} s^2$ and $KLD_{NPL} = 0.0689$), but when the scaling are applied to JET data, the superiority of the NPL model in terms of the indicators considered can be clearly seen; the fitted models are reported in table 6 and their statistical estimators for JET data in table 7.

The higher extrapolation capability of the scaling expressions in NPL form motivates a revision of the expected performance in terms of confinement time for ITER. Using the equations of table 4, the predicted value of the confinement time for ITER ($n_e = 10.3 \cdot 10^{19} m^{-3}$, $\kappa_a = 1.70$, $I_p = 15$ MA, $R = 6.2$ m, $P = 87$ MW) is about $2.96^{3.46}_{4.14}$ seconds to be compared to the $3.6^{3.13}_{4.14}$ seconds of the traditional extrapolations obtained with power law scalings (IPB98). The non-linear scaling expression foresees a similar value but slightly lower confinement time for ITER compared to the traditional scaling expressions. The two estimates agree within the confidence intervals but would tend to diverge more for larger devices such as DEMO. This is due to the effect of the saturation term, which tends to be more significant at higher densities.

5. Results in terms of dimensionless quantities

The procedure described in section 3, consisting of symbolic regression plus non-linear fitting, has been also applied to the ITPA database in terms of dimensionless variables. The best scaling expression obtained is given by the following equation (3) and will be referred as AdNPL from now on:

$$\tau \cdot \omega_{ci} = (1.13)^{1.15}_{1.11} \cdot 10^{-6} \cdot \frac{\kappa_a^{1.93^{3.12}_{1.70}} \beta^{0.37^{0.41}_{0.33}} M^{0.57^{0.67}_{0.46}}}{\rho^{2.19^{2.22}_{2.16}} \nu^{0.40^{0.42}_{0.39}} q^{0.16^{0.23}_{0.08}}} \cdot \frac{-0.072^{-0.060}_{-0.085} \cdot \kappa_a^{1.18^{1.40}_{0.94}}}{+ - 0.009^{-0.006}_{-0.011} \cdot q^{1.08^{1.21}_{0.94}} + 0.15^{0.17}_{0.13} \cdot M^{0.07^{0.19}_{-0.05}}$$
 (3)

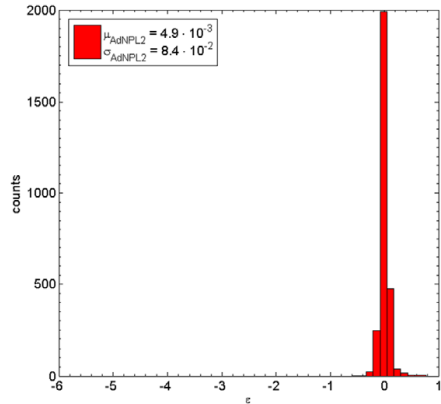


Figure 6. Residuals of the AdNPL model of $\tau \cdot \omega_{ci}$ in terms of dimensionless independent variables.

This time, in addition to a traditional power law factor, some saturation terms are included which are now additive. With regard to the dimensionality, it should be observed that all the additive terms are dimensionless and therefore the multiplicative constants are pure numbers.

To appreciate better the quality of the scaling expression (3), the residuals have been plotted in figure 6, which shows that their pdf can be quite well approximated with a zero centred Gaussian. It is worth emphasizing that regressing in terms of these non-dimensional quantities is another added value of our proposed methods. The used ITPA database presents too many collinearities and the term $\tau \omega_{ci}$ is not sufficiently independent from the dimensionless quantities to simply apply log regression. Since, as will be shown later, the new scaling given by equation (3) provides the same confinement time for ITER as the one using the dimensional quantities, this fact increases significantly the confidence in the obtained results.

Relation (3) has been compared with some of the most credited scaling expressions reported in the literature. In particular the two formulations chosen for the comparison are given in [15].

Since they have been derived starting from PL1 and PL2 [15], they have been respectively labelled as AdPL1, equation (4), and AdPL2, equation (5), from now on. Equation AdPL1 is:

$$\tau \cdot \omega_{ci} = 7.214 \times 10^{-8} \cdot \frac{M^{0.96} \epsilon^{0.73} \kappa_a^{3.3}}{\rho^{2.70} \beta^{0.90} \nu^{0.01} q^{3.0}}$$
 (4)

Again, to better appreciate the quality of the scaling expression, the residuals have been plotted in figure 7, which shows that their pdf cannot be well approximated with a zero centred Gaussian.

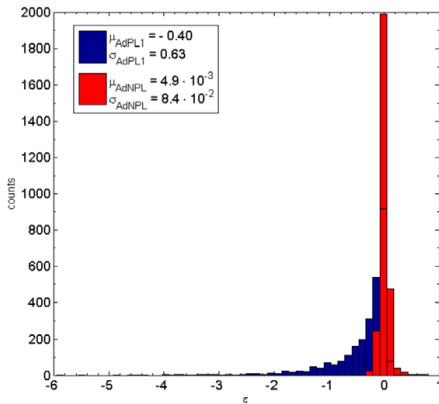


Figure 7. Residuals of equations AdPL1 and AdNPL.

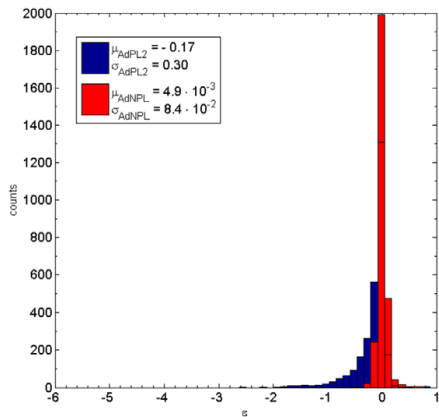


Figure 8. Residuals of equations AdPL2 and AdNPL.

Table 8. Statistical estimators used to qualify the scalings reported in terms of dimensionless quantities.

	k	AIC	BIC	MSE	KLD
AdPL1	9	-1650.59	-2533.00	0.5518	0.3316
AdPL2	9	-6034.11	-6744.95	0.1157	0.1875
AdNPL	14	-13 833.82	-13 758.91	0.715×10^{-2}	0.0567

The other main scaling expression suggested in [15] is AdPL2:

$$\tau \cdot \omega_{ci} = 1.836 \times 10^{-8} \cdot \frac{M^{0.49} \kappa_a^{3.34}}{\rho^{2.67} \beta^{0.57} v^{0.14} q^{1.84} \epsilon^{0.19}} \quad (5)$$

Also in this case the indicators are significantly worse than those of the equation in AdNPL form. The lower quality of this model for the interpretation of the ITPA database is easy to appreciate by inspection of the residuals reported in figure 8.

Finally table 8 summarizes the statistical estimators of the models expressed in terms of dimensionless quantities above:

The extrapolation capability of the non-power model has been tested as well. Again the non-linear fits have been

performed on the subset of data where all the JET’s entries have been removed and the fitted model can be found in table 9. The subset of data used to fit the free parameters of the AdNPL model considered contains 1411 entries. For the power law scaling, the original expressions, obtained over the entire database, have been retained (equations (4) and (5)).

The statistical estimators described above (AIC, BIC, MSE) have then been computed using the subset of JET’s data previously removed. The results are reported in the table 10, from which the superior extrapolation capability of the AdNPL scaling is evident in all indicators.

It is worth pointing out that the power law scalings AdPL1 and AdPL2 were derived in [15] using the entire database, including JET data. The fact that the new scaling expression AdNPL, derived by applying our approach only to the smaller devices, manages to extrapolate to JET better than such scalings is another very important proof of the quality of the new proposed methodology.

The quality of the AdNPL scaling and its good extrapolation behaviour to JET data have motivated the analysis of its estimate for ITER. In the following table 11, the prediction of the AdNPL scaling expression for ITER is compared to the ones of the other two AdPLs scalings from the literature. Moreover, fixing the ITER’s parameters, the trends of equations (3), (4) and (5) with the elongation κ_a and plasma volume have been reported in figure 9.

Another observation, which confirms the quality of the results obtained with the proposed methodology, is the general agreement between the estimates of the confinement time obtained both in terms of dimensional and dimensionless quantities. Indeed both scalings, NPL and AdNPL, provide in general very similar estimates of the confinement time over the experimental database available. This is shown graphically in figure 10, which reports the energy confinement time estimated by the expression NPL versus AdNPL. Also the extrapolation to ITER of the two scaling expressions are very similar as reported in figure 11. This remarkable agreement not only increases the confidence in the results but also highlights another advantage of the proposed methodology. As mentioned at the beginning of the section, in the literature the scaling expressions as functions of dimensionless quantities are typically derived by simple mathematical manipulation of the ones expressed in terms of dimensional quantities. They are therefore not the results of an independent exercise in regression. This is due to the limits of the databases, which present too many collinearities and dependencies of τ from the regressors when expressed in dimensionless form. Indeed the technique used to derive power laws, log regression, is based on the following assumptions: (a) no dependencies between the independent variable and the regressors, (b) no collinearity between the regressors and (c) normal distribution of the uncertainties (error bars) in all the variables. The available datasets typically do not satisfy any of these conditions.

On the other hand, symbolic regression is not based on the assumptions of log regression. It has indeed been tested with a series of numerical tests that the methodology proposed in this paper is robust against the aforementioned limitations of the available databases. A confirmation can be also obtained by the inspection of the obtained models, which are statistically much better than the ones in power law form obtained by rearranging the dimensional scalings.

Table 9. Non-dimensional non-power law model (AdNPL) fitted on the subset of data without JET entries.

$$\text{AdNPL} \quad (1.13)_{1.11}^{1.16} \times 10^{-6} \cdot \frac{\kappa_a^{1.571,82} \rho^{0.290,35} M^{1.001,22}}{\rho^{2,172,21} v^{0.390,41} q^{0.550,65}} - 0.062_{-0.070}^{-0.053} \cdot \kappa_a^{0.760,97} + -0.007_{-0.009}^{-0.004} \cdot q^{0.720,91} + 0.13_{0.12}^{0.14} \cdot M^{-0.06_{-0.15}^{0.03}}$$

Table 10. Statistical estimators for the extrapolation to JET of the dimensionless scaling expressions According to all statistical indicators AdNPL outperforms the traditional power laws.

	<i>k</i>	AIC	BIC	MSE	KLD
AdPL1	9	-294.94	-1102.55	79.905×10^{-2}	0.573
AdPL2	9	-2435.49	-3072.78	17.226×10^{-2}	0.283
AdNPL	14	-5610.85	-5723.52	1.756×10^{-2}	0.230

Table 11. Comparison of the extrapolated confinement times to ITER.

Equation	τ (s)
AdNPL	$2.97_{2.78}^{3.16}$
AdPL1	3.66
AdPL2	3.29
NPL	$2.96_{2.53}^{3.46}$

The saturation terms tend to smooth the trend of the confinement time when the quantities approach ITER’s values. In particular, as can be seen clearly in figure 9, the AdPL1 and AdPL2 foresee a quite abrupt increase of τ close to ITER’s values of various quantities, outside of the range where there can be any experimental confirmation of such an improvement. This is a general and quite problematic behaviour of all power law scalings.

6. Discussion, conclusions and further developments

In this paper, symbolic regression via genetic programming has been applied to the derivation of empirical scaling expressions for the energy confinement time in Tokamaks. The analysis has been particularized for the H-mode of confinement in terms of both dimensional and dimensionless quantities. The examples used for the present investigation belong to the ITPA international database, which include all of the most relevant machines in the world.

Contrary to the main results reported in the literature, the obtained empirical scalings are not in the form of power laws. Indeed they present either multiplicative or additive saturation terms.

These new expressions have been obtained with a methodology, symbolic regression via genetic programming, which generalizes previous attempts to find non-power law scalings [17–22]. Indeed in the previous studies devoted to non-power law scalings, the mathematical form of the scaling expressions had been assumed ‘a priori’ from empirical or theoretical considerations. On the contrary, using the techniques presented in this paper, even the mathematical forms of the scalings are purely data-driven, being selected by symbolic regression on the basis of the fitness function.

The superior quality of these new scalings, compared to the traditional power laws, has been demonstrated first of all with the help of a series of statistical indicators. To

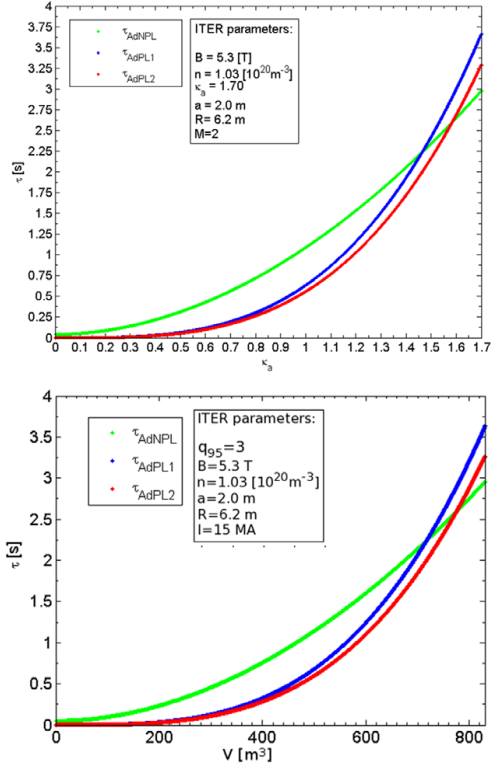


Figure 9. Comparison of AdPL1,2 and AdNPL scaling behaviour with the elongation and plasma volume at ITER’s parameters. The plasma volume has been chosen because it enters into other three dimensionless quantities; β , v^* , ρ^* .

complement this analysis, the extrapolation capability of the new scalings has been verified by dedicated investigations of different groups of devices (small and large machines) and of different parameters ranges (low and high currents). On the basis of the new found scalings, the confinement time to be expected in an ITER class device is about 20% lower than the predictions of the traditional power laws. This is due to the excess rigidity of the power law scalings (irrespective of the fact that they are expressed in terms of dimensional or dimensionless quantities), which probably tend to overestimate the confinement time in the case of large extrapolations. In any case, for ITER the estimates of the non-power law scalings and the IPB98 overlap within the confidence intervals. However, the difference is more significant for the generation of devices of the size of DEMO. This is due to the fact that the saturation term tends to become more important the larger the device.

On the other hand, the effect of the saturation with increasing density can be seen even in the present largest

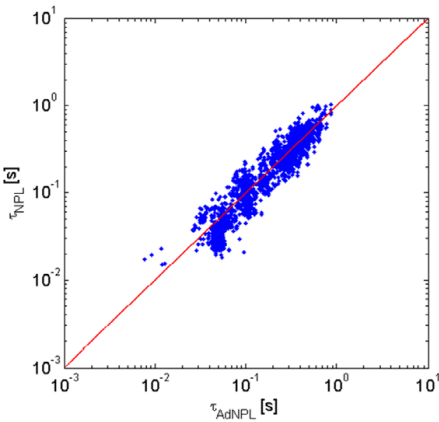


Figure 10. The estimates of the scaling expressions NPL and AdNPL for the entries of the ITPA database. The general agreement between the two empirical scalings is evident since they do not present any systematic discrepancy.

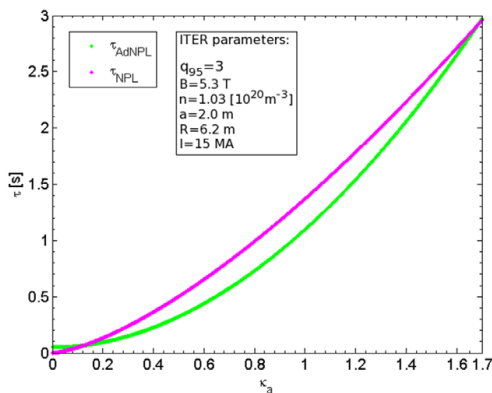


Figure 11. Comparison of NPL and AdNPL scalings with elongation at ITER's parameters.

devices, particularly JET, as shown in figure 12, which shows a comparison of the NPL scaling expression, found using the ITPA database with the usual DB3 selection, and the traditional IPB98 and EIV scalings. From the point of view of the physical interpretation, in our opinion the available database is not of sufficient quality to derive detailed conclusions. Anyway, this saturation seems to be linked to the plasma collisionality; above a certain level of this parameter, the confinement does not continue to improve with density as a power law. The more flexible symbolic regression identifies this dependence on collisionality as a saturation term, instead of an inverse power as is the case for the power law scalings IPB98(y,2) and EIV (see their dimensionless version reported in equations (4) and (5)). This saturation of the confinement with density is in line with the evidence reported in [16]. On the other hand, the available database does not contain a sufficient scan in triangularity to determine how this effect would be affected by the plasma shape, as was found again in [16] (the average

triangularity in the ITPA database is only 0.22 with a σ of about 0.1).

With respect to future developments, the obtained results are expected to provide significant inputs to the developments of physics based models of the energy transport [23–25]. Indeed the validation of transport models is one of the main scientific drives of research in JET, given the programme of experiments with different fuel mixtures on the route to the next D–T campaign. In this perspective, the proposed technique should be also applied to new databases, explicitly conceived to study the confinement in metallic devices. Indeed, even if the devised methodology is very powerful and the obtained results are statistically quite sound, these data-driven methods can learn only what is contained in the data. Therefore, particularly in the perspective of providing reliable extrapolations to ITER, specific and more updated databases should be built, to take into account the recent progress in the development of scenarios and the effects of the different wall materials. Dedicated studies should also address the issue of finding the most appropriate experiments to be carried out in order to discriminate between the various scalings, beyond what can be done with a statistical analysis of the presently available data sets. In this direction, certainly JET operation at high current with the new ITER Like Wall [26] should receive high priority, since validated data for optimized discharges around 4 and 5 MA is completely missing. A full D–T campaign in JET should also provide essential new information and allow answering most of the questions remained open after the DTE1 in 1997 [27].

The same methodology, which is absolutely general, can also be applied to other problems, since almost all the scaling expressions in the Tokamak community are expressed in terms of power laws. It is also worth mentioning that the developed technique of symbolic regression via genetic programming can also be used to extract symmetries and invariants from experimental databases [8]; therefore one natural application could be the validation of the dimensionless variables which are normally used to investigate the energy confinement in Tokamaks. Indeed the dimensionless quantities normally used in the literature, and therefore adopted also in this paper, have been derived from theoretical considerations but their adequacy has never been experimentally verified.

Appendix A. Symbolic regression via genetic programming for the identification of scaling expressions and their selection

As mentioned in the introduction, this paper describes the application of advanced techniques of symbolic regression (SR) via genetic programming (GP) to the problem of deriving scaling expressions for the confinement time from large databases. The main advantage of the proposed approach consists of practically eliminating any assumption about the form of the scaling expressions. The methods developed indeed allow identifying the most appropriate mathematical expression for the regression equations, the so called best unconstrained empirical model structure (BUEMS), and to demonstrate that it has the potential to better interpret the present experimental data for the confinement time in comparison with power laws (PLs). This appendix describes

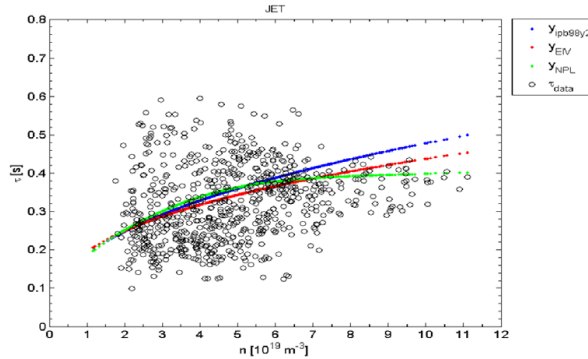


Figure 12. Scaling with the density for JET: $I = 2.239$ T; $M = 2.0$; $P = 10.129$ MW; $R = 2.917$ m; $\epsilon = 0.321$; $k_a = 1.589$. The green line is the new non-power scaling, obtained applying the DB3 selection to the entire ITPA database.

the mathematical basis of the tools implemented to perform the analysis used in the rest of the work. SR via GP is described in some detail in section A.1. The statistical criteria to qualify the obtained scaling expressions are described in section A.2 and the non-linear fitting procedures are briefly introduced in section A.3.

A.1. Genetic programming for database exploration

As mentioned before, the main objective of SR is to identify, for a given finite dataset, a class of appropriate model structures to describe the system under study without ‘*a priori*’ hypotheses (BUEMS). Solutions of varying levels of complexity can be generated and evaluated to obtain the best trade-off between accuracy and computational complexity. In this study, SR analysis has been performed using a genetic programming approach. SR via genetic programming is a non-parametric, non-linear technique that looks for both the appropriate model structure and the optimal model parameters simultaneously [8]. This approach provides a natural extension of the traditional linear and non-linear regression methods that fit parameters to an equation of a given model structure. GP is a systematic, domain-independent method that merely creates and searches for the best individual computer program (CP), i.e. the best mathematical expression for modelling the available database, among several possible randomly generated ones. The basic steps in a GP algorithm are shown in figure A1. The first step is the generation of the initial population of CPs (formulas in our case) and then the algorithm finds out how well an element of the population works according to some appropriate metrics. This performance of each model is quantified by a numeric value called fitness function (FF). In the second phase, as with most evolutionary algorithms, genetic operators (reproduction, crossover and mutation) are applied to individuals that are probabilistically selected on the basis of the FF, in order to generate the new population. That is, better individuals are more likely to have more child elements than inferior individuals. When a stable and acceptable solution, in terms of complexity, is found or some other stopping condition is met (e.g. a maximum number of generations or a tolerated error limits are reached), the algorithm provides the solution with best performance in terms of the FF.

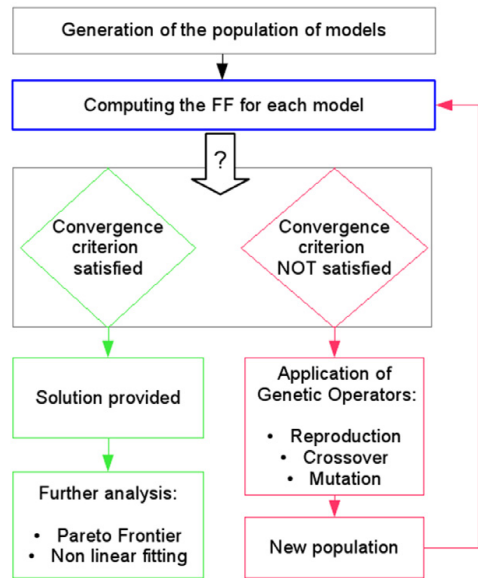


Figure A1. The basic flow chart of symbolic regression via genetic programming for the best unconstrained empirical model selection.

In this work, CPs are composed of functions and terminal nodes and can be represented as a combination of syntax trees, see figure A2. The function nodes can be standard arithmetic operations and/or any mathematical functions, squashing terms as well as user-defined operators. The function nodes included in the analysis performed in this paper are reported in table 1.

The terminal nodes can be independent variables or constants (integer or real). An example of a program representing the expression $3 \cdot P + B \cdot I^{0.5}$ is shown in figure A2. In this particular case, the function nodes set (F) is composed of multiplication, power, addition $F = \{*, +, \wedge\}$.

The terminal nodes set (T) in this example is composed of three variables and two constants $T = \{B, P, I, 3, 0.5\}$. The functions and terminals must satisfy two important conditions,

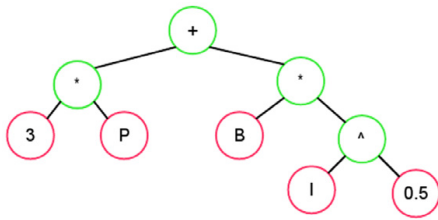


Figure A2. An example of syntax tree structure for the function $3 \cdot P + B \cdot I^{0.5}$. The function operator nodes (green) and the variable or constant nodes (red) are reported.

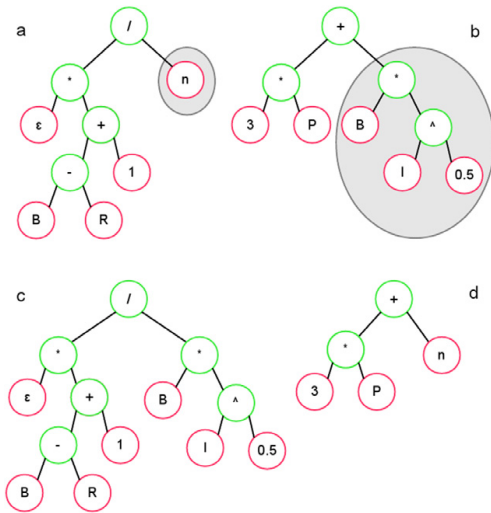


Figure A3. Crossover operation in genetic programming. (a) and (b) are the two selected models of the population used to produce the models (c) and (d) of the following iteration. The grey areas intersect the black branches, randomly selected during the genetic operation. Then all the leaves attached to these branches are swapped to produce the offspring (c) and (d).

in order to find an appropriate representation of the problem. These conditions are the closure property and the sufficiency property. The closure property includes protection of the function set and the terminal set against all inadmissible argument values, e.g. protection against negative square roots, division by zero, etc. The sufficiency property consists of the selection of the appropriate functions and terminals to solve the problem at hand.

The initial population of CP is formed by stochastic combining functions and terminals nodes and then it is evolved stochastically, generation by generation, to be converted into new, better populations. As mentioned before, evolution is achieved by using genetic operations such as reproduction, crossover and mutation. Reproduction involves selecting the program from the current population and allowing it to survive by copying it into the new population. The crossover operation involves choosing nodes in two parent trees and swapping the respective branches thus creating two new offsprings. Figure A3 illustrates the crossover operation. For example, if

the expressions for parent I (a) and parent II (b) are as follows before crossover:

$$\text{Parent I : } \frac{\varepsilon \cdot (B - R + 1)}{n}; \text{ Parent II : } 3 \cdot P + B \cdot I^{0.5}$$

the resulting offsprings (c) and (d) after the crossover operation are:

$$\text{Offspring I : } \frac{\varepsilon \cdot (B - R + 1)}{B \cdot I^{0.5}}; \text{ Offspring II : } 3 \cdot P + n.$$

A mutation operation consists of selecting a random node from the parent tree and substituting it with a newly generated random tree within the terminals and functions available.

As with most data-driven modelling tools, special attention must be paid to avoid overfitting the candidate models to the provided data. In this work, various forms of parsimony have been introduced and they operate at least at three different levels [9]. Already at this stage of building the trees, a method has been implemented which optimizes both fitness and syntax tree size. The shortest individual, the one having fewer nodes in its tree, is selected as the winner when two individuals are equally fit. This technique is particularly effective in controlling code dimension bloat, which is a phenomenon consisting of an excessive syntax tree growth without a corresponding improvement in fitness.

The first step in GP consists of selecting the initial population and therefore, together with the choice of the basis functions and operators, defines the search space, or phase space, which the algorithm will explore. This includes all the CPs, i.e. candidate BUEMS, which can be constructed by composing the initial population in all possible ways. In order to assure that the most appropriate solution is found, it is important to start with a sufficiently large initial population. Of course there is no theoretical criterion for determining the appropriate size of the initial population but a practical approach consists of increasing it until no significant new solutions are identified. At this point one can reasonably assume that the limitations are due to the database available more than to the exploratory technique. In its turn, the FF allows knowing which elements are appropriate to model the system under study. Fitness can be measured in many ways. To derive the results presented in this paper, the AIC criterion has been adopted [10] for the FF. The AIC form used is:

$$\text{AIC} = 2k + n \cdot \ln(\text{RMSE}) \quad (\text{A1})$$

In equation (A1), RMSE is the root mean square error, k is the number of nodes used for the model and n the number of y_{data} provided, so the number of entries in the database (DB). The FF parametrized above allows considering the goodness of the models, thanks to the RMSE, and at the same time their complexity is penalized by the dependence on the number of nodes. It is worth pointing out that the better the model, the lower its AIC. This is the second level of protection against overfitting. Another relevant comment regards the choice of the RMSE to determine the quality of the fit of the various models. This choice is driven by the fact that the RMSE satisfies very general statistical properties. In particular, it can be easily demonstrated that the RMSE is an unbiased estimator that maximizes the likelihood of the results in the case of Gaussian errors. This is the main reason why the

RMSE is so widely used in the statistical community [11, 13]; moreover its unbiased character makes the RMSE the best candidate to the present application, meant at verifying what is the most suitable mathematical expression for the scaling expressions. Indeed these classical statistical properties are not satisfied by the alternative indicators used in the literature and based on the logarithmic or relative deviations between the models and the data [15]. The choice of these alternative indicators was motivated by the 'a priori' choice of trying to fit power laws to the data and they are not the most adequate alternative for a more general exploration of the databases, as undertaken with the methodology proposed in this paper. Moreover these alternative indicators, based on the logarithmic or relative deviations, tend to penalize the contributions of large devices, in particular the entries of large τ (due to the saturating trend of the log function). This is not advisable in the case of extrapolations to ITER. Indeed the examples at large τ are already only a minority and if anything their importance should be emphasized and not reduced, as it happens if the quantity to be minimized by the fit is not the RMSE but it is proportional to $\log \tau$. In any case, it is also worth mentioning that more advanced but statistically sound indicators for the FF have been developed, in particular to better take into account both the distribution of the residuals and the errors in the measurements. Particularly powerful is the method of the geodesic distance on Gaussian manifolds [22]. On the other hand, it has already been checked that the implementation of such more sophisticated techniques to the ITPA database would not alter in any significant way the conclusions of the present paper.

A.2. Final model selection

However, the best result provided by the algorithm is not necessarily the best solution to the given problem. A more solid output can be found computing the Pareto frontier (PF). The PF is another tool designed to find the best compromise between the complexity of the models and the quality of their fit to the data. The complexity of the models is quantified by the number of nodes they contain; their goodness of fit is given by a suitable quantifier, the Bayesian information criterion (BIC) in our case. The PF is a plot of the BIC versus the complexity of the models. Typically, for each level of complexity, the three best models (according to BIC) are retained. Therefore, the PF is a reduced collection of BUEMS where each element represents the best models (according to the FF) for the subgroup of individuals having the same number of nodes. The PF is then visualized as reported in figure A4, plotting fitness versus complexity. The final solution, i.e. the required model, is finally chosen looking at the saturation part of the PF curve, after which an increase in the complexity of the models does not translate into a significant improvement in their quality (does not translate into a significant reduction in the BIC). This is the third level of protection against overfitting and allows finding a trade-off between the goodness of fit and complexity.

As mentioned, in order to increase confidence in the selection, these models are classified using a Bayesian criterion. Indeed, while the AIC criterion is used for the FF, the BIC is used for the PF to increase the generalization capability of the model selection. The BIC form used is:

$$\text{BIC} = n \cdot \ln(\sigma_{(\epsilon)}^2) + k \cdot \ln(n), \quad (\text{A2})$$

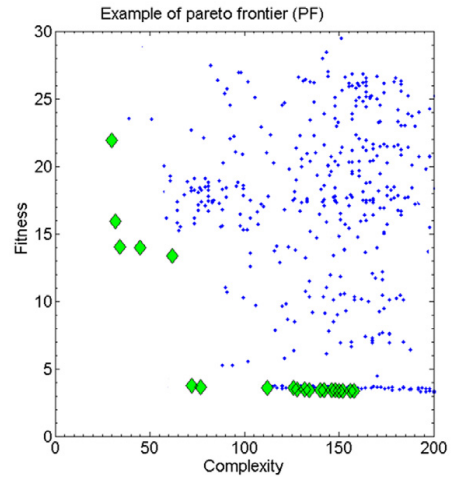


Figure A4. The plot shows an example of a Pareto frontier: the best models are plotted in green (the whole pool of models is in blue). In our case, fitness is quantified by the BIC indicator and complexity by the number of nodes in the model.

where $\epsilon = y_{\text{data}} - y_{\text{model}}$ are the residuals, $\sigma_{(\epsilon)}^2$ their variance, calculated with respect to the mean of the residuals, and the other symbols are defined in analogy with the AIC expression. Again the better the model, the lower its BIC.

With regard to the use of the two indicators AIC and BIC, it should be noticed that AIC is typically defined in terms of the sum of the square residuals (the application of the square root is immaterial). BIC is traditionally defined in terms of the variance, in which the difference is taken from the average of the residuals. So conceptually the two indicators are different and it is reassuring when, as in our analysis, they both give the same response on the quality of the models. We would also like to point out that, in any case, minor variations in the definition of these criteria are immaterial since the absolute values of the indicators are not important and what matters is the relative ranking of the models (which we have checked is unaffected by differences in the definitions).

The confidence and the stability of the chosen BUEMS are also important aspects of the analysis. To achieve this goal, several runs of SR via GP are launched varying the maximum number of trees and varying the initial population size. The analysis is performed along the lines previously described each time and in this way the chances of finding a good BUEMS are enhanced. To reduce the probability that relevant solutions are missed, a typical approach (the one that we have adopted) consists of increasing the number of trees and enlarging the initial population until the results are consistent and not vary with these parameters. In general, the models discussed in this paper have been selected out of a population of about 200 000 BUEMS.

A.3. Non-linear fitting

Once selected the best model with symbolic regression as described in the previous section, a non-linear fitting technique,

discussed briefly in this section, has been applied to improve the behaviour of the BUEMS on the data. Basically SR via GP is used to determine the functional form of the BUEMS and then the exact parameters of the models are determined by the non-linear fitting. Indeed optimized routines for non-linear fitting exist, which guarantee good results and are computationally efficient. They also provide confidence intervals for the parameters of the models. It is worth mentioning that the previous criteria, AIC and BIC, used to quantify the quality of the models, have been computed for the non-linearly fitted models.

The algorithm implemented for the non-linear fits [11, 23, 24, 25] aims at finding the best parameters \vec{c} minimizing the sum of squares of the residuals:

$$\begin{aligned} \min_{LB \leq \vec{c} \leq UB} & \left[\sum (\vec{e}(\vec{x}; \vec{c}, \vec{c}_0))^2 \right] \\ = \min_{LB \leq \vec{c} \leq UB} & \left[\sum (\vec{y}_{\text{data}}(\vec{x}) - \vec{y}_{\text{model}}(\vec{x}; \vec{c}, \vec{c}_0))^2 \right]. \quad (\text{A3}) \end{aligned}$$

The algorithm uses a trust region method based on an interior reflective Newton method. In equation (1) \vec{c}_0 stands for the vector of initial conditions provided by the genetic algorithm, the upper bounds (UB) and the lower bounds (LB) define instead the ranges of variation where the requested parameters \vec{c} can be found and are obtained after the first iteration. Those boundaries correspond in fact to the 99% of confidence level of their initial conditions \vec{c}_0 . The recursive procedure developed prevents the parameters to exceed those initial boundaries; moreover it determines the stability of both constants and exponents in \vec{c} to reach convergence. For this reason, a tolerance of 10^{-6} has been set for the difference between the values assumed by the fitted parameters between two successive iterations. Once the difference falls below the previous value, again the Jacobian and the residuals are used to estimate the parameters' confidence levels (95%). Finally, the weights (previously calculated in the first step of the procedure) can be easily applied by multiplying each term in the previous sum by the required weight.

Once fitted, in order to increase the generalization of the analysis and to make easier the comparison between different models, the RSS (sum of squared residuals) is used instead of the RMSE in equation (A1) and at the same time the number of parameters (p) plus one replaces the number of nodes for the complexity (k) both in equation (A1) and in equation (A2), so k is $k = p + 1$.

The best BUEMS, after the non-linear fitting, are then qualified by an additional estimator, the Kullback–Leibler divergence (KLD), calculated using the kernel density estimation (KDE) [12]. The KDE is the representation of the continuous probability distribution function of the selected model $p(\vec{y}_{\text{model}}(\vec{x}))$ and of the experimental data $q(\vec{y}_{\text{data}}(\vec{x}))$. Then the aim of the KLD is to quantify the difference between

the computed KDEs, in other words to quantify the information lost when $p(\vec{y}_{\text{model}}(\vec{x}))$ is used to approximate $q(\vec{y}_{\text{data}}(\vec{x}))$ [13]. The KLD is defined as:

$$\text{KLD}(P||Q) = \int p(x) \cdot \ln(p(x)/q(x)) dx, \quad (\text{A4})$$

Where the symbols have been defined as above. The Kullback–Leibler divergence assumes positive values and is zero only when the two pdfs, p and q , are exactly the same. Therefore the smaller the KLD is, the better the BUEM approximates the data, i.e. the less information is lost by representing the data with the model.

References

- [1] Wesson J. 2004 *Tokamaks* 3rd edn (Oxford: Clarendon)
- [2] Barenblatt G.I. 2003 *Scaling* (Cambridge: Cambridge University Press)
- [3] Mitchell M. 2009 *Complexity: a Guided Tour* (Oxford: Oxford University Press)
- [4] Murari A. et al 2013 *Nucl. Fusion* **53** 043001
- [5] Murari A. et al 2012 *Nucl. Fusion* **52** 063016
- [6] Connor J.W. and Taylor J.-B. 1977 *Nucl. Fusion* **17** 5
- [7] Kadomtsev B.B. 1975 *Sov. J. Plasma Phys.* **1** 389–91
- [8] Schmid M. and Lipson H. 2009 *Science* **324** 81–5
- [9] Koza J.R. 1992 *Genetic Programming: On the Programming of Computers by Means of Natural Selection* (Cambridge, MA: MIT)
- [10] Hirotsugu A. 1974 A new look at the statistical model identification *IEEE Trans. Autom. Control* **19** 716–23
- [11] Douglas B. and Donald W. 1988 *Nonlinear Regression Analysis and Its Applications* (New York: Wiley)
- [12] Silverman B.W. 1986 *Density Estimation for Statistics and Data Analysis* (London: Chapman and Hall)
- [13] Burnham K.P. and Anderson D.R. 2002 *Model Selection and Multi-Model Inference: A Practical Information-Theoretic Approach* 2nd edn (Berlin: Springer)
- [14] The International H-Mode Confinement Database Version DB3v13f <http://efdasql.ipp.mpg.de/hmodepublic/DataDocumentation/Datainfo/DB3v13/db3v13.htm>
- [15] McDonald D.C. et al 2007 *Nucl. Fusion* **47** 147–74
- [16] Saibene G. et al 1999 *Nucl. Fusion* **39** 1133 doi:10.1088/0029-5515/39/9/307
- [17] Takizuka T. 1998 *Plasma Phys. Control. Fusion* **40** 851–5
- [18] Thomsen K. et al 2002 *Plasma Phys. Control. Fusion* **44** A429–35
- [19] Kardaun O.J. et al 2000 *Proc. 18th IAEA Fusion Energy Conf. (Sorrento, Italy, 2000)* ITERP/04 www.iaea.org/programmes/rip/physics/fec2000/html/node238.htm
- [20] Kardaun O.J. 2005 *Classical Methods of Statistics* (Berlin: Springer)
- [21] Murari A. et al 2015 *Plasma Phys. Control. Fusion* **57** 014008
- [22] Peluso E. et al 2014 *Plasma Phys. Control. Fusion* **56** 114001
- [23] Bateman G. et al 2003 *Plasma Phys. Control. Fusion* **45** 1939
- [24] Polevoi A.R. et al 2002 *J. Plasma Fusion Res. Ser.* **5** 82
- [25] Boucher D. and The 1D ITER Modelling Working Group 2000 *Nucl. Fusion* **40** 1955
- [26] Lioure A. et al 2005 *Fusion Eng. Des.* **74** 141–6
- [27] Thomas P.R. et al 1998 *Phys. Rev. Lett.* **80** 5548

MICROWAVE AND FAR INFRARED DIAGNOSTICS

A. Krämer-Flecken

Institut für Energie und Klimaforschung / Plasmaphysik, Forschungszentrum Jülich
D-52425, Jülich, Germany

I. INTRODUCTION

The measurement of plasma quantities is a difficult task since the plasma cannot be treated like *normal* material. The properties of a plasma with an electron density $\leq 1 \times 10^{20} \text{ m}^{-3}$ and temperatures up to several keV asks for sophisticated probes. Any measurement of plasma quantities with solid probes will yield interactions with the plasma and cause a perturbation of the measured quantity. Inside a hot plasma those methods are not applicable, since they cause a contamination which, on the long run, ends in a disruption of the plasma. Therefore it is necessary to use optical properties as refraction and reflection as tool for plasma diagnostic. Plasmas in fusion experiments are transparent when looked with human eyes. However, choosing the right wavelength where refraction effects are large, plasma properties can be accessed. The propagation of millimetre and sub millimetre waves in a plasma is quite sensitive to refraction and reflection. In addition those waves are less demanding regarding their installation requirements on fusion facilities either tokamak or stellerator due to the little space requirements. Microwave radiation can easily be guided in wave guides, either oversized or fundamental ones, which can be bend around corners and which widens the area of operation. Furthermore due to the rapid growing application in telecommunication, active as well as passive microwave components have become less expensive and more powerful.

Refraction and reflection allows to obtain information on the plasma density from the refractive index, when actively probed by microwaves. An other way of diagnosing a hot plasma is the measurement of the emitted radiation in the microwave range. With both methods main plasma parameters as the electron density and the electron temperature can be measured quite accurate and reliable. However, also the measurement of fluctuations in density and temperature and the determination of the plasma current density are possible with sophisticated microwave diagnostics. Using more than one observation location and performing cross correlation analysis yields information on the propagation of the plasma and the properties of turbulent structures can be achieved under certain assumptions. Those measurements contribute a lot on the understanding of turbulent transport and

the interaction of different scales from microscopic (*turbulence*) to macroscopic (*flows*).

In the following section the propagation of electro magnetic waves in a plasma is reviewed. Sections III to VI are devoted to different diagnostic techniques. Section VII gives an outlook on future applications.

II. THE DISPERSION RELATION FOR THE PROPAGATION IN PLASMAS

Starting point is the *Appleton-Hartree* equation [1] which relates the refractive index N to the probing frequency ω .

$$\begin{aligned} N^2 &= 1 - \frac{A \cdot (1-A)}{1-A-1/2B^2 \sin^2 \theta \pm C} \quad (1) \\ A &= \frac{\omega_{pe}^2}{\omega^2} \quad ; \quad B = \frac{\omega_{ce}}{\omega} \\ C &= \left[(1/2B^2 \sin^2 \theta)^2 + (1-A)^2 B^2 \cos^2 \theta \right]^{1/2} \end{aligned}$$

Here ω_{pe} denotes the plasma frequency and ω_{ce} the cyclotron frequency:

$$\omega_{pe} = \sqrt{\frac{n_e e^2}{\epsilon_0 m_e}}; \quad \omega_{ce} = \frac{eB}{m_e \gamma} \quad (2)$$

γ takes into account relativistic effects, e denotes the electron charge, m_e the electron mass, n_e is the electron density and B the local magnetic field. The angle θ in Eq. 1 denotes the angle between the wave vector and the magnetic field. In the case $\theta = 0$ the propagation is parallel to the magnetic field. For $\theta = \pi/2$ we have a perpendicular propagation. In this case two solutions for the refractive index are possible, depending on whether the electric field vector of the wave \mathbf{E} is parallel to the magnetic field (*O-Mode*) or perpendicular (*X-Mode*). The refractive index for both cases is given in eq. 3.

$$\begin{aligned} O-Mode \quad N^2 &= 1 - \frac{\omega_{pe}^2}{\omega^2} \quad (3) \\ X-Mode \quad N^2 &= 1 - \frac{\omega_{pe}^2 (\omega^2 - \omega_{pe}^2)}{\omega^2 (\omega^2 - \omega_{pe}^2 - \omega_{ce}^2)} \end{aligned}$$

All microwave diagnostics studying the propagation of millimetre waves are based on these equations, regardless of being applied in fusion plasmas, weather broadcast, or climate research.

III. INTERFEROMETRY

A standard tool for measuring the electron density n_e within a plasma is an interferometer. In this case we have the refractive index for X -Mode which is investigated with the additional assumption that $\omega_{ce}/\omega \ll 1$, neglecting the effects of the magnetic field. The measurement of the electron density is done by comparing the phase change of two wave trains, one travelling through the plasma, and another travelling through vacuum or air and which is used as reference. The phase change for a given wave number k an frequency is then given by:

$$\Delta\Phi = \int (k_{plasma} - k_0)dl = \int (N - 1) \frac{\omega}{c} dl \quad (4)$$

The above equation can be rewritten with the use of the critical electron density n_c at the cut-off layer where $N = 0$. From Eq. 2 we achieve the critical density as

$$n_c = \frac{\epsilon_0 m_e \omega^2}{e^2} \quad (5)$$

yielding for the phase change:

$$\begin{aligned} \Delta\Phi &= \frac{\omega}{c} \int \left(\sqrt{1 - \frac{n_e}{n_c}} - 1 \right) dl \\ &\approx \frac{\omega}{2cn_c} \cdot \int n_e dl \end{aligned} \quad (6)$$

Here, it has been assumed that $n_e \ll n_c$, truncating the expansion of the square root expression after the first term. Such a phase change can be measured by an interferometer.

Several types of interferometers exist. Two arm interferometer like *Michelson Interferometer* or *Mach-Zehnder-Interferometer* (Fig. 1) and multiple beam interferometer as *Fabry-Perot-Interferometer*.

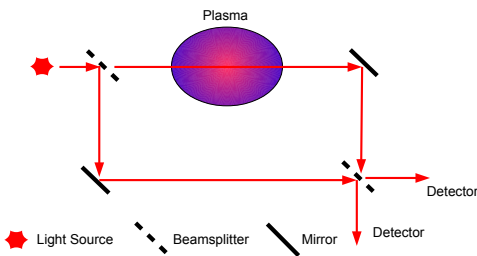


Figure 1: Schematic view of a Mach-Zehnder Interferometer

The major difference between the Michelson- and the Mach-Zehnder-Interferometer is the fact that the reference as well as the plasma path are only passed once in the Mach-Zehnder set-up. Two major drawbacks of all those types of interferometer are:

- The ambiguity of phase changes for $\Delta\Phi = n \cdot \pi$

- Amplitude variations due to refraction or absorption of the beam

To overcome those problems the frequency of the reference wave is shifted with a rotating grating. The detector will mix the two incoming frequencies from the plasma path ω_1 and the reference path ω_2 and yield an intermediate frequency $\Delta\omega_0 = \omega_1 - \omega_2$ and its higher harmonics. Such a detection scheme is called a heterodyne receiver. An additional phase change due to the plasma yield $\Delta\omega = \Delta\omega_0 + d\Phi/dt$. This allows a distinction between positive and negative phase changes.

To allow for interferometric measurements of n_e the following conditions have to be fulfilled.

- Sufficient power level for splitting the beam into radial separated chords and enough to detect at the same time 1% modulation with a time resolution $\leq 100 \mu s$
- No cutoffs or resonances in the plasma for the desired frequency deduced by the maximum n_e which can be achieved
- Small angular deviation of the beam ($\alpha \leq 10 \text{ mrad}$)

An interferometer-polarimeter of Mach-Zehnder type [3] using a HCN-laser operating at a frequency of 800 GHz was installed at TEXTOR (see Fig. 2) where the signals are detected by pyroelectric detectors. As can be seen from Eq. 6 the interferometric phase shift is integrated along the line of sight yielding line averaged densities. However, of importance is the local electron density and its profile. To fulfill an accurate calculation of the local density from the phase shift, tomographic methods have to be used. The phase shift has to be measured within a poloidal cross section of the tokamak with several chords at different radial position. Therefore assumption about the shape and symmetry of the plasma have to be made. With an inversion procedure (Abel-Inversion) a density profile is calculated.

A draw back of the previous mentioned short wavelength is the sensitivity to vibrations of the interferometer frame. Already small vibrations yield a disturbance of the path length and therefore an error in the phase measurement. To overcome this problems (i) the optics has to be mounted in a rigid frame or (ii) two different wavelength should be used. The shorter wavelength measures the disturbance of the diagnostic and the longer wavelength measures the refractive effects due to the plasma. In more sophisticated experiments it is even possible to detect the disturbance of the path length and try to adjust the path length by a moving mirror. Another problem is the bending of the chords. The plasma acts itself as a lens. Specially in the case of steep density gradients at the plasma boundary the changes in the refractive index will be quite large. As a consequence

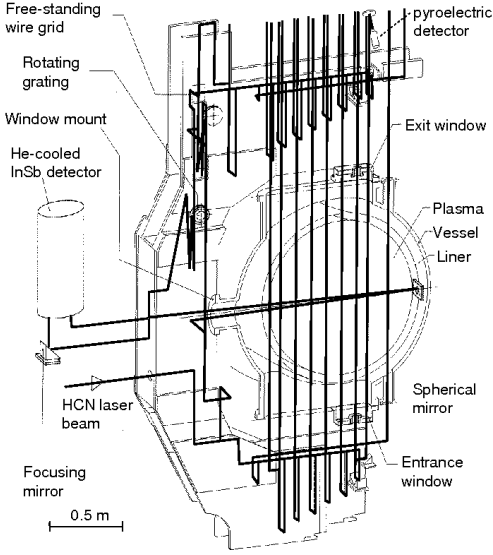


Figure 2: Schematic view of the nine channel HCN-interferometer-polarimeter as it was installed at TEXTOR. The thick lines show the optical path of the nine vertical, the horizontal and the reference channels.

the optical path length will increase and yield larger phase delays or the deviation will result in a loss of signal. In this case the inversion procedure will result in density profiles with higher edge densities and smaller one in the plasma center. From the geometrical point of view a multi chord interferometer is best suited for devices with circular plasma cross section. In D-shaped plasma only a few chords can be realized, mainly due to the restricted access from the top of the vessel. In this case other diagnostics are needed to calculate the required density profiles.

A. Dispersion Interferometry

The main drawback of a Mach-Zehnder or Fabry-Perot interferometer is the sensitivity to vibrations, specially for large devices like ITER and DEMO. This drawback can be overcome by using a second interferometer with a different wavelength and operated at the same path as the first one. or by using a dispersion interferometer [4, 5] which is not sensitive to phase changes due to vibrations. Probing and reference path use the same geometrical path but at different frequencies. The initial beam at frequency ω is partly doubled in frequency. Therefore frequency doubling crystals are used. Both waves at 1^{st} and 2^{nd} harmonic propagate through the plasma. After passing the plasma the 1^{st} harmonic is again doubled in frequency. In a next step the original frequency is filtered out. The interference pattern of the two waves at 2^{nd} harmonic are detected by a photo detector (see

Fig. 3). The phase difference is the difference between twice the phase of the fundamental frequency and the phase of the 2^{nd} harmonic travelling through the plasma and can be expressed by:

$$\Delta\Phi = \frac{\omega}{c} \int [N(\omega) - N(2\omega)] dl \quad (7)$$

With the equation for the refractive index N_O the phase change can be written as:

$$\Delta\Phi = \frac{3e^2}{8\pi\epsilon_0 m_e c^2} \lambda \langle n_e l \rangle \quad (8)$$

with λ being the probing wavelength and $\langle n_e l \rangle$ the line integrated density. It should be noted that $\Delta\Phi$ increases with the used wave length. However, a large λ will be more limited by refraction. A compromise for the used wave length is found in CO_2 -Laser at 28.3 THz corresponding to $\lambda \approx 10 \mu m$. Such a system is installed e.g. at LHD [6] for density control. It has a temporal resolution of 300 μs and a sensitivity of $\langle n_e l \rangle_{min} \leq 3 \times 10^{17} m^{-2}$.

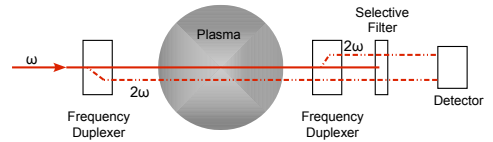


Figure 3: Principle scheme of a dispersion interferometer from [7].

IV. POLARIMETRY

Due to the magnetic field the refractive index is different for the two circular components of a linear polarized incident wave. In the case of a plasma current, generating a poloidal magnetic field, the interferometer-polarimeter set-up shown in Fig. 2 is sensitive to the parallel component of the poloidal magnetic field [3]. For a propagation of the wave parallel ($\theta = 0^\circ$) to the magnetic field component, the refractive index can be achieved from Eq. 1 retaining only first order terms in B, then we get:

$$N_{X,O}^2 \approx 1 - A \pm AB \cos\theta \quad (9)$$

The difference in N causes a different propagation speed of the O- and X-mode wave, which causes a rotation of the electric field vector of a linearly polarized wave (*Faraday Rotation*). This is a rotation of the polarization plane. The phase change along the propagation direction (z -axis) is given by:

$$\Delta\Phi = \frac{\omega}{c} (N_X - N_O) z \quad (10)$$

The Faraday rotation angle α depends only on B and n_e . It can be expressed by the measured phase change and making use of Eq. 9 where only the first order terms in ω_{ce}/ω are considered.

$$\begin{aligned}\alpha &= \frac{\Delta\Phi}{2} = \frac{e}{2m_e c} \int \frac{n_e \mathbf{B} \cdot d\mathbf{l}}{n_e(1 - n_e/n_c)^{1/2}} \\ &\approx \frac{e}{2m_e c} \int \frac{1}{n_c} \cdot n_e \mathbf{B} \cdot d\mathbf{l}\end{aligned}\quad (11)$$

This last approximation is valid if the ratio of electron density to critical density (n_c) is less than one. With the measurement of α the poloidal magnetic field can be estimated. The approximation is only depending on n_c which itself is a function of the used wavelength and the magnetic field, so that a numerical approach can be expressed by

$$\begin{aligned}\alpha [\text{degree/cm}] &= 1.5 \times 10^{-17} \lambda^2 [\text{mm}] \\ &\times n_e [\text{cm}^{-3}] B [\text{Gauss}]\end{aligned}\quad (12)$$

After the measurement of the poloidal magnetic field at different radial positions the plasma current profile $j(r)$ as well as the q -profile can be estimated.

V. REFLECTOMETRY

Reflectometry measurements are based on the reflection of a probing microwave (ω_{ref}) at a cutoff layer (R_{co}) corresponding to a cut-off frequency (ω_{co}). The phase of the reflected wave contains information on the position of the cut-off layer and information on the density fluctuations [8]. At R_{co} the refractive index is $N = 0$ and depends on the polarization of the launched microwave (e.g. selected by the orientation of the launching and receiving antenna). The phase change can be calculated by Eq. 13,

$$\Phi = \frac{2\omega}{c} \int_{R_{edge}}^{R_{co}} N_{X,O}(R, \omega) dR - \frac{\pi}{2}\quad (13)$$

where c denotes the speed of light and $N_{X,O}$ the refractive index for X - or O -mode polarization as deduced from Eq. 3. At the R_{co} a phase jump of $\pi/2$ will arise. Reflectometry can be done in O -Mode and X -Mode, respectively. In case of X -Mode reflectometry N_X is a function of the magnetic field and it has the advantage that $n_e(r) = 0$ at $\omega_{co} = \omega_{ce}$ which offers a stable initialization condition for the measurement of density profiles. Another advantage of X -Mode reflectometry is the larger access in the radial range of the density profile. With O -mode reflectometry only half of the profile can be measured, since a reflectometer can not look behind the horizon. Concerning its accuracy the radial resolution depends on the density scale length and the fluctuation level. Reflectometry is therefore a good tool for plasma density profile measurements in the gradient region and for

density fluctuation (turbulence) measurements. The detection of the reflected signal is similar to interferometry. The reflected and the reference signal at a slightly different are mixed. The resulting intermediate frequency serves together with the carrier as input for a quadrature detector which produces two output signals with 90° phase difference for each antenna. An overview on the diagnostic potential of the reflectometry can be found in [9].

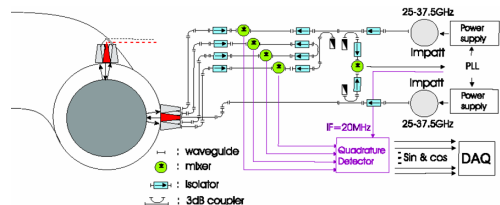


Figure 4: Schematic view and principal of the measurement of the heterodyne poloidal correlation reflectometer at TEXTOR. Microwave switches not shown in the figure allow to switch between signals from top and midplane array.

A. Density Profiles

The determination of the density profile was somewhat difficult in the past due to the large sweep times of the available microwave generators. The sweep time of the generators should be less or equal the life time of the fluctuation which is in the order of 10-20 μs . Today's technique allows a sweep time less than 10 μs using hyperabrupt varactor tuned oscillators (HTO) [10, 11, 12]. In this case the fluctuations can be considered as frozen during one sweep of the oscillator. For profile measurements both polarizations can be used. Independent from the polarization the net time delay (τ) is given by:

$$\tau(f) = \frac{d\Phi}{d\omega} = f_B \left(\frac{df}{dt} \right)^{-1}\quad (14)$$

Here f_B denotes the beat frequency of the reference and the reflected wave and $d\Phi/d\omega(f)$ denote the group delay. It is essential to know the frequency response on the evolution of the generator voltage, because it causes uncertainties in the estimation of the time delay. The density profile is reconstructed from an initialization procedure, which in case of O -mode could be quite complicated. Furthermore the sampling rate for such a system should be large, so that the fluctuations can be treated as frozen. In today set ups a sampling frequency up to 100 MHz and more is necessary to have a good frequency resolution during one sweep.

B. Turbulence and Rotation Measurements

In general reflectometry is most sensitive to long wavelength turbulence. With one launching and receiving antenna information on the phase fluctuation

can be retrieved from reflectometry. This can be related to density fluctuations as long as the phase fluctuation are small and not saturated. However, at the plasma edge the turbulence level becomes large and small angle scattering effects disturb the measurement. It makes the estimation of the turbulence level more complicated and sometimes even impossible.

The use of more than one receiving antenna surrounding the launcher allows the calculation of cross correlation as function of the toroidal and poloidal separation of antennae. The so called Correlation Reflectometry (CR) is often used to measure turbulence properties. This can be done either by using (i) an array of antennae measuring at toroidally and/or poloidally separated positions or (ii) by two reflectometers operating at different frequencies to obtain radial information on the turbulence structure and on the radial transport. A combination of both methods is possible as well. Using antennae arrays poloidally or toroidally separated, as shown in Fig. 4, yield further information on the poloidal or toroidal structure of the turbulence, e.g. poloidal correlation length (λ_{\perp}) and decorrelation time (τ_{dc}). However, the propagation time Δt between receiving antenna must fulfil the condition $\Delta t = \Delta s/v_{\perp} \leq \tau_{dc}$, where Δs is the distance between the correlated antennae. In Fig. 5 an example from poloidal CR shows the complex amplitude and cross phase spectra deduced from the quadrature detectors.

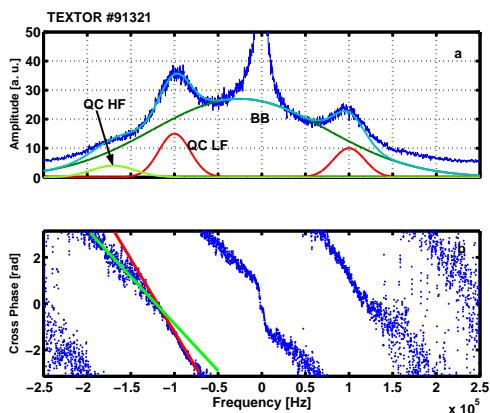


Figure 5: (a) Amplitude spectrum obtained from reflectometry showing the different fluctuation components. (b) The different propagation velocities are determined from the slopes in the cross phase spectrum.

From the complex amplitude spectrum different types of fluctuations can be recognized. Most pronounced are broad band fluctuations (BB) and the quasi coherent modes at low and high frequency (QC LF and QC HF). The different propagation velocities of the quasi

coherent mode are obvious from the different slopes in the cross phase spectrum. For signals from poloidal separated antennae the angular velocity (Ω_{turb}) of the turbulence is measured from the crossphase (Φ) between the signals from two or more antennae [13].

$$\Omega = \frac{2\pi \alpha}{d\Phi/df}, \quad (15)$$

where α is the angle between the antennae. With the assumption that the additional phase velocity of the turbulence is small compared to the poloidal plasma velocity $\Omega_{turb} \approx \Omega_{Plasma}$ is valid. From the knowledge of the diamagnetic drift velocity (v_{dia}) the estimation of the radial electric field $E_r = (v_{turb} - v_{dia}) \cdot B$ where $v_{turb} = \Omega_{turb} \cdot r_c$, is possible. Here, r_c is the radius of the flux surface where the reflection takes place. Furthermore fluctuations in Ω_{turb} can be deduced if the sampling frequency is large enough compared to the frequency of the instability under investigation.

Recently it has been demonstrated that poloidally and toroidally separated antennae allow the determination of the inclination angle of the magnetic field line at r_c [14]. The projection of the distance of different antennae combinations on the direction of v_{\perp} , B_{\perp} (see Fig. 6) yield different values for delay time Δt . With the assumption of a constant v_{\perp} the ratio of the measured delay time is proportional to the magnetic pitch angle.

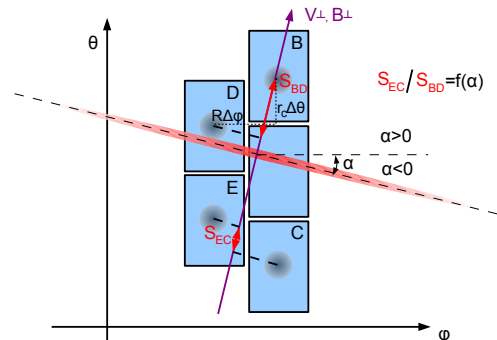


Figure 6: Schematic view of an antennae array. It shows the projection on the v_{\perp} axis for combinations BD and EC.

An alternative method to deduce plasma velocity is the Doppler reflectometry [15]. Here the plasma velocity is deduced from the Doppler shift of the receiving microwave. Instead of measuring the 0th order reflection which is used in standard reflectometry higher order diffraction is used for Doppler reflectometry (see Fig. 7). In most cases a tilted antenna is used for the launching and receiving microwave. In this case the tilting angle is adjusted to measure the -1st order of diffraction and a monostatic antenna arrangement is sufficient. Such an set up is sensitive to

certain wave number values (k_{\perp}) depending on the tilt angle.

$$k_{\perp} = 2k_0 \sin \alpha_{\text{tilt}} \quad (16)$$

Here k_0 is the wave number of the probing microwave in vacuum. If the reflection layer in the plasma is propagating with a velocity v_{\perp} , a frequency shift of $\Delta\omega = -v_{\perp} \cdot k_{\perp}$ is observed. As for CR, Doppler reflectometry is able to deduce the radial electric field when the phase velocity of the turbulence can be neglected. Doppler reflectometry extends the measurement of turbulence properties to higher k_{\perp} values and opens the window to electron temperature gradient driven turbulence. In case several Doppler reflectometry systems are operated at different frequencies cross correlation analysis can provide information on radial wavelength of the turbulence. A challenge

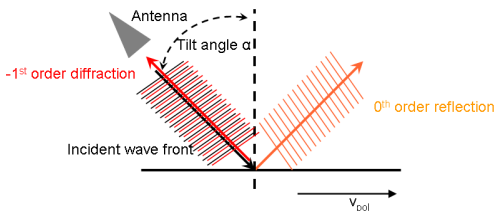


Figure 7: Principle of Doppler reflectometry. The 1st order diffraction contains information on the propagation of the turbulence.

for Doppler reflectometry is the development of non-mechanical steerable antennae which can work at different centre frequencies and where a small variation of the centre frequency causes a wide variation in the tilt angle.

A further diagnostic mainly to study the small scale fluctuations is the upper hybrid resonance (UHR) scattering [16, 17]. The principle relies on the backscattering of a launched X-mode microwave at the UHR. After mixing the local and the time delayed received waves a spectrum is obtained. The amplitude of the spectral components depends on the time delay between the launched and the received wave and allows to estimate the wave number of density fluctuations. At the UHR also a conversion from X- to O-mode takes place. The backscattered O-mode component contains information on magnetic fluctuations. If the receiving X-mode antennae is replaced by a O-mode sensitive horn it is in principle possible to measure magnetic fluctuations as well.

VI. ECE DIAGNOSTIC

In this section the properties of the radiation emitted by the plasma are investigated. A review on the theoretical aspects of the propagation of microwave radiation in a plasma can be found in [18].

The radiation results from gyrating electrons at a frequency ω_{ce} ,

$$\omega_{ce} = \frac{e \cdot B}{m_e \cdot \gamma} \quad (17)$$

where γ is the relativistic mass factor. Due to relativistic effects the radiation is emitted also in higher harmonics of ω_{ce} . Having a spatial varying toroidal magnetic field as in a tokamak where $B_t \propto 1/R$ a relation between the emitted frequency and the location within the plasma is possible. In the case of a maxwellian energy distribution of the electrons the intensity of the emitted radiation can be related to the temperature. The emitted frequency spectrum can be described by Planck's equation. In a fusion plasma $\hbar\omega \ll kT_e$ is fulfilled and the Rayleigh-Jeans approximation can be used.

$$I(\omega) = B(\omega) = \frac{\omega^2 \cdot T_e}{8 \cdot \pi^3 \cdot c^2} \quad (18)$$

The measurement of the intensity of the emitted frequency alone is not sufficient. Also the transport of the radiation from its point of emission within the plasma to the observing antenna has to be taken into account. The transport of the radiation is described by

$$\frac{dI}{ds} = j(\omega) - I \cdot \alpha(\omega) \quad (19)$$

where s is the ray path and α the absorption coefficient and j the emissivity which are itself a functions of the frequency. The differential equation can be integrated yielding

$$I(s_2) = I(s_1) \cdot e^{-\tau_{21}} + \frac{j}{\alpha} \cdot [1 - e^{-\tau_{21}}], \quad \tau_{21} = \tau_2 - \tau_1 \quad (20)$$

where τ is the optical depth defined by:

$$\tau = \int \alpha(\omega) ds \quad (21)$$

The absorption coefficient is itself a function of local plasma parameters as n_e , T_e , the polarization of the wave (e.g. X- or O-Mode) and the harmonic number. With respects to cut-off's a suitable measurement of the electron temperature is performed for X-mode perpendicular propagation $\theta = 90^\circ$. In this case τ can be calculated from a WKB approach as outlined in paper by Bornatici [18].

For optical thick plasmas ($\tau \gg 1$) the first term on the right side of Eq. 20 becomes small, yielding:

$$T_e^{rad} = \frac{\omega^2 \cdot T_e}{8 \cdot \pi^3 \cdot c^2} \cdot (1 - e^{-\tau}) \quad (22)$$

As mentioned above, the propagation of electron cyclotron radiation in a plasma is limited by resonances and cut-off's. To find those positions we start from the *Appleton-Hartree relation* (Eq. 1) again. As already known from the first section the refractive index decides about cut-off and absorption frequencies for

the propagation in *X-Mode*. Cut-off and resonances are depending on the local B - and n_e -values. For $N^2 = 0$ a cut-off will reflect the wave. If $N^2 = \infty$ a resonance will absorb the wave. As can be seen from the Eq. 3 for *X-Mode* propagation perpendicular to the magnetic field we get the following equation for cut-off,

$$\omega_{CO1,2} = \sqrt{\frac{(2\omega_{pe}^2 + \omega_{ce}^2)}{2} \pm \sqrt{\frac{(2\omega_{pe}^2 + \omega_{ce}^2)^2}{4} - \omega_{pe}^4}} \quad (23)$$

and for resonances in the plasma we get:

$$\omega = \omega_{pe} \quad (24)$$

$$\omega = \sqrt{\omega_{pe}^2 + \omega_{ce}^2} \quad (25)$$

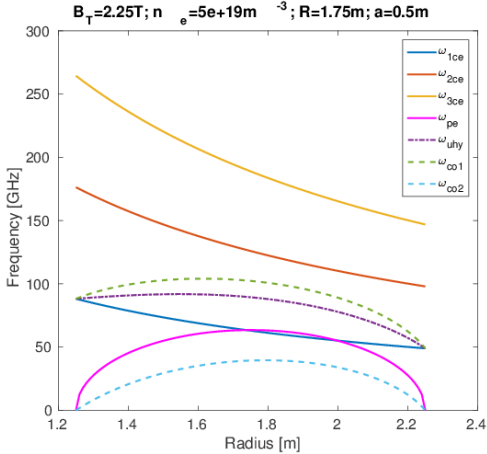


Figure 8: Cut-offs and resonances for a parabolic n_e -profile and $B_t = 2.25$ T and $n_e^{max} = 5 \times 10^{19} \text{ m}^{-3}$ and $R_0 = 1.75$ m. Furthermore the first three harmonics of the electron cyclotron frequency are shown

From Fig. 8 it becomes clear that the 1^{st} harmonic can not be used for ECE-measurements since $\omega_{ce} \leq \omega_{pe}$ for $1.8 \leq R \leq 2$ m. But as long as the n_e is small enough the 2^{nd} harmonic is very well suited to measure the electron temperature. However for an increased density the cut-off frequency ω_{co1} overcomes the 2^{nd} harmonic. Already when the local n_e reaches 80 – 85% of the cut-off density the 2^{nd} harmonic intensity drops, because of the divergence of the antenna beam [19]. In this case the 3^{rd} harmonic must be used. Disadvantage of this method is that the plasma is not optical thick for the 3^{rd} harmonic. Also multiple reflections of the radiation due to the plasma facing walls have to be taken into account. Therefore the first term in Eq. 20 is not zero and reflections from the wall have to be taken into account.

The reflection coefficient ρ of the wall is material depending. For a wall covered by graphite tiles $\rho = 0.7$ is achieved [20]. The equation for the estimation of the temperature has to be modified

$$T_e^{rad} = \frac{\omega^2 \cdot T_e}{8 \cdot \pi^3 \cdot c^2} \cdot \frac{(1 - e^{-\tau})}{1 - \rho \cdot e^{-\tau}} \quad (26)$$

This method needs the knowledge of the local electron density and temperature when calculating the optical depth. The measurement of T_e from 3^{rd} harmonic is restricted to a small frequency range where the frequency range of 2^{nd} and 3^{rd} harmonic do not overlap (see Fig. 8). Otherwise a mixture of both harmonics will be measured and yield wrong T_e -values.

The radiation measurement at frequencies above $f = 70$ GHz is difficult since the amplifier in this frequency range are noisy and the total amplification of the signal has to be around 80 dB, due to the low input power. To overcome this problem heterodyne radiometers are used for the measurement of T_e . They have a local oscillator for down conversion of the input frequency. As local oscillators Gunn-diodes made of GaAs are used because they are stable in frequency and have long lifetime compared with other microwave sources. The HF-frequency is mixed with the frequency of the local oscillator, yielding an intermediate frequency IF. The IF will pass a narrow filter with $\Delta f = 100 - 200 \text{ MHz}$. This filter is responsible for the radial resolution of the radiometer. The noise temperature of such a radiometer is below $T_{sys} \leq 1000 \text{ K}$. Unfortunately it is not possible to sweep the Gunn-diode over a large frequency range with constant output power therefore a broad-band mixer is used which covers the region from 2 GHz to 10 GHz. With a multiplexer and additional narrow bandpass filters T_e can be measured at several frequencies using only one LO-oscillator. This kind of radiometer has in general a higher noise temperature of $T_{sys} \approx 4000 \text{ K}$. A typical example of a modern ECE diagnostic is shown in fig. 9. The system is installed at Tore Supra [21] and is operated with 4 local oscillators. The mixer cover a frequency range of 2 GHz to 18 GHz and after the mixer the signal is filtered and splits into 8 channels each. In total 32 radial positions can be measured with the system. Beside heterodyne radiometer Michelson-Interferometer or a grating polychromator are used to measure T_e . The Michelson-Interferometer is mostly used to measure the emitted microwave radiation over a large frequency range (e.g. 1^{st} – 4^{th} harmonic). This is done by a vibrational or pneumatically mirror in the device, allowing a scan over a large frequency range within ≈ 10 ms. Since the power transferred to detector is very small the detector noise has to be reduced as much as possible by cooling with liquid helium.

VII. AN OUTLOOK TO FUTURE APPLICATIONS

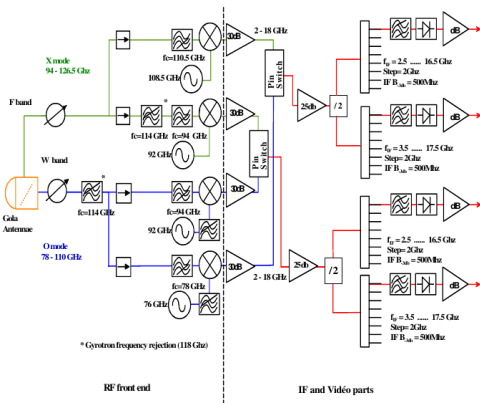


Figure 9: Modern set up of an ECE system at Tore Supra. The black dashed line shows the separation between the high frequency and the IF part.

What are the main directions in the development of microwave diagnostics? The rapid increase in the development of microwave components for the automotive sector will make standard reflectometry diagnostics for today devices more cheap. Together with smaller antennae correlation measurements of turbulence structures could be realised easier. Furthermore the investigations towards 2-dimensional images from the plasma in the range of microwave frequencies needs advanced antennae technique. First experiments using ECE imaging are successfully implemented at AUG [22]. Recent investigations of synthetic aperture microwave imaging for passive and active operation have been started at MAST [23]. The system operates with a time resolution of 10 μ s and records images at 16 different frequencies. With such a system propagation as well as the pitch angle of turbulence can be studied

Beside the more technical oriented development new diagnostic ideas show up as the measurement of the local magnetic field from the pitch angle or equivalent to measure the ellipticity of the reflected beam cross-section (the axis is aligned with the magnetic field) using coherent detection techniques with two orthogonal components [24].

REFERENCES

1. I.H. HUTCHINSON, *Principles of Plasma Diagnostic*, (2nd ed.), New York, NY: Cambridge University Press, p. 109
2. N.C. LUHMANN, *Instrumentation and Techniques for Plasma Diagnostics*, in *Infrared and Millimeter Waves*, Vol. 2, Academic Press, New York, (1979)
3. H.R. KOSLOWSKI, H. SOLTWISCH, *Fusion Engineering and Design*, **34-35**, 143-150, (1995)

4. F.A. HOPF et al, *Opt. Lett.*, **5**, 386, (1980)
5. V.P. Drachev et al., *Rev. Sci. Instrum.* ,**64**, (1993), pp 1010–1013
6. Akiyama et al., 15th International Conference on Laser aided Plasma Diagnostic, October 13-19, 2011, Jeju, Korea, DOI:10.1088/1748-0221/7/01/C01055
7. P.A. BAGRYANSKY et al., *Rev. Sci. Instrum.* ,**77**, 053501, (2006)
8. R. Nazikian et al., *Phys. Plasmas*, **8**, (2001), pp 1840-1855
9. Special issue on reflectometry, Editor G.D. CONWAY, *Nucl. Fusion* **46**, (2006), No. 9
10. A. Silva et al., *Rev. Sci. Instrum.*, **67** ,(1996), pp 4138–4145
11. T. Tokuzawa et al., *Rev. Sci. Instrum.*, **68** ,(1997), pp 443–445
12. Ph. MOREAU, *Rev. Sci. Instrum.*, **71** ,(2000), pp 74–81
13. A. KRÄMER-FLECKEN et. al, *Nucl. Fusion*, **44**, (2004), pp 1143-1157
14. A. KRÄMER-FLECKEN et. al, *Rev. Sci. Instrum.*, **81**, (2010), 113502
15. M. HIRSCH et al., *Rev. Sci. Instrum.*, **72**, (2001), pp 324–327
16. I. FIDONE et al., *Phys. Fluids*, **16**, (1973), 1680
17. D.G. BULYGINSKIY et al., *Phys. Plasmas*, **8**, (2001), 2224
18. M. BORNATICI, *Plasma Physics*, **24**, No. 6, 629, (1982)
19. W.H.M. CLARK, *Plasma Physics*, **25**, No. 12, 1501, (1983)
20. A. KRÄMER-FLECKEN, P.C. DE VRIES, *Proceedings on the tenth workshop of ECE and ECRH*, p. 209, World Scientific, Singapore, (1997)
21. J.L. Ségui et al., *Rev. Sci. Instrum.* **76**, 123501 (2005)
22. I.G.J. Classen et al., *Rev. Sci. Instrum.*, **81**, 10D929 (2010)
23. V.F. Shevchenko et al., *JINST*, **7**, (2012), DOI: 10.1088/1748-0221/7/10/P10016
24. A. STEGMEIR et al., *Fusion Engineering and Design* **86** (2011) 29282942

PLASMA SPECTROSCOPY

R.J.E. Jaspers

Science and Technology of Nuclear Fusion, Applied Physics, Eindhoven University of Technology
P.O. Box 513, 5600 MB Eindhoven, The Netherlands

ABSTRACT

A brief introduction into the spectroscopy of fusion plasmas is presented. Basic principles of the emission of ionic, atomic and molecular radiation is explained and a survey of the effects, which lead to the population of the respective excited levels, is given. Line radiation, continuum radiation, opacity and line broadening mechanisms are addressed. To access the core of a fusion reactor, active spectroscopic techniques have been developed, of which charge exchange recombination spectroscopy and Thomson scattering are treated in some detail.

I. INTRODUCTION

The beauty of a plasma relies in its optical emission: being it the Aurora Borealis, a lightning stroke or even the sunlight. Moreover, observations of spectra from plasma have contributed considerable in the development of the quantum theory. Finally, the lightning industry is fully dominated by the spectral emission of plasmas. For fusion plasmas, the beauty however lies much more in the diagnostic relevance itself: instead of learning about the atomic structure, this light comprises a wealth of quantitative information on the plasma environment itself. With appropriate background knowledge of the emission processes, quantities like the ion densities, the temperature or current distribution can be concealed from measuring the spectral intensity. Figure (1), a typical example of a spectrum in the VUV wavelength range of a tokamak is sufficient to illustrate this point. The information in the spectrum is hidden in its parameters: intensity, wavelength, spectral width and polarization. This lecture will address the basic features to relate these measurable quantities to the plasma parameters of interest. The instrumentation and techniques employed for these spectroscopy measurements will be briefly touched, as are some examples of active spectroscopic techniques. This lecture is not intended as an extensive review. Excellent textbooks are already available for that purpose (for instance [1, 2, 3, 4, 5, 6]).

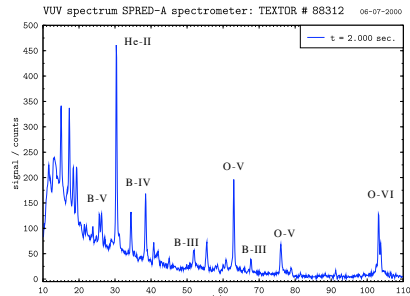


Figure 1: Typical example from TEXTOR of the spectral emission in the EUV/VUV wavelength range, for a standard ohmic discharge after boronisation. From W. Biel-FZJ

II. RADIATIVE PROCESSES

Plasma spectroscopy deviates from atomic physics in the fact that it is not the atomic structure of primary relevance but the dependence of the emission on the plasma conditions, i.e. the environment of the radiating atom. Therefore, here we assume the electronic energy structure of the atoms (or ions or molecules) for granted. Just as a short reminder, for the simplest case of an electron in a central field of a nucleus of charge Z , the energy levels E_n are given by the Rydberg formula:

$$E_n = R_y Z^2 / n^2 \quad (1)$$

with R_y is the Rydberg constant and n the principle quantum number. For more electron systems, the same still holds if n is replaced by $n_{eff} = n - d$, d being the quantum defect. For molecules, the energy associated with vibrational or rotational motion adds to the energy in Eq. 1. External electric and magnetic field might also contribute to changes in the energy levels (Zeeman and Stark effect), leading in general to complicated energy level diagrams. A transition between

two levels E_i and E_j will be accompanied by the emission ($E_i > E_j$) or absorption ($E_i < E_j$) of a photon with a frequency ν_{ij} given by:

$$h\nu_{ij} = E_i - E_j \quad (2)$$

In a plasma the atoms and ions will undergo transitions between these states through different radiative and collisional processes. In general the radiative processes include spontaneous decay, absorption, stimulated decay, all between bound states and recombination transition of free electrons into a bound state. Collisional processes include electron impact excitation / de-excitation, impact ionization and three body recombination. The spectral intensity distribution of the plasma depends on the population density of the energy levels, which in turn depends on the relative weights and cross-sections of these processes. Whereas in general this collisional radiative model is a quite complex system, some limiting case are discussed here to give a flavor of the essential ingredients. The first case is the complete thermal equilibrium. Then the radiation field has reached the blackbody level (so emission and absorption are in equilibrium) and the atoms adopt the Boltzmann distribution between all possible states. In practice, the radiation field is rather weak and this situation is essentially never reached. Local thermal equilibrium (LTE) is less restrictive. Here the condition for the radiation to be thermal is dropped. For LTE all population and depopulation processes are in equilibrium with their reverse processes. Also in this case the relative population of states of on atom or ion is given by the Boltzmann distribution:

$$n_i/n_j = g_i/g_j \exp(-\Delta E_{ij}/kT) \quad (3)$$

Where $g_{i,j}$ are the statistical weights of the states participating in the transition. For LTE the densities of the successive ionization stages is then given by the Saha equation:

$$\frac{n_e n_{i+1}}{n_i} = \frac{g_{i+1}}{g_i} \left[\frac{2m_e^3}{h} \left(\frac{2\pi T}{m_e} \right)^{3/2} \right] \exp\left(-\frac{\chi_i}{kT}\right) \quad (4)$$

where χ_i the ionization potential. Also this distribution holds only for high densities or for high quantum numbers, i.e. not the situation we are normally interested in when diagnosing fusion plasmas. For those conditions the so-called Corona model is a good approximation. The basic assumption here is that all transitions to higher levels are collisional (i.e. electron impact excitation, impact ionization or dielectronic recombination) and to lower levels are radiative (decay or recombination). So absorption effect or collisional de-excitation is negligible, which holds for low enough densities. For

this corona equilibrium one obtains the following relation between the different ionization stages:

$$\frac{n_{i+1}}{n_i} \approx 10^8 \frac{\zeta}{n_0} \frac{1}{\chi_i^2} \frac{kT}{\chi_i} \exp\left(-\frac{\chi_i}{kT}\right) \quad (5)$$

with ζ the number of electrons in the outer shell. As an application of the Saha and coronal equation, Figure 2 shows the relative carbon line intensities for different ionization stages as a function of the temperature. This figure illustrates the differences in emission depending on the population processes. In case of coronal equilibrium the temperature required for a line to appear is considerably larger than in thermal equilibrium (Saha). Since the temperature is a radial profile in a tokamak, an accurate treatment of the distribution of the ionization stages is also necessary for a radial localization of the radiation.

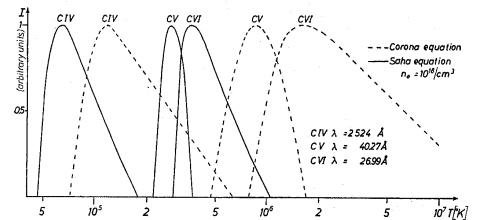


Figure 2: Relative carbon line intensities for different ionization stages as a function of temperature calculated from the Corona model and the thermal equilibrium. From [7]

The more important use of the collisional radiative modeling (or its simplification of the coronal assumption) is the conversion of measured intensities to ion densities of fluxes. The excited state density can be directly obtained from the measured line intensity, provided the Einstein coefficient A_{ij} for the transition from state i to j is known. To relate this to the density of the ground state, the parameter of interest, an appropriate model (e.g. corona equilibrium, LTE, etc.) is needed. The determination of the particle confinement time τ_p from the flux Φ_A serves as an illustrative example. The emission coefficient ϵ for the transition of an upper level i to a lower level j is defined by:

$$\epsilon = \frac{1}{4\pi} n_A^* A_{ij} \quad (6)$$

where n_A^* is the density of the excited state of ion A. What we are interested however is the density of the ground state n_A instead of n_A^* . Now, for the corona equilibrium, the collisional excitation into the excited

levels from the ground state can be related to the radiative decay to all lower levels:

$$n_A^* \sum_{k < i} A_{ik} = n_A n_e \langle \sigma_{ex} v_e \rangle \quad (7)$$

Here $\sum A_{ik}$ is the transition probability from level i into all lower states k and $\langle \sigma_{ex} v_e \rangle$ the excitation rate coefficient by electron collisions from the ground state (a function of T_e). The branching ratio is defined by $\Gamma = A_{ij} / \sum_{k < i} A_{ik}$. Using this we find for the measured intensity I_{tot} :

$$I_{tot} = h\nu \int_{r_1}^{r_2} c dr = \frac{h\nu\Gamma}{4\pi} \int_{r_1}^{r_2} n_A(r) n_e(r) \langle \sigma_{ex} v_e \rangle dr \quad (8)$$

Returning now to the parameter of interest, Φ_A , the flux of atoms into the plasma. Assuming that all atoms are ionized on their way into the plasma, one may readily obtain: $\Phi_A = n_a n_e \langle \sigma_i v_e \rangle$, with σ_i the ionization cross-section and n_a the neutral density of the atoms. Inserting this into eq. 8, relates the flux to the measured intensity:

$$\Phi_A = \frac{4\pi I_{tot} \int_{r_1}^{r_2} n_a n_e \langle \sigma_i v_e \rangle dr}{h\nu\Gamma \int_{r_1}^{r_2} n_a n_e \langle \sigma_{ex} v_e \rangle dr} \approx \frac{4\pi I_{tot}}{h\nu} \frac{S}{XB} \quad (9)$$

with $S \equiv \langle \sigma_i v_e \rangle$, $X \equiv \langle \sigma_{ex} v_e \rangle$ and $B \equiv \Gamma$. For expression (9) the assumption is made that the ratio of the cross-sections do not vary appreciably over the observed region. The ratio $S/(XB)$ represents the ionization events per photon and includes all the relevant rate coefficients from the collisional radiative modeling. Suitable packages exist for these calculations, like ADAS [8]. The final step now to arrive at the particle confinement time in steady state is by integrating the flux over the outer surface of the plasma:

$$\tau_p \equiv N_a / \Phi_A^{tot} = \frac{h\nu}{16\pi^3 a R} \left(\frac{XB}{S} \right) \frac{N_A}{I_{tot}} \quad (10)$$

where in the case of hydrogen the assumption can be made that $n_A \approx n_e$, the total number of electrons.

III. OPACITY

In the description above we have tacitly assumed that absorption of radiation is negligible. If spontaneous decay from an upper level to a lower level occurs, the reverse process, absorption of the same photon by the lower level is possible as well. To quantify this, one can calculate the absorption coefficient κ_ν , defined as the absorbed fraction of radiation I^0 per unit length x [3]:

$$\kappa_\nu = \frac{dI_\nu(x)}{dx} \frac{1}{I_\nu^0(x)} = \frac{e^2}{4m_e c \epsilon_0} n_l f_{lu} P(\nu) \quad (11)$$

The last equality relates the cross section for absorption to the oscillator strengths f_{lu} (related to the Einstein coefficients A_{ul}) and the density of the absorbing particles n_l . In this equation $P(\nu) = P(\lambda)c/\lambda^2$ represents the normalized line shape. For a Doppler broadened line (see below), we can rewrite this as a mean free path of the photon $mfpl_\lambda$ before it gets absorbed as:

$$\begin{aligned} mfpl_\lambda &= (\kappa_\lambda)^{-1} = \frac{4m_e \epsilon_0 c}{e^2} \sqrt{\frac{2kT_i}{m_i}} / (n_l f_{lu} \lambda_0 \sqrt{\pi}) \\ &= 5 \times 10^{17} \frac{\sqrt{T_e} [eV]}{n_1 [m^{-3}]} [m] \end{aligned} \quad (12)$$

Where in the last equality the values for the Lyman- α line ($\lambda_0 = 122nm$, $f_{12} = 0.4162$), have been used. Only in that case the density of the ground state, neutral hydrogen, is sufficiently large that the opacity might be noticeable: In the divertor for a typical neutral density of $n_H = O(10^{20} m^{-3})$ absorption of the light is expected within a few cm. For almost all other transitions, the absorption can be neglected (justifying the assumption that the plasma is not in thermal equilibrium).

IV. LINE BROADENING

Next to the intensity, the other directly accessible spectral characteristic to be measured is the line width. The width of a spectral line is governed by three different processes: the natural line width, Doppler Broadening and pressure broadening. The natural line width, related to the finite lifetime of an excited state as characterized by the Einstein coefficient A ($\Delta\lambda \approx \lambda^2 A_{ij} / (\pi c)$), is in all practical cases negligible in a fusion plasma. The Doppler effect on the contrary, is the dominant mechanism for line broadening. Applying the Doppler effect over the Maxwellian ion velocity distribution function gives rise to a Gaussian line shape $P(\lambda)$:

$$P(\lambda) d\lambda = \sqrt{\frac{m_i c^2}{2\pi k T_i \lambda_0^2}} \exp -\frac{m_i c^2 (\lambda - \lambda_0)^2}{2k T_i \lambda_0^2} \quad (13)$$

with a width (expressed here as FWHM: full width at half maximum) $\delta\lambda$:

$$\Delta\lambda_D = \sqrt{\frac{8kT_i \ln 2}{m_i c^2}} \lambda_0 \quad (14)$$

with k the Boltzmann constant and λ_0 the unshifted line. This equation 14 shows the ease at which spectral measurement can provide the ion temperatures T_i of the plasma. The final broadening mechanism we address here is pressure broadening, or also called Stark broadening or collisional broadening. This effect result from the fact that the radiating ions experience a change in

the electric field due to the presence of neighboring ions. Detailed calculations of this effect are extremely complicated, but for hydrogen some good approximations exist [9]:

$$\Delta\lambda_S = 0.54\alpha_{1/2}n_{20}^{2/3}nm \quad (15)$$

with $\alpha_{1/2}$ a constant resulting from the calculations ($\alpha_{1/2} \approx 0.08$ for the Balmer- β transition) and n_{20} the electron density in units of $10^{20}m^{-3}$. For typical tokamak conditions ($n_{20} < 1$), this broadening is negligible compared to the Doppler broadening, even for temperatures as low as 1 eV . Only in the divertor region densities might be sufficiently high for this to become appreciable.

V. CONTINUUM RADIATION

Up to know the discussion on the radiation was limited to transitions involving bound states of the electrons. However, the emission by free electrons deserves a prominent place as well in this discussion. In general radiation is emitted if a free particle is accelerated. This can occur as a result of an electron experiencing either an electric or magnetic field. The latter results in cyclotron radiation, associated with the gyro motion of the electron. This is left out of the discussion here, since it is treated in the microwave diagnostics part of this lecture course [10]. For the former one the dominant term is the varying electrical fields experienced by the electron moving in the Coulomb field of an ion. In case the final state of the electron is also free, this is called bremsstrahlung. If after the encounter with the ion, the free electron occupies a bound state, the radiation is referred to as recombination radiation. Both types are observed as continuum radiation, due to the free nature of the electron. The continuum spectrum extends from the plasma frequency up to the x-ray region (with photon energies of the order of the electron temperature).

The derivation of the bremsstrahlung can be done instructively by considering the power emitted by an electron during an accelerated motion and apply this to a Coulomb collision. For small impact parameters of the collision quantum mechanical effects then come into play. The final expression obtained for the emissivity per unit of frequency ϵ_ν of the continuum spectrum for one ion species Z is (see for instance [4]):

$$\epsilon(\nu) = n_e n_i Z^2 \left(\frac{e^2}{4\pi\epsilon_0} \right)^3 \frac{8\pi}{2\sqrt{3}m_e^2 c^3} \left(\frac{2m_e}{\pi T_e} \right)^{1/2} e^{-\frac{h\nu}{T_e}} \times \left[\bar{g}_{ff} + G_n \frac{\zeta}{n^3} \frac{\chi_i}{T_e} e^{\frac{\chi_i}{T_e}} + \sum_{\nu=n+1}^{\infty} G_\nu \frac{2Z^2 R_y}{\nu^3 T_e} e^{\frac{z^2 R_y}{\nu^2 T_e}} \right] \quad (16)$$

The first term in brackets is the free-free contribution, the second the recombination term into the lowest unfilled shell (n) and the third term to all other shells. The symbols used here are: G the Gaunt factor describing the quantum mechanical effects, \bar{g}_{ff} the Maxwell averaged free-free Gaunt factor, ζ the number of unfilled positions ion the lowest shell, χ_i the ionization potential and R_y the Rydberg energy (13.6 eV). Evaluating this expression shows that recombination is negligible for $\lambda \gg hc/Z^2 R_y \approx 100nm$ or for all wavelengths if $T_e \gg Z^2 R_y$. So in the visible the bremsstrahlung dominates the continuum radiation. Furthermore, note the square dependence on the density and the (evaluating the exponent) much weaker $T_e^{1/2}$ dependence.

Apart from an additional power loss term for the plasma, the practical use of the bremsstrahlung measurement lays in the diagnostic application: plotting the continuum over a broad wavelength range on a logarithmic scale allows to deduce the electron temperature directly from the slope of the plot. Furthermore another primary quantity that can be obtained from these bremsstrahlung measurement is the effective ionic charge of the plasma, Z_{eff} . By summing the emission from eq. 16 over all ionic species and invoking quasi neutrality ($n_e = \sum n_i Z_i$), Z_{eff} is defined as the factor over which the bremsstrahlung exceeds that of hydrogen, and thus can be regarded as a kind of mean ionic charge of the plasma:

$$\sum_i n_e n_i Z_i^2 \equiv n_e^2 Z_{eff}^2 \Rightarrow Z_{eff} = \sum n_i Z_i^2 / \sum n_i Z_i \quad (17)$$

These measurements are usually done in the visible wavelength range, due to the relatively less cumbersome absolute calibration effort. Precaution should be taken however, to select a wavelength range free of line radiation from atoms, ions or molecules.

VI. ACTIVE DIAGNOSTICS

Contrary to this passive emission, active techniques can be used to induce specific radiation, leading to even more detailed information. One of the main reasons to use active spectroscopy is that it can access the core of the fusion plasmas. At the high temperatures required for the fusion process all the light elements in the core are fully ionized and do not emit any line radiation. By active techniques, spectral emission can be induced, and as such measurements of, for instance, the temperature from the Doppler shift is still possible. Typical examples here are the use of lasers or atomic beams. From the laser aided diagnostics, two techniques are considered here: laser induced

fluorescence, LIF and the scattering of radiation by the electrons in the plasma: Thomson scattering, TS. Beam aided spectroscopy will be exemplified by charge exchange recombination spectroscopy, CXRS and Beam Emission Spectroscopy (including Motional Stark Spectroscopy).

VI.A. Laser Induced Fluorescence

The LIF technique is based on the excitation of atoms (or ions or molecules) by the absorption of laser radiation, and the measured spontaneous emission of the subsequent decay (either to the same level or to another level). To illustrate the principle of LIF, consider the simplest scheme of a two-level system (see also [12]). Then the rate equation for the excited state population is given by:

$$\frac{dN_2}{dt} = N_1(W_{12} + Q_{12}) - N_2(W_{21} + Q_{21} + A_{21}) \quad (18)$$

with $N_{1,2}$ the population of the lower and upper level respectively, and $W_{12,21}$ the laser-induced absorption and stimulated emission rate, $Q_{12,21}$ the collisional excitation rate and quenching rate and A_{21} the spontaneous emission rate. It is clear that even in steady state, it is non-trivial to relate the fluorescence signal (proportional to A_{21}) to the number of electrons in the excited level N_2 . For sufficiently strong lasers power densities S_p , the absorption and stimulated emissions (W) become so large that the N_2 population approaches saturation. This requirement on the laser power needed to reach this saturation is then determined by the condition that the stimulated absorption rate equals the spontaneous emission, which typically amount to 10 kW/cm^2 . In this saturation limit, one finds:

$$n_{ph} = \frac{(N_1 + N_2) g_2 k}{g_1 + g_2} A_{21} \quad (19)$$

where n_{ph} is the number of fluorescence photons per s, $g_{1,2}$ the statistical weights of the two levels and

$$k = \frac{V\tau\Delta\Omega}{4\pi} \quad (20)$$

a geometrical factor consisting of V the sampling volume, τ the transmission of the collection optics, and $\delta\Omega$ the solid angle.

Although the above is an oversimplification of the real system, it demonstrates the main principle. The main advantages of this LIF technique over usual passive spectroscopy are at least two-fold. The first arise from the ability to localize the region of the measurement by crossing the laser line with the viewing optics. Second is the advantage of detecting signals which otherwise would be lost in a large background. LIF has

been used in fusion research to determine several parameters like neutral densities [13], ion densities and velocities or magnetic fields [14]. A typical setup is shown in Fig. 3.

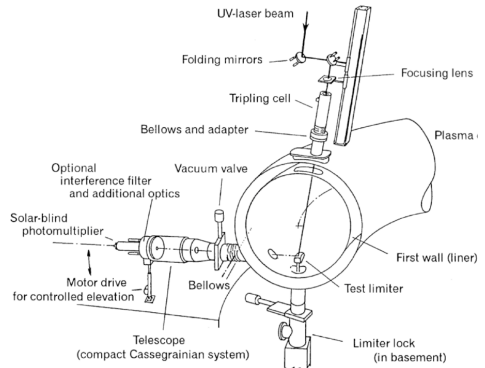


Figure 3: Experimental setup for LIF on TEXTOR edge plasma [15].

VI.B. Thomson Scattering

Thomson scattering is one of the most basic and common diagnostics at nearly every magnetic confinement device. Usually it provides profiles of electron temperature and density, but additional information, like the fast ion density or current density can be obtained as well from it, depending on arrangement of the system. Contrary to the sections before, where the radiation from the plasma itself was discussed, here the principle of the system is based on the scattering of electromagnetic waves by free electrons. This process was theoretically described by as early as 1903 by Thomson [16] and one of the first demonstrations to a tokamak was given in 1969 at the Russian tokamak T3 [17].

Scattering of monochromatic electromagnetic radiation from hot electrons in a plasma leads to a spectral broadening of the light due to the Doppler effect. Depending on the wavelength of the incident light, the scattering on individual electrons can be added or collective effects due to the correlated interactions between the plasma electrons have to be taken into account. The criteria to determine which regime applies is given by the Salpeter parameter α [18]:

$$\alpha = (k\lambda_D)^{-1} = \frac{\lambda_0}{4\pi\lambda_D \sin(\theta/2)} \quad (21)$$

where $\lambda_D = 7.4 \times 10^3 \sqrt{T_e[\text{eV}]/n_e[\text{m}^{-3}]}$ is the Debye length, k the scattering vector and θ the angle between incident and scattered wave. For $\alpha \ll 1$ the resulting

spectrum is determined by the scattering of individual electrons. This type is referred to as incoherent Thomson scattering. For $\alpha \geq 1$ the scattering from different electrons and their surrounding field will add up coherently, since there is a negligible phase difference between them. This is coherent Thomson scattering and although scattering takes place on the electrons, since they are surrounding the ion in the Debye sphere, information on the ion can be extracted from the scattered signal [19, 20]. A third regime is given by $\alpha \sim O(10)$. In that case $\lambda_0 \sin(\theta/2)$ is of the same order as the correlation length of the density fluctuations in the plasma (of the order of the ion Larmor radius) and the collective motion of the electrons can be observed [21]. Plenty of excellent review and lecture papers on Thomson scattering exist, including the collective effects [12, 4]. Therefore we concentrate in the remainder only on the basics of incoherent Thomson scattering, by far the most applied system.

The differential Thomson cross section can be derived by considering the acceleration experienced by an electron under the action of the electromagnetic field of an incident wave. For the common case of linearly polarized incident light, this leads to:

$$\frac{d\sigma_T}{d\Omega} = r_0^2 \sin^2 \phi \quad (22)$$

with $r_0 = e^2/(4\pi\epsilon_0 m_e c^2)$ the classical electron radius. This shows immediately the small value of the cross-section ($8 \times 10^{-30} m^{-2}$) and the fact that the scattering is maximum in a plane perpendicular to the incident \mathbf{E}_0 ($\phi = 90^\circ$). The scattered laser power is then given as:

$$P_s = P_0 \frac{d\sigma_T}{d\Omega} \sin^2 \phi n_e \Delta L \Omega S(k, \omega) \quad (23)$$

with P_0 the incident power, ΔL the length of the scattering volume and $S(k, \omega)$ the form factor describing the frequency shift resulting from the electron motion (and also the correlation effects in case of coherent scattering). For the case of a Maxwellian distribution function this form factor becomes for the incoherent case:

$$S(\lambda_s) = \frac{1}{\Delta\lambda_e \sqrt{\pi}} \exp - \left(\frac{\lambda_s - \lambda_0}{\Delta\lambda_e} \right)^2 \quad (24)$$

Here λ_s is the wavelength of the scattered radiation and $\Delta\lambda_e$ the 1/e width of the resulting spectrum:

$$\Delta\lambda_e = \frac{2\lambda_0}{c} \sin\left(\frac{\theta}{2}\right) \sqrt{\frac{2k_B T_e}{m_e}} = 1.94 \sqrt{T_e [eV]} [mm] \quad (25)$$

In the last expression the values for a ruby laser ($\lambda_0=694.3$ nm) and perpendicular scattering have been inserted. Note that the above derivation has neglected relativistic effects. However, for plasmas of typically 1-10 keV they become important due to two effects: the

Thomson cross-section is appreciably decreased due to the mass defect by the factor $1/\gamma^2$ and the fact that the electron radiates preferentially in the forward direction (the "headlight" effect). An analytical description of this is provided by [22] and gives rise to distortion of the Gaussian spectrum, most apparent as a blueshift of the spectrum.

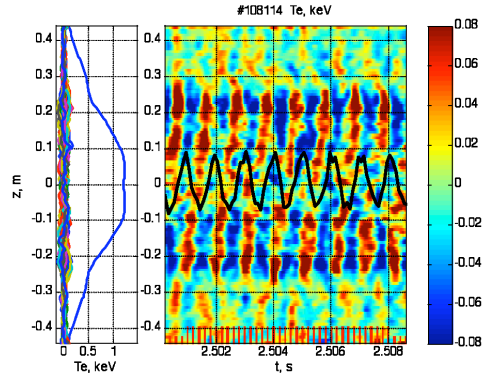


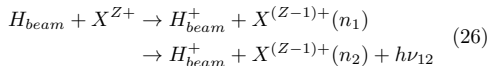
Figure 4: Typical result of the TEXTOR Thomson scattering system. Depicted here is the temperature evolution of magnetic islands in the plasma. The averaged profile (left) has been subtracted. The black line indicates the rotation of islands as measured with ECE. Temperature structures as small as 10 eV can be recognized (on a 1.5 keV background).

Several different Thomson scattering system are in use nowadays: (1) using repetitive lasers in combination with filter spectrometers to achieve relatively high temporal resolution. Since the Thomson scattering cross-section is so low (ratio of detected power over incident power is about 10^{-15} , (see Eq./ 23) strong lasers are required, with only a limited repetition frequency. However by packing several of these lasers (e.g. Nd:YAG lasers at 30 Hz) together and firing them independently, still high temporal resolutions can be achieved [23]. (2) LIDAR, which is based on a time of flight measurement of the back-scattered light of a short laser pulse. Presently only one such system is operational, at JET [24], but it is envisaged to develop such a system as well for ITER, since it has the big advantage that only one access window for both the laser and collection optics is required. (3) TV systems, which image the full laser cord on a CCD or CMOS cameras and thus have an excellent spatial resolution of less than a cm. Most advanced system in this respect is the TEXTOR Thomson system. Here the plasma is part of the laser cavity, allowing the operation of a multi pulse ruby laser at sufficiently high power. By adjusting the laser

path such that the laser pulse can travel up to 12 times through the plasma typically a burst of 60 pulses at 5 kHz repetition frequency and 60 J of effective laser power can be reached [25]. This high power, combined with the high spatial and temporal resolution allows to observe the dynamic of small structures in the plasma, like the rotation of magnetic islands, see Fig. 4.

VI.C. Charge eXchange Recombination Spectroscopy

The exchange of an electron between a hydrogen neutral and fully ionized particles is a resonant process which has its maximum cross section in the energy range of a few tens of keV for the light ions (H, He, B, Be, C, N, O, Ne, Ar) that are typically encountered in the tokamaks. In this energy range (10-100 keV) it is the dominant ionization process of neutral beams heating the plasma. These heating beams can thus be also used to induce line radiation from the plasma core. For an arbitrary plasma ion X capturing the electron from the hydrogen neutral beam, the reaction is written as:



where $h\nu_{12}$ representing the photon due to the radiative decay from the excited level n_1 to the level n_2 . The thus emitted spectrum entails the information from the core ions: its width squared proportional to the ion temperature (14), the Doppler shift to the core rotation along the line of sight and the intensity proportional to the ion density. Apart from the bare fact that this method allows to access the fusion core at all, the other big advantage of this method is that it is a local measurement: the recorded emission originated from the intersection of the neutral beam and the line of sight. This allows to obtain ion temperature, ion rotation and ion density profiles over the full plasma radius. Furthermore, the principle shell into which the electron will be caught can be approximated by $n_2 \approx Z^{3/4}$ for CX from the ground state (see [4]). For light elements like Carbon and Neon higher levels are populated, which allows transitions into the visible wavelength region, making the recording relatively easy. For helium this is only true to certain extent. A typical example of a carbon spectrum is shown in Fig. 5. (Note: carbon is usually used due its relatively uncomplicated spectral shape and its presence in all plasmas, since carbon is used as the most common wall material and thus diffuse into the core plasma. For future reactors, this might not be the case, since carbon has to be avoided because of its tritium retention capability). Over the past three decades the CXRS diagnostic has been developed to an extent that it is now the main core ion diagnostic [26].

For ITER a dedicated diagnostic neutral beam system (with an energy of 100 keV) is envisaged, since CXRS is the sole possibility to diagnose the helium ash density in the core [27].

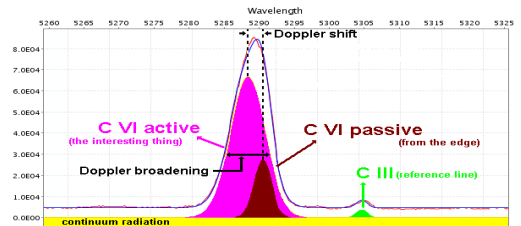


Figure 5: Typical carbon spectrum of the TEXTOR Charge Exchange Recombination System. The measured line originated from $C^{5+}(n = 8 \rightarrow n = 7)$ at $\lambda = 529nm$. Without the neutral beam, only a passive line originating from the plasma edge is observed. When the beam is switched on the active component appears: its width being representative of the carbon temperature, its Doppler shift is related to the ion rotation along the line of sight and the intensity is a measure of the carbon density.

Complications with this method arise mainly from two issues: i) apart from the active CX components, also emission from the same passive line, coming from the cold edge plasma, appears. This emission is always present, and originated either from CX reactions with neutrals from the wall instead of the beam or from the impact excitation of the non-fully stripped ion $X^{(Z-1)+}$ in the plasma edge. Discrimination between the active and passive components can be done by a modulated neutral beam (as envisaged for ITER) or by a (cumbersome) fitting procedure. ii) the neutral beam is attenuated towards the plasma centre (due to the ionization processes, of which CX itself is the dominant one). For large plasmas this makes the signal rather weak in the centre. For ITER, where only 1% of the beam particles arrive in the centre, this can be compensated only by a large light collection system. The beam attenuation complicates also the derivation of the ion density from the intensity signal (proportional to $n_X n_{beam}$). An accurate knowledge of the beam density in the observed volume is thus required and can be obtained from attenuation codes (calculating the integrated beam ionization along the beam path) or from measuring the beam density directly from the direct emission from the beam itself (i.e. the beam excitation by electron/ion impact collisions). Both methods rely on atomic cross-section of the relevant processes, which are still subject to investigations or validation [28].

VI.D. Beam Emission Spectroscopy

Detecting the emission from the neutral beam itself has three interesting applications: Firstly, the determination of the beam density, as discussed in the previous section, with the aim to obtain the ion density profile from CXRS measurements. Secondly, the fluctuations in the intensity of the beam emission is related to the fluctuations on the electron density. On DII-D a 2D system based on this measurement has been constructed, which showed both the fluctuation levels as the flows of the tubulent structures in the plasma [29]. However, the most renown application of the beam emission is related to the Motional Stark Effect (MSE). The fast beam neutrals, moving in a large magnetic field, experience a Lorentz electric field in their reference frame ($\mathbf{E} = \mathbf{v}_{\text{beam}} \times \mathbf{B}$), which gives rise to a Stark splitting of their energy levels. A typical example of such hydrogen beam spectrum at the Balmer- α transition is given in Fig. 6. From the Stark splitting ($\sim E$), or the polarisation (\sim direction of E), information on the amplitude or direction of the magnetic field (\mathbf{B}) can be obtained, since \mathbf{v}_{beam} is accurately known. Typical MSE diagnostics employ an interference filter to select one component from the spectra with a polarisation direction parallel or perpendicular to \mathbf{B} . Measuring the polarisation angle of this line then determines the magnetic field direction, which is used as input parameter to the plasma equilibrium codes, constraining the current density profile [30].

VII. INSTRUMENTATION

Key to the success of the plasma spectroscopy is the instrumentation. The choice of the instrument depends heavily on the wavelength of interest. Typically one can distinguish: a) the visible range ($h\nu \sim 2 - 3\text{eV}$), mainly for passive spectroscopy in the plasma edge, since only their temperature is low enough that the atoms or ions exhibiting these low energy transition are available, 2) the UV/VUV range ($h\nu \sim 3 - 120\text{eV}$) typical of higher ionization stages of impurity ions as they occur in the confined region of the plasma and 3) X-ray measurements ($h\nu \sim 0.12 - 10\text{keV}$), typical of highly charged states as they occur in plasma regions of 1 keV or more, so sensitive to the core of the plasma. For all these ranges, a spectral instrument should obey the following characteristics: a high resolving power $R = \Delta\lambda/\lambda$ to discriminate the different lines, high light transmission T and good imaging quality. The most used types in all ranges are grating spectrometers, as they can combine all these properties simultaneously. Prism instruments, Fabry-Pérot interferometer

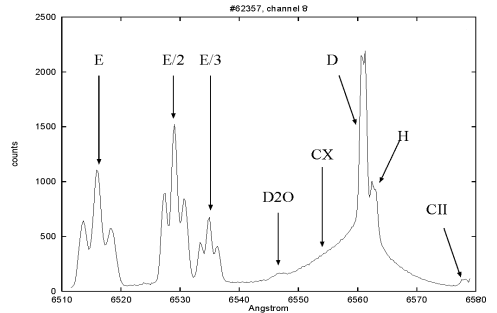


Figure 6: Typical spectrum of the Balmer- α emission of a Neutral Beam Heated discharge at TEXTOR. The Blue shifted Doppler lines originate from Balmer $n = 3 \rightarrow n = 2$ emission, which is splitted due to the motional Stark effect. This emission is polarised either parallel or perpendicular with respect to the Lorentz electric field $E_L = v \times B$. (The three separate groups are due to the different energy species in the neutral beam at 50, 25 and 16.7 keV)

and Fourier transform spectrometers are used only for special purposes.

VII.A. Spectrometer

The dispersion of a grating spectrometer is governed by the grating equation:

$$m\lambda = d(\sin\alpha + \sin\beta) \quad (27)$$

with m the diffraction order, d the line separation and α, β the angles of the incident and reflected light respectively. The resolving power is then determined by the total number of illuminated lines N : $R = Nm$. Densities of 6000 lines/mm can be attained on a 10 cm grating, yielding a resolving power of 6×10^5 in the first order. The intensity of the diffracted light depends on the shape of the lines. Ruled gratings are optimized (in reflectivity) with respect to a certain *blaze* angle corresponding to a certain wavelength. Efficiencies can be as high as 70 % at this wavelength. A special category are *Echelle* gratings, where one has comparatively few lines/mm but one operates this at high diffraction orders, so even achieving $R \sim 10^6$. Disadvantage there is the problem of many overlapping orders (i.e Eq. 27 fulfilled for different wavelengths at different orders m).

Another characteristic of the spectrometer is its etendue E or light throughput, representing the total light collection efficiency. It is given by the product of the area A of the entrance slit and the acceptance angle Ω , related to relative aperture $F/\#$:

$$E = A\Omega = \frac{\pi}{4} \frac{A}{(F/\#)^2}. \quad (28)$$

Since the etendue is cannot be increased in optical system, the spectrometer's etendue usually limits the light collection efficiency. To acquire a reasonably high signal to noise ratio for CXRS in the core of ITER, a high resolution, high etendue spectrometer has been designed with an unsurpassed etendue of $E = 1\text{mm}^2\text{sr}$ [31].

Spectrometers consist typically of the optics to collimate the light from the entrance slit towards the dispersive element (like the grating) and then image the dispersed light back to the exit slit where a detector might be located. Different types of optical arrangements exist, like the Czerny Turner or Littrow mount for the visible wavelength range. These are designed such to eliminate or minimize the optical aberrations and attain good image quality. If concave grating are used, the need for collimating and focussing is eliminated, which is particularly useful in the VUV en XUV regions, where conventional mirrors are ineffective. For even shorter wavelengths, the gratings are used at grazing incidence, to minimize the absorption losses. In X-ray one typically employs crystals instead of ruled gratings, where the diffraction occurs according to the Bragg condition for the atomic planes. An example is shown in Fig. 7 of a conventional Johann Crystal spectrometer [32]. More advanced present day designs have optimized this to have an imaging capability as well. This now allows to obtain profiles of ion temperature and rotation on large tokamaks [33].

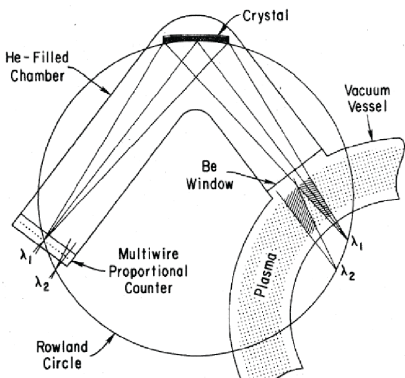


Figure 7: Example of a Johann Crystal spectrometer for application in the X-ray region. From [32]

VII.B. Coherence Imaging

The other alternative to obtain spectral information is by measuring the coherence of light. An example of this is a Fourier transform spectrometer, but other

arrangements are possible as well. An elegant example of this was developed for instance at WEGA [34]. Such systems monitor in two dimensions the temporal coherence of an isolated spectral line using polarization interferometric techniques. For quasi-monochromatic illumination, the signal, S (interferogram), at the output ports of a two-beam interferometer is given by:

$$S = \frac{I_0}{2}(1 + \zeta \cos \phi) \quad (29)$$

where I_0 is the source brightness, ζ is the fringe contrast and ϕ is the phase delay of the interferometer. When the emission line is now broadened, i.e. with increasing temperature, the fringe visibility decreases. To observe changes to the fringe visibility, it is necessary to modulate the optical path length (phase delay) in order to extract the fringe amplitude. This modulation is achieved electro-optically using a step-modulation pattern that is synchronized with the camera frame rate. Using a fast CCD camera this system can obtain the spectrum in 2D, since the spectral information is moved to the time domain. Further extensions to this system are being explored to use it for Zeeman or Motional Stark measurements [35].

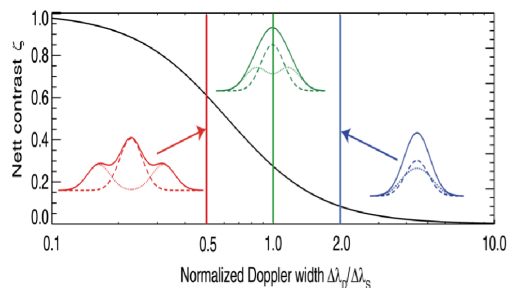


Figure 8: The calculated maximum net contrast ζ versus the ratio of Doppler width $\Delta\lambda_D$ and Stark separation $\Delta\lambda_s$. The insets show the multiplet line-shapes for ratios 0.5, 1 and 2, corresponding to different polarization angles. (From [35])

ACKNOWLEDGMENTS

This paper builds upon lectures given at previous editions of the Carolus Magnus Summer School by Dr. A. Pospieszczyk (FZ-Jülich), Dr. A.J.H. Donné (FOM Rijnhuizen) and Dr. B. Schweer (FZ-Jülich) and the author is much indebted to them.

REFERENCES

1. H.R. GRIEM, *Plasma Spectroscopy*, McGraw Hill, New York, (1964).
2. H.R. GRIEM, *Principles of Plasma Spectroscopy* Cambridge University Press, Cambridge (1997).
3. T. FUJIMOTO, *Plasma Spectroscopy*, Clarendon Press, Oxford, (2004).
4. I.H. HUTCHINSON, *Principles of Plasma Diagnostics*, Cambridge University Press, Cambridge, (2002).
5. W. LOCHTE-HOLTGREVE, *Plasma Diagnostics* North-Holland, Amsterdam (1968).
6. A.A. OVSYANNIKOV, ed: *Plasma Diagnostics*, Cambridge International Science Publishing, Cambridge (2000).
7. A. POSPIESZCZYK, *Spectroscopy*, Transaction of Fusion Science and Technology **49-2T** (2006) 395.
8. Atomic Data Analysis Structure, see: <http://adas.phys.strath.ac.uk>.
9. H.R. GRIEM, *Spectral Line Broadening by Plasmas*, Academic Press, New York, (1974).
10. A. KRÄMER-FLECKEN, this lecture course.
11. B. SCHWEER, *Atomic Beams for Plasma Diagnostics*, this issue.
12. A.J.H. DONNÉ *Laser-aided Plasma Diagnostics*, Trans. of Fusion Science and Technology, **49-2T** (2006) 375.
13. G.T. RAZDOBARIN *et al.*, *Nuclear Fusion* **19**, 1439 (1979).
14. W.P. WEST *et al.*, *Rev. Sci. Instrum.* **57** 1552 (1986).
15. Ph. MERTENS and A. POSPIESZCZYK, *Journal of Nuclear Materials* **266-269** 884 (1999).
16. J.J THOMSON, *Conduction of Electricity through Gases* University Press Cambridge (1903) p. 268.
17. N.J. PEACOCK *et al.*, *Nature* **224**, 488 (1969).
18. E.E. SALPETER, *Phys. Rev.* **120**, 1528 (1960).
19. R. BEHN, *et al.*, *Phys.Rev. Lett.* **62** 2833 (1989).
20. H. BINDSLEV *et al.*, *Phys. Rev. Lett* **83** 3206 (1999).
21. A. SEMET, *et al. Phys. Rev. Lett.* **45** 445 (1980).
22. A.C. SELDEN *Phys. Lett.* **79A** 5 (1980).
23. R. SCANNELL, *et al. Rev. Sci. Instrum.* **79** 10E730 (2008).
24. C.W. GOWERS, *et al. Rev. Sci. Instrum.* **66** 471 (1995).
25. M.Yu. KANTOR, *et al.*, *Plasma Physics and Controlled Fusion* **51** 055002 (2009).
26. R.C. ISLER, *Plasma Physics and Controlled Fusion* **36** 171 (1994).
27. D. THOMAS, *et al.*, *Fusion Science and Technology* **53** 487 (2008).
28. E. DELABIE, *et al.*, *Plasma Physics and Controlled Fusion* **52** 125008 (2010).
29. G. MCKEE, *et al.*, *Rev. Sci. Instrum.* **74** 2014 (2003).
30. D. WROBLEWSKI and L.L. LAO *et al.*, *Rev. Sci. Instrum.* **63** 5140 (1992).
31. W. BIEL, *et al.*, *Fusion Engineering and Design* **86 (6-8)** 548 (2011) .
32. G. BERTSCHINGER, *et al.*, *Physica Scripta* **T83** 132 (1999).
33. A. INCE-CUSHMAN, *et al.*, *Rev. Sci. Instrum.* **79** 10E302 (2008).
34. J. CHUNG, *et al.*, *Plasma Physics and Controlled Fusion* **47** 919 (2005)
35. J. HOWARD, *et al.*, *Plasma Physics and Controlled Fusion* **50** 125003 (2008)

Diagnosics for plasma-material interaction studies

A. Kreter

*Forschungszentrum Jülich GmbH, Institut für Energie- und Klimaforschung – Plasmaphysik,
52425 Jülich, Germany*

Abstract

The manuscript is accompanying the corresponding lecture at the 12th Carolus Magnus Summer School on Plasma and Fusion Energy Physics. The contribution is focused on surface analysis and erosion-deposition diagnostics frequently applied in the fusion relevant research on plasma-material interaction. The definitions of real-time, in-situ, in-vacuo and ex-situ diagnostics are given. The working principles of the following surface analysis tools are described and examples of their applications are given: thermal desorption spectrometry (TDS); scanning electron microscopy (SEM) including the option of focused ion beam (FIB); ion beam analysis (IBA) methods of nuclear reaction analysis (NRA) and Rutherford back-scattering (RBS); and secondary ion mass spectrometry (SIMS). Two methods of erosion-deposition measurements are introduced: quartz microbalance (QMB) and marker techniques.

1. Introduction

The availability of the fusion reactor is crucial for its economic operation and is to a large extent determined by plasma material interaction (PMI). There are two main PMI issues limiting the availability of the reactor: the lifetime of the wall components and the operational safety. The first wall will suffer from heat loads and particle bombardment, causing erosion of materials and limiting the lifetime of the first wall components. The safety issues are connected to the restrictions on the amount of radioactive tritium and dust stored in the reactor vacuum vessel.

PMI studies in both large-scale, at close-to-reactor conditions, and lab-scale, at well-defined conditions, devices are necessary for a better understanding of the background processes, refined predictions for the reactor and finding solutions to critical issues [1]. Therefore, the methods to determine PMI related values, i.e. material erosion and deposition and fuel retention, are important experimental tools in the fusion research.

There are numerous surface analysis techniques analysing the physical and chemical properties of the material surface. E.g. an overview table in the book by

G.A. Somorjai [2] lists 60 "most frequently used surface characterization techniques". In this paper, only a fraction of the techniques, which are most relevant to the PMI research, are covered, along with the methods for studying erosion and deposition of the wall materials.

2. Definitions of real-time, in-situ, in-vacuo and ex-situ

Material samples can be analysed in different ways concerning the temporal and spatial scale of analysis. The following nomenclature has been established for the description of different methods, here listed in order of the time point of their application or data availability: "real-time", "in-situ", "in-vacuo" and "ex-situ" ("post-mortem").

The real-time techniques deliver the data during the investigated process. They are often used for the real-time, or feedback, control of the process. Usually, less complex, robust methods are applied real-time for the control purposes.

In-situ (lat.: "in position") methods are, similarly to the real-time ones, applied during the investigated process, e.g. during the plasma exposure of a material sample. However, the data analysis often requires

additional efforts after the actual experiment, e.g. for the conversion of the raw diagnostics data to the meaningful data describing the particular PMI process. Therefore, the data of the in-situ measurements typically becomes available after the experiment. Nevertheless the in-situ data often provides valuable insights in the temporal evolution of the investigated process. In-situ methods of PMI including optical emission spectroscopy are the topic of a different lecture.

In-vacuo (lat.: "in vacuum") methods are applied after the investigated process, e.g. after the plasma exposure of a material sample, but before the exposure of samples to air. Typically they are conducted in the same vacuum chamber. Plasma-exposed surfaces are often chemically activated, exposure to air changes the chemical state of the surface, e.g. by oxidation. Therefore, it is favourable to analyse the sample surface in-vacuo.

Ex-situ (lat.: "out of position") methods are applied after the investigated process and after the exposure to air. In some cases the influence of air is minimised by the use of sealable enclosures, called "desiccators", which are pumped down or filled with inert gas, for the sample storage and transport. However, it cannot be excluded, that the sample surface changes its characteristics between the exposure and the ex-situ analysis. "Post-mortem" (lat.: "after death") is a term equivalent to "ex-situ".

It is usually quite challenging to install and operate a diagnostic for the in-situ or in-vacuo surface analysis. However, the largely increased value of the data with respect to the ex-situ methods and the technical progress in the analysis tools make the use of these techniques more popular. Despite their advantages, in-situ and in-vacuo analysis solutions have a significant downside of high complexity and costs.

Therefore, most PMI experiments still rely on the ex-situ surface analysis techniques. Another reason for the predominant use of ex-situ is that the material samples can be transported to various laboratories specializing in particular analysis techniques, thus increasing the versatility and quality of analyses.

One example of in-situ analysis in the DIONISOS plasma facility [3] at MIT, USA is given in figure 1(a). Here, an ion beam accelerator is used for the ion beam analysis simultaneously during the plasma exposure, providing insight on the dynamics of PMI processes. Figure 1(b) shows the in-vacuo surface analysis station of PISCES-B [4]. The samples are extracted from the target station, after termination of the plasma discharge, by a swing-linear manipulator and inserted in the surface analysis station, where Auger electron spectroscopy (AES), X-ray photoelectron spectroscopy (XPS) and secondary ion mass spectrometry (SIMS) techniques can be applied. For the PSI-2 device [5], the application of the laser based techniques including LID and LIBS is envisaged for in-vacuo surface characterization in the target exchange and analysis chamber (figure 1(c,d)). The sample carrier can be retracted after the exposure to plasma by a linear manipulator to the target exchange and analysis chamber, where it can be analysed by the laser based techniques. Mass spectrometry can be used for measurement of the desorbed deuterium, and a 2D optical spectroscopy system can be applied to detect the light intensity at a wavelength corresponding to a certain element on the surface. The plasma operation in PSI-2 can be continued with the retracted sample carrier using a removable plasma dump. The vacuum valves separate the exposure and the analysis regions of the vessel.

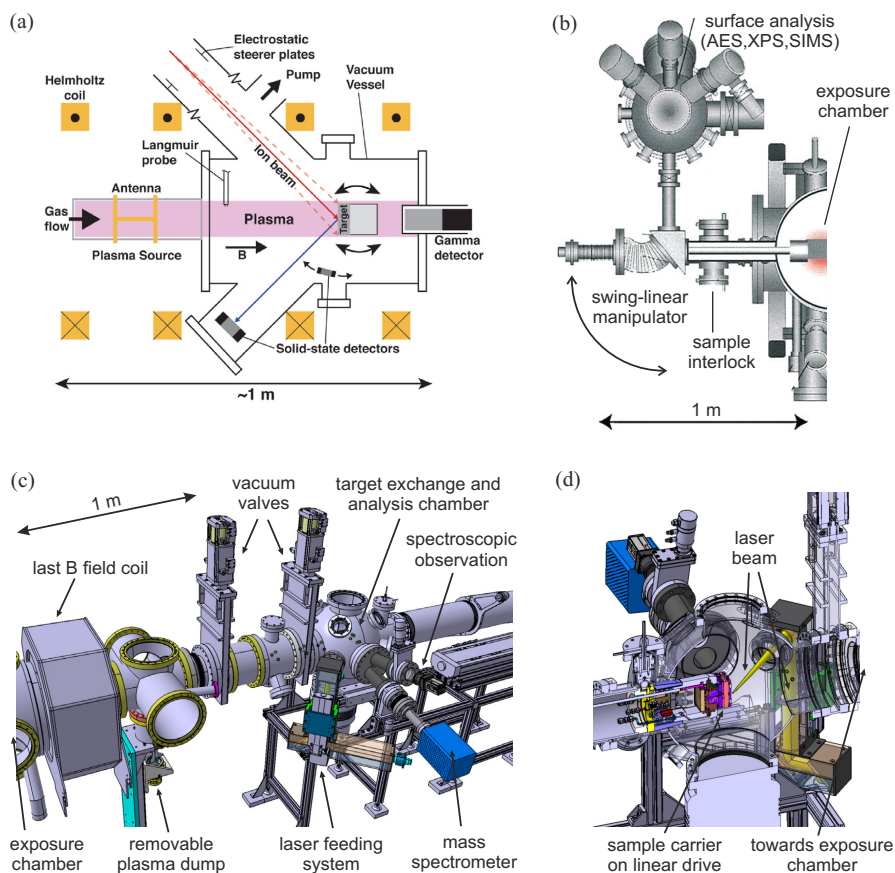


Figure 1. (a) In-situ ion beam analysis in DIONISOS [3]; (b) in-vacuo analysis station of PISCES-B [4]; (c) PSI-2 target exchange and analysis chamber with a laser feeding system for in-vacuo analysis; (d) cross-section of the opposite side of the PSI-2 target exchange and analysis chamber including an illustration of a sample exposed to a laser beam [5].

3. Surface analysis techniques

3.1 Thermal desorption spectrometry (TDS)

Thermal desorption spectrometry (TDS) is a frequently applied technique for the analysis of the gas, i.e. hydrogen isotopes, retention in samples. The gas is retained in various trapping sites in the material. By heating up of the sample the gas atoms escape the traps, diffuse to the sample surface and are released from the sample. In a TDS apparatus (figure 2(a)), the samples are heated in a compact vacuum chamber by a surrounding furnace. The

ramp rate of temperature is defined by the power of the furnace feedback controlled by the thermocouple measurements at the sample inside the vacuum chamber. Therefore, the technique is also often referred to as temperature programmed desorption (TPD). Partial pressures of different gas components are measured by a residual gas analyser (RGA), which is calibrated for the relevant masses by calibrating leaks. Typical temperature ramp rates are 0.1 K/s – 10 K/s. A faster ramp results in a higher signal but a lower temperature resolution in comparison with a slower ramp. The typical heaters which are used for TDS are infrared lamp or resistive

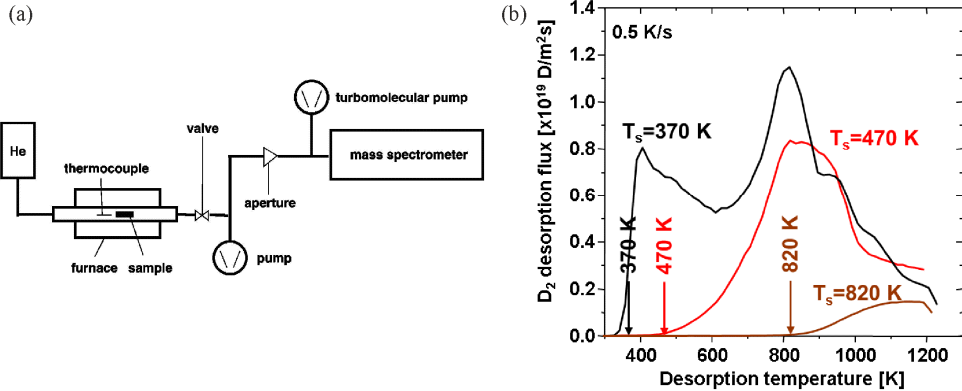


Figure 2. (a) Scheme of TDS system; (b) examples of spectra from thermal desorption. Temperatures at which the samples were exposed to deuterium plasma are indicated.

furnace.

Figure 2(b) shows an example of thermal desorption spectra of mass 4 (deuterium D_2) for carbon fibre composite (CFC) samples exposed to PISCES-A deuterium plasma at different temperatures [6]. The peaks correspond to different trapping sites of D in CFC. The distribution of deuterium in the sample bulk and a finite diffusion time out of the sample during the heating ramp lead to the peak broadening. The integral of the curve gives the total amount of deuterium in the sample released as D_2 molecules. Various methods are available to analyse the TD spectra, including sophisticated numerical codes describing the transport of solute gases in solids such as TMAP [7] and CRDS [8].

Laser induced desorption (LID) is a method in which a laser is used to heat up samples. The method can be seen as TDS with an extremely fast ($\sim 1-10$ ms) heating ramp. In this mode, the temperature resolution of the desorbed signal is completely lost, only the total amount can be measured. However, the method is fast and can be applied with a lateral resolution along the sample surface, e.g. to obtain a 2D mapping of the gas retention.

3.2 Scanning electron microscopy (SEM) and focused ion beam (FIB)

Scanning electron microscopy (SEM) is an electron beam based method of the surface analysis. The incident e-beam of $\sim 1-30$ kV is scanned across the surface and causes emission of secondary electrons (SE mode of operation) and backscattered electrons (BSE mode of operation) (figure 3(a)).

The SE mode is the most frequently used operation mode of SEM. It provides the surface topology by measuring the intensity of secondary electrons, which is a function of the angle between the surface and the detector. The imaging is provided by the rastering (scanning) of the e-beam along the surface. Figure 3 (b) shows an example of an SEM image taken in the SE mode.

The BSE mode provides the information on the elemental composition of the surface. It uses the fact that the intensity of backscattered electrons is a function of atomic mass of the scattering element. Heavy elements on the surface correspond to a bright part of the image, while light elements result in a dark part of the image (figure 3(c)).

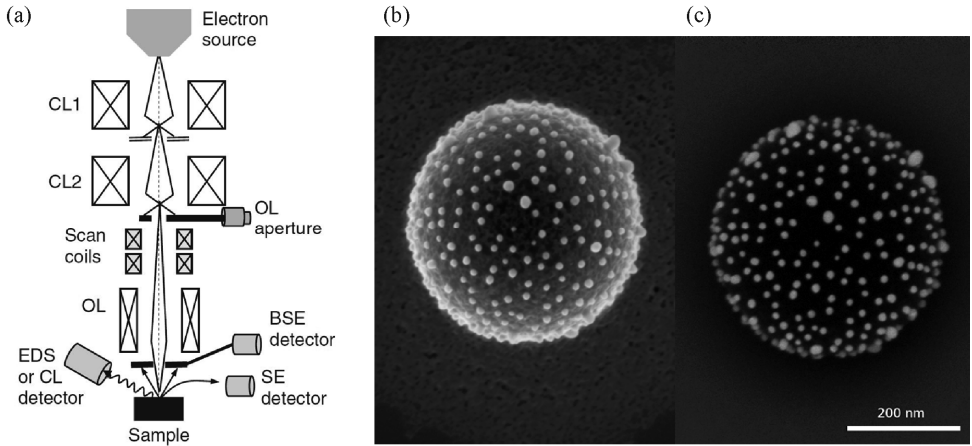


Figure 3. (a) Scheme of a SEM apparatus [9]; examples of (b) SE and (c) BSE operational modes of a SEM system: gold nanoparticles on polystyrene sphere. The SE image provides surface topography, while the BSE image gives material contrast [10].

The focused ion beam (FIB) technique is used for the nano-machining of the surface, e.g. surface cross-sectioning or preparation of small specimens. After the FIB treatment the surface is typically analysed by SEM. In a FIB instrument, an ion beam, typically Ga^+ , is rastered over the sample causing well controlled sputtering. Figure 4 shows a scheme of the application of FIB for the surface cross-sectioning with the subsequent SEM analysis, as well as SEM images of the surface topology and cross-section of a nano-structured tungsten surface, also known as tungsten fuzz.

3.3 Ion beam analysis (IBA): nuclear reaction analysis (NRA) and Rutherford back-scattering (RBS)

Ion beam analysis (IBA) techniques rely on a high energy (~1 MeV) ion beam produced, e.g., by a tandem accelerator. Several beam lines for different experiments are usually attached to the accelerator. In the example of the in-situ surface analysis given in figure1(a), the linear plasma device DIONISOS is attached to one of the beam lines delivering the ion beam from the accelerator. There are numerous IBA techniques available, with nuclear reaction

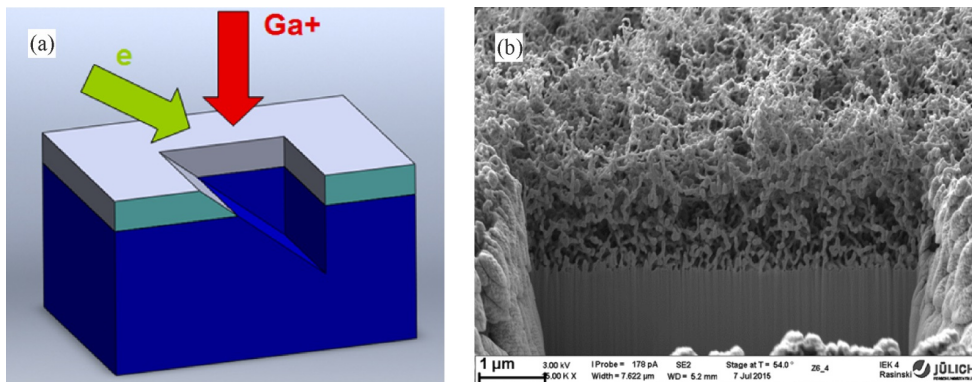


Figure 4. (a) Scheme of FIB application; (b) SEM image of a FIB cross section for nano-structured surface of a tungsten sample exposed to He plasma, also known as tungsten fuzz [11].

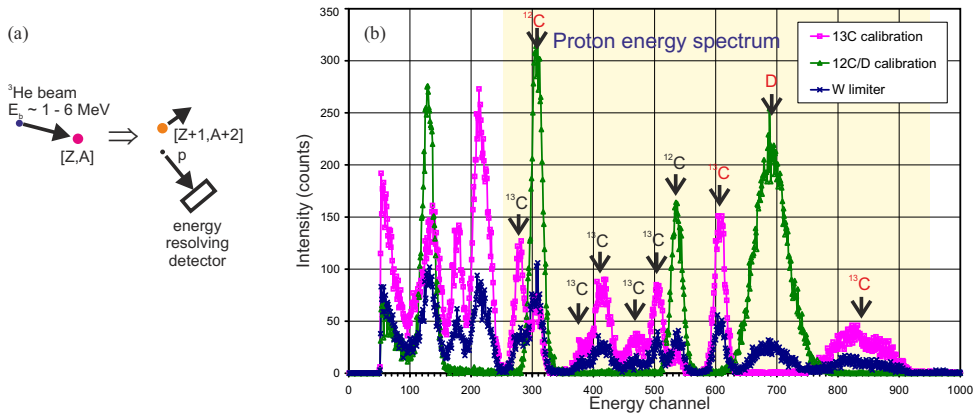


Figure 5. (a) Measurements scheme of NRA and (b) examples of NRA spectra for carbon-deuterium co-deposition layer on a tungsten test limiter after a $^{13}\text{CH}_4$ tracer injection experiment in TEXTOR as well as $^{12}\text{C}/\text{D}$ and ^{13}C reference samples [13]. Peaks from reactions which were used for the analysis are marked red.

analysis and Rutherford back-scattering being the most frequently used in the fusion related PMI research.

For nuclear reaction analysis (NRA), a ^3He beam in a range of energies 1-6 MeV is usually used, because ^3He reacts with many fusion relevant materials. The frequently used nuclear reactions with ^3He are: $\text{D}(^3\text{He},\text{p})^4\text{He}$, $^{12}\text{C}(^3\text{He},\text{p})^{14}\text{N}$, $^{13}\text{C}(^3\text{He},\text{p})^{15}\text{N}$, $^9\text{Be}(^3\text{He},\text{p})^{11}\text{B}$ and $^{11}\text{B}(^3\text{He},\text{p})^{13}\text{C}$, all of them having protons as one of the reaction product. The detection of further elements using other beams, i.e. H, D and Li, and reactions is possible. Figure 5(a) shows a measurement scheme of NRA. The method can determine the absolute amount of material in a maximal analysis depth of $\sim 1\text{-}10\ \mu\text{m}$, depending on the material and the ion beam energy. It has a moderate sensitivity of $\sim 10^{15}$ atoms/ cm^2 . The amount of the material can be determined by a cross-calibration with a sample with a known amount of material, or by using available reaction cross-section. Most of the PMI relevant reactions are incorporated in the IBA data analysis software SIMNRA [12]. A typical lateral resolution of $\sim 1\ \text{mm}$, corresponding to the beam diameter, can be reduced down to $\sim 10\ \mu\text{m}$ using the $\mu\text{-NRA}$ technique. NRA has a poor depth resolution, which can be

improved by the use of beams of different energies and therefore different probing depths for the same sample. Figure 5(b) shows examples of NRA spectra for $^{12}\text{C}/\text{D}$ and ^{13}C reference samples and from a mixed $^{12}\text{C}/^{13}\text{C}/\text{D}$ layer deposited on a tungsten test limiter in the tokamak TEXTOR [13].

For Rutherford back-scattering (RBS), a ^4He beam in a range of energies 1-6 MeV is usually used. A ^3He beam can also be used, thus RBS and NRA measurements can be combined. However, the market price of ^3He gas is significantly higher than of ^4He . Figure 6 shows a scheme of the RBS technique and an example of RBS spectrum. The energy of backscattered beam particles is $E_R = K(m_b, m_s, \theta, d) \times E_b$, where the kinematic factor K is a function of the beam particle mass m_b , scattering particle mass m_s , scattering angle θ and depth d and E_b is the beam energy. The method provides quantitative depth profiles of elements on the sample surface. The maximal analysis depth is typically $\sim 5\ \mu\text{m}$. The technique has a high sensitivity $\sim 10^{12}$ atoms/ cm^2 . The lateral resolution is of $\sim 1\ \text{mm}$ (beam diameter), similarly to NRA. RBS suffers from a pure discrimination of heavy elements with similar masses and has a limited applicability for mixed material layers and high-Z substrates.

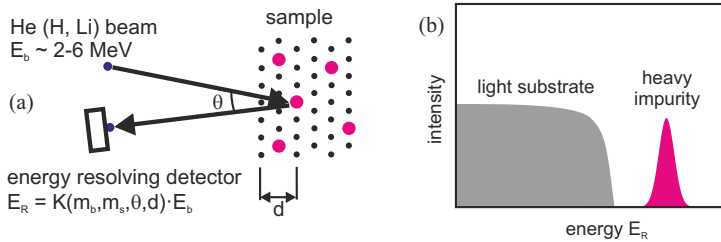


Figure 6. (a) Measurements scheme of RBS and (b) typical RBS energy spectrum for a heavy impurity on a light substrate.

3.4 Secondary ion mass spectrometry (SIMS)

Secondary ion mass spectrometry (SIMS) utilises ion probing beams in a range of energies of $\sim 1\text{-}30$ keV. The primary beam causes the emission of secondary ions from the sample, which are then analysed by a mass spectrometer delivering information on the elemental surface composition. Figure 7(a) shows the scheme of a SIMS apparatus. It usually incorporates at least two primary ion beam sources, e.g. an oxygen primary ion beam for probing of electropositive surface constituents and a caesium primary ion beam for electronegative elements. In some SIMS devices, an additional ion beam is used for the surface sputtering to obtain a

high quality depth profiling. The method has a high lateral resolution of ~ 100 nm - $1\ \mu\text{m}$. The modern SIMS devices, especially those equipped with a time-of-flight (TOF) mass spectrometer, have a high mass resolution and are able to resolve different molecular fragments. One drawback of the method is that only sputtered ion are analysed. The neutrals, which are the majority of sputtered particles, get lost. The process of the production of secondary ions is complex. Therefore, SIMS typically delivers qualitative but not quantitative information on the material composition. If the depth profiling is applied, the sputtering rate of the SIMS apparatus can be calibrated by measuring the depth of the SIMS crater by a surface profilometer.

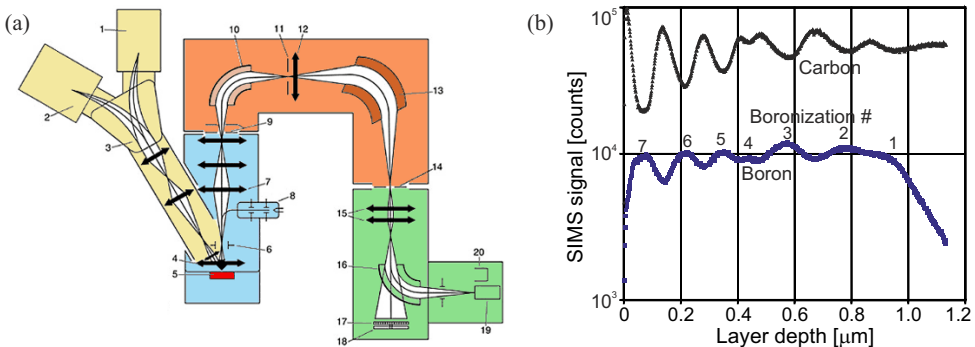


Figure 7. (a) Scheme of a SIMS apparatus: (yellow) primary ion column consisting of (1) and (2) ion sources, (3) primary beam mass filter, (4) immersion lens, (blue) secondary ion extraction system consisting of (5) specimen, (6) dynamic transfer system, (7) transfer optical system, (8) electron flood gun, (orange) mass spectrometer consisting of (9) entrance slit, field aperture, (10) electrostatic analyser, (11) energy slit, (12) spectrometer lens, (13) electromagnet, (14) exit slit, (green) detection system consisting of (15) projection lenses, (16) electrostatic sensor, (17) and (18) ion detectors and (19) Faraday cup [14]; (b) SIMS depth profile of a layer deposited on a collector probe installed for one experimental campaign in TEXTOR showing anti-correlated signals of carbon from the tokamak operation and boron from the boronizations [15].

Figure 7(b) shows an example of the SIMS depth profiling of a mixed layer deposited on a collector probe during a full experimental campaign in the tokamak TEXTOR [15]. The SIMS measurement was stopped when the signals dropped by a factor of two, corresponding to the bottom of the layer. Then the crater depth of 1.1 μm was measured by a stylus profilometer, thus, the sputtering rate of SIMS was obtained. The layer consists mainly of carbon from the normal plasma operation, with carbon being the main plasma impurity in TEXTOR, and boron from the boronisation wall conditioning. Seven boronisations were performed during the experimental campaign, which is reflected in the SIMS depth profiling.

4. Measurements of erosion and deposition

4.1 Quartz microbalance (QMB)

The quartz microbalance (QMB) technique uses the fact that the quartz (SiO_2) crystals have a resonant frequency changing with their mass. Quartz crystal microbalance (QCM) is a different notation for the technique. For commercially available quartz crystals for QMB, the resonant frequency is usually a few MHz, decreasing when gaining mass with a rate of $\sim 10^{-08}$ g/Hz, thus providing a high mass

sensitivity corresponding to about one monolayer of deposition on the quartz surface. Electronics measuring the crystal frequency have to be placed close to the detector, which increases the complexity of the QMB application in fusion devices. Another drawback is the sensitivity of the resonant frequency on the surrounding temperature. In fusion devices the particle flux is typically accompanied by a significant heat flux. Therefore, the influence of temperature on the QMB signal has to be monitored. It is often done by a second, reference, quartz, which is placed close to the first, measuring quartz. The reference quartz has similar temperature as the measuring one, but is mechanically covered to prevent any deposition on it and to keep its initial mass. Thus, the reference quartz has only the temperature response and can therefore be used for the temperature compensation of the measuring quartz.

The piezoelectric constant of quartz drops sharply for temperatures $>300^\circ\text{C}$ and reaches zero at the Curie point of 573°C . Therefore, QMB systems are typically installed in remote areas of a fusion device, where the heat flux is low. Material eroded from plasma facing components under the plasma impact is transported to remote areas where it is collected by QMB systems. Therefore, although actually measuring deposition, QMB systems are used as in-situ

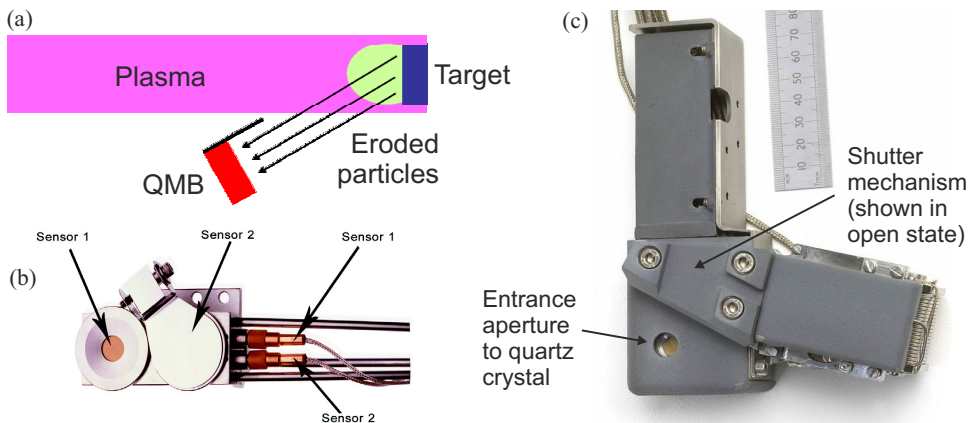


Figure 8. (a) Measurement scheme of QMB; (b) commercial dual QMB sensor [16]; (c) QMB diagnostic used at JET is protected by a graphite cover against heat loads [17,18].

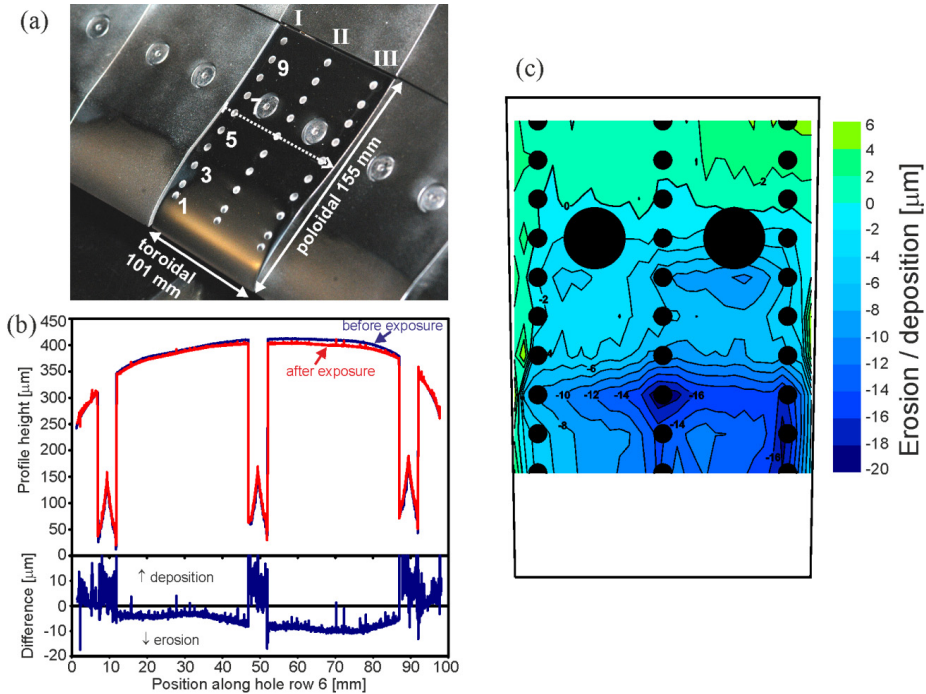


Figure 9. (a) View of the special limiter tile in TEXTOR after the exposure for one experimental campaign. The dimensions of the tile and the positions of the marker holes are indicated. The dotted line represents the position and the direction of the X axis in (b); (b) surface height profile measured by optical profilometry before and after the exposure; (c) 2D reconstruction of the erosion and deposition pattern of the limiter tile. Negative values represent erosion, positive values deposition.

erosion monitors of the plasma facing components.

Figure 8 shows the scheme of QMB application in a plasma device as well as photographs of commercially available QMB systems [16] and of a QMB system for the in-situ application in the tokamak JET [17,18].

4.1 Application of marker tiles

There are numerous methods which can quantify the amount of deposition on a certain sample or a tokamak wall tile. It is significantly more complicated to measure the erosion, something which is absent. A well-established method is marker techniques. Markers have to be prepared on samples or wall tiles in advance, before their exposure. The wall components equipped with markers are also called "smart tiles".

Typically the installation of "smart tiles" at the wall needs the air vent of the vessel, which is done between experimental campaigns. Therefore, unlike the in-situ QMB method, the marker technique is campaign-averaged. Markers can be e.g. well-defined layers of material deposited on a substrate in a combination suitable for the applied surface analysis techniques. The marker layers are characterised before and after the exposure. The difference is then the amount of eroded material. Techniques like RBS or SIMS are often used for the marker characterisation.

Another approach of markers is the application of reference points on the sample surface which are not subjected to erosion. The reference points can be e.g. recessed grooves or pits, which bottom is shaded from the eroding plasma flux. Figure 9(a) shows a marker tile of the main toroidal

limiter in TEXTOR made of isotropic graphite, which was used to determine the erosion-deposition pattern over the full tokamak campaign [19]. 3×10 drill holes were used as the reference points. It was found out by SIMS that up to several μm of deposition was accumulated in the recessed holes during the experimental campaign. It was taken into account when comparing the surface profiles measured by the optical surface profilometry before and after the exposure (figure 9(b)). A full erosion-deposition pattern of the tile surface was reconstructed by combining the surface profiles across the recessions done in both toroidal and poloidal directions (figure 9(c)).

References

- [1] A. Kreter, *Reactor-relevant plasma-material interaction studies in linear plasma devices*, Fusion Sci. Technol. **59** (2011) 51.
- [2] G.A. Somorjai, *Introduction to Surface Chemistry and Catalysis*, published by John Wiley & Sons, ISBN 978-0471031925 (1994).
- [3] G.M. Wright et al., *An experiment on the dynamics of ion implantation and sputtering of surfaces*, Rev. Sci. Instrum. **85** (2014) 023503.
- [4] R.P. Doerner, M.J. Baldwin and K. Schmid, *The influence of a beryllium containing plasma on the evolution of a mixed-material surface*, Phys. Scr. **T111** (2004) 75.
- [5] A. Kreter et al., *Linear plasma device PSI-2 for plasma-material interaction studies*, Fusion Sci. Technol. **68** (2015) 8.
- [6] A. Kreter et al, *Fuel retention in carbon materials under ITER-relevant mixed species plasma conditions*, Phys. Scr. **T138** (2009) 014012
- [7] G.R. Longhurst, *TMAP7 User Manual*, Idaho National Laboratory, INEEL/EXT-04-02352 (2008).
- [8] M. Oberkofler, M. Reinelt, Ch. Linsmeier, *Retention and release mechanisms of deuterium implanted into beryllium*, Nucl. Instrum. Meth. B **269** (2011) 1266.
- [9] *Low Voltage Electron Microscopy: Principles and Applications*, Editors: D.C. Bell, N. Erdman, published by John Wiley & Sons, ISBN: 9781119971115 (2013), DOI: 10.1002/9781118498514.
- [10] Carl Zeiss Microscopy GmbH, *ZEISS Gemini Optics - High Resolution Images On Real World Samples*, EN_42_050_016, CZ 05-2015, <http://www.zeiss.com/geminisem>.
- [11] M. Rasinski, M. Wirtz, private communication.
- [12] M. Mayer, *SIMNRA User's Guide*, Report IPP 9/113, Max-Planck-Institut für Plasmaphysik, Garching, Germany (1997).
- [13] A. Kreter et al, *Investigation of carbon transport by $^{13}\text{CH}_4$ injection through graphite and tungsten test limiters in TEXTOR*, Plasma Phys. Control. Fusion **48** (2006) 1401.
- [14] J.W. Valley et al., *4-Ion Microprobe Analysis of Oxygen, Carbon, and Hydrogen Isotope Ratios*, Reviews in Econ. Geology **7** (1998) 73.
- [15] A. Kreter et al., *Long-term carbon transport and fuel retention in gaps of the main toroidal limiter in TEXTOR*, J. Nucl. Mater. **438** (2013) S746.
- [16] INFICON, *Front Load Dual Sensor*, cibe23a1-a, <http://www.inficon.com>.
- [17] H.G. Esser et al., *Effect of plasma configuration on carbon migration measured in the inner divertor of JET using quartz microbalance*, J. Nucl. Mater. **337-339** (2005) 84.
- [18] A. Kreter et al., *Nonlinear impact of edge localized modes on carbon erosion in the divertor of the JET tokamak*, Phys. Rev. Lett. **102** (2009) 045007.
- [19] A. Kreter et al., *Long-term erosion and deposition studies of the main graphite limiter in TEXTOR*, Phys. Scr. **T128** (2007) 35.

FUSION PRODUCT DIAGNOSTICS OF TOKAMAK PLASMAS

Vasily Kiptily

*Culham Centre for Fusion Energy
EURATOM Association, Culham Science Centre, Abingdon, OX14 3DB United Kingdom
vasili.kiptily@ccfe.ac.uk*

ABSTRACT

This lecture reviews the fusion product diagnostics that are currently used for study of tokamak plasmas. Neutrons and charged fusion product measurement techniques as well as γ -ray diagnostics will be described together with examples obtained in experiments on JET (UK). Developments for ITER are discussed. The detailed information on the issues of the lecture can be found in the reviews [1-3].

I. INTRODUCTION

Fusion product diagnostics can be used to determine a fusion reaction rate, which indicates how close the plasma is to the ultimate goal of making a power plant based on nuclear fusion. However, these diagnostics can also provide large amounts of additional information, such as ion temperatures, the thermonuclear fraction in the fusion reaction rate, degree of fast-ion confinement, fast-ion loss mechanism, etc.

Each section of this lecture contains a general explanation of these systems, showing some experimental results obtained on working machines. A lot of useful information on the behaviour of energetic particles and their degree of confinement is provided in present D-D experiments since non-thermal ions contribute dominantly to the fusion reaction rate. Here are D-D reactions



and



have been the primary diagnostic tools. The $D\text{-}{}^3\text{He}$ reaction



has been used for diagnosing the plasma when ${}^3\text{He}$ is introduced for the discharge.

In future D-T experiments on ITER, the contribution of the fusion reaction



will be increased and the combination of several neutron measurement systems will provide the absolute fusion output and neutron fluence on the first wall. Cross-sections of the fusion reactions are well known (see Fig.1) and can simply be calculated using parameters from [4].

Together with neutron measurement, NPA, γ -ray and the fast-ion/ α -particle loss measurements play important roles in

research on burning plasma physics and hence in the self-heating burning control of the device.

II. NEUTRON DIAGNOSTICS

This chapter is dedicated to measurements of the neutron emission rate, neutron emission profiles and energy spectra. There have been several review articles on neutron diagnostics, and Ref.5 is recommended for the neutron diagnostics details.

II.A. Neutron emission rate measurements

The absolute measurement of neutron emission rate from the whole plasma is a very important diagnostic as a fusion power monitor in fusion experiments with D-D or D-T plasmas. So, the neutron emission rate will be used as a feedback parameter for fusion output control in ITER or other burning plasma devices.

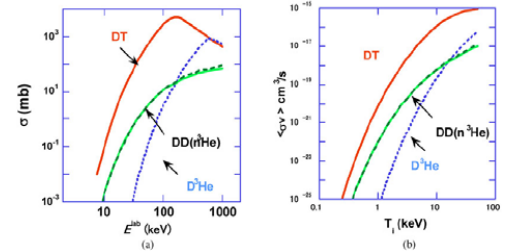


Fig.1. Fusion cross sections (a) as a function of the CM energy of the reacting particles and fusion reactivities (b) for Maxwellian ion distributions as a function of ion temperature T_i .

In fusion experiments with auxiliary heating, such as NBI, the neutron emission rate changes from 10^4 – 10^6 over the time scale of the fast ion slowing-down time (~ 100 ms). Therefore, the detector of the neutron emission rate must have a wide dynamic range and fast response time and also be immune to spurious signals from hard X-rays and γ -rays. To implement these two requirements simultaneously, a fast response neutron detector that selectively produces a large signal only for neutrons is used in combination of two operation modes: a pulse-counting mode and the current mode. The BF_3 proportional counters, ${}^3\text{He}$ proportional counters, and ${}^{235}\text{U}$ fission chambers are the most commonly used neutron detectors [6]. The BF_3 and ${}^3\text{He}$ proportional counters utilize ${}^{10}\text{B}(n,\alpha){}^7\text{Li}+2.78$ MeV and ${}^3\text{He}(n,p)\text{T}+0.77$ MeV reactions, respectively. The ${}^{235}\text{U}$ fission chambers utilize the

$^{235}\text{U}(n,\text{fission})$ reaction producing ~ 200 MeV of energy. As the energy dependence of these reactions is proportional to $E^{-1/2}$, these detectors are more sensitive to low-energy neutrons. To detect higher-energy neutrons, these detectors are often used with moderators to slow down fast neutrons. A fission chamber is an ionization chamber with electrodes coated with fissile material such as ^{235}U or ^{238}U , and ionization of the chamber gas is caused by fission fragments produced at the electrode with kinetic energy of 50 to 200 MeV. Here, it should be noted that ^{238}U fission chambers are sensitive only to fast neutrons because the $^{238}\text{U}(n,\text{fission})$ reaction has a threshold of ~ 1 MeV.

The neutron activation system provides time-integrated measurements of the total neutron yield with high degree of accuracy using well-known neutron reaction cross-sections. If the irradiation point is installed near the plasma, the relation between the neutron emission rate in the whole plasma and the neutron flux at the irradiation point should be calibrated by neutron Monte Carlo calculation with precise machine modelling.

The primary goals of the neutron activation system are to maintain a robust relative measure of fusion energy production with stability and a wide dynamic range, to enable accurate absolute calibration of fusion power. Fluxes of D-D and D-T neutrons can be measured easily with several foils with different threshold energy reactions. From the ratio of D-D and D-T neutron fluxes, the triton burn-up ratio in D-D plasmas and the D/T fuel ratio (n_d/n_t) in D-T plasmas can be derived. A sophisticated multi-foil activation technique using an unfolding code can provide a neutron energy spectrum at the irradiation point which is useful for testing of the neutron transport calculations.

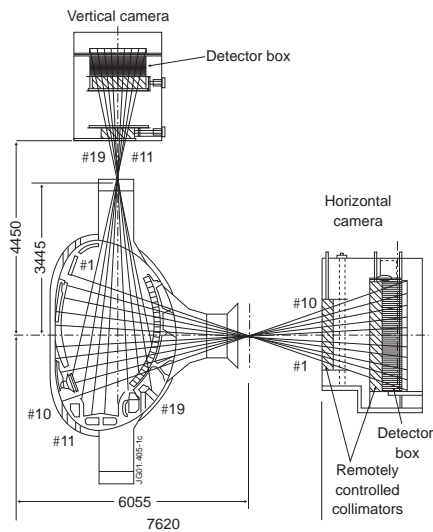


Fig.2 Schematic view of JET neutron profile monitor.

The neutron activation method using solid samples is used for accurate measurement of the neutron yield in many fusion devices. At current large tokamaks, pneumatic operated sample transfer systems are employed using polyethylene capsules. JET

has multiple irradiation positions with different poloidal locations, while JT-60U has a single position of the irradiation end in a horizontal port. A capsule with sample foils can be transferred to the selected irradiation end via a “carousel” switching system from a capsule loader in the γ -ray counting station before a plasma shot. After the plasma shot, each capsule returns to the γ -ray counting station by the pneumatic transfer system. Gamma-rays from the activated samples are measured with HPGe or NaI(Tl) scintillation detectors. In the case of fissile samples, such as ^{232}Th or ^{238}U , delayed neutrons from the irradiated samples are measured with high-sensitivity neutron detectors, such as ^3He or BF_3 proportional counters.

II.B. Neutron emission profile systems

The neutron source in fusion plasmas consists of a thermonuclear component and a component produced by fast fuel ions (deuterons, tritons). The thermonuclear neutron source profile is usually a function of the magnetic surfaces, but this is not true for the neutron source component related to fast ions. Their behaviour in reactor plasmas is crucially important, especially in driven regimes approaching the ignition. Measurements of spatial and energy distributions of fast confined fuel ions are very important for optimization of NBI and ICRF heating and current drives.

Neutron source profile measurement is the principal method for the measurement of fast fuel ion distributions. Because of non-symmetric deposition of NBI and ICRF-driven ion distributions on magnetic surfaces, the two-dimensional (2-D) neutron source profile measurements are required. This requirement is becoming stronger for optimization of ignition in reactors and plasmas influenced by magneto-hydrodynamic (MHD) instabilities.

The primary function of a neutron profile monitor is to measure the neutron emissivity over a poloidal cross section of the plasma using line-integrated measurements recorded by neutron detectors viewing the plasma along a number of chords (lines of sight). Knowledge of the absolute detection efficiency of the system enables us to obtain the total instantaneous neutron yield from the tokamak independently supplementing the results obtained using other techniques, such as neutron activation or neutron flux monitors.

The JET neutron profile monitor is a unique instrument among diagnostic systems available at large fusion devices. The solution adopted in JET for imaging of the noncircular plasma neutron source is to use two fan-like multi-collimator detector arrays as illustrated in Fig.2. A nine-channel camera is positioned above the vertical port to view downward through the plasma (vertical camera), while a ten-channel assembly views horizontally from the side (horizontal camera). The collimation can be remotely adjusted by use of two pairs of rotatable steel cylinders. Each channel is equipped with a set of three different detectors: a NE213 liquid organic scintillator with pulse shape discrimination (PSD) electronics for simultaneous measurement of 2.5 MeV D-D neutrons, 14-MeV D-T neutrons, and γ -rays; a BC418 (Bicron) plastic scintillation detector for measurement of 14-MeV D-T neutrons; and a CsI(Tl) photodiode for measuring the fast-electron bremsstrahlung and γ -ray emission in the range between 0.2 and 6 MeV. Each NE213 detector-photomultiplier unit is equipped with two PSD units allowing neutrons to be separated from γ -rays and providing the necessary energy discrimination. The Bicron scintillators are located in front of

the NE213 scintillators and are coupled to PMTs via a light guide. They are sufficiently small and therefore relatively

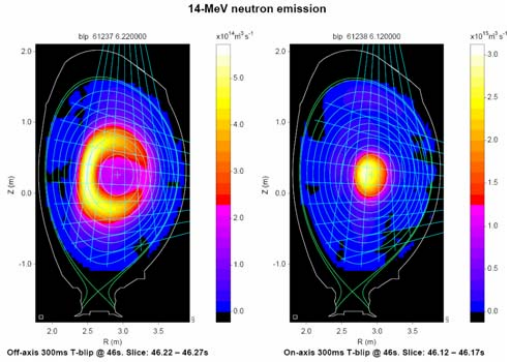


Fig.3 Tomographic reconstruction of data obtained with JET neutron cameras in TTE: left – off-axis tritium NBI blip; right – on axis one.

insensitive to γ -rays with $E_\gamma > 2$ MeV. The detection efficiencies for each of the 19 channels (and for both D-D and D-T neutrons) are determined computationally and by taking into account accelerator-based absolute calibrations of the scintillation detectors. The JET also complements activation systems and neutron flux monitors, providing an independent estimate of the absolute neutron yield from the plasma.

The JET profile monitor allows 2-D images to be obtained from the plasma neutron emission. Tomographic deconvolution of the line-integrated measurements is carried out with TOMO5 code [7] to obtain a 2-D mapping of the neutron emission rate. The plasma coverage by neutron profile arrays is adequate for neutron tomography, although neighbouring channels are 15 to 20 cm apart and have a width of ~ 7 cm as they pass near the plasma centre.

Capabilities of this method are illustrated in Fig.3 or two

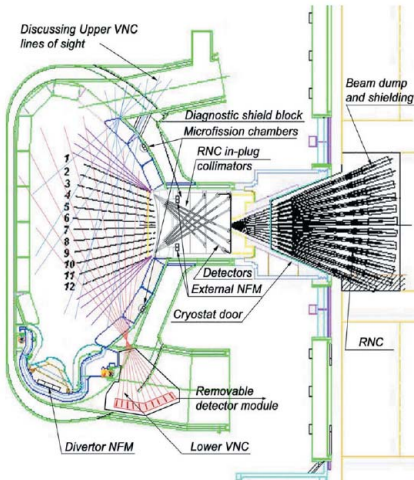


Fig. 4. Arrangement of the 2-D neutron source strength and energy distribution measurements in ITER.

JET discharges with injection of tritium beam into D-D plasmas in the Trace Tritium Experiments (TTE). These discharges were characterized by the off-axis and on-axis injections into L-mode monotonic current profile plasmas. In the off-axis injection case, a banana-shape 14-MeV neutron emission is on the high-field site. The on-axis beam-injection generates neutron emission in the plasma centre.

The necessity of 2-D neutron profile measurements in ITER arises from the fact that, due to fast ion components, the neutron source profile will not be constant on magnetic surfaces, especially during ICRH, NBI, sawtooth oscillations, excitation of Alfvén eigenmodes, and in advanced tokamak regimes with strongly negative magnetic shear. The 2-D neutron source strength and energy distribution measurements in ITER could be made by joint application of radial neutron camera (RNC) including compact in-plug collimators and vertical neutron cameras (VNC) showed in Fig.4. The RNC consists of 12x3 fan-shaped arrays of collimators viewing the plasma through a special shielding plug in equatorial port #1 and additional channels placed inside this equatorial port.

Several possible arrangements of the VNC have been studied, including distributed and upper VNC. The main concept of the lower VNC arrangement is to place the VNC shielding module inside a divertor port with collimators viewing the plasma through the gaps in the divertor cassettes, the blanket

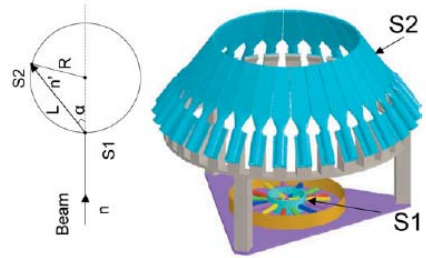


Fig. 5. Scheme of TOFOR spectrometer.

modules, and the triangular support.

III.C. Neutron spectrometry

The neutron emission spectrometry is a multi-function diagnostic the information of which is derived from measurement of the energy distribution of the direct and scattered neutron flux from plasmas.

The spectrum of direct plasma neutron emission reflects the relative motions of the fuel ions given by their velocity distributions. The neutron emission varies in both intensity and spectrum shape as the plasma heating conditions are changed. With ohmic heating, the ions are in thermal equilibrium and the spectrum shape will be almost precisely Gaussian and the effective ion temperature, T_i , can be deduced simply from the fwhm of the measured spectrum, $\text{fwhm} = 82.5(T_i)^{1/2}$ for d-d plasmas and $178(T_i)^{1/2}$ for d-t plasmas (keV units). Intensity of neutron emission depends on the fusion reaction rate $R \propto n_1 n_2 \langle \sigma v \rangle_{T_i}$, where n_1, n_2 , are the local ion densities and $\langle \sigma v \rangle_{T_i}$ is a fusion reactivity. This temperature is actually an average along the line-of-sight through the plasma. However, since the neutron emission is strongly localized near the plasma centre, the line-

averaged temperature is typically only about 10% lower than the central temperature. The thermal neutron emission is isotropic and has a characteristic peak energy, $E_0(T_i)$. Neutron emission spectra with auxiliary heating (NBI, ICRH) of plasmas have a non-Gaussian shape. Furthermore, rotation of the plasmas relative to a detector leads to the peak energy shift due to the fusion reaction kinematics.

At present JET is the tokamak best equipped for neutron diagnosing with high-performance spectrometers installed. One of them, spectrometer TOFOR is dedicated to measuring 2.5-MeV D-D neutrons in DD plasmas and can reach count rates in the 100-kHz range [8]. It is placed in the roof lab looking vertically down on the plasma at a distance of ~ 20 m with the sight line perpendicular through the plasma core.

Principles of the TOF spectrometer are shown on Fig.5: an incoming neutron being scattered from a proton in scintillator S1 to scintillator S2 with both detectors placed on the constant TOF sphere. The lower panel shows a model of the TOF spectrometer designed for optimized rate (TOFOR); the height is ~ 1 m [8].

There is also an upgrade version of the MPR spectrometer (MPRu) for measurement of the entire fusion neutron spectrum in the energy range ≈ 1.5 to 18 MeV. The incoming neutrons produce proton recoils in the polyethylene target foil. The

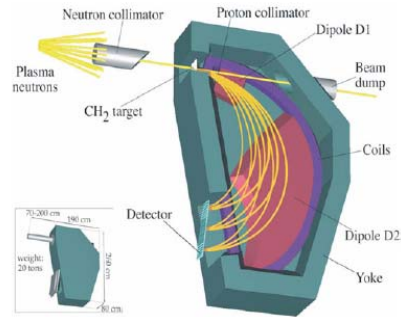


Fig. 6. Scheme of the magnetic proton recoil spectrometer (MPR)

A flux of neutral hydrogen (D, T) atoms is produced in the plasma by three processes: (a) CX with background neutrals, (b) radiative recombination of protons (deuterons, tritons) and electrons, and (c) electron capture from hydrogen-like impurity ions. The ratio between these three processes varies depending on particle energy and position in the plasma. The first two processes are dominant in the thermal energy range below 100

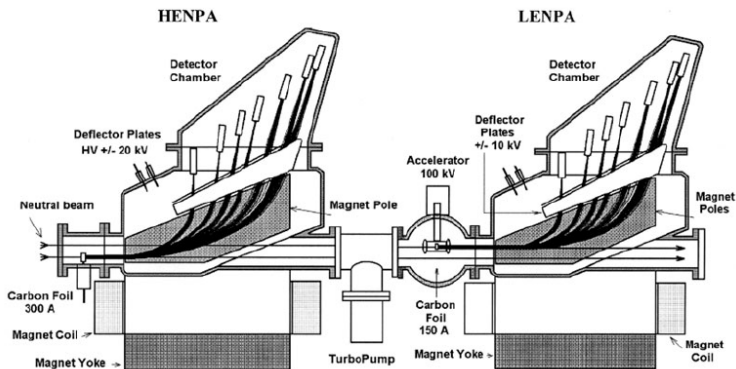


Fig. 7. Layout of NPA diagnostic set up proposed for ITER [12].

forward-going protons are focused, analyzed in the pole gap of D1 and D2 magnet and counted in the detector array at the focal plane exit (Fig.6). This is a high-performance instrument for diagnosis of D-T plasmas with count rates in the megahertz range [9]. For D plasmas, it is complementary to TOFOR.

III. NEUTRAL PARTICLE ANALYSERS [2]

The charge exchange (CX) neutral particle analysis provides straightforward information concerning parameters of the plasma ion component. The energy spectra of neutral atomic fluxes emitted by the plasma provide not only the ion temperature but also the ion energy distribution function. The latter is important both for understanding the particle and energy confinement mechanisms of the ion component and for studying the behaviour of ions produced by neutral beam heating and by application of ICRF heating.

to 200 keV, with recombination dominating in the central part of the plasma in large tokamaks. The last process is prevalent in the suprathermal energy range above 100-200 keV. According to this, the thermal energy range is used to study the bulk plasma ion component, whereas the suprathermal range is suitable for the study of high energy ions generated by auxiliary heating like ICRH or produced by fusion reactions in the plasma.

In the suprathermal range, the neutral flux is produced mainly by H^+ , D^+ , T^+ ions undergoing electron capture from hydrogen-like low-Z impurity ions. In the case of He^{2+} ions, neutralization in the MeV range occurs by double electron capture from helium-like low-Z impurity ions. The most probable donors for electron capture in large plasma machines like JET are helium-like carbon and beryllium ions because carbon and beryllium are the main low-Z impurities in these machines and their densities in the plasma core are higher than the density of H^0 . At energies $E > 100$ keV, the hydrogen-like

ions Be^{3+} and C^{5+} are rather effective donors for neutralization of H^+ in comparison with the residual H^0 atoms.

Neutralization of confined alphas on impurities in D-T plasma creates the possibility to detect the energy spectrum of the fast He^0 atoms and to derive the confined α -particle distribution function. The first successful attempt to do this was made on JET [10]. Another option to measure the flux of suprathermal atoms is to use the pellet CX technique. These measurements obtained with the use of lithium (or boron) pellets injected into the plasma were used in TFTR for measuring the distributions of ICRF-driven H^+ -ions and fusion alpha particles [11]. For lithium pellets, H^+ and He^{2+} ions interacted with the pellet ablation cloud of Li^+ to form an equilibrium neutral fraction as a result of the reactions $\text{H}^+ + \text{Li}^+ \rightarrow \text{H}^0 + \text{Li}^{2+}$ and $^4\text{H}^{2+} + \text{Li}^+ \rightarrow ^4\text{He}^0 + \text{Li}^{3+}$.

Neutral particle analyzers (NPA) have the following general features. The neutral particle flux from a plasma enters the analyzer and is partially ionized by stripping collisions with molecules in a gas-filled stripping cell or by passing through a thin foil (e.g., a 5- to 40-nm thick carbon foil). The resulting secondary ions are separated by mass and by energy with superimposed or adjacent (tandem-type) electric and magnetic fields or by time-of-flight (TOF) analysis. Then they are detected by a set of ion detectors. Scintillation counters, channeltrons, or microchannel plates (MCPs) combined in chevron-type units can be used as ion detectors. Sets of detectors (from 5 up to 40 per mass species) are normally used in NPAs followed by time-resolved electronics providing measurements of the energy spectra and their time variation. NPAs are calibrated using H/D atom beams of known energy and intensity. In the last decade solid-state detectors, and in particular natural diamond detectors (NDDs), were introduced for detection and energy analysis of the neutral particle fluxes from plasmas.

A superimposed E||B concept in which the electric field region was spatially displaced to follow the magnetic field region (i.e., tandem E||B) was developed in PPPL. The tandem E||B NPA enables simultaneous measurement of multiple mass species (e.g. H, D, and T or ^3He). Similar instruments have been developed for JT-60 and JET.

There are two important tasks for CX neutral particle diagnostics in ITER. The first task is the measurement of the

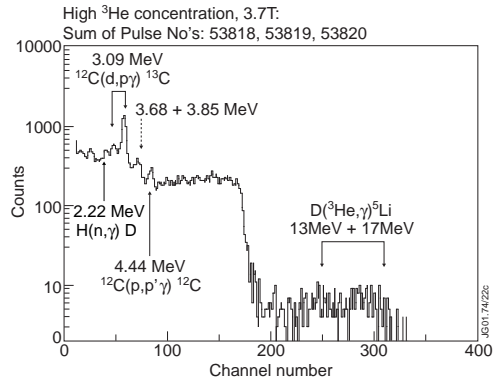


Fig. 8. Sum of gamma-ray energy spectra measured during three 2MA/3.7T discharges with ICRF heating tuned to $\omega = \omega_{3\text{He}}$ in deuterium JET plasma with high ^3He concentration, $\eta_{\text{He}} \approx 20\%$. [14]

hydrogen isotope composition of the plasma on the basis of measurements of neutralized fluxes of corresponding hydrogen ions, namely, protons, deuterons, and tritons in the 10- to 200-keV energy range. One of the main tasks of the ITER control system is to provide an optimal D-T ratio in the plasma. The second task of neutral particle diagnostics is the measurement of the distribution functions of MeV ions generated by auxiliary heating and fusion reactions. This includes measurement of the confined D-T α -particle distribution function by detection of He atom energy spectra in MeV range.

Figure 7 presents a tandem arrangement of two NPAs, which is proposed to be used on ITER. The NPA system consists of two devices: a low-energy NPA (LENPA) for the 10 to 200 keV energy range for providing measurement control of the isotope ratio and a high-energy NPA (HENPA) for the energy range 0.1 to 4 MeV to measure the fast ion and confined α -particle distribution functions by detection of the energy spectra of the neutralized fast ions and α -particles. Both the HENPA and the LENPA view along a major radius close to the equatorial plane of the torus and through the same straight vacuum opening of 20-cm diameter at the blanket face in the ITER port. Both analyzers can operate simultaneously because the LENPA is shifted horizontally to ensure an independent line of sight. Analyzers were successfully tested and used on JET.

IV. GAMMA-RAY DIAGNOSTICS

One of the most important techniques used for studying fast-ion behaviours in fusion devices is nuclear reaction γ -ray diagnostics [13]. Measurements on the tokamaks Doublet-III, TFTR, JT-60U and JET have shown that an intense γ -ray emission is produced when fast ions (fusion products, ICRF-driven ions and NBI-injected ions) react either with plasma fuel ions or with the plasma impurities such as beryllium, boron, carbon and oxygen. On JET, the γ -ray emission measurements are routinely used to interpret different fast ion physics effects arising during ICRF and NBI heating.

There are three sources of fast particles that can give rise to a γ -ray emission from plasmas. Firstly, fusion reactions between the plasma fuel ions produce fusion products such as fast tritons, protons, ^3He and ^4He ions with MeV-energies. Secondly, ICRF heating of H- and ^3He -minority ions accelerates these ions to energies in the MeV range. There are also ICRF schemes to accelerate D, T and ^4He ions. Thirdly, NBI heating introduces D, T, H, ^4He and/or ^3He ions. Fast ions born in plasma produce line spectra due to their nuclear reactions with low-Z plasma

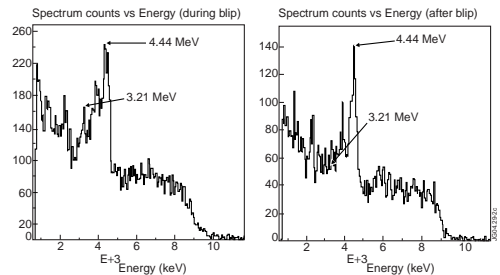


Fig. 9. Gamma-ray spectra measured in JET discharge with deuterium NBI heating and tritium 300-ms blip [16].

impurities. The fusion product neutrons interact with the structural materials, generating a continuous γ -ray background. A typical γ -ray spectrum recorded during ICRF heating with ^3He -ions shown in Fig.8. The 17-MeV γ -rays from the $\text{D}(^3\text{He}, \gamma)^3\text{Li}$ reaction, which used in JET as an indicator of the ICRF power deposition efficiency, were observed.

More than 15 essential nuclear reactions have been identified in the γ -ray spectra recorded at JET. Particularly, the reaction $^9\text{Be}(\alpha, n\gamma)^{12}\text{C}$, the significance of which was investigated in detail in Ref.15 for the fusion-born α -particle measurements. This is type of resonant reaction, which has thresholds. The presence of the 4.44-MeV peak in the γ -ray spectra is evidence for the existence of alphas with energies that exceed 1.7 MeV. The 3.21-MeV γ -rays indicate that the alphas with energies in excess of 4 MeV exist in the plasma. As an example, Fig.9 shows two γ -ray spectra, recorded in the same JET discharge: the left hand side plot shows the spectrum during 300-ms T-beam blip, the right one shows the spectrum just after the NBI blip. During the injection two γ -ray peaks, 4.44 MeV and 3.21 MeV are observed, however, in the post-blip time-slice the 3.21-MeV peak becomes rather weak. This is an effect of changes in the distribution function, i.e. the result of a shift of the high-energy tail to the low-energy range due to the α -particle slowing-down.

IV.A. Gamma-ray spectrometers in JET

In JET γ -ray energy spectra are measured with two different devices, one with a horizontal and one with a vertical line of sight through the plasma centre [14]. The first spectrometer is a calibrated bismuth germinate, $\text{Bi}_4\text{Ge}_3\text{O}_{12}$ (BGO) scintillation detector that is located in a well-shielded bunker and views the plasma tangentially. In order to reduce the neutron flux and the γ -ray background, the front collimator is filled with polythene. Behind the scintillation detector there is an additional dump of polythene and lead. The γ -rays are continuously recorded in all JET discharges over the energy range 1-28 MeV, with an energy resolution of about 4% at 10 MeV. The second device for the γ -ray energy spectrum measurements is a $\text{NaI}(\text{Tl})$ scintillation detector viewing the plasma vertically through the centre.

IV.B. Gamma-ray emission profile measurements

Spatial profiles of the γ -ray emission in the energy range $E_\gamma > 1$ MeV have been measured in JET using the Gamma Cameras, which have ten horizontal and nine vertical collimated lines of sight. Each collimator defines poloidal-viewing extent at the centre of plasma of about 10 cm (Fig.3). The detector array is comprised of 19 $\text{CsI}(\text{Tl})$ photo-diodes (10 mm \times 10 mm \times 15 mm). Although the system was developed for neutron measurements and the shielding is not entirely adequate for γ -ray measurements, in discharges with ICRF heating the γ -ray measurements are successful.

In the Gamma Cameras the line-integral γ -ray brightness along the viewing direction is measured. Experimental data obtained for the 19 lines of sight are tomographically reconstructed to get the local γ -ray emissivity in a poloidal cross-section. In these reconstructions the full geometry of the collimators and detector efficiencies were taken into account, but small effects of attenuation and scattering of the γ -rays were neglected. It is assumed that the distribution of the low-Z

impurities is uniform in the plasma core as confirmed by atomic spectroscopy measurements. For the tomographic reconstruction a constrained optimisation method [7] is used, which was successfully applied earlier to soft x-ray, bolometer and neutron measurements at JET. The effective spatial resolution of the diagnostic in these experiments is about 7cm.

The today data acquisition system accommodates the γ -ray count-rate measurement in four energy windows. This allows allocating specific γ -ray peaks in the windows to be counted separately. A typical example of the tomographic reconstruction of the measured line-integrated profiles is shown in Fig.10. It is seen clearly that the γ -ray emission profile produced by fast D-ions (right-hand figure) differs from the profile from ^4He -ions (left-hand figure) accelerated by ICRF [17]. This effect can be explained by the difference in pitch-angle distribution between ^4He beam-ions injected into the plasma quasi-tangentially and isotropic D-minority ions.

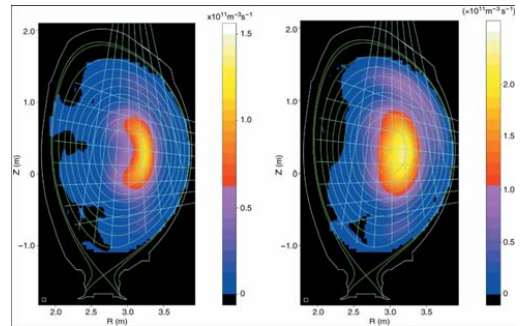


Fig. 10. Tomographic reconstructions of 4.44-MeV γ -ray emission from the reaction $^9\text{Be}(\alpha, n\gamma)^{12}\text{C}$ (left) and 3.09-MeV γ -ray emission from the reaction $^{12}\text{C}(d, p\gamma)^{13}\text{C}$ (right) deduced from simultaneously measured profiles [17].

IV.C. Gamma-ray measurements in ITER

The gamma-ray diagnostics based on $\text{D}(T, \gamma)^5\text{He}$ and $^9\text{Be}(\alpha, n\gamma)^{12}\text{C}$ reactions could provide important information on behaviour of the fusion alpha particles in ITER, where Be impurity is supplied from the first wall. The main idea of the technique consists of a comparison of both the 3.5-MeV alpha-particle birth profile (17-MeV γ -rays) and that of the confined α -particles slowed down to 1.7 MeV (4.4-MeV γ -rays). These measurements could be performed with a dedicated γ -ray profile camera, which is similar to the neutron/gamma camera currently in operation on JET. For time-resolved profile measurements, efficient γ -ray spectrometers and neutron attenuators, in each channel of the cameras, are needed.

General requirements of the spectrometers are high efficiency and peak-to-background ratio. It could be a single crystal spectrometer with heavy scintillator or a detector-array, which allow measurement of γ -rays in the energy range from 1 to 30MeV. The feasibility of the measurements also depends on the quality of neutron suppression of the collimators. A more convenient neutron filter is based on ^6LiH . It is compact, effective, and transparent for γ -rays and does not produce interfering γ -rays in the high energy range. A 30-cm sample of

the ${}^6\text{LiH}$ filter reduces 2.4-MeV neutron flux to ~ 900 times and the 15-MeV neutron flux to ~ 30 times.



Fig.11. The scintillation probe installed in JET vessel.

The performance characteristics of the neutron ${}^6\text{LiH}$ attenuator were comprehensively investigated during experiments on JET [18]. The attenuator was used with collimated BGO spectrometer. The detector was placed in the laboratory above the tokamak and separated from it by a high-density concrete shielding 2-m thick. Analysis of the spectra (recorded with and without the ${}^6\text{LiH}$ attenuator) showed that without the attenuator γ -rays produced in reactions of the inelastic fast-neutron scattering by the detector material made the main contribution to the background counting rate of the detector. In the spectra measured with the ${}^6\text{LiH}$ attenuator, the background peaks are highly suppressed.

Gamma-ray cameras with such neutron filters seem to be the best candidates for measuring γ -ray spectra in the presence of high neutron fluxes typical of D-T reactor plasmas. The γ -ray cameras could be integrated with radiation shields of radial and vertical neutron cameras and have the same type of fan-shaped viewing geometry. Gamma-ray spectrometry induced by α -particles from beryllium tiles on the first wall using ${}^9\text{Be}(\alpha, n){}^{12}\text{C}$ reaction was proposed to measure the lost α -particle strength [19].

IV. MEASUREMENT OF FAST ION LOSSES

Fast ions, such as heating ions and α -particles, should be well confined until they transfer their energy to the plasma. In particular, α -particle heating will be needed to sustain ignition in fusion reactor plasma. Fundamental confinement properties can be studied by measurement of the α -particles loss. From the view point of machine protection, it is important to monitor the bombardment location and the heat load on the first wall. A clear understanding of loss mechanism is required to carry the fusion program to a real reactor. The temporal behaviour of lost alpha signals, and measurement of pitch angle and energy distribution are very important to understand the underlying physics, such as first orbit loss, toroidal field ripple loss, ICRH-induced loss and MHD induced loss.

In large tokamaks, like JET, a substantial part of the fusion-produced fast ions are confined. Dedicated probes were developed, and classical confinement properties, MHD induced losses, ripple effects, etc., are studied. For example, the alpha-particle loss measured by a scintillation probe [20] located at the TFTR vessel bottom showed dependence of loss ratios on the

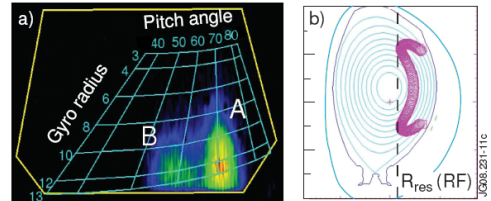


Fig.12. a) 2-D footprint of fast ion losses: fusion alphas from D^3He -reaction (A) and first orbit losses of p&T-fusion products from DD-reaction (B) observed on the scintillator plate; b) an orbit reconstruction for detected losses of type A [23].

plasma current in the ion grad- B drift direction [21].

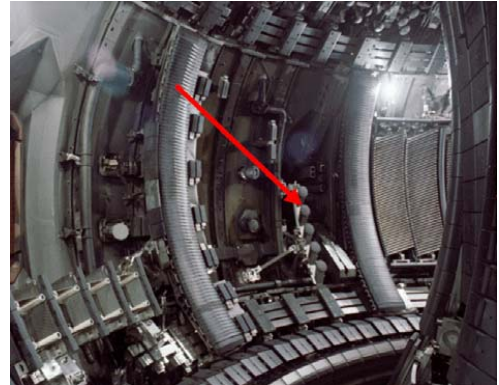


Fig.13. The Faraday Cup array installed in JET vessel.

Figure 11 shows the JET scintillator probe [22] in the vessel. Light emitted from the scintillator is divided by a beam splitter into two detection paths and is detected by the PMT array and charge-coupled device (CCD) camera. The PMT signals have high time resolution up to 1 kHz. The 2-D image obtained with the CCD camera provides information on both gyro-radius and pitch-angle simultaneously (Fig.12). As these probes are capable of resolving the energy and pitch angles of escaping fast ions with good time resolution, there is a great possibility of study of the MHD-induced losses.

In addition to SP the newly installed Faraday Cup array [24] could detect lost fusion alphas at multiple poloidal locations (Fig.13). The array consists of nine detectors spread over five poloidal locations below the mid-plane just outside the plasma at low magnetic field side of the JET torus. Along the major radius, the detectors are equally spaced in three locations. A detection of the temporal evolution of the fast α -particle current signals in the radially and poloidally distributed detectors can

provide a map of lost particle fluxes at different locations with time resolution of about 1 ms.

The Faraday Cups is the main measurement tools for time-resolved pitch angle and energy measurement of lost alphas in ITER. The self-heating of a D-T plasma by fusion-produced α -particles is the key to the realization of self-sustainable ignition of a thermonuclear plasma for fusion reactors. The loss of the α -particles means a deterioration of the heating input power. Moreover, the localization of alpha-particle bombardment on the first wall surface may induce serious damage. This is one of the key problems in ITER.

V. SUMMARY

Fusion product measurements, measurements of neutrons, γ -rays, and escaping MeV-ions produced in D-D, D-T, and other nuclear reactions are commonly used for diagnosing fusion plasmas magnetically confined. In D-D experiments on present devices, fusion reaction between a thermal and a non-thermal ion and that between non-thermal ions contribute substantially to the fusion reaction rate. Many interesting studies on energetic ion behaviours have been done by fusion product diagnostics. The recent publication on that issue can be found in [25 - 32]. For D-T fusion experiments on ITER, where the neutron emission rate will increase by more than of 10^3 from present large tokamaks and the thermonuclear fraction will be boosted as the self-heating source from α -particles becomes dominant, the fusion product diagnostics will be more important and will play the essential role, not only on the measurement of the fusion output power, but also on self-heating burning plasma studies.

ACKNOWLEDGMENTS

This work was funded jointly by the United Kingdom Engineering and Physical Sciences Research Council and by the European Communities under the contract of Association between EURATOM and UKAEA. This work was carried out within the framework of the European Fusion Development Agreement. The views and opinions expressed herein do not necessarily reflect those of the European Commission.

REFERENCES

1. M. SASAO, T. NISHITANI, J. KALLNE, V. KIPTILY, A. KRASILNIKOV and S. POPOVICHEV, "Chapter 9: Fusion product diagnostics", *Fusion Sci. and Tech.*, **53**, 604 (2008).
2. A. KISLYAKOV, A.J.H. DONNE, L.I. KRUPNIK, S.S. MEDLEY and M.P. PETROV, "Chapter 8: Particle diagnostics", *Fusion Sci. and Tech.*, **53**, 577 (2008).
3. V. G. KIPTILY, F. E. CECIL, and S. S. MEDLEY, *Plasma Phys. Control. Fusion*, **48**, R59 (2006).
4. H-B. BOSCH and G. M. JALE, *Nucl. Fusion*, 611 (1992).
5. O. N. JARVIS, *Plasma Phys. Control. Fusion* **36**, 209 (1994).
6. G. F. KNOLL, *Radiation Detectors*, John Wiley and Sons, New York (1979).
7. L.C. INGESSON et al *Nucl. Fusion* **38** 1675 (1998).
8. M. GATU et al., *Rev. Sci. Instrum.*, **77**, 10E702 (2006).
9. L. GIACOMELLI et al., *Nucl. Fusion*, **45**, 1191 (2005).
10. S. E. SHARAPOV et al., *Nucl. Fusion*, **40**, 1363 (2000).
11. R. K. FISHER et al., *Phys. Rev. Lett.*, **75**, 846 (1995).
12. V. I. AFANASIEV et al., *Europhysics Conference Abstracts*, **27A**, O-4.4D (2003).
13. V. G. KIPTILY, F. E. CECIL, and S. S. MEDLEY, *Plasma Phys. Control. Fusion*, **48**, R59 (2006).
14. V. G. KIPTILY et al., *Nucl. Fusion*, **42**, 999 (2002).
15. V.G. Kiptily, *Fusion Technology*, **18**, 583 (1990).
16. V. G. KIPTILY et al., *Phys. Rev. Lett.*, **93**, 115001 (2004).
17. V. G. KIPTILY et al., *Nucl. Fusion*, **45**, L21 (2005).
18. I.N. CHUGUNOV et al., *Instrum. and Exp. Techniques*, **51**, 166 (2008).
19. V.G. KIPTILY et al., *Fusion Technology*, **22**, 454. (1992).
20. S.J. ZWEBEN, *Nucl. Fusion*, **29**, 825 (1989).
21. S.J.ZWEBEN et al., *Plasma Phys. Control. Fusion*, **39**, A275 (1997).
22. S. BAUMEL et al., *Rev. Sci. Instrum.* **75**, 3563 (2004).
23. V. KIPTILY et al., *Nucl. Fusion*, **49**, 065030 (2009).
24. D.S. DARROW et al., *Rev. Sci. Instrum.* **75**, 3566 (2004).
25. D.S. DARROW et al *Rev. Sci. Instrum.* **81**, 10D330 (2010).
26. V.G. KIPTILY et al, *Nuclear Fusion* **50** (2010) 084001.
27. M. TARDOCCHI et al *Phys Rev Letters* **107**, 205002 (2011)
28. T. GASSNER et al, *Phys. Plasmas* **19** (2012) 032115
29. M. NOCENTE et al, *Nucl. Fusion* **52** (2012) 063009
30. F.E. CECIL et al., *Nucl. Fusion* **52** (2012) 094022
31. V.G. KIPTILY et al, *Plasma Phys. Control.Fusion* **54** (2012) 074010
32. V.G. KIPTILY et al, *Plasma and Fusion Research* **8** (2013) 2502071.

STATUS AND OUTLOOK OF FUSION RESEARCH

Wolfgang Biel^{a,b}

^a*Institute of Energy and Climate Research, Forschungszentrum Jülich GmbH, D-52425 Jülich, Germany*

^b*Department of Applied Physics, Ghent University, B-9000 Ghent, Belgium*

ABSTRACT

Fusion research aims to develop fusion as a promising energy source for the future. The latest status of fusion research is represented in the physics and technology basis of the large tokamak ITER [1] currently under construction, which is expected to produce for the first time significant fusion power ($P_{fus} \sim 500$ MW) over periods of several minutes. After a successful operation of ITER, several countries are planning the development of demonstration reactors with net electricity production to prepare the ground for commercialisation. While the main mission of ITER is the demonstration of a hot plasma mainly heated by fusion alpha particles, future efforts must be targeted towards improving the performance and availability of the reactor, and demonstrating the economic perspective for commercial fusion energy.

Within this paper we present an overview on the status of fusion and on our current understanding of the main features of a tokamak fusion reactor. Aiming for a quantitative treatment, a coupled set of non-linear equations is used to describe and predict the reactor performance based on a limited set of input quantities in a self-consistent way (systems code approach). Operational limits related to both plasma operation and machine components are discussed and an optimisation strategy to define the various plasma and machine parameters is outlined.

I. INTRODUCTION

The controlled fusion of the hydrogen isotopes deuterium (D) and tritium (T) has a great potential to provide substantial contributions to the energy supply of mankind for the future. Fusion research is on the one hand aiming to improve our basic understanding of fusion plasmas and of the principles of confining and controlling them, and on the other hand a targeted approach is pursued to develop the first fusion power plant which will be feeding electrical energy into the grid. Specifically, the European Roadmap for Fusion [2] is providing a plan on how to conduct the development of a demonstration reactor (DEMO), aiming for a net electricity production of 300...500 MW by the mid of this century. In this plan, the development and successful operation of the ITER tokamak [1] is seen as a cornerstone.

ITER is supposed to produce for the first time plasma pulses with a significant fusion power $P_{fus} = 500$ MW at an energy amplification factor of $Q = P_{fus}/P_{ext} = 10$ over a pulse duration of $t_{pulse} = 400$ s, where P_{ext} denotes the externally supplied plasma heating power. Due to the size and the complexity of the ITER project which is currently under development in Cadarache, France, these decisive results can realistically be expected only after 2030.

The mission of ITER is focussed towards the physics of a fusion plasma which is predominantly heated by the alpha particles generated via fusion, and to a demonstration of several reactor relevant technologies. The target value of $Q = 10$ would however not yet be suitable for efficient net electricity production, since the external plasma heating consumes electrical power, and therefore

$$(1) \quad P_{el,net} \sim \eta_{el} P_{therm} - \frac{P_{ext}}{\eta_{ext}} \sim P_{therm} \left(\eta_{el} - \frac{1}{\eta_{ext} Q} \right).$$

In case of a thermodynamic efficiency for conversion of thermal power to electricity of $\eta_{el} \sim 0.3$, and for a typical efficiency for the production of the external plasma heating power from electrical power of $\eta_{ext} \sim 0.3$ [3], a value of $Q = 10$ represents just the “break-even” above which net electricity production would become possible. Thus, in order to produce net electricity, DEMO will have to obtain an energy amplification factor of $Q \gg 10$, where the exact value is however not important and is hence not regarded as an optimisation quantity.

Considering the timescale of the ITER project as well as the budgetary limitations, the remaining period until the year ~ 2050 for achieving DEMO operation with electricity production appears quite short. Hence this ambitious goal can only be achieved if many of the main physics and technology developments for ITER can be smoothly transferred towards DEMO, such that only a limited amount of major new developments will be needed after ITER. In this respect the tokamak concept, together with the ITER developments, is the most developed magnetic confinement concept, and it has therefore been adopted as the “baseline” for a DEMO fusion reactor in the European Roadmap. In the following, we describe some aspects of the tokamak as needed for the systems description of the reactor. For a more detailed description of the tokamak principle and the status of related research we refer to the textbook by Wesson [4].

II. PHYSICS PRINCIPLES RELEVANT TO THE DESIGN OF A TOKAMAK FUSION REACTOR

A. Basics of fusion

A thermal pure DT plasma with a D-T ratio of 50:50, where the alpha particle power is compensating the power losses from the plasma, can be sustained (“ignited plasma”) if the burn condition is fulfilled [4]

$$(2) \quad n_{DT} k_B T_i \tau_E > 3 \cdot 10^{21} \text{ keV} \cdot \text{s} \cdot \text{m}^{-3}.$$

Here n_{DT} denotes the density of deuterium and tritium ions, k_B is the Boltzmann constant, T_i the ion temperature and

$$(3) \quad \tau_E = \frac{W_{plasma}}{P_{heat}}$$

is the global energy confinement time, with W_{plasma} being the stored kinetic energy in the plasma and P_{heat} the heating power absorbed in the plasma. Hence the energy confinement time is a measure of the quality of the thermal insulation of the plasma.

A minimum value of the triple product needed for ignition is found in the range of $T_i = 10 \dots 20$ keV. Assuming this temperature range and a fuel ion density of $n_{DT} \sim 10^{20} \text{ m}^{-3}$, the burn condition can be fulfilled if the energy confinement time amounts $\tau_E \sim$ several seconds.

The fusion power density produced in a thermal DT plasma with D-T ratio 50:50 follows from the equation

$$(4) \quad \frac{P_F}{V} = \frac{1}{4} n_{DT}^2 \langle \sigma v \rangle_{DT} E_{DT},$$

where $\langle \sigma v \rangle$ denotes the rate coefficient for the DT fusion reaction, see fig. 1, and $E_{DT} = 17.59$ MeV is the energy released per fusion event. A functional expression for the fusion rates was presented by Bosch et al. [5].

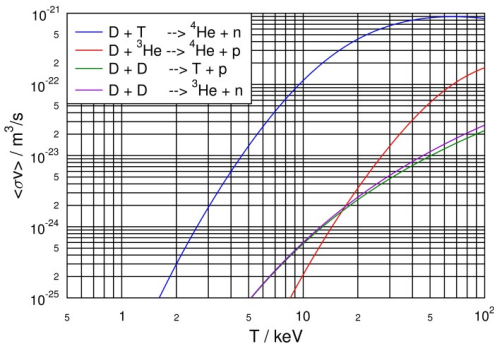


Figure 1: Fusion rate coefficients after Bosch et al. [5]

In the presence of plasma impurities with charge state Z ,

$$(5) \quad n_{DT} = n_e - \sum Z n_Z := f_{nDT} n_e,$$

where n_Z denotes the density of ion species Z and the summation comprises all ion species apart from deuterium and tritium.

B. The tokamak principle

The most widely used principle to confine a hot fusion plasma in a magnetic field is the tokamak, a toroidal plasma confinement system. In a tokamak, toroidal field (TF) coils generate a strong toroidal magnetic field, forcing the charged particles in the plasma to gyrate along the field lines. A purely toroidal field would however lead to a loss of the plasma particles into radial outward direction via particle drifts, originating from the curvature and inhomogeneity of the field. These losses can be suppressed by adding a poloidal field (PF) component.

In the tokamak the poloidal field is generated by driving a current in the plasma, using the central solenoid (CS) coil as the primary and the plasma as the secondary winding of a transformer. The helical magnetic field resulting from the superposition of TF and PF field components has a field line structure in the form of nested magnetic surfaces – in the absence of radial motion any particle following its field line would stay on its magnetic surface. A vertical magnetic field, which is generated by poloidal field coils, interacts with the plasma current to provide a radially inward $j \times B$ force to counteract the Lorentz and pressure forces acting in radial outward direction, thereby keeping the diameter of the plasma torus constant.

The geometry of the basic tokamak plasma is described by the major radius R_0 and minor radius a of the torus, as well as the safety factor q . This safety factor measures the number of toroidal turns which are needed until a screwed field line would come back to the same poloidal position. The outer boundary of the plasma (minor plasma radius a) in a tokamak can be defined by two different ways.

In a simple tokamak, the most protruding wall element, the so called “limiter”, will cut a magnetic field line, thus defining the outermost magnetic surface: all magnetic field lines inside of this surface are closed, while all field lines outside are open and are ending on the wall elements. The limiter is the area where most of the plasma wall interaction and heat exhaust takes place. The impinging particles are being neutralised, and the continuous plasma flux towards the limiter causes some neutral particle compression in front of it. This effect can be used to pump away impurities like the helium ash from the plasma of a fusion reactor. Usually a limiter is constructed from a material with high melting point and good thermal conductivity, together with a smooth surface shaping, in order to withstand the very high heat loads in the plasma wall contact.

However, in most modern tokamaks large poloidal field coils are employed to elongate the plasma in vertical direction, generating „X-points“ at the locations where the poloidal fields of the plasma current and of the

PF coil just cancel. Thus the strongest (innermost) X-point defines the “separatrix” which divides the magnetic field lines into two categories: Inside the separatrix, all field lines are closed and they lie on nested magnetic surfaces. Outside the separatrix, all magnetic field lines are open and they impinge, eventually after several toroidal turns, onto a wall element within the so called “divertor” which is usually located below the main plasma. If the distance between first wall of the main chamber and plasma edge is chosen large enough, the particles lost from the main plasma in radial direction may not touch the first wall but stream along the field lines down towards the divertor. On their way they cool down via radiation and collisions and finally form a relatively cold plasma of high density (“divertor plasma”) in front of the divertor target plates. This concept was designed to separate the plasma wall interaction zone from the core plasma, to make the heat loads to the first wall more tolerable than in a limiter tokamak, and to facilitate the Helium pumping by the neutral particle compression arising from the plasma flow towards the target plates followed by neutralisation. In most cases only one main divertor is used in a so called “single null” configuration, where the plasma geometry can be described by the two new parameters elongation κ and triangularity δ in addition to the major and minor radius.

For the following discussion of the main dependencies of fusion power in a divertor tokamak, it is convenient to write all equations in terms of dimensionless quantities:

a	Minor plasma radius at the tokamak midplane / m
R_0	Major plasma radius at the tokamak midplane / m
n_{20}	Electron density / 10^{20} m^{-3}
n_{DT}	Fuel ion density / 10^{20} m^{-3}
n_Z	Density of ions with charge state Z / 10^{20} m^{-3}
N_{GW}	Greenwald number $N_{GW} = n/n_{GW}$
T_k	Plasma temperature / keV
I_M	Plasma current / MA
B_0	Magnetic field at the tokamak axis $R = R_0 / T$
q_{95}	Safety factor at a radial location of 95% flux
P_M	Power / MW
W	Energy / MJ
V	Plasma volume / m^3
τ_E	Energy confinement time / s

C. High confinement regime (H-mode)

An important feature of divertor tokamaks is the occurrence of improved plasma confinement in case of sufficiently strong plasma heating. In this so called “H-mode” [6] the observed energy confinement time τ_E can be a factor ~ 2 higher than in the low confinement (“L-mode”) regime. The H-mode is related to the formation

of a transport barrier and a “pedestal” of the pressure at the plasma edge. The properties of the H-mode have been widely investigated on many divertor tokamaks, deriving the empirical IPB98(y,2) scaling law by a nonlinear fitting procedure using data from a large number of discharges [7]:

$$(6) \quad \tau_E = 0.173 H_H I_M^{0.93} R_0^{1.39} a^{0.58} \kappa^{0.78} n_{20}^{0.41} B_0^{0.15} P_{loss,M}^{-0.69}.$$

In eq. (6) the confinement enhancement factor H_H is a measure of the actual confinement quality relative to standard H-mode ($H_H = 1.0$), and we have eliminated the dependency on the isotope composition by assuming a DT plasma with $n_D = n_T$.

In order to achieve and maintain H-mode conditions, the power losses $P_{loss} = P_{heat} - P_{rad,core}$ across the separatrix via convection and conduction have to exceed the H-mode power threshold P_{LH} ($P_{rad,core}$ denotes the radiated power from the core plasma). Within this paper, we use the empirical scaling presented by Martin et al. [8]

$$(7) \quad P_{LH,M} = 1.72 n_{20}^{0.78} B_0^{0.77} a^{0.98} R_0^{1.00}.$$

D. Operational limits in a tokamak plasma

In order to maximise the fusion power density according to eq. (4), both the plasma density and temperature should be maximised. However, the parameter range in which the plasma in a tokamak fusion reactor can be operated is governed by several operational limits which are only briefly recalled here. For a more detailed treatment, we refer to the literature [4, 9].

First, the line averaged plasma density is limited by the empirical “Greenwald limit” [10]:

$$(8) \quad n_{20} \leq n_{GW} = \frac{I_M}{\pi a^2}.$$

Increasing the plasma density to values above n_{GW} leads to a termination (disruption) of the discharge by an instability. Stable tokamak operation can only be obtained if, for a desired plasma density, the plasma current is large enough or the plasma radius small enough. However, the plasma current within a divertor tokamak is limited via a second requirement, such that the safety factor q_{95} (number of toroidal turns after which a magnetic field line closes with one poloidal turn) measured at a radial location of 95% flux must stay above a value of 2 in order to avoid a disruption caused by an external kink mode [11]

$$(9) \quad q_{95} = 5 \frac{a^2 B_0}{I_M R_0} f \geq 2,$$

where we have used the geometric shape factor [7]

$$(10) \quad f = \frac{1 + \kappa^2(1 + 2\delta^2 - 1.2\delta^3)}{2} \frac{1.17 - 0.65 a/R_0}{(1 - (a/R_0)^2)^2}.$$

From eqs. (9) and (10) it is evident that choosing larger elongation and triangularity would increase the shape factor f and hence open a route to allow for larger plasma current and hence higher density. The vertical elongation κ and the triangularity δ of the plasma are defined by the equilibrium between the plasma pressure and the action of the poloidal field coils onto the plasma. However, increasing the elongation by enhancing the attractive forces induced by the PF coils located above and below the plasma would make the vertical plasma position more and more unstable. In order to control the vertical position, the response of the control system must be faster than the growth rate of the vertical instability. The limiting factors here are first the large inductivity of the PF coils, second the limitations for both the maximum voltage and maximum power to be supplied to the coils, and third the damping by eddy currents induced in the blanket and structures between PF coils and plasma. Based on these boundary conditions the plasma elongation has to be limited towards a value that can be safely controlled. According to experimental and modelling results, for DEMO a maximum controllable elongation at the X-point of

$$(11) \quad \kappa_{x,\max} = 1.5 + \frac{0.5}{A-1}$$

has been proposed [12], where $A = R_0/a$ is the aspect ratio of the plasma. Following eq. (9), another route to attain higher plasma current and hence higher plasma density would be opened by increasing the magnetic field B_0 or reducing the major radius R_0 while keeping the minor radius constant.

As a third requirement, the plasma pressure in a tokamak is limited by the ‘‘Troyon limit’’ [4]

$$(12) \quad \beta_N \equiv 100 \beta \left/ \frac{I_M}{a B_0} \right. \leq \beta_{N,\max},$$

where

$$(13) \quad \beta \equiv \frac{P}{B_0^2 / 2\mu_0}$$

is the normalised plasma pressure (‘‘beta’’). For discharges of the ‘‘ELMy H-mode’’ type the empirical limitation for the normalised beta is $\beta_{N,\max} = 3.5$. In case of a reactor design based on ‘‘conservative’’ physics and technology assumptions as discussed below, the expected beta is low enough so that the beta limit will not be further discussed in the following.

E. Systems description of a tokamak reactor

In the following, we present a simple quantitative description of the main elements of a tokamak fusion reactor. Writing for the kinetic plasma energy

$$(14) \quad W_{plasma} \sim 3 n k_B T V_{plasma},$$

assuming $T_e = T_i = T$, neglecting the radial dependencies of both n and T , and inserting into eq. (3), we obtain

$$(15) \quad T_k = 1.05 \frac{\tau_E (P_{\alpha,M} + P_{ext,M})}{\kappa a^2 R_0 n_{20}}.$$

Here, we have assumed that the total heating power is given by the sum of alpha heating power and external heating power, $P_{heat} = P_\alpha + P_{ext}$, and we have approximated the core plasma volume by the expression

$$(16) \quad V_{plasma} \sim 2\pi^2 \kappa a^2 R_0.$$

The system of equations (4), (6) and (15) already allows to perform a 0-D description of the tokamak fusion reactor and to predict the expected fusion power output for a given set of pre-defined input parameters, namely the plasma geometry (a , R_0 , κ and δ), plasma density, magnetic field B_0 , plasma current (safety factor) and confinement quality H_H . This procedure, together with a treatment of plasma radiation (see below) also represents the essence of the plasma physics module in more sophisticated so called ‘‘fusion reactor systems codes’’ [13,14,15,16]. For simplicity we will use in the following discussion radially constant (mean) values for plasma density and temperature. However, extending the description towards using prescribed radial profiles is straightforward and this is the usual approach by systems codes.

For a discussion on the principles for optimisation of a fusion reactor, this set of equations is somewhat involved and hence impractical. We therefore proceed with simplifying the description further by restricting the discussion to cases where the plasma temperature is in the range of $T = 10 \dots 20$ keV, where the rate coefficient shows approximately a quadratic dependence with plasma temperature and hence

$$(17) \quad P_\alpha = V_{plasma} n_D n_T \langle \sigma v \rangle_{DT} \times \frac{17.59}{5} \text{ MeV} \\ \sim 0.0016 n_{20}^2 T_k^2 V_{plasma} [\text{MW}]$$

Furthermore, it is convenient to substitute plasma current and density in the expressions for confinement time (6) and plasma temperature (15) by the expressions for the dimensionless quantities q_{95} and $N_{GW} = n/n_{GW}$, yielding

$$(18) \quad \tau_E = 0.935 H_H R_0^{0.05} a^{2.44} \kappa^{0.78} f^{1.34} N_{GW}^{0.41} q_{95}^{-1.34} B_0^{1.49} P_M^{-0.69} \\ \text{and} \\ (19) \quad T_k = 0.62 H_H R_0^{0.05} a^{0.44} \kappa^{-0.22} f^{0.34} \times \\ N_{GW}^{-0.59} q_{95}^{-0.34} B_0^{0.49} (P_{\alpha,M} + P_{ext,M})^{0.31}.$$

Neglecting for the moment the radiated power and the heating power, i.e. assuming $P_{heat} = P_{loss} = P_\alpha$, we obtain after some algebra a single equation describing the alpha heating power generated in a tokamak fusion reactor operated at H-mode (‘‘tokamak fusion reactor equation’’)

$$(20) \quad P_{\alpha,M} = 10^{-4} H_H^{5.26} a^{7.58} R_0^{-2.37} \kappa^{1.47} f^{7.05} N_{GW}^{2.16} q_{95}^{-7.05} B_0^{7.84}$$

In this equation, the dimensionless formulations of the density limit and the current limit

$$(21) \quad N_{GW} \leq 1 \text{ and}$$

$$(22) \quad q_{95} \geq 2$$

have to be observed. For the geometrical parameters of the tokamak used in eq. (20), the following condition applies:

$$(23) \quad R_0 > a + b + c + r_{CS},$$

where c denotes the radial thickness of the TF coil and r_{CS} the radius of the central solenoid.

Using N_{GW} , the beta limit ($\beta_N < 3.5$) can be reformulated as

$$(24) \quad T_k \leq 1.35 B_0 a / N_{GW}.$$

After solving the equations above for a set of input parameters, the resulting temperature T_k (eq. 15) should be in agreement with condition (24) to avoid the pressure driven instabilities leading to a plasma disruption.

In a reactor under steady state conditions all the power which is heating the core plasma has to be exhausted from the plasma, without damaging the wall or divertor. We express the power entering into the divertor via

$$(25) \quad P_{Div} \approx P_{loss} \approx P_\alpha + P_{ext} - P_{rad,core}.$$

Practically, the radiated power $P_{rad,core}$ in the core plasma can be adjusted in a wide range by adding medium- or high-Z impurities like Argon, Krypton or even Xenon to the plasma [17]. A simple empirical expression for the total radiated power from a tokamak plasma was presented by Matthews et al. [18],

$$(26) \quad P_{rad} \approx 0.16 (Z_{eff} - 1) S^{0.94} n_{20}^{1.9} [MW],$$

where S denotes the surface area of the plasma. However, the power loss across the separatrix has to significantly exceed the H-mode threshold (eq. 7) in order to avoid a sudden drop of confinement back to low confinement (L-mode) conditions. Furthermore, the radiation loss parameter L_Z , which is defined via the relation

$$(27) \quad P_{rad,Z} = n_Z n_e L_Z,$$

typically shows an increase with decreasing electron temperature over a wide range of temperatures, which implies that highly radiative plasmas are difficult to control: any sudden drop of confinement and plasma temperature would lead to an increase of radiation and hence to a further cooling of the plasma. This is not reflected in the eq. (26), which hence only can serve as a rough approximation for the radiated power.

Within the divertor region, a large fraction of P_{Div} still has to be radiated in order to distribute the power to larger parts of the target plates and hence keep the peak loads below the tolerable values.

In addition to the output power of a tokamak fusion reactor, a second important optimisation quantity is the plasma pulse duration which can be achieved. This pulse duration depends on the plasma current, the ohmic resistance and plasma inductivity, the amount of non-inductive current driven by the external heating [3] or by the “bootstrap” effect [4], and on the available total flux swing [19]. The total flux Φ_0 available from the central solenoid (CS) and (to some extent) from the other poloidal field (PF) coils,

$$(28) \quad \Phi_0 \approx 1.1 \times 2\pi r_{CS}^2 B_{max,CS},$$

where $B_{max,CS}$ denotes the maximum magnetic field obtained in the CS coil and the factor 1.1 accounts for a conservative estimate of the additional flux provided by the PF coils. During the plasma discharge, this total flux is consumed by the ignition Φ_{ignit} , by the build-up of the magnetic energy stored in the plasma current, and by ohmic losses. After having tuned the CS coil from $B_{max,CS}$ towards the final value of $-B_{max,CS}$, the plasma current has to be ramped down and the discharge has to be stopped. Approximating the ohmic losses during current ramp-up using the Ejima approximation $\Phi_{OH,ramp-up} \sim 0.5\mu_0 R_0 I_P$ [20], we obtain for the pulse duration

$$(29) \quad t_{pulse} \approx \frac{\Phi_0 - \Phi_{ignit} - (0.5\mu_0 R_0 + L_{plasma}) I_P}{R_{plasma} (I_P - I_{noninduct})},$$

where R_{plasma} denotes the ohmic resistance of the plasma during the flat-top period, and $I_{noninduct}$ is the non-inductive part of the total plasma current. According to eq. (29), long pulse operation can be attained by increasing Φ_0 or by enhancing the non-inductive current. In case of full noninductive current drive ($I_{noninduct} = I_P$), which is the domain of “advanced tokamak” studies [21], steady state operation is obtained, where usually high confinement quality $H_H > 1.0$ is assumed, allowing for higher plasma pressure and hence larger bootstrap current, while lower values for the total plasma current are chosen with $q_{95} = 4 \dots 6$ in order to keep the level of the required external current drive within reasonable limits.

III. TECHNOLOGICAL ISSUES RELEVANT TO REACTOR OPTIMISATION

Before continuing the discussion of eq. (20) and the reactor optimisation strategy, we briefly recall a number of technological issues relevant to the definition of reactor parameters.

A. Magnetic field coils

From Eq. (20) it can be seen that the fusion power depends strongly on the toroidal magnetic field B_0 in the plasma centre, if the safety factor q_{95} , the Greenwald fraction N_{GW} , the confinement quality H_H and the plasma geometry as defined by the four parameters R_0 , a , κ and δ are kept constant. The latest status of superconducting magnet coil technology for fusion is

represented by the development of the ITER coils [22]. Two important limitations have to be observed for the TF coils design. First, the current density in the superconducting materials at a given temperature and magnetic field must be kept below a limit to avoid back-transition to normal conductivity. Thus the size of the winding pack of the TF coils is defined by these requirements together with Biot-Savart's law describing the required Amp-turns

$$(30) \quad B_{tor}(R) = \frac{\mu_0}{2\pi} \frac{NI}{R},$$

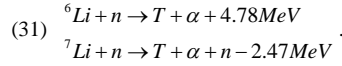
where N is the total number of windings (product of number of coils and number of windings per coil), I is the current per winding and R the distance from the torus centre. Second, the coils are subject to the "hoop" force which acts to expand each conductor and the TF coil as a whole, and a strong radial force driving all conductors away from the plasma centre. Both forces have to be supported by the coil design. For this purpose, the cable in conduit approach has been adopted for ITER. Here the individual brittle SC conductors ("strands") are packed together with Copper strands, needed in cases of quench of the superconductive state, into stainless steel housings to form a robust cable structure which supports the whole set of strands against the forces. These SC cables are then wound into radial plates which are designed to accept the overall forces acting on the cables. The radial plates itself are mounted into a thick steel casing taking the overall forces acting onto the coil. The ITER TF coil structure, with a radial coil thickness in the order of $c \sim 1$ m and with a maximum field at the inner leg of the TF coil of $B_{max} = 11.6$ T, is subject to stresses of up to 600 MPa, which is near the limits of the steel that is used here. Aiming for even higher toroidal magnetic fields would imply

- increasing the number of Amp-turns according to eq. (30), which means increasing the area needed for the winding pack;
- on the same time, strongly reducing the current density in the SC strands, since the permissible current density in the SC conductor decreases with magnetic field, which means another increase in the area of the winding pack;
- finally, increasing the amount of steel in the radial plates and coil housings to accept the stronger forces.

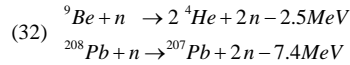
From all three effects together it follows that, in order to obtain higher magnetic field B_{max} , the radial dimension of the TF coils c would have to be enlarged proportional to a high power of the magnetic field. Practically, from the current status of magnet technology for fusion, the values of $B_{max,TF} = 11.6$ T and $B_{max,CS} = 13$ T achieved for the ITER design are regarded as a technical limitation, which also defines the framework for the DEMO design studies undertaken in Europe [23].

B. Blanket design

While ITER can be operated using tritium that is available on earth, e.g. produced as a side product from fission plants, the tritium consumption of a DEMO reactor will be so large (several 10 kg per year) that the tritium will have to be produced on-site by a breeding process using the fusion neutrons. For this purpose, the plasma of a DEMO reactor will be almost completely surrounded by a breeding blanket, where Lithium is being converted to tritium using the reactions



Natural Lithium consists of 7.4% ${}^6\text{Li}$ and 92.6% ${}^7\text{Li}$, but the cross section for the first (exothermic) reaction is more than two orders of magnitude larger for the case of thermalized neutrons, as compared to the peak of the cross section for the second (endothermic) reaction. A pure breeding blanket cannot obtain a tritium breeding rate (TBR, ratio between produced and consumed tritium) of 100 percent, since a fraction of the primary fusion neutrons will unavoidably be lost due to absorption in the structural material of the blanket, and due to geometrical neutron losses related to the necessary openings for plasma diagnostic, heating and fuelling systems, as well as within the divertor [24]. Therefore the overall number of available neutrons has to be increased by a neutron multiplication process. For this purpose, the following reactions are being considered:



In addition to the generation of neutrons, another main function of the blanket is the power exhaust in a way that permits the efficient use of the thermal power to produce electrical energy.

For the design of the blanket, various technical implementations and different options are under development. If Beryllium is used as multiplier, both the Lithium breeder and the Beryllium are commonly foreseen in the form of small solid pebbles within the blanket module. Designs based on Lead as multiplier are normally based on mixing both breeder and multiplier and operating the Pb:Li mixture at temperatures of several hundred degrees as a liquid metal. Regarding the choice of coolants, various options are being considered, namely water cooling, Helium gas cooling and (in case of Pb:Li) the liquid metal itself, as well as dual-coolant options using the combination of water and Helium, or liquid metal and water. Helium as coolant could provide higher exit temperatures than water and hence allow for higher thermodynamic efficiency, but the large amounts of gas needed for cooling require significant pumping power, which largely reduces the overall efficiency again. In addition to the TBR and the overall thermodynamic efficiency also the thickness of the blanket is an important optimisation criterion for the

reactor: The distance b between plasma and TF coil on the inboard side of the tokamak is related to the magnetic field in the plasma, B_0 , and the field B_{max} at the inner leg of the TF coil according to Biot-Savart's law via

$$(33) \quad B_0 = B_{max} \left(1 - \frac{a+b}{R_0} \right).$$

Hence reducing b would allow for larger magnetic field in the plasma B_0 , leading to an increase of fusion power when keeping all other quantities constant. However, the quantity b is defined as the sum of several radial dimensions:

- the radial distance needed between plasma edge and first wall in order to protect the first wall from overheating,
- the thickness of the breeding blanket, including the space needed for the cooling manifold at the backside of the blanket,
- shielding and vacuum vessel thickness.

In a tokamak reactor with full tritium breeding the total distance between the inner radial edge of the plasma and the inner leg of the TF coil cannot be made significantly smaller than $b \sim 1.8$ m. Since this is a quantity essentially not scaling with the size of a fusion reactor, the quantity b represents a lower limitation for the overall radial dimensions of the reactor.

In the European programme towards a DEMO reactor, the Helium Cooled Pebble Bed (HCPB) and the Helium Cooled Lithium lead (HCLL) concepts being pursued as the main concepts, while the Dual Coolant Lithium Lead (DCLL) and the Water Cooled Lithium Lead (WCLL) designs are regarded as alternative approaches [25].

C. First wall and divertor

The first wall in the main chamber of a DEMO fusion reactor has to withstand a typical level of average stationary surface heat loads due to radiated power and particles emitted from the core plasma in the order of less than 0.5 MW/m^2 , where some local inhomogeneities due to the magnetic field and wall structure have to be expected. On top of this a typical stationary neutron wall load in the order of $1\text{-}2 \text{ MW/m}^2$ provides the main part of the power produced from the fusion processes, which is mainly deposited into the first 10-30 cm of the blanket. The stationary heat loads at the first wall can reasonably be covered by installing a sufficiently dense (mm ... cm) network of coolant channels into the involved components. In this area, a low activation steel like EUROFER is foreseen as structural material.

Strong transient heat loads to the first wall can be generated by plasma disruptions and they are a major area of concern already for ITER [26]. During a plasma disruption, the confining nested magnetic field structure breaks down due to rapid changes in the plasma current and current profile, which leads to a rapid loss of a major part of the stored kinetic energy to the wall ("thermal

quench") within a short time of the order of $\tau_{TQ} \leq 1$ ms. The main strategy for ITER, besides avoidance of disruptions, is the disruption mitigation via fast and massive particle injection into the plasma once a disruption can no longer be avoided. The injected particles get excited and radiate major fractions of the stored energy, thereby distributing the heat loads to larger areas. Assuming that half of the stored thermal energy from the DEMO plasma $W_{th} \sim 1$ GJ would be radiated to the first wall within a time of $\tau_{TQ} \sim 1$ ms, and assuming a toroidal and poloidal asymmetry of a factor 2 each, the resulting maximum heat impact factor η [27] on DEMO is in the order of

$$(34) \quad \eta = \frac{W}{A_{eff} \sqrt{\tau_{TQ}}} \sim 40 \frac{MJ}{m^2 s^{0.5}}$$

(W is the deposited energy, A_{eff} the effective wall area), which is only slightly below the melt limit for tungsten but already above the limit where surface cracks of several 100 microns depth have to be expected. Thus only a low number of disruptions is permissible on DEMO even with application of a perfect mitigation system.

The divertor target plates have to withstand the highly peaked stationary power fluxes that are transporting the power, which has been convected and conducted across the separatrix, along the field lines down to the divertor region. The peak power flux densities expected for ITER are in the order of $10\text{...}20 \text{ MW/m}^2$. To accommodate for these extreme heat loads, the divertor target plates of ITER are constructed using a castellated tungsten surface connected to a Cu:Cr:Zr alloy structure, where a dense network of cooling channels serves for heat removal using water at $100 \text{ }^\circ\text{C}$ as coolant.

For a future DEMO reactor, staying above the H-mode threshold (eq. 7) implies that the expected stationary peak power flux densities are comparable or even larger than on ITER. On the other hand, several routes of modifications are being pursued to develop the DEMO divertor aiming for specific improvements as compared to the ITER divertor:

- Utilising the divertor heat for electricity production at acceptable efficiency would require a coolant temperature of $> 250 \text{ }^\circ\text{C}$.
- The material Cu:Cr:Zr used on ITER should be replaced by a material which has low activation properties, in order to minimise the amount of radioactive waste with longer decay times.

On top of the stationary loads, edge localised modes (ELMs) associated with the standard H-mode would provide strong pulsed heat loads to the divertor surface. Uncontrolled ELMs would deposit energies of several 10 MJ per ELM on ITER, and up to 100 MJ per ELM on DEMO [28], which would lead to surface melting if no mitigation measures are taken. While ITER is aiming to mitigate ELMs by employing resonant magnetic perturbations and ELM pacing via Pellet injection, the

required ELM mitigation factor for DEMO and the requirements for reliability of ELM suppression are so high that a change in the dis-charge scenario, i. e. an intrinsically ELM-free discharge type, appears favourable.

The power exhaust problem explained above is currently seen as the most important issue where substantial progress will be needed in order to make commercial fusion viable, and intense R&D is being pursued to develop solutions. In the current stage of fusion research, Tungsten is widely regarded as the prime choice for first wall and divertor surface materials, since it first provides high resilience against erosion by physical sputtering due to its high atomic mass, second high resilience against stationary and transient heat loads due to the good thermal conductivity and the high melting point, and third it shows acceptable levels of activation after neutron irradiation. In the current EU DEMO development it is therefore seen as the baseline solution for both the first wall as well as the divertor material.

However, even when assuming that the power flow across the separatrix is being reduced via core plasma radiation down towards the H mode threshold, $P_{SOL} \sim P_{LH}$, the remaining power flux density towards the divertor target plates may be still too high. To solve this problem, three main alternative approaches to the baseline divertor are being pursued: First, divertor strike point sweeping with an amplitude of several 10 cm and a frequency in the order of 1 Hz is being explored as an option to distribute the power fluxes over a larger part of the divertor target. Second, novel magnetic configurations are being investigated, aiming to reduce the power flux densities to the divertor by a magnetic field structure which is spreading the field lines from the edge plasma onto larger parts of the divertor target. Third, parts of the divertor surface could be made of liquid metal which is flowing and thereby enhancing the heat removal due to its heat capacity. None of these concepts has reached sufficient maturity until now, so that these are not foreseen in the current ITER design.

IV. DESIGN OPTIMISATION OF A TOKAMAK FUSION REACTOR

Having summarised the main physics and technological constraints for tokamak fusion reactor design, we can now proceed discussing the tokamak fusion reactor equation (20) and suitable optimisation criteria. In order to better show the explicit dependencies on technical quantities that can be independently chosen, we substitute eq. (33) into eq. (20). Moreover, considering also the case of plasma dilution by impurities, we use $f_{nDT} = n_{DT}/n_e$ and $s_{nz} = \sum n_z/n_e$ and obtain a more detailed version of the tokamak fusion reactor equation

$$(35) \quad P_{\alpha,M} = 0.004 H_H^{5.26} a^{7.58} R_0^{-2.37} \kappa^{1.47} f^{7.05} \times N_{GW}^{2.16} \left(\frac{f_{nDT}}{1 + f_{nDT} + s_{nz}} \right)^{5.26} q_{95}^{-7.05} B_{max}^{7.84} \left(1 - \frac{a+b}{R_0} \right)^{7.84}.$$

We note that there is still the dependence of the shape factor f from the elongation, triangularity and aspect ratio, see eq. (10). Furthermore, the maximum controllable elongation depends on the aspect ratio according to eq. (11). However, in order to keep the reactor equation reasonable simple, we will not substitute these further.

Equation (35) can now be used to discuss the recipe for optimisation of a tokamak fusion reactor. In general, for a reactor ultimately the cost of electricity (CoE) should be minimised, which means maximisation of the net electrical output power while minimising the overall reactor cost for initial investment, operation, maintenance, shutdown and disposal. The presentation of a full fusion reactor cost model is beyond the scope of the present paper. However, as a first approximation, we may assume that the cost of electricity is proportional to the total volume of the tokamak components (blanket, vessel, coils, etc.), hence

$$(36) \quad CoE \sim \frac{V_{tokamak}}{P_{el,net}}$$

In further determining the optimum choice of parameters in eq. (35), the maximisation of many individual parameters may be desirable but a number of operational and technical limits have to be obeyed:

- The TF coil system should be optimised for the maximum technically possible magnetic field B_{max} , which amounts $\sim 12 \dots 13$ T according to current technology as described above.
- The radial build should be optimised for minimum blanket thickness, hence $b \sim 1.8$ m.
- The maximum possible plasma current compatible with good MHD stability should be chosen, yielding $q_{95} \sim 3$.
- A high plasma density should be chosen, which is favourable for both high fusion power but also for power exhaust (detached divertor). This means operation near the Greenwald limit with $N_{GW} \sim 1$, noting that this density limit is related to the edge plasma density, so that in case of peaked density profiles a mean density of $N_{GW} \sim 1$ is viable.
- The elongation should be chosen such that a reliable control of the vertical plasma position is possible: $\kappa \sim 1.6 \dots 1.8$. On the same time, the triangularity should be maximised with respect to the limits of what is achievable based on the feasibility and cost of PF coils.
- A stable plasma scenario should be chosen with high core radiation but observing the requirement of $P_{loss} > P_{LH}$. We note that for highly radiative H-mode usually $H_H \leq 1$ is found [29,30]. On the other hand, since the confinement scaling (eq. 6) was elaborated while neglecting the radiation correction assuming $P_{loss} = P_{heat}$, an effective confinement quality of $H_H = 1.0$ may be seen as viable for DEMO [31].

Making use of these boundary conditions in a consistent fashion, only two open parameters are left, namely the

major plasma radius R_0 and aspect ratio $A = R_0 / a$, which can now be selected independently to choose the target fusion power and pulse duration of the tokamak reactor.

V. SELECTED NUMERICAL RESULTS

In the following, we present selected numerical results derived from the reactor systems model described above, where profile effects have been included. In figure 2 the cost of electricity is displayed using a conservative set of input parameters $H_H = 1.0$, $N_{GW} = 1.0$, $q_{95} = 3$, $P_{ext} = 50$ MW, $B_{max,TF} = B_{max,CS} = 13$ T, $b = 1.8$ m, while for the elongation eq. (11) was used and for the triangularity $\delta = (\kappa - 1)/2$ was assumed. The range of plotted data covers the range in which numerical solutions were found in agreement with the chosen input data and with a power flow across the separatrix $P_{sep} > P_{LH}$.

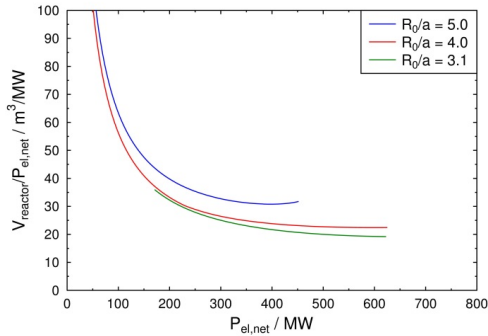


Figure 2: Cost of electricity for different aspect ratios

This simplified cost of electricity figure typically shows a steep decrease with increasing electrical output power (reactor size), up to a point of saturation at a few 100 MW from which onwards a further increase of the reactor size does not lead to further improvement. The main reasons for this observed saturation are:

- Increasing the machine size leads to an increase of plasma temperature. However, for plasma temperatures of $T > 20$ keV the fusion rate coefficient shows only a moderate increase, with saturation above $T > 40$ keV, see fig. 1.
- With increasing major radius R_0 , the absolute achievable plasma density due to the Greenwald limit decreases, which becomes evident when inserting eq. (9) in eq. (8). On the same time however, the magnetic field in the plasma B_0 can be increased according to eq. (33), if B_{max} is kept constant.
- With increasing fusion power and reactor size a larger fraction of the power has to be radiated in order to keep the divertor load below the limits. This is accomplished via impurity seeding, causing additional plasma cooling and some dilution of the fuel, both reducing the further increase in fusion power.

Based on the results of fig. 2 we may conclude that the optimisation of cost of electricity leads us towards a minimum plant size in the order of several 100 MW electrical output power. This refers to a typical minor plasma radius of $a \sim 2.5 \dots 2.8$ m, i.e. a reactor size about 25...40 percent larger than ITER.

The pulse duration for the same cases is displayed in figure 3. We note that for large aspect ratio the achievable pulse duration can be substantially longer than for small aspect ratio. The main reason is that with the larger R_0 more space is available in the centre of the tokamak, which allows installing a larger CS coil which can provide a larger total flux Φ_0 .

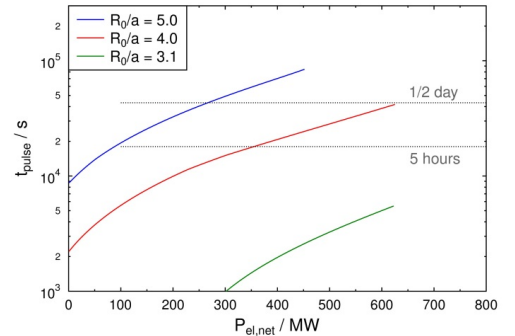


Figure 3: Pulse duration for different aspect ratios

The numerical examples presented above demonstrate that the two main dimensional parameters a and R_0 are suitable parameters to define the tokamak geometry based on target values for electrical output power and pulse duration, after having defined all other parameters from eq. (35) according to operational and technical limits.

Defining several technical and physics parameters near their limits, namely elongation, triangularity, plasma density and safety factor, we can see that in eq. (35) the fusion power depends on the product of high powers of confinement quality H_H , magnetic field B_{max} and reactor dimensions. We may conclude that, for a defined target fusion power, a reduction of the size of the tokamak (minor and major radius) could be achieved if a higher magnetic field $B_{max} > 13$ T or a better plasma confinement $H_H > 1$ could be obtained as compared to the status of today's fusion research. Improving the plasma confinement and designing stronger magnetic field coils are therefore subjects of ongoing research. However, a more compact tokamak with high fusion power would have to solve the even stronger power exhaust problems arising from the higher power densities.

VI. THE STELLARATOR: AN ALTERNATIVE CONFINEMENT CONCEPT

Instead of driving a current in the plasma, the necessary helical structure of the confining magnetic field in a

toroidal system can be fully defined by external magnetic field coils. This is the approach of the stellarator, with the largest currently existing devices being the Heliotron type device LHD [32] and the optimised stellarator W7-X [33,34]. Important intrinsic advantages of the stellarator are [34] first the possibility of steady state plasma operation without the need to maintain a plasma current, second the fact that the confining field structure is fully determined from outside, so that plasma instabilities cannot lead to an sudden loss of confinement like in a tokamak. On the other hand, the externally defined helical field structure is associated with a non-axisymmetric complex geometry of field lines, with a large fraction of trapped plasma particles, and causing significant challenges for the machine design and engineering. While the drift losses of trapped particles from the complex confining field structure can be reduced by the optimised field structure [33, 34], the engineering issues towards a future stellarator reactor design remain challenging [35] in particular with respect to coil geometry and magnetic forces, as well as the overall maintenance concept.

Within the European fusion research, the development of the stellarator is being pursued as a promising alternative to the tokamak and may become the candidate approach for a DEMO fusion reactor after successful operation of W7-X.

VII. SUMMARY

Within this paper, we have summarised the status and prospects of the development towards a tokamak fusion reactor. For this purpose, a numerical model was proposed which describes the main features of the tokamak reactor based on a limited number of input parameters. Defining the values for a number of plasma physics and technological quantities nearby the known limits, the main dimensions of the tokamak, a and R_0 , remain as optimisation quantities, from which the net electrical output power and the pulse duration of the tokamak can be derived in a straight-forward manner.

REFERENCES

[1] www.iter.org
 [2] Romanelli F. et al., Fusion electricity, <https://www.euro-fusion.org/wp-content/uploads/2013/01/JG12.356-web.pdf> (2012)
 [3] Wagner F. et al., Plasma Phys. Control. Fusion **52** (2010) 124044
 [4] Wesson J., Tokamaks, Oxford Univ. Press, 4th Edition (2011)
 [5] Bosch H. S. et al., Nucl. Fusion **32** (1992) 611
 [6] Wagner F., Plasma Phys. Control. Fusion **49** (2007) B1

[7] ITER Physics Expert Group on Confinement and Transport et al., Nucl. Fusion **39** (1999) 2175
 [8] Martin Y. R. et al., J. of Physics: Conf. Series **123** (2008) 012033
 [9] Koslowski H. R., these proceedings (2015)
 [10] Greenwald M., Plasma Phys. Control. Fusion **44** (2002) R27
 [11] ITER Physics Expert Group on Disruptions, Plasma Control, and MHD and ITER Physics Basis Editors, Nucl. Fusion **39** (1999) 2251
 [12] Zohm H. et al, Nucl. Fusion **53** (2013) 073019
 [13] Kovari M. et al., Fusion Engin. Design **89** (2014) 3054
 [14] Johner J., Fusion Sci. Technol. **59** (2011) 308
 [15] Dragojlovic Z. et al., Fusion Engin. Design **85** (2010) 243
 [16] Zohm H., Fusion Sci. Technol. **58** (2010) 613
 [17] Kallenbach A. et al., Nucl. Fusion **52** (2012) 122003
 [18] Matthews G. F. et al., J. Nucl. Materials **241-243** (1999) 450
 [19] Sheffield J., Rev. Mod. Phys. **66** (1994) 1015
 [20] Ejima S. et al. Nucl. Fusion **22** (1982) 1313
 [21] Wolf R. C., Plasma Phys. Control. Fusion **45** (2003) R1
 [22] Mitchell N. et al., Fusion Engin. Design **84** (2009) 113
 [23] Duchateau J.-L. et al., Fusion Engin. Design **89** (2014) 2606
 [24] Zeng S. and Todd T., Fusion Engin. Design, in press (2015)
 [25] Boccaccini L., Fusion Sci. Technol. **64** (2013) 615
 [26] Lehnen M. et al., J. Nucl. Materials **463** (2015) 39
 [27] Hirai T. et al., Fusion Engin. Design **82** (2007) 389
 [28] Wenninger R. et al., Nucl. Fusion **54** (2014) 114003
 [29] Rapp J. et al., Nucl. Fusion **49** (2009) 095012
 [30] Asakura N. et al., Nucl. Fusion **49** (2009) 115010
 [31] Ward D. J., Plasma Phys. Control. Fusion **52** (2010) 124033
 [32] Iiyoshi, A., et al., Fusion Technol. **17** (1990) 169
 [33] Gasparotto M. et al., Fusion Engin. Design **89** (2014) 2121
 [34] Helander P. et al., Plasma Phys. Control. Fusion **54** (2012) 124009
 [35] Schauer F. et al., Fusion Engin. Design **88** (2013) 1619

THE BIG STEP FROM ITER TO DEMO

J. Ongena , R.Koch, Ye.O.Kazakov

Laboratorium voor Plasmafysica - Laboratoire de Physique des Plasmas
Koninklijke Militaire School - Ecole Royale Militaire
Association "EURATOM - Belgian State", B-1000 Brussels, Belgium
Partner in the Trilateral Euregio Cluster (TEC)

N. Bekris

European Fusion Development Agreement
JET Close Support Unit, Culham Science Centre
Culham, OX14 3DB, United Kingdom

D.Mazon

Institut de Recherche sur la Fusion par Confinement Magnetique
CEA Cadarache, 13108 St Paul-lez-Durance, France

ABSTRACT

Extrapolation of the knowledge base towards a future fusion power reactor is discussed. Although fusion research has achieved important milestones since the start and continues achieving successes, we show that there are still important challenges that have to be addressed before the construction and operation of an economical fusion power reactor. Both physics and technological questions have to be solved. ITER is a significant step that will lead to major progress; for a DEMO reactor however, there will still be outstanding physics and engineering questions that require further R&D. This paper introduces some of the main topics to illustrate the challenges that lie in front of us.

I. INTRODUCTION

The decision to build ITER has been a very important step towards the realization of a fusion energy source. However, as we will show in the paper, there are still major challenges beyond ITER that must be resolved. DEMO, should be a practical demonstration of electricity generation on a power-plant scale that satisfies various socio-economic goals; it will include a closed tritium fuel cycle, and demonstrate a high level of safety and low environmental impact. Such a DEMO device will be a major milestone towards a fusion energy source that can economically compete with other energy sources. DEMO programmes are different in different parts of the world, although there is the common plan to try to have an operational DEMO device around the middle of this century.

DEMO is currently based on the tokamak, as this is the most advanced fusion concept to date, and plasma parameters approaching those of a reactor are foreseen in

ITER. Reactor studies are also being developed for Helical Devices (see e.g. [1-4]). However, a decision on a next step stellarator/helical device can only take place when the main results of the current large helical devices in operation or construction have been obtained. The largest helical device currently in operation is LHD (Large Helical Device, in the National Institute for Fusion Science (NIFS), close to Nagoya, Japan). The construction of the largest stellarator in the world Wendelstein 7-X (Max-Planck Institute, Greifswald, Germany) is nearly finished with first operations foreseen for beginning 2015. In this paper, we will therefore restrict ourselves to the discussion of a tokamak fusion reactor.

The European Fusion Development Agreement (EFDA) has released recently (November 2012) a roadmap for the realization of fusion electricity to the grid by 2050 [5]. This roadmap covers three periods: (i) the upcoming European Research Framework Programme, Horizon 2020, (ii) the years 2021-2030 and (iii) the period 2031-2050.

ITER is the key facility of the roadmap as it is expected to achieve most of the important milestones on the path to fusion power. The vast majority of resources proposed for Horizon 2020 are dedicated to ITER and its accompanying experiments. The second period is focused on maximizing ITER exploitation and on preparing the construction of DEMO. Building and operating DEMO is the subject of the last roadmap phase (time horizon about 2050).

To lead a coordinated effort in the EU (building on efforts done in the past) towards DEMO, the Power Plant Physics and Technology Department (PPP&T) has been established under EFDA in 2011 [6].

The aims of the DEMO studies in Europe are:

- to quantify key physics and technology prerequisites for DEMO;
- to identify the most urgent technical issues that need to be solved in physics and technology;
- to plan and implement supporting physics and technology R&D.

Two DEMO design options are currently being investigated by PPP&T. (See Table I for main characteristics):

- DEMO Model 1: A “conservative baseline design” that could be delivered in the short to medium term, based on the expected performance of ITER with reasonable improvements in science and technology i.e. a large, modest power density, long-pulse inductively supported plasma in a conventional plasma scenario.
- DEMO Model 2: an “optimistic design” based upon more advanced assumptions which are at the upper limit of what may be achieved, leading to a steady state plasma scenario where a large fraction of the plasma current is induced non-inductively, i.e. without making use of the transformer. This is currently a rather speculative option.

Device Operation Mode	DEMO 1 Pulsed	DEMO 2 Steady State
P_{th} (MW)	2200	2700
P_{net} (MW)	500	500
P_{rec} (MW)	594	600
P_{aux} (MW)	50	350
R_0 (m)	9.0	8.15
a (m)	2.25	3.0
I_p (MA)	14.1	19.8
B_t (T) on axis	6.8	5.0
f_{BS}	32%	40%
$H_{98(y,2)}$	1.2	1.3
β_N ($\beta_{N,th}$)	2.7 (2.2)	3.4 (2.8)

Table I: Main parameters of the early DEMO 1 and more advanced DEMO 2 model currently under investigation by the PPP&T Department of EFDA. Shown are the thermal output power (P_{th}), the net electrical power to the grid (P_{net}), the recirculating power (P_{rec}), the auxiliary heating power (P_{aux}), major radius (R_0) and minor radius (a) of the device, plasma current (I_p), toroidal magnetic field on axis (B_t), the bootstrap current fraction (f_{BS}), the enhancement factor H with respect to IPB98(y,2) scaling law and the normalized toroidal beta with (β_N) and without fast particle energy content, i.e. taking into account only the thermal plasma parameters ($\beta_{N,th}$)

Although ITER will bring significant advances, there remains a large gap between ITER and DEMO. Main differences between ITER and DEMO are summarized in Table II.

The power needed to drive the necessary plasma current additional to the bootstrap current for DEMO 2 (12MA) would be 480MW if one assumes a current drive efficiency of 0.05A/W and a wall plug efficiency for the heating system of 0.5 (See Section II.C). Without further improvements in alternative ways to maintain the plasma current, steady-state tokamak operation is a real challenge. A quasi-continuous tokamak operation was shown in JET and HT-7A and ISTTOK.

II. Technological Development Needs for DEMO

II.A Divertor concept

Of great importance is the design of the divertor. The power load to the divertor in DEMO can be estimated as follows. The area A of power deposition at the divertor targets can be approximated by $2\pi R \lambda_{SOL} F_{exp}$, where λ_{SOL} is the power decay length in the midplane scrape-off layer (SOL) and F_{exp} is the flux expansion from midplane to divertor targets. For DEMO with $R \sim 9m$, $F_{exp} \sim 3-4$ and $\lambda_{SOL} \sim 0.01m$ this results in $A \sim 2.3m^2$. We took the value of $\lambda_{SOL} \sim 0.01m$ as a first approximation from existing experiments, as it seems to depend only weakly on the size of the machine. The power arriving at the targets is the sum of the additional heating power and the alpha power from the fusion reactions. With an alpha power between 400 and 500 MW, and an additional heating power between 50 and 350 MW, one then finds a power flux density orthogonal to the divertor target plates between 200 and 370 MW/m². This number can be reduced by tilting the target plates, e.g. over an angle of 20°, leading to 190 and 350 MW/m² or a bit lower with further optimization, of the angle of inclination. Nevertheless, the numbers obtained in that way are still far in excess of the material limit of 10-20MW/m².

The first option is a conventional ITER like divertor combined with high radiation in the plasma edge to spread the heat load as homogeneously as possible over the much larger first wall surface. A possibility could be offered by seeding with appropriate impurities up to radiation fractions around 90-95%. Impurities that are currently under investigation in divertor tokamaks are N₂, Ar and Ne or a mix of them. The question is however if such regimes are compatible with sufficiently good fusion performance. Main topics for investigation are thus: (i) the effect on confinement of the seeded impurities, (ii) the effect of penetration of the impurities to the plasma centre (and/or how to avoid the pollution of the centre by the seeded impurities) and (iii) the stability of the discharge, because of the closeness to the radiation limit. It is not clear at the

moment if a satisfactory solution can be found meeting all these requirements, and thus alternative solutions have to be explored as well.

ITER	DEMO
Experimental Device	Close to commercial plant
400s pulses Long interpulse time	Long pulses, high duty cycle or steady state
Many diagnostics	Minimum set of diagnostics only needed for operations
Many H&CD systems	Reduced set of H&CD systems
No T breeding required	Self sufficient T breeding
316 SS structural material	Reduced activation structural material
Modest n-fluence, low dpa Low material damage	High n-fluence, high dpa Significant material damage

Table II: Main differences between ITER and DEMO

A more advanced option consists in using innovative divertor configurations, aiming at increasing the area of power deposition.

A very early innovative concept was the doublet [7] which later was implemented in the Doublet-I (1968-1969) and subsequent Doublet-II and Doublet-III devices in General Atomics, San Diego, USA. Recently several other options have been proposed:

- X-divertor [8] where using additional coils two more X-points are created close to the targets, to further open the flux lines and spread the power over a larger target plate area;
- Super-X divertor [9], a modification of the previous concept to move the outer strike point to a larger major radius. This allows not only to increase the area of power deposition (which is mainly proportional to the major radius at the divertor target due to the near constancy of λ_{SOL} as a function of machine size) but also to increase the distance between the targets and the plasma, and thus improves impurity screening;
- Snowflake divertor (SF) [10], named after its shape around the X-point resembling a natural snowflake. It can be generated by three toroidal currents located at the corners of an isosceles triangle: the plasma current itself and two divertor coils. This concept increases not only the area of power deposition by the larger connection lengths and perpendicular transport but also increases radiation because of the larger divertor volume.

- However the SF configuration is unstable: slight variations in the currents of the coils lead to another configuration with a double null; this is the quasi snowflake (QSF) divertor [11,12]. If the distance between the two nulls is small, then the properties of the QSF are close to that of the SF. The question is then what is the optimal distance between the nulls. A detailed assessment is given in [13].

- Recently also the cloverleaf divertor [14] has been proposed, named after the shape of the full magnetic configuration resembling a four petal clover-leaf. It can be generated by four toroidal currents: the plasma current itself, two divertor coils located symmetrically around the vertical axis and one on the axis. Main recent configurations are illustrated in Figs. 1a and 1b.

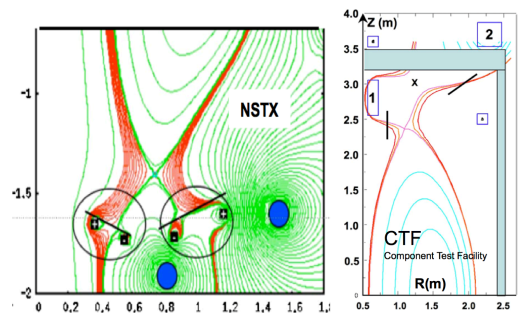


Fig. 1a: The X-divertor (left) and super-X divertor (right)

In using these alternative divertor configurations one aims at (i) decreasing the stationary and peak heat fluxes on the divertor targets and at the same time (ii) minimizing the erosion of the targets. This should be obtained by facilitating access to detachment (power and particle) by decreasing the plasma temperature below 3 eV for volume recombination to occur, improving the stability of the radiating region and increasing the wetted area [15]. At the same time (i) central plasma pollution should be avoided to minimize influence on the plasma reactivity and core radiation should be limited to allow for a sufficiently large power flux across the LCFS in order to get access to H-mode operation; (ii) the neutral particle pumping capability should be maintained. These configurations will require substantial research before becoming feasible. E.g some simulations predict that the total current in the poloidal coils could be up to ~20 times the plasma current, in case they cannot be constructed close to the plasma due to e.g. difficulties in providing sufficient neutron shielding in DEMO [16].

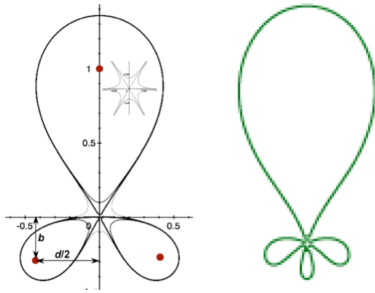


Fig. 1b: The snowflake (left) and clover-leaf (right) divertor configurations.

An additional or alternative tool to render the power exhaust capability of the divertor compatible with DEMO requirements is the use of advanced plasma facing materials such as e.g. liquid metals. The basic advantage of liquids is that they cannot be damaged by interaction with energetic plasma particles, thus showing no defect accumulation, cracking, or other surface modifications. At the same time the eroded material can be replaced in situ by e.g. capillary forces or other means. Flowing liquids offer also in principal the option to adopt larger heat fluxes using the material flow and its heat capacity. The main drawbacks are possible instabilities of the liquids in the plasma environment and the material evaporation. Candidate elements under investigation are Li, Ga, Al and Sn. Best candidates are Al, Ga and Sn because they allow for a low evaporation and sputtering rate while working at sufficiently high surface temperatures (around 1000K).

Before being able to use these two alternative options to the standard divertor in DEMO, one has to evaluate their potential “costs”.

For the alternative divertor configurations this means mainly: problems arising from the increased complexity of the magnetic configuration, the compatibility with neutron shielding of the poloidal coils, constraints arising from the need for remote maintenance and increased demands on the control of the magnetic configuration.

For the liquid metals this means: avoiding core contamination with metal impurities (this implies essentially to avoid solutions that rely on evaporation), investigate potential limitations on the use of liquid metals arising from instabilities leading to splashing of the liquid in the presence of (eddy) currents and strong magnetic fields, learning how to cope with the narrow surface temperature window for operations (too high temperatures lead to too large evaporation rates).

II.B Structural materials

Defining structural and first wall materials for DEMO is another major challenge. A central issue is the material degradation due to irradiation with 14 MeV neutrons. The neutrons collide with lattice atoms, pushing them out of their equilibrium sites, leaving a vacancy and an interstitial atom. A quantity to characterize this is number of displacements per atom in the crystal lattice or dpa [17]. The migrating defects can recombine, agglomerate, form voids, interact with existing dislocations and grain boundaries etc. This leads to a number of material changes such as e.g. hardening, embrittlement, swelling and creep with the danger of losing the properties needed to guarantee the integrity of the whole device. A database providing information on the degradation of potential candidate materials thus needs to be generated.

Existing neutron sources provide only a limited answer, mainly because the average neutron energy is either too low, in fission reactors it is about 2 MeV, far below the needed 14 MeV, or too high, in the hundreds MeV range as with spallation sources. The answers can only be found by the construction of a dedicated device capable of generating the required fluxes of 14 MeV neutrons to simulate the neutronic conditions in a fusion power plant. This device should: (i) qualify the candidate materials for fusion reactors; (ii) generate the necessary data for the design, licensing and safe operation of DEMO; (iii) deepen the fundamental understanding of the radiation response of materials to high flux and energy neutron irradiation (that would allow the design of new materials for future reactors). The current proposal for such a device is IFMIF [18] (International Fusion Materials Irradiation Facility, Fig. II) in the framework of the Broader Approach Agreement between Japan and Europe.

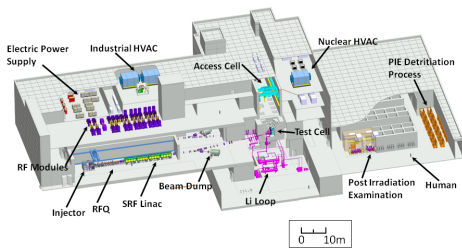


Fig. II: Overview of the IFMIF 14 MeV neutron facility for irradiation studies.

IFMIF is an accelerator-driven source of neutrons, using ${}^{\text{nat}}\text{Li}(d,xn)$ nuclear reactions (where ${}^{\text{nat}}\text{Li}$ represents natural Lithium consisting of 92.6% ${}^7\text{Li}$ and 7.4% ${}^6\text{Li}$) to produce 14 MeV neutrons that simulate the conditions in flux and neutron spectrum for the first wall of DEMO and ensuing Fusion Power Plants. The symbol ${}^{\text{nat}}\text{Li}(d,xn)$ represents a whole set of reactions (e.g. [19, page 38]) that fall in several categories: so-called deuteron break-up reactions

(where the deuteron falls apart in proton and neutron, with both half the energy of the deuteron), deuteron stripping reactions [20] (sometimes also confusingly called break-up reactions, in which one nucleon of the deuteron is stripped off, leaving a free proton or neutron at half the energy of the incoming fast deuteron), nuclear reactions in which a new (unstable) nucleus is formed (e.g. ${}^7\text{Li}(d,n){}^8\text{Be}$, ${}^6\text{Li}(d,n){}^7\text{Be}$) and “evaporation” reactions in which neutrons from the Li nucleus are ejected (e.g. ${}^7\text{Li}(d,na)$, ${}^7\text{Li}(d,np){}^7\text{Li}$, ${}^7\text{Li}(d,nn){}^7\text{Be}$, ${}^7\text{Li}(d,nd){}^6\text{Li}$) [21]. Each of those reactions is characterized by a different output cone for the resulting neutrons. Nuclear reactions have the broadest cone, as in the centre of mass reference frame, the reaction products have an isotropic velocity distribution. The stripping reactions result in the most narrow output cone, and are also the main source of 14 MeV neutrons in IFMIF [20, 22].

Material irradiation experiments require stable, continuous irradiation with high availability. IFMIF will achieve this using two 40 MeV, continuous wave (CW) linear deuteron accelerators, each delivering 125 mA beam current, thus resulting in two accelerated deuteron beams of 5MW. Both beams strike a concave flowing lithium target under an angle of 9° , with a footprint of 200mm x 50 mm. About 6% of the collisions result in a neutron [23], thus providing an intense neutron flux of about 10^{18} n/m²/s with a broad energy peak at 14 MeV [24]. As the energy deposited in the target is about 1 GW/m², a value that cannot be supported by any solid target, it consists of a flowing liquid. The heat is evacuated with the liquid lithium, which flows at a nominal speed of 15 m/s at a temperature of 523 K. The average temperature rise in the liquid is about 50 K during its 3.3ms crossing of the two 5MW beams. The liquid is again cooled to 523 K in a quench tank using a series of heat exchangers. The inventory of liquid Li in IFMIF is about 10m³. Many more very interesting recent technical developments can be found in reference [25].

The neutron flux in the test area falls off with distance from the lithium target, and the highest-value regions can be characterized as providing a damage production rate > 20 dpa/y in a volume of 0.5 liter capable to house around ~1000 testing specimens in 12 capsules independently cooled with He gas.

IFMIF, presently in its Engineering Validation and Engineering Design Activities (EVEDA) phase is validating the main technological challenges of the accelerator, target and test facility with the construction of full scale prototypes [26] (a deuteron accelerator at 125 mA and 9 MeV; three different lithium loops (Brasimone (ENEA), Oarai (JAEA) and Osaka University); a High Flux Test Module and He cooling gas prototype in KIT and Small Specimens Test Technique in Japanese Universities). Concurrently, an IFMIF Intermediate Engineering Design

Report has been prepared to allow the construction of IFMIF on time and schedule within less than one decade whenever the Fusion community demands a fusion relevant neutron source indispensable for the next steps after ITER.

II.C Heating systems

Heating DEMO will require important further physics and technological progress on all heating systems currently in use on large tokamaks. All of them have advantages and disadvantages and at this time none of them should be excluded for DEMO since a careful assessment can only be reasonably done after ITER.

To a large extent, the size of the device dictates new needs. Taking the example of NBI, and as explained further on in this paper, if one would use the current systems as e.g. used at JET, with an acceleration voltage of up to ~120 keV, one would only penetrate a fraction of the minor radius of DEMO (and also ITER). Much higher particle energies are needed in the range of 1-2 MeV to deposit close to the plasma core in DEMO plasmas. But this new requirement implies that the current positive ion acceleration technique cannot be used, as the neutralization efficiency is very low at high acceleration energy. Instead negative ions have to be used and thus we are faced with the following major challenges for NBI: how to efficiently produce negative ions, how to design an accelerator in the MeV range and how to increase neutralization efficiency using a gas target as neutralizer? (the possibility of using photo-ionization is under investigation [27]). This is just one example that should illustrate the difficulties of extrapolating current knowledge to a reactor.

	GENERATION EFF. η_{CD}	CD Efficiency γ_{CD} (10^{20} AW ⁻¹ m ²)	WALL PLUG CD EFF. $\eta_{CD} \times \gamma_{CD}$
ICRH	60-70%	0.23-0.32 Central or off-axis deposition	0.14-0.22
LHCD	40-50%	0.3 Off-axis deposition	0.12-0.15
ECRH	20-30%	0.35-0.40 Central deposition	0.07-0.12
NNBI	20-40%	0.3-0.45 Central deposition	0.06-0.18

Table III: Overview of the current status of auxiliary heating systems in terms of the Generation Efficiency η_{CD} (Fast Neutrals, Waves), Current Drive (CD) Efficiency γ_{CD} and the efficiency from wall plug power to plasma current $\eta_{CD} \times \gamma_{CD}$

An important characteristic of heating systems is the potential for substituting in part the plasma current that

normally is induced by the transformer, in view of extending the pulse length (in case of the pulsed DEMO 1) or steady state operation (for DEMO 2). This is expressed by the so-called current drive efficiency γ defined as $n_e R_0 I_{CD} / P_{CD}$ with R_0 the major radius (m) or the tangency radius in case of NBI, I_{CD} the magnitude of the driven current (A), P_{CD} the auxiliary heating power used (W), and n_e the plasma density (in 10^{20} m^{-3}). As DEMO 2 is rather speculative, with more special CD requirements, only the DEMO 1 case is considered below.

An overview of the present expectations for the different heating systems is given in Table III. The CD efficiency values are taken from [28]. They are computed for conditions optimized for DEMO 1. In this table the generation efficiency (second column) is taken from existing systems, notwithstanding the fact that the sources assumed in the computations of γ_{CD} do not exist for ECRH (250-280 GHz) and NBI (1.5 MeV). Of final importance is the wall plug power efficiency to generate current, and a figure of merit is shown in the last column. From the requirement of minimization of the recirculating power in a reactor, it is clear that further work is needed on all systems to improve this number.

It should also be noted that: (i) the physical mechanisms leading to off-axis current drive by NBI are not fully understood [29]; (ii) LHCD is only depositing in the edge ($\rho > 0.7-0.8$); (iii) that ECRH and NBI are more ‘robust’ to couple the generated power to the plasma, as power deposition is not so much depending on the edge plasma profiles as in the case of ICRH and LHCD.

For NBI, a huge effort is being put in the development of the high energy, high power ($2 \times 16.5\text{MW}$, 1 MeV acceleration voltage) neutral beam injectors for ITER. To this end the PRIMA (Padova Research on ITER Megavolt Accelerator [30]) lab is under construction with as main experiments MITICA (Megavolt ITER injector and Concept Advancement [31]) and SPIDER (Source for Production of Ions of Deuterium Extracted from an RF plasma [32]). For DEMO continued efforts will be needed, building on the experiences from ITER, to reliably and efficiently accelerate and neutralize particles at energies between 1 and 2 MeV.

For ECRH, long pulse high frequency (250-280 GHz) sources with improved efficiency need to be developed. Existing sources (at lower frequencies $\sim 100-140$ GHz) have currently a rather low efficiency for wave generation (20-30%). This could be increased, possibly by recovering the electron beam energy in the gyrotron in “depressed collectors” [33]. A possible drawback of the use of ECRH is the large amount of stray radiation that occurs in case of badly absorbing plasma scenarios, as then several 10s of MW of microwave power will be ‘sloshing’ around in the

device and finally arrive at first wall components, inside the diagnostic ports, etc... causing potentially large local damage (melting, burning).

In the case of ICRH the main development need is in improving the coupling of the waves over the (large and evanescent) gap between the antenna and the Last Closed Magnetic Surface of DEMO plasmas. This could imply to go to higher frequencies (~ 200 MHz) and/or special gas fuelling techniques in the edge to provide a propagating layer of gas in front of the antenna, without perturbing the confinement performance of the burning plasma of DEMO. LHCD has similar problems of large distance coupling. In addition, due to the large density and temperature in DEMO, the wave absorption occurs very close to the edge limiting its possibilities for driving current in the plasma core.

An important parameter to take into account in planning heating systems for future devices is the amount of power that is deposited in the plasma center. A comparison between ICRH and NBI is instructive in this discussion. A good approximation to the $1/e$ length of penetration of a neutral particle beam is given by

$$L_{\text{NBI}} \sim E_{\text{NBI}} / [180 \times (1 + \delta(E, n_e, Z_{\text{eff}})) \times A \times n_e]$$

with E_{NBI} the energy of the injected neutral atoms (in keV), A the atomic mass of the injected atom (in amu), and n_e the line-averaged density (in 10^{20} m^{-3}). Multistep ionization is taken into account by the factor $\delta(E, n_e, Z_{\text{eff}})$ [33b]. For JET, with $E_{\text{NBI}} \sim 120\text{keV}$, $n_e \sim 5 \times 10^{19} \text{ m}^{-3}$ and $\delta(E, n_e, Z_{\text{eff}}) \ll 1$ one finds $L_{\text{JET}} \sim 0.7\text{m}$, close to the value for the plasma radius $a_{\text{JET}} \sim 0.9\text{m}$. If such a system would be applied for ITER, with expected $n_e \sim 1 \times 10^{20} \text{ m}^{-3}$, one finds for $L_{\text{ITER}} \sim 0.35\text{m}$ using the same value for $E_{\text{NBI}} = 120\text{keV}$, i.e. only about $1/4$ of the minor radius of ITER ($a_{\text{ITER}} \sim 2\text{m}$). In other words, mainly the outer edge of the plasma is heated. To reach the plasma centre of ITER, the injected particle energy has therefore to be increased. For DEMO, the voltage requirements are even higher to reach the centre.

	$E_{\text{NBI, D}}$	L_{NBI}	Edge NBI power deposition $P_{\text{abs}}(r/a \geq 0.5)$	Central NBI power deposition $P_{\text{abs}}(r/a \leq 0.5)$
ITER	1 MeV	1.4m	63%	37%
DEMO	1 MeV	1.4m	76%	24%
	2 MeV	2.8m	51%	49%
	3 MeV	4.2m	60%	39%

Table IV: Values for the edge and central power deposition for various values of the injected energy of neutral D atoms in ITER and DEMO. To deposit dominantly in the plasma center, very high injection energies are required.

Table IV gives an overview of the off-axis, centrally deposited and shine-through power for ITER and DEMO, for various values of E_{NBI} (tangential injection). Shine-through power is less than 1% for all cases mentioned.

The situation is totally different of ICRH (and also for ECRH). This heating method, on the contrary, offers the possibility to deposit a significantly larger fraction of launched power closer to the center. Indeed, the fraction of power deposited in the outer shell ($r/a > 0.5$) can be made less than 10%, in clear contrast to NBI as illustrated in Table IV. In fact, this can be further optimized. With a proper choice of wave frequency and heating scenario, more than 80% of the launched ICRH power can be absorbed within the plasma zone $r/a < 0.2$.

II.D Tritium Self Sufficiency

The Test Breeder Blanket Module (TBM) is an essential concept in the development of a future commercial reactor such as DEMO.

Any future fusion power plant reactor which will exploit the deuterium-tritium (D-T) fusion reaction to produce energy, needs to be tritium self-sufficient. Indeed, although D is relatively easy to find in sea water (its natural abundance is 0.015 %) tritium does not exist as such, and therefore, it has to be generated artificially. The easiest way to get tritium is to recover it from the Heavy Water fission Reactors (HWR) where it is produced as a by-product. Presently we estimate that about 1.7 kg per year can be produced from the Darlington Tritium Removal Facility in Canada and another 0.7 kg per year from similar South Korean reactors.

However, the operation of a commercial fusion power plant, such as DEMO, operating at the GW fusion power level, will require much more tritium. Indeed, per GW produced (thermal) power, about 55 kg tritium are needed for a full power year (FPY), or ~0.150 kg tritium per full power day.

Understandably, there is not enough tritium for a commercial fusion machine and therefore, every future fusion power plant will have to breed its own tritium needs. Therefore, one of the major objectives of ITER is to demonstrate that the current blanket technology is able not only to breed tritium, but also to extract and purify it before injecting it back into the fusion machine.

Tritium breeding requirements are quite demanding, as the process is based on the nuclear reaction between the neutron generated by the fusion reaction, taking place in the plasma and the lithium based compound, filling the blanket surrounding the torus. There are two possible ways to produce tritium in the blanket. Either by the neutron-alpha (n, α) reaction on ${}^6\text{Li}$, or by the ($n, n'\alpha$) reaction on ${}^7\text{Li}$, both lithium isotopes have a natural abundance (92.4%

and 7.6% respectively). To increase as much as possible the efficiency of the above mentioned nuclear reaction the blanket must contain not only lithium based ceramic material but also a neutron multiplier.

According to the current road map toward production of fusion energy, ITER might be the only opportunity for testing mockups of breeding blankets, called Test Blanket Modules, in a real fusion environment [34]. For this purpose, three equatorial ports will be dedicated to the test TBMs where each TBM port will receive two independent TBMs.

At present, the following six independent TBM Systems are foreseen for tests in ITER [35]:

- the Helium Cooled Ceramic Breeder (HCCB) and the Lithium Lead Ceramic Breeder (LLCB) for installation in Equatorial Port #02.
- the Helium Cooled Lithium Lead (HCLL) and the Helium Cooled Pebble Bed (HCPB) for installation in Equatorial Port #16;
- the Water Cooled Ceramic Breeder (WCCB) and the Dual Coolant Lithium Lead (DCLL) for installation in Equatorial Port #18;

Since the nineties the European Breeding Blanket Programme has been developing two DEMO relevant blanket concepts, the helium cooled pebble bed and the helium cooled lithium lead. For both concepts the use of lithium as breeder material is being proposed, but while the HCLL Blanket uses liquid lead as neutron multiplier, the HCPB employs beryllium. Both concepts are Helium cooled and the use of martensitic steel as structural material [36] is being considered.

In order to attain the tritium self-sufficiency, the Tritium Breeding Ratio (TBR) needs to exceed unity (best >1.1). The TBR is the ratio between the T produced in the blanket to T consumed in the plasma. The TBR value should be very accurate, as an uncertainty as small as 1% translates into 1–2 kg of T per FPY for 2–3 GW fusion power [37].

Although tritium production is an essential factor to take into account, the *Tritium extraction* operation is not less important. Indeed, the tritium bred by neutron capture in a lithium-containing blanket has to be continuously extracted by a closed loop operation and then removed from the loop for its subsequent re-introduction into the machine.

In this respect, there are several ancillary systems foreseen to carry out these operations, which are briefly described below. Firstly, the Tritium Extraction System (TES), which is foreseen to extract tritium from the lithium ceramic beds and beryllium multiplier. The TES will operate with a low-pressure helium stream (0.11MPa) and will contain approximately 0.1% pure hydrogen. The addition of hydrogen into the helium stream is absolutely necessary as

it enhances the tritium release by the isotope exchange mechanism. Under such conditions the TES accomplishes the tritium extraction from the ceramic blanket in the two main chemical forms, HT and HTO. The subsequent separation, from the purging helium gas, of all diluted tritiated gaseous components, independent of their chemical form (HT, HTO, CH₃T, etc) constitutes the *Tritium removal* operation. Finally, after an ultimate chemical processing the tritium will be recovered in the Isotope Separation System (ISS), before it is sent downstream to the Storage and Delivery System (SDS), which is the main system feeding the machine with deuterium and tritium.

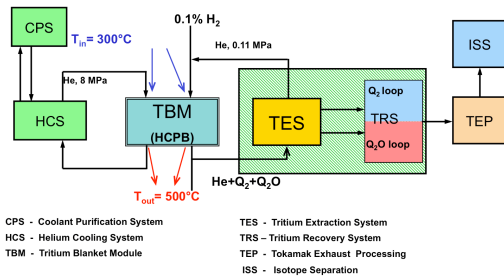


Fig. III. Flow diagram of the TES, HCS and CPS of the Test Blanket Module for ITER

Beside the TES the blanket has also to be featured with another high pressure He loop. Indeed, the thermal power, of around 3 GW (in DEMO), is extracted by means of the Helium Coolant System (HCS). In the HCS the He flows at a pressure of 8 MPa through the first wall and blanket cooling plates, which are made in EUROFER 97 martensitic steel. The inlet and outlet temperatures of the primary coolant are 300 and 500°C respectively. At such temperatures non-negligible tritium permeation cannot be avoided from the blanket modules into the He primary coolant (HCS) [37a]

Consequently, a complementary closed helium loop called Coolant Purification System (CPS) must be designed in order to remove the tritium permeated into the coolant stream. The tritium removal from He coolant has also the beneficial effect to keep the tritium inventory low in the HCS, minimising the tritium release (i) into the reactor vault in the case of a LOss of Coolant Accident (LOCA) and thus also (ii) in the secondary water-steam circuit through the steam generators. For this reason, a deep and critical analysis of the possible candidate CPS processes has to be carried out, in view of the selection of the most appropriate system and its engineering design.

A possible flow diagram of the main tritium processing systems for such a blanket concept (HCPB or HCLL) is shown in Fig. III.

After ITER important steps still have to be taken before arriving at a design for DEMO. Compared to ITER, the DEMO requirements are more demanding: the surface heat flux is about a factor of two larger, the first wall irradiation damage about 30 times larger, the neutron wall load about 3 times larger, and the local (i.e. not the full blanket) tritium production up to a factor of 10 higher [38].

II.E Diagnostics for DEMO

This paragraph raises a very important and challenging problem. Indeed many diagnostics which are currently operating in present days tokamaks and are straightforwardly being adapted to be operating in ITER cannot be directly transposed to DEMO. Worse even, many of them will simply not be working during high duty cycle burning plasma experiments [39]. Indeed the application to a steady state thermonuclear burning plasma environment induces many problems to fusion diagnostics mainly due to radiation damage, deposition of dust, influence of alpha particle bombardment, tile erosion, high heat fluxes and neutron fluence [40].

The most simple but essential diagnostic in tokamaks, the magnetics diagnostic, will already be strongly affected by radiation-induced conductivity effects in their insulators, in particular those close to the plasma that will be used for identification and control of fast instabilities. Sometimes it will be not possible to get any measurement from magnetic diagnostics depending on their specific location in the torus. An alternative solution for the measurement of the plasma shape could be to use another diagnostic that is not directly used for that purpose like tomographic Soft-X-Ray (SXR) measurements or bolometers. But this then implies a strong shielding against radiation. For a fusion reactor it is also essential to develop techniques for the detection of dust particles and erosion of the first wall (among others, also to avoid water leaks etc). These techniques are starting to be applied to laboratory samples but we need to expand these techniques in order to survey larger areas, using e.g. articulated beams. The α -particles from fusion reactions, the main source of heating in DEMO, will need to be diagnosed accurately, including their spatial distribution in the plasma. But this is a measurement that is not developed in present devices and where we have a substantial need for further developments. The measurement of escaping fast particles is also a very important problem to tackle, as the techniques currently being employed are extremely difficult to extrapolate to burning plasmas. More problematic even are all the diagnostics based on the use of fast injected neutrals from neutral beams. As stated above in Section II.C, depending on the plasma size, much higher acceleration voltages are needed, still not accessible by current technologies. Limits to the maximum acceleration voltage could thus limit the penetration of the fast particles and this would mean that the radial extent of ion

temperature, rotation and current density profiles etc. would be rather limited. Also here, new measurement techniques need to be developed and tested in actual devices. More general, backscattered neutrons will affect the signal to noise ratio of practically all the diagnostics and their associated electronics and proper shielding or transfer of the information to a safe distance from the plasma using optical systems will be required [41]. But the reduced transparency of optical fibres under neutron irradiation should be strongly reduced. More general, the influence neutron irradiation on all optical elements used in various diagnostics, as well on the reflectivity of mirrors will need to be studied, maybe in the new high energy neutron generation facilities like IFMIF (see Section II.B) On top of this we have to consider the difficulties related to the acquisition of data in discharges that are lasting for days or weeks, compared to the current maximum discharge time of several tens of minutes. One important consequence of long pulse operation will be the need for a regular calibration of the diagnostics, e.g. to be triggered on demand. Indeed, the hostile environment in a fusion reactor is expected to cause severe drifts of the electronics and accelerated aging of various diagnostic components used for detection. This would imply for example calibration sources of various kinds to be permanently installed on the tokamak and remotely manipulated.

Progress in fusion energy science is strongly linked with diagnostic developments in order to measure the necessary data needed for checking the theory. Diagnostics are thus essential to further improve our understanding of the physical mechanisms and properties of the plasma. Because of the challenges sketched above, it could well be that unfortunately, we are forced to accept that only a limited number of diagnostics in DEMO will be present. This then has an immediate and important consequence for feedback control of the plasma: indeed diagnostics are the sensors that are providing real time information required for the plasma control systems to steer the different actuators (heating power, current drive systems, fuelling, plasma positioning, etc). Controlling in real time the DEMO plasma to maintain a safe and reliable plasma performance is thus becoming a challenge with a limited set of sensors. Most importantly, it is questionable whether plasma profile control, necessary for advanced tokamak scenarios [42] can be achieved in DEMO due to the rather high number of sensors needed for the real-time reconstruction with sufficient spatial resolution of the plasma equilibrium [43]. One potential solution that needs to be tested in actual devices (preferably in ITER) is to develop and validate interpretative and predictive modelling tools that could be used for the control systems. This then requires the development of synthetic diagnostics to validate the reconstruction through comparison with the limited set of diagnostic measurements on a DEMO device. In ITER such techniques should be developed, tested and

optimized. In any case, even if limited, robust diagnostics will have to be implemented. The development of diagnostics providing simultaneously several informations on the plasma behaviour should be encouraged. A typical example could be the SXR diagnostic cited previously which could possibly be used to study impurity transport and MHD instabilities but – if combined with tomographic reconstruction – could provide information about the plasma shape, magnetic axis, photon temperature etc... It is clear that there is a huge need for an extensive R&D programme focused on the specific problems of implementing diagnostics in the harsh environment of a fusion reactor.

III. Physics Needs for DEMO

III.A High Density Operation and Plasma Fuelling

High density operation is an evident advantage for any fusion reactor but it is challenging. There are several density limiting mechanisms, but there is no comprehensive theory. One of the main limits is the so-called Greenwald limit [44] which is based on the empirical observation that it is difficult to run the device above a line integrated density defined by $n_e = I_p / (\pi a^2)$, with n_e the line-averaged central density (in 10^{20} m^{-3}), I_p the plasma current (in MA) and a (in m) the minor radius (or minor axis of the elliptic cross-section). Moreover, in H-Mode the density profile is usually rather flat. To arrive at a peaked profile, pellet injection may provide a possible option that should be explored. For application to DEMO, optimization of the size and the speed of the pellets will be needed in order to penetrate the plasma sufficiently to fuel beyond the pedestal region of the plasma profiles.

III.B MHD Stability

Reactor requirements for high β values arise from two major considerations: high fusion power and high bootstrap current fraction. In advanced scenarios, it is generally assumed that operation is possible near the ideal magneto-hydrodynamic (MHD) limit (the so-called “no-wall limit”), usually stated as $\beta_N = 4 \times I_i$ with β_N the so-called normalized beta value (i.e. the value of β normalized to the Troyon limit value for β [45]) and I_i the internal inductance of the plasma current. However, the real β limit could be significantly lower, due to the presence of neoclassical tearing modes (NTMs) or resistive wall modes (RWM). To mitigate this, a stabilizing wall and active feedback would be required [46, 47]. In the hybrid regime, the assumption is usually made that β_N values up to 3.5 can be sustained, thereby not exceeding the “no-wall limit”. Also here neoclassical tearing modes could cause limitations, and control using localized electron cyclotron current drive (ECCD) would be needed.

III.C Alpha particle physics studies

ITER will be the first fusion experiment where a large amount of fusion alphas will be present during the high performance deuterium-tritium experiments. A simple formula relates the fraction of self-heating f by alpha particles to the Q value of the plasma : $f = Q/(Q+5)$. With $Q=10$ in ITER, we find $f = 66\%$; with $Q=30-50$ as expected for DEMO, $f = 85-90\%$. In a tokamak plasma there exists a series of discrete Alfvén eigenmodes, in the frequency gaps of the Alfvén wave continuum [48]. These gaps can be due to toroidicity, elongation, triangularity, helicity etc... Frequency gaps are important because radially extended, weakly damped modes that are not subject to continuum damping can exist in these gaps, resulting in the so-called Toroidal Alfvén Eigenmodes (TAEs), Helicity-induced Eigenmodes (HAEs) etc...). Alfvén modes can become unstable if resonances occur between the velocities of the energetic particles above the Alfvén velocity $v_A = c/\sqrt{\mu_0\rho}$ (where c is the speed of light, μ_0 the magnetic permeability of vacuum, and ρ is the mass density of the charged particles in the plasma) and the wave phase velocity. These Alfvén modes can lead to the loss of the energetic alphas with possible serious damage to the first wall as a consequence.

Detection of alpha particles in a burning plasma is another important topic to be developed. A clever method is not to detect directly the alpha particle but physical effects of its presence. In JET this has been demonstrated using γ rays originating from nuclear reactions between the fast alphas and intrinsic plasma impurities. In the period when JET was still equipped with the carbon inner wall (i.e. before May 2011), there were always traces of Be present in JET due to a Be evaporation technique used to condition the wall. Gamma rays from the reaction ${}^9\text{Be}({}^4\text{He},n\gamma){}^{12}\text{C}$ were used to indirectly detect the alpha particles [49]. With the Be wall now installed in JET, this is an evident reaction to use, and the same is true for ITER. For DEMO, one has likely to choose another reaction as Be is not an appropriate wall material for a reactor device. Using a two dimensional set of γ ray cameras around the device one would be able to perform 2D tomographic reconstructions of the alpha population in the plasma. However, the γ ray detectors should be shielded against the severe neutron emission in ITER and DEMO with special neutron filters [50].

III.D Confinement and Operational scenarios

By modifying in a clever way the current profile using current drive or by freezing the current profile in a non-relaxed state by heating the plasma early in its evolution after the plasma breakdown, some confinement improvement can be obtained. A sketch of the resulting profiles of the safety factor q are shown in Fig. IV. Profiles

with strongly reversed shear $s = (r/q) dq/dr$ correspond to advanced modes, those with a flat q profile in the center to the so-called hybrid mode. Confinement enhancement factors up to 1.4-1.5 have been obtained for the hybrid mode, and higher values for the advanced modes. However, advanced modes have a tendency to be unstable, as they are characterized by peaked pressure profiles, often leading to an excess of the β limit in the plasma centre, which then leads to triggering of instabilities.

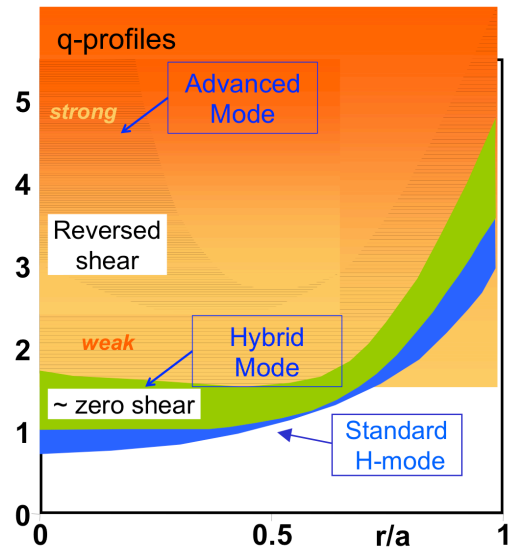


Fig IV. Profiles of the safety factor for H-Mode, hybrid-mode and advanced mode operational scenarios.

DEMO should deliver 500MW net electrical power to the grid, as discussed in the introduction of this paper. This can be done in a pulsed way or in steady-state. In many previous studies a steady-state DEMO was a primary goal. This is of course the most attractive way of operation, but it remains very challenging and requires values for e.g. β and bootstrap fraction that are hardly attainable in existing tokamaks. Advanced modes are also natural candidates for steady state operation, as the strong density gradients lead to large (non-inductive) bootstrap currents. However, they also need substantial active real-time control, which could be problematic, especially if only a limited set of diagnostics would be possible on DEMO, given that only a fraction of the power and the current is controllable in a reactor. More recent studies therefore also envisage a pulsed DEMO, with the hybrid mode as operational scenario, demonstrated by the ongoing PPP&T work in Europe (See Table 1). Advantage of pulsed operation is that the underlying operational scenarios have a much broader physics base. A major disadvantage of pulsed operation is the thermal fatigue of the first wall and

structural material and the bigger size of the machine (mainly due to the larger central solenoid needed), hence a more costly device.

Both in JET and ASDEX one finds that in a majority of discharges with metallic walls confinement in H-Mode is reduced by ~20% compared to the same scenario with a Carbon wall and a similar reduction holds for the L-H threshold [51]. The reduction in confinement with respect to carbon devices can be (partly) overcome by seeding of nitrogen [52]. The reasons for these changes are not yet understood and are subject of future research. Note however that most of these discharges are obtained at a low to moderate heating power level and at rather high gas fuelling, a fact that could play a role in the observed confinement reduction. This example alone shows again that one has to be careful with straight extrapolating the current understanding to a fusion power reactor.

III.E Disruption mitigation

A disruption is defined as a sudden loss of thermal energy and particle confinement, due to a global MHD instability. It leads to a rapid decay of the plasma current, and is often preceded by a triggering MHD instability. Plasma disruptions lead to a fast and irreversible loss of thermal and magnetic energy. The energy stored in the plasma is promptly released to the surrounding structures. Large toroidal loop voltages can accelerate run-away electrons, which may hit the vessel walls, causing metallic components to melt. Elongated plasma configurations can lose vertical stability; if this occurs at full plasma current and thermal energy, it is called a vertical displacement event (VDE). When the plasma loses its equilibrium vertical position and comes in contact with the wall part of its current (known as a halo current) can flow through the wall. The average poloidal halo current contributes to the vertical force on the vessel, while the magnitude of the local halo current density puts additional requirements to the mechanical design of in-vessel components. Currents induced in conductive in-vessel components, due to the plasma displacement and/or the plasma current decay, also produce local and global forces. The deposition of energy on plasma-facing components during disruptions can have a major impact on the lifetime of these components, and it is one of the main factors that have been taken into account for the determination of the divertor plasma-facing materials in ITER [53].

The importance of avoiding disruptions in ITER and DEMO is clear: the electromechanical forces induced by disruptions scale roughly with the square of the plasma current; the runaway electron energy scales very strongly with plasma current.

The challenge for ITER and DEMO will be to limit the number of disruptions to an absolute minimum. As disruptions are unavoidable, they can be mitigated if their approach is known with sufficient warning. To this end a disruption predictor needs to be developed, which can be continuously trained, starting with a very small number of events. The most effective mitigation technique at the moment is massive gas injection [54, 55]: several bar* ℓ of a noble gas (Ar and Ne preferred) are injected at high pressure. This is used to precipitate the quench via a radiative collapse. This results reliably in short disruptions, with consequently less opportunity to develop electromechanical loads, whereby most of the energy is lost fairly uniformly by radiation, rather than locally conducted to the wall as it would if the radiation was low both during the thermal quench and the current quench. Massive gas injection might also prevent or suppress the generation of runaway electrons, however this has not been experimentally demonstrated yet [56].

Another option is to inject a so-called large shattered deuterium-neon mixture pellet [57]. This technique consists of injecting a large cryogenic pellet (in DIII-D 15 mm diameter and 20mm long, with speeds up to 600 m/s) and shattering it into sub-millimeter fragments by impacting it on metal plates or using a curved tube. Shattering the pellet is necessary to protect the inner wall from damage by impact of a large remnant of the originally injected pellet. Shattering also helps to increase the global pellet surface area and also generates a 'spray' of smaller pellet particles thus increasing the ablation rate. This technique has been successfully applied to terminate plasma discharges and may be useful for suppression or dissipation of runaway electrons [58]. Before being applicable for DEMO, further work is needed. Questions to be solved are: the optimal material mixtures, size and speed of the pellets, and in how far can this be realized with existing technology. Indeed, a fast response time could mean a close proximity to the plasma. This poses many engineering challenges to the injector technology for both Massive Gas Injection and Scattered Pellet Injection, due to the presence of strong magnetic fields and high radiation levels.

III.F ELM Mitigation

Operating ITER in the reference H-Mode scenario at 15MA and $Q=10$ requires good confinement, accompanied by a sufficient pedestal pressure. The strong gradients that occur in the edge region often drive strong MHD instabilities that lead to Edge Localized Modes (ELMs). The plasma energy from the pedestal region is expelled from the pedestal region in very short timescales during ELMs (~ 100 μ s) and can cause serious damage to the plasma facing components. In ITER it is expected that ELM energy losses could correspond to 20% of the

pedestal energy, or an energy loss ΔW_{ELM} of $\sim 20\text{MJ}$ per ELM, equivalent to a power loss in the range of 100-200 GW. In DEMO the power losses will be even larger. Mitigation of the power losses caused by these ELMs is thus mandatory. Two techniques are being pursued: (i) keeping the plasma edge conditions such that good confinement is reached, but with pedestal pressure below (but close to) the stability limits. This could possibly be achieved by applying external magnetic perturbations or could be reached in confinement regimes with small ELMs; (ii) destabilizing the plasma edge, by triggering an ELM (using external means) before the stability limit is reached. This can be done by applying a perturbation to the edge such that the ELM instability is triggered at a lower pressure than the stability limit. This technique is based on the experimental observation that the energy loss during an ELM, ΔW_{ELM} , is inversely proportional to the ELM frequency [59]. Faster ELMs lead thus to a lower energy loss per ELM.

Techniques that are currently investigated to reduce the ELM energy loss are: (i) working in a confinement regime with small ELMs [60] (ii) shallow pellet injection from the Low Field Side [61], (iii) moving the plasma up and down on a short timescale (“plasma kicks”) [62] and (iv) Resonant Magnetic Perturbation (RMP) coils [63]. All of these need further research before being applicable to DEMO; questions are: (i) are confinement regimes with small ELMs transferable to DEMO? (ii) pellet injection has to be made compatible with strong neutron irradiation and handling of tritium; (iii) in how far are fast kicks a possibility, if this requires coils that are close to the plasma; (iv) the results with RMPs up to now are not very conclusive with respect to ELM mitigation, even for application to ITER; much more work will be needed there before such a system will be ready for use on DEMO; in addition it is likely that these RMP coils should sit close to the plasma to be effective, and then neutron irradiation constraints could cause difficulties to implement this method.

III.G Exhaust Pumping Systems

A fusion reactor can only successfully be operated if the ash of the fusion reaction (He) can be successfully removed. Because of the fact that the T burn-up is rather low (a few percent), the exhaust gas will consist largely in D-T fuel that has not undergone a fusion reaction plus possibly other gases used to reduce peak heat loads to the plasma facing components by edge radiation. Extrapolation of the ITER pumping systems to DEMO is not straightforward. Indeed, although they have extremely large pumping speeds, can be made tritium compatible, work under high magnetic fields and neutron loads and require relatively low maintenance (a minimum of moving parts), they have also important drawbacks for a reactor:

they build up (large) hydrogen inventories with the consequent risk for explosions and thus require regular regenerations; this interferes with long pulse or continuous DEMO operations. A review of the various options indicates the need for diffusion and liquid ring pumps, together with a new type, the metal-foil pump, based on super-permeation of hydrogen and its isotopes through metallic foils, pioneered by Prof. Waelbroeck and his team (IPP, KFA-Juelich) [64]. As the metal foil pump works only for hydrogen and its isotopes it could be used to separate directly the hydrogenic fraction close to the torus, (where these could be immediately recycled) and thus could reduce to a large extent the gas throughput to the gas exhaust system [65, 66]. Such a combination of pumps is currently under investigation in the THESEUS facility in KIT, Karlsruhe [67]. An excellent overview of the current state of work can be found in [68].

CONCLUSIONS

This paper tries to illustrate the physical and technological developments that are needed before the construction of a fusion power reactor can take place. ITER will contribute to enhance our knowledge on several important aspects, but still a large step has to be taken from ITER to DEMO. The increase in size of the device a main factor driving the development needs: disruptive forces are much higher, ELM loads will be much larger, the heat load on the wall will increase, the size of the plasma is such that e.g. NBI particles need much higher energies to penetrate, etc... These are only a few examples which show that further developments are needed for currently available systems before becoming ready for use in a reactor. The need for new components, materials or systems is another factor. New physics phenomena (like the presence of a large population of fast alpha particles from fusion reactions) is a third factor contributing to continued R&D. These points clearly demonstrate that every step in fusion science is pushing the limits of what is currently known in physics and technology. In some cases even new, purpose-built laboratories have to be constructed, as illustrated in the paper.

We all know that fusion is a challenging undertaking and that patience will be needed, but it is more than worth the effort given the difficulties we are facing in the future with our current energy supply and its suspected influence on climate. It will be evidently up to you, young researchers, to tackle these interesting and very important problems. If successful, this will be your very important contribution to the benefit of all people on earth.

ACKNOWLEDGEMENTS

The following colleagues are gratefully acknowledged for stimulating and interesting discussions during the preparation of this paper: Kristel Crombé and André Messiaen (ERM-KMS, Brussels), Juan Knaster (IFMIF, Rokkasho), Gianfranco Federici (EFDA PPP&T Department, Garching), Joerg Hobirk (IPP-Garching), Francesco Gnesotto (Consortio RFX, Padova), Paula Siren (VTT, Helsinki), Volker Phillips (IEK-4/Plasmaphysik, FZ-Juelich), Domenico Frigione and Giuseppe Calabrò (ENEA, Frascati), Valeria Riccardo (JET, Culham) and Larry Baylor (ORNL, Oak Ridge).

REFERENCES

- [1] C.D.Beidler et al., “Stellarator Fusion Reactors – An Overview”, *Proc. 12th International Toki Conference on Plasma Physics and Controlled Nuclear Fusion (ITC-12)*, (11-14 Dec 2001, Toki-city, Japan), Paper XI-3 (2001).
- [2] H.Wobig, T. Andreeva et al., “Development of the Wendelstein line towards a Helias Reactor”, *Proc. 36th EPS Plasma Physics Conference (29 June – 3 July 2009, Sofia, Bulgaria)*, Paper P4.192 (2009).
- [3] A.Sagara et al., “Conceptual design activities and key issues on LHD-type reactor FFHR”, *Fusion Eng. Des.* **81**, 2703 (2006).
- [4] A.Sagara et al., “Improved structure and long-life blanket concepts for heliotron reactors”, *Nucl. Fusion* **45**, 258 (2005).
- [5] F.Romanelli et al. “Fusion Electricity: A roadmap to the realization of fusion energy”, EFDA, ISBN 978-3-00-040720-8 (2012).
- [6] G.Federici et al., “EU DEMO Design and R&D Studies”, *25th Symp. Fus. Eng. (SOFE), 10-14 June 2013, San Francisco, USA*, paper WO1-1 (2013).
- [7] T. Ohkawa, H.G. Voorhies, “Plasma-Current Multipole Experiments”, *Phys. Rev. Lett.* **22**, 1275 (1969).
- [8] M. Kotschenreuther, et al., “On heat loading, novel divertors, and fusion reactors”, *Phys. Plasmas* **14**, 072502 (2007).
- [9] P.M. Valanju, et al., “Super-X divertors and high power density fusion devices”, *Phys. Plasmas* **16**, 056110 (2009).
- [10] D.D. Ryutov, “Geometrical properties of a “snowflake” divertor”, *Phys. Plasmas* **14**, 064502 (2007).
- [11] V.Pericoli et al., “Preliminary 2D code simulation of the quasi-snowflake divertor configuration in the FAST tokamak”, *Fus. Eng. Design* **121**, 282 (2013).
- [12] G.Calabrò et al., “FAST/EAST snowflake similarity studies”, paper presented at 7th IAEA Technical Meeting on Steady State Operation of Magnetic Fusion Devices Aix en Provence, France, 14-17 May, 2013.
- [13] D.D. Ryutov et al., “A snowflake divertor: a possible solution to the power exhaust problem for tokamaks”, *Plasma Phys. Control. Fusion* **54**, 124050 (2012).
- [14] D.D. Ryutov, M. Umansky, “Divertor with a third-order null of the poloidal field”, *Phys. Plasmas* **20**, 092509 (2013).
- [15] M. V. Umansky et al., “Analysis of geometric variations in high-power tokamak divertors”, *Nucl. Fusion* **49**, 075005 (2009).
- [16] R.Ambrosino et al., “Advanced Configuration Magnetic Design”, presented at the *European Fusion Programme Workshop, (3-5 December 2012 Ericeira Portugal)*.
- [17] M.I.Norgett et al., “A proposed method of calculating displacement dose rates”, *Nucl. Eng. Design* **33**, 50 (1975).
- [18] IFMIF Comprehensive Design Report, International Energy Agency (IEA) Implementing Agreement for a Program of Research and Development on Fusion Materials, January 2004.
- [19] J.A.Hassberger et al., “Preliminary Assessment of interactions between the FMIT deuteron beam and liquid-lithium target”, *Hanford Engineering Development Laboratory Report*, HEDL-TME 82-28 (1983).
- [20] R.Serber “The production of high energy neutrons by stripping”, Report MDDC-1238, US Atomic Energy Commission, Oak Ridge, Tennessee, 21 July 1947; see also R.Serber, “The production of High Energy Neutrons by Stripping”, *Phys. Rev.* **72**, 1008 (1947).
- [21] M.Hagiwara et al., “Measurement of Neutron Emission Spectra in Li(*d, xn*) reaction with thick and thin targets for 40-MeV Deuterons”, *Fusion Sci. Techn.* **48**, 1320 (2005).
- [22] T.Ye et al., “Analysis of deuteron breakup reactions on ⁷Li for energies up to 100MeV”, *Phys.Rev.C* **80**, 014604 (2009).
- [23] I.C.Gomes et al., “Neutronics of a D-Li source. An overview”, *Fus. Eng. Design* **28**, 724-729 (1995);

F.M.Mann et al., “Neutrons from D+Li and the FMIT Irradiation Environment”, *Hanford Engineering Development Laboratory Report*, HEDL-TC-1459 (1981).

[24] J.Knaster et al., “IFMIF, a fusion relevant neutron source for material irradiation. Current Status”. *Proc. 11th International Symposium on Fusion Nuclear Technology, (16-20 Sept. 2013, Barcelona)*, paper O6B.1 (2013).

[25] J.Knaster et al., “Assessment of the beam-target interaction of IFMIF: a state of the art”, *Proc. Of the 11th International Symposium on Fusion Nuclear Technology (16-20 September 2013, Barcelona)* paper P3-090.

[26] J.Knaster et al., “IFMIF: overview for the validation activities”, *Nucl.Fusion* **53**, 116001 (2013).

[27] A.Simonin, “SIPHORE: Conceptual Study of a High Efficiency Neutral Beam Injector Based on Photo-detachment for Future Fusion Reactors”. *AIP Conf. Proc.*, **1390**, 494 (2011); also: R.McAdams, “Beyond ITER: Neutral beams for a demonstration fusion reactor (DEMO)”, *Rev. Sci. Instr.* **85**, 02B319 (2014)

[28] H.Zohm et al., “Assessment of H&CD System Capabilities for DEMO”, *Proc. 40th EPS Plasma Physics Conference (1-5 July 2013, Helsinki, Finland)*, Paper O3.108 (2013).

[29] S.Günter et al., “Conditions for NBI Current Profile Control on ASDEX Upgrade”, *Proc. 31st EPS Plasma Physics Conference (28 June - 2 July 2004, London, United Kingdom)*, Paper O1.02 (2004).

[30] P.Sonato et al., “Status of PRIMA, The Test Facility for ITER Neutral Beam Injectors”, *Proc. 3rd Int. Symp. On Negative Ions, Beams and Sources (NIBS 2012, 3-7 Sept. 2012, Jyväskylä, Finland)*, *AIP Conf. Proc.* **1515**, 549-558 (2013).

[31] R. Hemsworth et al., “Status of the ITER heating neutral beam system”, *Nucl. Fusion* **49** 045006 (2009); L.R.Grisham et al., “Recent improvements to the ITER neutral beam system design”, *Fus. Eng. and Design* **87**, 1805 (2012).

[32] P.Sonato et al., “The ITER full size plasma source device design”, *Fus. Eng. and Design* **84**, 269 (2009).

[33] M.Thumm, “MW gyrotron development for fusion plasma applications”, *Plasma Physics Contr. Fusion*, **45** A143 (2003); A.Litvak et al., “Innovation on high-power long-pulse gyrotrons”, *Plasma Physics Contr. Fusion*, **53**, 124002 (2011).

[33b] R.K.Janev et al. “Penetration of energetic neutral beams into fusion plasmas”, *Nucl. Fusion* **29**, 2125 (1989)

[34] Y. Poitevin et al., “The test blanket modules project in Europe: From the strategy to the technical plan over next 10 years” *Fusion Engineering and Design* **82**, 2164 (2007).

[35] L.M.Giancarli, et al., Overview of the ITER TBM Program. *Fusion Engineering and Design* **87**, 395 (2012).

[36] L.V. Boccaccini et al., “The EU TBM systems: Design and development programme”, *Fusion Engineering and Design* **84**, 333 (2009).

[37] Laila A. El-Guebaly, Siegfried Malang. Toward the ultimate goal of tritium self-sufficiency: Technical issues and requirements imposed on ARIES advanced power plants. *Fus. Eng. Design* **84**, 2072 (2009).

[37a] B. Bornschein, C. Day, D. Demange, T. Pinna, “Tritium management and safety issues in ITER and DEMO breeding blankets”, *Fusion Engineering and Design* **88** (2013) 466–471

[38] E.Magnani et al., “DEMO relevance of the test blanket modules in ITER—Application to the European test blanket modules”, *Fus. Eng. Design* **85**, 1271 (2010).

[39] A.J.H. Donné et al., ‘Diagnostics for plasma control on DEMO: challenges of Implementation’ *Nucl. Fusion* **52** 074015 (2012).

[40] K.M Young et al., “An Assessment of the Penetrations in the First Wall Required for Plasma Measurements for Control of an Advanced Tokamak Plasma Demo”, *Fusion Sci. Technol.* **57** 298–304 (2010).

[41] A.T.Ramsey et al., “D-T radiation effects on TFTR diagnostics”, *Rev. Sci. Instrum.* **66** 871–876 (1995).

[42] D. Moreau, D. Mazon et al., ‘Plasma models for real-time control of advanced tokamak scenarios’, *Nucl. Fusion*, **51** 063009 (2011).

[43] D. Mazon et al., “Equinox: a real-time equilibrium code and its validation at JET”, *World Scientific Book Series on Nonlinear Science, Series B*, vol. 15, World Scientific, pp. 327–333 (2010)

[44] M.Greenwald et al., “A New Look at Density Limits”, *Nucl. Fusion* **28**, 2199 (1988).

[45] F.Troyon et al., “MHD-Limits to Plasma Confinement”, *Plasma Phys. Control. Fusion* **26**, 209 (1984).

- [46] A.Garofalo et al., “Sustained rotational stabilization of DIII-D plasmas above the no-wall beta limit”, *Phys. Plasmas* **9**, 1997 (2002).
- [47] E.J.Strait et al., “Wall stabilization of high beta tokamak discharges in DIII-D”, *Phys.Rev.Lett.*, **74**, 2483 (1995).
- [48] W.W.Heidbrink, “Basic physics of Alfvén instabilities driven by energetic particles in toroidally confined plasmas”, *Phys.Plasmas* **15**, 055501 (2008).
- [49] V.G.Kiptily et al., “First Gamma-Ray Measurements of Fusion Alpha Particles in JET Trace Tritium Experiments”, *Phys.Rev.Lett.* **93**, 115001 (2004).
- [50] V.G.Kiptily et al., “Gamma-ray imaging of D and ⁴He ions accelerated by ion-cyclotron-resonance heating in JET plasmas”, *Nucl. Fusion* **45**, L21-L25 (2005).
- [51] M.N.A Beurskens et al., “L–H Power Threshold, Pedestal Stability and Confinement in JET with a Metallic Wall”, *Proc. 24th IAEA Fusion Energy Conference, (8-13 October, San Diego, USA)*, paper EX/P7-20 (2012).
- [52] J.Schweinzer et al., “Overview of ASDEX Upgrade “Improved H–mode “ Scenario Development”, *Proc. 24th IAEA Fusion Energy Conference, (8-13 October, San Diego, USA)*, paper EX/P2-03 (2012).
- [53] V.Riccardo et al., “Disruption Studies in JET.” *Fusion Science and Technology* **53**, no.4, 1064 (2008).
- [54] M.Lehnen et al., “Disruption mitigation by massive gas injection in JET”, *Nucl Fusion*, **51**, 123010 (2011).
- [55] M.Lehnen et al., “Impact and mitigation of disruptions with the ITER-like wall in JET”, *Nucl. Fusion* **53**, 093007 (2013).
- [56] E.M.Hollmann et al., “Control and dissipation of runaway electron beams created during rapid shutdown experiments in DIII-D”, *Nucl. Fusion* **53**, 083004 (2013).
- [57] N.Commaux et al., “Demonstration of rapid shutdown using large shattered deuterium pellet injection in DIII-D”, *Nucl. Fusion* **50**, 112001 (2010).
- [58] N.Commaux et al., “Novel rapid shutdown strategies for runaway electron suppression in DIII-D”, *Nucl. Fusion* **51**, 103001 (2011).
- [59] G.M.Fishpool, “Loss of confinement due to reduction of the edge pedestal in JET”, *Nucl. Fusion* **38**, 1373 (1998).
- [60] N. Oyama et al., “Pedestal conditions for small ELM regimes in tokamaks”, *Plasma Phys. Contr. Fusion* **48**, A171 (2006).
- [61] P.Lang et al., “ELM pace making and mitigation by pellet injection in ASDEX Upgrade”, *Nucl. Fusion* **44**, 665 (2004).
- [62] A.W.Degeling et al, “Magnetic triggering of ELMs in TCV”, *Plasma Phys. Control. Fusion*, **45**, 1637 (2003).
- [63] T.E.Evans et al., “Suppression of large edge localized modes with edge resonant magnetic fields in high confinement DIII-D plasmas”, *Nucl. Fusion* **45**, 595 (2005).
- [64] H.Hackfort, K.Bösche, F.Waelbroeck, J.Winter, P.Wienhold, “Hydrogen Pumping and Compression by Superpermeation through Iron”, *J.Nucl. Mat.* **144**, 10 (1987).
- [65] Th. Giegerich et al., “Conceptuation of a continuously working vacuum pump train for fusion power plants”, *Fusion Eng. Design*, **88**, 206 (2013).
- [66] Chr. Day et al., “The Direct Internal Recycling concept to simplify the fuel cycle of a fusion power plant”, *Fusion Eng. Design*, **88**, 616 (2013).
- [67] Th. Giegerich et al., “The THESEUS facility – a test environment for the torus exhaust vacuum pumping system of a fusion power plant”, *Proc. 25th Symposium on Fusion Engineering (10-14 June 2013, San Francisco, USA)*, paper TO3-4 (2013).
- [68] Chr. Day et al., “Exhaust Pumping of DT Fusion Devices: Current State-of-the-art and a Potential Roadmap to a Power Plant”, *Proc. 25th Symposium on Fusion Engineering (10-14 June 2013, San Francisco, USA)*, paper TO3-2 (2013).

THE NUCLEAR ASPECTS OF A FUSION POWER PLANT: NEW CONSTRAINTS AND CHALLENGES

V. Massaut

SCK•CEN, Boeretang 200, 2400 Mol, Belgium, vmassaut@sckcen.be

Carolus Magnus Summer School – Bad-Honef – September 2013

Fusion would deliver a new source of energy from the mid of this century. But the fusion research has now to make an important step forward by switching from pure plasma physics, based on Hydrogen and Deuterium plasma, to burning plasmas, implying the use of radioactive fuel (the Tritium) and the production of intense neutron flux. These aspects bring with them the change of fusion devices from laboratory (or industrial) facilities to nuclear facilities, with all the necessary precautions which are involved. The nuclear aspects of fusion reactors and power plants have an impact on various domains of the facilities: the approach of safety, security and radioprotection, the resistance of materials to neutron bombardments, the activation of material and the needs of remote handling, the effects of radiations on instruments and functional components, and last but not least the impact on radioactive waste production and recycling. All these aspects will be handled shortly in this first approach of the "nuclearization" of fusion reactors and facilities.

I. INTRODUCTION

Fusion has been developed since several years in various countries in the world to be able to propose a new source of energy for mankind. Fusion being the process driving the sun and stars has demonstrated to be able to be a very important source of energy. But its control and confinement on Earth proved to be much more difficult than foreseen. The very high temperature or very high densities to be reached drove the focus of the research up to now on these aspects of high temperatures (for the magnetic confinement facilities: tokamaks and stellarators) or high densities (like in the inertial confinement fusion)¹, and not on the nuclear aspects of the machines. Nevertheless, now that we are approaching the construction of reactors allowing "burning plasma", i.e. facilities which will produce large amount of fusion power, the nuclear aspects of the installations are

¹ We will mostly base our analysis on magnetic confinement fusion, as this one is probably more advanced and closer to the production of energy, but the main data and information are valid also for inertial confinement, once D-T mixture will be used.

becoming more and more important and have to be taken into account in the design and operation of such facilities.

This lecture will focus mostly on the impacts of the nuclear character of the future machines and will thus consider that the reader has already a sufficient knowledge of fusion facilities, and in particular of tokamak type installations. One considers also that a sufficient basic knowledge of nuclear physics is present, although some of the main phenomena will be reminded or shortly introduced.

Finally, this lecture is only an introduction to a very broad domain, which is currently studied and developed by a lot of scientists among the World. For further information or deeper analysis of the different areas which will be only superficially approached, the reader is sent to the literature on the different areas. The nuclear aspects of a fusion power plant are surely important features which need to be taken into account when one intends to design and build such a future source of energy.

II. THE REASONS OF THE NUCLEAR APPROACH

Fusion reaction is a nuclear process, involving the nucleus of the atoms; this is already a first reason to consider fusion as a nuclear process (the actual name of fusion being in fact "thermonuclear fusion"). Nevertheless, if the process did not involve radioactive materials, several aspects of the nuclearization would have been strongly simplified. Unfortunately, as in most nuclear processes and reactions, the fusion reaction implies the presence of radioactive isotopes and materials.

In fusion reactors, the presence of radioactive materials can be seen as having three main origins:

- the use of tritium as fuel, tritium being a radioactive species, with a rather short half-life;
- the activation of the materials facing the plasma or being exposed to neutrons coming from the plasma and the fusion reactions;
- the transport of radioactive contamination through the cooling fluids and in the air of the auxiliary buildings and areas.

The third origin is in fact more a consequence of the two other ones, but it brings the needs of precaution sometimes far away from the source of the activity.

Let us try to have some facts and figures about the different nuclear aspects mentioned above and let us start with the tritium.

Tritium is an isotope of Hydrogen; but unlike the Deuterium (one proton, one neutron) which is a stable species to be found in seawater, tritium (1 proton, 2 neutrons) is radioactive, i.e. it disintegrates naturally by emitting a beta radiation (an electron) having a rather low energy (5.7 keV), to become an ^3He nucleus (2 protons and 1 neutron). The half-life of tritium (i.e. the time after which half of the original atoms have disintegrated) is about 12.32 years.

It is good to remember that after 5 half-lives the activity has decreased by a factor 32 (2^5), while after 10 half-lives the activity has decreased by a factor close to one thousand (2^{10}), and 20 half-lives divides the activity by a factor close to one million (2^{20}).

The mass of tritium is about three times the one of Hydrogen and 1.5 the one of Deuterium. This can play a certain role in the particles kinetics within the plasma. Finally the fact that tritium decays in Helium has also two important impacts: it creates He in the material in which it can diffuse, and it creates another source of He within the plasma, after the one of the fusion reaction itself:



Another important aspect is the high diffusivity of tritium, which follows here the properties of its main element, hydrogen. Thus such an isotope can diffuse through solid materials (like steel or other metals) easily if the temperature is high.

Finally, for the aspect of safety and health effects, it is important to know the ratio between the tritium activity and the induced dose in the human body. This figure is very small and in the order² of 10^{-11} Bq/Sv:

Dose factor (radiotoxicity) of [1]:

Tritium (gaseous)	= $1,8 \cdot 10^{-15}$ Sv/Bq
Tritiated water (aqueous)	= $1,8 \cdot 10^{-11}$ Sv/Bq
Organically bound Tritium (OBT)	= $4,1 \cdot 10^{-11}$ Sv/Bq

This very small figure shows the low health impact of tritium on the body. Nevertheless, as for any other radioactive isotope, the ALARA principle must apply and the irradiation (mostly internal irradiation, by inhalation or ingestion) should be kept as small as reasonably possible. To have an idea of the activity content of tritium mass, one can also remember that 1g of T_2 gas represents about 10 000 Ci or $3,7 \cdot 10^{14}$ Bq

² For those not very familiar with the Sievert, let us remind that the natural background of radiation fluctuates between 0.5 and tens mSv per year (thus around $1 \mu\text{Sv/h}$) and the max. occupational planned dose for a nuclear worker is set at 20 mSv/y [2].

The table 1 below gives a summary of the principal properties of tritium.

Property	Value	Unit
Half – life	12.32	year
Beta energy	5.7	keV
Atomic mass	3,0160492	a.m.u.
Tritiated water dose factor	$1,8 \cdot 10^{-11}$	Sv/Bq

Table 1: main properties of Tritium

Let us now look at the activation aspect of materials facing the plasma or able to get some neutrons coming from the reaction. An important aspect is the neutron energy and the neutron flux (or better the so-called fluence, i.e. the integrated neutron flux over the time the material is exposed to the neutrons) which hits the various components of a fusion reactor. The most exposed components are indeed the plasma facing components or PFC. But as one can see on fig.1 (giving a developed view of the facing components of the research tokamak JET), the PFC can be very diverse, and one should not only focus on the blanket and first wall; heating antenna shields and limiters (if any), diagnostic windows or first mirrors, viewing systems, etc. are all facing the plasma, in a neutronic sense. If for plasma physics, a small geometrical recede changes strongly the plasma wall interaction, for neutrons, not influenced by the magnetic fields, this does not play any role.

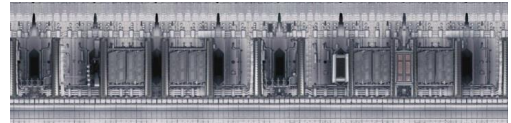


Figure 1: Outer wall of JET (developped)

The neutrons have several types of interactions with matter, which gives different macroscopic effects on components and systems. Neutrons can have elastic and inelastic interactions, knocking atoms from their original positions (often one single neutron induces a cluster of knocked atoms, and loses his energy by several elastic or inelastic interactions). Neutrons can also be absorbed by some atoms inducing transmutations of the original atoms. When the neutron is absorbed, it normally disappears, or can lead to an instable atom re-emitting one or several other neutrons. The transmuted nuclei are often radio-active, and their radioactivity can lead to the emission of a proton (leading to Hydrogen formation in the material) or to the emission of an alpha particle, leading to the creation of Helium inside the material. Finally the created radioactive species are often emitting gamma (or beta) rays leading to ionization and thus

important influence on chemical bonds. The neutrons, by knocking atoms, by absorption or by the induced radioactivity are also producing heat in the material, (called “nuclear heating”) which could be very significant for materials directly exposed to the neutron source. This is also the main route of transporting the created energy to the cooling fluid and subsequently to the turbine. Further analysis on this aspect will be done in the chapter IV.

Let us just still make a short comparison with fission neutrons, for having some ideas of the orders of magnitude and to feel a bit the importance of this aspect. In fission, each reaction creates about 200 MeV of energy, from which 2.5 neutrons are created in average, taking with them energy of around 2 MeV. This means that the neutrons take away about 2% of the total energy created, the remaining 98% being left in the fuel material by the recoils of the fissioned atoms. In fusion the situation is rather different! Each reaction produces around 17 MeV, from which the created neutron takes away around 14 MeV, or 82% of the total energy (the remaining 18% being transported by the alpha particle which stays in and gives its energy to the plasma). Comparing both situations, for the same overall energy production of the plant, the energy deposited by the neutrons is 33 times higher in fusion! The energy per neutron being about 7 times higher for fusion neutrons, the total number of neutrons for the same power is thus almost 5 times larger than in fission... Thus the total surface of the first wall of a fusion reactor gets 5 times more neutrons with an energy 7 times higher³. This gives only an idea of the issue at stake.

Finally, we should not forget the transport of activated materials through the cooling fluid and even by the atmosphere during maintenance and opening of the vacuum vessel. This transport, which is common and rather well known in fission reactors, depends a lot on the fluid physico-chemical conditions (temperature, pressure, purity, pH, oxygen content etc...) and is probably the main cause of activity dispersion in the plant. Moreover the transport and deposition of radioactive species induces exposition of workers to radiations, and is thus an important factor to consider. This topic will be analysed in chapter IV below.

III. THE NUCLEAR SAFETY AND CONFINEMENT, THE SECURITY AND THE RADIOPROTECTION

One of the first impacts of the presence of radioactive materials and species in a fusion power plant is surely the safety aspect and the radioprotection. Nuclear safety is of prime importance in a fusion power plant

³ To be more scientifically correct, we should speak about the neutron flux, for which the ratio is more complicated. This comparison is only given here to have some taste of the difference.

although the absence of fission fuel and its radioactive content reduces strongly the risks and source term in case of an accident compared to fission plant.

Nevertheless, the confinement of the radioactive species, present in a fusion reactor, in all cases of operation (up to the less credible accident) has to be assured in order to avoid any spread of radioactive contamination in the environment and to avoid absolutely any need of evacuation of the population in the surrounding of the plant in any case. This is probably one of the main objectives of the safety approach of a fusion power plant design. The aspects of radioprotection of the workers and operators will be analysed further.

The basis of the safety approach for a fusion power plant can be taken from the ITER Generic Site Safety Report [3]. Let us thus first define the safety objectives:

“ITER’s safety objectives address the potential hazards in ITER from normal operation, accidents and waste:

- (1) ensure in normal operation that exposure to hazards within the premises is controlled, kept below prescribed limits, and minimised;
- (2) ensure in normal operation that exposure to hazards due to any discharge of hazardous material from the premises is controlled, kept below prescribed limits, and minimised;
- (3) prevent accidents with high confidence;
- (4) ensure that the consequences, if any, of more frequent events are minor and that the likelihood of accidents with higher consequences is low;
- (5) demonstrate that the consequences from internal accidents are bounded as a result of the favourable safety characteristics of fusion together with appropriate safety approaches so that there may be, according to IAEA guidelines [IAEA96], technical justification for not needing evacuation of the public (external hazards are site dependent, but are considered for a generic site);
- (6) reduce radioactive waste hazards and volumes.”

One can also consider the safety principles used for the ITER GSSR [3], as basic principles for a fusion power plant (although the experimental character of ITER has also some specific aspects, which are not taken into account here):

Defence-in-Depth

All activities are subject to overlapping levels of safety provisions so that a failure at one level would be compensated by other provisions. Priority shall be given to preventing accidents. Protection measures shall be implemented in sub-systems as needed to prevent damage to confinement barriers. In addition, measures to mitigate the consequences of postulated accidents shall be provided, including successive or nested barriers for confinement of hazardous materials.

Passive Safety

Passive safety shall be given special attention. It is based on natural laws, properties of materials, and internally stored energy. Passive features, in particular minimisation of hazardous inventories, help assure ultimate safety margins. (...)"

Potential safety concerns that must be considered during the design process to minimize challenges to the public safety function of confinement of radioactive and/or hazardous materials include, but should not be limited to the following [4]:

- a. ensuring afterheat removal when required;
- b. providing rapid controlled reduction in plasma energy when required;
- c. controlling coolant energy (e.g., pressurized water, cryogen);
- d. controlling chemical energy sources;
- e. controlling magnetic energy (e.g., toroidal and poloidal field stored energy);
- f. limiting airborne and liquid releases to the environment.

Tritium

From the DOE Guidance [5], Tritium system design should include features which minimize the environmental release of tritium and exposure of personnel, minimize quantities of tritium available for release during accidents or off-normal events, and minimize the unintended conversion of elemental tritium to an oxide form. Consistent with facility safety analysis, design features should include:

1. Segmentation of the tritium inventory such that release of all tritium from the single largest segmented volume has acceptable consequences;
2. Confinement barriers to reduce tritium environmental release to an acceptable level;
3. Materials and equipment which are tritium compatible and minimize exposure of tritium to oxygen; and
4. Cleanup systems to recover gaseous tritium released within any confinement barrier or to process streams exhausting to atmosphere.

Aspects of Security

Beyond the safety aspects of a fusion plant, the security (i.e. the physical protection against unfriendly acts or terrorism) of the installation is also an aspect to be developed. The main item to defend is probably the tritium inventory (see below), but the diversion of activated or contaminated materials should also be taken into account as well as sabotage actions or even external attacks.

Fortunately, the "source term" in a fusion plant is limited to its activated (and contaminated) components and to the tritium inventory. As the

activated species are mostly bound within solid components (first wall and blanket module; divertor, etc), except for the produced dust and for the components coolant, the main source of easily escaping radio-nuclide is the tritium inventory. That is why a particular attention is placed towards the monitoring and control of the tritium inventory, and to the separation of this inventory in small parts not possible to mobilize together.

The purposes of requirements placed on tritium control, accountability, and physical protection at fusion facilities are to [4]:

- a. meet legal requirements for environmental releases, waste disposal, and transportation of tritium;
- b. prevent the diversion of the material for unauthorized use;
- c. gain knowledge of the process efficiency, that is, how much tritium is produced and used in processes under investigation;
- d. meet the requirements of the safety authorities;
- e. assure operational safety of the facilities by providing knowledge of the location and form of tritium;
- f. prevent unwanted buildup of tritium within a facility; and
- g. protect and control tritium commensurate with its monetary value.

Tritium is the predominant nuclear material used at fusion facilities. It is of interest because of safety concerns, its monetary value, and possible unauthorized diversion for other applications.

Other nuclear material that must be controlled and accounted for at fusion facilities includes depleted uranium (U-238) and deuterium. Depleted uranium is used for storage of tritium, fission chambers, and various radioactive check- and calibration-sources. The control and accountability of these materials is relatively straightforward and does not present significant problems for operating facilities. The scope and extent of the accountability program for these materials should be based on the monetary value of the material and should include inventories and some measurements.

ALARA and radioprotection optimization

The ALARA approach ("As Low As Reasonably Achievable") is not only an acronym but has led to a complete approach of the radioprotection optimization. Indeed the principle which is behind this acronym implies several aspects which should be taken into account. The term "Reasonably" for instance is probably one of the most important; it translates into 'reasonably' regarding the economic and social impact and constraints. Therefore this principle can almost be opposed to the "As Low As Technically Possible", which should also mean 'at every cost!' And this can have ethical implications. Indeed, one

can protect anybody from even not harmful risks with high economic impact. But as the overall available money is always limited, for any type of project or practice, this means that this money (used for nothing) is no more available for other means (like e.g. modernizing a hospital or promoting R&D against cancer etc...).

On the other hand the radioprotection optimization approach under the ALARA principle should also take into account the whole lifecycle of the involved component or activity. As example, let us take the development of low activation materials (for facilitating the remote handling of the maintenance); this is good for the maintenance activity, but in the overall study one should also take into account the effects on the waste management and even the final effect after disposal... Moreover the ALARA approach can be done at the design phase of a facility as it allows to make large gains with limited (but smart) investments.

IV. THE NUCLEAR “CLEANLINESS” AND TRANSPORT OF RADIOACTIVITY

Materials exposed to neutron flux have to present a cleanliness above normal industrial standard, as the production of activated products often depends on trace impurities (in materials) or on traces of impurities on materials. In the case of fusion reactors, the components and materials situated inside the vacuum vessel and exposed to the plasma and to the low vacuum needed for operating the system, already imply a sufficient cleanliness of the exposed materials. Nevertheless, these components are not the only ones exposed to the neutron flux, and probably most of the difficulties will happen in the cooling circuits and any other loops allowing some fluid to circulate for a while in front of the neutron source. For instance, in fission power plant, most of the occupational dose is due to the contamination of the primary loop and the transport of radioactive species from the core of the reactor to the surface of the whole cooling loops. This will surely also happen in fusion power plant, where the exposed surface of the cooling fluid is rather important (although the mass of the cooling fluid is probably lower than in an LWR where the complete core and auxiliary are immersed in the primary water).

A. Contamination and Activated Corrosion Products (ACP)

One nuclear aspect, which forms an important factor for the exposure of workers and operators, is the radioactive contamination of cooling circuits. Moreover it can have also an impact on the waste management from fusion reactor decommissioning and large maintenance works. Therefore, it appears to be important to study this topic and take profit of the return of experience from fission.

Areas with large deposition surfaces and strong temperature gradients, like the heat exchangers and steam generators, constitute often large sources of radiations influencing the maintenance of the facilities. The main radio-isotope playing a role in fission plants in this domain is the Cobalt-60. With a half-life of 5.24 years and a double gamma-rays above 1 MeV, this radio-isotope represents, in fission reactors, one of the most important source of radiations originating from activation. In fusion reactors, where most of the water cooling loops are mostly foreseen in stainless steel, the presence of Cobalt in the water chemistry is quasi unavoidable. But one big difference is the neutron energy, as the production of Co-60 from the stable Co-59 has its largest cross-section for thermal neutrons. But other threshold reactions can happen at high neutron energy (above 1 MeV) and the neutron energy spectrum can be degraded when reaching the cooling fluids, which can even further slowdown the neutron flux.

Some of the potential radio-isotopes, presenting a role in radioactive contamination of the cooling circuits are given below.

Isotope	Type of radiation	Half-Life	Origin	Implication on	Specific Problem
Co-60	Gamma (strong)	5.25 y	Activation (neutron in steel)	Operations	Shielding
C-14	Beta	5730 y	Activation (neutron in graphite)	Contaminat ⁿ , Dispersion	Carbon chemistry
Nb-94	Beta Gamma	20 000y	Activation in steel	Waste	Long Half-life (present in steel)
Ni-63	Beta	100 y	Activation (in steel)	Waste	Stainless steel constituent
Eu-152	Beta-gamma	13.4 y	Activation (in concrete)	Contaminat ⁿ ,	Present in concrete
Eu-154		8.2 y		Waste	

Table 2: some of the important radionuclides for radioprotection (ORE) and waste management aspects.

The actual rate of erosion/dissolution/deposition depends on a lot of other parameters, like the water chemistry, the local water velocity, the temperature differences, the solubility of various elements etc... which makes the modeling of this phenomenon rather complex. (see fig.2)

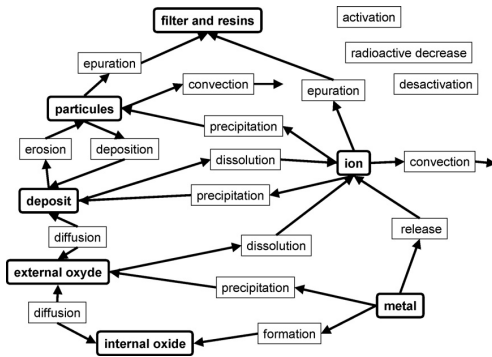


Figure 2: the various interactions and transport routes of radionuclides in cooling medias [6]

Nevertheless, based on fission experience, several aspects should be taken into account:

- envisage the possibility of decontaminating the loop during shutdown and maintenance periods;
- foresee sufficient shielding (or potential shielding space) around large exposed surface components (like heat exchangers);
- avoid spaces with stagnant fluid or with abrupt flow changes;
- keep the water chemistry under good control, and filter + purify water sufficiently (often, the filtration/purification loop is made on a by-pass of the main flow. Consider sufficient by-pass flow rate to avoid accumulation of ACP).

B. Airborne contamination and radioactive species transport during maintenance.

During shut down and maintenance outages of fusion plants, the vacuum vessel will be put at atmospheric pressure and can even be opened towards the external world for introducing remote handling inspection and repair machines. This opening brings the possibility of dispersing the existing contamination from the vessel internals towards the outside world. The main contamination sources being the tritium trapped in the metal structures and the dust deposited everywhere in the vacuum vessel. This dust is activated and can also contain some trapped tritium.

To mitigate as much as possible this source of contamination several processes can be put in place. The first one is indeed to collect the contaminants at the source; i.e. detritiating as much as possible the vacuum vessel and its internals, and collecting or removing the dust as soon as the vessel is open. Nevertheless, none of these actions can insure 100% of removal. Therefore, when opening the vacuum vessel (including ports and neutral beam injectors) one should insure a pressure cascade between the outside atmospheric pressure and the

inside pressure of the vessel, using adapted ventilation system. Several levels of the cascade should avoid or reduce the risk of contamination spread.

These effects have an impact on the occupational radiation exposure of the operators, but also on the consequences of an accident, on the waste management and on the needed handling systems for components replacement and repairs.

V. FUNDAMENTALS OF THE NEUTRONS INTERACTION WITH MATTER

Neutrons are, as indicated by their names, neutral particles, constitutive of the atom nucleus. Neutrons are ejected with high energy from the plasma (about 14 MeV or $1.93 \cdot 10^8$ m/s). But neutrons have various interactions with matter. Let us summarize the most important ones (see also fig. 3 below):

- it goes through the material without interactions; this can mostly happen as the neutrons are not charged, and if they have a high energy (or speed) most of them would not "see" the atoms of the matter;
- it can undergo elastic scattering against (mostly) light atoms, i.e. like bouncing of billiard balls, and sharing its energy between the neutron and the knocked atoms. This is for instance what is used for the slowing down of neutrons in thermal fission reactors;
- it can undergo what is called inelastic scattering, where the neutron is absorbed by the target atom, which re-emits another neutron with another energy;
- it can be absorbed by an atomic nucleus, leading to excitation and transmutation of the atom, and/or to several types of reactions implying the emission of other particles (n,p ; n,α ; n,γ ; etc...); the n,γ reaction is also called "radiative capture";
- or it can induce fission of heavy nuclei (mostly of the actinides of the periodic table).

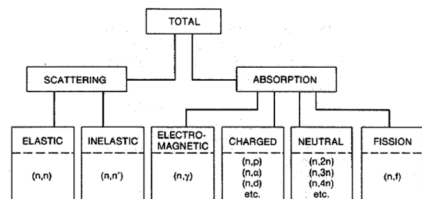


Figure 3: Various categories of neutron interactions. The letters separated by commas in the parentheses show the incoming and outgoing particles. [7]

and model. Most effects models are currently based on empirical equations tuned to fit the experimental results obtained in various types of irradiations conditions. The most known materials for high energy (> 1 MeV) neutrons effects, are austenitic stainless steels (type AISI 304, 316 and specific grades) which were developed for the fast breeder reactors and are also used as internals in the Light Water Reactors operated today.

Moreover, the effects of neutron irradiation are inherently multiscale, in space, time and number of atoms concerned. It varies indeed from instantaneous effects (ps) to long terms effects (Gs), from submicroscopic effects (Å, nm) to large macroscopic effects (m) and concerns small clusters from 10^2 to 10^{31} atoms ... [8]

In the figure below are summarized some typical effects of irradiation on stainless steels.

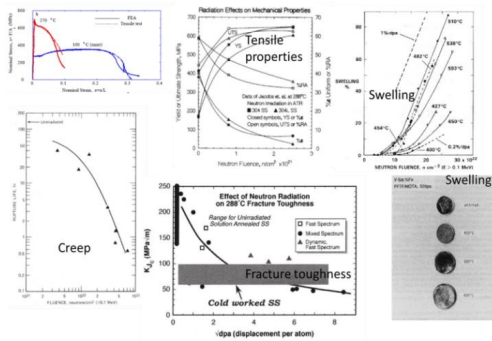


Figure 6: Typical effects of neutrons on austenitic stainless steels (example of effects on tensile properties, creep resistance, fracture toughness and swelling) [8]

The effects of the microstructure of the metals are also important factors to take into account. Metallic materials are often constituted of "grains" which consist of single crystals (bcc, fcc, hcp, ...). The grains present different orientations and are separated by grain boundaries. Most of the metals used in structural materials (and in steels) are alloys which are composed of several alloying elements, and some impurities. For the neutron effects, even the impurities can have an important impact on the microstructure. Finally, for modeling and understanding of the phenomena happening in the microstructure of the materials, one has to take into accounts the defect structures: dislocations, gas bubbles, cavities (voids), vacant lattice sites (vacancies), interstitials.

Point defects (vacancies and interstitials) are created by the radiations. They undergo reactions and aggregations (clustering), as they can move and diffuse in materials. The modeling of these effects and of their

diffusion and effects on the macroscopic properties of the materials is currently a subject of a lot of research (see e.g. [9]).

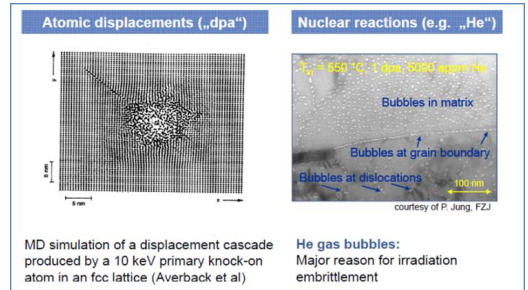


Figure 7: view of the effects of "damages"(dpa) and gas formation in metallic materials (A. Möslang, 2009)

Finally, the choice of the alloying elements (and of the following impurities) is very important also for the activation of the components, with implications on remote handling constraints and waste management. Fusion reactors being often much larger (in volume) than fission reactors, and the replacement of the Plasma Facing Components (PFC) being foreseen at rather high frequency (e.g. replacement every 3 or 5 years of the divertors) this aspect of low activation or reduced activation material is very important for the overall environmental impact of fusion. Therefore the selection of the alloys and alloying elements is also constraint by this aspect [10] (e.g. one should avoid Re as alloying element as it gives rise to long lived radionuclides). See also the chapter IX below.

The current R&D on structural material in magnetic fusion mostly focuses on the ferritic/martensitic steel, more particularly to the reduced activation alloy called "Eurofer".

A second aspect, which should also be looked at, is the effect of neutron irradiation on plasma facing components. Here the material challenge is still more severe: the material must be compatible with the high thermal heat flux (up to 10 MW/m² on the divertor), the sputtering and blistering due to particles impacts, the compatibility with the plasma (low Z material), together with the radiation damages and transformations. Moreover, the PFC must present a low tritium trapping behavior to avoid tritium inventory buildup in the plasma facing materials and in flakes and dust.

All these qualities together do not lead to a lot of remaining materials. For plasma compatibility (low Z) and high heat flux (and high temperature) resistance, the Carbon composites seems to give the most interesting answers, but they show a tendency to have a high tritium retention. For plasma compatibility and sputtering, this is

the case for Beryllium; but this element has bad sputtering resistance qualities and is not very well fitted for high heat flux; it is moreover toxic and thus difficult to handle. Vanadium and Vanadium alloys seems to present some potentiality but their radiation induced damages are precluding their use. Finally, today the R&D focuses mostly on Tungsten and Tungsten alloys for its high heat flux resistance, low sputtering behavior and relatively good behavior towards the neutron irradiation which compensates for its high Z property. Silicon Carbide fibers in Silicon Carbide matrix (SiC/SiCf) seems also promising but is far to be developed sufficiently.

An example is the sputtering rate: for low Z material like Carbon, the erosion is of the order of 3mm/burn-year while for Tungsten it is around 0.1 mm/burn-year [Wirth].

VII. THE RADIATION RESISTANCE OF DIAGNOSTICS AND FUNCTIONAL COMPONENTS

The effects of neutrons on organic or amorphous materials is also important for diagnostics, instrumentation and remote handling components. Changes in the insulation resistance of insulators, darkening of glass and optical components, changes in the lubricating properties of oils or embrittlement of the components can play an important role in the design and selection of materials for the measuring instruments or functional materials of fusion facilities.

Functional components are concerned by the neutron irradiation and the impact on their operation and "function". We will focus here mostly on diagnostics and instrumentation components and equipment. Up to now this equipment, to measure the various plasma parameters, was designed to resist to the high vacuum and sometimes high temperature environment, plus the presence of strong electro-magnetic fields.

The nuclear environment adds another difficulty to these components. First of all, the presence of neutrons and of strong gamma field (due to the radioactive decay of neutron activated metallic component in the vacuum vessel) precludes the use of most organic materials as insulator. In high radiation environment, only mineral insulation (like MgO or Al₂O₃) ceramic insulation materials can be used.

The use of semi-conductors must also be done with care, and high electronic circuit integration in high level radiation field is not advisable.

The use of optical components (windows, fiber optics, even mirrors) can also be influenced by the presence of radiations and the selection of the specific materials and assembly process must be done with great care and after intensive testing in similar conditions.

Several studies have been carried out during the last 10 to 20 years to develop and test radiation hardened

components and systems. Nevertheless, sophisticated systems and highly integrated circuits tends to show strong sensitivity to radiations.

One can give here some generic and simplified trends shown by various components under radiation (but for more details, please refer to the literature):

- In high radiation fields, use mostly mineral; insulators instead of organic ones;
- Semi-conductors can be sensitive to radiations and circuits have to be designed fault-tolerant if used in semi-hard radiation fields (never directly in the strong neutronic field);
- Optical instruments (and their bonding system) tends to be radiation sensitive if not selected carefully; the presence of impurities in the glass can have dramatic impact on the properties;
- Fiber optics show in general the same trend as optical glasses, but some typical fiber types can resist to some radiation levels allowing to use them in specific locations.

There is a range of effects on insulating and functional materials that one can summarize in the following list :

- Radiation-induced conductivity (RIC);
- Radiation induced electrical degradation (RIED);
- Radiation-induced electromotive force (RIEMF);
- Radiation-induced thermo-electric sensitivity (RITES);
- Radiation induced absorption (RIA) for optical components;
- Radioluminescence (RL or RIE) e.g. in fiber optics
- Nuclear heating;
- Change in other properties such as activation, transmutation and swelling.

For further details on the impact on diagnostics and remote handling, see also the lecture of A. Donné.

VIII. THE ACTIVATION OF MATERIALS AND THE REMOTE HANDLING

The activation of materials has been described above. The very high activation level (giving up to tens of kGy/h radiation field) of the plasma facing components induces the impossibility to have human intervention in the plasma chamber after the D-T reactions. Moreover, the rather long distance of actions of neutrons and the transport of activated product also preclude human intervention in the vicinity of the vacuum vessel and of the neutral beam lines.

The principal elements that are leading to activation in the metallic parts (first wall, shielding, divertor, blanket,...) surrounding the plasma are the nickel, chromium, iron, cobalt and copper leading to the production of Co-60, Mn-54, Cr-51, Cu-64... Other

isotopes are also produced, depending on the alloying elements used and the impurities present in the metals. The activation data is a rather complex topic as it depends on the local neutron flux, the operation and exposure data, the presence of impurities in the metals etc. The activation leads e.g. to high requirements in the purity of the metals (removal of several important impurities [10]) but also on the potential alloying elements. As example, there is currently an optimization study for the tungsten alloy to be used for power plant divertors. Beyond the mechanical and thermal behavior in irradiated situation, the used alloying elements should not lead to high activation for handling purposes, but also for waste management and environmental impact aspects (see chapter IX below).

Therefore, remote handling has to be used for all inspection, maintenance and repair works to be carried out in these areas, as well as for decommissioning. Remote handling is thus a real challenge for these activities, as it has to work in a rather harsh environment (high radiations, temperature, vacuum for some case). Moreover, the geometry and the available space for maintenance and repair are also rather complex and limited leading to challenging operations and complicated movements.

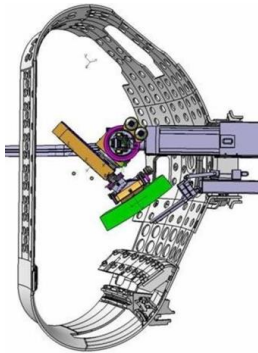


Figure 8: remote handling of ITER shielding block (ITER.org)

Several R&D works are currently on going for developing the needed equipment and testing the components in the foreseen environment. A first trial was already made at JET, for replacing remotely the complete first wall.

Several aspects need to be taken into account for the design of remote handling systems:

- the accessibility of the component to replace (some "tiles" or first wall components in the torus are not easily accessible);
- the weight of the heaviest component or tool to be handled by the RH system (some pieces can be

very heavy: the divertor cassettes in ITER for instance are already weighing more than 10 tons);

- the limited access through narrow ports;
- the potential contamination by dust (from beryllium, tungsten or carbon, with tritium content and activated products);
- the high to very high gamma radiation field (more than 30 kGy/h);
- the unavailability of direct viewing conditions (only televisual connection);
- the ultra-high vacuum and nuclear cleanliness requirements.

The main impacts of the nuclear aspects of a fusion plant concerns the resistance to radiations of all components (actuators, motors, sensors, ...) and the necessary cleanliness and easiness to wash the potential contamination of the manipulators and vehicles.

The resistance to radiations can lead to special developments of the whole systems (like e.g. the use of water instead of oil for hydraulic high payload manipulators) [11] , to the use of radiation resistant sensors and vision systems (this implying the same approach as for the diagnostics systems - see chapter VII above) and the development of actuators and motors with limited (or even no) organic content and specific insulation and lubricant materials.

The development of such remote handling system, with strong request and resistance to severe and harsh environment is also a technical challenge for today's technology.

IX. THE RADIOACTIVE WASTE AND RECYCLING

Even if fusion would not produce long lived radioactive waste, regarding the high volume and mass surrounding the plasma chamber, fusion will probably produce, by far, much more quantity of short lived waste than any other facilities. But the quantity and mostly the "quality" of the generated radioactive waste (i.e. its radioactive lifetime and its possibility to be recycled) depends strongly on the individual constituents of the materials facing the plasma (incl. impurities).

Therefore, it is of very high importance for the design and selection of the materials facing the plasma but also likely to be bombarded by neutrons, to take these aspects of waste management and recycling into consideration.

Several studies have already been carried out in this domain (see e.g. [12, 13, 14]) but a lot remains to be done to develop the necessary process and infrastructure allowing to dismantle, condition and recycle the materials generated by the regular maintenance and replacement of a fusion plant.

To give some idea of the magnitude of the problem, the structural and functional metallic material situated around the plasma in one of the European fusion power plant conceptual design (PPCS-AB) had a mass of about 97,000 tons! This represents 13 times the mass of the Eiffel tower... And the mass of the replaceable components in ITER (divertors and first wall) represents a (potentially activated) mass of about 800 tons (above 2000 with the shielding).

Once again the first mitigation technique of this issue is to treat the problem at the source; i.e. developing materials without isotopes leading to long-lived radionuclides [waste1] and developing materials with a strong control on the impurities level (often the impurities, even at trace levels, can have an impact on the long lived waste stream). Moreover, the design of the components has to be such that their dismantling and the separation of the different constituents (made of different materials) must be easy to carry out remotely.

On the other side, methods and process for recycling/reuse of material have to be developed, to avoid generating too much waste for disposal. Recycling and reuse means to handle, work on and refabricate (slightly) radioactive materials into new elements for re-use in fusion reactors or recycle within the nuclear industry. Clearance and free release is another way of disposing materials, if the remaining radioactivity (after decay storage) is low enough to have negligible effects on the populations and environment.

The question is whether it is feasible to fabricate the complex units of a fusion plant under remote control conditions. Indeed, for the higher activity pieces it will not be possible to reuse highly activated materials for shielding or other "simple" purposes, unless radioisotopes are removed during reprocessing. Reuse of these materials in a fusion power plant or an advanced fission next-generation reactor seems the only option. Therefore, sophisticated fabrication and testing processes have to be looked at in detail and limits must be defined if applicable. The use of refractory materials (such as Nb, Mo, Ta, W, Re) may need innovative approach.

This would lead to a material cycle approach, as follows, if all the steps can be developed on time and with the available technology:

FUSION POWER MATERIAL CYCLE

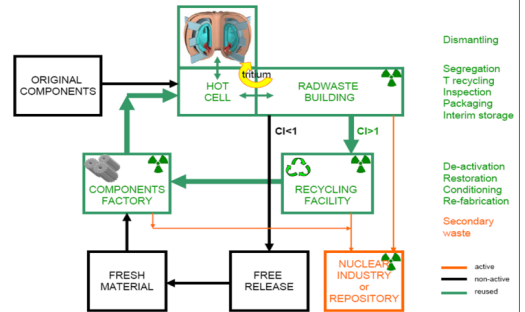


Figure 9: Fusion power potential material cycle [11]

To summarize this topic, there are still some open questions, which have to be solved or answered in order to reduce the generated waste amount and tend towards a low radioactive waste production (and thus low environmental impact) from fusion energy production:

- Definition of undesirable alloying elements;
- Assessment of radioactivity build-up by repeated reuse of structural materials;
- Dismantling and separation of different materials from complex components: different steps to follow and impact on design requirements;
- Developing processes for the production of material suitable for recycling;
- Fabrication of complex components using recycled materials by remote handling and related design approach;
- Acceptable limits for processing of radioactive materials in foundries;
- Study of (Li-Pb) breeder refurbishment by chemical process for reuse.

The back end of material re-use is thus an important factor in preparing the future of fusion power.

X. CONCLUSIONS

The nuclear aspects of a fusion power plant are rather new to tackle. Up to now, only very few machines (JET, TFTR) in the world have worked in D-T plasmas, with very limited amount of tritium (the total amount in JET was 20 g, to be compared with the 3 kg foreseen in ITER) and a very low neutron flux on the walls and in-vessel components compared to the ones expected in ITER and future fusion power plants.

The nuclear aspects of a plant are various and must be taken into account in parallel with other issues; moreover, the experience gained in fission power plant can be very valuable for drawing lessons and taking the best solutions for different aspects.

Beside the safety aspects (including the radioprotection of the workers and population), one can understand that the aspects of materials properties and the impact of neutrons and the nuclear environment on these materials are of prime importance.

ACKNOWLEDGMENTS

The author wants to thank the various colleagues who helped him to summarize the various aspects of this large domain, and in particular Inge Uytendhouvern, Dmitry Terentyev, Mageshwaran Ramesh, Nicolas Castin, Chris Dylst from SCK•CEN, Luigi Di Pace from ENEA, Patrick Lorenzetto from F4E and Sergio Ciattaglia from ITER-IO. This work, partly supported by the European Communities under the contract of Association between EURATOM and the Belgian State, was carried out within the framework of the European Fusion Programme with financial support from SCK•CEN. The views and opinions expressed herein do not necessarily reflect those of the European Commission.

REFERENCES

1. *Colloque A.N.C.L.I.* ; "Les risques sanitaires de l'exposition au tritium: conclusions du scientifique des experts 'article 31' Euratom [archive]" (4-5/11/2008), Orsay, France.
2. A D Wrixon, REVIEW; New ICRP recommendations, *J. Radiol. Prot.* **28** (2008) 161–168.
3. ITER – Generic Site Safety Report, *G 84 RI 1 R02*, (July 2004).
4. DOE handbook supplementary guidance and design experience for the fusion safety standards doe-std-6002-96 and doe-std-6003-96, *DOE-HDBK-6004-99*, (Jan. 1999).
5. DOE STANDARD; Safety of magnetic fusion facilities: guidance, *DOE-STD-6003-96*, (May 1996).
6. A. Molander, "Corrosion and Water Chemistry Aspects Concerning the Tokamak Cooling Water Systems of ITER", EFDATW5-TVM-LIP, *STUDSVIK/N-06/186*, (2006).
7. P. Rinard, US-NRC, "Passive Non Destructive Assay of nuclear materials", Doug Reilly, Norbert Ensslin and Hastings Smith Jr. editors; *NUREG/CR 5550; LA-UR-90-732*, Chapter 12, (March 1991).
8. B. Wirth, D. Olander (UCB) and R. Odette (UCSB), "An Introduction to the Effect of (Neutron) Irradiation on the Microstructure and Properties of Structural Alloys", *NE 220, Nuclear Engineering Department, University of California, Berkeley Presentation*, (Spring 2008).
9. S.L. Dudarev et al., "The EU programme for modelling radiation effects in fusion reactor materials: An overview of recent advances and future goals.", *Journal of Nuclear Materials* 386–388 (2009) 1–7.
10. M. Desecures, L. El-Guebaly et al., "Study of radioactive inventory generated from W-based components in ITER and PPCS fusion designs", *Fusion Engineering and Design*, in press, (2013).
11. G. Dubus "Development of a water hydraulics remote handling system for ITER maintenance", *Presentation at IARP/EURON RISE'08* (Jan. 2008).
12. V. Massaut et al., "State of the art of fusion material recycling and remaining issues", *Fusion Engineering and Design*, **82** (2007) 2844–2849.
13. L. El-Guebaly, V. Massaut, K. Tobita, L. Cadwallader, "Goals, challenges, and successes of managing fusion activated materials", *Fusion Engineering and Design*, **83** (2008) 928–935.
14. L. Di Pace et al., "Radioactive Waste Management of Fusion Power Plants", in Chapter 14, *Radioactive Waste*, Ed. by Rehab Abdel Rahman, ISBN 978-953-51-0551-0, InTech Publisher, (April 2012).

Band / Volume 285

**Spektrale aktinische Flussdichten und Photolysefrequenzen -
Untersuchungen in der atmosphärischen Grenzschicht und der freien
Troposphäre**

I. M. Lohse (2015), VI, 111, VII-XXIII pp

ISBN: 978-3-95806-086-9

Band / Volume 286

**Neue Charakterisierungsmethoden für die Gasdiffusionslage in PEM-
Brennstoffzellen vor dem Hintergrund produktionsprozessbedingter
Materialschwankungen**

S. M. Bach (2015), VIII, 149 pp

ISBN: 978-3-95806-088-3

Band / Volume 287

**Using the anisotropy of electrical properties for the characterization
of sedimentological structures and preferential flow processes**

S. Al-Hazaimay (2015), xxii, 94 pp

ISBN: 978-3-95806-090-6

Band / Volume 288

**Aktivitätsuntersuchungen und Methoden zur Regeneration von
Katalysatoren für die autotherme Reformierung von Dieselmotoren**

K. Löhken (2015), II, 147 pp

ISBN: 978-3-95806-093-7

Band / Volume 289

**Large-Scale Three Dimensional Modelling
of a Direct Methanol Fuel Cell Stack**

J. W. McIntyre (2015), 138 pp

ISBN: 978-3-95806-094-4

Band / Volume 290

**Abscheidung von Wärmedämmschichtsystemen mit dem Plasma Spray-
Physical Vapor Deposition- (PS-PVD-) Prozess – Untersuchung des
Prozesses und der hergestellten Schichten**

S. Rezanka (2015), XII, 204 pp

ISBN: 978-3-95806-095-1

Band / Volume 291

**Characterization & Modification of Copper and Iron Oxide Nanoparticles
for Application as Absorber Material in Silicon based Thin Film Solar Cells**

M. R. Nuys (2015), XII, 123 pp

ISBN: 978-3-95806-096-8

Band / Volume 292

Interpretation of L-band brightness temperatures of differently tilled bare soil plots

M. Dimitrov (2015), XIV, 116 pp

ISBN: 978-3-95806-098-2

Band / Volume 293

Atrazine in the environment 20 years after its ban: long-term monitoring of a shallow aquifer (in western Germany) and soil residue analysis

D. S. Vonberg (2015), 149 pp

ISBN: 978-3-95806-099-9

Band / Volume 294

Yttria-Stabilized Zirconia / Gadolinium Zirconate Double-Layer Plasma-Sprayed Thermal Barrier Coating Systems (TBCs)

E. Bakan (2015), viii, 131 pp

ISBN: 978-3-95806-100-2

Band / Volume 295

Hydration and dehydration at the tropical tropopause

C. Schiller (2015), 72 pp

ISBN: 978-3-95806-101-9

Band / Volume 296

Influence of Impurities on the Fuel Retention in Fusion Reactors

M. Reinhart (2015), 140 pp

ISBN: 978-3-95806-105-7

Band / Volume 297

The role of abiotic processes in the formation and degradation of gaseous nitrogen compounds in the soil

J. Heil (2015), XIV, 106 pp

ISBN: 978-3-95806-106-4

Band / Volume 298

12th Carolus Magnus Summer School on Plasma and Fusion Energy Physics

edited by Kristel Crombé (2015), 468 pp

ISBN: 978-3-95806-107-1

Weitere *Schriften des Verlags im Forschungszentrum Jülich* unter
<http://wwwzb1.fz-juelich.de/verlagextern1/index.asp>

**Energie & Umwelt /
Energy & Environment
Band / Volume 298
ISBN 978-3-95806-107-1**

